U.PORTO
FEUP FACULDADE DE ENGENHARIA
UNIVERSIDADE DO PORTO

Structural Mechanics of Thin-Ply Laminated Composites

Albertino Arteiro

Thesis submitted to the Faculty of Engineering of the University of Porto – FEUP
in partial fulfillment of the requirements for the degree of
Doctor in Mechanical Engineering

Supervisors
Prof. Dr. Pedro Manuel Ponces Rodrigues de Castro Camanho
Dr. Giuseppe Catalanotti

Programa Doutoral em Engenharia Mecânica (PRODEM)
Departamento de Engenharia Mecânica (DEMec)
Faculdade de Engenharia (FEUP)
Universidade do Porto (UP)

"I roamed the countryside searching for answers to things I did not understand. Why shells existed on the tops of mountains along with the imprints of coral and plants and seaweed usually found in the sea. Why the thunder lasts a longer time than that which causes it, and why immediately on its creation the lightning becomes visible to the eye while thunder requires time to travel. How the various circles of water form around the spot which has been struck by a stone, and why a bird sustains itself in the air. These questions and other strange phenomena engage my thought throughout my life."

Leonardo da Vinci

À Carina
e aos meus pais

Acknowledgements

First of all, I would like to express my gratitude to my supervisors, Prof. Dr. Pedro P. Camanho, for the opportunity to engage in this doctoral programme and for the institutional and endless scientific support, and Dr. Giuseppe Catalanotti, for the valuable discussions and important advice.

I gratefully acknowledge the financial support provided by the Portuguese Government's Fundação para a Ciência e a Tecnologia, under grant SFRH/BD/88593/2012, funded by Programa Operacional Potencial Humano/Fundo Social Europeu (POPH/FSE). The financial support provided by AIRBUS (Hamburg, Germany) under project *2genComp — second generation Composites* is also gratefully acknowledged. In particular, I am thankful to Dr. Peter Linde (AIRBUS, Germany), for all his support, for the useful discussions, and for the continuous interest in this work.

I also acknowledge Dr. Joël Cugnoni and Dr. Robin Amacher (EPFL, Switzerland) and North Thin Ply Technology, LLC group (Penthalaz, Switzerland) for providing the carbon/epoxy laminates used in the hole size effect study and all data required in the analyses, and for the useful discussions. I am also grateful to Chomarat (Le Cheylard, France) and Oxeon AB (Borås, Sweden) for providing, respectively, the non-crimp fabrics and the spread-tow fabrics used in experimental campaigns reported in this thesis, and to VX Aerospace (Leesburg, Virginia USA) and Aldila (Poway, California USA) for manufacturing the material used in the preliminary stages of this work.

I would like to thank Eng. Célia Novo (INEGI, Portugal) for the help provided during production of the composite plates manufactured from Chomarat's non-crimp fabrics and Oxeon AB's spread-tow fabrics, and Eng. Joaquim Fonseca for the help provided during production of the test specimens.

The support and professionalism provided by Dr. José Xavier (UTAD, Portugal) in handling the Digital Image Correlation system employed in the extensive experimental programme carried out during this thesis is also acknowledged, as well as the support and flexibility of Andreia Durães (INEGI, Portugal), Eng. Miguel Figueiredo and Rui Silva (FEUP, Portugal), for providing the necessary means to perform these tests in the labs they are in charge of.

I am also thankful to Emília Soares (FEUP, Portugal) for the help with the preparation of the micrography samples, and to Prof. Dr. Josep Costa (Universitat de Girona, Spain) for providing the X-ray radiographies presented in this thesis.

I would also like to express my gratitude to Prof. Stephen W. Tsai (Stanford University, California USA), for the incredible opportunity to collaborate with him and to join the Department of Aeronautics and Astronautics of Stanford University, and for the experienced advice regarding professional and personal life.

I must also mention those who collaborated with me in the period of this thesis, namely Dr. António R. Melro (Bristol University, UK), Dr. Matthias Vogler (Hannover, Germany), Prof. Dr. José D.D. Melo (Federal University of Rio Grande do Norte, Brazil), and my current and former colleagues Ricardo Pinto, Cláudia Cardoso, Carolina Furtado, Rodrigo Tavares, Mahmoud Hayati and Hélder Mata.

For the interest and encouraging words, I would like to thank Prof. Dr. António T. Marques, Prof. Dr. Paulo M.S.T. de Castro and Prof. Dr. Francisco M.A. Pires (FEUP, Portugal), and Prof. Dr. Albert Turon (Universitat de Girona, Spain).

Last, but not least, I must thank Carina, my parents José Alberto and Maria Virgília, and my family.

Abstract

This thesis presents an experimental and numerical study of the mechanical response of spread-tow thin-ply laminates, which complements the preliminary studies on the unnotched and notched response of this new class of advanced composites.

The design of laminates using thin plies is known for a series of advantages, including superior material uniformity, smoother ply drops, reduced crimp and tow flexure, laminate homogenisation, possibility of using smaller relative fibre orientations, and faster and simpler design, with great potential for better optimised laminates. Thin-ply laminates are therefore highly attractive, being present in the advanced composites market in the form of different reinforcement configurations.

In terms of structural performance, some of the benefits of ply thinness include higher longitudinal compressive strength, higher *in situ* strengths, higher resistance to delamination, higher laminate tensile and compressive strengths, higher low-velocity impact resistance, improved fatigue response, and higher bearing strengths. However, due to the damage suppression capability of thin-ply laminates, notched coupons or structures made of thin plies are prone to early unstable failure across the ligament sections, resulting in lower notched strengths. In addition, the understanding of the effect of ply thickness on the damage tolerance of multidirectional laminates is still limited.

An extensive experimental test campaign on different reinforcement configurations with different areal weights was performed aiming at assessing in greater detail the effect of ply thickness on the structural mechanics of thin-ply composites. In general, notched thin-ply laminates exhibit a brittle type of net-section failure mode, with negligible subcritical damage. As the specimens' size increases, a decrease of the notched strengths is observed, which tend to a notch-sensitive material response. On the other hand, the tensile notched strength of high-grade laminates, which can be considerably lower than the strengths of thin-ply laminates for the smaller coupons, increase with size, approaching their unnotched strengths for sufficiently large coupons.

In general, the effects of using thin plies are not only observed in laminates produced from unidirectional tapes but also in spread-tow textile composites. The ability of thin-ply textile multidirectional laminates to delay or suppress subcritical damage growth results in an improved tensile unnotched strength and in superior compressive and in-plane shear strengths. However, it is also responsible for premature failure of the notched configurations loaded in tension. The effect of using thin-ply textile composites in mechanically fastened joints is not as important as in unidirectional tape laminates.

To study the effect of 0° ply blocking on the blunting mechanisms and notched response of structural thin-ply laminates, an additional test campaign is performed using non-crimp fabrics. Improvements of the notched behaviour are observed when adopting a laminate configuration with blocked 0° plies and spread-tow thin plies along the transverse and off-axis orientations. More importantly, this is achieved without compromising the unnotched tensile and compressive strengths of thin-ply laminates.

To further understand the effects of geometry on the deformation and fracture of ultra-thin spread tows embedded in a multidirectional laminate, computational micro-mechanical analyses are also carried out. The proposed three-dimensional computational micro-mechanics framework is able to accurately represent the micro-mechanical response of ultra-low grades, including the mechanics of transverse cracking onset and propagation in tension and compression, the constraining

effect observed in the laminae embedded in multidirectional laminates, the gradual, slow stress relaxation and progressive transverse cracking observed in very thin plies, the reduction in crack opening displacement of the transverse cracks with ply thinness, the formation of thin necks of matrix material around the regions where interfacial damage is more pronounced, and the *in situ* effect. When comparing the results of the micro-mechanical simulations with the predictions from analytical models available in the literature for the *in situ* effect, similar trends are obtained.

New three-dimensional failure criteria are also presented in this thesis to predict failure in a single unidirectional ply. These failure criteria have an invariant formulation and are based on structural tensors, enabling an elegant coordinate system-free description of anisotropy using isotropic tensor functions. A pragmatic approach to estimate the orientation of the fracture plane for composite laminates under transverse, matrix-dominated failure is proposed. To account for the effect of ply thickness when the laminae are embedded in a multidirectional laminate, appropriate definitions of the *in situ* properties are derived in the framework of the invariant-based failure criterion for transverse failure mechanisms. The failure predictions are in good agreement with the experimental data available in the literature, and with the predictions of computational micro-mechanics.

The proposed failure criteria is then implemented in a Smeared Crack Model to predict ply failure mechanisms in composite laminates. A preliminary verification, based on single-element tests and on simple models with different levels of refinement, shows that the proposed implementation is not only consistent with respect to the proposed damage idealisation and to mesh objectivity, but it can also be seen as a valid tool to predict failure of multidirectional laminates using only properties determined from tests carried out at the lamina level.

Macro-mechanical analysis methods based on analytical tools formulated at the homogenised laminate level are proposed to enhance the predictive capability of the strength and failure of composite structures, and for more reliable and easier design methodologies. The recently proposed Trace theory and Master Ply concept and the concept of Omni Strain Failure Envelopes and the Unit Circle failure criterion are described. These theories show great potential to simplify design allowable generation and to make material screening similar to that of metals, since only 0° coupons need to be tested in tension and compression. Moreover, laminate design becomes substantially simpler.

To predict the notched response of composite laminates, a Finite Fracture Mechanics model is proposed. With this model, more reliable analyses of the notched response of laminated plates with through-penetration damage are obtained without requiring fitting parameters or complex Finite Element Analyses. Furthermore, only independently measured material properties are necessary.

It is important to stress that, using thin plies, the potential for simpler and faster design procedures is enormous, and that all benefits of the superior specific properties of advanced composites can be exploited to further improve the performance of high-end applications. Even though it is recognised that the apparent brittle failure behaviour of thin-ply laminates may be unsuitable for applications with unpredictable loading conditions, laminate design concepts based on combinations of thin-thick plies, pseudo-ductile lay-ups or hybrid configurations, which exhibit higher structural margins, can help widening the range of applications of composite structures.

Resumo

Esta tese apresenta um estudo de caracterização e análise mecânica e estrutural de laminados ultrafinos, complementando assim estudos preliminares baseados em testes experimentais e em métodos de análise da resposta ao entalhe desta nova classe the materiais avançados.

O design the laminados utilizando camadas ultrafinas é reconhecido por uma série de vantagens, incluindo uma boa relação custo-benefício, excelente qualidade e uniformidade do material, transições entre camadas mais suaves, reduzida ondulação dos reforços, possibilidade de utilizar menores orientações relativas entre camadas, e design mais rápido e mais simples, com grande potencial para laminados mais otimizados. Os laminados ultrafinos são, por isso, bastante atrativos, estando já presentes no mercado sob a forma de diferentes tipos de reforços.

Relativamente à resposta estrutural, alguns dos benefícios das camadas ultrafinas incluem maior resistência à compressão longitudinal, resistências *in situ* mais elevadas, maior resistência à delaminagem, laminados mais resistentes à tração e à compressão, maior resistência ao impacto de baixa velocidade, melhor resposta à fadiga e maior resistência ao esmagamento. No entanto, devido à capacidade de supressão de dano destes materiais, a sua resistência ao entalhe é inferior. Para além disso, a compreensão do efeito da espessura da camada na tolerância ao dano é ainda limitada.

Uma longa campanha experimental em diferentes reforços com gramagens distintas é levada a cabo com o objetivo de investigar em detalhe o efeito da espessura da camada na resposta estrutural de laminados ultrafinos. Em geral, os laminados ultrafinos com entalhes, sujeitos a cargas de tração, exibem modos de dano tipicamente frágeis ao longo da secção útil, sendo que a ocorrência de dano subcrítico é desprezável. Com o aumento do tamanho dos provetes ocorre uma redução da resistência, que tende para uma resposta sensível ao entalhe. Por outro lado, a resistência ao entalhe de materiais com camadas de gramagem elevada, que pode ser bastante reduzida no caso dos provetes mais pequenos, aumenta com o tamanho dos provetes, tendendo para a resistência do laminado "intacto" no caso de provetes suficientemente grandes.

Em geral, o efeito de utilizar camadas ultrafinas observa-se não só em laminados produzidos a partir de camadas unidirecionais, mas também a partir de compósitos têxteis. A capacidade dos laminados multidirecionais à base de têxteis ultrafinos em suprimir a ocorrência de dano resulta em resistências à tração superiores no caso de laminados "intactos". As resistências à compressão e ao corte também aumentam. Contudo, esta supressão de dano é também responsável pela rotura prematura dos laminados com entalhe sujeitos a cargas de tração. A utilização de têxteis ultrafinos parece não ter um efeito tão importante na resistência ao esmagamento como no caso dos laminados com reforços unidirecionais.

Para estudar o efeito da espessura da camada a 0° nos mecanismos de dano e na resposta ao entalhe de laminados estruturais ultrafinos, é realizada uma campanha de testes adicionais, utilizando tecidos "não-entrelaçados". Esta campanha mostra que é possível obter uma melhoria notória na resposta ao entalhe quando se combinam camadas a 0° mais espessas com camadas ultrafinas ao longo das orientaçõe transversal e fora do eixo. Mais importante, esta melhoria da resposta ao entalhe é conseguida sem deteriorar as resistências à tração e à compressão do laminado ultrafino.

Análises de micromecânica computacional são utilizadas nesta tese para estudar a resposta mecânica das camadas ultrafinas no interior de laminados multidirecionais. Com o modelo tridimensional proposto é possível representar com exatidão a resposta micromecânica de camadas ultrafinas, incluíndo a iniciação e a propagação de fissuras transversais

em tração e em compressão, o efeito de restrição observado nas camadas transversais no interior de laminados multidirecionais, a relaxação gradual e lenta das tensões e a progressão de fissuras transversais em camadas interiores ultrafinas, a redução da abertura das fissuras transversais com a diminuição da espessura da camada, a formação de pequenos ligamentos de material da matriz através das fissuras transversais nas zonas onde a decoesão fibra-matriz é mais pronunciada, e o efeito *in situ*. Quando comparados com as previsões de modelos analíticos para o efeito *in situ*, os resultados dos modelos de micromecânica computacional apresentam as mesmas tendências.

Um novo conjunto de critérios de rotura é também apresentado nesta tese, com o objetivo de prever a rotura de camadas unidirecionais. Este conjunto de critérios fenomenológicos apresenta uma formulação baseada em invariantes e em tensores estruturais, permitindo uma descrição elegante da anisotropia do material compósito que não depende do sistema de eixos, utilizando funções tensoriais isotrópicas. Uma abordagem pragmática permite estimar a orientação do plano de rotura transversal no caso de dano na matriz. De modo a ter em conta o efeito da espessura da camada no interior de laminados multidirecionais, as definições das propriedades *in situ* são formuladas a partir das relações do critério de rotura transversal baseado em invariantes. Em geral, as previsões dos critérios de rotura estão de acordo com outros modelos tridimensionais, com os dados experimentais disponíveis na literatura e com os resultados obtidos utilizando micromecânica computacional.

Os critérios de rotura propostos são depois implementados num "*modelo de fissuração distribuída*" para simular a rotura e a propagação de dano em materiais compósitos laminados. Uma verificação preliminar baseada em modelos de um só elemento e em modelos simples com malhas de elementos finitos com diferentes níveis de refinamento mostram que a implementação proposta é não só consistente em relação à idealização do modelo de dano proposto e à objetividade numérica da malha de elementos finitos, mas deve também ser vista como uma ferramenta válida para prever a rotura de laminados multidirecionais utilizando como *inputs* apenas propriedades obtidas ao nível da camada.

Finalmente são apresentados métodos de análise macromecânicos baseados em soluções analíticas formuladas ao nível do laminado homogeneizado como forma de melhorar a capacidade de previsão da resistência e modo de rotura de estruturas compósitas, e assim obter metodologias de análise apropriadas dotadas de simplicidade compatível com a análise preliminar e otimização de estruturas em materiais compósitos. Assim, são descritos sucintamente a teoria do *Traço* e o conceito de "*Camada Mestra*" para a previsão da rigidez e as *Omni-Envelopes de Rotura no Espaço de Deformação* e o critério de rotura do *Círculo Unitário* para a previsão da resistência de laminados multidirecionais. Estas teorias apresentam grande potencial para simplificar a obtenção das propriedades admissíveis utilizadas em design, tornando os procedimentos de seleção de materiais nas fases de design preliminar semelhantes aos procedimentos utilizados com os metais, visto que passa a ser apenas necessário proceder ao teste de amostras unidirecionais a 0° em tração e em compressão. Para além disso, o design de laminados torna-se consideravelmente mais simples.

Para prever a resposta ao entalhe de laminados multidirecionais, o modelo de Mecânica da Fratura Finita proposto recentemente é descrito. Com este modelo é possível obter melhores previsões da resposta ao entalhe de placas laminadas com entalhes sem recorrer a parâmetros de calibração ou a modelos de elementos finitos. Para além disso, as propriedades materiais necessárias podem ser obtidas através de testes independentes.

É importante ter em conta que, utilizando laminados ultrafinos, existe enorme potencial para tirar partido de métodos de análise simplificados, e assim beneficiar das propriedades específicas dos compósitos para melhorar a performance das aplicações de ponta que usam estes materiais. Apesar de se reconhecer que a aparente fragilidade dos laminados ultrafinos pode limitar a sua utilização em aplicações com condições de carregamento imprevisíveis, a adoção de conceitos como laminados combinando camadas ultrafinas e camadas mais espessas, de laminados pseudo-dúcteis ou configurações híbridas, que apresentam maior "*acomodamento*" estrutural, poderá expandir o campo de aplicações estruturais dos materiais compósitos.

Contents

List of Figures

List of Figures

List of Tables

Part I

Introduction

Chapter 1

Introduction

When developing new manufacturing technologies and new composite materials, understanding their potential benefits and drawbacks with respect to manufacturing, processing, mechanical properties, design, and cost-effectiveness is extremely important for their successful introduction into new markets and new applications. Due to the increasing use of carbon fibre-reinforced polymers in airframes, when promising new technologies appear, the aeronautical industry tries to follow up their development, aiming to improve the performance of the aero-structures based on these materials. The present research aims to improve the understanding of the structural mechanics of spread-tow thin-ply laminates, in terms of the mechanical and fracture characterisation and analysis of this new class of advanced composites. In the remaining of this chapter, a brief introduction to the increasing importance of composite materials in the design and development of new structures, particularly for the aeronautical industry, is presented. Then, the motivation and the objectives of the present research are introduced, and, finally, the thesis layout and organisation is described.

1.1. Background

As the term indicates, a *composite material* arises from the macroscopic combination of two or more different materials, resulting in a third useful material with superior properties than those of the individual constituent materials acting independently [1, 2]. Typically, composite materials refers to materials having strong fibres — continuous or discontinuous — or particles acting as the reinforcement, surrounded by a weaker matrix material, which distributes the reinforcements, protects them against environmental influences, and transfers the load between them. Particularly, a composite may consist of polymers that have continuous fibres imbedded in them, the so-called *fibre-reinforced polymers* (FRPs). Advanced FRPs are often fabricated in the form of *laminates*, consisting of a number of thin layers, called *laminae* or *plies*, stacked together, each one oriented in a given direction.

But the concept of composite materials is not a human creation of the recent days; in fact, composite materials are very common in nature, existing since the first complex organisms appeared on Earth. Muscular systems and wood, both comprising a combination of fibrous systems surrounded by a matrix material, are typical examples of biological composite materials. The first evidences of man-made composite materials date from the Egyptian era, where straw and mud where burnt together by the Israelites to form tougher bricks for construction, and strips of stems of the papyrus plant were laid up side by side and put on top of each other in perpendicular directions by the Egyptians to manufacture papyrus paper. Later, the Mongols invented the first composite bows using a combination of wood, bone and animal tissues bonded with animal glue, and pressed and wrapped with birch bark, providing the Mongols with a smaller, incredibly manageable, powerful and accurate weapon. Not too far, the Japanese samurai were manufacturing their swords combining a softer steel in the inner core with a hard steel, forged with a U-shape, in the outer region of the blade, providing it with high toughness and high superficial hardness. In the 19^{th} century, steel reinforced concrete appeared, revolutionizing architecture and civil engineering.

Yet, advanced composite materials, as they are known today, gained shape in the 20th century. First, the advent of the glass fibres in the 1930's, and their application in the quickly growing aeronautic industry, in the naval industry, mainly during the world war II, and in the beginning of the space age in the 1950's. Then, the first patent for production of carbon fibres in the 1960's, and later, the introduction of boron and aramid fibres in the late 1960's and early 1970's, respectively.

Nevertheless, high-end composites technology has evolved in the aerospace industry only in the last thirty years, whose rapidly expanding applications in the recent past have provided much optimism for the future of this technologically advanced materials. Filament-wound pressure vessels using glass fibres were the first strength critical application of modern composites. After these, many US Air Force programmes promoted the introduction of aero-structures made of composites. The F-111 horizontal stabilizer was the first flight-worthy composite component. It was followed by the production of composite parts such as stabilizers and rudders for the F-14, F-15 and F-16 military aeroplanes, for example. In the early 1980's, composite materials became part of commercial aeroplanes too, namely in the Boeing 767, the Antonov 124 and the Airbus A310-300. Nowadays, nearly all aeroplanes use composites extensively [3], having been now introduced in primary structure components in the most recent long range aeroplanes such as the centre wing box, the fuselage or the wings [4, 5]. And there is still great potential for further application, not only in the aeroplanes' main structures, but also in their engines, namely in the fans and outer casings.

Besides the aeronautical industry, application of advanced FRPs is gradually increasing in a wide spectrum of industrial components and customers, gradually evolving from secondary, non-critical applications to (lightweight) primary load-bearing structural applications; this is the case of the automotive industry [6–8], motivated, for example, by the weight-increase induced by the new advanced powertrain systems for hybrid and electric vehicles. One reason for this wider application of FRPs is because components made of composite materials can be engineered to offer outstanding mechanical (stiffness and strength), fatigue, ballistic, thermal, corrosion, and electro-magnetic properties, typically with reduced weight. Such characteristics promote/improve the use of renewable energy and generally result in a far more sustainable lifestyle. This is becoming even more apparent as the significance of life cycle assessment is being recognised. Another reason is due to all existing processing techniques. Composites give designers and engineers tremendous freedom in terms of both form and function. Compound curves and complex geometries can be readily incorporated, maximizing structural integrity and performance. Furthermore, composites also favour the development of integrated design when a part or component is suitable to be manufactured in "*one shot*", avoiding laborious joining and fitting operations.

1.2. Motivation

1.2.1. New technological developments

Knowledge of the constituent material properties is important when defining a composite structure for a given application and in understanding how that structure will respond to the various stimuli likely to be imposed on it. When new composites arise, resulting from the development of new manufacturing technologies, understanding their potential benefits and drawbacks with respect to manufacturing, processing, material properties, design, and cost-effectiveness is extremely important for their successful introduction into new markets and applications.

The use of carbon fibre-reinforced polymers (CFRP) in airframes increased drastically in the last few years. However, to ensure safe operation, currently large safety margins are used in the design of composite structures when compared with alternative materials. This is due to the lack of knowledge and predictive capability of the mechanical response and of the complex failure behaviour of composite materials, limiting full exploitation of their benefits. This is also due to the high susceptibility of CFRPs to subcritical damage mechanisms, which degrade their mechanical performance without showing any external evidence of damage. Accordingly, when promising new composite technologies appear, the aeronautical industry tries to follow up their development, aiming to improve the performance of the aero-structures [9].

Owing to overcome the inherent brittleness and difficult recyclability of thermoset matrices, which compose most of the advanced FRPs currently used in structural applications, fibre-reinforced thermoplastics (FRTPs) have been receiving

growing interest from the industry. The advantages of FRTPs over traditional FRPs include higher strain to failure, higher fracture toughness and damage tolerance, longer shelf life, and ability to reshape and reuse/recycle. However, due to a reduced performance/cost ratio and manufacturing difficulties (thermoplastic matrices have very high viscosities at processing temperatures, which may result in a large void content due to inadequate impregnation), their application in structural parts is still very limited.

One possible method to toughen FRPs, which is becoming increasingly popular nowadays, particularly in airframe construction, is "*interleaving*". This technology refers to the sandwiching of thin layers of resin "interleaves" between the plies of a laminate, employing two different resins in the composite system: the matrix resin in the *prepreg* sheets and the interleaf resin that provides interlaminar toughening [10]. Alternatively, the interlaminar fracture toughness of laminates can also be enhanced by "*particulate toughening*", through selective hybridisation of thermoset and thermoplastic resins [10]. This second approach is achieved by dispersing a particulate thermoplastic polymer into the thermoset base resin, selectively localised onto the surface of the *prepreg*. A heterogeneous interlaminar resin layer is formed taking advantage of thermoset's good processability and thermoplastic's high fracture toughness. Both approaches are known to provide great improvements of the interlaminar fracture toughness, either in mode I or mode II, and high compressive strength after impact due to damage growth suppression [10, 11].

An alternative technique used to restrict interlaminar damage growth, and consequently to improve the impact resistance and post-impact residual strength of laminated polymer composites, at the same time it aids fabrication, consists in inserting transverse reinforcing threads by *stitching* [12, 13]. Even though applications of this concept to provide through-the-thickness reinforcement of composite structures already exist for some decades [14], recent efforts have been put on the development and application of this technology, namely on the aerospace and aeronautical industries. However, it has not only been observed that the efficiency of stitching is greatly dependent on the nature and extent of the fracture modes occurring on the base composite material, as it has also been recognised that the insertion of the through-the-thickness reinforcement inevitably perturbs the internal configuration of the laminate, introducing, for instance, fibre breakage, layer waviness and resin-rich regions near the reinforcing yarns, which act as stress concentration sites and induce additional damage modes in the material. The compressive strength, for example, is particularly vulnerable to the introduction of the stitching yarns [12, 13].

Another promising design approach is related to the concept of *variable-stiffness laminates*. While in industry FRPs are usually designed using a constant fibre orientation in each ply (typically 0°, 90° and ±45°), variable-stiffness laminates imply that fibre paths are not necessarily straight, but can be continuously curved, resulting in variable in-plane fibre orientations [15–17]. Hence, the stiffness properties at every point of the laminate can be varied independently, introducing additional freedom in locally tailoring the properties of the composite panel and increasing the design space [15, 18].

The curvilinear fibre paths of variable-stiffness laminates can be manufactured using *automated fibre placement*[1] [16–18], whose introduction in the production of aero-structures made possible the current application of high performance composite laminates in large components for aeroplanes (e.g. fuselage barrels and main wing boxes). Nevertheless, application of this technique in the industry has been limited to the production of conventional, constant fibre orientation laminae [17].

The production of variable-stiffness laminates is characterised by manufacturing constraints imposed (i) by the maximum amount of steering that is possible with a fibre placement machine (to avoid wrinkling at the inner side of the steering tow) [18, 19], and (ii) by the minimum cut length (defined by the distance between the cutting mechanism and the clamps or rollers that hold the tows within the fibre placement machine) [18, 19]. Nevertheless, they can be beneficial and practical for structural applications [16, 19], having already proven enhanced dynamic properties, through increased optimal fundamental frequency [15, 18], and better buckling response (up to a factor of two or higher) [18, 19, 21, 22].

[1] Automated fibre placement is an automated manufacturing process that consists of laying up a laminate by deposition of composite tows on a tool (mandrel or mould) using a robot and a computerised head that feeds, guides and cuts the individual tows. This process is able to locally vary the thickness and curvature within each ply with great precision, even on complex shapes [17–19]; besides, a benefic relationship has been observed between the stress distribution and the repeatable levels of inhomogeneity typical of this production technique, which are larger than those found in traditional tape laminates, promoting split cracking and resulting in a lower notch sensitivity of tow-placed laminates [20].

1.2. Motivation

The beneficial structural performance of variable-stiffness laminates is the result of stress redistribution inside the laminate caused by the varying in-plane stiffness [16], conducting to non-uniform stress states and principal load paths redirection [19]. However, due to in-plane fibre angle variation, variable-stiffness panels typically exhibit gaps, resulting in small resin rich areas, and/or overlaps between adjacent courses, conducting to ply thickness variations, which affect the structural response, manufacturing time and/or surface quality of the final products [16, 17, 21, 22].

Regarding tentative improvements of the intralaminar damage resistance of laminated composites, a technology often seen as promising is *hybridisation*. Hybrid laminates are composite laminates comprising a combination of different reinforcing materials. Different types of hybridisation include (i) laminae of two or more composite material systems combined in a ply-by-ply hybrid structure (i.e. inter-ply hybrid) [23, 24] (ii) combination of metal-foils and polymer-based plies (i.e. Fibre Metal Laminates (FMLs)), (iii) materials with tows of more than one fibre type combined in a repeating pattern within each individual ply (often manufactured using automated fibre placement) [20, 25] or as hybrid weaves (with different materials in the warp and weft [14]), forming intra-ply hybrid structures, or (iv) a combination of two or more different types of fibres, such as carbon and fibreglass, carbon and aramid, or different grades of carbon fibres, into an intermingled structure (tows, tapes, fabrics and other forms) [25, 26]. Generally, hybrid laminates are either available in the market (e.g. FMLs), or they can be easily obtained from commercially available raw materials [23, 25, 26].

Hybrid laminates are known to offer higher toughness and lower notch sensitivity (i.e. lower reduction in residual strength with increasing notch size) than conventional carbon laminates [25]. Moreover, hybridisation can be used to tailor laminate stiffness and circumvent catastrophic failure in composites [27]. For instance, laminae combining low-elongation stiff fibres, such as carbon fibres, which provide initial stiffness and a warning before failure, with high-elongation fibres, which provide a stable failure at high strains, arresting crack propagation and providing further load-bearing capacity, show higher strains to failure than pure carbon laminae [27], a material behaviour described as pseudo-ductile [23, 26]. Nevertheless, this is achieved reducing the stiffness and increasing the amount of subcritical damage mechanisms such as matrix splitting and delamination in the laminate [25].

In terms of out-of-plane response, when subjected to impact and post-impact compression loads, hybrid laminates exhibit less visual damage on both top and bottom faces, smaller projected delamination areas, and better relative residual compressive strength (related to the compressive strength of non-impacted specimens); these results can be improved placing the stiffer laminae in the outer plies of the laminate [24]. Hybrid laminates can, therefore, be designed to meet a good balance between in-plane and out-of-plane properties, weight, and material cost, not achieved by the extreme cases defined, for example, by the expensive, stiff carbon fibre-, or by the heavy, damage tolerant glass fibre-based laminates [24].

However, composite materials that use more than one type of fibre are far more difficult to shred and recycle than composites made with a single fibre type (after shredding and matrix digestion, the mix of fibres that results is difficult to reuse) [25]. In addition, developing or applying analysis methods for prediction of the mechanical behaviour of hybrid laminates is not straightforward, particularly because additional material characterisation, not always easily available, is required, such as the interlaminar fracture toughness between two different adjacent materials in inter-ply hybrid laminates [24].

More recently, other concepts have arisen to create a pseudo-ductile behaviour on traditionally brittle composites, providing them with a significantly nonlinear response. One of these concepts exploits unidirectional (UD) composites with aligned discontinuous carbon fibres [28] or overlapped discontinuities at the ply level [29]. Hybrid configurations combining aligned discontinuous carbon fibres with continuous fibreglass were also suggested [30].

Due to progressive interlaminar damage, promoted by the pre-existing discontinuities in the laminate, a significantly nonlinear response can be obtained under tensile loading, as long as the aspect ratio is sufficiently high to support load transfer [28, 29]. UD composites with aligned discontinuous fibres or overlapped discontinuities are able to retain similar stiffness (around 90%) of the baseline continuous composite, but only approximately 40% of the tensile strength. Nonetheless, this pseudo-ductile behaviour may be of great interest for certain applications, in which loading conditions are not fully predictable [29], with further improvements foreseen as the introduction of thicker and tougher interfaces (for

instance through interleaving) has the potential to increase the strain-to-failure of these materials [29]. Moreover, discontinuous fibre reinforced composites can be advantageous in manufacturing structural parts with complex geometries due to their superior formability [28]. However, a loss of the high strength-to-weight ratio that characterises advanced composite materials has to be tolerated, and the best compromise between strength, pseudo-ductility and formability needs to be evaluated from application to application through appropriate material tailoring.

1.2.2. Spread-tow thin-ply technology

In spite of the improved specific properties of composite laminates and the new technological developments described in section 1.2.1, their heterogeneity at the meso-scale still poses some limitations regarding their mechanical performance. These limitations include the weak interfaces between plies, the low resistance to high thermal loads due to the mismatch of mechanical properties, and the residual stresses due to the difference in the coefficients of thermal expansion (both between plies of different orientation and between the fibres and matrix).

It has been claimed [31] that these limitations can be overcome through the introduction of new materials, such as functionally graded materials, whose material properties, even though heterogeneous, vary continuously from surface to surface, avoiding interface problems. Despite their high potential, their application in structural mechanics is still scarce, and laminated composites are still the most viable, improved solution for high performance structures. Besides, the limitations previously enumerated can be diminished, or even suppressed, using a recent technology, already available commercially and of great interest: the *spread-tow thin-ply technology* [32, 33].

This technique is able to continuously and stably open fibre tows, and produce flat and straight plies with dry ply thicknesses as low as 0.02 mm, considerably below the standard for CFRP low grade tapes. The potential benefits of such ultra-thin plies are considerable. On one hand, the use of thinner plies allows the production of thinner and lighter laminates and structures. On the other hand, per given laminate thickness, more plies can be accommodated (particularly interesting for thin laminates), increasing the design space and leading to a possibility of using smaller relative fibre angles between adjacent plies. This is beneficial when it comes to interfacial fracture between plies [34]. Also, by reducing the ply thickness in a multidirectional laminate, the *in situ* effect, characterised by an increase in transverse strength of a lamina constrained between two plies with a different fibre orientation, gains additional importance. Matrix cracking and delamination can, therefore, be suppressed [35–39] without the use of special resins and/or through-the-thickness reinforcements, providing high strength, enhancing fatigue life, and improving resistance to leakage events. In terms of design and manufacturing, the spread-tow plies exhibit improved fibre orientation and distribution, potentially leading to fewer weak zones. There is also a huge potential for improved textile and non-crimp fabric reinforcements, whose handling and lay-up procedures, even over complex shapes, are much easier [40]; thinner fibre tows can result in lower crimp angles and in a reduced impact of the stitching yarns.

However, most studies in the literature addressing the effect of ply thinness on the mechanical response of laminated composites were limited to a minimum ply thickness of 0.125 mm. Studies assessing the mechanics of thin-ply laminates only appeared in recent years, and most of them are preliminary. Furthermore, the effect of ply thinness and the use of thin plies in different reinforcement configurations, such as woven or non-crimp fabrics, as well as the comprehensive assessment of the damage mechanisms involved in the failure of thin-ply laminates and the applicable analysis tools, were not studied in detail in an industrial context.

1.3. Objectives

The present research aims to improve the understanding of the structural mechanics of spread-tow thin-ply laminates, in terms of the mechanical and fracture characterisation and analysis of this new class of advanced composites, namely by complementing previous preliminary experimental and analysis studies on the notched response of spread-tow thin-ply laminates. A thorough experimental test campaign comparing laminates produced from the same material system with different areal weights and reinforcement configurations will be presented. Different spread-tow reinforcements combined into laminates based on the same baseline from the aeronautic industry will be studied. This will enable the detailed understanding of some of the advantages and potential weaknesses of thin-ply configurations.

In addition, numerical and analytical analyses at different length-scales need to be conducted to improve the understanding of the applicability of current and innovative analysis methods to predict the mechanical behaviour and structural response of thin-ply laminates. To understand the effect of ply thickness on the meso-mechanical behaviour of composite laminae, detailed computational micro-mechanical analyses are proposed. Models at the meso-scale, formulated at the ply level, will be introduced as innovative numerical tools to model the detailed failure sequence of laminates in general, and thin-ply composites in particular. Finally, macro-mechanical analysis methods based on analytical tools formulated at the homogenised laminate level will be used to enhance the predictive capability of the strength and failure of composite structures, and for more reliable and easier design methodologies. Focus will be placed on attempts to identify and explore potential benefits of this new type of advanced composite materials in a systematic manner.

1.4. Thesis layout

In part II, the state-of-the-art of the spread-tow thin-ply technology is presented, with some remarks on manufacturing and design with thin-ply laminates and a description of some of the commercially available spread-tow reinforcements. The description of the state-of-the-art is followed by a comprehensive literature review, where the microstructural effect of ply thinness on the mechanical response of UD laminae, the effect of ply thickness scaling on the mechanical response of composite laminates and current applications of thin plies are discussed.

In part III, the experimental test campaign carried out in the scope of this thesis is presented. In chapter 3, the hole size effect on laminated composites incorporating spread-tow thin plies is studied. Open-hole and centre-notched tension tests are performed on laminates with the same nominal thickness produced from unidirectional *prepregs* of the same material system but with different ply thicknesses. In chapter 4, an experimental test campaign is carried out to study the structural response of aerospace-grade plain weave spread-tow fabrics of different grades, including a detailed assessment of the structural response of laminates based on a baseline of the aeronautical industry. Special focus is placed on the effect of tow thickness on the structural response of textile composites. In chapter 5, the effect of 0° ply blocking on the blunting mechanisms and notched response of a structural laminate based on a baseline of the aeronautical industry is investigated, with the aim to improve the notched response of structural thin-ply laminates. Due to the intrinsic design advantages, thin-ply non-crimp fabric layers were employed.

Part IV presents different numerical and analytical modelling strategies of ply damage mechanisms at different length-scales. In chapter 6, a three-dimensional computational micro-mechanics framework is used to study the mechanical response of ultra-thin spread tows embedded in a multidirectional laminate and assess the effect of ply thickness on the mechanical response of laminated composites (i.e. the *in situ* effect). The results of the micro-mechanical model are then compared with the predictions from analytical models for the *in situ* effect, with the aim of validating both modelling strategies. In addition, a truthful insight into the mechanics of thin-ply laminates is sought using the proposed micro-mechanical model, including a better understanding of their damage mechanics and of the mechanisms that preclude both microcracking and delamination. In chapter 7, new three-dimensional failure criteria for fibre-reinforced composite materials are presented, based on structural tensors that represent the material symmetries of the respective anisotropy class as an intrinsic material property, enabling an elegant coordinate system-free description of anisotropy using isotropic tensor functions. In addition, a pragmatic approach is proposed to estimate the orientation of the fracture plane for composite laminates under transverse, matrix-dominated failure. To account for the effect of ply thickness when the laminae are embedded in a multidirectional laminate, appropriate definitions of the *in situ* properties are derived in the framework of the invariant-based failure criterion for transverse failure mechanisms. Finally, the proposed failure criteria are validated using several case studies available in the literature based on experimental testing and on a strategy employing computational micro-mechanics. In chapter 8, this new set of failure criteria is implemented in a Smeared Crack Model.

In part V, macro-mechanical analysis models for laminate failure prediction are introduced. Chapter 9 presents an overview of the recently proposed Trace theory and Master Ply concept, which employ an invariant-based approach to stiffness, with great potential to simplify design allowable generation. Then, an introduction to the concept of Omni Strain Failure Envelopes and to the Unit Circle failure criterion is presented. These concepts introduce a new invariant-based approach to strength that greatly simplifies the macro-mechanical failure analysis of homogenised laminates. Using the

invariant-based approaches to stiffness and strength, a simple sizing method that is able to account for weight and lay-up time savings is described, making lay-up and material screening for a given application much easier. In chapter 10, analysis methods based on simple solutions formulated at the homogenised laminate level are used to predict the notched response of composite laminates. Because traditional analysis methods are not able to capture the bridging processes that occur in the presence of large through-the-thickness cracks, a recently proposed Finite Fracture Mechanics model is reformulated to take into account the crack resistance curve of the material. With the proposed model, the notched response of laminated plates with large through-penetration damage can be obtained using only independently measured material properties and without requiring fitting parameters or complex Finite Element Analyses.

Finally, part VI presents the conclusions of the work carried out in this thesis, and enumerates the topics that should be subject of future analysis and further development towards the understanding of the structural mechanics of thin-ply laminated composites.

Part II

State-of-the-art and literature review

Chapter 2

State-of-the-art and literature review

In the domain of commercial aeroplanes, advanced laminated composites, namely carbon fibre-reinforced polymers, have seen an increasing use in the airframe and other aeronautical structures. In order to satisfy the increasing demand of carbon laminates, and fibre-reinforced polymers in general, new technologies are being developed. One of this technologies — the *spread-tow thin-ply technology* — is able to produce composites in which the laminate consists of particularly thin plies. These laminates, hereafter referred to as *thin-ply laminates*, comprise several potential advantages. This chapter aims to describe the current state-of-the-art and recent developments regarding this new technology, including remarks on manufacturing and design with thin-ply laminates and a description of some of the commercially available spread-tow reinforcements. In addition, a comprehensive literature review is presented, where the microstructural effect of ply thinness on the mechanical response of UD laminae, the effect of ply thickness scaling on the mechanical response of composite laminates and current applications of thin plies are discussed. This chapter will be important in defining the main benefits and potential drawbacks of thin-ply laminates, in understanding how thin plies can be used to facilitate the design process and improve the structural performance of composite structures, and in providing new perspectives for improvements and innovative applications of spread-tow fibre reinforcements.

2.1. Introduction

The use of composite materials in structural applications has significantly increased during the last few years. This is mainly because composites have properties which are very different from conventional isotropic engineering materials. For example, composite materials may exhibit superior specific properties (strength-to-weight and stiffness-to-weight ratios), fatigue resistance, corrosion resistance, and thermal stability, making them well suited for structures in which the weight is a fundamental variable in the design process. In addition, composite materials are also well suited for damage tolerant design by the proper selection of fibre reinforcement patterns at damage critical regions, achieving better stress redistribution and load paths redirection. Also, structural components requiring high stiffness and strength, impact resistance, complex shape and high volume production are suitable candidates to be manufactured using composite materials.

An example of continuously increasing application of composite materials is the commercial aeronautical industry. Advanced laminated composites, namely carbon fibre-reinforced polymers (CFRPs), have seen an increasing use in structural applications in the airframe and other aeronautical structures. When compared to other materials, CFRP-based aero-structures offer (i) weight saving, which leads to fuel saving, increase in payload, and/or increase in range, improving performance, (ii) good fatigue resistance, which leads to enhanced life and savings in the long-term cost of the component, and (iii) good corrosion resistance, which means fewer requirements for inspection, resulting in savings on maintenance cost [2]. However, because laminated composites are heterogeneous materials, their damage behaviour is quite different from that of commonly used materials (metals, for instance), generally more complicated, and dependent

on several factors, such as the properties of the constituent materials, the fibre orientation, the stacking sequence, or the nature of loading, to mention just a few.

Typical damage mechanisms include the matrix-dominated transverse cracking (or microcracking) and delamination, and fibre breakage, either brittle fracture or pull-out failure in tension or shear-driven fracture or fibre kinking in compression. Usually, matrix-dominated damage mechanisms occur first. Transverse cracking through the thickness of the ply typically occurs as the first-ply failure (FPF) mode, followed by delamination, induced by the transverse cracks or starting at the free edges. Fibre-breakage only happens at the last failure stage, most times in a catastrophic manner. However, laminated composites can totally lose their structural integrity only due to matrix-dominated damage (both microcracking and delamination), without any fibre breakage.

To satisfy the increasing demand of carbon composites, and fibre-reinforced polymers (FRPs) in general, new technologies are being developed to improve the performance of CFRP-based composite structures. One of this technologies — the *spread-tow thin-ply technology* [32, 33] — is able to continuously and stably open thick fibre tows, such as 12k filament tows or higher, and cost-effectively produce flat and straight plies with dry ply weights of less than 100 g/m^2, which can be as low as 20 g/m^2, without damaging the filament fibres.

2.2. Tow spreading concept and state-of-the-art

2.2.1. Spread-tow thin-ply technology

There have been a few efforts in the past to reduce the ply thickness below the conventional 0.125 mm. However, they typically required costly and slow processes, likely to damage the fibres during processing, like filament cutting and fluffing caused by the strong external forces in which these techniques relied [38]. The tow spreading technology [32, 33, 41–43], developed by the Industrial Technology Centre in Fukui Prefecture, Fukui-city, Japan, avoided these limitations, being able to cost-effectively produce flat and straight plies with dry ply thicknesses as low as 0.02 mm, without damaging the filament fibres.

However, early references to a pneumatic tow spreader date to the middle 1970's. Daniels [44, 45] patented an apparatus for pneumatically spreading thin carbon filaments from a tow bundle using what was called a "*Venturi spreader*". In the beginning of the 1990's, Marchello and co-workers [46–49], at NASA's Langley Research Centre, used a pneumatic spreading device, with a configuration different from the one developed by the Industrial Technology Centre in Fukui Prefecture, to develop dry powder *towpreg* processes for production of both thermoplastic and thermosetting composites. In the middle 1990's, Kim and Gray Jr. [50] also patented a pneumatic spreading technique based on the Venturi effect used for producing carbon fibre tapes suitable for use in the production of metal matrix composites by physical vapour deposition [50, 51].

But the tow spreading technique as it is known today was firstly proposed by Kawabe et al. [32], consisting of a roll part for a preliminary opening, and a pneumatic part for the main opening, which is key in the effectiveness and success of the process. This technique was successfully applied by Kawabe and co-workers [32, 33] to carbon and glass fibre tows, who reported that a much more widely opened tow could be obtained by this combined method, as compared to any of the singular processes. More recently [52], Harmoni Industry Co., Ltd., from Fukui-city, obtained a patent for manufacturing the tow spreading machines based on this pneumatic process.

Figure 2.1 shows a schematic of the pneumatic tow spreading technique. Following a pragmatic description of Sihn et al. [53], when air flows around both sides of the tow, the difference in the velocity of the airflow, near and away from the tow, results in a pressure difference at these locations. This pressure difference creates an aerodynamic force that helps the filament fibres to lose the tension momentarily (leftmost drawing in figure 2.1). As the tow spreading begins, air flows between the filaments, helping the tow to spread more and faster (middle and rightmost drawings). The wider the tow is spread, the thinner the tow thickness becomes. Reductions of the areal weight (i.e. weight per unit area) of conventional 12k tows by approximately 500% have already been reported [54]. Moreover, tow spreading machines can also be used in tow hybridisation procedures [26].

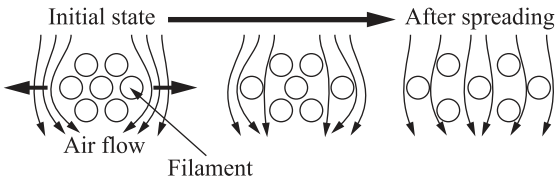

Fig. 2.1. Schematic front view of the tow spreading process with a pneumatic method (after Sihn et al. [53]).

2.2.2. Remarks on manufacturing and design with thin-ply laminates

Thin-ply laminates show some clear advantages in terms of manufacturing that arise directly from the tow spreading process. For example, tow spreading has the potential to use heavy tow yarns, such as 100k or 200k, to cost-effectively obtain wider or smaller tows (e.g. 12k), which may help to reduce the production costs of ultra-thin plies. In addition, the improved surface appearance due to the unique uniformity of the tow spreading may help reducing part production costs in terms of surface finishing and painting. This unique uniformity of the tow spreading also results in an improved fibre orientation and distribution, as well as a better dispersion and uniformity of the plies, potentially conducting to laminates with fewer weak zones, such as voids or resin rich areas.

Because of the plies thinness, ply drops in thin-ply composite structures are much smoother, since each drop can be much smaller, decreasing stress concentrations and improving their structural performance. On the other hand, when used in woven fabrics, ultra-thin plies reduce the crimp angle, and consequently tow flexure, improving the mechanical properties of this kind of reinforcements.

At first, it might appear that part production using thin-ply laminates will result in a clear disadvantage: per laminate thickness, more plies will have to be accommodated, which may result in an increased processing effort, as high as the number of plies (or the thinness of the plies) to be incorporated. But this may only happen if the same manufacturing and design concepts used today with conventional laminates are applied to thin-ply laminates. In other words, the effective use of thin-ply laminates relies on a substantially different approach to composites manufacturing and design, which must take advantage of the unique properties of laminated structures.

For example, for the same laminate thickness, more plies can be accommodated as repeated sublaminates, and laminate homogenisation is possible for the laminate thicknesses currently used in advanced structural design, making mid-plane symmetry irrelevant due to negligible thermal warpage [3, 55]. This enables a simpler lay-up process, since reversing the stacking sequence at the mid-plane is no longer needed. Continuous stacking becomes possible, and processing time, cost, waste and stacking errors can be reduced. Besides, by avoiding the symmetry rule, the laminate design space widens and optimisation for out-of-plane loading and damage tolerance, where non-symmetric laminates may perform better, is made easier [56]. For example, in the design of stringers for aero-structures, whose criteria is governed by warpage, optimisation may rely only on topological optimisation, as with thin-ply laminates warpage is null. Moreover, as the ply thickness decreases, the potential for overall laminate thickness reduction on compression buckling- and damage tolerance-driven laminate design increases [57].

On the other hand, because the layers are more finely dispersed, thin-ply laminates are stronger and tougher. Due to an improved *in situ* effect (section 2.4.1), the strength properties of the composite are optimised and matrix cracking is restricted, bringing FPF closer to ultimate laminate failure, and suppressing the delaminations that originate at the tips of transverse cracks. This laminae fine dispersion also results in lower interlaminar stresses, restricting delamination at the free edges. In addition, having more plies per laminate thickness also leads to the possibility of using smaller relative fibre orientations between adjacent plies, which further improves delamination resistance [34].

Homogenisation and the absence of subcritical damage mechanisms such as matrix cracking and delamination before final failure makes design much faster and simpler. Instead of conducting complex ply-by-ply progressive failure analysis to determine ply failures (the number of plies can be substantially higher than in conventional laminates), the equivalent stiffness and strength of a laminate can be calculated directly using very simple analysis tools, such as classical laminated

plate theory (a successful application of this modelling strategy can be found in Ref. [58]), and closed-form and rapid solutions can be used in the design of composite structures without relying on high safety factors.

The use of equivalent properties rather than the ply-by-ply approach also has advantages in computational analysis (such as the finite element method). By taking the homogenised laminate instead of simulating each ply individually, the overall CPU time and memory needed for simulations can be significantly shorten, especially when the number of layers in the laminate is large. Moreover, the suppression of subcritical damage mechanisms allows simpler models to be used in the numerical strength prediction of thin-ply laminates, avoiding highly nonlinear numerical models such as cohesive damage models or complex continuum damage mechanics models. If such simpler, but reliable, analysis methodologies, particularly interesting when the design procedures involve optimisation, are added to the intrinsic superior strength and increased design space of thin-ply laminates (the number of plies and, consequently, the discrete laminate thickness domain increase with ply thinness, even for already thin laminates), better optimised laminates and higher consistency in defining safety factors can be readily obtained, resulting in weight savings and, consequently, in cost reduction. Therefore, if designed with the appropriate tools, production of composite structures based on thin-ply laminates can be very competitive.

Optimisation of thin-ply laminates may also rely on the concept of anisotropy of unbalanced laminates, to take advantage of bend-twist coupling, for example. Because homogenisation is made possible by the use of ultra-thin plies, so that an asymmetric lay-up will not warp, thin-ply laminates can be engineered to behave similarly to a homogeneous anisotropic material. And this can be done using sublaminates with as few as two different fibre orientations (e.g. $[+\alpha/-\beta]_{nT}$). On one hand, anisotropic, bi-angle laminates, for example, are easier to homogenise than laminates with three- or four-angle sublaminates, and thinner homogeneous laminates can be obtained. On the other hand, bi-angle laminates are less prone to subcritical damage, such as microcracking, than conventional four-angle laminates, attributed to the increased compatibility between both plies, resulting in higher strength; this compatibility between adjacent plies and, consequently, the FPF strength increase as the difference between the off-axis angles decrease. Hence, thin-ply anisotropic laminates can be designed to reduce the gap between FPF and last-ply failure (LPF) in such a way that microcracking can be completely avoided before final failure.

Anisotropic, unbalanced laminates that have shear coupling, i.e. its stretching and distortion are coupled, unlike quasi-isotropic laminates, exhibit both types of deformation when subjected to bending or twisting loading. Therefore, the material and ply orientations can be selected so the resulting stretching and distortion can work against or for each other for the benefit of laminate performance, something not available when traditional balanced building blocks are used [59, 60]. Instead of avoiding coupling, it is possible to reduce weight simply by using anisotropy, which is unique in composite materials [60]. This feature has been long recognised for its potential for controlling or designing the deformation counter-effects on each of the loading types, usually referred to as *passive aeroelastic tailoring* [59]. In addition, laminate sizing and optimisation becomes simpler, since the off-axis ply angles are better continuous variables than the discrete ply count of conventional *black aluminium* with the ten-percent rule.

2.2.3. Spread-tow thin-ply reinforcements

As already mentioned, the spread-tow thin-ply technology is commercially available, and different companies worldwide are already producing ultra-thin unidirectional (UD) carbon tapes. An example is the North Thin Ply Technology, LLC group (Penthalaz-Cossonay, Switzerland), a joint venture of the US company North Technology Group and the Swiss company Createx.

North Thin Ply Technology, LLC is able to produce thin-ply structures with a ply weight of 30 g/m^2, but they can go as low as 15 g/m^2. They manufacture dry or pre-impregnated thin-ply UD tapes, or use automated tape laying to make customised pre-assembled stacks of plies off-the-mould for easy and fast handling. These solutions allow companies currently manufacturing advanced carbon fibre-reinforced composite structures based on UD *prepregs* to readily adopt thin-ply laminates in their design scheme, without huge efforts in terms of adaptation to new manufacturing processes and/or design concepts. In addition, the automated tape laying technology allows these companies to save extra processing efforts when it comes to stacking all plies together, due to the ability of pre-selecting specific thin-ply sublaminates in

accordance with the manufacturing requirements, which can be integrated afterwards in the component or structure being manufactured, followed by the curing process.

But the thinner and wider tows obtained with tow spreading show unique benefits that open a broad range of new possibilities in terms of design and manufacturing of composite structures. These include not only ultra-thin UD tapes, but most importantly new, innovative kinds of carbon fibre reinforcements.

Fabric reinforcements, for instance, show great potential for application in primary structures for aerospace and aeronautic applications [61], as well as for crash-relevant structural parts for the automotive industry [7, 62]. Crimp configurations of fibre yarns have been introduced as a first attempt to develop appropriate substitutes to traditional UD laminates that meet the growing demand of enhanced out-of-plane properties, higher impact and delamination resistance[1] [63], low manufacturing costs, and easier lay-up[2], handling and storage[3]. With the advent of the spread-tow ultra-thin plies, new fabric configurations have emerged, with promising advantages.

For example, Oxeon AB (Borås, Sweden), besides ultra-thin UD tapes with areal weights from 21 g/m^2 and ply thicknesses as low as 0.02 mm, is also producing spread-tow fabrics (STFs), trademarked TeXtreme®. Instead of yarns, Oxeon AB uses spread tapes in the weaving process, which can be incorporated in individually adjustable angular orientations $[+\alpha/-\beta]$. These novel concepts conduct not only to better structural performance, but also to a much larger design space, circumventing some of the limitations of conventional fabrics that would not allow their use in composite primary structures.

With thin-ply fabrics, fibre bundles are not only thinner, but they are also wider (20 mm to 50 mm), resulting in a flatter fabric, with fewer interlacing points and better surface finish than conventional ones. Such fabric configurations are also characterised by minimal fibre waviness, and therefore lower crimp frequency and smaller crimp angles, even for simple woven structures such as plain weaves (2.5° compared to 45° crimp angles in conventional fabrics) [54, 64], allowing the filaments to immediately carry tensile or compressive loads without first having to straighten.

Due to the thinner and wider spread tows, the amount of matrix between the tows of thin-ply fabrics is very small, resulting in overall composite fibre volume fractions very close to the local fibre volume fraction of the spread tows [66, 67]. As a result, the performance of thin-ply fabrics approaches that of laminates made of UD tapes; compared to conventional fabrics, considerable weight reductions can be obtained. On the other hand, they are considerably more drapable than UD reinforcements, allowing their use in components manufactured by liquid moulding techniques. STFs are also less susceptible to out-of-plane damage and delamination, making them ideal for applications where damage tolerance is the design driving factor.

In alternative to weave textiles, non-crimp fabric (NCF) systems have been developed and proposed as reliable reinforcements able to provide enhancements in the out-of-plane and impact performance. In spite of requiring expensive machinery, its mass production results in low manufacturing costs. NCFs consist of UD plies with oriented fibre tows stitched or knitted together through the thickness with a non-structural binding yarn [40, 68]; therefore, unlike woven

[1] Due to the nonplanar interlaminar structure of woven fabrics, delamination cracks interact with matrix regions and the weave structure during its propagation, experiencing substantial growth resistance, which increases with increasing weave index and changes with crack propagation direction (higher for propagation along the weft yarns than along the fill yarns) [63].

[2] Shamsudin and York [64], for instance, suggest that laminate tailoring using woven fabrics is suitable for added functionality and weight reduction through the introduction of mechanical interactions between the in-plane and out-of-plane deformations (also discussed for general laminate configurations in section 2.2.2). For example, textile architectures with square symmetry (e.g. plain weave, 2×2 twill weave, or 4×4 twill weave, etc.) are known not to show thermal distortion due to their balanced nature, which means that the laminates constructed of these materials possess a "*hygro-thermally curvature-stable*" or "*warp-free*" condition, not exhibiting thermal distortion independently of the individual ply orientations used or the laminate stacking sequence definition [64]. This can be advantageous from a design point of view because mechanical coupling can be obtained without incurring on thermal warpage, thanks to the meso-structure of square symmetric reinforcements.

[3] Even though textile composites are inferior in terms of in-plane mechanical properties (both stiffness and strength), they offer a lower cost production alternative for composite structures; since they are manufactured as dry fibre preforms, which hold together without any polymer thread or matrix, they can be shipped, stored, draped (within limits that depend on the type of fabric) and moulded with relative ease, making them particularly suitable for liquid moulding techniques [14]. Besides, textiles can be advantageous for applications requiring high strain to failure, high fracture toughness (e.g. Ref. [65]), low notch sensitivity, and high damage resistance and tolerance [14].

fabrics, crimp or waviness are typically negligible. On the other hand, NCFs are generally thicker, but more flexible than UD tapes, and the storage, lay-up and draping costs with respect to the manufacturing of final parts can be reasonably lower. For instance, since NCFs are pre-plied in multiple directions, automated, continuous lay-up is possible, with no gaps during part fabrication and without having to consider the splice locations in the production process of composite stiffeners[4] [69].

Unlike UD tapes, NCFs not only ensure the highest quality standards in *prepregging*, but also in liquid moulding techniques [40], since the fine stitching provides the necessary rigidity to the fibre bundles, avoiding their displacement during handling of the dry reinforcement and during resin injection. In addition, this fine stitching can significantly enhance damage resistance and tolerance, as well as the through-the-thickness strength. Even though stitching may cause filament damage, it generally does not generate dangerous failure modes in the same extent as crimp textile reinforcements. When compared to UD tapes, a slight reduction of the in-plane elastic and strength properties caused by the yarns and associated resin-rich areas is observed [40, 68, 70, 71], especially in compression [68].

With the introduction of thin-ply NCFs, new approaches to composites design become possible. An example is the concept of bi-angle NCFs introduced by Chomarat (Le Cheylard, France), which uses a multiaxial machine with an off-line spreading process of the starting tows to mass-produce bi-angle NCFs with low areal weights and low off-axis angles (below 30°). In this process, the desired off-axis ply is pre-plied and tied to the 0° ply. When the ultra-thin plies are stitched together to form an NCF, fibre dispersion in each ply is as uniform as a conventional *prepreg*. In fact, due to the high quality of the NCFs produced by tow spreading, the effect of stitching is lower, either under quasi-static [72] or fatigue loading [73].

The bi-angle configuration of these NCFs is also advantageous, making them particularly suitable for continuous, one- or two-axis asymmetric stacking of (anisotropic) composite laminates, which can be many times faster than the standard four-axis lay-up of UD plies. As discussed previously (section 2.2.2), the adoption of an anisotropic design can be extremely interesting when combined bending and twisting loads and deformations are present, without additional efforts in terms of processing if bi-angle NCFs with shallow off-axis angles are used with continuous one- or two-axis lay-up.

2.3. Microstructural effect on the mechanical response of UD laminae

The unique uniformity of the tow spreading has motivated the study of the effect of ply thinness on the mechanical response of the UD lamina. Amacher et al. [36, 37, 58] performed an extensive experimental characterisation of the mechanical response of thin-ply laminates, from tests at the lamina level (UD properties) to tests at the laminate and structural levels (e.g. open-hole fatigue, bearing tests and impact). Carbon fibre-epoxy composites with ply areal weights ranging from 30 g/m^2 to 300 g/m^2 were produced from the same batch of fibres and matrix and tested. At the lamina level, the results have shown no significant influence of the ply thinness on the elastic and strength properties of the UD lamina, except for longitudinal compression. In this case, the UD specimens with the thinner plies have clearly shown higher compressive strength (approximately 20% on average). This enhanced compressive strength was attributed to the more uniform microstructure of spread-tow thin plies. Optical micrographs presented by Amacher et al. [36, 37, 58] showed that the microstructure of the laminate made of thicker plies was fairly inhomogeneous (figure 2.2a), with varying fibre volume fraction along its microstructure (in the range of 42% to 64%) due to fibre rearrangement and resin flow during the low-viscosity phase of the curing cycle. This heterogeneous microstructure is responsible for earlier micro-instabilities of the fibres that conduct to premature compressive failure of the laminate [36, 37, 58]. As the ply thickness decreased (figures 2.2b and c), a better uniformity of the microstructure was achieved, becoming practically homogeneous for the lowest grades.

The better uniformity of spread-tow laminae has also potential consequences on the interlaminar fracture toughness of thin-ply laminates. As it is well known, the interlaminar fracture, or delamination, of UD composites is characterised

[4] In the typical fabrication process of composite stiffeners using UD tapes, the location of the splice, where the pieces meet side-by-side, must be controlled such that they do not align in the thickness direction.

(a) High-grade UD lamina (300 g/m^2). (b) Low-grade UD lamina (100 g/m^2). (c) Spread-tow UD lamina (30 g/m^2).

Fig. 2.2. Optical micrographs of carbon fibre-epoxy composites of different grades (after Amacher et al. [37]).

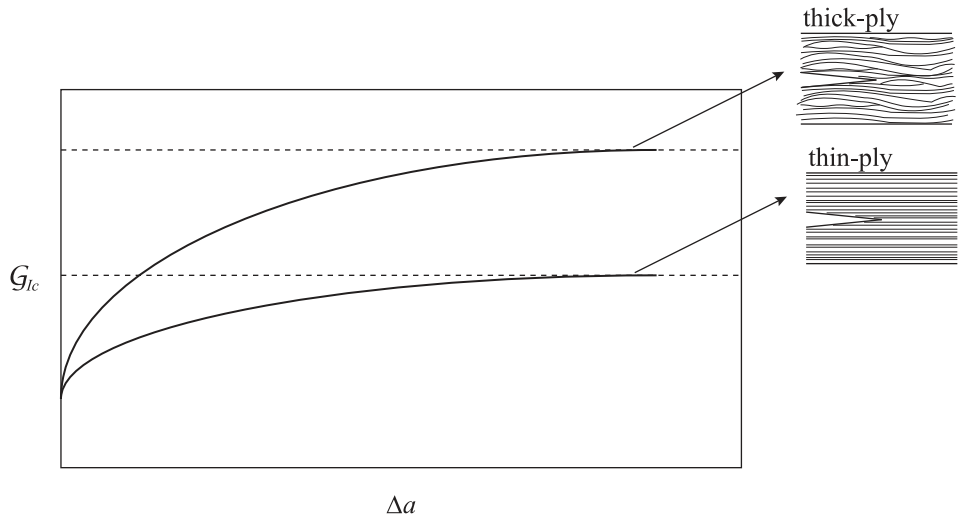

Fig. 2.3. Schematic showing the potential effect of the uniformity of spread-tow laminae on the crack resistance curve associated with interlaminar fracture of UD composites.

by a crack resistance curve (or $\mathcal{R}$-curve) [74–77], i.e. an apparent increase of the fracture toughness with crack extension. This can be attributed to bridging phenomena involved in the separation process after interlaminar fracture initiation, particularly fibre bridging, which induces tractions acting at high displacements and extending into the crack wake [76, 77]. The extremely uniform microstructure of ultra-thin plies means that the potential for large-scale fibre bridging in UD composites is reduced when compared to more heterogeneous grades — schematic on figure 2.3. Consequently, a flatter $\mathcal{R}$-curve, characterised by a lower steady-state value of the fracture toughness, can be expected for crack propagation parallel to the fibres.

2.4. Effect of ply thickness scaling on the mechanical response of composite laminates

As discussed in section 2.2.2, thin plies have intrinsic advantages in terms of the mechanical response of composite laminates. For instance, higher delamination resistance due to lower interlaminar stresses and higher *in situ* strengths are two clear benefits that may conduct to an improved mechanical response of thin-ply laminates when compared to conventional ones. However, the effect of these benefits must be properly quantified, and other potential advantages must be identified in a systematic manner by means of detailed experimental programmes, complemented by analytical models and numerical, finite element (FE)-based analysis, which should be carried out to improve understanding and prediction of the mechanical behaviour of thin-ply laminates.

2.4. Effect of ply thickness scaling on the mechanical response of composite laminates

In the past years, the effect of ply thickness on the mechanical response of composite laminates was mostly based on studies addressing the effect of ply thickness scaling. Although this approach does not give a definitive answer regarding the mechanical response of today's thin-ply laminates (most of these studies were restricted to a minimum nominal ply thickness of 0.125 mm, considerably above the 0.03 mm commercially available today), it gives very interesting clues about the consequences of using ultra-thin plies in laminated composites.

The fracture process of high performance composite laminates is quite complex, involving *intralaminar* (e.g. matrix transverse cracking, brittle fibre fracture, fibre-matrix shearing and fibre kinking) and *interlaminar* (delamination) damage mechanisms, whose individual effects and interactions must be understood. However, only a few studies in the literature regard exhaustively the effect of ply thickness scaling on each of these failure modes. A review concerning the effect of ply thickness scaling on the mechanical response and structural integrity of composite laminates, including *in situ* effects, delamination resistance, size effects, intralaminar fracture toughness, impact resistance and damage tolerance, fatigue and bearing strength, is presented in the next sections.

2.4.1. Matrix cracking and *in situ* effect

When embedded in a multidirectional laminate, the laminae whose fibre orientation is perpendicular to the loading direction develops matrix cracks that induce the deterioration of the mechanical performance of the laminate, prompt other damage modes (e.g. delamination), and creates pathways for chemicals and other substances (critical for applications such as chemical tanks and pressure vessels) [78]. These matrix cracks typically occur at strains lower than the failure strain of the entire laminate [35, 38]. Either under static or fatigue loading, damage onset is generally the result of the nucleation, propagation and multiplication of transverse cracks [79].

As suggested in the literature, the actual strengths of the transverse plies are not only higher than those measured in UD coupons, but they reportedly increase with decreasing ply thickness [35, 38, 80–85]. The crack density in embedded transverse plies is also known to increase with decreasing ply thickness [35, 80, 84–89]. This is caused by the constraining effect imposed by the neighbouring plies, which reduces the available elastic energy within the transverse ply, delaying damage propagation in the matrix [38, 58, 82, 90].

Several experimental studies in the literature show that the transverse tensile strength (Y_T) and the in-plane shear strength (S_L) of a ply are function of ply thickness [91–97] and fibre orientation (or stiffness) of the adjacent plies [94, 95]. On the other hand, analysis methods show that they are also a function of the ply's position in the laminate [81]. This is a deterministic size effect that occurs at the meso-scale, known as the *in situ* effect. Therefore, the ply strengths cannot be treated as intrinsic lamina properties [94, 95], but as *in situ* properties that depend on material and geometrical factors.

Typically, the *in situ* properties are taken into account by using fracture mechanics models that predict the relation between the ply thickness, its fracture toughness and the *in situ* strengths [81, 98], whose accurate determination is necessary for implementation of physically based failure criteria for prediction of transverse damage mechanisms in multidirectional laminates [81, 99–108]. In fact, it has been shown that using as ply properties those measured directly from UD plies to predict the strength of multidirectional laminates, regardless of ply orientation or laminate thickness, results in very conservative predictions that can differ substantially from the experimental results [83, 95, 102, 109].

It is noted that, in the case of in-plane shear, linear elastic fracture mechanics (LEFM) alone is not able to accurately predict the *in situ* strength. In this case, the nonlinear shear response typically observed in laminated composites must be included in the prediction models [81].

It is also interesting to note that the response of glass-fibre and carbon-fibre reinforced composites to matrix cracking is generally different [87]. In the case of glass-fibre reinforced cross-ply laminates, after the initial cracks occur, a sharp increase in crack density is observed as the applied load is increased. However, the average crack density then tends to a limiting value which depends on the transverse ply thickness: the thinner the transverse ply, the higher the crack density at saturation. For carbon-fibre reinforced composites, crack density typically does not reach a saturation value, since fracture of the 0° plies, which have lower strain-to-failure, interrupts further development of transverse cracking [87].

Nevertheless, as observed for the glass-fibre reinforced laminates, the crack density measured as the applied load increases is higher for the case of thinner carbon transverse plies.

Another important difference between glass-fibre and carbon-fibre reinforced composites is related to the stiffness reduction. Whereas glass-fibre reinforced laminates are characterised by a high stiffness reduction due to matrix cracking, in carbon-fibre composites it is typically low.

2.4.1.1. Transverse tension

In the late 1970s, tensile tests in different glass fibre-reinforced polymer cross-ply laminates with constant fibre volume fraction, constant longitudinal (0°)-ply thickness and different transverse (90°)-ply thicknesses were performed by Bailey and co-authors [91–93]. It was observed that, as the thickness of the 90° plies is reduced, transverse cracking changes from multiple occurrences to slow crack growth, small edge cracks and, finally, complete crack suppression, evidencing cracking constraint in the 90° plies (figure 2.4).

Flaggs and Kural [94] showed that the transverse stress at onset of transverse cracking in the 90° laminae of $[\pm\theta/90_n]_S$ carbon/epoxy laminates is a function not only of the 90° laminae thickness, but also a function of the orientation of the adjacent $\pm\theta$ laminae (figure 2.5). Similar results for the influence of ply thickness on the transverse strength of carbon/epoxy laminates were obtained later by Boniface et al. [96] for distinct resin systems, viz. a single phase and a toughened resin.

Herakovich [110], in a study about the effect of ply thickness on the mechanical response of angle-ply laminates, has shown that the ultimate stress, the strain to failure and the toughness (measured as the area under the experimentally obtained stress-strain curves) of angle-ply laminates is higher when plies of the same orientation are dispersed through the laminate instead of blocked together. He observed that failure of all blocked-ply laminates was due to matrix cracking across the width of each angle ply, and due to delamination at the plus/minus interfaces, with no fibre failure.

Conversely, failure in the dispersed-ply angle-ply laminates with small off-axis angles was characterised by a single crack across the width of the specimen, parallel to the fibre direction of the outer layer [110]. The plies with the same fibre orientation of the outer plies exhibited matrix-dominated failure, while fibre-dominated failure was observed at the remaining plies. Delamination was almost absent.

The results presented by Herakovich [110] not only showed the effect of ply thickness on the ply's transverse strength (only matrix-dominated failure was observed on the blocked-ply laminates), but also demonstrated the effect of ply position in the laminate. Matrix cracks starting from the outer plies (which have lower *in situ* strengths) defined the plane of failure in the dispersed-ply laminates with small off-axis angles.

Dvorak and Laws [98] compared the predictions of an analytical model for the *in situ* strengths, based on LEFM, with experiments on T300/934 carbon/epoxy. They showed that the *in situ* transverse tensile strength decreases with

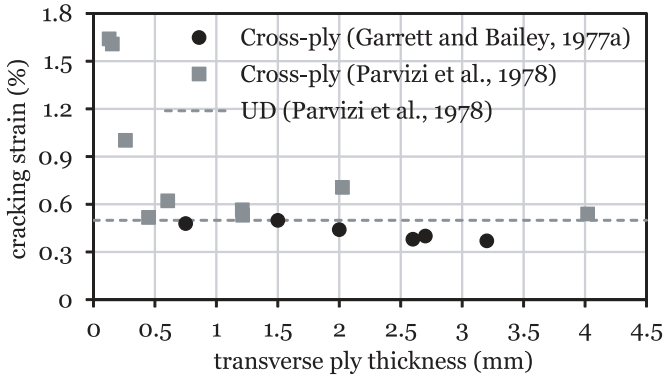

Fig. 2.4. Cracking strain of different glass fibre-reinforced polymer cross-ply laminates (after Refs. [91, 92]).

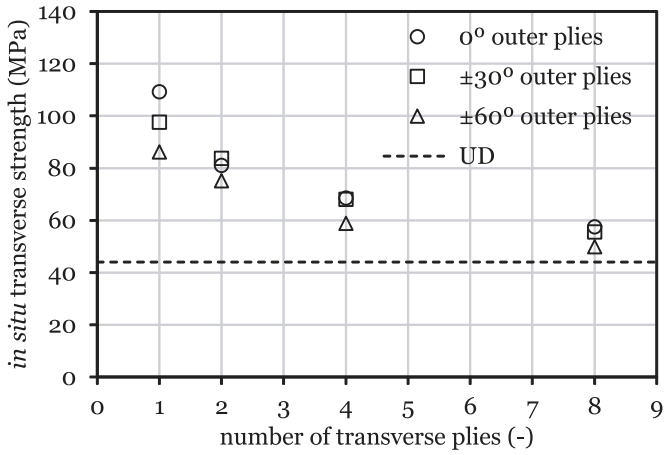

Fig. 2.5. *In situ* effect on the transverse tensile strength of an embedded ply (after Flaggs and Kural [94]).

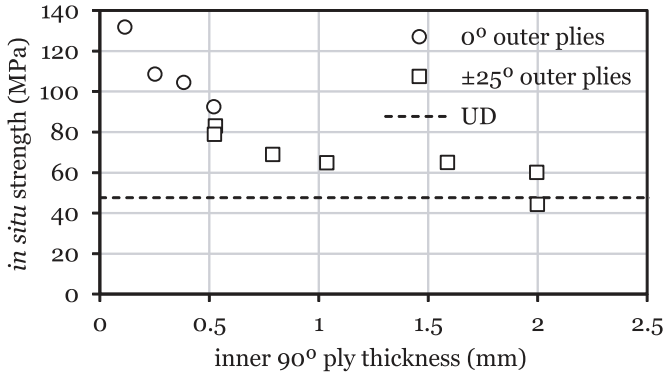

Fig. 2.6. *In situ* transverse tensile strength of an inner 90° ply (after Dvorak and Laws [98]).

increasing inner 90° ply thickness (figure 2.6), and that fracture mechanics models are able to accurately predict the *in situ* effect.

Chang et al. [101], conducted a parametric study using a progressive damage model formulated taking into account the *in situ* effect. A substantial reduction in the maximum failure load of open-hole angle-ply and cross-ply laminates under tensile loading due to ply clustering in the laminates was predicted. The extent of damage was more extensive in the laminates with ply clustering. Adolfsson and Gudmundson [90] performed an experimental investigation concerning matrix cracking in different stacking sequences, including cross-ply laminates with blocks of 1 to 8 transverse plies, among others. A severe degradation of the elastic properties with increasing transverse ply thickness were observed on cross-ply laminates. In addition, Lavoie et al. [111] reported that stress concentrations on longitudinal plies arising from transverse cracking on thicker 90° degree plies may induce premature laminate failure too. Lavoie and Adolfsson [112], based on experiments on carbon-epoxy multidirectional laminates, showed that laminates with thicker ply blocks developed matrix cracks due to thermal residual stress, as opposite to laminates with thinner ply blocks, where no thermally induced matrix cracks could be identified.

In a different approach, Yokozeki et al. [113] investigated the propagation of transverse cracks on the width direction. In particular, they addressed the effect of specimen configuration and transverse ply thickness. According to these authors, quasi-isotropic CFRP laminates with thinner transverse plies are less susceptible to transverse crack initiation or propagation, with edge cracks occurring at higher strain levels than in thicker 90° plies. Nonetheless, the damage process is approximately the same independently of the 90° ply thickness, with the edge crack density growing rapidly after initiation as the applied strain increases. The edge cracks barely propagate in the width direction before saturation of the edge crack density. When saturation occurs, the edge cracks start propagating widthwise and average crack lengths

increase rapidly. Yokozeki et al. [113] observed that the saturation density in quasi-isotropic laminates with thinner 90° plies is higher than in thicker 90° plies, and that the former are less susceptible to propagation of transverse cracks in the width direction. In cross-ply laminates, the edge crack density and widthwise propagation of transverse cracks occurred simultaneously. As observed in the quasi-isotropic laminates, the laminates with thinner 90° plies were less susceptible to the onset and propagation of transverse cracking in the width direction.

Sasayama et al. [114] studied the effect of ply thickness on FPF of multidirectional, quasi-isotropic composite laminates, manufactured using thin plies with a nominal thickness of 0.05 mm. These authors monitored the occurrence of FPF using acoustic emission during tensile tests. They clearly observed an increase in the initial failure stress with decreasing laminae thickness.

Huchette [88], which addressed transverse cracking of carbon/epoxy T700SC/M21 cross-ply laminates with varying mid-90° ply thickness, reported an increasing applied stress at the appearance of the first transverse crack when decreasing ply thickness, resulting from the *in situ* effect. Moreover, the increase in transverse crack density with applied load was much faster as the ply thickness decreased, with a much higher transverse crack density at final laminate failure for the laminates with thinner mid-90° plies. In addition, Huchette [88] performed a numerical study about the effect of the orientation of the plies adjacent to the mid-90° lamina on the variation of the compliance of the laminate due to transverse cracking, showing that a reduction of the stiffness of the adjacent plies promotes transverse cracking; nevertheless, according to his predictions, this influence was not remarkable. Finally, Huchette [88] showed the influence of the position of the 0° plies on transverse cracking of off-axis plies in quasi-isotropic laminates tested under tension, demonstrating the constraining effect imposed by the stiffer plies. Both thicker off-axis plies and off-axis plies adjacent to each other had shown earlier transverse cracking than thinner off-axis plies constrained by 0° laminae.

Yokozeki et al. [78] also performed a study addressing the effect of ply thickness and intersecting angle (defined by the authors as the relative orientation between adjacent plies) on crack formation of multidirectional laminates. Their results showed that thinner plies and smaller intersecting angles restrict matrix crack propagation in oriented plies adjacent to cracked 90° plies, in spite of increasing the density of matrix microcracking.

Sihn et al. [53] performed uniaxial tensile static tests on both unnotched and open-hole specimens to study the effect of ply thickness on FPF and transverse microcracking. Spread-tow carbon/epoxy quasi-isotropic specimens, with two different lay-ups, were tested. The laminates were manufactured using thin plies with a thickness of 0.04 mm. One laminate was scaled at the sublaminate level (no ply blocking), and the other at the ply level (with blocks of five thin plies). The laminates' nominal thickness was the same. The results obtained indicated suppression and/or delay of microcracking and splitting damage in the thin-ply laminated composites, with and without the open-hole. From the analysis of X-ray photos and acoustic emission counts, it was clear that, with thinner plies, FPF is delayed nearly up to the ultimate failure stress, either with or without the presence of a stress concentration.

Pierron et al. [115, 116] also investigated the effect of ply thickness on the initial damage process, testing glass/epoxy quasi-isotropic laminates with a centrally located open-hole subjected to tensile loading. Two lay-ups with the same thickness were compared, one comprising ply-level scaling (thick ply blocks), another comprising sublaminate-level scaling (single ply blocks). Full-field optical measurements based in the grid method were used to conduct such investigation. Much lower loads at first surface cracking were reported for laminates with thick ply blocks.

O'Higgins et al. [117] carried out an experimental study to determine the effect of ply thickness on the open-hole tensile characteristics of carbon and S2-glass fibre-reinforced polymer cross-ply laminates. Blocked-ply and dispersed-ply stacking sequences were analysed. In both stacking sequences, damage in the CFRP cross-ply laminates was characterised by axial splits in the 0° plies, accompanied by matrix cracks in the 90° plies; in addition, areas of triangular delamination were evident along the length of the axial splits in both stacking sequences. However, the damage zones in the blocked sequences were much more extensive, with much easier growth of split cracks in the 0° plies. Dispersed-ply laminates tended to arrest growth of the split cracks. Similar trends were observed for the S2-glass fibre-reinforced polymer cross-ply laminates, except for the extent of matrix cracking, which was much reduced due to the less brittle nature of the matrix material used by O'Higgins et al. [117] in their experiments.

2.4. Effect of ply thickness scaling on the mechanical response of composite laminates

Takagi et al. [118] and Ogihara and Nakatani [119] studied the effect of ply thickness on the damage resistance of angle-ply CFRPs. These authors have shown that angle-ply laminates with 0.05 mm thick plies exhibit higher strength and higher strain to failure than angle-ply laminates of similar stacking sequence with 0.60 mm thick ply blocks. Through numerical analysis, it was shown that thin-ply angle-ply laminates have an intrinsic superior resistance to matrix-dominated damage mechanisms.

Takeuchi and co-authors [35, 120] experimentally evaluated transverse cracking constraining on thin-ply carbon/epoxy cross-ply laminates. The thickness of the inner 90° layer varied between 0.040 mm (single ultra-thin ply) and 0.160 mm (block of four ultra-thin plies). A much lower crack-opening displacement (COD) was observed for the thin 90° ply when compared to blocks of two and four plies. This was clearly a constraining effect caused the stiff 0° plies adjacent to the inner 90° ply. For the thickest transverse laminae, the matrix crack extension, which occurred suddenly through the lamina thickness, led to stress relaxation, whereas, for the thinner transverse laminae, matrix cracking extended gradually, eventually without penetrating completely through the thickness, making stress relaxation much more difficult. The higher stress field maintained in the thinner transverse laminae caused, therefore, new matrix cracks to occur, increasing the crack density. A crack suppression effect was shown to exist, supposedly caused by a decrease in the Energy Release Rate (ERR) at the crack tip as the ply thickness decreases.

In a complementary study, Saito et al. [38] numerically investigated matrix cracking restriction in the inner transverse ply in a thin-ply laminate, and the effect of the stiffness of the adjacent plies, in order to clarify the mechanisms of transverse damage suppression in thin-ply laminates. A two-dimensional micro-mechanical model, simulating a representative volume element (RVE) of an embedded ply subjected to transverse tensile loading, where fibres and matrix were discretely represented, was used.

Saito et al. [38] used a bilinear elastic-plastic constitutive model to represent the mechanical behaviour of the matrix. Failure was assumed to occur when the tensile or shear strains in the matrix reached their critical values, and the moduli of failed matrix was reduced to 10% of the original moduli. A "*weak interfacial strength*" was assumed between matrix and fibres, modelled using cohesive elements in the interfaces. The fibres distribution in the RVE of the 90° ply was modelled mimicking the *in situ* observations on the actual specimens tested by Saito et al. [35]. The widths of the RVEs were defined using the experimentally observed crack density information, such that the area modelled along the length direction contained only one transverse crack. Standard boundary conditions were applied to the RVE. An initial thermal step was performed to account for the residual stresses of the curing process in the RVE. According to Saito et al. [38], the numerical results were consistent with previous experiments [35], with drastic penetration of the transverse cracks for thicker 90° plies. Changing the orientation of the outer plies adjacent to the inner 90° layer from 0° to 45°, faster matrix crack propagation was observed, confirming the effect of the stiffness of adjacent plies on the constraining imposed to the 90° laminae [94].

Based on numerical predictions and experimental results on T700SC/M21 cross-ply laminates, Laurin et al. [89] demonstrated that the stress applied at the onset of transverse cracking increases substantially with decreasing transverse ply thickness and that, at failure, crack density is higher in the cross-ply laminates with thinner mid-90° plies, similarly to what was observed by Huchette [88].

Erçin et al. [121], while studying size effects on the tensile failure of open-hole composite laminates, measured the FPF loads, associated with the *in situ* strengths, of two laminates, with and without blocked 90° plies at the surface. In-house scripts that postprocess the data from full-field measurements of the displacements in the surface 90° plies, obtained with digital image correlation (DIC), were used. It was observed that the laminate with thicker (blocks of two) outer 90° plies had a FPF load 10% lower than the laminate with a single outer 90° ply in each surface, clearly evidencing the *in situ* effect. Also, as a consequence, the in-plane transverse tensile and shear strengths of the first laminate were lower than those of the second.

Arteiro et al. [122], in a study addressing the notched response of quasi-isotropic NCF thin-ply laminates, have shown that the tensile unnotched strength increases when the maximum ply thickness in a laminate is kept to the minimum. This improved plain strength was attributed by the authors to the higher *in situ* strengths in the laminate.

Amacher et al. [36, 37, 58] identified, by acoustic emission monitoring, the stress at the onset of damage (FPF) in tensile unnotched specimens of quasi-isotropic laminates of different grades, including 30 g/m^2 ultra-thin plies. The same carbon/epoxy material system was used in all laminates, which had the same thickness. A large increase (of about 230%) has been reported for the stress at the onset of damage when decreasing the grade of the UD plies from 300 g/m^2 to the ultra-thin 30 g/m^2. In order to clarify the nature of this size effect, Amacher et al. [36, 37, 58] also tested thick-ply laminates produced from blocks of ten 30 g/m^2 ultra-thin plies and from individual 300 g/m^2 plies. No substantial difference was found between these two laminates, demonstrating that the observed size effect was not related to changes in intrinsic ply properties, but to a deterministic *in situ* effect.

For intermediate ply thicknesses, a linear trend was reported by Amacher et al. [58]. Additionally, it was observed that, for the laminates with the thinnest plies, the onset of damage occurred at a stress just 3% lower than the ultimate stress, and nearly no damage was identified before final failure. It is also interesting to note that the ultimate strength of the unnotched specimens increased 39% and 42% when decreasing the grade of the UD plies from 300 g/m^2 to 100 g/m^2 and to 30 g/m^2, respectively. These results were attributed to an increased stability of intralaminar cracking in the transverse and angle plies close to the free edges and to the suppression of damage propagation before fibre fracture in the 0° plies conducted to catastrophic laminate failure.

In the same study, Amacher et al. [36, 37, 58] addressed the notched tensile strength of the same quasi-isotropic laminates. The ultimate notched strength of the thin-ply laminate was considerably lower than that of the thick-ply laminate (about 26%), attributed to the absence of early subcritical damage in the thin-ply laminates, which prevented local stress redistribution at the hole boundaries and led to a brittle type of failure[5]. The onset of damage in the thin-ply laminate occurred at a stress 38% higher than in the thick-ply laminate, very close to the ultimate failure stress. Amacher et al. [36, 37, 58] also reported a clear transition from a progressive, multi-mode failure in the thick-ply laminate to a brittle type of net-section failure mode for the thin-ply laminate, with an intralaminar crack propagating from the notch boundary perpendicularly to the loading direction. This clearly evidenced the damage suppression capability of thinner plies, particularly advantageous in the case of fatigue loading [36, 37, 58] (see also section 2.4.6).

Guillamet et al. [39, 123] studied the onset and progression of transverse matrix cracking in dispersed- and blocked-ply regions of an NCF thin-ply laminate by monitoring the free edges of unnotched specimens. They observed that the region with ply blocking is the critical one in terms of transverse cracking, with considerably lower critical strains. These authors have also shown that transverse cracking is delayed in the dispersed-ply region, occurring very close to laminate failure, or even suppressed, evidencing the *in situ* effect.

Herráez et al. [124], employing a simpler constitutive, bi-dimensional computational micro-mechanical model, have argued that the transverse ply strength corresponding to the initiation and propagation of a transverse crack through the thickness was independent of the ply thickness. These authors also argued that this is in accordance with the thick-ply solution of the *in situ* effect theory [81, 98], since the model they employed could not capture widthwise propagation of the matrix cracks. However, this argument contradicts not only the numerical observations presented elsewhere [38, 84], as it contradicts experimental evidence from Saito et al. [35]. Moreover, it is not clear whether taking the homogenised stress in the transverse ply at the onset of damage growth, as Herráez et al. [124] did, is the best measure of the actual strength of the embedded transverse ply. In fact, after the first crack or strain localisation band as started to propagate, strain relaxation occurs across the transverse ply, and most load is carried out by the adjacent homogenised laminae.

Herráez et al. [124] also argued that transverse cracks propagate from the interface between the inner and outer plies towards the centre of the ply. Even though this is a phenomenon typically seen on oblique cracking [125] (which could be captured by the computational micro-mechanical model presented in chapter 6), transverse crack growth generally starts at the centre of the ply (as small fibre-matrix decohesions) where the constraining effect of the adjacent stiffer plies is minimum, propagating towards the interfaces between plies, as predicted numerically [38, 84], analytically [83], and observed experimentally Saito et al. [35], Huchette [88], París et al. [126].

[5]Further explanations about the effect of subcritical damage suppression on the notched response of composite laminates is given in section 2.4.3.2.

2.4.1.2. In-plane shear

Chang and Chen [95] performed shear tests on carbon/epoxy UD and cross-ply laminates using a rail shear testing fixture. As the ply thickness increased, the shear strength decreased and reached a lower plateau, clearly demonstrating that the ply thickness has a significant effect on the shear strength (similar results were obtained previously by Chang et al. [127] in a simpler experimental programme).

2.4.1.3. Transverse and longitudinal compression and transverse shear

Experimental studies have also shown that a substantial reduction in longitudinal compressive and transverse shear strengths can result from transverse cracking (see Ref. [94] for earlier references). Therefore, the *in situ* properties previously described may also have an important effect on the delay of other matrix-dominated failure mechanisms, including fibre kinking. This can be addressed through the application of 3D phenomenological failure criteria [128, 129]. According to these models, when embedded in a multidirectional laminate, not only the transverse tensile strength and the in-plane shear strength (calculated using the models proposed by Camanho et al. [81]), but also the transverse compressive strength[6] (Y_C) and the transverse shear strength (S_T) are *in situ* properties. In addition, assuming that kink bands[7] are triggered by localised matrix failure in the vicinity of misaligned fibres [128, 129], the *in situ* effect has also a direct, positive influence on the resistance of multidirectional laminates to fibre kinking, therefore affecting the longitudinal compressive behaviour of laminated composites.

Kawabe et al. [133] studied the effect of ply thickness on the compressive properties in multidirectional, quasi-isotropic composite laminates with the same nominal thickness. Ply thicknesses starting from 0.045 mm were addressed. Thick-ply laminates were manufactured blocking plies with the same fibre orientation. A clear *in situ* effect in compression has been reported by these authors.

Yokozeki et al. [134] investigated the ply thickness effect on the damage resistance and tolerance of carbon/epoxy laminates by means of unnotched and open-hole compression testing. Two laminates made of the same material system and with the same in-plane stiffness, total thickness and lay-up ratios (same percentage of plies along each lay-up direction) were manufactured using either conventional (145 g/m^2) or thin-ply (75 g/m^2) UD tapes. Plain strength compression results demonstrated an increase in compressive strength (16%) of the thin-ply laminate, even though the compressive behaviours of the conventional and thin-ply laminates were almost identical. The compressive notched strength of the thin-ply laminate was also slightly higher (9%) than the conventional laminate. This is an evidence of the previously mentioned *in situ* effect in compression.

Erçin et al. [121] has reported a higher compressive unnotched strength for laminates having dispersed plies when compared to partially blocked-ply laminates. These results could be attributed to an *in situ* effect in compression.

Arteiro et al. [122] have also shown a strength improvement in the compressive unnotched strength of quasi-isotropic NCF thin-ply laminates whose maximum ply thickness is kept to the minimum (no ply blocking). Similar conclusions were also obtained when compared to conventional CFRP laminates [135]. This has been attributed to damage restraining inside the laminate, as well as to an improved *in situ* strength in compression.

Amacher et al. [37, 58] studied the effect of ply thickness on the notched response of quasi-isotropic laminates under quasi-static compressive loading. A notched compressive strength improvement of 18% was reported when decreasing the grade of the UD plies from 300 g/m^2 to 30 g/m^2. The same trend was observed for the onset of damage, assessed by acoustic emission monitoring. In the thin-ply laminates, failure occurred in a localised band of lateral fibre kinking, with no evidence of intralaminar cracking or delamination, which were observed in thick-ply laminates. These results were attributed to an intrinsically higher compressive strength of the spread-tow plies [58] (see also section 2.3). However, they also show how the constraining effect on thinner plies delays the occurrence of kink bands, due to the suppression of matrix cracking.

[6] Often referred to as "*wedge fracture*", a matrix-dominated failure mode caused by high transverse compressive stresses in embedded laminae [109].
[7] Crack-like type of failure occurring in laminae subjected to compressive loadings in the fibre direction [130–132].

It should be noted that, while there is no direct experimental evidence of the *in situ* effect for transverse compression, recent test results obtained in structural details indicate that ply thickness affects the compressive strengths. For example, the results presented by Amacher et al. [37, 58] show that the bearing strength (see also section 2.4.7) increases with decreasing ply thickness, which can be justified by the increase of the transverse and longitudinal compressive strengths of thin-ply laminates.

As a final remark, it is also noted that, in the simplest design methodologies, composite laminates are usually designed not to be loaded over a critical load corresponding to the FPF strain, in order to avoid the occurrence of microcracking. But for most conventional laminates, the FPF strain is much lower than the ultimate strain of the laminate, and the advantages of composites regarding their high specific modulus and strength are not fully utilised [136]. If, by reducing the ply thickness, microcracking can be avoided, suppressing the gap between FPF and LPF, thin-ply laminates can be regarded as clearly advantageous in terms of the design process when compared to conventional laminates. For instance, as shown by Amacher et al. [37], simple closed-form solutions, such as the classical laminated plate theory, can be used to predict the strength of thin-ply laminates, with relative errors around 3%, using only the ply properties and without implementing stiffness degradation, as failure ends up being dominated by the ultimate failure strain in the fibres.

2.4.2. Delamination

Structural collapse in a composite structure is caused by the evolution of different types of damage mechanisms, such as matrix transverse cracking and fibre fracture or *delamination*. The extent of these types of damage strongly depend upon geometry, fibre orientation and stacking sequence [137–139].

Delamination is the result of the failure of the thin resin layer existing between two different oriented plies. It is one of the most common types of damage in laminated fibre-reinforced composites due to their relatively weak interlaminar strengths, namely when there is no reinforcement in the thickness direction [10, 105, 137, 140–144]. This failure mechanism is particularly important for the structural integrity of composite structures because, typically, no visual defect is visible on the surface or free edges, making it difficult to detect during visual inspection [104, 137, 143]. The study of the effect of ply thickness on delamination initiation and growth cannot, therefore, be neglected.

Delamination damage is known to happen because of excessive interlaminar normal and shear stresses at the ply boundaries, and may develop during manufacture (due to incomplete curing or introduction of foreign particles), from impact damage, or from the interlaminar stresses that develop at geometric discontinuities, such as free edges, curved sections, sudden changes of cross sections, ply drop-offs, stiffener terminations and flanges, bonded and bolted joints, and access open-holes [105, 140, 142, 145–148]. Furthermore, delaminations may grow under both static and cyclic loading, affected by a number of other factors such as inhomogeneities or residual thermal strains [137, 140, 142–145, 149–151]. Delamination growth redistributes the stresses in the plies of a laminate and may influence residual stiffness, residual strength and fatigue life, generally conducting to a significant loss of structural integrity, including reduction of the bending stiffness and compressive load-carrying capacity caused by local buckling [105, 137, 140–142, 145, 150, 152].

Characterisation of the interlaminar fracture behaviour of composites is generally performed in terms of a critical ERR (or *interlaminar fracture toughness*), associated with delamination onset and growth [140, 149, 153]. However, measurement of the interlaminar fracture toughness involves complex data reduction because it is an energy-based parameter that can be influenced not only by the accuracy of the measured load and displacement, but also by the accuracy of the measured crack length and corresponding change in compliance [153, 154].

Interlaminar fracture parameters are also known to depend (moderately) on the relative orientation between the adjacent plies. This dependency arises from several factors, such as delamination surface morphology, (intralaminar) cracking of the adjacent plies, fibre bridging, etc. [151]. The most conservative interlaminar fracture properties are obtained testing UD FRPs [151], due to favourable surface morphology, resulting in a guiding effect of the reinforcing fibres [151], and due to the absence of transverse cracking in the adjacent plies. However, multidirectional ply interfaces, which are the most common in laminate design, are more prone to delamination. This happens not because they are less resistant to

interlaminar fracture, but because the highest interlaminar stresses in multidirectional laminates occur at the interfaces between plies of different orientation. Still, since delamination testing of UD FRPs is much simpler and much more reliable than testing interlaminar fracture in multidirectional interfaces[8], and due to their conservative character, the use of the properties measured in UD coupons is the preferred method to predict delamination growth, giving the most reliable results [151].

The most common source of interlaminar damage is *free-edge delamination* (FED). It occurs as a result of the high interlaminar stresses that develop at the free edges due to the mismatch in Poisson contraction of the individual plies with different orientations, and due to the fact that fibres are broken at the laminate edges when the specimen is cut (this may happen even for an UD composite) [144, 149, 155]. These edge delaminations typically occur between 90° plies and adjacent angle plies, with delaminations forming initially in a thumbnail shape and rapidly becoming a delaminated strip that grows across the specimen width [149].

Although FED is considered a stable fracture process, besides reducing the laminate modulus as it propagates [149], it can have a major effect not only on the response to out-of-plane loading, but also on in-plane failure of composite laminates [144]. Depending on the thickness of the plies (or ply blocks), the unnotched tensile strength of multidirectional laminates may be controlled by this subcritical failure mechanism, without reaching the stresses expected on the basis of the UD tensile strengths even when single low-grade 0.125 mm thick plies are used in each lamina [144].

Delamination may also be induced by matrix cracks parallel to the fibre direction [148]. *Matrix cracking-induced delamination* (MCID) is caused by the interlaminar stresses that develop at the tips of the matrix cracks, originating local delaminations that form and propagate at the interface between the cracked ply and the neighbouring ply. Both experimental evidence and analysis models have shown that the importance of this phenomenon increases with increasing ply thickness (or ply blocking) and increasing mismatch angles between plies [148, 149]. On one hand, this results from the lower *in situ* strengths of thicker and less constrained plies (due to higher mismatch angles), conducting to earlier ply cracking. On the other hand, higher interlaminar stresses, which occur at the interfaces of thicker plies with higher mismatch angles, promote delamination onset and propagation at those interfaces. Typically, delamination failure of composite laminates occurs as a combination of MCID and FED, which, when occurring at the same interface, may congregate in a single interlaminar crack spanning the whole net section of the composite.

Delamination is one of the most important fatigue damage mechanisms too. This is particularly important because mechanical fatigue, especially high-cycle fatigue, is a common cause of failure, involving several damage mechanisms that result in the degradation of the structure [156–158]. Although polymer matrix composite materials with continuous fibres, in particular carbon fibres, are very effective under high cycle fatigue loading due to the ability of the fibres to transmit and disperse the high-frequency vibration loads, these materials, when subjected to high cycle fatigue, usually experience damage initiation by transverse cracking in the matrix. While not affecting the structural response and the resistance to intralaminar damage propagation, these transverse cracks induce local delaminations, which propagate under fatigue loading, eventually conducting to the total loss of structural integrity of the laminate [159].

Another important precursor of delamination in composite materials is low velocity impact (LVI). In this type of events, local delaminations arise below and around the impact location, which are generally not visible with the naked eye. This type of damage is particularly critical for the compressive strength of the impacted composite laminate [152] (more details will be presented in section 2.4.5).

In the early 1980's, O'Brien [140, 149] conducted analysis programmes to characterise delamination onset and growth in composite laminates. Based on analysis and experimental data, O'Brien [140] showed that delaminations form at a lower nominal applied strain in thicker laminates of identical stacking sequences, scaled by increasing the number of ply repetitions (i.e., by increasing the ply thickness). Similar results have been reported elsewhere [87]. Based on a free-edge

[8]Delamination testing of UD FRPs avoids several problems that clearly invalidate the characterisation of the interlaminar fracture properties in multidirectional interfaces, namely (i) mode mixity in delamination propagation between plies of different orientation, (ii) curing residual stresses, (iii) non-uniformity of the ERR components, (iv) bending-twisting coupling, (v) development of intralaminar damage in the adjacent plies and other dissipation mechanisms, (vi) crack wandering and bifurcations, and (vii) change in propagation interface and delamination crack migration [151]

stress analysis, Tsai [3] have demonstrated that a drastic decrease in the delamination stress is observed as a function of the increasing repeating index of a sublaminate within a laminated structure. This increase in strength can also be rationalised by a damage distribution argument; i.e., when the plies in a laminate are dispersed, each ply group represents a smaller percentage of the total laminate.

O'Brien [149] has also shown, again through both experiments and analysis, that increasing the ply thickness (or ply blocking) decreases the MCID onset strains. O'Brien [149] also noticed that increasing the thickness of transverse plies changes the predominant type of interlaminar failure from FED to MCID; the latter is then responsible for higher local strain concentrations in the neighbouring plies, precipitating early laminate failures, below the nominal strength of the adjacent plies. Lavoie and Adolfsson [112], based on experiments on carbon-epoxy multidirectional laminates, showed that MCID are generally absent in laminates with thin ply blocks subjected to monotonic tensile loading. Huchette [88], based on experimental results on cross-ply laminates, showed that the length of local delaminations increase much faster in laminates with thicker transverse laminae.

Sihn et al. [53], analysed the effect of ply thickness on the extent of delamination on unnotched and open-hole specimens subjected to tensile loading. For the same laminate thickness, it was observed that laminates with thicker plies (or thicker ply blocks), besides extensive microcracking, developed large delaminations starting from the free edges. While thin-ply specimens retained linearity nearly up to the ultimate failure stress, thick-ply specimens have shown unrecoverable severe damage due to microcracks and delamination. With the open-hole defect, a large increase of the strain and delamination extent near the hole edge of the thick-ply specimens was observed, whereas in the thin-ply specimens the hole edges were kept undamaged nearly up to final fracture.

Herakovich [139], in a historical review regarding the mechanics of composites, showed the significant effects of stacking sequence for tensile tests on angle-ply laminates with different stacking sequences. When the layers are stacked in an alternating fashion, the mode of failure is primarily due to fibre breakage. In contrast, when the layers are grouped together, edge effects and interlaminar shear stresses dominate, with the specimen failing due to delamination at a much lower axial stress.

In a preliminary numerical study towards the understanding of the effect of thin plies in delamination resistance, Camanho et al. [146] performed a finite element analysis (FEA) to evaluate the influence of ply thickness on the FED onset strain and growth using generalised plain strain elements and user defined cohesive elements [137]. Different carbon/epoxy symmetric and asymmetric laminates, with dispersed or clustered 0.04 mm thick plies, were simulated. Delamination onset strain was found to increase considerably when the ply thickness was reduced. Note that, based on numerical studies (e.g. Ref. [160]), it has been shown that independently of the type of failure observed in laminates with ply thicknesses equal to or above the conventional 0.125 mm, either pull-out or delamination failure modes, neglecting delamination results in an overprediction of the ultimate strengths; in fact, modelling delamination is critical even when delamination is not the major failure mode [160]. For thin-ply laminates, this may not be the case.

Camanho et al. [146] also performed a numerical analysis on the delamination resistance of ply-drops (skin-stiffener). For the same applied strain, the ply-drop with blocked plies exhibited much higher interlaminar stresses, inducing delaminations before the ply-drop with thin plies. The critical strain for blocked-ply laminates was much lower than for thin-ply laminates, with the latter clearly showing higher delamination resistance.

In an attempt to achieve pseudo-ductility in high performance CFRPs by creating controlled subcritical failure mechanisms, Czél et al. [29], Czél and Wisnom [161] studied the behaviour of UD discontinuous-ply laminates under tensile loads. The discontinuous-ply laminates were obtained introducing designed ply discontinuities through the laminate thickness. According to Czél et al. [29], Czél and Wisnom [161], laminates with thinner ply blocks had strains to failure almost three times higher than laminates with thicker ply blocks. Whereas the former exhibited a stable, highly nonlinear stress-strain response, the latter failed suddenly, without remarkable nonlinearity. Moreover, the discontinuous-ply laminates with thinner ply blocks exhibited a slightly higher initial modulus and a much higher failure stress. These laminates exhibited significant displacements of the adjacent blocks around the resin pockets formed by the plies discontinuities. A non-uniform shear stress distribution along the long overlaps, with peaks around the plies discontinuities, made relatively

early damage initiation and accumulation possible. Due to the higher shear load transfer capacity, a stable mode II delamination propagation before final failure was possible, yielding the stable nonlinear behaviour just mentioned. Besides, the thin ply blocks and the long overlaps resulted in a negligible role of the resin pockets in the tensile load transfer. Compared to UD continuous-ply laminates, small differences in initial modulus were observed, as well as a reasonably high tensile strength, which was reached after significant nonlinear behaviour, with no sudden failure. On the other hand, the thick ply blocks of the alternative UD discontinuous-ply laminates resulted in an uniform shear stress on the interfaces, also promoted by small overlaps, which reached the shear strength of the interface and conducted to sudden, premature failure of the laminates without any stable delamination propagation.

Guillamet et al. [39, 123], in their experimental study, also addressed the onset and progression of free-edge and MCID in dispersed- and blocked-ply regions of unnotched NCF thin-ply laminates. They observed that delamination originating from the free edges or matrix cracks were drastically reduced, or even suppressed, in the dispersed-ply region. Besides lower *in situ* strengths, which resulted in premature delamination induced by matrix cracks, ply blocking also contributed to higher interlaminar stress concentrations in adjacent interfaces, resulting in earlier onset of FED.

Based on visual observation and video recording, Amacher et al. [58] were able to report the nature and sequence of damage progression in quasi-isotropic laminates with different ply thicknesses. According to these authors, thick-ply laminates showed a progressive failure mode, which started by transverse and shear cracking of the 90° and ±45° plies, followed by massive delamination. Laminates with intermediate ply thicknesses have also shown a progressive type of failure, within a more limited delamination area, followed by a more abrupt final failure. However, thin-ply laminates did not exhibit delamination or other subcritical failure mechanisms before final fracture, resulting in higher unnotched strengths.

Due to the low through-the-thickness strength typical of conventional composite laminates, their use in applications with important out-of-plane stresses, such as those observed in L-shaped structures (typical of box structures, such as wings or wind turbine blades), is generally restrict. In fact, there are difficulties in replacing metallic curved sections by composite ones due to delamination failure caused by the through-the-thickness, out-of-plane reactions. In an attempt to improve the structural performance of L-shaped members, Arca [162] compared the interlaminar properties of conventional UD tapes and thin-ply NCFs, and performed structural tests on L-shaped structures. He observed that thin-ply NCFs not only show higher interlaminar fracture toughness, but they also show an improved structural performance on L-shaped structures.

2.4.3. Size effects

Because of the material heterogeneity at the constituent scale and at the ply scale, the analysis of failure due to cracking in composite materials resulting from stress concentrations is complex and dependent on many factors [25, 163]. For example, it is well known that, due to the discrete nature of its damage mechanisms, the mechanical response of composite laminates depends on the samples' scale (or volume), even when all other characteristics are preserved. Such dependence is known as *size effect* [131, 155, 164]. Therefore, it is very important to consider the effect of specimen size on strength when carrying out tests on composites, and to take it into account when using strength data from small coupons in the design of large load-bearing structures such as composite fuselages for aeroplanes[9] [131, 155, 164–166]. If size effects are not appropriately taken into account, designers may be forced to use unreasonably high safety factors and conduct costly full-scale structural tests than would be necessary. Moreover, according to Bažant [131, 164, 167], "*scaling laws are the most fundamental aspect of every physical theory*", and "*if the scaling is not understood, a viable theory does not exist*".

There are different sources for the size effects observed in composite materials, and in quasi-brittle materials in general. A statistical size effect may arise from the fact that the larger the structure, the greater the probability to encounter in its

[9]Even though full-scale experiments are usually carried out in aerospace engineering for certification purposes, accurate knowledge of the size effects affecting the structural performance of the composite materials used in large load-bearing parts is crucial to reduce design costs with respect to extrapolation of data from small-size coupons to large scale components, namely by reduction or suppression of experimental testing campaigns on intermediate scales.

volume a material element of a given critically small strength (weakest link). This is the classical size effect theory, and it can be described by *Weibull theory* using the statistical distribution with the same name[10] [131, 164]. More recently, though, due to the uniformity and quality of modern composite laminates, it has been shown that the Weibull theory has become inappropriate for use with laminated composites at the macroscopic level, where complex failure mechanisms develop and interact [111].

When a large fracture process zone (FPZ) or a long stable crack, or both, can develop before reaching the maximum load, the size effect due to strength randomness becomes inapplicable. This is the case of quasi-brittle materials, including FRP laminates, which typically develop a non-negligible FPZ, compared with the structural dimensions [131, 165, 168]. The statistical size effect is overwhelmed by the effect of stress redistributions caused by stable, gradual fracture propagation and consequent energy release, resulting in a *deterministic* (non-statistical) *size effect* [131, 164, 165]. This is particularly evident in the presence of stress concentrations caused by notches and holes, since, in this case, the material adjacent to the notch tips or hole edges fails first, and the influence of statistical variation of material strength is negligible [160].

When the FPZ is negligibly small, the fracture process is assumed to occur in one point (the crack tip), and LEFM applies [164]. It defines the strongest possible deterministic size effect, in which the nominal strength is inversely proportional to the square root of structure size. However, fracture of quasi-brittle materials is characterised by a finite FPZ (or characteristic length of the material), non-negligible compared to any structural dimension [164]. Consequently, the concept of *quasi-brittle size effect* has to be introduced [131], bridging the limiting cases of non-brittle (ductile — no size effect) and brittle (driven by LEFM — strongest possible size effect) behaviours[11] [164]. The key to the quasi-brittle size effect is the combination of the concept of strength or yield with fracture mechanics; in other words, fracture propagation will depend on both the fracture energy and (yield) strength of the material [131]. The quasi-brittle size effect is, thus, transitional between a plasticity-like theory and LEFM. Alternatively, the quasi-brittle size effect can also be described by a cohesive crack, characterised by a softening stress-displacement law for the crack opening.

When it comes to the particular case of laminated composites, it has been observed that this kind of quasi-brittle materials show remarked size effects due to the propagation of cracks in tension, and due to the propagation of kink bands in compression [131]. Although statistical size effects can also be observed in composite materials, due to its greater importance in the failure prediction of large load-bearing structures, only the deterministic size effect will be addressed in the present section.

2.4.3.1. Size effects in smooth coupons

On a detailed study addressing size effects on unnotched multidirectional composite laminates, based on different test campaigns, Lavoie et al. [111] reported that the tensile strength scaling on smooth quasi-isotropic laminates was absent as long as delamination was avoided, which could be observed on sublaminate-level scaled laminates, where the basic sublaminate is repeated as often as it is required (the ply thickness is kept constant and equal to the thickness of a single lamina independently of the laminate thickness). For these laminates, the constraining effect imposed by the off-axis plies on dispersed 0° plies resulted in a brittle type of failure mode. Quasi-isotropic laminates with ply-level scaling, where plies of the same orientation are stacked together to increase the effective ply thickness, exhibited less constraint on the blocked 0° plies, which resulted in split cracking and delamination from the off-axis plies. A size effect on the tensile strength could be identified, independently of specimen width or volume. However, according to Lavoie et al. [111], the origin for this size effect was in the grips.

[10] This is valid for perfectly brittle failure, in which the structural failure is caused by failure of one negligibly small RVE (it is considered that a structure fails as soon as a microscopic crack becomes macroscopic) [164, 168]. For ductile (or plastic) failure, the statistical distribution must be Gaussian (normal), since the failure load is a weighted sum of contributions of random strength values of RVEs along the failure surface, all of which fail simultaneously [168].

[11] It should be noted that, as discussed by Bažant [164], the meaning of the term *quasi-brittle* is relative. If the size of the quasi-brittle structure is sufficiently large compared to the material inhomogeneities, its behaviour approaches that of a perfectly brittle structure; on the other hand, if the size of the quasi-brittle structure is sufficiently small, with the FPZ extending over the cross section of the structure, its behaviour approaches that of a non-brittle (ductile) material [164].

Lee and Soutis [169, 170], even though focused on the scaling effects in open-hole composite specimens loaded in compression, also addressed the scaling effects in smooth coupons of carbon/epoxy quasi-isotropic laminates. Stacking sequences were based either in a sublaminate-level scaling, or in a ply-level scaling. The unnotched compressive strength of the ply-level scaled specimens was found to reduce with increasing specimen dimensions, an effect attributed to the blocked 0° ply thickness (increase of fibre waviness and void content), free edge effect and residual thermal stresses. The compressive strength of the sublaminate-level scaled specimens was unaffected regardless of the specimen dimensions.

Wisnom et al. [171] studied the size effects on tensile unnotched specimens, and how the ply thickness affects them. Quasi-isotropic carbon/epoxy laminates scaled at the ply and sublaminate level were tested. For the same laminate thickness, specimens with sublaminates repetition always exhibited higher failure stress than specimens with ply blocking. Furthermore, whereas changing the laminate thickness by ply-level scaling resulted in a strength reduction, laminate thickness scaling using sublaminates repetition resulted in an increase of strength. All specimens scaled at the sublaminate level behaved similarly, with no load drops or visual indications of damage prior to ultimate failure, characterised by a fairly clean break across the width in the gauge section; delamination did not occur before ultimate failure. In specimens scaled at the ply level, matrix cracks were visually observed on their surfaces, and delamination damage propagated at increasing load until catastrophic fibre failure of the longitudinal plies.

2.4.3.2. Hole size effect

The presence of a hole or any other discontinuity in a composite structure introduces high local stresses which may result in the development of subcritical damage that sometimes is not present in smooth components. This gives rise to a particular size effect form named *hole size effect*. It is characterised by a change in strength of laminates with a centrally located circular hole of different sizes, but constant stress concentration across the width (i.e. constant width-to-hole diameter ratio[12]) [144, 163, 172], and it is generally dependent on many factors, such as lamina constituents, stacking sequence, laminate thickness and ply thickness.

2.4.3.2.1. Tension When a notched coupon is loaded in tension, localised delaminations, starting at matrix cracks in the off-axis plies, occur at the hole edge, extending and joining up, and stepping through the thickness locally; splitting in the 0° plies may also occur. This localised damage, which blunts the notch, affects the stress concentration at the hole edge, and consequently the notched strength. But as the hole size increases, it becomes more difficult for the delaminations to join up and link through the thickness, and for splitting to occur, causing a reduction in strength [144, 163].

However, the hole size effect does not always result in the same trends for all laminates. It depends on the laminate design, in particular on the ply (block) thickness [144]. According to Wisnom and co-authors [144, 163], the different trends observed for the hole size effect are explained by the role of subcritical damage, in particular delamination [144], in the laminates' failure mode. In other words, even though conventional laminates show similar subcritical damage modes, their extent will determine the ultimate failure stress and predominant failure mechanism.

Laminates with sufficiently thin plies fail by fibre fracture, because the fibre failure stress is reached before extensive delamination growth [144, 163]. Intralaminar fracture initiates at the hole edge and propagates across the width, conducting either to pull-out or brittle fracture, depending on the extent of subcritical damage mechanisms. Extensive pull-out is typically observed in the smaller specimens, and brittle fracture in the larger ones. In fact, as the hole size increases, delamination propagation becomes more difficult, reducing further the blunting effect of delamination and splitting, and decreasing the notched strength, giving rise to the conventional hole size effect.

With sufficiently thick plies (or thick ply blocks), delamination, which is the predominant failure mechanism, easily propagates across the specimen's width and then along the specimen's length, especially for small hole sizes and small width-to-hole diameter ratios [144, 163]. In general, before failure of the 0° plies, matrix splitting propagates from the hole edge along the off-axis plies, followed by complete gauge section delamination. At this point, the specimen loses

[12]It is important to note that when the width is kept constant for varying hole sizes, the varying stress distribution across the width (typically represented by finite width correction factors) may obscure the underlying size effects [172].

its structural integrity, and it can be considered to have failed[13] [173]. Increasing the hole size, and keeping constant the width-to-hole diameter ratio, it becomes harder for the delaminations to propagate and join up across the wider ligaments, which may still occur before fibre fracture. Consequently, complete loss of structural integrity is delayed and the notched strength increases, resulting in an inverse hole size effect.

For laminates with an intermediate ply (block) thickness, a transition of failure mechanisms, from delamination to fibre failure, may occur as the coupon size increases. Specimens with small holes may fail by delamination, and specimens with large holes may fail by fibre fracture. In these cases, the competing failure mechanisms result in a flat response, with an almost constant notched strength over a range of hole sizes [144, 163].

Wisnom and co-authors [144, 163] have also concluded that the hole diameter-to-ply block thickness ratio is the critical parameter affecting how easily delaminations propagate, and therefore it is the critical parameter affecting how the laminates' strength change with changing hole diameters. For high hole diameter-to-ply block thickness ratios, extensive delamination is not likely to occur. On the other hand, for low hole diameter-to-ply block thickness ratios, the risk of premature delamination is substantially higher, resulting in lower notch sensitivity.

Green et al. [163] performed an extensive experimental programme to study the effect of scaling on the tensile strength of notched composite laminates. In a similar, but more detailed work, Hallett et al. [174] experimentally and numerically evaluated the damage growth in notched composite laminates under tensile loading, namely by interrupted testing. Particularly, the effect of ply thickness was investigated by testing carbon/epoxy quasi-isotropic laminates with stacking sequences based either on sublaminate-level scaling or ply-level scaling. Both works [163, 174] showed that an increase in ply thickness led to a decrease in failure stress. For laminates with single ply blocks, damage was restricted to the outermost sublaminate, inhibiting its propagation through the thickness of the laminate. This led to a fibre failure mode, with either pull-out or brittle appearance. For laminates with thicker ply blocks, when the 45/90 interface delamination at the hole propagated across the width and reached the specimen edge, the delamination stepped through the 45/90 and 90/−45 interfaces, via 90° and −45° matrix cracks, to the −45/0 interface, isolating the 0° plies. This conducted to complete gauge section delamination of the −45/0 interface, resulting in early delamination failure.

Wisnom and Hallett [144] also performed open-hole tension tests on dispersed-ply and blocked-ply quasi-isotropic carbon/epoxy laminates with the same stacking sequence and laminate thickness but varying ply block thickness and varying number of sublaminates. Results showed that specimens scaled at the sublaminate level failed by fibre fracture before reaching the stress necessary to delaminate across the width, with the strength decreasing with increasing hole size. Specimens with (four) blocked plies all delaminated, with the failure stress increasing with increasing hole diameter (this inverse hole size effect was also observed by Green et al. [163] and Hallett et al. [174]). Finally, specimens with intermediate ply block thicknesses showed intermediate response, with the small ones failing by delamination and the large ones by fibre failure, achieving a constant strength over a range of hole sizes. Accordingly, it was notorious that delamination, either starting from the intersection of transverse cracks or from the free edges, had a crucial role in the in-plane strength, failure mode and hole size effect on open-hole tension of quasi-isotropic laminates. Premature failure was observed, especially for narrow specimens, small holes and thick ply blocks, due to overall gauge section delamination, as already discussed.

Erçin et al. [121] observed that the decrease in tensile strength of open-hole specimens with size is more pronounced in laminates with dispersed plies than with blocked plies. These authors also observed that the notched strength of partially blocked-ply laminates is higher than that of dispersed-ply laminates, confirming the importance of fibre-matrix splitting in the 0° plies as a notch blunting mechanism.

Arteiro et al. [122, 135] studied the notched response of quasi-isotropic NCF thin-ply laminates with centrally located open holes. Both experimental [122] and analytical [135] analyses were employed in a conjugate study. Two distinct laminates were addressed, one with dispersed plies, the other with some plies with the same fibre orientation blocked

[13] Even though specimens failing by delamination are able to sustain additional loading, in general due to the load carrying capacity of the remaining 0° ligaments, delamination is still considered an appropriate definition of failure because these specimens had effectively lost their structural integrity [172]. Final failure may occur at lower or higher applied stresses depending on the stability of delamination propagation [172].

together. When compared to other CFRP laminates with similar stacking configurations, no substantial differences were found either in the effects of hole size nor in the notch sensitivity of thin-ply laminates. It was also demonstrated that, by proper laminate design with thin plies, it is possible to decrease the notch sensitivity while reducing the development of subcritical damage, such as delamination and matrix cracking, to a minimum [135].

Finally, it is important to stress that in laminates with thin plies (or thin ply blocks), since extensive delamination is not likely to occur, failure analysis may be considerably simplified since accurate closed-form solutions to predict the notched strength of such laminates are readily available (e.g. Refs. [175–182]). On the other hand, for laminates with thick ply blocks, the risk of premature delamination is substantially higher, and traditional design methods are not able to predict the notched response of such laminates [163, 179]; in spite of exhibiting lower notch sensitivity, their mechanical response can only be analysed using complex nonlinear FEA, generally unsuitable for preliminary design and optimisation [183].

2.4.3.2.2. Compression For the hole size effect in compression, three distinct failure mechanisms, all associated with catastrophic failure, have been observed depending on the scale and lay-up, with similarities to those identified in tension (section 2.4.3.2.1): brittle fibre fracture (shear-driven or microbuckling), push-out between plies and delamination [172]. Laminates with sufficiently thin plies exhibit a brittle fracture straight across the laminate. Since subcritical damage mechanisms, e.g. delamination and fibre splitting, are inhibited by the constraining effect of the thinner sublaminates, the stress in the 0° plies increases to a level enough to trigger fibre kinking, resulting in a brittle failure. Laminates with thicker plies (or thicker ply blocks) typically show fracture of the angle plies and local delamination or push-out between plies. In this case, delamination and splitting occur before fibre kinking, delaying fibre fracture. For sufficiently thick laminates with thick plies, delamination failure, with no fibre fracture, may also occur.

Lee and Soutis [169, 170] studied the scaling effects in open-hole composite specimens loaded in compression, including the ply thickness effect. Carbon/epoxy quasi-isotropic laminates were fabricated comprising either blocked (ply-level scaling) or distributed plies (sublaminate-level scaling). The compressive notched strengths obtained for the ply-level scaled specimens were higher than those obtained for the sublaminate-level scaled specimens. This result could be attributed to stress redistribution that occurs due to local damage around the hole in the ply-level scaled specimens. This local damage, which appears in the form of fibre/matrix splitting at a lower applied compressive stress than in the sublaminate-level scaled specimens, reduces the stress concentration factor at the edge of the hole, delaying the final failure to a higher applied stress. If the local damage does not occur, or occurs just prior to catastrophic failure (which is the case of sublaminate-level scaled specimens), the composite laminate behaviour is closer to brittle behaviour, resulting in a lower failure stress.

Erçin et al. [121] reported a more pronounced decrease of the compressive notched strength with size in laminates with dispersed plies, attributed to subcritical damage occurring in greater extent in partially blocked-ply laminates. Except for the smallest specimens, the compressive notched strength of partially blocked-ply laminates was higher than that of dispersed-ply laminates. It was also noted that the detrimental effect of load reversal from tension to compression is more pronounced in the notched specimens, with reported open-hole tensile strengths 66–91% higher than the open-hole compressive strengths, whereas the unnotched tensile and compressive strengths differ in 48%.

Arteiro et al. [122, 135] also studied the notched response of quasi-isotropic NCF thin-ply laminates in compression. When compared to conventional CFRP laminates with similar stacking configurations, even though no atypical differences were found, the studied thin-ply laminates have shown a slightly inferior notched response. However, the higher notch sensitivity exhibited by the NCF thin-ply laminates was attributed to the remarkably high compressive unnotched strength of these laminates when compared to conventional ones (see also section 2.4.1), resulting in a reduced relative performance of the notched specimens. Still, as in the tensile case, it was also demonstrated that, by proper laminate design, it is possible to decrease the notch sensitivity of a laminate while reducing the development of subcritical damage to a minimum [135].

It is noted that the results presented by Lee and Soutis [169, 170], Erçin et al. [121] and Arteiro et al. [122, 135] on ply-level and sublaminate-level scaled laminates not always agree with those obtained by Lee and Soutis [184] (sec-

tion 2.4.3.3) and by Yokozeki et al. [134] and Amacher et al. [37, 58] (section 2.4.1.3), who reported equal or higher compressive notched strengths for the laminates with thinner plies. Clarification about the effect of ply thinness on the compressive notched response of composite laminates is therefore a topic of great interest.

2.4.3.3. Effect of laminate thickness

Lee and Soutis [184] studied the stacking sequence effects on the compressive failure strength of quasi-isotropic carbon/epoxy composite laminates with varying laminate thickness, by means of static compressive testing in smooth and open-hole specimens. Tests on sublaminate-level and ply-level scaled laminates were reported. The strength values obtained from the sublaminate-level scaled specimens were slightly higher or just similar to those obtained from the ply-level scaled specimens, in both unnotched and open-hole specimens. The reason for this effect was explained by the fibre waviness, void content, free edge effect and stress distribution in blocked and dispersed 0° plies.

The unnotched sublaminate-level scaled specimens did not show any thickness effects, since their compressive strength was practically constant regardless of the specimen thickness [184]. The failure, which occurred suddenly in a crushing failure mode, involved a combination of fibre kinking in the 0° plies, delamination between 0° and ±45° plies, splitting parallel to the fibres at 0° and ±45° plies, and matrix cracking and crushing in the 90° plies, without a global buckling influence. For the unnotched ply-level scaled specimens, which showed the previous failure characteristics but in a more pronounced way, a strength reduction with increasing thickness was observed. Fibre waviness and void content were found to be the main parameters contributing to the thickness effect on the compressive failure strength of the ply-level scaled specimens.

The compressive strength of the open-hole specimens increased with increasing thickness on both dispersed-ply and blocked-ply laminates [184]. This was explained by the introduction of out-of-plane bending in the window area of the anti-buckling device, magnifying the stress field near the hole and causing damage initiation and final failure at a lower applied load in the thinner specimens.

Wisnom et al. [172] gathered extensive recent work on scaling of unnotched and open-hole specimens, and discussed the effect of laminate thickness on the strength of laminates. They show that the open-hole tensile strength of ply-level scaled specimens decreases with increasing thickness, in a trend similar to that observed in unnotched specimens. This is attributed to the type of failure observed in thick ply-level scaled specimens, which is characterised by extensive delamination. Sublaminate-level scaled specimens show a slight reduction in tensile notched strength with increasing laminate thickness, remaining constant for increasingly thicker laminates. The higher strength for the thinner laminates is attributed to a decrease in stress concentration caused by the failure that develops on the surface plies (which represent a greater portion of the laminate than in the thicker ones) before reaching the 0° plies.

2.4.4. Intralaminar fracture toughness

Characterisation and prediction of the fracture toughness associated with *intralaminar* failure modes involving fibre breakage is also an important issue regarding the effect of ply thickness on damage onset and subsequent propagation [185]. In fact, the intralaminar fracture toughness not only plays an important role in the assessment of the damage tolerance of composite structures and their behaviour during damage propagation [65, 185–188], as it is also relevant in the definition of the softening laws used in recent computational analysis models [106, 108, 189, 190] and in establishing the energy equilibrium equations used in closed-form solutions [181, 182] that predict the ultimate strength of composite laminates.

Fibre breakage can take place during both longitudinal tensile or compressive loading. In particular for carbon/epoxy systems, the energy released by these failure processes is much larger than for those involving matrix or matrix-fibre bond failures [191].

When subjected to direct in-plane loading, laminates may fail under *intralaminar fibre tensile failure*, characterised by fibre-matrix debonding and subsequent pull-out and fibre fracture, under *intralaminar fibre compressive failure*, whose failure can initiate as either shear-driven fibre failure or fibre kinking, and under *intralaminar matrix failure*, characterised

by matrix cracking either longitudinally or transversely with respect to the fibres [192]. Because they are intrinsic properties to the material system and, for a given loading condition, formation and propagation of damage within a laminate is lay-up dependent, care must be taken when determining the fracture toughness associated with each of these failure modes.

According to a review by Laffan et al. [192], although intralaminar fracture toughness has received relatively little attention from the scientific community in the past[14], nowadays, this type of characterisation plays an increasingly important role, mainly due to the application of large composite primary structures. The collection of work related to tensile failure reveals a varied approach in terms of specimen configuration, size and data reduction, despite the existence of an ASTM standard (ASTM E 1922 – 97 [193]). Works on compressive failure are even less comprehensive [192].

It is important to stress that, even though the fracture toughness can be characterised by a single parameter such as the critical ERR or the critical Stress Intensity Factor, it may be represented more accurately in the form of an $\mathcal{R}$-curve, relating the change in the critical ERR with crack growth. In fact, the experimental characterisation of several composite materials and different lay-ups has shown that composite laminates exhibit a fracture resistance behaviour resembling an $\mathcal{R}$-curve type of response, whose damage growth resistance was primarily due to (i) load redistribution resulting from microcracking, splitting and/or delamination, which relieve the stress concentration and delays fracture to higher applied loads [20, 182, 194–196], and (ii) bridging by the intact fibres of the plies that are adjacent to the principal load-carrying plies with broken fibres [194, 195]. Crack growth stability is therefore necessary for good data acquisition. However, $\mathcal{R}$-curves are not currently addressed by the ASTM E 1922 – 97 standard test method [192, 193].

2.4.4.1. Compact Tension/Compression

According to Laffan et al. [192], the *Compact Tension* (CT) configuration is perhaps the most widely used specimen configuration for intralaminar fracture toughness measurement of composites. In order to resolve some problems with undesirable failure modes, such as damage beneath the central loading point in three point bending and crack growth perpendicular to the desired growth direction in CT specimens (particularly in highly orthotropic laminates), an *Overheight Compact Tension* (OCT) configuration [197, 198]) has also been used in intralaminar fracture toughness testing of composite laminates. The OCT configuration is particularly suitable for testing the intralaminar fracture toughness of tougher material systems, where the previously mentioned undesirable failure modes tend to appear.

A configuration similar to the CT test specimen has also been used for characterisation of the compressive fracture toughness of composite laminates by reversal of the loading configuration. This is known as the *Compact Compression* (CC) test specimen [191, 192].

CT-type tests are usually devised such that extraneous damage modes are minimised and a brittle type of crack progression occurs from the pre-machined notch to measure the intralaminar fracture toughness of the laminate or of the lamina (in the latter, associated with longitudinal, fibre fracture) [198]. Nonetheless, these undesired damage mechanisms may still occur, eventually affecting the accurate characterisation of the intralaminar fracture toughness.

Li et al. [198] experimentally investigated the interaction between subcritical damage in the form of splitting and delamination, promoted by proper laminate design, with progressive fibre failure. In particular, they investigated the effect of having dispersed and blocked plies in the thickness direction, by means of interrupted testing, to capture the damage process as it occurred before the onset of fibre failure (ultrasonic C-scanning and X-ray was used to determine the extent of delamination). Carbon/epoxy laminates, including dispersed and blocked cross-ply and quasi-isotropic lay-ups, were tested. OCT tests were used together with an anti-buckling support attached to the back face of the specimen to evaluate stable crack growth so that the composite damage zone could be investigated.

The results presented by Li et al. [198] showed that, in dispersed-ply laminates, damage growth was restricted, promoting fibre failure and crack growth through the whole thickness, since the local stress at the notch tip was higher due

[14] The lack of attention for intralaminar fracture of composites in the past was partially due to (i) a lack of confidence in composite materials, resulting in them not being used in primary structures where this type of characterisation is more useful, and (ii) a lack of modelling capabilities that can use the parameters effectively [192].

to the reduced blunting effect of subcritical damage. The load curves of the dispersed ply specimens were approximately linear before the first load drop. The through-the-thickness crack progressed across the width of the specimen in a series of small "jumps" which resulted in further load drops. For these laminates, the overall trend was crack progression at approximately constant load, with much smaller load jumps in the quasi-isotropic laminates than in cross-ply laminates. This might suggest that the ±45° plies can help reducing the stress accumulation in the 0° plies and foster smoother or more stable fibre breakage progression.

In contrast, blocked-ply laminates promoted a larger amount of splitting and delamination and caused a larger damage process zone [198]. Due to the development of splitting and delamination, the load curves showed a larger degree of nonlinearity. These laminates generally failed suddenly due to blocked plies pulling out via delamination. It was also observed that damage initiation (FPF) of blocked-ply laminates occurred earlier than in dispersed-ply laminates with the same thickness. However, this resulted in a significant reduction of the stress concentration at the notch tip that ultimately conducted to a tougher laminate. Finally, it was noticed that in the case of blocked-ply laminates the process zone became so large that the specimen size was no longer sufficient. According to Li et al. [198], if the delamination were to be allowed to continue to grow in a larger specimen, eventually the fibre failure stress at the notch would be exceeded and a through-the-thickness crack would have eventually started to propagate.

Laffan et al. [185] investigated the use of different data reduction methods for calculation of the intralaminar fracture toughness of carbon/epoxy laminates using the CT specimen configuration. The area method, the ASTM E 399 – 90 standard test method [199] (established for isotropic materials, in particular metals), the $\mathcal{J}$-integral/Virtual Crack Closure Technique (VCCT) method (based on FEA), the compliance calibration method (CCM), using the optically measured crack length, and the modified compliance calibration method (MCCM), using the effective crack length, were studied. According to Laffan et al. [185], the area method is simpler, but must use optically measured crack growth (Δa), becoming more sensitive to errors for low Δa and insensitive to $\mathcal{R}$-curve effects for large Δa. In addition, for stick-slip crack growth, it requires interpolating the load vs. displacement curve between critical loads. The ASTM E 399 – 90 standard test method [199] allows to choose the initial a/w ratio which gives accurate initiation values, but relies on optically measured crack length, and the use of a function $f(a/w)$ for isotropic materials renders it inappropriate. The $\mathcal{J}$-integral/VCCT method eliminates any error from differentiating a fitted curve such as that in the CCM and MCCM, but relies on optically measured crack length and the use of FEA adds complexity. The CCM works well if the compliance vs. crack length curve can be sufficiently populated, but, once again, relies on optically measured crack length, and the data points for the compliance calibration curve are dictated by specimen crack jumps, which may result in areas not being populated. Finally, the MCCM does not require optical crack length measurement (when using effective crack length), but requires additional experimental work or adds the complexity of using FEA to obtain the compliance vs. crack length curve.

An alternative data reduction procedure has been proposed by Catalanotti et al. [200] based on the DIC technique. This method involves an automated algorithm that post-processes the full-field data provided by the DIC system during the CT test (or similar), and it is used to automatically detect the crack tip location, quantifying the crack length without any visual inspection. Based on the displacement and strain fields obtained from the DIC technique, the $\mathcal{J}$-integral can be calculated and the $\mathcal{R}$-curve generated, obviating the need of complex pre- and post-processing of the test data [200].

Laffan et al. [201] studied the size and lay-up effects on the mode I intralaminar tensile fracture toughness of carbon/epoxy associated with fibre fracture. According to this study, there is no significant effect of scaling the specimen in-plane size. However, the use of very small specimens can result in undesirable failure modes, such as shear out of the loading holes. On the other hand, the use of very large specimens has no benefits on the results, making them impractical in terms of material usage. On the other hand, the thickness of the specimen demonstrated a significant effect in the fracture toughness of the tested carbon/epoxy laminates. The thicker specimen showed lower intralaminar fracture toughness associated with fibre fracture (28% for initiation and 14% for propagation), even though no significant difference between the fracture surfaces of thinner and thicker specimens was observed. Furthermore, the thick specimen showed an increasing $\mathcal{R}$-curve trend, unlike the thin specimen. These results indicate one of the weaknesses of using the CT configuration for characterisation of the mode I intralaminar tensile fracture toughness of advanced composite materials.

2.4. Effect of ply thickness scaling on the mechanical response of composite laminates

In order to address lay-up effects, Laffan et al. [201] measured the $\mathcal{R}$-curves of dispersed- and blocked-ply carbon/epoxy laminates. The apparent intralaminar fracture toughness of the fibre tensile failure mode was found to increase (almost twice) when the thickness of the 0° layer was increased, attributed to an increase in fibre pull-out in the thicker 0° layers. Hence, Laffan et al. [201] have claimed that the intralaminar fracture toughness associated with mode I crack propagation perpendicularly to the fibre direction is not simply a material property, but rather an *in situ* material property. Based on this assumption, Chen et al. [160] employed a cohesive zone model accounting for a thickness-dependent mode I intralaminar fracture toughness perpendicular to the fibre direction in the prediction of the tensile strength of open-hole laminates. Since no quantitative mathematical model that describes this thickness dependency has been proposed, these authors applied a simple linear scaling of the fracture toughness of blocked 0° plies, multiplying the fracture toughness of a single 0° ply by the number of plies blocked together, based on the experiments carried out by Laffan et al. [201] (even though different material systems have been addressed in these works). They concluded that accounting for this dependency is necessary to predict thickness size effects in multidirectional laminates based either on ply-level scaling or on sublaminate-level scaling (due to the symmetry 0° ply block), without detailing the effect of other (subcritical) damage mechanisms. Besides, no parametric study has been shown about the influence of the assumption regarding the linear scaling of the mode I intralaminar fracture toughness of blocked 0° plies on the predicted results.

Teixeira et al. [202] determined the intralaminar fracture toughness of several carbon/epoxy laminates and correlated such values with the intralaminar fracture toughness of the individual plies. The authors reported an intralaminar fracture toughness at propagation for a block of two 0° plies as being almost three times greater than that of a single ply, even though no clear information was mentioned about the type of failure and the extent of other failure mechanisms than clear intralaminar fibre breakage. In addition, no notable difference in the intralaminar fracture toughness of quasi-isotropic laminates with dispersed plies and with blocked plies was found.

In a preliminary study, Fernandes [203] suggested a ply thickness dependence of the ERR associated with intralaminar fracture of composites perpendicularly to the fibre direction. However, the occurrence or extent of other failure mechanisms and their effect on the results was not reported (from the scanning electron microscopy fracture surfaces presented by Fernandes [203], interlaminar cracks due to delamination or split cracking in the CT specimens with 0.150 mm thick plies could be observed), as well as the reliability of the CT test specimen for the tested materials; hence, this work can be seen as an intriguing, but not conclusive contribution.

From the previous discussion, it can be argued that the experimental work carried out by Laffan et al. [201], Teixeira et al. [202] and Fernandes [203] does not provide sufficient data to conclude about the effect of ply thickness on the intralaminar fracture toughness of composite laminates. For example, damage spreading from the pre-inserted notch of scaled CT specimens with anti-buckling guides, without clear through-the-thickness fracture propagation, was observed by Bergan et al. [204]. No steady-state fracture toughness could be obtained with the proposed specimen geometries due to subcritical damage propagation, which smeared damage evolution in a region relatively large compared to the size of the specimen. Moreover, in recent studies carried out by Xu et al. [166, 205], it was shown that local fibre breakage is delayed in thicker 0° ply blocks due to the propagation of longer splits and extensive delamination, which can be attributed to the lower constraint [111] and higher interlaminar stresses at the interfaces adjacent to the 0° ply blocks.

According to Xu et al. [166, 205], the split cracks and local delaminations in the vicinity of the crack tips blunt the stress concentration in a greater extent than in single 0° plies. Therefore, crack restraining in thick 0° plies cannot be attributed solely to an intrinsically higher fracture resistance, as the apparent increase of fracture toughness may be due to the development of a large damage process zone containing substantial splitting and delamination, which modifies the stress field in the vicinity of the notch tip. Hence, further studies are required to improve the knowledge on the effect of ply thinness on the intralaminar fracture toughness associated with mode I crack propagation perpendicularly to the fibre direction. Furthermore, the use of an alternative method to measure the $\mathcal{R}$-curve is strongly recommended.

Finally, it should be noted that accounting for a higher intralaminar fracture toughness on the numerical simulation of blocked plies (e.g. Ref. [160]) is simply a means of accounting for the extra stress relaxation that results from the development of a larger damage process zone containing extensive split cracking and localised delaminations that are

not addressed in the constitutive formulation that accounts for intralaminar damage mechanisms. It is not clear if such virtual fracture toughness scaling will remain applicable for more complex loading scenarios that differ substantially from the simple scenarios used for intralaminar fracture characterisation, and that may change the sequence and extent of the blunting mechanisms.

2.4.4.2. Size effect law

CT-type test specimens have shown deficiencies in characterising the intralaminar fracture toughness of new, tougher composite systems [65, 187, 206, 207], woven composites [65, 208], and thin laminates [182]. Among other factors, this inadequacy can be attributed to no fracture propagation in the desired growth direction due to significant buckling of the unnotched end [182, 206], to difficulties in locating the tip of the FPZ [208], to very high coefficients of variation of the measured properties [208], to the inability to get the right fracture properties (e.g., the $\mathcal{R}$-curve) due to the occurrence of subcritical failure mechanisms (namely delamination and splitting) that blunt self-similar intralaminar fracture propagation [198, 204, 205, 208][15], or to the effect of specimens' size on the sequence and type of failure [205][16].

On the other hand, there is also the need to measure the fracture toughness and the corresponding $\mathcal{R}$-curve associated with the propagation of a kink band in polymer composites. However, the CC test specimen has demonstrated inadequacy, as discussed in detail by Catalanotti and co-authors [187, 207]. On one hand, the correction factor used in the data reduction of the CC test method does not account for the contact tractions that occur on the crack faces. On the other hand, the CC test specimen triggers diffused damage during the propagation of the kink band that artificially increases the value of the measured fracture toughness and renders the detection of the tip of the kink band impossible, making this test method unreliable for the determination of the $\mathcal{R}$-curve.

In order to obviate the drawbacks of CT- and CC-type test specimens, recently, a methodology based on the *size effect law* [209] has been proposed to measure the intralaminar fracture toughness and the $\mathcal{R}$-curve of composite laminates in mode I, both tensile [65, 210] and compressive modes [187], and in mode II[17] [188]. As discussed by Bažant [164], measurement of the size effect offers a robust way to determine the fracture characteristics of quasi-brittle materials.

According to this methodology, the $\mathcal{R}$-curve can be measured taking into account that, for different characteristic sizes w_n, assuming that the size effect law, $\bar{\sigma}^{\infty} = \bar{\sigma}^{\infty}(w)$, is known, the driving force curves $\mathcal{G}_I$ at the ultimate remote stresses $\bar{\sigma}^{\infty}(w_n)$ are tangent to the $\mathcal{R}$-curve. In other words, the $\mathcal{R}$-curve can be determined as the envelope of the driving force curves at the ultimate remote stresses (e.g. Ref. [211]).

This methodology has provided a robust way for determining the steady-state value of the $\mathcal{R}$-curve for polymer composites without relying on complex test setups and post-processing analyses, and without the need to pinpoint the location

[15] Blanco et al. [208], in their experimental study, used a Doubly-Tapered Compact Tension (2TCT) specimen to measure the intralaminar fracture toughness of a five-harness satin carbon composite. Even though they concluded that the 2TCT specimen was suitable to characterise the tensile fracture properties of woven composites, correct $\mathcal{R}$-curves could not be identified, and the coefficients of variation of the measured fracture properties were as high as 17%. It is noted that intralaminar fracture toughness characterisation of woven composites was successfully achieved, for instance, by Catalanotti et al. [65].

[16] Xu et al. [205] tested OCT specimens scaled by a factor of two, up and down, and observed that long splits blunt the stress concentration and prevent fibre breakage of the thicker 0° plies, and that the amount of delamination adjacent to the thick 0° plies becomes quite substantial in the later stages of fracture propagation. The large splits and extensive delamination cause a sudden loss of stiffness in the specimens and blunt self-similar intralaminar fracture propagation, independently of the OCT specimen size. Moreover, scaled OCT specimens show distinct final failure mechanisms, with the smaller suffering compressive failure of the unnotched end, and the larger exhibiting buckling after a short period of stable fracture growth after the peak load. Similar buckling failure was observed by Arteiro et al. [182] on thinner OCT specimens, but without fracture growth at all.

[17] The knowledge of the $\mathcal{R}$-curve associated with intralaminar fracture of fibre-reinforced composites in mode II can be very valuable in the direct extension to mode II of existing analysis methods [179, 181, 182] and computational procedures [189] initially formulated for mode I fracture. However, until very recently, no characterisation procedure has been proposed for measuring the $\mathcal{R}$-curve of fibre-reinforced composites in mode II [188, 207]. Catalanotti and Xavier [188] proposes the use of the Iosipescu test method to determine the intralaminar fracture toughness and $\mathcal{R}$-curve in mode II using the size effect law. This test method was chosen (i) because it is typically used to measure the elastic properties of polymer composites, (ii) because it has the ability to apply an uniform shear stress field in the gauge section of the cracked specimen, and (iii) because of its dissemination in the scientific community (no novel test setup is required). Nevertheless, since the experimental device is standardised, it is not possible to scale specimens of the same geometry to use the classical size effect method, and the full $\mathcal{R}$-curve cannot be extracted from experiments. This is overcome extracting the size effect law by mapping the part of the $\mathcal{R}$-curve that can be obtained. All details can be found in Ref. [188].

of the crack tip to measure the crack length at different load values. In fact, only the ultimate stresses of *geometrically similar specimens*[18] (not mandatory, but providing simpler and more accurate analyses [164]) of different sizes with a *positive geometry*[19] are required [65, 187, 188].

Using the size effect law, Catalanotti et al. [65] obtained the $\mathcal{R}$-curve associated with intralaminar fracture of different carbon/epoxy systems and reinforcements (including non-crimp and woven fabrics). Scaled double edge-notched specimens were used. The intralaminar fracture toughness and the corresponding $\mathcal{R}$-curve of multidirectional laminates or of the 0° ply were obtained in cases where a CT-type test method had failed (e.g. Refs. [182, 206]).

One of the laminates characterised by Catalanotti et al. [65] was an NCF thin-ply laminate, with a minimum nominal ply thickness of 0.08 mm. When compared to conventional laminates (with a nominal ply thickness of 0.125 mm), the value of the intralaminar fracture toughness of the 0° ply, estimated using the model presented by Camanho and Catalanotti [212], have not evidenced any inherent brittleness for this kind of laminated composites; in fact, in spite of using an epoxy resin not certified for aerospace applications, the intralaminar fracture toughness of the NCF thin-ply laminate was slightly higher than that measured for an aerospace-grade carbon/epoxy.

2.4.4.3. Centre-Notched Tension/Compression

The *Centre-Notched Tension* (CNT) specimen configuration has also been used for the measurement of the fracture toughness of composite laminates (see, for instance, Ref. [212]). In addition, a similar configuration has also been used for characterisation of the compressive fracture toughness of composite laminates, by reversal of the loading direction — *Centre-Notched Compression* (CNC) [192, 212].

However, a centre-notched specimen alone only provides a single value of the intralaminar fracture toughness, which is below the steady-state value unless a sufficiently large centre-notched specimen, able to develop the full FPZ, is tested; the characterisation of the $\mathcal{R}$-curve is not possible. Still, the determination of the fracture toughness can be important for application of strength prediction methods based on classical LEFM or based on Finite Fracture Mechanics [179, 180].

Erçin et al. [121] measured the tensile and compressive intralaminar fracture toughness of two distinct laminates of the same carbon/epoxy material system and same in-plane stiffness using, respectively, the CNT and CNC test configurations. One laminate had dispersed plies, whereas the other had blocks of two plies with the same fibre orientation in the outermost layers. A tensile and a compressive intralaminar fracture toughness 9% and 10% lower was reported for the laminate with dispersed plies.

Arteiro et al. [122] determined and compared the tensile and compressive intralaminar fracture toughnesses of quasi-isotropic NCF thin-ply laminates with and without ply blocking. CNT and CNC specimens were tested. In the tensile case, an intralaminar crack, dominated by fibre fracture, could be observed in both laminates, with and without ply blocking. The former exhibited a pull-out failure mode, with some signs of splitting and delamination, whereas the latter exhibited a brittle failure surface. Still, the difference in the value of the intralaminar fracture toughness was only 1%. In compression, no major differences were observed in the failed specimens, which exhibited a net-section failure mode dominated by fibre kinking. A difference in compressive fracture toughness below 5% was obtained.

Using the analytical model proposed by Camanho and Catalanotti [212], Arteiro et al. [122] predicted the tensile and compressive fracture toughnesses of the 0° plies, and no substantial differences were observed between the two laminates, either in the tensile or compressive cases. It was also observed that the predicted values were not far from those typically obtained in CFRP laminates used in the aeronautical and aerospace industries, in agreement with Catalanotti et al. [65].

[18] Geometrically similar specimens have constant ratio between the characteristic dimension, e.g. the specimen's width, and the other dimensions, namely the crack length and the gauge length of the specimen.

[19] In structures with a positive geometry, the ERR at constant load must increase with crack extension [165]. In other words, the correction factor for the structure's geometry must be an increasing function of the crack length. Nearly all notched fracture specimens have a positive geometry [165].

Later, Arteiro et al. [182] used the $\mathcal{R}$-curve associated with intralaminar fracture obtained by Catalanotti et al. [65] for a thin-ply NCF to predict the Large Damage Capability (LDC) of this material system. In addition, detailed LDC tests were carried out to assess the residual strength of NCF thin-ply laminates with a large through-the-thickness central notch. Both predictions and experiments have shown that this new material system is characterised by a quasi-brittle intralaminar fracture behaviour, with extensive crack bridging, eliminating any evidence of inherent brittleness of laminates composed of thin-plies. In the experiments, a large, stable damage process zone before ultimate failure could be observed, with almost no subcritical damage such as delamination or splitting, showing the ability of thin-ply laminates to suppress subcritical damage without incurring on a perfectly brittle fracture behaviour.

2.4.4.4. Other testing configurations

Other testing configurations have been used for intralaminar fracture toughness characterisation of composite laminates. Also derived from an existing ASTM standardised configuration for metals, such as the CT configuration, *three-point bending* configuration has been used in composites characterisation [192]. Other configurations are the *Single/Double Edge-Notched Tension* configurations. According to Laffan et al. [192], these configurations have been used for intralaminar fracture toughness characterisation of carbon, E-glass, Kevlar and boron/epoxy systems.

2.4.5. Impact resistance and damage tolerance

In general, load bearing structures made of composite laminates, particularly those used in aeronautical and aerospace structures, must have their design driven by damage tolerance considerations (i.e., some level of damage must be assumed to exist in the composite structure), since compression and shear failures become critical when associated with pre-existing local defects [186, 213]. In addition, composite laminates are known to be very susceptible to the introduction of such defects by external events during operation and maintenance services.

A common source of local defects is out-of-plane impact by foreign objects. However, not all impacts produce the same type of damage. Whereas in ballistic impacts the damage is very localised and easily noticed, in *low-velocity impact* (LVI) both global deflections and localised contact forces produce a global structural response [214], resulting in complex interactions between different failure mechanisms, such as indentation, matrix cracking, fibre-matrix interface debonding and pull-out, fibre breakage, delamination and, eventually, penetration [12, 13, 215]. In some cases, the interaction between the different failure mechanisms may result in localised subsurface damage, typically termed *barely visible impact damage* (BVID), that is difficult to identify by external inspection and is often left undetected during maintenance routines. From a damage tolerant point of view, LVI is, therefore, of greater concern, because it can grow invisibly, continuously degrading the residual properties of the composite material until catastrophic failure [12, 13].

Impact damage affects considerably the residual compressive and shear strengths of the composite material due to the appearance of instabilities and overloading, and consequent failure of undamaged areas [152], reducing the load-carrying capacity and the structural integrity of composite structures [24, 152, 213, 216–220]. Therefore, structural characterisation of the *impact resistance* (or *damage resistance*), which is concerned with the creation of damage directly from the impact event, and *damage tolerance*, which addresses the structural integrity associated with a given damage condition, is of great importance. These structural properties are traditionally assessed by means of LVI and *compression after impact* (CAI) testing, respectively.

If thin-ply laminates are able to suppress the onset of the microcracking and delamination damage (as discussed in sections 2.4.1 and 2.4.2), it can be expected that a similar superiority can be observed under impact loading [53, 221]. In laminates with thick plies (or thick ply blocks), the number of interfaces available for delamination is reduced, resulting in a fewer number of larger delaminations when subjected to impact loading. This is prejudicial for the impact response of the laminate [222].

However, the effect of ply thickness on the damage tolerance, assessed by means of the residual compressive strength, where the greatest reduction in loading is observed due to laminae buckling in the delaminated areas, is not totally clear [218–220, 222, 223]. In fact, due to a reduction in the plate bending stiffness, the residual compressive strength of laminated composites decreases if the size of the delaminations created by impact is large, which is expected to occur

in thick-ply laminates, but also if the number of delamination planes increases, which happens when the number of plies in a laminate increases [220, 222], as in the case of thin-ply laminates. This observation highlights the importance of understanding, through both experimental and advanced numerical analyses, the effect of ply thickness on impact resistance and damage tolerance of laminated composites.

Hitchen and Kemp [216] investigated the effect of the stacking sequence on the impact resistance and damage tolerance of a carbon/epoxy composite laminate, performing LVI and CAI tests. After LVI testing, the lay-ups with higher number of interfaces (i.e. thinner ply blocks) showed the smaller total delamination areas, attributed to a higher energy absorption for delamination initiation. The CAI strength, however, showed no trend with the number of interfaces; in other words, ply thickness did not show any effect in the residual strength of the tested plates.

Fuoss et al. [223] experimentally and numerically examined the effect of blocking plies together in the impact resistance of carbon/epoxy composite laminates by means of LVI testing and quasi-static simulations. Stacking sequences with no ply blocking and groupings of two and three plies were investigated. Ply blocking was found to reduce the damage resistance in a laminate. Dispersed-ply laminates contained the smallest damage area, whereas laminates with blocks of three plies had twice the damage area of the former. The location of the ply blocks also had an effect on the damage resistance. A larger damage area was observed when the ply grouping was located near the impact and back faces of the laminate, whereas a better configuration was achieved by uniformly distributing the ply grouping through the laminate. According to this study, stacking together plies with the same fibre orientation increase the stress concentration at the adjacent interfaces, due to the increased bending stiffness within that ply group, creating larger delaminations. Ply grouping also reduces the number of interfaces available for delamination, since delaminations can occur only at interfaces that contain different fibre orientations between the adjacent plies. Because delamination acts as an energy absorbing mechanism, reducing the number of locations available for delamination results in an increase of the delaminations size at the remaining interfaces.

In a study carried out by de Freitas and Reis [219], impact resistance and damage tolerance of two different carbon/epoxy composite systems were assessed by means of LVI and CAI. Results have shown that the delaminated area after impact is highly dependent on the number of interfaces between plies, which increases with decreasing ply thickness. Higher delaminated areas were observed in laminates with fewer interfaces, i.e., in laminates with thick plies. However, the compressive residual strength was scarcely affected by the stacking sequence.

Sihn et al. [53] conducted LVI testing on thin- and blocked-ply laminates and compared C-scan images showing the size and depth of the delamination damage due to impact loading. CAI tests were also performed. The C-scan images indicated that the overall size of delamination damage was similar for thin-ply and blocked-ply specimens. However, the stress-strain behaviour after the CAI tests indicated less severe delamination damage in the thin-ply laminates. These results, even though preliminary, did not completely agree with those from Refs. [216, 219, 223].

Aymerich and co-authors [12, 13] studied and compared the behaviour of blocked- and dispersed-ply cross-ply laminates under LVI and CAI, aiming to study the effect of the extent and type of damage on the performance of through-the-thickness stitching reinforcements. It was reported that, for laminates comprising ply blocking, the introduction of stitching does not affect the initiation of delamination under LVI, acting, in fact, as triggering locations for matrix cracking. However, it decreases the total delamination area, because of the bridging effect exerted by the unbroken stitching yarns. Negligible effect on the CAI performance and failure modes was observed, even though delamination growth was restricted. A possible explanation is the detrimental effect of the stitching yarns on the compressive strength of the laminate.

For laminates with dispersed plies, stitching was seen to degrade the response to LVI, caused by a suppression or delay of delamination at the interface closer to the impact side and by inducing fibre fracture in the opposite plies [12, 13]. Dispersed-ply laminates, either stitched or not, had smaller delaminated areas when compared to blocked-ply laminates. The CAI performance, however, improved with the introduction of the stitching yarns, due to the bridging effect they exerted. Unlike the blocked-ply laminates, the stitching yarns in the dispersed-ply laminates were not prone to fail during LVI, resulting in a superior CAI performance. It was also noticed that the improvement of the CAI performance of the

dispersed-ply laminates increased with increasing impact energy. This study shows how dispersed-ply laminates are able to suppress subcritical damage mechanisms occurring under LVI, and how these laminates take greater advantage of the through-the-thickness reinforcements when it comes to improvements of their residual strength.

Yokozeki et al. [134] also characterised the damage tolerance of thin-ply carbon/epoxy laminates by means of CAI testing. This comparative study addressed laminates with the same in-plane stiffness, total thickness and lay-up ratios, but manufactured using either conventional (145 g/m^2) or thin-ply (75 g/m^2) UD tape (see also section 2.4.1). It was performed to clarify the effectiveness of the compressive and damage tolerance characteristics of spread-tow thin-ply laminates. The LVI and CAI test results show that the projected post-impact delamination areas were almost identical between conventional and thin-ply laminates; however, the CAI strength of thin-ply laminates were slightly higher (8%) than that of conventional laminates, which may result from the narrow delamination widths and superior resistance against delamination growth observed in thin-ply laminates. These results agree with those obtained by Sihn et al. [53], while contradicting those obtained in Refs. [216, 219, 223].

In a later study, Yokozeki et al. [221] assessed in more detail the damage resistance of spread-tow thin-ply laminates by means of quasi-static indentation, claiming that the tested carbon/epoxy laminates exhibit similar mechanical response and damage process under transverse dynamic and static loading [213]. Conventional and thin-ply quasi-isotropic laminates (the same used in the previous study [134]) were tested. Results showed that matrix cracking was first observed in the back surface ply, and delaminations were induced inside both conventional and thin-ply laminates. However, in the conventional laminates, accumulation and growth of delaminations and matrix cracking was observed, whereas sudden fibre fractures occurred in the thin-ply laminates. Accordingly, it was considered that the thin-ply laminates had higher damage resistance against matrix cracking and delamination under out-of-plane transverse loading than the conventional ones, contrary to the conclusions made in the previous research [134], which reported similar results for LVI testing of both laminates.

González et al. [220] studied the effect of ply thickness on rectangular, flat, monolithic laminated composite plates subjected to drop-weight LVI (their results have also been discussed by Camanho et al. [146]). Various stacking sequences comprising dispersed and blocked plies were used to study ply thickness effects. All laminates had the same nominal thickness, but different ply block thicknesses and different number of interfaces. In spite of having similar stiffness, the resulting impact responses of all laminates were quite different. According to this study, the use of thick ply blocks reduces the impact resistance of the structure, because increasing the ply thickness (i) the delamination threshold load and the peak force were both reduced under equal impact conditions, and (ii) the response was elongated in time, and larger delaminations were created due to the reduced number of available interfaces. González et al. [220] also evaluated the effect of ply thickness on damage tolerance, assessed by CAI tests. Unlike impact resistance, the damage tolerance did not seem to be reduced by increasing the ply thickness. For the same impact conditions, all laminates showed similar residual compressive strengths (confirming the results obtained in Refs. [216, 219, 223]).

Saito et al. [224] focused their study on the effect of ply thinness on the impact damage morphology of quasi-isotropic CFRP laminates. They reported a drastic decrease in transverse cracking in the thin-ply laminates. Transverse cracks occurred at every ±45° plies located above the 0° layers in conventional laminates, inducing delaminations along their interfaces. For thin-ply laminates, a single transverse crack at the middle thicker ply (due to laminate symmetry) could be observed in the cross section of the specimens, connected to a large delamination that tended to propagate in a specific interface. Using a non-standard CAI test apparatus, they observed a noticeable increase of the CAI strength of the thin-ply laminates when compared to the laminates with conventional ply thicknesses, even though the CAI failure morphologies were not very different. In spite of having a larger projected delamination area (due to the extensive propagation of a single delamination), the resulting sublaminates of the thin-ply laminates were substantially thicker than those originated in the thick-ply laminates, where delaminations were observed along several interfaces. According to Saito et al. [224], the superior CAI strength observed in the thin-ply laminates was related not only to the damage morphology resulting from the LVI event, but also to their intrinsically higher compressive strength, attributed to the improved fibre alignment of the thin plies, which were finely dispersed between plies of different fibre orientation, restraining fibre kinking.

2.4. Effect of ply thickness scaling on the mechanical response of composite laminates

Sebaey et al. [222] studied the effect of 0°-ply blocking (or clustering) on the damage resistance and tolerance of laminates with fibre orientations not limited to the conventional 0°, 90° and ±45° angles (referred to as "dispersed laminates") by means of LVI and CAI testing. Laminates with similar in-plane and equivalent bending stiffnesses were tested: a conventional quasi-isotropic laminate (baseline), with no ply blocking, and two dispersed laminates with blocks of four and two 0° plies in the mid-plane and in the outer layers, respectively. These authors showed that ply blocking has a negative effect on the impact response of dispersed laminates. On the other hand, improvements on the damage tolerance and post-impact response up to 30% were reported when introducing 0°-ply blocking, namely at the outer layers, possibly due to an increase of the bending stiffness of the surface sublaminates.

In their extensive experimental programme on ply thickness effects, Amacher et al. [58] observed that, under impact, laminates with very thin plies (0.03 mm thick) exhibit a quasi-brittle failure with extensive intralaminar cracking across the fibres. Important delamination areas were observed, apparently induced by the large intralaminar cracks. On the other hand, laminates with intermediate ply thicknesses (0.10 mm) exhibited the best performance, minimising the projected damage area. Local intralaminar fracture and local indentation could be observed in the impact area. For thick-ply laminates (0.30 mm thick plies), delamination is predominant, and intralaminar fracture is barely observed for the impact energies used in these tests.

With the aim of contributing for the development of modelling methods for thin-ply weaves, Olsson [225] presented an analytical model to assess large mass impact response and damage growth in thin-ply composite laminates. The model was formulated taking into account damage due to ply shear cracking, delamination, bending failure and membrane failure. Based on the predictions of the proposed model and on experimental evidence, Olsson [225] suggested that, whereas in conventional laminates delamination occurs relatively early, causing a change to membrane dominated behaviour and negligible bending strains, thin-ply laminates show higher resistance to delamination, resulting in bending-dominated compressive fibre failure. Even though Olsson [225] was not certain about the origin of this behaviour, experimental observation suggests that delamination in impacted thin-ply laminates is generated by fibre fracture, rather than being the cause of it. An additional factor pointed out by Olsson [225] is related to the effect of higher *in situ* transverse shear strengths in thin-ply laminates. Olsson [225] suggests that the transverse shear cracks that typically occur in laminates with plies of conventional thickness, which can deflect into delaminations, tend to shift to longitudinal shear cracks in thin-ply laminates. These longitudinal shear cracks should induce intralaminar crack growth that is likely to be associated with a higher toughness due to bridging and a more tortuous crack path. This may have an effect on the global impact response of thin-ply laminates.

In an interesting work, still to be published, González et al. [226] tested carbon/epoxy quasi-isotropic laminates with the same thickness but produced by stacking plies of different areal weights, corresponding to mean cured ply thicknesses of 0.03 mm, 0.10 mm and 0.30 mm. Drop-weight impact tests were performed. When subjected to LVI, the thin-ply laminates exhibited a brittle response, characterised by substantial intralaminar damage and indentation, as well as partial penetration for the highest energy level. From these experiments, a lower threshold for BVID can be expected for thin-ply laminates. Compared to the thick-ply laminates, peak loads about 40% lower have been obtained for the highest energy level. However, the projected delamination areas have not been presented yet, and no clear conclusions can be made about the impact resistance of the tested laminates.

It must be recognised that no clear, general conclusion can be drawn about the effect of ply thickness scaling on the impact resistance and damage tolerance of composite laminates. One possible problem has to do with appropriate laminate definition to properly address the effect of ply thickness on complex types of loading such as LVI and CAI.

According to Lopes et al. [227], it is important to ensure that both the in-plane and the bending stiffness of the lay-ups under study are kept constant, to avoid misinterpretations of the results, something not specifically taken into account in previous studies. In fact, in out-of-plane LVI events, which are generally governed by global deflections, bending stiffness plays an important role on the way damage develops on the impacted laminate, since, in such situations, the delaminated area is highly dependent on the out-of-plane displacement of the laminate during impact [227]. Further research, including experimental testing together with reliable analytical [220] and numerical (FE) [228] analyses on laminates designed with

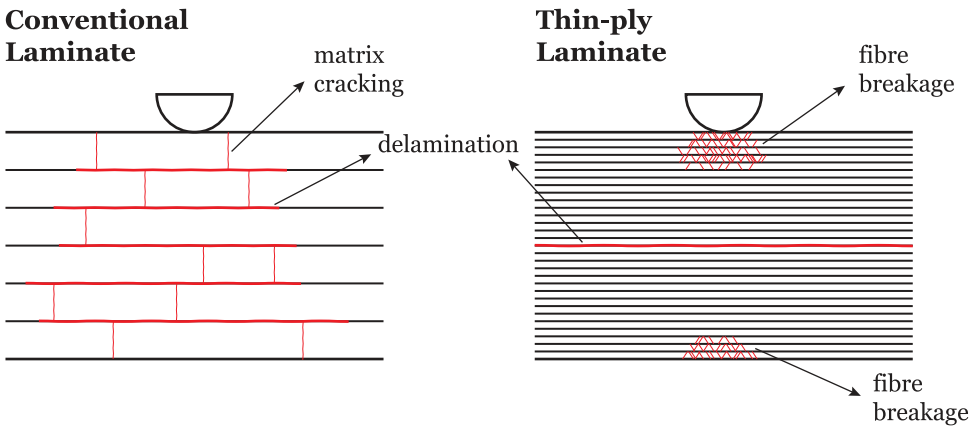

Fig. 2.7. Schematic showing the differences between the impact damage morphology of conventional and thin-ply laminates.

the same in-plane and bending stiffnesses [227], is therefore crucial for a better understanding of the effect of ply thickness scaling on damage resistance and tolerance of composite laminates.

In addition, from previous work on the impact response of thin-ply laminates, it is becoming clear that these laminates exhibit a characteristic behaviour that differs substantially from conventional composites. Matrix cracking and sequential delamination beneath the impact point are practically suppressed [224].

Instead, fibre breakage on both impacted and non-impacted faces [58, 221, 226] due, respectively, to very high compressive and tensile stresses, and a large delamination at or around the mid-surface [224] where the highest shear stresses occur, seem to be the relevant damage mechanisms in impacted thin-ply composites (figure 2.7). Deeper indentation fingerprints can also be expected due to the high local compressive stresses beneath the impactor, which may reduce the threshold for BVID, as suggested by González et al. [226]. Hence, from the damage resistance and damage tolerance point of view, thin-ply laminates have to be addressed differently from conventional composites [225]. The particular mechanical response of thin-ply laminates must be taken into account in the design process to fully exploit their special features. For instance, it may be necessary to design thin-ply composite structures specifically for impact resistance instead of damage tolerance.

Because the threshold for BVID and the extent of internal damage at this threshold are significantly lower than in conventional laminates, it can be assumed that the corresponding degradation of the structural integrity is equally lower for impact events in thin-ply laminates whose damage is left undetected. Therefore, for a given application, the design must be driven by the resistance to impact damage, in order to ensure that it does not occur under normal circumstances, and not by the residual strength for a given level of pre-existing damage that cannot be detected. It is not clear, though, what the optimum solution for a given application with important out-of-plane dynamic requirements would be, if a conventional low-grade laminate designed for damage tolerance, or a thin-ply laminate designed for damage resistance. Studying the effect of ply thinness is therefore of great importance to understand objectively how to address damage resistance and damage tolerance of thin-ply laminates, for instance conducting experimental testing and analyses on spread-tow thin-ply and conventional laminates designed with the same in-plane and bending stiffnesses [227].

2.4.6. Fatigue

Even though high performance reinforcements such as carbon fibres are known not to suffer from fatigue damage, providing composite materials with a greater fatigue life than comparable metallic structures [173], cyclic loading is still a very important precursor of subcritical damage mechanisms in composite laminates. These include matrix cracking, which occurs in the very early stages of the fatigue life of the material, and, more importantly, delamination, which constitutes its largest portion [173, 229, 230]. On the other hand, fibre failure represents just a short damage accumulation phase at the end of fatigue life [230].

2.4. Effect of ply thickness scaling on the mechanical response of composite laminates

In the case of notched coupons under fatigue loading, the development of subcritical damage is enhanced, as the relative damage growth rates will not be the same and matrix-dominated failure modes such as matrix cracking and delamination are likely to become more dominant before fibre failure. In addition, damage development is more progressive and more dispersed in the 90° plies than in quasi-static loading [173]. For example, depending on the load severity, sudden or gradual delamination propagation may occur in specimens subjected to tension-tension open-hole fatigue tests [173]. On the other hand, matrix cracking and splitting can occur in specimens tested under fatigue at loads as low as 40% of the static notched strength, with delamination practically absent [173].

Because the reduction of the ply thickness is known to suppress subcritical damage mechanisms, it is believed that it should also have an important effect on fatigue behaviour of advanced composites. Moreover, the certification of primary composite structures, especially for aeronautical applications, is typically based on "no growth" criteria for delaminations emanating from stress raisers such as ply drop-offs or free-edges (for instance, in open holes) [230]. Therefore, the intrinsic ability of thin-ply laminates to delay the initiation and growth of delamination may also result in benefits when it comes to certification of airborne composite structures.

Furthermore, suppression of matrix-dominated failure mechanisms (as observed, for instance, not only in thin-ply laminates, but also in tougher thermoplastic-based matrix composites), may favour fibre failure in the vicinity of the notch boundary, reducing the long-term fatigue performance of the composite laminate [173]. Therefore, assessing the effect of ply thinness on the fatigue response of smooth and notched coupons and structures is deemed very important, in order to clarify the effect of these conflicting mechanisms.

In a thorough review, Berthelot [87] addressed the development of transverse cracking and delamination in cross-ply laminates subjected to quasi-static and fatigue loading. Regarding transverse cracking in fatigue, Berthelot [87] reported that the constraining effect in thin transverse plies generally leads to limited growth of cracks through the specimen width, whereas thicker plies show generalised transverse crack propagation through the ply width, in particular for high applied maximum fatigue stresses.

Nishikawa et al. [66, 231] studied the fatigue behaviour of thin-ply and conventional CFRPs. Plain-woven fabrics manufactured using very thin and wide spread tows were tested under tension-tension fatigue loading. The experimental results showed that the fatigue lives of spread-tow plain-woven laminates were higher than those of conventional types. It was also observed that fatigue crack formation and propagation were constrained by using thin plies. Similar conclusions regarding tension-tension fatigue testing were also reported by Yokozeki et al. [134] when studying thin-ply laminates of carbon/epoxy UD tapes.

Sihn et al. [53] performed tensile fatigue tests in thin-ply and blocked-ply carbon/epoxy laminates. Unnotched and open-hole specimens were tested. From the unnotched tensile fatigue testing, it was observed that, unlike thin-ply laminates, blocked-ply laminates show increasing edge strain near the free edges as the fatigue cycles increase. Besides, X-ray photographs of the tested specimens have shown extensive microcracking and FED on the blocked-ply laminates, whereas thin-ply laminates did not show any visible damage. On open-hole tensile fatigue, some splitting around the open hole on the thin-ply laminate was observed, with no delamination along the specimen outer edges or microcracking. For the thick-ply laminate, massive delaminations around the open hole and outer edges, plus microcracking along all ply angles, were observed.

Amacher et al. [36, 37, 58] also studied the effect of ply thickness on the response to open-hole tension-tension fatigue. Quasi-isotropic laminates of different grades, including 30 g/m^2 ultra-thin plies, were tested. Very significant improvements for the onset of damage and, in some cases, ultimate strength were obtained when decreasing the ply thickness. This was related to a major change in the damage progression and failure modes of the laminates, caused by a systematic delay or even suppression of transverse cracking and delamination growth in thin-ply laminates, resulting in no stiffness degradation nor damage occurrence. Thick-ply laminates, on the other hand, exhibited a progressive damage accumulation by delamination and transverse/shear cracking of the 90° and ±45° plies, resulting in a clear fatigue life reduction trend. From these results, it was therefore clear that using thin plies delays the onset of damage, resulting in a substantial increase of the fatigue lifetime [58].

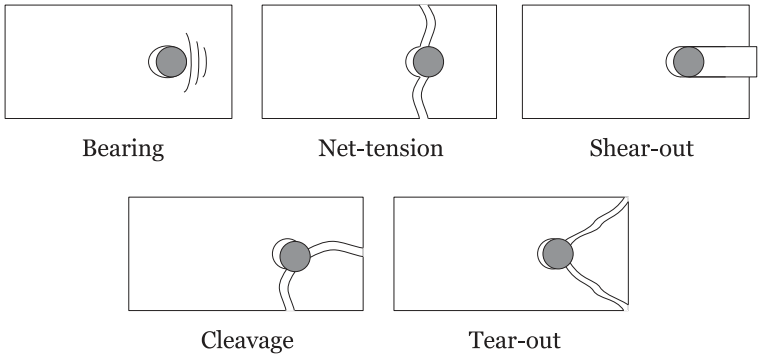

Fig. 2.8. Joint failure modes (after Ref. [237]).

2.4.7. Bearing strength

Virtually every large-scale composite structure, particularly for application in the aeronautical and space industries, contains joints. The reasons behind their use are well known, but manufacturing constraints and requirements related to accessibility to the structure, quality control, structural integrity assessment and part replacement are the main ones [232–235]. Among the types of joints used in large-scale composite structures, mechanically fastened joints are particularly common, and often the only feasible solution [181]. They are used in composite structures since the 1960's, when high modulus, high strength composites first came into use [25], and the proliferation of composite materials in aero-structures in recent years did not limit the usage of mechanical fastening, mostly because they are relatively inexpensive to manufacture and can be disassembled [235, 236]. However, due to the stress concentrations created, mechanically fastened joints are generally the critical part of a composite structure, as they are a source of weakness and compliance [235]; consequently, the soundness of the joint design procedure used is reflected on the overall weight and cost of the composite structure [235]. In fact, with the aim to reduce cost and number of holes in composite components, and to reduce the weight by eliminating build-ups for fastener countersinking and bearing strength, it is generally recommended to use adhesive bonding for thin, lightly loaded composite structures, restricting the use of mechanical fastening to thicker, more heavily loaded structures [25].

The behaviour of composites in bolted joints differs considerably from that of metals. The quasi-brittle nature of composite materials requires more detailed analysis to address the different failure modes occurring in the vicinity of the loaded fasteners. In composites, the stress concentrations dictate the components static strength to a larger extent than in metals due to the absence of yielding, conducting to less efficient joints. Therefore, when designing composite joints, several factors need to be taken into account, namely the brittleness of the composite laminate, the use of highly orthotropic laminates that promote high stress concentrations, the anisotropy in both stiffness and strength properties, and geometrical parameters such as edge distances and hole spacings [25, 235].

In addition, different failure modes can occur in mechanically fastened joints in composite laminates. Bearing, net-tension, shear-out, cleavage and tear-out failure can occur due to in-plane loading [237] — figure 2.8. Failure of mechanically fastened joints can also occur due to out-of-plane loading, typically resulting in a pull-through failure mode.

One of the most common failure modes is bearing failure (figure 2.8), which occurs predominantly when the fastener diameter is a small fraction of the plate width. This is a progressive failure mode and occurs when the laminate is no longer capable of sustaining the accumulated local damage [233, 236, 238]. Before final failure, nonlinearities in the load-displacement relation appear, with damage starting as localised delaminations, followed by matrix cracks through the laminae thickness, which lead to further delaminations [238]. Bearing failure is also related to fibre-buckling and fibre-matrix crushing [100]. Its damage is typically characterised by an elongation of the hole [233].

The bearing strength of a laminate, i.e. the load corresponding to bearing failure, is often taken as the measure of a laminate's mechanical performance when subjected to local compressive efforts, typical of mechanically fastened

joints. Since bearing failure is non-catastrophic, being characterised by a progressive accumulation of damage and by the corresponding permanent deformation of the hole, different definitions can be used: maximum load sustained by the joint, the first load drop, the onset of nonlinearity in the bearing strain-bearing stress relation, or a limit value for the permanent deformation of the hole. The correct definition of bearing strength is not clear, as it depends on the permanent deformation in the hole and on the damage mechanisms occurring in the material [235]. Nonetheless, comparisons for the same definition are generally accurate and allow a reliable source of analogy between different laminates.

Given the ability of thin-ply laminates to delay, or even suppress, subcritical, progressive damage mechanisms such as delamination and matrix cracking, an improved performance of these materials when subjected to bearing loads is expected. For example, Camanho and Matthews [239], by means of a 3D FE model, have shown that laminates with thinner ply blocks lead to higher delamination onset loads and smaller initial delaminated areas, evidencing the advantage of using thin plies in composite mechanical joints.

In the early 1980's, Garbo and Ogonowski [240] performed an extensive study addressing the design strength and life of mechanically fastened composite joints, including stacking sequence effects. Laminates with the same in-plane stiffness but different 0° ply block thicknesses were studied. Tests under different environments were conducted: room temperature dry and elevated temperature wet. They observed that laminates with thicker blocks of 0° plies have lower bearing strengths, independently of the environmental testing conditions.

More recently, in a study addressing the notched response of NCF thin-ply laminates, Arteiro et al. [122] have shown that these laminates, in relative terms, have an improved bearing performance when compared to aerospace-grade composite systems. With a normalised bearing strength up to approximately 20% higher, such improved performance was attributed to the ability of thin-ply laminates to suppress the onset and propagation of damage mechanisms such as matrix cracking, delamination, fibre kinking and through-the-thickness shear cracking.

Amacher et al. [36, 58] performed single lap bearing tests, under standard and hot-wet (90°C) environmental conditions, on quasi-isotropic laminates of different grades, including 30 g/m^2 ultra-thin plies. All tested specimens had the same nominal thickness. When compared to the thick-ply (300 g/m^2) laminates, the thin-ply laminates exhibited a bearing strength improvement of 23% and 138% for the standard and hot-wet conditions, respectively. The occurrence of macroscopic through-the-thickness damage in the thin-ply laminates was negligible in both conditions, compared to the extensive delamination and matrix cracking observed in the thick-ply laminates.

2.5. Applications of thin plies

Besides the previous works about thin-ply laminates focused on the effect of ply thickness on the mechanical response of composites [35–38, 53, 58, 66, 84, 85, 122, 123, 133–135, 162, 182, 221, 224, 225], other studies have been published in the recent years about the application of thin-ply laminated composites as an effort not only to better understand this new type of materials, but also to exploit their potential benefits.

Moon et al. [241] studied some solutions to improve not only the mechanical properties, but also the resistance against low earth orbit (LEO) environment of carbon/epoxy composite laminates for aerospace applications, including the use of spread-tow thin plies. Quasi-isotropic laminates with 0.125 mm thick plies (conventional low grade *prepreg*) and 0.060 mm thick plies (thin-ply laminate) were investigated. Both laminates had the same thickness. Results showed that the tensile strength of the thin-ply laminate was slightly higher, either with (12.1%) or without (8.9%) LEO environment exposure. Conventional laminates showed a sudden large increase in strain and load drops induced by progressive failure of the specimens, including matrix cracking, delamination and fibre breakage (these phenomena were especially evident with LEO environment exposure). In contrast, thin-ply laminates exhibited stable stress/strain curves (even with LEO environment exposure), meaning that less progressive damage had occurred before fibre failure due to the high constraining effect between the thin plies.

El-Dessouky et al. [54] studied the production and mechanical response of a thermoplastic matrix reinforced by a thin-ply plain weave textile. This application was motivated by the low crimp level and closest proximity of adjacent tows

within the woven structure of STFs that should enable better resin wet out than conventional textiles. These authors compared a spread-tow 12k plain weave fabric and a conventional 3k 5-harness satin, both impregnated with polyphenylene sulphide thermoplastic resin. It was shown that the void content was higher in the case of the conventional fibre-reinforced thermoplastic (FRTP), promoted by the more compacted fibre tows that made it difficult for the viscous resin flow to reach the innermost regions of the tows. In contrast, the spread-tow FRTP exhibited wider inter-fibre spacing, which enabled easier flow of the resin inside the tow and, consequently, better fibre wetting, resulting in lower void content. The lower crimp angles in the spread-tow FRTP also resulted in considerably smaller resin rich areas, which was reflected in better mechanical properties. An experimental programme focused on the flexural properties of these composite materials showed that the spread-tow FRTP, which was thinner and lighter than the conventional one, exhibited slightly better specific modulus and significantly higher specific strength.

Kuraishi et al. [69] evaluated the applicability of a thin-ply NCF to aero-structural parts through the fabrication trial of a representative stiffener. Part compression (crippling) testing and flat coupons testing, including LVI, were performed. According to these authors, the ply thinness contributed for the good quality of the parts manufactured; the thin-ply NCF conformed to the tool without local bridging or wrinkling. Even though no improvements were found for the residual resistance to impact damage, part production using thin-ply NCFs was considered a promising low cost option.

Czél and Wisnom [23] studied the introduction of ultra-thin carbon plies in glass/epoxy composites to produce, through hybridisation, a pseudo-ductile high strength material. Motivated by the lower ERRs of thinner plies, which delay the propagation of intra- and interlaminar cracks, they have suggested the combination of the benefits of both ultra-thin plies and hybridisation to exploit the full pseudo-ductility potential of these material structures.

According to Czél and Wisnom [23], the use of carbon thin plies with outer glass/epoxy laminae is a good combination because (i) there is a significant difference in strains to failure and stiffness of the constituents, resulting in a considerable change in properties, (ii) hybridisation is possible since both materials come in similar *prepreg* forms, with compatible resin systems, (iii) thin-ply *prepregs* are commercially available, (iv) the damage tolerant outer glass/epoxy laminae act as protective layers, avoiding damage of the thin carbon plies during manufacturing (and suppressing grip stress concentrations during experimental testing), and (v) the translucent character of the glass/epoxy laminae facilitates delamination visual detection. Moreover, the mode II ERR, which is the parameter governing the stable failure behaviour of ply-by-ply hybrid laminates after failure of the ply with lower ultimate strain (i.e. the carbon ply), depends on the thickness of the low strain-to-failure layer. Thinner (carbon) low-strain layers originate a lower mode II ERR, delaying delamination, which is potentially the most unstable failure mechanism in ply-by-ply hybrid laminates.

Czél and Wisnom [23] showed that, in hybrid composites with standard carbon ply thicknesses, failure generally occurs as a single fracture in the low-strain (carbon) layer, instantaneously followed by unstable delamination, which appears on the stress-strain diagrams as a significant load drop. Only then comes a stress recovery as the high strain (glass) fibres pick up all the load. But using a thin-ply hybrid laminate, these authors have shown that the failure behaviour is, instead, characterised by progressive fragmentation or multiple cracking of the carbon layer, with some local delaminations around the carbon ply cracks, followed by stable localised pull-out. The sudden stress drop observed in conventional hybrid laminates is, thus, replaced by a stable transition between the stress peaks of the intact hybrid and the stress carried by the fibreglass layers after fracture of the carbon ply. This stable transition appears as a significant change in slope of the stress-strain curves, resulting in the desired pseudo-ductile behaviour.

To obtain a more stable pseudo-ductile failure type, Czél et al. [242] proposed a hybrid continuous glass/discontinuous carbon fibre-reinforced laminate configuration. The hybridisation approach is similar to that studied by Czél and Wisnom [23], but replacing the mid-continuous carbon layer by a discontinuous one. This special discontinuous carbon layer resulted in an improvement of the tensile failure character over the continuous hybrid configuration by replacing the significant stress drop that occurs upon the continuous carbon layer fragmentation with a gradual degradation of the tangent stiffness.

Fuller and Wisnom [243, 244] exploited the damage suppression capability of thin-ply angle-ply carbon/epoxy laminates to achieve a pseudo-ductile behaviour under uniaxial tension through fibre reorientation towards the direction of

loading. The fibre rotation, via a scissoring action permitted by matrix plasticity, resulted in large strains to failure and post-yield stiffening. However, in conventional angle-ply laminates, failure often occurs prematurely due to matrix cracking and delamination (e.g. Ref. [139]). Suppressing these damage mechanisms through the use of ultra-thin plies, pseudo-ductile, high-performance laminates can be obtained. X-ray computed tomography imaging had shown that damage within the gauge area was very limited, and that failure was a local event rather than a complex combination of different damage mechanisms, as observed in conventional angle-ply laminates. Failure occurred across all plies, with no signs of edge delamination. Large nonlinear strains were observed in the tested thin-ply angle-ply laminates, resulting in a promising pseudo-ductile behaviour. The so-called "*thin-ply effect*" ensured that the post-yield condition was well-defined and damage free, preserving the structural integrity of these laminates up to failure, in spite of the highly nonlinear response.

Fuller and Wisnom [244] also showed how thin-ply angle-ply laminates can be tailored for strength or ductile behaviour according to requirements simply by modifying the fibre angle, even though there was obviously a compromise between strength and ductility. In addition, based on this delamination and matrix cracking suppression capability inherent to thin-ply laminates, Fuller and Wisnom [245] proposed a simple analytical modelling approach for thin-ply angle-ply laminates based solely on the plasticity of the matrix, valid only for in-plane uniaxial tensile loading, though. Yet, this could be a very useful tool for preliminary design and optimisation of high-performance pseudo-ductile carbon composites (which do not rely on complex, costly and time consuming production or tailoring techniques and can be readily obtained from products available in the market).

Combining the approaches discussed in Refs. [23, 243], a pseudo-ductile behaviour has been achieved by Fuller et al. [246] using thin-ply angle-ply laminates with central UD thin plies through fragmentation of the latter and dispersed local delamination. With this new approach, Fuller et al. [246] intended to take advantage of the nonlinear stress-strain response and damage suppression exhibited by thin-ply angle-ply laminates, improving the laminate modulus, "pseudo-yield" stress and ultimate strain by combining these lay-ups with centrally located UD plies. Before the onset of fragmentation of the centre 0° ply, a roughly linear stress-strain response was observed. After fragmentation onset, which occured at the longitudinal failure strain of the central 0° ply, the stress remained approximately constant, as it was steadily transferred from the fragmented UD ply to the outer angle plies, until a point from which the angle plies take up any further loading. From this point, reloading at a lower modulus is observed, until final laminate failure.

More recently, Baley et al. [247] reviewed the application of the spread-tow thin-ply technology as a means to improve the quality of composite racing yachts construction. As observed by Arteiro et al. [122], the combination of the spread-tow thin-ply technology with out-of-autoclave production methods (using vacuum bag-only *prepregs*) results in laminates of great quality. This makes high performance composite structures reliable for racing yacht manufacturing by avoiding the use of autoclaves, which impose limitations on production rate, production time (due to long thermal cycles), energy consumption, and structures' size [247].

2.6. Concluding remarks

Ultra-thin plies manufactured using the spread-tow thin-ply technology present a series of advantages in terms of design and structural performance. The former include (i) potential to use heavy tow yarns, such as 100k or 200k, to cost-effectively obtain low-grade and thin-ply tows, (ii) improved surface appearance, fibre orientation and distribution, and better dispersion and uniformity of plies, (iii) smoother ply drops, (iv) reduced crimp angle and tow flexure when used in woven fabrics, (v) laminate homogenisation, making mid-plane symmetry irrelevant due to negligible thermal warpage, and making the concepts of anisotropy of unbalanced laminates and passive aeroelastic tailoring doable, (vi) possibility of using smaller relative fibre orientations between adjacent plies, and (vii) faster and simpler design due to the absence of subcritical damage mechanisms such as matrix cracking and delamination, showing potential for better optimised laminates and higher consistency in defining safety factors.

All these potential advantages make the spread-tow thin-ply technology highly attractive for a number of lightweight and structural applications. It is, therefore, not surprising to see that different reinforcement configurations produced using

this technology, including ultra-thin UD tapes, STFs and thin-ply NCFs, are already commercially available.

In terms of structural performance, the literature shows that some advantages are intrinsic to the ply thinness obtained with the spread-tow thin-ply technology, either as UD lamina or when incorporated into multidirectional laminates. These advantages include (i) higher UD longitudinal compressive strength, (ii) higher *in situ* strengths, (iii) higher resistance to delamination due to lower interlaminar ERRs, (iv) higher laminate tensile and compressive strengths, (v) higher LVI resistance, (vi) improved fatigue response, and (vii) higher bearing strengths, which are either the result of microstructural uniformity or the result of subcritical damage suppression.

However, the damage suppression capability of thin-ply laminates has also a potential negative effect on the mechanical response of coupons or structures containing notches. In this case, damage suppression reduces the blunting effect that provides conventional notched composites with a more gradual failure behaviour. Consequently, notched coupons or structures made of thin plies are prone to early unstable failure across the ligament sections, resulting in lower notched strengths.

Moreover, the possible drawbacks or benefits of spread-tow thin-ply laminates with respect to other aspects of their structural performance are not clear. For instance, it is not clear what is the effect of ply thinness on the intralaminar fracture toughness associated with tensile and compressive longitudinal fracture perpendicular to the fibre direction. In addition, contradicting results about the effect of ply thickness scaling on the compressive notched strength and damage tolerance (or CAI strength) of advanced composite laminates were found in the literature.

In spite of the great number of publications which address the effect of ply thickness scaling on the mechanical and structural response of advanced composite laminates, a thorough study including different spread-tow reinforcement configurations with areal weights below the conventional low-grade is still missing. Furthermore, a discussion about the modelling and design strategies for laminates made of spread-tow reinforcements, and hints on how these advanced laminates can be used to facilitate the design process and improve the structural performance of composite structures is of great importance for the understanding and acceptance of the spread-tow thin-ply technology as a valuable tool to reduce weight and cost of composite structures. Also, a detailed understanding of the micro-mechanical origins of the *in situ* effect is still missing, which can be addressed, for instance, by means of computational micro-mechanical models.

It is recognised that the brittle failure behaviour of thin-ply laminates may be unsuitable for applications with unpredictable loading conditions, where high safety factors are used to ensure the risk of catastrophic failure is acceptably low [26]. But in this case, laminate design concepts based on combinations of thin-thick plies [222, 248], pseudo-ductile lay-ups [243] or hybrid configurations [23, 161], which exhibit higher structural "*forgiveness*", can help widening the range of applications of composite structures.

Finally, it should be noted that more sustainable and improved design of composite structures, in particular for the aeronautical industry, can only be achieved if relying on the most advanced theories for failure prediction, which must also be simple enough for ready understanding and application at an industrial level. In fact, according to Bažant [131], "*some segments of the engineering community need to be educated in the concepts of fracture mechanics, including the size effect aspects, in order to be willing to accept new improved design procedures, e.g., for concrete structures and fiber composites*".

Part III

Experimental test campaign

Chapter 3

Hole size effects in thin-ply laminates

Laminates with sufficiently thin plies are known to fail by fibre fracture, delaying or suppressing subcritical damage mechanisms such as delamination and fibre-matrix splitting. In spite of the enhanced mechanical performance provided by this damage suppression capability, a negative impact on the notched response of structures loaded in tension is expected. In fact, inhibiting local stress redistribution at the vicinity of the notch results in premature brittle failure of the composite. This disadvantage has been actually pointed out as one of the main obstacles to the widespread use of thin plies. In this chapter, an assessment of the hole size effect on laminated composites incorporating spread-tow thin plies is presented. Open-hole and centre-notched tension tests are performed on laminates with the same nominal thickness produced from unidirectional *prepregs* of the same material system but with different ply thicknesses. Unlike previous studies addressing the effect of ply thickness on the hole size effect, the intermediate- and thick-ply laminates were obtained from unidirectional tapes of different areal weight. In order to understand the differences of using blocked plies or high-grade systems, an alternative thick-ply laminate with thin plies blocked together was used.

3.1. Introduction

The increasing use of composite laminates in the design of structural parts also requires a better understanding of the mechanical performance and structural integrity of these materials, especially in the presence of high stress concentrations. Many composite structures, such as those used in the aeronautical industry, contain filled and opened cut-outs for joining and access purposes. The presence of a hole or any other discontinuity in a composite structure introduces high local stresses which may result in the development of sub-critical damage mechanisms that sometimes are not present in smooth components. When loaded in tension, localised delaminations, starting at matrix cracks in the off-axis plies, occur in the vicinity of the hole before the final collapse of the laminate, extending and joining up, and stepping through the thickness locally; splitting in the 0° plies may also occur. This localised damage, which blunts the notch, affects the stress concentration at the hole edge, and consequently the notched strength [144, 163].

Composite structures are also highly susceptible to severe discrete sources of damage, such as impacts from bird strikes or fuselage penetration in aeroplanes with open rotary engines. The stress concentrations originating from geometrical discontinuities and from discrete damage result in high stress and strain gradients not present in unnotched laminates, decreasing the strength and conducting to the growth of large damage process zones [196].

In general, before final failure, composite laminates develop subcritical ply damage, which can be regarded as a fracture process zone (FPZ). For very small specimens, the FPZ affects the entire width of the laminate, and the notched strength tends to the unnotched strength. On the other hand, the size of the FPZ in large specimens is negligible when compared to the characteristic dimensions of the specimen. This relative dimension of the FPZ with respect to the specimen size justifies the different strengths observed in small and large specimens [183].

For instance, delamination [144, 163] and fibre-matrix splitting in the 0° plies [121] are known to play an important

role on the tensile notched response and size effect of notched composite laminates. Extensive gauge section delamination, which is prone to occur on laminates with sufficiently thick plies, causes the strength to increase with structural size [144, 163]. However, total loss of structural integrity is likely to occur before failure of the 0° plies due to complete gauge section delamination. Fibre-matrix splitting, on the other hand, is typical of laminates with intermediate ply thickness, and acts as an important notch blunting mechanism [121], improving the notched strength of laminates while maintaining the conventional hole size effect (decreasing strength with increasing structural size). This is typically the most desirable notched behaviour.

Laminates with sufficiently thin plies generally fail by fibre fracture, delaying or suppressing subcritical damage mechanisms such as delamination and fibre-matrix splitting. The enhanced mechanical performance of thin-ply laminates is mainly due to the ability to delay the onset of damage typically observed in composite materials. In general, thin-ply composites exhibit enhanced unnotched strengths [53, 58, 122, 134], potential for improved compressive response [122, 134] and higher fatigue resistance [53, 58, 66, 134]. However, the delay of damage onset has a negative impact in notched structures loaded in tension [58], since it inhibits local stress redistribution at the vicinity of the notch leading to premature brittle failure of the composite. This disadvantage has been pointed out as one of the main obstacles to the introduction of thin plies in a large scale.

Previous studies addressing the effect of ply thickness on the hole size effect were limited to a minimum ply thickness of 0.125 mm [144, 163]. In this chapter, an assessment of the hole size effect on laminated composites incorporating spread-tow thin plies [32] is presented.

Open-hole tests are typically used to study the behaviour of composite laminates with stress concentrations and to assess the effect of size in composite materials. These tests are also required for generation of allowables to support the *Building Block Approach* for composite structures and to meet damage resistance/tolerance requirements in airframe design [25]. In addition, these tests are important for the definition of material/lay-up and geometric parameters ("*characteristic distances*") used in semi-empirical closed-form models [175, 176, 235] for the prediction of the mechanical behaviour of notched composite laminates, and are often used to validate design tools based on analytical methods [25, 121, 135, 175–177, 179, 180, 182, 249].

Additionally, notched specimen configurations are used in the design process of composite structures to account for the strength reductions, or *residual strengths*, of laminates with discrete sources of damage [25]. The Centre-Notched Tension (CNT) configuration is perhaps the most widely used.

In the present chapter, quasi-isotropic (QI) carbon fibre-reinforced polymer (CFRP) laminates of the same material system and same laminate thickness, but with different ply thicknesses, are studied. Open-Hole Tension (OHT) and centre-notched tests are performed on laminates produced from unidirectional (UD) *prepregs* with ply thicknesses between 0.03 mm and 0.30 mm. Unlike previous studies addressing the effect of ply thickness on the hole size effect, the intermediate- and thick-ply laminates were not obtained by blocking together plies with the same orientation, but using plies of different areal weight. In order to understand the differences of using blocked plies or high-grade systems, an alternative thick-ply laminate with thin plies blocked together was also included in the present study.

3.2. Material characterisation and experimental procedure

In this work, three UD *prepreg* tapes of different fibre areal weight — 30 g/m^2, 100 g/m^2 and 300 (2×150) g/m^2 — were used to study hole size effects in laminates of different ply thicknesses. The UD *prepreg* tapes were produced at North Thin Ply Technology, LLC (Penthalaz-Cossonay, Switzerland) from M40JB carbon fibres and ThinPreg™ 80EP/CF epoxy resin using the same batches in order to minimise scatter related with material provision.

QI laminates, $[45/90/-45/0]_{nS}$, with the same nominal thickness $t = 2.4$ mm, were manufactured and cured in autoclave following the recommended curing cycle (80°C, 8 hours, 5 atm peak pressure) [37, 58]. The uniformity of the specimen thickness was assured by two aluminium plates with very tight planar tolerances separated by precisely machined spacers. The consolidated ply thicknesses for 55% fibre volume fraction were determined in a preliminary

study at École polytechnique fédérale de Lausanne (EPFL), Switzerland, using optical microscopy and image processing techniques [37, 58]. The fibre volume fraction of each plate was then calculated from its total fibre weight and thickness [37, 58].

Three laminates with different ply thicknesses were tested in this experimental work: a $[45/90/-45/0]_{10S}$ laminate ($n = 10$) with 30 g/m^2 plies (nominal ply thickness around 0.03 mm), hereafter referred to as *THIN*; a $[45/90/-45/0]_{3S}$ laminate ($n = 3$) with 100 g/m^2 plies (nominal ply thickness around 0.10 mm), hereafter referred to as *INTERMEDIATE*; and a $[45/90/-45/0]_S$ laminate ($n = 1$) with 300 g/m^2 plies (nominal ply thickness around 0.30 mm), hereafter referred to as *THICK*. A fourth laminate, $[45_{10}/90_{10}/-45_{10}/0_{10}]_S$, hereafter referred to as *THICK - PLY LEVEL*, equivalent to the *THICK* laminate (same nominal ply thickness) but obtained blocking together plies with 30 g/m^2 with the same fibre orientation, was also tested to assess the effect of blocking together plies with the same fibre orientation instead of using plies with higher areal weight on the notched response of thick-ply laminates.

OHT tests were performed on specimens with a centrally located hole with different in-plane dimensions, scaled by a factor between 2 and 6, to study the hole size effect. Additionally, CNT tests were performed to estimate and compare the mode I intralaminar laminate fracture toughness, $\mathcal{K}_{Ic}$, of the different laminates.

All tests were performed under displacement control, at a controlled speed of 1 mm/min, in an Instron 4208 electro-mechanical universal testing machine with a load capacity of 300 kN, equipped with a 100 kN load cell. Wedge grips were used to hold and load the specimens.

Table 3.1 shows the test matrix that summarises the experimental programme, where L is the specimen length, W is the specimen width, d is the hole diameter of open-hole specimens, and $2a$ is the notch length of centre-notched specimens. The width-to-hole diameter and the width-to-notch length ratios, W/d and $W/(2a)$ respectively, are kept constant and equal to 6. Despite the reduced number of specimens per geometry and per laminate available, generally only 2, the results for each case did not deviate considerably, and the mean value is representative of the actual response for the corresponding laminate and geometry.

All specimens were cut to nominal dimensions using a diamond-coated disk. The holes of the open-hole specimens were drilled using a drilling machine according to the specifications for this type of materials, using two plates of a similar carbon/epoxy laminate between the specimens to avoid damaging the outer plies at the insertion and exit points. The notch of the centre-notched specimens were obtained using a milling machine equipped with a 1 mm drill bit, ensuring a distance of 1 mm between the notch faces and a notch tip radius of 0.5 mm. Again, two plates of a similar carbon/epoxy laminate were used between the specimens to avoid damaging the outer plies. The notch tips of the centre-notched specimens were not sharpened since, based on a previous work by Camanho and Catalanotti [212], no relevant difference between the mode I laminate fracture toughness of specimens with and without sharpened notch tips is expected. In fact, after the damage process has developed from the notch tips, the actual crack tip can be considered *sharp*, and this should not affect the value of the fracture toughness at unstable crack propagation [65, 187].

3.3. Instrumentation

In the field of experimental mechanics, the computer-aided processing of full-field images provided by optical methods is becoming more and more important. Techniques based on digital image processing, together with appropriate post-processing algorithms, are able to manage large amounts of data, which are common in full-field optical methods, with a high degree of automation. Particularly interesting is the ability of some of these techniques to retrieve displacement and strain fields by computations of the camera images only [250]. Most of these techniques record pattern images before and after deformation at different load steps, retrieving the displacement fields by remapping the images after deformation to the reference image in the undeformed state [250–252].

Digital image correlation (DIC) is an optical-numerical full-field and non-contact technique for the measurement of two-dimensional (2D) or three-dimensional (3D) displacement and strain fields at the surface of objects with painted

3.3. Instrumentation

Table 3.1
Size effect test matrix.

Geom. ID	no. spec. (-)	W/d (-)	$W/(2a)$ (-)	L (mm)	W (mm)	t (mm)	d (mm)	$2a$ (mm)
THIN								
Geom. 1	2	6	-	240	6	2.4	1	-
Geom. 2	2	6	-	240	12	2.4	2	-
Geom. 5	∗	6	-	240	36	2.4	6	-
Geom. 6	2	-	6	240	24	2.4	-	4
INTERMEDIATE								
Geom. 1	3	6	-	240	6	2.4	1	-
Geom. 2	3	6	-	240	12	2.4	2	-
Geom. 4	2	6	-	240	24	2.4	4	-
Geom. 5	∗	6	-	240	36	2.4	6	-
Geom. 6	2	-	6	240	24	2.4	-	4
THICK								
Geom. 1	2	6	-	240	6	2.4	1	-
Geom. 2	2	6	-	240	12	2.4	2	-
Geom. 5	∗	6	-	240	36	2.4	6	-
THICK - PLY LEVEL								
Geom. 1	2	6	-	240	6	2.4	1	-
Geom. 2	2	6	-	240	12	2.4	2	-
Geom. 3	2	6	-	240	18	2.4	3	-
Geom. 4	2	6	-	240	24	2.4	4	-
Geom. 6	3	-	6	240	24	2.4	-	4

∗ Test results from Amacher et al. [58].

speckle patterns [196, 251]. This technique is increasingly used in experimental mechanics, allowing the qualitative and quantitative study of the mechanical behaviour of complex materials.

The displacement field is measured based on pattern recognition by analysing the geometrical deformation of the images of the surface of interest, exploiting the correspondence between the speckle pattern recorded before and after loading. For this purpose, the initial (undeformed) image is mapped by subsets (facets) containing a finite number of pixels, within which an independent measurement of the displacement is calculated. The DIC technique uses a correlation algorithm which identifies areas of matching grey level values between the speckle pattern in each subset of the deformed and undeformed images [253]. Therefore, a stochastic speckle pattern must be applied to the surface of the object to provide random grey level variations. The quality of the speckle pattern and the size of the random spots is fundamental to the precision of the measured displacement field [253].

The subset size in the plane of the object will define the displacement spatial resolution. Typically, a larger subset size will improve the precision of the measurements but will also degrade the spatial resolution. Moreover, large subsets increase the computation time, which is proportional to subset size [254, 255]. Thus, a compromise must be found according to the application to be handled, particularly attending to the size of the region of interest, the optical system (magnification and resolution), and the quality of the average speckle size obtained by the painting technique [200, 253, 256]. The subset step (i.e., the distance between adjacent subsets) can also be set for controlling the total number of measuring points over the region of interest, and for enhancing the spatial resolution by slightly overlapping adjacent subsets [187, 200].

The strain field is computed as the numerical derivative of the displacement field using displacement data from neighbouring subsets. The number of neighbouring subsets (or strain computation size) is defined by a base length, which determines the number of subsets on each side of the strain computation window. The total number of subsets is, therefore, the square of the base length.

It is interesting to note that the subset size that minimises both the displacement measurement error and the strain measurement error are generally different [254], and the definition of the most suitable subset size typically results in a compromise between adequate displacement and strain measurements. Furthermore, definition of the optimal subset size will depend on the strain gradients [254], which occur near regions of stress concentration such as cut-outs. Smaller subsets are generally required when high strain gradients are present [254].

Besides the quality of the speckle pattern, subset size, and subset step definition, other factors affecting the accuracy of DIC are the sub-pixel optimisation algorithm, subset shape function, sub-pixel intensity interpolation scheme, image noise, camera lens distortion, lighting, quality of parallelism of the lens and the sample surfaces, and presence of out-of-plane movements (in 2D DIC systems) [196, 255]. Nevertheless, DIC has proven to be a versatile technique because it does not need an elaborate specimen preparation or test setup, requiring just a common camera to store the images to be processed later [196].

The experimental monitoring of damage and fracture phenomena in composite materials using optical full-field techniques has not only gained attention in the past [250], but it is still subject of interest given the possibility to study in detail and identify the complex failure behaviour of these materials [5, 121, 122, 182, 196]. In fact, the specific characteristics of the mechanical response and failure behaviour of composite materials such as heterogeneity, anisotropy and high strain gradients due to the development of extensive damage process zones make it desirable to obtain global full-field data when performing experimental characterisation on these materials rather than local measurements from traditional electrical strain gauges and extensometers [196]. For example, Caminero et al. [196] has shown that the identification of the regions with high localised strains from full-field measurements using DIC can give a good representation of the damage pattern developing inside the laminate. A comparison with the results from penetrant enhanced X-ray radiography showed that the damage figure identified with both techniques matched very well [196].

In the present chapter, the DIC technique was used to evaluate the displacement and strain fields of the 45° outer plies, and to assess damage formation and development near the notch tips. The ARAMIS DIC-2D v6.0.2 developed by GOM [257] was used. The optical system was equipped with an 8-bit Baumer 138 Optronic FWX20 camera, with a resolution of 1624×1236 pixels^2 and a sensor format of 1/1.8". For higher versatility, due to the range of coupon configurations under study (section 3.2), the digital camera was coupled with a Nikon AF Micro-Nikkor 200 mm f/4D IF-ED lens for image grabbing. A subset size of 15×15 pixels^2 and a subset step of 13×13 pixels^2 were used. A slightly overlapping of 2 pixels between adjacent subsets was chosen in order to enhance the spatial resolution. The measured strain was computed using a strain base length of 5 subsets, with a strain validity code of 55.0%, and using the total strain method. The adopted configuration and the measuring parameters, which lead to an expected spatial resolution in the order of 2×10^{-2} pixels and a strain resolution in the range 0.01-0.04% [187], are summarised in tables 3.2 and 3.3.

For mobility and adaptability, the optical system was mounted on a multi-axis ($x - y$) positioning stage (for fine adjustments) in a tripod facing the testing machine. Two Raylux 25 white light LEDs were used on either side of the camera to ensure an even illumination of the test specimen's surface and to avoid over-exposition (i.e., the saturation of pixels over the field of view) [255, 256].

In the DIC technique, an important issue is speckle pattern recognition [250]. Before testing, the test specimens need to be sprayed with white and black ink to generate a speckle pattern, i.e., a random and contrasted distribution of granular spots. Following [253], a pattern of black spots on a white background was chosen to improve the contrast of the speckle pattern and to maximise the natural variation of grey levels. Hence, a thin coating of white matte paint was applied on the specimens' surfaces.

To ensure a suitable speckle pattern, an airbrush (Iwata Custom 181 Micron CM-B model) with a fluid nozzle of 0.18 mm in diameter was used to apply the black spots. With this marking technique, the accurate uniformity, isotropy and spot size ideal for the smaller specimens can be achieved [187], leaving less bare invariable background colour exposed within the subset [253].

The setup of the image grabbing frame started by positioning the optical system perpendicularly to the surface of the

Table 3.2
Configuration of the DIC system.

Camera-lens optical system	
CCD camera	Baumer 138 Optronic FWX20
	8-bit
	Resolution: 1624×1236 pixel^2
	Sensor format of 1/1.8”
Lens	Nikon AF Micro-Nikkor 200 mm f/4D IF-ED
	Lens aperture: $f/16$
DIC measuring parameters	
Facet size	15×15 pixel^2
Facet step	13×13 pixel^2
Strain base length	5 subsets
Strain validity code	55.0%
Strain computation method	Total
Acquisition frequency	1 Hz
DIC resolution	
Spatial resolution	2×10^{-2} pixels [187]
Strain resolution	0.01-0.04% [187]

Table 3.3
Optical system parameters.

Specimen geometry	Shutter time (ms)	Working distance (mm)	Captured region (approx.) (mm^2)	Conversion factor (approx.) (mm/pixel)
W = 6 mm	10	375	6 × 6	0.0056
W = 12 mm	13	538	12 × 10	0.0088
W = 18 mm	13	681	18 × 13	0.0119
W = 24 mm	18	872	24 × 17	0.0157

specimen mounted into the testing machine. A level ruler was used to ensure a correct alignment. The lens was adjusted to be in focus with regard to the surface of interest, setting the lens aperture to $f/4$ (where f is the focal length of the lens) to minimise the depth of field. The lens aperture was then closed to $f/16$ to improve the depth of field during testing. The shutter time was set in the range of 10–18 ms, maximising the grey levels distribution over the 8-bit dynamic range of the camera while avoiding saturation of the image [253].

3.4. Results and discussion

Amacher et al. [58] conducted unnotched tension tests on the same laminates manufactured from M40JB/ThinPreg™ 80EP/CF carbon/epoxy. Table 3.4 shows, for each laminate, the fibre volume fraction, V_f, the laminate tensile unnotched strength, X_T^L, and the laminate tensile unnotched strength normalised for a fibre volume fraction $V_f = 55\%$ [37, 58].

The ultimate strength of the unnotched specimens increased 39% and 42% when decreasing the grade of the UD plies from 300 g/m^2 to 100 g/m^2 and 30 g/m^2, respectively (table 3.4). These results were attributed to an increased stability of intralaminar cracking in the transverse and angle plies close to the free edges and to the suppression of damage propagation until fibre fracture in the 0° plies [58].

Amacher et al. [58] also identified the stress at the onset of damage (first-ply failure) by acoustic emission monitoring. A large increase (of about 230%) was reported for the stress at the onset of damage when decreasing the grade of the UD plies from 300 g/m^2 to 30 g/m^2. For intermediate ply thicknesses, a linear trend was reported [58]. Additionally, it was observed that, for the laminates with the thinnest plies, the onset of damage occurred at a stress just 3% lower than the ultimate stress, and nearly no damage could be identified before final failure.

Table 3.4
Fibre volume fraction and tensile unnotched strength of the tested laminates. Measurements performed by Amacher et al. [58].

Laminate	V_f (%)	X_T^L (MPa)	$X_{T,\,55\%}^L$ (MPa)
THIN	52.81	814	847
INTERMEDIATE	55.55	842	832
THICK	56.55	612	595
THICK - PLY LEVEL	56.29	544	532

The role of ply thickness on damage growth in notched coupons is similar to that observed in the unnotched specimens, but with a more profound effect on the structural response due to the presence of the stress concentration. Figures 3.1 to 3.4 show representative test specimens for the different geometries and laminates after testing. Different failure modes can be observed for the specimens of different ply thicknesses and different geometry/scale.

Observing the specimens of the *THIN* laminate on figure 3.1, it can be seen that, for specimens with a hole diameter of 2 mm or a 4 mm long notch, a brittle type of net-section failure mode has occurred, where subcritical damage such as transverse cracking or delamination is absent. Indeed, observing figure 3.5, which shows the surface longitudinal strain field of a representative specimen with a 2 mm hole, it can be seen that, before final fracture, damage is restricted to the hole free edge, and that, in spite of having a 45° surface ply, it propagates in a plane perpendicular to the loading direction, and not parallel to the fibre direction. On the other hand, the specimens with a 1 mm hole (the smallest) all exhibited a fibre-dominated pull-out failure mode, where delaminations with a triangular shape, extending from the hole edge to the free edge and connected to matrix cracks in the 45° outer layers (aligned with the fibre direction), can be observed.

The failure mode observed in the *THIN* specimens with a 1 mm hole was very similar to that observed in the *INTERMEDIATE* specimens with the same geometry. However, in the latter, some split cracks in the 45° outer layers were also observed — see figure 3.2. The same type of fibre-dominated pull-out failure mode was observed in the remaining *INTERMEDIATE* specimens, where delaminations with a triangular shape across the specimens' width and matrix and splitting cracks in the 45° outer layers were identified. For example, observing figure 3.6, which shows the surface longitudinal strain field of a representative specimen with a 2 mm hole, transverse cracks in the 45° surface ply can be identified before ultimate failure, starting where the fibre direction is tangent to the hole free edge, and propagating in the fibre direction (compare with figure 3.5). By increasing the ply thickness from 0.03 mm (*THIN* laminate) to 0.10 mm (*INTERMEDIATE* laminate), a modification of failure has occurred for the wider specimens, which changed from brittle to pull-out failure, with extensive subcritical damage.

For the *THICK* and *THICK - PLY LEVEL* laminates (figures 3.3 and 3.4), a completely different, matrix-dominated failure mode, common to all specimens, was observed. Before fibre fracture of the 0° plies, extensive delamination had

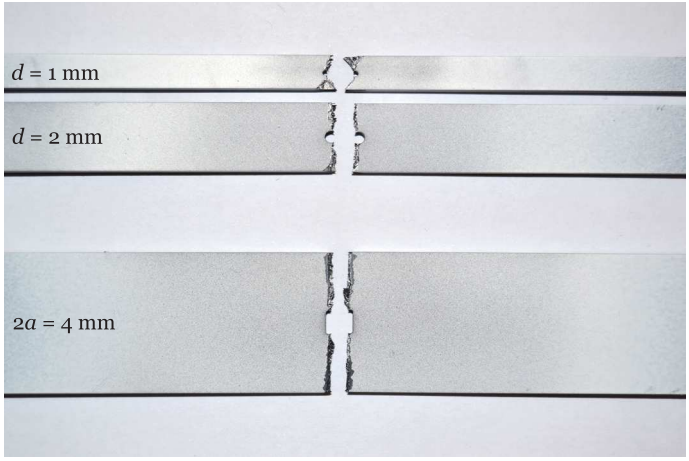

Fig. 3.1. Representative specimens of the *THIN* laminate after testing.

3.4. Results and discussion

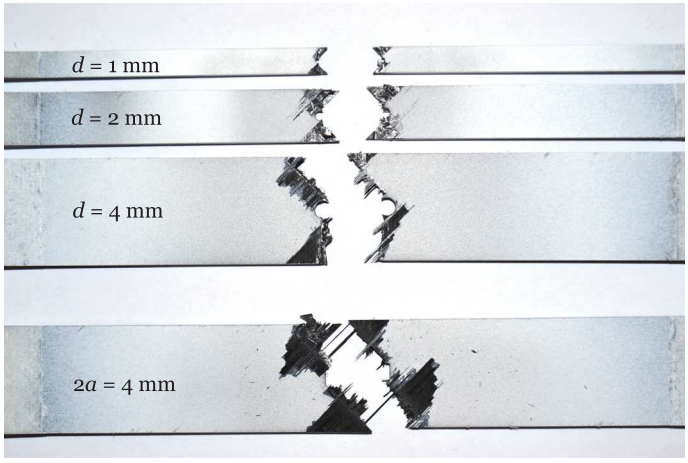

Fig. 3.2. Representative specimens of the *INTERMEDIATE* laminate after testing.

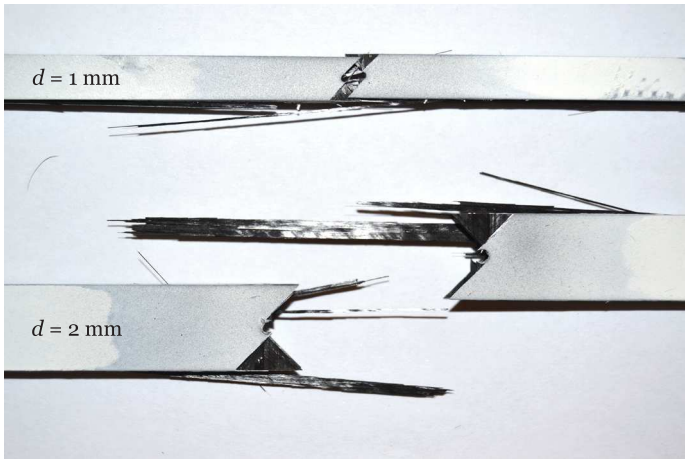

Fig. 3.3. Representative specimens of the *THICK* laminate after testing.

Fig. 3.4. Representative specimens of the *THICK - PLY LEVEL* laminate after testing.

occurred, propagating across the entire gauge section and terminating at the free edges and end tabs. The ±45° and 90° plies failed due to transverse cracking.

Observing the surface longitudinal strain fields of representative specimens of the *THICK* and *THICK - PLY LEVEL* laminates with a 2 mm hole, figures 3.7 and 3.8 respectively, it can be seen that transverse cracks in the 45° outer ply, parallel to the fibre direction and starting where the fibre direction is tangent to the hole free edge, extended across the specimens' width, terminating at the free edges. The outer 45° ply, as well as the inner 90° and −45° plies, failed before the specimens' final fracture, separating from the 0° plies, as can be seen in figure 3.9. After overall gauge section delamination, before fibre fracture, only the 0° plies sustained the load, and the specimens had lost their structural integrity. Therefore, in such cases, the notched strength, $\bar{\sigma}^{\infty}$, was determined as the maximum applied remote stress before delamination had propagated across the entire gauge section, reaching the end tabs. This point typically coincided with an abrupt, noticeable decrease of the applied remote stress in the remote stress-displacement curve, as can be seen in figure 3.10 for a representative *THICK - PLY LEVEL* open-hole specimen with a 1 mm hole.

Table 3.5 shows the mean value of the remote stress at failure, or notched strength, $\bar{\sigma}^{\infty}$, obtained in the experimental tests. Following Amacher et al. [58], the remote stress at failure normalised for a fibre volume fraction $V_f = 55\%$, $\bar{\sigma}^{\infty}_{55\%}$ is also presented. Finally, the normalised notched strength, $\bar{\sigma}_N$, calculated dividing the mean notched strength, $\bar{\sigma}^{\infty}$, by the corresponding unnotched strength, X_T^L (table 3.4):

$$\bar{\sigma}_N = \frac{\bar{\sigma}^{\infty}}{X_T^L} \tag{3.1}$$

is also shown. For reference, table 3.5 also provides the corresponding specimen width and the hole diameter or notch length. The OHT results are summarised in figure 3.11 for the different laminates as a function of the hole diameter.

The notched strengths of the *THIN* and *INTERMEDIATE* laminates decrease as the hole diameter increases (table 3.5 and figure 3.11). This is attributed to the type and extent of subcritical damage growth before ultimate failure. As the hole diameter increases, the relative size of the damage process zone becomes comparatively small with respect to the dimensions of the open hole, decreasing the blunting effect and, consequently, resulting in early failure across the ligament width.

Nevertheless, independently of the specimen geometry, the *INTERMEDIATE* laminate has a notched strength greater than the *THIN* laminate (table 3.5 and figure 3.11a). Interestingly, observing the results normalised for a fibre volume fraction $V_f = 55\%$ (figure 3.11b), it can be seen that, for the smallest specimens (hole diameter of 1 mm) the notched strengths are virtually the same (see also table 3.5). Hence, for very small specimens, reducing the ply thickness below the standard does not result in a different notched response. In fact, for such geometries, identical failure modes were observed for the *THIN* and *INTERMEDIATE* laminates (figures 3.1 and 3.2). Because the ligament width is so small, delaminations, which may start at matrix cracks near the hole, quickly propagate across the width of the specimens in both laminates, even for very small ply thicknesses, resulting in similar blunting effects and, consequently, in similar strength degradation due to the presence of the notch. It is noted that a small difference between the strengths of the *THIN* and *INTERMEDIATE* laminates was also observed in the unnotched coupons (table 3.4) [58].

For hole diameters greater than 1 mm, subcritical damage in the *THIN* laminate is almost absent (figures 3.1 and 3.5). Consequently, the blunting effect is suppressed, increasing the stress concentration at the hole edge as the hole diameter increases, resulting in the brittle type of net-section failure mode previously described.

The *INTERMEDIATE* laminate exhibits extensive subcritical damage before fibre-dominated pull-out failure, and a modest blunting effect in the regions of higher stress concentration is still observed for hole diameters of 2 mm and 4 mm, delaying unstable net-section intralaminar fracture. In this case, the stress concentration increases with increasing hole diameter, but not as rapidly as in the case of the *THIN* laminate.

Regarding the laminates with thick plies, both *THICK* and *THICK - PLY LEVEL* laminates exhibit an inverse size effect, originally reported in Refs. [144, 163]. As the hole diameter increases, the ligament width increases too, and

3.4. Results and discussion

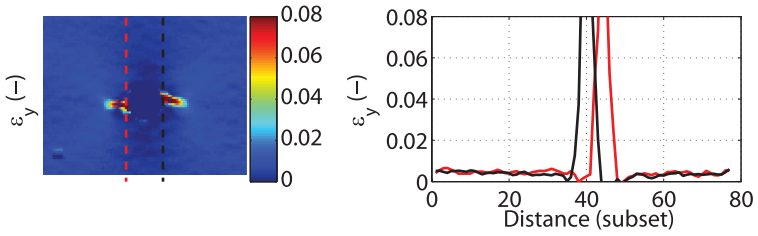

Fig. 3.5. Surface longitudinal strain field, ε_y, of a representative specimen of the *THIN* laminate with a 2 mm hole before ultimate failure and longitudinal strain measured along two lines tangent to the hole boundaries, parallel to the y-(loading) direction.

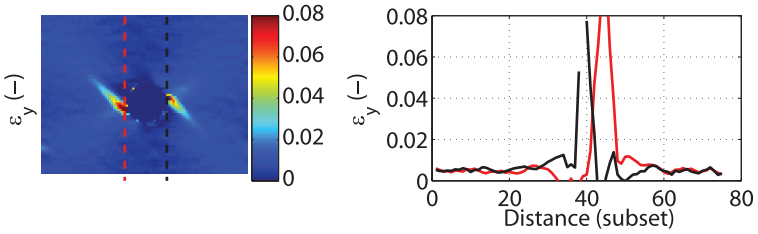

Fig. 3.6. Surface longitudinal strain field, ε_y, of a representative specimen of the *INTERMEDIATE* laminate with a 2 mm hole before ultimate failure and longitudinal strain measured along two lines tangent to the hole boundaries, parallel to the y-(loading) direction.

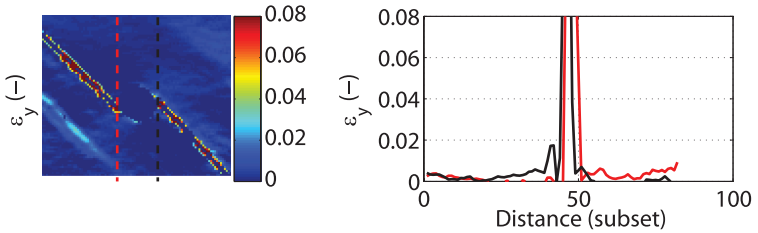

Fig. 3.7. Surface longitudinal strain field, ε_y, of a representative specimen of the *THICK* laminate with a 2 mm hole after losing its structural integrity and longitudinal strain measured along two lines tangent to the hole boundaries, parallel to the y-(loading) direction.

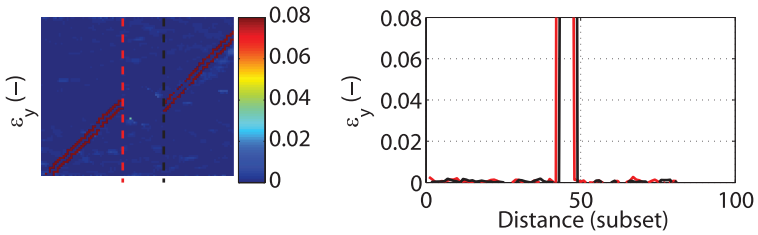

Fig. 3.8. Surface longitudinal strain field, ε_y, of a representative specimen of the *THICK - PLY LEVEL* laminate with a 2 mm hole after losing their structural integrity and longitudinal strain measured along two lines tangent to the hole boundaries, parallel to the y-(loading) direction.

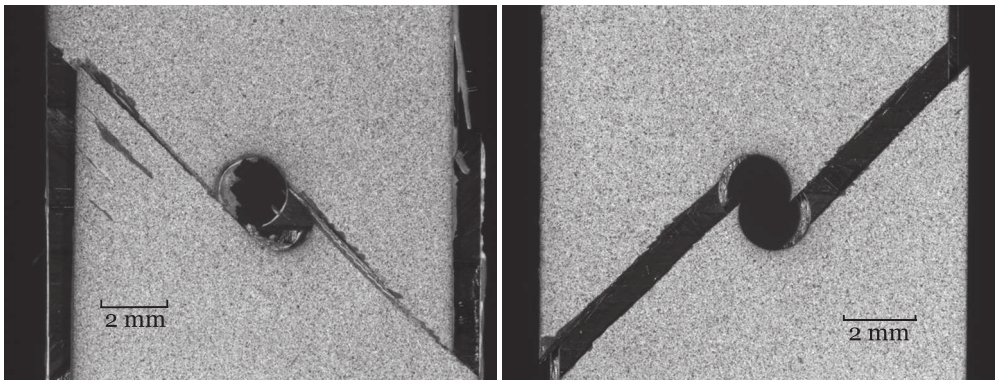

(a) *THICK* laminate specimen. (b) *THICK - PLY LEVEL* laminate specimen.

Fig. 3.9. Representative specimens of the *THICK* and *THICK - PLY LEVEL* laminates with a 2 mm hole after losing their structural integrity (pictures obtained with the DIC optical system).

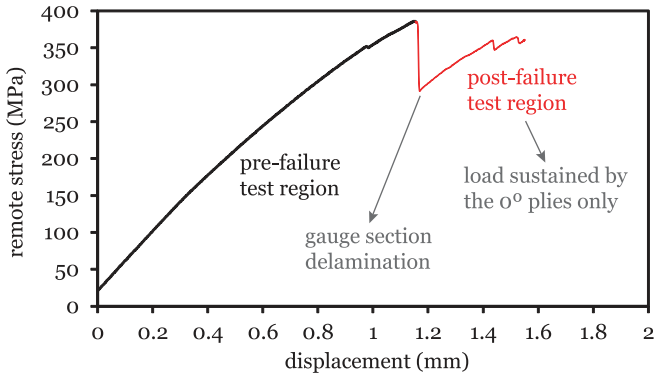

Fig. 3.10. Representative remote stress-displacement curve for a *THICK - PLY LEVEL* open-hole specimen with a 1 mm hole. Both pre-failure and post-failure test regions are shown.

delamination propagation across the specimens' width is more difficult. The stress field at the hole edge is severely modified due to the development of extensive subcritical damage across the gauge section. Consequently, the notched strengths increase, becoming higher than the notched strengths of the laminates with thinner plies (table 3.5 and figures 3.11a and 3.11b).

A very interesting result is presented in figure 3.11c. For specimens with hole diameters of 1 mm and 2 mm, independently of the ply thickness, very similar normalised notched strengths, $\bar{\sigma}_N$, were obtained, with a maximum difference of approximately 4% and 2%, respectively (in the latter case, excluding the *THIN* laminate). This suggests that, for such geometries, the stress concentration and blunting effect at the hole edge is practically insensitive to the ply thickness. When the ligament width is sufficiently small, widthwise delamination seems to be the governing damage mechanism. Hence, the stress required to propagate the delamination across the ligament width, which increases with decreasing ply thickness (due to lower interlaminar stresses and interlaminar energy release rates at the interfaces between plies of different orientation), will apparently define the notched strength of the laminate.

However, it is important to note that, in this analysis, the size effect on unnotched laminates is not taken into account (the tensile unnotched strengths shown in table 3.4 were measured from 24 mm wide specimens only [58]). As shown by Wisnom et al. [171], the unnotched strength is, in fact, size dependent as well, decreasing with decreasing specimen's volume in the case of sublaminate level scaling, and increasing with decreasing specimen's volume in the case of ply level scaling. Nonetheless, because the studied geometries are not significantly different, and because the size effects on smooth coupons are far less important than in notched coupons, it is believed that the general trends discussed before would still

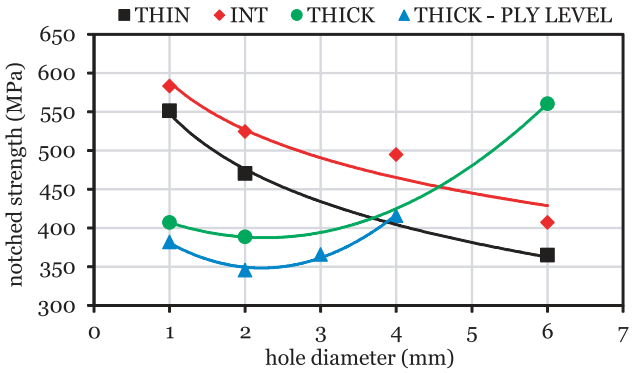

(a) Mean notched strength vs hole diameter.

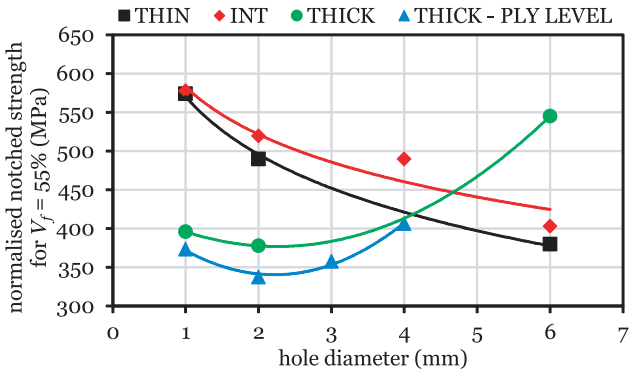

(b) Mean notched strength normalised for a fibre volume fraction V_f = 55% vs hole diameter.

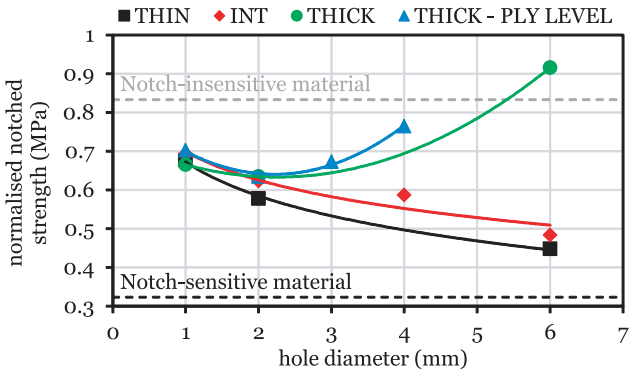

(c) Normalised notched strength vs hole diameter.

Fig. 3.11. Experimental results for the open-hole tests.

Table 3.5
Experimental results for the hole size effect study: mean tensile notched strengths, $\bar{\sigma}^{\infty}$, and corresponding coefficients of variation (C.V.), tensile notched strengths normalised for a fibre volume fraction $V_f = 55\%$, $\bar{\sigma}^{\infty}_{55\%}$, and normalised tensile notched strengths, $\bar{\sigma}_N$.

Geom. ID	W (mm)	d (mm)	$2a$ (mm)	$\bar{\sigma}^{\infty}$ (MPa) (C.V.)	$\bar{\sigma}^{\infty}_{55\%}$ (MPa)	$\bar{\sigma}_N$ (-)
THIN						
Geom. 1	6	1	-	551 (0.3%)	574	0.677
Geom. 2	12	2	-	470 (0.3%)	490	0.578
Geom. 5	36	6	-	365 (∗)	384	0.453
Geom. 6	24	-	4	387 (1.0%)	403	0.475
INTERMEDIATE						
Geom. 1	6	1	-	583 (0.7%)	577	0.693
Geom. 2	12	2	-	524 (2.2%)	519	0.623
Geom. 4	24	4	-	494 (1.9%)	490	0.587
Geom. 5	36	6	-	407 (∗)	403	0.483
Geom. 6	24	-	4	487 (2.5%)	482	0.579
THICK						
Geom. 1	6	1	-	407 (1.1%)	396	0.665
Geom. 2	12	2	-	388 (3.4%)	378	0.635
Geom. 5	36	6	-	560 (∗)	545	0.916
THICK - PLY LEVEL						
Geom. 1	6	1	-	382 (1.0%)	373	0.702
Geom. 2	12	2	-	345 (0.8%)	337	0.635
Geom. 3	18	3	-	366 (0.4%)	357	0.672
Geom. 4	24	4	-	416 (2.4%)	406	0.764
Geom. 6	24	-	4	413 (1.8%)	403	0.759

∗ Test results from Amacher et al. [58].

be valid if size dependent unnotched strengths were considered.

Figure 3.11c also shows the predictions for a *notch-sensitive material*, whose normalised notched strength is a function of the stress concentration factor K_t ($\bar{\sigma}_N = 1/K_t$), and the predictions for a *notch-insensitive material*, whose normalised strength is a function of the geometry ($\bar{\sigma}_N = 1 - d/W$). For a QI laminate with a centrally located circular hole, the stress concentration factor K_t can be obtained as [258]:

$$K_t = \frac{2 + (1 - d/W)^3}{1 - d/W} \tag{3.2}$$

For the smaller specimens, a slight reduction in strength with increasing hole size is observed in all laminates (figure 3.11c), which exhibit similar trends for hole diameters below 2 mm. However, as size increases further, the tensile notched strengths of the *THIN* and *INTERMEDIATE* laminates tend to a notch-sensitive material response, whose mechanical behaviour depends strongly on the stress concentration factor at the hole boundary. On the other hand, the tensile notched strengths of the *THICK* and *THICK - PLY LEVEL* laminates increase towards a notch-insensitive material response, whose mechanical behaviour becomes independent of the stress concentration at the notch. In fact, for specimens with large ligament widths (e.g. in the specimens with a hole diameter of 6 mm), the notched response of the *THICK* (and probably of the *THICK - PLY LEVEL*) laminate tends to the unnotched strength of the laminate. This indicates that, after delamination propagation across the ligament width, the stress concentration in the vicinity of the hole is not sufficiently high to break the intact 0° plies, and delamination takes place along the unnotched gauge section. Failure eventually occurs due to complete gauge section delamination as in the unnotched specimens, resulting in tensile notched strengths approximately equal to the tensile unnotched strengths. Nevertheless, it is important to stress that the development of large-scale subcritical damage, in particular delamination, which may propagate unstably in finite, abrupt steps,

is typically highly undesirable due to the early loss of structural integrity and due to the severe reduction of the laminates' residual compressive and shear strengths.

3.5. Concluding remarks

OHT tests were performed on specimens with a centrally located hole with different in-plane dimensions, scaled by a factor between 2 and 6, to study the hole size effect on QI CFRP laminates of the same material system and same laminate thickness, but different ply thicknesses: 0.03 mm, 0.10 mm and 0.30 mm. Three different failure modes were observed. In general, thin-ply laminates, with 0.03 mm thick plies, exhibited a brittle type of net-section failure mode, where subcritical damage such as transverse cracking or delamination were absent. Only the smallest specimens, with a hole diameter of 1 mm, exhibited a fibre-dominated pull-out failure mode, where delaminations with a triangular shape, extending from the hole edge to the free edge and connected to matrix cracks in the 45° outer layers, were observed. The same type of fibre-dominated pull-out failure mode, with extensive subcritical damage, was also observed in the laminate with 0.10 mm thick plies, which, in addition, exhibited split cracks in the 45° outer plies. The thick-ply laminates, with 0.30 mm thick plies, obtained using either 300 g/m^2 laminae or blocks of ten 30 g/m^2 laminae with the same orientation, exhibited a matrix-dominated failure mode, characterised by extensive delamination, which propagated across the gauge section, terminating at the free edges and end tabs, and by transverse cracking of the ±45° and 90° plies. Even though thick-ply laminates did not fail catastrophically, they lost their structural integrity due to complete gauge section delamination.

For very small specimens, reducing the ply thickness below the standard (e.g. from 0.10 mm to 0.03 mm) did not result in a different notched response. For specimens with a small ligament width, delaminations, which start at matrix cracks near the hole (or other stress concentration), quickly propagate across the width of the specimen. However, as the in-plane dimensions increase, subcritical damage in the thin-ply laminate is practically suppressed, decreasing the blunting effect and, consequently, increasing the stress concentration at the hole edge. The suppression of subcritical damage results in a brittle type of net-section failure mode, as discussed. The laminate with 0.10 mm thick plies exhibited extensive subcritical damage before fibre-dominated pull-out failure, and the blunting effect was still observed for hole diameters of 2 mm and 4 mm. In this case, the stress concentration increased with increasing in-plane dimensions, but not as rapidly as in the case of the thin-ply laminate.

For the thick-ply laminates, an inverse size effect was obtained [144, 163], and no significant difference was found in the notched response of thick-ply laminates manufactured with 300 g/m^2 plies or by blocking together ten 30 g/m^2 plies with the same fibre orientation.

An interesting finding is related with the fact that, for the smallest specimens, the normalised notched strengths, $\bar{\sigma}_N$, were practically independent of the ply thickness. Hence, when the ligament width is sufficiently small, widthwise delamination seems to be the governing damage mechanism, and the stress required to propagate the delamination across the ligament width, which increases with decreasing ply thickness (due to lower interlaminar stresses and interlaminar energy release rates at the interfaces between plies of different orientation), will apparently define the notched strength of the laminate. It is believed that these conclusions are valid even though the size effect on unnotched laminates was not taken into account.

But as the specimens' size increases, the tensile notched strengths of the laminates with thinner plies tend to a notch-sensitive material response, whose mechanical behaviour depends strongly on the stress concentration factor at the hole boundary. On the other hand, the tensile notched strengths of the thick-ply laminates tend to their unnotched strengths. This indicates that, after delamination propagation across the ligament width, the stress concentration in the vicinity of the hole is not sufficiently high to break the intact 0° plies, and delamination takes place along the unnotched gauge section. Failure eventually occurs due to complete gauge section delamination as in the unnotched specimens, resulting in tensile notched strengths approximately equal to the tensile unnotched strengths. Nevertheless, it is important to stress that the development of large-scale subcritical damage, in particular delamination, which may propagate unstably in finite, abrupt steps, is typically highly undesirable due to the early loss of structural integrity and due to the severe reduction of the laminates' residual compressive and shear strengths.

In the future, the present study can be complemented by testing specimens with larger geometries and different notch shapes, for instance to understand the effect of ply thinness on the Large Damage Capability of composite laminates. In addition, new experimental studies identical to the present one but addressing the effect of ply thinness on the filled-hole and unnotched size effects, as well as size effects in compression, would certainly boost the understanding of the structural behaviour of spread-tow composite laminates. The introduction of enhanced resin formulations and the study of the effect of lay-up and the effect of inter- and intra-ply hybridisation on the structural response of laminates with conventional and spread-tow reinforcements would be of great value as well.

Chapter 4

Effect of tow thickness on the structural response of aerospace-grade spread-tow fabrics

Ultra-thin plies open a broad range of new possibilities in terms of design and manufacturing of composite structures. These include not only ultra-thin UD tapes, but most importantly new, innovative kinds of carbon fibre reinforcements. This is the case of the spread-tow fabrics developed by Oxeon AB (Borås, Sweden), trademarked TeXtreme®. Instead of yarns, TeXtreme® is produced using spread tapes in the weaving process. Consequently, the fibre bundles are not only thinner, but they are also wider, resulting in a flatter fabric, with fewer interlacing points, minimal fibre waviness and overall composite fibre volume fractions very close to the local fibre volume fraction of the spread tows. As a result, the performance of STFs approaches that of laminates made of UD tapes. In the present chapter, an experimental test campaign is carried out to study the structural response of aerospace-grade plain weave STFs of different grades, including a detailed assessment of the structural response of laminates based on a baseline of the aeronautical industry.

4.1. Introduction

The effect of ply thickness on the onset of ply damage (transverse cracking) and delamination is extremely important for the prediction of the mechanical response of laminated composite structures. This is of particular significance when dealing with the most recent spread-tow, ultra-thin grades, where dry ply thicknesses can be extremely low.

The use of thinner plies enables the production of thinner and lighter laminates and structures. Additionally, per given laminate thickness, more plies can be accommodated (particularly interesting for thin laminates), increasing the design space and leading to a possibility of using smaller relative fibre angles between adjacent plies. This is beneficial when it comes to interfacial fracture between plies [34]. Also, by reducing the ply thickness in a multidirectional laminate, matrix cracking and delamination can be delayed [35, 37, 38] without the use of special resins and/or through-the-thickness reinforcements, providing high strength, enhancing fatigue life, and improving resistance to leakage events.

In terms of design and manufacturing, spread-tow plies are known to exhibit improved fibre orientation and distribution, potentially leading to fewer weak zones. One direct consequence is the enhancement of the longitudinal compressive strength of unidirectional (UD) thin-ply laminates, attributed to the more uniform microstructure of spread-tow thin plies [58]. Other benefits include easier homogenisation (opening perspectives for automated, continuous lay-up) and potential to use heavier tow yarns, which can significantly reduce production costs.

In addition, the thinner and wider tows obtained with tow spreading show unique benefits that open a broad range of new possibilities in terms of design and manufacturing of composite structures. These include not only ultra-thin UD

tapes, but most importantly new, innovative kinds of carbon fibre reinforcements.

Oxeon AB (Borås, Sweden), for instance, is producing spread-tow fabrics (STFs), trademarked TeXtreme®, which use spread tapes in the weaving process instead of conventional yarns. Interestingly, fibre bundles are not only thinner, but they are also wider, resulting in a flatter fabric, with fewer interlacing points and better surface finish than conventional ones. Such fabric configurations are also characterised by minimal fibre waviness, and therefore lower crimp frequency and smaller crimp angles [54, 64], allowing the filaments to immediately carry tensile or compressive loads without first having to straighten.

Due to the thinner and wider spread tows, the amount of matrix between the tows of thin-ply fabrics is also very small, resulting in overall composite fibre volume fractions very close to the local fibre volume fraction of the spread tows [66, 67]. As a result, the performance of thin-ply fabrics approaches that of laminates made of UD tapes.

In the present work, an experimental test campaign is carried out to study the structural response of aerospace-grade plain weave STFs of different grades. The test campaign includes basic characterisation of the STFs, performed on basic cross-ply laminates, and the detailed assessment of the structural response of laminates based on a baseline of the aeronautical industry.

4.2. Material selection and manufacturing

Oxeon AB's T700SC TeXtreme® STFs pre-impregnated with HexPly® M21 toughened epoxy resin from Hexcel were selected for this study. Two plain weave configurations with different areal weights were used: 160 g/m^2 and 240 g/m^2 STFs, with nominal fabric layer thicknesses around 0.16 mm and 0.24 mm respectively.

Table 4.1 shows the elastic properties of T700GC/M21 carbon/epoxy, where E_{11T} and E_{11C} are respectively the longitudinal Young's moduli in tension and compression, E_{22} is the transverse Young's modulus, ν_{12} and ν_{23} are respectively the in-plane and out-of-plane Poisson's coefficients, and G_{12} is the in-plane shear modulus. These properties were determined by in-plane tensile or compressive tests on 0° and 90° plies [88], tensile tests on $[\pm 45]_S$ laminates Huchette [88], and out-of-plane compressive tests [259] on laminates from *prepregs* with an areal weight of 268 g/m^2 (cured ply thickness of 0.262 mm) [88, 259]. Nevertheless, it was shown that the effect of ply areal weight on the basic UD properties of composite materials is negligible, except on the longitudinal compressive strength (attributed to the more uniform microstructure of spread tows) [58].

It is also important to note that whereas the STFs used in the present work are made of T700SC fibres, the elastic properties in table 4.1 were obtained from *prepregs* with T700GC fibres, which use a different sizing. Nevertheless, it is believed that, while fibre sizing may affect the strength of the composite material, the effect on the elastic properties should be negligible. In addition, the elastic properties presented in table 4.1 were determined in a UD composite, and in spite of the more uniform microstructure and lower waviness of STFs, it is not clear how well these UD properties translate into the properties of the individual STF layers.

Basic elastic and strength characterisation of the 160 g/m^2 and 240 g/m^2 STFs is performed on UD textile laminates of different thicknesses. Thinner plain weave laminates were selected for the strength characterisation in tension, and thicker laminates for the strength characterisation in compression and for the fracture characterisation in tension and compression. Two laminates, one of each STF grade, were also designed based on a damage tolerance optimised baseline laminate for aeronautical applications. Table 4.2 shows the stacking sequences definition, where \$ stands for symmetric with respect to the middle layer (which is not repeated). The 0° fibre orientation is coincident with the loading direction.

Table 4.1
T700GC/M21 elastic properties [88, 259].

E_{11T} (GPa)	E_{11C} (GPa)	E_{22} (GPa)	ν_{12} (-)	ν_{23} (-)	G_{12} (GPa)
130.0	114.0	8.3	0.32	0.54	4.5

Table 4.2
Stacking sequence definitions of the T700SC/M21 STF laminates.

Laminate ID	STF lay-up sequence	Laminate stacking sequence
Basic elastic and strength characterisation		
UDA240	$[0]_8$	$[(0/90)]_{4S}$
UDB240	$[0]_{18}$	$[(0/90)]_{9S}$
UDA160	$[0]_{12}$	$[(0/90)]_{6S}$
UDB160	$[0]_{26}$	$[(0/90)]_{13S}$
Structural characterisation		
DTO240	$[0/45_2/0/45_2/0]$	$[(0/90)/(45/-45)/(45/-45)/(0/90)]_\$$
DTO160	$[0/45/0/45_2/0/45_2/0/45/0]$	$[((0/90)/(45/-45))_2/(45/-45)/(0/90)]_\$$

Table 4.3
Basic characteristics of the T700SC/M21 STF laminates.

Laminate ID	STF grade	Orientation and number of STF layers			Nominal laminate
		[0]	[45]	Total	thickness (mm)
UDA240	240 g/m^2	8	0	8	1.92
UDB240	240 g/m^2	18	0	18	4.32
UDA160	160 g/m^2	12	0	12	1.92
UDB160	160 g/m^2	26	0	26	4.16
DTO240	240 g/m^2	3	4	7	1.68
DTO160	160 g/m^2	5	6	11	1.76

All selected laminates are balanced and symmetric (due to the plain weave configuration). The multidirectional structural laminates are orthotropic. Note that, since each plain weave has 0° and 90° spread tapes in their configuration, the [0] and [45] STF plies can be translated respectively into (0/90) and (45/−45) biaxial layers. The laminate stacking sequences with respect to the tape orientations are also shown in table 4.2.

Table 4.3 shows the basic characteristics of each laminate. As can be observed, the laminates of the different STF grades were defined in order to match the laminate thickness and elastic properties.

All laminates were prepared for curing in a vacuum bag and cured using an autoclave. The autoclave cure cycle was defined by setting a heat-up rate of 2°C/minute from room temperature to 180°C, holding at 180°C for 120 minutes and cooling down at a rate of 2°C/minute. A gauge autoclave pressure of 4 bar was applied throughout the cure cycle. One 300×300 mm^2 plate of laminates *UDA240* and *UDA160*, three 300×300 mm^2 plates of laminates *UDB240* and *UDB160*, and six square plates of laminates *DTO240* and *DTO160* (two 300×300 mm^2, two 330×330 mm^2 and two 400×400 mm^2 plates) were produced, in a total of 20 plates. After curing, each plate was cut to the specimens' nominal dimensions using a diamond-coated disk.

4.3. Experimental test programme

4.3.1. Fabric tensile unnotched strength

In the design process of composite structures, the evaluation of candidate laminate configurations under a prescribed set of loading conditions by means of experimental testing alone is unfeasible, prohibitively expensive and time consuming. Also, laminate-level stress analysis, where the measured laminate strengths under single stress component tests are translated into anticipated strength estimates for combined stress cases, is limited to the laminates for which test data is available. Therefore, the analysis of laminates is generally performed by means of ply-level stress analysis, which requires the knowledge of the basic material properties of a composite lamina [25].

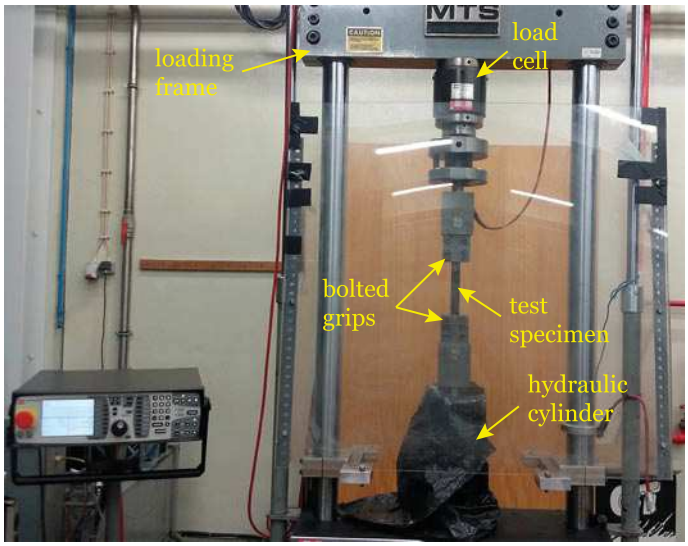

Fig. 4.1. MTS 810 servo-hydraulic testing frame and tensile experimental setup.

Despite the most recent advances in micro-mechanical analysis methods [260, 261], due to the complexity of the failure process of UD or textile fibre composites, it is still desirable to regard the strength of laminae subjected to a single principal stress component as a quantity to be measured experimentally, rather than deduced from constituent properties. Consequently, tests on UD laminae are essential in establishing the allowables for the individual plies, which are used as the inputs to lamina failure theories [25].

Plain weave unnotched specimens with a nominal width (W) of 25 mm and a nominal length (L) of 300 mm were tested in tension, following the ASTM D3039/D3039M – 14 test standard [262]. The tests were performed on laminates *UDA240* and *UDA160* (tables 4.2 and 4.3) under displacement control, at a speed of 1.0 mm/min, in an MTS 810 servo-hydraulic testing machine with a load capacity of 250 kN, equipped with a 250 kN load cell (figure 4.1). The test data was acquired directly by the testing machine commands module, with an acquisition frequency of 5.0 Hz.

The specimens were fixed to the load frame using a bolted clamping rig with six M10 bolts (figure 4.1) fastened with a torque of up to 80 Nm. Strips of Dexter sandpaper with coarse grains were inserted between the specimen surfaces and the grips to improve the load transfer capability of the bolted clamping system and prevent sliding. The gauge length was set to 150 mm.

4.3.2. Fabric compressive unnotched strength

Plain weave unnotched specimens were also tested in compression. The tests were performed on laminates *UDB240* and *UDB160* (tables 4.2 and 4.3), under displacement control, at a controlled speed of 0.1 mm/min, in an Instron 4208 electro-mechanical universal testing machine with a load capacity of 300 kN and equipped with a 100 kN load cell (figure 4.2). Following Koerber et al. [263], unnotched specimens with a nominal width (W) of 10 mm and a nominal length (L) of 20 mm (figure 4.3a) were tested using an end-loading test rig with a self-alignment system (figure 4.3b).

The self-alignment system consists of two parts connected by a spherical joint, which allows small rotations and avoids premature failure of the specimen that might occur due to the lack of parallelism between the faces in contact with the test rig. Due to the high compressive strength of the specimen in the fibre direction, polished tungsten-carbide (TC) inserts were used to avoid damage on the contact surfaces of the test fixture caused by the endings of the stiff carbon fibres [263, 264]. In addition, a thin layer of molybdenum disulphide (MoS_2) was used between the specimen end-surfaces and the surfaces of the rig to minimise friction [263]. The test data was acquired using a Spider 8 data logger, with an acquisition frequency of 5.0 Hz.

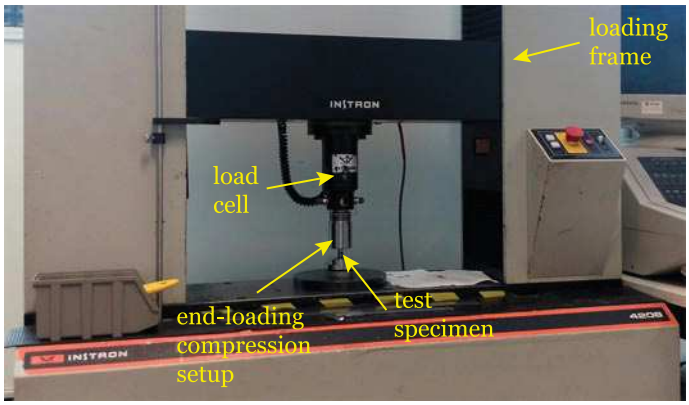

Fig. 4.2. Instron 4208 universal testing machine and end-loading compression test setup.

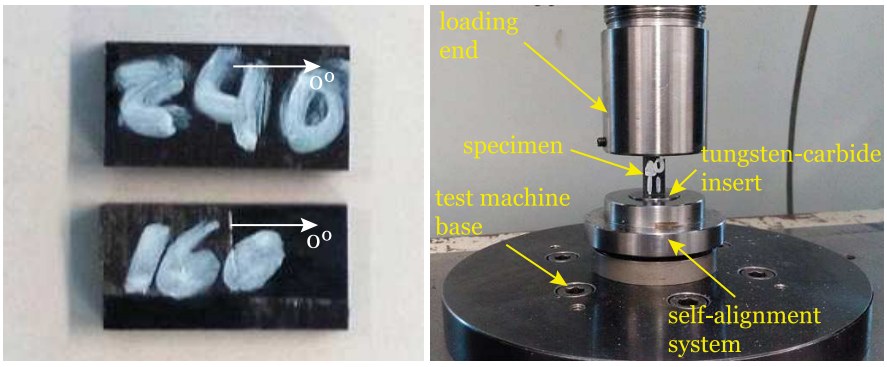

(a) Specimens. (b) Compression test system.

Fig. 4.3. Representative fabric unnotched compression specimens and compression test rig with self-alignment system.

4.3.3. Fabric off-axis compression tests

In composite parts and structures, the states of stress and deformation are never limited to a single stress component. Therefore, the understanding of the mechanical behaviour of UD composites and laminates under combined stresses is fundamental for the development of constitutive models and analysis tools that accurately represent the response of the composite material under general stress states.

Off-axis specimens are a simple alternative to induce combined transverse and shear deformation in UD composites, without requiring complex multiaxial test setups. A combined stress state with respect to the material axes can be obtained by simple uniaxial loading [79, 264], requiring just rather simple specimens and an uniaxial testing machine.

Experimental yield and failure envelopes for combined transverse and in-plane shear loading can be easily derived from the experimental data, and used to validate yield and failure criteria [263, 265]. In addition, the observed off-axis stress-strain relations allow the identification of damage initiation and failure mechanisms [263, 265], which are needed to develop and validate reliable composite material models that able to predict experimentally observed nonlinearities and the progressive evolution of damage until ultimate failure under multi-axial loading conditions [108, 266–268].

In the present work, 15° and 30° off-axis compression tests were performed. These tests were carried out on the *UDB240* and *UDB160* laminates (tables 4.2 and 4.3) under displacement control, at a controlled speed of 0.1 mm/min. An Instron 4208 electro-mechanical universal testing machine with a load capacity of 300 kN and equipped with a 100 kN load cell was used to load the specimens, and the test data was acquired using a Spider 8 data logger, with an acquisition frequency of 5.0 Hz.

Following Koerber et al. [263], unnotched specimens with a nominal width (W) of 10 mm and a nominal length

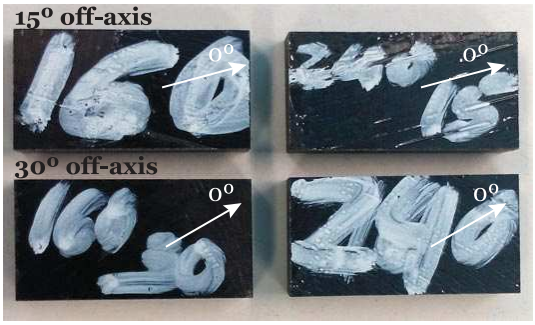

Fig. 4.4. Representative plain weave off-axis compression test specimens.

(L) of 20 mm (figure 4.4) were tested using the same end-loading test rig used in the UD unnotched compression tests (section 4.3.2). Polished TC inserts were used to avoid damage on the contact surfaces of the test fixture (figure 4.3b) and a thin layer of MoS_2 was used between the specimen end-surfaces and the surfaces of the rig to minimise friction [263, 264]. As reported elsewhere [264], the smooth contact surface is essential in off-axis compression tests to allow the induced extension-shear coupling to fully develop under uniaxial compression loading. In fact, the friction between the specimen end-surfaces and the rig contact surfaces are known to affect the off-axis compressive strength data if appropriate lubrication is not used [264].

To determine the strength components of the off-axis tests, $\bar{\sigma}_{11}$, $\bar{\sigma}_{22}$ and $\bar{\sigma}_{12}$, the measured axial compressive strength in the loading coordinate system, $\bar{\sigma}_x$, needs to be transformed into the material coordinate system. This can be performed employing a simple coordinate transformation [263]:

$$\bar{\sigma}_{11} = \bar{\sigma}_x \cos^2\theta \tag{4.1}$$

$$\bar{\sigma}_{22} = \bar{\sigma}_x \sin^2\theta \tag{4.2}$$

$$\bar{\sigma}_{12} = -\bar{\sigma}_x \sin\theta\cos\theta \tag{4.3}$$

where the transformation angle $\theta = \theta_0 + \Delta\theta$ consists of the initial off-axis angle θ_0 and the additional fibre rotation $\Delta\theta$ occurring due to the extension-shear coupling effect [263]. The additional fibre rotation $\Delta\theta$ can be measured via post-processing of the measurements performed using the DIC technique. Hence, the correct off-axis angle can be used in the transformation in equations (4.1)–(4.3). It is important to note that the strength components of the off-axis tests, $\bar{\sigma}_{11}$, $\bar{\sigma}_{22}$ and $\bar{\sigma}_{12}$, expressed in the material coordinate system, are not the ply strengths for uniaxial loading along the main material directions.

4.3.4. Fabric mode I tensile crack resistance curve — size effect of Double Edge-Notched Tension (DENT) specimens

Characterisation and prediction of the fracture toughness associated with intralaminar failure modes involving fibre breakage is currently a fundamental issue in the understanding and design of advanced composite structures. In fact, the intralaminar fracture toughness not only plays an important role in the assessment of the damage tolerance of composite structures and their behaviour during damage propagation [65, 185–188], as it is also relevant in the definition of the softening laws used in recent computational analysis models [106, 108, 189, 190] and in establishing the energy equilibrium equations used in closed-form solutions [181, 182] that predict the ultimate strength of composite structures.

Moreover, fracture characterisation is also essential in understanding size effects in the notched response of composite laminates. In fact, any other source of size effects (namely statistical size effects) is overwhelmed by the effect of stress redistributions caused by stable, gradual fracture propagation and consequent energy release, resulting in a deterministic (nonstatistical) size effect [131, 164, 165]. This is particularly evident in the presence of stress concentrations caused by

notches and holes, because in this case the material adjacent to the notch tips or hole edges fails first, and the influence of statistical variation of material strength is negligible [160].

When the fracture process zone (FPZ) is negligibly small, the fracture process is assumed to occur in one point (the crack tip), and linear elastic fracture mechanics (LEFM) applies [164]. However, quasi-brittle materials, including fibre-reinforced polymer (FRP) laminates, can develop non-negligible FPZ, compared with the structural dimensions [131, 165, 168], before reaching the maximum load.

In fact, it has been observed that laminated composites show remarked size effects due to the propagation of cracks in tension, and due to the propagation of kink bands in compression [131]. In particular for carbon/epoxy systems, the energy consumed by failure mechanisms involving fibre breakage is much greater than for those involving matrix or matrix-fibre bond failures [191].

Even though the fracture toughness can be characterised by parameters such as the critical Stress Intensity Factor (SIF), $\mathcal{K}_{Ic}$, or the critical energy release rate (ERR), $\mathcal{G}_{Ic}$, it may be represented more accurately in the form of a *crack resistance curve* (or $\mathcal{R}$-curve), relating the change in the critical ERR with crack growth. In fact, the experimental characterisation of several composite materials and different lay-ups has shown that composite laminates exhibit a fracture resistance behaviour resembling an $\mathcal{R}$-curve type of response, whose damage growth resistance was primarily due to (i) load redistribution resulting from microcracking, splitting and/or delamination, which relieve the stress concentration and delays fracture to higher applied loads [182, 194–196], and (ii) bridging by the intact fibres of the plies that are adjacent to the principal load-carrying plies with broken fibres [194, 195]. Crack growth stability is therefore necessary for good data acquisition. However, $\mathcal{R}$-curves are not currently addressed by standard test methods [192].

Recently, a robust methodology has been proposed to measure the intralaminar fracture toughness and the $\mathcal{R}$-curve of composite laminates in mode I [65, 187, 210] based on the size effect law [164, 209]. The size effect law can be calibrated using a set of scaled *geometrically similar specimens* with *positive geometry* [65, 187, 188], whose results can then be fitted using, for instance, one of the regression methods proposed in Ref. [209].

In the present work, the mode I tensile crack resistance curve of the plain weave STFs is determined using the methodology proposed by Catalanotti et al. [65]. According to this methodology, the $\mathcal{R}$-curve of a composite laminate can be measured taking into account that, for different characteristic sizes w_n, assuming that the size effect law, $\bar{\sigma}^{\infty} = \bar{\sigma}^{\infty}(w)$, where $\bar{\sigma}^{\infty}$ is the ultimate remote stress, is known, the driving force curves $\mathcal{G}_I$ at the ultimate remote stresses $\bar{\sigma}^{\infty}(w_n)$ are tangent to the $\mathcal{R}$-curve. In other words, the $\mathcal{R}$-curve can be determined as the envelope of the driving force curves at the ultimate remote stresses (see, e.g., Ref. [211]). Mathematically, this means that the ultimate remote stresses can be obtained solving the following system of equations [65]:

$$\begin{cases} \mathcal{G}_I(\Delta a) = \mathcal{R}(\Delta a) \\ \dfrac{\partial \mathcal{G}_I(\Delta a)}{\partial \Delta a} = \dfrac{\partial \mathcal{R}(\Delta a)}{\partial \Delta a} \end{cases} \tag{4.4}$$

where Δa is the crack extension. Taking x and y as the preferred axes of the material (figure 4.5), for a two-dimensional orthotropic body the ERR in mode I, $\mathcal{G}_I$, for a crack propagating in the y-direction is [269, 270]:

$$\mathcal{G}_I = \frac{1}{\acute{E}} \mathcal{K}_I^2 \tag{4.5}$$

where the equivalent modulus $\acute{E}$ is given as:

$$\acute{E} = \left(\frac{1+\rho}{2E_x E_y} \right)^{-1/2} \mu^{-1/4} \tag{4.6}$$

In equation (4.6), ρ and μ are two elastic parameters, given, respectively, by [270]:

4.3. Experimental test programme

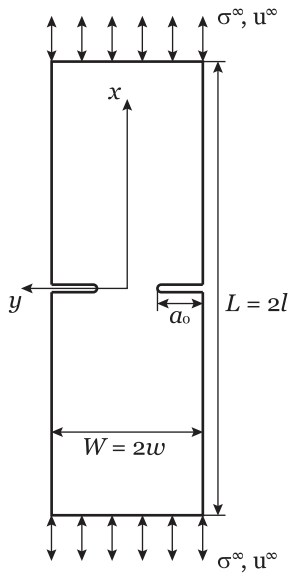

Fig. 4.5. Double edge-notched specimen configuration.

$$\rho = \frac{\left(E_x E_y\right)^{1/2}}{2G_{xy}} - \left(\nu_{xy}\nu_{yx}\right)^{1/2} \tag{4.7}$$

and:

$$\mu = \frac{E_y}{E_x} \tag{4.8}$$

Using the orthotropy rescaling technique [269, 270], the SIF in equation (4.5), $\mathcal{K}_I$, can be written in a generic form as:

$$\mathcal{K}_I = \sigma^{\infty}\sqrt{w}\,\kappa(\alpha,\rho,\varphi) \tag{4.9}$$

where σ^{∞} is the remote stress, w is a characteristic dimension, $\varphi = \mu^{-1/4}\varpi$, $\alpha = a/w$ and $\varpi = w/l$ are the shape parameters, and $\kappa(\alpha,\rho,\varphi)$ is a generic correction factor that accounts for both geometry and orthotropy of the material. a and l are, respectively, the crack length and half gauge length ($l = L/2$). Using equation (4.9) in equation (4.5), and defining $\alpha_0 = a_0/w$ as the initial value of the shape parameter (where a_0 is the initial crack length), the driving force curves read:

$$\mathcal{G}_I(\Delta a) = \frac{1}{\acute{E}} w\,(\sigma^{\infty})^2\,\kappa^2\left(\alpha_0 + \frac{\Delta a}{w},\rho,\varphi\right) \tag{4.10}$$

At the ultimate remote stress, $\bar{\sigma}^{\infty}$, the following expression for $\mathcal{R}(\Delta a)$ can be obtained substituting equation (4.5) in the first equation of (4.4):

$$\mathcal{R}(\Delta a) = \frac{1}{\acute{E}} w\,(\bar{\sigma}^{\infty})^2\,\kappa^2\left(\alpha_0 + \frac{\Delta a}{w},\rho,\varphi\right) \tag{4.11}$$

Differentiating equation (4.11) with respect to w, assuming that *geometrically similar specimens* (α_0 and ϖ independent of w) of different sizes with *positive geometry* (where the correction factor κ is an increasing function of the crack

Table 4.4
Size effect DENT test matrix.

Geometry ID	L_s (mm)	L (mm)	W (mm)	a_0 (mm)
A	300±1	200±1	10.0±0.1	3.00±0.03
B	300±1	150±1	20.0±0.2	6.00±0.03
C	300±1	150±1	30.0±0.3	9.00±0.03
D	300±1	150±1	40.0±0.4	12.00±0.03
E	300±1	150±1	50.0±0.5	15.00±0.03

length) are tested, and taking into account that, by definition, the $\mathcal{R}$-curve is size independent (i.e., $\partial\mathcal{R}/\partial w = 0$), the following equation is obtained:

$$\frac{\partial}{\partial w}\left[w\,(\bar{\sigma}^{\infty})^2\,\kappa^2\right] = 0 \tag{4.12}$$

Knowing the size effect law, $\bar{\sigma}^{\infty} = \bar{\sigma}^{\infty}(w)$, equation (4.12) can be solved for $w = w(\Delta a)$. Using $w = w(\Delta a)$ in equation (4.11), the $\mathcal{R}$-curve, $\mathcal{R}(\Delta a)$, is obtained.

Following Catalanotti et al. [65], scaled Double Edge-Notched Tension (DENT) specimens were tested. Table 4.4 shows the size effect DENT test matrix, where W is the total specimen width, L_s is the total specimen length, L is the gauge length (free length between grips), and a_0 is the machined edge notch length. The characteristic dimension w is taken as half specimen width ($w = W/2$), and the edge notch length-to-width ratio is kept constant in all scaled specimens ($\alpha_0 = a_0/w = 0.6$). The tests were performed on laminates *UDB240* and *UDB160* (tables 4.2 and 4.3).

The edge notches were obtained using a milling machine equipped with a 1 mm drill bit, ensuring a distance of 1 mm between the notch faces. Carbon-epoxy sacrificial plates were used at the top and bottom faces of the specimens to avoid damage during the machining process. The notch tip was not sharpened because, after the damage process has developed from the notch tips, the actual crack tip can be considered *sharp*, and this should not affect the value of the fracture toughness at unstable crack propagation [187].

For materials with $0 \leq \rho \leq 4$, the generic correction factor $\kappa(\alpha, \rho, \varphi)$ can be replaced by the finite-width correction (FWC) factor for isotropic materials, which in the case of sufficiently long specimens ($\varphi \approx 0$) can be written as $f(\alpha)$, multiplied by a correction factor for the orthotropy of the material, $\chi(\rho)$ [270]. However, as discussed by Catalanotti et al. [65], for highly orthotropic materials, with $\rho > 4$ (which is typically the case of cross-ply laminates), the generic correction factor κ, which takes into account both geometry and orthotropy dependence, should be determined, using, for instance, parametric computational fracture mechanics techniques [65].

Catalanotti et al. [65] built a parametric model of a double edge-cracked plate in Python to calculate the correction factor κ for different values of α, ρ and φ using the commercial Finite Element (FE) package Abaqus. The Virtual Crack Closure Technique (VCCT) was used to calculate the ERR. The details of the FE model are given in Ref. [65].

For a sufficiently long specimen ($\varpi < 0.5$), the correction factor κ can be written as [65]:

$$\kappa(\alpha, \rho) = \sqrt{\tan\frac{\pi\alpha}{2}} \sum_{i=1}^{M}\sum_{j=1}^{N} \Phi_{ij}\alpha^{i-1}\rho^{j-1} \tag{4.13}$$

where Φ_{ij} is the element of the matrix $\mathbf{\Phi}$ of indexes i and j, and M and N are respectively the number of rows and columns of matrix $\mathbf{\Phi}$. The latter was calculated by Catalanotti et al. [65] and is given as:

$$\boldsymbol{\Phi} = \begin{bmatrix} 1.7482487564 & -0.053754159533 & 0.0040142704949 & -9.8480085881\text{E}-4 \\ -0.76896688866 & -0.0068632911438 & 0.0029984681658 & -0.00010108691939 \\ 0.85633404777 & 0.23922363475 & -0.023289123198 & 0.00062358861997 \\ -0.67470597429 & -0.25334178248 & 0.022297779266 & -0.00056784694513 \\ 0.18495379886 & 0.084067007027 & -0.0068989066533 & 0.00016783852495 \end{bmatrix} \tag{4.14}$$

All DENT tests were performed under displacement control, at a controlled speed of 1.0 mm/min, in an MTS 810 servo-hydraulic testing machine with a load capacity of 250 kN, equipped with a 250 kN load cell. The test data was acquired directly by the testing machine commands module, with an acquisition frequency of 5.0 Hz.

The 10 mm wide specimens (geometry A) were fixed to the load frame using a bolted clamping rig with four M8 bolts fastened with a torque of 35 Nm. The remaining specimen configurations were fixed using the same bolted clamping rig used in the UD unnotched tension tests (section 4.3.1), with six M10 bolts fastened with a torque of 55–60 Nm. Strips of Dexter sandpaper with coarse grains were inserted between the specimen surfaces and the grips to improve the load transfer capability of the bolted clamping system and prevent sliding.

4.3.5. Fabric mode I compressive crack resistance curve — size effect of Double Edge-Notched Compression (DENC) specimens

In composites, characterisation of the fracture behaviour associated with intralaminar failure involving fibre breakage is not limited to the tensile failure mode. Measuring the fracture toughness and the corresponding $\mathcal{R}$-curve associated with the propagation of a kink band is currently as important as in the tensile case, namely for the assessment of the fracture behaviour and for the definition of the softening laws used in recent computational analysis models [106, 108, 189, 190], as well as in establishing the energy equilibrium equations used in closed-form solutions [181, 182] that predict the ultimate strength of composite structures.

The compact compression (CC) test specimen [191, 192] has been used for characterisation of the compressive fracture toughness of composite laminates. However, the CC test specimen is deemed inadequate to perform reliable measures of the compressive intralaminar fracture toughness of composite laminates [187, 207]. On one hand, there are no adequate data reduction methods for the CC test specimen as the contact tractions that occur on the crack faces during kink band growth are not taken into account. On the other hand, the CC test specimen triggers diffused damage during the propagation of the kink band, which artificially increases the value of the measured fracture toughness and makes the detection of the tip of the kink band impossible, reading this test method unreliable for the determination of the $\mathcal{R}$-curve.

In order to obviate the drawbacks of the CC specimen, a methodology based on the size effect law [209] can be used to measure the mode I intralaminar fracture toughness and the $\mathcal{R}$-curve associated with the formation of a kink band [187]. In fact, because it is assumed to have a crack-like behaviour [131, 164, 271], the propagation of a kink band implies a size effect [164] and, consequently, a well defined $\mathcal{R}$-curve [187].

Following the reasoning presented in section 4.3.4, taking x and y as the preferred axes of the material (figure 4.5), for a two-dimensional orthotropic body the ERR in mode I, $\mathcal{G}_I$, for a crack propagating in the y-direction is given by equation (4.5), and using the orthotropy rescaling technique [269, 270], the SIF, $\mathcal{K}_I$, can be written in a generic form as shown in equation (4.9).

As in the tensile case, the size effect law can be calibrated using a set of scaled *geometrically similar specimens* and fitted using, for instance, one of the regression methods proposed in Ref. [209]. Following Catalanotti et al. [187], scaled Double Edge-Notched Compression (DENC) specimens were tested (figure 4.6).

Table 4.5 shows the size effect DENC test matrix, where W is the total specimen width, L is the specimen length (end loading), and a_0 is the machined edge notch length. The characteristic dimension w is taken as half specimen width ($w = W/2$), and the edge notch length-to-width ratio is kept constant in all scaled specimens ($\alpha_0 = a_0/w = 0.6$). The tests were performed on laminates *UDB240* and *UDB160* (tables 4.2 and 4.3).

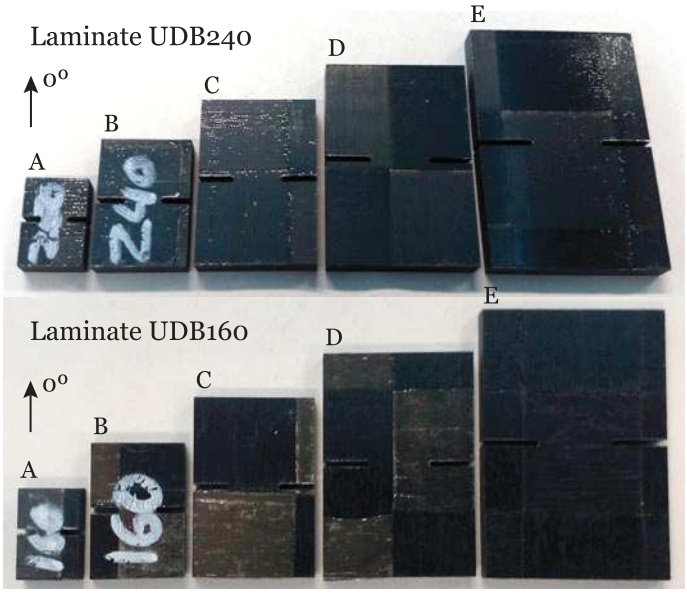

Fig. 4.6. Representative DENC test specimens.

Table 4.5
Size effect DENC test matrix.

Geometry ID	L (mm)	W (mm)	a_0 (mm)
A	15.0±0.1	10.0±0.1	3.00±0.03
B	22.5±0.1	15.0±0.1	4.50±0.03
C	30.0±0.1	20.0±0.2	6.00±0.03
D	37.5±0.1	25.0±0.2	7.50±0.03
E	45.0±0.1	30.0±0.3	9.00±0.03

The edge notches were obtained using a milling machine equipped with a 1 mm drill bit, as in the DENT test specimens, and carbon-epoxy sacrificial plates were used at the top and bottom faces of the specimens to avoid damage during the machining process. A separation of 1 mm between the crack faces could be ensured, avoiding contact between the crack faces after propagation of the kink band. As discussed by Catalanotti et al. [187], such contact would have invalidated the experimental results. Also discussed by Catalanotti et al. [187] is the fact that the semicircular shape of the notch tip does not affect the correct determination of the $\mathcal{R}$-curve because the notch tip shape does not influence the value of the fracture toughness in compression, and also because, after the initial propagation, the tip of the kink band that has formed can be considered equivalent to a *sharp* crack, which should not affect the value of the fracture toughness at unstable propagation.

The dimensionless function $\kappa(\alpha, \rho, \varphi)$, which accounts for the geometry and orthotropy of the material, can be defined using a parametric FE model and the VCCT, as proposed by Catalanotti et al. [187]. The parametric model was defined for specimens with a fixed width-to-length ratio $2\varpi = 2w/L = 2/3$ subjected to end loading (displacement applied on the top face and fixed bottom face). Frictionless contact was assumed. The calibration was performed having as variables the shape parameter α and the dimensionless parameter ρ, valid for the range $0 < \alpha < 1$ and $0 \leq \rho < 20$.

Using the results obtained in the FE analysis, Catalanotti et al. [187] approximated the correction factor $\kappa(\alpha, \rho)$ by the following polynomial function:

$$\kappa(\alpha, \rho) = \sqrt{\frac{\alpha}{1-\alpha} \sum_{i=1}^{M} \sum_{j=1}^{N} \Phi_{ij} \rho^{j-1} \alpha^{i-1}} \tag{4.15}$$

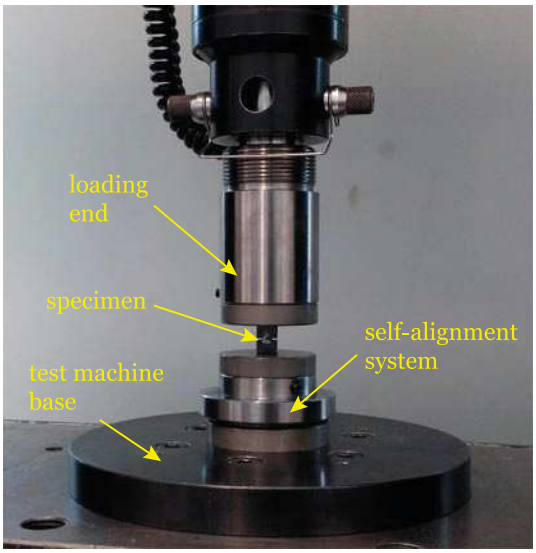

Fig. 4.7. DENC end-loading and self-alignment test setup.

where Φ_{ij} is the element of matrix $\mathbf{\Phi}$ at the row i and column j, and M and N are respectively the number of rows and columns of the matrix, which is given as [187]:

$$\mathbf{\Phi} = \begin{bmatrix} 4.315050777 & -0.1833177904 & 0.01642021976 & -4.829962430\text{E}-4 \\ -5.148136502 & -0.3554678337 & -9.974634025\text{E}-4 & 4.975387379\text{E}-4 \\ 2.385888075 & 1.339974300 & -0.05966399650 & 7.544565390\text{E}-4 \\ -0.2810124370 & -0.8040552990 & 0.04491874691 & -7.869467548\text{E}-4 \end{bmatrix} \tag{4.16}$$

It is important to stress that the matrices $\mathbf{\Phi}$ used in the dimensionless functions $\kappa(\alpha,\rho)$ in tension (section 4.3.4) and in compression, given respectively by equations (4.14) and (4.16), are different, since they were established for different boundary value problems.

Catalanotti et al. [187], by comparing the numerical solution obtained in the FE simulations with the polynomial approximation in equation (4.15), showed that the fitting is excellent. This polynomial approximation can, therefore, be used in the analytical model for implementation of the proposed formulation. Using the polynomial approximation of $\kappa(\alpha,\rho)$ defined by Catalanotti et al. [187] in the equations of the driving force curves given by equation (4.10), it is observed that the ERR is an increasing function of the crack length, and therefore the proposed specimen has a *positive geometry*.

All DENC tests were performed under displacement control, at a controlled speed of 0.1 mm/min, in an Instron 4208 electro-mechanical universal testing machine with a load capacity of 300 kN and equipped with a 100 kN load cell. The test data was acquired using a Spider 8 data logger, with an acquisition frequency of 5.0 Hz.

An end-loading test rig with a self-alignment system (figure 4.7), similar to the longitudinal and off-axis compression tests, was used [187]. A thin layer of MoS_2 was used between the specimen end-surfaces and the surfaces of the rig to minimise friction.

4.3.6. Laminate tensile unnotched strength

In the aeronautic industry, the derivation of lamina allowables for laminate design does not meet all requirements set by current regulations [25]. It is still considered that failure theories using lamina-level test data does not correlate well over the range of potential failure modes. Unless very conservative lamina values are used, laminate-level tests are required to verify the predicted failures. In addition, correction or modification factors must be applied to either the ply design values or elsewhere in the analysis. This is to account for lamination or structural load path effects which are not

Fig. 4.8. Representative laminate unnotched compression test specimens.

reflected in the lamina specimen tests. Additional testing or factors may also be needed to account for the production methods used to fabricate parts. To obtain these factors, tests of the actual laminates and structure must be conducted [25].

The experimental determination of the unnotched strengths of laminates is required not only for mechanical characterisation of a composite material, but also for the development of material scatter factors, for the definition of in-plane laminate strength design allowables, to evaluate specimen failure modes, and for preliminary laminate analysis [25]. Coupon level tests in unnotched configurations are also conducted to assess durability, manufacturing anomalies and environmental effects [25]. Moreover, knowledge of the laminate unnotched strengths is also required for application and validation of design tools based on analytical methods [25, 121, 135, 175–177, 179–182, 249].

In this work, unnotched specimens with a nominal width (W) of 25 mm and a nominal length (L) of 300 mm were tested in tension, following the ASTM D3039/D3039M – 14 test standard [262]. In order to assess the effect of the grade of the STFs on the mechanical response of structural, multidirectional laminates, the tests were conducted on laminates *DTO240* and *DTO160* (tables 4.2 and 4.3).

The unnotched tension tests were performed in an MTS 810 servo-hydraulic testing machine with a load capacity of 250 kN and equipped with a 250 kN load cell. The tests were conducted under displacement control, at a speed of 1.0 mm/min. The test data was acquired directly by the testing machine commands module, with an acquisition frequency of 5.0 Hz.

The specimens were fixed to the loading frame using the same bolted clamping rig used in the UD unnotched tension tests (section 4.3.1), with six M10 bolts fastened with a torque of 55–60 Nm. Strips of Dexter sandpaper with coarse grains were inserted between the specimen surfaces and the grips to improve the load transfer capability of the bolted clamping system and prevent sliding. The gauge length was set to 150 mm.

4.3.7. Laminate compressive unnotched strength

Compression testing of unnotched coupons is also required not only for mechanical characterisation, but also for the development of material scatter factors and strength design allowables, to evaluate specimen failure modes, for preliminary laminate analysis, to assess durability, manufacturing anomalies and environmental effects, and to apply and validate analytical design tools. Furthermore, compression unnotched tests are also performed to establish the baseline for damage tolerance analysis based on compression after impact testing.

In this work, unnotched compression tests were conducted on specimens with a nominal width (W) of 25 mm and a nominal length (L) of 305 mm (figure 4.8) of laminates *DTO240* and *DTO160* (tables 4.2 and 4.3). Following the ASTM D6484/D6484M – 14 test standard [272], a special test rig designed to prevent buckling was used in the compression tests.

The alignment of the clamping system with the axis of the testing machine was performed using two guiding pins with a diameter of 6 mm in the ends of the specimens. The guiding holes in the specimen (figure 4.8) were obtained using a drilling machine. Carbon-epoxy sacrificial plates were used at the insertion and exit points of the drill to avoid damage during the machining process.

The compression rig was clamped using M8 bolts fastened with a torque of 8 Nm. The tests were performed under displacement control, at a controlled speed of 1.0 mm/min, in a servo-hydraulic MTS 810 testing machine with a load capacity of 100 kN, equipped with a 100 kN load cell. The acquisition frequency was set to 5.0 Hz.

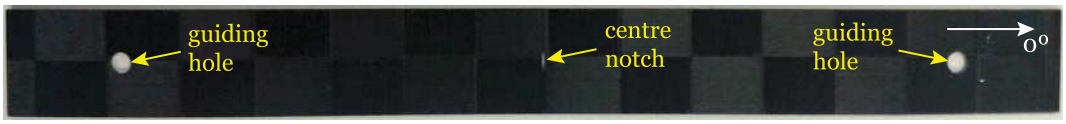

Fig. 4.9. Representative CNC test specimens.

4.3.8. Laminate tensile centre-notched strength

The increasing use of composite laminates in the design of structural parts requires a better understanding of the mechanical performance and structural integrity of these materials, especially in the presence of high stress concentrations, originated, for instance, by discrete sources of damage. Notched specimen configurations are often used in the design process of composite structures to account for the effects of such high stress concentrations [25]. The Centre-Notched Tension (CNT) configuration is perhaps the most widely used.

In the present work, CNT tests, based on the ASTM D5766/D5766M – 11 test standard [273] for open-hole tensile strength, are carried out to assess the tensile residual strength of STF laminates of different grades in the presence of discrete damage in the form of a straight notch. CNT specimens of laminates *DTO240* and *DTO160* (tables 4.2 and 4.3) with a nominal width (W) of 30 mm and a nominal length (L) of 300 mm were tested. A centre notch on each specimen with a nominal length ($2a$) of 5 mm was obtained using a milling machine equipped with a 1 mm drill bit, ensuring a distance of 1 mm between the notch faces and a width-to-notch length ratio ($W/2a$) equal to 6. Carbon-epoxy sacrificial plates were used at the top and bottom faces of the specimens to avoid damage during the machining process. Based on previous observations [212], the notch tips were not sharpened. On one hand, this avoids getting irregular notch faces that are inevitably obtained when using very sharp saws for that purpose [166], a process that can be very laborious. On the other hand, having a 1 mm diameter notch tip for all specimens shall not affect the results of the size effect study, as once the propagation of the damage process zone has initiated, its progression will dictate the final response.

The CNT tests were performed under displacement control, at a controlled speed of 1.0 mm/min, in an MTS 810 servo-hydraulic testing machine with a load capacity of 250 kN, equipped with a 250 kN load cell. The acquisition frequency was set to 5.0 Hz.

The specimens were fixed to the loading frame using the same bolted clamping rig used in the UD unnotched tension tests (section 4.3.1), with six M10 bolts fastened with a torque of 55–60 Nm. Strips of Dexter sandpaper with coarse grains were inserted between the specimen surfaces and the grips to improve the load transfer capability of the bolted clamping system and prevent sliding. The gauge length was set to 150 mm.

4.3.9. Laminate compressive centre-notched strength

A similar configuration to the CNT test has been used, for example, for characterisation of the compressive fracture toughness of composite laminates, by reversal of the loading configuration used in tensile fracture toughness testing [192, 212]. The Centre-Notched Compression (CNC) tests are useful for application and validation of strength prediction methods based on fast analysis tools such as LEFM or FFMs [179, 180], or based on more complex analysis models including strain-softening laws [25].

CNC tests were conducted on specimens with a nominal width (W) of 30 mm and a nominal length (L) of 300 mm were tested (figure 4.9). The CNC tests were performed on laminates *DTO240* and *DTO160* (tables 4.2 and 4.3). Following the ASTM D6484/D6484M – 14 test standard [272], a special test rig designed to prevent buckling was used.

The alignment of the clamping system with the axis of the testing machine was performed using two guiding pins with a diameter of 6 mm in the ends of the specimens. The guiding holes in the specimen (figure 4.9) were obtained using a drilling machine. A centre notch on each specimen with a nominal length ($2a$) of 5 mm (figure 4.9) was obtained using a milling machine equipped with a 1 mm drill bit, ensuring a width-to-notch length ratio ($W/2a$) equal to 6. Carbon-epoxy sacrificial plates were used at the top and bottom faces of the specimens to avoid damage during the drilling and machining processes.

Table 4.6
OHT test matrix.

Geometry	L_s (mm)	L (mm)	W (mm)	d (mm)
Large	300±1	150±1	30.0±0.3	5.00±0.06
Small	300±1	200±1	12.0±0.1	2.00±0.06

A separation of 1 mm between the crack faces could be obtained, avoiding contact between the crack faces after compressive failure. Avoiding such contact allows self-similar compressive fracture propagation at failure.

Moreover, as discussed in section 4.3.5, the semicircular shape of the notch tip does not affect the correct determination of compressive centre-notched strength because the notch tip shape does not influence the value of the fracture toughness in compression and, after the initial propagation, the tip of the kink band that has formed can be considered equivalent to a *sharp* crack, which should not affect the value of the notched strength observed at unstable propagation.

The rig was clamped using M8 bolts fastened with a torque of 8 Nm. Because some specimens were slightly longer than the end-loading compression rig, the ends outside the rig needed to be polished using a metallic rasp to ensure that the ends of the specimen coincided with the ends of the compression rig.

The tests were performed at a controlled speed of 1.0 mm/min, in a servo-hydraulic MTS 810 testing machine with a load capacity of 100 kN, equipped with a 100 kN load cell. The acquisition frequency was set to 5.0 Hz.

4.3.10. Open-Hole Tension (OHT) tests

In the current design process of advanced composite structures used, for instance, in the airframe, open-hole tests are typically required to study the behaviour of composite laminates with stress concentrations, to assess the effect of size in composite materials, to generate laminate allowables, and to meet damage resistance/tolerance requirements [25]. In addition, these tests are important in preliminary design of notched components for the definition of "*characteristic distances*" used in semi-empirical strength prediction models [175, 176, 235], and for validation of design tools based on analytical methods [25, 121, 135, 175–177, 179, 180, 182, 249].

In the present work, Open-Hole Tension (OHT) tests are carried out to evaluate the mechanical behaviour in the presence of stress concentrations and the effects of size in the STF laminates of different grades when subjected to tensile efforts. OHT tests, based on the ASTM D5766/D5766M – 11 test standard [273], were performed on laminates *DTO240* and *DTO160* (tables 4.2 and 4.3). OHT specimens of different sizes were tested under displacement control, at a controlled speed of 1.0 mm/min, in an MTS 810 servo-hydraulic testing machine with a load capacity of 250 kN, equipped with a 250 kN load cell. The test data acquisition frequency was set to 5.0 Hz.

Table 4.6 shows the OHT test matrix, where W is the total specimen width, L_s is the total specimen length, L is the gauge length (free length between grips), and d is the hole diameter. The width-to-hole diameter ratio (W/d) was constant and equal to 6. The open holes were obtained by a drilling machine, using carbon-epoxy sacrificial plates at the insertion and exit points of the drill to avoid damage during the machining process.

The 12 mm wide (small) OHT specimens were fixed to the load frame using a bolted clamping rig with four M8 bolts fastened with a torque of 35 Nm. The 30 mm wide (large) OHT specimens were fixed using the same bolted clamping rig used in the UD unnotched tension tests (section 4.3.1), with six M10 bolts fastened with a torque of 55–60 Nm. Strips of Dexter sandpaper with coarse grains were inserted between the specimen surfaces and the grips to improve the load transfer capability of the bolted clamping system and prevent sliding.

4.3.11. Open-Hole Compression (OHC) tests

In current airframe design guidelines, Open-Hole Compression (OHC) tests are often used directly in the analysis methods employed in the design process of composite structures or components [25]. OHC tests are also performed in part fabrication verification to assess typical failure modes of detail areas extracted from composite parts or sections [25].

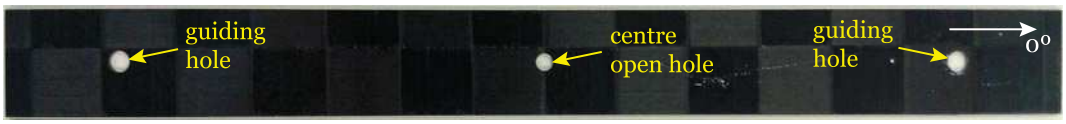

Fig. 4.10. Representative OHC test specimens.

In addition, the derivation of laminate allowables for structural design typically requires testing OHC specimens for the definition of correction or modification factors to account for defects or in-service damage events (design for damage tolerance) [25]. OHC tests can be performed to establish a lower bound for damage tolerance analysis, namely when the minimum damage size detectable by non-destructive inspection is specified or the typical size of the damage inflicted by low-velocity impact is known in advance, eventually replacing compression after impact testing. OHC is also a prescribed test of the *Building Block Approach* for composite structures [25].

Regarding the implementation of analysis methods for compressive failure modes, OHC test data can be used in the determination of "*characteristic distances*" used in semi-empirical tools [175, 176, 235]. Moreover, OHC tests have been used in the validation of physically-based analysis models derived from analytical solutions [121, 135].

In this work, OHC tests are conducted to evaluate the mechanical behaviour of the STF structural laminates *DTO240* and *DTO160* (tables 4.2 and 4.3) in the presence of stress concentrations, when subjected to compressive loadings. Specimens with a nominal width (W) of 30 mm and a nominal length (L) of 300 mm were tested (figure 4.10). The nominal hole diameter (d) was 5 mm, resulting in a width-to-hole diameter ratio (W/d) equal to 6.

Following the ASTM D6484/D6484M – 14 test standard [272], a special test rig designed to prevent buckling was used. The alignment of the clamping system with the axis of the testing machine was performed using two guiding pins with a diameter of 6 mm in the ends of the specimens. The centre hole and the guiding holes in the specimen (figure 4.9) were obtained using a drilling machine. Carbon-epoxy sacrificial plates were used at the top and bottom faces of the specimens to avoid damage during the drilling process.

The compression rig was clamped using M8 bolts fastened with a torque of 8 Nm. The tests were performed under displacement control, at a controlled speed of 1.0 mm/min, in a servo-hydraulic MTS 810 testing machine with a load capacity of 100 kN, equipped with a 100 kN load cell. The acquisition frequency was set to 5.0 Hz.

4.3.12. Bearing tests

Mechanically fastened joints are generally the critical part of a composite structure, as they are a source of weakness and compliance. Therefore, since the introduction of composite structures in the aeronautic and aerospace industries, new joint design solutions had been proposed. For example, specialised fasteners featuring larger tail footprint areas to improve pull-through and bearing strengths had been introduced in composites design, whereas rivets had been eliminated due to the low through-the-thickness composite laminate strength [25]. Use of aluminium fasteners was also eliminated due to galvanic corrosion susceptibility between carbon and aluminium [25]. More recently, innovative hybrid metal-composite laminated bolted joints were proposed to increase efficiency of mechanical fastening in composite structures [274].

Bearing failure is perhaps the most common failure mode in composite mechanically fastened joints, occurring predominantly when the bolt diameter is a small fraction of the plate width. Therefore, the bearing strength of a laminate, i.e. the load corresponding to bearing failure, is often taken as the measure of the performance of composite joints.

Because bearing failure is non-catastrophic, being characterised by a progressive accumulation of damage, different definitions of bearing strength can be used. Some definitions are the maximum load sustained by the joint, the first load drop, the onset of nonlinearity in the bearing strain-bearing stress relation, or a limit value for the permanent deformation of the hole. Even though the correct definition of bearing strength is not clear, as it depends on the permanent deformation in the hole and on the damage mechanisms occurring in the material [235], comparisons for the same definition are generally accurate and allow a reliable source of analogy between different laminates.

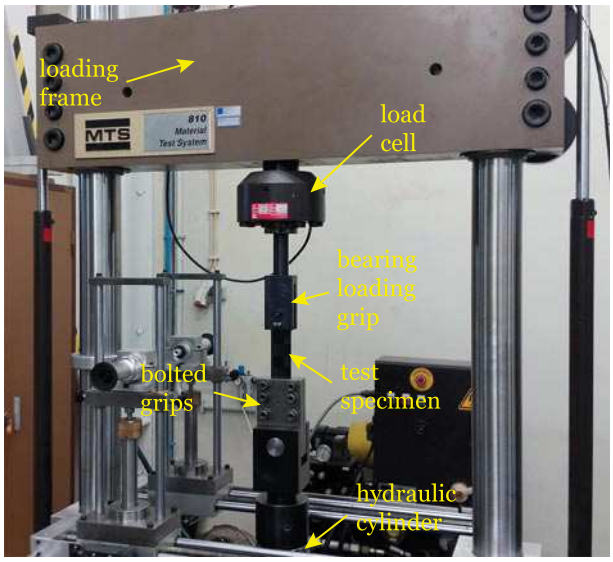

Fig. 4.11. MTS 810 testing machine and bolt-bearing test setup.

The bearing strength of a composite laminate also depends on the lateral support provided in the bearing region. Because most mechanically fastened joints include clamping pressure, bolt-bearing tests are typically used to characterise the bearing strength of laminates. In bolt-bearing tests, a "finger-tight" clamping pressure is applied to give conservative bearing stress results [235, 237]. In this configuration, washers are typically used.

Bolt-bearing tests were performed following the ASTM D5961/D5961M – 13 test standard [237]. Specimens with a nominal hole diameter $d = 6$ mm, end distance-to-hole diameter ratio $e/d = 6$, width-to-hole diameter ratio $W/d = 6$, and nominal length $L = 215$ mm were used. A bolt M6 was used with washers subjected to a "finger-tight" clamping pressure, corresponding to a torque $T = 2.2$ Nm.

The tests were conducted in a servo-hydraulic MTS 810 testing machine with a load capacity of 100 kN (figure 4.11), equipped with a 100 kN load cell. The tests were performed under displacement control, at a controlled speed of 1.0 mm/min.

The acquisition frequency was set to 5.0 Hz. The end of the specimen far from the bearing hole was clamped using a bolted clamping rig with six M10 bolts fastened with a torque of 55–60 Nm. Strips of Dexter sandpaper with coarse grains were inserted between the specimen end and the grip to improve the load transfer capability of the bolts clamping system and avoid sliding.

The alignment of the longitudinal axis of the gripped specimen with the test direction was performed using a guiding pin with a diameter of 4 mm. The bearing and guiding holes in the specimen were obtained using a drilling machine, with carbon-epoxy sacrificial plates at the insertion and exit points of the drill to avoid damage at the holes edges.

4.4. Instrumentation

The experimental monitoring of damage and fracture phenomena in composite materials using optical full-field techniques can be extremely useful to identify and understand the complex failure behaviour of these materials [5, 121, 122, 182, 196]. In this experimental programme, full-field measurements were performed using the digital image correlation (DIC) technique to obtain the surface in-plane displacement and strain fields of the outer (0/90) STF layer of different coupon configurations (section 4.3). These results are used to assist in the assessment of strain concentrations and to monitor the differences in damage formation and propagation in the low-grade and thin-ply STF laminates.

The surface in-plane displacement and strain fields of the different specimens were measured by means of a single camera, using the ARAMIS DIC-2D v6.0.2 system developed by GOM [257]. The optical system was equipped with an

Table 4.7
Configuration of the DIC system.

Camera-lens optical system	
CCD camera	Baumer 138 Optronic FWX20
	8-bit
	Resolution: 1624×1236 pixels^2
	Sensor format: 1/1.8”
Lens	Nikon AF Micro-Nikkor 200 mm f/4D IF-ED
DIC measuring parameters	
Subset size	15×15 pixels^2
Subset step	13×13 pixels^2
Strain base length	5 subsets
Strain validity code	55.0%
Strain computation method	Total
DIC resolution	
Spatial resolution	2×10^{-2} pixels [187]
Strain resolution	0.01-0.04% [187]

8-bit Baumer 138 Optronic FWX20 camera, with a resolution of 1624×1236 pixels^2 and a sensor format of 1/1.8”. For higher versatility, due to the range of coupon configurations under study (section 4.3), the digital camera was coupled with a Nikon AF Micro-Nikkor 200 mm f/4D IF-ED lens for image grabbing. In all test configurations, a subset size of 15×15 pixels^2 and a subset step of 13×13 pixels^2 were used. The measured strain was computed using a strain base length of 5 subsets, with a strain validity code of 55.0%, and using the total strain method. This configuration leads to an expected spatial resolution in the order of 2×10^{-2} pixels and a strain resolution in the range 0.01-0.04% [187]. The adopted configuration is summarised in table 4.7.

For mobility and adaptability, the optical system was mounted on a multi-axis ($x - y$) positioning stage (for fine adjustments) in a tripod facing the testing machine (figure 4.12). Two Raylux 25 white light LEDs were used on either side of the camera to ensure an even illumination of the test specimen’s surface.

In the present work, textured patterns were created across the gauge section of representative specimens of each laminate by means of aerosol or airbrush painting, depending on the scale of observation of each specimen configuration. When necessary, the observation surface of each specimen analysed with the DIC system was polished by hand using wolcraft® 280 sandpaper. This procedure is intended to prevent the specimen’s surface texture from influencing the quality of the applied speckle patterns [253]. All observation surfaces were then cleaned with acetone.

Following [253], a pattern of black spots on a white background was chosen to improve the contrast of the speckle pattern and to maximise the natural variation of grey levels. Hence, a thin coating of white matte paint was applied on the (smoothed) surfaces.

To ensure a suitable speckle pattern, for the smaller specimen configurations, with regions of interest smaller than 30–45 mm, an airbrush (Iwata Custom 181 Micron CM-B model) with a fluid nozzle of 0.18 mm in diameter was used to apply the black spots (figures 4.13 to 4.21). With this marking technique, the accurate uniformity, isotropy and spot size ideal for the smaller specimens can be achieved [187], leaving less bare invariable background colour exposed within the subset [253].

It is important to note that, in figures 4.13 to 4.21, the grey levels histograms were obtained for the entire pictures. Because the pixel count includes the pixels outside the marked specimen region, the histograms often present (large — figures 4.14, 4.15 and 4.17 — or small — figures 4.19 and 4.21) grey level peaks in the dark regions (low grey levels), or extended tails (figures 4.16, 4.18 and 4.20), depending on the aspect ratio of the marked specimen region and on the notch geometry and background lighting. The measurement region in each specimen, which includes only the region of interest, is defined using the correlation software before applying the image correlation algorithm.

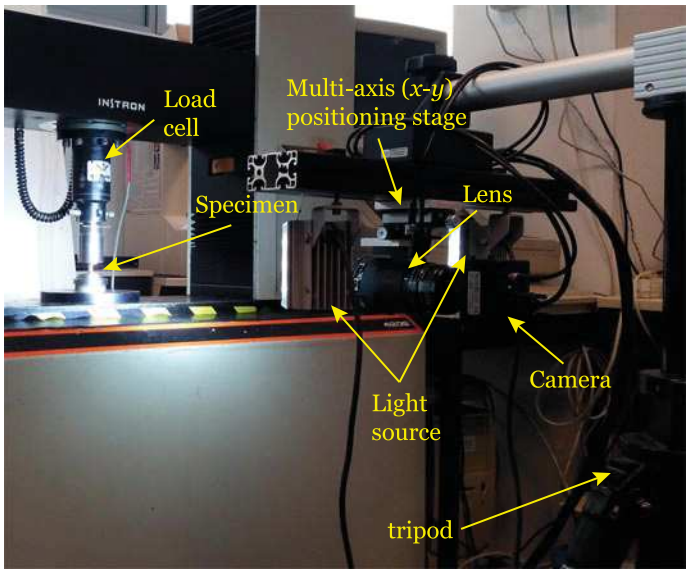

Fig. 4.12. Optical system setup.

Airbrush painting is generally regarded as the preferred marking technique. This is supported by simulations of pattern deformations and experimental validation against strain gauge readings [253]. However, very small speckles, which occupy only a small number of pixels on the camera sensor, reduce the uniqueness of the pattern and produce large variations in the identification of their size, shape and distribution relative to their original features, reducing the accuracy of the measurements [253]. Therefore, unless a set of different airbrushes are available, with different speckle size possibilities, alternative marking techniques are still required. In the current study, a coarser speckle pattern was required for the larger specimen configurations, which could not be obtained with the available airbrush. The speckle pattern was created by aerosol spray, applying a spot distribution of black paint on the white matte surface (figure 4.22).

Nevertheless, it should be noted that very large speckles decrease the randomness of the pattern, as speckles occupy larger portions of the subsets; an appropriate trade-off between speckle size, shape and density is therefore important to ensure the right conditions for the DIC measurements [253]. In the present work, the speckle patterns obtained with aerosol spray for the larger specimens show an adequate size and distribution of the black spots.

A level ruler was used to ensure a correct alignment when positioning the optical system perpendicularly to the surface of the specimen mounted into the testing machine. The lens was then adjusted to be in focus with regard to the surface of interest, setting the lens aperture to $f/4$ to minimise the depth of field. The lens aperture was then closed to $f/11$ or $f/16$ to improve the depth of field during testing. The shutter time was set in the range of 5.0–10.0 ms, maximising the grey levels distribution over the 8-bit dynamic range of the camera while avoiding saturation of the image [253]. One or two extension tubes of 20 mm, placed between the lens and the camera, were used in some cases to increase the depth of the optical field. The working distance, defined between the specimen's surface and the support of the camera, was set in the range of 530–1420 mm, depending on the size of the region of interest.

The captured region was defined according to the specimen configuration. In the case of the unnotched specimens tested in tension (sections 4.3.1and 4.3.6), the measured strain field can be used to track transverse matrix cracking in the surface transverse spread tow yarns, as well as longitudinal and transverse split cracking, before fibre-dominated catastrophic failure. In order to maximise the observation region in the specimen while maximising the resolution of the observations, the height of the observation window was defined by the specimen's width. The observation window was rotated by an angle of 90°, with the loading direction parallel to the DIC reference x-direction (figure 4.13).

In the unidirectional unnotched specimens tested in compression, in order to monitor compressive damage across the thickness, the full-field observations were performed along the edge of the specimens. The width of the DIC observation

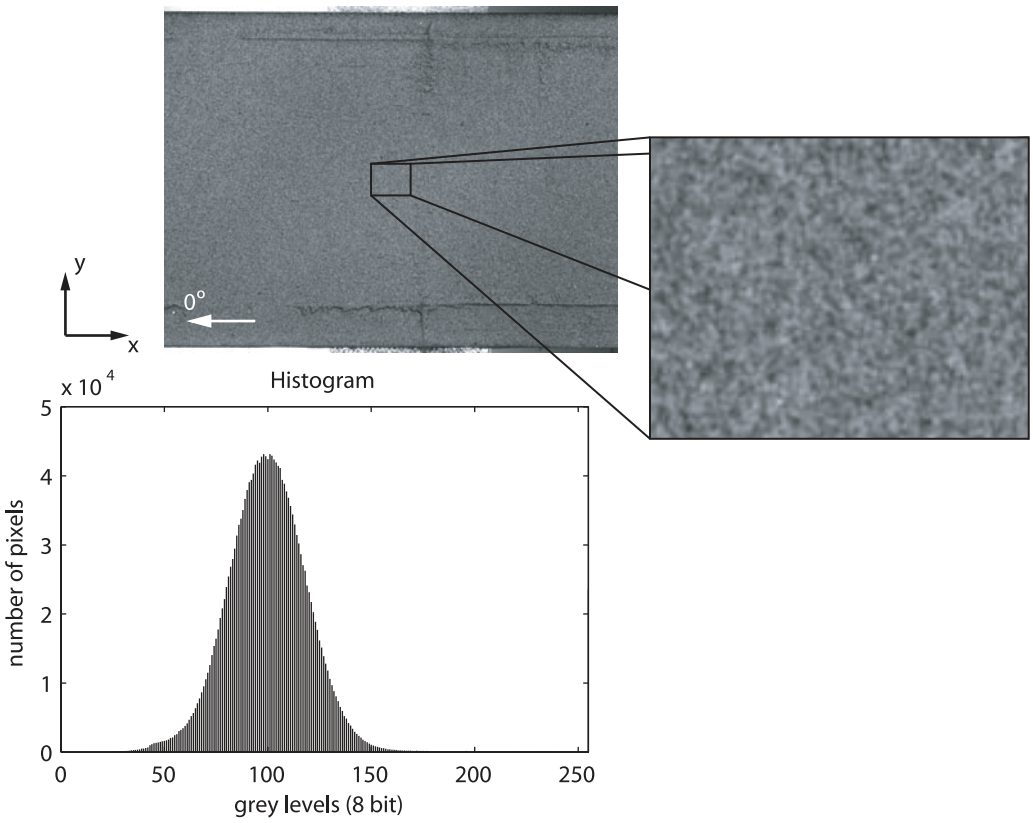

Fig. 4.13. Representative airbrush speckle pattern of an unnotched tension test specimen and corresponding grey levels histogram. The loading direction is parallel to the x-direction.

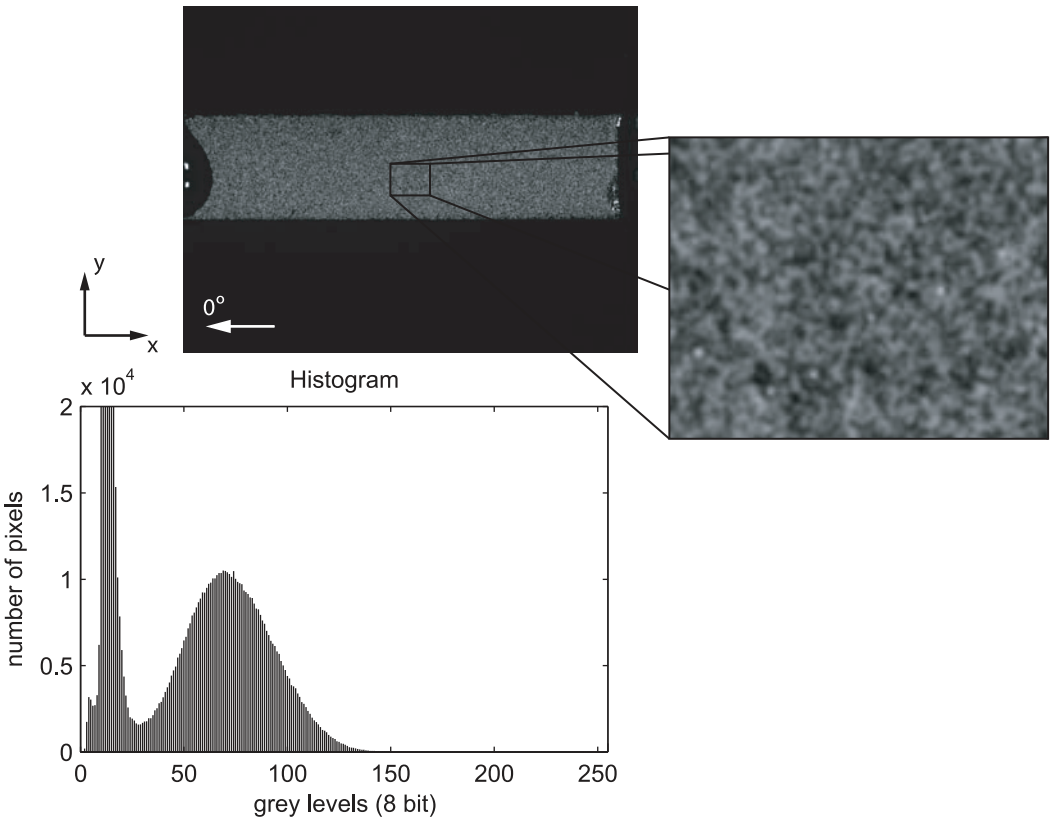

Fig. 4.14. Representative airbrush speckle pattern of an UD unnotched compression test specimen and corresponding grey levels histogram. The loading direction is parallel to the *x*-direction.

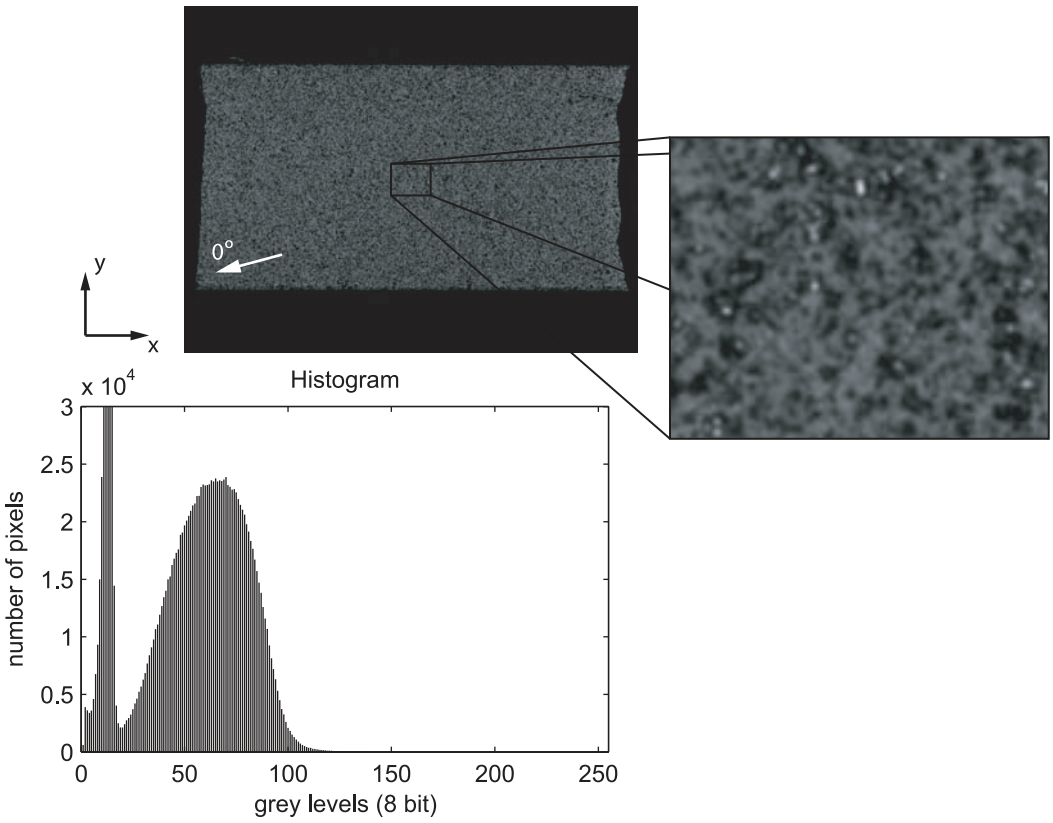

Fig. 4.15. Representative airbrush speckle pattern of an off-axis compression test specimen and corresponding grey levels histogram. The loading direction is parallel to the *x*-direction.

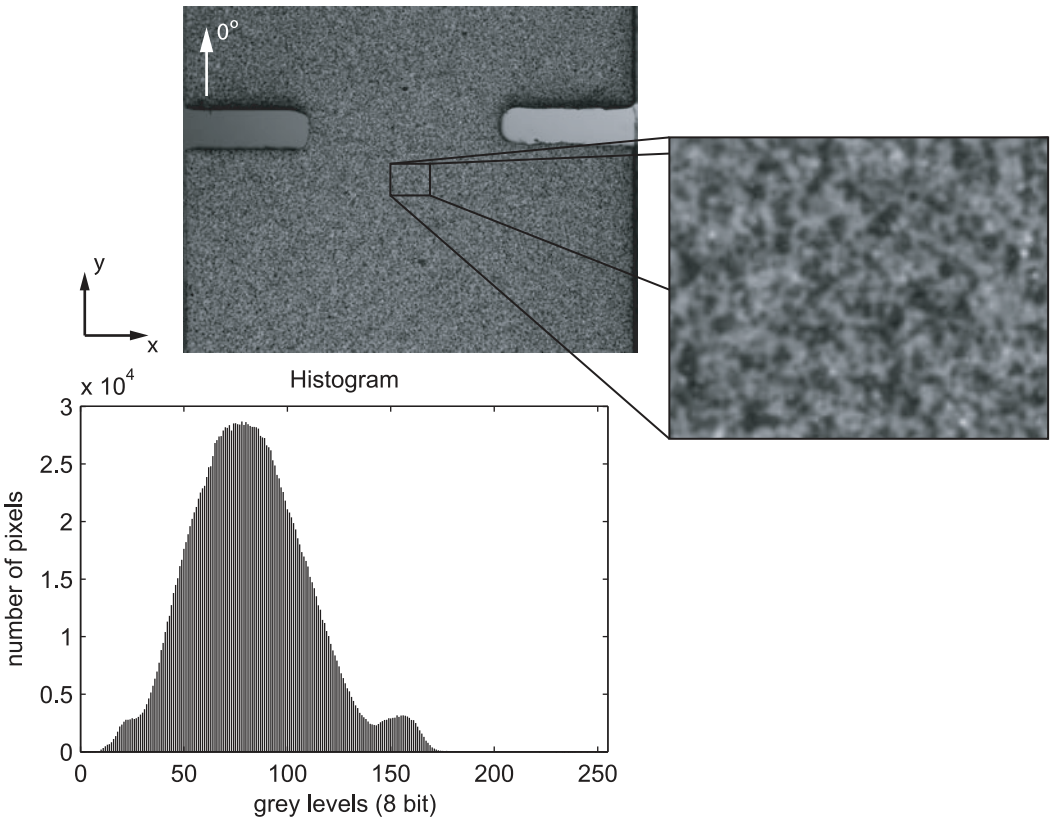

Fig. 4.16. Representative airbrush speckle pattern of a small DENT test specimen and corresponding grey levels histogram. The loading direction is parallel to the *y*-direction.

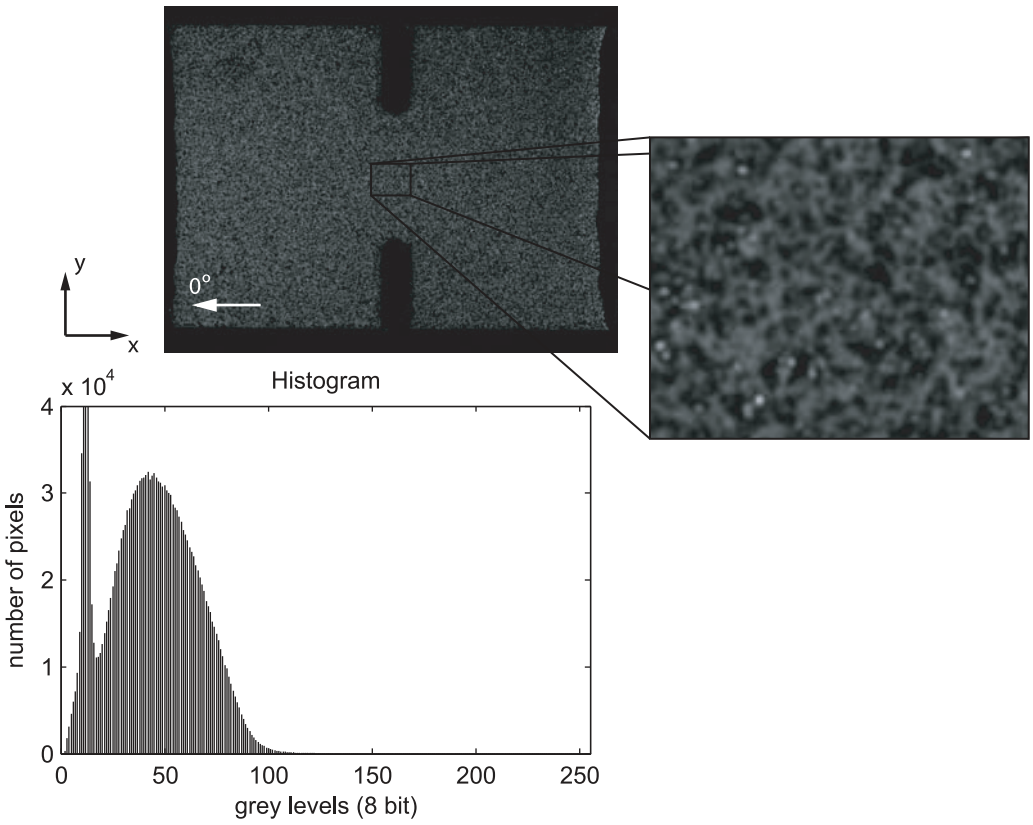

Fig. 4.17. Representative airbrush speckle pattern of a DENC test specimen and corresponding grey levels histogram. The loading direction is parallel to the x-direction.

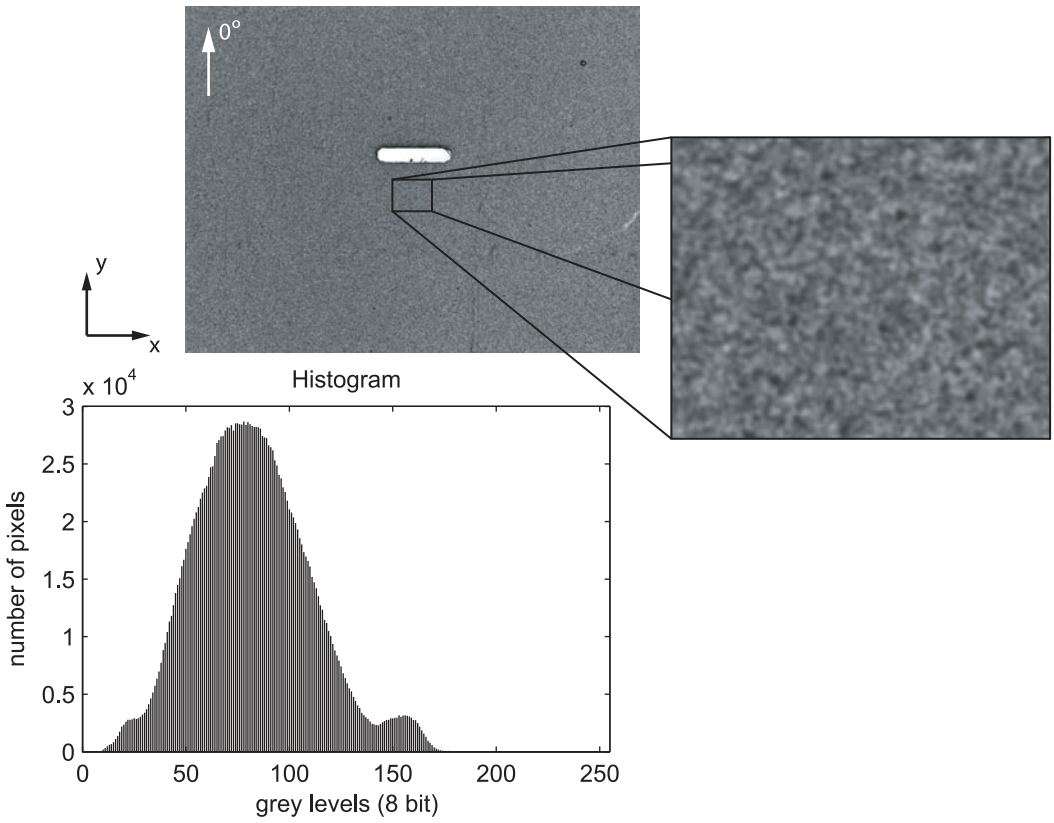

Fig. 4.18. Representative airbrush speckle pattern of a CNT test specimen and corresponding grey levels histogram. The loading direction is parallel to the *y*-direction.

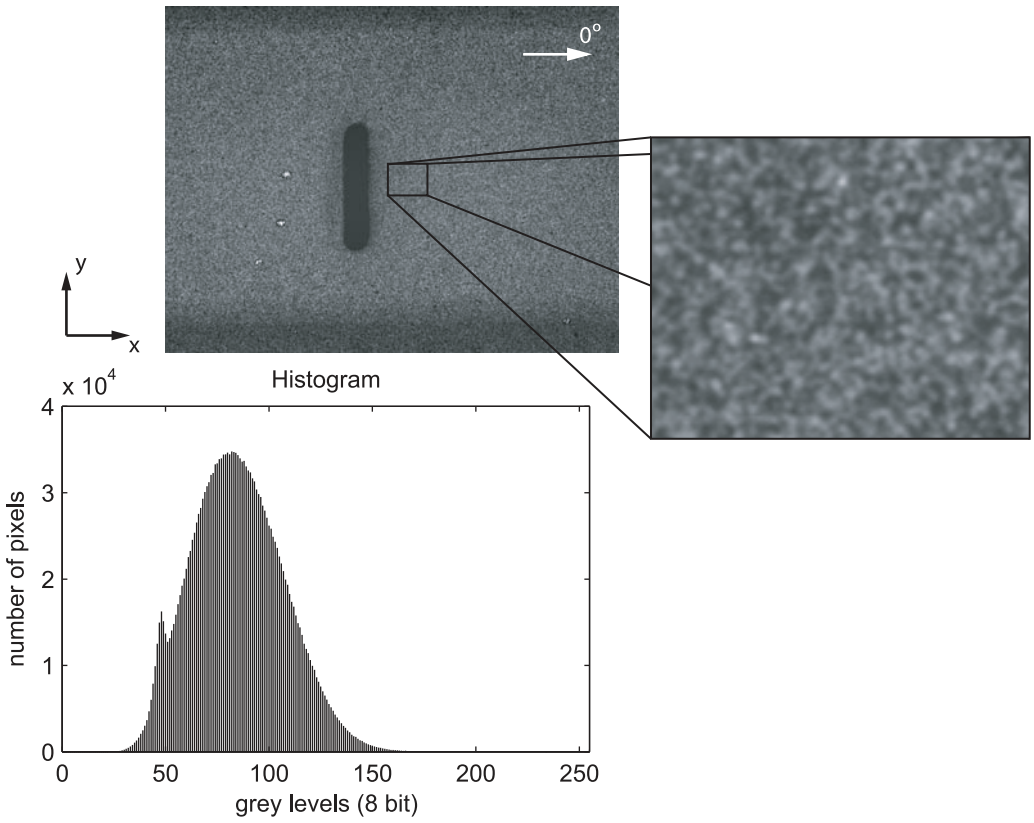

Fig. 4.19. Representative airbrush speckle pattern of a CNC test specimen and corresponding grey levels histogram. The loading direction is parallel to the x-direction.

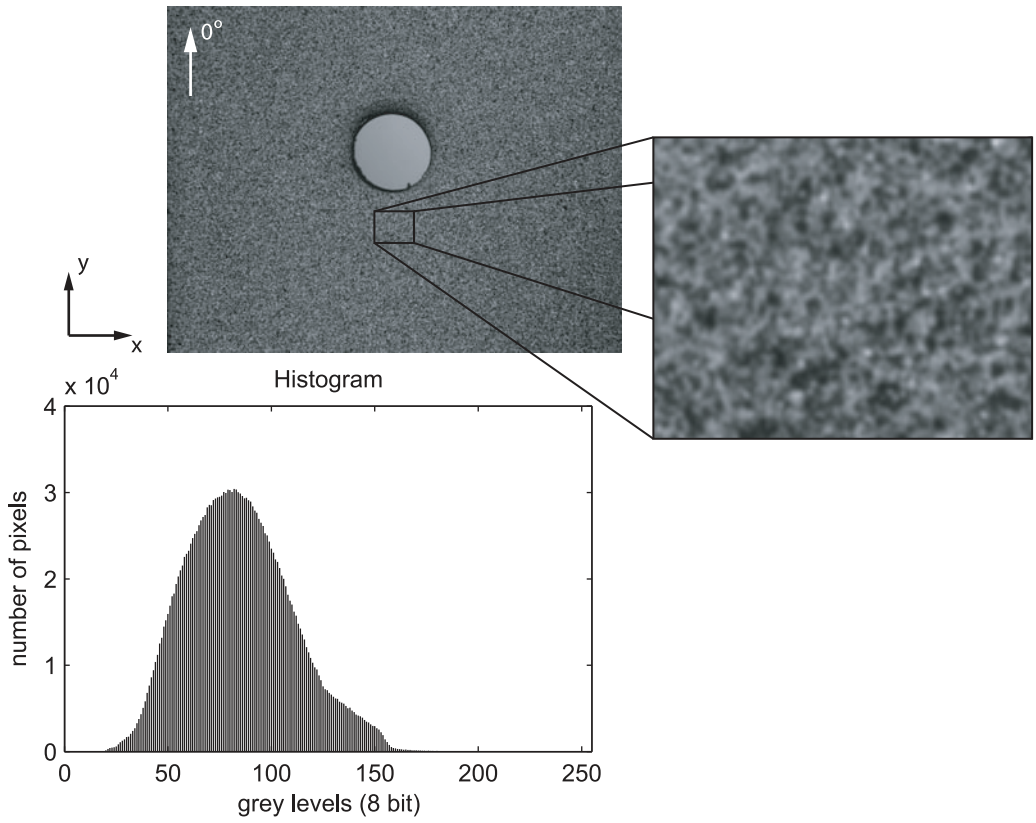

Fig. 4.20. Representative airbrush speckle pattern of an OHT test specimen and corresponding grey levels histogram. The loading direction is parallel to the *y*-direction.

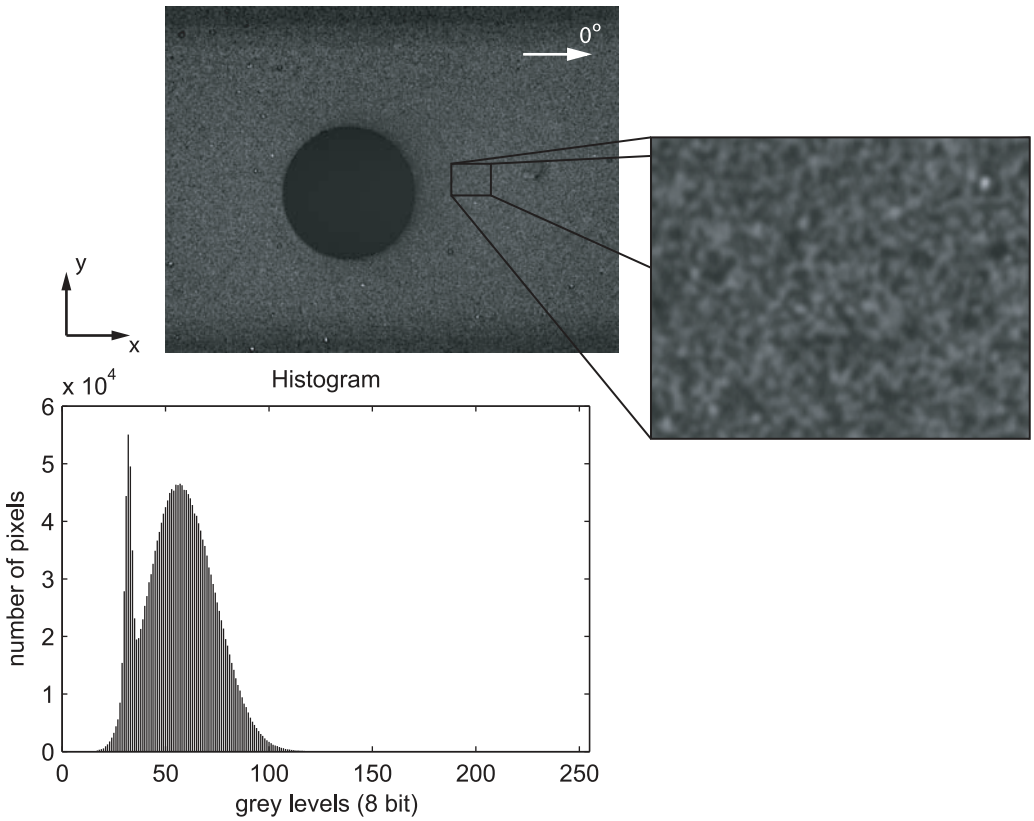

Fig. 4.21. Representative airbrush speckle pattern of an OHC test specimen and corresponding grey levels histogram. The loading direction is parallel to the x-direction.

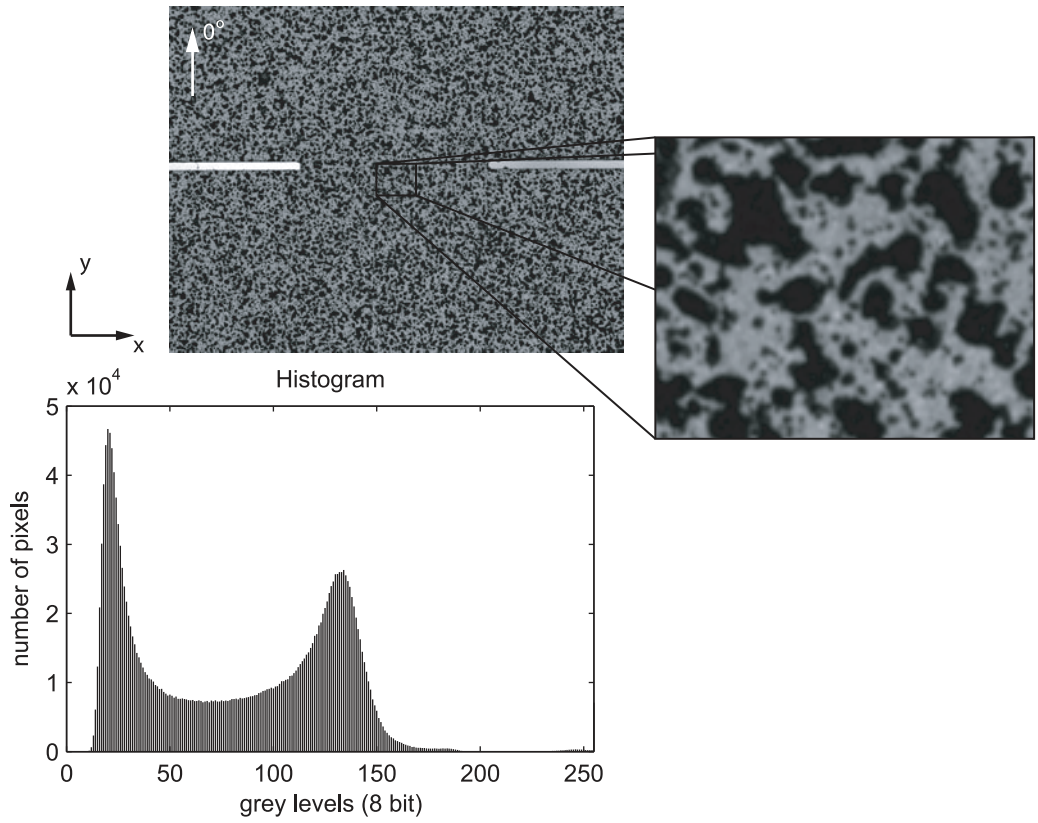

Fig. 4.22. Representative aerosol spray speckle pattern of a large DENT test specimen and corresponding grey levels histogram. The loading direction is parallel to the *y*-direction.

window was defined by the specimens' length to maximise the resolution of the observations while capturing the entire length of the specimens. Therefore, the observation window was rotated by an angle of 90° (figure 4.14).

The full-field measurements of the off-axis compression specimens were performed on the face of the specimens to measure the in-plane strain fields and fibre rotation, and to assess the correctness of the loading conditions and strain and damage localisation parallel to the fibre direction [263, 265]. The width of the DIC observation window was defined by the specimens' length to maximise the resolution of the observations while capturing the entire specimen. Therefore, the observation window was rotated by an angle of 90°, with the loading direction parallel to the DIC reference x-direction (figure 4.15).

The notched specimens were monitored using DIC to analyse the strain concentrations and the differences in damage formation and propagation from the notch boundaries. Because damage in the notched coupons is expected to occur along the notched plane, in the specimens tested in tension the width of the DIC observation window was defined by the specimens' width to maximise the resolution of the observations in the ligament section, with the loading direction parallel to the DIC reference y-direction (figures 4.16, 4.18, 4.20 and 4.22).

In compression, the full-field measurements performed on the DENC coupons were also used to assess problems in the load introduction due to possible misalignments in the loading system, and verify the validity of the tests performed. This can be done analysing the shear strain field γ_{xy} (e.g. figure 4.23), which must be perfectly antisymmetric with respect to the longitudinal axis of the specimen and zero all over the central part of the specimen and near each crack tip [187]. To observe the entire specimen's surface and maximise the field of view, the width of the observation window was set equal to the specimen's length. The captured images will consequently show the specimen rotated by an angle of 90°, with the loading direction parallel to the DIC reference x-direction (figure 4.17).

For the CNC and OHC tests (sections 4.3.9 and 4.3.11), a special test rig [272] was used to prevent buckling. The specimens were constrained in both faces, except along a small opening in the centre of the gauge section. Therefore, the full-field measurements were limited to this small window, and the strain concentrations and damage formation assessments were restricted to the vicinity of the notch boundaries. The size of the DIC observation window was defined by the size of this opening, with the loading direction parallel to the DIC reference x-direction (figures 4.19 and 4.21).

The conversion factors varied in the range of 0.0069–0.035 mm/pixel, depending on the coupon's size and region of interest for the different configurations. The acquisition frequency was set between 0.3 Hz and 2.0 Hz, depending on the test duration according to the expected maximum displacement and cross-head displacement rate. Table 4.8 shows the measuring parameters selected for each specimen configuration (section 4.3). Full-field measurements were performed in one specimen of each configuration presented in table 4.8.

In all tests performed with DIC full-field measurements, image acquisition started at the beginning of the test. However, in the compression tests performed using the end-loading setup with a self-alignment system (longitudinal compression, off-axis compression and DENC), the specimens were initially loaded up to approximately 1% of the maximum load at a displacement rate of 0.1 mm/min to ensure that the loading surface of the test setup was in contact with the specimens' top end, and to avoid recording meaningless data in the initial phase of adjustment of the specimen and self-alignment system, at which the applied load remains approximately constant and very close to zero. Then, a pre-load of approximately 10% of the maximum load was applied, again at a displacement rate of 0.1 mm/min, to perform the required adjustments of the image grabbing setup, avoiding potential parasitic movements in the initial loading stage that could affect not only the correct position of the specimen, but also the quality of the recorded images. The test specimens were subsequently unloaded to the previous position and finally loaded to failure.

4.5. Experimental results and discussion

4.5.1. Fabric tensile unnotched strength test results

The tensile unnotched strength of the STFs studied in the present work were obtained testing between 5 and 7 valid smooth coupons until failure. Figure 4.24 shows the remote stress-displacement curves of both laminates. The remote

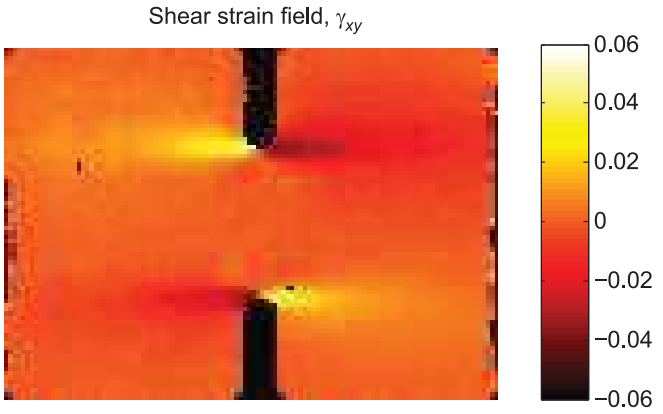

(a) Small DENC test specimen (geometry A) at an applied compressive load of 6.4 kN.

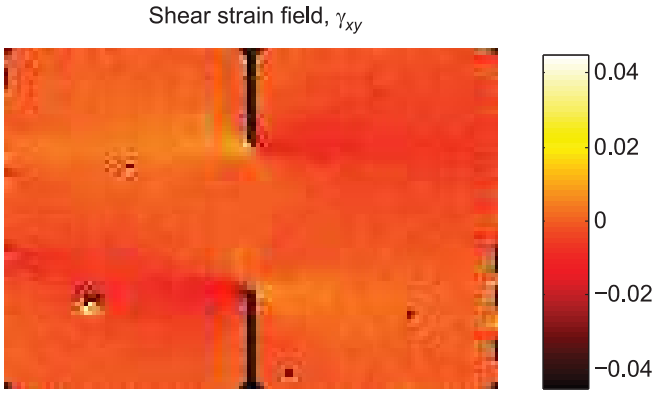

(b) Large DENC test specimen (geometry E) at an applied compressive load of 11.0 kN.

Fig. 4.23. Shear strain fields, γ_{xy}, of representative DENC test specimens. The loading direction is parallel to the horizontal axis of the specimens.

Table 4.8
Optical system parameters.

Specimen geometry	Laminate ID	Captured region (mm^2)	Conversion factor (mm/pixel)	Acquisition frequency (Hz)
Unnotched tension	*UDA240*	34.0×25.9	0.020960	0.5
	UDA160	34.0×25.9	0.020946	0.5
	DTO240	33.9×25.8	0.020891	1.0
	DTO160	33.9×25.8	0.020874	1.0
Unnotched compression	*UDB240*	19.0×14.5	0.011697	0.5
	UDB160	18.1×13.8	0.011149	0.5
15° off-axis compression	*UDB240*	20.4×15.5	0.012538	0.5
	UDB160	20.4×15.5	0.012533	0.5
30° off-axis compression	*UDB240*	20.4×15.5	0.012572	0.3
	UDB160	20.3×15.4	0.012495	0.4
DENT A	*UDB240*	11.3× 8.6	0.006956	1.0
	UDB160	11.8× 9.0	0.007292	1.0
DENT B	*UDB240*	22.2×16.9	0.013701	1.0
	UDB160	22.9×17.4	0.014075	1.0
DENT C	*UDB240*	32.4×24.7	0.019948	1.0
	UDB160	32.5×24.7	0.019996	1.0
DENT D	*UDB240*	42.7×32.5	0.026267	1.0
	UDB160	42.5×32.4	0.026178	1.0
DENT E	*UDB240*	56.0×42.6	0.034483	1.0
	UDB160	54.2×41.2	0.033356	1.0
DENC A	*UDB240*	15.1×11.5	0.009301	1.0
	UDB160	15.3×11.7	0.009439	1.0
DENC B	*UDB240*	22.1×16.9	0.013647	1.0
	UDB160	22.5×17.1	0.013843	1.0
DENC C	*UDB160*	28.9×22.0	0.017797	1.0
DENC D	*UDB240*	36.9×28.1	0.022732	0.8
DENC E	*UDB160*	45.5×34.7	0.028046	0.8
CNT	*DTO240*	31.1×23.7	0.019157	1.0
	DTO160	30.7×23.4	0.018894	1.0
CNC	*DTO240*	17.5×13.3	0.010782	1.0
	DTO160	17.9×13.6	0.011039	1.0
OHT small	*DTO240*	11.7× 8.9	0.007217	1.0
	DTO160	11.6× 8.8	0.007119	1.0
OHT large	*DTO240*	29.9×22.7	0.018388	1.0
	DTO160	29.7×22.6	0.018313	1.0
OHC	*DTO240*	17.5×13.3	0.010749	1.0
	DTO160	17.2×13.1	0.010616	2.0

stress, σ^{∞}, of each specimen was calculated dividing the applied load, P, measured by the load cell, by the corresponding specimen's cross-section area $S = W \times t$, where W is the specimen width and t is the laminate thickness. The cross-head displacement was measured directly by the testing machine's LVDT.

Both STFs exhibit approximately linear remote stress-displacement relations (figure 4.24). A minor nonlinearity is observed in some specimens of both laminates close to the ultimate remote stress.

In the *UDA240* low-grade STF laminate, the nonlinearities close to the peak remote stress, in some cases with small load drops, apparently occurred due to the development of subcritical damage, which was audible at applied remote stresses above about 80% of the ultimate remote stress. Nevertheless, all failed specimens of laminate *UDA240* show a catastrophic fibre-dominated failure mode (figure 4.25a). Extensive pull-out is not observed, mainly due to the absence of off-axis plies, but delamination between the STF layers and transverse and longitudinal split cracking of the spread-tow yarns have occurred, as demonstrated in figure 4.25a.

In the case of the *UDA160* thin-ply STF laminate, the minor nonlinearity can be either due to small-scale sliding between the sandpaper and the specimen surface inside the grips, with no effect on the final strength of the laminate, or due to the development of subcritical damage mechanisms before reaching the failure stress. During the tests, damage was audible for applied remote stresses above 90% of the ultimate strength, generally very close to catastrophic failure. All specimens exhibit a fibre-dominated failure mode, with evidence of transverse and longitudinal split cracking of the spread-tow yarns (figure 4.25b). The extent of gauge section delamination is reduced.

Some specimens failed in multiple places in the gauge section, in some cases close to the clamping grips. This is attributed to the sudden, highly catastrophic failure mode exhibited by both STF laminates.

Because no pre-existing defect was present (as in the notched specimens), the location of the section where final failure takes place cannot be known in advance. Assuming an even stress distribution in a smooth specimen, final failure should start in the weakest point of the laminate (internal material defect, region with higher concentration of subcritical failure mechanisms, or just material strength variability), and develop into a quick, very energetic fracture process that, at the moment of failure, may induce fracture of other regions in the highly stressed material. Compression damage may also occur in the specimen after tensile failure, when the specimen recovers from the very high elastic deformation.

It is important to stress that, even though it is recognised that clamping acts as a source of stress concentration, which may promote premature failure close to the clamped regions, special care in utilising adequate sandpaper inside the bolted clamping system and an adequate clamping torque helps minimising such risks. Since the deviations between the results of specimens of the same laminate are within an acceptable range (see figure 4.24), it is considered that all results presented herein are valid experimental data.

In order to assess the occurrence and extent of early damage, the DIC technique was used to monitor transverse cracking formation through analysis of the longitudinal strain field of the outer STF layer of representative specimens

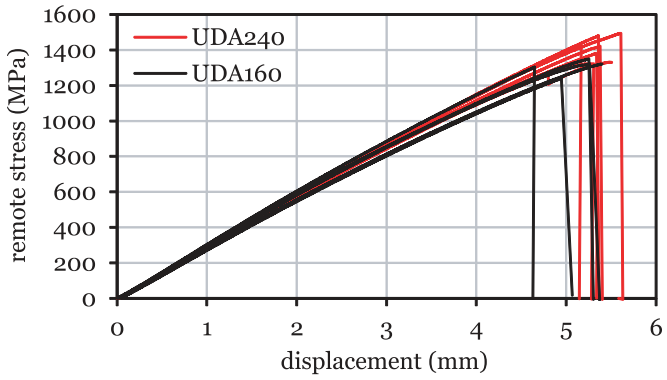

Fig. 4.24. Remote stress-displacement curves of the UD plain weave unnotched tension tests.

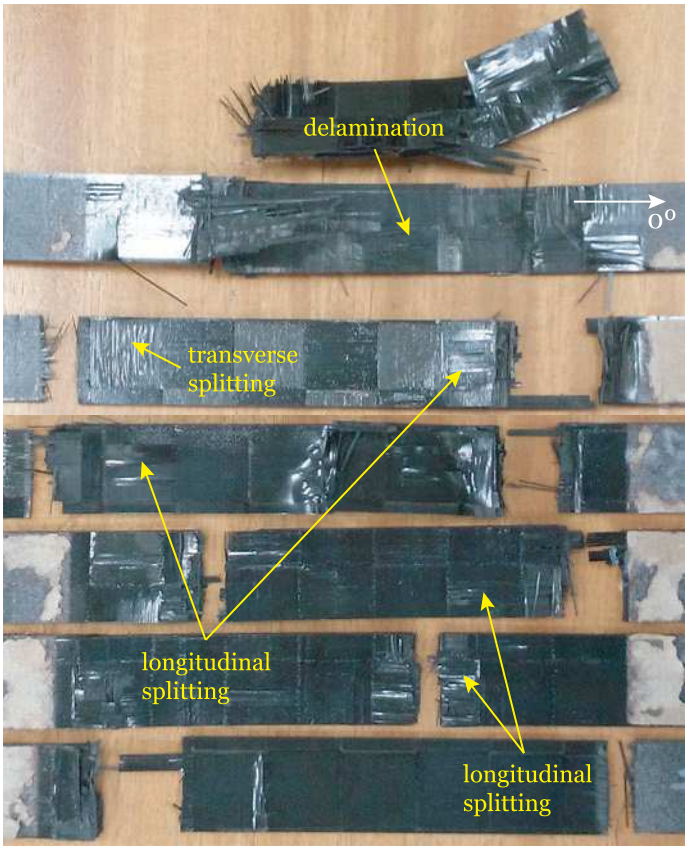

(a) Low-grade STF *UDA240*.

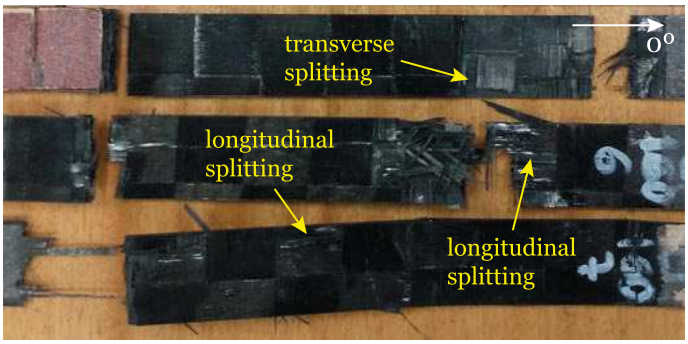

(b) Thin-ply STF *UDA160*.

Fig. 4.25. Representative UD plain weave unnotched tension test specimens after testing.

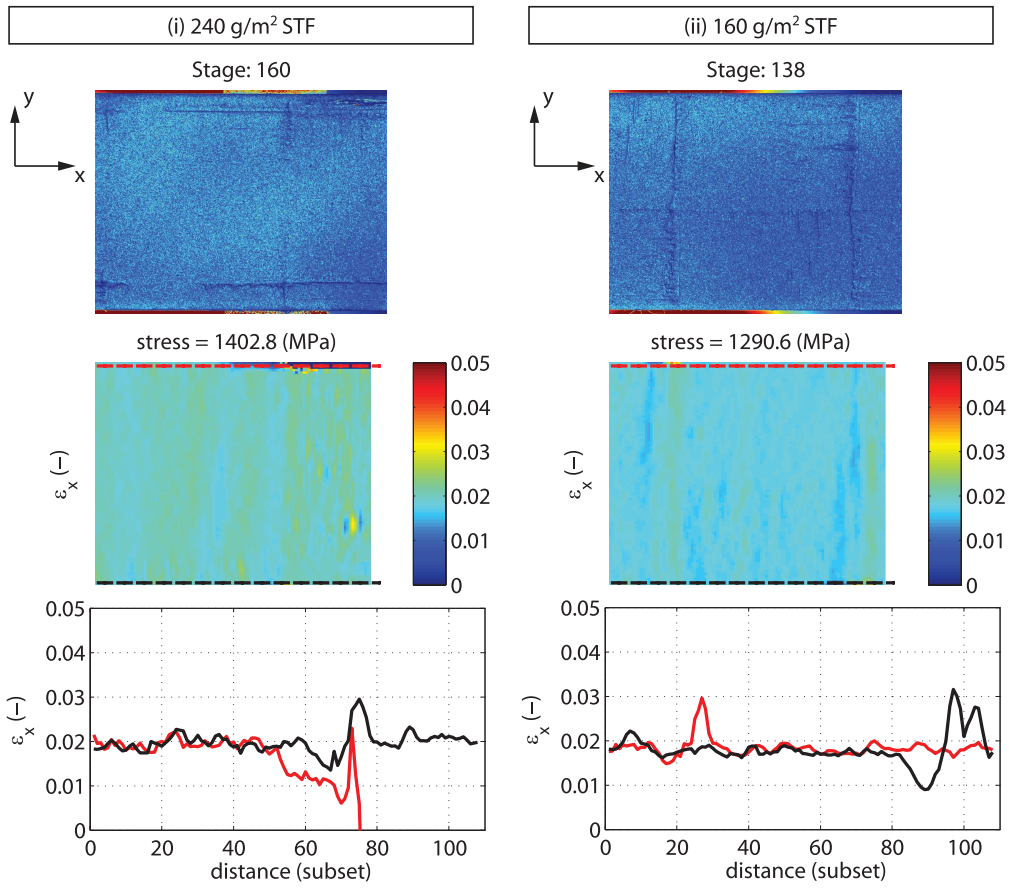

Fig. 4.26. Coloured distributions of grey levels (0–255), longitudinal strain fields, ε_x, and local longitudinal strain along the edges of the outer STF layer of representative UD unnotched tension test specimens of laminates (i) *UDA240* and (ii) *UDA160* obtained with the DIC technique at the stage prior to ultimate failure. The reference DIC coordinate system is depicted in the figures, where the *x*-axis is aligned with the loading direction.

of both laminates. Figure 4.26 shows the surface longitudinal strain field at the stage prior to final failure. The local longitudinal strain measured along two lines, parallel to the loading direction, near the free edges, are also presented. For reference, figure 4.26 also shows the corresponding coloured distribution of grey levels.

As can be observed, prior to ultimate failure, transverse matrix cracking has not occurred. In laminate *UDA240*, a longitudinal split can be observed at the top free edge, resulting in a lost of correlation (see the red line in the bottom plot of figure 4.26 (i)). In laminate *UDA160*, small strain concentrations at the free edges in the interlacing points can be observed. However, they do not indicate the occurrence of transverse damage before ultimate failure. This suggests that the extent of damage growth during the test is very small. It is also clear from figures 4.25 and 4.26 that the 240 g/m^2 STF is more susceptible to fibre-matrix splitting than the thinner 160 g/m^2 STF, and that both STF grades are able to preclude transverse matrix damage mechanisms. The later can be attributed not only to the thinness of spread-tow yarns (*in situ* effect), but also the the woven configuration.

A virtual strain gauge computed from the DIC measurements by averaging the longitudinal strains in an area with 3.18 mm in length by 1.78 mm in width, equivalent to the gauge area of a physical strain gauge, was used to obtain the remote stress-strain relations of representative unnotched tension test specimens [121, 122, 182, 187]. Figure 4.27 shows, for both STFs, the location of the gauge areas, drawn on the longitudinal strain field obtained with DIC at an applied remote stress equal to 20% of the ultimate remote stress, and the corresponding remote stress-strain relations.

A linear-elastic Finite Element Analysis (FEA) was performed to validate the implementation of the proposed virtual

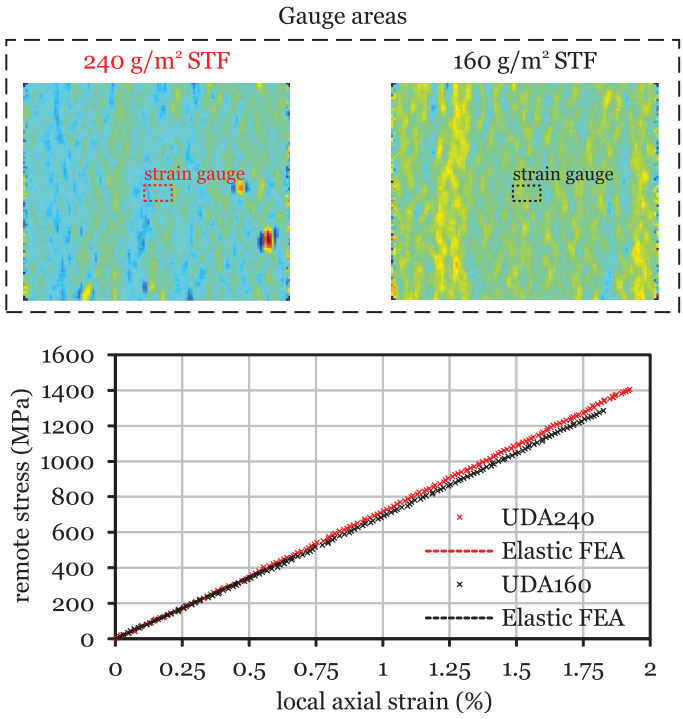

Fig. 4.27. Virtual strain gauge areas and remote stress-strain relations of representative UD plain weave unnotched tension test specimens. The loading direction is parallel to the horizontal axis of the specimens.

strain gauge approach, employing the same averaging procedure to compare with the obtained test data. The FE models were created with the commercial FE software Abaqus 6.12-1 [275] using a structured mesh of 1 mm long square 4-node plane stress elements with reduced integration (CPS4R). Only the gauge section was modelled.

In order to replicate the load and boundary conditions of the actual test setup, a longitudinal displacement (x-direction) of 1.00 mm was applied to the nodes on the top end, while fixing their remaining degrees of freedom. The nodes in the bottom end were all fixed (encastre boundary condition).

Each STF layer was represented by a [0/90] cross-ply sublaminate. The individual plies were modelled using a layerwise approach, explicitly defining each lamina, and respective ply orientation, by one integration point through the thickness of the CPS4R elements. The constitutive behaviour of each ply was defined by an orthotropic linear-elastic material model, using the elastic properties of T700GC/M21 (table 4.1). As explained in section 4.2, even though the material system of the STFs (T700SC/M21) has a different fibre sizing, it is believed that it shall not affect the elastic properties. It is also noted that the properties shown in table 4.1 are the properties of the UD ply, obtained from *prepregs* with a different areal weight. Nevertheless, assuming that the elastic properties are independent of the material grade [58] and that the spread-tow yarns of the plain weave STFs studied in the present work are sufficiently wide and straight (negligible waviness), it is believed that employing the elastic properties of table 4.1 in the FE model to represent the elastic behaviour of the STF layers is a valid approximation.

The results of the FEA are plotted together with the DIC data in figure 4.27. A remarkable correlation can be observed between the results of the FEA and the average strain measure obtained from the DIC data (figure 4.27), despite the assumptions regarding the material model. These results also validate the proposed virtual strain gauge approach. As expected for unnotched laminates with a fibre-dominated failure mode, linear stress-strain relations up to the ultimate remote stress were obtained in both laminates.

Table 4.9 shows the mean tensile unnotched strengths, X_T, of the 240 g/m^2 and 160 g/m^2 STFs, obtained respectively from laminates *UDA240* and *UDA160*, and the respective coefficients of variation. Interestingly, the tensile strength of the

Table 4.9
UD plain weave tensile unnotched strength (X_T) test results and respective coefficients of variation (C.V.).

Results	240 g/m^2 STF	160 g/m^2 STF
No. specimens	7	5
X_T (MPa)	1408	1307
C.V. (%)	4.4	2.8

thinner 160 g/m^2 STF is 7.2% lower than the tensile strength of the 240 g/m^2 STF. Previous experimental evidence [58] has shown that the longitudinal and transverse tensile strengths of UD tapes are not affected by the ply thickness. On the other hand, the tensile unnotched strength of laminates with thinner plies is higher than the tensile unnotched strength of laminates with thicker plies, or thicker ply blocks [53, 58, 121, 122, 171], with the higher extent of subcritical damage in the thick-ply laminates associated with earlier failure of the multidirectional composite. However, due to the woven reinforcement architecture, the apparent gradual failure process of the 240 g/m^2 STF, characterised by the development of internal damage in the form of split cracking of the spread-tow yarns prior to ultimate failure, relaxes the highly stressed fibres, delaying longitudinal fracture.

It is also recognised that, in general, thin-ply laminates have lower fibre volume fraction than conventional laminates [58]. This is not only due to the typically larger inter-fibre spacing exhibited by spread tows [54], but also due to the increased number of interfaces in thin-ply laminates resulting from the need to stack more plies for a given laminate thickness. Hence, even though both *prepregs*, produced from spread tows, have the same nominal resin content (35%), normalisation for the same fibre volume fraction, taking the 240 g/m^2 STF as reference, would result in a slightly higher tensile unnotched strength for the 160 g/m^2 STF, bringing it closer to the unnotched strength of the 240 g/m^2 STF. Nevertheless, since it was not possible to measure the real fibre volume fractions of the tested laminates, and because a reduction of fibre volume fraction due to manufacturing constraints is an important factor to account for in the analysis of the structural response of thin-ply laminates, normalisation for the same fibre volume fraction was not performed.

4.5.2. Fabric compressive unnotched strength test results

The compressive unnotched strength of the STFs studied in the present work were obtained testing between 5 and 6 valid smooth coupons until failure. Figure 4.28 shows the remote stress-displacement curves of both laminates. The remote stress, σ^{∞}, of each test was calculated dividing the applied load measured by the load cell by the corresponding specimen's cross-section area. The cross-head displacement was measured directly by the testing machine's LVDT.

Due to the adjustments in the self-alignment system (figure 4.3b), all specimens show a nonlinear remote stress-displacement relation in the beginning of the tests. After the adjusting stage, which can be in the range of approximately 40% of the maximum applied load, the remote stress-displacement relations become linear. Before failure, modest load drops occur in both STFs, with a negligible effect on the stiffness of the tested specimens. In some cases, the first load

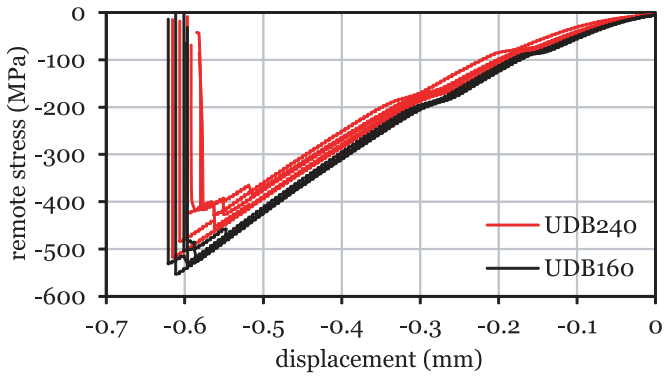

Fig. 4.28. Remote stress-displacement curves of the UD plain weave unnotched compression tests.

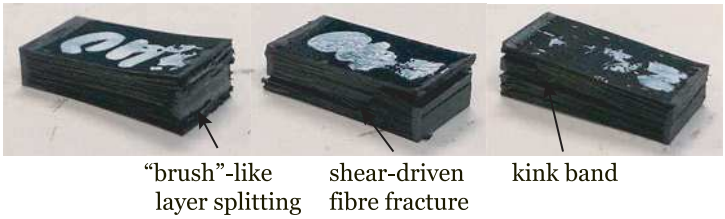

(a) Low-grade STF *UDB240*.

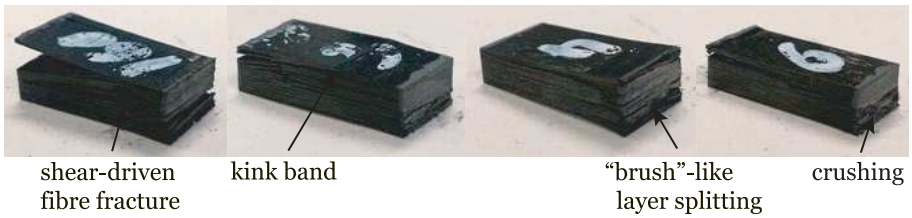

(b) Thin-ply STF *UDB160*.

Fig. 4.29. Representative UD plain weave unnotched compression test specimens after testing.

drop is also the peak load. Final failure is catastrophic in all laminates, characterised by a total loss of load-carrying capacity (the applied load stress suddenly drops to practically zero).

The load drops in the remote stress-displacement curves are attributed to the development of compressive damage, in the form of kink bands or brittle, shear-driven compressive cracks, which was audible during the tests. However, in all specimens of both STFs, ultimate failure is not due to the propagation of compressive fibre failure across the thickness of the specimen, but it occurs due to layer splitting along the length of the specimen, which becomes totally opened upon final failure (see figure 4.29).

After testing, sublaminate regions with longitudinal compressive failure, characterised by fibre kinking and shear-driven compressive fibre fracture, can be observed in the failed specimens of both STFs (figure 4.29). In the 160 g/m^2 STF (figure 4.29b), longitudinal compressive failure was also observed in thin outer sublaminates, which occurred upon the peak load.

Localised longitudinal compressive damage of thin sublaminates is apparently the damage mode that induces final failure of both STFs, conducting to out-of-plane splitting from the compression-damaged inner regions. After overall layer splitting, final longitudinal compressive failure becomes easier due to the loss of out-of-plane support of the thin intact sublaminates, resulting in the catastrophic response observed in figure 4.28.

However, not all specimens show clear compressive fibre failure away from the loading ends (figure 4.29). Some specimens exhibit a "brush"-like layer-splitting failure mode at one of the ends. Some specimens of the 160 g/m^2 STF also exhibited end crushing, with very short interlaminar cracks from the loaded surface. Nevertheless, as reported elsewhere [263], the different failure location appears to have no effect on the global response of the UD unnotched compression specimens, as can be observed, for instance, in figure 4.28.

It is important to note that, if a correct alignment of the specimen in the end-loading setup is not ensured, an invalid layer-splitting failure mode may occur, at applied load stresses considerably below the unnotched compressive strength of the STF. This is clear observing figures 4.30 and 4.31, which show the surface longitudinal strain field along the free edge of invalid UD unnotched compression test specimens, obtained with the DIC technique. The local longitudinal strain along the free edge tangent to the surfaces of the specimen is also shown. For reference, figures 4.30 and 4.31 also show the corresponding coloured distributions of grey levels. A misalignment in the load introduction, with local strain fields of different signs along opposite surfaces of the specimen, induces a premature out-of-plane failure mode at the over-loaded edges, reading the test results invalid.

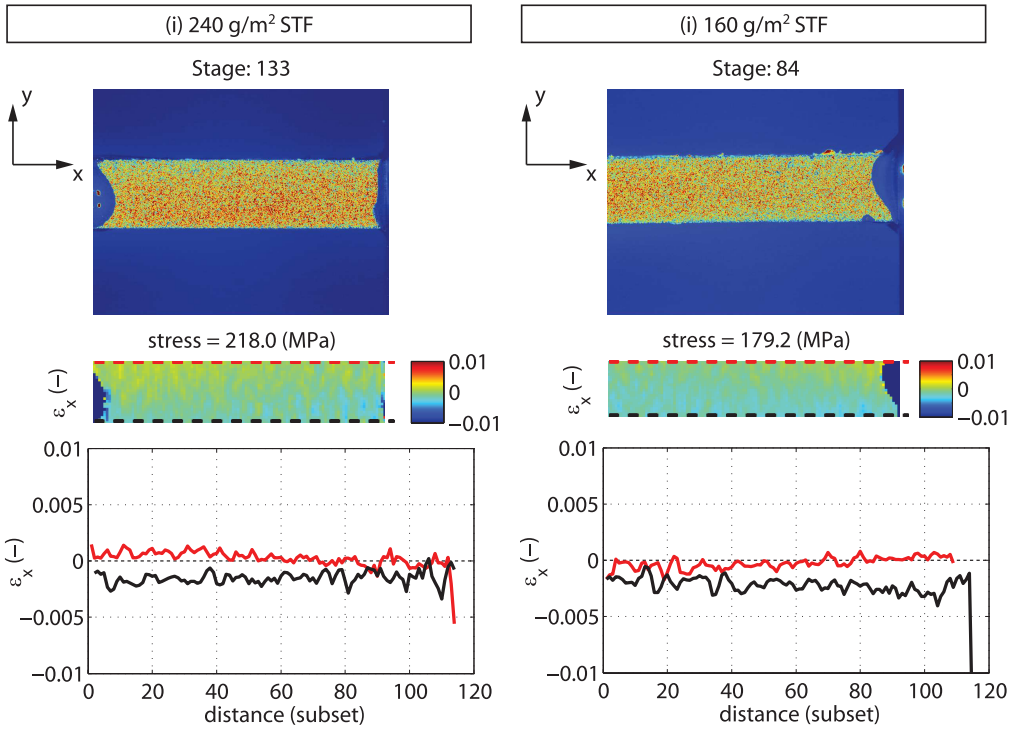

Fig. 4.30. Coloured distributions of grey levels (0–255), free edge longitudinal strain fields, ε_x, and local longitudinal strain tangent to the surfaces of invalid UD unnotched compression test specimens of laminates (i) *UDB240* and (ii) *UDB160* obtained with the DIC technique at a stage far from the maximum compressive stress. The reference DIC coordinate system is depicted in the figures, where the x-axis is aligned with the loading direction.

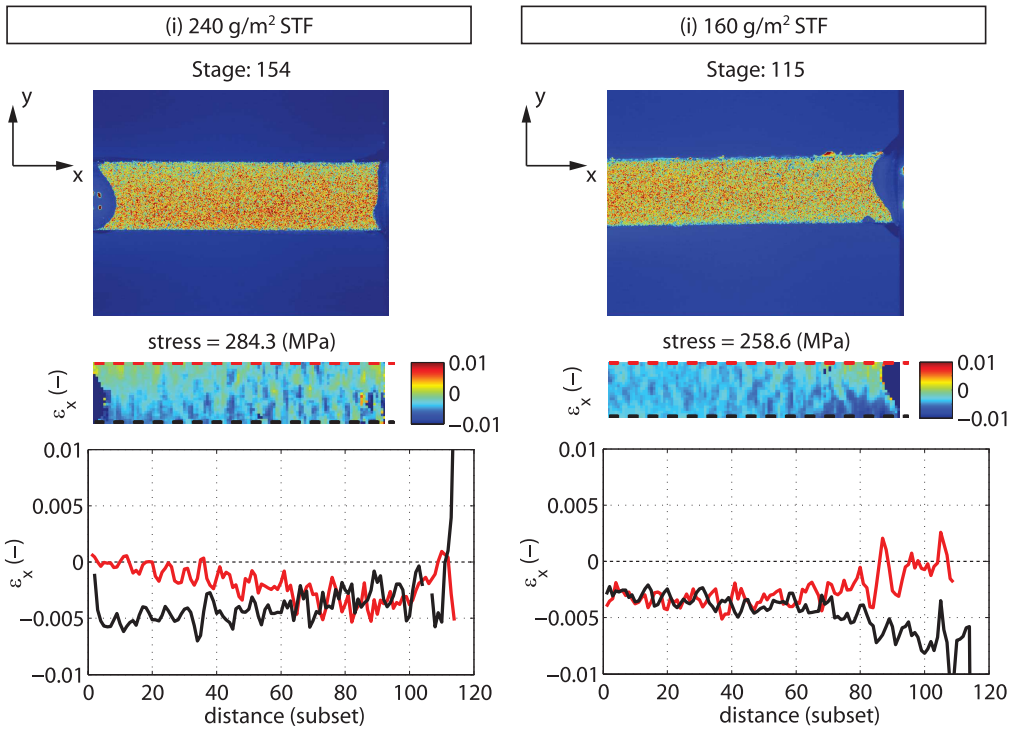

Fig. 4.31. Coloured distributions of grey levels (0–255), free edge longitudinal strain fields, ε_x, and local longitudinal strain tangent to the surfaces of invalid UD unnotched compression test specimens of laminates (i) *UDB240* and (ii) *UDB160* obtained with the DIC technique at the stage of maximum compressive stress. The reference DIC coordinate system is depicted in the figures, where the x-axis is aligned with the loading direction.

Table 4.10
UD plain weave compressive unnotched strength (X_C) test results (absolute values) and respective coefficients of variation (C.V.).

Results	240 g/m^2 STF	160 g/m^2 STF
No. specimens	6	5
X_C (MPa)	456	530
C.V. (%)	7.5	3.1

Table 4.10 shows the mean compressive unnotched strengths, X_C, of the 240 g/m^2 and 160 g/m^2 STFs, obtained respectively from laminates *UDB240* and *UDB160*, and the respective coefficients of variation. The thinner 160 g/m^2 STF exhibits a compressive unnotched strength 16.2% higher than the 240 g/m^2 STF.

Amacher et al. [58] has shown that, in the case of UD tapes, an improved lamina compressive behaviour is obtained due to the uniformity of the microstructure of spread-tow tapes. In the case of textile composites, the superior compressive unnotched response can be attributed not only to an improved uniformity of the microstructure, but also to a better uniformity of the reinforcement architecture, including lower fibre waviness and smaller crimp angles, which delay micro- and meso-instabilities in the fibre direction and, consequently, improve the longitudinal strength.

4.5.3. Off-axis compression test results

Off-axis compression tests were performed on 6 or 7 valid 15° and 30° off-axis specimens of each STF. All 15° off-axis specimens were tested to failure. Some 30° off-axis specimens were tested to failure, while others were stopped soon after the peak load. Figure 4.32 shows the axial stress-displacement curves of both off-axis configurations. In the compression tests of off-axis specimens with the proposed geometry (section 4.3.3) [263], determining the axial stress using the initial specimen cross section can result in an overprediction of the axial stress (and strengths) at high axial compressive strains due to a large barreling deformation of the off-axis specimens [263]. As suggested by Koerber et al. [263], the axial stress, σ_x (x denotes the loading direction), and the axial compressive strength, $\bar{\sigma}_x$, were therefore calculated dividing respectively the load signal, measured directly by the load cell, and the peak load by the true specimen cross section. The true cross-section area can be estimated by monitoring the relative displacement in the loading direction between two points in the in-plane displacement field near the top and bottom loading surfaces obtained from full-field measurements using the DIC technique. Following Koerber et al. [263], applying the volume consistency condition, the true specimen cross-section area, S, can be estimated as:

$$S = S_0 \frac{L_0}{L} = S_0 \left(1 - \frac{\Delta L}{L_0}\right)^{-1} \tag{4.17}$$

where $S_0 = W \times t$ is the initial cross-section area, L_0 and L are respectively the initial and current specimen length, and ΔL is the specimen length change given by the relative displacement in the loading direction between two points in the in-plane displacement field near the top and bottom loading surfaces. The cross-head displacement in figure 4.32 was measured directly by the testing machine's LVDT.

Due to adjustments in the self-alignment system, all specimens show a nonlinear axial stress-displacement relation in the beginning of the tests. After the adjusting stage, which can be in the range of 50% of the maximum applied load, the axial stress-displacement relations become linear.

In the 15° off-axis compression tests (figure 4.32a), a small nonlinearity before failure can be observed. In some specimens, failure is gradual, with the applied stress decreasing stably to values below one third of the maximum applied stress; in some cases, modest load drops can be observed. In other specimens, failure occurs suddenly, with a big load drop. Nevertheless, the different failure responses had no effect on the ultimate failure stress (see figure 4.32a).

Damage propagation in the 15° off-axis compression tests was audible only upon the peak load. Some 15° off-axis specimens show a remarked kink band across the thickness of the specimen, approximately perpendicular to the off-axis

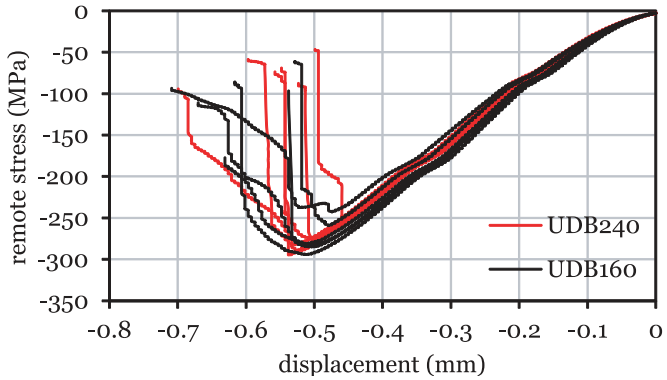

(a) 15° off-axis compression.

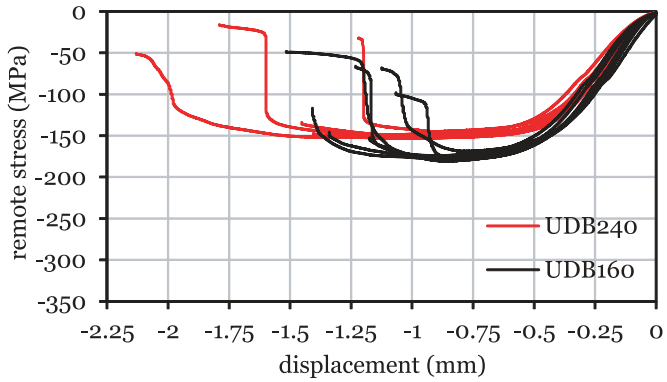

(b) 30° off-axis compression.

Fig. 4.32. Off-axis compression axial stress-displacement curves.

direction (figure 4.33a and b). In other specimens, a series of kink bands can form along the length of the specimen (figure 4.33a). Some kink bands did not penetrate completely through the thickness of the specimen, delaminating towards one of the specimen's ends (figure 4.33a). In general, surface crushing can also be observed on the failed specimens at the loaded ends, sometimes coinciding with the final load drop. In some cases, the kink bands formed very close to one of the specimen's ends. Small delaminations from the end surfaces are often observed. Some 15° off-axis specimens also exhibited a "brush"-like layer splitting failure mode, with no clear longitudinal compressive failure mode. Nevertheless, the different failure modes had not effect on the ultimate failure stress of the 15° off-axis compression tests (see figure 4.32a).

The 30° off-axis compression tests (figure 4.32b), show a high nonlinear response. Large deformations form almost a plateau in the range of the maximum applied stress, attributed to an accumulation of compressive damage. Ultimate failure generally occurs quickly, with a steep load drop. However, due to the large accumulation of damage, this sudden load drop is not catastrophic, but results from high material degradation.

During the 30° off-axis compression tests of the 240 g/m^2 STF, small sounds due to damage growth were audible at applied stresses as low as approximately 65% of the maximum stress. Damage is expected to have initiated in the form of matrix cracks parallel to the fibre direction [263]. During damage accumulation, small buckling edge delaminations of thin outer sublaminates were observed. Then, crushing of one of the corners of the loaded ends could be observed. Finally, the load started dropping quickly, apparently due to compression stability failure of the fibres or due to severe out-of-plane layer splitting. Sudden failure was generally audible.

Some failed specimens exhibit surface crushing, with a "brush"-like layer splitting failure mode (figure 4.33c). Remarked kink bands, approximately perpendicular to the off-axis direction, which penetrate partially through the thickness

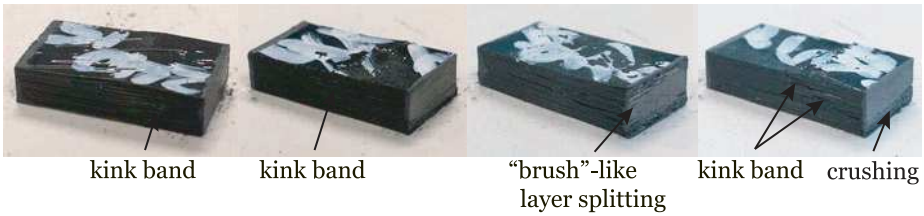

(a) *UDB240* 15° off-axis specimens.

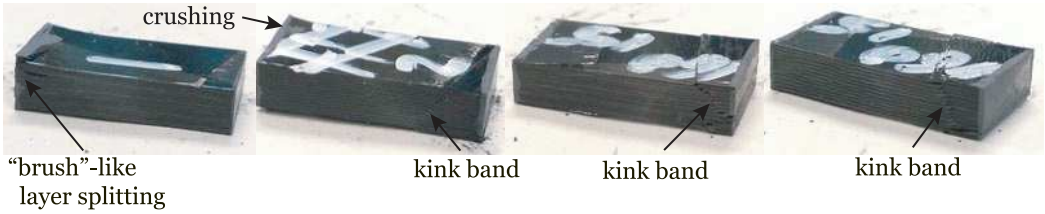

(b) *UDB160* 15° off-axis specimens.

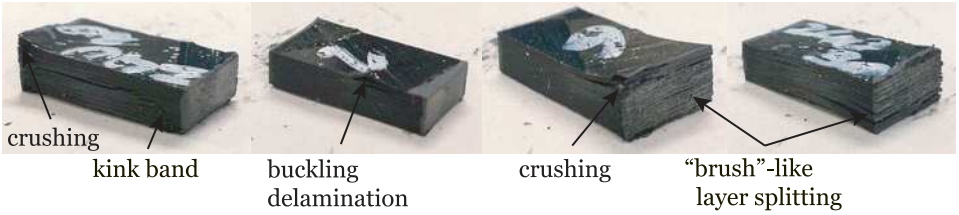

(c) *UDB240* 30° off-axis specimens.

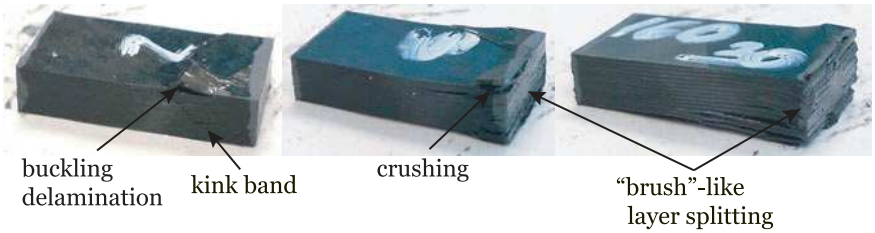

(d) *UDB160* 30° off-axis specimens.

Fig. 4.33. Representative off-axis compression test specimens after testing.

Table 4.11
Off-axis compression test results (absolute values) and respective coefficients of variation (C.V.).

Results	15° off-axis		30° off-axis	
	240 g/m^2 STF	160 g/m^2 STF	240 g/m^2 STF	160 g/m^2 STF
No. specimens	6	6	7	7
$\bar{\sigma}_x$ (MPa)	278	274	151	176
C.V. (%)	5.3	6.4	1.7	2.0

of the specimen, could also be observed. In some cases, delaminations propagated from the kink bands towards one of the specimen's ends, which prevented the kink bands from extending completely through the thickness.

In the 160 g/m^2 STF 30° off-axis specimens, small edge buckling delaminations initiated before the peak load, extending further after the peak load, eventually conducting to failure of the thin outer sublaminate. Kink band formation could be observed at the ultimate failure, resulting in a steep load drop. Further loading conducted to a stable growth of these kink bands through the thickness of the specimens. In some specimens, a "brush"-like layer splitting failure mode was also observed. In these cases, ultimate failure was due to a mixture of compressive failure of the fibres and severe out-of-plane layer splitting.

The failed 30° off-axis specimens of the 160 g/m^2 STF (figure 4.33d) exhibited remarked kink bands, which could penetrate completely through the thickness. These kink bands were inclined with respect to the out-of-plane direction, and approximately perpendicular to the off-axis direction. Small split cracks in the outer layers could be observed, apparently caused by surface damage due to kink band formation. Crushing of the corners of the specimens' ends could also be observed.

Figures 4.34 and 4.35 show sequences of the axial strain field obtained with the DIC technique of representative 30° off-axis specimens of the 240 g/m^2 and 160 g/m^2 STFs, respectively. The position of the loading stage in the axial stress-time relation and the local axial strain measured along the loading direction near the free edges are also presented. For reference, figures 4.34 and 4.35 also show the corresponding coloured distributions of grey levels.

At the peak load (figures 4.34 (ii) and 4.35 (ii)) regions of high strain localisation parallel to the fibre directions can be observed. In general, these regions coincide with the resin-rich interlacing points in the fabric. This localised plastic deformation added to the damage caused by compressive failure of the fibres is the main cause of the highly nonlinear behaviour observed in the axial stress-displacement and time relations (figures 4.32, 4.34 (iv) and 4.35 (iv), respectively). Measurements of the in-plane strain field in the loading coordinate system obtained using the DIC technique by performing an average over an area in the specimen centre equivalent to the area of a real strain gauge show the same nonlinear behaviour (figure 4.36[1]). In the present study, a 3.18 mm long and 1.78 mm wide area was chosen. The validity of this approach was already demonstrated via linear-elastic FEA of test configurations with a more representative linear response (see, for instance, section 4.5.1 and figure 4.27).

Table 4.11 shows the mean axial compressive strength, $\bar{\sigma}_x$, of the 240 g/m^2 and 160 g/m^2 STFs for the 15° and 30° off-axis tests, and the respective coefficients of variation. Interestingly, the axial compressive strength of the 15° off-axis specimens is virtually the same; it differs by just 1.3%, below the material scatter. In fact, observing figure 4.32a and figure 4.33a and b, no difference can be observed between the mechanical response and failure modes of the 240 g/m^2 and 160 g/m^2 STFs. On the other hand, the thinner 160 g/m^2 STF exhibits a 30° off-axis axial compressive strength 16.9% higher than the 240 g/m^2 STF (a difference in the range of that observed for the unnotched compressive strength, section 4.5.2). However, figure 4.32b shows that the 240 g/m^2 STF exhibits higher axial strain-to-failure when compared with the 160 g/m^2 STF. Observing figure 4.33c and d, a slightly brittler failure mode can be observed for the 160 g/m^2 STF, but no relevant difference in the sequence and extent of the failure mechanisms is observed.

[1]In the 30° off-axis specimen of the 160 g/m^2 STF, good correlation data could not be obtained soon after the peak load due to out-of-plane movements caused by fast compressive damage propagation and end crushing. Therefore, in figure 4.36, only the DIC data with good correlation was post-processed.

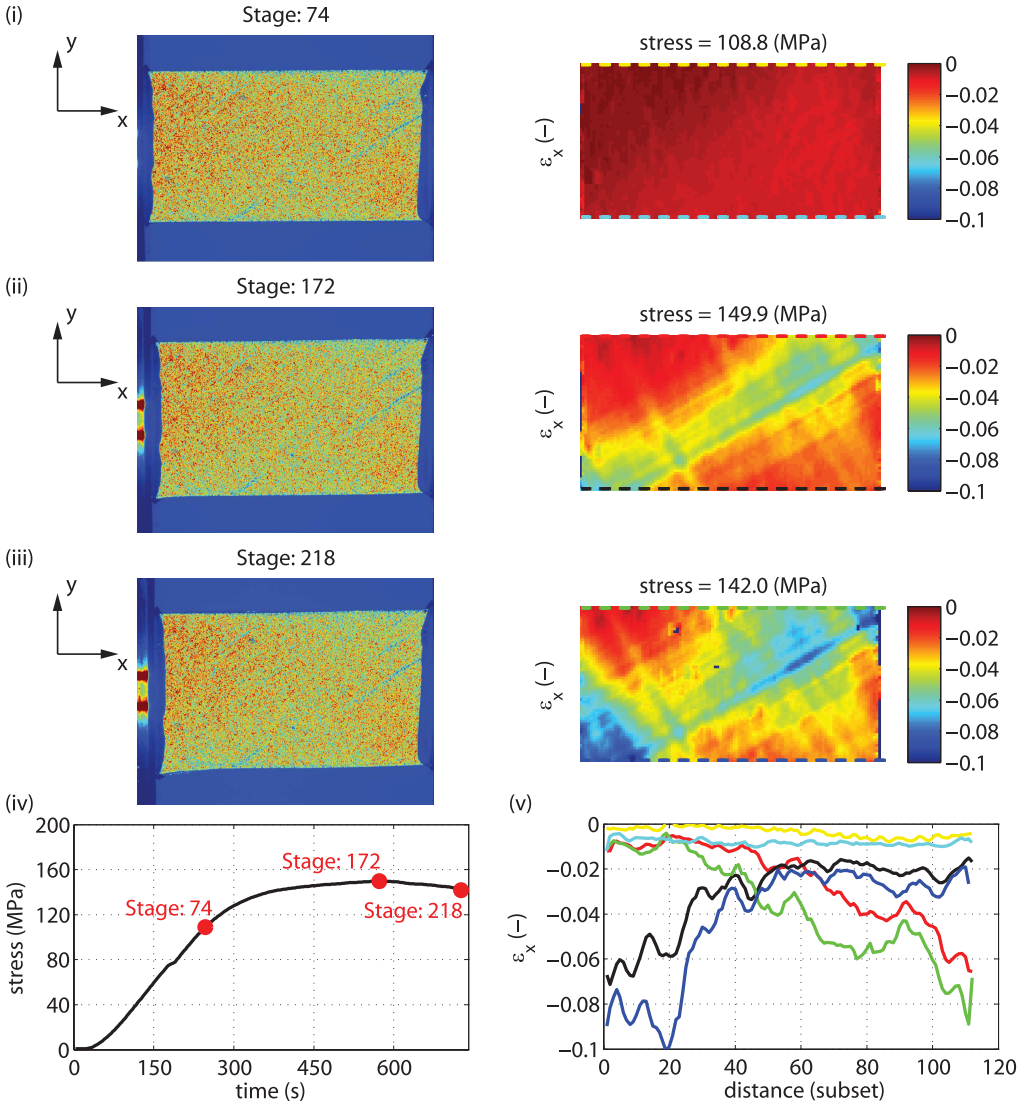

Fig. 4.34. Coloured distributions of grey levels (0–255) and axial strain fields, ε_x, of a representative 30° off-axis specimen of the 240 g/m^2 STF obtained with the DIC technique at the stages of (i) onset of nonlinearity, (ii) maximum applied stress and (iii) before failure due to out-of-plane layer splitting. (iv) Position of the stages in the axial stress-time relation. (v) Local axial strain measured along two lines parallel to the loading direction near the free edges. The reference DIC coordinate system is depicted in the figure, where the x-axis is aligned with the loading direction. The stresses are given in absolute values.

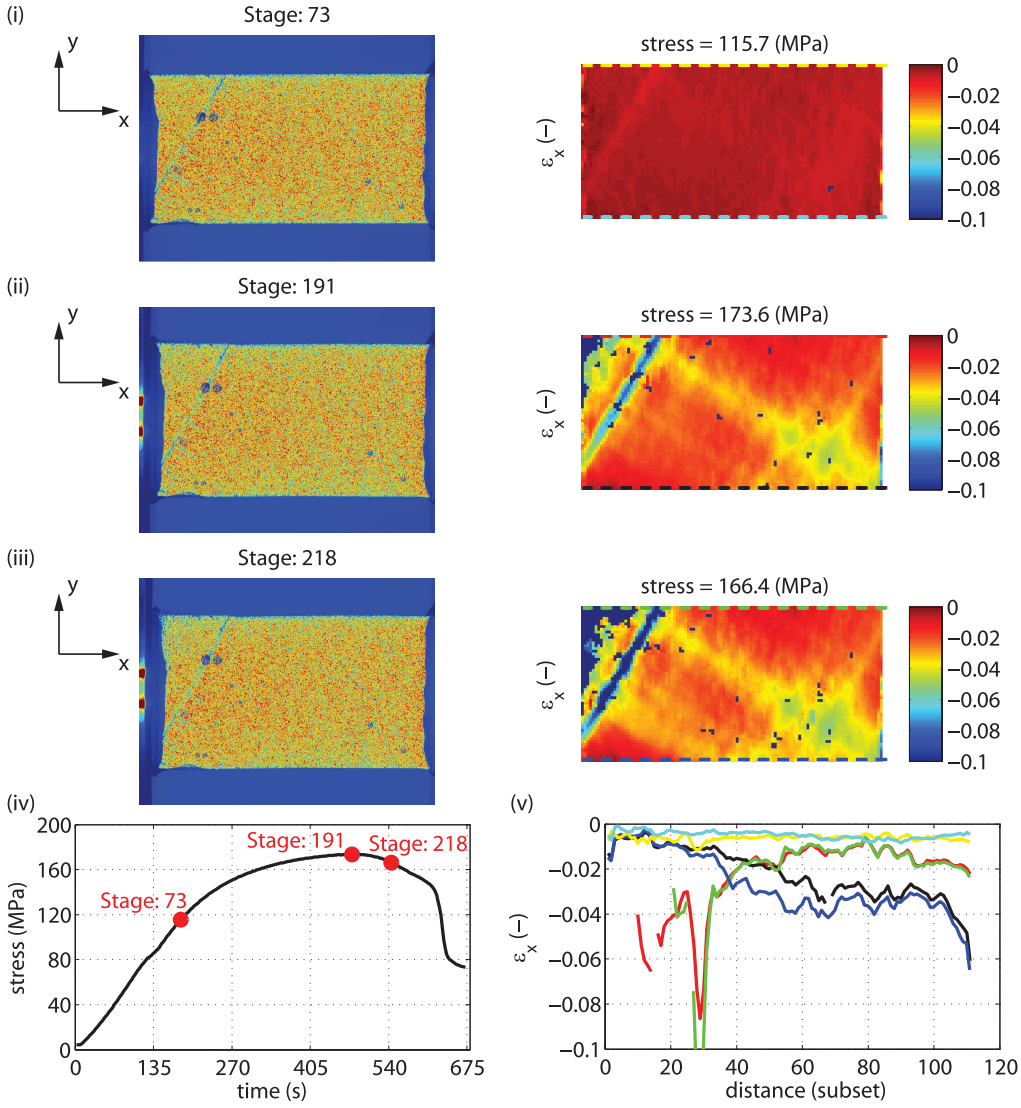

Fig. 4.35. Coloured distributions of grey levels (0–255) and axial strain fields, ε_x, of a representative 30° off-axis specimen of the 160 g/m^2 STF obtained with the DIC technique at the stages of (i) onset of nonlinearity, (ii) maximum applied stress and (iii) before failure due to out-of-plane layer splitting. (iv) Position of the stages in the axial stress-time relation. (v) Local axial strain measured along two lines parallel to the loading direction near the free edges. The reference DIC coordinate system is depicted in the figure, where the x-axis is aligned with the loading direction. The stresses are given in absolute values.

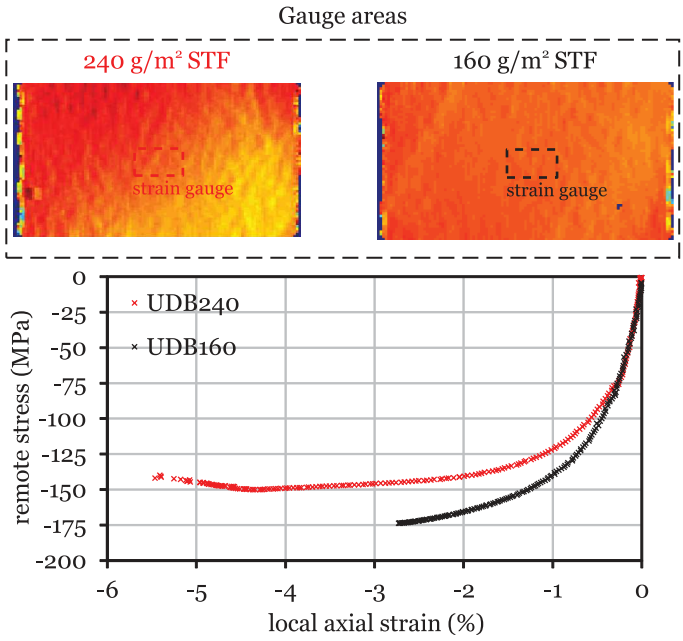

Fig. 4.36. Virtual strain gauge areas and axial stress-strain relations of representative 30° off-axis compression test specimens. The loading direction is parallel to the horizontal axis of the specimens.

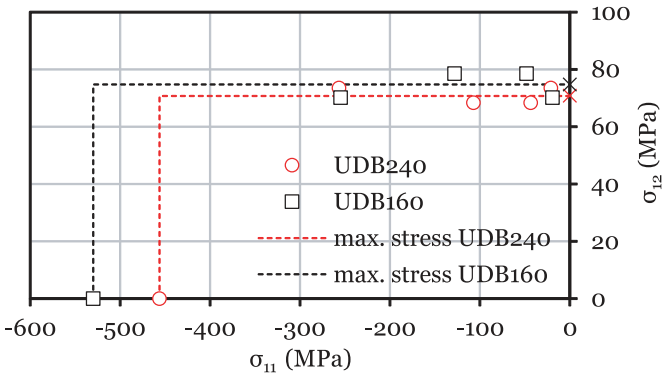

Fig. 4.37. Failure envelopes for the combined compression/in-plane shear stress space.

Equations (4.1)–(4.3) can now be used to determine the strength components of the off-axis tests in the material coordinate system, $\bar{\sigma}_{11}$, $\bar{\sigma}_{22}$ and $\bar{\sigma}_{12}$, using the measured axial compressive strength in the loading coordinate system, $\bar{\sigma}_x$. Figure 4.37 shows the failure envelope of each STF grade for the combined compression/in-plane shear stress space σ_{11}–σ_{12}.

A compressive stress component, σ_{22}, also exists in the transverse (weft)-direction of the investigated textile composites. Nevertheless, this stress component is small compared with the stress component in the longitudinal (warp)-direction, σ_{11}.

Due to the balanced amount of fibres in the warp- and weft-direction, it can be assumed that the corresponding compressive strengths are equal (i.e. $X_C = Y_C$), and the 15° and 30° off-axis data can be used to represent fictitious 75° and 60° off-axis specimens, respectively. By simply interchanging the warp and weft stress components, the data points for fictitious 75° and 60° off-axis specimens can be obtained. These data points are also plotted in the σ_{11}–σ_{12} stress diagram of figure 4.37.

As observed by Koerber et al. [263] for a 5-harness-satin textile carbon-epoxy composite, an approximately constant value of the in-plane shear stress at failure was obtained regardless of the applied multiaxial stress state. A maximum

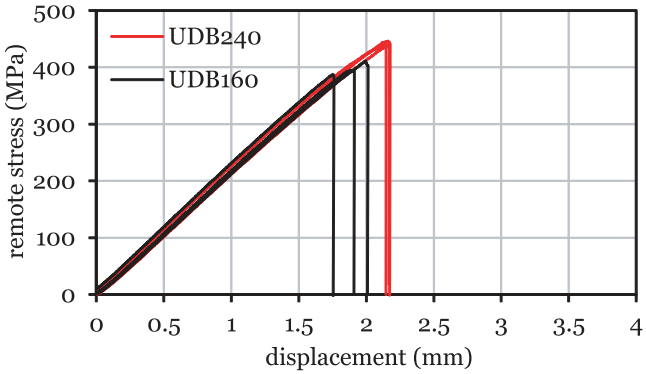

Fig. 4.38. Remote stress-displacement curves for the 10 mm wide DENT test specimens (geometry A).

stress failure criterion seems therefore suitable to represent the failure envelopes of the STFs studied in the present work (see figure 4.37). As noted by Koerber et al. [263], by comparison, UD composites subject to a combined transverse compression/in-plane shear loading exhibit an in-plane shear stress component at failure that, for low values of the transverse compressive stress component, is higher than the in-plane shear strength of the UD composite.

Assuming that a maximum stress failure criterion adequately approximates the failure envelopes in the σ_{11}–σ_{12} stress space, the obtained off-axis data can be used to estimate the in-plane shear strengths (S_L) of the STFs investigated in the present study (see × data points in figure 4.37). The resulting in-plane shear strengths are $S_L = 71$ MPa and $S_L = 75$ MPa for the 240 g/m^2 and 160 g/m^2 STF, respectively, a difference of 5.6%.

The 160 g/m^2 STF, which exhibits a slightly brittler response, as discussed before (figure 4.33), seems to have a slightly higher shear strength. The particular meso-structure of the textile composites, which resembles a cross-ply laminate, apparently promotes a thinness effect on the in-plane shear strength.

In fact, figure 4.37 shows that the thinner 160 g/m^2 STF not only exhibits a markedly superior behaviour in compression, attributed to the uniformity of the thinner reinforcement architecture of the 80 g/m^2 individual spread-tow yarns (section 4.5.2), but also a slightly higher in-plane shear strength, which can be attributed to the ability of the thinner spread-tow yarns to suppress microcracking caused by shear loading (*in situ* effect [81]). Nevertheless, the resulting nonlinear strain-to-failure is reasonably lower than the 240 g/m^2 STF (see figure 4.32b).

It is important to note that only one specimen per off-axis configuration and STF grade was monitored using the DIC technique. Therefore, the relative displacement results used to estimate the specimen length change and determine the true cross-section area of each specimen (equation (4.17)) were extrapolated from the full-field measurements obtained from one specimen with the same off-axis angle and STF grade. Similarly, the correct off-axis angle at failure, θ (equations (4.1)–(4.3)), was obtained from the DIC data of a single specimen per off-axis configuration and STF. It is therefore assumed that, at failure, the shear angle is the same for all specimens of the same initial off-axis angle and STF grade. Since full-field data was not available for all specimens in the present work, it is believed that this approximations not only meet the objectives of this study, as they also provide the most reasonable data given the limited amount of information available.

4.5.4. Fabric mode I tensile crack resistance curve

For each STF and DENT geometry configuration, 3 specimens were tested to failure. Figures 4.38 to 4.42 show, for the different geometries, the remote stress-displacement curves of both laminates. The remote stress, σ^∞, of each test was calculated dividing the applied load measured by the load cell by the corresponding specimen's cross-section area. The cross-head displacement was measured directly by the testing machine's LVDT.

All DENT specimen configurations exhibit an approximately linear remote stress-displacement curve until close to the peak load (figures 4.38 to 4.42). As the size of the specimens increases, small load drops before ultimate failure become

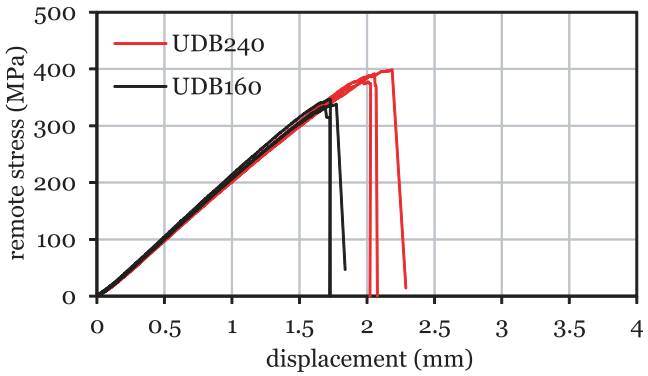

Fig. 4.39. Remote stress-displacement curves for the 20 mm wide DENT test specimens (geometry B).

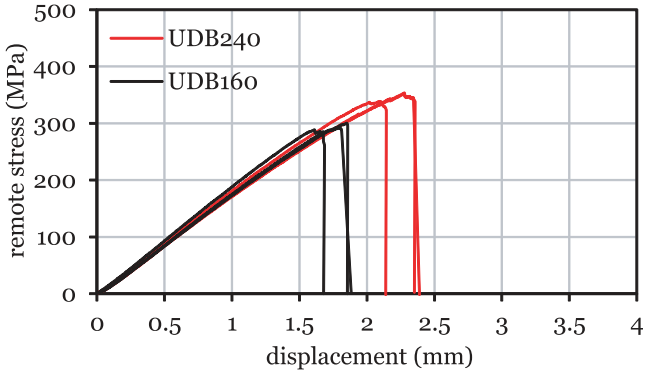

Fig. 4.40. Remote stress-displacement curves for the 30 mm wide DENT test specimens (geometry C).

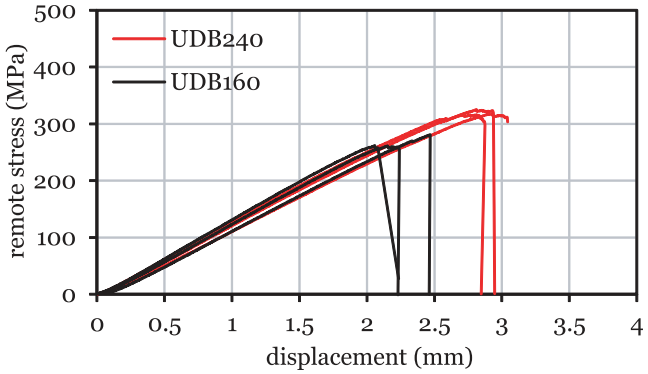

Fig. 4.41. Remote stress-displacement curves for the 40 mm wide DENT test specimens (geometry D).

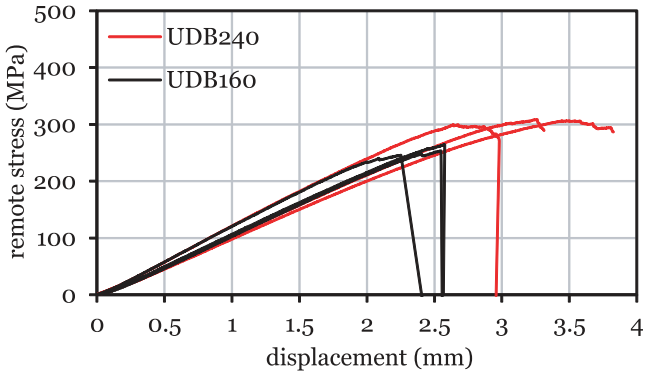

Fig. 4.42. Remote stress-displacement curves for the 50 mm wide DENT test specimens (geometry E).

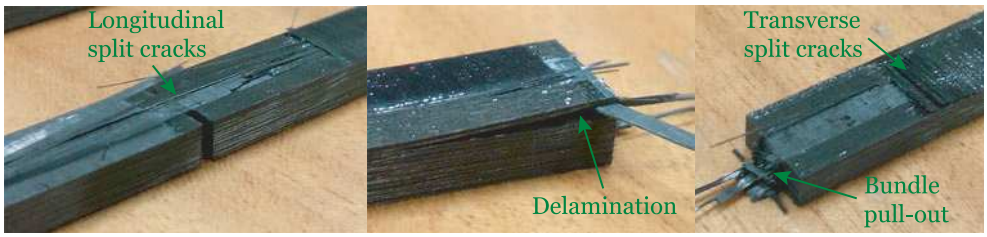

(a) Low-grade STF *UDB240*.

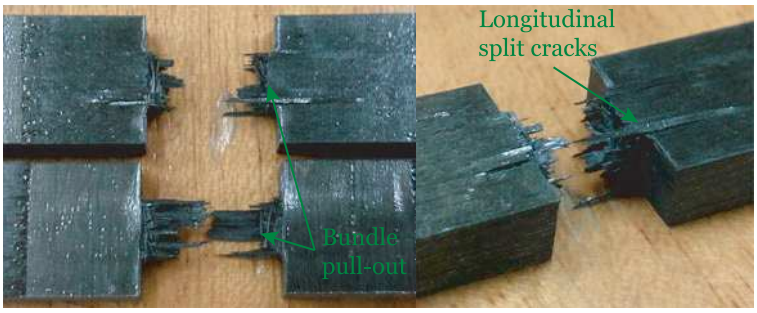

(b) Thin-ply STF *UDB160*.

Fig. 4.43. Details of representative 10 mm wide (geometry A) DENT test specimens after testing.

more frequent, affecting the stiffness of the specimens and conducting to a nonlinear behaviour. This response towards the specimens failure is attributed to stable damage growth in the form of intralaminar fracture and fibre-matrix splitting of the spread-tow yarns. It is interesting to note that these small load drops occur at lower applied remote stresses in the 160 g/m^2 STF, which also exhibits a shorter nonlinear response. This observation indicates that, even though the onset of severe damage growth occurs earlier in the 160 g/m^2 STF, the load-carrying capacity during stable damage propagation is substantially higher in the 240 g/m^2 STF, namely in the largest specimen configurations (figures 4.41 and 4.42).

However, during the tests, the onset of damage was generally audible before the occurrence of load drops in the remote stress-displacement relations, while the specimens' response was still approximately linear. For the smaller specimens (geometry A) of the 240 g/m^2 STF, internal damage growth was generally audible at applied remote stresses around 410 MPa (92% of the ultimate remote stress). For the 160 g/m^2 STF, noise produced by internal damage growth occurred just before ultimate failure. Notice that, in the smaller specimens (figure 4.38), the remote stress-displacement relations are approximately linear up to ultimate failure. Hence, the occurrence of early subcritical damage in the 240 g/m^2 STF has apparently the ability to delay final intralaminar fracture when compared with the 160 g/m^2 STF, despite the linear response observed in both STFs (figure 4.38).

Figure 4.43 shows the DENT specimens with geometry A after testing. Both STFs exhibit a fibre-dominated failure mode, characterised by fibre bundle pull-out across the fractured ligament section. The specimens of the 240 g/m^2 STF (figure4.43a) show very long surface split cracks in the spread-tow yarns aligned with the loading direction, propagating from the ligament section along the gauge length. In addition, delamination and split cracking of the spread tows perpendicular to the loading direction can also be observed. On the other, the 160 g/m^2 STF shows very small split cracks in the spread tows aligned with the loading direction, arising from the ligament section.

For the 20 mm wide specimens (geometry B), internal damage growth in the 240 g/m^2 STF was audible above 290 MPa (75% of the ultimate remote stress). Internal damage growth was audible in the 160 g/m^2 STF at applied remote stresses above approximately 300 MPa (88% of the ultimate remote stress). In both STFs, damage onset occured earlier than the first load drop in the remote stress-displacement curves (figure 4.39). Interestingly, even though internal subcritical damage growth starts earlier in the 240 g/m^2 STF, severe damage growth, which originates the load drops and nonlinear response, occurs first in the 160 g/m^2 STF. Therefore, subcritical damage growth appears to play an important role in delaying severe damage growth and catastrophic intralaminar failure of the tested specimens.

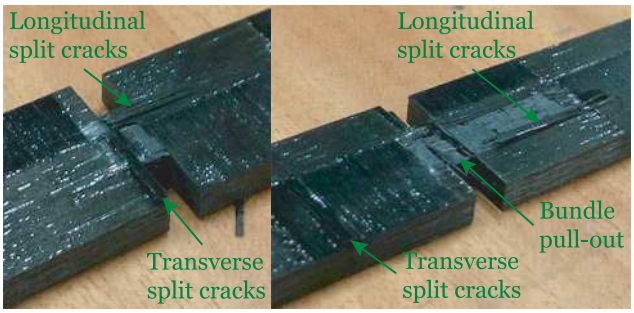

(a) Low-grade STF *UDB240*.

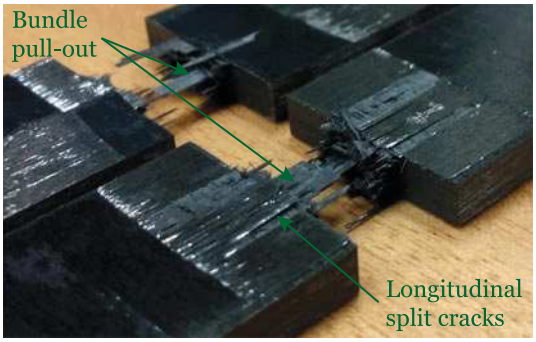

(b) Thin-ply STF *UDB160*.

Fig. 4.44. Details of representative 20 mm wide (geometry B) DENT test specimens after testing.

After testing, the DENT test specimens with geometry B (figure 4.44) show a fibre-dominated failure mode, characterised by fibre bundle pull-out across the ligament section. The specimens of the 240 g/m^2 STF (figure 4.44a) exhibit longitudinal and transverse split cracks in the spread-tow yarns aligned and perpendicular to the loading direction, respectively. The split cracks can be observed not only close to the plane of the edge notches, but also along the gauge section. Split cracks in the spread-tow yarns aligned with the loading direction can also be observed in the 160 g/m^2 STF (figure 4.44b).

For the 30 mm wide specimens (geometry C) of the 240 g/m^2 STF, internal damage growth was audible above approximately 280 MPa (83% of the ultimate remote stress). In the last stages of loading and after the peak load, the noise produced by damage growth indicated the occurrence of stable fibre breakage. Internal damage growth was also audible in the 160 g/m^2 STF at applied remote stresses around 260 MPa (89% of the ultimate remote stress).

After testing (figure 4.45), both STFs exhibit a fibre-dominated failure mode, characterised by fibre bundle pull-out across the ligament section. Split cracks in the spread tows aligned with the loading direction can be observed in all DENT test specimens with geometry C.

For the 40 mm wide specimens (geometry D), internal damage growth in the 240 g/m^2 STF was audible above 240 MPa (77% of the ultimate remote stress). Internal damage growth was also audible in the 160 g/m^2 STF, at applied remote stresses around 220 MPa (78% of the ultimate remote stress). In both STFs, as the applied remote stress approached the maximum remote stress, noise due to the occurrence of stable fibre breakage was perceptible, which eventually extended after the peak load.

A fibre-dominated failure mode, characterised by fibre bundle pull-out across the ligament section, can be observed in all DENT test specimens with geometry D (figure 4.46). Long split cracks in the spread-tow yarns aligned with the loading direction can be observed in the 240 g/m^2 STF (figure 4.46a), propagating from the ligament section along the gauge length through several transverse yarns. In the 160 g/m^2 STF (figure 4.46b), small split cracks in the spread-tow yarns parallel and perpendicular to the loading direction starting at the ligament section can be observed.

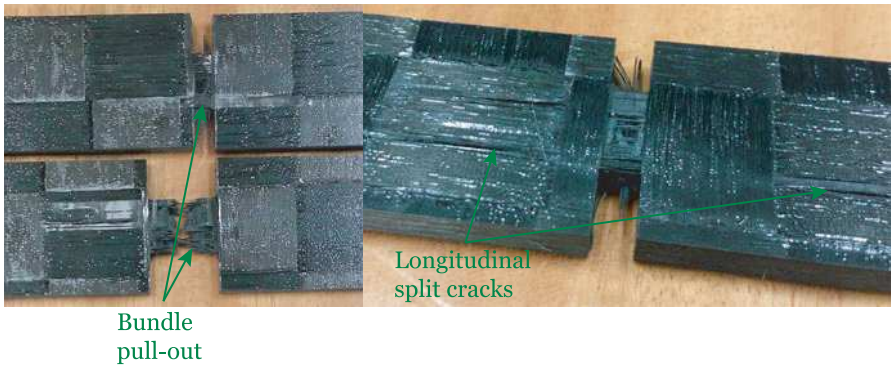

(a) Low-grade STF *UDB240*.

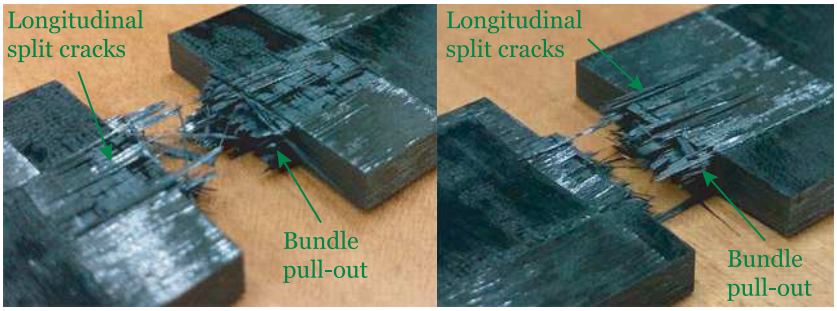

(b) Thin-ply STF *UDB160*.

Fig. 4.45. Details of representative 30 mm wide (geometry C) DENT test specimens after testing.

(a) Low-grade STF *UDB240*.

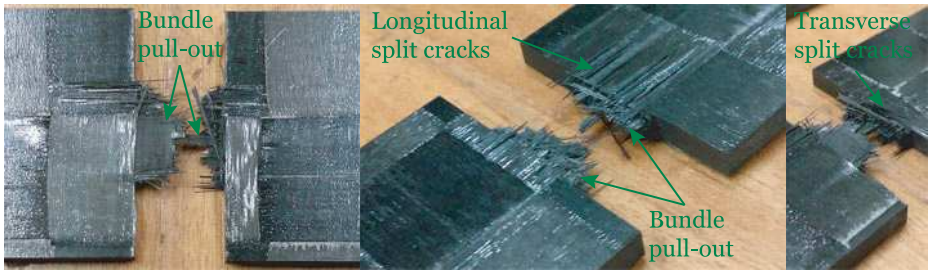

(b) Thin-ply STF *UDB160*.

Fig. 4.46. Details of representative 40 mm wide (geometry D) DENT test specimens after testing.

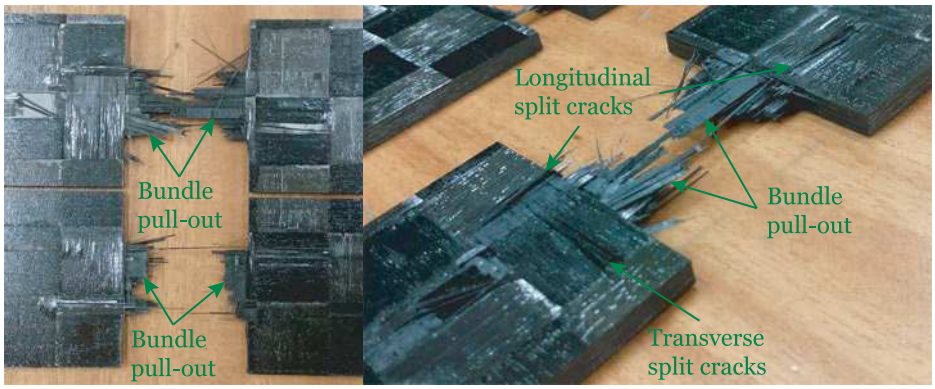

(a) Low-grade STF *UDB240*.

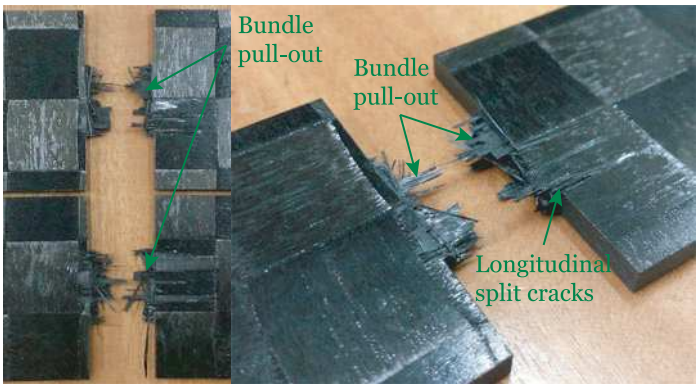

(b) Thin-ply STF *UDB160*.

Fig. 4.47. Details of representative 50 mm wide (geometry E) DENT test specimens after testing.

For the 50 mm wide specimens (geometry E) of the 240 g/m^2 STF, internal damage growth was audible above approximately 240 MPa (80% of the ultimate remote stress), indicating stable damage propagation after the peak load and after high nonlinearity, stronger after the peak load. Internal damage growth was also audible in the 50 mm wide specimens of the 160 g/m^2 STF at applied remote stresses around 220 MPa (92% of the ultimate remote stress). It is interesting to note that, whereas the extent of the nonlinear response of the 160 g/m^2 STF almost does not change with the size of the specimens, stable damage growth at approximately constant applied remote stress in the 240 g/m^2 STF becomes more and more important as the specimens become larger (figure 4.42).

The DENT test specimens with geometry E show a fibre-dominated failure mode too, with extensive fibre bundle pull-out across the ligament section (figure 4.47). In addition, the 240 g/m^2 STF (figure 4.47a) exhibits long split cracks in the spread tows parallel and perpendicular to the loading direction arising from the ligament section and propagating along the gauge length. The 160 g/m^2 STF (figure 4.47b) shows small split cracks in the spread tows parallel to the loading direction, close to the notched plane.

Figures 4.43 to 4.47 show that, for all DENT specimen configurations, and in spite of exhibiting the same type of failure mode, failure of the 240 g/m^2 STF is characterised not only by a larger degree of fibre bundle pull-out across the fracture plane when compared with the 160 g/m^2 STF, but it is also characterised by more diffuse subcritical damage mechanisms, particularly longitudinal and transverse fibre-matrix splitting. These differences in the post-failure damage mechanisms are intimately related with the different notched responses observed in figures 4.38 to 4.42. The 240 g/m^2 STF generally exhibits a long range of stable damage growth, in particular as the size of the specimens increases. This is related with the stable propagation of internal longitudinal split cracking, resulting in the longer fibre bundle pull-outs, as well as surface split cracking along the spread-tow yarns parallel or perpendicular to the loading direction. The 160 g/m^2 STF, though, exhibits a short range of stable damage growth, resulting in a brittler failure mode. This can be attributed

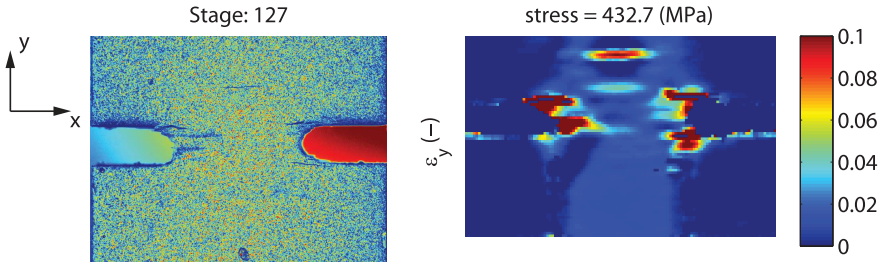

(a) 240 g/m^2 STF.

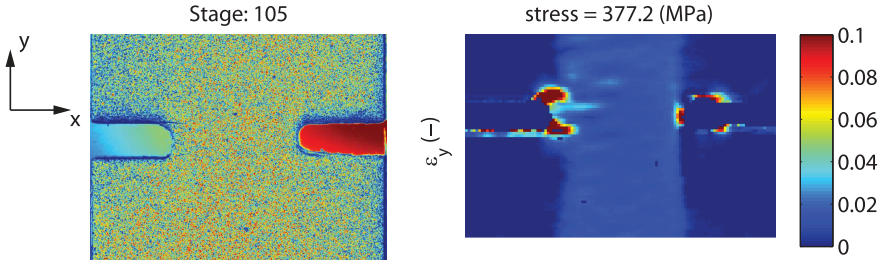

(b) 160 g/m^2 STF.

Fig. 4.48. Coloured distribution of grey levels (0–255) and longitudinal strain field, ε_y, of representative 10 mm wide DENT test specimens (geometry A) obtained with the DIC technique at the stages before final failure. The reference DIC coordinate system is depicted in the figures, where the y-axis is aligned with the loading direction.

to the lower interlaminar (and inter-bundle) stresses originated in the thin-ply laminated structure, which delay damage mechanisms such as fibre-matrix splitting, which have a very important blunting effect [121, 276].

The previous observations can be confirmed assessing the longitudinal strain field obtained from DIC measurements of representative specimens of the different configurations, shown in figures 4.48 to 4.52. For reference, figures 4.48 to 4.52 also show the corresponding coloured distribution of grey levels.

Due to the shape of the notch tip and relative size of the notch height and specimen width, in the smallest DENT specimens (figure 4.48) intralaminar fracture does not necessarily start or propagate along the notch mid-plane, but it eventually occurs along the planes of the straight free edges of the notches. This is particularly evident in the 240 g/m^2 STF (figure 4.48a), even though it can be observed in both STFs (see detailed pictures of the ligament section before ultimate failure in figure 4.53).

Figure 4.48a also shows that damage in the 240 g/m^2 STF is not restricted to the the ligament section, with small transverse cracks visible in the gauge section. The longitudinal strain concentration along a band with the size of the ligament section also anticipates the occurrence of internal longitudinal split cracking, resulting in the pull-out failure mode observed in figure 4.43.

As the size of the DENT specimens increases, surface damage in the 160 g/m^2 STF remains confined to the tips of the edge notches. The occurrence of internal longitudinal split cracking can still be anticipated due to the longitudinal strain concentration along a band with the size of the ligament section as the applied remote stress increases towards the maximum remote stress (see figures 4.49b to 4.52b). The lack of stress relaxation in the vicinity of the notch tips conducts to early unstable fracture of the 0° spread-tow yarns after short stable damage growth, resulting in a brittler failure mode, as discussed before.

In the 240 g/m^2 STF, though, diffuse intralaminar damage and surface longitudinal split cracking become more frequent as the size of the DENT specimens increases (see figures 4.54a to 4.57a). The longitudinal strain concentration along a band with the size of the ligament section is now bounded by the surface split cracks (figures 4.49a to 4.52a),

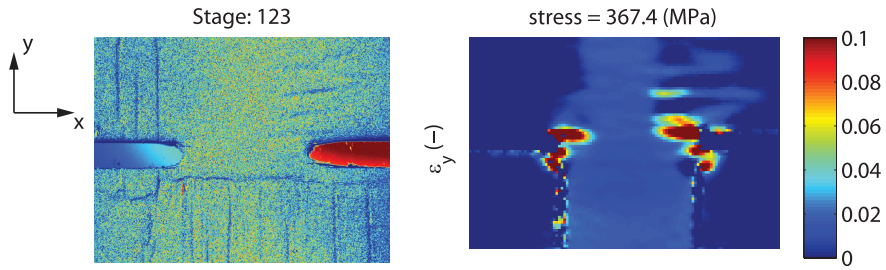

(a) 240 g/m^2 STF.

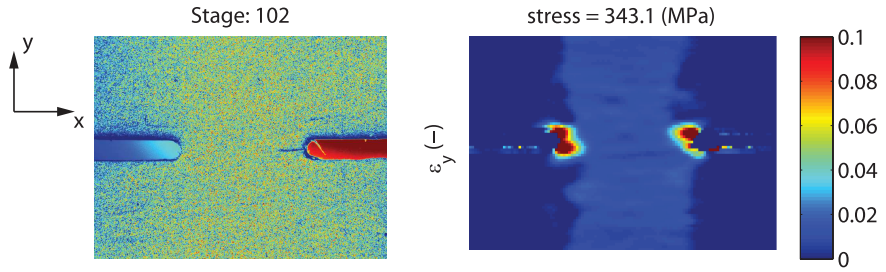

(b) 160 g/m^2 STF.

Fig. 4.49. Coloured distribution of grey levels (0–255) and longitudinal strain field, ε_y, of representative 20 mm wide DENT test specimens (geometry B) obtained with the DIC technique at the stages before final failure. The reference DIC coordinate system is depicted in the figures, where the y-axis is aligned with the loading direction.

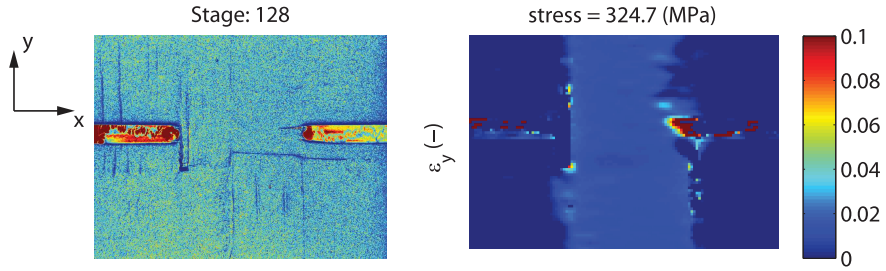

(a) 240 g/m^2 STF.

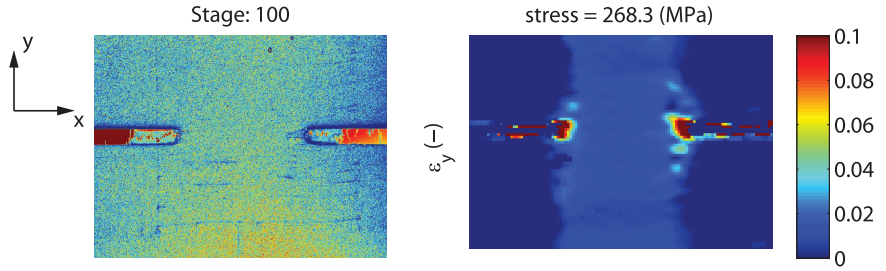

(b) 160 g/m^2 STF.

Fig. 4.50. Coloured distribution of grey levels (0–255) and longitudinal strain field, ε_y, of representative 30 mm wide DENT test specimens (geometry C) obtained with the DIC technique at the stages before final failure. The reference DIC coordinate system is depicted in the figures, where the y-axis is aligned with the loading direction.

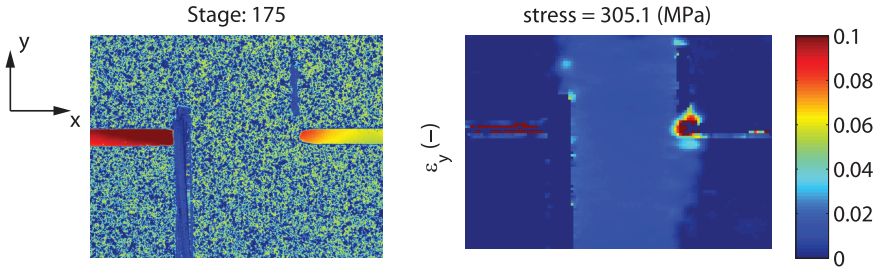

(a) 240 g/m^2 STF.

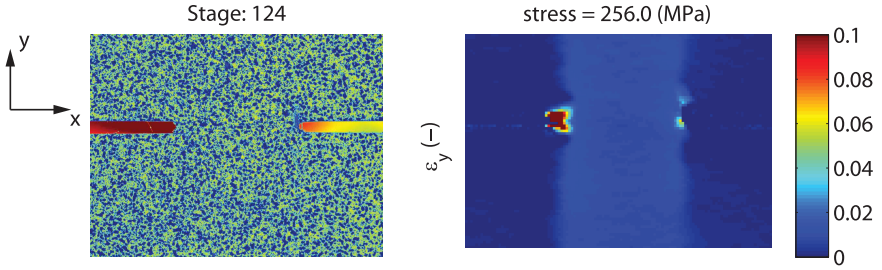

(b) 160 g/m^2 STF.

Fig. 4.51. Coloured distribution of grey levels (0–255) and longitudinal strain field, ε_y, of representative 40 mm wide DENT test specimens (geometry D) obtained with the DIC technique at the stages before final failure. The reference DIC coordinate system is depicted in the figures, where the y-axis is aligned with the loading direction.

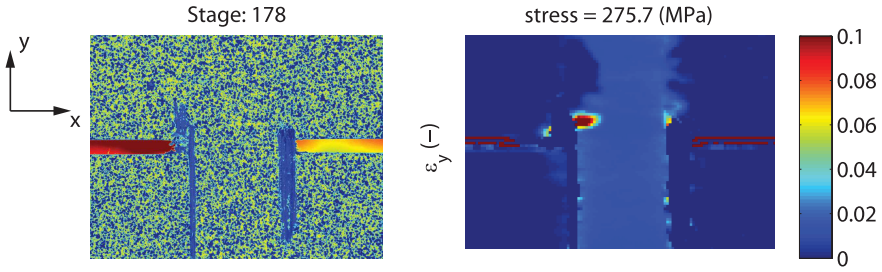

(a) 240 g/m^2 STF.

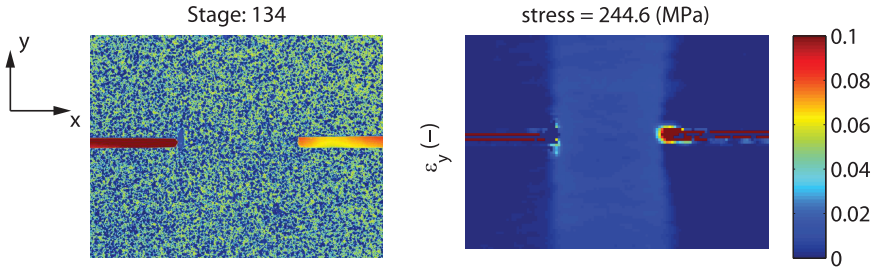

(b) 160 g/m^2 STF.

Fig. 4.52. Coloured distribution of grey levels (0–255) and longitudinal strain field, ε_y, of representative 50 mm wide DENT test specimens (geometry E) obtained with the DIC technique at the stages before final failure. The reference DIC coordinate system is depicted in the figures, where the y-axis is aligned with the loading direction.

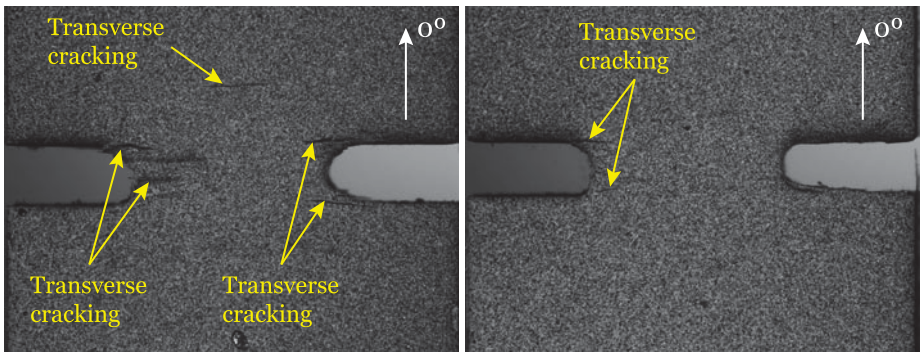

(a) 240 g/m^2 STF. (b) 160 g/m^2 STF.

Fig. 4.53. Detailed pictures of the ligament section of representative 10 mm wide DENT test specimens (geometry A) before ultimate failure. Pictures captured with the DIC image grabbing system.

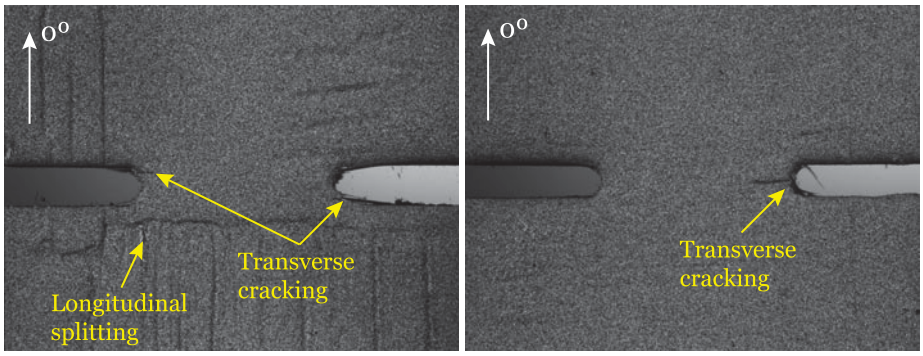

(a) 240 g/m^2 STF. (b) 160 g/m^2 STF.

Fig. 4.54. Detailed pictures of the ligament section of representative 20 mm wide DENT test specimens (geometry B) before ultimate failure. Pictures captured with the DIC image grabbing system.

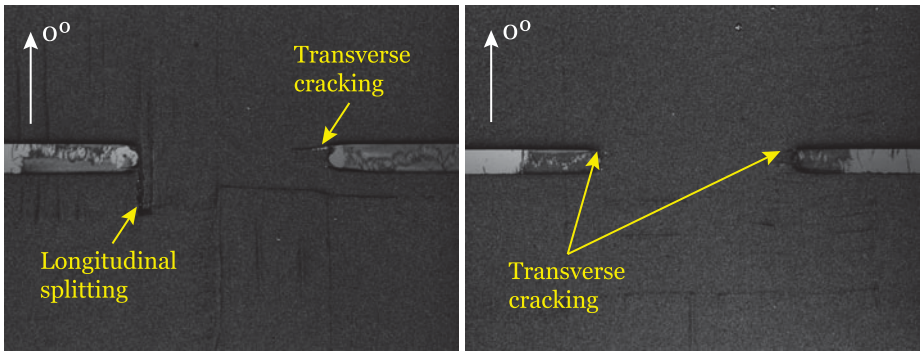

(a) 240 g/m^2 STF. (b) 160 g/m^2 STF.

Fig. 4.55. Detailed pictures of the ligament section of representative 30 mm wide DENT test specimens (geometry C) before ultimate failure. Pictures captured with the DIC image grabbing system.

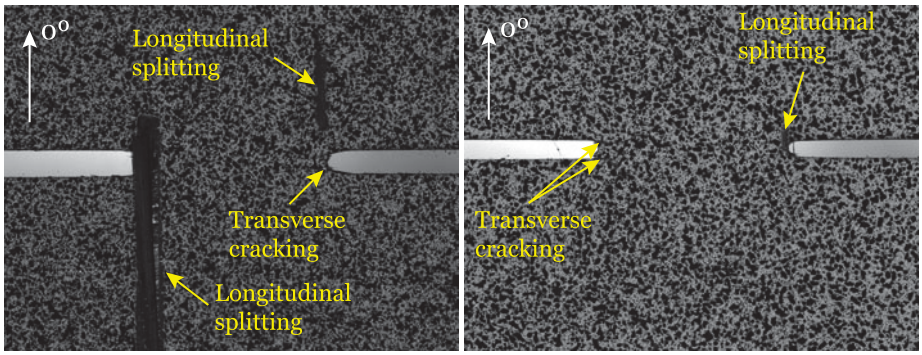

(a) 240 g/m^2 STF. (b) 160 g/m^2 STF.

Fig. 4.56. Detailed pictures of the ligament section of representative 40 mm wide DENT test specimens (geometry D) before ultimate failure. Pictures captured with the DIC image grabbing system.

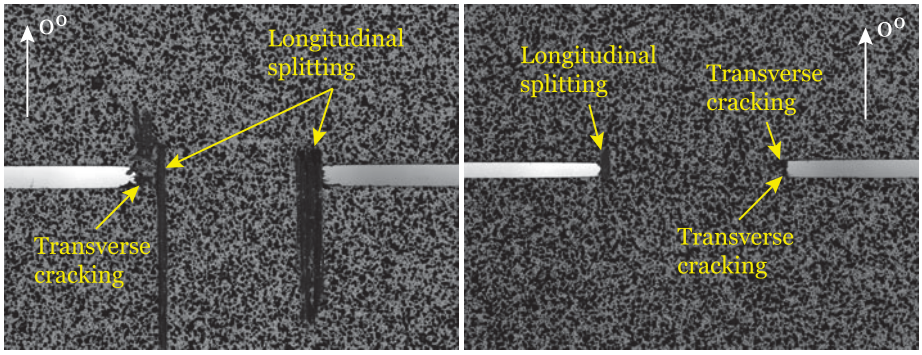

(a) 240 g/m^2 STF. (b) 160 g/m^2 STF.

Fig. 4.57. Detailed pictures of the ligament section of representative 50 mm wide DENT test specimens (geometry E) before ultimate failure. Pictures captured with the DIC image grabbing system.

making the occurrence of internal longitudinal split cracking more evident. Both internal and surface split cracks greatly affect the strain distribution in the vicinity of the notch (as it is noticeable from figures 4.48a to 4.52a), blunting the strain concentration and, consequently, delaying unstable fracture of the 0° spread-tow yarns.

From the previous discussions, it is clear that strong stress relaxation has occurred in both STFs before unstable intralaminar fracture, more importantly in the low-grade 240 g/m^2 STF. It is also important to stress that the determination of the $\mathcal{R}$-curve associated with mode I tensile intralaminar fracture assumes that all damage mechanisms can be lumped into the intralaminar damage process zone represented by the measured $\mathcal{R}$-curve. This includes not only stable intralaminar fracture of the longitudinal and transverse spread-tow yarns, but also blunting mechanisms not confined to the vicinity of the noth tips, such as split cracking.

However, if strong stress relaxation occurs in the vicinity of the notch (as observed before), such assumption is no more valid. Consequently, the $\mathcal{R}$-curve may not be representative of the damage process associated with mode I tensile intralaminar fracture alone, but associated with a combination of non-negligible mechanisms whose characterisation will not represent a material property, but rather a structural response. In this case, direct comparison between different materials (or even different reinforcement grades) cannot be performed due to the impossibility to identify appropriately which mechanisms are actually involved in the fracture process and in which extent. Any assessment may have to be restricted to a structural integrity analysis, and not to material characterisation.

To assess possible load asymmetries and the effects of strain concentration near the tips of the edge notches, remote stress-local axial strain relations were obtained with virtual strain gauges computed from the DIC data [121, 122, 182,

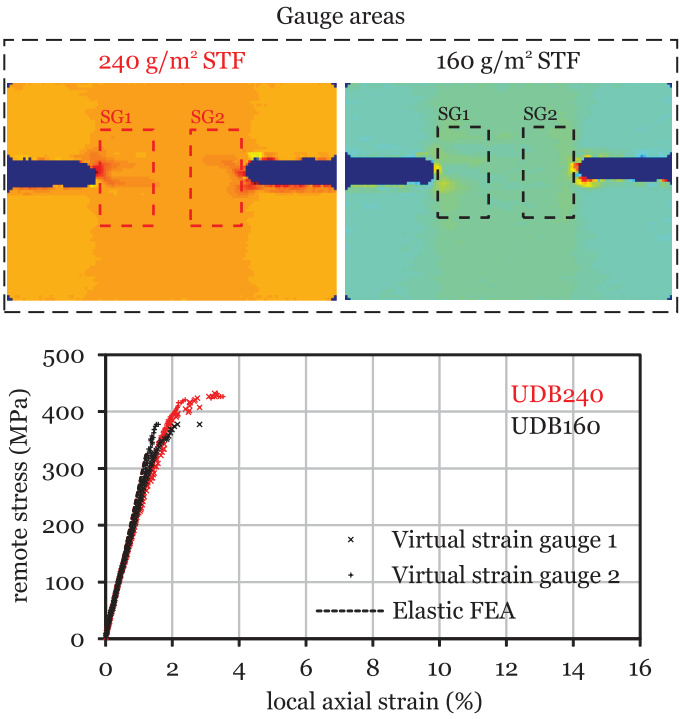

Fig. 4.58. Virtual strain gauge areas and remote stress-local axial strain relations for representative 10 mm wide DENT test specimens (geometry A). The loading direction is parallel to the vertical axis of the specimens.

187]. The strain measurements of the virtual strain gauges were obtained averaging the results of the DIC in an area equivalent to the gauge area of physical strain gauges. Gauge areas with 3.18 mm in length by 1.78 mm in width were used.

Two virtual strain gauges (*SG1* and *SG2*) were placed at the tips of the edge notches. Figures 4.58 to 4.62 show, for each specimen configuration and for both STFs, the location of the gauge areas (*SG1* and *SG2*) drawn on the longitudinal strain field obtained with DIC at an applied remote stress equal to 20% of the ultimate remote stress, and the remote stress-local axial strain relations obtained with this numerical procedure.

Previous studies [121, 122, 182, 187] using a similar DIC system configuration have shown that the data obtained with physical and virtual strain gauges is virtually the same, even for regions with high strain concentrations. To further validate the proposed virtual strain gauge approach and the accuracy of the results, a linear-elastic FEA was performed for each specimen geometry, employing the same averaging procedure to compare with the data measured with virtual strain gauges.

The FE models were created using the commercial FE software Abaqus 6.12-1 [275]. A structured mesh of CPS4R elements with a minimum in-plane size five times smaller than the notch tip radius (or 0.1 mm) were used at the notch tip to accurately represent the notch geometry and capture the strain concentrations. In the FE model, only the gauge section was represented, i.e. the gripped regions were not modelled. Figures 4.63a and 4.64a show a detail of the mesh of the 10 mm wide (geometry A) and 50 mm wide (geometry E) FE models, respectively.

In order to replicate the load and boundary conditions of the actual test setup, a longitudinal displacement (x-direction) of 1.00 mm was applied to the nodes on the top end, while fixing their remaining degrees of freedom. The degrees of freedom of the nodes in the bottom end were all fixed (encastre boundary condition).

The individual plies of the composite lay-up were modelled using a layerwise approach, explicitly defining each lamina, and respective ply orientation, by one integration point through the thickness of the plane stress elements. The constitutive behaviour of each ply was defined by an orthotropic linear-elastic material model, using the elastic properties

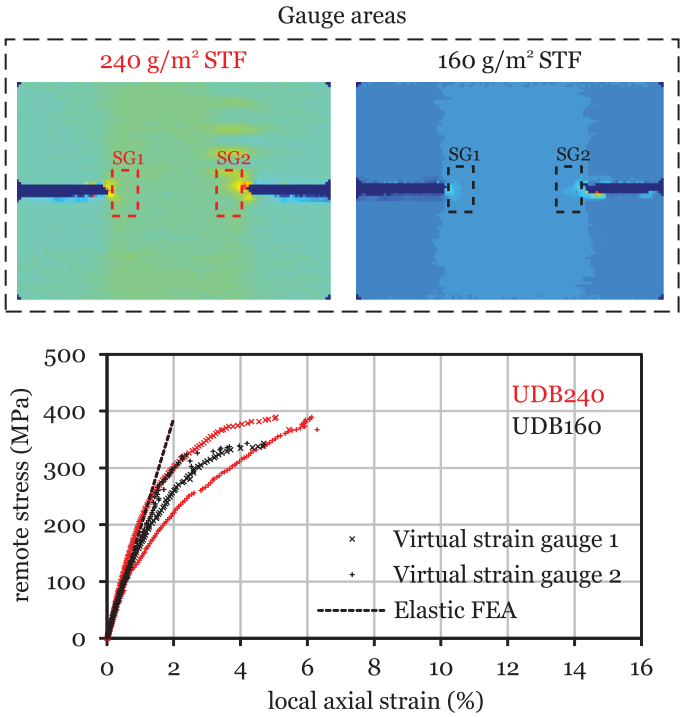

Fig. 4.59. Virtual strain gauge areas and remote stress-local axial strain relations for representative 20 mm wide DENT test specimens (geometry B). The loading direction is parallel to the vertical axis of the specimens.

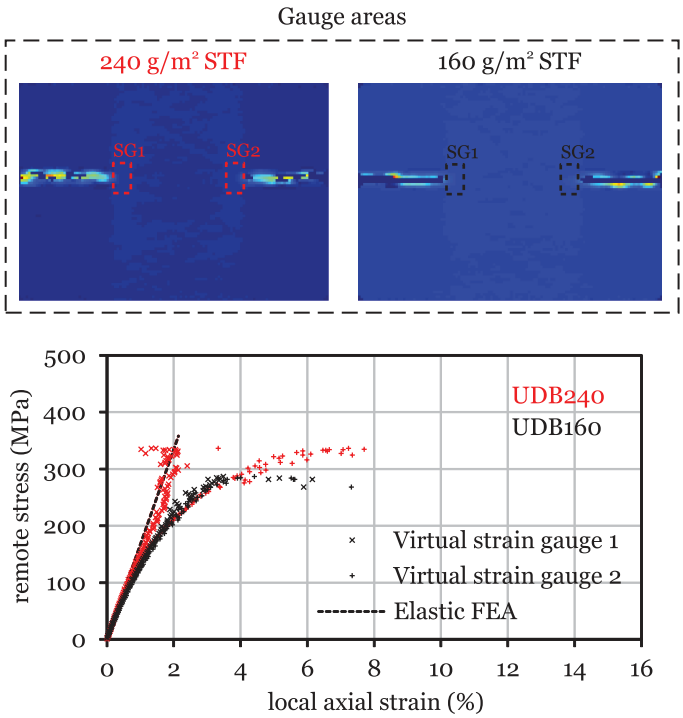

Fig. 4.60. Virtual strain gauge areas and remote stress-local axial strain relations for representative 30 mm wide DENT test specimens (geometry C). The loading direction is parallel to the vertical axis of the specimens.

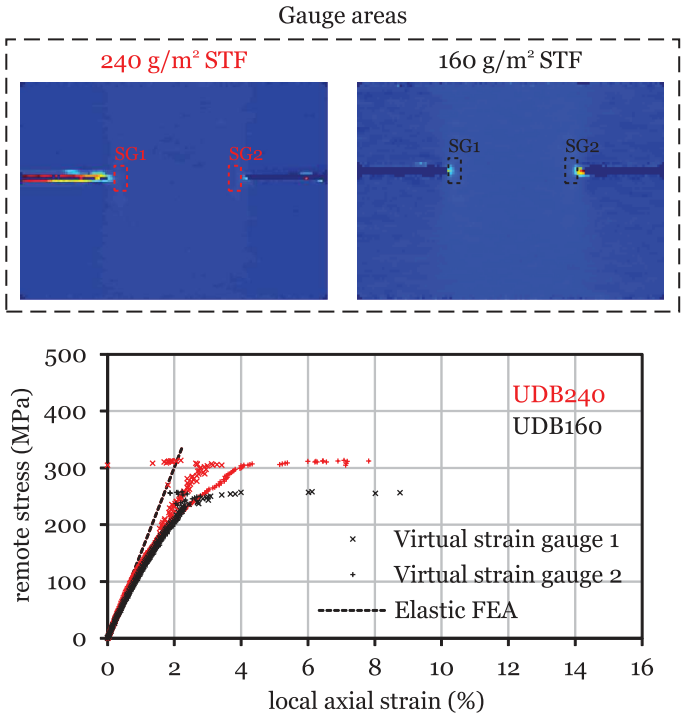

Fig. 4.61. Virtual strain gauge areas and remote stress-local axial strain relations for representative 40 mm wide DENT test specimens (geometry D). The loading direction is parallel to the vertical axis of the specimens.

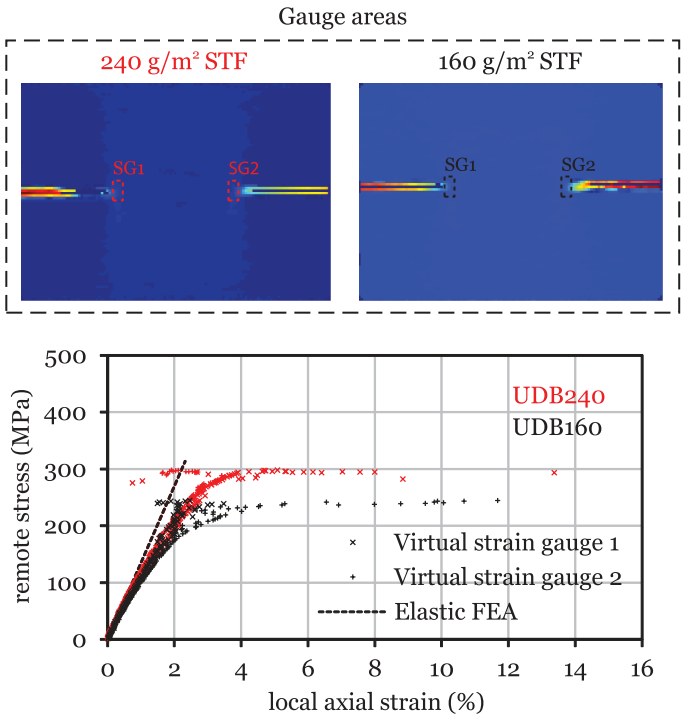

Fig. 4.62. Virtual strain gauge areas and remote stress-local axial strain relations for representative 50 mm wide DENT test specimens (geometry E). The loading direction is parallel to the vertical axis of the specimens.

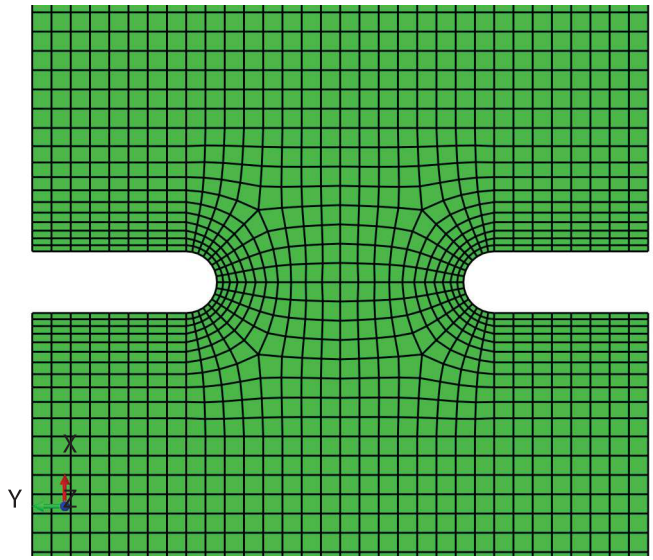

(a) Mesh detail.

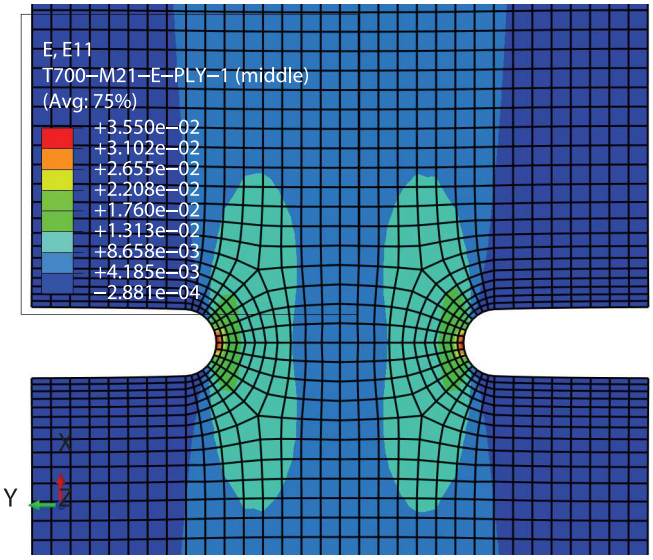

(b) Longitudinal strain field of the outer ply.

Fig. 4.63. Mesh detail of the FE model of a 10 mm wide DENT specimen (geometry A) and longitudinal strain field of the outer ply.

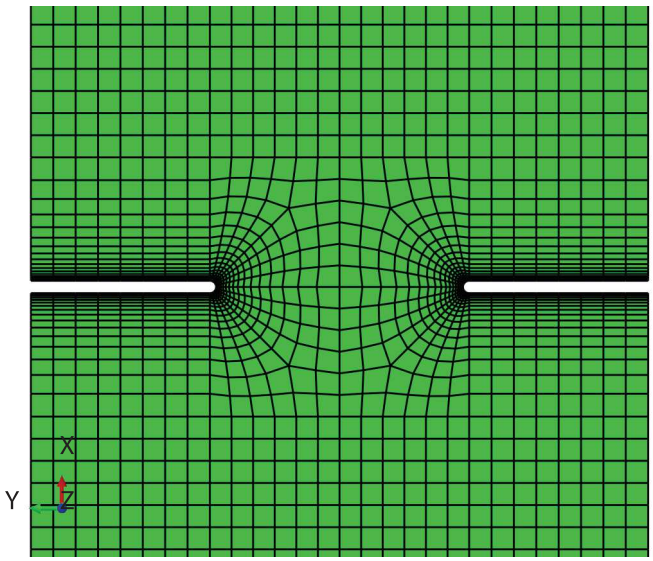

(a) Mesh detail.

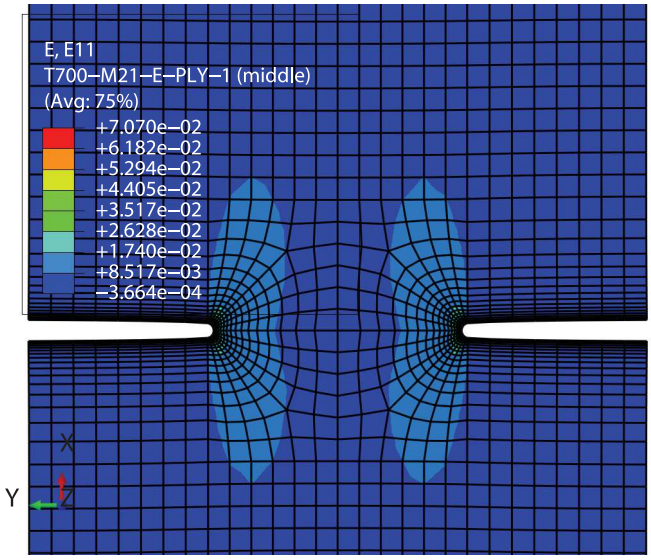

(b) Longitudinal strain field of the outer ply.

Fig. 4.64. Mesh detail of the FE model of a 50 mm wide DENT specimen (geometry E) and longitudinal strain field of the outer ply.

Table 4.12
Mean ultimate remote stresses ($\bar{\sigma}^{\infty}$) and coefficients of variation (C.V.) of the DENT tests.

Results	Geometry ID				
	A	B	C	D	E
240 g/m^2 STF					
No. specimens	3	3	3	3	3
$\bar{\sigma}^{\infty}$ (MPa)	443	390	348	319	305
C.V. (%)	0.6	2.1	1.9	1.3	1.2
160 g/m^2 STF					
No. specimens	3	3	3	3	3
$\bar{\sigma}^{\infty}$ (MPa)	398	339	293	268	254
C.V. (%)	2.5	1.6	1.7	3.4	3.0

of T700GC/M21 (table 4.1). As demonstrated in section 4.5.1, despite the assumptions regarding the adoption of the properties of a material system with a different fibre sizing obtained from *prepregs* with a different areal weight (section 4.2), a remarkable correlation could be observed between the results of the FEA and the average strain measure obtained from the DIC data for the smooth STF coupons (figure 4.27), validating their use in the FEA. For reference, figures 4.64b and 4.64b show the longitudinal strain field of the outer ply of the 10 mm wide (geometry A) and 50 mm wide (geometry E) FE models, respectively.

The results of the FEA are plotted together with the DIC data in figures 4.58 to 4.62. As can be observed, before the onset of damage localisation at the notch tips, i.e. in the initial linear stress-strain relation, the numerical results are in very good agreement with the measured strains, validating the proposed virtual strain gauge approach, namely for application on regions of high strain concentration. It is important to note that virtual strain gauges are particularly advantageous in the analysis of the local strains in locations of high strain concentration, as, unlike real strain gauges, they do not suffer from premature signal saturation due to the development of a damage process zone in the gauge area [182], unless fracture of the observation surface occurs, which may conduct to loss of correlation due to pilling of the painted speckle pattern.

Figures 4.58 to 4.62 show that, before the stress-strain relation becomes highly nonlinear due to damage growth in the gauge area, the results for both strain gauges of the same coupon is virtually the same, confirming that an adequate test setup has been employed, resulting in a good load symmetry at the tips of the edge notches. In general, the onset of damage localisation in the vicinity of the notch tips, corresponding to the onset of nonlinearity in the stress-strain relation, is delayed in the 240 g/m^2 STF compared with the 160 g/m^2 STF. As discussed earlier, this can be attributed to the blunting effect caused by the development of longitudinal split cracking in the 240 g/m^2 STF, which relaxes the strain concentration in the longitudinal spread-tow yarns, delaying intralaminar damage localisation.

Table 4.12 shows the average results for the ultimate remote stress and corresponding coefficients of variation. These results are summarised in figure 4.65, which shows the mean ultimate remote stress as a function of the initial edge notch length, which is proportional to the specimen's size (geometrically similar specimens).

For the same specimen size (i.e., for the same edge notch length), the 240 g/m^2 STF exhibits higher notched strength than the 160 g/m^2 STF (table 4.12 and figure 4.65). This confirms the better notched response of the low-grade material (see also figures 4.38 to 4.42).

As already discussed, the superior notched response of the 240 g/m^2 STF can be attributed to the improved blunting effect of the damage mechanisms that precede intralaminar fracture, in particular longitudinal split cracking, potentiated by the higher interlaminar (inter-bundle) stresses at the interfaces of the thicker 0° spread-tow yarns. As expected, as the specimen's size increases, the mean ultimate remote stress of both STFs decreases, following a similar trend. This means that the proposed specimen configuration has positive geometry, a requirement for the determination of the $\mathcal{R}$-curve using the size effect law.

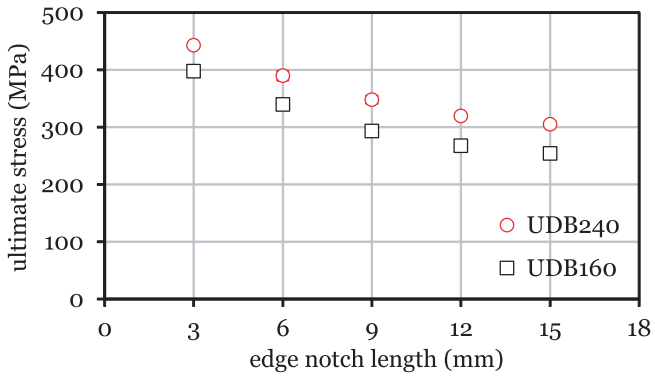

Fig. 4.65. Mean ultimate remote stress as a function of the initial edge notch length of the DENT tests.

The size effect law regression proposed in Ref. [209] that best fit the experimental data of both STFs is the *linear regression II*, which can be written as [65]:

$$\text{Linear regression II:} \quad \frac{1}{w\,(\bar{\sigma}^{\infty})^2} = \acute{A}\,\frac{1}{w} + \acute{C} \tag{4.18}$$

where $\acute{A}$ and $\acute{C}$ are the fitting parameters, given in table 4.13. Figure 4.66 shows the experimental results and the best fitting for the size effect laws of the plain weave STFs.

Using the fitting parameters shown in table 4.13, it is now possible to calculate the length of the FPZ, l_{fpz}, and the steady-state value of the fracture toughness, $\mathcal{R}_{ss}$, of the STFs as [65]:

$$\text{Linear regression II:} \quad l_{fpz} = \frac{\kappa_0}{2\acute{\kappa}_0}\frac{\acute{A}}{\acute{C}} \tag{4.19}$$

$$\mathcal{R}_{ss} = \frac{\kappa_0^2}{\acute{E}}\frac{1}{\acute{C}} \tag{4.20}$$

where $\kappa_0 = \kappa|_{\alpha=\alpha_0}$ and $\acute{\kappa}_0 = \partial\kappa/\partial\alpha|_{\alpha=\alpha_0}$ are, respectively, the value of the correction factor that accounts for both geometry and orthotropy of the material and the value of its derivative with respect to α calculated at the initial crack length ($\alpha_0 = a_0/w$), and $\acute{E}$ is the equivalent modulus given in equation (4.6). Table 4.14 shows the values of l_{fpz} and $\mathcal{R}_{ss}$ obtained for both STFs.

Figure 4.67 shows the $\mathcal{R}$-curves of the plain weave STFs obtained as the envelopes of the crack driving force curves calculated using the size effect laws of figure 4.66. Unlike most experimental results available in the literature, which consider the $\mathcal{R}$-curve to start from some initial nonzero value of $\mathcal{R}$, the $\mathcal{R}$-curve presented in figure 4.67 starts from zero. However, as stressed, for instance, by Bažant and Kazemi [277], an $\mathcal{R}$-curve that starts from some initial nonzero value implies that the crack tip can sustain a singular stress field without showing any damage, which is unreasonable. The fact that the $\mathcal{R}$-curve starts from zero means that the process zone forms right at the beginning of loading and that there is

Table 4.13
Fitting regressions and parameters for the size effect laws of the plain weave STFs.

STF configuration	Regression fit [209]	Fitting parameters
240 g/m^2 STF	Linear regression II	$\acute{A}$ = 3.5780E – 06 MPa^{-2} mm^{-1}
		$\acute{C}$ = 2.9917E – 07 MPa^{-2}
160 g/m^2 STF	Linear regression II	$\acute{A}$ = 3.8486E – 06 MPa^{-2} mm^{-1}
		$\acute{C}$ = 4.8684E – 07 MPa^{-2}

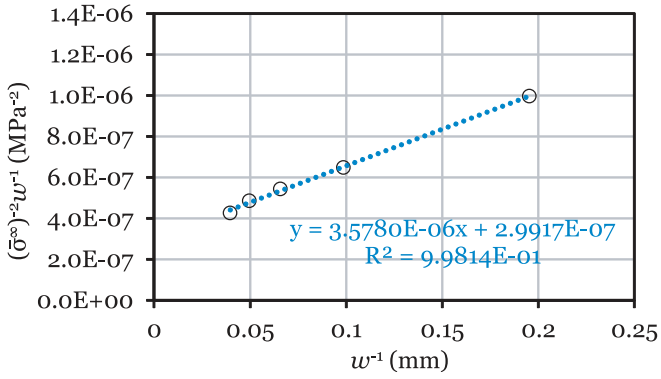

(a) 240 g/m^2 STF: linear regression II.

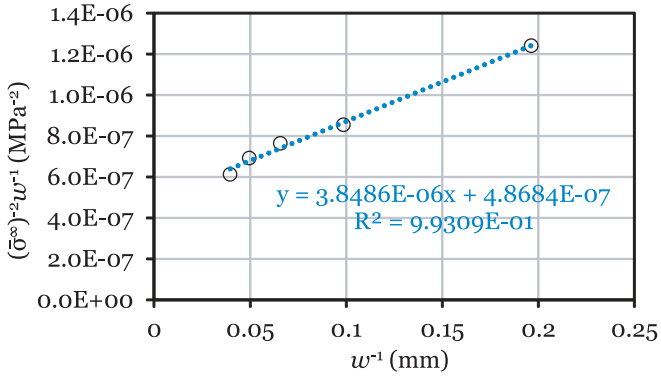

(b) 160 g/m^2 STF: linear regression II.

Fig. 4.66. Experimental results and best fitting for the size effect laws of the plain weave STFs.

never any singularity at the crack tip, which is more physically reasonable. For FRPs exhibiting a relatively large bridging zone, however, it is observed that the initial rising part of the $\mathcal{R}$-curve is considerably steep, which is the reason why, in practice, a nonzero initial value of $\mathcal{R}$ is often used.

To simplify the implementation of the $\mathcal{R}$-curve in numerical or analytical models, Catalanotti et al. [65] used the following fitting equation:

$$\mathcal{R}(\Delta a) = \begin{cases} \mathcal{R}_{ss}\left[1-(1-\zeta\,\Delta a)^{\eta}\right], & \Delta a \le l_{fpz} \\ \mathcal{R}_{ss} & , \ \Delta a > l_{fpz} \end{cases} \tag{4.21}$$

where ζ and η are the parameters that best fit the formula to the respective $\mathcal{R}$-curve. In the present work, these parameters were obtained using a nonlinear least squares method with a Trust-Region algorithm, available in the commercial software Matlab [278]. The parameters that best fit the $\mathcal{R}$-curves of both STFs are given in table 4.14. Figure 4.68 shows the $\mathcal{R}$-curves and the corresponding fitting curves for both laminates. As can be observed, the fitting formulae agree very well with the analytical envelopes. A comparison of the $\mathcal{R}$-curves of both laminates is given in figure 4.69.

Table 4.14 and figure 4.69 show that the $\mathcal{R}$-curve of the low-grade STF obtained from the size effect law calibrated from

Table 4.14
Parameters of the $\mathcal{R}$-curves and fitting formulae of the plain weave STFs.

STF configuration	l_{fpz} (mm)	$\mathcal{R}_{ss}$ (N/mm)	ζ (mm^{-1})	η (-)
240 g/m^2 STF	3.66	277	0.2276	3.690
160 g/m^2 STF	2.42	170	0.3505	3.607

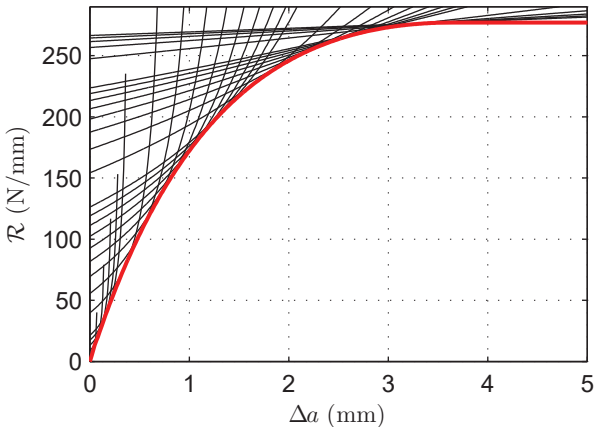

(a) 240 g/m^2 STF.

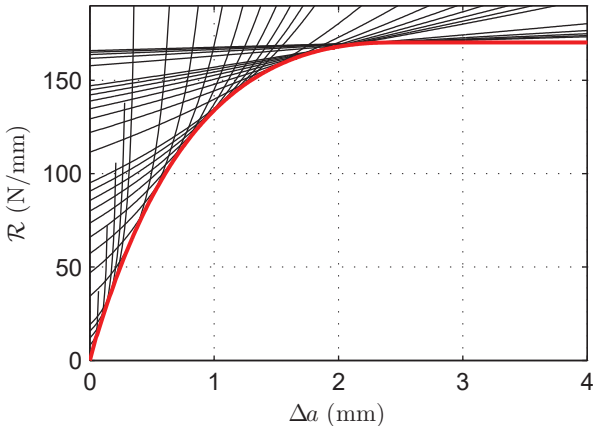

(b) 160 g/m^2 STF.

Fig. 4.67. Crack driving force curves and resulting $\mathcal{R}$-curves of the plain weave STFs for mode I longitudinal intralaminar fracture.

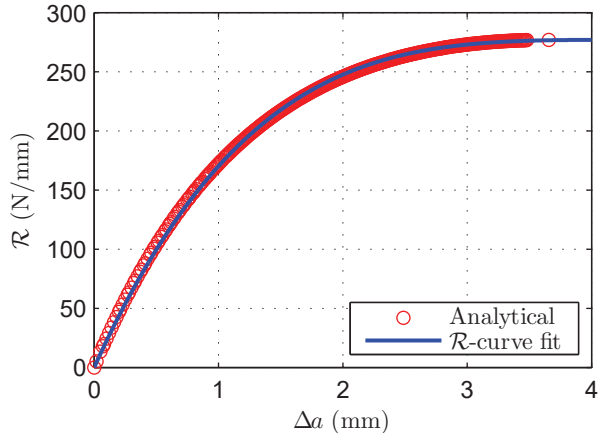

(a) 240 g/m^2 STF.

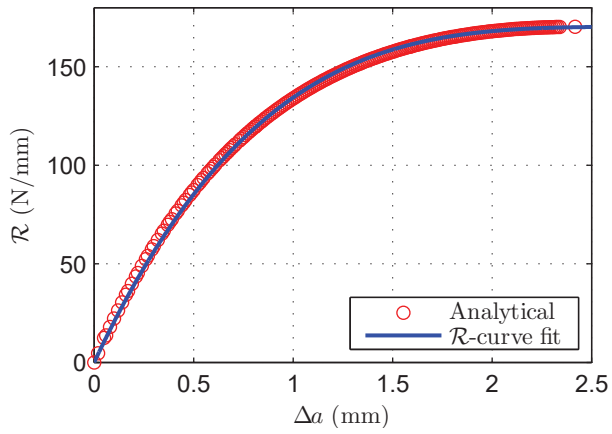

(b) 160 g/m^2 STF.

Fig. 4.68. Analytical and fitted $\mathcal{R}$-curves of the plain weave STFs.

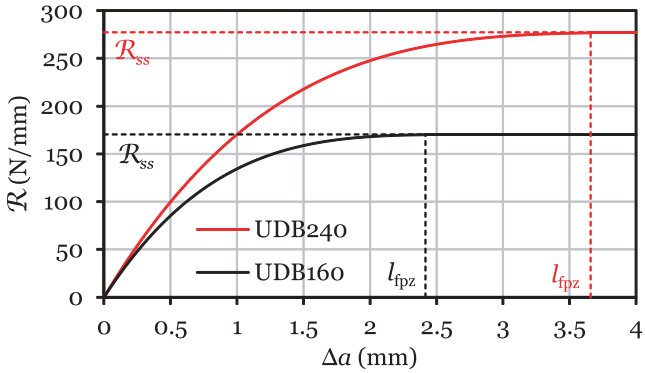

Fig. 4.69. Comparison of the $\mathcal{R}$-curves for mode I longitudinal intralaminar fracture of the plain weave STFs.

the DENT tests performed in this study (figure 4.66) is characterised, respectively, by a length of the FPZ and a steady-state value of the fracture toughness 1.51 times larger and 1.63 times higher than the thin-ply STF. Such improved fracture toughness could be expected given the superior notched response of the low-grade STF observed in figures 4.38 to 4.42, and in table 4.12 and figure 4.65.

However, as already discussed, this improved fracture toughness and notched response of the low-grade STF is attributed to the blunting effect of the damage mechanisms that precede intralaminar fracture, in particular longitudinal split cracking (see figures 4.43 to 4.47 and 4.48 to 4.52); it cannot be attributed to an intrinsically higher fracture toughness of the thicker spread-tow yarns.

In fact, the extent of blunting damage mechanisms in the two STFs, which modifies the stress distribution in the vicinity of the notch tips, was significantly different, and clear, self-similar intralaminar fracture did not occur. Larger DENT specimen configurations would be required to minimise the effect of the blunting mechanisms acting at the notch tips, to accurately determine $\mathcal{R}_{ss}$.

It is important to note that the $\mathcal{R}$-curve determined from the size effect law is defined such that $\mathcal{R}_{ss}$ is the energy required for crack growth in an infinitely large specimen. Hence, $\mathcal{R}_{ss}$ calculated using the size effect law is size and geometry independent. However, because the size effect law is not exact, this should be regarded as an approximation. These results highlight the importance of adequately selecting both specimen configurations and range of coupon dimensions in calibrating the size effect laws to accurately derive the $\mathcal{R}$-curves with this methodology. Nonetheless, these results demonstrate that promoting subcritical damage mechanisms, in particular longitudinal fibre-matrix splitting, by increasing the thickness (or grade) of the 0° yarns has the potential to improve substantially the fracture resistance and notched response of spread-tow laminates. And this is obtained while avoiding the most detrimental interlaminar damage and transverse matrix cracking.

Finally, it is noted that, for some materials, the $\mathcal{R}$-curve may change slightly with specimen shape (e.g. Refs. [211, 277, 279, 280]). However, the differences in the $\mathcal{R}$-curve, which generally do not affect $\mathcal{R}_{ss}$, may result either from the statistical scatter of the experimental tests carried out to calibrate the size effect law (e.g. Ref. [211]), or due to the effect of the shape correction functions κ, which vary with the different specimen shapes. In fact, because l_{fpz} is dependent on κ and on its derivative, l_{fpz} is more sensitive to experimental or numerical error than $\mathcal{R}_{ss}$ (e.g. Refs. [279, 280]).

4.5.5. Fabric mode I compressive crack resistance curve

Between 2 and 7 valid DENC specimens of each STF and geometry were tested to failure. Figures 4.70 to 4.74 show, for the different geometries, the remote stress-displacement curves of both STFs. The remote stress, σ^{∞}, of each test was calculated dividing the applied load by the corresponding specimen's cross-section area. The applied load was measured by the load cell and the displacement is the cross-head displacement of the testing machine. Due to the adjustments in the self-alignment system (figure 4.7), all specimen configurations show a nonlinear remote stress-displacement relation

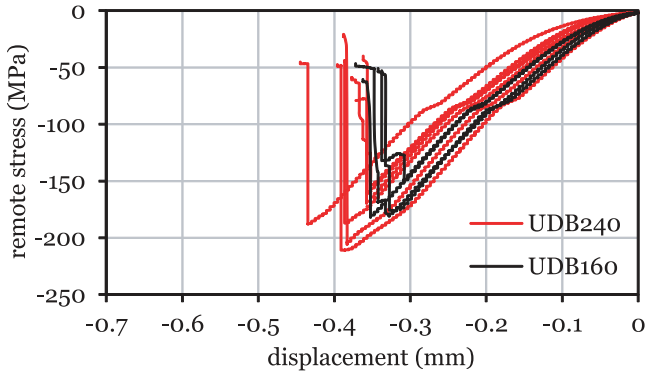

Fig. 4.70. Remote stress-displacement curves for the 10 mm wide DENC specimens (geometry A).

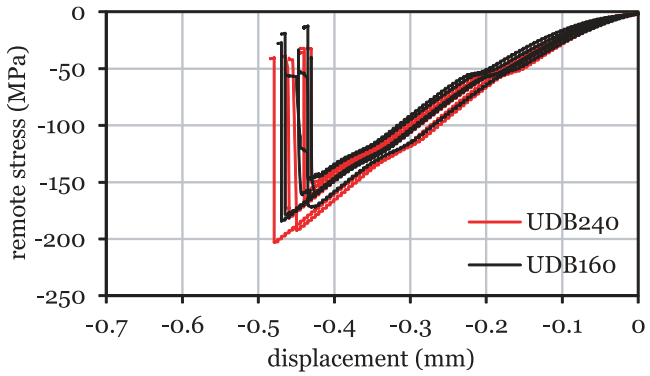

Fig. 4.71. Remote stress-displacement curves for the 15 mm wide DENC specimens (geometry B).

in the beginning of the tests. No remarkable difference is observed between the results of the two STFs.

Figures 4.75 to 4.79 show representative DENC test specimens of each configuration after testing. In general, all specimen configurations fail with the propagation of intralaminar compressive damage along the ligament section of the notched plane, connecting the edge notch tips. No difference was observed in the failure modes exhibited by the 240 g/m^2 and 160 g/m^2 STFs.

Some 10 mm wide DENC specimens (geometry A) exhibited lateral interlaminar damage between plies close to the surface, propagating from the notched section towards the specimen's ends. Kinked thin sublaminate groups could also be observed. The 15 mm, 20 mm and 25 mm wide DENC specimens (geometries B, C and D) exhibited lateral interlaminar damage too, with small longitudinal or transverse split cracks at the outer spread-tow yarns close to the ligament section. In the 30 mm wide specimens (geometry E), long longitudinal or transverse split cracks at the surface spread-tow yarns along the specimens' gauge length or across the width could also be observed.

Final catastrophic failure coincided with a large load drop (figures 4.70 to 4.74) and a strong noise caused by longitudinal compressive failure. However, prior to catastrophic failure, small load drops occurred in some specimens of all configurations, either preceding or following the peak applied remote stress, more frequently in the smaller DENC configurations of the 160 g/m^2 STF. On the other hand, in some of the largest specimens, internal damage growth was audible as the applied load was approaching the ultimate remote stress.

In some 20 mm wide specimens (geometry C), internal damage growth in the 240 g/m^2 STF was audible at applied remote stresses above 130 MPa (87% of the ultimate remote stress). In the 160 g/m^2 STF, noise produced by internal damage could be detected at applied remote stresses between 110 MPa and 150 MPa (80% to 99% of the ultimate remote stress).

For the 25 mm wide specimens (geometry D), internal damage growth in the 240 g/m^2 STF was audible at approxi-

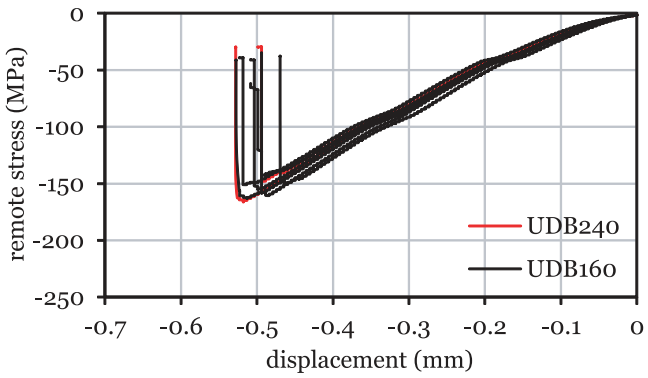

Fig. 4.72. Remote stress-displacement curves for the 20 mm wide DENC specimens (geometry C).

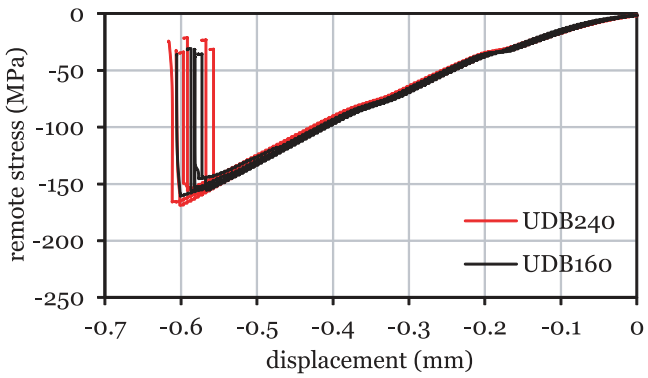

Fig. 4.73. Remote stress-displacement curves for the 25 mm wide DENC specimens (geometry D).

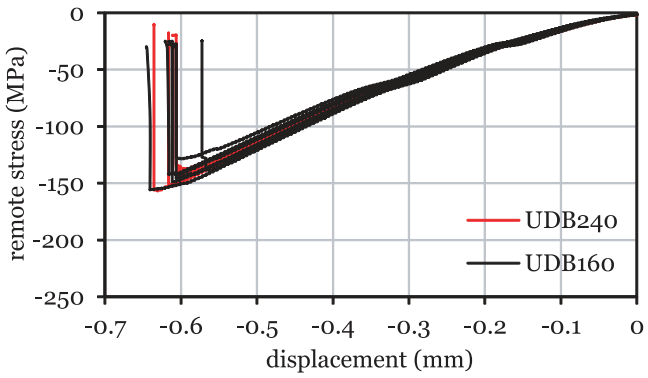

Fig. 4.74. Remote stress-displacement curves for the 30 mm wide DENC specimens (geometry E).

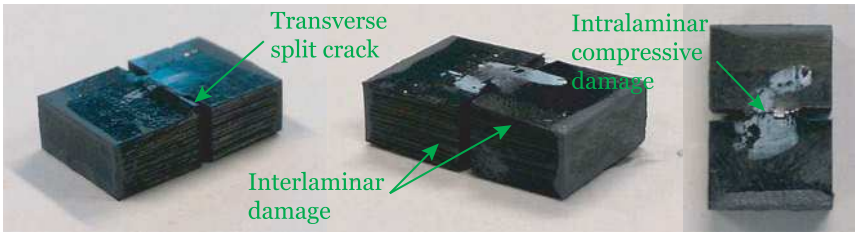

Fig. 4.75. Representative 10 mm wide DENC specimens (geometry A) after testing.

Fig. 4.76. Representative 15 mm wide DENC specimens (geometry B) after testing.

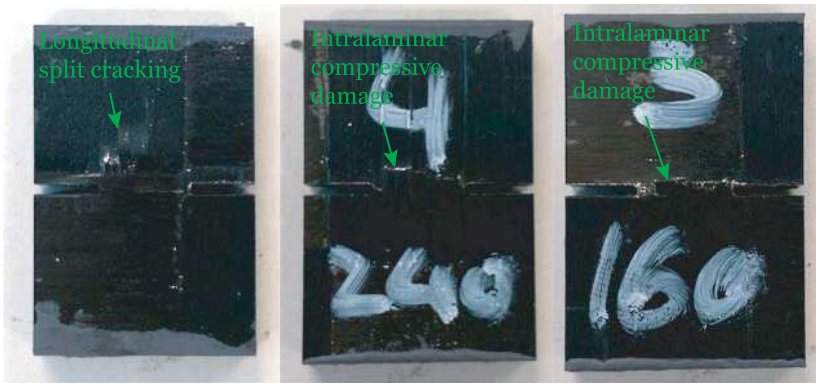

Fig. 4.77. Representative 20 mm wide DENC specimens (geometry C) after testing.

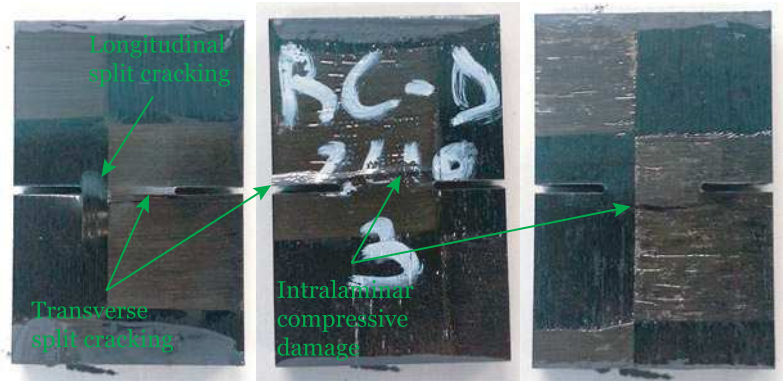

Fig. 4.78. Representative 25 mm wide DENC specimens (geometry D) after testing.

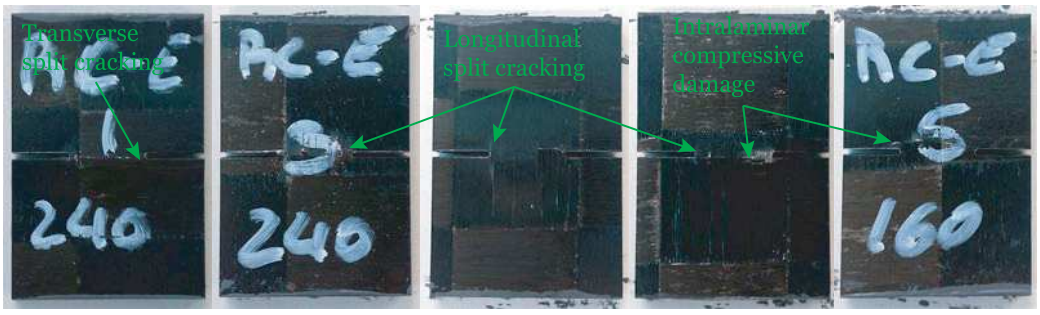

Fig. 4.79. Representative 30 mm wide DENC specimens (geometry E) after testing.

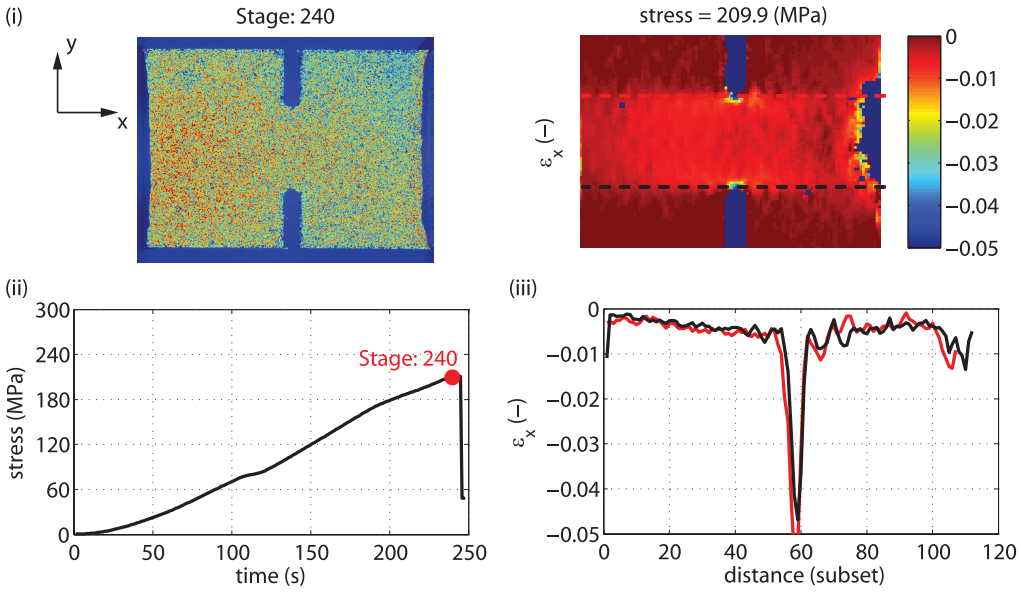

Fig. 4.80. (i) Coloured distribution of grey levels (0–255) and longitudinal strain field, ε_x, of a representative 10 mm wide 240 g/m^2 STF DENC test specimen (geometry A) obtained with the DIC technique at the stage prior to unstable propagation of intralaminar compressive damage along the notched plane. (ii) Position of the stage in the remote stress-time relation. (iii) Local longitudinal strain measured along two lines tangent to the tips of the edge notches over the length of the specimen. The reference DIC coordinate system is depicted in the figure, where the x-axis is aligned with the loading direction. The stresses are given in absolute values.

mately 130 MPa (85% of the ultimate remote stress) or above. Internal damage growth was also audible during the tests of of the 160 g/m^2 STF at applied remote stresses around 110 MPa (74% of the ultimate remote stress), in some cases with apparent compressive fibre failure at approximately 130 MPa (i.e. 96% of the ultimate remote stress) and above.

For the 30 mm wide specimens (geometry E), internal damage growth in the 240 g/m^2 STF was audible at approximately 100 MPa (66% of the ultimate remote stress) or above. In the 160 g/m^2 STF, internal damage growth was audible above 70 MPa (53% of the ultimate remote stress), more frequently above approximately 140 MPa (96% of the ultimate remote stress) as the applied remote stress was approaching the ultimate failure stress.

The noise produced by the specimens of both laminates during the tests indicates that damage occurs in the DENC test specimens before intralaminar compressive failure takes place in the notched plane. However, it is interesting to note that fibre compressive failure, which might be identified by a stronger characteristic noise, apparently occurs at the final stages of damage propagation, close to final specimen failure. Hence, it can be stated that, as fibre compressive failure initiates, it prompts quick intralaminar compressive damage growth, which rapidly conducts to catastrophic failure of the specimen.

Figures 4.80 to 4.86 show the longitudinal strain fields and the local longitudinal strain measured along two lines tangent to the tips of the edge notches and parallel to the loading direction obtained with the DIC technique on representative specimens of some of the tested DENC configurations. The analysis and localisation of the peaks, discontinuities or even loss of data correlation in the longitudinal strain field, namely in the vicinity of the tips of the edge notches, can be used to identify the onset and propagation of intralaminar surface damage in the DENC test specimens. For reference, the coloured distributions of grey levels and the remote stress-time relations are also shown.

As can be observed, little or no damage occurred before unstable intralaminar compressive damage propagation across the surface ligament width of the tested specimens. Internal damage growth during the test can, therefore, be attributed to small local events that, as shown in figures 4.70 to 4.74 and in figures 4.80 to 4.86 had little or no effect on the mechanical response of the DENC test specimens of the tested STFs.

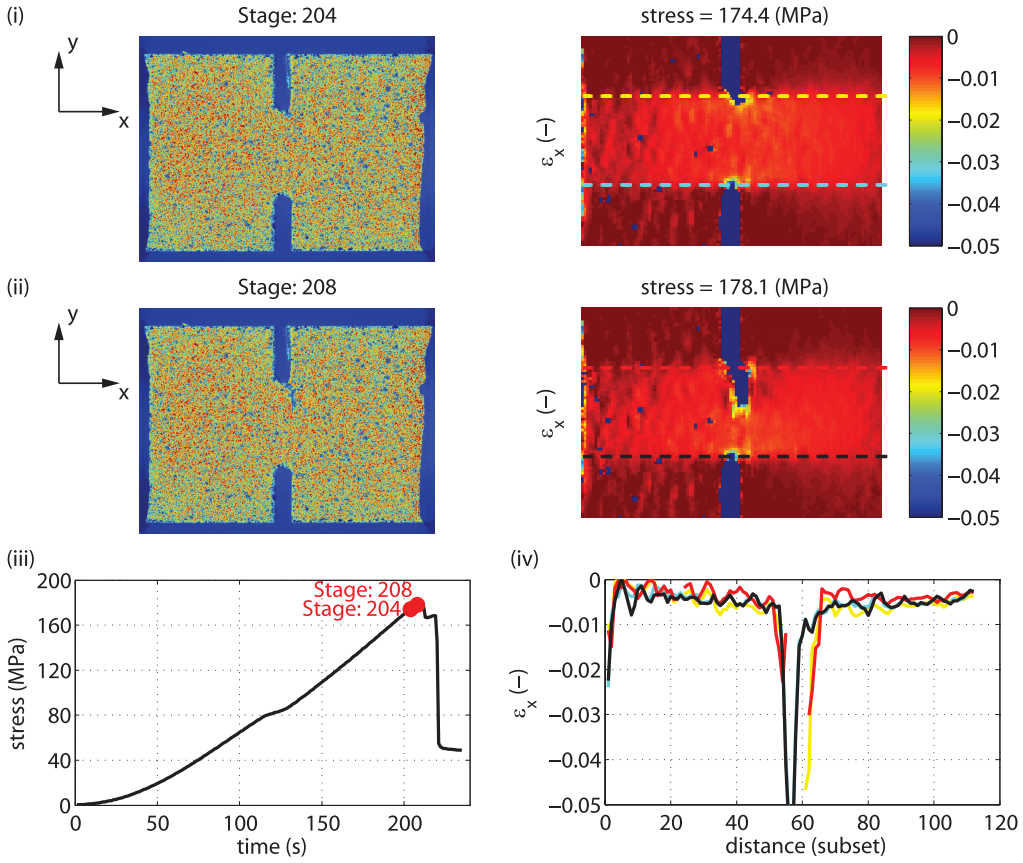

Fig. 4.81. Coloured distributions of grey levels (0–255) and longitudinal strain fields, ε_x, of a representative 10 mm wide 160 g/m^2 STF DENC test specimen (geometry A) obtained with the DIC technique at the stages of (i) onset of intralaminar compressive damage growth and (ii) before unstable propagation along the notched plane. (iii) Position of the stages in the remote stress-time relation. (iv) Local longitudinal strain measured along two lines tangent to the tips of the edge notches over the length of the specimen. The reference DIC coordinate system is depicted in the figure, where the x-axis is aligned with the loading direction. The stresses are given in absolute values.

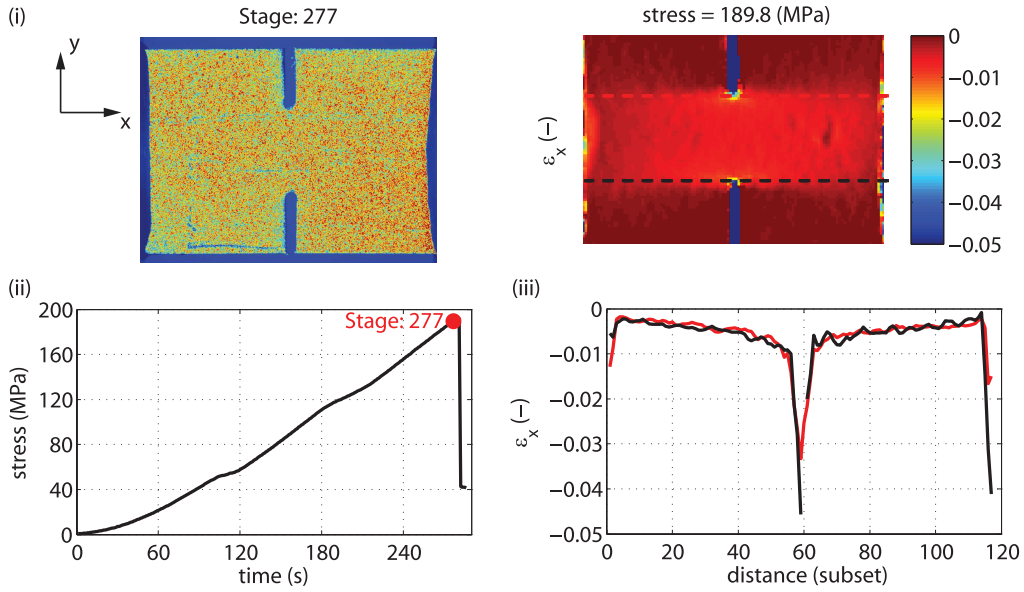

Fig. 4.82. (i) Coloured distribution of grey levels (0–255) and longitudinal strain field, ε_x, of a representative 15 mm wide 240 g/m^2 STF DENC test specimen (geometry B) obtained with the DIC technique at the stage prior to unstable propagation of intralaminar compressive damage along the notched plane. (ii) Position of the stage in the remote stress-time relation. (iii) Local longitudinal strain measured along two lines tangent to the tips of the edge notches over the length of the specimen. The reference DIC coordinate system is depicted in the figure, where the x-axis is aligned with the loading direction. The stresses are given in absolute values.

Interestingly, surface intralaminar compressive failure across the ligament width (figure 4.87) generally occurred before the peak load. Final failure, corresponding to the big load drop observed in all remote stress-displacement curves (figures 4.70 to 4.74), in some cases occurred after a short sequence of small load drops or after a short load plateau. This observation suggests that intralaminar compressive failure of the tested STFs occurs quickly, but in a progressive mode, starting close to the surface of the specimen, and then penetrating through the specimen's cross-section, resulting in a total loss of the load-carrying capacity. This progressive but quick failure mode means that the adopted specimen scaling configuration is suitable for the characterisation of the mode I intralaminar compressive fracture properties of the STFs investigated in the present study.

The progressive but catastrophic failure mode exhibited by the tested STFs is characteristic of the compression fracture process typically observed in fibre-reinforced composites, in particular fibre kinking. The latter is originated by local micro-structural defects or local instabilities that trigger kink band propagation when local matrix cracking occurs in the vicinity of the misaligned, micro-buckled fibres [103, 281, 282].

It is important to note that compressive failure may, therefore, initiate predominantly in one face of the specimen either due to the characteristics of the tested material (acceptable situation), but also due to load misalignment (undesirable). Nevertheless, based on post-failure analysis of the tested specimens and based on the analysis of the displacement and strain fields measured with the DIC technique when available, valid loading conditions in all cases presented in figures 4.80 to 4.86 and in figure 4.87 were assured by appropriate loading setup.

In figures 4.75 to 4.79 and in figure 4.87 it is also noted that, in a few specimens, surface net-section fracture between the tips of the edge notches did not always occur across the mid-plane of the ligament section, but slightly above or slightly below. Nevertheless, post-failure analysis of the tested specimens show that laminate intralaminar compressive fracture through the thickness occurred primarily on the notched plane.

The remote stress-local axial strain relations of representative DENC test specimens of both STFs were determined using virtual strain gauges computed from the DIC measurements. The local strains were obtained averaging the longitudinal strains in an area equivalent to the gauge area of physical strain gauges. Strain gauge areas 3.18 mm long and

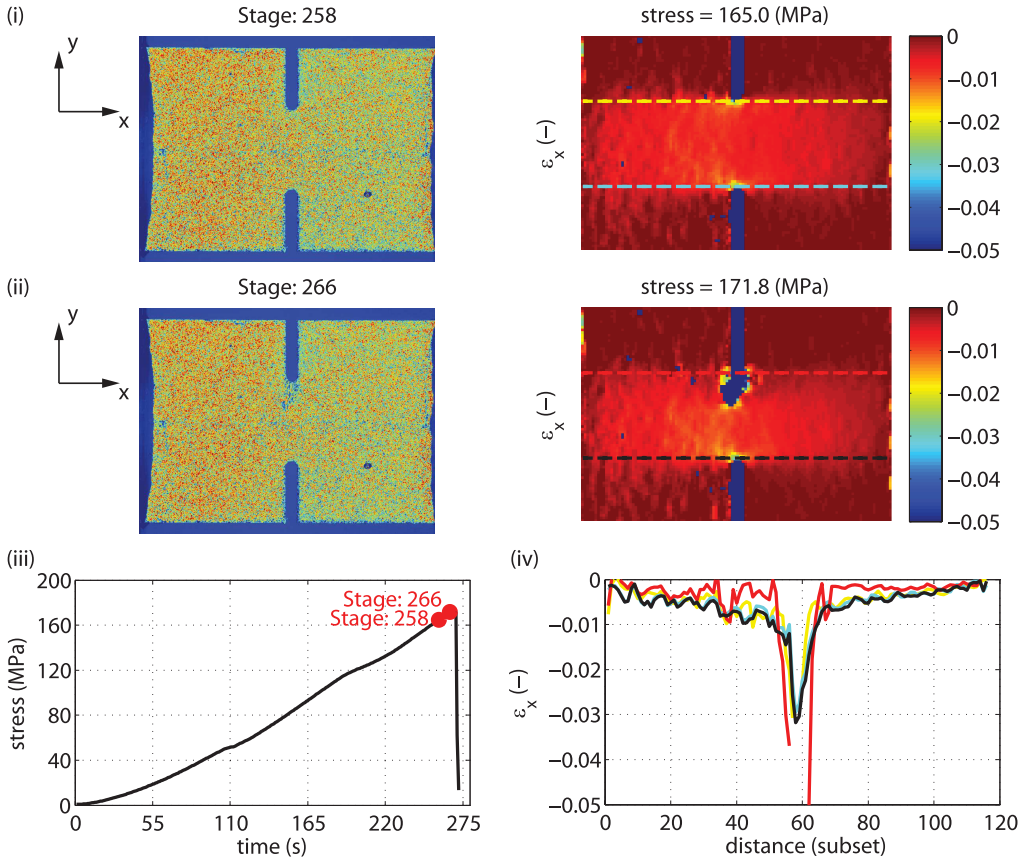

Fig. 4.83. Coloured distributions of grey levels (0–255) and longitudinal strain fields, ε_x, of a representative 15 mm wide 160 g/m^2 STF DENC test specimen (geometry B) obtained with the DIC technique at the stages of (i) onset of intralaminar compressive damage growth and (ii) before unstable propagation along the notched plane. (iii) Position of the stages in the remote stress-time relation. (iv) Local longitudinal strain measured along two lines tangent to the tips of the edge notches over the length of the specimen. The reference DIC coordinate system is depicted in the figure, where the x-axis is aligned with the loading direction. The stresses are given in absolute values.

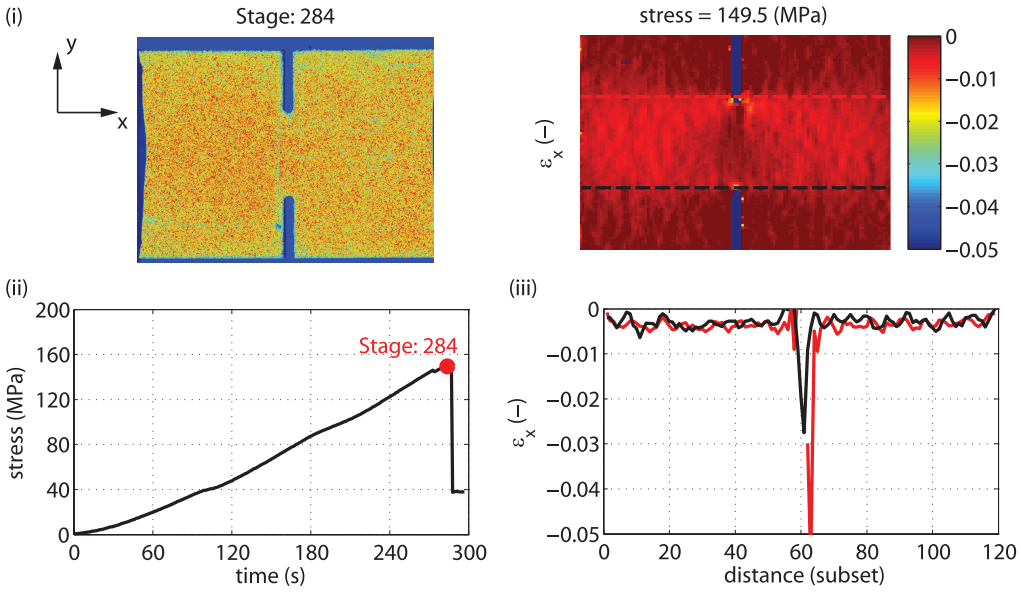

Fig. 4.84. (i) Coloured distribution of grey levels (0–255) and longitudinal strain field, ε_x, of a representative 20 mm wide 160 g/m^2 STF DENC test specimen (geometry C) obtained with the DIC technique at the stage prior to unstable propagation of intralaminar compressive damage along the notched plane. (ii) Position of the stage in the remote stress-time relation. (iii) Local longitudinal strain measured along two lines tangent to the tips of the edge notches over the length of the specimen. The reference DIC coordinate system is depicted in the figure, where the x-axis is aligned with the loading direction. The stresses are given in absolute values.

1.78 mm wide were selected. Two virtual strain gauges (*SG1* and *SG2*) were placed below and above the ligament section. Figures 4.88 to 4.92 show the location of the gauge areas (*SG1* and *SG2*) drawn on the longitudinal strain field obtained with DIC at an applied remote stress equal to 20% of the ultimate remote stress, and the corresponding remote stress-local axial strain relations.

A linear-elastic FEA was performed for each specimen geometry to compare with the virtual strain gauge data from the experiments (figures 4.88 to 4.92). This analysis is intended to validate the accuracy of the proposed virtual strain gauge approach, and also to evaluate the quality of the load introduction setup. To perform this analysis, the same averaging procedure as in the virtual strain gauges has been employed in the post-processing of the FEA.

The FE models were created with the commercial FE software Abaqus 6.12-1 [275] using a structured mesh of CPS4R elements. At the notch tip, finite elements with a minimum in-plane size five times smaller than the notch tip radius (or 0.1 mm) were used to accurately represent the notch geometry and capture the strain concentrations. Figures 4.93a and 4.94a show the mesh of the 10 mm wide (geometry A) and 30 mm wide (geometry E) FE models, respectively.

A longitudinal displacement (x-direction) of −0.10 mm was applied to the nodes on the top end, leaving the displacement in the transverse direction free in both ends; following Catalanotti et al. [187], it is assumed that the contact between the specimen and the loading system is frictionless. The remaining degrees of freedom in the top and bottom ends were fixed.

The individual plies of the composite lay-up were modelled using a layerwise approach, explicitly defining each lamina, and respective ply orientation, by one integration point through the thickness of the plane stress elements. Each ply was assumed orthotropic and linear-elastic. The elastic properties of T700GC/M21 (table 4.1) were used.

As demonstrated in section 4.5.1 and discussed in section 4.5.4, despite the assumptions regarding the adoption of the properties of a material system with a different fibre sizing obtained from *prepregs* with a different areal weight (section 4.2), a remarkable correlation could be observed between the results of the FEA and the average strain measure

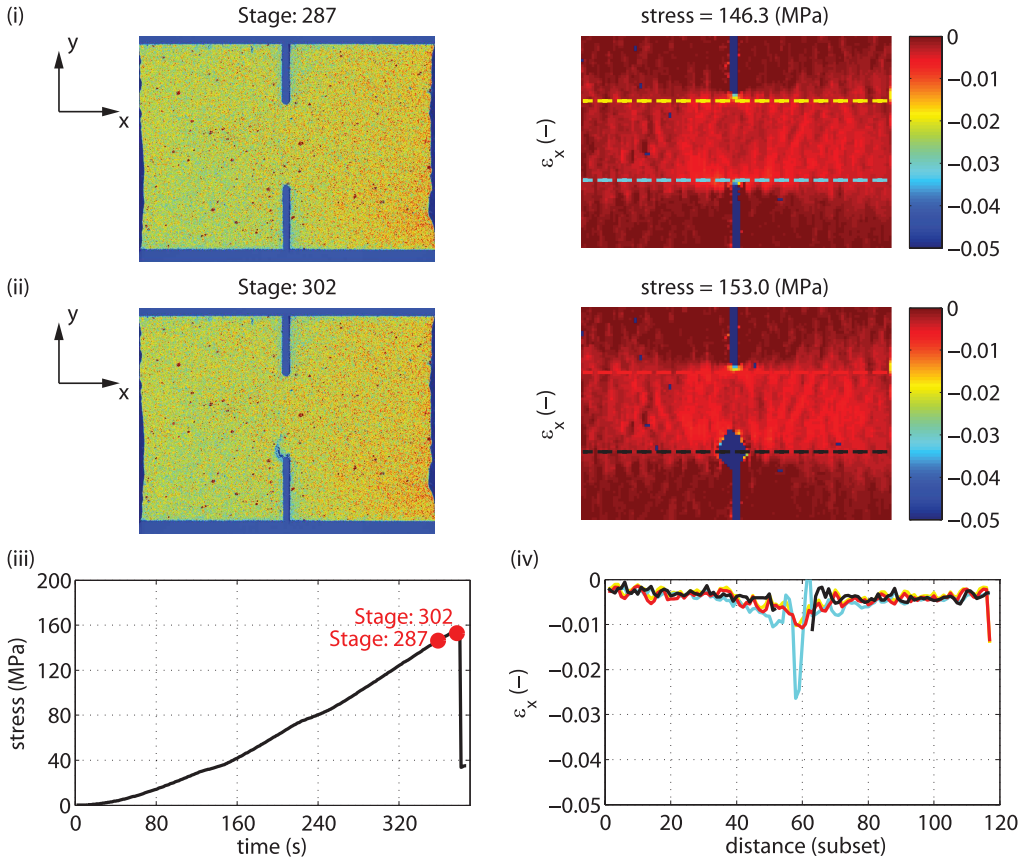

Fig. 4.85. Coloured distributions of grey levels (0–255) and longitudinal strain fields, ε_x, of a representative 25 mm wide 240 g/m^2 STF DENC test specimen (geometry D) obtained with the DIC technique at the stages of (i) onset of intralaminar compressive damage growth and (ii) before unstable propagation along the notched plane. (iii) Position of the stages in the remote stress-time relation. (v) Local longitudinal strain measured along two lines tangent to the tips of the edge notches over the length of the specimen. The reference DIC coordinate system is depicted in the figure, where the x-axis is aligned with the loading direction. The stresses are given in absolute values.

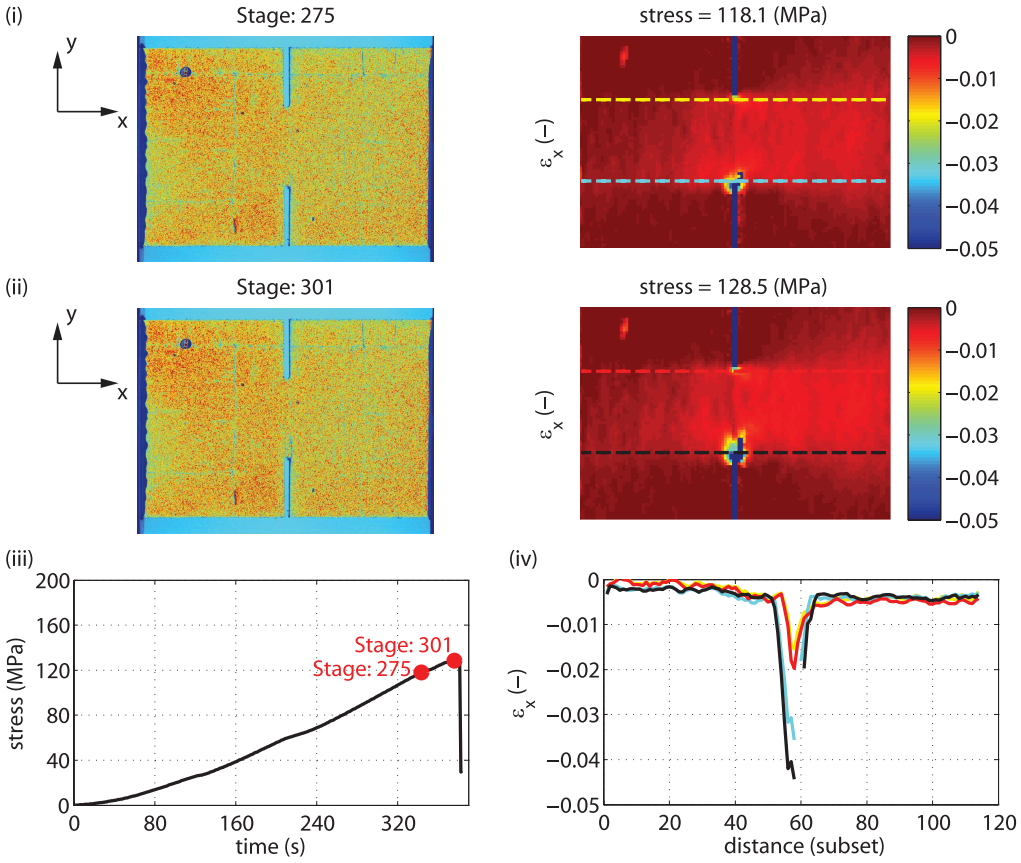

Fig. 4.86. Coloured distributions of grey levels (0–255) and longitudinal strain fields, ε_x, of a representative 30 mm wide 160 g/m^2 STF DENC test specimen (geometry E) obtained with the DIC technique at the stages of (i) onset of intralaminar compressive damage growth and (ii) before unstable propagation along the notched plane. (iii) Position of the stages in the remote stress-time relation. (v) Local longitudinal strain measured along two lines tangent to the tips of the edge notches over the length of the specimen. The reference DIC coordinate system is depicted in the figure, where the x-axis is aligned with the loading direction. The stresses are given in absolute values.

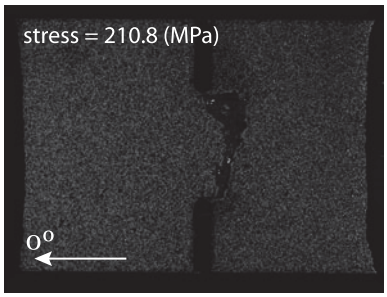

(a) Geometry A: 240 g/m^2 STF.

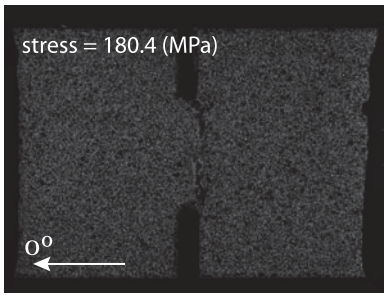

(b) Geometry A: 160 g/m^2 STF.

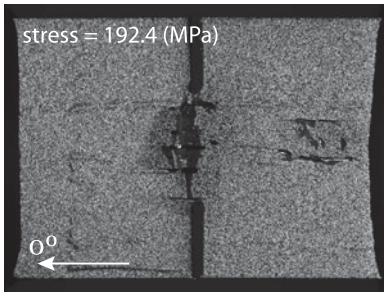

(c) Geometry B: 240 g/m^2 STF.

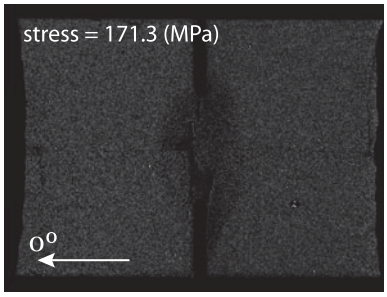

(d) Geometry B: 160 g/m^2 STF.

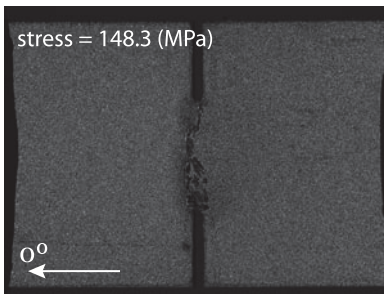

(e) Geometry C: 160 g/m^2 STF.

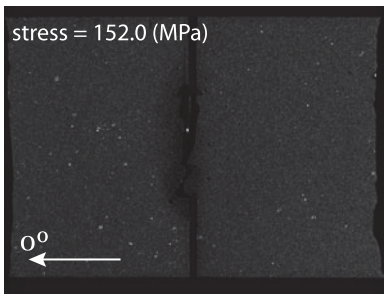

(f) Geometry D: 240 g/m^2 STF.

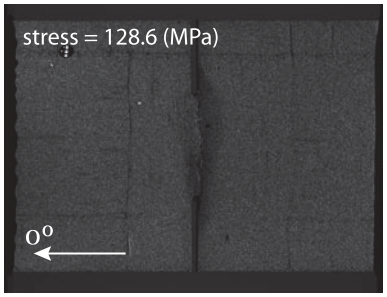

(g) Geometry E: 160 g/m^2 STF.

Fig. 4.87. Detailed pictures of the ligament section of representative DENC test specimens before ultimate failure (close to the peak load). Pictures captured with the DIC image grabbing system.

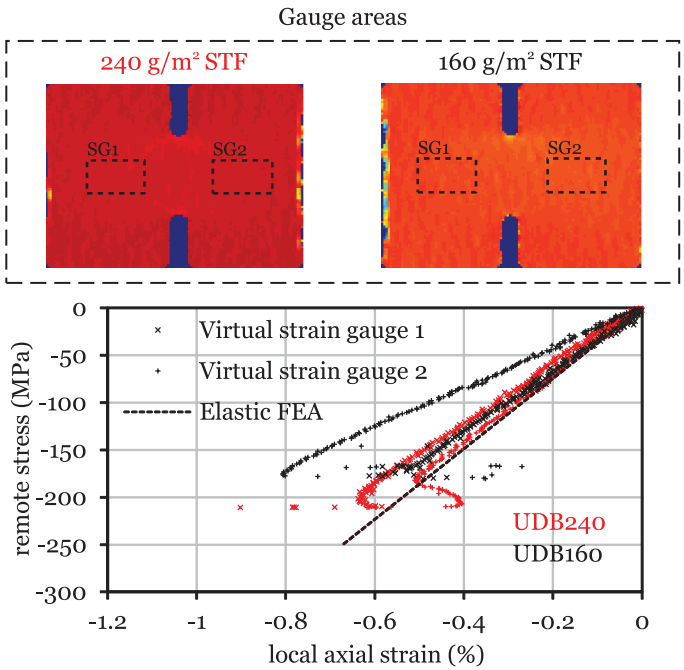

Fig. 4.88. Virtual strain gauge areas and remote stress-local axial strain relations for representative 10 mm wide DENC test specimens (geometry A). The loading direction is parallel to the horizontal axis of the specimens.

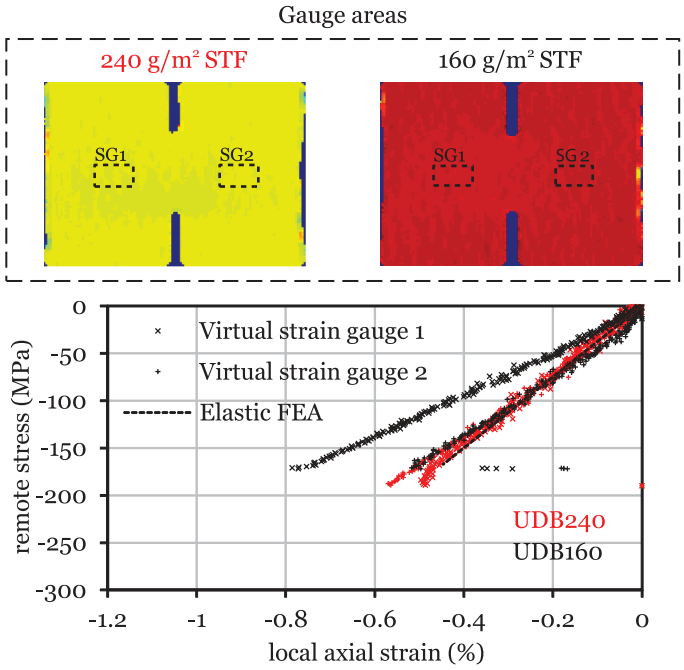

Fig. 4.89. Virtual strain gauge areas and remote stress-local axial strain relations for representative 15 mm wide DENC test specimens (geometry B). The loading direction is parallel to the horizontal axis of the specimens.

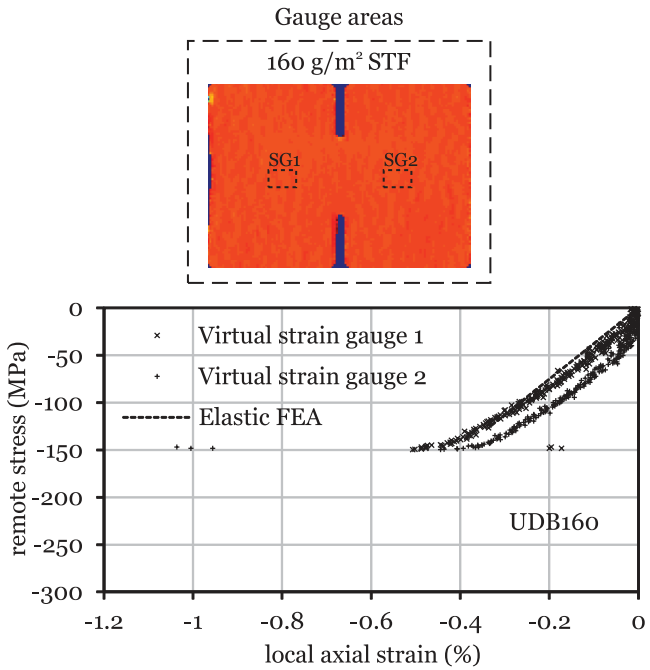

Fig. 4.90. Virtual strain gauge areas and remote stress-local axial strain relations for a representative 20 mm wide DENC test specimen (geometry C). The loading direction is parallel to the horizontal axis of the specimen.

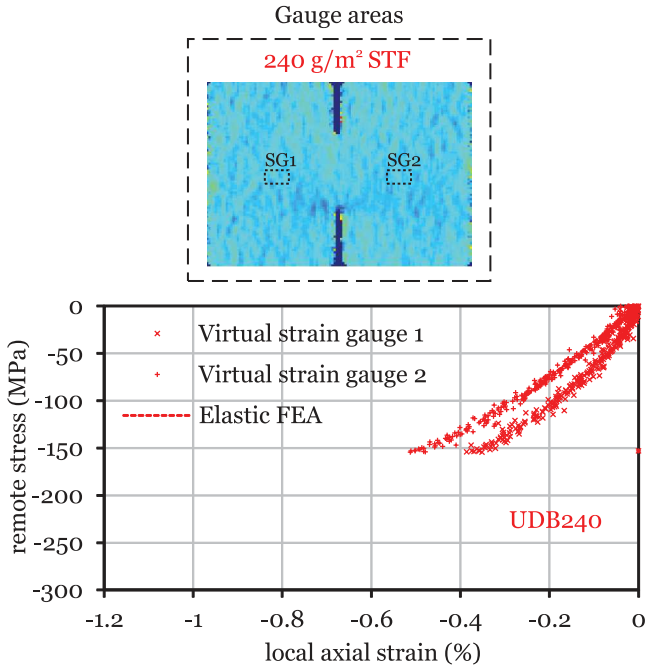

Fig. 4.91. Virtual strain gauge areas and remote stress-local axial strain relations for a representative 25 mm wide DENC test specimen (geometry D). The loading direction is parallel to the horizontal axis of the specimen.

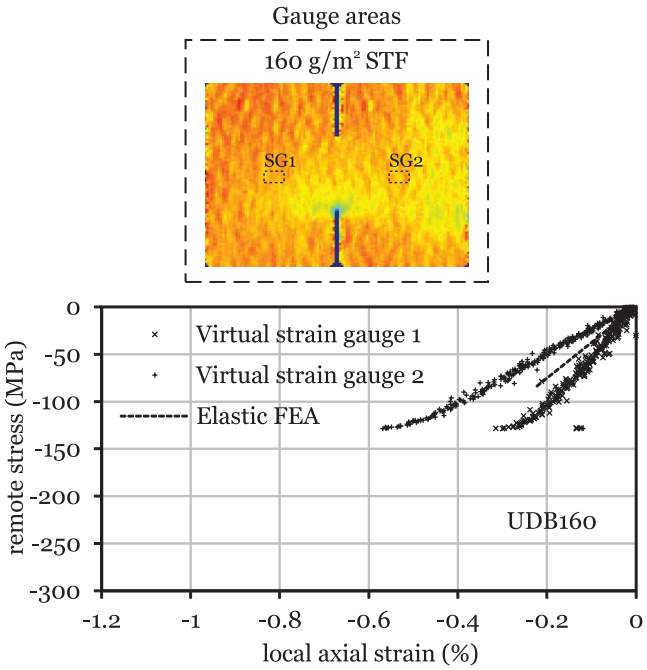

Fig. 4.92. Virtual strain gauge areas and remote stress-local axial strain relations for a representative 30 mm wide DENC test specimen (geometry E). The loading direction is parallel to the horizontal axis of the specimen.

obtained from the DIC data for the smooth STF coupons (figure 4.27), validating their use in the FEA. For reference, figures 4.93b and 4.94b show the longitudinal strain field of the outer ply of the 10 mm wide (geometry A) and 30 mm wide (geometry E) FE models, respectively.

The results of the FEA are plotted together with the DIC data in figures 4.88 to 4.92. In general, a good correlation between the FEA and the measured strains is obtained. Nevertheless, in some specimens, the results of one or both virtual strain gauges deviate slightly from the reference FEA results.

The uneven relation between the data of some virtual strain gauges and the FEA results can be attributed to the adopted load introduction setup, which was assumed frictionless in the FEA [187], even if it is recognised that friction can affect the overall response of the tested specimens despite the use of a lubricant between the specimens' ends and the loading supports [265]. The fracture response, though, is believed to be unaffected by the friction between the specimens' ends and the loading supports, as it invariably occurred at the notched plane, thus validating the obtained results. The discrepancies may also result from correlation problems in some regions of the specimens monitored by DIC, or from asymmetry in the position of the virtual strain gauges, namely in the larger specimens, whose relative dimensions of the averaging areas with respect to the specimens dimensions can be small, and consequently more susceptible to variations. This can result from the non-uniform strain distribution (e.g. figures 4.93b and 4.94b), but also from local effects, such as strain oscillations, which gain additional importance when the averaging area is relatively small (e.g. figure 4.92).

Figures 4.88 to 4.92 confirm that both STFs exhibit a very similar compressive notched response. For each geometry, not only the ultimate remote stress (figures 4.70 to 4.74), but also the failure mode (figures 4.75 to 4.79) and fracture behaviour (figures 4.80 to 4.86 and 4.88 to 4.92) are similar.

Table 4.15 and figure 4.95 show, respectively, the average results for the ultimate remote stress of the tested DENC specimens and corresponding coefficients of variation, and the mean ultimate remote stress as a function of the initial edge notch length, which is proportional to the specimen's size (geometrically similar specimens). As expected, as the specimen's size increases, the mean ultimate remote stress of both STFs shows a decreasing trend. This means that the proposed specimen configurations have positive geometry, a requirement for the determination of the $\mathcal{R}$-curve using the size effect law.

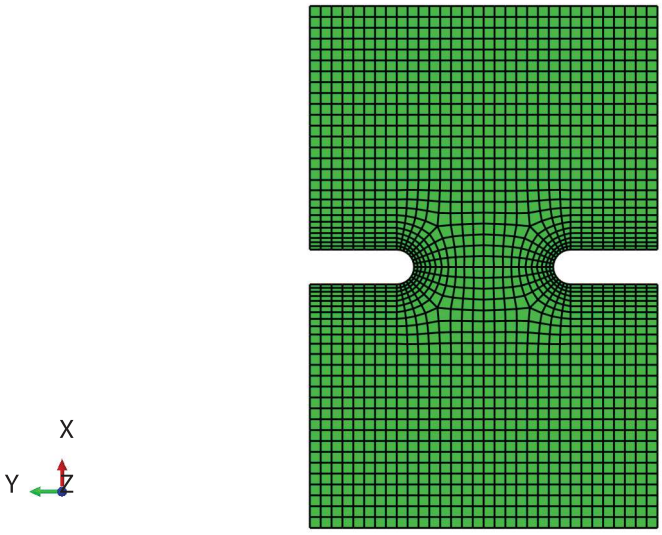

(a) FE mesh.

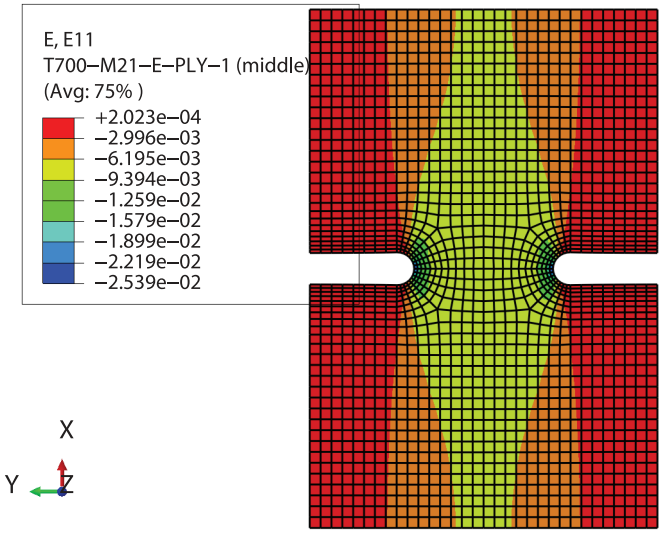

(b) Longitudinal strain field of the outer ply.

Fig. 4.93. Mesh detail of the FE model of a 10 mm wide DENC specimen (geometry A) and longitudinal strain field of the outer ply.

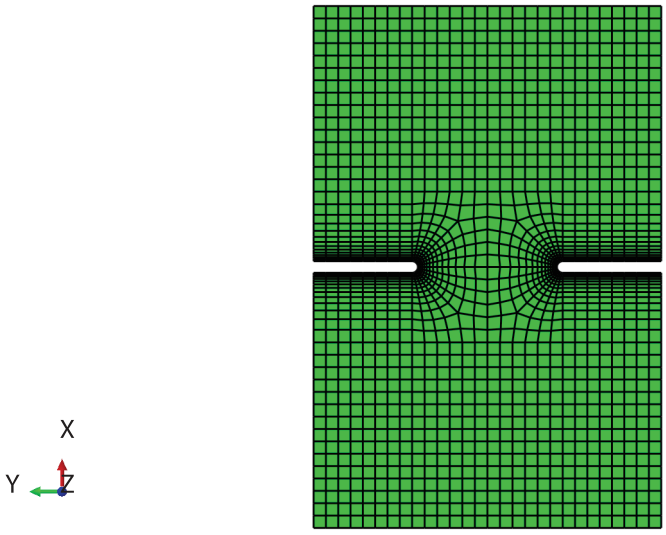

(a) FE mesh.

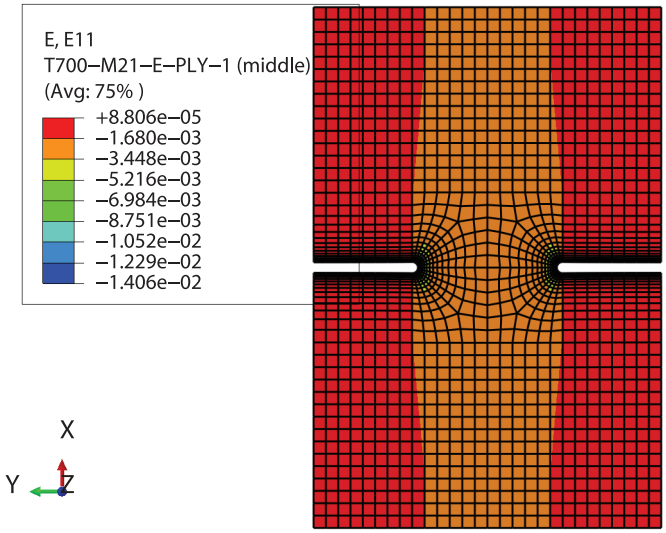

(b) Longitudinal strain field of the outer ply.

Fig. 4.94. Mesh detail of the FE model of a 30 mm wide DENC specimen (geometry E) and longitudinal strain field of the outer ply.

Table 4.15
Absolute values of the mean ultimate remote stress ($\bar{\sigma}^{\infty}$) and coefficients of variation (C.V.) of the DENC tests.

Results	Geometry ID				
	A	B	C	D	E
240 g/m^2 STF					
No. specimens	7	7	2	6	6
$\bar{\sigma}^{\infty}$ (MPa)	182	176	157	157	146
C.V. (%)	11.1	9.7	5.8	5.1	4.6
160 g/m^2 STF					
No. specimens	4	7	6	6	7
$\bar{\sigma}^{\infty}$ (MPa)	173	165	154	154	143
C.V. (%)	7.3	8.1	4.5	3.0	5.5

Interestingly, the compressive notched strengths os the smallest specimens of the 240 g/m^2 STF are slightly higher than for the 160 g/m^2 STF. However, as the size of the specimens increases, their notched strengths tend to the same values.

The experimental data of both STFs can now be fitted by one of the size effect law regressions proposed in Ref. [209]. The regression that best fit the DENC test results is the linear regression II (equation (4.18)), whose fitting parameters ($\acute{A}$ and $\acute{C}$) are given in table 4.16. Figure 4.96 shows the experimental results and the best fitting for the size effect laws of the plain weave STFs in compression.

Using the fitting parameters shown in table 4.16, it is now possible to calculate the length of the FPZ, l_{fpz}, and the steady-state value of the fracture toughness, $\mathcal{R}_{ss}$, in compression of the plain weave STFs (equations (4.19) and (4.20), respectively). Table 4.17 shows the values of l_{fpz} and $\mathcal{R}_{ss}$ obtained for both laminates.

Figure 4.97 shows the $\mathcal{R}$-curves of the STFs obtained as the envelopes of the crack driving force curves calculated using the size effect laws of figure 4.96. To simplify the implementation of the $\mathcal{R}$-curve in numerical or analytical models, following Catalanotti et al. [65], equation (4.21) is used to fit the $\mathcal{R}$-curves of figure 4.97. The parameters that best fit the $\mathcal{R}$-curves of the 240 g/m^2 and 160 g/m^2 STFs are given in table 4.17, which were obtained using a nonlinear least squares method with a Trust-Region algorithm available in the commercial software Matlab [278]. Figure 4.98 shows the $\mathcal{R}$-curves and the corresponding fitting curves for both STFs. As in section 4.5.4, the fitting formulae agree very well with the analytical envelopes.

Figure 4.99 shows a comparison of the $\mathcal{R}$-curves of both laminates. Unexpectedly, the 160 g/m^2 STF is characterised, respectively, by a length of the FPZ and a steady-state value of the fracture toughness 42.9% larger and 16.2% higher than the 240 g/m^2 STF, despite the very similar notched response depicted, for instance, in figure 4.95. These results should, therefore, be treated with caution.

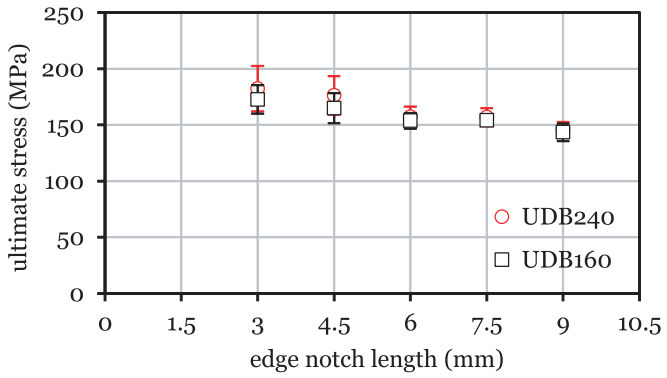

Fig. 4.95. Absolute values of the mean ultimate remote stress as a function of the initial edge notch length of the DENC tests.

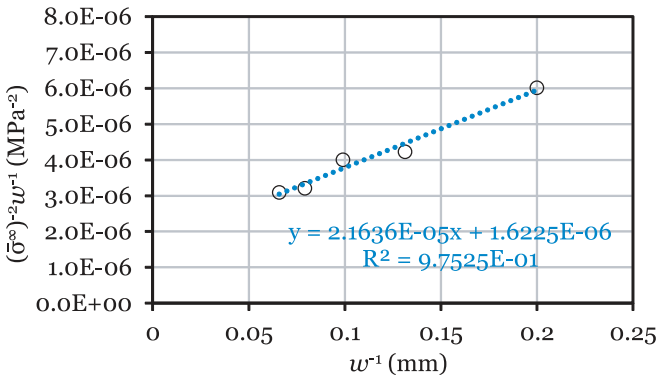

(a) 240 g/m^2 STF: linear regression II.

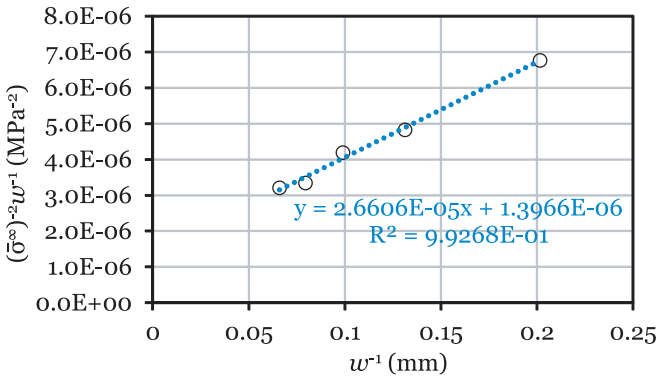

(b) 160 g/m^2 STF: linear regression II.

Fig. 4.96. Experimental results and best fitting for the compressive size effect laws of the plain weave STFs.

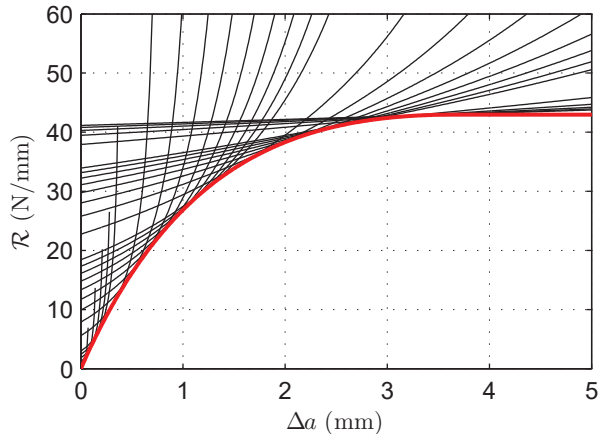

(a) 240 g/m^2 STF.

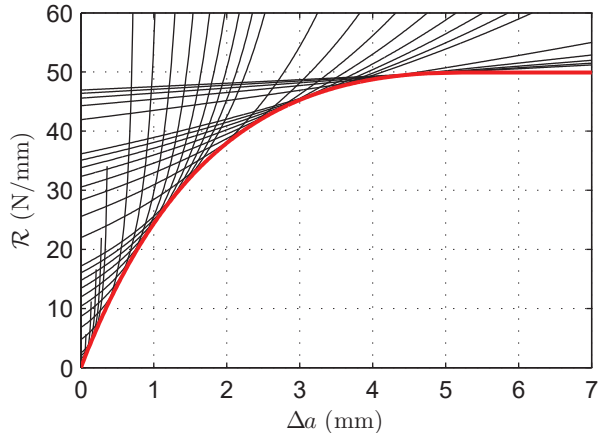

(b) 160 g/m^2 STF.

Fig. 4.97. Crack driving force curves and resulting $\mathcal{R}$-curves of the plain weave STFs for mode I longitudinal intralaminar compressive fracture.

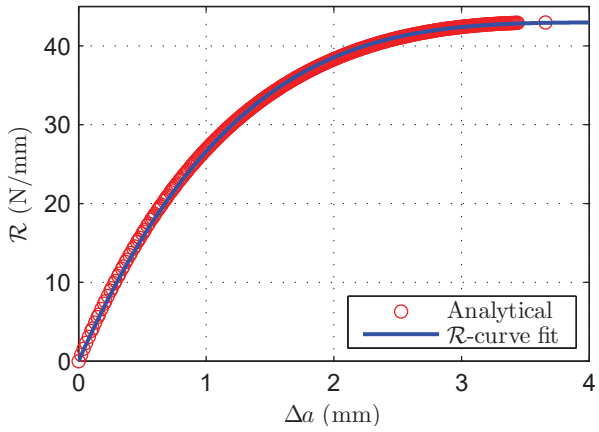

(a) 240 g/m^2 STF.

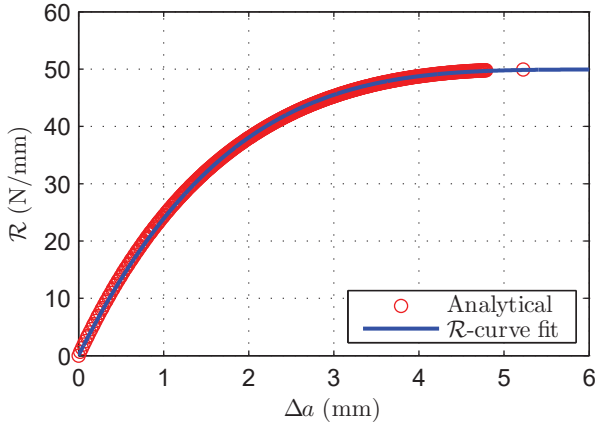

(b) 160 g/m^2 STF.

Fig. 4.98. Analytical and fitted compressive $\mathcal{R}$-curves of the plain weave STFs.

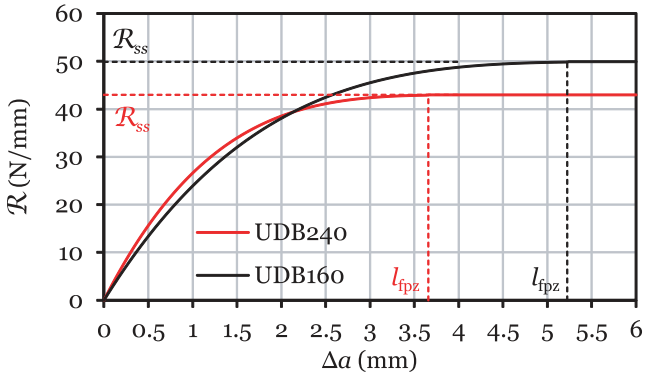

Fig. 4.99. Comparison of the $\mathcal{R}$-curves for mode I longitudinal intralaminar compressive fracture of the low-grade 240 g/m^2 and thin-ply 160 g/m^2 plain weave STFs.

Table 4.16
Fitting regressions and parameters for the compressive size effect laws of the plain weave STFs.

STF configuration	Regression fit [209]	Fitting parameters
240 g/m^2 STF	Linear regression II	$\acute{A}$ = 2.1636E – 05 MPa^{-2} mm^{-1}
		$\acute{C}$ = 1.6225E – 06 MPa^{-2}
160 g/m^2 STF	Linear regression II	$\acute{A}$ = 2.6606E – 05 MPa^{-2} mm^{-1}
		$\acute{C}$ = 1.3966E – 06 MPa^{-2}

Table 4.17
Parameters of the $\mathcal{R}$-curves and fitting formulae of the plain weave STFs in compression.

STF configuration	l_{fpz} (mm)	$\mathcal{R}_{ss}$ (N/mm)	ζ (mm^{-1})	η (-)
240 g/m^2 STF	3.66	43.0	0.2276	3.690
160 g/m^2 STF	5.23	49.9	0.3505	3.607

As discussed before, figure 4.95 shows that the compressive notched strengths obtained for the smaller specimens of the 240 g/m^2 STF are slightly higher than for the 160 g/m^2 STF. However, as the size of the specimens increase, the compressive notched strengths tend to the same values. This is translated in a steeper strength reduction, or steeper size effect law (figure 4.96), which conducts to the determination of a lower steady-state value of the fracture toughness and a smaller FPZ for the 240 g/m^2 STF.

According to these results, for even larger specimens, the compressive notched strength of the 240 g/m^2 STF would keep decreasing faster than the 160 g/m^2 STF, with the latter providing higher compressive notched strengths. However, if the compressive notched strengths of the STFs is to become nearly the same as the size of the specimens keeps increasing, as figure 4.95 suggests, then a more similar size effect law would be expected. It is therefore suggested that characterisation of the compressive notched response of the STFs studied in the present work must rely on testing of larger geometrically-similar DENC specimens.

4.5.6. Laminate tensile unnotched strength test results

Two multidirectional laminates, *DTO240* and *DTO160* (tables 4.2 and 4.3), produced, respectively, from the low-grade 240 g/m^2 and thin-ply 160 g/m^2 plain weave STFs based on a damage tolerance optimised baseline laminate for aeronautical applications, were tested to address the effect of ply grade on structural laminates made of textile composites. The laminate tensile unnotched strengths were obtained testing to failure 5 smooth specimens of each laminate. Figure 4.100 shows the remote stress-displacement curves of both laminates, where the remote stress, σ^{∞}, was calculated dividing the applied load, measured by the load cell, by the cross-section area, and the cross-head displacement was measured directly by the testing machine's LVDT.

Figure 4.100 shows that the thin-ply laminate *DTO160* is characterised by an approximately linear remote stress-displacement relation up to ultimate failure. The low-grade laminate *DTO240*, on the other hand, shows a minor nonlinear behaviour close the ultimate remote stress, resulting in a slightly lower unnotched strength compared with laminate *DTO160*.

In the low-grade laminate *DTO240*, the nonlinearities close to the peak remote stress, in some cases with small load drops, apparently occurred due to the development of subcritical damage, which was audible at applied remote stresses as low as 63% of the ultimate remote stress, but it may also have been originated by plastic deformation of the off-axis STFs. In the thin-ply laminate *DTO160*, internal damage growth was not audible at applied remote stresses below 78% of the maximum applied remote stress.

At failure, both laminates exhibited a catastrophic failure mode (figure 4.100), preceded by an intense noise produced by internal longitudinal fracture just before the specimens fail. This effect was particularly evident in laminate *DTO240*, since severe damage propagation was audible for applied remote stresses above 92% of the ultimate remote stress.

The extent of damage growth prior to ultimate failure becomes readily apparent observing the unnotched coupons after

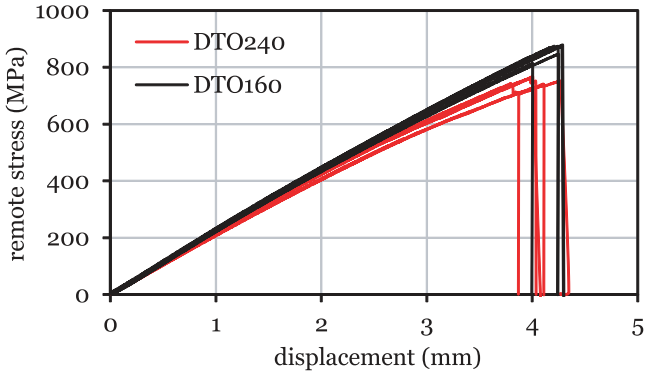

Fig. 4.100. Remote stress-displacement curves of the laminate unnotched tension tests.

testing to failure (figure 4.101). Both laminates exhibit a fibre-dominated failure mode. However, laminate *DTO240* is characterised by extensive pull-out, with transverse and longitudinal split cracking along the transverse and longitudinal spread/tow yarns, respectively (figure 4.101a). A diffuse failure region is observed, without a clear fracture plane. The thin-ply laminate *DTO160*, as expected, show a brittler net-section failure mode, with the fracture plane perpendicular to the loading direction (figure 4.101b). Matrix damage and fibre-matrix splitting was effectively preclude when reducing the yarns grade from 240 g/m^2 to 160 g/m^2, resulting in an improved unnotched response (see figure 4.100).

Figure 4.101b shows that some specimens of the thin-ply laminate *DTO160* failed in multiple places in the gauge section, in some cases close to the clamping grips. This is attributed to the brittle failure mode exhibited by this laminate. Since no damage accumulation has occurred before ultimate failure, a quick, very energetic fracture process takes place at the moment of failure, which may induce fracture on other regions of the highly stressed material. Compression damage has also occurred in the specimen after tensile failure, when the specimen recovers from the very high elastic deformation. In laminate *DTO240*, though, since pre-failure damage accumulation has occurred, ultimate failure takes place on the region with the highest degree of degraded material (figure 4.101a).

As stressed in section 4.5.1, even though it is recognised that clamping acts as a stress concentrator, which may promote premature failure close to the clamped regions, special care in utilising adequate sandpaper inside the bolted clamping system and an adequate clamping torque helps minimising such risks. Since the deviations between the results of specimens of the same laminate are within an acceptable range (see figure 4.24), it is considered that all results presented herein are valid experimental data.

In order to assess the occurrence and extent of early damage, the DIC technique was used to monitor transverse cracking formation through analysis of the longitudinal strain field of the outer STF layer of representative specimens of both laminates. Figure 4.102 shows the surface longitudinal strain field at the stage prior to ultimate failure. The local longitudinal strain measured along two lines, parallel to the loading direction, near the free edges, are also presented. For reference, figure 4.102 also shows the corresponding coloured distribution of grey levels.

As can be observed in figure 4.102, prior to ultimate failure, transverse matrix cracking or fibre-matrix splitting has not occurred in laminate *DTO160*. Two small discontinuities are observed in the gauge section, but it was not clear if they were caused by internal damage growth, resulting in a local split, or just due to local pilling of the white paint caused by the high applied strain. Nevertheless, a reasonably smooth strain distribution is observed, even at the free edges, similarly to what was observed in figure 4.26 (ii) for the plain weave UD specimen.

In laminate *DTO240*, extensive free-edge surface transverse cracking and longitudinal splitting along the 0° spread-tow yarns tangent to the free edges can be observed (figure 4.102 (i)). As discussed in section 4.5.1 (figures4.25 and 4.26), the 240 g/m^2 STF is more susceptible to fibre-matrix splitting than the thinner 160 g/m^2 STF, not only along the longitudinal spread-tow yarns, but also along the transverse yarns. Figure 4.102 also shows that, in laminate *DTO240*, not only the extent of subcritical damage before ultimate failure is remarkable, but it also occurs and propagates at applied remote

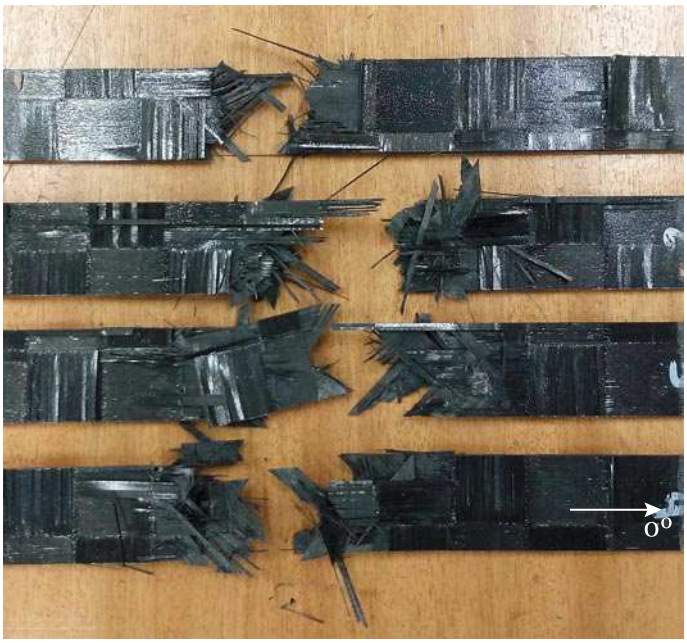

(a) Low-grade laminate *DTO240*.

(b) Thin-ply laminate *DTO160*.

Fig. 4.101. Representative unnotched tension test specimens after testing.

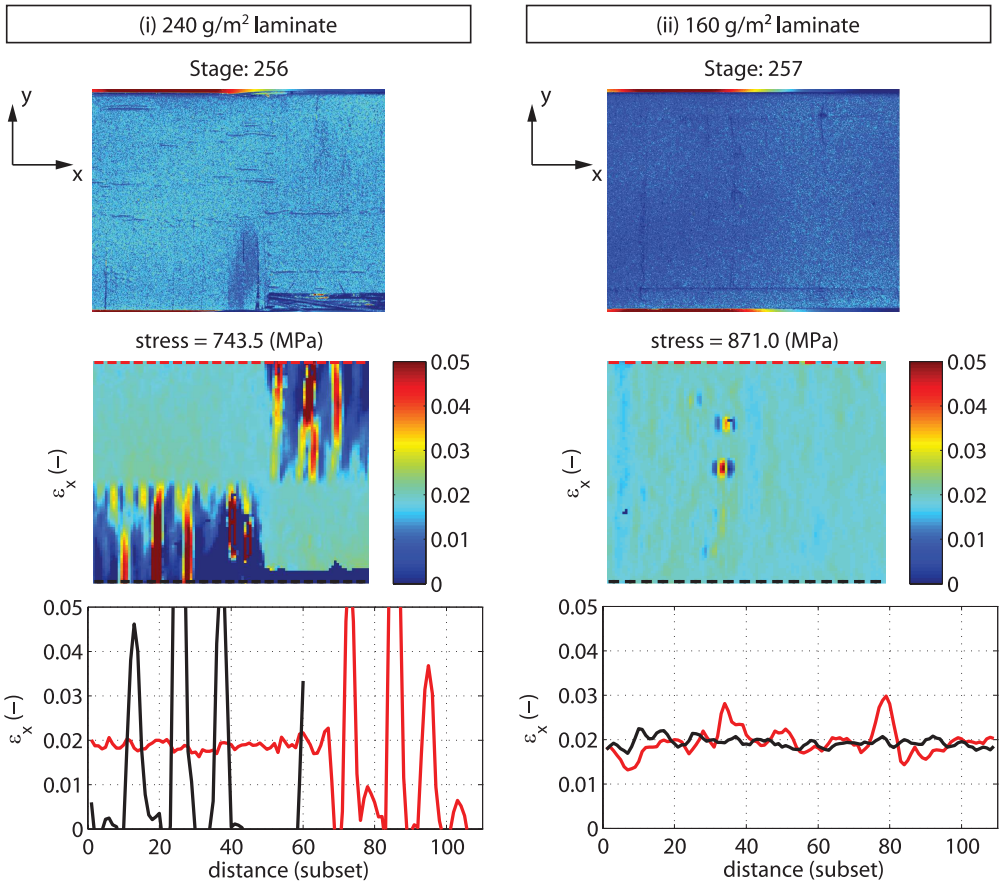

Fig. 4.102. Coloured distributions of grey levels (0–255), longitudinal strain fields, ε_x, and local longitudinal strain along the edges of the outer STF layer of representative unnotched tension test specimens of laminates (i) *DTO240* and (ii) *DTO160* obtained with the DIC technique at the stage prior to ultimate failure. The reference DIC coordinate system is depicted in the figures, where the x-axis is aligned with the loading direction.

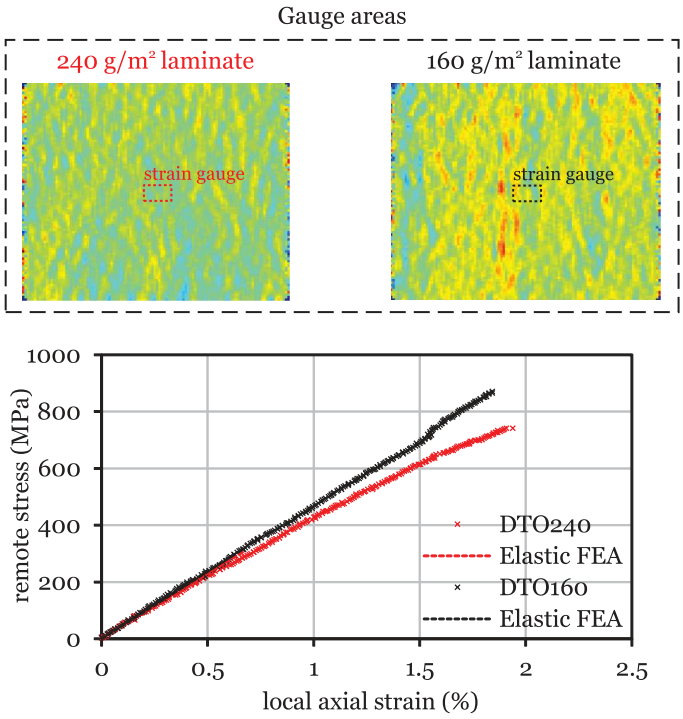

Fig. 4.103. Virtual strain gauge areas and remote stress-strain relations of representative unnotched tension test specimens. The loading direction is parallel to the horizontal axis of the specimens.

stresses considerably below the maximum stress. By precluding such damage mechanisms, laminate *DTO160* is able to sustain reasonably higher applied loads. Interestingly, gauge section delamination has not been observed in the tested laminates (figure 4.101).

A virtual strain gauge computed from the DIC measurements by averaging the longitudinal strains in an area with 3.18 mm in length by 1.78 mm in width, equivalent to the gauge area of a physical strain gauge, was used to obtain the remote stress-strain relations of representative unnotched tension test specimens [121, 122, 182, 187]. Figure 4.103 shows, for both laminates, the location of the gauge areas, drawn on the longitudinal strain field obtained with DIC at an applied remote stress equal to 20% of the ultimate remote stress, and the corresponding remote stress-strain relations.

A linear-elastic FEA was performed to validate the implementation of the proposed virtual strain gauge approach, employing the same averaging procedure, to compare with the obtained test data. The FE models were created with the commercial FE software Abaqus 6.12-1 [275] using a structured mesh of 1 mm long square CPS4R elements. Only the gauge section was modelled.

In order to replicate the load and boundary conditions of the actual test setup, a longitudinal displacement (x-direction) of 1.00 mm was applied to the nodes on the top end, while fixing their remaining degrees of freedom. The nodes in the bottom end were all fixed (encastre boundary condition).

Each STF layer was represented by a [0/90] cross-ply sublaminate. The individual plies were modelled using a layerwise approach, explicitly defining each lamina, and respective ply orientation, by one integration point through the thickness of the CPS4R elements.

The constitutive behaviour of each ply was defined by an orthotropic linear-elastic material model. Assuming that fibre sizing, material grade and reinforcement configuration does not affect the elastic properties of the material system studied in the present work (as demonstrated in section 4.5.1), the elastic properties of T700GC/M21 (table 4.1) were used in the material definition.

Table 4.18
Laminate tensile unnotched strength (X_T^L) test results and respective coefficients of variation (C.V.).

Results	240 g/m^2 laminate	160 g/m^2 laminate
No. specimens	5	5
X_T^L (MPa)	753	857
C.V. (%)	1.3	2.9

The results of the FEA are plotted together with the DIC data in figure 4.103. The correlation is remarkable, is spite of the assumptions regarding the material model. These results also validate the proposed virtual strain gauge approach.

Figure 4.103 also shows that, as discussed before, whereas the thin-ply laminate *DTO160* is characterised by an approximately linear remote stress-strain relation up to final failure, a minor nonlinear behaviour is observed for the low-grade laminate *DTO240*. The fact that a nonlinear stress-strain relation is obtained from a local measurement demonstrates that the captured nonlinearity is due to the material behaviour and not to external factors (such as problems in the loading setup). As explained earlier, this nonlinear behaviour can be attributed to the development of subcritical damage, as well as to plastic deformation of the off-axis STF layers.

Table 4.18 shows the mean laminate tensile unnotched strengths, X_T^L, of both laminates, and respective coefficients of variation. As expected, and unlike the results for the UD unnotched coupons, the thin-ply laminate *DTO160* has a tensile unnotched strength 13.9% higher than laminate *DTO240*. This improved unnotched response, already observed in previous work [53, 58, 122, 171], is attributed to the damage suppression capability of laminates made of thinner reinforcements, delaying ultimate failure to values closer to the strength of the reinforcing layers aligned with the loading direction.

The apparent superior longitudinal strength of the low-grade 240 g/m^2 STF reported in section 4.5.1 did not translate into a superior laminate strength. If, in the former, subcritical damage growth apparently resulted in relaxation of the stress applied to the longitudinal yarns, which delayed ultimate failure, in the latter, damage of the spread-tow yarns adjacent to those aligned with the loading direction caused local stress redistributions that promoted early failure of the longitudinal yarns in regions of high stress concentration due to the presence of transverse and off-axis cracks and localised delaminations.

4.5.7. Laminate compressive unnotched strength test results

The compressive unnotched strength of two multidirectional laminates, *DTO240* and *DTO160* (tables 4.2 and 4.3), produced, respectively, from the low-grade 240 g/m^2 and thin-ply 160 g/m^2 plain weave STFs, were determined testing 3 smooth coupons until failure. Figure 4.104 shows the remote stress-displacement curves of both laminates. The remote stress, σ^∞, of each test was calculated dividing the applied load measured by the load cell by the specimen's cross-section area. The cross-head displacement was measured directly by the testing machine's LVDT.

Due to adjustments in the end-loading anti-buckling setup in the early stages of loading, a nonlinear remote stress-displacement relation is observed in the beginning of the tests (figure 4.104). The range of the adjusting stage, which varies considerably between specimens, is not higher than approximately 20% of the maximum applied load. Before failure, small load drops can be observed in some specimens of both laminates, with a negligible effect on the stiffness of the tested specimens. Final failure is sudden and catastrophic, characterised by a big load drop.

The load drops in the remote stress-displacement curves (figure 4.104) can be attributed to the development of compressive damage before ultimate failure. This was more evident in the thin-ply laminate *DTO160*, since noise due to internal damage growth was audible at applied remote stresses above 80% of the ultimate remote stress.

After testing, all specimens exhibited a net-section failure mode (figure 4.105). Failure of both laminates is characterised by a complex combination of damage mechanisms, including fibre kinking, wedge transverse fracture, delamination and surface fibre/matrix splitting.

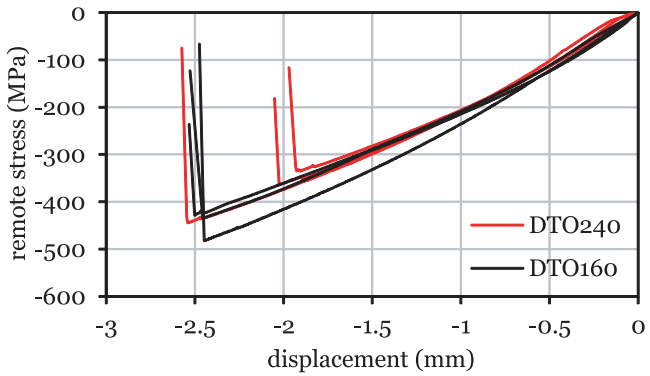

Fig. 4.104. Remote stress-displacement curves of the laminate unnotched compression tests.

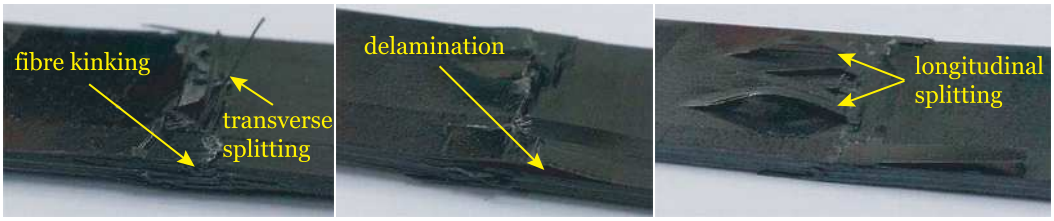

(a) Low-grade laminate *DTO240*.

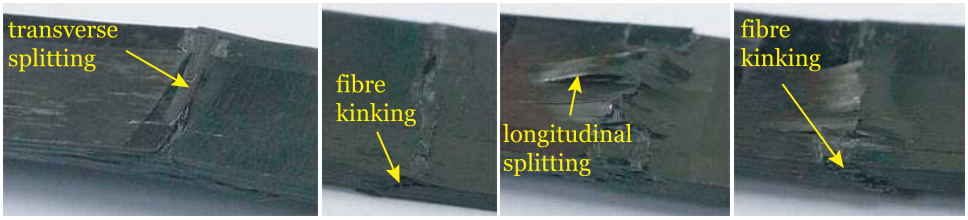

(b) Thin-ply laminate*DTO160*.

Fig. 4.105. Representative laminate unnotched compression test specimens after testing.

The thin-ply laminate *DTO160* (figure 4.105b) exhibits a slightly brittler failure mode, with a more clear through-the-thickness fracture plane, inclined with respect to the mid-plane of the specimen. Delamination between STF layers is absent. In laminate *DTO240* (figure 4.105b, on the other hand, a more diffuse fracture region is observed, including free-edge delamination along the outer STF layers. Interestingly, upon final failure, some specimens of both laminates exhibited longitudinal split cracking caused by buckling of the outer STF layers. Nevertheless, this failure mechanism apparently did not have any effect on the final response of the tested specimens.

Table 4.19 shows the mean laminate compressive unnotched strengths, X_C^L, of laminates *DTO240* and *DTO160*, and respective coefficients of variation. Laminate *DTO160* exhibits a compressive unnotched strength 17.7% higher than laminate *DTO240*, which can be attributed to the uniformity of the thinner reinforcement architecture of the 160 g/m^2 STFs of laminate *DTO160*. In fact, as discussed in section 4.5.2, the thinner 160 g/m^2 STF exhibited higher compressive strength than the low-grade 240 g/m^2 STF, as the better uniformity of the spread-tow yarns, lower fibre waviness and smaller crimp angles of the former delay micro-instabilities in the fibre direction, allowing the longitudinal yarns to carry higher loads.

It is noted from figure 4.104 and from table 4.19 that the variation in the test results of laminate *DTO240* is atypically high. Since no problem was observed in the loading setup, and no uncharacteristic compressive response (figure 4.104) or failure mode (figure 4.105a) was detected on the specimens of laminate *DTO240*, the variation of the ultimate failure stress should also be attributed to the less uniform reinforcement configuration of laminate *DTO240*. In fact, when

Table 4.19
Laminate compressive unnotched strength (X_C^L) test results (absolute values) and respective coefficients of variation (C.V.).

Results	240 g/m^2 laminate	160 g/m^2 laminate
No. specimens	3	3
X_C^L (MPa)	381	448
C.V. (%)	12.1	5.4

a reinforcement is less uniform, the susceptibility to variations of its uniformity (fibre waviness and crimp angle) is expected to increase, resulting in higher variations of the mechanical response too. Hence, the lower uniformity of the structure of the low-grade STF apparently results not only on lower compressive strengths but also on higher variability of the respective results (the same trend was observed in section 4.5.2 for the compressive response of the STFs — see table 4.10). A similar effect of the uniformity of the microstructure on the compressive strength and on its variability has also been observed by Amacher et al. [37, 58] for UD tapes of different grades.

4.5.8. Laminate tensile centre-notched strength test results

Centre-notched coupons of laminates *DTO240* and *DTO160* were tested to failure in the present work. Tensile centre-notched tests were performed in 3 specimens of each laminate. Figure 4.106 shows the remote stress-displacement curves, where the remote stress, σ^{∞}, was calculated dividing the applied load, measured by the load cell, by the cross-section area, and the cross-head displacement was measured directly by the testing machine's LVDT.

All CNT specimens exhibit an approximately linear remote stress-displacement curve until ultimate failure (figure 4.106). Small load drops can be observed near the peak load, with no effect on the stiffness of the specimens. These small load drops can be attributed to damage growth from the notch tips before unstable catastrophic failure.

However, during the tests, internal damage growth was generally audible before the occurrence of the load drops in the remote stress-displacement relations. In laminate *DTO240*, noise due to internal damage growth was audible at applied remote stresses above approximately 370 MPa (78% of the ultimate remote stress), becoming stronger as the applied remote stress approached the maximum remote stress, above approximately 450 MPa (95% of the ultimate remote stress). In laminate *DTO160*, internal damage growth was audible at applied remote stresses above 390 MPa (or above 82% of the ultimate remote stress), becoming stronger above approximately 480 MPa (97% of the ultimate remote stress).

Figure 4.107 shows the notched plane of representative CNT specimens after testing. Both laminates exhibit a fibre-dominated pull-out failure mode. However, the low-grade laminate *DTO240* (figure 4.107a) exhibit a more diffuse failure zone. Some specimens do not exhibit a clear fracture plane, whereas others exhibit diffuse fracture predominantly along the −45° direction, including pull-out and delamination of large fibre bundles.

The failed specimens of the thin-ply laminate *DTO160* (figure 4.107b) exhibit fracture predominantly along the −45°

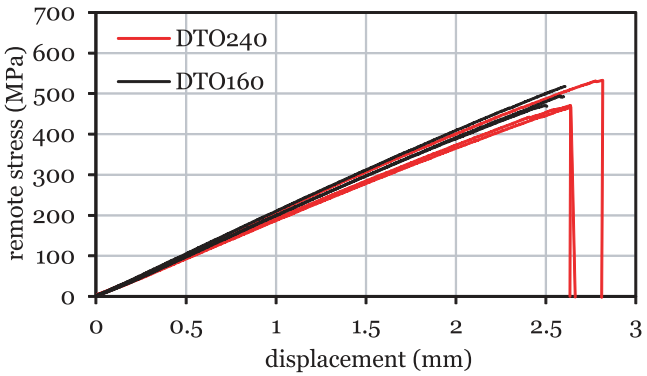

Fig. 4.106. Remote stress-displacement curves of the CNT tests.

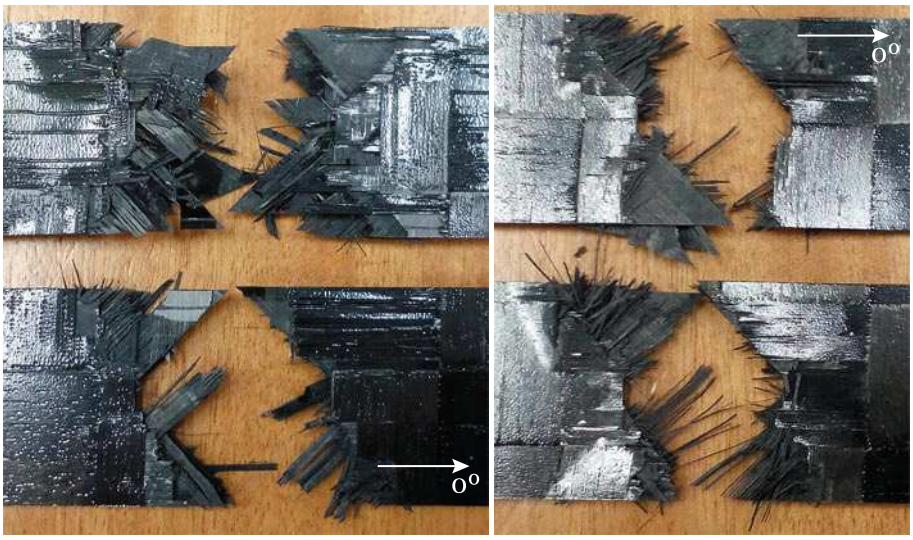

(a) Low-grade laminate *DTO240*. (b) Thin-ply laminate *DTO160*.

Fig. 4.107. Details of representative CNT test specimens after testing.

direction, with fibre bundle pull-out and delaminations with a triangular shape due to intralaminar fracture along the 45° direction of some off-axis STF layers. Longitudinal splitting of the 0° spread-tow yarns can be observed in the specimens of both laminates.

To understand the sequence and extent of damage before unstable intralaminar fracture and fibre bundle pull-out, the development of the damage process zone can be investigated analysing the longitudinal strain fields obtained from the DIC measurements of representative specimens of both laminates (figures 4.108 and 4.109). In laminate *DTO240* (figure 4.108), surface discrete intralaminar damage from the notch tips appears reasonably before the peak remote stress, but does not penetrate stably along the lateral ligament sections. Before unstable intralaminar fracture, surface transverse split cracks form in the 90° spread-tow yarns, while surface longitudinal splitting in the vicinity of the notch tips blunt the strain concentration. Close to the maximum applied remote stress (figures 4.108 (ii) and (iii)), a straight band in the strain field, bounded by the notch tips and parallel to the loading direction, indicates the occurrence of internal longitudinal split cracking tangent to the notch tips, which acts as a strong blunting mechanism, preventing intralaminar damage growth until catastrophic failure of the 0° spread-tow yarns.

In laminate *DTO160* (figure 4.109), surface discrete intralaminar damage from the notch tips starts close to the peak remote stress (figures 4.109 (i) and (iv)), and propagates quickly across the width, along the off-axis directions (figures 4.109 (ii), (iii) and (v)). Close to the peak remote stress (figures 4.109 (ii) and (iii)), a straight band in the strain field, bounded by the notch tips and parallel to the loading direction, indicates the occurrence of internal longitudinal split cracking tangent to the notch tips. However, it does not prevent the occurrence of discrete intralaminar damage growth, with catastrophic failure of the 0° spread-tow yarns occurring soon after the onset of intralaminar damage propagation from the notch tips.

To assess possible load asymmetries and the effects of strain concentration in the vicinity of the notch tips, remote stress-local axial strain relations were obtained with virtual strain gauges [121, 122, 182, 187], computed averaging the results from the DIC data in an area equivalent to the gauge area of physical strain gauges (figure 4.110). Gauge areas with 3.18 mm in length and 1.78 mm in width were used. Two virtual strain gauges (*SG1* and *SG2*) were placed at the tips of the central notch. The location of the gauge areas (*SG1* and *SG2*) are presented in figure 4.110, depicted over the longitudinal strain field obtained with DIC at an applied remote stress equal to 20% of the ultimate remote stress.

To validate the implementation of the virtual strain gauges in the vicinity of strain concentration sites, a linear-elastic

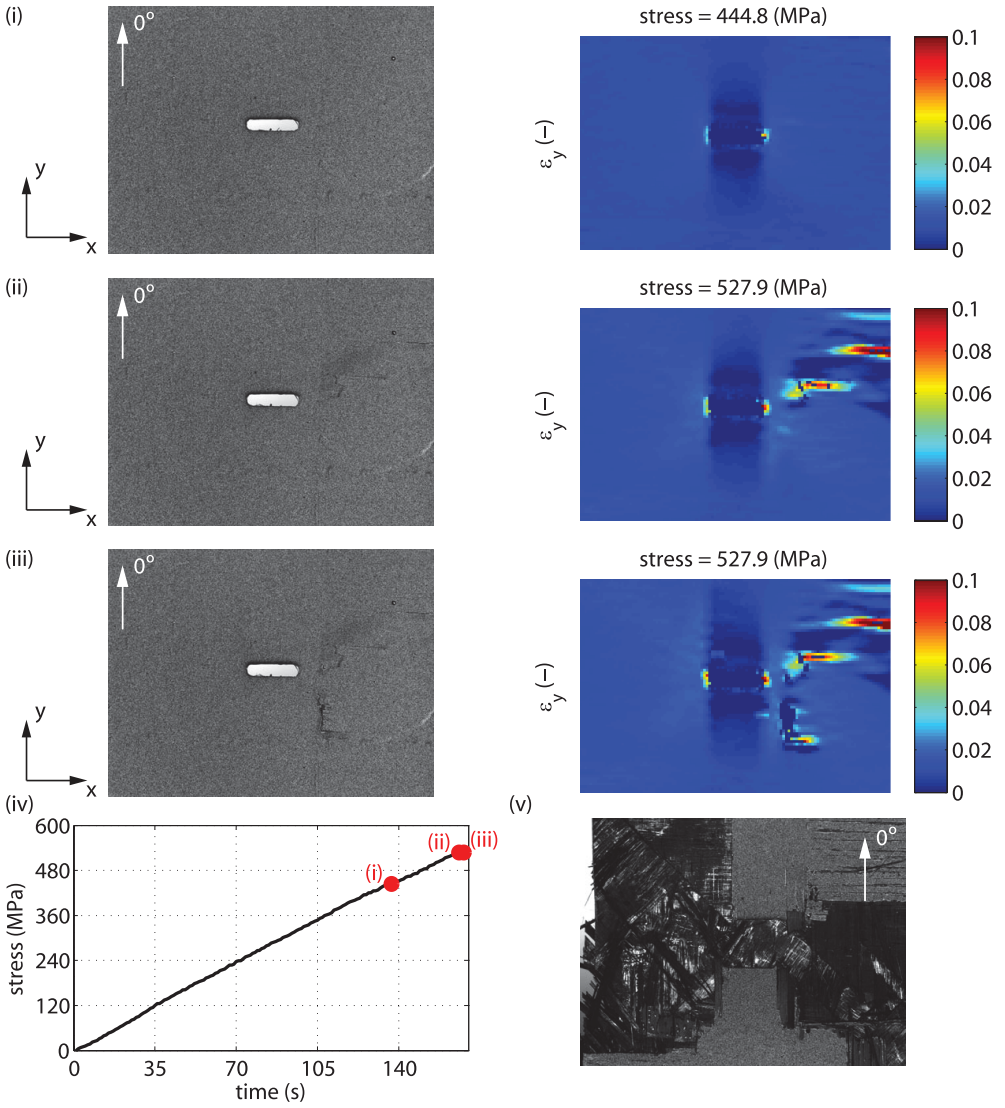

Fig. 4.108. Specimen's surface and longitudinal strain fields, ε_y, of a representative CNT test specimen of laminate *DTO240* obtained with the DIC system at the stages of (i) onset of intralaminar cracking, (ii) at the peak remote stress and (iii) before ultimate failure. (iv) Remote stress-time relation. (v) Specimen's surface after failure obtained with the DIC image grabbing setup. The reference DIC coordinate system is depicted in the figure, where the *y*-axis is aligned with the loading direction.

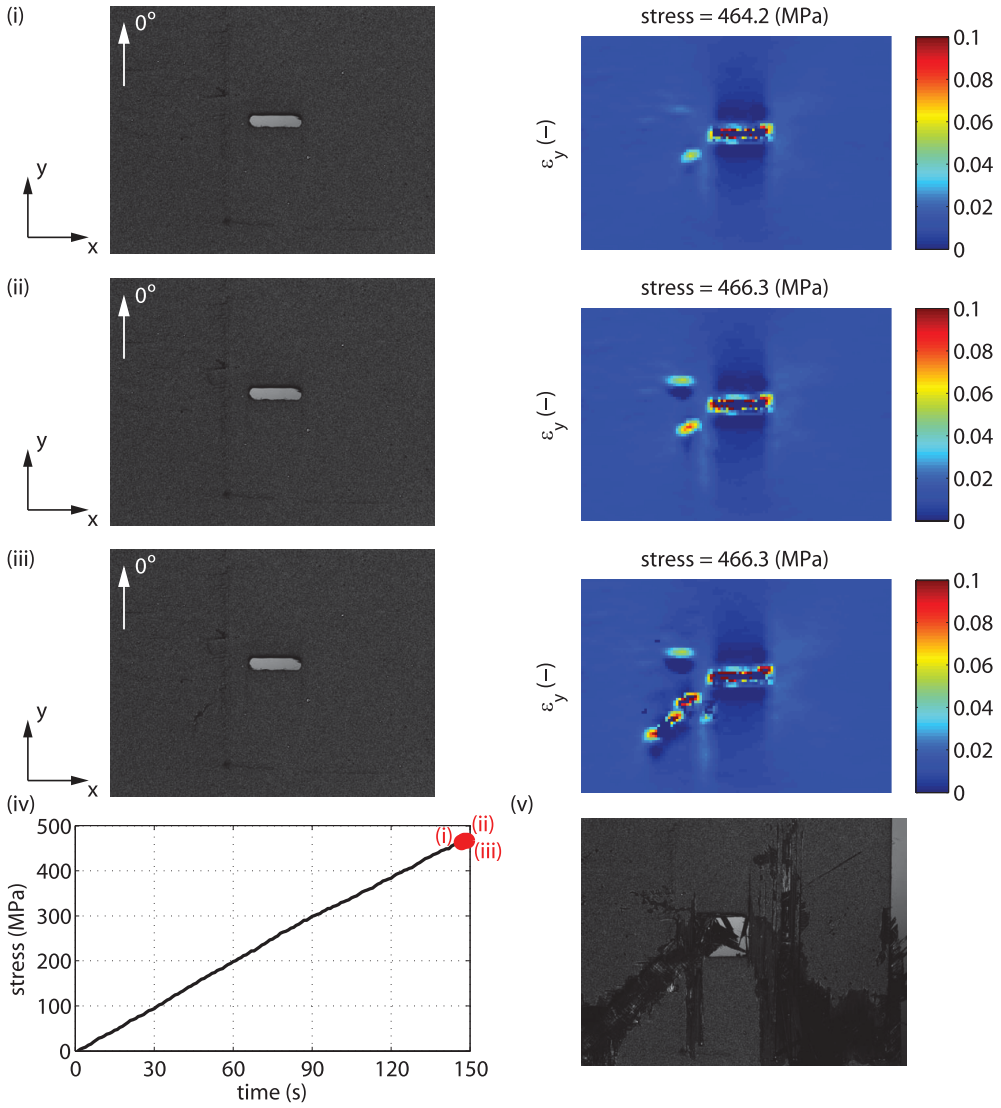

Fig. 4.109. Specimen's surface and longitudinal strain fields, ε_y, of a representative CNT test specimen of laminate *DTO160* obtained with the DIC system at the stages of (i) onset of intralaminar cracking, (ii) at the peak remote stress and (iii) before ultimate failure. (iv) Remote stress-time relation. (v) Specimen's surface after failure obtained with the DIC image grabbing setup. The reference DIC coordinate system is depicted in the figure, where the *y*-axis is aligned with the loading direction.

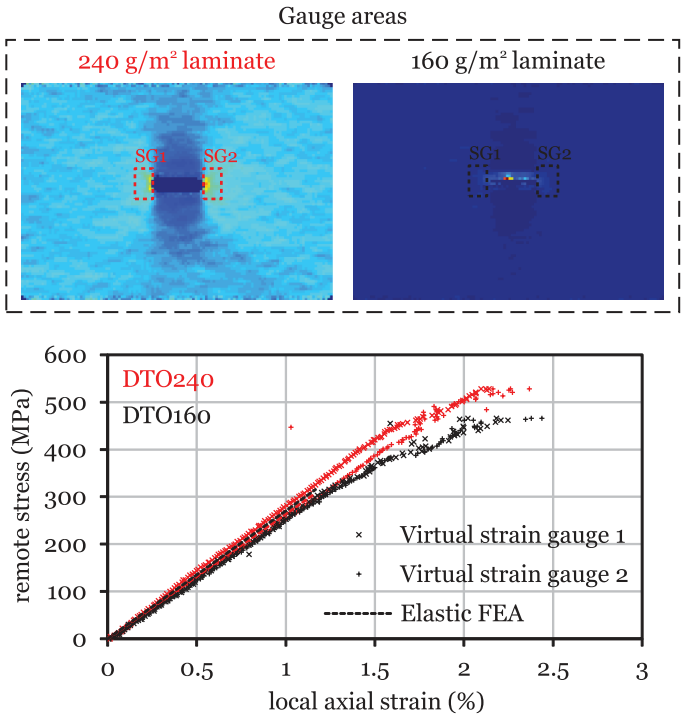

Fig. 4.110. Virtual strain gauge areas and remote stress-local axial strain relations for representative CNT test specimens. The loading direction is parallel to the vertical axis of the specimens.

FEA was performed for each laminate, employing the same averaging procedure. The FE models were created with the commercial FE software Abaqus 6.12-1 [275] using a structured mesh of CPS4R elements. At the notch tip, finite elements with a minimum in-plane size five times smaller than the notch tip radius (or 0.1 mm) were used to accurately represent the notch geometry and capture the strain concentrations. In the FE model, only the gauge section was modelled. Figure 4.111a shows a detail of the mesh of a CNT FE model.

To replicate the load and boundary conditions of the actual test setup, a longitudinal displacement (x-direction) of 1.00 mm was applied to the nodes on the top end. The remaining degrees of freedom were fixed. An encastre boundary condition was applied to the nodes in the bottom end by fixing all degrees of freedom.

Each STF layer was represented by a [0/90] cross-ply sublaminate. The individual plies of the composite lay-up were modelled using a layerwise approach, explicitly defining each lamina, and respective ply orientation, by one integration point through the thickness of the plane stress elements. The constitutive behaviour of each ply was defined by an orthotropic material model, using the elastic properties of T700GC/M21 (table 4.1). It is assumed that fibre sizing, material grade and reinforcement configuration does not affect the elastic properties of the material system studied in the present work (e.g. section 4.5.1). Figure 4.111b shows the longitudinal strain field of the outer ply of a CNT FE model.

The results of the FEA are plotted together with the DIC data in figure 4.110. As can be observed, the numerical results are in very good agreement with the linear range of the measured stress-strain relations, validating the application of the virtual strain gauge approach in the present analysis.

For the same laminate, the linear stress-strain relations before onset of strain localisation in the vicinity of the notch tips (figure 4.110) are either coincident (laminate *DTO160*) or reasonably similar (laminate *DTO240*), demonstrating that a good load symmetry was achieved, thus validating the adopted test setup. It is important to note that, because the virtual strain gauges are placed in the vicinity of high strain concentration sites, small changes in their position may alter the stress-strain relation. Nevertheless, very satisfactory results were obtained.

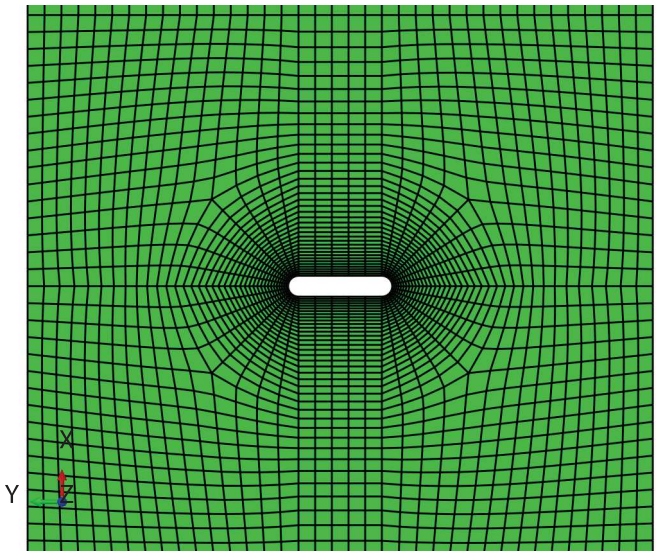

(a) Mesh detail.

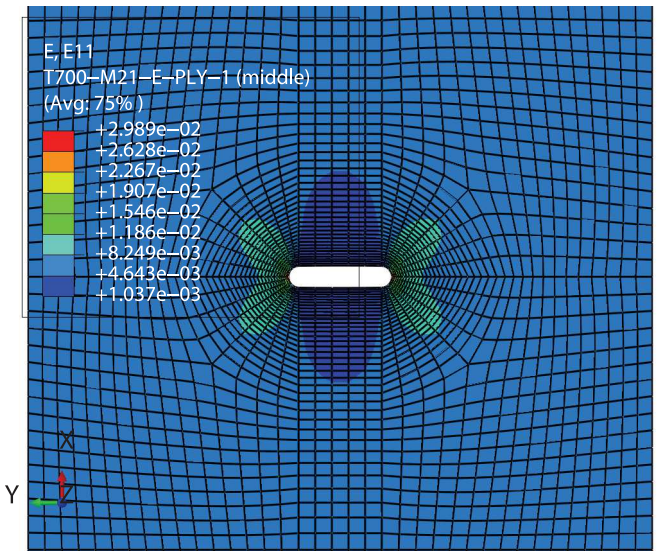

(b) Longitudinal strain field of the outer ply.

Fig. 4.111. Mesh detail of the FE model of a CNT specimen and longitudinal strain field of the outer ply.

Table 4.20
Laminate tensile centre-notched strength ($\bar{\sigma}^{\infty}$) test results and respective coefficients of variation (C.V.).

Results	240 g/m^2 laminate	160 g/m^2 laminate
No. specimens	3	3
$\bar{\sigma}^{\infty}$ (MPa)	490	494
C.V. (%)	6.2	3.9

Interestingly, even though the onset of surface discrete intralaminar damage from the notch tips in laminate *DTO160* was seen to occur close to the peak remote stress (figure 4.109), a nonlinear behaviour in the vicinity of the notch tips can be observed in figure 4.110 reasonably before ultimate failure. This nonlinear response can be attributed to the development of internal damage, which blunts the strain concentration and modifies the surface strain field. A similar trend can be observed for laminate *DTO240*.

Table 4.20 shows the average results for the ultimate remote stress of the CNT tests, and corresponding coefficients of variation. It is interesting to note that the tensile centre-notched strengths of laminates *DTO240* and *DTO160* differ by just 0.9%. It can be concluded, therefore, that they are virtually the same, in spite of the differences in the morphology and extent of the failure mechanisms involved in the fracture process. The similarity of the experimental results can be attributed to the development of internal longitudinal split cracking tangent to the notch tips before ultimate failure of both laminates, as suggested by the straight bands in the strain field, parallel to the loading direction, observed in figures 4.108 and 4.109. However, the susceptibility of the thicker spread-tow yarns of laminate *DTO240* to develop early subcritical damage results in a diffuse failure mode due to the propagation of transverse and longitudinal split cracking.

Laminate *DTO160*, on the other hand, prevents the occurrence of diffuse damage (figures4.107b and 4.109), while providing sufficient internal blunting mechanisms that delay ultimate intralaminar fracture. It is noted that similar tensile centre-notched strengths for thin-ply laminates with and without ply blocking were already obtained in previous work [122].

4.5.9. Laminate compressive centre-notched strength test results

Centre-notched coupons of laminates *DTO240* and *DTO160* were also tested to failure in compression. The tests were performed on 3 specimens of each laminate. Figure 4.112 shows the remote stress-displacement curves, where the remote stress, σ^{∞}, was calculated dividing the applied load, measured by the load cell, by the cross-section area, and the cross-head displacement was measured directly by the testing machine's LVDT.

Due to adjustments in the end-loading anti-buckling setup in the early stages of loading, a nonlinear remote stress-displacement relation is observed in the beginning of the tests (figure 4.112). The range of the adjusting stage, which varies between specimens, is not higher than approximately 20% of the maximum applied remote stress.

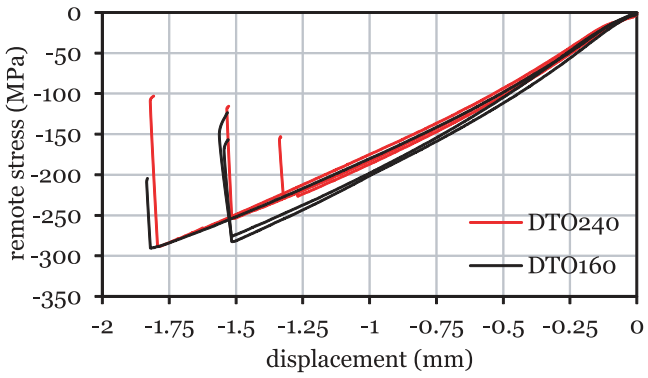

Fig. 4.112. Remote stress-displacement curves of the CNC tests.

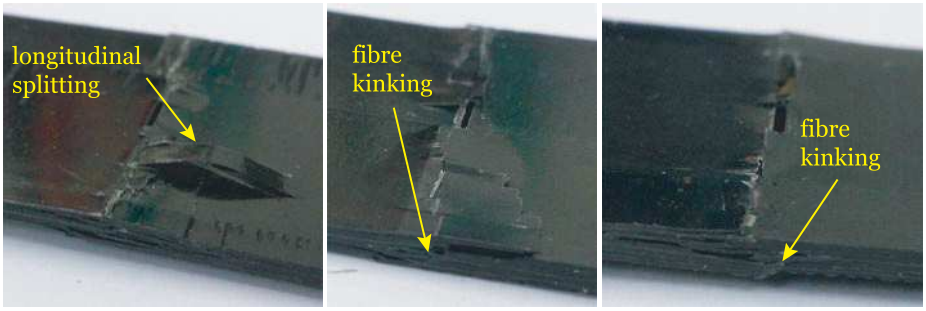

(a) Low-grade laminate *DTO240*.

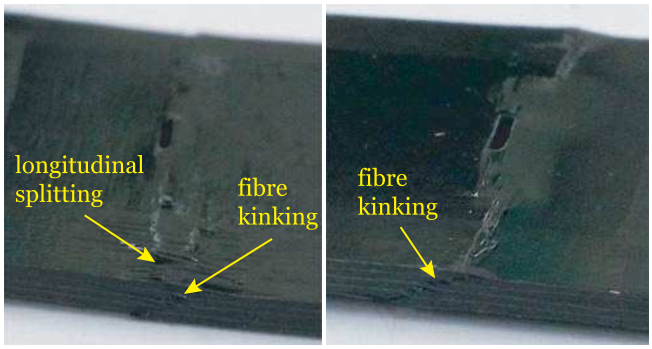

(b) Thin-ply laminate*DTO160*.

Fig. 4.113. Representative CNC test specimens after testing.

Before ultimate failure, small load drops can be observed in some specimens of laminate *DTO240* (figure 4.112), near or after the peak load. These load drops, which have a negligible effect on the stiffness of the tested specimens, can be attributed to the development of compressive damage before ultimate failure. Damage growth was also perceptible during the tests due to noise produced by the development of a damage process zone ahead of the notch tips, which was audible at applied remote stresses of approximately 200 MPa (or approximately 70% of the ultimate remote stress) and above.

In laminate *DTO160*, internal damage growth was audible just before ultimate failure. Since no load drops were observed in the remote stress-displacement curves (figure 4.112), it can be concluded that compressive damage was precluded until final collapse of the ligament section ahead of the notch tips.

Both laminates exhibited a catastrophic failure mode, characterised by a steep load drop (figure 4.112). It is noted that the applied remote stress does not drop to zero due to the contact forces between the fracture surfaces.

After testing, all specimens exhibited a net-section failure mode (figure 4.113). However, failure of laminate *DTO240* (figure 4.113a) is characterised by a complex combination of damage mechanisms, including fibre kinking, wedge transverse fracture and surface fibre/matrix splitting. Longitudinal split cracking caused by buckling of the outer STF layers was also observed, similarly to the unnotched specimens (figure 4.105a).

On the other hand, failure of laminate *DTO160* (figure 4.113b) is dominated by fibre kinking, which propagates across the ligament section ahead of the notch tips. Clear kink bands have formed across the thickness of the laminate, along a plane inclined with respect to the loading direction. Small longitudinal split cracks at the free edges are also observed is some specimens, due to buckling of the thin outer layers.

To understand the sequence and extent of compressive damage before unstable fracture, the development of the damage process zone can be investigated analysing the longitudinal strain fields obtained from DIC measurements of representative specimens of laminates *DTO240* (figure 4.114) and *DTO160* (figure 4.115). Interestingly, the surface damage morphology and extent exhibited by both laminates is very similar.

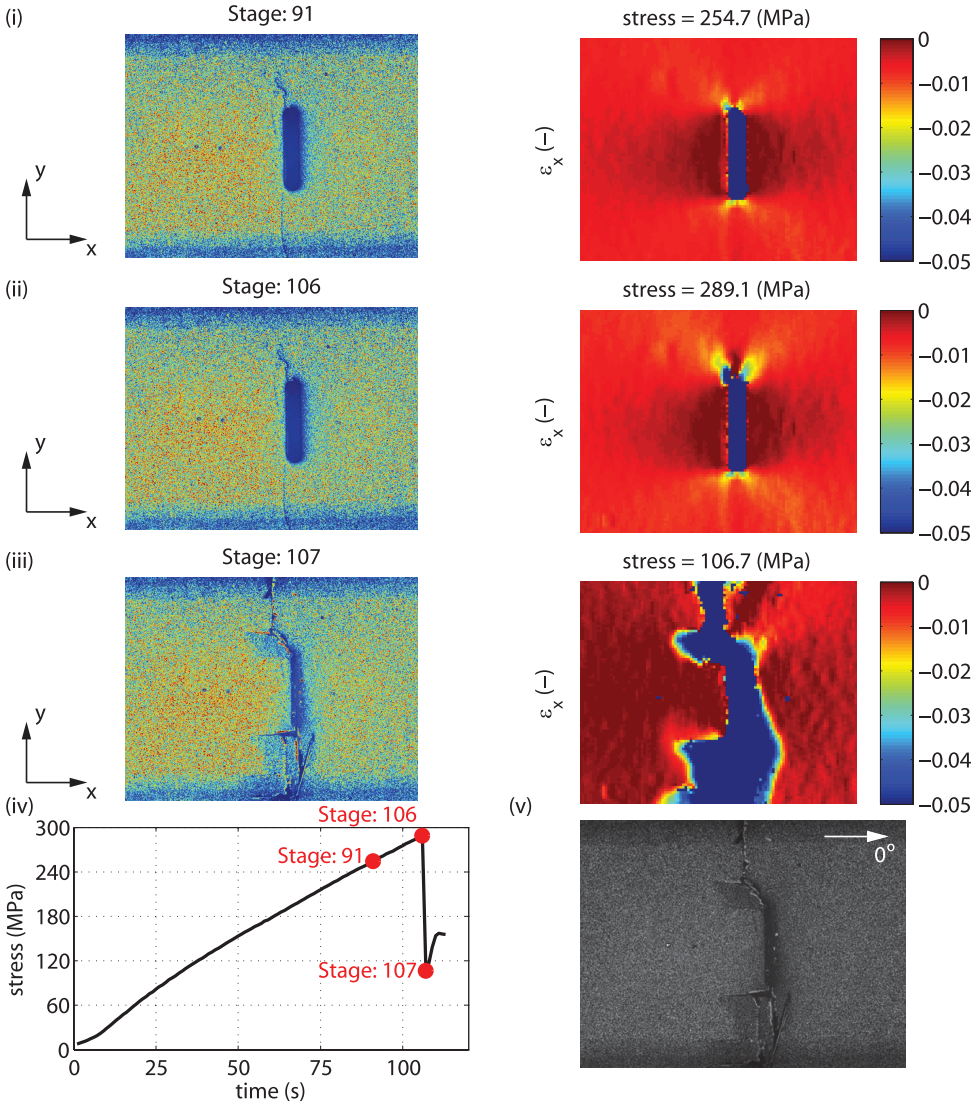

Fig. 4.114. Coloured distribution of grey levels (0–255) and longitudinal strain fields, ε_x, of a representative CNC test specimen of laminate *DTO240* obtained with the DIC system at the stages of (i) onset of compressive intralaminar cracking, (ii) at the peak remote stress and (iii) after ultimate failure. (iv) Remote stress-time relation. (v) Specimen's surface after failure obtained with the DIC image grabbing setup. The reference DIC coordinate system is depicted in the figure, where the x-axis is aligned with the loading direction.

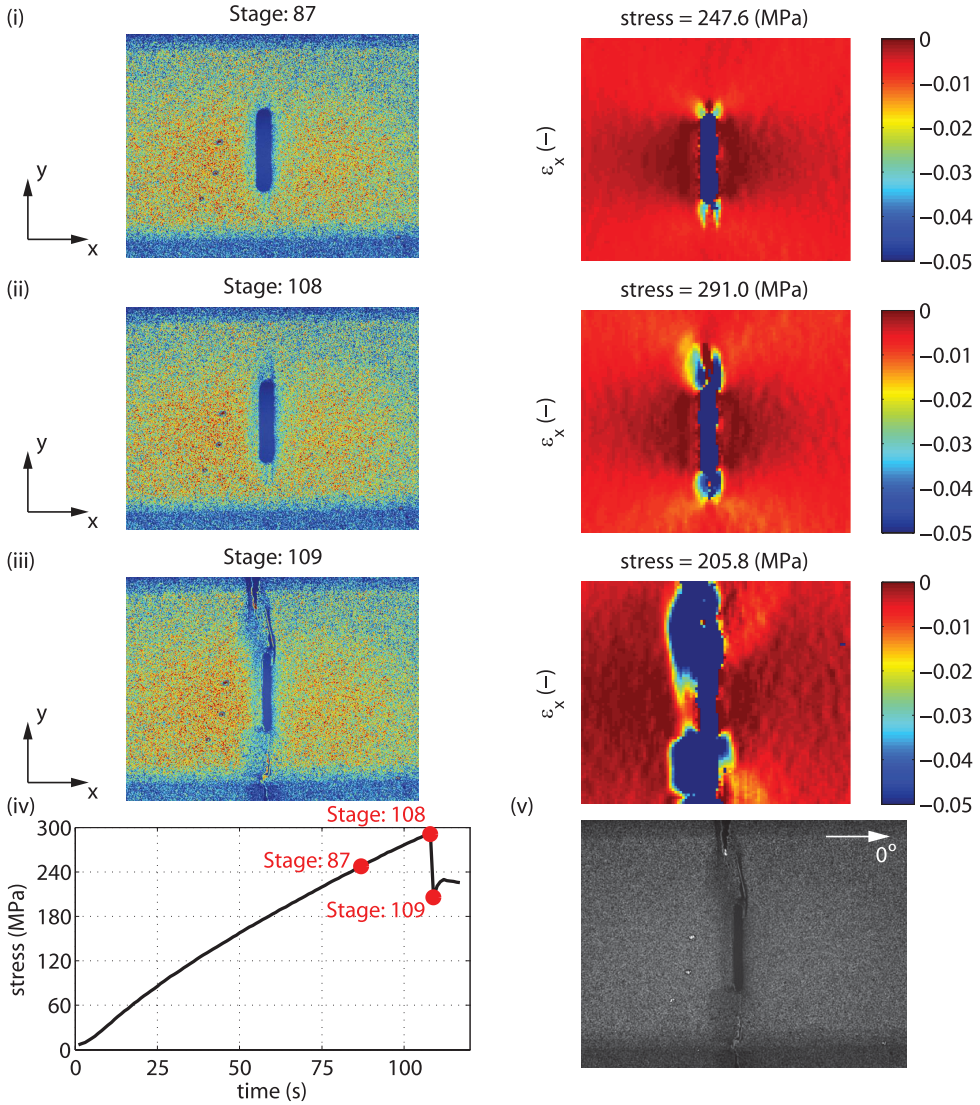

Fig. 4.115. Coloured distribution of grey levels (0–255) and longitudinal strain fields, ε_x, of a representative CNC test specimen of laminate *DTO160* obtained with the DIC system at the stages of (i) onset of compressive intralaminar cracking, (ii) at the peak remote stress and (iii) after ultimate failure. (iv) Remote stress-time relation. (v) Specimen's surface after failure obtained with the DIC image grabbing setup. The reference DIC coordinate system is depicted in the figure, where the x-axis is aligned with the loading direction.

4.5. Experimental results and discussion

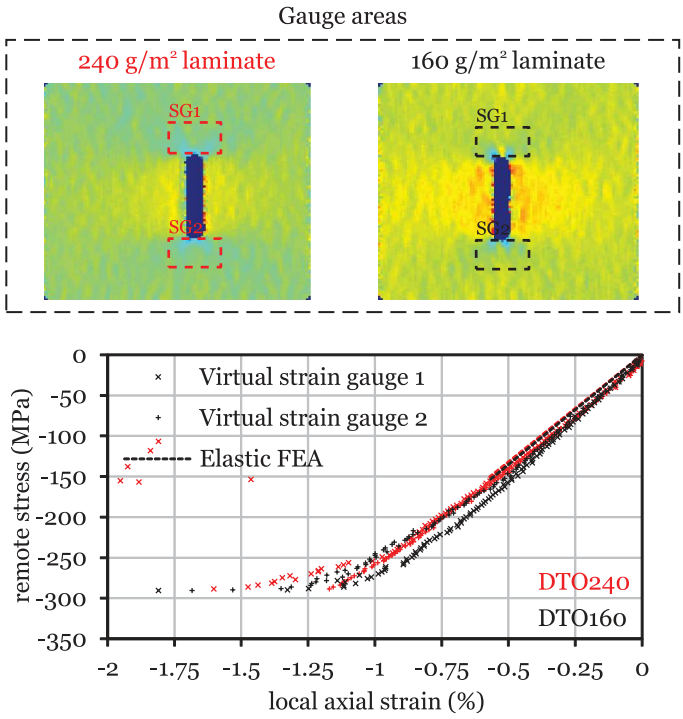

Fig. 4.116. Virtual strain gauge areas and remote stress-local axial strain relations for representative CNC test specimens. The loading direction is parallel to the horizontal axis of the specimens.

Figures 4.114 and 4.115 show that propagation of discrete damage from the notch tips starts early before ultimate failure in both laminates. However, stable damage growth is confined to the vicinity of the notch tips[2]. Unstable propagation across the ligament width occurs upon final failure. This suggests that the development of subcritical damage is reduced and that ultimate failure, either more diffuse, as in laminate *DTO240*, or brittler, as in laminate *DTO160*, is governed by the mechanism that conducts to unstable fracture of the laminates.

In order to assess possible load asymmetries and the effects of strain concentration, remote stress-local axial strain relations were obtained with virtual strain gauges [121, 122, 182, 187], computed averaging the results from the DIC data in an area equivalent to the gauge area of physical strain gauges (figure 4.116). Gauge areas with 3.18 mm in length and 1.78 mm in width were used. Two virtual strain gauges (*SG1* and *SG2*) were placed at the tips of the central notch. The location of the gauge areas (*SG1* and *SG2*) are presented in figure 4.116, depicted over the longitudinal strain field obtained with DIC at an applied remote stress equal to 20% of the ultimate remote stress.

As in previous sections, linear-elastic FEA were performed to validate the implementation of the virtual strain gauges. The FE models were created with the commercial FE software Abaqus 6.12-1 [275] using a structured mesh of CPS4R elements. At the notch tip, finite elements with a minimum in-plane size five times smaller than the notch tip radius (or 0.1 mm) were used to accurately represent the notch geometry and capture the strain concentrations. Figure 4.117a shows a detail of the mesh of a CNC FE model.

A longitudinal displacement (x-direction) of -1.00 mm was applied to the nodes on the top end, leaving the displacement in the transverse direction free in both ends. The remaining degrees of freedom in the top and bottom ends were fixed.

Each STF layer was represented by a [0/90] cross-ply sublaminate. The individual plies of the composite lay-up were modelled using a layerwise approach, explicitly defining each lamina, and respective ply orientation, by one integration

[2]It should be noted that only a small region of the CNC specimen centered with the notch, corresponding to the window in the anti-buckling compression rig [272], was monitored using DIC (sections 4.3 and 4.4)

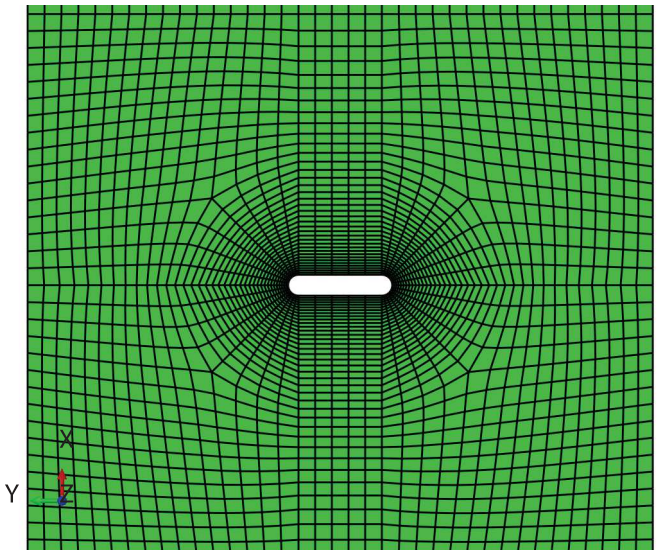

(a) Mesh detail.

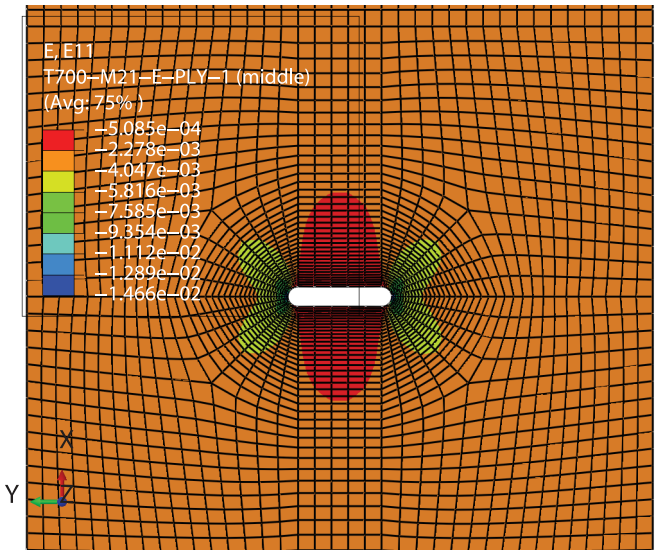

(b) Longitudinal strain field of the outer ply.

Fig. 4.117. Mesh detail of the FE model of a CNC specimen and longitudinal strain field of the outer ply.

Table 4.21
Laminate compressive centre-notched strength ($\bar{\sigma}^{\infty}$) test results (absolute values) and respective coefficients of variation (C.V.).

Results	240 g/m^2 laminate	160 g/m^2 laminate
No. specimens	3	3
$\bar{\sigma}^{\infty}$ (MPa)	256	283
C.V. (%)	9.9	2.1

point through the thickness of the plane stress elements. The constitutive behaviour of each ply was defined by an orthotropic linear-elastic material model, using the elastic properties of T700GC/M21 (table 4.1). It is assumed that fibre sizing, material grade and reinforcement configuration does not affect the elastic properties of the material system studied in the present work (e.g. section 4.5.1). Figure 4.117b shows the longitudinal strain field of the outer ply of a CNC FE model.

The results of the FEA are plotted together with the DIC data in figure 4.116. As can be observed, the numerical results are in very good agreement with the linear range of the measured stress-strain relations, validating the application of the virtual strain gauge approach in the present analysis. Moreover, for the same laminate, the linear stress-strain relations before onset of strain localisation in the vicinity of the notch tips is almost coincident, demonstrating that a good load symmetry was achieved, thus validating the adopted test setup.

No substantial difference between the compressive notched response of both laminates is observed in figure 4.116. However, strain localisation in the vicinity of the notch tips, captured by the onset of nonlinearity in the stress-strain relation, seems to occur earlier in the thin-ply laminate *DTO160*. Nonetheless, the range of nonlinear deformation does not change substantially between laminates.

Table 4.21 shows the average results for the ultimate remote stress of the CNC tests, and corresponding coefficients of variation. Following the trends observed for the compressive unnotched strength (section 4.5.7), the thin-ply laminate *DTO160* exhibits an improved compressive notched response compared with the low-grade laminate *DTO240*, with a compressive centre-notched strength 10.3% higher than the latter.

A brittler failure mode, as exhibited by laminate *DTO160*, where diffuse damage mechanisms, such as transverse and split cracking and interlaminar damage, are absent, seems to provide an improved compressive response, either or not in the presence of stress concentrations. Also, as discussed in sections 4.5.2 and 4.5.7, the thinner 160 g/m^2 STF exhibits higher compressive strength than the low-grade 240 g/m^2 STF. This is attributed to a better uniformity of the spread-tow yarns, resulting in lower fibre waviness and smaller crimp angles which delay micro-instabilities in the fibre direction, allowing the longitudinal yarns to carry higher loads.

It is interesting to note that, whereas subcritical damage growth acts as a blunting mechanism in tension, reducing the stress concentration and delaying unstable intralaminar damage propagation, in compression it seems to promote early unstable fracture of the longitudinal spread-tow yarns. Assuming that fibre kinking is the critical failure mechanism that, upon unstable growth, conducts to ultimate compressive failure, the growth of subcritical damage, which is generally matrix dominated, may result in an early loss of the lateral support provided to the highly compressed fibres, conducting to premature compressive failure. For instance, the occurrence of subcritical damage mechanisms prior to ultimate failure in the low-grade laminate *DTO240*, promoted premature kinking of small sublaminates, connected by diffuse interlaminar and intralaminar damage mechanisms (see figure 4.113a). Also, precluding the occurrence of subcritical damage can delay compressive failure until a kink band is formed across the thickness of the laminate, as observed in the thin-ply laminate *DTO160* (figure 4.113b), conducting to an improved compressive response.

4.5.10. OHT test results

OHT tests were performed on laminates *DTO240* and *DTO160*. For each laminate and OHT geometry (table 4.6), 3 specimens with a centrally located open hole were tested to failure. Figure 4.118 shows, for the different geometries, the remote stress-displacement curves of both laminates, where the remote stress, σ^{∞}, was calculated dividing the applied

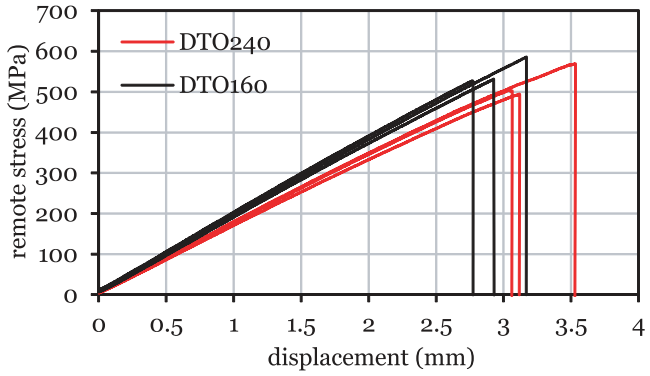

(a) Hole diameter: 2 mm (small).

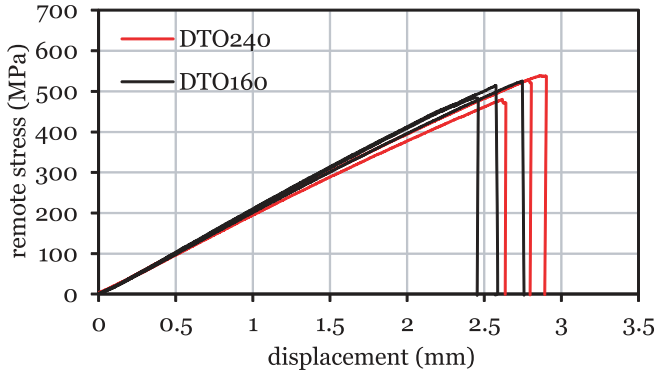

(b) Hole diameter: 5 mm (large).

Fig. 4.118. Remote stress-displacement curves of the OHT tests.

load, measured by the load cell, by the cross-section area, and the cross-head displacement was measured directly by the testing machine's LVDT.

All OHT specimens exhibited an approximately linear remote stress-displacement curve until ultimate failure (figure 4.118). Small load drops can be observed close to the peak load, more importantly in the large OHT specimens (figure 4.118b), caused by damage growth in the vicinity of the open hole just before unstable catastrophic failure.

However, during the tests, internal damage growth was generally audible before the occurrence of the load drops in the remote stress-displacement relations. This suggests that internal subcritical damage growth may have started reasonably before than figure 4.118 suggests.

In laminate *DTO240*, noise due to internal damage growth was audible at applied remote stresses above approximately 460 MPa (81% of the ultimate remote stress) in the small coupons, and above 430 MPa (90% of the ultimate remote stress) in the larger coupons. In the latter, stronger noise produced by severe damage growth, which coincided with the load drops in the remote stress-displacement curves (figure 4.118), was audible just before ultimate failure.

In the small coupons of laminate *DTO160*, noise due to internal damage growth was audible either at applied remote stresses above approximately 540 MPa (91% of the ultimate remote stress), or only upon ultimate failure. In the large OHT specimens, internal damage growth was audible above 450 MPa (or above 88% of the ultimate remote stress). As expected, internal damage growth in the vicinity of the open hole was delayed in the thin-ply laminate *DTO160*.

Figures 4.119 and 4.120 show, respectively, the open-hole sections of representative small and large OHT specimens after testing. As can be observed, both laminates exhibit a fibre-dominated pull-out failure mode, independently of the coupon geometry.

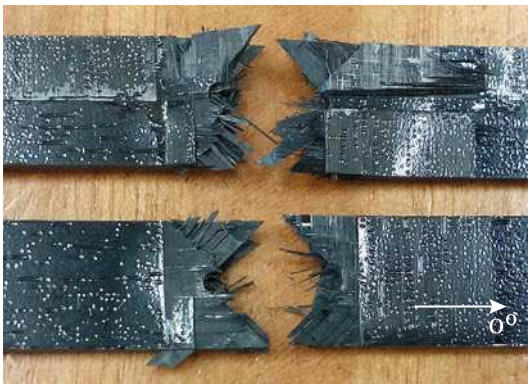

(a) Low-grade laminate *DTO240*.

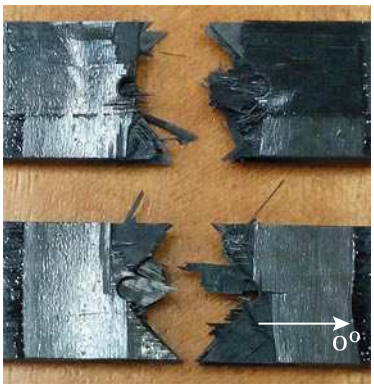

(b) Thin-ply laminate *DTO160*.

Fig. 4.119. Details of representative OHT test specimens with a hole diameter of 2 mm after testing.

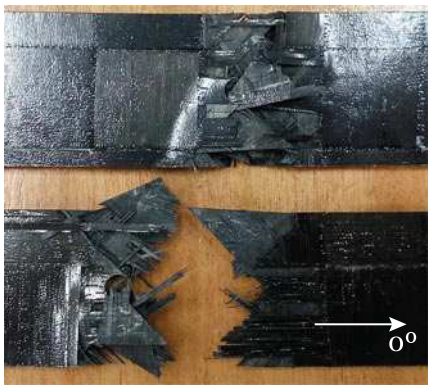

(a) Low-grade laminate *DTO240*.

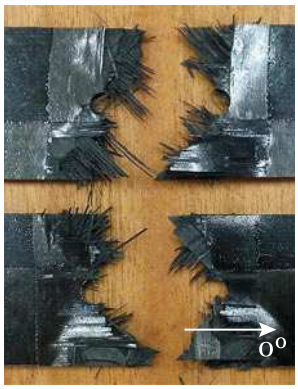

(b) Thin-ply laminate *DTO160*.

Fig. 4.120. Details of representative OHT test specimens with a hole diameter of 5 mm after testing.

The small OHT specimens of the low-grade laminate *DTO240* (figure 4.119a) exhibit a diffuse fracture plane either perpendicular or at 45° with the loading direction, dominated by fibre bundle pull-out and split cracking of the longitudinal and off-axis spread-tow yarns. Transverse split cracking and delamination of the outer STF layers are also observed in the open-hole section of the failed specimens.

The thin-ply laminate *DTO160* exhibit a brittler failure mode, with the fracture plane predominantly at 45° with the loading direction (figure 4.119b). Fibre bundle pull-out and split cracking of the longitudinal and off-axis spread-tow yarns are also observed, but in lesser extent than in laminate *DTO240*. Laminate *DTO160* also exhibits delaminations with triangular shape across the ligament width, caused by straight intralaminar fracture of some off-axis STF layers along the 45° direction tangent to the open hole boundary.

In the larger OHT specimens, the extent of diffuse damage increases in both laminates. Failure of laminate *DTO240* is characterised by pull-out of the spread-tow yarns, without a clear fracture plane (figure 4.120a). Large split cracks in the longitudinal and off-axis spread-tow yarns and delamination between STF layers across the ligament width are also observed. Laminate *DTO160* exhibits a diffuse fracture plane, with fibre bundle pull-out of the off-axis spread-tow yarns and delaminations with triangular shape due to intralaminar fracture of some off-axis STF layers (figure 4.120b).

To understand the sequence and extent of damage before unstable intralaminar fracture and fibre bundle pull-out, the development of the damage process zone can be investigated analysing the longitudinal strain fields obtained from the DIC measurements of representative specimens of both laminates (figures 4.121 to 4.124). In laminate *DTO240*, the small OHT specimen (figure 4.121) exhibits longitudinal split cracking tangent to the hole boundary. Intralaminar

fracture perpendicular or at an angle with the loading direction is absent before ultimate failure. Surface split cracking of the longitudinal spread-tow yarns at the free edges can also be observed, resulting in the diffuse failure mode presented in figure 4.119a.

The absence of surface discrete intralaminar fracture in the small OHT specimen of laminate *DTO240* (figure 4.121) can be attributed to the short ligament section relative to the size of the fibre-matrix splits that form before ultimate failure. Because the split cracks and surrounding local delaminations occupy a relatively large region in the vicinity of the open hole, the blunting effect is tremendous, precluding stable intralaminar cracking before catastrophic failure of the longitudinal spread-tow yarns.

In laminate *DTO160* (figure 4.122), even though surface damage is not captured until final failure, a straight band in the strain field, bounded by the open-hole diameter and parallel to the loading direction, indicates the occurrence of internal longitudinal split cracking tangent to the hole boundary. As in laminate *DTO240*, a tremendous blunting effect caused by the relatively large damage process zone in the vicinity of the open hole delays intralaminar cracking until catastrophic failure of the longitudinal spread-tow yarns.

In the larger specimens, because the size of the damage process zone is relatively smaller, intralaminar cracking perpendicular to the loading direction is observed in both laminates (figures 4.123 and 4.124). In laminate *DTO240* (figure 4.123), a diffuse damage process zone in the vicinity of the open hole started early before ultimate failure, propagating into transverse intralaminar cracking ahead of the open hole boundary and into longitudinal splitting tangent to the hole free edge, conducting to the diffuse failure mode shown in figure 4.120a.

In laminate *DTO160* (figure 4.124), clear intralaminar fracture ahead of the hole boundary along the ligament section can be observed, starting reasonably before ultimate failure. Interestingly, after stable propagation, transverse intralaminar fracture eventually originates other damage mechanisms ahead of the crack tips, namely longitudinal split cracking. This combination of damage mechanisms seems to be responsible for the diffuse pull-out failure mode exhibited by the large OHT specimens of laminate *DTO160* (figure 4.120b).

To investigate the effects of strain concentration in the vicinity of the open hole, remote stress-local axial strain relations were obtained with virtual strain gauges [121, 122, 182, 187], computed averaging the results from the DIC data in an area equivalent to the gauge area of physical strain gauges (figures 4.125 and 4.126). Gauge areas with 3.18 mm in length by 1.78 mm in width were used.

Two virtual strain gauges (*SG1* and *SG2*) were placed in the vicinity of the hole boundary, centered with respect to the ligament section plane. The location of the gauge areas (*SG1* and *SG2*) are presented in figures 4.125 and 4.126, depicted over the longitudinal strain field obtained with DIC at an applied remote stress equal to 20% of the ultimate remote stress.

To validate the implementation of the virtual strain gauges in the vicinity of the open holes, linear-elastic FEA were performed and post-processed employing the same averaging procedure as in the test data. The FE models were created with the commercial FE software Abaqus 6.12-1 [275] using a structured mesh of CPS4R elements. At the vicinity of the hole, finite elements with a minimum in-plane size ten times smaller than the open hole radius were used to accurately represent the notch geometry and capture the strain concentrations. In each FE model, only the gauge section was modelled. Figure 4.127a shows the detail of a mesh.

To replicate the load and boundary conditions of the actual test setup, a longitudinal displacement (x-direction) of 1.00 mm was applied to the nodes on the top end. The remaining degrees of freedom were fixed. A clamped boundary condition was applied to the nodes in the bottom end.

Each STF layer was represented by a [0/90] cross-ply sublaminate. The individual plies of the composite lay-up were modelled using a layerwise approach, explicitly defining each lamina, and respective ply orientation, by one integration point through the thickness of the plane stress elements. The constitutive behaviour of each ply was defined by an orthotropic linear-elastic material model, using the elastic properties of T700GC/M21 (table 4.1). It is assumed that fibre

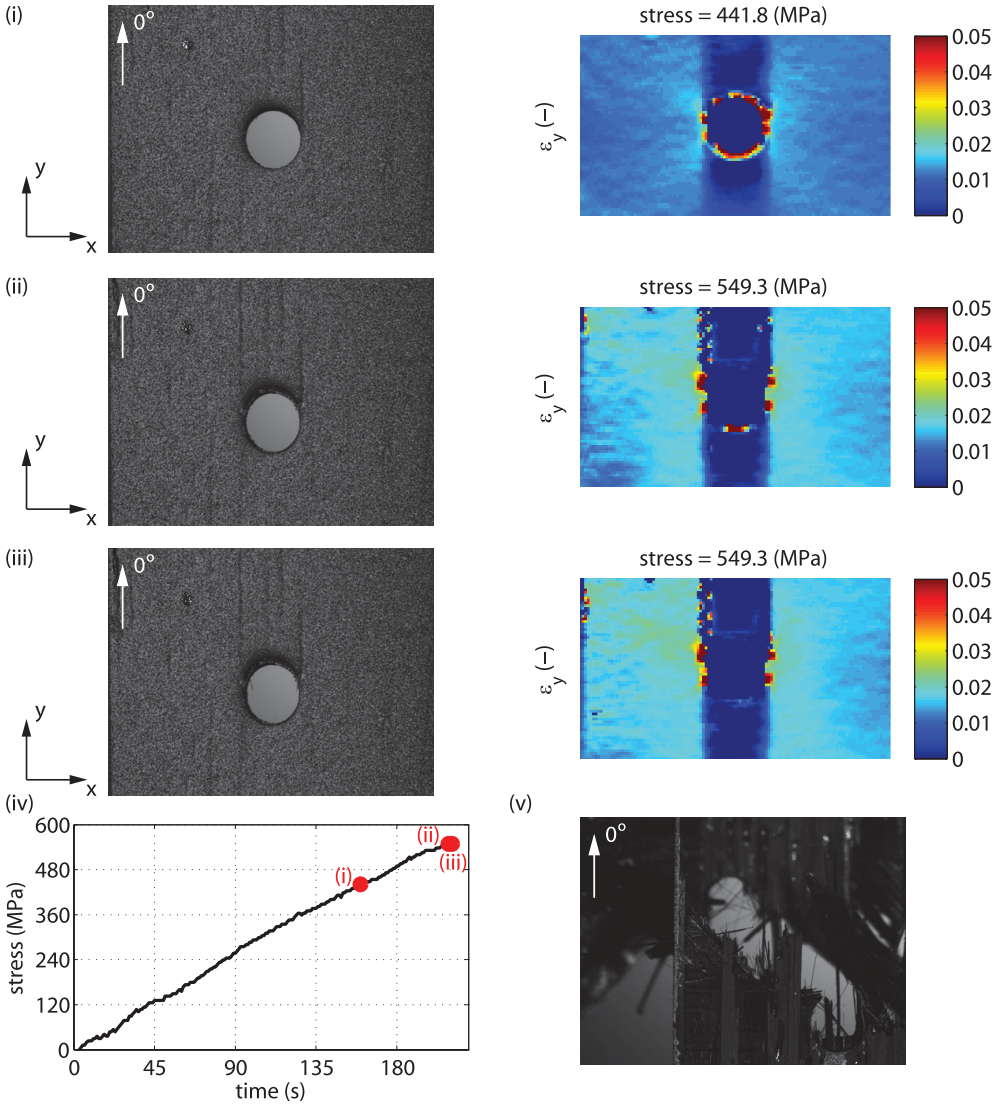

Fig. 4.121. Specimen's surface and longitudinal strain fields, ε_y, obtained with the DIC system from a representative OHT test specimen of laminate *DTO240* with a hole diameter of 2 mm at the stages of (i) onset of longitudinal split cracking tangent to the hole boundary, (ii) at the peak remote stress and (iii) before ultimate failure. (iv) Remote stress-time relation. (v) Specimen's surface after failure obtained with the DIC image grabbing setup. The reference DIC coordinate system is depicted in the figure, where the *y*-axis is aligned with the loading direction.

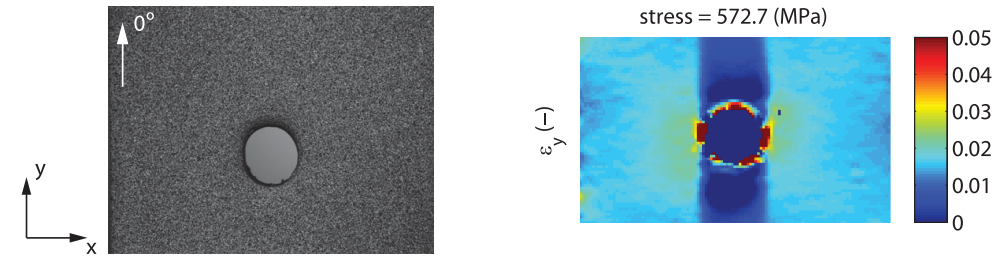

Fig. 4.122. Specimen's surface and longitudinal strain field, ε_y, obtained with the DIC system from a representative OHT test specimen of laminate *DTO160* with a hole diameter of 2 mm at the peak remote stress, before ultimate failure. The reference DIC coordinate system is depicted in the figure, where the *y*-axis is aligned with the loading direction.

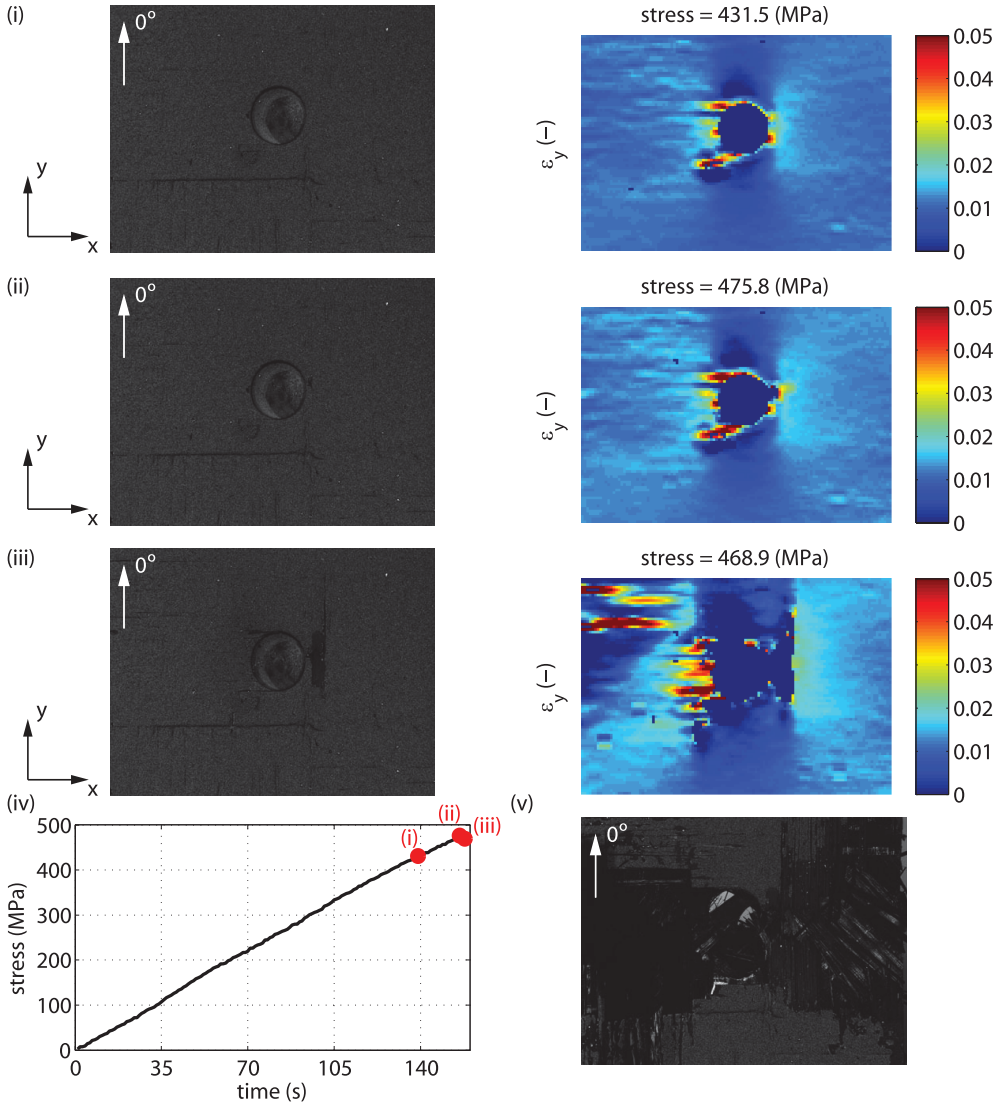

Fig. 4.123. Specimen's surface and longitudinal strain fields, ε_y, obtained with the DIC system from a representative OHT test specimen of laminate *DTO240* with a hole diameter of 5 mm at the stages of (i) onset of surface intralaminar cracking from the hole boundary, (ii) at the peak remote stress and (iii) before ultimate failure. (iv) Remote stress-time relation. (v) Specimen's surface after failure obtained with the DIC image grabbing setup. The reference DIC coordinate system is depicted in the figure, where the *y*-axis is aligned with the loading direction.

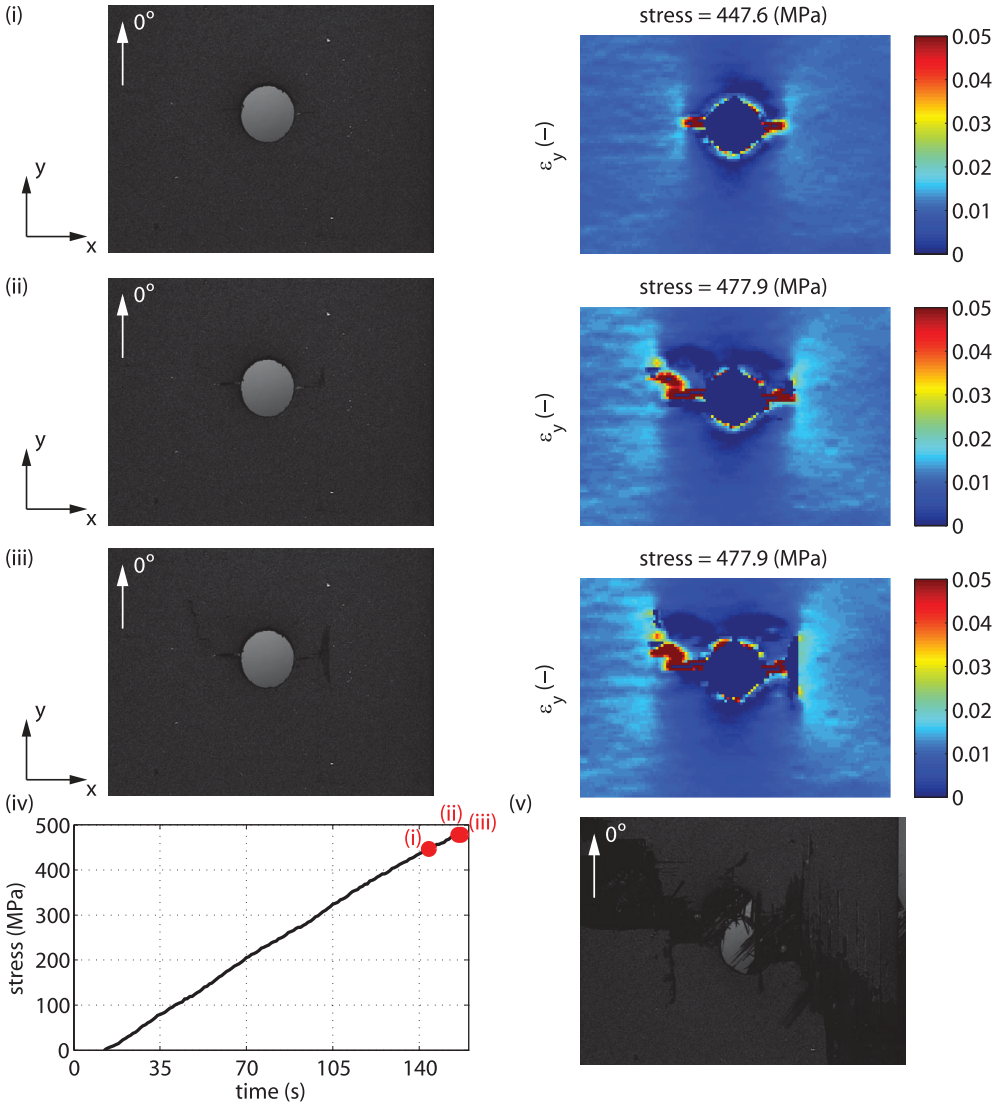

Fig. 4.124. Specimen's surface and longitudinal strain fields, ε_y, obtained with the DIC system from a representative OHT test specimen of laminate *DTO160* with a hole diameter of 5 mm at the stages of (i) onset of surface intralaminar cracking from the hole boundary, (ii) at the peak remote stress and (iii) before ultimate failure. (iv) Remote stress-time relation. (v) Specimen's surface after failure obtained with the DIC image grabbing setup. The reference DIC coordinate system is depicted in the figure, where the y-axis is aligned with the loading direction.

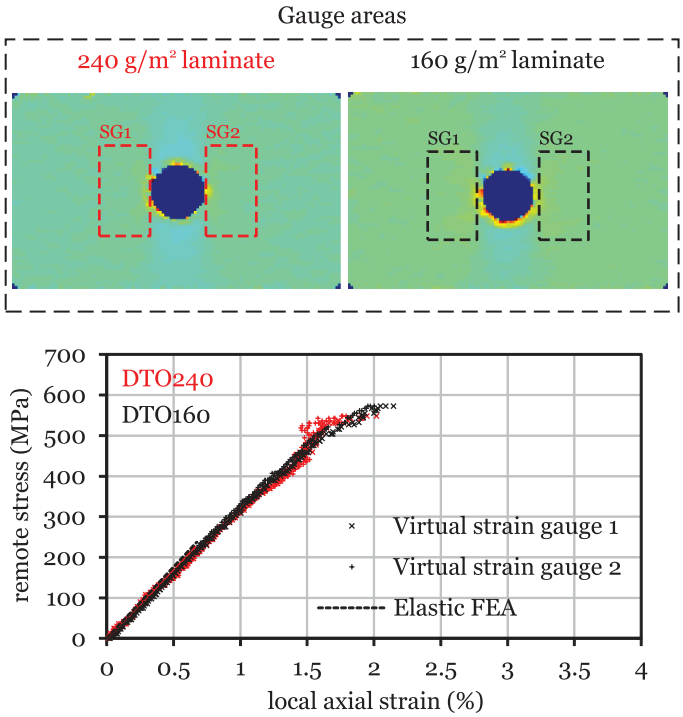

Fig. 4.125. Virtual strain gauge areas and remote stress-local axial strain relations for representative OHT test specimens with a hole diameter of 2 mm. The loading direction is parallel to the vertical axis of the specimens.

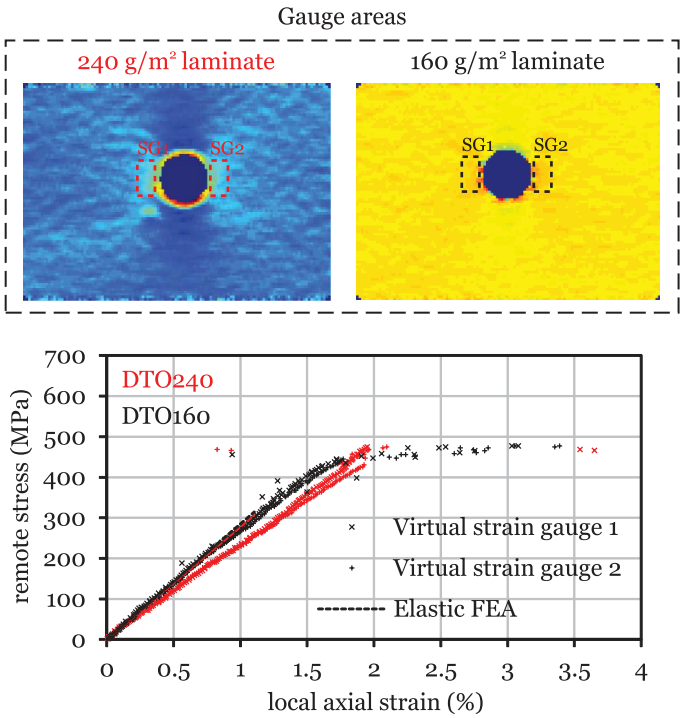

Fig. 4.126. Virtual strain gauge areas and remote stress-local axial strain relations for representative OHT test specimens with a hole diameter of 5 mm. The loading direction is parallel to the vertical axis of the specimens.

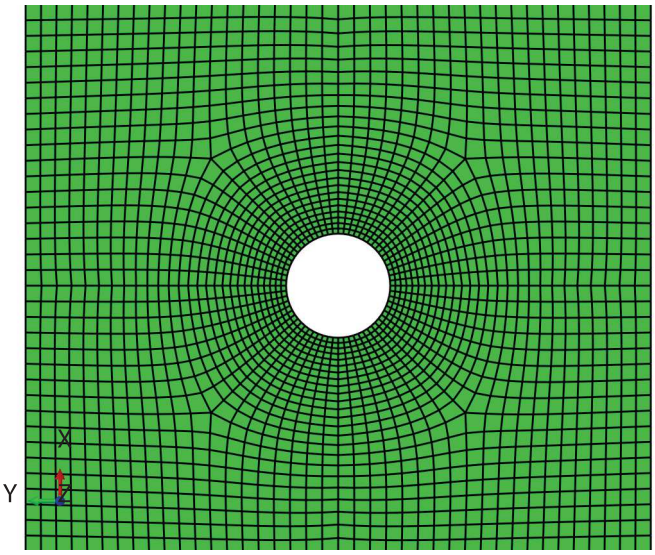

(a) Mesh detail.

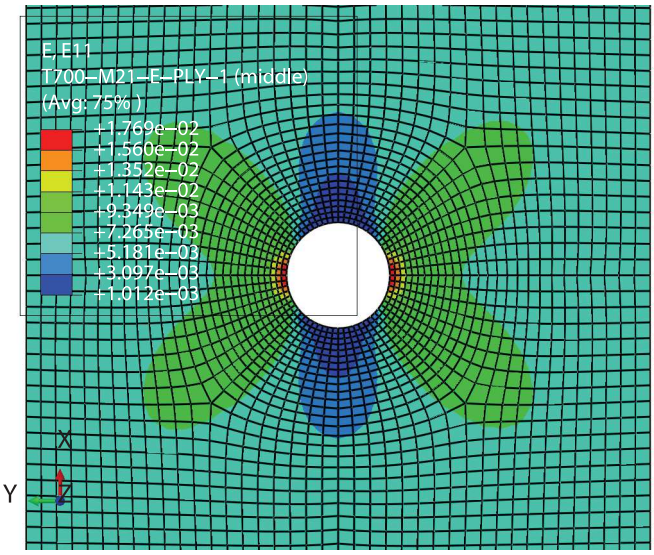

(b) Longitudinal strain field of the outer ply.

Fig. 4.127. Mesh detail of the FE model of an OHT specimen with a hole diameter of 5 mm and longitudinal strain field of the outer ply.

Table 4.22
Mean ultimate remote stresses ($\bar{\sigma}^{\infty}$) and coefficients of variation (C.V.) of the OHT tests.

Results	Hole diameter: 2 mm		Hole diameter: 5 mm	
	DTO240	*DTO160*	*DTO240*	*DTO160*
No. specimens	3	3	3	3
$\bar{\sigma}^{\infty}$ (MPa)	523	548	515	508
C.V. (%)	6.3	4.9	4.9	3.4

sizing, material grade and reinforcement configuration does not affect the elastic properties of the material system studied in the present work (e.g. section 4.5.1). Figure 4.127b shows the longitudinal strain field of the outer ply of an OHT FE model.

The results of the FEA are plotted together with the DIC data in figures 4.125 and 4.126. As can be observed, the linear range of the measured stress-strain relations are in good agreement with the numerical results, validating the application of the virtual strain gauge approach in the present analysis. Moreover, for the same laminate, and for both geometries, the linear stress-strain relations, which precede the onset of strain localisation, obtained from the virtual strain gauges placed in opposite positions with respect to the centre hole agree very well, demonstrating that load symmetry was guaranteed by the adopted test setup.

Interestingly, for the same geometry, no substantial difference between the notched response of laminates *DTO240* and *DTO160* is observed in figures 4.125 and 4.126. Strain localisation in the vicinity of the hole boundary, corresponding to the onset of nonlinearity in the stress-strain relation, occurs before ultimate failure, but grows quickly towards unstable intralaminar fracture.

As observed in figures 4.121 and 4.122, the dominant surface damage mechanism that precede ultimate failure of the specimens with a hole diameter of 2 mm is longitudinal split cracking tangent to the hole boundary, which does not form a clear strain localisation band or region that can be captured by the virtual strain gauge (figure 4.125). In this case, the nonlinear response can be attributed to the development of internal damage, which blunts the strain concentration and modifies the surface strain field.

Table 4.22 shows the average results for the ultimate remote stress of the OHT tests, and corresponding coefficients of variation. As expected, as the hole size increases (with constant width-to-hole diameter ratio), the tensile strength of the open-hole specimens decreases, an effect that is generally regarded as the conventional hole size effect. However, the strength reduction in laminate *DTO240* is only marginal (in the range of 1.4%, below the tests scatter), whereas in laminate *DTO160* it is in the range of 7.3%.

It is important to note that the hole size effect can be attributed to the relative size of the damage process zone in the vicinity of the open hole with respect to the characteristic dimension of the coupon or structure. As this characteristic dimension becomes larger, the relative size of the damage process zone becomes smaller, reducing the blunting effect in the vicinity of the stress concentration and conducting to early unstable failure of the structure.

As discussed before, prior to ultimate failure, laminate *DTO240* develops a relatively large damage process zone, either in the form of longitudinal splitting (figure 4.121) or diffuse transverse intralaminar cracking (figure 4.123). Failure is characterised by pull-out of the spread-tow yarns, without a clear fracture plane (see, for instance, figure 4.120a). In addition, large split cracks in the longitudinal and off-axis spread-tow yarns and delamination between STF layers across the ligament width could be observed. The similar blunting effect of the diffuse damage mechanisms that grow in laminate *DTO240*, independently of coupon size, results in a marginal difference between the open-hole tensile strengths of the small and large coupons (table 4.22).

The thin-ply laminate *DTO160* exhibits a brittler failure mode (figures 4.119b and 4.120b), characterised by intralaminar fracture ahead of the hole boundary along the ligament section, which, after stable propagation, eventually conducts to other damage mechanisms, namely longitudinal split cracking (figure 4.124). Consequently, as the coupon size increases,

the relative size of the damage process zone becomes smaller, reducing the blunting effect and the notched strength.

Comparing the two laminates, it is interesting to note that, for the specimens with a hole diameter of 2 mm, laminate *DTO160* exhibits an ultimate remote stress 4.9% higher than laminate *DTO240*. On the other hand, the ultimate remote stress of the specimens with a hole diameter of 5 mm is virtually the same, as it differs by just 1.4%.

In the specimens with a hole diameter of 2 mm, the larger extent of diffuse damage in laminate *DTO240* seems initially to blunt the notch, but, after extensive growth, it may precipitate early failure, either due to overloading of the longitudinal spread-tow yarns or due to local stress concentrations caused by the subcritical damage mechanisms adjacent to the load-carrying longitudinal yarns. In laminate *DTO160*, because the ligament section is sufficiently small, the lower extent of diffuse damage is enough to effectively blunt the notch, without precipitating early failure of the longitudinal spread-tow yarns as in laminate *DTO240*. These results suggest that, for small-notch coupons, the structural response tends to the unnotched behaviour.

In the specimens with a hole diameter of 5 mm, the relatively smaller damage process zone exhibited by laminate *DTO160* results in a conventional size effect, characterised by a decrease of its strength. The open-hole tensile strength of laminate *DTO240* is practically unchanged. Nevertheless, the strength of both laminates is still very similar. It can be assumed, though, that as the coupon size increases further the tensile notched strength of laminate *DTO160* will keep decreasing faster than laminate *DTO240*, whose tensile notched strength is expected to become higher than the tensile notched strength of laminate *DTO160*.

4.5.11. OHC test results

OHC tests were performed on 3 specimens of each laminate. Figure 4.128 shows the remote stress-displacement curves, where the remote stress, σ^{∞}, was calculated dividing the applied load, measured by the load cell, by the cross-section area. The cross-head displacement was measured directly by the testing machine's LVDT.

Due to slack in the anti-buckling setup in the early stages of loading, a nonlinear remote stress-displacement relation is observed in the beginning of the tests (figure 4.128). The range of the adjusting stage, which varies between specimens, is not higher than approximately 30% of the maximum applied remote stress. After the initial adjustments inside the anti-buckling rig, the remote stress-displacement relations become linear-elastic until ultimate failure.

During the tests, internal damage growth could be detected by the characteristic noise produced by the development of a damage process zone ahead of the hole boundary. In laminate *DTO240*, it could be detected at applied remote stresses above 210 MPa (87% of the ultimate remote stress), becoming more frequent close to the peak remote stress, above 230 MPa (95% of the ultimate remote stress). In some OHC specimens of laminate *DTO160*, internal damage growth was also audible before ultimate failure, at applied remote stresses around 230 MPa (89% of the ultimate remote stress) and above.

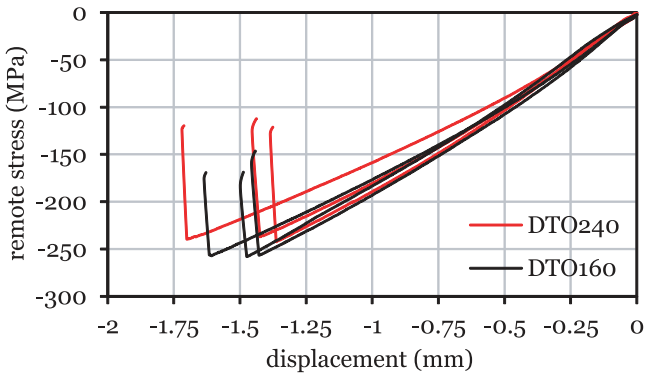

Fig. 4.128. Remote stress-displacement curves of the OHC tests.

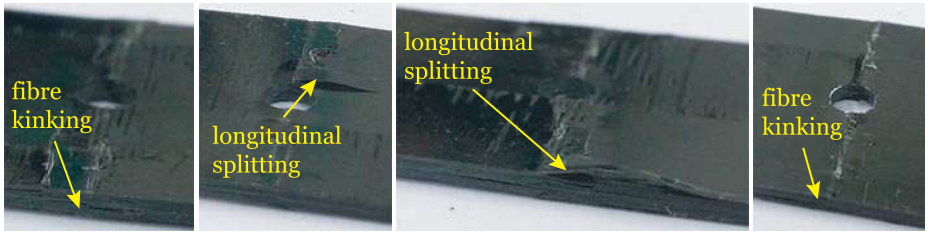

(a) Low-grade laminate *DTO240*.

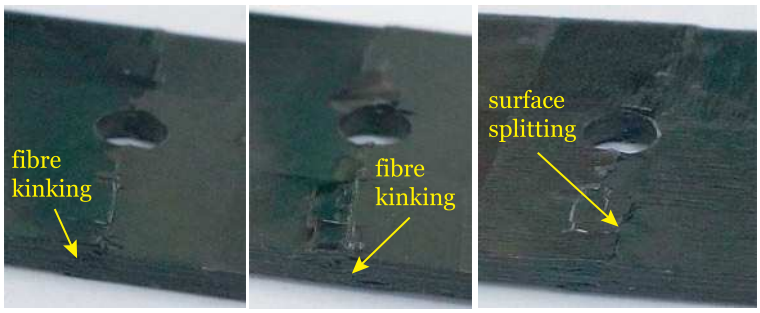

(b) Thin-ply laminate*DTO160*.

Fig. 4.129. Representative OHC test specimens after testing.

Both laminates exhibited a catastrophic failure mode, characterised by a steep load drop (figure 4.128). It is noted that the applied remote stress does not drop to zero due to the contact forces between the fracture surfaces.

After testing, all specimens exhibited a net-section failure mode (figure 4.129). However, failure of laminate *DTO240* (figure 4.129a) is characterised by a complex combination of damage mechanisms, including fibre kinking, wedge transverse fracture and surface fibre/matrix splitting. Longitudinal split cracking caused by buckling of the outer STF layers was also observed, similarly to the unnotched and centre-notched specimens (figures 4.105a and 4.113a).

Failure of laminate *DTO160* (figure 4.129b) is dominated by fibre kinking, which propagates across the ligament section ahead of the hole boundary. Clear kink bands have formed across the thickness of the laminate, along a plane inclined with respect to the loading direction. Surface splitting due to intralaminar compressive fracture of the outer STF layers along the fracture plane is also observed.

To assess the sequence and extent of compressive damage before unstable fracture, the development of the damage process zone can be investigated analysing the longitudinal strain fields obtained from the DIC measurements of representative specimens of both laminates (figures 4.130 and 4.131). Analysis of the strains fields of laminates *DTO240* and *DTO160* indicates that intralaminar compressive damage growth from the hole boundary starts early before ultimate failure in both laminates. However, in laminate *DTO240* (figure 4.130) surface intralaminar compressive damage propagates quickly across the ligament width, whereas in laminate *DTO160* (figure 4.130) surface intralaminar compressive damage growth is limited to the vicinity of the open hole, propagating unstably upon ultimate failure. The ability of the thin-ply laminate *DTO160* to delay the propagation of intralaminar damage has apparently resulted in an improved compressive notched response (see figure 4.128 and compare figures 4.130 and 4.131).

To assess the effects of strain concentration and damage growth in the vicinity of the open hole boundary, remote stress-local axial strain relations were obtained with virtual strain gauges [121, 122, 182, 187], computed averaging the results from the DIC data in an area equivalent to the gauge area of physical strain gauges (figure 4.132). Gauge areas with 3.18 mm in length and 1.78 mm in width were used. Two virtual strain gauges (*SG1* and *SG2*) were placed at the tips of the central notch. The location of the gauge areas (*SG1* and *SG2*) are presented in figure 4.132, depicted over the longitudinal strain field obtained with the DIC technique at an applied remote stress equal to 20% of the ultimate remote stress.

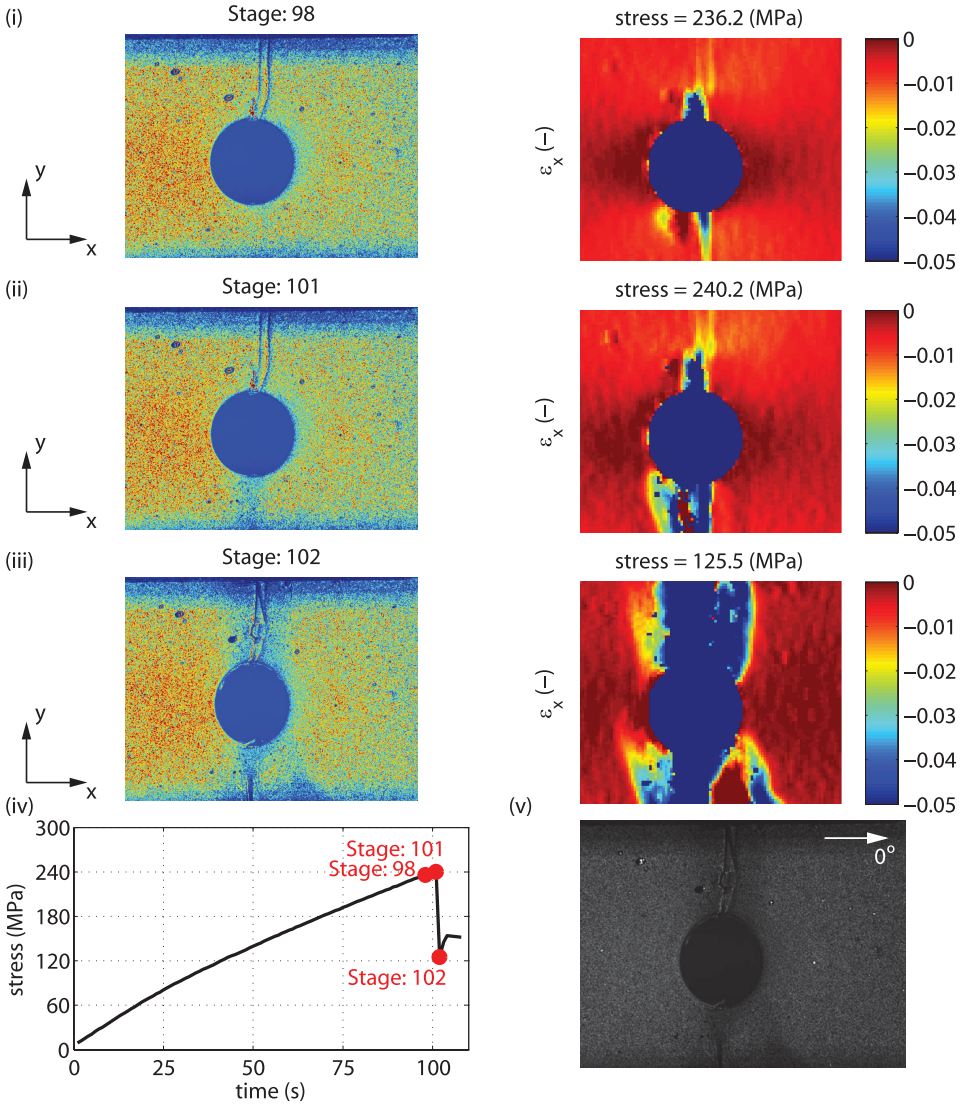

Fig. 4.130. Coloured distribution of grey levels (0–255) and longitudinal strain fields, ε_x, of a representative OHC test specimen of laminate *DTO240* obtained with the DIC system at the stages of (i) onset of compressive intralaminar cracking, (ii) at the peak remote stress and (iii) after ultimate failure. (iv) Remote stress-time relation. (v) Specimen's surface after failure obtained with the DIC image grabbing setup. The reference DIC coordinate system is depicted in the figure, where the x-axis is aligned with the loading direction.

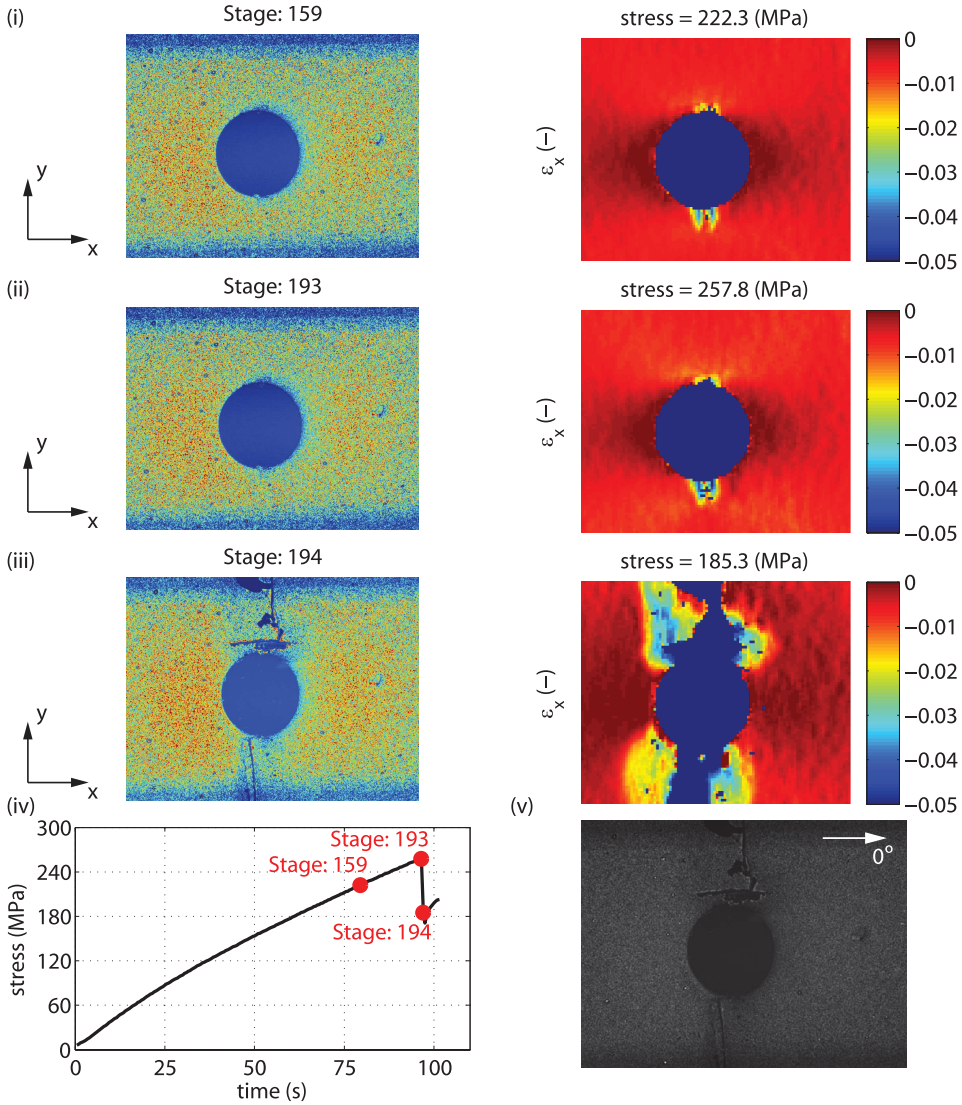

Fig. 4.131. Coloured distribution of grey levels (0–255) and longitudinal strain fields, ε_x, of a representative OHC test specimen of laminate *DTO160* obtained with the DIC system at the stages of (i) onset of compressive intralaminar cracking, (ii) at the peak remote stress and (iii) after ultimate failure. (iv) Remote stress-time relation. (v) Specimen's surface after failure obtained with the DIC image grabbing setup. The reference DIC coordinate system is depicted in the figure, where the x-axis is aligned with the loading direction.

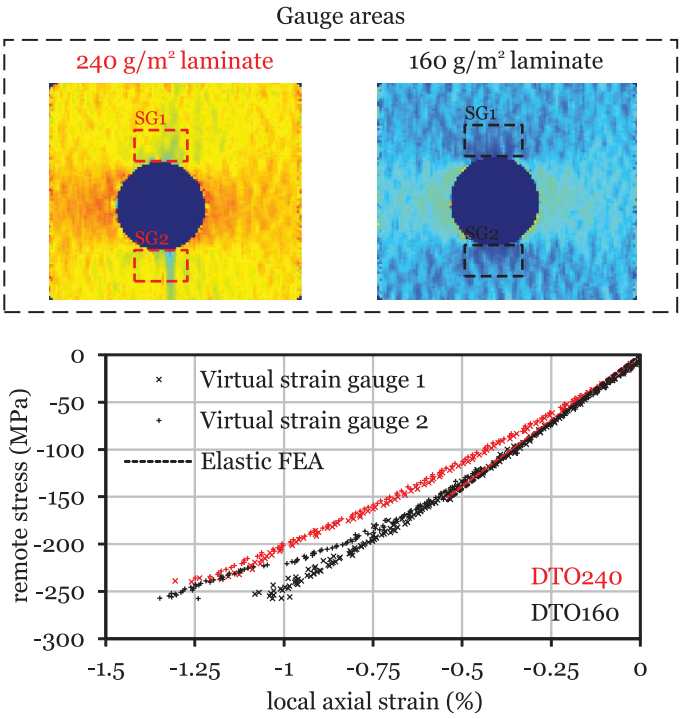

Fig. 4.132. Virtual strain gauge areas and remote stress-local axial strain relations for representative OHC test specimens. The loading direction is parallel to the horizontal axis of the specimens.

As before, linear-elastic FEA were performed to validate the implementation of the virtual strain gauges. The FE models were created with the commercial FE software Abaqus 6.12-1 [275] using a structured mesh of CPS4R elements. At the notch tip, finite elements with a minimum in-plane size ten times smaller than the open hole radius (or 0.25 mm) were used to accurately represent the notch geometry and capture the strain concentrations. Figure 4.133a shows a detail of the mesh of an OHC FE model.

A longitudinal displacement (x-direction) of -1.00 mm was applied to the nodes on the top end, leaving the displacement in the transverse direction free in both ends. The remaining degrees of freedom in the top and bottom ends were fixed.

Each STF layer was represented by a [0/90] cross-ply sublaminate. The individual plies of the composite lay-up were modelled using a layerwise approach, explicitly defining each lamina, and respective ply orientation, by one integration point through the thickness of the plane stress elements. The constitutive behaviour of each ply was defined by an orthotropic linear-elastic material model, using the elastic properties of T700GC/M21 (table 4.1). It is assumed that fibre sizing, material grade and reinforcement configuration does not affect the elastic properties of the material system studied in the present work. Figure 4.133b shows the longitudinal strain field of the outer ply of an OHC FE model.

The results of the FEA are plotted together with the DIC data in figure 4.132. As can be observed, the numerical results agree reasonably well with the linear range of the measured stress-strain relations, validating the application of the virtual strain gauge approach in the present analysis. Moreover, for the same laminate, the stress-strain relations before onset of strain localisation in the vicinity of the notch tips is almost coincident, demonstrating that a good load symmetry was achieved, thus validating the adopted test setup.

In figure 4.132, it is noted that laminate *DTO240* (in red) appears to exhibit a nonlinear stress-strain relation soon after the beginning of the test, unlike laminate *DTO160*. However, this cannot be attributed to early damage growth, but to the existence of an interlacing point, coincident with the ligament section, on the surface STF of laminate *DTO240* (see figure 4.130).

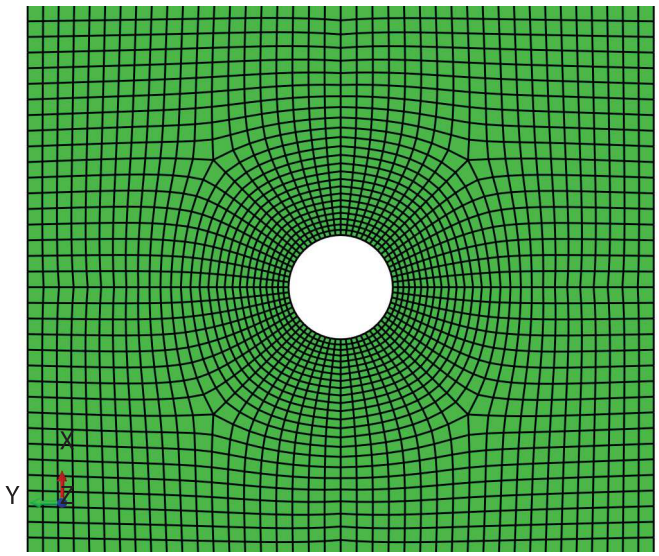

(a) Mesh detail.

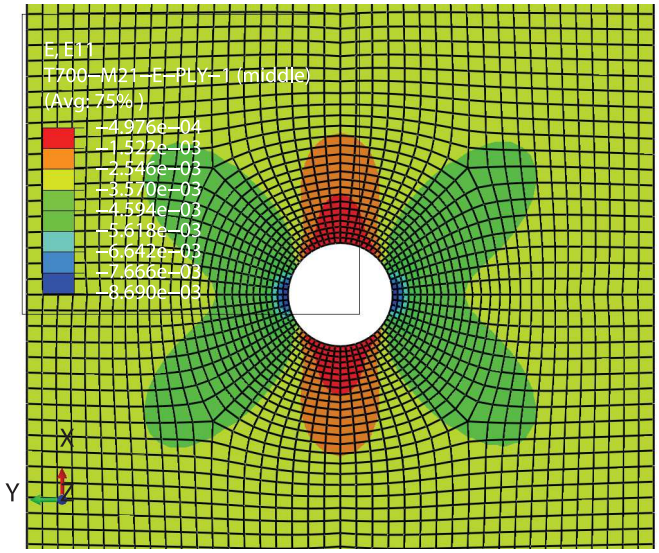

(b) Longitudinal strain field of the outer ply.

Fig. 4.133. Mesh detail of the FE model of an OHC specimen and longitudinal strain field of the outer ply.

Table 4.23
Absolute values of the mean ultimate remote stresses ($\bar{\sigma}^{\infty}$) and respective coefficients of variation (C.V.) of the OHC tests.

Results	240 g/m^2 laminate	160 g/m^2 laminate
No. specimens	3	3
$\bar{\sigma}^{\infty}$ (MPa)	239	257
C.V. (%)	0.9	0.2

Nevertheless, in general, no substantial difference between the compressive notched response of both laminates is observed in figure 4.132. As discussed before, strain localisation in the vicinity of the open hole seems to occur earlier in laminate *DTO160* (see also figures 4.130 and 4.131).

Table 4.23 shows the average results for the ultimate remote stress of the OHC tests, and corresponding coefficients of variation. Following the trends observed for the compressive unnotched and centre-notched strengths (sections 4.5.7 and 4.5.9), the thin-ply laminate *DTO160* exhibits an improved compressive notched response compared with the low-grade laminate *DTO240*, with an open-hole compressive strength 7.4% higher than the latter.

As suggested in section 4.5.9, a brittler failure mode, as exhibited by laminate *DTO160*, where diffuse damage mechanisms, such as transverse and split cracking, are absent, seems to provide an improved compressive response, either or not in the presence of stress concentrations. Furthermore, the thinner 160 g/m^2 STF exhibits higher compressive strength than the low-grade 240 g/m^2 STF. This is attributed to a better uniformity of the spread-tow yarns, resulting in lower fibre waviness and smaller crimp angles which delay micro-instabilities in the fibre direction, allowing the longitudinal yarns to carry higher loads.

Interestingly, whereas subcritical damage growth acts as a blunting mechanism in tension, reducing the stress concentration and delaying unstable intralaminar damage propagation, in compression it seems to promote early unstable fracture of the longitudinal spread-tow yarns. As observed in laminate *DTO240* (figure 4.130), fast damage propagation across the ligament width can occur soon after strain localisation in the vicinity of the hole boundary.

Assuming that fibre kinking is the critical failure mechanism that, upon unstable growth, conducts to ultimate compressive failure, the growth of subcritical damage, which is generally matrix dominated, may result in an early loss of the lateral support provided to the highly compressed fibres, conducting to premature compressive failure. For instance, the occurrence of subcritical damage mechanisms prior to ultimate failure in the low-grade laminate *DTO240*, promoted premature kinking of small sublaminates, connected by diffuse interlaminar and intralaminar damage mechanisms (figure 4.129a). Precluding the occurrence of subcritical damage, as observed in laminate *DTO160* (figure 4.113b), can delay compressive failure until a kink band can form through the thickness of the laminate, improving the compressive response.

4.5.12. Bearing test results

4.5.12.1. Bearing strengths

In this work, 3 bolt-bearing specimens of each laminate, *DTO240* and *DTO160*, were tested to failure. As expected, all specimens exhibited a bearing failure mode, resulting from local compressive damage in the bearing hole region. Representative specimens after testing are shown in figure 4.134. Besides local compressive failure and crushing of the load-bearing surface, which is the typical failure mode observed in composite laminates subjected to bearing loads [122, 235], split cracking of the longitudinal and transverse spread-tow yarns of the outer layers was also observed in the region outside the washer, after permanent deformation of the hole. No relevant difference between the failure modes of laminates *DTO240* and *DTO160* is observed.

Figure 4.135 shows the bearing stress-bearing strain relations of both laminates. The bearing stress, σ^{br}, is defined as:

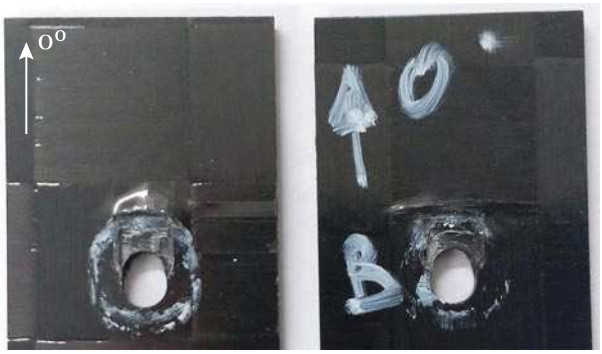

(a) Low-grade laminate *DTO240*.

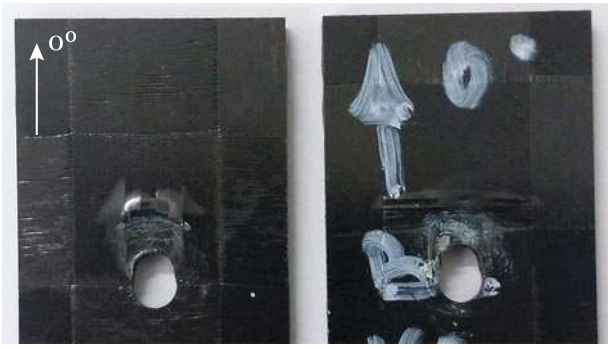

(b) Thin-ply laminate*DTO160*.

Fig. 4.134. Bearing hole region of representative bolt-bearing specimens after testing.

$$\sigma^{br} = \frac{P}{d\,t} \tag{4.22}$$

where P is the applied load measured by the load cell, d is the hole diameter and t is the laminate thickness. The bearing strain, ε^{br}, is determined from the total axial deformation of the specimen's gauge length, measured directly from the cross-head displacement of the testing machine:

$$\varepsilon^{br} = \frac{\Delta}{K\,d} \tag{4.23}$$

where Δ is the cross-head displacement and K is a parameter that depends on the bearing test configuration [237]. For double-shear tests $K = 1.0$ [237].

The bearing stress-bearing strain curves of both laminates are linear up to approximately 50% of the maximum bearing stress, exhibiting a small kink before the response becomes nonlinear. A similar response was already reported elsewhere [122].

The nonlinearity in the bearing stress-bearing strain curves is attributed to the propagation of matrix cracks and to the initiation of fibre kink bands [122, 235]. For bearing stresses greater than the initial peak bearing stress, after the first load drop, extensive matrix cracking and fibre kinking are typically observed [235]. Subcritical damage mechanisms start to interact, resulting in permanent damage such as through-the-thickness shear cracks, whose propagation conducts to the sudden load drops shown in figure 4.135, as well as to permanent hole deformation.

The large load drop observed in both laminates at bearing strains around or above 30% (figure 4.135) were typically accompanied by a strong noise due to sudden, permanent damage propagation in the specimens' bearing region. Nonetheless, the initiation of less severe damage growth in laminate *DTO240* was audible above loads corresponding

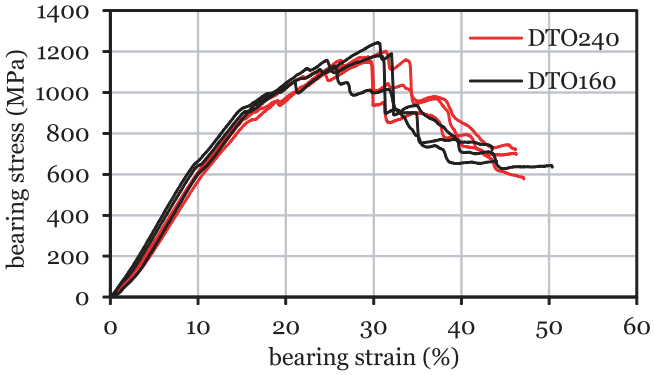

Fig. 4.135. Bearing stress-bearing strain relations for the bolt-bearing tests.

approximately to a 2% offset bearing strain, whereas in laminate *DTO160* it was only audible close to the first load drop in the bearing stress-bearing strain curves.

After the large load drop (figure 4.135), subsequent damage propagation takes place in a rather continuous way, with the bearing stress decreasing slowly. At this point, extensive hole deformation occurs and continuous damage growth is audible until the test is finally stopped.

As explained in section 4.3.12, a clear interpretation of bearing strength does not exist, and different definitions can be used. Table 4.24 shows the average test results and respective coefficients of variation for the bearing strengths of laminates *DTO240* and *DTO160* adopting some of the most common definitions used in the literature, namely the average bearing stress at the onset of nonlinearity, the average bearing stress at the first load drop, the average bearing stress for an offset bearing strain of 2% and 6%, and the average maximum bearing stress. The offset bearing strains were determined following the ASTM D5961/D5961M – 13 test standard [237]. The offset is performed based on a bearing chord stiffness, E^{br}, which was determined from the bearing strain obtained from the total axial deformation of the specimen's gauge length, measured directly from the cross-head displacement. The bearing chord stiffness is defined as [237]:

$$E^{br} = \frac{\Delta\sigma^{br}}{\Delta\varepsilon^{br}} \tag{4.24}$$

where $\Delta\sigma^{br}$ and $\Delta\varepsilon^{br}$ are the change in bearing stress and bearing strain over the chord stiffness range, respectively. Figure 4.136 shows two representative bearing stress-bearing strain curves indicating the bearing strength definitions adopted in table 4.24.

In a previous work [235], based on the experimental data obtained in both bolted and pinned joints, a conservative definition of the ultimate bearing strength was suggested, corresponding to the first nonlinearity in the bearing stress-bearing strain relation. Using this definition it is possible to safely increase the applied load before the load-carrying capacity has been lost (i.e. before the load drops to lower values). Furthermore, there are no shear cracks in the material, and the resulting permanent hole deformation is small. This is, therefore, a suitable bearing strength definition to use in the design of mechanical joints for composite structures, since permanent hole deformation, which increases the bolt-hole clearance and, in turn, leads to fretting fatigue, can be avoided.

It should be noted, though, that the first nonlinearity in the bearing stress-bearing strain relation does not necessarily indicate that the actual load-carrying capacity of a composite laminate subjected to bearing loads has been achieved, specially in bolted joints, due to the lateral support provided in the bearing region. In fact, after the first nonlinearity, composite laminates exhibit an additional load-carrying capacity, which in some cases can duplicate the bearing stress before the load starts dropping (e.g. figure 4.136).

Hence, as an alternative, the bearing stress at the first load drop can be used as a reliable measure of the bolted joint bearing strength [122], in particular for the purpose of joint failure strength assessment and material/lay-up scrutiny. It is

Table 4.24
Average test results for the bolt-bearing strengths and respective coefficients of variation (C.V.).

Results		240 g/m^2 laminate	160 g/m^2 laminate
No. specimens		3	3
Average bearing stress at the onset of nonlinearity			
σ^{br}_{nonlin}	(MPa)	628	629
C.V.	(%)	5.0	2.7
Average bearing stress at the first load drop			
σ^{br}_{drop}	(MPa)	1106	1093
C.V.	(%)	9.5	2.8
Average bearing stress for an offset bearing strain of 2%			
$\sigma^{br}_{2\%offset}$	(MPa)	884	925
C.V.	(%)	1.3	1.6
Average bearing stress for an offset bearing strain of 6%			
$\sigma^{br}_{6\%offset}$	(MPa)	1057	1065
C.V.	(%)	2.4	3.4
Average maximum bearing stress			
σ^{br}_{max}	(MPa)	1171	1184
C.V.	(%)	1.9	3.9

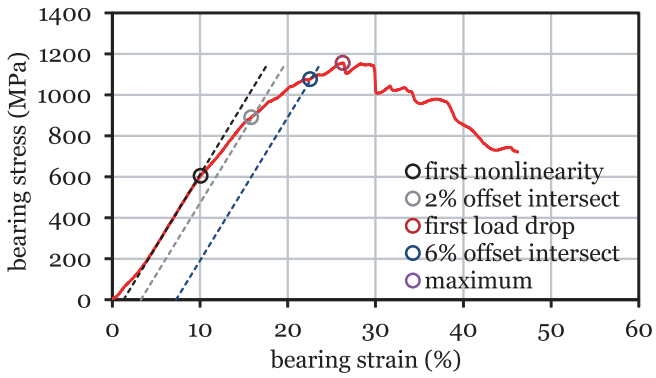

(a) Low-grade laminate *DTO240*.

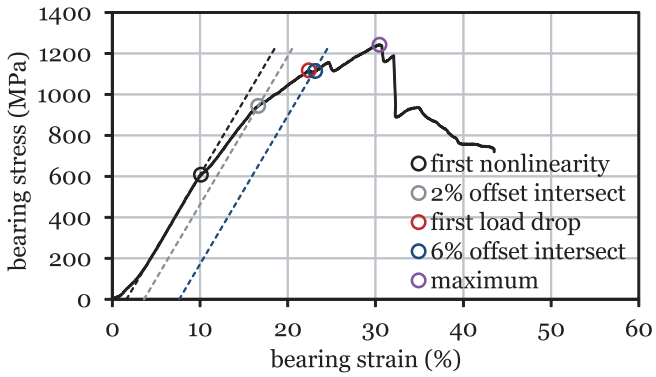

(b) Thin-ply laminate*DTO160*.

Fig. 4.136. Representative bearing stress-bearing strain curves and alternative definitions of bearing strength.

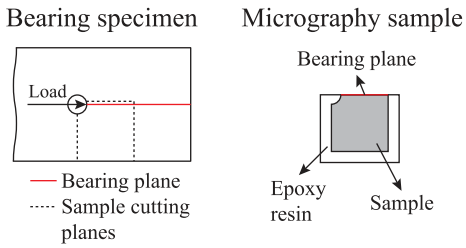

Fig. 4.137. Micrography sample illustration.

interesting to note that, whereas the bearing stress at the onset of nonlinearity is related to the onset of damage [235] (i.e. first-ply failure), the bearing stress at the first load drop is governed by the propagation of damage mechanisms such as matrix and shear cracking and fibre kinking (i.e. last-ply failure).

Composite joints loaded to high offset bearing strains or up to the maximum load sustained by the joint show already extensive damage in the bolt-bearing region, and present an excessively high permanent deformation of the hole. The maximum bearing stress is also associated with local catastrophic failure of the joint, and typically followed by large load drops (figures 4.135 and 4.136). Their use to characterise the bearing strength of a bolted joint is therefore undesirable. Nevertheless, the bearing strengths corresponding to these definitions were also included in table 4.24.

Interestingly, figure 4.135 and table 4.24 show that laminates *DTO240* and *DTO160* exhibit practically the same bearing response. This conclusion is independent of the bearing strength definition used (table 4.24), except for the average bearing stress for an offset bearing strain of 2%, which is 5% higher in laminate *DTO160*. This indicates that the thin-ply laminate *DTO160* exhibits a slightly higher resistance to the propagation of subcritical damage mechanisms at the initial stages of permanent damage (figure 4.135). During the tests, it was noticed that noise caused by internal damage growth before severe hole deformation in laminate *DTO160* was detected later after laminate *DTO240*. Nonetheless, the resistance to severe damage growth (first load drop) and the maximum load-carrying capacity (maximum bearing stress) of both laminates is virtually the same (table 4.24).

4.5.12.2. Interrupted bolt-bearing test results

A more accurate explanation for the difference of the bearing response of the low-grade and thin-ply STF laminates can be obtained identifying the distinct damage mechanisms at different loading stages. Hence, interrupted bolt-bearing tests were performed in 3 specimens of each laminate, corresponding to three different loading levels: onset of nonlinearity, first load drop and offset bearing strain of 6%[3]. Each sample was subsequently analysed by optical microscopy. Micrographies on through-the-thickness sections of the bearing plane (figure 4.137) were obtained, providing a more precise picture of the failure process occurring on the bearing tests, allowing the detailed identification of individual damage mechanisms [235, 238].

After loading each specimen to the desired load level, the test was stopped and the specimen unloaded. The surface to be analysed was marked on the specimen, and each sample obtained by cutting a section of the specimen using a diamond-coated disk (figure 4.137). To avoid inflicting additional damage on the bearing plane due to the cutting process, the sample was cut in a plane parallel to the surface to be analysed, at a distance of the bearing plane of approximately 1 mm. The sample was then embedded into an epoxy resin for handling. The surface of the resin parallel to the composite surface to be analysed was ground on a rotary grinder. Watered silicon carbide grinding paper of 180, 320, 800, 2500 and 4000 grit were sequentially used. Final polishing was obtained using different cloths impregnated with 3 μm and 1 μm synthetic diamond particles.

[3]The bearing stress for an offset bearing strain of 2% is typically reported as a measure of the bearing strength [235, 237]. However, in the present study (section 4.5.12.1), it does not yield permanent damage, occurring before the first load drop (figure 4.136). This is because the bearing strain was determined from the total axial deformation of the specimen's gauge length, measured directly from the cross-head displacement of the testing machine, and not from the axial deformation of the region surrounding the hole, as specified in the ASTM D5961/D5961M – 13 test standard [237]. The bearing stress for an offset bearing strain of 6% has been used instead.

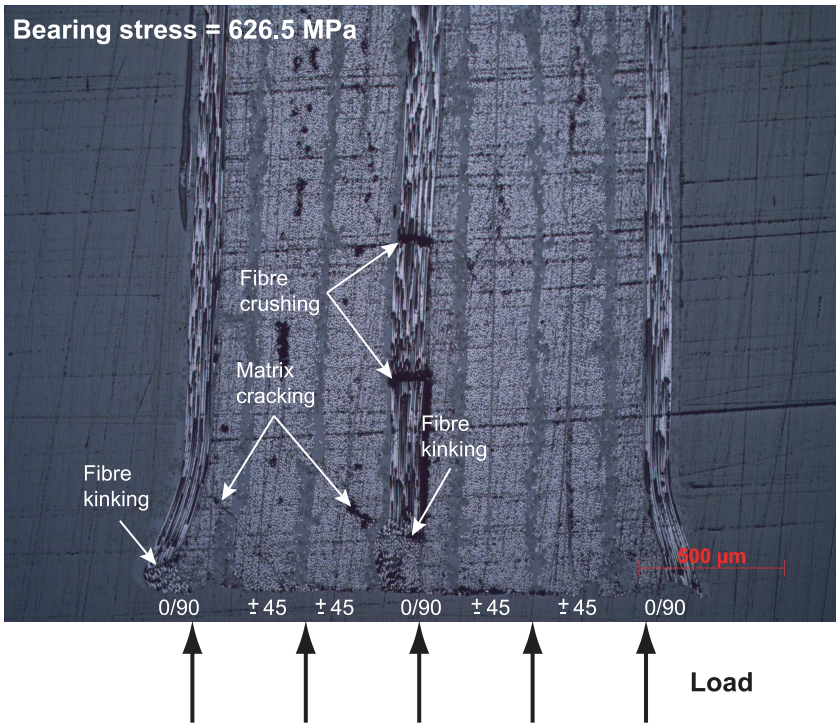

Fig. 4.138. Bearing plane of laminate *DTO240* at the onset of nonlinearity. Magnification factor of 5×.

The polished samples were examined at different magnification factors and the micrographies captured by a digital camera attached to the optical microscope. Starting from the through-the-thickness plane tangent to the hole (figure 4.137), micrographies were taken until no further damage was visible.

Figures 4.138 and 4.139 show, respectively, the through-the-thickness micrographies of the bearing planes of specimens of laminates *DTO240* and *DTO160* at the onset of nonlinearity. In both laminates, fibre kinking and shear-driven matrix cracking can be observed. In laminate *DTO240*, fibre crushing can also be observed along the centre 0° spread-tow yarn (figure 4.138). As suggested in section 4.5.12.1, the onset of nonlinearity in the bearing stress-bearing strain relations (figures 4.135 and 4.136) is associated with the initiation of permanent damage mechanisms such as fibre kink bands and matrix cracks (see also Ref. [235]). It is interesting to note that the extent of matrix cracking in laminate *DTO160* is noticeably lower than in laminate *DTO240*, indicating that compressive matrix-dominated fracture is effectively delayed in the thinner STFs and that an *in situ* effect is compression exists.

At the first load drop (figures 4.140 to 4.144), extensive fibre kinking and shear-driven matrix cracking is observed. These damage mechanisms are not restricted to the vicinity of the hole edge, occurring along the bearing plane far from the loading surface (figures 4.141, 4.143 and 4.144). Moreover, their interaction leads to the formation of through-the-thickness shear cracks, which are responsible for the first load drop observed in the bearing stress-bearing strain relations (figures 4.135 and 4.136).

In laminate *DTO240*, even though fibre kinking along the 0° spread-tow yarns has occurred not only close to the loading surface but also far from this region (figure 4.141), through-the-thickness shear cracking is limited to the vicinity of the hole edge (figure 4.140). It is also noted that, as opposed to laminate *DTO160* (figures 4.142 to 4.144), in laminate *DTO240* fibre compressive failure far from the loading surface is apparently driven by fibre micro-instabilities, ultimately resulting in the formation of kink bands that can occur sequentially, very close to each other (figure 4.141). This "softer" longitudinal compressive failure mode has apparently the ability to delay the more severe through-the-thickness shear cracking.

In laminate *DTO160*, a "brittler" longitudinal compressive failure mode is observed, with more pronounced kink

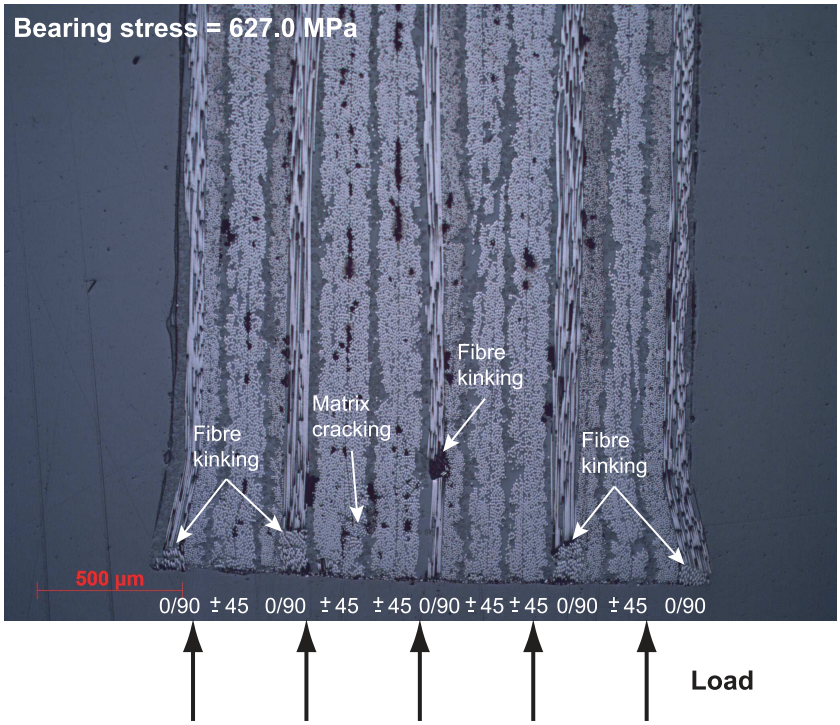

Fig. 4.139. Bearing plane of laminate *DTO160* at the onset of nonlinearity. Magnification factor of 5×.

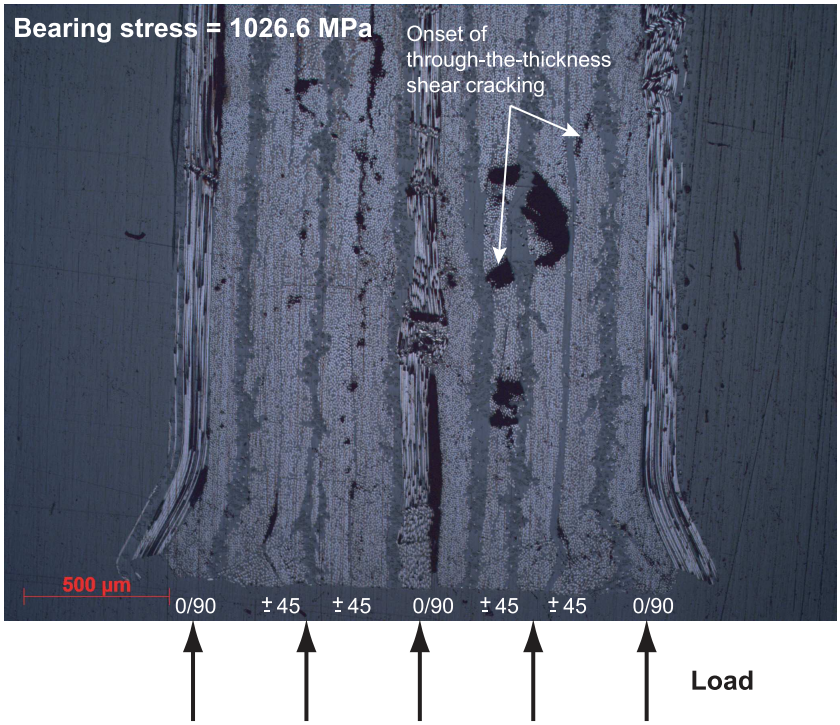

Fig. 4.140. Bearing plane of laminate *DTO240* at the first load drop. Magnification factor of 5×.

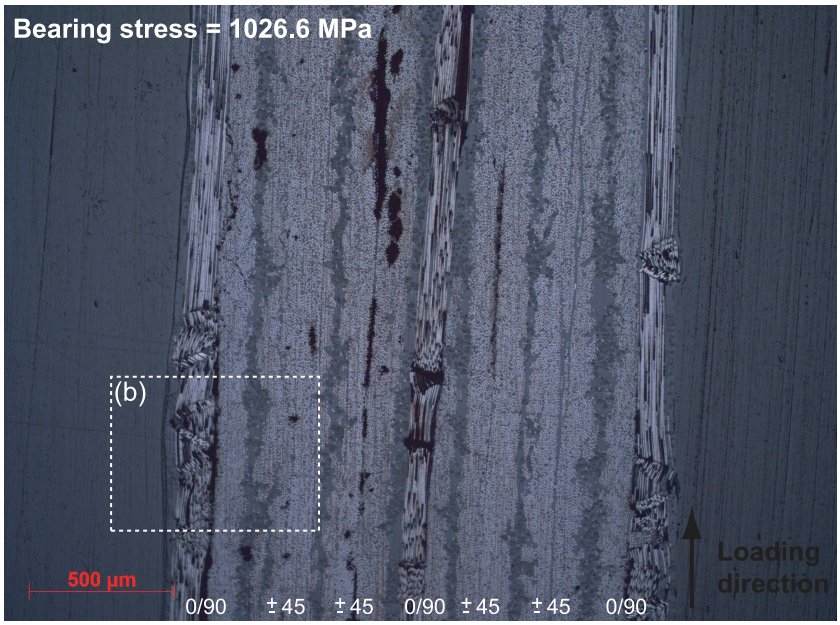

(a) Magnification factor of 5×.

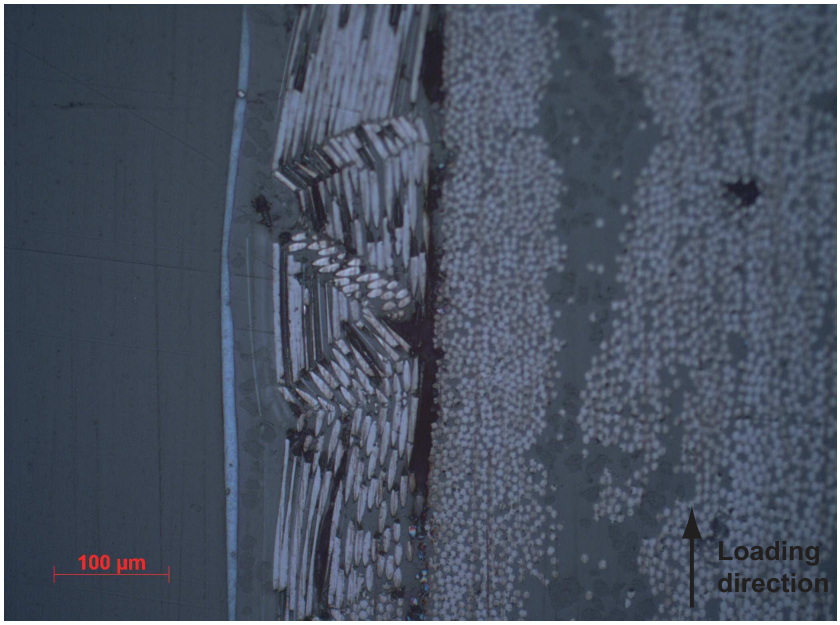

(b) Magnification factor of 20× (detail from (a)).

Fig. 4.141. Bearing plane of laminate *DTO240* at the first load drop at approximately 1.8 mm from the hole edge.

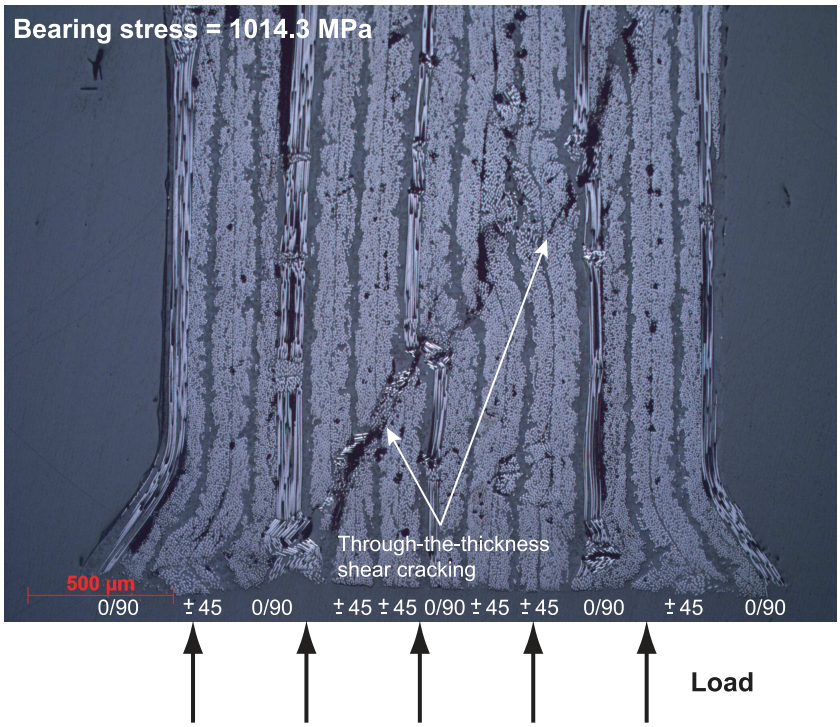

Fig. 4.142. Bearing plane of laminate *DTO160* at the first load drop. Magnification factor of 5×.

bands along the 0° spread-tow yarns not only close to the loading surface but also far from this region, as well as shear-driven fibre fracture (figure 4.144b). Through-the-thickness shear cracking is not limited to the vicinity of the hole edge (figure 4.142), occurring also far from the loading surface (figures 4.143 and 4.144), apparently promoted by the formation of the brittler kink bands in the thinner spread-tow yarns of laminate *DTO160*.

Interestingly, the interaction of the damage mechanisms involved in the failure process of the two laminates affects differently the formation of the through-the-thickness shear cracks. Whereas through-the-thickness shear cracking in laminate *DTO240* occurs gradually due to the propagation of fibre kinking and matrix cracking through the thickness of the laminate (figures 4.138 and 4.140), the suppression of matrix cracking in laminate *DTO160* delays the occurrence of fibre compressive failure, which eventually propagates suddenly in the form of brittler kink bands or shear-driven oblique fracture, inducing quick through-the-thickness shear cracking. However, in spite of the different interactions, the formation of through-the-thickness shear cracking occurs simultaneously in both laminates, leading to the same average bearing stress at the first load drop (table 4.24).

After the first load drop and formation of the first through-the-thickness shear cracks, further loading conducts to additional matrix cracking and fibre kinking, promoting the formation and propagation of the shear cracks along the bearing plane (figures 4.145 to 4.150). At an offset bearing strain of 6%, extensive through-the-thickness shear cracking can be observed in laminate *DTO240*, not only in the vicinity of the hole edge (figure 4.145), but also far from this region (figures 4.146 and 4.147). This indicates that as matrix cracking and fibre kinking grow inside the material, shear cracks form and propagate gradually as a result of their interaction. Propagation of the through-the-thickness shear cracks apparently promotes shear-driven fibre fracture in laminate *DTO240* too (figure 4.146). In laminate *DTO160* (figures 4.148 to 4.150), subsequent loading leads to the propagation of the marked shear cracks formed upon the first load drop, induced by the brittler kink bands and by the shear-driven fibre fractures. Fibre and matrix crushing at the hole edge become more and more important with subsequent loading (e.g. figure 4.148a).

In spite of the differences in the damage morphology of the STF grades, because the governing failure mechanisms are essentially the same, the bearing response is very similar (see figures 4.134 and 4.136 and table 4.24). In fact, after the first load drop, through-the-thickness shear cracking is known to govern the bearing response of composite laminates,

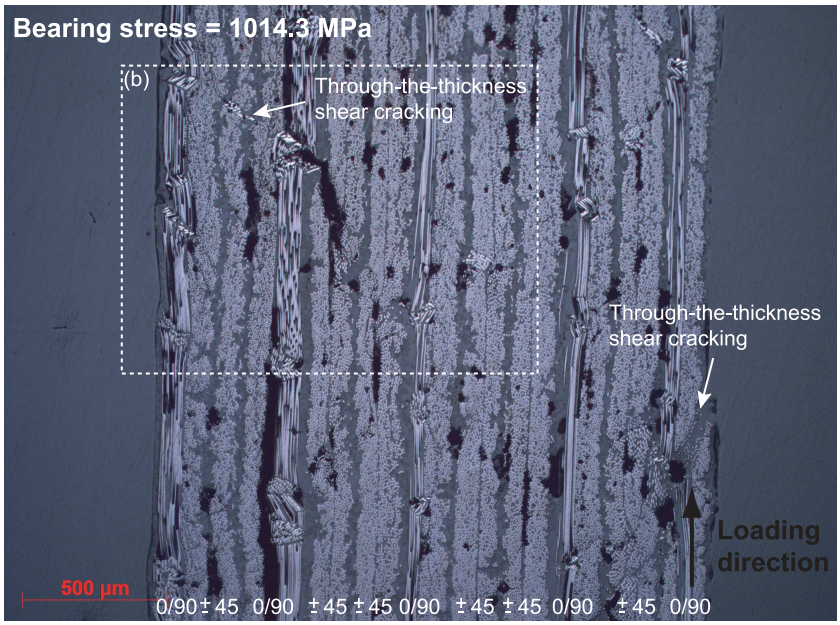

(a) Magnification factor of 5×.

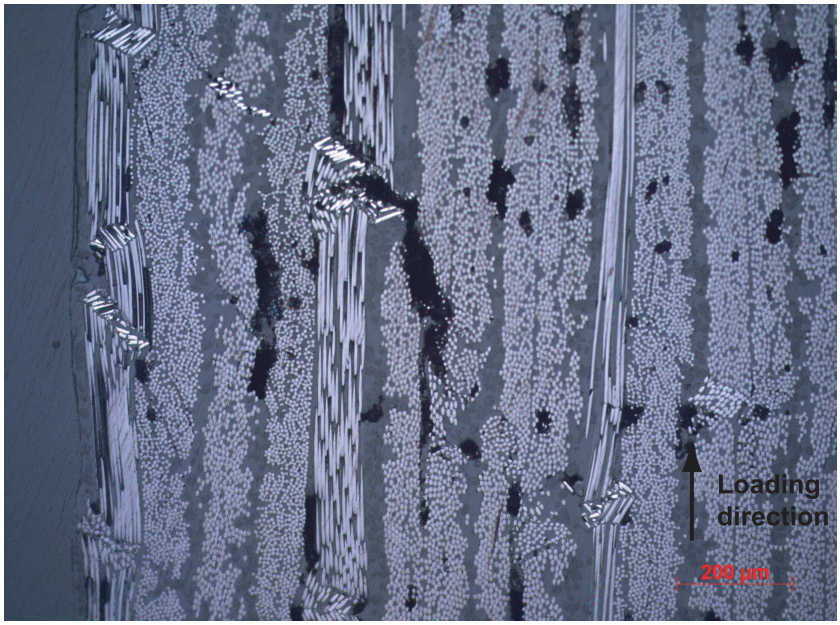

(b) Magnification factor of 10× (detail from (a)).

Fig. 4.143. Bearing plane of laminate *DTO160* at the first load drop at approximately 1.8 mm from the hole edge.

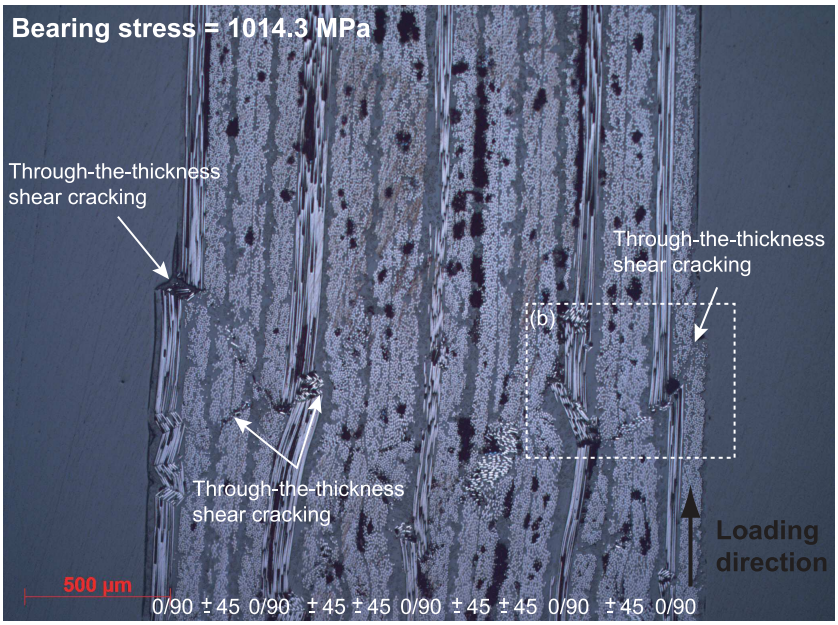

(a) Magnification factor of 5×.

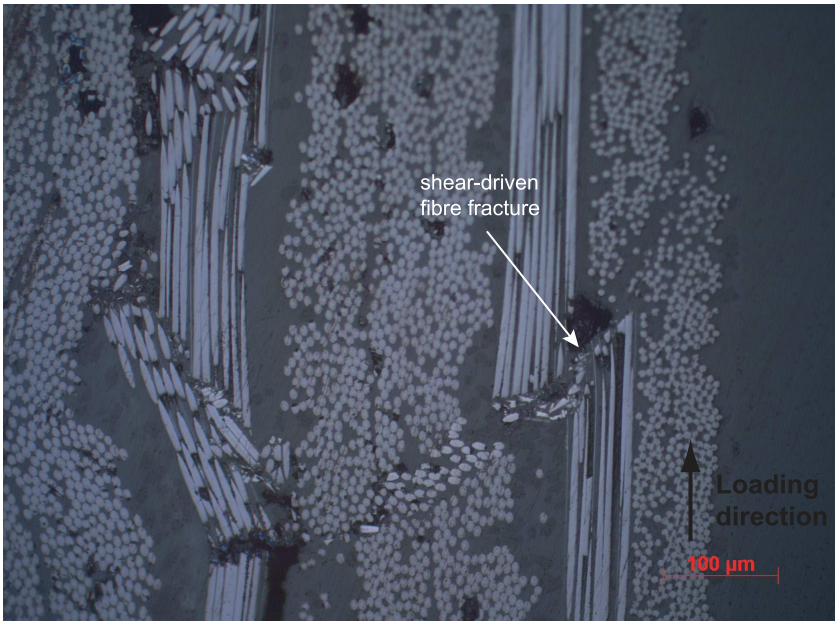

(b) Magnification factor of 20× (detail from (a)).

Fig. 4.144. Bearing plane of laminate *DTO160* at the first load drop at approximately 3.7 mm from the hole edge.

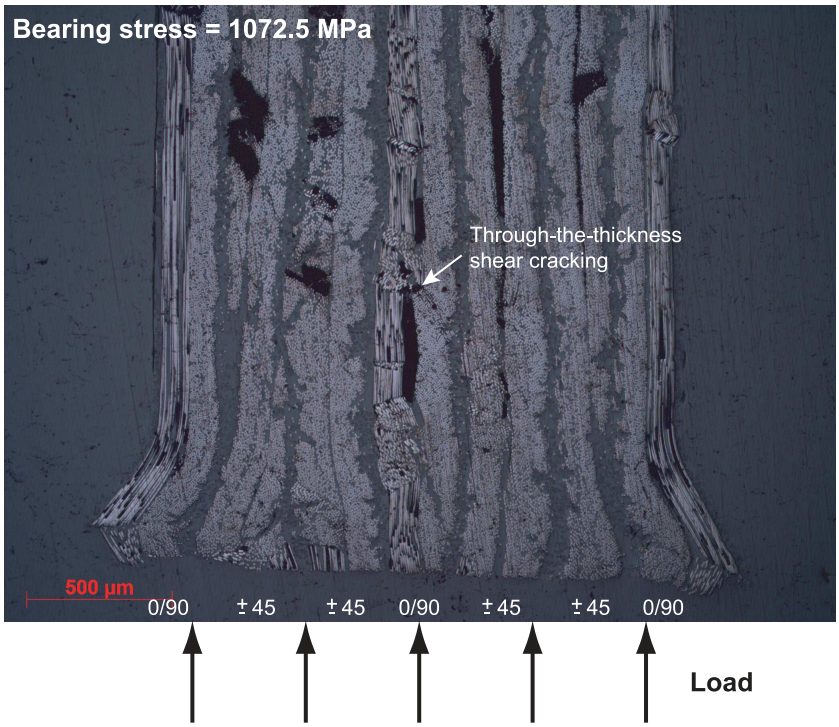

Fig. 4.145. Bearing plane of laminate *DTO240* at an offset bearing strain of 6%. Magnification factor of 5×.

as already discussed elsewhere [235]. Even though the morphology and growth mechanisms of these shear cracks are different in laminates *DTO240* and *DTO160*, their extent is similar, as well as the overall bearing response.

However, it is interesting to note that, before the first load drop, matrix cracking and kink band formation are delayed in laminate *DTO160* (compare figures 4.138 and 4.139), even though their onset occur at approximately the same bearing stress (at the onset of nonlinearity). This delay of damage propagation can be attributed to a thinness (or *in situ*) effect, conducting to the slightly higher bearing stress at an offset bearing strain of 2% of laminate *DTO160* (table 4.24).

Finally, it should be noted that, whereas previous studies [58, 122] have shown that the structural performance of mechanically fastened joints of laminates with thin UD plies can be considerably better than laminates made of low or high grade UD tapes, the same thinness effect was not observed in the present study, in spite of the improved compressive response of the thinner 160 g/m^2 STF (section 4.5.2) and of the corresponding multidirectional laminate (sections 4.5.7, 4.5.9 and 4.5.11). This can be attributed to the local nature of the damage mechanisms induced by bearing loads. If at the coupon level the uniformity of the thinner STFs play an important role in delaying the micro-instabilities that conduct to compressive failure, at the local level of bearing damage the same role is expectably smaller. Moreover, it is important to stress that, in the present study, the thickness of the yarns is not as different as in previous studies [58, 122], and that the yarns of both grades of the STFs were obtained by tow spreading, ensuring a very good homogeneity of the microstructure in spite of the different thicknesses.

Nevertheless, a compressive damage constraining effect promoted by the yarns thinness, as well as a change in the damage morphology were observed in figures 4.138 to 4.150. Hence, it can be argued that, for a wider range of ply thicknesses, the distinct damage morphologies will eventually play a positive role in improving the bearing response of the thin-ply composite, as reported in Refs. [58, 122].

4.6. Concluding remarks

With the aim to study the structural response of aerospace-grade plain weave STFs of different tow thicknesses, an experimental test campaign was carried out which included basic characterisation of the STFs and the detailed assessment

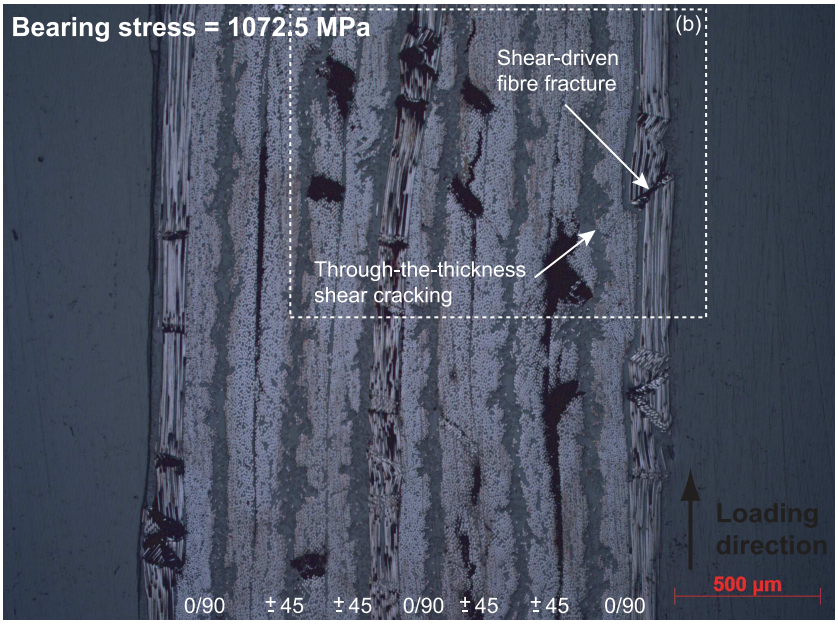

(a) Magnification factor of 5×.

(b) Magnification factor of 10× (detail from (a)).

Fig. 4.146. Bearing plane of laminate *DTO240* at an offset bearing strain of 6% at approximately 1.8 mm from the hole edge.

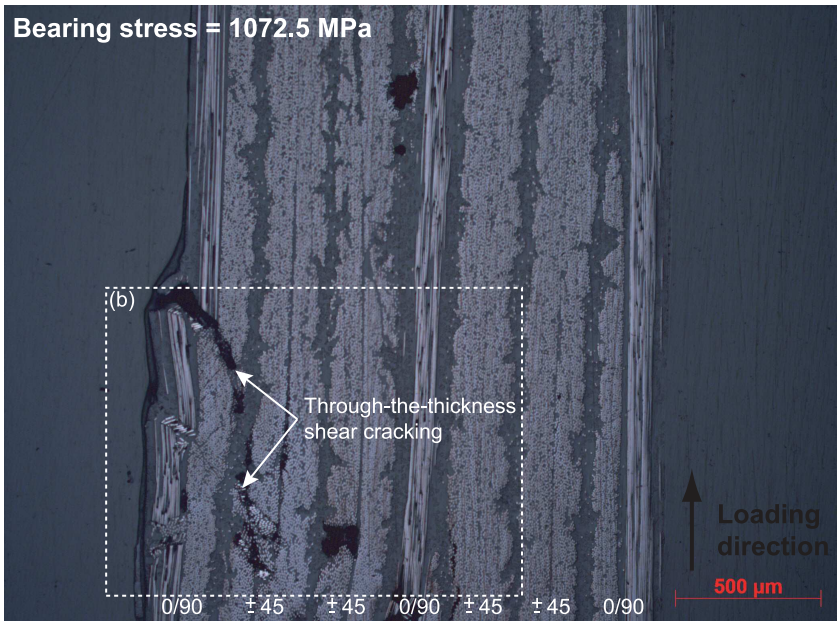

(a) Magnification factor of 5×.

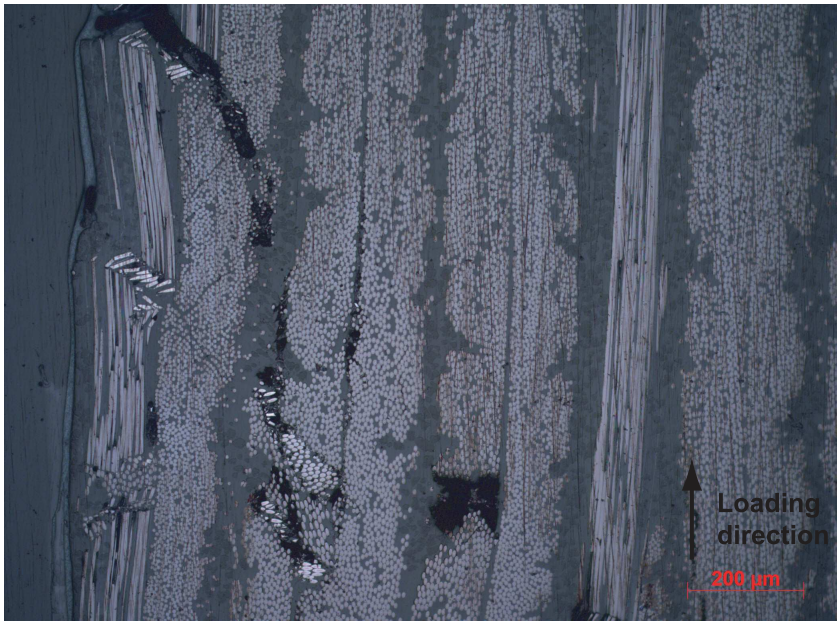

(b) Magnification factor of 10× (detail from (a)).

Fig. 4.147. Bearing plane of laminate *DTO240* at an offset bearing strain of 6% at approximately 3.7 mm from the hole edge.

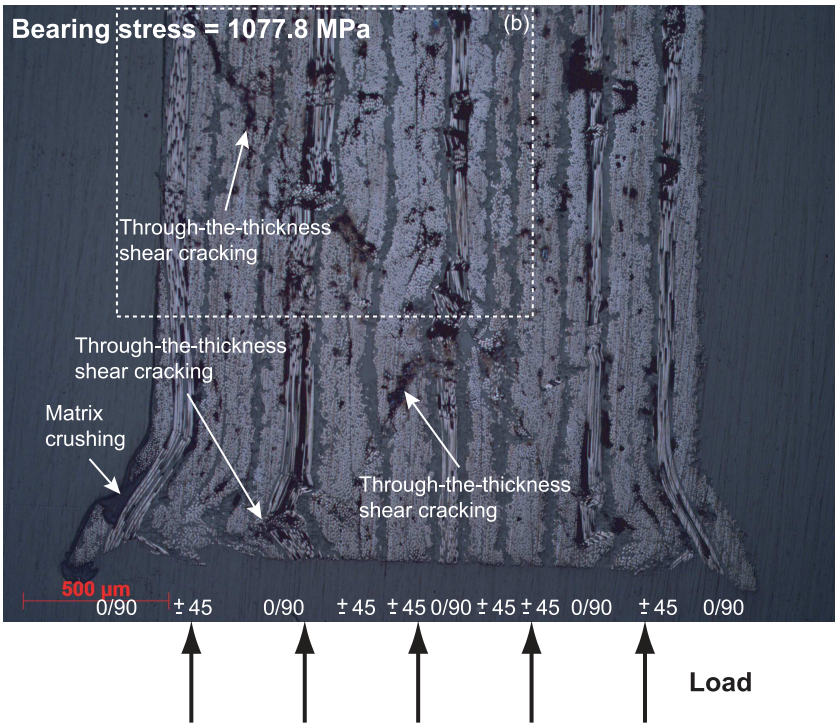

(a) Magnification factor of 5×.

(b) Magnification factor of 10× (detail from (a)).

Fig. 4.148. Bearing plane of laminate *DTO160* at an offset bearing strain of 6%.

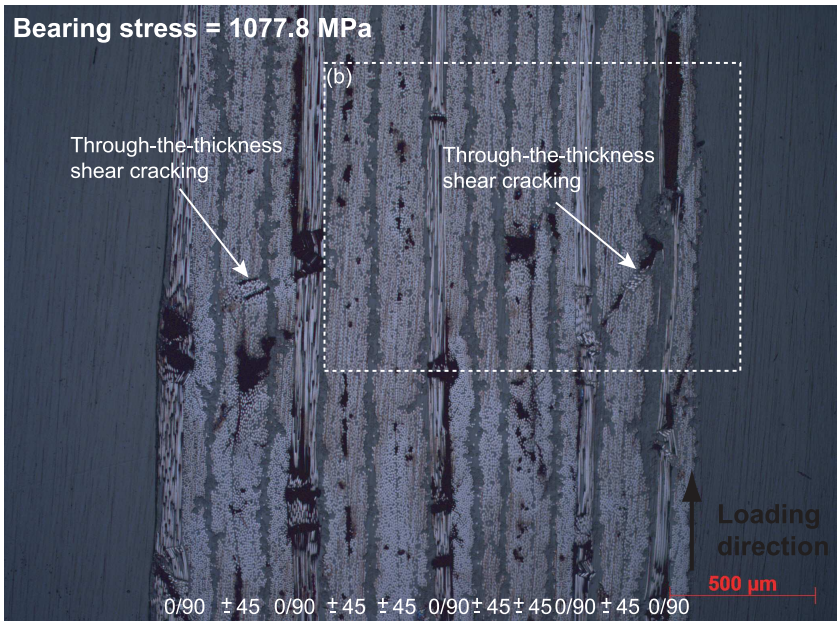

(a) Magnification factor of 5×.

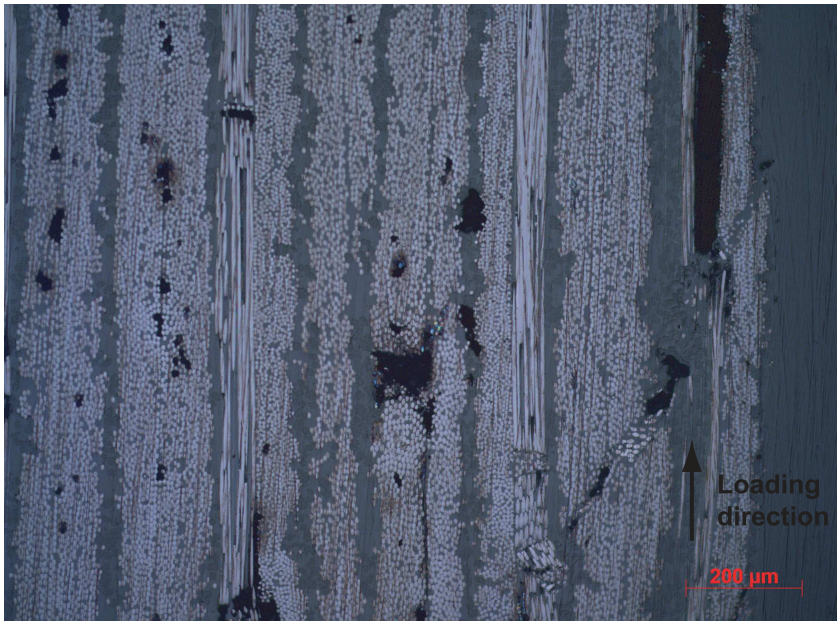

(b) Magnification factor of 10× (detail from (a)).

Fig. 4.149. Bearing plane of laminate *DTO160* at an offset bearing strain of 6% at approximately 1.8 mm from the hole edge.

4.6. Concluding remarks

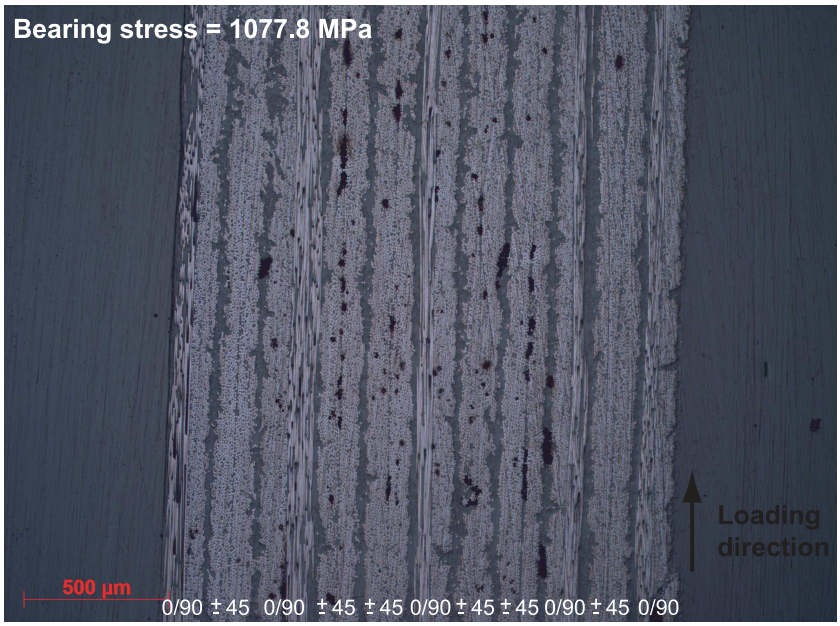

Fig. 4.150. Bearing plane of laminate *DTO160* at an offset bearing strain of 6% at approximately 3.7 mm from the hole edge. Magnification factor of 5×.

of the structural response of laminates based on a baseline of the aeronautical industry.

The thin-ply 160 g/m^2 STF exhibited a tensile strength 7.2% lower than the low-grade 240 g/m^2 STF. Even though ultimate failure of both reinforcement configurations was characterised by a catastrophic fibre-dominated failure mode, the latter exhibited delamination between the STF layers and transverse and longitudinal split cracking of the spread-tow yarns. On the other hand, the thin-ply 160 g/m^2 STF showed evidence of transverse and longitudinal split cracking of the spread-tow yarns, but the extent of gauge section delamination was reduced.

Previous work [58] has shown that the longitudinal and transverse tensile strengths of UD tapes is not affected by the material grade. However, the tensile unnotched strength of multidirectional laminates with thinner plies is known to be higher than the tensile unnotched strength of laminates with thicker plies, or thicker ply blocks [53, 58, 121, 122, 171]. In fact, the extent of subcritical damage in the thick-ply laminates is generally associated with earlier failure of the multidirectional composite. However, apparently due to the woven reinforcement architecture, the ability of the 240 g/m^2 STF to develop internal damage in the form of split cracking of the spread-tow yarns before ultimate failure relaxes the fibre strains, delaying longitudinal fracture.

In compression, the trend changes dramatically. The thinner 160 g/m^2 STF exhibits a compressive unnotched strength 16.2% higher than the 240 g/m^2 STF, in agreement with what has been observed in UD tapes [58]. This improved behaviour can be attributed to the uniformity of the thinner reinforcement architecture of the 80 g/m^2 individual spread-tow yarns of the 160 g/m^2 STF, including lower fibre waviness and smaller crimp angles, which delays micro-instabilities in the fibre direction and, consequently, improves the longitudinal strength.

To understand the mechanical behaviour of the plain weave STFs under study subjected to combined stresses, off-axis compression tests were performed in addition to longitudinal compression. Interestingly, the axial compressive strength of the 15° off-axis specimens was virtually the same, with no significant difference between the mechanical response and failure modes of the 240 g/m^2 and 160 g/m^2 STFs. However, the thinner 160 g/m^2 STF exhibited a 30° off-axis axial compressive strength 16.9% higher than the 240 g/m^2 STF, a difference in the range of that observed for the longitudinal compressive strength. The 240 g/m^2 STF exhibited higher axial strain-to-failure than the 160 g/m^2 STF. Moreover, the latter was characterised by a slightly brittler failure mode, even though no relevant difference in the sequence and extent of the failure mechanisms was observed.

An approximately constant value of the in-plane shear stress at failure was obtained regardless of the applied multiaxial stress state. A maximum stress failure criterion was therefore assumed as a suitable model to represent the failure envelopes of the STFs studied in the present work in the σ_{11}–σ_{12} stress space. Consequently, the obtained off-axis data could be used to estimate the in-plane shear strengths of the STFs. Following this approach, it was estimated that the 160 g/m^2 STF has an in-plane shear strength 5.6% higher than the 240 g/m^2 STF. The particular meso-structure of the textile composites, which resembles a cross-ply laminate, apparently promotes a thinness effect on the in-plane shear strength, which can be attributed to the ability of the thinner spread-tow yarns to suppress microcracking caused by shear loading (*in situ* effect [81]). The slightly lower nonlinear strain-to-failure is a result of this damage suppression capability.

To obtain the mode I tensile and compressive $\mathcal{R}$-curves associated with longitudinal intralaminar fracture, DENT and DENC tests were performed, respectively. As expected, both DENT and DENC specimen configurations had positive geometry, i.e. as the specimen's size increased, the mean ultimate remote stress decreased, a requirement for the determination of $\mathcal{R}$-curves using the size effect law.

As expected, for the same specimen size, the 240 g/m^2 STF exhibited higher tensile notched strengths than the 160 g/m^2 STF, confirming the better notched response of the low-grade STF. The superior notched response of the 240 g/m^2 STF was attributed to the improved blunting effect of the damage mechanisms that precede intralaminar fracture, in particular longitudinal split cracking, potentiated by the higher interlaminar stresses at the interfaces of the thicker 0° spread-tow yarns.

The mode I tensile $\mathcal{R}$-curve of the low-grade STF was characterised, respectively, by a length of the FPZ and a steady-state value of the fracture toughness 1.51 times larger and 1.63 times higher than the thin-ply STF, a result of the superior tensile notched response of the low-grade STF. However, this improved fracture toughness and notched response of the low-grade STF was attributed to an improved blunting effect of damage mechanisms such as longitudinal split cracking. No intrinsically higher fracture toughness of the thicker spread-tow yarns was observed. In fact, the extent of blunting damage mechanisms in the two STFs, which alters significantly the stress distribution in the vicinity of the stress concentration points, was substantially different, and clear, self-similar intralaminar fracture has not occurred. Nonetheless, these results demonstrate that promoting subcritical damage mechanisms, in particular longitudinal fibre-matrix splitting, by increasing the thickness (or grade) of the 0° yarns has the potential to improve substantially the fracture resistance and notched response of spread-tow laminates, while avoiding more detrimental interlaminar damage and matrix cracking.

In compression, slightly higher notched strengths were obtained for the smaller specimens of the 240 g/m^2 STF. However, as the size of the specimens increased, the compressive notched strengths tended to the same values. This was translated into a steeper strength reduction, or steeper size effect law, for the 240 g/m^2 STF. Consequently, the 160 g/m^2 STF exhibited a length of the FPZ and a steady-state value of the fracture toughness 42.9% larger and 16.2% higher than the 240 g/m^2 STF, respectively, despite the very similar notched response of both STFs. In fact, the results obtained suggested that the compressive notched strengths of the STFs should tend to the same value if the size of the specimens keeps increasing. In such case, a more similar size effect law would be expected. It is therefore suggested that characterisation of the compressive notched response of the STFs studied in the present work must rely on testing of larger geometrically-similar DENC specimens. This shall certainly be the subject of future work.

After characterisation of the STFs, two multidirectional laminates produced from the STFs based on a damage tolerance optimised baseline laminate for aeronautical applications were tested to address the effect of tow grade on the structural response of textile composites. As expected, and unlike the results for the UD unnotched coupons, the thin-ply laminate exhibited a tensile unnotched strength 13.9% higher than the low-grade laminate.

This improved unnotched response, already observed in previous work [53, 58, 122, 171], was attributed to the damage suppression capability of laminates made of thinner reinforcements, delaying ultimate failure to values closer to the strength of the reinforcing layers aligned with the loading direction. In fact, prior to ultimate failure, transverse matrix cracking or fibre-matrix splitting did not occur in the thin-ply laminate. On the other hand, in the low-grade laminate, extensive free-edge surface transverse cracking and longitudinal splitting along the 0° spread-tow yarns tangent to the

free edges were observed, due to a higher susceptibility of the low-grade STFs to fibre-matrix splitting than the thinner 160 g/m^2 STF, not only along the longitudinal spread-tow yarns, but also along the transverse yarns. Moreover, in the low-grade laminate not only the extent of subcritical damage before ultimate failure is remarkable, but it also occurs and propagates at applied remote stresses considerably below the maximum stress. By precluding such damage mechanisms, the thin-ply laminate was able to sustain reasonably higher applied loads. Interestingly, gauge section delamination was not observed in both laminates.

In compression, following the trend of the UD STFs, the thin-ply laminate, produced from 160 g/m^2 STFs, exhibits a compressive unnotched strength 17.7% higher than the low-grade STF laminate, which can be attributed to the uniformity of the thinner reinforcement architecture of the ultra-thin 160 g/m^2 STFs, characterised by intrinsically higher longitudinal strength, as discussed before.

It is noted, though, that the variation in the test results of the low-grade STF laminate is atypically high. Since no problem was observed in the loading setup, and no uncharacteristic compressive response or failure mode was detected on the specimens of laminate *DTO240*, the variation of the ultimate failure stress should also be attributed to the less uniform reinforcement configuration of laminate *DTO240*. In fact, when a reinforcement is less uniform, the susceptibility to variations of its uniformity (fibre waviness and crimp angle) is expected to increase, resulting in higher variations of the mechanical response too. Hence, the lower uniformity of the structure of the low-grade STF apparently resulted not only on lower compressive strengths but also on higher variability of the respective results. A similar effect of the uniformity of the microstructure on the compressive strength and on its variability has also been observed by Amacher et al. [37, 58] for UD tapes of different grades.

To study the notched response of the multidirectional STF laminates, the evolution of damage mechanisms on notched coupons with different notch configurations and subjected to tensile and compressive loading scenarios was also investigated in the present study. In the case of centre-notched specimens loaded in tension, different damage morphologies were observed in the thin-ply and low-grade STF laminates. In the latter, surface discrete intralaminar damage from the notch tips appears reasonably before the peak remote stress, but does not penetrate stably along the ligament width. Before unstable intralaminar fracture, surface transverse split cracks formed in the 90° spread-tow yarns, while surface longitudinal splitting in the vicinity of the notch tips blunted the strain concentration. In the thin-ply STF laminate, surface discrete intralaminar damage from the notch tips only started near the peak remote stress, propagating quickly across the width, along the off-axis directions.

Modifications of the longitudinal strain field indicated the occurrence of internal longitudinal split cracking tangent to the notch tips in both laminates. In the low-grade STF laminate, this damage mechanism had a strong blunting effect, preventing intralaminar damage growth until catastrophic failure of the 0° spread-tow yarns. In the thin-ply laminate, on the other hand, internal longitudinal split cracking did not prevent the occurrence of discrete intralaminar damage growth, with catastrophic failure of the 0° spread-tow yarns soon after the onset of intralaminar damage propagation from the notch tips.

Interestingly, the tensile centre-notched strengths of the thin-ply and low-grade STF laminates were virtually the same, in spite of the differences in the morphology and extent of the failure mechanisms involved in the fracture process. The similarity of the notched responses can be attributed to the development of internal longitudinal split cracking tangent to the notch tips before ultimate failure of both laminates, even though, the susceptibility of the thicker spread-tow yarns of the low-grade laminate to develop early subcritical damage results in a diffuse failure mode due to the propagation of transverse and longitudinal split cracking.

The thin-ply laminate prevented, to some extent, the occurrence of diffuse damage, while providing sufficient internal blunting mechanisms that delayed ultimate intralaminar fracture. The ability to preclude transverse damage mechanisms is also believed to play an important role in delaying ultimate failure, because the extent of blunting mechanisms such as longitudinal split cracking was noticeably lower than in the low-grade laminate. It is noted that similar tensile centre-notched strengths for thin-ply laminates with and without ply blocking were already obtained in previous work [122].

In compression, propagation of discrete damage from the notch tips started early before ultimate failure in both laminates. However, stable damage growth was confined to the vicinity of the notch tips. Unstable propagation across the ligament width occurred upon final failure.

Following the trends observed for the smooth coupons, the laminate made of thin-ply 160 g/m^2 STFs exhibited a brittler failure mode, where diffuse damage mechanisms, such as transverse and split cracking and interlaminar damage, were absent, resulting in an improved compressive notched response. A compressive centre-notched strength 10.3% higher than the strength of the laminate made of low-grade 240 g/m^2 STFs was obtained.

It is interesting to note that, whereas subcritical damage growth acts as a blunting mechanism in tension, reducing the stress concentration and delaying unstable intralaminar damage propagation, in compression it seems to promote early unstable fracture of the longitudinal spread-tow yarns. Assuming that fibre kinking is the critical failure mechanism that, upon unstable growth, conducts to ultimate compressive failure, the growth of subcritical damage, which is generally matrix dominated, may result in an early loss of the lateral support provided to the highly compressed fibres, conducting to premature compressive failure. In the low-grade laminate, subcritical damage promoted premature kinking of small sublaminates, connected by diffuse interlaminar and intralaminar damage mechanisms. However, precluding the occurrence of subcritical damage can delay compressive failure until a kink band is formed across the thickness of the laminate, as observed in the thin-ply laminate, resulting in an improved compressive response.

In the case of open-hole specimens loaded in tension, a size effect on the notched strength was observed in both laminates. As the hole diameter increased from 2 mm to 5 mm (with constant width-to-hole diameter ratio), the tensile strength of the open-hole specimens decreased. However, the strength reduction in the low-grade laminate was marginal (in the range of 1.4%, below the tests scatter), whereas in the thin-ply laminate it was in the range of 7.3%.

This size effect can be attributed to the relative size of the damage process zone in the vicinity of the notch with respect to the characteristic dimensions of the test coupons. In general, as the characteristic dimensions become larger, the relative size of the damage process zone becomes smaller, reducing the blunting effect and conducting to early coupon failure.

In the low-grade laminate, prior to ultimate failure, a relatively large damage process zone was formed, comprising either longitudinal splitting or diffuse transverse intralaminar cracking. Failure was characterised by pull-out of the spread-tow yarns, without a clear fracture plane. In addition, large split cracks in the longitudinal and off-axis spread-tow yarns and delamination between STF layers across the ligament width could be observed. The similar diffuse damage mechanisms that propagated independently of the coupon size resulted in a similar blunting effect in the vicinity of the open holes, conducting to the marginal difference between the open-hole tensile strengths of the small and large coupons.

The thin-ply laminate, on the other hand, exhibited a brittler failure mode, characterised by intralaminar fracture ahead of the hole boundary along the ligament section. As usual, as the coupon size increased, the relative size of the damage process zone became smaller, and the strength decreased.

Comparing the two laminates, it is interesting to note that, for the specimens with a hole diameter of 2 mm, the thin-ply laminate exhibited an ultimate remote stress 4.9% higher than the low-grade laminate. On the other hand, the ultimate remote stress of the specimens with a hole diameter of 5 mm was virtually the same (it differed by just 1.4%).

In the specimens with a hole diameter of 2 mm, the larger extent of diffuse damage in the low-grade laminate, in an initial stage, blunted the notch, but, after extensive growth, it precipitated early failure, either due to overloading of the longitudinal spread-tow yarns or due to local stress concentrations caused by the subcritical damage mechanisms adjacent to the longitudinal spread-tow yarns. In the thin-ply laminate, because the ligament section is sufficiently small, the lower extent of diffuse damage was enough to effectively blunt the notch, without precipitating early failure of the longitudinal spread-tow yarns as in the low-grade laminate. These results suggest that, for small-notch coupons, the structural response tends to the unnotched behaviour.

4.6. Concluding remarks

In the specimens with a hole diameter of 5 mm, the relatively smaller damage process zone exhibited by the thin-ply laminate resulted in a conventional size effect, characterised by a decrease of its strength, whereas the open-hole tensile strength of the low-grade laminate was practically unchanged. Nevertheless, the strength of both laminates is still very similar. It can be assumed, though, that as the coupon size increases further the tensile notched strength of the thin-ply laminate will keep decreasing faster than the low-grade laminate, whose tensile notched strength is expected to become higher than the tensile notched strength of the thin-ply laminate.

Following the trends observed for the compressive unnotched and centre-notched strengths, the thin-ply laminate exhibited an improved compressive notched response compared with the low-grade laminate, with an open-hole compressive strength 7.4% higher than the latter. As suggested before, the brittler failure mode exhibited by the thin-ply laminate, where diffuse damage mechanisms, such as transverse and split cracking, are absent, provides an improved compressive response, either or not in the presence of stress concentrations.

In order to investigate the effect of the yarn thickness on the structural performance of the STF laminates, bolt-bearing tests were performed. A similar bearing response was obtained for both laminates. The thin-ply STF laminate exhibited a slightly higher resistance to the propagation of subcritical damage mechanisms at the initial stages of permanent damage, but the resistance to severe damage growth (first load drop) and the maximum load-carrying capacity (maximum bearing stress) of both laminates was practically the same.

It is interesting to note that, whereas previous studies [58, 122] have shown that the structural performance of mechanically fastened joints of laminates with thin UD plies can be considerably better than laminates made of low or high grade UD tapes, the same thinness effect was not observed in the present study, in spite of the improved compressive response of the thinner 160 g/m^2 STF and of the corresponding multidirectional laminate. This can be attributed to the local nature of the damage mechanisms induced by bearing loads. If at the coupon level the uniformity of the thinner STFs play an important role in delaying the micro-instabilities that conduct to compressive failure, at the local level of bearing damage the same role is expectably smaller. Moreover, it is important to stress that, in the present study, the thickness of the yarns is not as different as in previous studies [58, 122], and that the yarns of both grades of the STFs were obtained by tow spreading, ensuring a very good homogeneity of the microstructure in spite of the different thicknesses. Nevertheless, a compressive damage constraining effect, promoted by the yarns thinness, was observed. In addition, a change in the damage morphology from a "softer" longitudinal compressive failure mode, characterised by the formation of kink bands driven by fibre micro-instabilities, to a "brittler" longitudinal compressive failure mode, with more pronounced kink bands along the 0° spread-tow yarns and shear-driven fibre fracture, was evident when decreasing the ply thickness. Hence, it can be argued that, for a wider range of ply thicknesses, the distinct damage morphologies will eventually play a positive role in improving the bearing response of the thin-ply composite, as reported in Refs. [58, 122].

This experimental programme has shown that, in general, the ply thinness effect observed in laminates produced from UD tapes [53, 58, 122] is also present in spread-tow textile composites. In spite of an unexpectedly lower tensile longitudinal strength of the UD fabric, the ability of the thinner STF to delay or suppress subcritical damage growth resulted in an improved tensile unnotched strength when incorporated in a structural multidirectional laminate. However, suppressing subcritical damage mechanisms reduced the blunting effect in the presence of stress concentrations, resulting in premature failure of the notched configurations loaded in tension. This was particularly evident in the case of the UD STF laminates used for characterisation of the mode I tensile $\mathcal{R}$-curves of the STFs. In structural multidirectional laminates, the effect of subcritical damage suppression on the notched strengths was not so evident, on one hand due to excessive subcritical damage growth in the low-grade STF laminate, and, on the other hand, due to an effective blunting effect in the thin-ply STF laminate promoted by the selected lay-up.

In compression, due to the positive effect of the uniformity of the crimp configuration and homogeneity of the individual yarns, which benefit from a thinner configuration, a substantial improvement of the compressive response of the thin-ply configuration over a low-grade configuration was observed, demonstrating the merit of ultra-thin reinforcements in improving the compressive response of composite laminates. This positive effect is not restricted to unnotched coupons, but it was also observed in the notched configurations. In fact, subcritical damage growth tended to promote early unstable

fracture of the longitudinal spread-tow yarns due to an early loss of the lateral support provided to the highly compressed fibres, conducting to premature compressive failure of the thicker configurations.

Chapter 5

Effect of 0° ply blocking on the structural response of aerospace-grade non-crimp fabric thin-ply laminates

The enhanced mechanical performance of thin-ply laminates is mainly due to the ability to delay the onset of damage typically observed in composite materials. However, the delay of damage onset has a negative impact in notched structures loaded in tension, since it inhibits local stress redistribution at the vicinity of the notch. In this chapter, a strategy to improve the notched response of structural laminates is proposed. To keep the occurrence of detrimental subcritical damage mechanisms, such as transverse cracking and delamination, to a minimum, spread-tow thin plies were chosen to design a structural laminate based on a baseline of the aeronautical industry. Due to the intrinsic design advantages, thin-ply NCF layers were employed. In order to improve local blunting near geometrical stress concentrations, such as holes or through-the-thickness cracks, a detailed study on the effect of 0° ply blocking is carried out, with particular emphasis on the blunting mechanisms and notched response.

5.1. Introduction

Laminates with sufficiently thin plies are known to fail by fibre fracture, showing extensive pull-out in the smaller specimens or a brittle fracture in the larger ones, and the strength decreases with increasing hole size [144, 163]. However, laminates with sufficiently thick plies fail by delamination, and the strength increases with increasing hole diameter [144, 163]. Laminates with intermediate ply thickness show an intermediate response; in some cases, a constant strength over a range of hole sizes may be achieved [144, 163].

The different trends observed for the hole size effect are explained by the role of subcritical damage in the laminates' failure mode [144, 163], in particular delamination [144]. In other words, even though conventional laminates show similar subcritical damage modes, their extent will determine the ultimate failure stress and failure mechanism.

The enhanced mechanical performance of thin-ply laminates is mainly due to the ability to delay the onset of damage typically observed in composite materials. However, the delay of damage onset has a negative impact in notched structures loaded in tension [58], since it inhibits local stress redistribution at the vicinity of the notch. Studies addressing this disadvantage, which has been pointed out as one of the main obstacles to the introduction of thin plies in a large scale, and ways of avoiding it without compromising the advantages of thin plies, namely the enhanced unnotched strengths and potential for improved compressive notched strengths, are, unfortunately, scarce.

Based on the previous observations, a strategy to improve the notched response of structural laminates is proposed in this chapter. Transverse cracking is known to promote premature failure due to stress concentrations on the load carrying

plies. In addition, delamination may conduct to the loss of structural integrity, particularly in compression. Hence, to keep the occurrence of these detrimental subcritical damage mechanisms to a minimum, spread-tow thin plies were chosen to design a structural laminate based on a baseline of the aeronautical industry. In particular, due to the intrinsic design advantages, thin-ply non-crimp fabric (NCF) layers were employed (section 2.2.3). To promote local blunting near geometrical stress concentrations, such as holes or through-the-thickness cracks, a detailed study on the effect of 0° ply blocking on the structural behaviour of this aerospace-grade laminate is carried out, with particular emphasis on the blunting mechanisms (split cracking and local delamination) and notched response. Focus is placed on the understanding of the effect of the number of 0° plies, their thickness and position in the laminate. To accomplish this objective, a detailed experimental programme was carried out on two stacking sequences, with dispersed and blocked 0° plies. Laminate strength and fracture mechanics properties were evaluated, in both tension and compression, and structural tests, essential for laminate scrutiny in the aeronautical industry, were carried out to understand the effects of laminate design on the complex behaviour of structural details.

5.2. Material selection and manufacturing

Chomarat's T700GC/M21 C-Ply™ bi-angle NCFs, with an areal weight of 75 g/m^2 per layer, were used in the present experimental campaign. Each layer is made of 12k tow-spread T700GC carbon fibres, pre-plied and mechanically sewn with fine stitching yarns, forming bi-axial NCFs. Two configurations are used in the present work, (0/45) and (0/−45) bi-angle layers. Both configurations are pre-impregnated with Hexcel's M21 toughened epoxy resin. Table 4.1 shows the elastic properties of T700GC/M21 carbon/epoxy, where E_{11T} and E_{11C} are respectively the longitudinal Young's moduli in tension and compression, E_{22} is the transverse Young's modulus, ν_{12} and ν_{23} are the in-plane and out-of-plane Poisson's coefficients, and G_{12} is the shear modulus.

It is noted that the properties presented in table 4.1 were determined from *prepregs* with an areal weight of 268 g/m^2 (cured ply thickness of 0.262 mm) [88, 259]. Nevertheless, Amacher et al. [58] showed that the effect of ply areal weight on the basic unidirectional (UD) properties of composite materials is negligible, except on the longitudinal compressive strength. Assuming that stitching does not affect the elastic behaviour, it is reasonable to represent the individual UD plies of the NCF layers using the properties presented in table 4.1.

A stacking sequence of bi-angle NCFs was defined based on a damage tolerance optimised baseline laminate for aeronautical applications, with *dispersed* 0° plies. An alternative stacking sequence was also defined, but with *blocked* 0° plies. Table 5.1 shows the stacking sequences definition, where n is the number of repetitions, and the 0° fibre orientation is coincident with the loading direction. Both stacking sequences are oriented, 0°-dominated (*hard laminates*), and, following standard design rules, they are both balanced and symmetric. Due to the latter restriction — laminate symmetry — both C-Ply™ NCF configurations had to be used to reproduce the stacking sequences in table 5.1. Table 5.2 shows the C-Ply™ NCF lay-up sequences.

In total, four laminates were investigated, with $n = 1$ (baseline) for tensile tests and $n = 2$ for compressive tests. The choice for thicker laminates for the compressive tests was made to avoid buckling on end-loading experimental setups. The baseline ($n = 1$) laminates have a total of 12 C-Ply™ NCF layers and a nominal laminate thickness of 1.8 mm. The thicker ($n = 2$) laminates, for compression testing, have 24 C-Ply™ NCF layers and a nominal laminate thickness of 3.6 mm.

Thanks to the pre-plied off-axis plies, these laminates were manufactured by two-axis hand lay-up (in the 0° and 90° directions), reducing substantially the time spent with the lay-up process. They were then prepared for curing in a vacuum

Table 5.1
Stacking sequence definitions.

Laminate ID	Stacking sequence
dispersed	$[(90/-45)/(0/45)/(0/45)/(90/-45)/(0/45)/(0/-45)]_{nS}$
blocked	$[(90/-45)/(45/0)/(0/45)/(90/-45)/(45/0)/(0/-45)]_{nS}$

Table 5.2
C-Ply™ NCF lay-up sequences.

Laminate ID	NCF lay-up sequence[†‡]
dispersed	$(A(90)/A/A/A(90)/A/B)_n//(-A/-B/-B(90)/-B/-B/-B(90))_n$
blocked	$(A(90)/-B/A/A(90)/-B/B)_n//(-A/A/-B(90)/-B/A/-B(90))_n$

[†] A: (0/45) NCF
[†] A(90): (0/45) NCF rotated 90°: (90/−45)
[†] -A: inverted (0/45) NCF: (−45/0)
[†] -A(90): inverted (0/45) NCF rotated 90°: (45/90)
[‡] B: (0/−45) NCF
[‡] B(90): (0/−45) NCF rotated 90°: (90/45)
[‡] -B: inverted (0/−45) NCF: (45/0)
[‡] -B(90): inverted (0/−45) NCF rotated 90°: (−45/90)

bag and cured in an autoclave. The autoclave cure cycle was defined by setting a heat-up rate of 2°C/minute from room temperature to 180°C, holding at 180°C for 120 minutes and cooling down at a rate of 2°C/minute. A gauge autoclave pressure of 4 bar was applied throughout the cure cycle. A total of 11 square plates of each baseline laminate were produced, with in-plane dimensions of 300×300 mm^2 (4 plates) and 400×400 mm^2 (7 plates), as well as one square plate of each thick laminate, with in-plane dimensions of 400×400 mm^2. After curing, each plate was cut to the specimens' nominal dimensions using a diamond-coated disk.

5.3. Experimental test programme

5.3.1. Laminate mode I tensile crack resistance curve

The experimental characterisation of several composite materials and different lay-ups in the past has shown that composite laminates exhibit a fracture resistance behaviour resembling an $\mathcal{R}$-curve type of response, whose damage growth resistance was primarily due to (i) load redistribution resulting from microcracking, splitting and/or delamination, which relieve the stress concentration and delays fracture to higher applied loads [182, 194–196], and (ii) bridging by the intact fibres of the plies that are adjacent to the principal load-carrying plies with broken fibres [194, 195]. Fracture characterisation is, therefore, essential in understanding size effects [131, 164, 165] in the notched response of composite laminates, in assessing the damage tolerance of composite structures [65, 185–188], and in the definition of the softening laws used in recent computational analysis models [106, 108, 189, 190] and in establishing the energy equilibrium equations used in closed-form solutions [181, 182] that predict the ultimate strength of composite structures.

In the present work, the laminate mode I tensile crack resistance curve ($\mathcal{R}$-curve) of both *dispersed* and *blocked* laminates is determined using the methodology recently proposed by Catalanotti et al. [65] based on the size effect law [209]. Taking x and y as the preferred axes of the material (figure 4.5), for a two-dimensional orthotropic body the energy release rate (ERR) in mode I, $\mathcal{G}_I$, for a crack propagating in the y-direction is given by equation (4.5). Using the orthotropy rescaling technique [269, 270], the Stress Intensity Factor (SIF), $\mathcal{K}_I$, can be written in the generic shown in equation (4.9).

Using equation (4.9) in equation (4.5), and defining $\alpha_0 = a_0/w$ as the initial value of the shape parameter (where a_0 is the initial crack length and w is the characteristic dimension), an expression for the driving force curves, $\mathcal{G}_I$, is derived (equation (4.10)). At the ultimate remote stress, $\bar{\sigma}^{\infty}$, the driving force curves are tangent to the $\mathcal{R}$-curve, and an expression for $\mathcal{R}(\Delta a)$ can be obtained (equation (4.11)). Taking into account that, by definition, the $\mathcal{R}$-curve is size independent (i.e., $\partial\mathcal{R}/\partial w = 0$), and assuming that *geometrically similar specimens* (α_0 and ϖ independent of w, where $\varpi = w/l$ and l is half gauge length, $l = L/2$) of different sizes with *positive geometry* (where the correction factor κ is an increasing function of the crack length a) are used to calibrate the size effect law, $\bar{\sigma}^{\infty} = \bar{\sigma}^{\infty}(w)$, the $\mathcal{R}$-curve, $\mathcal{R}(\Delta a)$, can be obtained.

Following Catalanotti et al. [65], scaled Double Edge-Notched Tension (DENT) specimens were tested (figure 5.1). Table 5.3 shows the size effect DENT test matrix, where W is the total specimen width, L_s is the total specimen length, L is the gauge length (free length between grips), and a_0 is the machined edge notch length. The characteristic dimension w is

5.3. Experimental test programme

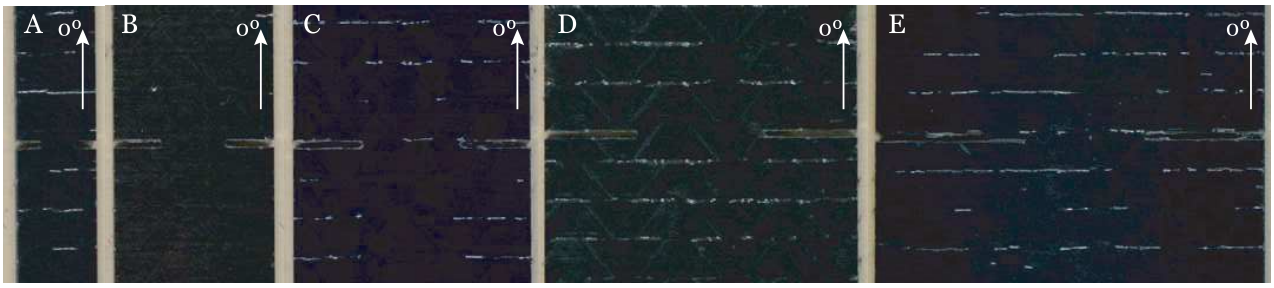

Fig. 5.1. Detail of the edge-notched section of representative DENT test specimens.

Table 5.3
Size effect DENT test matrix.

Geometry ID	L_s (mm)	L (mm)	W (mm)	a_0 (mm)	Hydraulic clamping pressure (bar)
A	300±1	150±1	10.0±0.1	3.00±0.03	< 25
B	300±1	150±1	20.0±0.2	6.00±0.03	50
C	300±1	150±1	30.0±0.3	9.00±0.03	50
D	300±1	150±1	40.0±0.4	12.00±0.03	50
E	300±1	150±1	50.0±0.5	15.00±0.03	50

taken as half specimen width ($w = W/2$), and the edge notch length-to-width ratio is kept constant in all scaled specimens ($\alpha_0 = a_0/w = 0.6$).

The edge notches (figure 5.1) were obtained using a milling machine equipped with a 1 mm drill bit, ensuring a distance of 1 mm between the notch faces. Carbon-epoxy sacrificial plates were used at the top and bottom faces of the specimens to avoid damage during the machining process. The notch tip was not sharpened, since, based on previous work [212], the fracture toughness of specimens with and without sharpened notch tips is virtually the same. In fact, after the damage process has developed from the notch tips, the actual crack tip can be considered *sharp*, and this should not affect the value of the fracture toughness at unstable crack propagation [187].

Following Bao et al. [270], for materials with $0 \leq \rho \leq 4$, where ρ is the elastic parameter given in equation (4.7), the generic correction factor $\kappa(\alpha, \rho, \varphi)$ (where $\varphi = \mu^{-1/4}\varpi$ and μ is the elastic parameter given in equation (4.8)) can be replaced by the finite-width correction (FWC) factor for isotropic materials, which in the case of sufficiently long specimens ($\varphi \approx 0$) can be written as $f(\alpha)$, multiplied by a correction factor for the orthotropy of the material, $\chi(\rho)$ [65]:

$$\kappa(\alpha, \rho) = f(\alpha)\chi(\rho) \tag{5.1}$$

For a double edge cracked plate, the FWC factor, $f(\alpha)$, can be derived e.g. from Tada et al. [283] as:

$$f(\alpha) = \sqrt{\pi\alpha}\left[1 + 0.122\cos^4\left(\frac{\alpha\pi}{2}\right)\right]\sqrt{\left(\frac{2}{\alpha\pi}\right)\tan\left(\frac{\alpha\pi}{2}\right)} \tag{5.2}$$

The orthotropy dependence factor, $\chi(\rho)$, is given as [270]:

$$\chi(\rho) = 1 + 0.1(\rho - 1) - 0.016(\rho - 1)^2 + 0.002(\rho - 1)^3 \tag{5.3}$$

All DENT tests were performed under displacement control, at a controlled speed of 1.0 mm/min, in an Instron 4208 electro-mechanical universal testing machine with a load capacity of 300 kN, equipped with a 300 kN load cell. Hydraulic grips were used to hold and apply the tensile load to the test specimens (figure 5.2). Different hydraulic clamping pressures

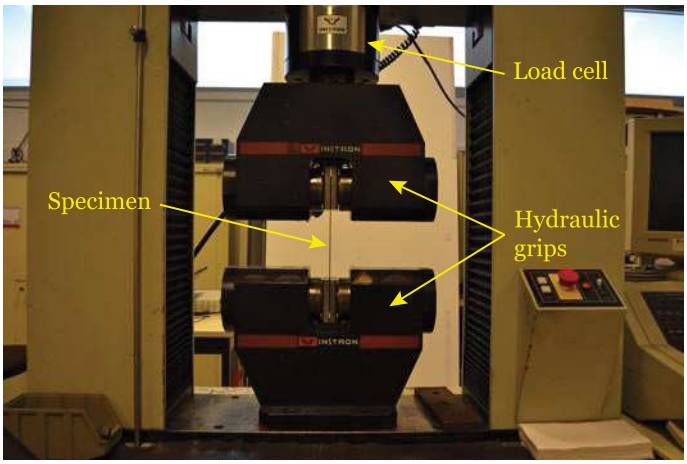

(a) General view of the test setup.

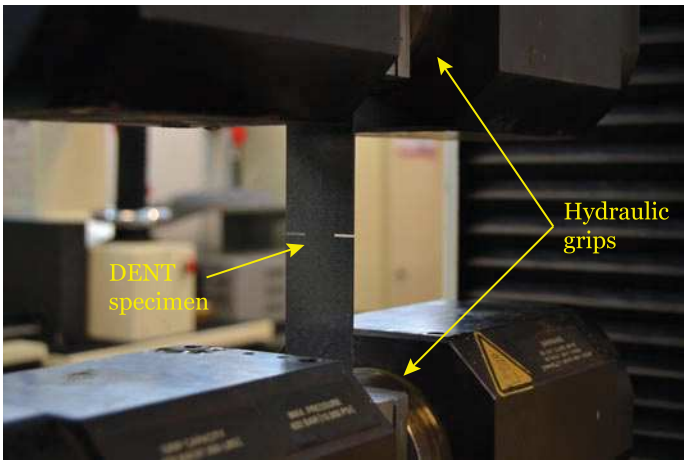

(b) Detail of a mounted DENT test specimen.

Fig. 5.2. DENT test setup.

were applied to the DENT test specimens, depending on their size, to avoid excessive damage on the outer NCF layers (table 5.3). The test data was acquired using a Spider 8 data logger, with an acquisition frequency of 5.0 Hz.

5.3.2. Laminate mode I compressive crack resistance curve

In composites, characterisation of the fracture toughness and the corresponding $\mathcal{R}$-curve associated with the propagation of a kink band is very important. As in the tensile case, the assessment of the fracture behaviour and the definition of the softening laws used in recent computational analysis models [106, 108, 189, 190], as well as the establishment of the energy equilibrium equations used in closed-form solutions [181, 182] that predict the ultimate strength of composite structures applied to compressive loading scenarios require a reliable methodology to measure the compressive intralaminar fracture toughness and $\mathcal{R}$-curve of composite laminates [187, 207]. In the present work, the methodology based on the size effect law [209] recently proposed by Catalanotti et al. [187] is employed.

Scaled Double Edge-Notched Compression (DENC) specimens (figure 5.3) were used to calibrate the size effect law. Table 5.4 shows the size effect DENC test matrix, where W is the total specimen width, L is the specimen length (end loading), and a_0 is the machined edge notch length (figure 4.5). The characteristic dimension w is taken as half specimen width ($w = W/2$), and the edge notch length-to-width ratio is kept constant in all specimens ($\alpha_0 = a_0/w = 0.6$).

The edge notches were obtained using a milling machine equipped with a 1 mm drill bit, and carbon-epoxy sacrificial plates were used at the top and bottom faces of the specimens to avoid damage during the machining process. A separation

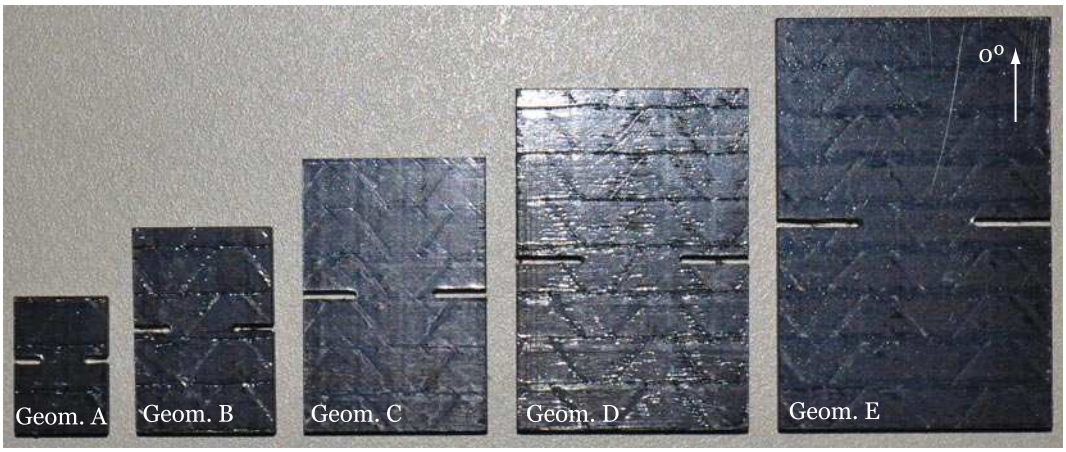

Fig. 5.3. Representative DENC test specimens.

Table 5.4
Size effect DENC test matrix.

Geometry ID	L (mm)	W (mm)	a_0 (mm)
A	15.0±0.1	10.0±0.1	3.00±0.03
B	22.5±0.1	15.0±0.1	4.50±0.03
C	30.0±0.1	20.0±0.2	6.00±0.03
D	37.5±0.1	25.0±0.2	7.50±0.03
E	45.0±0.1	30.0±0.3	9.00±0.03

of 1 mm between the crack faces could be ensured, avoiding contact between the crack faces after propagation of the kink band, which would have invalidated the experimental results [187]. The semicircular shape of the notch tip shall not affect the correct determination of the $\mathcal{R}$-curve because, on one hand, the notch tip shape does not influence the value of the fracture toughness in compression, and, on the other hand, after the initial propagation, the tip of the kink band that has formed can be considered equivalent to a *sharp* crack [187].

The dimensionless function $\kappa(\alpha, \rho, \varphi)$ that accounts for both geometry and orthotropy of the material, required to determine the $\mathcal{R}$-curve, $\mathcal{R}(\Delta a)$ (equation (4.11)), is defined using a parametric finite element (FE) model and the Virtual Crack Closure Technique (VCCT), as proposed by Catalanotti et al. [187]. The parametric model was defined for specimens with a fixed width-to-length ratio $2\varpi = 2w/L = 2/3$ subjected to end loading (displacement applied on the top face and fixed bottom face). Frictionless contact was assumed. The calibration was performed having as variables the shape parameter α and the dimensionless parameter ρ, valid for the range $0 < \alpha < 1$ and $0 \leq \rho < 20$.

It is noted that the model presented by Catalanotti et al. [187] was initially proposed for $[0/90]_{n\mathrm{S}}$ cross-ply laminates ($E_x = E_y$). Hence, the parameter μ was not taken into account by Catalanotti et al. [187] in the calibration of the dimensionless function κ, as its value was constant and equal to one — see equation (4.8). However, based on the results presented by Bao et al. [270] on orthotropy rescaling, the effect of neglecting this parameter is small for the shape of the specimen and for the laminates used in the present work.

Using the results obtained in the FE analysis, Catalanotti et al. [187] approximated the correction factor $\kappa(\alpha, \rho)$ by the polynomial function given in equation (4.15), where Φ_{ij} is the element of matrix $\mathbf{\Phi}$ (equation (4.16)) at the row i and column j, and M and N are respectively the number of rows and columns of the matrix. Catalanotti et al. [187], by comparing the numerical solution obtained in the FE simulations with the polynomial approximation in equation (4.15), showed that the fitting is excellent. This polynomial approximation can, therefore, be used in the analytical model for implementation of the proposed formulation.

All DENC tests were performed under displacement control, at a controlled speed of 0.1 mm/min, in an Instron 4208 electro-mechanical universal testing machine equipped with a 100 kN load cell (figure 5.4a). Following Catalanotti et al.

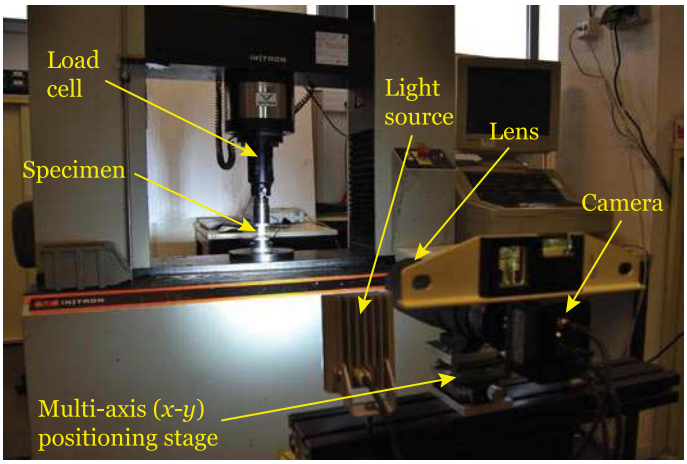

(a) General view of the test and image grabbing setup.

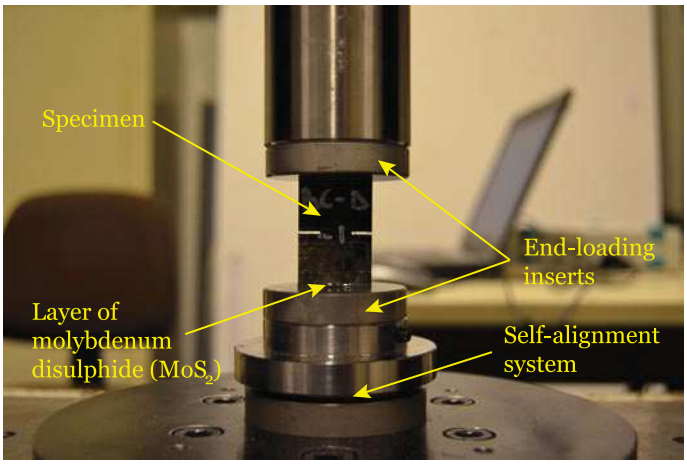

(b) Detail of the end-loading and self-alignment test setup.

Fig. 5.4. DENC test setup.

[187], an end-loading test rig with a self-alignment system (figure 5.4b), based on the test setup initially proposed by Koerber et al. [265] for quasi-static off-axis compression testing of unidirectional specimens, is used in the present work. The self alignment system consists of two parts connected by a spherical joint, which allows small rotations and avoids premature failure of the specimen that might occur due to the lack of parallelism between the faces in contact with the test rig. A thin layer of molybdenum disulphide (MoS_2) was used between the specimen end-surfaces and the surfaces of the rig to minimise friction. The test data was acquired using a Spider 8 data logger, with an acquisition frequency of 5.0 Hz or 10.0 Hz.

It is important to stress that, unlike the compact compression (CC) test specimen [191, 192], the determination of the $\mathcal{R}$-curve associated with the compressive intralaminar fracture of composite laminates using the methodology proposed by Catalanotti et al. [187] based on the size effect law [209] is performed without the need to identify the location of the tip of the kink band. In fact, locating the tip of the kink band on CC test specimens is not possible, as this specimen configuration triggers diffused damage during the propagation of the kink band, which also results in an artificial increase of the measured fracture toughness. Furthermore, there are no adequate data reduction methods for the CC test specimen as the contact tractions that occur on the crack faces during kink band growth are not taken into account. The methodology employed in the present work [187] is therefore deemed the most appropriate to measure the compressive $\mathcal{R}$-curve of the *dispersed* and *blocked* laminates and assess the effect of 0° ply blocking on the compressive notched response of thin-ply laminates.

5.3.3. Laminate tensile unnotched strength

According to current aeronautical design guidelines, the unnotched strengths of laminates are usually determined not just for the sake of mechanical characterisation, for the development of material scatter factors and for the definition of in-plane laminate strength design allowables [25], but also to evaluate specimen failure modes, for preliminary laminate analysis, to assess durability, manufacturing anomalies and environmental effects [25], and for application and validation of design tools [25, 175–177, 179–182, 249]. In the present work, unnotched tension tests are performed to assess the effect of 0° ply blocking on the tensile strength and failure modes of thin-ply laminates.

Unnotched specimens with a nominal width (W) of 25 mm and a nominal length (L) of 300 mm were tested, following the ASTM D3039/D3039M – 14 test standard [262]. The tests were performed under displacement control, at a speed of 1.0 mm/min, in an Instron 4208 electro-mechanical universal testing machine equipped with a 300 kN load cell (figure 5.5a). The test data was acquired using a Spider 8 data logger, with an acquisition frequency of 5.0 Hz.

Hydraulic grips were used to clamp the specimens to the test frame (figure 5.5b). Hydraulic clamping pressures between 100 bar and 150 bar were used. One specimen of the *dispersed* laminate and two specimens of the *blocked* laminate were tested with 2 mm thick, 75 mm long aluminium tabs to avoid failure inside the hydraulic grips. To glue the tabs, the surfaces of the adherents were polished by hand with wolcraft® 280 sandpaper and cleaned with acetone, and a 2-component epoxy adhesive Araldite® 420 A/B was used. The gauge length was set to 150 mm.

5.3.4. Laminate compressive unnotched strength

Compression testing of unnotched coupons is also a typical requirement of current aeronautical design guidelines [25]. Mechanical characterisation, development of material scatter factors and strength design allowables, evaluation of specimen failure modes, preliminary laminate analysis, assessment of durability, manufacturing anomalies and environmental effects, application and validation of design analytical methods, and establishment of the pristine baseline for damage tolerance analysis based on compression after impact (CAI) testing are some of the possible applications.

In this work, unnotched specimens with a nominal width (W) of 25 mm and a nominal length (L) of 305 mm were tested in compression to assess the effect of 0° ply blocking on the compressive strength and failure modes of thin-ply laminates. Following the ASTM D6484/D6484M – 14 test standard [272], a special test rig designed to prevent buckling was used in the compression tests, as shown in figure 5.6. The alignment of the clamping system with the axis of the testing machine was performed using two guiding pins with a diameter of 6 mm in the ends of the specimens. The guiding holes in the specimen were obtained using a drilling machine. Carbon-epoxy sacrificial plates were used at the insertion and exit points of the drill to avoid damage during the machining process. The compression rig was clamped using M8 bolts fastened with a torque of 8 Nm. The tests were performed under displacement control, at a controlled speed of 1.0 mm/min, in a servo-hydraulic MTS 810 testing machine with a load capacity of 250 kN, using a 250 kN load cell. The test data was acquired directly by the testing machine commands module, with an acquisition frequency set to 5.0 Hz.

5.3.5. Laminate tensile centre-notched strength — size effect study

In the design of structural composite parts, the understanding of the mechanical performance and structural integrity of composite materials, especially in the presence of high stress concentrations, is fundamental. In fact, composite structures are highly susceptible to severe discrete sources of damage. Furthermore, due to the discrete nature of its damage mechanisms, the residual strength of composite laminates in the presence of through-penetration damage is known to change significantly with size [25].

In general, it is possible to distinguish between small-notch ("*strength-dominated*") and large-notch ("*toughness-dominated*") strengths [25]. Such dependence, or *size effect* [131, 155, 164], must be considered when using strength data from small coupons in the design of large load-bearing structures such as composite fuselages for aeroplanes [131, 155, 164–166]. Therefore, tests on notched coupons are important in studying the mechanical response of composite

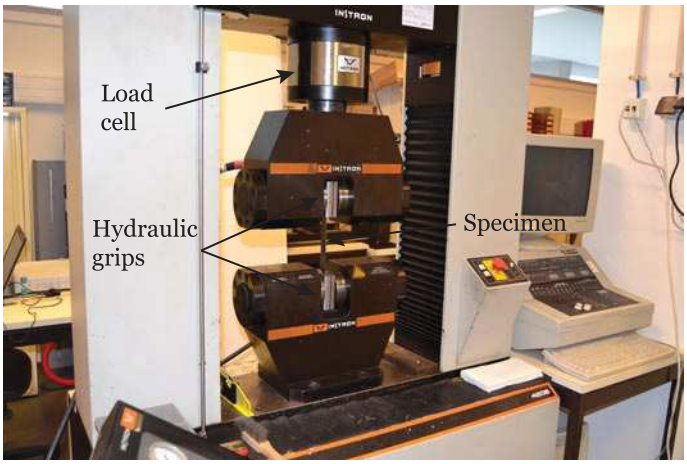

(a) General view of the test setup.

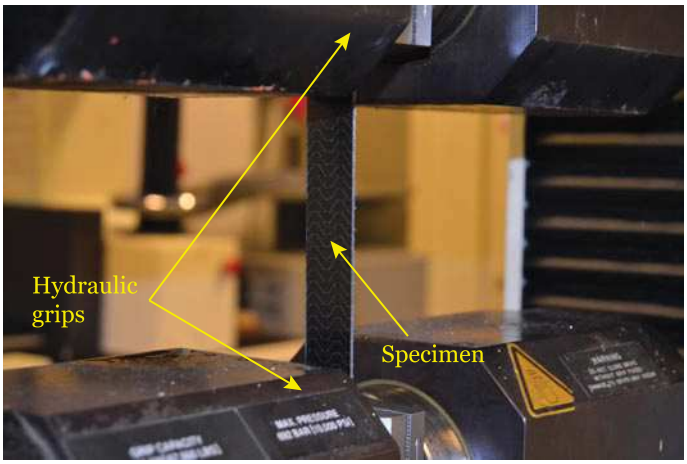

(b) Detail of a mounted unnotched tension test specimen.

Fig. 5.5. Laminate unnotched tension test setup.

laminates with stress concentrations and in assessing the effect of size on strength, as well as in defining material/lay-up and geometric factors often used in design.

In the present work, Centre-Notched Tension (CNT) tests were performed on scaled specimens to study the evolution of damage mechanisms in thin-ply laminates with *dispersed* and *blocked* 0° plies. Table 5.5 shows the CNT size effect test matrix. The width-to-notch length ratio is kept constant and equal to 6 in all specimens (figure 5.7).

The central notches were obtained using a milling machine equipped with a 1 mm drill bit, ensuring a distance of 1 mm between the notch faces. Carbon-epoxy sacrificial plates were used at the top and bottom faces of the specimens to avoid damage during the machining process.

Based on previous observations [212], the notch tips were not sharpened. This avoids getting irregular notch faces that are inevitably obtained when using very sharp saws for that purpose [166], a process that can be very laborious. Additionally, having a 1 mm diameter notch tip for all specimens shall not affect the results of the size effect study, as once the propagation of the damage process zone has initiated, its progression will dictate the final response.

All CNT tests were performed under displacement control, at a controlled speed of 1.0 mm/min, in an Instron 4208 electro-mechanical testing machine equipped with a 300 kN load cell. The test data was acquired with an acquisition frequency of 5.0 Hz using a Spider 8 data logger.

Fig. 5.6. Laminate compressive test setup, with anti-buckling test rig [272].

Hydraulic grips were used to hold and apply the tensile load to the test specimens — see figure 5.8. Different hydraulic clamping pressures were applied to the CNT test specimens depending on their size. Table 5.5 shows the hydraulic clamping pressure applied to the different CNT specimens.

Because the 82 mm wide hydraulic grips were narrower than the largest CNT specimen configurations (see table 5.5 and figure 5.8), aluminium tabs, 2 mm thick and 100 mm long, were used to increase the rigidity of the clamped regions. To glue the tabs, the surfaces of the adherents were polished by hand with wolcraft® 180 and 280 sandpaper and cleaned with acetone. Different adhesives were used depending on their availability. For the 108 mm and 144 mm wide specimens, and for three 180 mm wide specimens of the *dispersed* laminate, a 2-component epoxy adhesive Araldite® 420 A/B was used. For one 180 mm wide specimen of the *dispersed* laminate and two 180 mm wide specimens of the *blocked* laminates, a 2-component polyurethane adhesive SikaForce®-7710 L100, with SikaForce®-7010 Hardener, was used. For three 180 mm wide specimens of the *blocked* laminates, a 2-component Araldite® bisphenol-A based epoxy resin was used.

5.3.6. Bolt-bearing tests

The behaviour of composites in bolted joints differs considerably from that of metals. The quasi-brittle nature of composite materials requires more detailed analysis to address the different failure modes occurring in the vicinity of the

Table 5.5
CNT size effect test matrix.

Notch length (mm)	Width (mm)	Length (mm)	Gauge length (mm)	Hydraulic clamping pressure (bar)
6.00±0.06	36.0±0.1	300±1	150±1	100
12.00±0.06	72.0±0.1	300±1	150±1	150
18.00±0.06	108.0±0.1	400±1	200±1	200
24.00±0.06	144.0±0.1	400±1	200±1	250
30.00±0.06	180.0±0.1	400±1	200±1	300

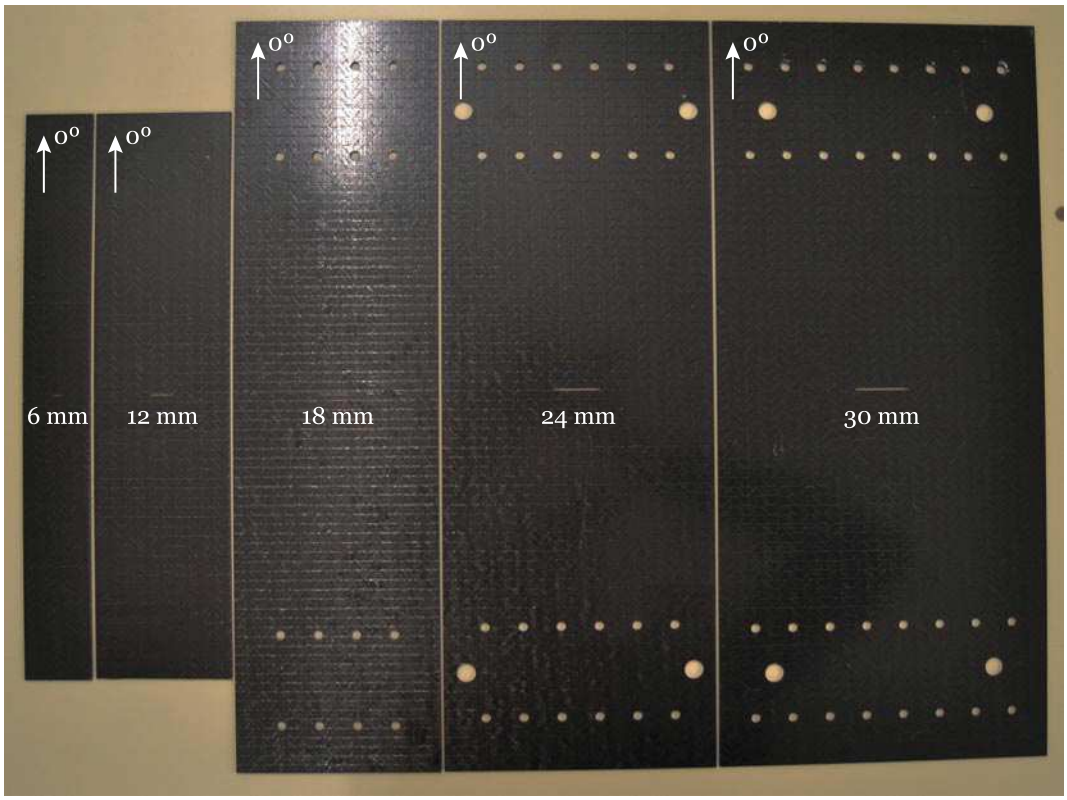

Fig. 5.7. Representative CNT test specimens.

loaded fasteners. Moreover, in composites, the stress concentrations dictate the components static strength to a larger extent than in metals due to the absence of yielding, conducting to less efficient joints.

Different failure modes can occur in composite mechanically fastened joints due to in-plane loading (figure 2.8). Bearing, net-tension, shear-out, cleavage and tear-out failure are typical examples [237]. Nevertheless, the most common is perhaps bearing failure, which occurs predominantly when the tool diameter is a small fraction of the plate width. In fact, the bearing strength of a laminate is the most common measure of a laminate's mechanical performance when subjected to the local compressive efforts typical of mechanically fastened joints.

Because the bearing strength of a composite laminate depends on the lateral support provided in the bearing region, two different experimental configurations are possible, namely bolt-bearing tests and pin-bearing tests. In bolt-bearing tests, a "finger-tight" clamping pressure is applied in the bearing region of the laminate to give conservative bearing stress results [235, 237]. In this configuration washers can be used.

In pin-bearing tests, no clamping pressure is applied. It is noted that the absence of clamping pressure in the pin-bearing tests results in lower bearing stresses than in a bolted joint [235, 284]. Therefore, not taking into account the clamping pressure in joint design acts as a safety factor. However, most mechanically fastened joints include clamping pressure. Thus, it is controversial which test is more appropriate [284].

Following the ASTM D5961/D5961M – 13 test standard [237], bolt-bearing tests were performed on the *dispersed* and *blocked* laminates to assess the effect of 0° ply blocking on the structural performance of composite bolted joints. Specimens with a nominal hole diameter $d = 6$ mm, end distance-to-hole diameter ratio $e/d = 6$, width-to-hole diameter ratio $W/d = 6$, and nominal length $L = 215$ mm were used. A bolt M6 was used with washers subjected to a "finger-tight" clamping pressure, corresponding to a torque $T = 2.2$ Nm.

The tests were performed under displacement control in a servo-hydraulic MTS 810 testing machine with a load capacity of 100 kN, at a controlled speed of 1.0 mm/min. A 100 kN load cell was used. The acquisition frequency was set

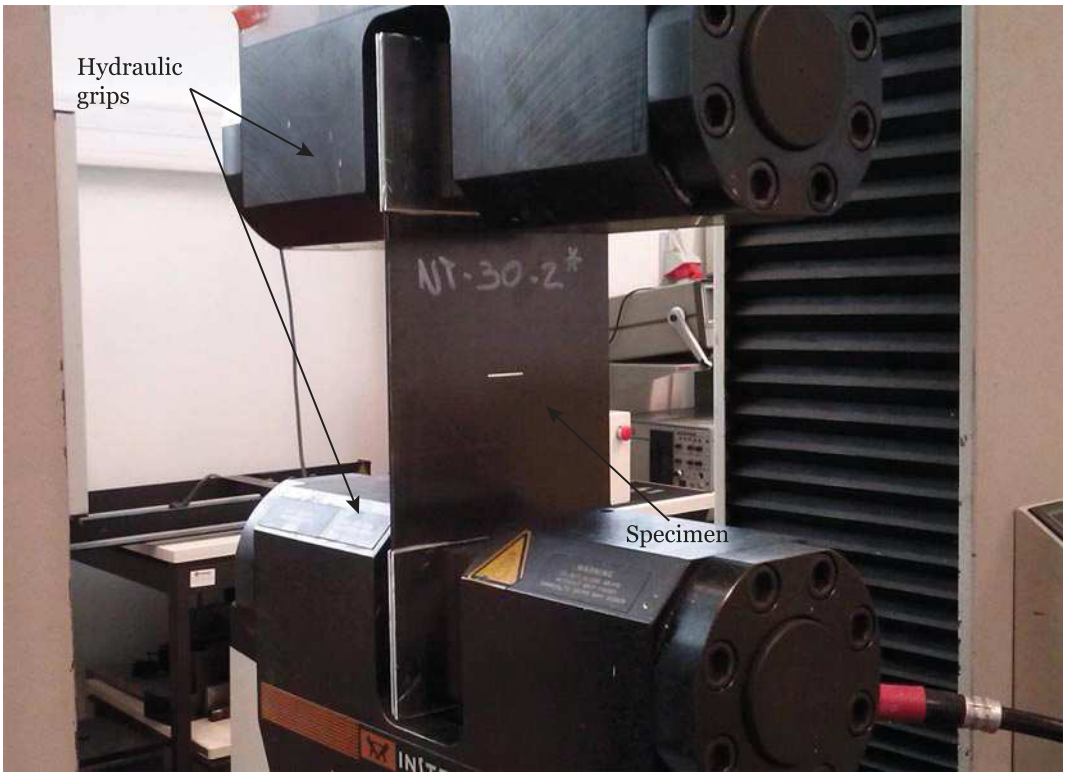

Fig. 5.8. CNT test setup, with a 180 mm wide specimen mounted into the hydraulic grips.

to 5.0 Hz. The end of the specimen far from the bearing hole was clamped using a bolted clamping rig with six M10 bolts fastened with a torque between 55 and 60 Nm. Strips of BUEHLER-MET II GRIT80/P80 silicon carbide grinding paper were inserted between the specimens and the grip to improve the load transfer capability of the bolts clamping system and avoid sliding. The alignment of the longitudinal axis of the gripped specimen with the test direction was performed using a guiding pin with a diameter of 4 mm. The bearing and guiding holes in the specimen were obtained using a drilling machine, with carbon-epoxy sacrificial plates at the insertion and exit points of the drill to avoid damage at the holes edges.

5.3.7. Pin-bearing tests

As described in section 5.3.6, the bearing strength of a composite laminate depends on the lateral support provided in the bearing region. In pin-bearing tests, where no clamping pressure is applied in the bearing region of the laminate, the bearing strength is lower than that of a bolted joint, defining the lowest bound for the bearing strength of a composite laminate. Pin-bearing tests can also be useful in characterising the actual resistance of a laminate to localised compressive loading, given the absence of the external support which precludes damage onset and propagation.

In the present study, pin-bearing tests are performed (i) to understand the failure morphology of thin-ply laminates subjected to a local compressive effort, which, to the author knowledge, has not been done yet in previous experimental campaigns on thin-ply laminates (e.g. Refs. [53, 58, 122]), (ii) assess the effect of changing the joint configuration and how detrimental is removing the lateral support provided in the bearing region in thin-ply laminates, and (iii) assess the effect of 0° ply blocking on the development of the damage mechanisms promoted by local compressive failure.

The pin-bearing tests were performed following the ASTM D5961/D5961M – 13 test standard [237], using specimens with a nominal hole diameter $d = 6$ mm, end distance-to-hole diameter ratio $e/d = 6$, width-to-hole diameter ratio $W/d = 6$, and nominal length $L = 215$ mm. A 6 mm diameter pin was used to load the bearing hole.

The tests were performed under displacement control in a servo-hydraulic MTS 810 testing machine with a load

capacity of 100kN, at a controlled speed of 1.0 mm/min. A 100 kN load cell was used. The acquisition frequency was set to 5.0 Hz. The end of the specimen far from the bearing hole was clamped using a bolted clamping rig with six M10 bolts fastened with a torque between 55 and 60 Nm. Strips of BUEHLER-MET II GRIT80/P80 silicon carbide grinding paper were inserted between the specimens and the grip, similarly to the bolt-bearing tests. The alignment of the longitudinal axis of the gripped specimen with the test direction was performed using a guiding pin with a diameter of 4 mm.

The bearing and guiding holes in the specimen were obtained using a drilling machine. Carbon-epoxy sacrificial plates at the insertion and exit points of the drill were used to avoid damage at the holes edges.

5.3.8. Net-tension strength and size effect

Even though bearing failure is, in practice, the most common failure mode in composite mechanically fastened joints, when the hole diameter is large compared with the specimen's width, or when the bolt spacing in a multi-hole bolted joint is comparatively small, net-tension failure (figure 2.8) is likely to occur. This can drastically change the strength of the joint [181]. The critical value of the width-to-hole diameter ratio or bolt spacing that defines the change from bearing failure to net-tension failure depends on the material, ply percentages and stacking sequence. For quasi-isotropic laminates, for instance, this ratio is about 3–4 [181].

Net-tension tests were preformed in the present work to study the effect of 0° ply blocking on the net-tension failure mode of composite bolted joints. This is an important structural test, specified by the most important design guidelines in aeronautics, because, as a geometry-dependent feature often used directly in the analysis methods, it is required in the derivation of in-plane laminate allowables [25]. The results of these tests can also be used to validate the most recent design tools used to predict net-tension failure of mechanically fastened joints in composite laminates [181].

These tests were carried out based on the ASTM D5961/D5961M – 13 test standard [237], using specimens with a nominal hole diameter $d = 6$ mm, end distance-to-hole diameter ratio $e/d = 6$, and nominal length $L = 215$ mm. To study the effect of geometry, specimens with nominal widths (W) of 9 mm and 12 mm were tested.

A bolt M6, subjected to a torque $T = 2.2$ Nm ("finger-tight" clamping pressure), with a washer was used to load the bearing hole. The specimen was clamped at the end far from the bearing hole using a bolted clamping rig with four M8 bolts fastened with a torque between 35 and 40 Nm. Strips of BUEHLER-MET II GRIT80/P80 silicon carbide grinding paper were inserted between the specimens and the grip, similarly to the bearing tests. The alignment of the longitudinal axis of the gripped specimen with the test direction was performed using a guiding pin with a diameter of 4 mm. The bearing and guiding holes were obtained using a drilling machine, with carbon-epoxy sacrificial plates at the insertion and exit points of the drill to avoid damage at the holes edges.

The tests were performed under displacement control, at a speed of 1.0 mm/min, in a servo-hydraulic MTS 810 testing machine with a load capacity of 100 kN. A 100 kN load cell was used, and the acquisition frequency was set to 5.0 Hz.

5.4. Instrumentation

The use of optical full-field techniques to monitor damage and fracture phenomena can be extremely useful in identifying and understanding the complex failure behaviour of composite materials [5, 121, 122, 182, 196]. With the aim of assessing the effect of 0° ply blocking on the structural and notched response of thin-ply laminates, global full-field data on regions with high strain gradients, caused by the presence of geometrical discontinuities and by the development of damage process zones, is used in the present work to support the experimental analysis and the material and fracture characterisation that is carried out.

The digital image correlation (DIC) technique is used in this experimental programme to measure the surface in-plane displacement and strain fields. This data is then used to assist in the assessment of stress concentrations and transverse cracking onset and propagation on the surface plies, and to observe the differences in damage formation and propagation in the numerous coupon configurations studied in the present work.

Table 5.6
Configuration of the DIC system.

Camera-lens optical system	
CCD camera	Baumer 138 Optronic FWX20
	8-bit
	Resolution: 1624×1236 pixels^2
	Sensor format: 1/1.8”
Lens	Nikon AF Micro-Nikkor 200 mm f/4D IF-ED
	Lens aperture: f/11
DIC measuring parameters	
Subset size	15×15 pixels^2
Subset step	13×13 pixels^2
Strain base length	5 subsets
Strain validity code	55.0%
Strain computation method	Total
DIC resolution	
Spatial resolution	2×10^{-2} pixels [187]
Strain resolution	0.01-0.04% [187]

The surface in-plane displacement and strain fields of the different specimens were measured by means of a single camera, using the ARAMIS DIC-2D v6.0.2 system developed by GOM [257]. The optical system was equipped with an 8-bit Baumer 138 Optronic FWX20 camera, with a resolution of 1624×1236 pixels^2 and a sensor format of 1/1.8”. For higher versatility, due to the range of coupon configurations under study (section 5.3), the digital camera was coupled with a Nikon AF Micro-Nikkor 200 mm f/4D IF-ED lens for image grabbing. In all test configurations, a subset size of 15×15 pixels^2 and a subset step of 13×13 pixels^2 were used. A slightly overlapping of 2 pixels between adjacent subsets was chosen in order to enhance the spatial resolution. The measured strain was computed using a strain base length of 5 subsets, with a strain validity code of 55.0%, and using the total strain method. This configuration leads to an expected spatial resolution in the order of 2×10^{-2} pixels and a strain resolution in the range 0.01-0.04% [187]. The adopted configuration is summarised in table 5.6.

For mobility and adaptability, the optical system was mounted on a multi-axis ($x - y$) positioning stage (for fine positioning adjustments) in a tripod positioned facing the testing machine (figure 5.4a). Two Raylux 25 white light LEDs were used on either side of the camera to ensure an even illumination of the test specimen’s surface and to avoid over-exposition [255, 256].

Before testing, the test specimens were sprayed with white and black ink to generate a speckle pattern. Depending on the scale of observation of each specimen configuration, the textured patterns were created by means of aerosol or airbrush painting.

When necessary, the observation surface of each specimen analysed with the DIC system was first polished by hand with KL 361 J-FLEX P180 sandpaper, BUEHLER-MET II GRIT280/P320 silicon carbide grinding paper and/or BUEHLER-MET II GRIT400/P800 silicon carbide grinding paper. This prevents the specimen’s surface texture from influencing the quality of the applied speckle patterns [253]. All observation surfaces were then cleaned with acetone.

Following [253], a pattern of black spots on a white background was chosen to improve the contrast of the speckle pattern and to maximise the natural variation of grey levels. Hence, a thin coating of white matte paint was applied on the (smoothed) surfaces.

In order to ensure a suitable speckle pattern, for the smaller specimen configurations, with regions of interest smaller than 35–45 mm, an airbrush (Iwata Custom 181 Micron CM-B model) with a fluid nozzle of 0.18 mm in diameter was used to apply the black spots (figures 5.9 to 5.12). With this marking technique, the accurate uniformity, isotropy and spot

size ideal for the smaller specimens can be achieved [187], leaving less bare invariable background colour exposed within the subset [253]. Airbrush painting is, in fact, the preferred marking technique, a statement supported by simulations of pattern deformations and experimental validation against strain gauging readings [253].

However, for the larger specimen configurations, a coarser speckle pattern was required, which could not be obtained with the available airbrush. Very small speckles, which occupy only a small number of pixels on the camera sensor, reduce the uniqueness of the pattern and produce large variations in the identification of their size, shape and distribution relative to their original features, reducing the accuracy of the measurements [253]. Therefore, for the larger specimens, the speckle pattern was created by aerosol spray, carefully applying a spot distribution of black paint on the white matte surface (figures 5.13 and 5.14). It should be noted, though, that very large speckles decrease the randomness of the pattern, as speckles occupy larger portions of the subsets. An appropriate trade-off between speckle size, shape and density is therefore important to ensure the right conditions for the DIC measurements [253]. In the present work, observation of the speckle patterns obtained with aerosol spray for the larger specimens (e.g. figures 5.13 and 5.14) show that sufficiently good size and distribution of the speckles could be obtained.

It should be noted that, in figures 5.9 to 5.14, the grey levels histogram was obtained for the entire picture, and the pixel count includes the pixels outside the marked region, resulting in large (figures 5.9 to 5.11 and figure 5.13) or small (figures 5.12 and 5.14) grey level peaks in the dark regions (low grey levels), depending on the marked region aspect ratio and notch geometry. The measurement region in each specimen, which includes only the region of interest, is defined using the correlation software before applying the image correlation algorithm.

The displacement and strain fields were measured on the outer 90° ply. This allows the monitoring of transverse cracking in the laminate, which is typically the first damage mechanism occurring in conventional multidirectional composite laminates. In general, matrix cracks, which occur in the transverse and off-axis plies of multidirectional laminates considerably before final failure, not only induce delamination onset and propagation between plies of different orientation, but they also create high local stress concentrations on the adjacent longitudinal (0°) plies, causing early fibre fracture, which results in premature laminate failure.

According to Ref. [81], in the case of transverse outer plies the energy release rate is magnified due to the proximity of the slit crack to the surface of the laminate. In other words, for the same transverse ply thickness, matrix cracking is expected to occur first in an outer ply. Therefore, since all transverse plies of both thin-ply laminates under study have the same thickness, it is expected that growth of transverse matrix cracks will initiate in the outer 90° ply monitored by the DIC system, providing a lower bound for the occurrence of transverse failure mechanisms in the laminates.

The setup of the image grabbing frame started by positioning the optical system perpendicularly to the surface of the specimen mounted into the testing machine. A level ruler was used to ensure a correct alignment. The lens was adjusted to be in focus with regard to the surface of interest, setting the lens aperture to $f/4$ (where f is the focal length of the lens) to minimise the depth of field. The lens aperture was then closed to $f/11$ in all tests to improve the depth of field during testing (table 5.6). The shutter time was set in the range of 4.0–20.0 ms, maximising the grey levels distribution over the 8-bit dynamic range of the camera while avoiding saturation of the image [253]. One or two extension tubes of 20 mm, placed between the lens and the camera, were used in some cases to increase the depth of the optical field. The working distance, defined between the specimen's surface and the support of the camera, was set in the range of 451–2587 mm, depending on the size of the region of interest.

The captured region was defined according to the specimen configuration. For the DENT test specimens (section 5.3.1), the observation window was centered along the longitudinal direction by the edge notches, and its size defined by the width of the specimen (figures 5.9 and 5.13), in order to measure the strain concentration and observe damage propagation from the notch tip.

For the DENC test specimens (section 5.3.2), the size of the observation window was defined by the size of the specimen, in order to not only measure the strain concentration and observe compressive failure from the notches, but also to assess problems in the load introduction due to possible misalignments in the loading system, and verify the

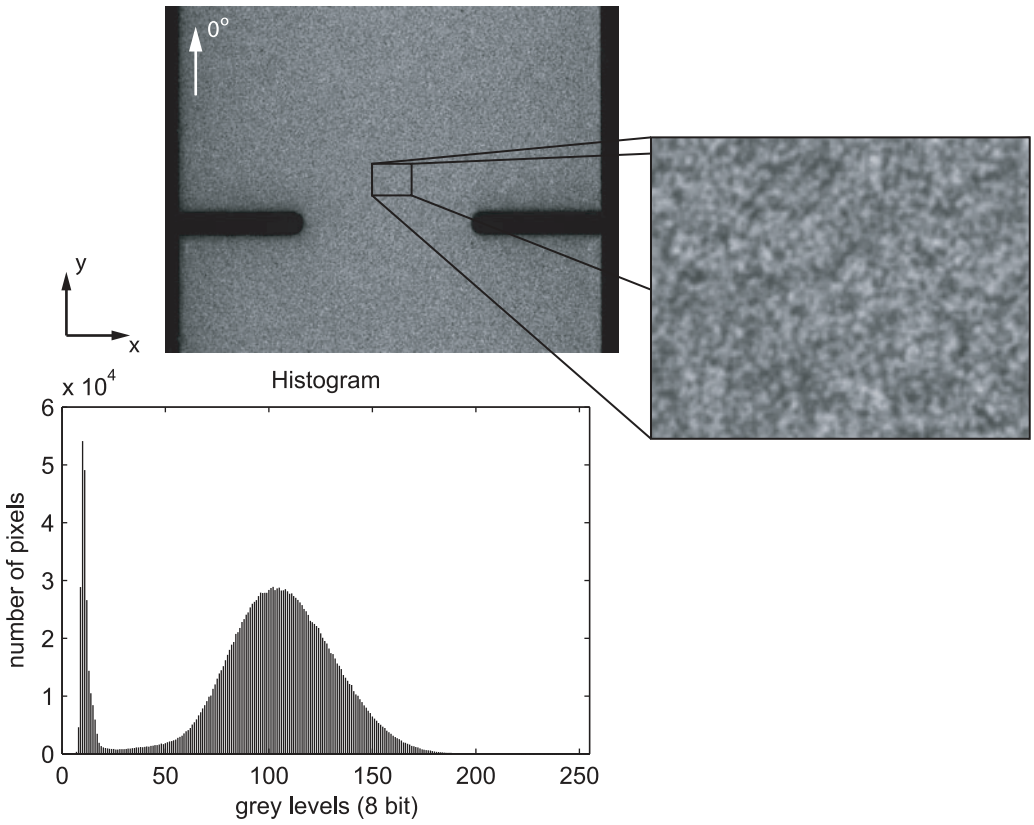

Fig. 5.9. Representative speckle pattern of a small DENT test specimen, obtained with an airbrush, and corresponding grey levels histogram. Example of a *blocked* 20 mm wide DENT test specimen (geometry B). The loading direction is parallel to the *y*-direction.

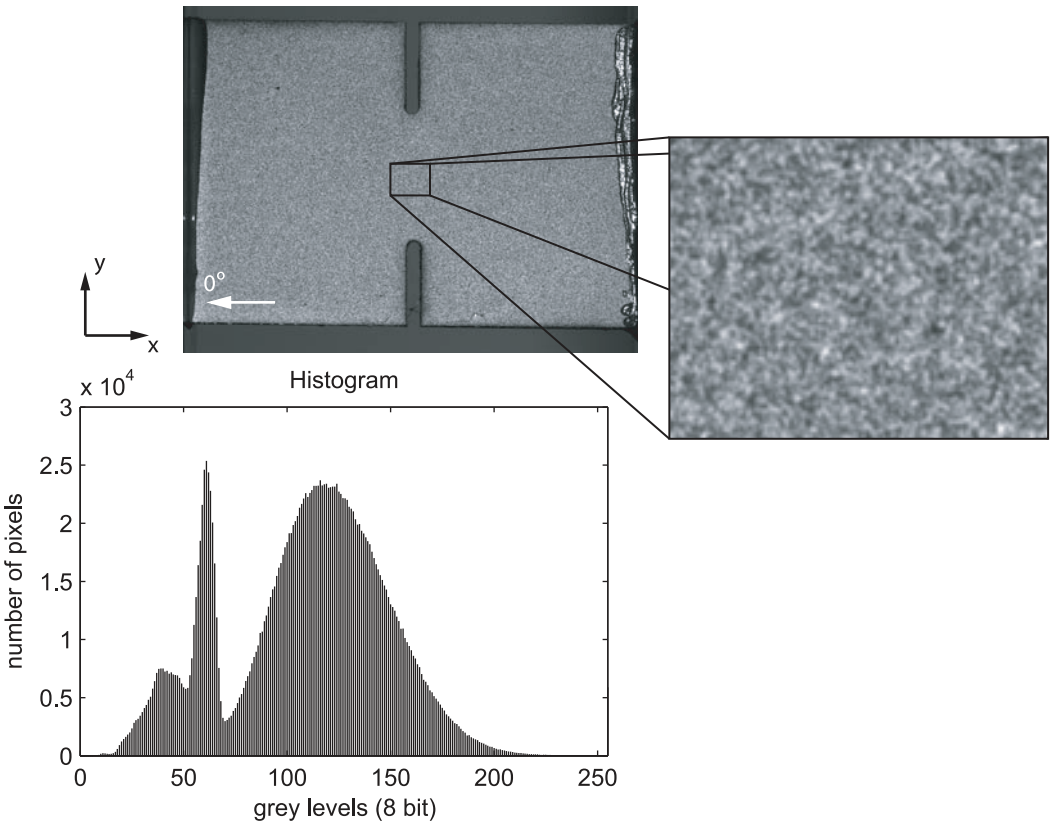

Fig. 5.10. Representative speckle pattern of a DENC test specimen, obtained with an airbrush, and corresponding grey levels histogram. Example of a *blocked* 20 mm wide DENC test specimen (geometry C). The loading direction is parallel to the x-direction.

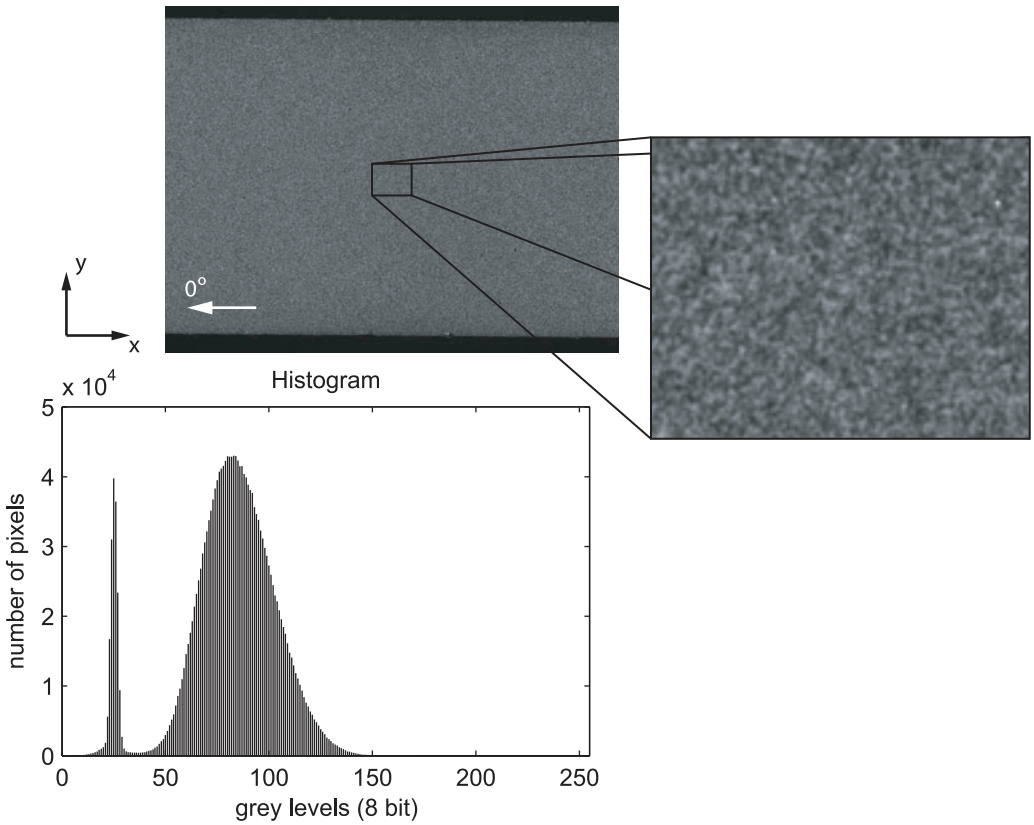

Fig. 5.11. Representative speckle pattern of an unnotched tension test specimen, obtained with an airbrush, and corresponding grey levels histogram. Example of a *blocked* unnotched test specimen. The loading direction is parallel to the x-direction.

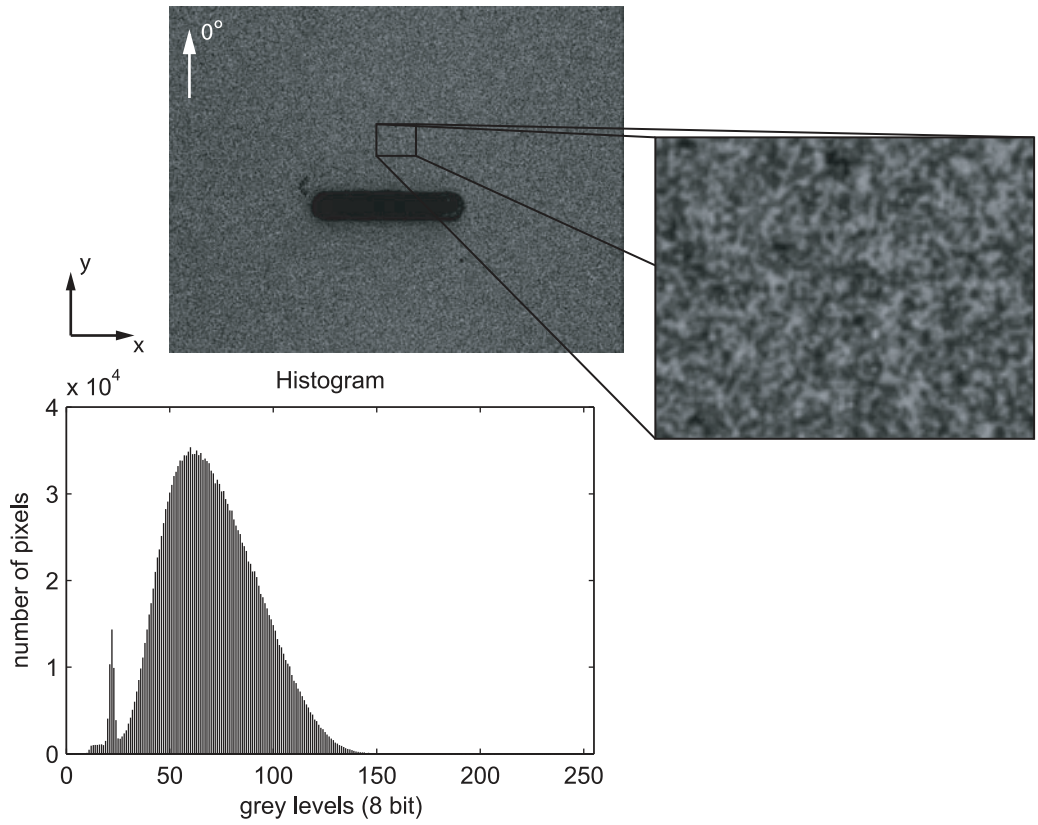

Fig. 5.12. Representative speckle pattern of a small CNT test specimen, obtained with an airbrush, and corresponding grey levels histogram. Example of a *blocked* 36 mm wide CNT test specimen. The loading direction is parallel to the *y*-direction.

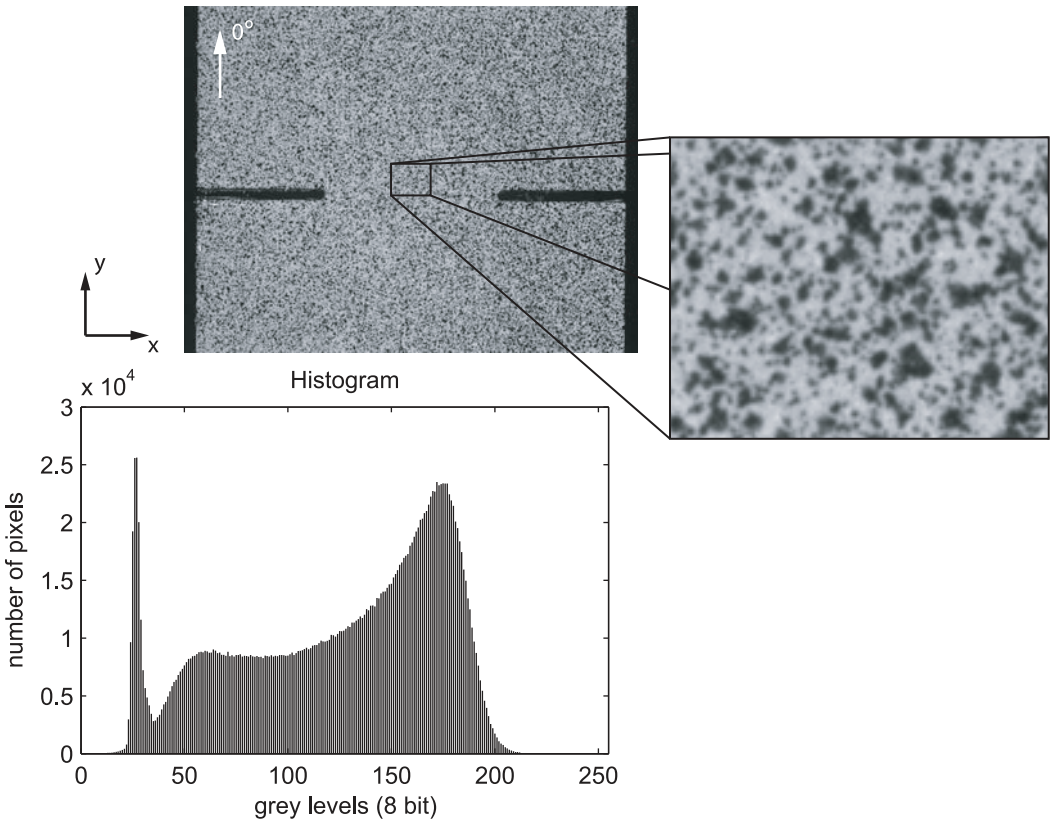

Fig. 5.13. Representative speckle pattern of a large DENT test specimen, obtained with an aerosol spray, and corresponding grey levels histogram. Example of a *blocked* 40 mm wide DENT test specimen (geometry D). The loading direction is parallel to the *y*-direction.

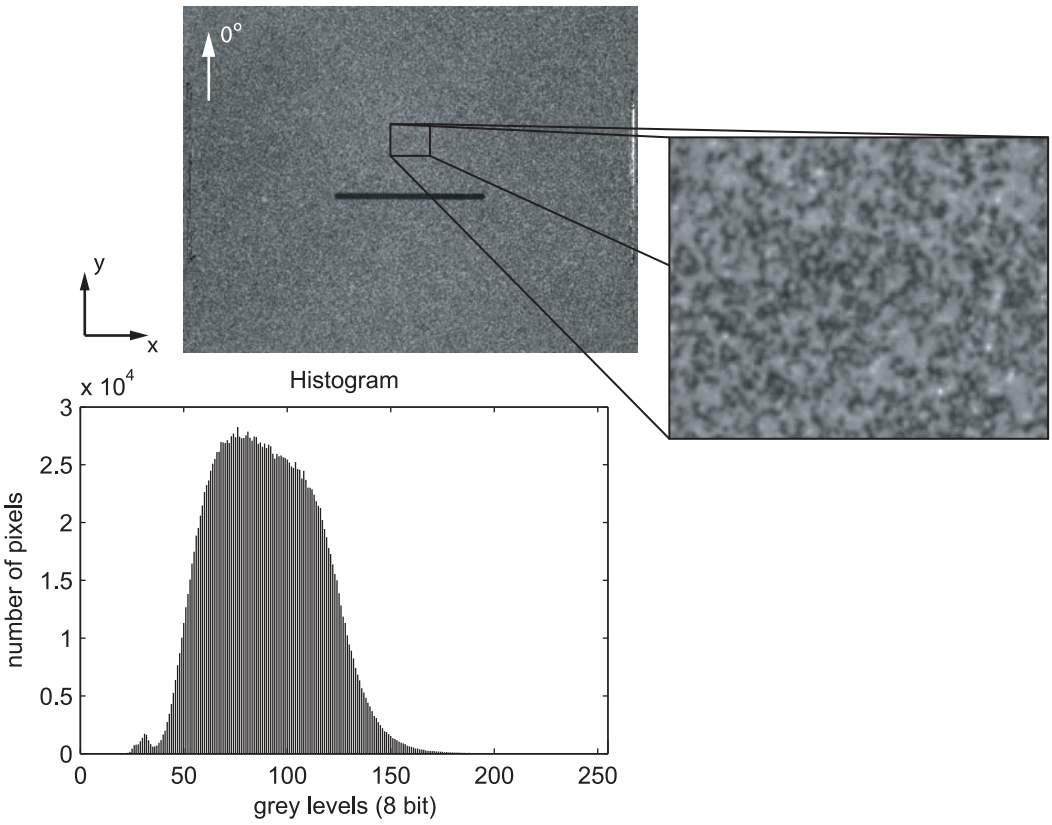

Fig. 5.14. Representative speckle pattern of a large CNT test specimen, obtained with an aerosol spray, and corresponding grey levels histogram. Example of a *blocked* 144 mm wide CNT test specimen. The loading direction is parallel to the *y*-direction.

validity of the tests performed. This can be done analysing the shear strain field γ_{xy} (e.g. figure 5.15), which must be perfectly antisymmetric with respect to the longitudinal axis of the specimen and zero all over the central part of the specimen and near each edge crack tip [187]. To observe the entire specimen's surface and maximise the field of view, the width of the observation window is set equal to the specimen's length. The captured images will consequently show the specimen rotated by an angle of 90° (figure 5.10).

In the case of the unnotched tension test specimens (section 5.3.3), the measured strain field can be used to track transverse cracking onset and growth from the free edges of the outer 90° ply of the specimen before fibre-dominated catastrophic failure. In order to maximise the captured region in the specimen while maximising the resolution of the observations, the height of the observation window was defined by the specimen's width. The captured region was, therefore, rotated by an angle of 90°, with the loading direction parallel to the DIC reference x-direction (figure 5.11).

For the CNT test specimens (section 5.3.5), the observation window was centered along the transverse and longitudinal direction by the centre of the notch, and its size set in width to three times the notch length (figures5.12 and 5.14). This observation window configuration was defined based on previous experiments in small and large size CNT coupons (Refs. [122, 182] respectively), allowing the measurement of the strain concentration at the notch tips and the assessment of stable damage propagation from the notch while maximising the field of view of the notched region.

The conversion factor varied in the range of 0.0069–0.0770 mm/pixel, depending on the coupon's size and region of interest for the different configurations. The acquisition frequency was set between 0.5 Hz and 1.0 Hz, depending on the test duration, according to the expected specimen's maximum displacement and cross-head displacement rate. Tables 5.7 and 5.8 show the measuring parameters selected for each specimen configuration (section 5.3) of the *dispersed* and *blocked* laminates (section 5.2), respectively. Full-field measurements were performed in at least one specimen of each configuration presented in tables 5.7 and 5.8.

In all tests performed with DIC full-field measurements, image acquisition started at the beginning of the test. However, in the DENC tests, to avoid recording meaningless data in the initial phase when adjustments on the specimen and self-alignment system take place while the applied load remains approximately constant and very close to zero, the specimens were initially loaded up to approximately 1% of the maximum load at a displacement rate of 0.1 mm/min, ensuring contact between the loading surface of the test setup and the specimens' top end (see figure 5.4b). Then, a pre-load of approximately 10% to 15% of the maximum load was applied, again at a displacement rate of 0.1 mm/min, to perform the required adjustments of the image grabbing setup, avoiding potential parasitic movements in the initial loading stage that could affect not only the correct position of the specimen with respect to the image grabbing setup, but also the quality of the recorded images. The DENC test specimens were subsequently unloaded to the previous position and finally loaded to failure.

5.5. Experimental results and discussion

5.5.1. Laminate mode I tensile crack resistance curve

Between 2 and 7 valid specimens were tested for each laminate and DENT geometry configuration. All specimens were tested until failure. Figures 5.16 to 5.20 show, for the different geometries, the remote stress-displacement curves of both laminates. The remote stress, σ^{∞}, of each test was calculated dividing the applied load, P, measured by the load cell, by the corresponding specimen's cross-section area, $S = W \times t$, where t is the laminate thickness. The cross-head displacement was measured directly by the testing machine. Due to the clamping pressure of the hydraulic grips, all DENT specimens had a small pre-loading before the beginning of the test, between 9 MPa and 24 MPa, below 8% of the ultimate remote stress. A nonlinear remote stress-displacement relation is also observed in all specimen configurations in the beginning of the tests due to small adjustments inside the grips as the load is applied.

Figures 5.21 and 5.22 show, respectively, representative DENT test specimens of the *dispersed* and *blocked* laminates after testing. All specimen configurations of both laminates fail due to the sudden propagation of an intralaminar crack across the notched plane, connecting the edge notches.

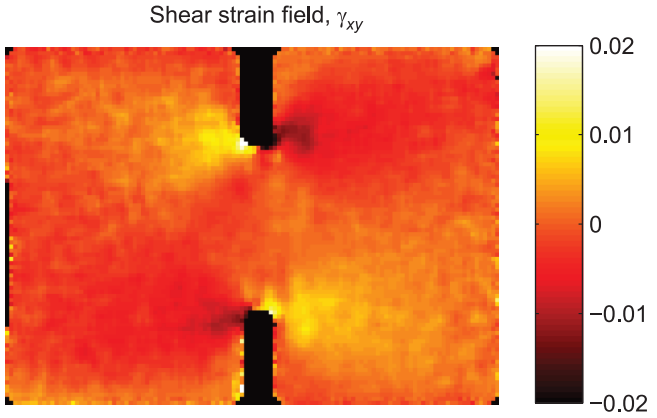

(a) *Blocked* 10 mm wide DENC test specimen (geometry A) at an applied compressive load of 4.1 kN.

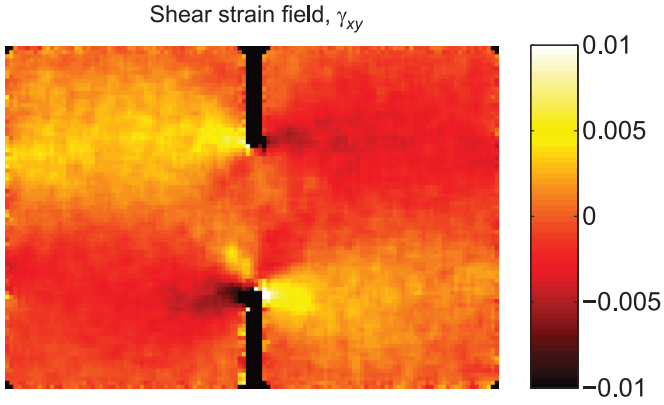

(b) *Blocked* 30 mm wide DENC test specimen (geometry E) at an applied compressive load of 13.2 kN.

Fig. 5.15. Shear strain fields, γ_{xy}, of representative DENC test specimens.

Table 5.7
Optical system parameters for specimens of the *dispersed* laminate.

Specimen geometry	Captured region (mm^2)	Conversion factor (mm/pixel)	Acquisition frequency (Hz)
DENT A	9.6×7.1	0.007004	1.0
DENT B	19.7×14.5	0.013287	1.0
DENT C	29.8×21.9	0.019617	1.0
DENT D	39.3×29.5	0.026045	1.0
DENT E	49.8×36.6	0.031628	1.0
DENC A	13.4×10.0	0.008912	1.0
DENC B	21.1×14.9	0.014004	1.0
DENC C	28.7×20.0	0.018720	1.0
DENC D	35.4×25.5	0.022535	1.0
DENC E	43.2×29.4	0.027241	1.0
UNT†	31.5×24.8	0.022231	0.5
CNT 6‡	17.8×11.5	0.011201	1.0
	17.8×11.7	0.011150	1.0
CNT 12‡	35.6×25.5	0.022826	1.0
	36.8×26.6	0.023223	1.0
CNT 18‡	54.2×39.0	0.034447	1.0
	51.1×36.7	0.032489	1.0
CNT 24‡	83.0×59.0	0.052743	1.0
	84.6×61.2	0.052882	1.0
CNT 30‡	105.6×77.9	0.066578	1.0
	122.2×90.1	0.077042	1.0

† Unnotched tension (section 5.3.3)
‡ Notch length (section 5.3.5)

Table 5.8
Optical system parameters for specimens of the *blocked* laminate.

Specimen geometry	Captured region (mm^2)	Conversion factor (mm/pixel)	Acquisition frequency (Hz)
DENT A	9.8×6.7	0.006946	1.0
DENT B	20.0×14.6	0.013356	1.0
DENT C	29.6×22.4	0.019608	1.0
DENT D	39.4×29.9	0.026099	1.0
DENT E	49.3×35.8	0.031618	1.0
DENC A	13.9×10.1	0.008925	1.0
DENC B	21.1×15.1	0.013978	1.0
DENC C	28.0×19.9	0.018708	1.0
DENC D	35.3×25.2	0.022279	1.0
DENC E	42.8×29.7	0.027195	1.0
UNT†	31.2×24.5	0.022207	0.5
CNT 6‡	18.0×11.6	0.011256	1.0
	17.8×11.5	0.011204	1.0
CNT 12‡	35.0×24.3	0.022252	1.0
	37.0×27.0	0.023883	1.0
CNT 18‡	59.0×42.1	0.037202	1.0
	55.5×40.7	0.035575	1.0
CNT 24‡	83.7×60.4	0.052798	1.0
	77.7×57.0	0.049826	1.0

† Unnotched tension (section 5.3.3)
‡ Notch length (section 5.3.5)

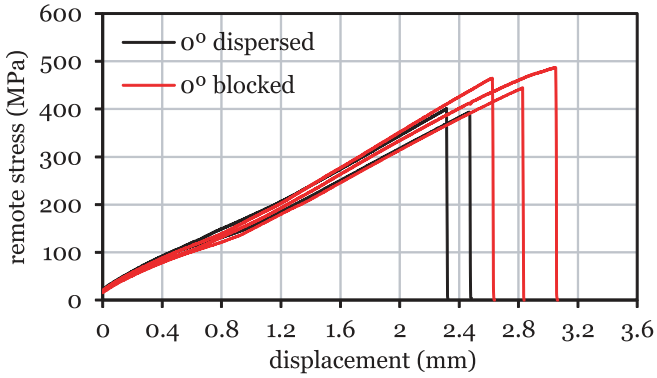

Fig. 5.16. Remote stress-displacement curves for the 10 mm wide DENT specimens (geometry A).

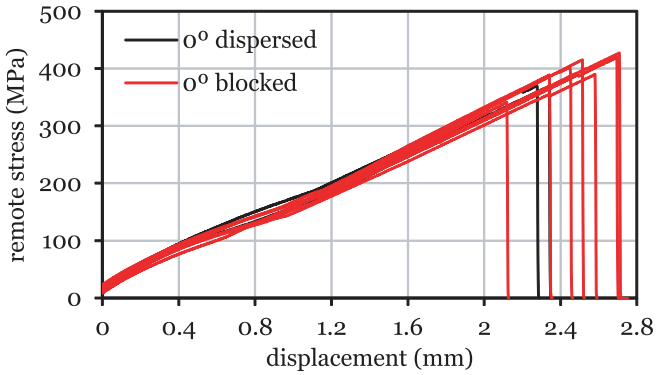

Fig. 5.17. Remote stress-displacement curves for the 20 mm wide DENT specimens (geometry B).

However, during the tests, the development of a fracture process zone (FPZ) prior to ultimate failure was audible in all specimen configurations. In some specimens, particularly in the largest, the development of the FPZ coincided with small load drops in the remote stress-displacement curves, with a negligible effect on the stiffness of the tested specimens (figures 5.18 to 5.20).

For the smaller specimens (geometry A) of the *dispersed* laminate, internal damage growth was audible above 340 MPa (86% of the ultimate remote stress). For the *blocked* laminate, internal damage growth was audible above approximately 380 MPa (or 87% of the ultimate remote stress), reaching a maximum applied remote stress reasonably above the *dispersed* laminate (figure 5.16). Hence, in the case of small ligament widths, blocking the 0° plies delayed not only the growth of severe (audible) damage to higher applied remote stresses, but also ultimate failure, resulting in an improved notched response.

For the 20 mm wide specimens (geometry B), internal damage growth in the *dispersed* laminate was audible above 300 MPa (81% of the ultimate remote stress), with apparent stable fibre fracture above approximately 320 MPa (or 86% of the ultimate remote stress). Internal damage growth was audible in the *blocked* specimens at applied remote stresses above approximately 240 MPa (57% of the ultimate remote stress), with apparent stable fibre fracture above approximately 300 MPa (74% of the ultimate remote stress), in some cases coinciding with the small load drops in the remote stress-displacement curves (figure 5.17).

For the 30 mm wide specimens (geometry C) of the *dispersed* laminate, internal damage growth was audible above approximately 240 MPa (74% of the ultimate remote stress), with apparent stable fibre fracture. Internal damage growth was also audible in the *blocked* specimens, at applied remote stresses above approximately 190 MPa (or 58% of the ultimate remote stress), stronger and apparently with stable fibre fracture above approximately 300 MPa (or 87% of the ultimate remote stress).

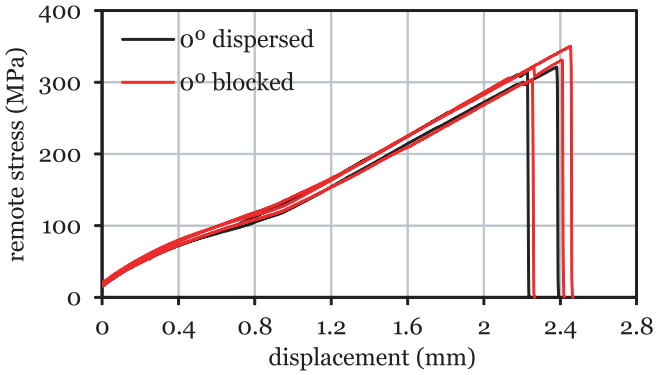

Fig. 5.18. Remote stress-displacement curves for the 30 mm wide DENT specimens (geometry C).

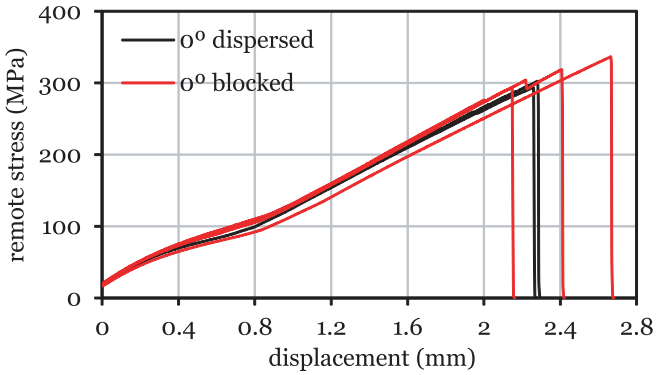

Fig. 5.19. Remote stress-displacement curves for the 40 mm wide DENT specimens (geometry D).

For the 40 mm wide specimens (geometry D), internal damage growth in the *dispersed* laminate was audible above approximately 180 MPa (59% of the ultimate remote stress), with apparent stable fibre fracture at applied remote stresses above 220 MPa (74% of the ultimate remote stress). Internal damage growth was also audible in the *blocked* specimens, at applied remote stresses above 210 MPa (72% of the ultimate remote stress), stronger and apparently with stable fibre fracture above approximately 270 MPa (84% of the ultimate remote stress). As the size of the specimens increased, the range of stable discrete damage growth, between the onset of more severe damage, including fibre breakage (which produces a very characteristic sound), and ultimate failure, increased as well.

For the 50 mm wide specimens (geometry E) of the *dispersed* laminate, internal damage growth was audible above 140 MPa (45% of the ultimate remote stress), stronger and apparently with stable fibre fracture at applied remote stresses above approximately 200 MPa (64% of the ultimate remote stress). Lateral free-edge damage could be observed in the middle block of −45° plies (symmetry plane) of the tested specimens of the *dispersed* laminate, above and below the notched plane (figure 5.23).

Internal damage growth was also audible in the 50 mm wide specimens (geometry E) of the *blocked* laminate at applied remote stresses above approximately 180 MPa (61% of the ultimate remote stress), stronger and apparently with stable fibre fracture above 240 MPa (90% of the ultimate remote stress). Similarly to the *dispersed* laminate, some lateral free-edge damage could be observed on the middle block of −45° plies (symmetry plane) of the tested specimens, with evidence of split cracking on the ±45° plies.

The noise audible during the tests due to damage in the specimens indicates that the onset of damage occurs earlier and stable propagation of the damage process zone takes longer in the larger specimen configurations. On the other hand, observation of the broken specimens indicates that this damage process zone mostly comprises intralaminar damage, confined to the notched plane, where final intralaminar fracture takes place.

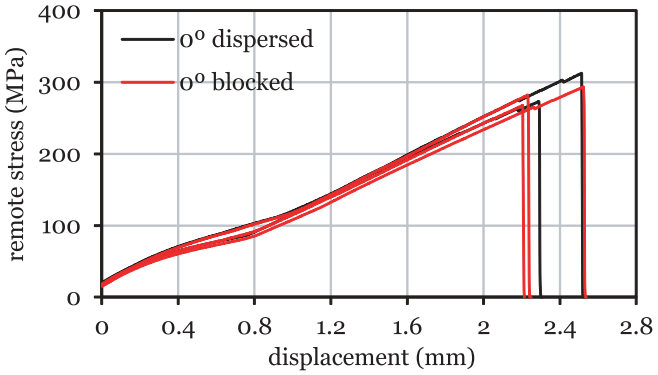

Fig. 5.20. Remote stress-displacement curves for the 50 mm wide DENT specimens (geometry E).

This becomes even more evident by analysing the longitudinal strain fields obtained from the DIC measurements of representative specimens of the different configurations (figures 5.24 to 5.28). For reference, figures 5.24 to 5.28 also show the corresponding coloured distributions of grey levels.

As can be observed in figures 5.24 to 5.28, as the size of the specimens increases, the length of the damage process zone starting from the tips of the edge notches increases too. In addition, transverse damage normal to the loading direction in the larger specimen configurations is confined to the notched plane, whereas strain localisation bands anticipate the occurrence of transverse cracking on the outer 90° ply of the smaller specimens along their gauge section. It is also noted that these transverse localisation bands are more pronounced on the *blocked* laminate. Their formation is linked to the higher stress levels reached by the smaller specimens, particularly of the *blocked* laminate.

Figures 5.24 to 5.28 also show that, particularly for the smaller specimens (figures 5.24 to 5.26), the damage process zone is not always perpendicular to the loading direction; starting from the tips of the edge notches, it can grow along the −45° ply direction before fracture of the notched plane. Although the damage process zone would be expected to grow perpendicularly to the loading direction and across the notched plane, which eventually occurs upon unstable crack propagation and final failure (see detailed pictures of the notched plane after ultimate failure in figures 5.29 and 5.30), in these cases stable damage growth apparently occurs due to the development of a −45° split crack inside the laminate. This shows how analysis of the surface strain fields measured with the DIC technique can be useful in evaluating the occurrence of internal damage mechanisms in the laminate.

The growth of the damage process zone along a direction not aligned with the outer ply also shows that through-the-thickness intralaminar fracture starts and propagates before the occurrence of transverse matrix cracking, which is generally the first damage mechanism occurring in a multidirectional laminate. This can be attributed to the *in situ* effect [81, 94, 98].

Figures 5.21 to 5.30 also show that, for both laminates, the adopted specimen configuration leads to failure due to the development of a self-similar intralaminar damage process zone. Strong stress relaxation due to the occurrence of subcritical damage mechanisms was not observed. This is a requirement for the determination of the $\mathcal{R}$-curve associated with tensile mode I intralaminar fracture.

Even though lateral free-edge damage could be observed on the larger specimens after testing (figure 5.23), it is not clear if these damage mechanisms have occurred before or after unstable intralaminar fracture. In fact, the analysis of the longitudinal strain fields, measured with the DIC technique, at different stages of loading do not show evidence of stress relaxation due to failure mechanisms other than intralaminar damage growth perpendicular to the loading direction and across the notched plane. It is therefore reasonable to assume that the damage mechanisms that conduct to the observed free-edge damage can be lumped into the intralaminar damage process zone represented by the measured $\mathcal{R}$-curve.

To assess possible load asymmetries and the effects of strain concentration near the tips of the edge notches, remote stress-local axial strain relations were obtained with virtual strain gauges computed from the DIC data [121, 122, 182,

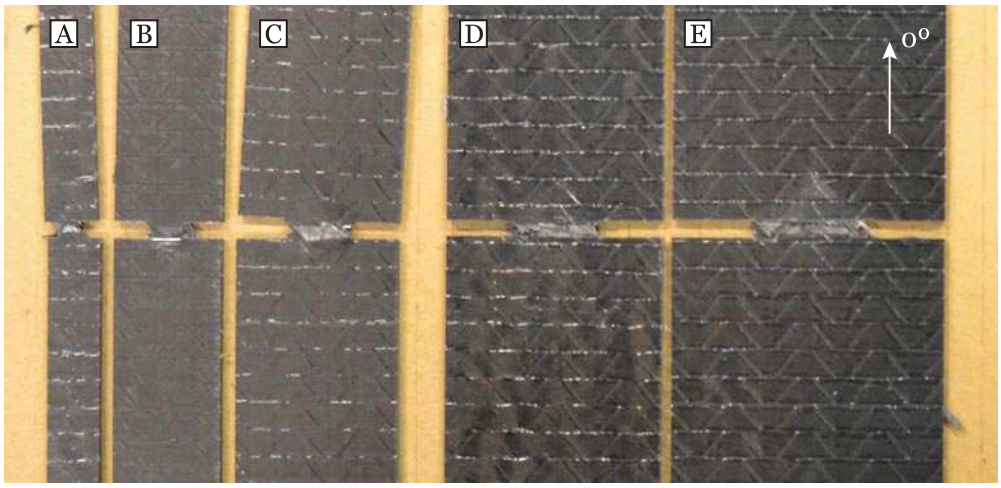

Fig. 5.21. Representative DENT test specimens of the *dispersed* laminate after testing.

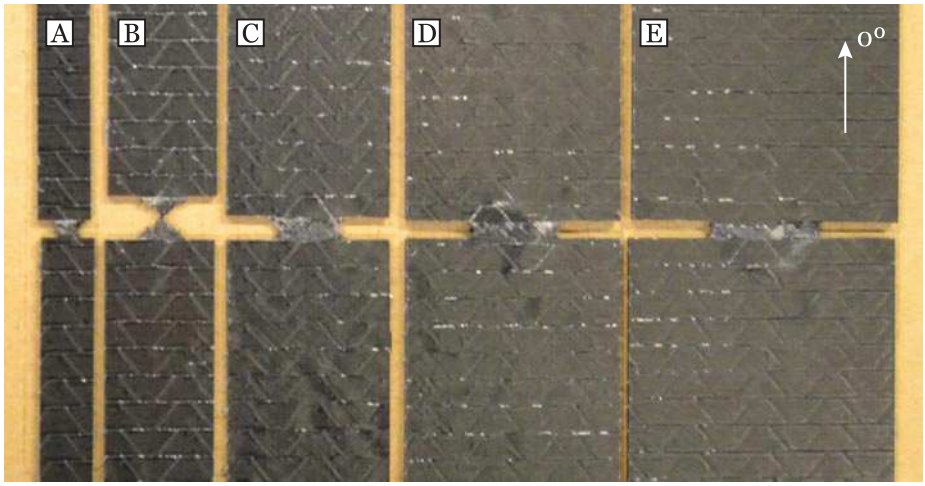

Fig. 5.22. Representative DENT test specimens of the *blocked* laminate after testing.

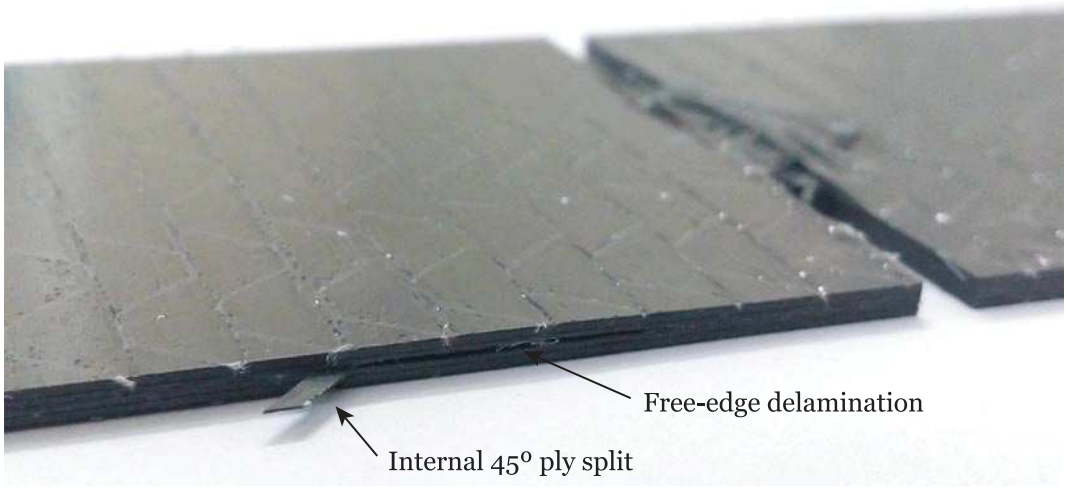

Fig. 5.23. Detail of a 50 mm wide DENT specimen (geometry E) after testing.

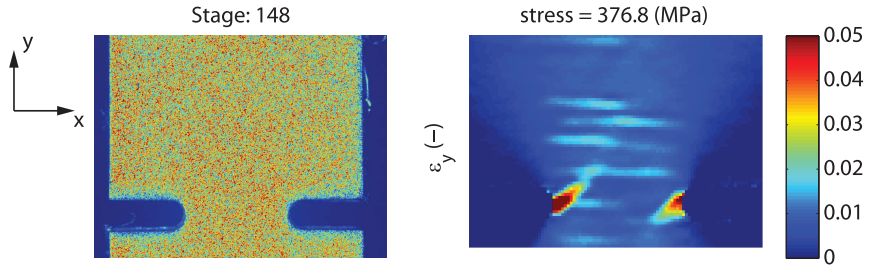

(a) *Dispersed* laminate.

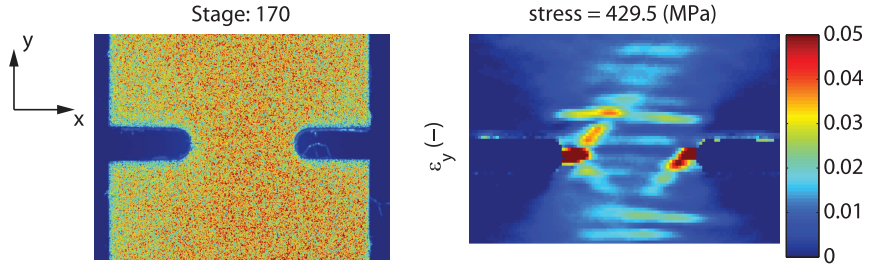

(b) *Blocked* laminate.

Fig. 5.24. Coloured distributions of grey levels (0–255) and longitudinal strain fields, ε_y, of the outer 90° ply of representative 10 mm wide DENT test specimens (geometry A) obtained with the DIC technique at the stage before ultimate failure. The reference DIC coordinate system is depicted in the figures, where the y-axis is aligned with the loading direction.

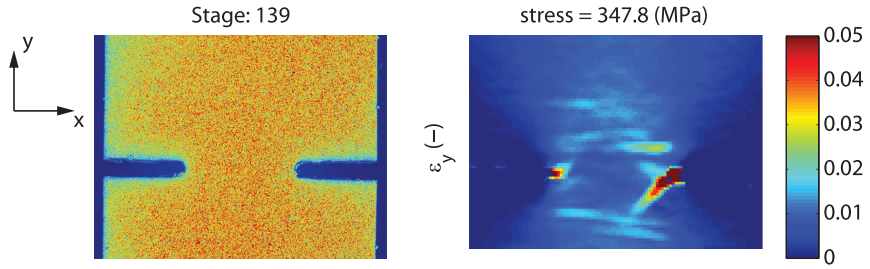

(a) *Dispersed* laminate.

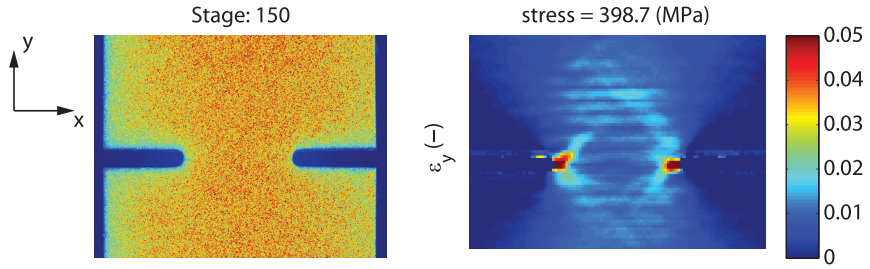

(b) *Blocked* laminate.

Fig. 5.25. Coloured distributions of grey levels (0–255) and longitudinal strain fields, ε_y, of the outer 90° ply of representative 20 mm wide DENT test specimens (geometry B) obtained with the DIC technique at the stage before ultimate failure. The reference DIC coordinate system is depicted in the figures, where the y-axis is aligned with the loading direction.

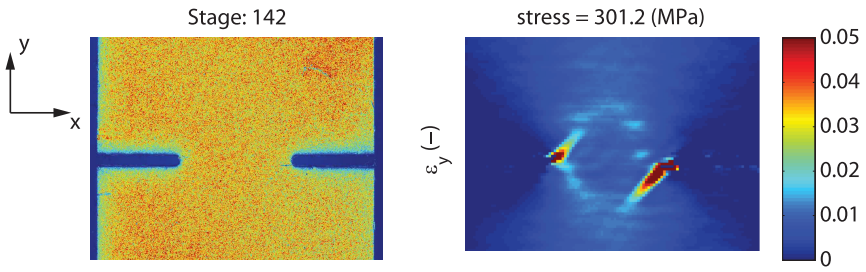

(a) *Dispersed* laminate.

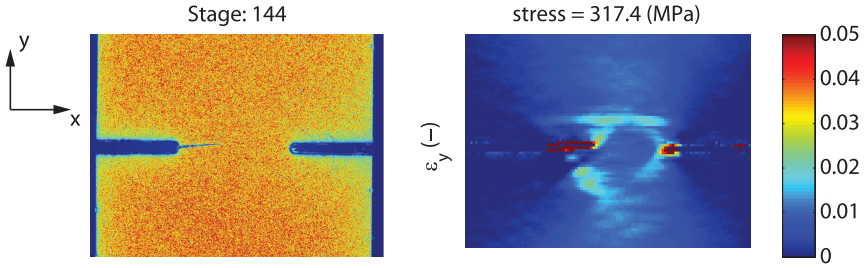

(b) *Blocked* laminate.

Fig. 5.26. Coloured distributions of grey levels (0–255) and longitudinal strain fields, ε_y, of the outer 90° ply of representative 30 mm wide DENT test specimens (geometry C) obtained with the DIC technique at the stage before ultimate failure. The reference DIC coordinate system is depicted in the figures, where the *y*-axis is aligned with the loading direction.

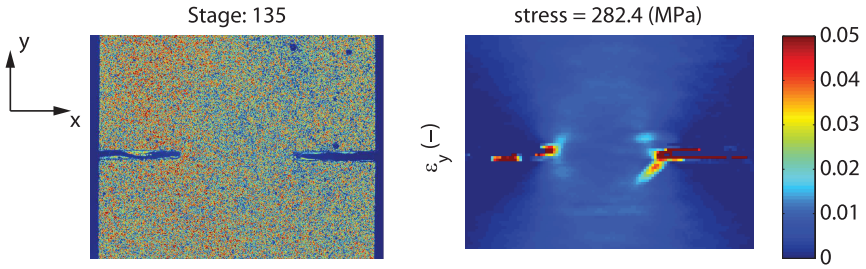

(a) *Dispersed* laminate.

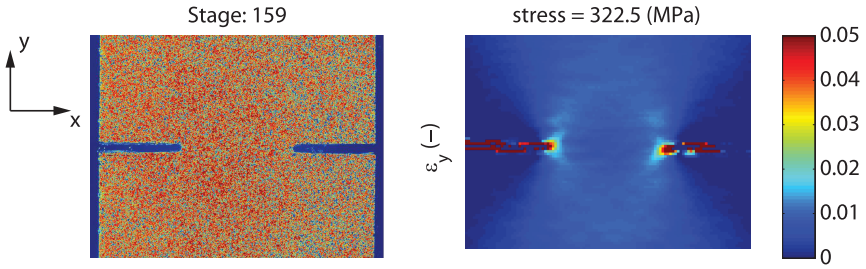

(b) *Blocked* laminate.

Fig. 5.27. Coloured distributions of grey levels (0–255) and longitudinal strain fields, ε_y, of the outer 90° ply of representative 40 mm wide DENT test specimens (geometry D) obtained with the DIC technique at the stage before ultimate failure. The reference DIC coordinate system is depicted in the figures, where the *y*-axis is aligned with the loading direction.

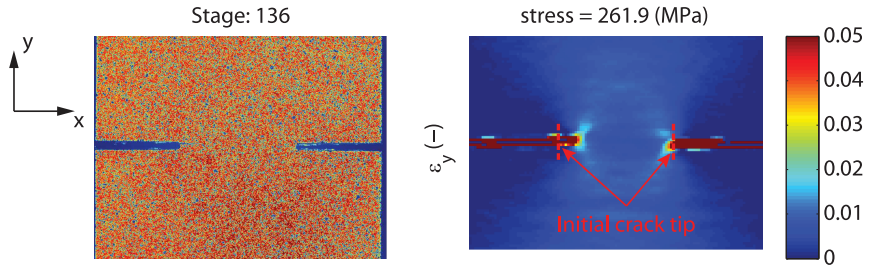

(a) *Dispersed* laminate.

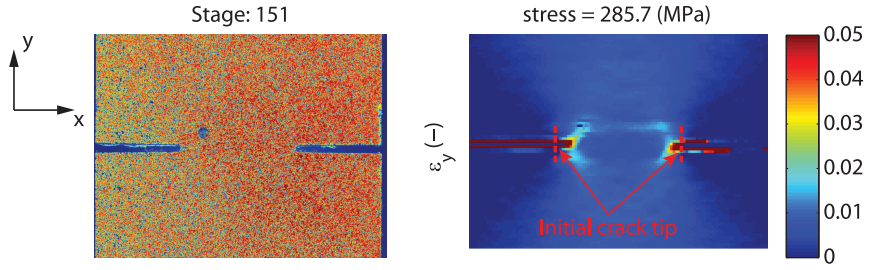

(b) *Blocked* laminate.

Fig. 5.28. Coloured distributions of grey levels (0–255) and longitudinal strain fields, ε_y, of the outer 90° ply of representative 50 mm wide DENT test specimens (geometry E) obtained with the DIC technique at the stage before ultimate failure. The reference DIC coordinate system is depicted in the figures, where the y-axis is aligned with the loading direction.

187]. The strain measurements of the virtual strain gauges were obtained averaging the results of DIC in an area equivalent to the gauge area of physical strain gauges. Gauge areas with 3.18 mm in length by 1.78 mm in width were used. Two virtual strain gauges (*SG1* and *SG2*) were placed at the tips of the edge notches. Figures 5.31 to 5.35 show, for each specimen configuration and for both laminates, the remote stress-local axial strain relations obtained with this numerical procedure. For reference, the location of the gauge areas (*SG1* and *SG2*) are also presented, plotted on the longitudinal strain field obtained with the DIC technique at an applied remote stress corresponding to 20% of the ultimate remote stress.

Previous studies [121, 122, 182, 187] using a similar DIC system configuration have shown that the data obtained with physical and virtual strain gauges is virtually the same. To further validate the proposed virtual strain gauge approach and the accuracy of the results, a linear-elastic Finite Element Analysis (FEA) was performed for each specimen geometry, employing the same averaging procedure to compare with the data measured with virtual strain gauges.

The FE models were created with the commercial FE software Abaqus 6.12-1 [275] using a structured mesh of 4-node plane stress elements with reduced integration (CPS4R). At the notch tip, finite elements with a minimum in-plane size five times smaller than the notch tip radius (or 0.1 mm) were used to accurately represent the notch geometry and capture the strain concentrations. In the FE model, only the gauge section was represented, i.e. the gripped regions were not modelled. Figures 5.36a and 5.37a show details of the meshes of the 10 mm wide (geometry A) and 50 mm wide (geometry E) FE models, respectively.

In order to replicate the load and boundary conditions of the actual test setup, a longitudinal displacement (x-direction) of 1.00 mm was applied to the nodes on the top end, while fixing their remaining degrees of freedom. The nodes in the bottom end were all fixed (clamped boundary condition).

The individual plies of the composite lay-up were modelled using a layerwise approach, explicitly defining each lamina, and respective ply orientation, by one integration point through the thickness of the plane stress elements. The constitutive behaviour of each ply was defined by an orthotropic linear-elastic material model using the elastic properties of T700GC/M21 (table 4.1). Figures 5.36b and 5.37b show the longitudinal strain field of the outer ply of the 10 mm

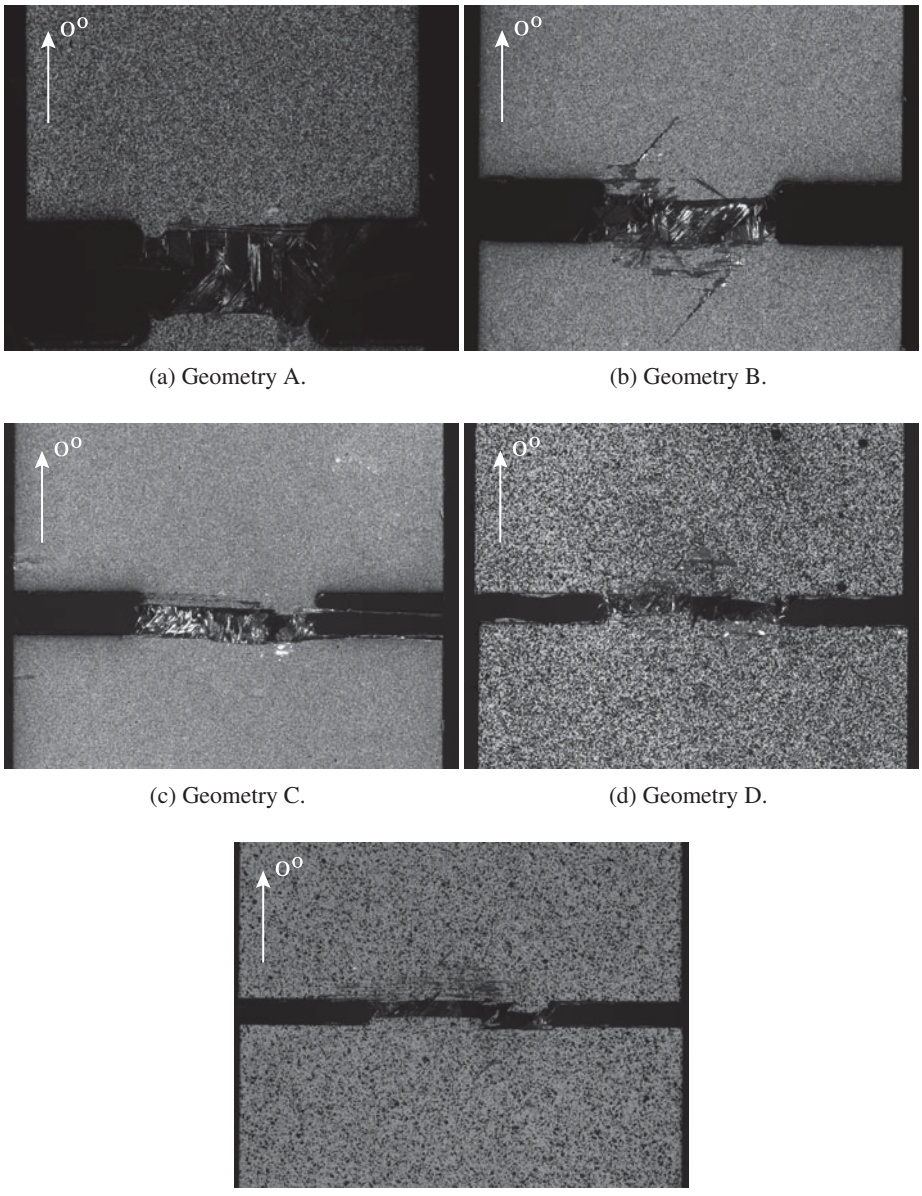

(a) Geometry A.

(b) Geometry B.

(c) Geometry C.

(d) Geometry D.

(e) Geometry E.

Fig. 5.29. Detailed pictures of the notched plane of representative DENT test specimens of the *dispersed* laminate immediately after ultimate failure. Pictures captured with the DIC image grabbing system.

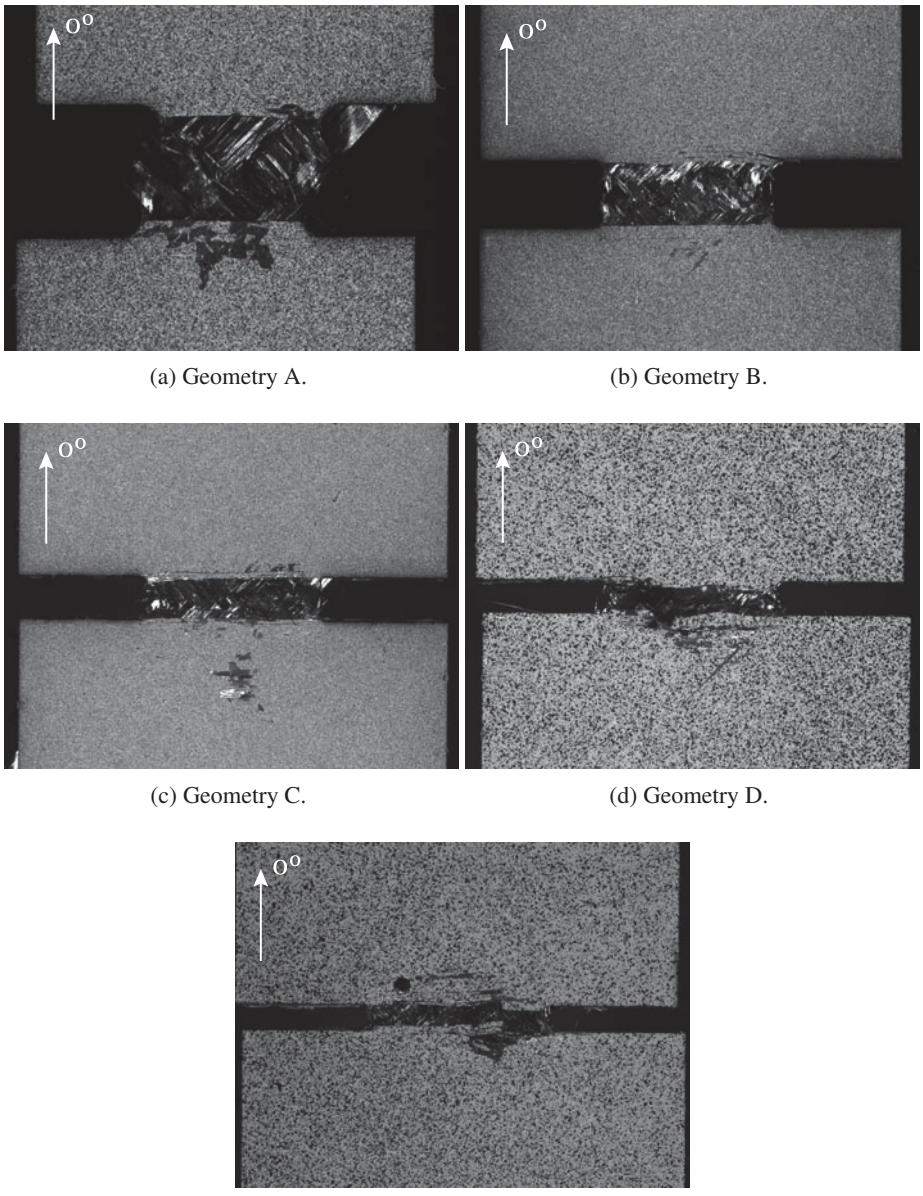

(a) Geometry A.

(b) Geometry B.

(c) Geometry C.

(d) Geometry D.

(e) Geometry E.

Fig. 5.30. Detailed pictures of the notched plane of representative DENT test specimens of the *blocked* laminate immediately after ultimate failure. Pictures captured with the DIC image grabbing system.

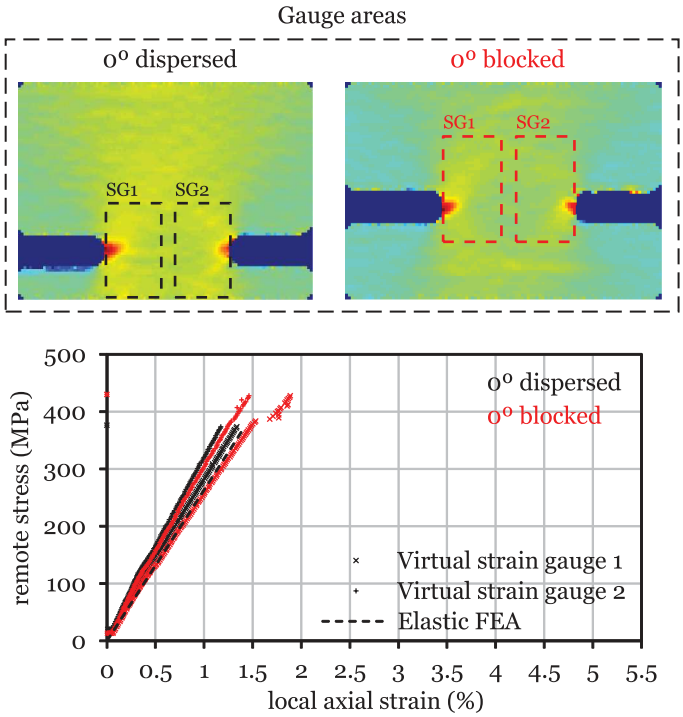

Fig. 5.31. Virtual strain gauge areas and remote stress-local axial strain relations of representative 10 mm wide DENT test specimens (geometry A). The loading direction is parallel to the vertical axis of the specimens.

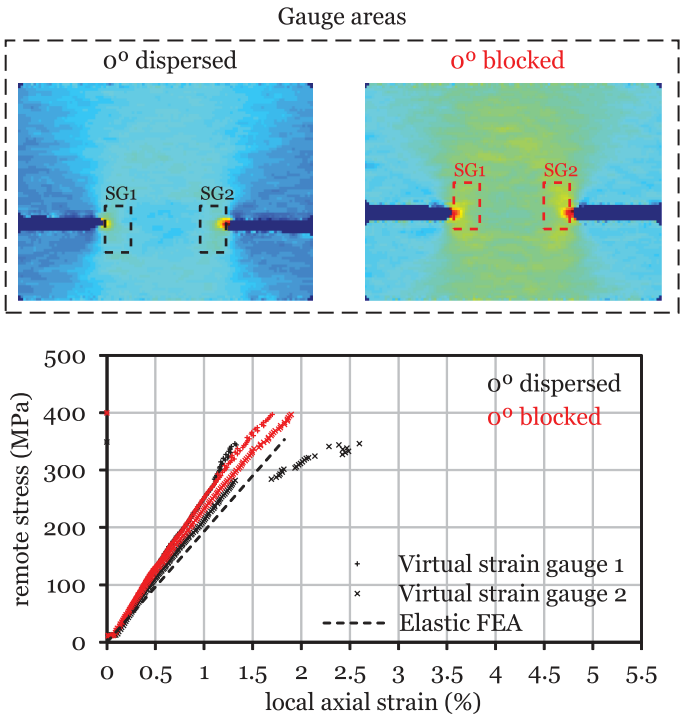

Fig. 5.32. Virtual strain gauge areas and remote stress-local axial strain relations of representative 20 mm wide DENT test specimens (geometry B). The loading direction is parallel to the vertical axis of the specimens.

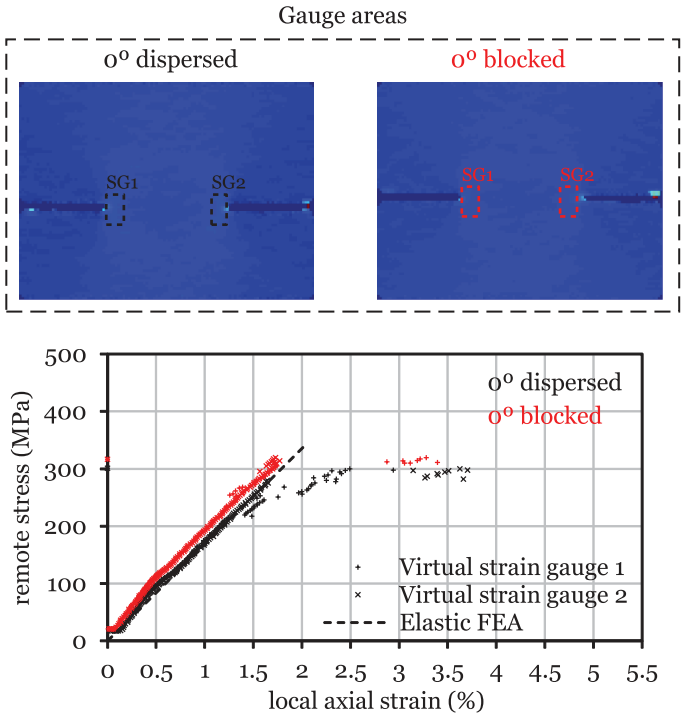

Fig. 5.33. Virtual strain gauge areas and remote stress-local axial strain relations of representative 30 mm wide DENT test specimens (geometry C). The loading direction is parallel to the vertical axis of the specimens.

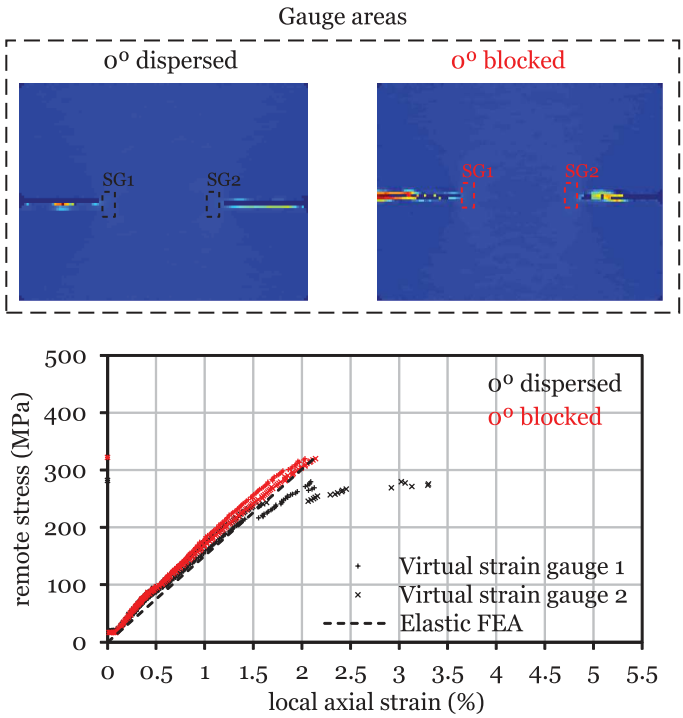

Fig. 5.34. Virtual strain gauge areas and remote stress-local axial strain relations of representative 40 mm wide DENT test specimens (geometry D). The loading direction is parallel to the vertical axis of the specimens.

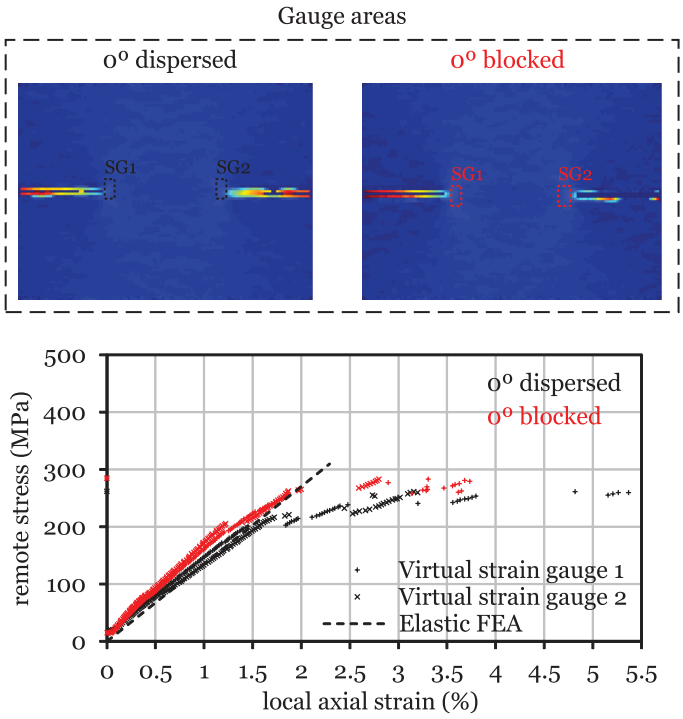

Fig. 5.35. Virtual strain gauge areas and remote stress-local axial strain relations of representative 50 mm wide DENT test specimens (geometry E). The loading direction is parallel to the vertical axis of the specimens.

wide (geometry A) and 50 mm wide (geometry E) models on the mesh detail shown in figures 5.36a and 5.37a, respectively.

The results of the FEA are plotted together with the DIC data in figures 5.31 to 5.35. As it can be observed, the numerical results are in very good agreement with the measured strains, validating the proposed virtual strain gauge approach, namely for application on regions of high strain concentration. It is interesting to note that virtual strain gauges computed from the DIC measurements are particularly advantageous in the analysis of the local strains in locations of high strain concentration because, unlike real strain gauges, they do not suffer from premature signal saturation due to the development of a damage process zone in the gauge area [182], unless fracture of the observation surface or pilling of the background speckle pattern occurs.

For the same laminate, figures 5.31 to 5.35 show that the results of both virtual strain gauges in the initial loading stages (linear range), before high local strain increments caused by strain localisation in the gauge area, match very well. This shows that an adequate test setup was used, resulting in good load alignment with regard to the position of the edge notches.

Interestingly, figures 5.31 to 5.35 also show that, in general, the onset of damage growth from the notch tips starts earlier in the *dispersed* laminate, since high local strain increments occur earlier in this laminate. In the case of the smaller specimens (figure 5.31), the earlier onset of damage growth in the *dispersed* laminate conducts to unstable propagation, resulting in a linear stress-strain relation up to ultimate failure.

Because the thickness of the 90° outer ply is the same for the *dispersed* and *blocked* laminates, and its neighbour ply, immediately below, has the same orientation (−45°) in both laminates (therefore not affecting the local constraining effect), it is clear that this earlier onset of damage is not caused by an *in situ* effect; instead, internal stress relaxation occurs inside the *blocked* laminate, which delays the onset of through-the-thickness intralaminar damage growth. It is noted that, contrary to the *dispersed* laminate, the 0° ply blocking in the *blocked* laminate results in higher stress concentrations in the adjacent interfaces, promoting delamination and internal splitting between the adjacent plies. Also, in the *blocked*

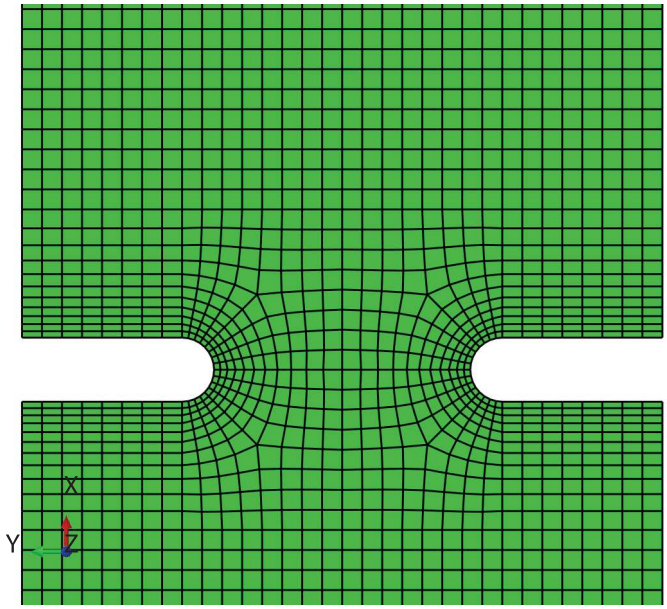

(a) Mesh detail.

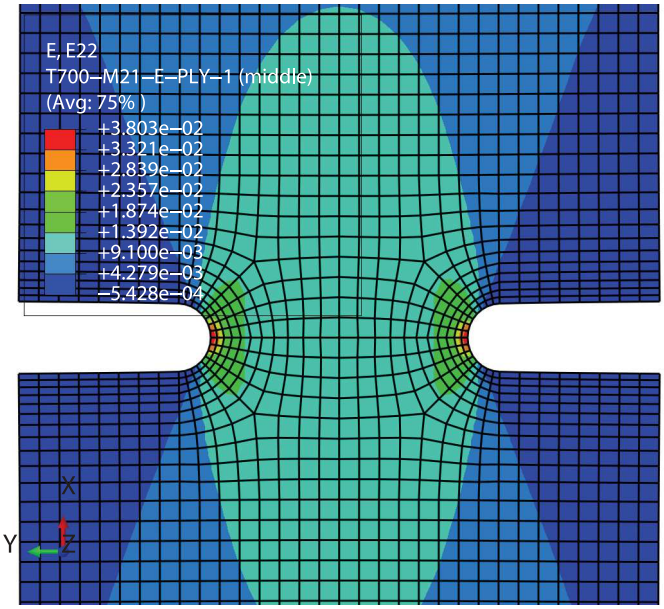

(b) Longitudinal strain field of the outer ply.

Fig. 5.36. Mesh detail of the FE model of a 10 mm wide DENT specimen (geometry A) and longitudinal strain field of the outer ply.

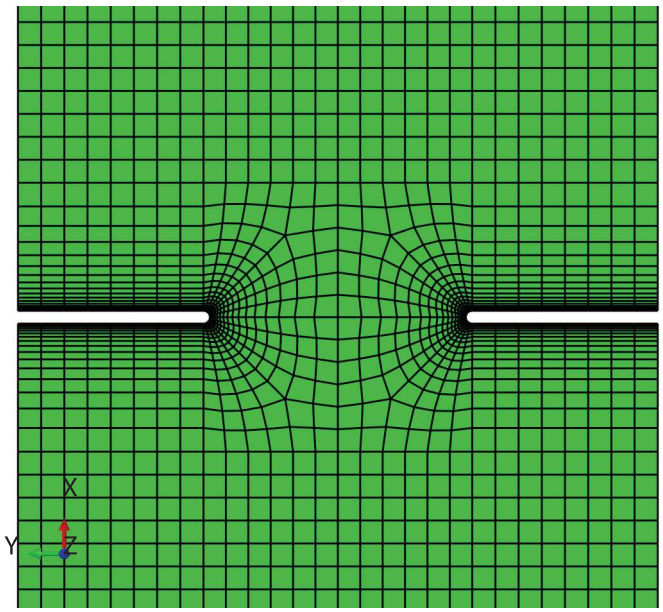

(a) Mesh detail.

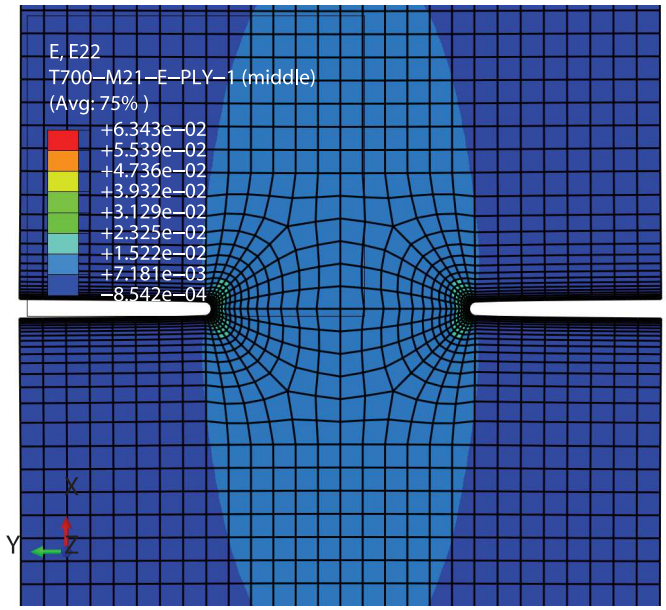

(b) Longitudinal strain field of the outer ply.

Fig. 5.37. Mesh detail of the FE model of a 50 mm wide DENT specimen (geometry E) and longitudinal strain field of the outer ply.

5.5. Experimental results and discussion

Table 5.9
Mean ultimate remote stresses ($\bar{\sigma}^{\infty}$) and coefficients of variation (C.V.) of the DENT tests.

Results	Geometry ID				
	A	B	C	D	E
***Dispersed* laminate**					
No. specimens	2	2	2	2	2
$\bar{\sigma}^{\infty}$ (MPa)	397	370	318	298	293
C.V. (%)	1.0	0.2	1.0	1.4	6.7
***Blocked* laminate**					
No. specimens	3	7	3	3	3
$\bar{\sigma}^{\infty}$ (MPa)	465	398	329	316	281
C.V. (%)	3.7	6.7	5.7	5.5	3.7

laminate, some of the adjacent NCF bi-angle layers are stacked with relative ply orientations of 90°, contributing to higher interlaminar stress concentrations between these plies.

In the present case, the increased internal stress relaxation in the *blocked* laminate is most probably caused by internal split cracking of the blocked 0° and −45° plies [111, 117, 166, 205]. Transverse matrix cracking and delamination, which are generally more detrimental to the laminates integrity, are believed to play a minor role in this relaxation process.

As explained in section 5.4, for the same ply thickness, transverse cracking occurs earlier in the outer plies, as in this case the energy release rate is magnified due to the proximity of the slit crack to the surface of the laminate [81]. Since, in the present study, transverse matrix cracking is not observed in the outer ply, it can be concluded that matrix cracking has most likely not occurred inside the laminate too. On the other hand, as the ply thickness decreases, delamination onset is known to occur very close to laminate failure [149]. For ply thicknesses below the conventional low grades (i.e. below 0.125 mm), as in the present study, delamination can be completely suppressed [53, 58, 122].

Table 5.9 shows the average results for the ultimate remote stress and corresponding coefficients of variation. These results are summarised in figure 5.38, which shows the mean ultimate remote stress as a function of the initial edge notch length, which is proportional to size in the case of geometrically similar specimens.

As expected, as the size of the specimens increases, the mean ultimate remote stress decreases. This means that, as expected, the proposed specimen configuration has positive geometry, a requirement for the determination of the $\mathcal{R}$-curve using the size effect law.

It is interesting to note that the ultimate remote stresses of the *blocked* laminate, which are the highest for the first four specimen configurations, tend to the same values of the ultimate remote stresses of the *dispersed* laminate as the initial edge notch length increases, becoming slightly lower for the larger specimen configuration (table 5.9 and fig-

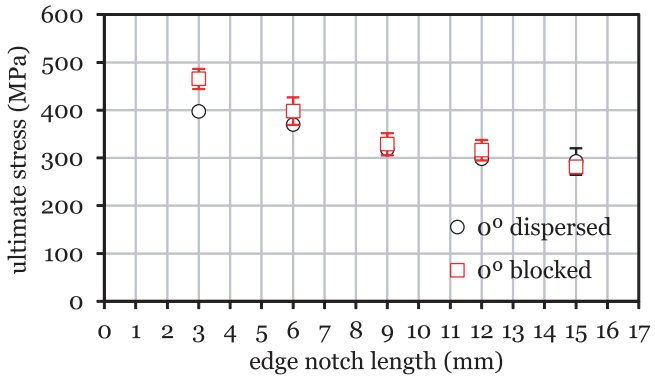

Fig. 5.38. Mean ultimate remote stress as a function of the initial edge notch length of the DENT tests.

Table 5.10
Fitting regressions and parameters for the size effect laws of the *dispersed* and *blocked* laminates.

Laminate	Regression fit [209]	Fitting parameters
Dispersed laminate	Linear regression II	$\acute{A}$ = 4.8277E − 06 MPa^{-2} mm^{-1}
		$\acute{C}$ = 2.9741E − 07 MPa^{-2}
Blocked laminate	Linear regression I	A = 3.9493E − 07 MPa^{-2}
		C = 2.6515E − 06 MPa^{-2} mm^{-1}

ure 5.38). This result shows that, as the size of the specimens increases, the effect of internal stress relaxation due to the blunting mechanisms promoted by the thicker blocks of 0° plies, namely internal split cracking, becomes less and less important.

This observation is in accordance with the general nonlinear fracture mechanics principles. For sufficiently large structures (or coupons), the size of the FPZ tends to a limit value that will become negligibly small when compared to any characteristic dimension of the structure. At this point, the fracture toughness reaches a constant (steady-state) value, and the principles of linear elastic fracture mechanics become applicable.

The change in the stacking sequence of the laminates under study, which have the same in-plane properties, only affects the extent of internal subcritical damage mechanisms. Assuming that these damage mechanisms can be lumped into a damage process zone, it is expected that, as the specimens become sufficiently large, the difference in the notched response of the *dispersed* and *blocked* will become negligible.

The size effect law regressions proposed in Ref. [209] that best fit the experimental data are *linear regression II* for the *dispersed* laminate and *linear regression I* for the *blocked* laminate. These linear regressions can be written as [65]:

$$\text{Linear regression I:} \quad \frac{1}{(\bar{\sigma}^{\infty})^2} = A\,w + C \tag{5.4}$$

$$\text{Linear regression II:} \quad \frac{1}{w\,(\bar{\sigma}^{\infty})^2} = \acute{A}\,\frac{1}{w} + \acute{C} \tag{5.5}$$

where A, C, $\acute{A}$ and $\acute{C}$ are the parameters that provide the best fitting to the size effect laws. These parameters, and the corresponding regressions, that best fit the size effect laws of the *dispersed* and *blocked* laminates are given in table 5.10. Figure 5.39 shows the experimental results and the fitted size effect laws.

Using the fitting parameters shown in table 5.10, it is now possible to calculate the length of the FPZ, l_{fpz}, and the steady-state value of the fracture toughness, $\mathcal{R}_{ss}$, of the *dispersed* and *blocked* laminates, according to their corresponding fitting regressions [65]:

$$\text{Linear regression I:} \quad l_{fpz} = \frac{\kappa_0}{2\acute{\kappa}_0}\frac{C}{A} \tag{5.6}$$

$$\mathcal{R}_{ss} = \frac{\kappa_0^2}{\acute{E}}\frac{1}{A} \tag{5.7}$$

$$\text{Linear regression II:} \quad l_{fpz} = \frac{\kappa_0}{2\acute{\kappa}_0}\frac{\acute{A}}{\acute{C}} \tag{5.8}$$

$$\mathcal{R}_{ss} = \frac{\kappa_0^2}{\acute{E}}\frac{1}{\acute{C}} \tag{5.9}$$

where $\kappa_0 = \kappa|_{\alpha=\alpha_0}$ and $\acute{\kappa}_0 = \partial\kappa/\partial\alpha|_{\alpha=\alpha_0}$ are, respectively, the value of the correction factor that accounts for both geometry and orthotropy of the material and the value of its derivative with respect to α calculated at the initial crack length

5.5. Experimental results and discussion

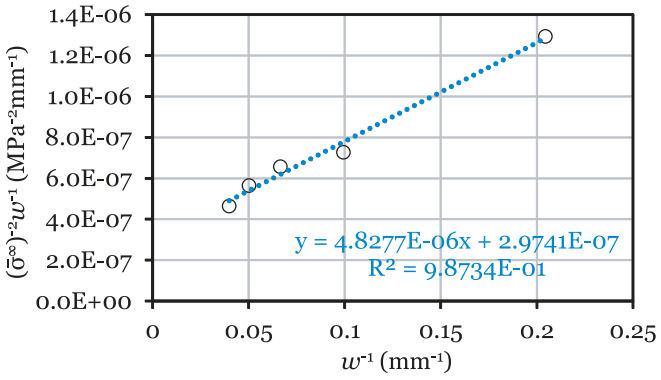

(a) *Dispersed* laminate: linear regression II.

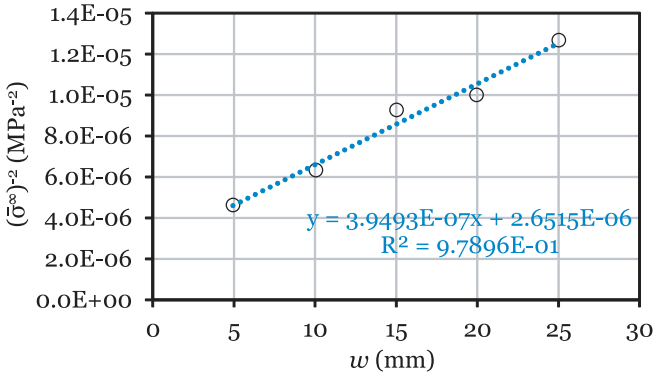

(b) *Blocked* laminate: linear regression I.

Fig. 5.39. Experimental results and best fitting for the size effect laws of the *dispersed* and *blocked* laminates.

($\alpha_0 = a_0/w$), and $\acute{E}$ is the equivalent modulus given in equation (4.6). Table 5.11 shows the values of l_{fpz} and $\mathcal{R}_{ss}$ obtained for both laminates.

Figure 5.40 shows the $\mathcal{R}$-curves of the *dispersed* and *blocked* laminates obtained as the envelopes of the crack driving force curves calculated using the size effect laws of figure 5.39. It is noted that most experimental results available in the literature consider the $\mathcal{R}$-curve to start from some initial nonzero value of $\mathcal{R}$. However, an $\mathcal{R}$-curve that starts from some initial nonzero value implies that the crack tip can sustain a singular stress field without showing any damage, which is unreasonable [277]. The $\mathcal{R}$-curve presented in figure 5.40 starts from zero, which means that the process zone forms right at the beginning of loading and that there is never any singularity at the crack tip, which is more physically reasonable. Nevertheless, for FRPs exhibiting a relatively large bridging zone, it is observed that the initial rising part of the $\mathcal{R}$-curve is considerably steep, which is the reason why, in practice, a nonzero initial value of $\mathcal{R}$ is often used.

To simplify the implementation of the $\mathcal{R}$-curve in numerical or analytical models, Catalanotti et al. [65] used the fitting formula presented in equation (4.21). The parameters ζ and η that best fit the formula to the $\mathcal{R}$-curves of the *dispersed* and *blocked* laminates are given in table 5.11. These parameters were obtained using a nonlinear least squares method with a Trust-Region algorithm, available in the commercial software Matlab [278]. Figure 5.41 shows the $\mathcal{R}$-curves and the corresponding fitting curves. As can be observed, the fitting formulae agree very well with the analytical envelopes.

Table 5.11
Parameters of the $\mathcal{R}$-curves and fitting formulae of the *dispersed* and *blocked* laminates.

Laminate	l_{fpz} (mm)	$\mathcal{R}_{ss}$ (N/mm)	ζ (mm^{-1})	η (-)
Dispersed laminate	5.31	175	0.1470	4.195
Blocked laminate	2.20	132	0.3731	3.946

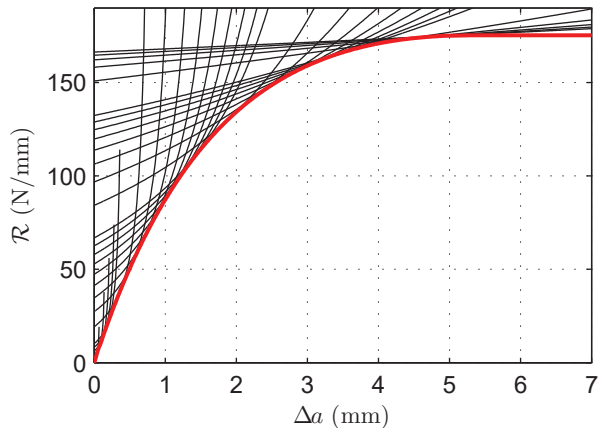

(a) *Dispersed* laminate.

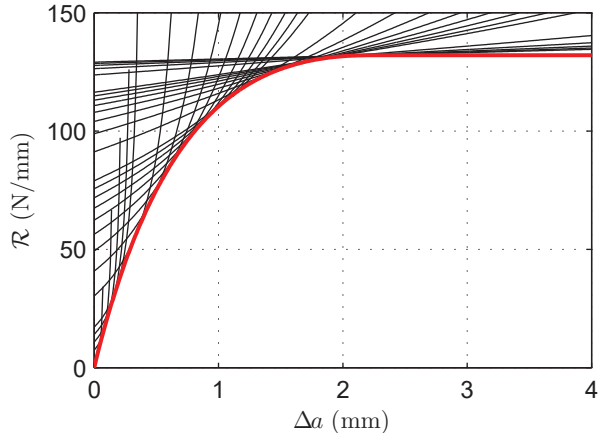

(b) *Blocked* laminate.

Fig. 5.40. Crack driving force curves and resulting $\mathcal{R}$-curves of the *dispersed* and *blocked* laminates for mode I longitudinal intralaminar fracture.

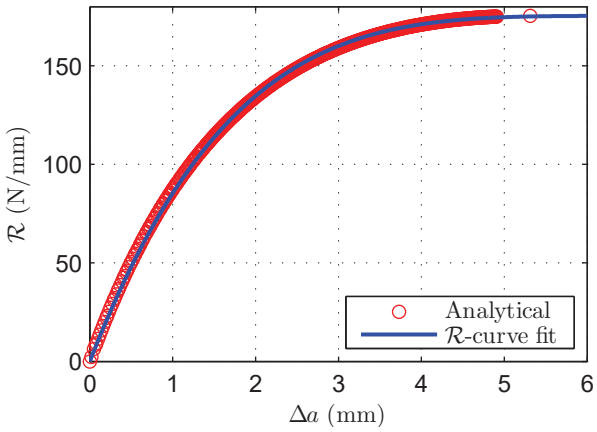

(a) *Dispersed* laminate.

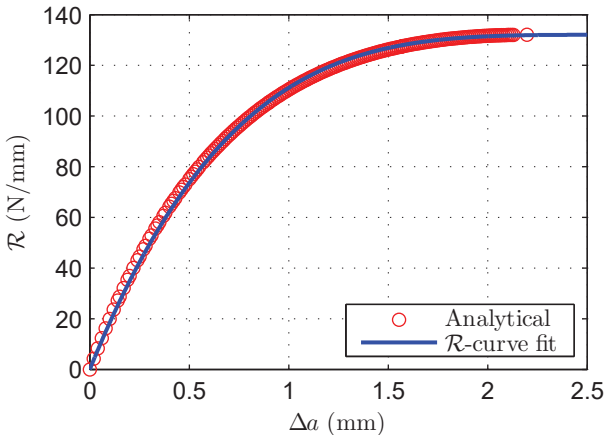

(b) *Blocked* laminate.

Fig. 5.41. Analytical and fitted $\mathcal{R}$-curves of the *dispersed* and *blocked* laminates.

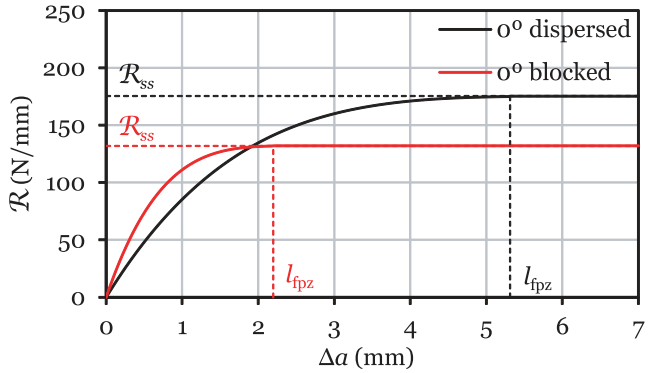

Fig. 5.42. Comparison of the $\mathcal{R}$-curves for mode I longitudinal intralaminar fracture of the *dispersed* and *blocked* laminates.

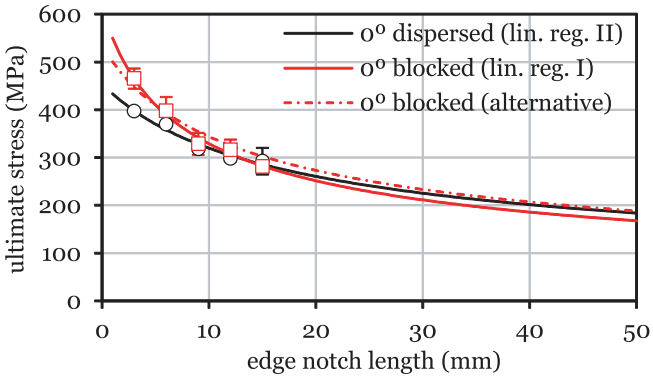

Fig. 5.43. Comparison between the size effect laws (equations (5.4) and (5.5)) and the experimental data used for calibration. Example of an alternative size effect law for the *blocked* laminate selected to reasonably fit the experimental results and give the same steady-state value of the fracture toughness of the *dispersed* laminate.

A comparison of the $\mathcal{R}$-curves of both laminates is given in figure 5.42. From table 5.11, it is observed that the length of the FPZ and the steady-state value of the fracture toughness of the *dispersed* laminate is, respectively, 2.42 times larger and 1.33 times higher than the *blocked* laminate. However, from the observation of the damage mechanisms and failure modes of the tested specimens, in particular of the larger coupons (geometry E), and taking into account that both laminates have the same material system, more similar $\mathcal{R}$-curves would be expected.

This difference in the results can be understood observing the experimental data plotted in figure 5.38 and resulting size effect laws (figure 5.43). The information provided by the available experimental data alone (figure 5.38), essentially shows a stronger strength reduction with size in the *blocked* laminate, despite its higher notched strength for the small coupons. Even though for the larger DENT specimen configuration tested in the present work (geometry E), the notched strengths of the *dispersed* and *blocked* laminates were not substantially different (see table 5.9 or figure 5.38), the resulting regressions predict reasonably lower notched strengths for the *blocked* laminate as size increases due to a steeper size effect law. This is translated in a brittler response and, consequently, in a shorter FPZ and lower fracture toughness.

The resulting $\mathcal{R}$-curves of the *dispersed* and *blocked* laminates (figure 5.42) clearly reflect these trends. The *blocked* laminate shows a fast rising $\mathcal{R}$-curve, typical of a brittler response, with a higher value of the fracture toughness for small crack extensions Δa (small coupons), resulting in higher notched strengths in these cases. However, because the size effect law of the *blocked* laminate decreases faster, its steady-state value of the fracture toughness is reached sooner, becoming reasonably lower for larger crack extensions (larger coupons), whereas the low rising $\mathcal{R}$-curve of the *dispersed* laminate keeps increasing until its higher steady-state value is reached.

To understand the effect of the calibration parameters of the fitting regression on the resulting size effect law and, consequently, on the derived $\mathcal{R}$-curve, in figure 5.43 an example of an alternative size effect law for the *blocked* laminate

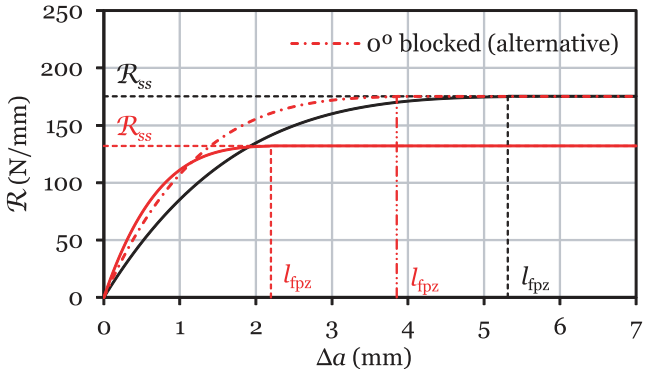

Fig. 5.44. Recalculation of the $\mathcal{R}$-curve for the *blocked* laminate, derived from an alternative size effect law selected to reasonably fit the experimental results and give the same steady-state value of the fracture toughness of the *dispersed* laminate.

is also plotted, obtained from linear regression I (equation (5.4)) but with different calibration parameters A and C. These parameters were selected to reasonably fit the experimental results (even though noticeably not as well as the parameters in table 5.10), and, at the same time, give the same steady-state value of the fracture toughness of the *dispersed* laminate.

Figure 5.44 shows the resulting alternative $\mathcal{R}$-curve. As can be observed, a small change in the shape of the size effect law (figure 5.43) conducts to remarkable changes in the shape and parameters of the $\mathcal{R}$-curve. In this case, the alternative $\mathcal{R}$-curve virtually resembles the observed material and laminate behaviour: for small crack extensions (small coupons), the *blocked* laminate exhibits a higher value of the fracture toughness; as the crack extension increases (i.e. for larger coupons), the fracture toughnesses of both laminates tend to the same steady-state value, the same trend observed by their notched strengths.

In the present case, testing a larger specimen configuration would most certainly help understanding if, as suggested before, for specimen geometries larger than the 50 mm wide configuration (geometry E) the notched strengths of both laminates tend to the same value. Notice that, according to the experimental data (figure 5.38) and resulting size effect laws (figure 5.43), the 50 mm wide specimens are at a turning point when comparing the two laminates. However, the trends are not known unless experimental results on larger specimens are obtained.

In fact, it is important to note that the $\mathcal{R}$-curve determined from the size effect law is defined such that $\mathcal{R}_{ss}$ is the energy required for crack growth in an infinitely large specimen, which is taken as size and geometry independent. However, because the size effect law is not exact, this should be regarded as an approximation. These results highlight the importance of adequately selecting both specimen configurations and range of coupon dimensions in calibrating the size effect laws to accurately derive the $\mathcal{R}$-curves with this methodology.

5.5.2. Laminate mode I compressive crack resistance curve

For each laminate and DENC configuration, between 4 and 10 valid specimens were tested to failure. The remote stress-displacement curves of the *dispersed* and *blocked* laminates are shown in figures 5.45 to 5.49 for the different geometries. The remote stress, σ^{∞}, of each test was calculated dividing the applied load by the corresponding specimen's cross-section area. The applied load was measured by the load cell and the displacement is the cross-head displacement of the testing machine. Due to adjustments in the self-alignment system (figure 5.4b), all specimen configurations show a nonlinear remote stress-displacement relation in the beginning of the tests.

Figure 5.50 shows representative DENC test specimens of the *dispersed* and *blocked* laminates after testing. The different specimen configurations fail with the propagation of intralaminar compressive damage along the ligament section. Final catastrophic failure always coincided with a large load drop in the remote stress-displacement curves and a strong noise caused by longitudinal compressive failure. However, prior to catastrophic failure, small load drops occurred in some specimens of all configurations, either preceding or following the peak applied remote stress (figures 5.45 to 5.49);

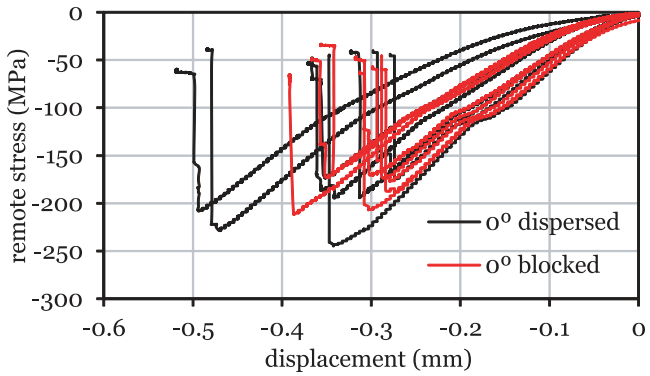

Fig. 5.45. Remote stress-displacement curves for the 10 mm wide DENC specimens (geometry A).

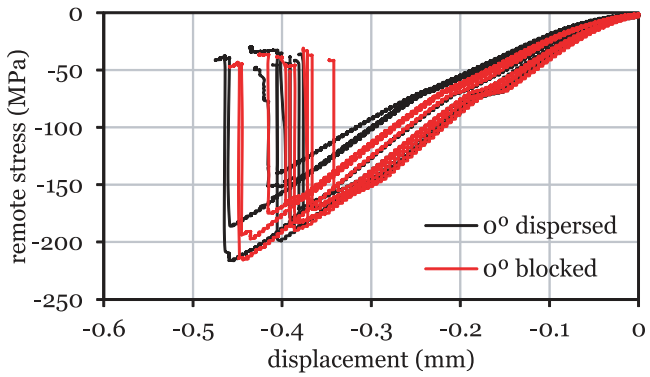

Fig. 5.46. Remote stress-displacement curves for the 15 mm wide DENC specimens (geometry B).

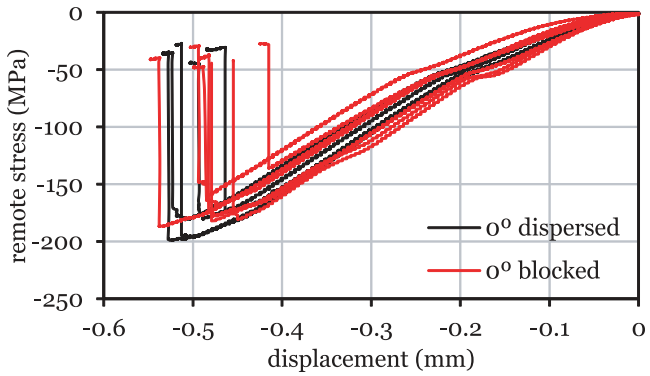

Fig. 5.47. Remote stress-displacement curves for the 20 mm wide DENC specimens (geometry C).

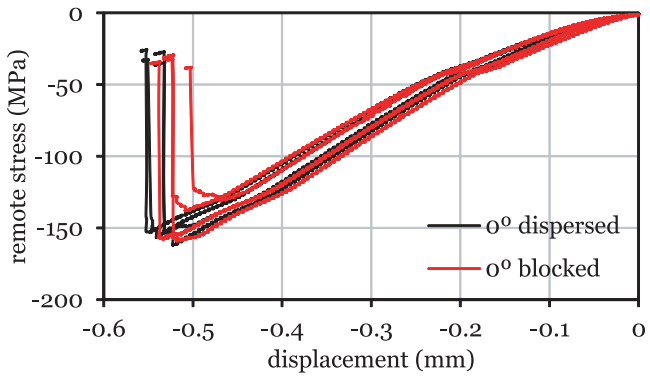

Fig. 5.48. Remote stress-displacement curves for the 25 mm wide DENC specimens (geometry D).

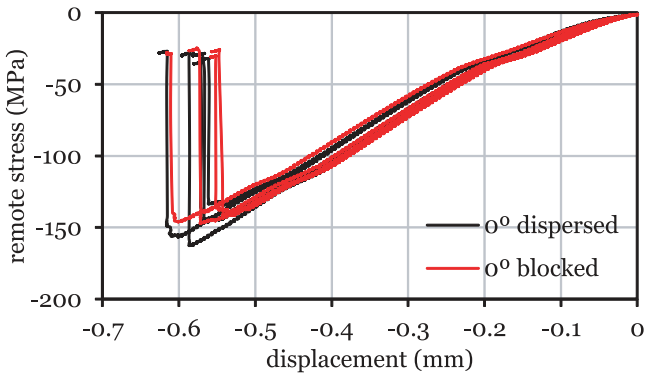

Fig. 5.49. Remote stress-displacement curves for the 30 mm wide DENC specimens (geometry E).

in addition, internal damage growth in the specimens was audible during the tests as the applied load approached the ultimate remote stress, indicating that stable damage growth occurred in the DENC test specimens before unstable intralaminar compressive failure across the notched plane.

In both laminates, internal damage growth was audible at applied remote stresses as low as 64% of the ultimate remote stress. In some specimens, damage growth above 89% of the ultimate remote stress could be attributed to compressive fibre failure, due to the stronger characteristic noise produced by this damage mechanism. In some of the largest specimens, stable intralaminar damage growth was also audible after the peak remote stress.

It is interesting to note that the onset of fibre compressive failure seems to have occurred at the final stages of damage propagation in both laminates, always close to the peak remote stress. Hence, it can be concluded that, as fibre compressive failure initiates, it prompts quick intralaminar compressive damage growth, which rapidly conducts to catastrophic specimen failure.

Figures 5.51 to 5.60 show the longitudinal strain field and the local longitudinal strain measured along two lines tangent to the tips of the edge notches and parallel to the loading direction, obtained with the DIC technique on representative specimens of the different configurations, whose analysis helps understanding the evolution of compressive damage in the DENC test specimens. For reference, the coloured distributions of grey levels and the remote stress-time relations are also shown.

The onset of intralaminar damage on the outer 90° ply, which can be easily identified observing the longitudinal strain fields and the local longitudinal strain tangent to the tips of the edge notches (figures 5.51 to 5.60), can occur at applied remote stresses as low as 80% of the ultimate remote stress. For the smaller specimens (geometries A and B), the onset of intralaminar damage occurs without producing visible damage or perceptible sounds during the test.

After the onset of intralaminar damage, stable damage propagation across the notched plane has apparently occurred in all specimen configurations of both laminates. However, this is not always visible in figures 5.51 to 5.60 because, in some specimens, stable compressive damage growth across the notched plane occurred predominantly in one face of the specimen, propagating unstably through the thickness as the specimen approached final fracture.

This type of failure behaviour is caused by the compressive damage mechanisms involved in the fracture process, in particular fibre kinking, which is originated by local micro-structural defects that trigger kink band propagation [103, 281, 282]. Hence, compressive failure may have initiated predominantly in one face of the specimen due to the characteristics of the tested material (acceptable situation), or due to load misalignment (undesirable situation). Nevertheless, in all cases presented in figures 5.51 to 5.60, valid loading conditions during the tests were assured by appropriate loading setup, verified by post-failure analysis of the tested specimen, and by analysis of the displacement and strain fields measured with the DIC technique.

In most cases, net-section fracture of the outer 90° ply preceded the ultimate remote stress; the only exceptions are

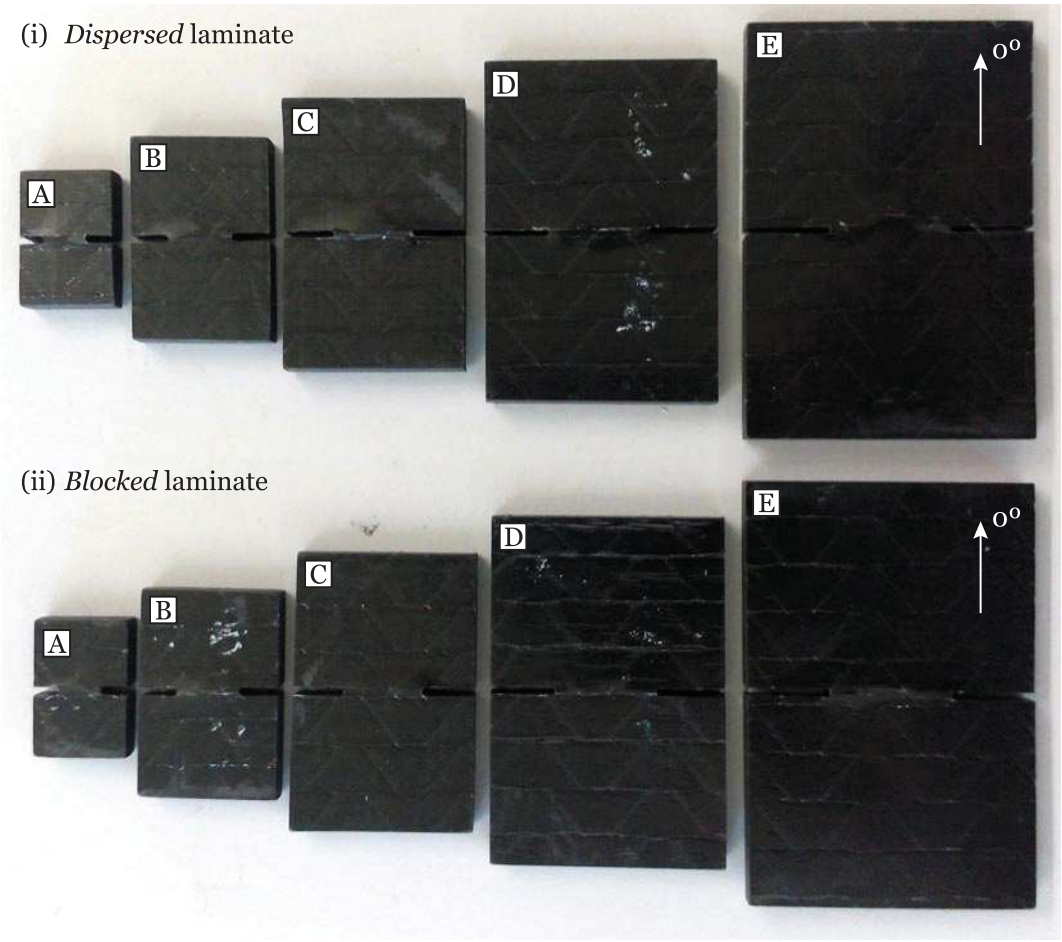

Fig. 5.50. Representative DENC test specimens after testing.

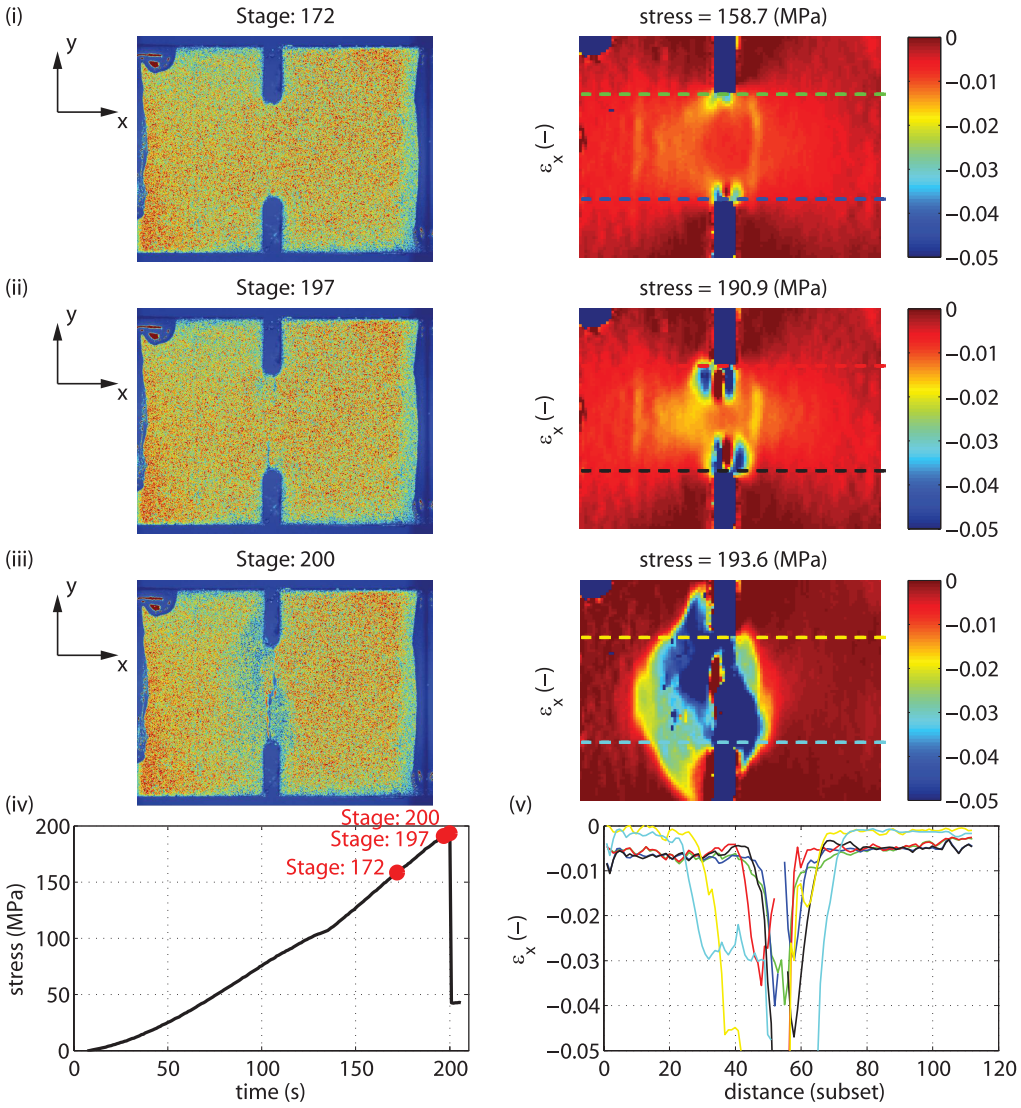

Fig. 5.51. Coloured distributions of grey levels (0–255) and longitudinal strain fields, ε_x, of the outer 90° ply of a representative 10 mm wide *dispersed* DENC test specimen (geometry A) obtained with the DIC technique at the stages of (i) onset of intralaminar compressive damage growth, (ii) before unstable propagation across the notched plane, and (iii) at the ultimate remote stress. (iv) Position of the stages in the remote stress-time relation. (v) Local longitudinal strain measured along two lines tangent to the tips of the edge notches and parallel to the loading direction. The reference DIC coordinate system is depicted in the figures, where the x-axis is aligned with the loading direction. The stresses are given in absolute values.

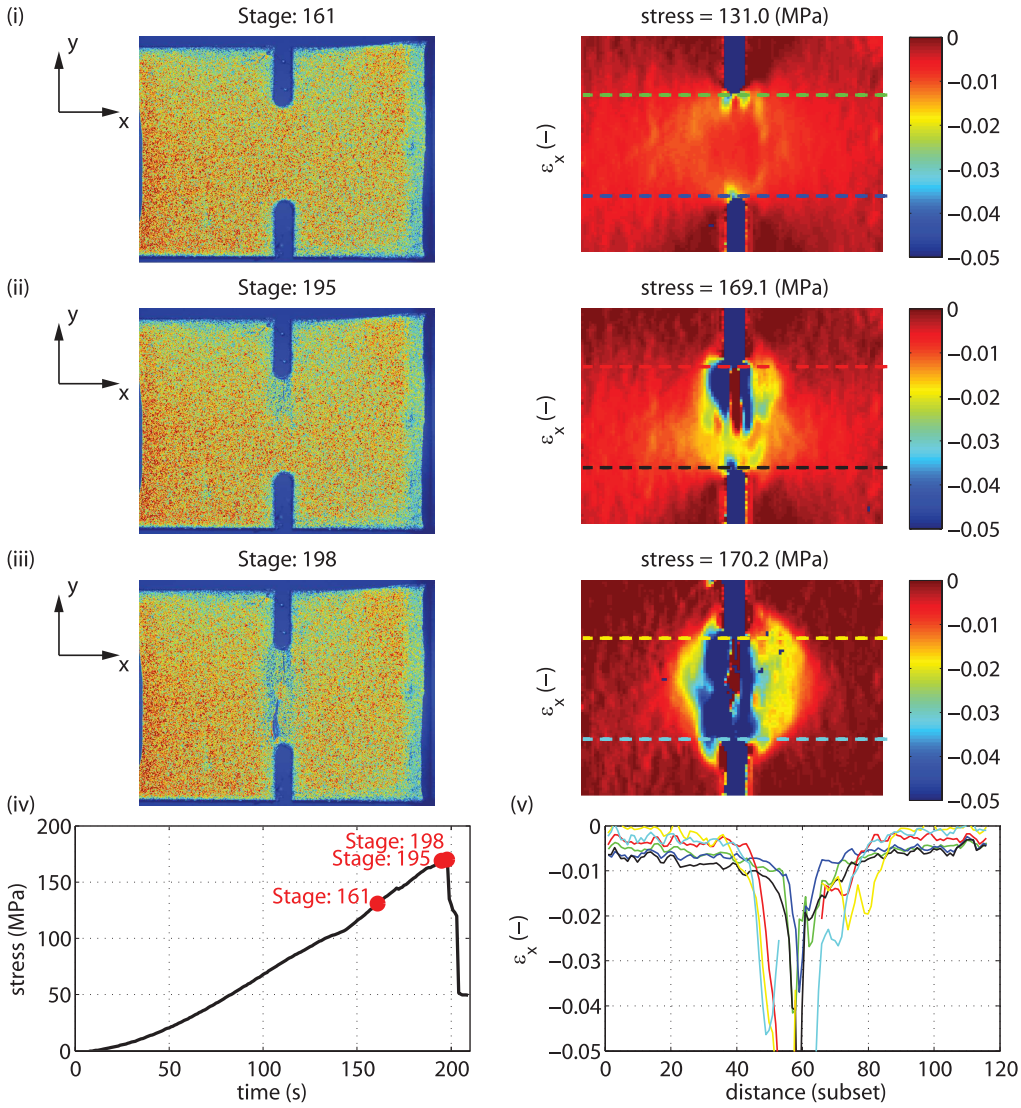

Fig. 5.52. Coloured distributions of grey levels (0–255) and longitudinal strain fields, ε_x, of the outer 90° ply of a representative 10 mm wide *blocked* DENC test specimen (geometry A) obtained with the DIC technique at the stages of (i) onset of intralaminar compressive damage growth, (ii) before unstable propagation across the notched plane, and (iii) at the ultimate remote stress. (iv) Position of the stages in the remote stress-time relation. (v) Local longitudinal strain measured along two lines tangent to the tips of the edge notches and parallel to the loading direction. The reference DIC coordinate system is depicted in the figures, where the x-axis is aligned with the loading direction. The stresses are given in absolute values.

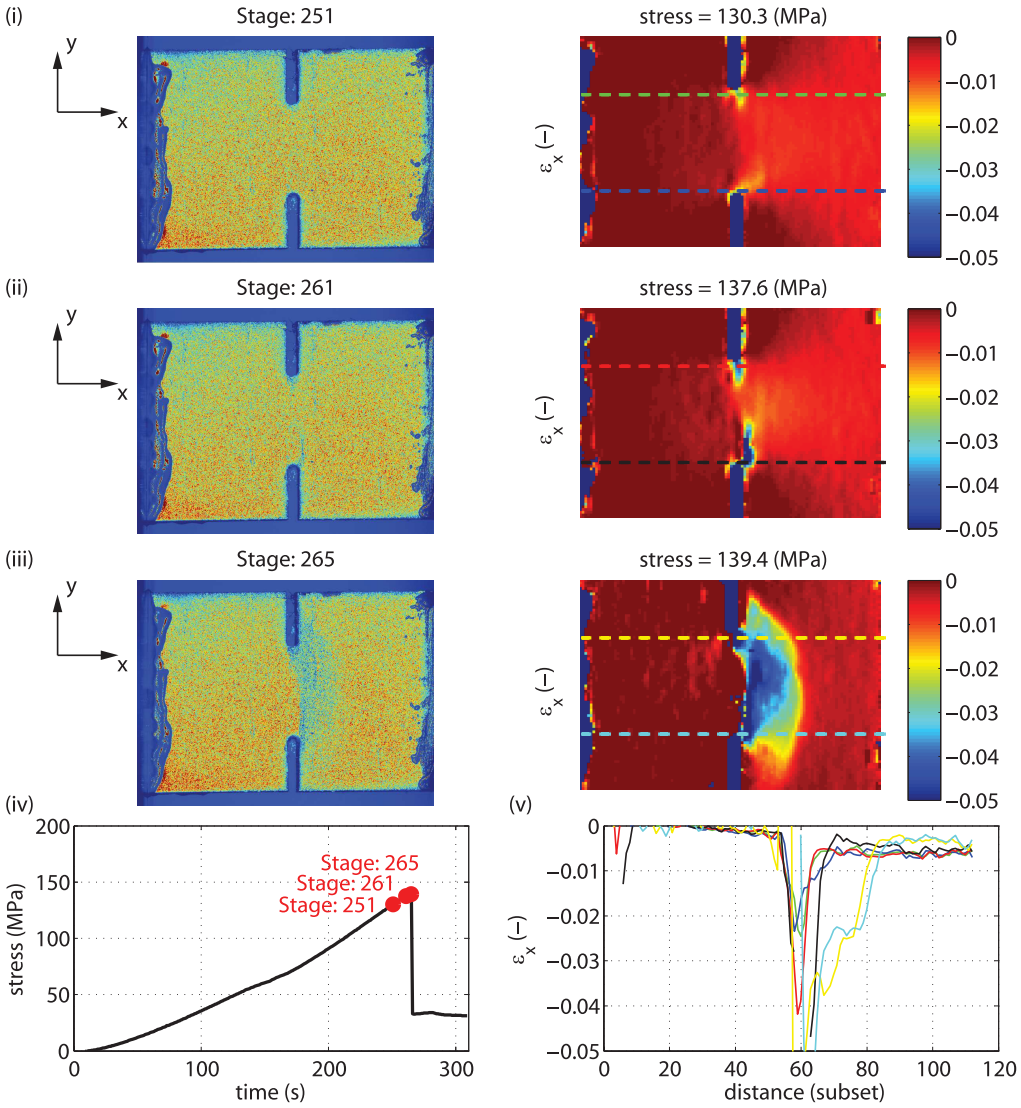

Fig. 5.53. Coloured distributions of grey levels (0–255) and longitudinal strain fields, ε_x, of the outer 90° ply of a representative 15 mm wide *dispersed* DENC test specimen (geometry B) obtained with the DIC technique at the stages of (i) onset of intralaminar compressive damage growth, (ii) before unstable propagation across the notched plane, and (iii) at the ultimate remote stress. (iv) Position of the stages in the remote stress-time relation. (v) Local longitudinal strain measured along two lines tangent to the tips of the edge notches and parallel to the loading direction. The reference DIC coordinate system is depicted in the figures, where the x-axis is aligned with the loading direction. The stresses are given in absolute values.

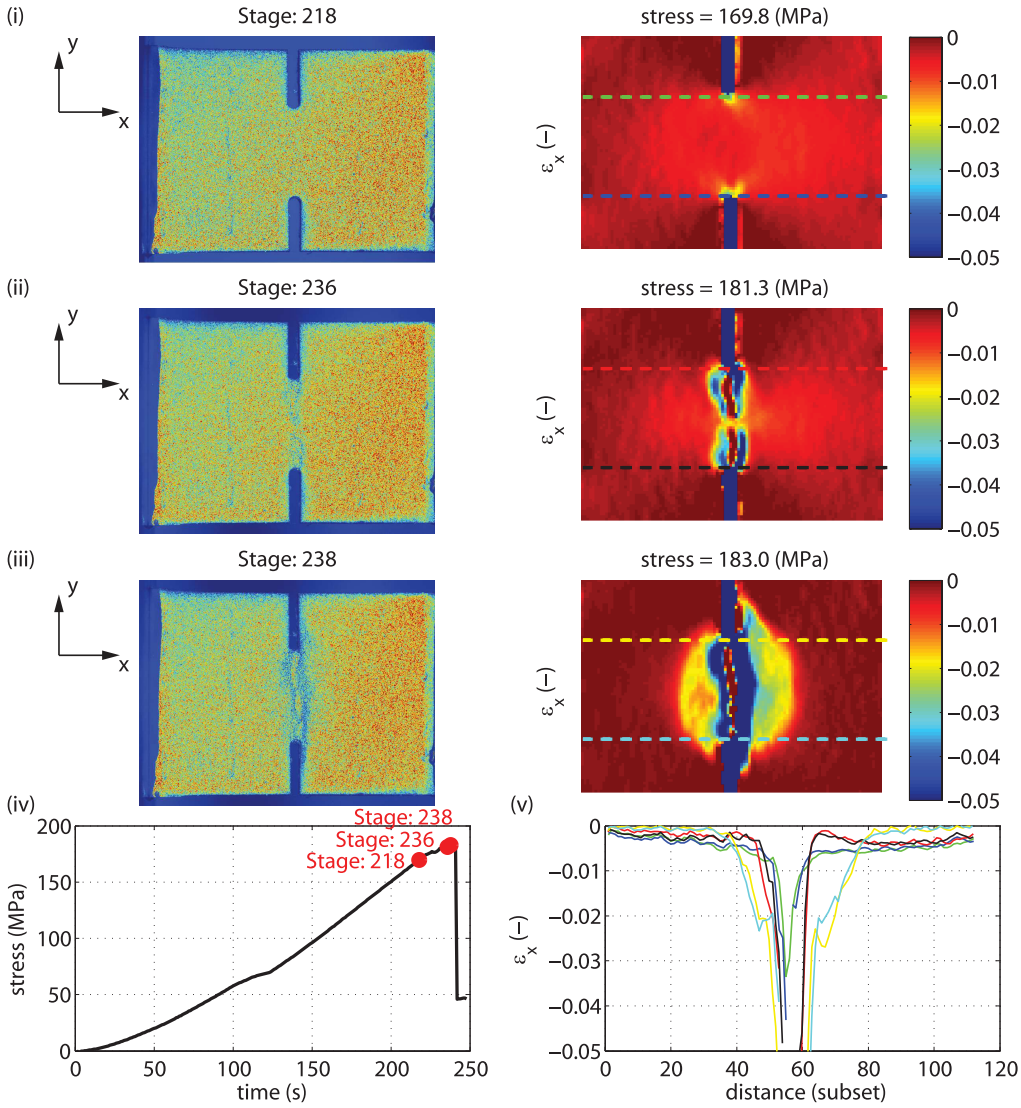

Fig. 5.54. Coloured distributions of grey levels (0–255) and longitudinal strain fields, ε_x, of the outer 90° ply of a representative 15 mm wide *blocked* DENC test specimen (geometry B) obtained with the DIC technique at the stages of (i) onset of intralaminar compressive damage growth, (ii) before unstable propagation across the notched plane, and (iii) at the ultimate remote stress. (iv) Position of the stages in the remote stress-time relation. (v) Local longitudinal strain measured along two lines tangent to the tips of the edge notches and parallel to the loading direction. The reference DIC coordinate system is depicted in the figures, where the x-axis is aligned with the loading direction. The stresses are given in absolute values.

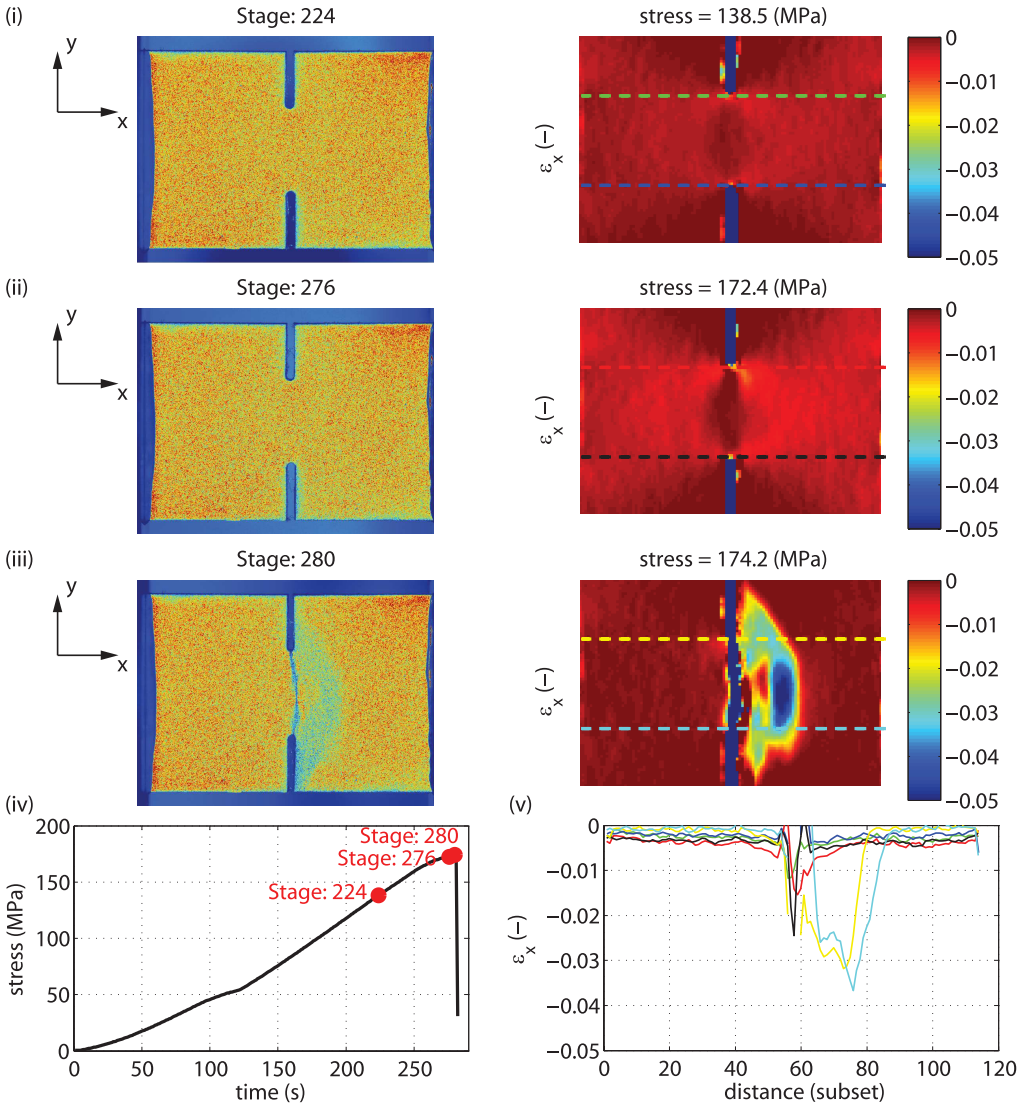

Fig. 5.55. Coloured distributions of grey levels (0–255) and longitudinal strain fields, ε_x, of the outer 90° ply of a representative 20 mm wide *dispersed* DENC test specimen (geometry C) obtained with the DIC technique at the stages of (i) onset of intralaminar compressive damage growth, (ii) before unstable propagation across the notched plane, and (iii) at the ultimate remote stress. (iv) Position of the stages in the remote stress-time relation. (v) Local longitudinal strain measured along two lines tangent to the tips of the edge notches and parallel to the loading direction. The reference DIC coordinate system is depicted in the figures, where the x-axis is aligned with the loading direction. The stresses are given in absolute values.

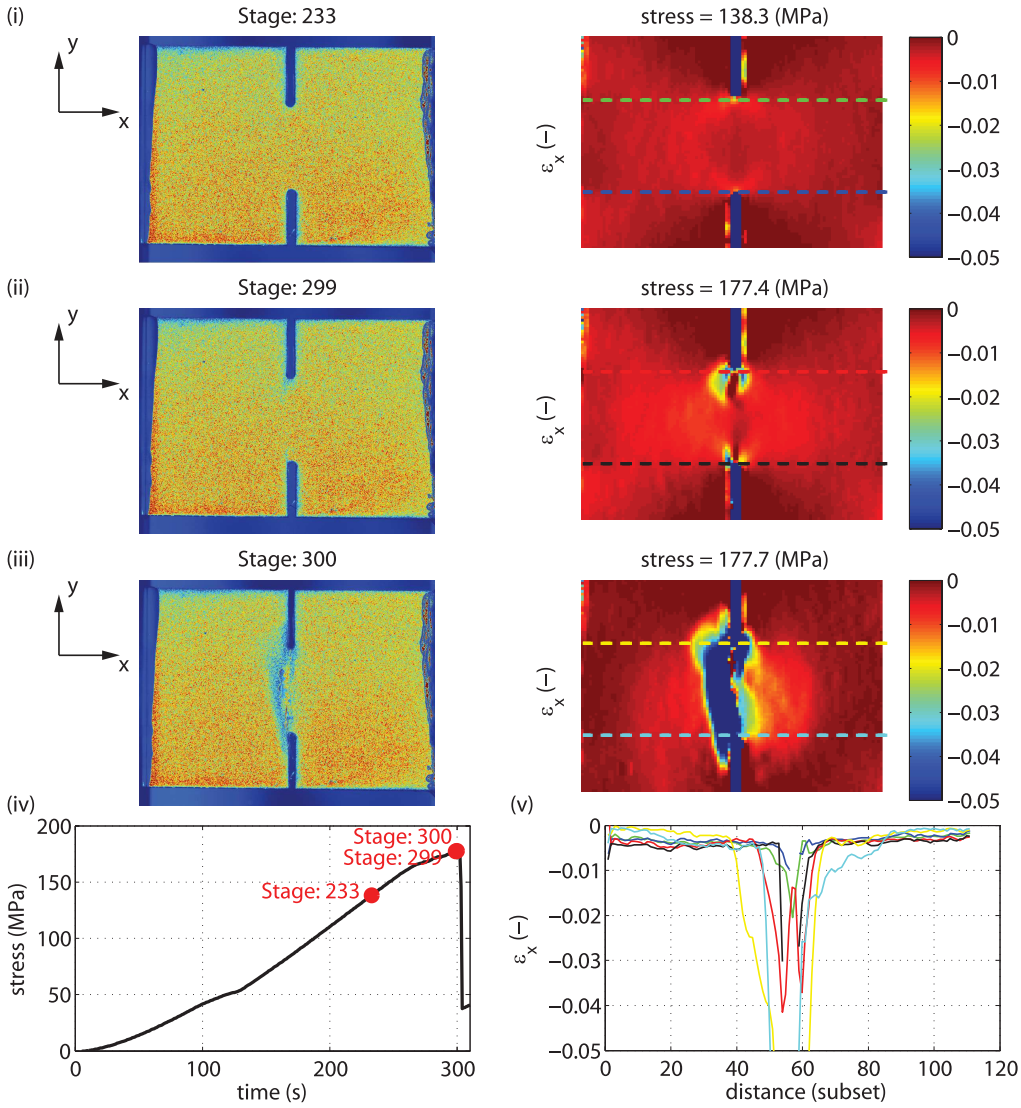

Fig. 5.56. Coloured distributions of grey levels (0–255) and longitudinal strain fields, ε_x, of the outer 90° ply of a representative 20 mm wide *blocked* DENC test specimen (geometry C) obtained with the DIC technique at the stages of (i) onset of intralaminar compressive damage growth, (ii) before unstable propagation across the notched plane, and (iii) at the ultimate remote stress. (iv) Position of the stages in the remote stress-time relation. (v) Local longitudinal strain measured along two lines tangent to the tips of the edge notches and parallel to the loading direction. The reference DIC coordinate system is depicted in the figures, where the x-axis is aligned with the loading direction. The stresses are given in absolute values.

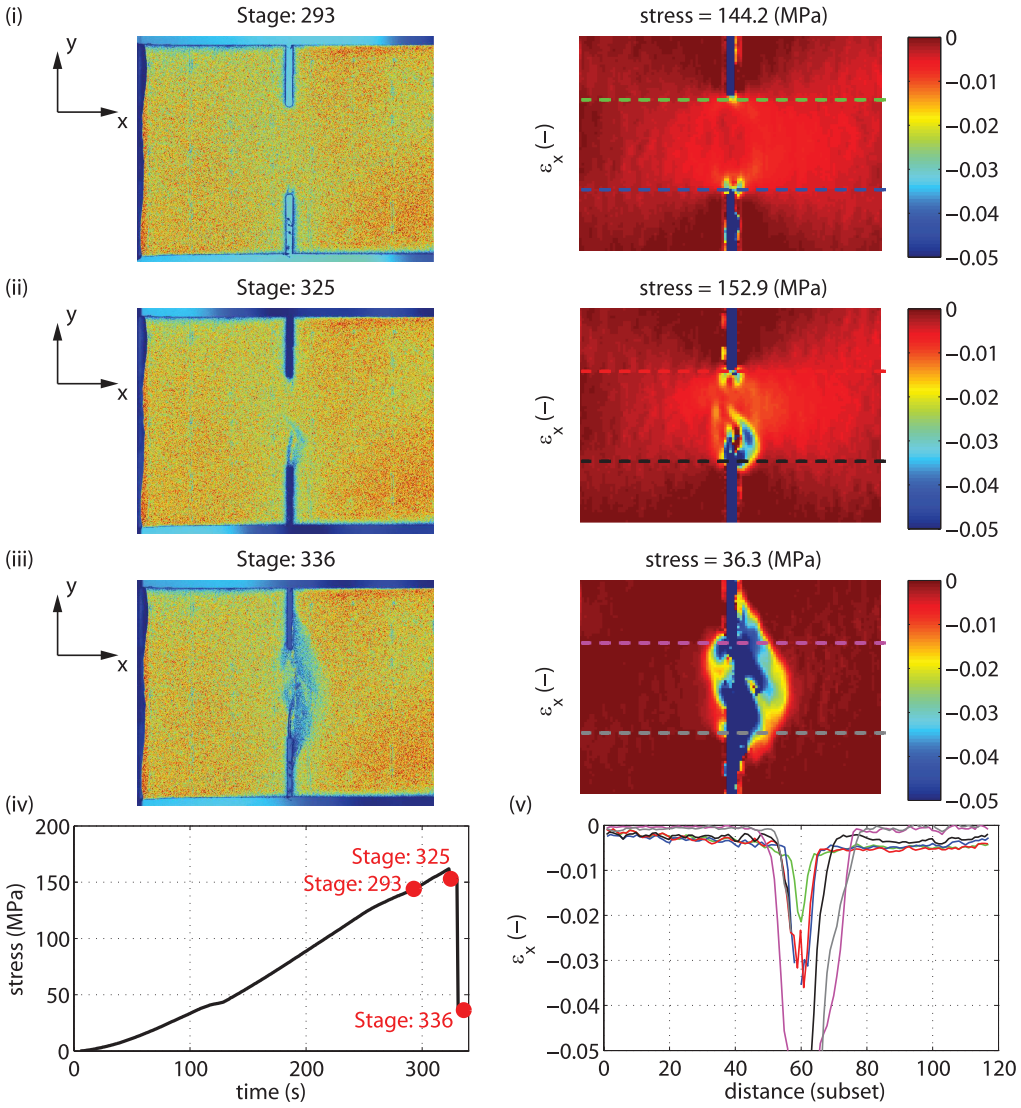

Fig. 5.57. Coloured distributions of grey levels (0–255) and longitudinal strain fields, ε_x, of the outer 90° ply of a representative 25 mm wide *dispersed* DENC test specimen (geometry D) obtained with the DIC technique at the stages of (i) onset of intralaminar compressive damage growth, (ii) after the ultimate remote stress, just before unstable propagation across the notched plane, and (iii) after specimen failure. (iv) Position of the stages in the remote stress-time relation. (v) Local longitudinal strain measured along two lines tangent to the tips of the edge notches and parallel to the loading direction. The reference DIC coordinate system is depicted in the figures, where the x-axis is aligned with the loading direction. The stresses are given in absolute values.

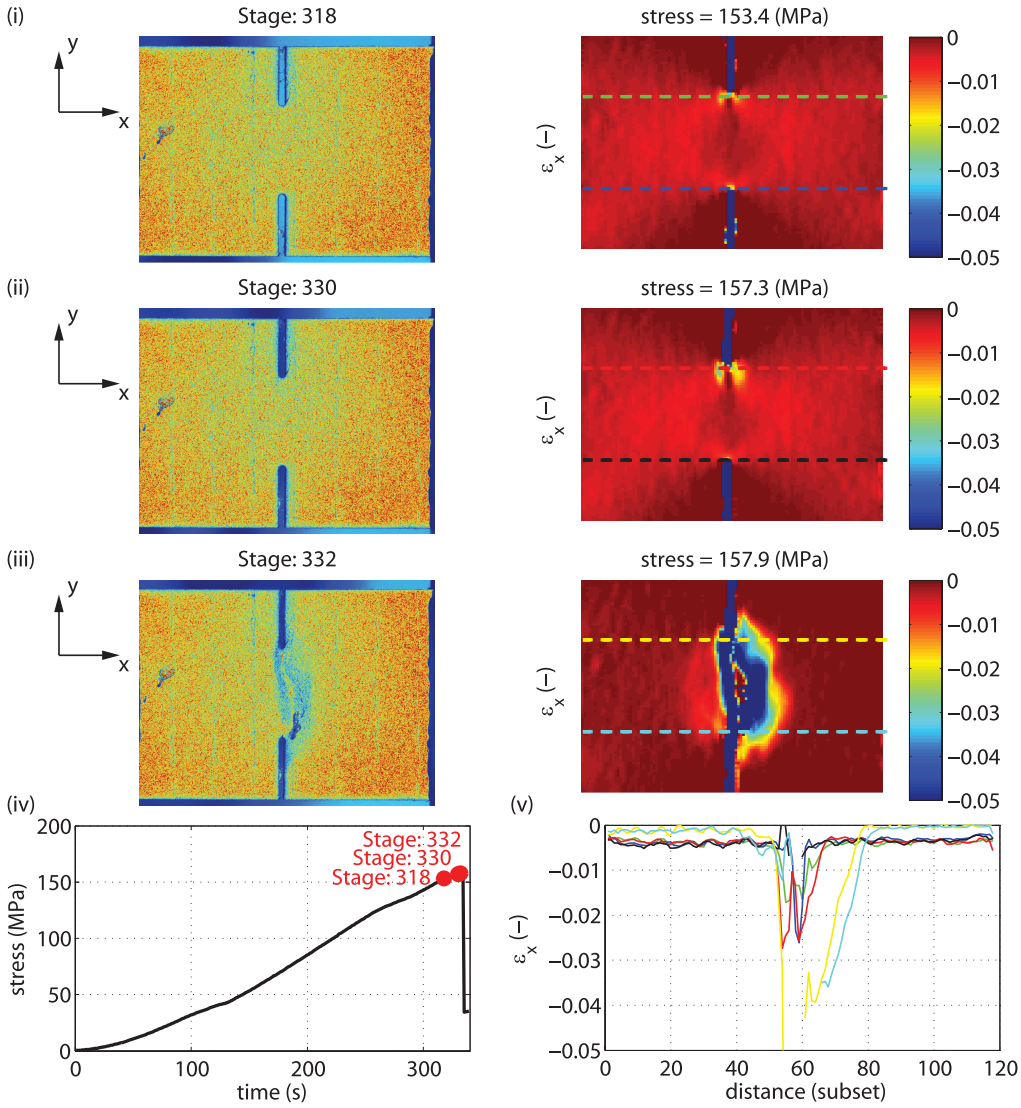

Fig. 5.58. Coloured distributions of grey levels (0–255) and longitudinal strain fields, ε_x, of the outer 90° ply of a representative 25 mm wide *blocked* DENC test specimen (geometry D) obtained with the DIC technique at the stages of (i) onset of intralaminar compressive damage growth, (ii) before unstable propagation across the notched plane, and (iii) at the ultimate remote stress. (iv) Position of the stages in the remote stress-time relation. (v) Local longitudinal strain measured along two lines tangent to the tips of the edge notches and parallel to the loading direction. The reference DIC coordinate system is depicted in the figures, where the x-axis is aligned with the loading direction. The stresses are given in absolute values.

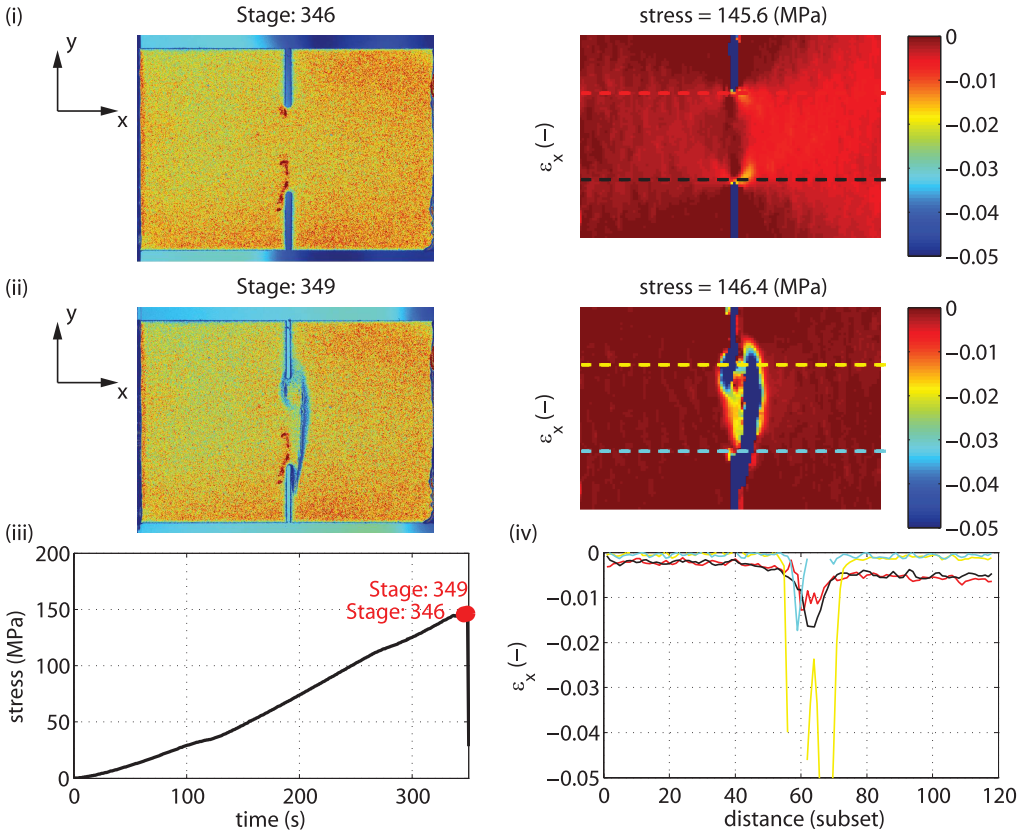

Fig. 5.59. Coloured distributions of grey levels (0–255) and longitudinal strain fields, ε_x, of the outer 90° ply of a representative 30 mm wide *dispersed* DENC test specimen (geometry E) obtained with the DIC technique at the stages of (i) onset and unstable propagation of intralaminar compressive damage across the notched plane and (ii) at the ultimate remote stress. (iii) Position of the stages in the remote stress-time relation. (iv) Local longitudinal strain measured along two lines tangent to the tips of the edge notches and parallel to the loading direction. The reference DIC coordinate system is depicted in the figures, where the x-axis is aligned with the loading direction. The stresses are given in absolute values.

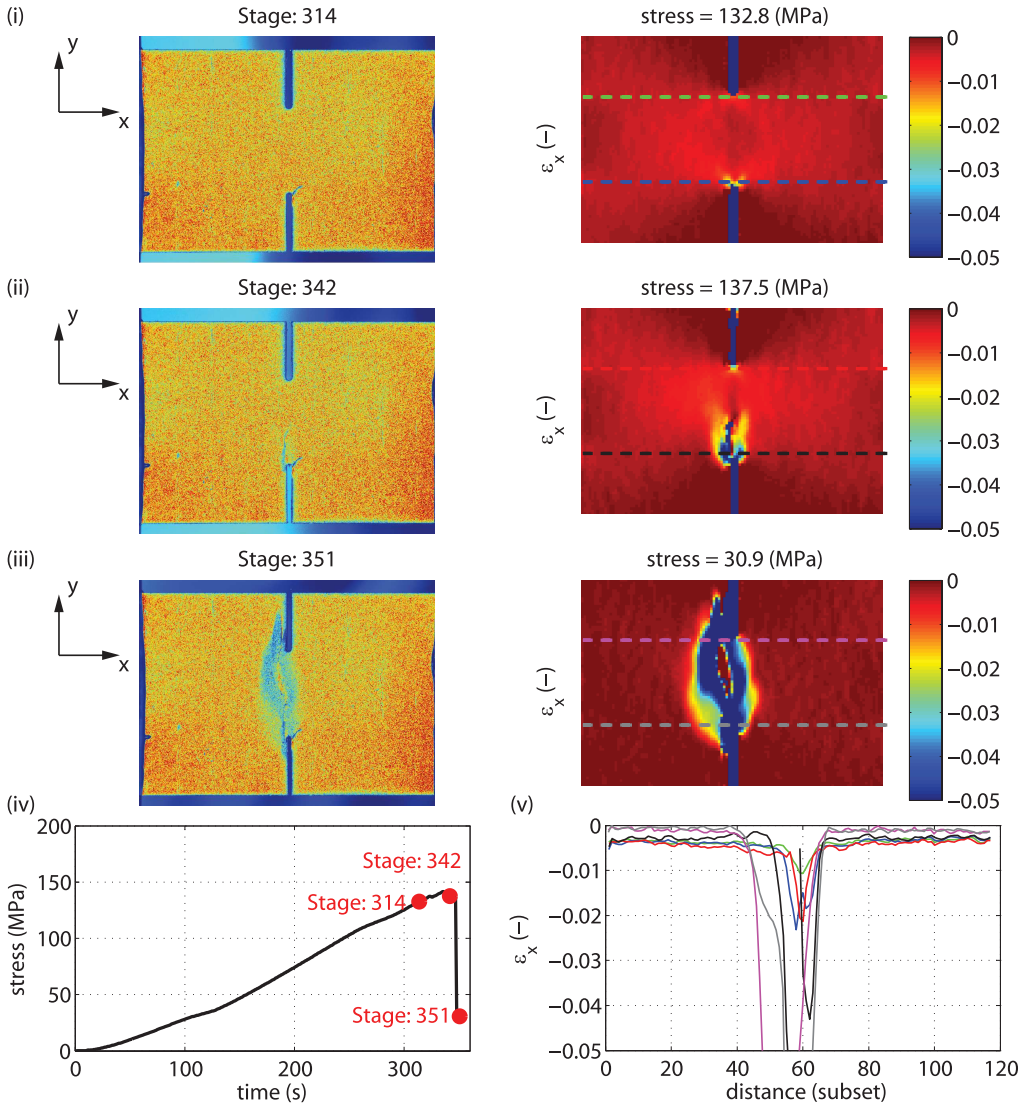

Fig. 5.60. Coloured distributions of grey levels (0–255) and longitudinal strain fields, ε_x, of the outer 90° ply of a representative 30 mm wide *blocked* DENC test specimen (geometry E) obtained with the DIC technique at the stages of (i) onset of intralaminar compressive damage growth, (ii) before unstable propagation across the notched plane, and (iii) after specimen failure. (iv) Position of the stages in the remote stress-time relation. (v) Local longitudinal strain measured along two lines tangent to the tips of the edge notches and parallel to the loading direction. The reference DIC coordinate system is depicted in the figures, where the x-axis is aligned with the loading direction. The stresses are given in absolute values.

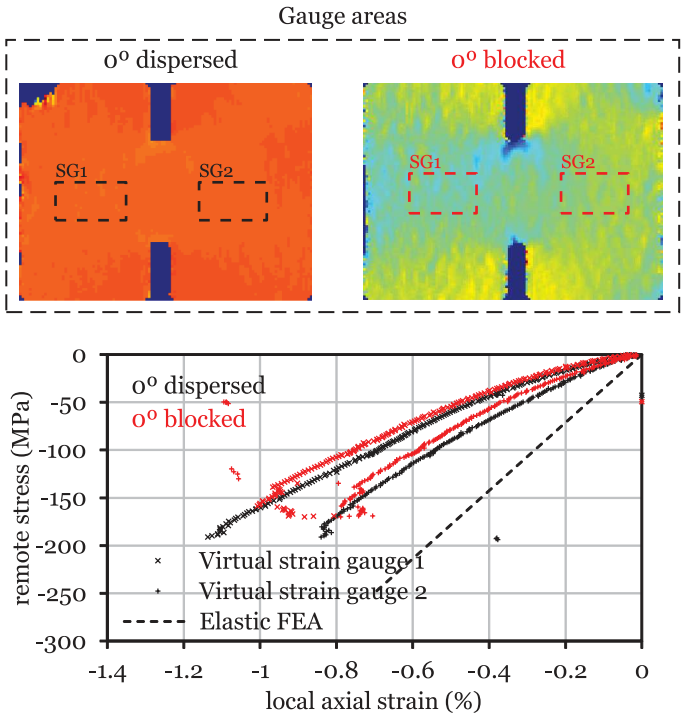

Fig. 5.61. Virtual strain gauge areas and remote stress-local axial strain relations of representative 10 mm wide DENC test specimens (geometry A). The loading direction is parallel to the horizontal axis of the specimens.

depicted in figures 5.57 and 5.60. In the latter, intralaminar compressive failure may have occurred predominantly in the other face of the specimen, before penetrating completely through the specimen's thickness. It is interesting to note, though, that, in all cases, fracture of the outer 90° ply occurred just before, or just after the ultimate remote stress, which indicates that when the fracture process zone propagates completely across the notched plane, intralaminar compressive damage, including kink band formation, penetrates rapidly through the thickness of the specimen, leading to the specimen failure. The adopted specimen scaling configuration results, therefore, in self-similar intralaminar compressive failure, suitable for the characterisation of the laminate mode I intralaminar fracture properties associated with the propagation of compressive damage.

The pictures of the specimens with the coloured distributions of grey levels in figures 5.51 to 5.60 also show that surface net-section fracture of the outer 90° ply between the tips of the edge notches did not always occur exactly across the notched plane, (e.g. figures 5.58 to 5.60). Nevertheless, post-failure analysis of the tested specimens show that laminate intralaminar compressive fracture occurred primarily on the notched plane (figure 5.50). Moreover, it is noted that the specimens with more irregular fracture planes are the ones that exhibited more unstable transverse compressive damage propagation in the outer 90° ply (with reduced intralaminar damage propagation from the notch tips), which may explain the more arbitrary transverse cracking path.

The remote stress-local axial strain relations of representative DENC test specimens of both laminates were determined using virtual strain gauges computed from the DIC measurements. The local strains were obtained averaging the longitudinal strains in an area equivalent to the gauge area of physical strain gauges: 3.18 mm long and 1.78 mm wide. Two virtual strain gauges (*SG1* and *SG2*) were placed below and above the ligament section. Figures 5.61 to 5.65 show the remote stress-local axial strain relations for each specimen configuration and for both laminates. For reference, figures 5.61 to 5.65 also show the location of the gauge areas (*SG1* and *SG2*) plotted on the longitudinal strain field obtained with DIC at an applied remote stress corresponding to 20% of the ultimate remote stress.

A linear-elastic FEA was performed for each specimen geometry to compare with the virtual strain gauge data from the experiments (figures 5.61 to 5.65). This analysis is intended, on one hand, to validate the accuracy of the proposed

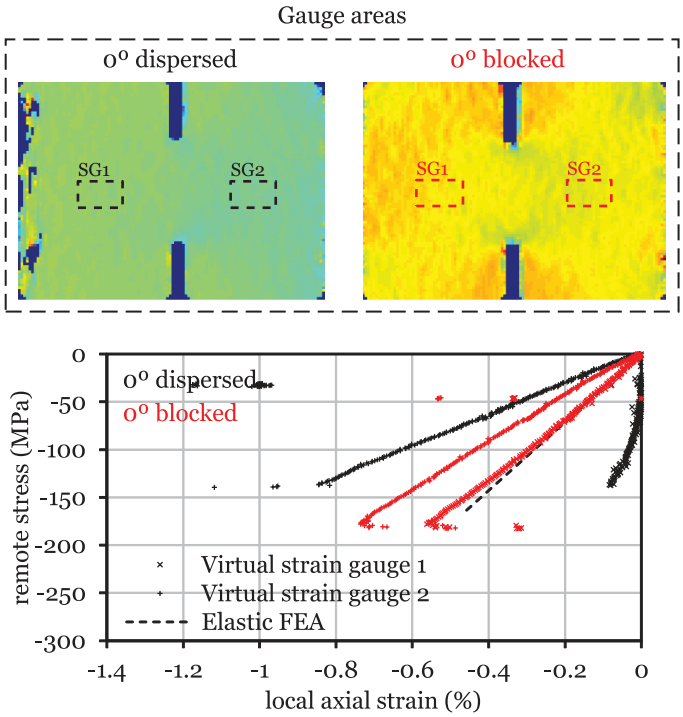

Fig. 5.62. Virtual strain gauge areas and remote stress-local axial strain relations of representative 15 mm wide DENC test specimens (geometry B). The loading direction is parallel to the horizontal axis of the specimens.

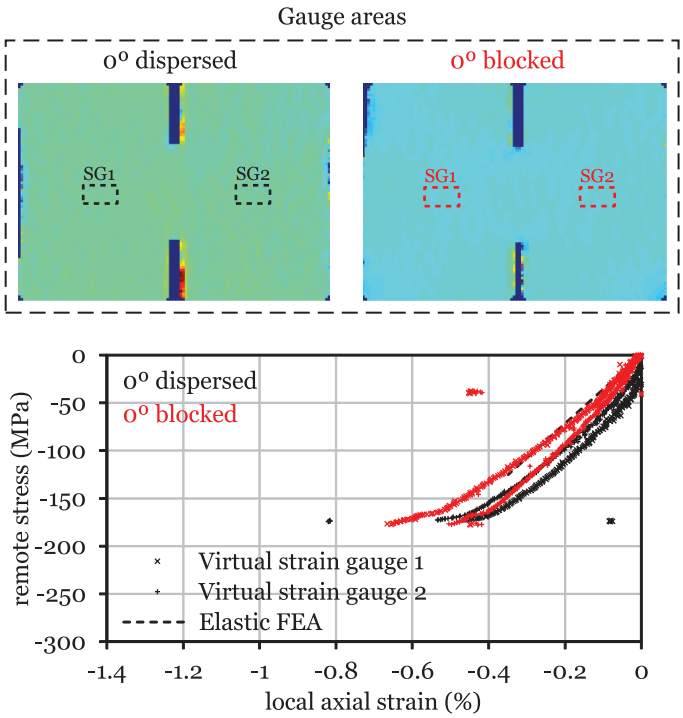

Fig. 5.63. Virtual strain gauge areas and remote stress-local axial strain relations of representative 20 mm wide DENC test specimens (geometry C). The loading direction is parallel to the horizontal axis of the specimens.

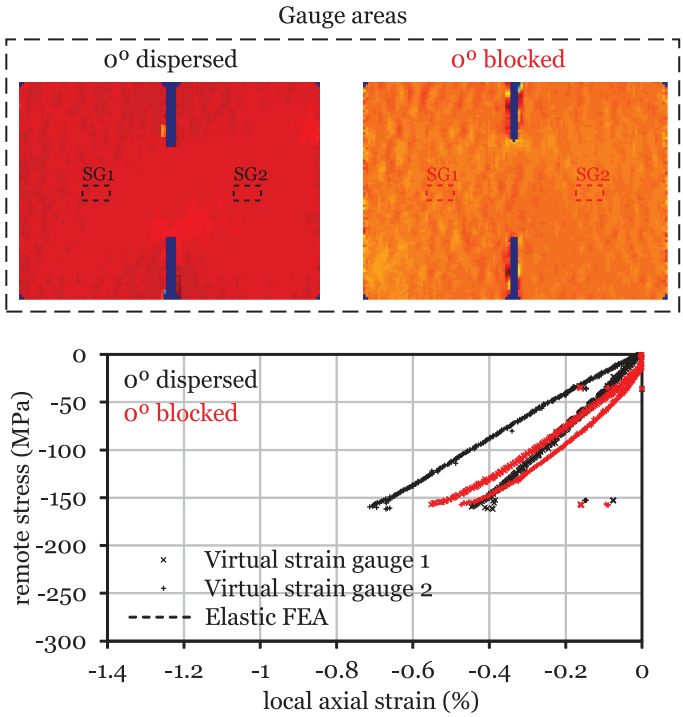

Fig. 5.64. Virtual strain gauge areas and remote stress-local axial strain relations of representative 25 mm wide DENC test specimens (geometry D). The loading direction is parallel to the horizontal axis of the specimens.

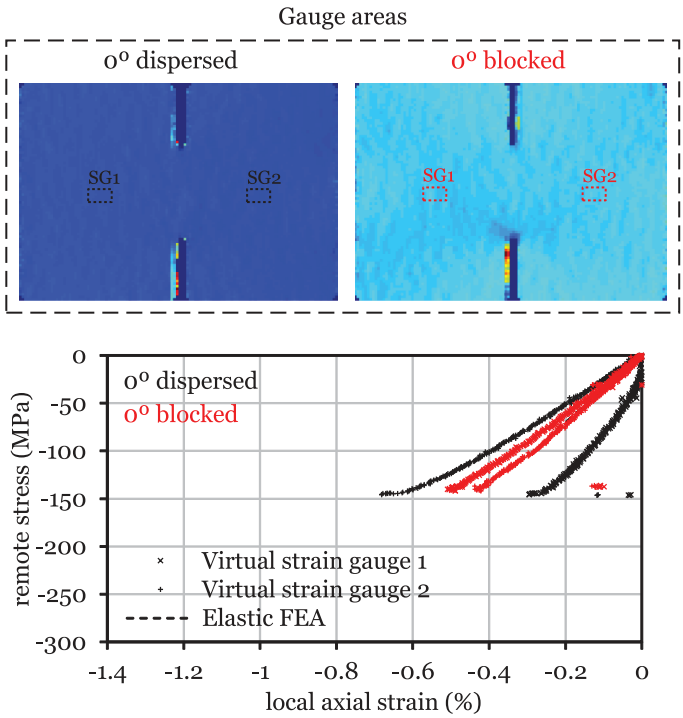

Fig. 5.65. Virtual strain gauge areas and remote stress-local axial strain relations of representative 30 mm wide DENC test specimens (geometry E). The loading direction is parallel to the horizontal axis of the specimens.

virtual strain gauge approach, and, on the other hand, to evaluate the global quality of the load introduction. To perform this analysis, the same averaging procedure as in the virtual strain gauges was employed in the post-processing of the FEA.

The FE models were created with the commercial FE software Abaqus 6.12-1 [275] using a structured mesh of CPS4R elements. At the notch tip, finite elements with a minimum in-plane size five times smaller than the notch tip radius (or 0.1 mm) were used to accurately represent the notch geometry and capture the strain concentrations. Figures 5.66a and 5.67a show the mesh of the 10 mm wide (geometry A) and 30 mm wide (geometry E) FE models, respectively.

A longitudinal displacement (x-direction) of -0.10 mm was applied to the nodes on the top end, leaving the displacement in the transverse direction free in both ends. Following Catalanotti et al. [187], it was assumed that the contact between the specimen and the loading system is frictionless. The remaining degrees of freedom in the top and bottom ends were fixed.

As in section 5.5.1, the individual plies of the composite lay-up were modelled using a layerwise approach, explicitly defining each lamina, and respective ply orientation, by one integration point through the thickness of the plane stress elements. The constitutive behaviour of each ply was defined by an orthotropic linear-elastic material model, using the elastic properties of T700GC/M21 (table 4.1). Figures 5.66b and 5.67b show the longitudinal strain fields of the outer ply of 10 mm wide (geometry A) and 30 mm wide (geometry E) FE models, respectively.

The results of the FEA are plotted together with the DIC data in figures 5.61 to 5.65. As it can be observed, the correlation with the measured strains is not always satisfactory, especially for the smallest specimens (geometry A, figure 5.61). On one hand, this uneven relation, in particular in the initial loading stages, may result from the load introduction setup, which was assumed frictionless in the FEA [187], even if it is recognised that, despite the use of a lubricant between the specimens' ends and the loading supports, friction can effectively affect the overall response of the tested specimens [265]. However, the fracture response of the tested specimens is believed to be unaffected by the friction between the specimens' ends and the loading supports, as failure invariably occurred at the notched plane, thus validating the obtained results. The discrepancies observed in the smaller specimens (figure 5.61) may also result from the large averaging area (or gauge area) compared to the specimens' size, whose results may be affected by its proximity to the loading ends. Nonetheless, the fact that both laminates exhibit a very similar response, shows that the results are actually consistent, validating the test results.

In the case of larger specimens (figures 5.62 to 5.65), the observed differences between the predicted stress-strain relations and the virtual strain gauge data is most certainly due to the variability typical of experimental procedures, as some of the numerical and experimental relations are in very good agreement. In fact, as the size of the averaging area becomes smaller comparatively to the size of the specimens, the local effects, such as strain oscillations, captured by the gauge area gain additional importance, and the averaging procedure loses its effectiveness in smearing such effects, providing a more local response.

From figures 5.51 to 5.65, it is observed that, in general, the *dispersed* and *blocked* laminates show a similar fracture response in compression. In fact, not only the ultimate remote stresses, for the same geometry, are similar (e.g. figures 5.45 to 5.49), but also the stresses at the onset of intralaminar damage growth. Because the thickness of the 90° outer ply is the same in both laminates, and the neighbour ply, immediately below, has the same orientation ($-45°$), the constraining effect on transverse compressive cracking of the outer ply is expected to be the same in both laminates (i.e. same *in situ* effect). The same surface cracking strain is therefore expected, as observed before, as long as internal blunting mechanisms are precluded or if they occur with the same extent, confirming the equivalent notched response of the *dispersed* and *blocked* laminates.

Table 5.12 and figure 5.68 show, respectively, the average results for the ultimate remote stresses of the tested DENC specimens and corresponding coefficients of variation, and the mean ultimate remote stress as a function of the initial edge notch length, which is proportional to size in the case of geometrically similar specimens. Globally, as the size of the

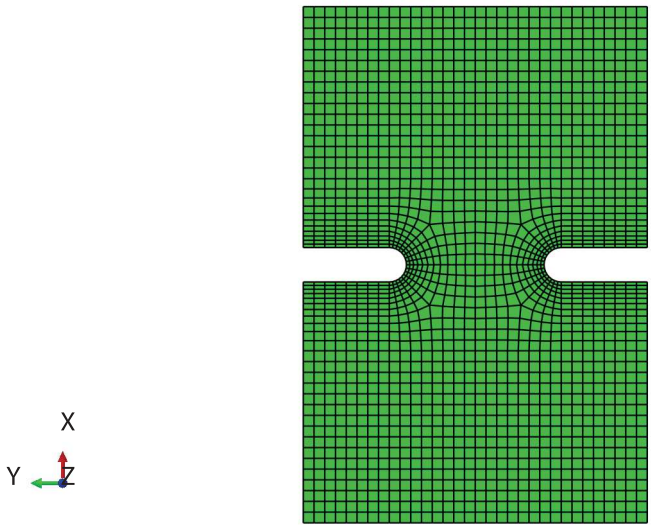

(a) FE mesh.

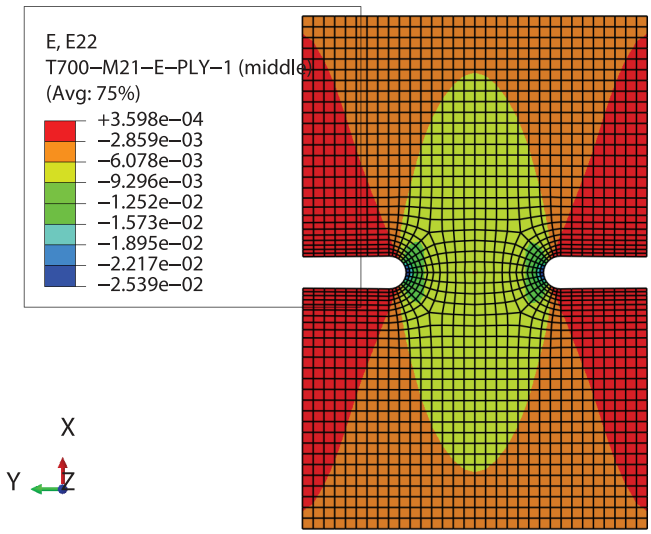

(b) Longitudinal strain field of the outer ply.

Fig. 5.66. Mesh detail of the FE model of a 10 mm wide DENC specimen (geometry A) and longitudinal strain field of the outer ply.

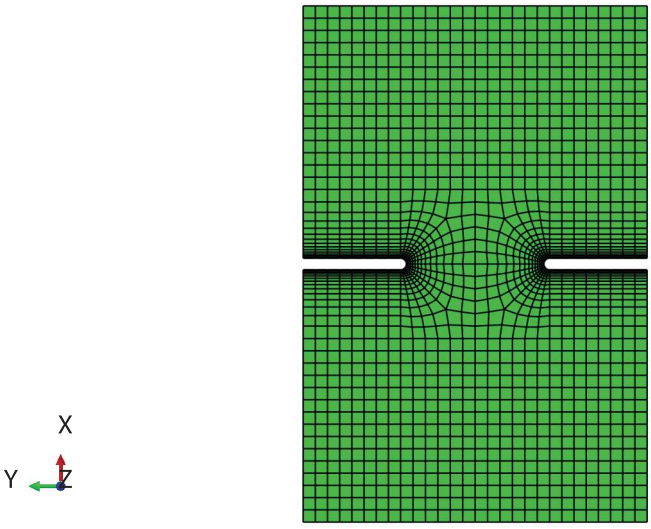

(a) FE mesh.

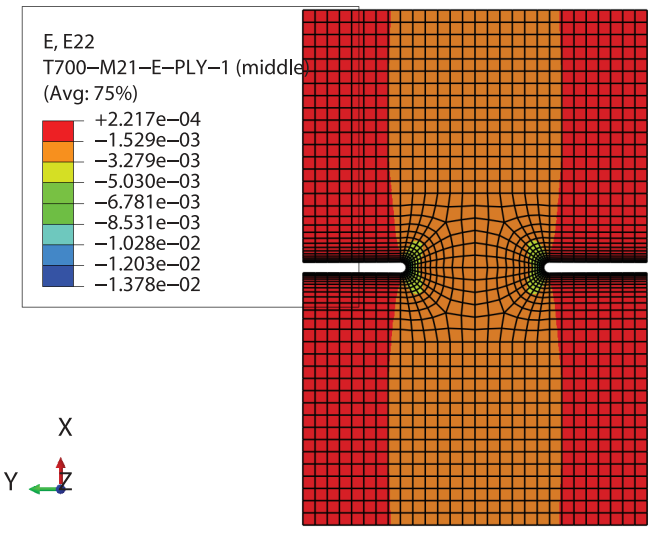

(b) Longitudinal strain field of the outer ply.

Fig. 5.67. Mesh detail of the FE model of a 30 mm wide DENC specimen (geometry E) and longitudinal strain field of the outer ply.

Table 5.12
Absolute values of the mean ultimate remote stress ($\bar{\sigma}^{\infty}$) and coefficients of variation (C.V.) of the DENC tests.

Results	Geometry ID				
	A	B	C	D	E
***Dispersed* laminate**					
No. specimens	8	10	5	4	5
$\bar{\sigma}^{\infty}$ (MPa)	198	175	186	156	149
C.V. (%)	13.1	12.9	5.1	2.4	6.6
***Blocked* laminate**					
No. specimens	8	10	7	4	4
$\bar{\sigma}^{\infty}$ (MPa)	184	179	170	147	144
C.V. (%)	8.6	9.1	9.5	8.3	1.7

specimens increases, the mean ultimate remote stress decreases. This means that, as expected, the proposed specimen configurations have positive geometry, a requirement for the determination of the $\mathcal{R}$-curve using the size effect law. Moreover, a similar size effect is observed in both laminates. Thus, it can be concluded that the effect of the change in the stacking sequence, i.e. the effect of grouping together the 0° plies, in the compressive fracture response of this particular lay-up is negligible. This becomes even more evident by determining the corresponding laminate mode I compressive crack resistance curves.

The size effect law regression proposed in Ref. [209] that best fit the experimental data of both laminates is linear regression II (equation (5.5)), whose fitting parameters ($\acute{A}$ and $\acute{C}$) are given in table 5.13. Figure 5.69 shows the experimental results and the best fitting for the size effect laws of the *dispersed* and *blocked* laminates.

Using the fitting parameters shown in table 5.13, it is now possible to calculate the length of the FPZ, l_{fpz}, and the steady-state value of the fracture toughness, $\mathcal{R}_{ss}$, in compression of the *dispersed* and *blocked* laminates (equations (5.8) and (5.9)). Table 5.14 shows the values of l_{fpz} and $\mathcal{R}_{ss}$ obtained for both laminates.

Figure 5.70 shows the $\mathcal{R}$-curves of the *dispersed* and *blocked* laminates obtained as the envelopes of the crack driving force curves calculated using the size effect laws of figure 5.69. To simplify the implementation of the $\mathcal{R}$-curve in numerical or analytical models, following Catalanotti et al. [65], equation (4.21) is used to fit the $\mathcal{R}$-curves of figure 5.70. The parameters that best fit the $\mathcal{R}$-curves of the *dispersed* and *blocked* laminates are given in table 5.14, which were obtained using a nonlinear least squares method with a Trust-Region algorithm available in the commercial software Matlab [278]. Figure 5.71 shows the $\mathcal{R}$-curves and the corresponding fitting curves for both laminates. As in section 5.5.1, the fitting formulae agree very well with the analytical envelopes.

Figure 5.72 shows a comparison of the $\mathcal{R}$-curves of both laminates. As expected from the analysis of the size effect relation in figure 5.68, the compressive $\mathcal{R}$-curves of the *dispersed* and *blocked* laminates are very similar in shape and

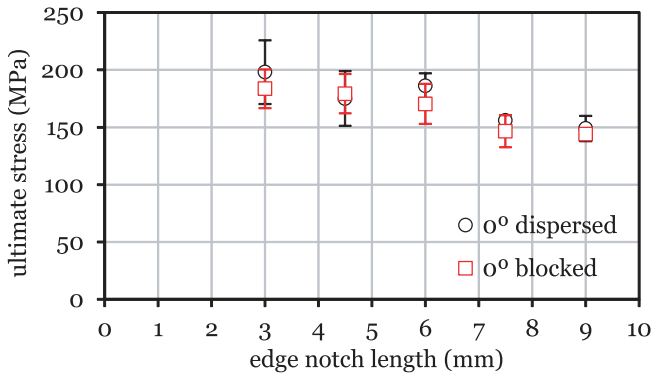

Fig. 5.68. Absolute values of the mean ultimate remote stress as a function of the initial edge notch length for the DENC tests.

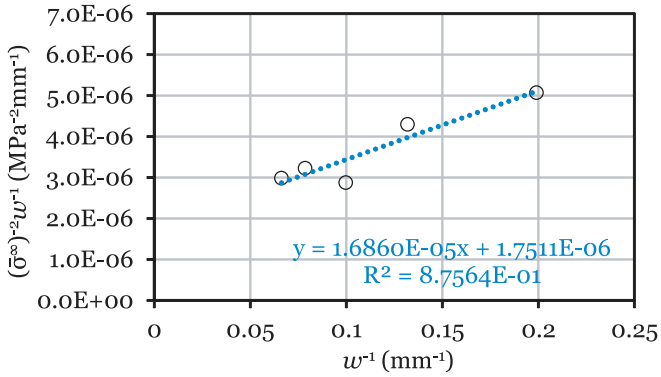

(a) *Dispersed* laminate: linear regression II.

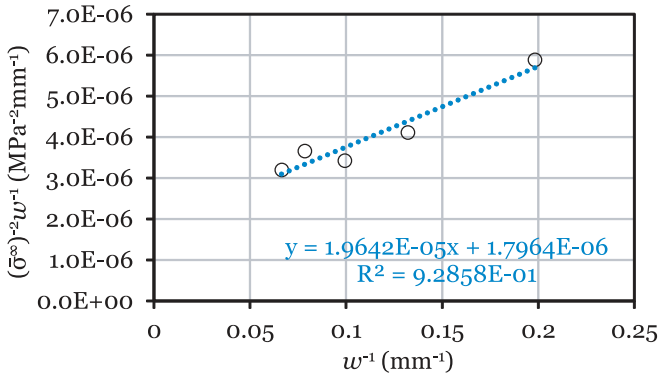

(b) *Blocked* laminate: linear regression II.

Fig. 5.69. Experimental results and best fitting for the compressive size effect laws of the *dispersed* and *blocked* laminates.

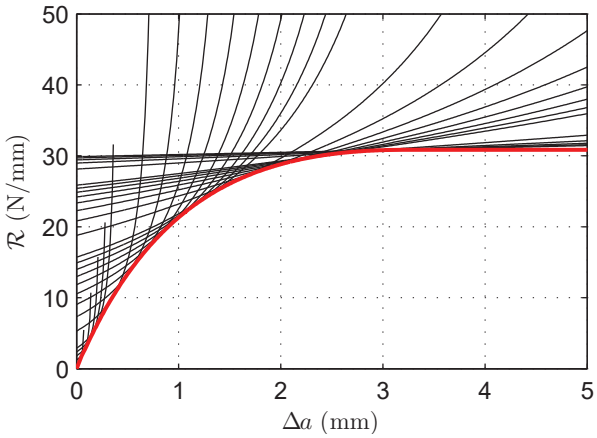

(a) *Dispersed* laminate.

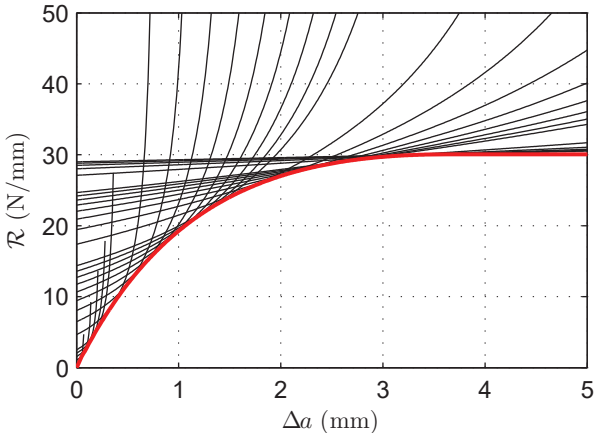

(b) *Blocked* laminate.

Fig. 5.70. Crack driving force curves and resulting $\mathcal{R}$-curves of the *dispersed* and *blocked* laminates for mode I longitudinal intralaminar compressive fracture.

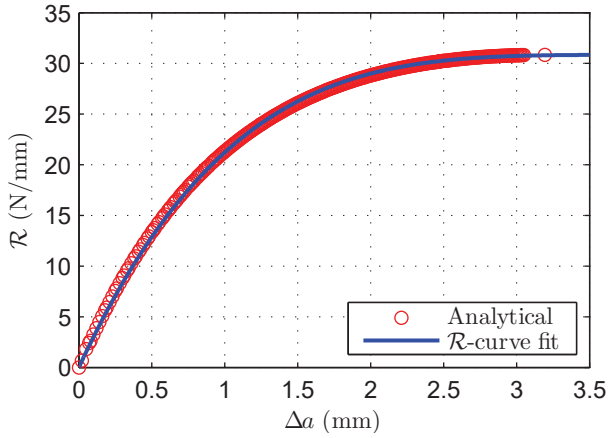

(a) *Dispersed* laminate.

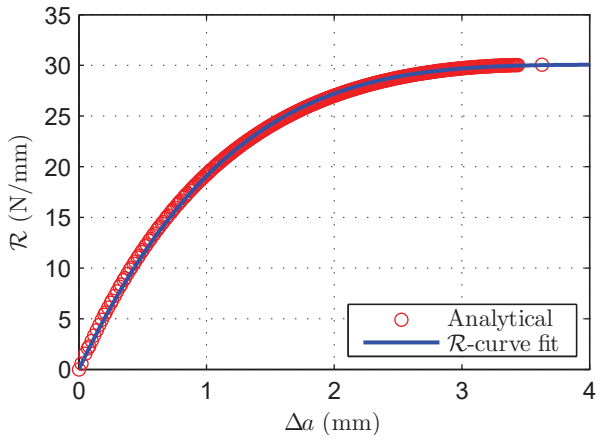

(b) *Blocked* laminate.

Fig. 5.71. Analytical and fitted compressive $\mathcal{R}$-curves of the *dispersed* and *blocked* laminates.

Table 5.13
Fitting regressions and parameters for the compressive size effect laws of the *dispersed* and *blocked* laminates.

Laminate	Regression fit [209]	Fitting parameters
Dispersed laminate	Linear regression II	$\acute{A}$ = 1.6860E − 05 MPa^{-2} mm^{-1}
		$\acute{C}$ = 1.7511E − 06 MPa^{-2}
Blocked laminate	Linear regression II	$\acute{A}$ = 1.9642E − 05 MPa^{-2} mm^{-1}
		$\acute{C}$ = 1.7964E − 06 MPa^{-2}

Table 5.14
Parameters of the $\mathcal{R}$-curves and fitting formulae of the *dispersed* and *blocked* laminates in compression.

Laminate	l_{fpz} (mm)	$\mathcal{R}_{ss}$ (N/mm)	ζ (mm^{-1})	η (-)
Dispersed laminate	3.19	30.8	0.2527	4.000
Blocked laminate	3.63	30.1	0.2210	4.034

in size, with approximately the same length of the FPZ, l_{fpz}, and same steady-state value of the fracture toughness, $\mathcal{R}_{ss}$. This result demonstrates the negligible effect of the 0° ply (block) thickness on the compressive notched response of hard laminates.

5.5.3. Laminate tensile unnotched strength test results

The plain tensile strengths of the *dispersed* and *blocked* laminates were obtained testing, respectively, 3 and 5 valid unnotched specimens until failure, under the conditions described in section 5.3.3. Figure 5.73 shows the remote stress-displacement curves of both laminates. Due to the clamping pressure of the hydraulic grips, the unnotched tension test specimens had a small pre-loading before the beginning of the test, negligible compared to the ultimate remote stresses. For the specimens tested without aluminium tabs, these pre-loads varied between −16 MPa and 2 MPa, below 1% of the ultimate remote stresses of the tested specimens. For the specimens with aluminium tabs, while the hydraulic clamping pressure was applied, a manual adjustment of the position of the cross-head of the testing machine needed to be performed to avoid excessive compressive deformation of the test specimens due to high compressive pre-loads. This manual adjustment was performed ensuring a pre-load close to zero at the testing clamping pressure.

Due to small adjustments inside the grips, the specimens tested without aluminium tabs exhibited an initially nonlinear remote stress-displacement relation (figure 5.73), resulting in a considerably higher applied displacement until failure. In the specimens with aluminium tabs, the superior rigidity of the gripped regions ensured that load could be immediately transferred to the specimens, with minimal adjustments inside the hydraulic grips. Moreover, any initial adjustments of the specimen inside the grips were suppressed by the manual adjustment of the position of the cross-head of the testing machine before the beginning of the test.

Figure 5.73 also shows that both laminates exhibit an approximately linear behaviour up to the ultimate remote stress, and no significant nonlinearity is observed before the peak load. These results suggest that extensive transverse cracking and delamination did not occur before final failure, which was dominated by fibre breakage (figure 5.74).

The level of damage in the tested specimens (figure 5.74) reveals the catastrophic type of failure typical of this test configuration. Failure systematically occurred in the gauge section of the specimens, which exhibit a fibre-dominated pull-out failure mode, with the failure section perpendicular to the applied load. In both laminates, local delaminations were observed in the damaged regions close to the centre of the gauge section, apparently caused by the catastrophic type of failure. However, the extent of delamination and pulled-out fibre bundles in the failed regions is slightly higher in the *blocked* laminate, suggesting a higher susceptibility to grow subcritical damage mechanisms. It is noted that, in one specimen of the *blocked* laminate (figure 5.74b), part of the specimen delaminated from one of the surfaces at the moment of failure. As explained in section 5.5.1, 0° ply blocking originates higher stress concentrations in the adjacent interfaces, which become more susceptible to delamination and splitting. Also, in the *blocked* laminate, some of the adjacent NCF bi-angle layers are stacked with relative ply orientations of 90°, conducting to higher interlaminar stress concentrations between these plies, promoting delamination in these interfaces.

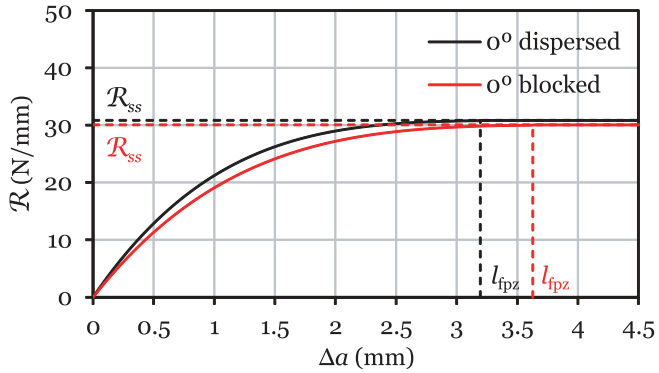

Fig. 5.72. Comparison of the $\mathcal{R}$-curves for mode I longitudinal intralaminar compressive fracture of the *dispersed* and *blocked* laminates.

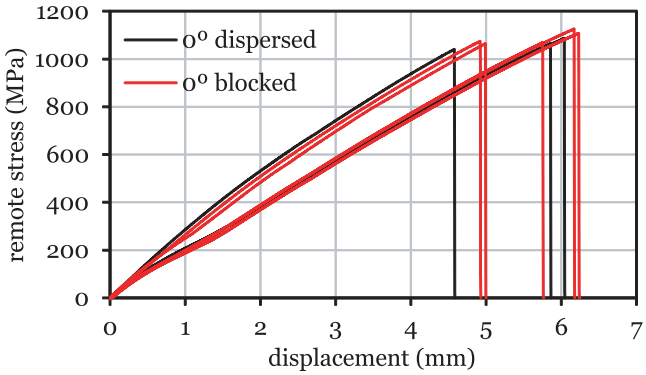

Fig. 5.73. Unnotched tension test results.

In most specimens, failure occurred in multiple places, in some cases close to the edges of the hydraulic grips (figure 5.74). Nevertheless, due to the sudden, highly catastrophic failure mode, it is impossible to identify exactly where failure occurs first. Since no pre-installed defect is present (as in the notched specimens), the location of the section where final failure takes place cannot be known in advance. Assuming an even stress distribution in a smooth specimen, final failure should start in the weakest point of the laminate (internal material defect, region with higher concentration of subcritical failure mechanisms, or just material strength variability), and develop into a quick, very energetic fracture process that, at the moment of failure, may prompt fracture of other regions in the highly stressed material. Severe compressive damage may also occur far from the failure section, typically close to the edges of the clamped region, when the specimen recovers from the very high elastic deformation.

It is also recognised that clamping can act as a source of stress concentration, namely at the edges of the clamped regions. If its effect is not properly addressed and minimised, clamping may affect the test results, promoting early failure close to the grips. Nevertheless, in the present study, the tests with the aluminium tabs, which, in some extent, reduce the stress concentrations at the grips, show that the deviations between the different specimens of the same laminate are not significant (e.g. figure 5.73), validating the results obtained in the present work.

Even though no damage could be observed in the unnotched specimens during the tests, internal damage growth was audible at applied remote stresses as low as 21% of the ultimate remote stress. With the applied load, noise due to internal damage growth would become more frequent, above applied remote stresses corresponding to 46% of the ultimate remote stress, eventually becoming stronger, due to fibre breakage, already close to ultimate failure, at applied remote stresses above 89% of the ultimate remote stress.

This perception indicates that, in spite of the absence of subcritical damage mechanisms in the regions far from the failure sections (figure 5.74), internal damage growth did apparently occur during the tests. It is interesting to note, though,

(a) *Dispersed* laminate.

(b) *Blocked* laminate.

Fig. 5.74. Unnotched tension test specimens after testing.

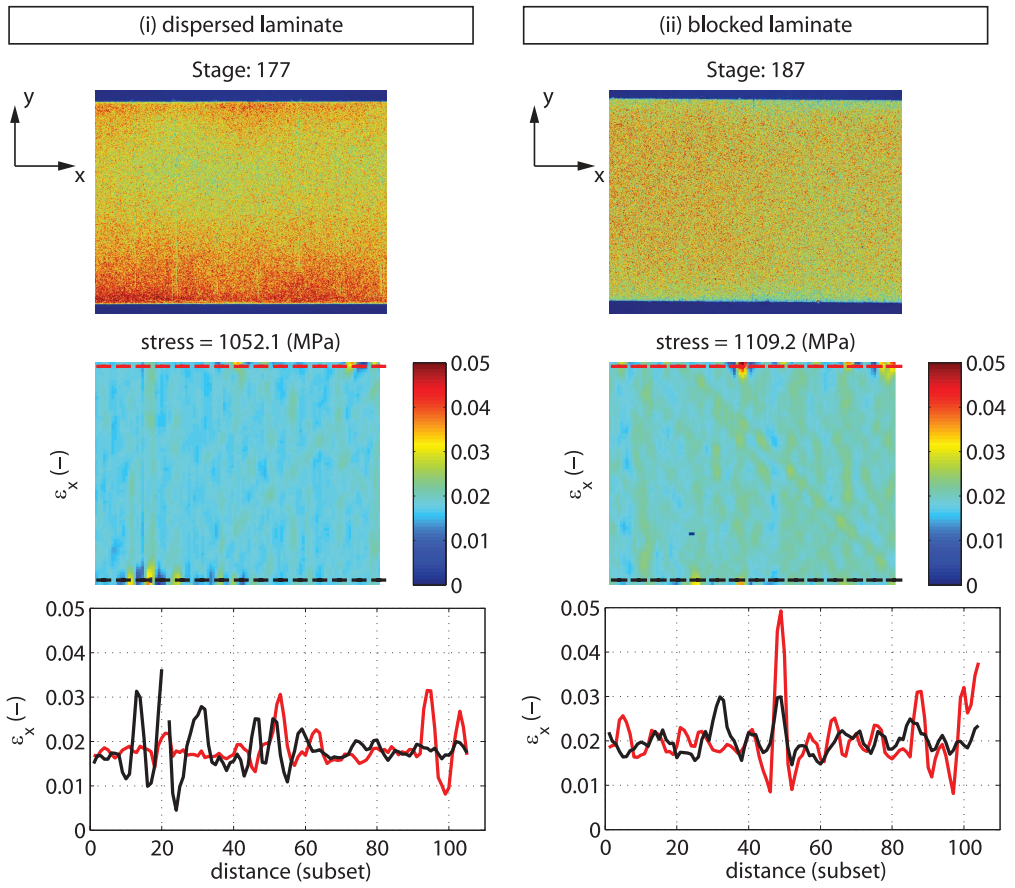

Fig. 5.75. Coloured distributions of grey levels (0–255), longitudinal strain fields, ε_x, and local longitudinal strain measured along the edges of the outer 90° ply of representative unnotched tension test specimens of the (i) *dispersed* and (ii) *blocked* laminates obtained with the DIC technique at the stage prior to ultimate failure. The reference DIC coordinate system is depicted in the figures, where the x-axis is aligned with the loading direction.

that the effect of these early damage mechanisms seemingly did not affect the overall mechanical response of the tested specimens, as no load drops or nonlinearities were observed in the remote stress-displacement curves (figure 5.73).

In order to assess the occurrence and extent of early damage, the DIC technique was used to monitor transverse cracking formation near the free-edges. Figure 5.75 shows the longitudinal strain field of the outer 90° ply of representative specimens of the *dispersed* and *blocked* laminates at the stage prior to ultimate failure. The local longitudinal strain measured along two lines, parallel to the loading direction, near the free edges, are also presented. For reference, figure 5.75 also shows the corresponding coloured distributions of grey levels.

As it can be observed, prior to ultimate failure of the unnotched specimens, onset of transverse matrix cracking has barely occurred, with regions of high strain concentration confined to the free edges, without extending through the specimens' width. Unlike conventional laminates with the same epoxy resin subjected to considerably lower remote stresses [121], transverse cracking is totally absent in this case, showing the potential of thin transverse plies to suppress subcritical failure mechanisms. This transverse cracking suppression capability is attributed to the *in situ* effect [81]. Due to the constraining effect imposed by the neighbouring plies, which reduces the energy release rate within the 90° ply, the actual strengths in the transverse plies increase with decreasing ply thickness, delaying [121] or even suppressing damage propagation in the matrix, as observed in the present study. This result becomes particularly interesting if taking into account that in the case of transverse outer plies the energy release rate is magnified due to the proximity of the slit crack to the surface of the laminate [81], which means that transverse matrix cracking in the inner plies will only occur at even higher applied remote stresses.

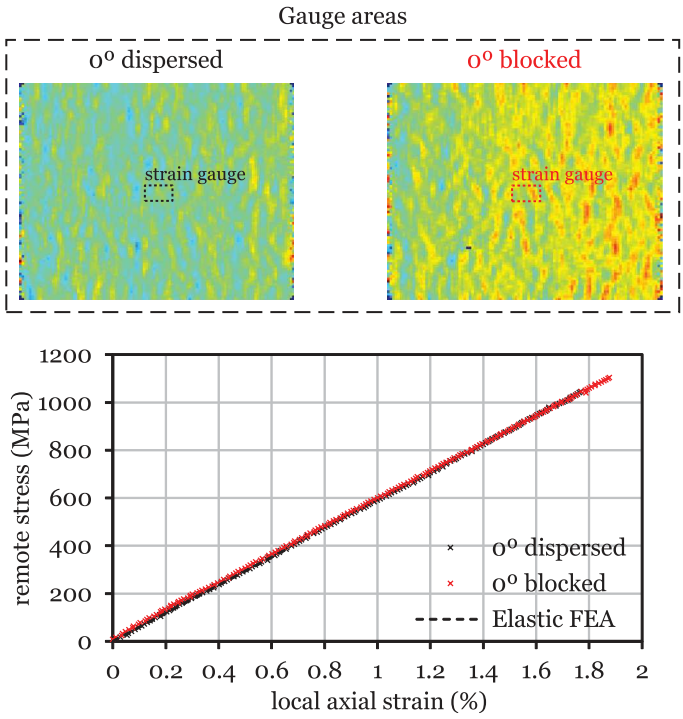

Fig. 5.76. Virtual strain gauge areas and remote stress-strain relations of representative unnotched tension test specimens. The loading direction is parallel to the horizontal axis of the specimens.

Figure 5.75 also shows that the difference between the two laminates is scarce or nonexistent. Hence, it can be assumed that the noise caused by internal damage growth in both laminates was, most likely, caused by occasional events, intrinsic to the material, which did not affect the global response or the results of the tests performed.

A virtual strain gauge computed from the DIC measurements by averaging the longitudinal strains in an area with 3.18 mm in length by 1.78 mm in width, equivalent to the gauge area of a physical strain gauge, was used to obtain the remote stress-strain relations of representative unnotched tension test specimens. Figure 5.76 shows, for both laminates, the location of the gauge areas, plotted on the longitudinal strain field obtained with DIC at an applied remote stress corresponding to 20% of the ultimate remote stress, and the respective remote stress-strain relations.

A linear-elastic FEA was performed to validate the implementation of the proposed virtual strain gauge approach, employing the same averaging procedure to compare with the obtained test data. The FE models were created with the commercial FE software Abaqus 6.12-1 [275] using a structured mesh of 1 mm long square CPS4R elements. Only the gauge section was modelled.

To replicate the load and boundary conditions of the actual test setup, a longitudinal displacement (x-direction) of 1.00 mm was applied to the nodes on the top end, while fixing their remaining degrees of freedom. The nodes in the bottom end were all fixed (encastre boundary condition).

The individual plies of the composite lay-up were modelled using a layerwise approach, explicitly defining each lamina, and respective ply orientation, by one integration point through the thickness of the CPS4R elements. The constitutive behaviour of each ply was defined by an orthotropic material model, using the elastic properties of T700GC/M21 (table 4.1). The results of the FEA are plotted together with the DIC data in figure 5.76.

A remarkable correlation can be observed between the results of the FEA and the average strain measure obtained from the DIC data, thus validating the proposed virtual strain gauge approach. As expected for unnotched laminates with a fibre-dominated failure mode, linear stress-strain relations up to the ultimate remote stress were obtained in both laminates.

Table 5.15
Laminate tensile unnotched strength (X_T^L) test results and respective coefficients of variation (C.V.).

Results	*Dispersed* laminate	*Blocked* laminate
No. specimens	3	5
X_T^L (MPa)	1064	1088
C.V. (%)	1.8	2.2

Table 5.15 shows the average results for the tensile unnotched strengths, X_T^L, of the *dispersed* and *blocked* laminates and the respective coefficients of variation. As can be observed, the tensile strengths of the tested laminates differ by just 2.3%, a difference within the variation of the tests. It can be concluded, therefore, that the tensile strength of both laminates is virtually the same.

It is interesting to note that, as reported elsewhere [53, 58, 121, 122], blocking together the off-axis and transverse plies with the same orientation has a detrimental effect on the tensile unnotched strength of multidirectional laminates. This is due to the higher interlaminar stresses and lower *in situ* strengths of laminates with thick plies, which cause early subcritical damage mechanisms adjacent to the load carrying 0° plies, acting as stress concentration points that promote early catastrophic longitudinal failure. Restricting ply blocking to the 0° plies, though, does not affect the final unnotched strength of the laminates (table 5.15), while potentiating the growth of damage mechanisms such as fibre-matrix splitting, which may be beneficial especially in improving the notched response of laminates.

5.5.4. Laminate compressive unnotched strength test results

The plain compressive strengths of the *dispersed* and *blocked* laminates were obtained testing 3 unnotched specimens of each laminate until failure, according to the procedures described in section 5.3.4. Figure 5.77 shows the remote stress-displacement curves of both laminates. As it can be observed, the remote stress-displacement relations of both laminates exhibit a nonlinear behaviour, suggesting that permanent damage or generalised plastic deformation develops before final failure. However, the post-failure behaviour of the *dispersed* and *blocked* laminates is remarkably different. The *dispersed* laminate shows a progressive failure mode, characterised by a series of load drops, which become larger as the specimen approaches final failure. Some load drops show reductions of the applied remote stress of approximately 10%. On the other hand, final failure of the *blocked* laminate occurs suddenly or soon after the first load drops, which are typically small, but occur at applied remote stresses higher than those of the first load drops observed in the *dispersed* laminate.

After testing, all specimens exhibited a net-section failure mode (figure 5.78). Failure of both laminates is characterised by a complex combination of damage mechanisms, including fibre kinking, brittle shear-driven fibre fracture, wedge transverse fracture, crushing and delamination, whose sequence is not easy to identify. In some specimens, multiple fracture planes, inclined with respect to the laminate midplane, have occurred, revealing the catastrophic type of failure of this test configuration.

The *dispersed* laminate has apparently a brittler failure mode, as the occurrence of fibre kinking is more limited, and a high degree of abrasion of the inclined crack surfaces, typical of shear-driven brittle compressive failure [285], is observed (figure 5.78a). The *blocked* laminate exhibits more irregular failure surfaces, dominated by fibre kinking. This suggests that blocking the 0° plies results in a higher susceptibility to grow kink bands before compressive failure.

In fact, assuming that kink bands are triggered by localised matrix failure in the vicinity of misaligned fibres, an *in situ* effect associated with the onset of fibre kinking in constrained 0° plies is likely to exist. In other words, thicker 0° plies, which have lower *in situ* transverse strengths, will have lower resistance to localised matrix failure in the vicinity of misaligned fibres, thus lowering the resistance to the onset of fibre kinking.

Limiting the development of kink bands, as in the *dispersed* laminate, results in a more gradual failure mode (figure 5.77). However, growth of severe damage apparently occurs earlier, initially as small events (first load drops), becoming more and more important as the specimen is loaded towards final failure.

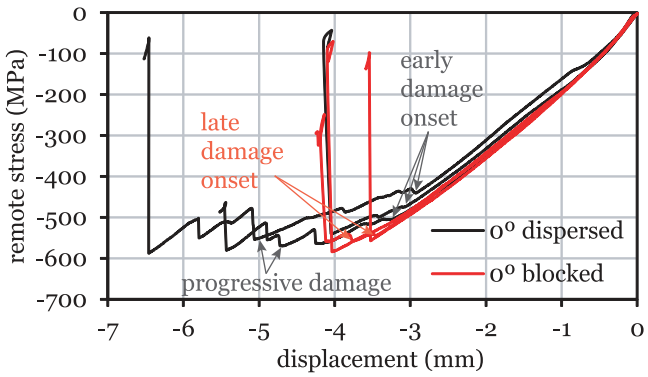

Fig. 5.77. Unnotched compression test results.

In the *blocked* laminate, the development of kink bands has apparently the potential to delay the onset of discrete compressive damage growth. However, final failure is catastrophic, propagating unstably once fibre kinking initiates (figure 5.77).

It is interesting to note that, despite the different responses of the *dispersed* and *blocked* laminates, the ultimate remote stress is remarkably similar. This suggests that final longitudinal compressive failure is not governed by the sequence of damage mechanisms that leads to failure of the 0° plies, but by the ply longitudinal compressive strength itself.

Table 5.16 shows the average results for the compressive unnotched strengths, X_C^L, of the *dispersed* and *blocked* laminates and the respective coefficients of variation. As can be observed, the compressive strengths of the tested laminates differ by just 0.5%, and, therefore, can be considered virtually the same.

It is interesting to note that previous work [121, 122] has shown that blocking together the off-axis and transverse plies with the same orientation has a detrimental effect on the compressive unnotched strength of multidirectional laminates, seemingly caused by higher interlaminar stresses and lower *in situ* strengths. However, restricting ply blocking to the 0° plies does not affect the final compressive unnotched strength of the laminates, in spite of the changes in the damage mechanisms (figure 5.78).

5.5.5. Laminate tensile centre-notched tests

5.5.5.1. Notched strengths and size effect

For both laminates, 2 or 3 valid specimens of each geometry configuration (section 5.3.5) were tested to failure. Figures 5.79 to 5.83 show the corresponding remote stress-displacement curves. As before, the remote stress, σ^{∞}, was calculated dividing the applied load, measured by the load cell, by the specimen's cross-section area. The cross-head displacement was measured directly by the testing machine. Due to the clamping pressure of the hydraulic grips, the CNT specimens had a small pre-loading before the beginning of the test, between −11 MPa and 23 MPa, below 5% of the ultimate remote stress. Due to small adjustments of the specimens in the loading setup, in the beginning of the tests a non-linear remote stress-displacement relation is observed, except in the larger specimen configuration (figure 5.83).

Small load drops in the remote stress-displacement curves (figures 5.79 to 5.83), more evident as the size of the specimens increases, indicate the development of a fracture process zone ahead of the notch tips. Internal damage growth

Table 5.16
Laminate compressive unnotched strength (X_C^L) test results (absolute values) and respective coefficients of variation (C.V.).

Results	*Dispersed* laminate	*Blocked* laminate
No. specimens	3	3
X_C^L (MPa)	569	566
C.V. (%)	3.7	2.2

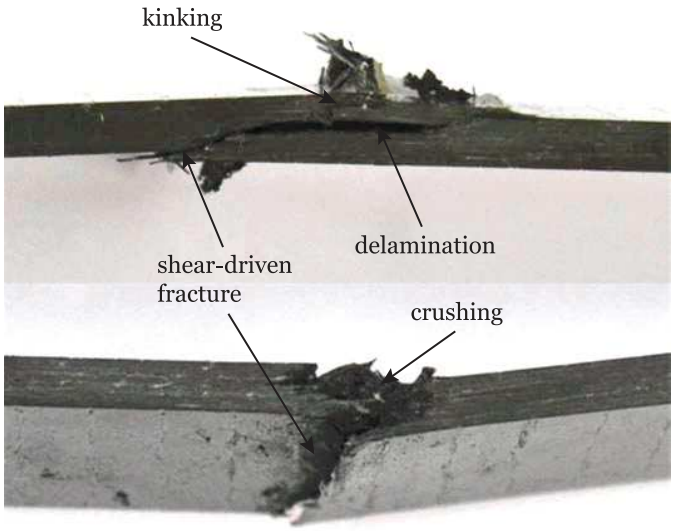

(a) *Dispersed* laminate specimens.

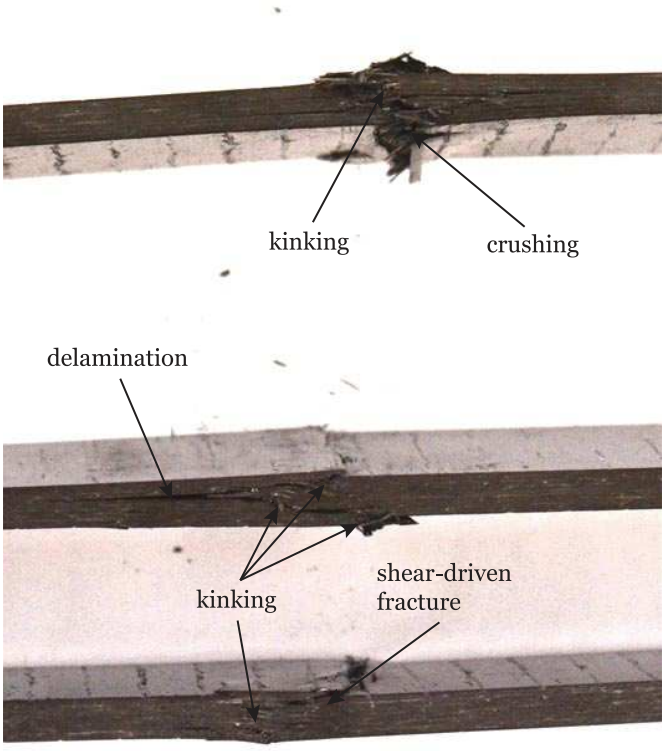

(b) *Blocked* laminate specimens.

Fig. 5.78. Details of the unnotched compression test specimens after testing.

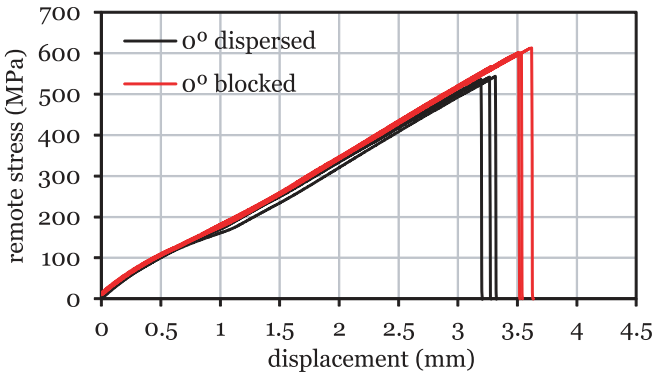

Fig. 5.79. Remote stress-displacement curves for the 36 mm wide CNT specimens.

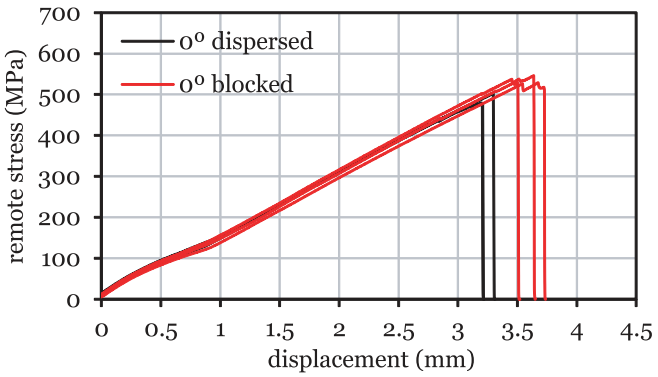

Fig. 5.80. Remote stress-displacement curves for the 72 mm wide CNT specimens.

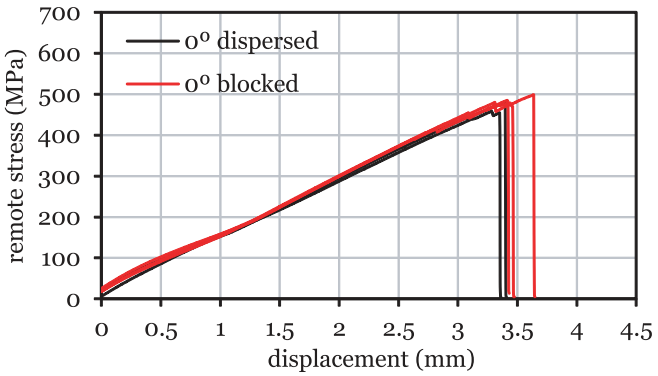

Fig. 5.81. Remote stress-displacement curves for the 108 mm wide CNT specimens.

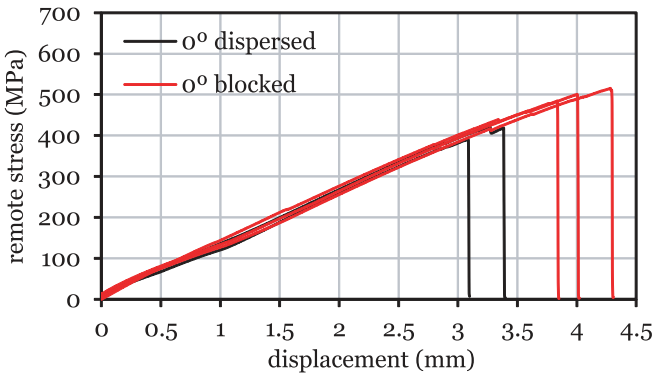

Fig. 5.82. Remote stress-displacement curves for the 144 mm wide CNT specimens.

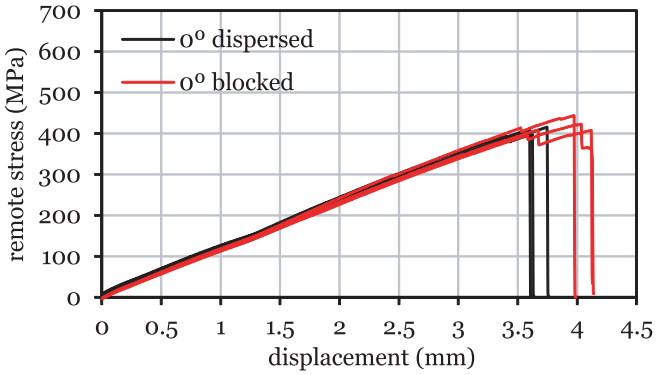

Fig. 5.83. Remote stress-displacement curves for the 180 mm wide CNT specimens.

could be heard during the tests of all specimen configurations. For the smaller, 36 mm wide specimens of the *dispersed* laminate, the noise produced by internal damage growth was audible above approximately 240 MPa (48% of the ultimate remote stress), becoming stronger above approximately 390 MPa (72% of the ultimate remote stress), apparently due to damage growth across the fibres. For the *blocked* laminate, internal damage growth was audible above 210 MPa (37% of the ultimate remote stress), becoming stronger above 470 MPa (82% of the ultimate remote stress). Closer to the maximum load (in general above 95% of the ultimate remote stress), the noise in both laminates became more frequent due to fast damage growth.

For the 72 mm wide specimens of the *dispersed* laminate, internal damage growth was audible above 250 MPa (50% of the ultimate remote stress), apparently across the fibres above 320 MPa (67% of the ultimate remote stress), coinciding with the small load drops in the remote stress-displacement curves (figure 5.80). Internal damage growth was also audible in the *blocked* laminate, at applied remote stresses above 280 MPa (56% of the ultimate remote stress). Fibre breaks, which produce a characteristic sound, were audible above 350 MPa (66% of the ultimate remote stress), becoming stronger above 380 MPa (72% of the ultimate remote stress). Closer to the maximum load (in general above 91% of the ultimate remote stress), the noise in both laminates became very strong and more frequent due to fast damage propagation, in some cases resulting in moderate load drops just before final failure (figure 5.80).

In some 108 mm wide specimens, internal damage growth in the *dispersed* laminate was audible at very low applied remote stresses, above approximately 125 MPa (28% of the ultimate remote stress). Nevertheless, severe damage propagation was only audible above approximately 290 MPa (65% of the ultimate remote stress), coinciding with the small load drops in the remote stress-displacement curves (figure 5.81). Internal damage growth was also audible in the *blocked* laminate at applied remote stresses above 290 MPa (61% of the ultimate remote stress), stronger and apparently with stable fibre fracture at approximately 390 MPa (80% of the ultimate remote stress). In both laminates, before final fracture, the noise became more frequent, practically uninterrupted for some seconds, due to fast and extensive damage growth.

In some 144 mm wide specimens of the *dispersed* laminate, internal damage growth was also audible at very low applied remote stresses, above 96 MPa (24% of the ultimate remote stress). More severe damage propagation, apparently comprising stable fracture across the fibres, was perceptible at applied remote stresses above 270 MPa (63% of the ultimate remote stress). At higher applied remote stresses, generally above 72% of the ultimate remote stress, the noise became more frequent due to fast damage growth, practically uninterrupted for several seconds.

In the *blocked* laminate, the onset of internal damage growth in the 144 mm wide specimens was audible at applied remote stresses above 210 MPa (44% of the ultimate remote stress). The characteristic noise produced by fibre breakage was audible above 300 MPa (61% of the ultimate remote stress), becoming stronger at approximately 370 MPa (74% of the ultimate remote stress), practically uninterrupted until final failure.

For the largest, 180 mm wide specimens, internal damage growth in the *dispersed* laminate was audible at approximately 170 MPa (41% of the ultimate remote stress), becoming stronger and more frequent at approximately 210 MPa

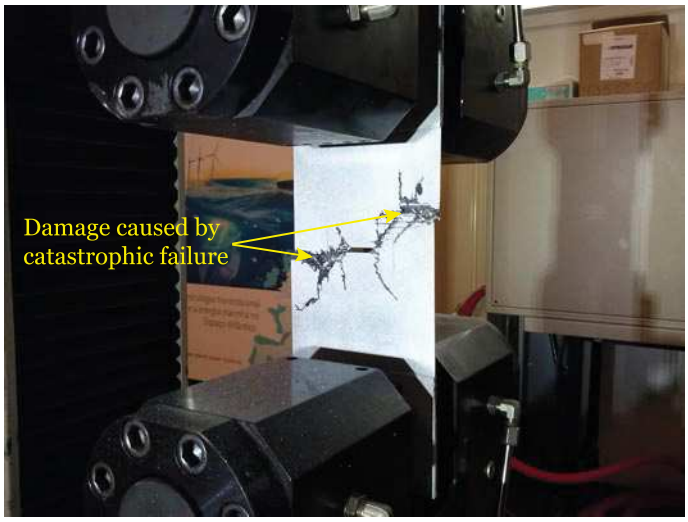

Fig. 5.84. Representative 144 mm wide specimen after testing before being removed from the loading setup.

(54% of the ultimate remote stress), caused by continuous damage growth and fibre breakage. Above 330 MPa (84% of the ultimate remote stress), and until final failure, the noise produced by internal damage growth became practically uninterrupted.

Internal damage growth was also audible in the 180 mm wide specimens of the *blocked* laminate at very low applied remote stresses, above approximately 125 MPa (28% of the ultimate remote stress). Fibre breakage and extensive split cracking were audible in the last stages of loading, as the specimens were approaching ultimate failure. This severe discrete damage, which included the propagation of huge internal split cracks, extending along the loading direction from the notched plane towards the specimen's ends, coincided with the occurrence of moderate to large load drops in the remote stress-displacement curves (figure 5.83).

Even though the degree of damage growth before ultimate failure can be substantially different between specimens of different sizes, all CNT test specimens of both laminates show a fibre-dominated failure mode, caused by the catastrophic propagation of an intralaminar crack after extensive damage growth ahead of the notch tips (figure 5.84). Figures 5.85 to 5.89 show the damaged regions of representative CNT specimens of the *dispersed* and *blocked* laminates after testing, as well as closer views of some damage mechanisms.

All failed specimens of the *dispersed* and *blocked* laminates show extensive diffuse damage, unlike quasi-isotropic specimens with a similar geometry and in a similar size range [122, 182, 212], which show brittler failure modes. In the 36 mm wide specimens (figure 5.85), split cracking in the $\pm 45^\circ$ plies and local delaminations from the notch tips can be observed. The 72 mm wide specimens (figure 5.86) exhibit split cracking in the $\pm 45^\circ$ plies too, with local delaminations at the free edges and along the damaged area. In both cases, a typical pull-out failure mode, with intralaminar fracture either perpendicular to or at an angle of -45° with the loading direction, can be observed.

The 108 mm wide specimens (figure 5.87) also show extensive damage, with evidence of brittle, unstable fracture after some damage growth from the notch tips. In the *blocked* laminate (figure 5.87b), stable damage propagation before final failure includes severe internal split cracking of the 0° plies, which conducts to longitudinal intralaminar fracture of the outer transverse plies across the fibres perpendicular to the loading direction. The 144 mm wide and 180 mm wide specimens (figures 5.88 and 5.89 respectively) show extensive damage too, with evidence of unstable fracture after damage propagation from the notch tips. Fibre pull-out can be observed. Stable damage growth is characterised by intralaminar fracture from the notch tips perpendicularly to the loading direction, followed by internal split cracking along the 0° and -45° directions. The latter conducts to longitudinal intralaminar fracture across the fibres of the outer transverse plies.

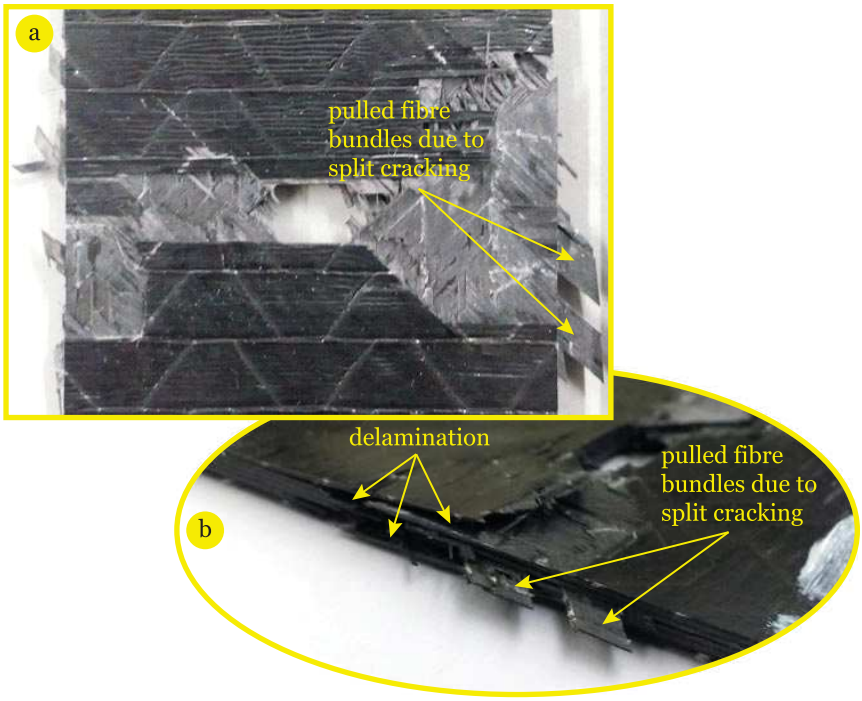

(a) *Dispersed* laminate.

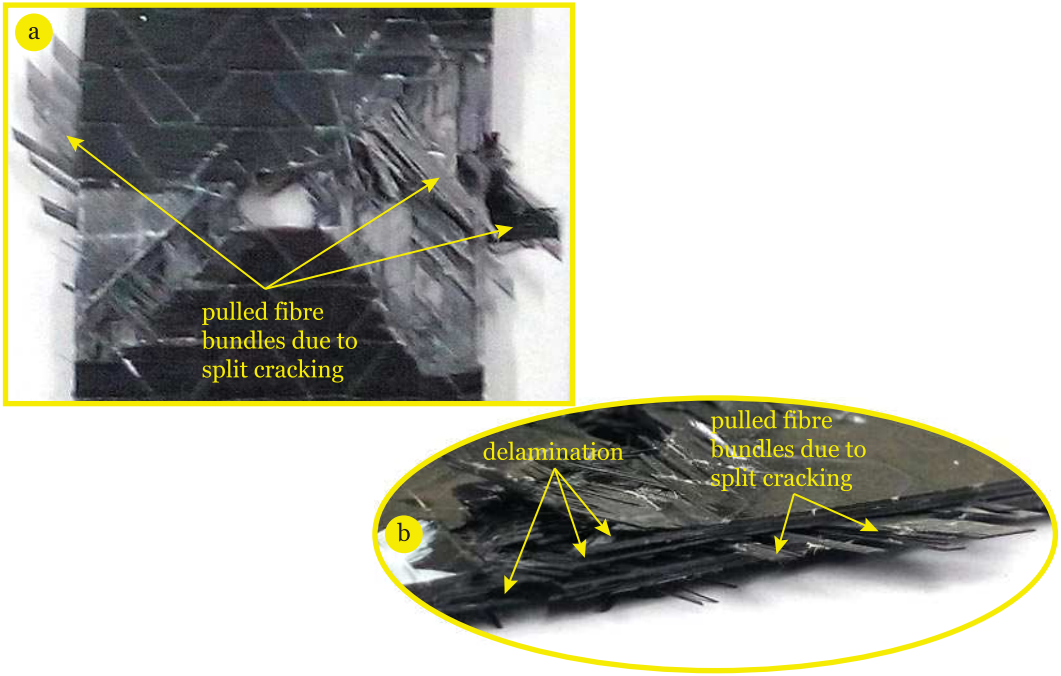

(b) *Blocked* laminate.

Fig. 5.85. Damaged section of representative 36 mm wide CNT specimens after testing, and closer views of some damage mechanisms.

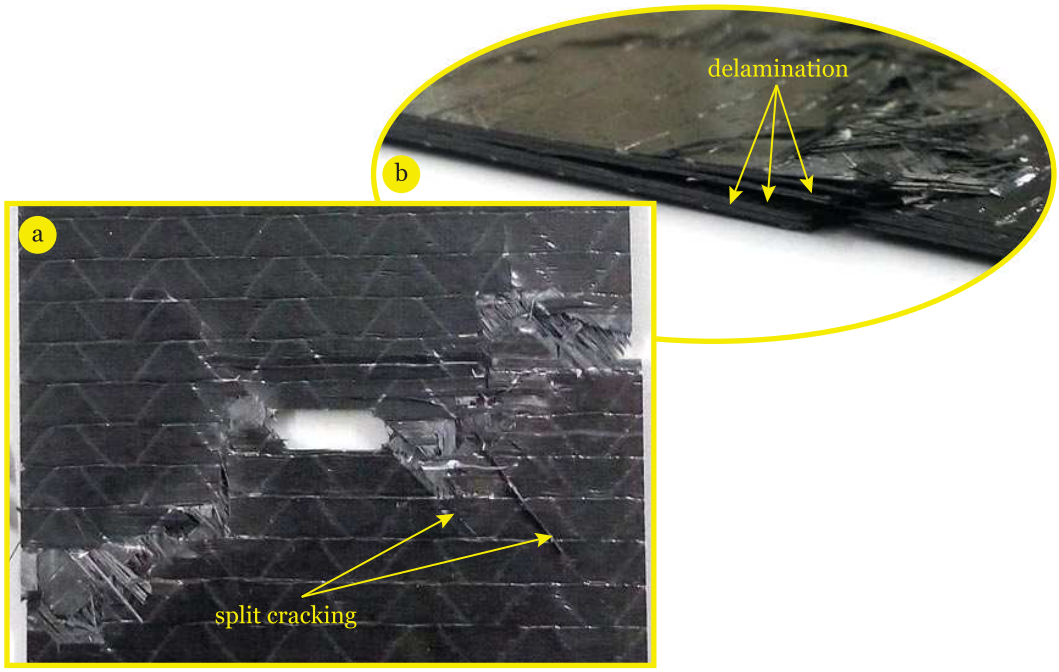

(a) *Dispersed* laminate.

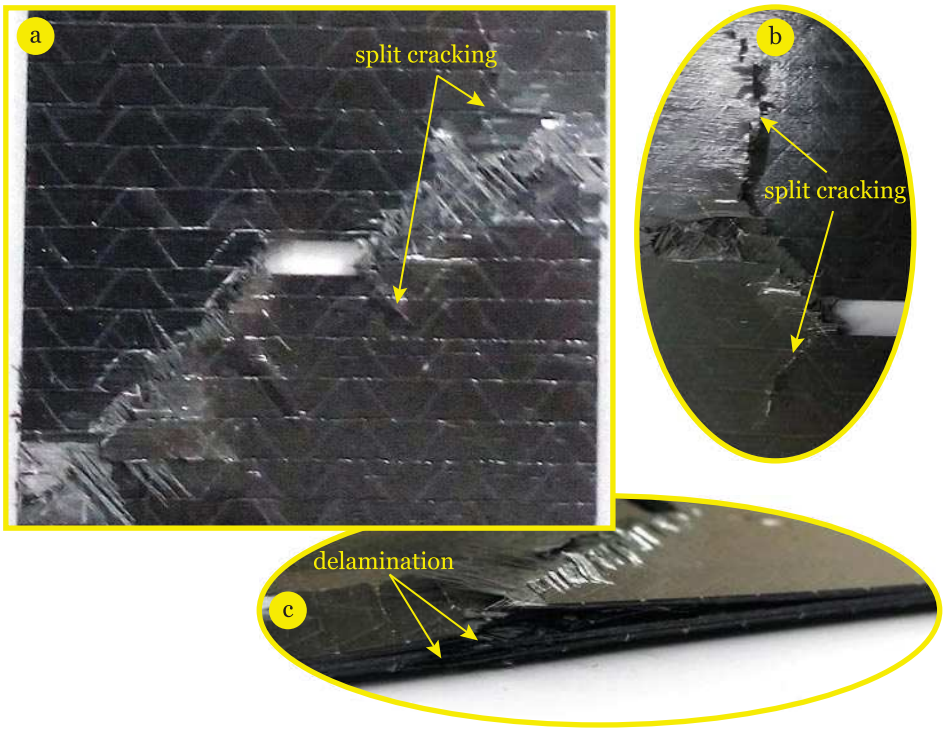

(b) *Blocked* laminate.

Fig. 5.86. Damaged section of representative 72 mm wide CNT specimens after testing, and closer views of some damage mechanisms.

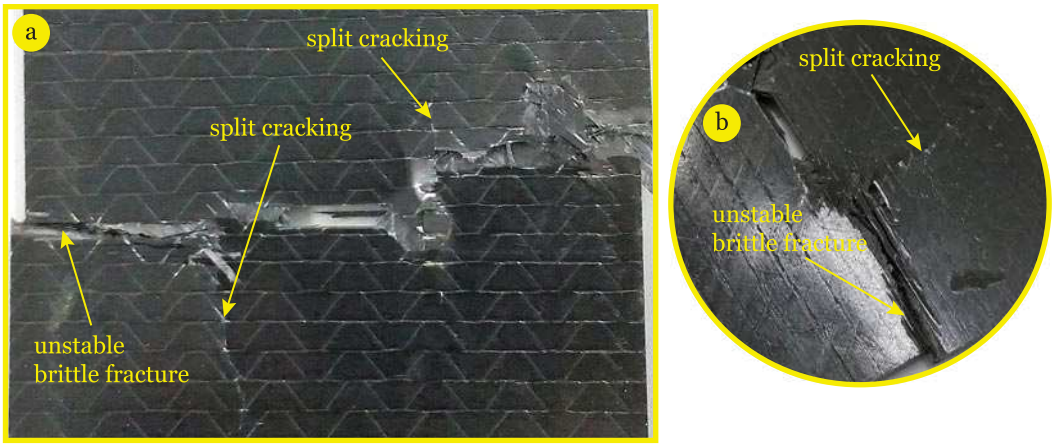

(a) *Dispersed* laminate.

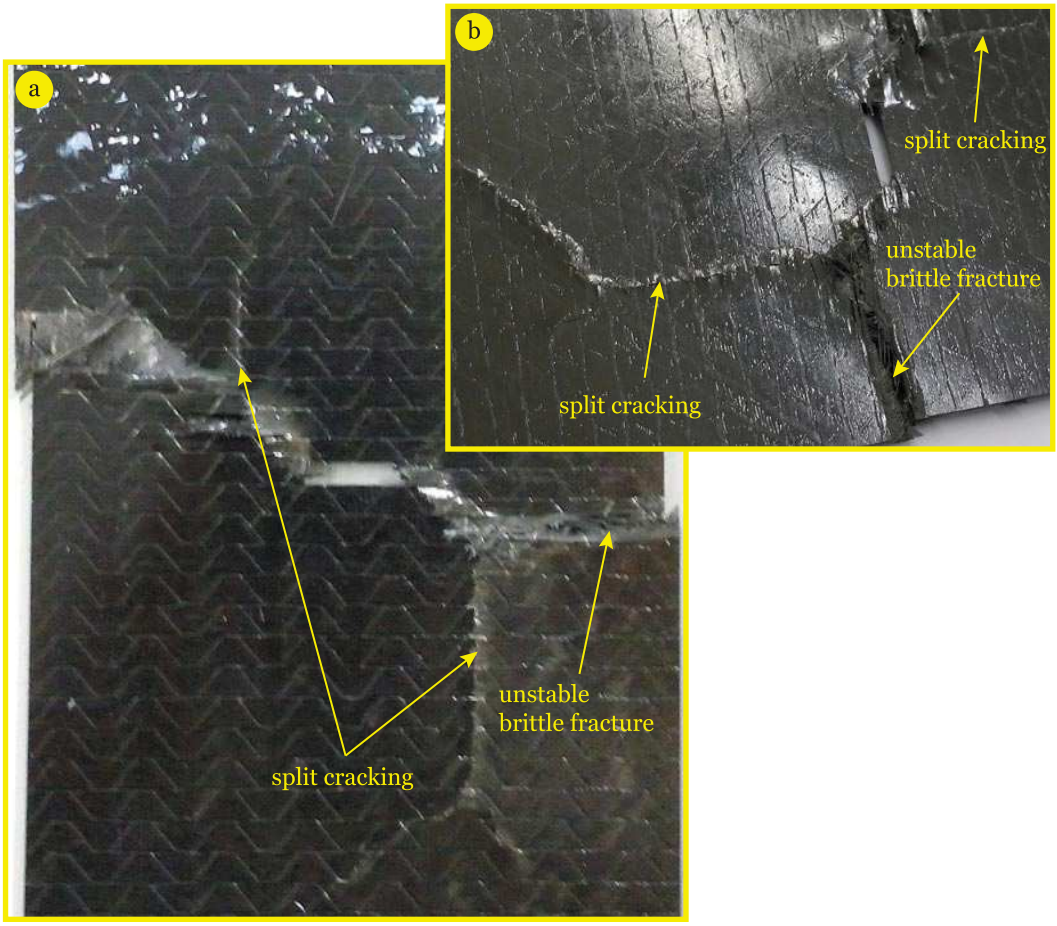

(b) *Blocked* laminate.

Fig. 5.87. Damaged section of representative 108 mm wide CNT specimens after testing, and closer views of some damage mechanisms.

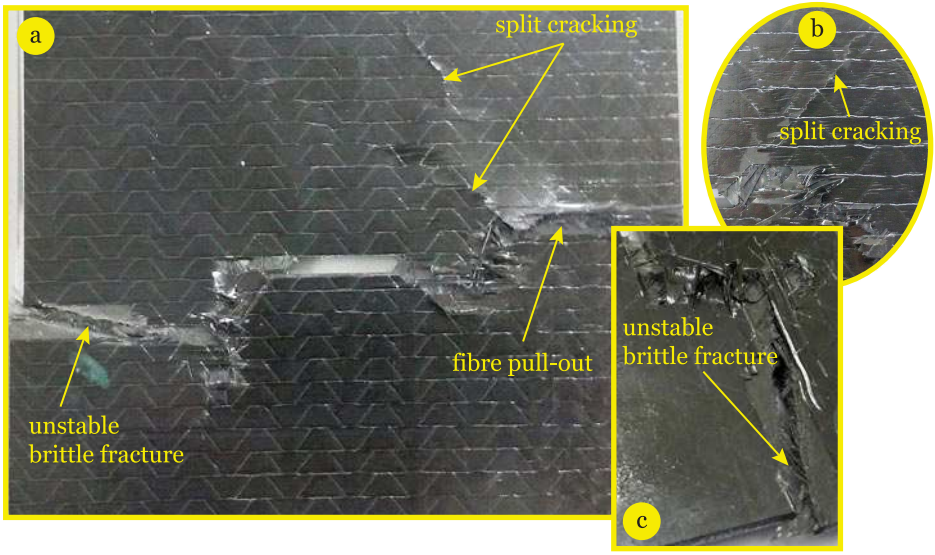

(a) *Dispersed* laminate.

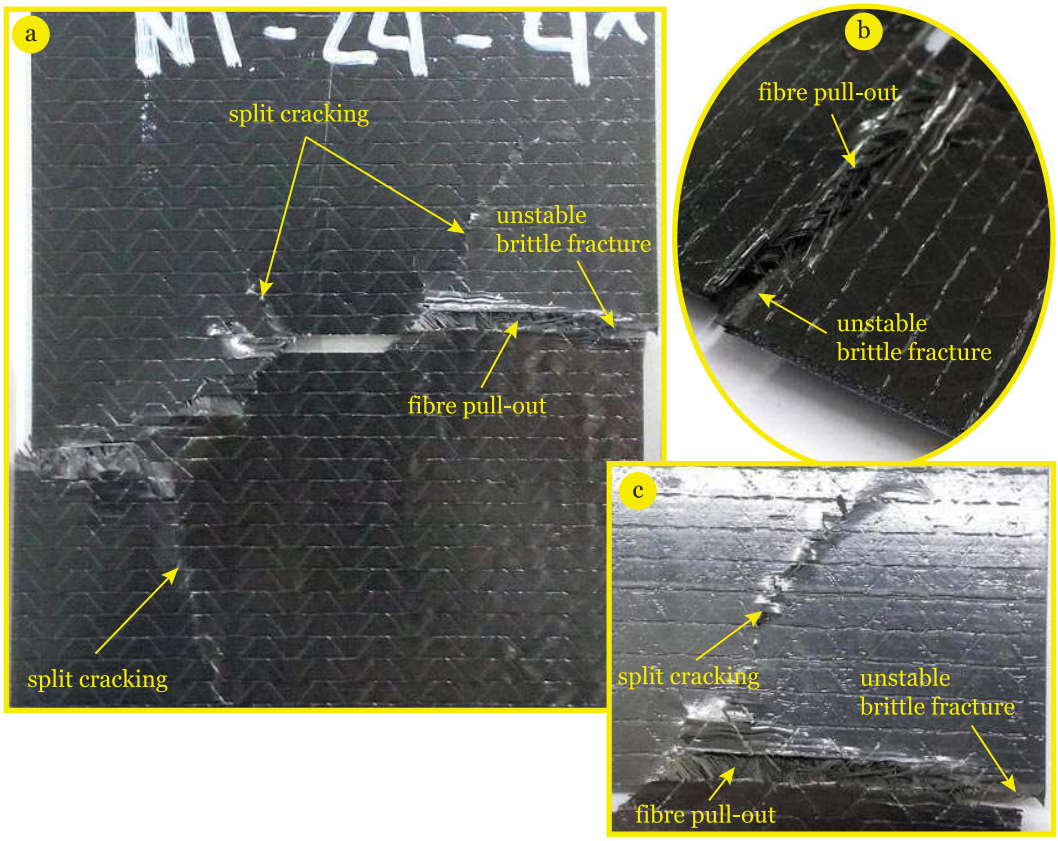

(b) *Blocked* laminate.

Fig. 5.88. Damaged section of representative 144 mm wide CNT specimens after testing, and closer views of some damage mechanisms.

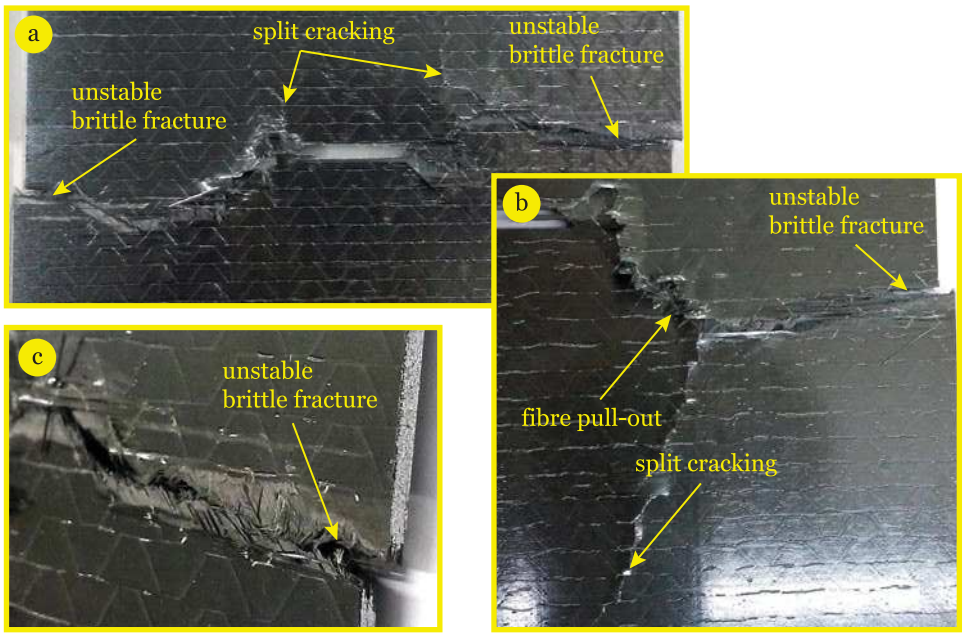

(a) *Dispersed* laminate.

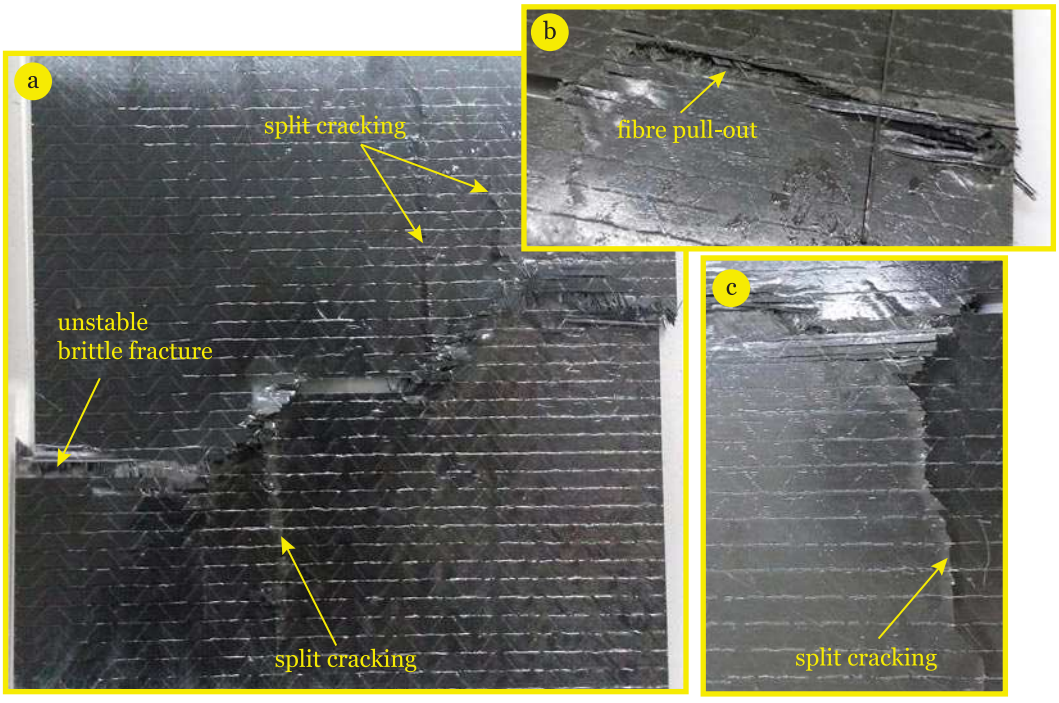

(b) *Blocked* laminate.

Fig. 5.89. Damaged section of representative 180 mm wide CNT specimens after testing, and closer views of some damage mechanisms.

5.5. Experimental results and discussion

Observation of the longitudinal strain fields obtained from the DIC measurements of representative specimens of the different configurations (figures 5.90 to 5.99) gives a complementary insight into the development of the damage process zone. At least one representative specimen of each laminate with the different sizes was assessed using the DIC technique, except for the 180 mm wide specimens of the *blocked* laminate. It is noted that figures 5.97 and 5.98 show the results of two representative CNT test specimens of the *blocked* laminate. The excellent agreement between these results show that the data obtained from a representative specimen is consistent, and that it can be extrapolated to the remaining specimens of the same laminate with the same geometry.

As the size of the specimens increases, the damage process zone starting from the notch tips becomes larger and more diffuse (figures 5.90 to 5.99). Even though all DIC measurements were performed on the outer 90° ply, diffuse damage, propagating predominantly along the off-axis ±45° directions, can be observed. Furthermore, as the size of the specimens increases (figures 5.94 to 5.99), longitudinal split cracks propagate quickly, after slow damage growth from the notch tips along the off-axis directions. Regions of high strain concentration with a triangular shape can be observed in the vicinity of the notch tips, specially in the smaller specimens of the *blocked* laminate (figures 5.91 and 5.93). These regions indicate the occurrence of localised transverse cracking and possibly delamination in addition to intralaminar fracture and longitudinal splitting.

In order to assess possible load asymmetries and the effects of strain concentration in the vicinity of the notch tips, remote stress-local axial strain relations were obtained with virtual strain gauges [121, 122, 182, 187], computed averaging the results from the DIC data in an area equivalent to the gauge area of physical strain gauges (figures 5.100 to 5.104). Gauge areas with 3.18 mm in length by 1.78 mm in width were used. Two virtual strain gauges (*SG1* and *SG2*) were placed at the tips of the centre notch. The location of the gauge areas (*SG1* and *SG2*) are presented in figures 5.100 to 5.104 for the different geometries and for both laminates, plotted over the longitudinal strain field obtained with DIC at an applied remote stress corresponding to 20% of the ultimate remote stress.

Figures 5.100 to 5.104 also show the results of a linear-elastic FEA, performed for each specimen geometry, which uses the same averaging procedure of the virtual strain gauges to compare with the data measured with the DIC technique. The FE models were created with the commercial FE software Abaqus 6.12-1 [275] using a structured mesh of CPS4R elements. At the notch tip, finite elements with a minimum in-plane size five times smaller than the notch tip radius (or 0.1 mm) were used to accurately represent the notch geometry and capture the strain concentrations. In the FE model, only the gauge section was represented, i.e. the gripped regions were not modelled. Figures 5.105a and 5.106a show a detail of the mesh of the 36 mm wide and 180 mm wide FE models, respectively.

To replicate the load and boundary conditions of the actual test setup, a longitudinal displacement (x-direction) of 1.00 mm was applied to the nodes on the top end. The remaining degrees of freedom were fixed. An encastre boundary condition was applied to the nodes in the bottom end by fixing all degrees of freedom.

The individual plies of the composite lay-up were modelled using a layerwise approach, explicitly defining each lamina, and respective ply orientation, by one integration point through the thickness of the plane stress elements. The constitutive behaviour of each ply was defined by an orthotropic material model, using the elastic properties of T700GC/M21 (table 4.1). For reference, figures 5.105b and 5.106b show the longitudinal strain field of the outer ply of the 36 mm wide and 180 mm wide models, respectively.

The results of the FEA are plotted together with the DIC data in figures 5.100 to 5.104. As can be observed, the numerical results are in very good agreement with the measured strains, validating the application of the virtual strain gauge approach in the present analysis.

The linear behaviour in the initial loading phase in figures 5.100 to 5.104 show that the data of the two virtual strain gauges positioned in the vicinity of the notch tips match very well in all tests. This result indicates that a good load symmetry was obtained, thus validating the adopted test setup. Moreover, not only the linear response was symmetric, but also the onset and propagation of strain localisation from the notch tips, given the similarity of the remote stress-local axial strain relations obtained at the opposite notch tips.

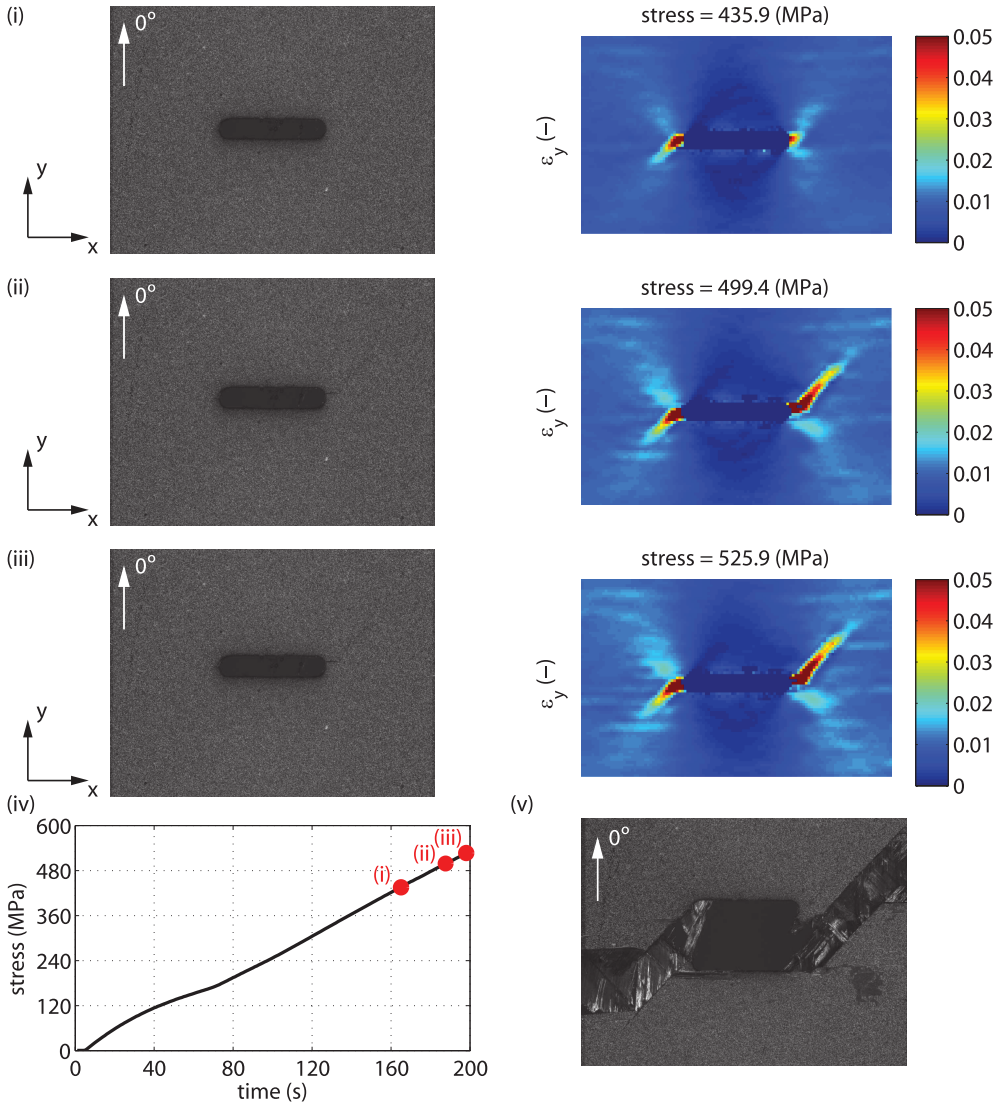

Fig. 5.90. Specimen's surface and longitudinal strain fields, ε_y, of the outer 90° ply of a representative 36 mm wide *dispersed* CNT test specimen obtained with the DIC system at the stages of (i) onset of transverse cracking, (ii) at 95% of the ultimate remote stress and (iii) at the ultimate remote stress. (iv) Remote stress-time relation. (v) Specimen's surface after failure obtained with the DIC image grabbing setup. The reference DIC coordinate system is depicted in the figures, where the *y*-axis is aligned with the loading direction.

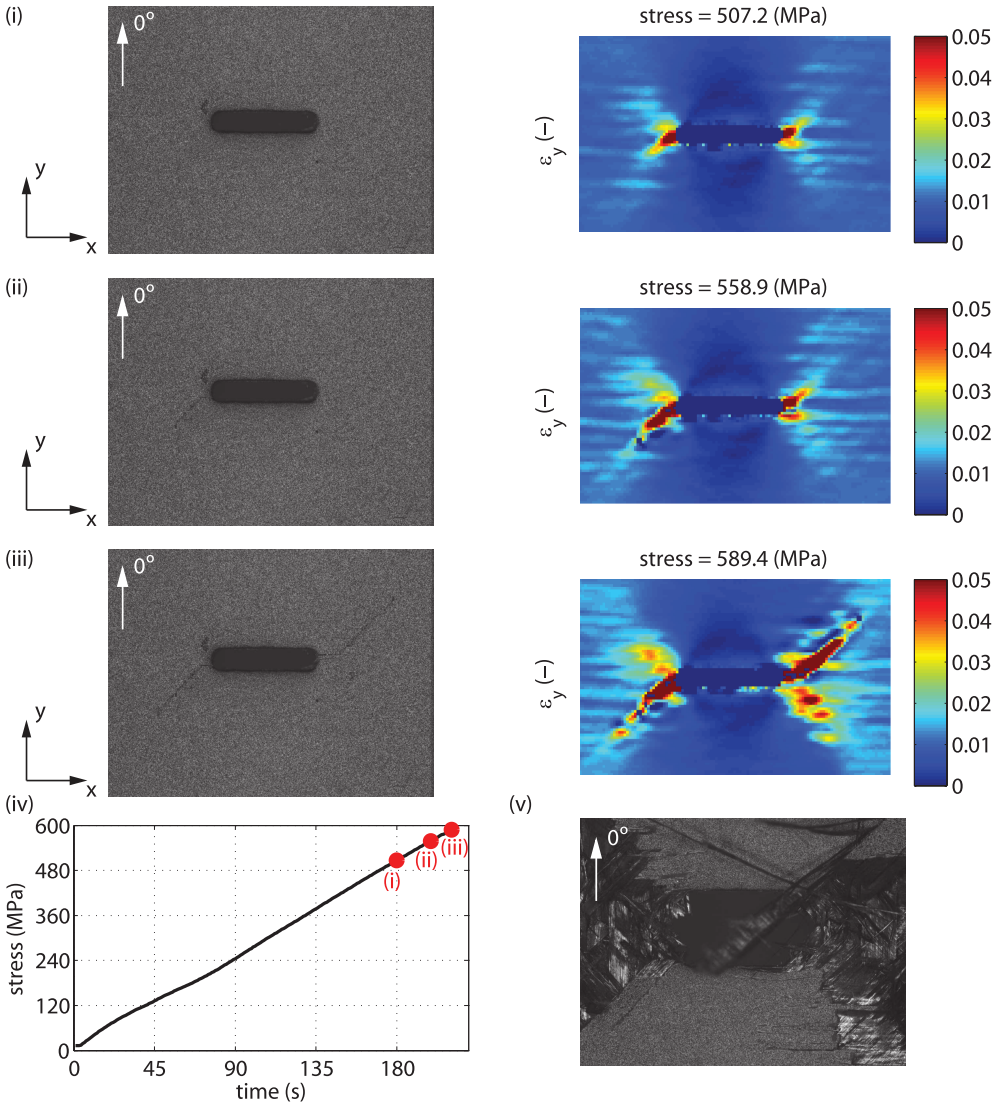

Fig. 5.91. Specimen's surface and longitudinal strain fields, ε_y, of the outer 90° ply of a representative 36 mm wide *blocked* CNT test specimen obtained with the DIC system at the stages of (i) onset of transverse cracking, (ii) at 95% of the ultimate remote stress and (iii) at the ultimate remote stress. (iv) Remote stress-time relation. (v) Specimen's surface after failure obtained with the DIC image grabbing setup. The reference DIC coordinate system is depicted in the figures, where the y-axis is aligned with the loading direction.

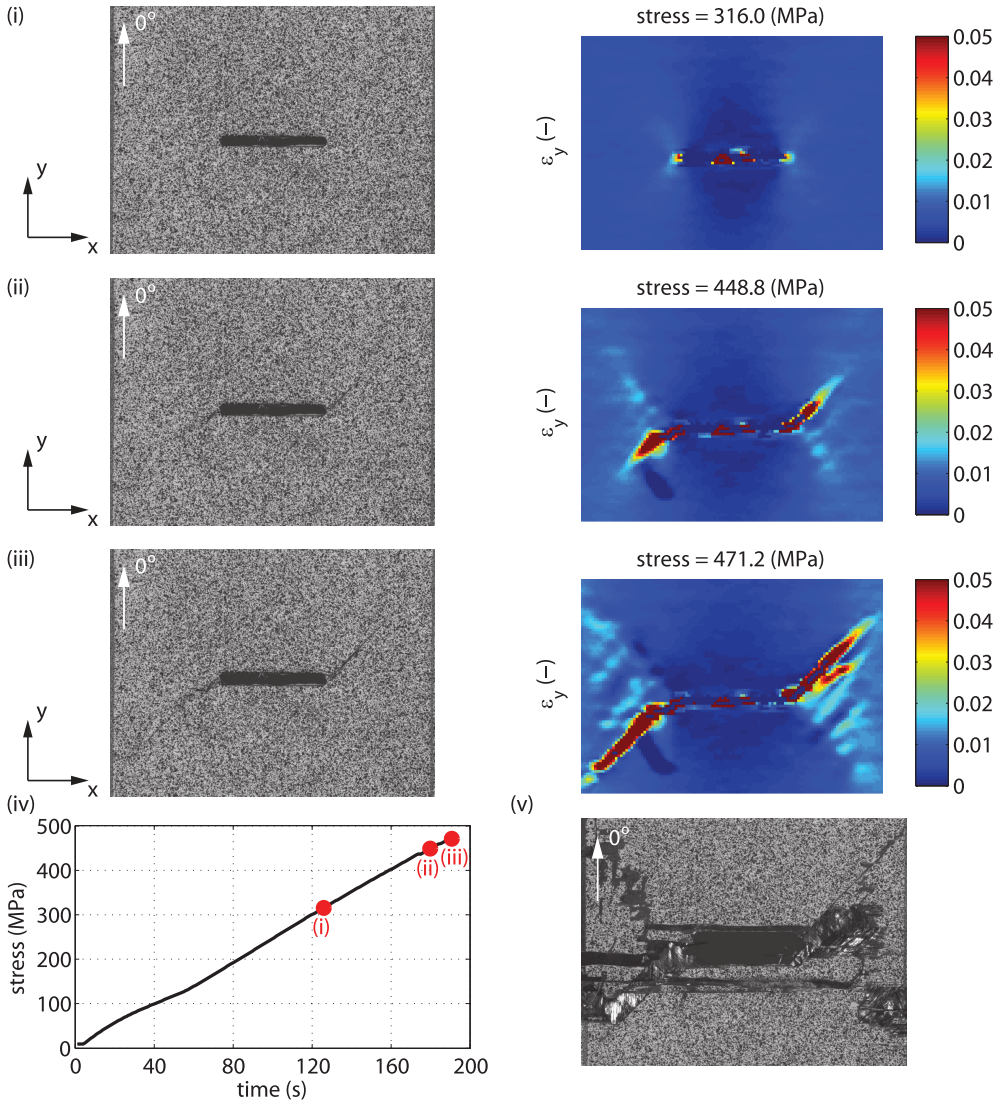

Fig. 5.92. Specimen's surface and longitudinal strain fields, ε_y, of the outer 90° ply of a representative 72 mm wide *dispersed* CNT test specimen obtained with the DIC system at the stages of (i) onset of transverse cracking, (ii) at 95% of the ultimate remote stress and (iii) at the ultimate remote stress. (iv) Remote stress-time relation. (v) Specimen's surface after failure obtained with the DIC image grabbing setup. The reference DIC coordinate system is depicted in the figures, where the *y*-axis is aligned with the loading direction.

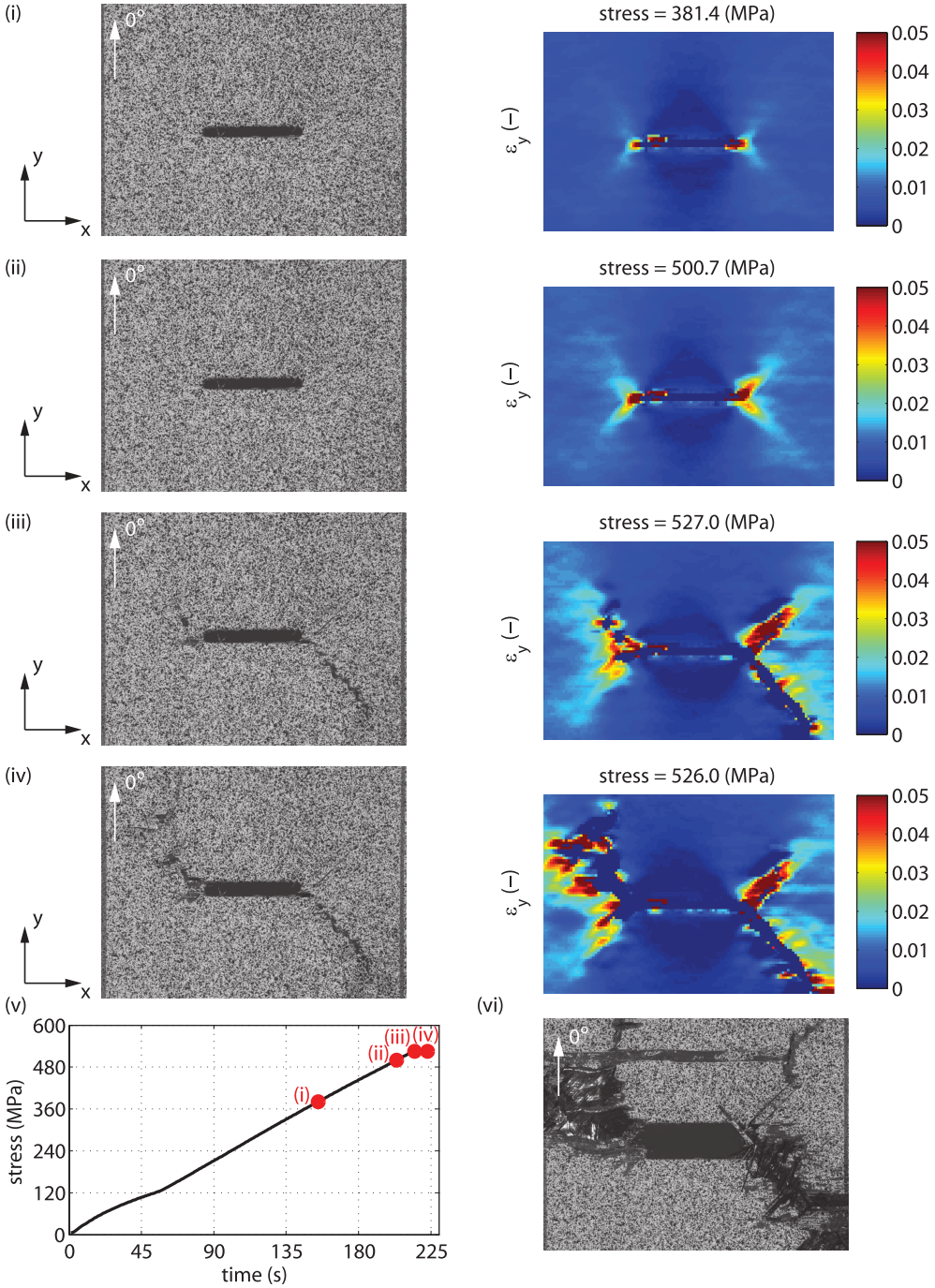

Fig. 5.93. Specimen's surface and longitudinal strain fields, ε_y, of the outer 90° ply of a representative 72 mm wide *blocked* CNT test specimen obtained with the DIC system at the stages of (i) onset of transverse cracking, (ii) at 95% of the ultimate remote stress, (iii) at the maximum remote stress and (iv) just before ultimate failure. (v) Remote stress-time relation. (vi) Specimen's surface after failure obtained with the DIC image grabbing setup. The reference DIC coordinate system is depicted in the figures, where the *y*-axis is aligned with the loading direction.

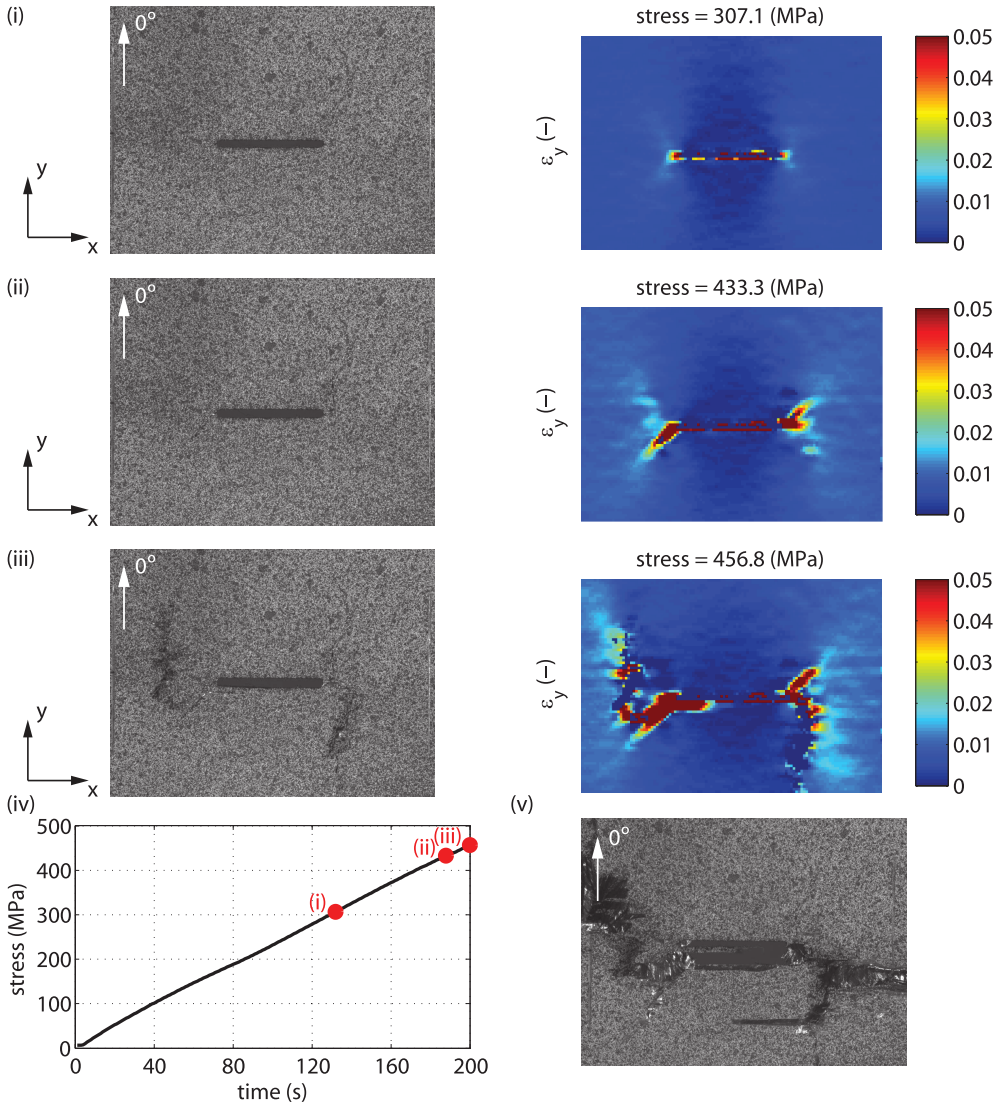

Fig. 5.94. Specimen's surface and longitudinal strain fields, ε_y, of the outer 90° ply of a representative 108 mm wide *dispersed* CNT test specimen obtained with the DIC system at the stages of (i) onset of transverse cracking, (ii) at 95% of the ultimate remote stress and (iii) at the ultimate remote stress. (iv) Remote stress-time relation. (v) Specimen's surface after failure obtained with the DIC image grabbing setup. The reference DIC coordinate system is depicted in the figures, where the *y*-axis is aligned with the loading direction.

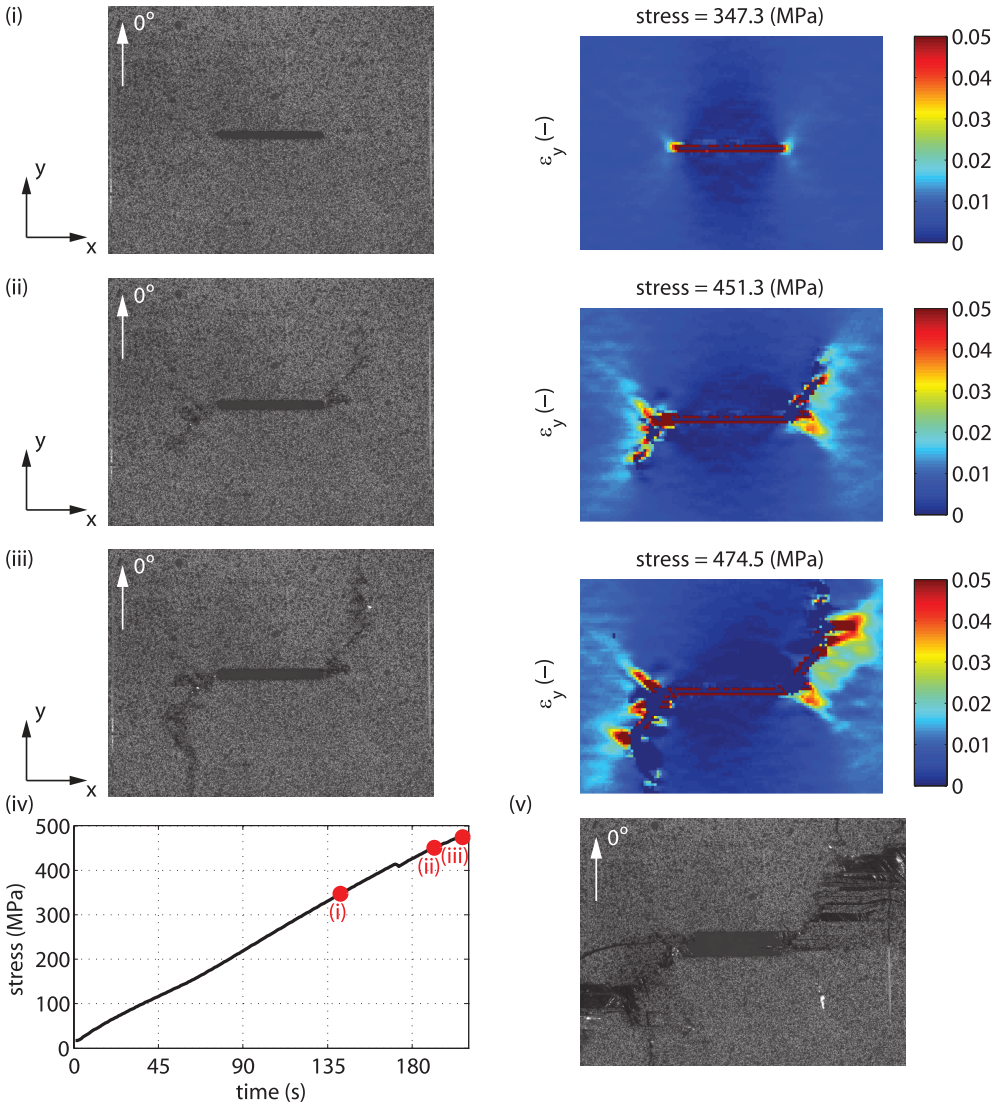

Fig. 5.95. Specimen's surface and longitudinal strain fields, ε_y, of the outer 90° ply of a representative 108 mm wide *blocked* CNT test specimen obtained with the DIC system at the stages of (i) onset of transverse cracking, (ii) at 95% of the ultimate remote stress and (iii) at the ultimate remote stress. (iv) Remote stress-time relation. (v) Specimen's surface after failure obtained with the DIC image grabbing setup. The reference DIC coordinate system is depicted in the figures, where the *y*-axis is aligned with the loading direction.

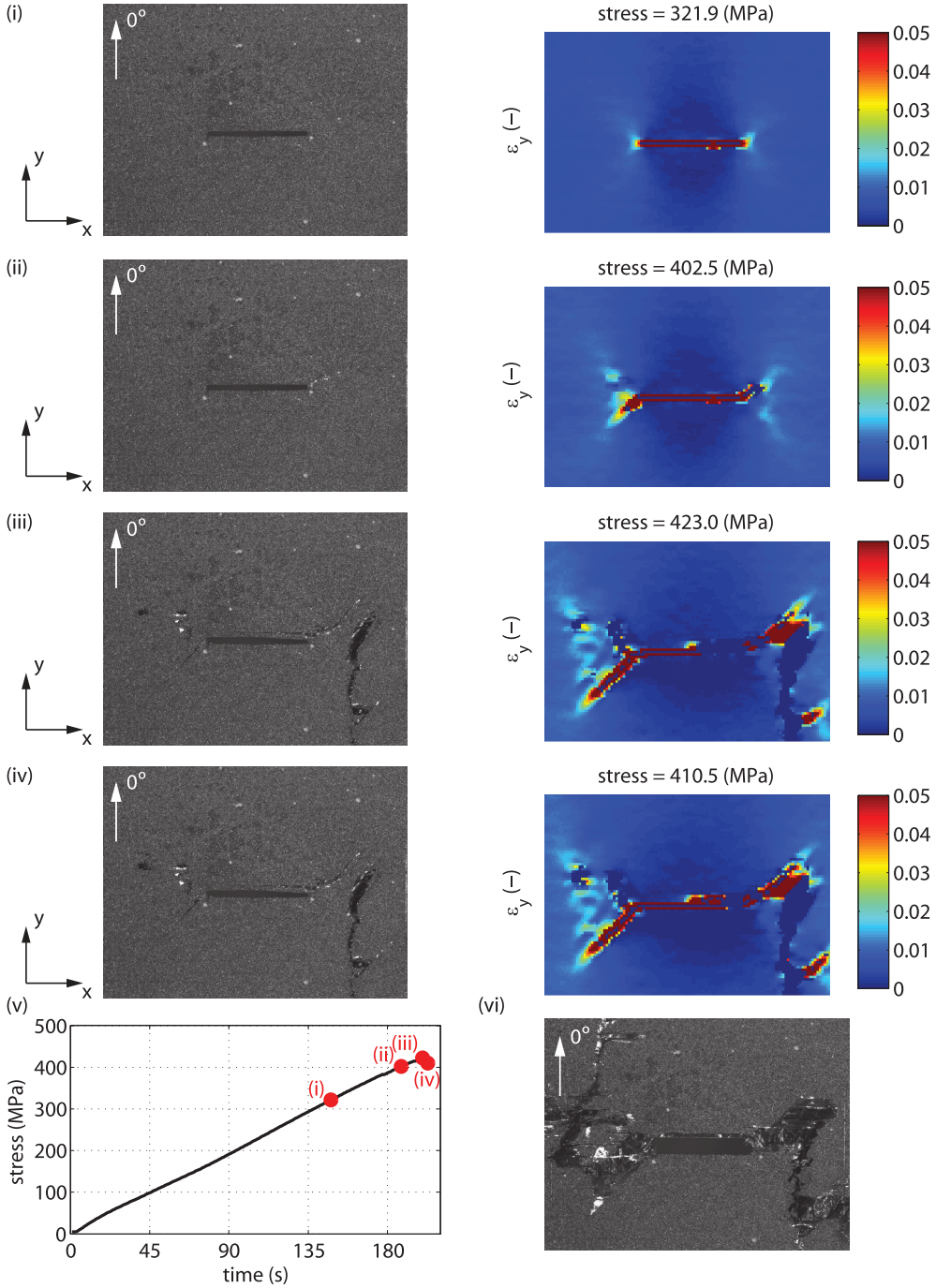

Fig. 5.96. Specimen's surface and longitudinal strain fields, ε_y, of the outer 90° ply of a representative 144 mm wide *dispersed* CNT test specimen obtained with the DIC system at the stages of (i) onset of transverse cracking, (ii) at 95% of the ultimate remote stress, (iii) at the maximum remote stress and (iv) just before ultimate failure. (v) Remote stress-time relation. (vi) Specimen's surface after failure obtained with the DIC image grabbing setup. The reference DIC coordinate system is depicted in the figures, where the *y*-axis is aligned with the loading direction.

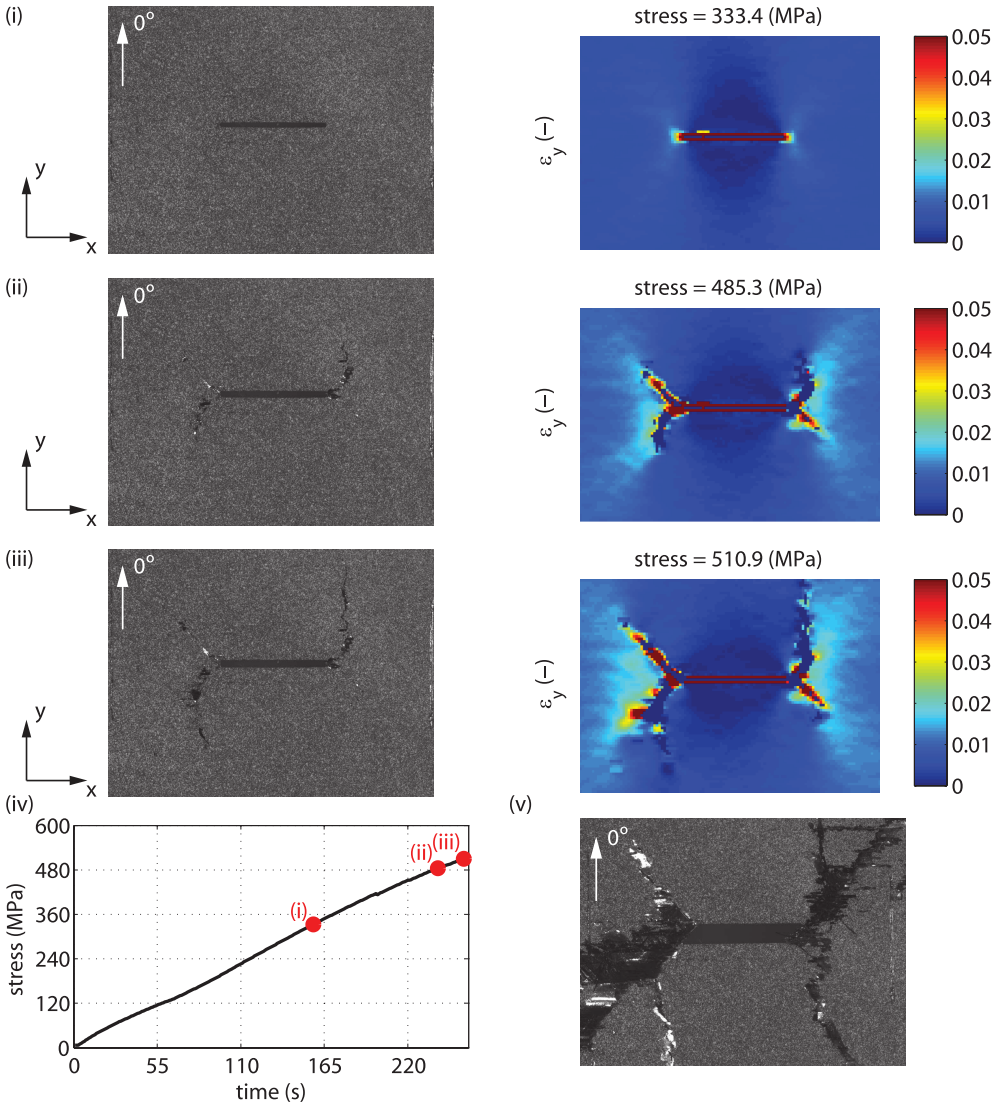

Fig. 5.97. Specimen's surface and longitudinal strain fields, ε_y, of the outer 90° ply of a representative 144 mm wide *blocked* CNT test specimen obtained with the DIC system at the stages of (i) onset of transverse cracking, (ii) at 95% of the ultimate remote stress and (iii) at the ultimate remote stress. (iv) Remote stress-time relation. (v) Specimen's surface after failure obtained with the DIC image grabbing setup. The reference DIC coordinate system is depicted in the figures, where the y-axis is aligned with the loading direction.

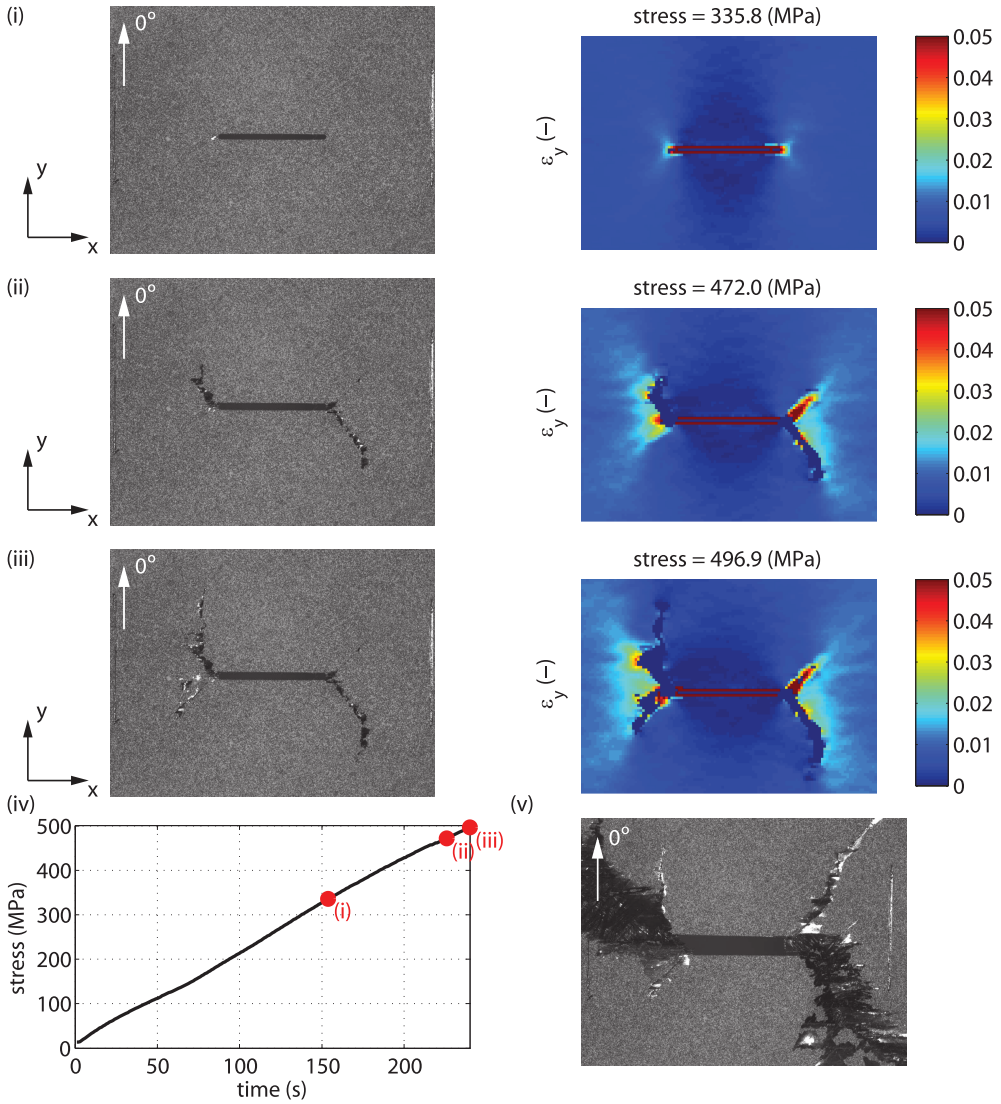

Fig. 5.98. Specimen's surface and longitudinal strain fields, ε_y, of the outer 90° ply of a second 144 mm wide *blocked* CNT test specimen obtained with the DIC system at the stages of (i) onset of transverse cracking, (ii) at 95% of the ultimate remote stress and (iii) at the ultimate remote stress. (iv) Remote stress-time relation. (v) Specimen's surface after failure obtained with the DIC image grabbing setup. The reference DIC coordinate system is depicted in the figures, where the *y*-axis is aligned with the loading direction.

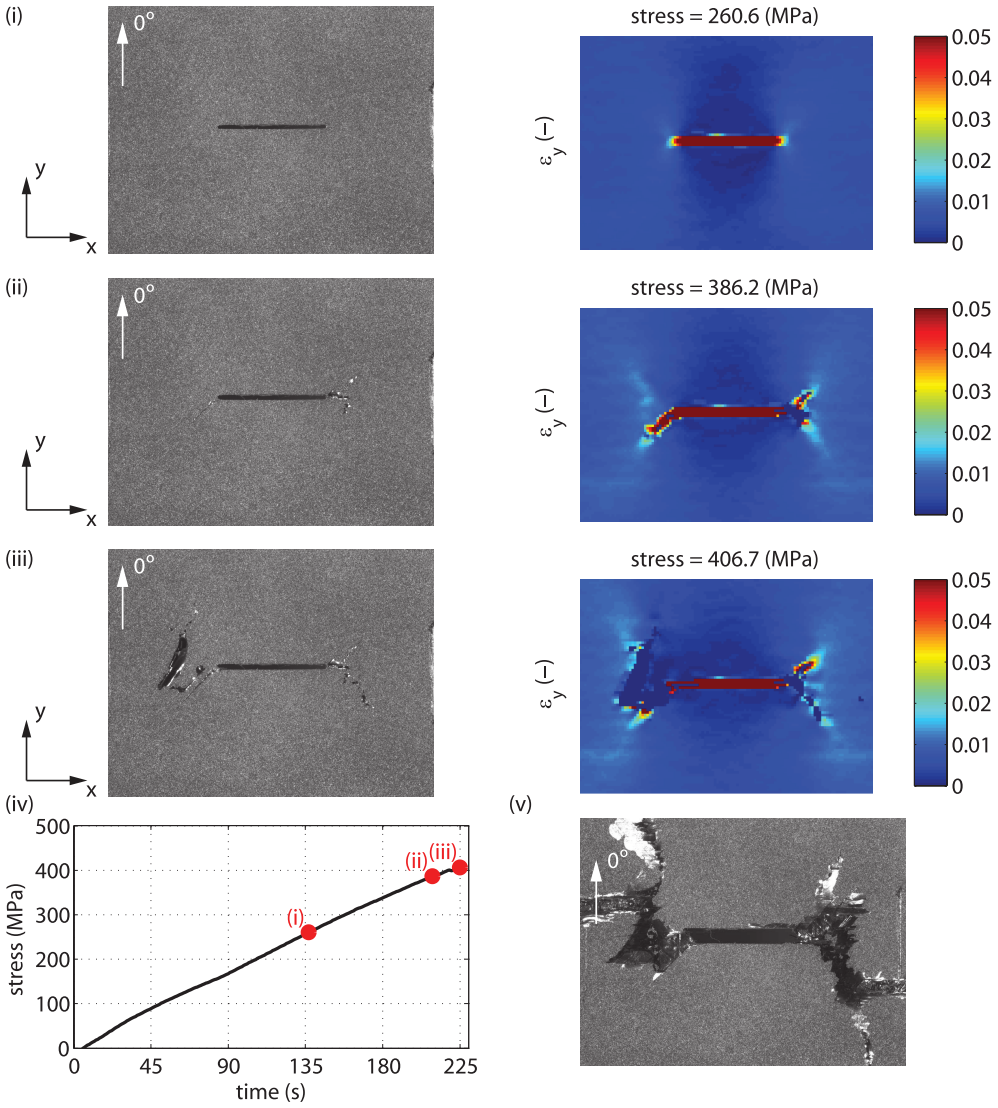

Fig. 5.99. Specimen's surface and longitudinal strain fields, ε_y, of the outer 90° ply of a representative 180 mm wide *dispersed* CNT test specimen obtained with the DIC system at the stages of (i) onset of transverse cracking, (ii) at 95% of the ultimate remote stress and (iii) at the ultimate remote stress. (iv) Remote stress-time relation. (v) Specimen's surface after failure obtained with the DIC image grabbing setup. The reference DIC coordinate system is depicted in the figures, where the *y*-axis is aligned with the loading direction.

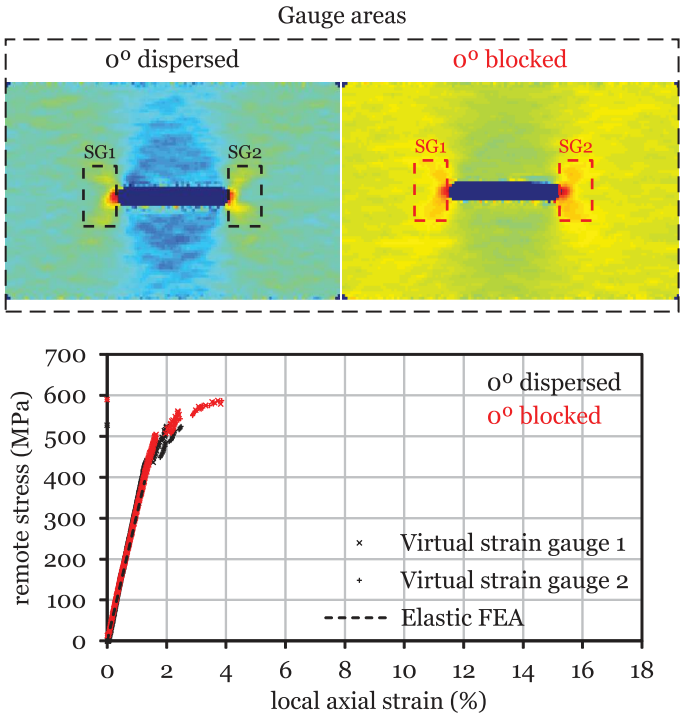

Fig. 5.100. Virtual strain gauge areas and remote stress-local axial strain relations of representative 36 mm wide CNT test specimens. The loading direction is parallel to the vertical axis of the specimens.

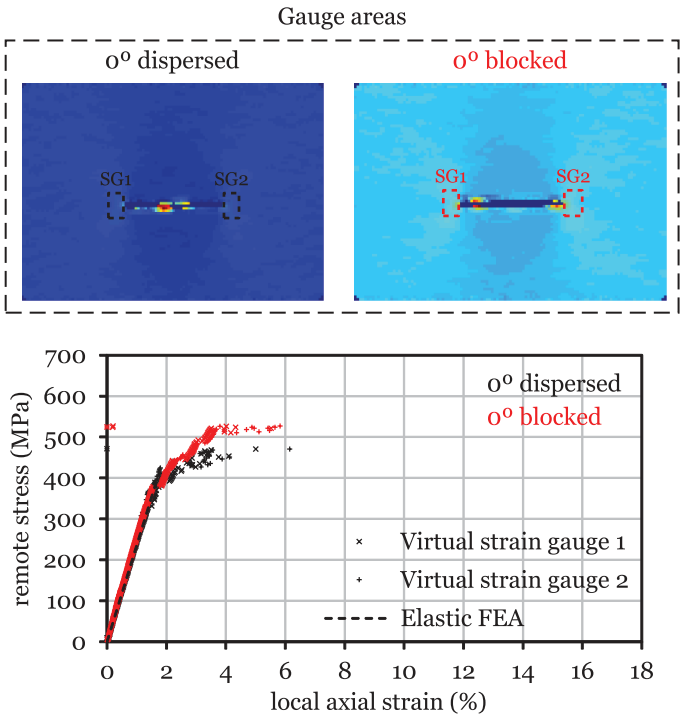

Fig. 5.101. Virtual strain gauge areas and remote stress-local axial strain relations of representative 72 mm wide CNT test specimens. The loading direction is parallel to the vertical axis of the specimens.

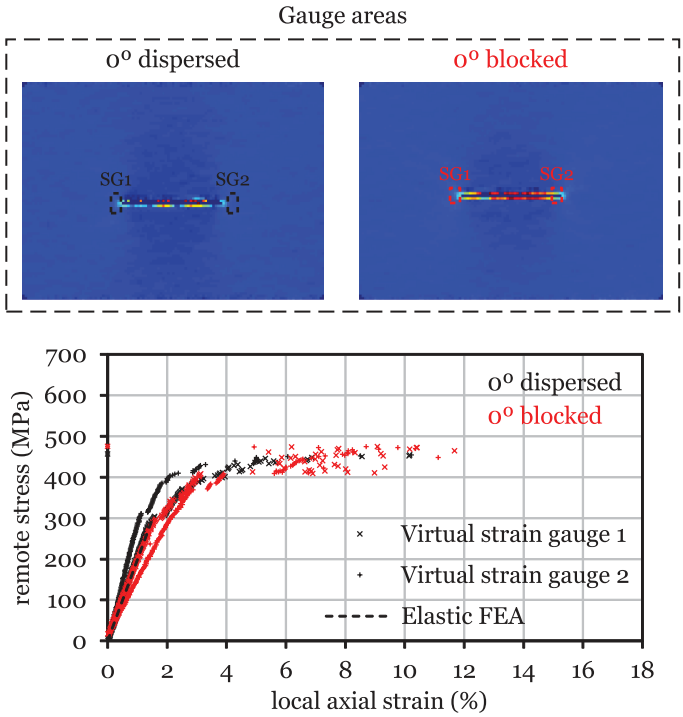

Fig. 5.102. Virtual strain gauge areas and remote stress-local axial strain relations of representative 108 mm wide CNT test specimens. The loading direction is parallel to the vertical axis of the specimens.

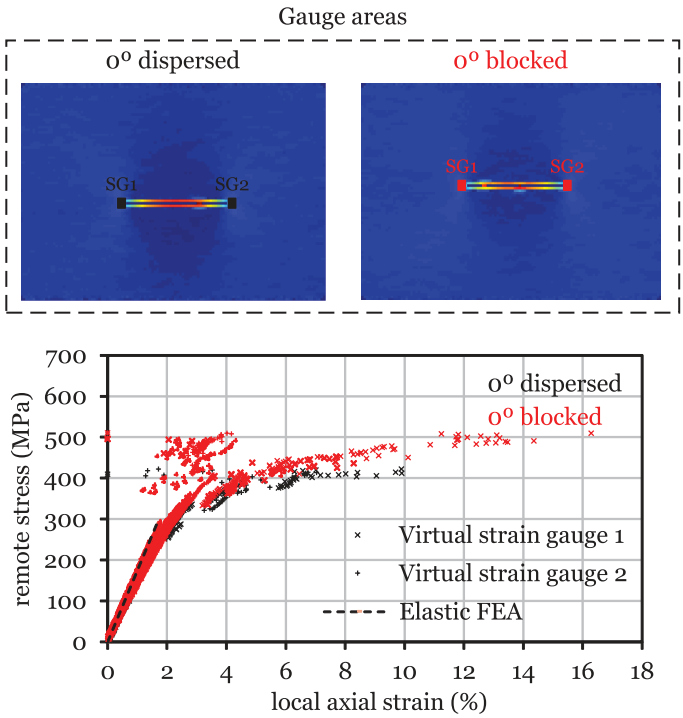

Fig. 5.103. Virtual strain gauge areas and remote stress-local axial strain relations of representative 144 mm wide CNT test specimens. The loading direction is parallel to the vertical axis of the specimens.

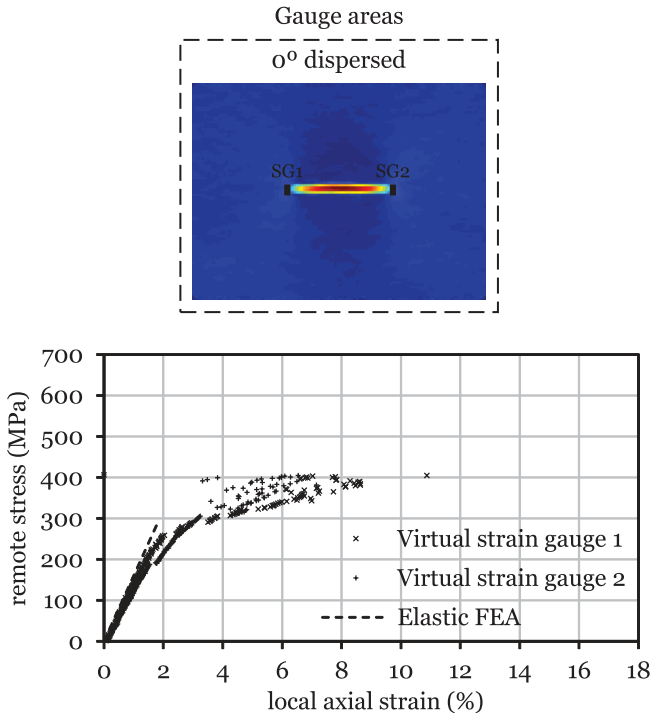

Fig. 5.104. Virtual strain gauge areas and remote stress-local axial strain relations of representative 180 mm wide CNT test specimens. The loading direction is parallel to the vertical axis of the specimens.

Figures 5.90 to 5.98 and figures 5.100 to 5.103 show that, in general, the onset of damage growth from the notch tips starts earlier in the *dispersed* laminate. Because the thickness of the 90° outer ply is the same for the *dispersed* and *blocked* laminates, and its neighbour ply, immediately below, has the same orientation (−45°) in both laminates (therefore not affecting the local constraining effect), it is clear that the earlier onset of damage in the *dispersed* laminate is not caused by an *in situ* effect. Instead, surface damage restraining in the *blocked* laminate can be attributed to stress relaxation caused by internal damage growth, which delays the onset of through-the-thickness intralaminar damage. It is noted that, contrary to the *dispersed* laminate, 0° ply blocking in the *blocked* laminate results in a lower constraining of the 0° plies and higher stress concentrations at the adjacent interfaces, promoting delamination and split cracking between the adjacent plies [111, 117, 166, 205]. Also, in the *blocked* laminate, some of the adjacent NCF bi-angle layers are stacked with relative ply orientations of 90°, conducting to higher interlaminar stress concentrations between these plies, contributing to an earlier onset of delamination in these interfaces. As explained in section 5.5.1, transverse matrix cracking and delamination, which are generally more detrimental to the laminates integrity, are believed to play a minor role in the tested laminates.

Table 5.17 shows the average results for the ultimate remote stress of the CNT tests and corresponding coefficients of variation. These results are summarised in figure 5.107, which shows the mean ultimate remote stress as a function of the nominal notch length, which is proportional to the size of the specimens (geometrically similar CNT specimens were tested). As expected, as the size of the specimens increases, the mean ultimate remote stress decreases (positive geometry).

Table 5.17 and figure 5.107 show that, in general, the ultimate remote stresses of the *blocked* laminate are higher than the ultimate remote stresses of the *dispersed* laminate. This can be attributed to higher stress relaxation in the vicinity of the notch tips of the *blocked* laminate due to longer longitudinal split cracking in the 0° plies, which blunts the notch and reduces the local stress concentration.

It is interesting to note that, as the size of the specimens increases, the ultimate remote stresses tend to the same value. This result shows that stress relaxation caused by the superior blunting effect of split cracking and local delamination

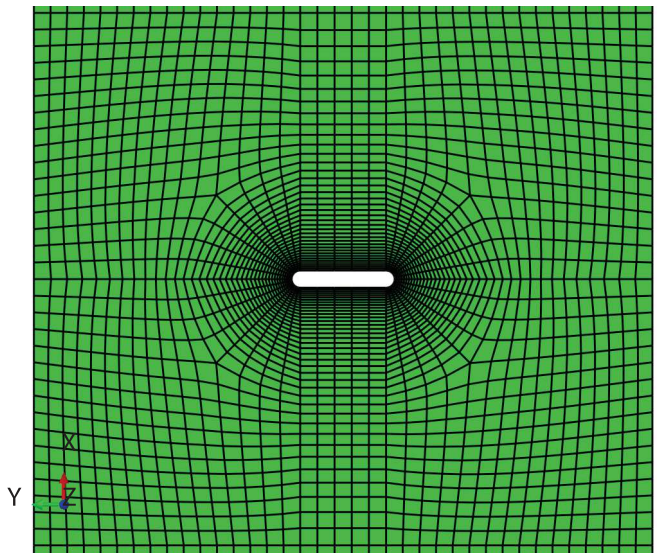

(a) Mesh detail.

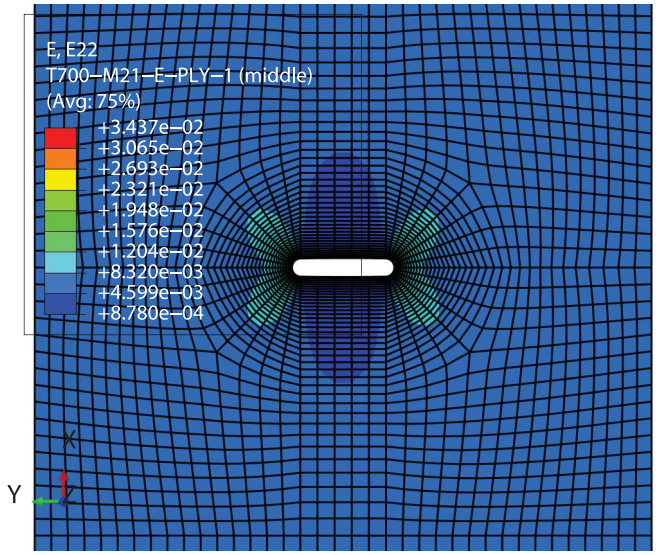

(b) Longitudinal strain field of the outer ply.

Fig. 5.105. Mesh detail of the FE model of a 36 mm wide CNT test specimen and longitudinal strain field of the outer ply.

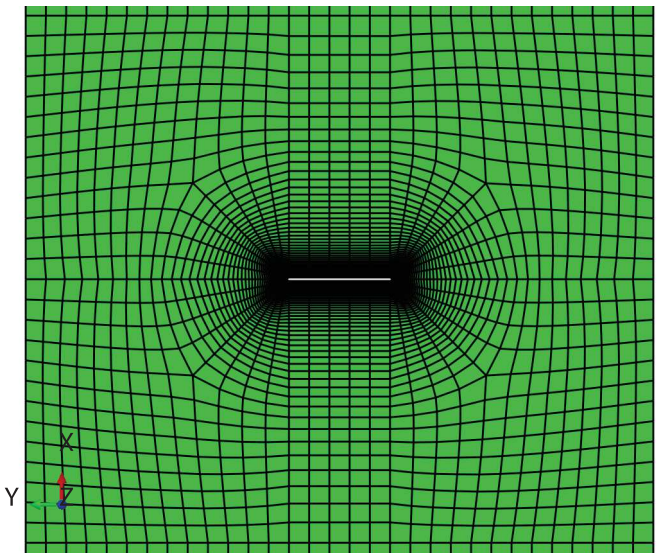

(a) Mesh detail.

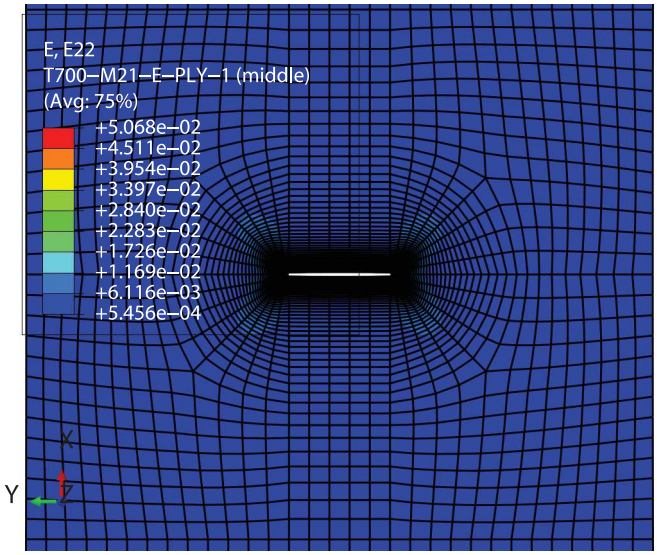

(b) Longitudinal strain field of the outer ply.

Fig. 5.106. Mesh detail of the FE model of a 180 mm wide CNT test specimen and longitudinal strain field of the outer ply.

Table 5.17
Mean ultimate remote stresses ($\bar{\sigma}^{\infty}$) and coefficients of variation (C.V.) of the CNT tests.

Results	Notch length (mm)				
	6	12	18	24	30
***Dispersed* laminate**					
No. specimens	3	3	2	3	3
$\bar{\sigma}^{\infty}$ (MPa)	540	486	469	414	407
C.V. (%)	0.6	2.3	2.3	4.0	1.9
***Blocked* laminate**					
No. specimens	3	3	3	3	3
$\bar{\sigma}^{\infty}$ (MPa)	605	534	487	500	425
C.V. (%)	0.9	1.5	1.7	2.5	3.5

in the *blocked* laminate, potentiated by the thicker blocks of 0° plies, becomes less and less important as the size of the specimens increases. As stressed in section 5.5.1, the size of the FPZ, which tends to a limit value, may become negligibly small for sufficiently large structures, and the fracture toughness then reaches a constant (steady-state) value. Because the laminates under study have the same in-plane properties, and the change in the stacking sequence affects only internal subcritical damage mechanisms, which can be lumped into a damage process zone, it is expected that, as the specimens become sufficiently large, the difference in their notched response will become smaller. A greater insight into the size of the damage process zone can be obtained through analysis of specimens subjected to interrupted testing at applied remote stresses close to the corresponding failure stress.

5.5.5.2. Interrupted centre-notched tension test results

Tests interrupted at applied remote stresses between 92% and 97% of the mean ultimate remote stresses were performed to study the damage mechanisms responsible for the stable development of the fracture process zone ahead of the notch tips. An additional test interrupted at 81% of the mean ultimate remote stress of a 180 mm wide specimen of the *blocked* laminate was also conducted.

To assess the extent of internal damage growth before ultimate failure, X-ray radiographies of some CNT specimens after interrupted testing are presented in figures 5.108 to 5.117. The scanning voltage was 45 kV (140 μA) and the exposure time for each radiograph was 2 s. It is noted that no X-ray radiographies were obtained on the 144 mm wide CNT test specimens. For reference, the schematics of the damage identified by external visual inspection are also shown in figures 5.109 to 5.117.

In the 36 mm wide specimen of the *dispersed* laminate tested to 94% of the ultimate remote stress (figure 5.108), no damage could be identified by external visual inspection after the test was interrupted. However, small split cracks in the off-axis plies can be identified in the X-ray radiographies, propagating from the centre notch tips and starting where the

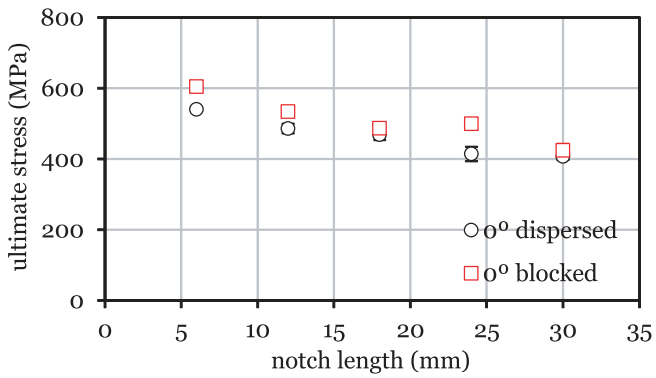

Fig. 5.107. Mean ultimate remote stress as a function of the nominal notch length of the CNT tests.

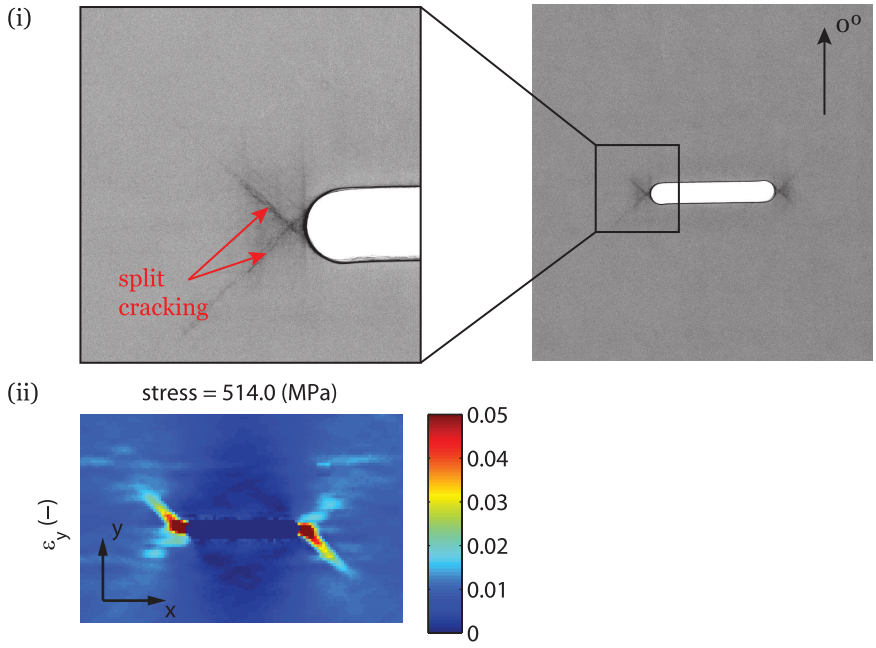

Fig. 5.108. Damage on the 36 mm wide CNT specimen of the *dispersed* laminate after interrupted testing at 94% of the mean ultimate remote stress. (i) X-ray radiographies of the complete centre notch and of a detail of the left notch tip. (ii) Longitudinal strain field, ε_y, on the outer 90° ply.

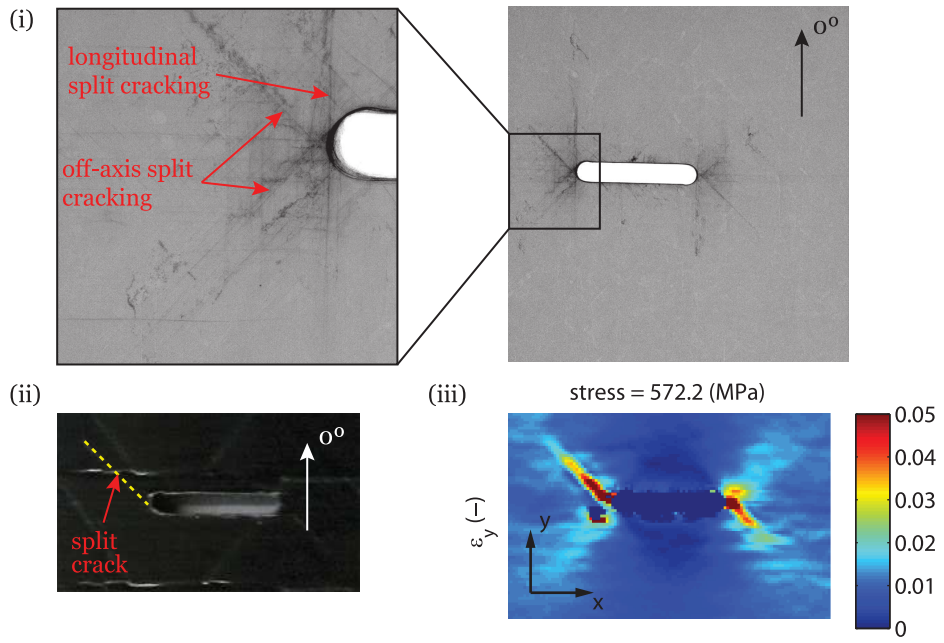

Fig. 5.109. Damage on the 36 mm wide CNT specimen of the *blocked* laminate after interrupted testing at 95% of the mean ultimate remote stress. (i) X-ray radiographies of the complete centre notch and of a detail of the left notch tip. (ii) Schematic of the damage identified by external visual inspection. (iii) Longitudinal strain field, ε_y, on the outer 90° ply.

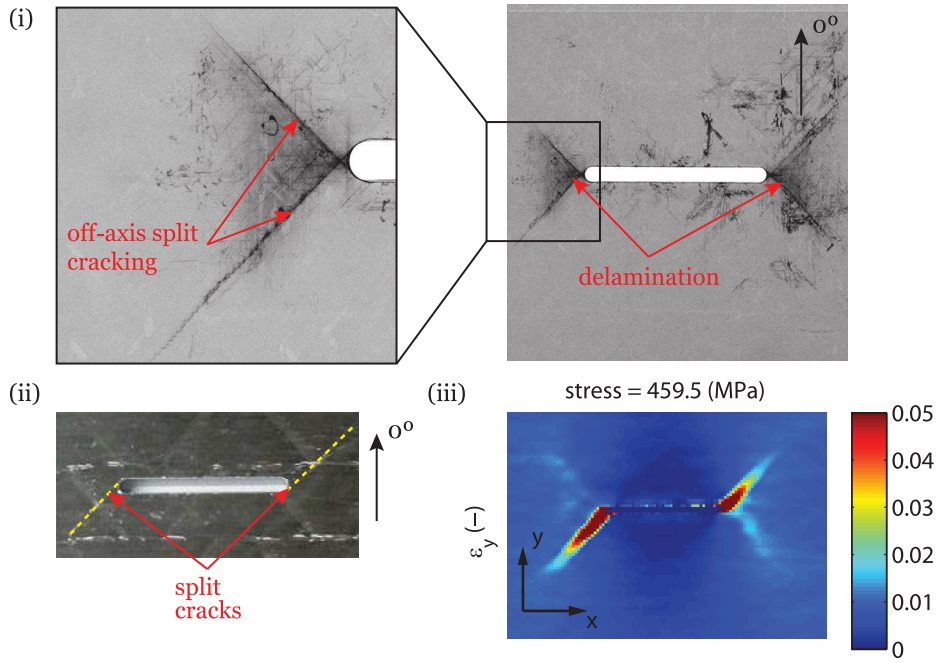

Fig. 5.110. Damage on the 72 mm wide CNT specimen of the *dispersed* laminate after interrupted testing at 95% of the mean ultimate remote stress. (i) X-ray radiographies of the complete centre notch and of a detail of the left notch tip. (ii) Schematic of the damage identified by external visual inspection. (iii) Longitudinal strain field, ε_y, on the outer 90° ply.

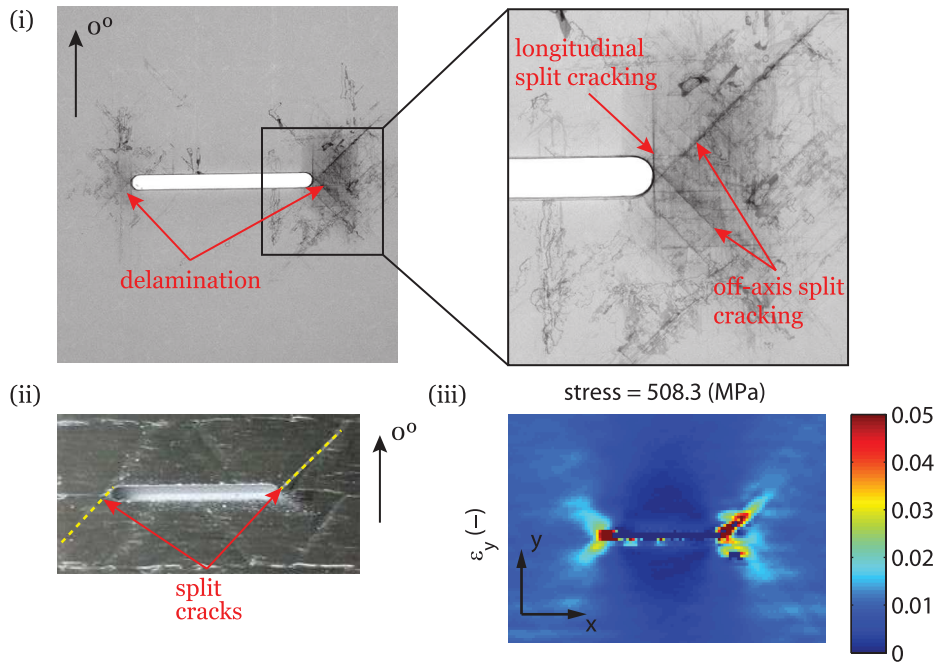

Fig. 5.111. Damage on the 72 mm wide CNT specimen of the *blocked* laminate after interrupted testing at 95% of the mean ultimate remote stress. (i) X-ray radiographies of the complete centre notch and of a detail of the right notch tip. (ii) Schematic of the damage identified by external visual inspection. (iii) Longitudinal strain field, ε_y, on the outer 90° ply.

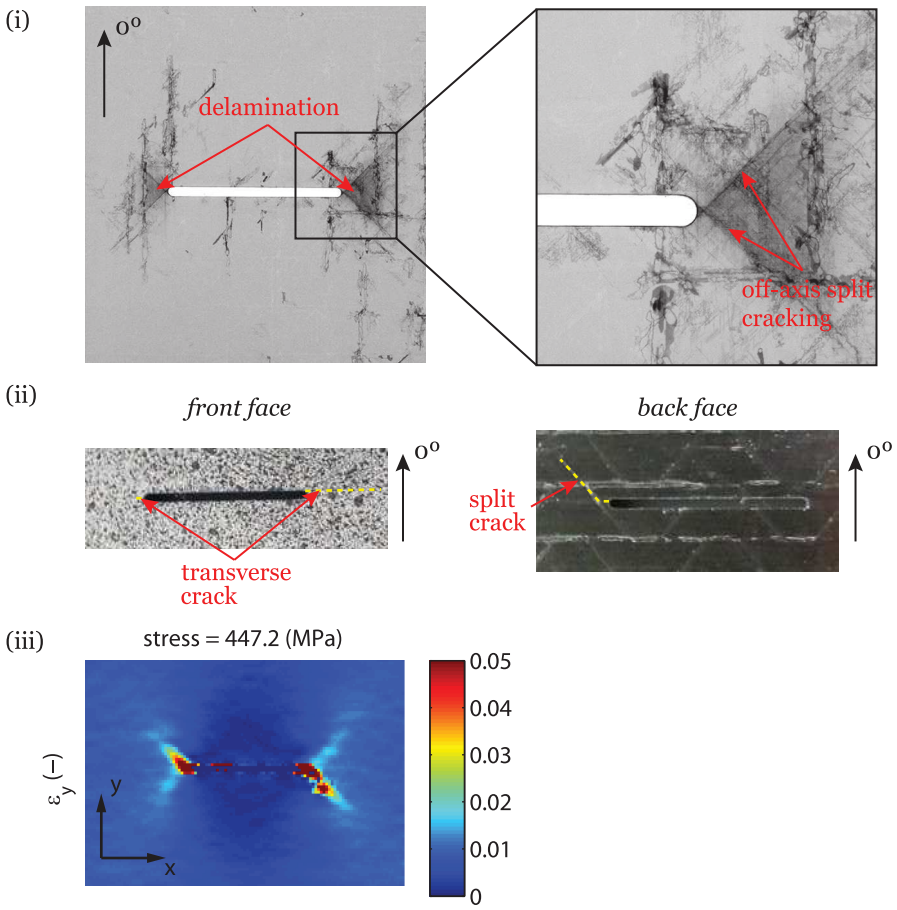

Fig. 5.112. Damage on the 108 mm wide CNT specimen of the *dispersed* laminate after interrupted testing at 97% of the mean ultimate remote stress. (i) X-ray radiographies of the complete centre notch and of a detail of the right notch tip. (ii) Schematic of the damage identified by external visual inspection. (iii) Longitudinal strain field, ε_y, on the outer 90° ply.

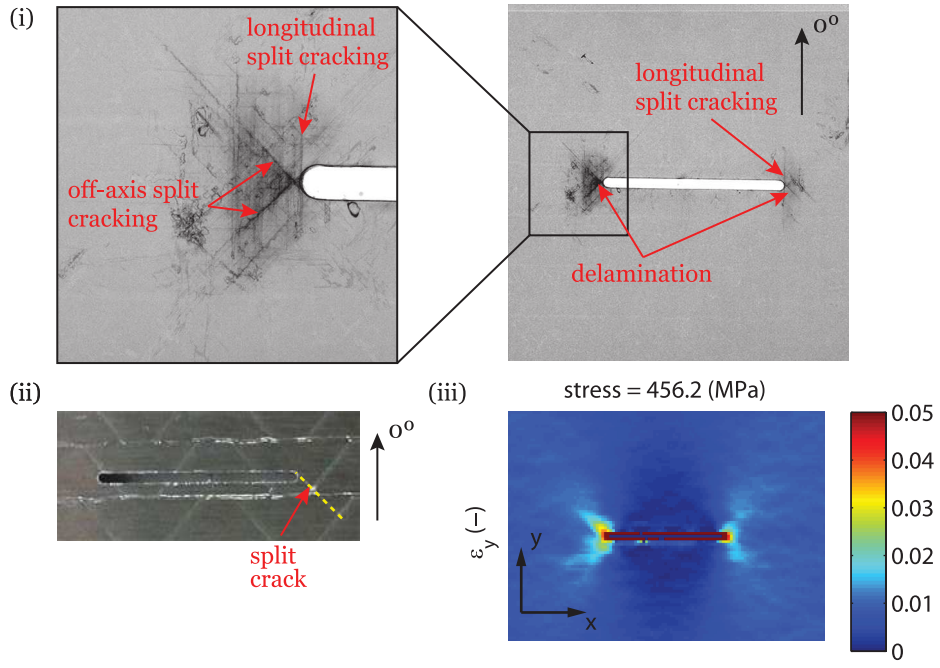

Fig. 5.113. Damage on the 108 mm wide CNT specimen of the *blocked* laminate after interrupted testing at 95% of the mean ultimate remote stress. (i) X-ray radiographies of the complete centre notch and of a detail of the left notch tip. (ii) Schematic of the damage identified by external visual inspection. (iii) Longitudinal strain field, ε_y, on the outer 90° ply.

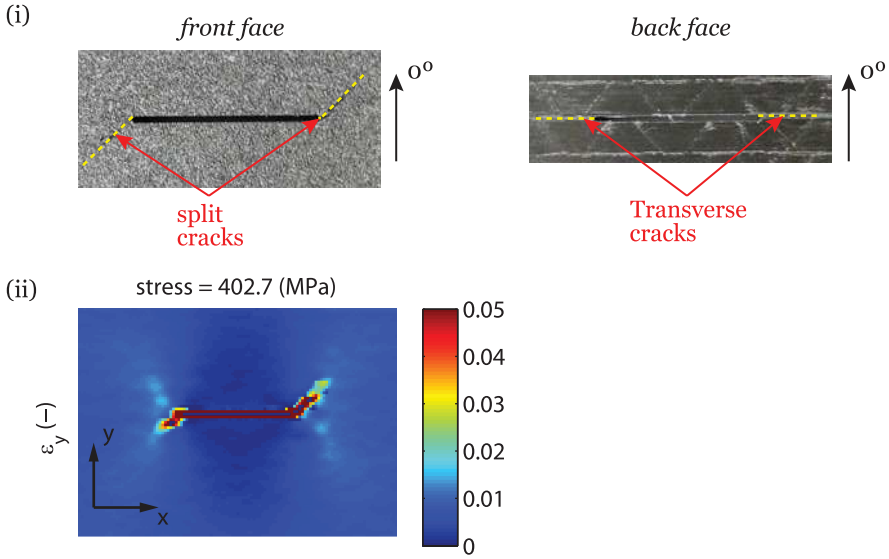

Fig. 5.114. Damage on the 144 mm wide CNT specimen of the *dispersed* laminate after interrupted testing at 95% of the mean ultimate remote stress. (i) Schematic of the damage identified by external visual inspection. (ii) Longitudinal strain field, ε_y, on the outer 90° ply.

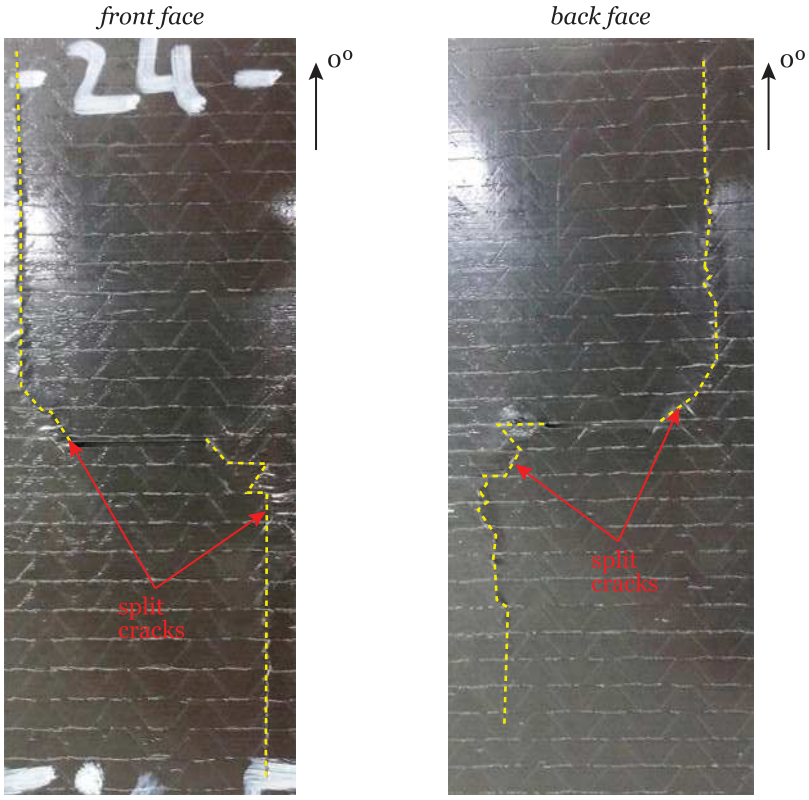

Fig. 5.115. Damage on the 144 mm wide CNT specimen of the *blocked* laminate after interrupted testing at 93% of the mean ultimate remote stress. Schematic of the damage identified by external visual inspection.

fibre direction is tangent to the semi-circular boundary of the notch tips, similarly to what has been observed in open-hole specimens [163, 174].

In the 36 mm wide specimen of the *blocked* laminate tested to 95% of the ultimate remote stress, a small split crack can be identified by visual inspection (figure 5.109 (ii)). But observing the X-ray radiographies (figure 5.109 (i)), internal off-axis and longitudinal split cracking, starting where the fibre direction is tangent to the notch tips, can be identified. As expected, external visual inspection alone is not able to provide the full extent of damage on specimens loaded to fractions of the ultimate failure stress.

In the 72 mm wide specimens of the *dispersed* and *blocked* laminates tested to 95% of the respective ultimate remote stresses (figures 5.110 and 5.111 respectively), off-axis split cracking ahead of the notch tips and delaminations with a triangular shape connecting these split cracks can be identified in the X-ray radiographies. The split cracks can also be identified by visual inspection. In the *blocked* laminate, in addition to off-axis split cracking and delamination, longitudinal split cracking is also observed in the X-ray radiographies (figure 5.111 (i)).

In the 108 mm wide specimens of the *dispersed* and *blocked* laminates tested, respectively, to 97% and 95% of the respective ultimate remote stresses (figures 5.112 and 5.113), off-axis split cracking and delamination ahead of the notch tips can be observed. In spite of the similar stress levels reached before interrupting the tests, the extent of damage is seemingly smaller in the specimen of the *blocked* laminate. This is related to the propagation of longitudinal split cracking tangent to the notch tips in the *blocked* laminate (figure 5.113), attributed to the thicker 0° plies, reducing the stress concentration in the vicinity of the notch [121, 276].

From visual inspection (figures 5.112 (ii) and 5.113 (ii)), small split cracks along the off-axis plies can be identified in the 108 mm wide specimens of both laminates. In addition, a transverse crack ahead of the notch tip can be observed in the outer 90° layer of the *dispersed* laminate (figures 5.112 (ii)).

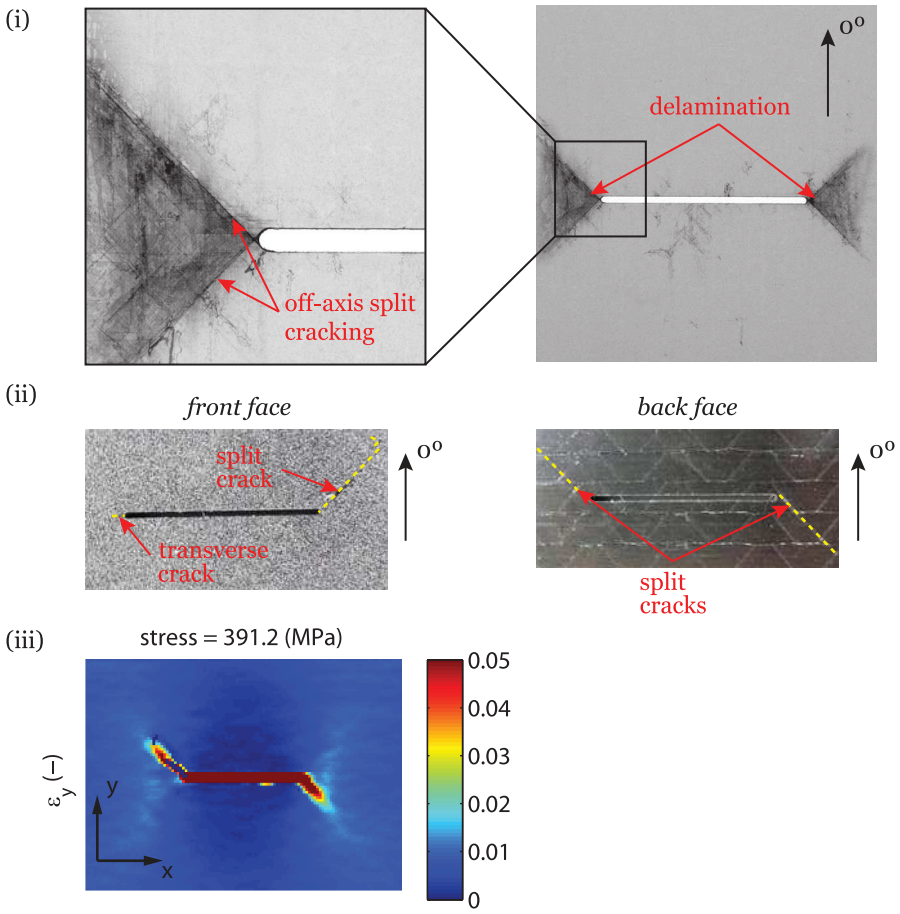

Fig. 5.116. Damage on the 180 mm wide CNT specimen of the *dispersed* laminate after interrupted testing at 94% of the mean ultimate remote stress. (i) X-ray radiographies of the complete centre notch and of a detail of the left notch tip. (ii) Schematic of the damage identified by external visual inspection. (iii) Longitudinal strain field, ε_y, on the outer 90° ply.

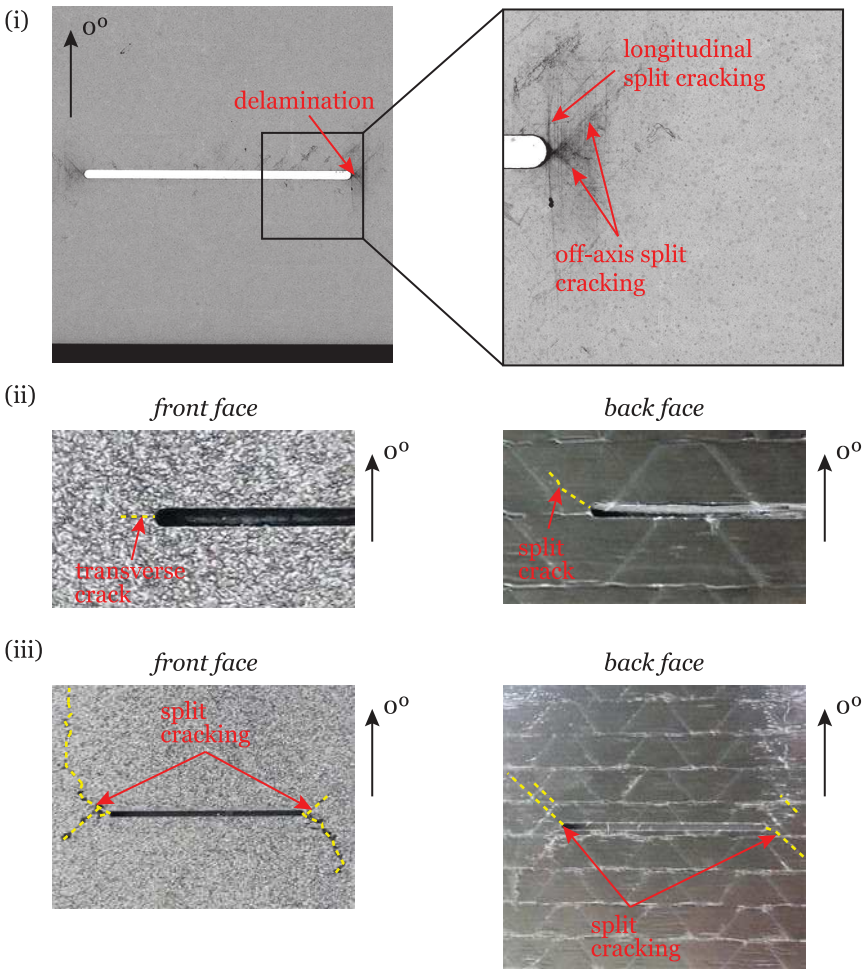

Fig. 5.117. Damage on the 180 mm wide CNT specimen of the *blocked* laminate. (i) X-ray radiographies of the complete centre notch and of a detail of the right notch tip after interrupted testing at 81% of the mean ultimate remote stress. Schematic of the damage identified by external visual inspection after interrupted testing at (ii) 81% and (iii) 92% of the mean ultimate remote stress.

In the 144 mm and 180 mm wide specimens of the *dispersed* laminate (figures 5.114 and 5.116), tested respectively to 95% and 94% of the ultimate remote stress, damage propagation from the notch tips could be identified by visual inspection. Visible damage includes external transverse cracks perpendicular to the loading direction and surface split cracks along the off-axis direction. X-ray radiographies of the 180 mm wide specimen of the *dispersed* laminate after interrupted testing at 94% of the mean ultimate remote stress (figure 5.116 (i)) show long split cracks in the off-axis plies and localised delamination with a triangular shape.

In the 144 mm wide specimen of the *blocked* laminate (figure 5.115), extensive damage has occurred at 93% of the ultimate remote stress. Severe split cracking propagating from the notch tips parallel to the loading direction towards the specimen's ends can be observed.

In the 180 mm wide specimen tested to 81% of the ultimate stress (figures 5.117 (i) and (ii)), small off-axis split cracks can be identified ahead of the notch tips. Localised delamination and longitudinal split cracking can also be identified in the X-ray radiographies (figure 5.117 (i)). Visual inspection of the specimen tested to 92% of the ultimate remote stress (figure 5.117 (iii)) shows split cracking starting at the ±45° plies before extending along the loading direction.

The assessment of the extent of damage and size of the fracture process zone of the interrupted tests can also be performed analysing the longitudinal strain fields obtained from the DIC measurements of representative specimens of the different configurations (figures 5.108 to 5.116). As observed in the specimens tested to failure (figures 5.90 to 5.99), although all DIC measurements were performed on the outer 90° ply, intralaminar damage propagates predominantly along the off-axis ±45° directions. The intralaminar cracks closer to the surface of the specimens can be clearly identified by the discontinuity in the strain field and by the straight strain localisation bands. Regions of strain concentration from the notch tips with a triangular shape can also be observed, related to the occurrence of internal damage growth.

It is interesting to note that, as observed elsewhere [196], the shape and extent of damage identified from the X-ray radiographies and from the surface longitudinal strain fields measured with DIC are globally in very good agreement. It can be assumed that this observation is also valid for the specimens tested to failure (figures 5.90 to 5.99).

Virtual strain gauges [121, 122, 182, 187], computed averaging the results from the DIC data in an area equivalent to the gauge area of physical strain gauges, were used to obtain the remote stress-local axial strain relations (figures 5.118 to 5.122) and assess possible load asymmetries and the effects of strain concentration in the vicinity of the notch tips. Gauge areas with 3.18 mm in length and 1.78 mm in width were used. Two virtual strain gauges (*SG1* and *SG2*) were placed at the tips of the central notch. The location of the gauge areas (*SG1* and *SG2*) are presented in figures 5.118 to 5.122 for the different geometries and for both laminates, depicted over the longitudinal strain field obtained with DIC at an applied remote stress equal to 20% of the ultimate remote stress. Figures 5.118 to 5.122 also show the results of a linear-elastic FEA, performed for each specimen geometry, which uses the same averaging procedure to compare with the data measured with the virtual strain gauges. The details of the FE model were given in section 5.5.5.1. The good agreement between the numerical results and the measured strains validates the application of the virtual strain gauge approach in the present analysis.

Similarly to the tests performed until failure, figures 5.118 to 5.122 show that the interrupted tests were also characterised by a good load symmetry, thus further validating the adopted test setup. Figures 5.118 to 5.120 also confirm the observation presented in section 5.5.5.1 that the onset of damage growth from the notch tips starts earlier in the *dispersed* laminate, caused by internal stress relaxation inside the *blocked* laminate, which delays the onset of through-the-thickness intralaminar damage growth.

5.5.5.3. Crack resistance curve

Because the CNT tests were performed using geometrically similar specimens with positive geometry (figure 5.107), these tests were used to calibrate the size effect law and determine the laminate $\mathcal{R}$-curve associated with diffuse fracture of the *dispersed* and *blocked* laminates. The effect of specimen geometry and size range can be addressed with this complementary study. However, it is important to stress that, since self-similar intralaminar fracture propagation from the notch tips was not obtained, these results should be regarded as merely indicative. In fact, after short stable intralaminar

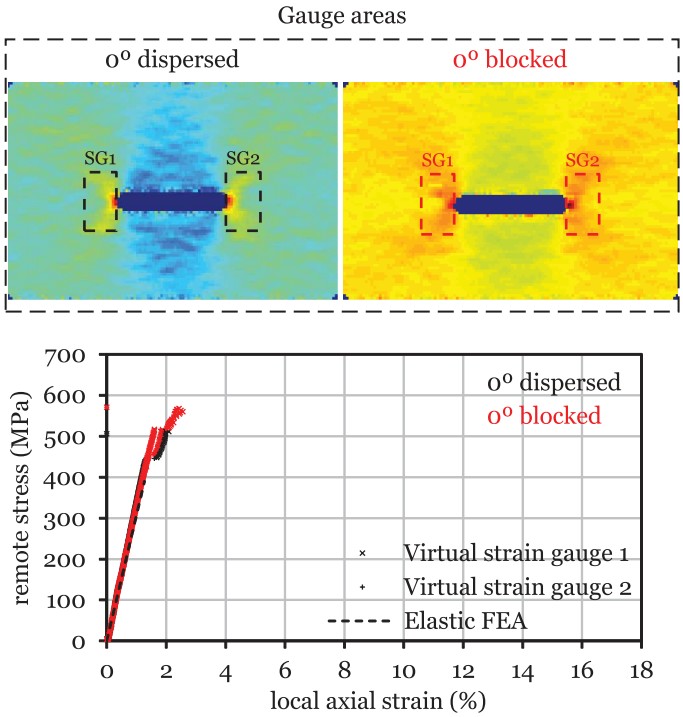

Fig. 5.118. Virtual strain gauge areas and remote stress-local axial strain curves for the 36 mm wide CNT test specimens subjected to interrupted testing. The loading direction is parallel to the vertical axis of the specimens.

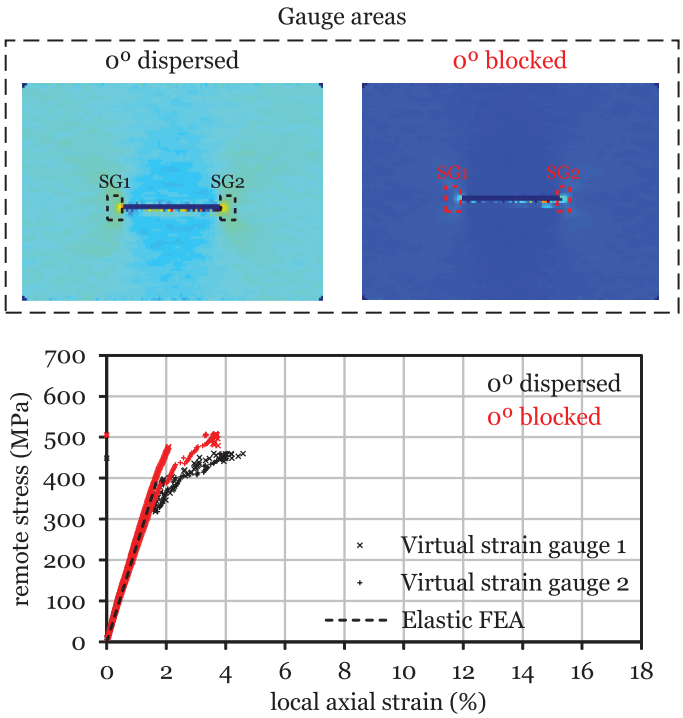

Fig. 5.119. Virtual strain gauge areas and remote stress-local axial strain curves for the 72 mm wide CNT test specimens subjected to interrupted testing. The loading direction is parallel to the vertical axis of the specimens.

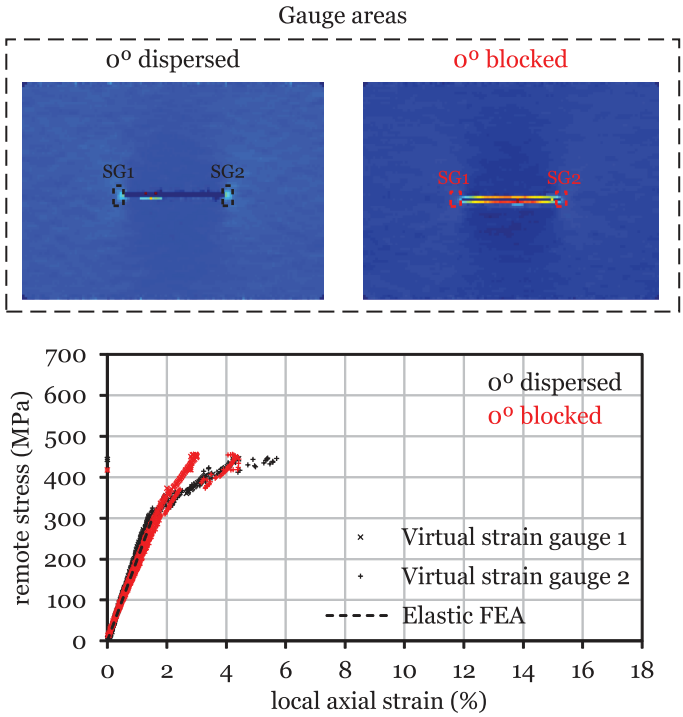

Fig. 5.120. Virtual strain gauge areas and remote stress-local axial strain curves for the 108 mm wide CNT test specimens subjected to interrupted testing. The loading direction is parallel to the vertical axis of the specimens.

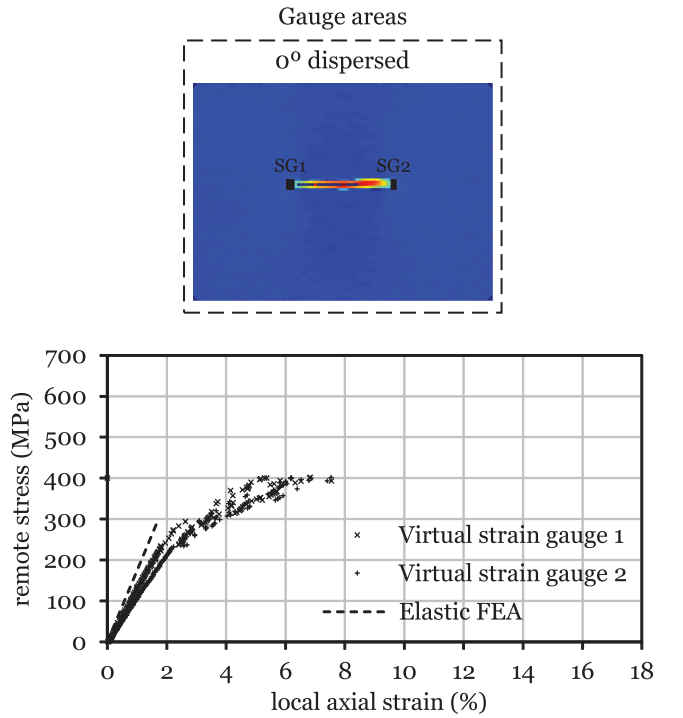

Fig. 5.121. Virtual strain gauge areas and remote stress-local axial strain curves for the 144 mm wide CNT test specimens subjected to interrupted testing. The loading direction is parallel to the vertical axis of the specimens.

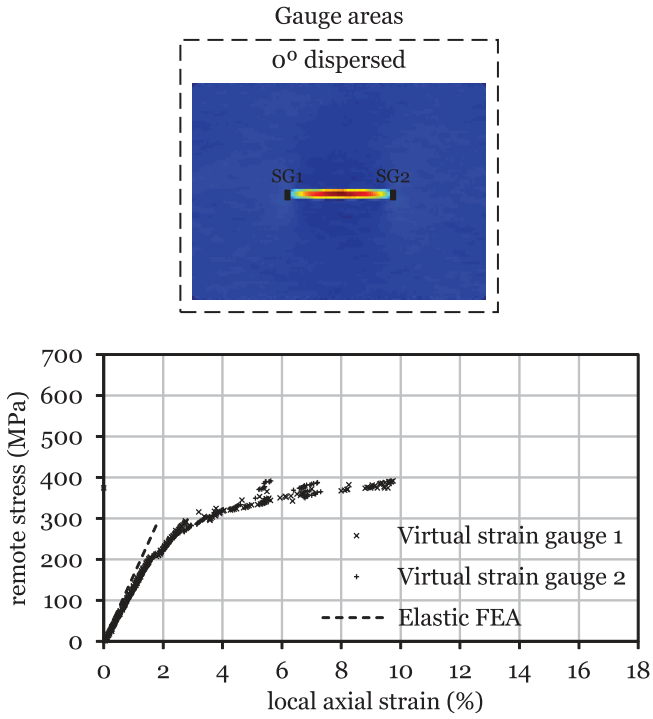

Fig. 5.122. Virtual strain gauge areas and remote stress-local axial strain curves for the 180 mm wide CNT test specimens subjected to interrupted testing. The loading direction is parallel to the vertical axis of the specimens.

Table 5.18
Fitting regressions and parameters for the size effect laws of the *dispersed* and *blocked* laminates calibrated from the CNT tests.

Laminate	Regression fit [209]	Fitting parameters
Dispersed laminate	Linear regression II	$\acute{A}$ = 2.7438E – 06 MPa^{-2} mm^{-1}
		$\acute{C}$ = 3.8314E – 08 MPa^{-2}
Blocked laminate	Linear regression II	$\acute{A}$ = 2.1258E – 06 MPa^{-2} mm^{-1}
		$\acute{C}$ = 3.4895E – 08 MPa^{-2}

damage growth, diffuse damage, including long 0° split cracks and localised delamination ahead of the notch tips, affected considerably the stress state in the vicinity of the crack tips (figures 5.90 to 5.99), reading these results unsuitable to determine the $\mathcal{R}$-curve of the *dispersed* and *blocked* laminates associated with pure mode I intralaminar fracture.

From the size effect law regressions proposed in Ref. [209], the regression that best fit the experimental data is *linear regression II*, given by equation (5.5). The fitting parameters that best approximate the observed trends are given in table 5.18. Figure 5.123 shows the experimental results and the best fitting for the size effect laws of the *dispersed* and *blocked* laminates obtained from the CNT tests.

For a centre-cracked plate, the FWC factor, $f(\alpha)$, can be derived e.g. from Chen et al. [286] as:

$$f(\alpha) = \sqrt{\frac{\pi\alpha}{1-\alpha^2}} \tag{5.10}$$

Using the fitting parameters shown in table 5.18, it is now possible to calculate l_{fpz} and $\mathcal{R}_{ss}$ for the *dispersed* and *blocked* laminates using respectively equations (5.8) and (5.9) (table 5.19).

Figure 5.124 shows the $\mathcal{R}$-curves of the *dispersed* and *blocked* laminates obtained as the envelopes of the crack driving force curves calculated using the size effect laws calibrated from the CNT test data (figure 5.123). To simplify the implementation of the $\mathcal{R}$-curve in numerical or analytical models, Catalanotti et al. [65] used equation (4.21) to fit the

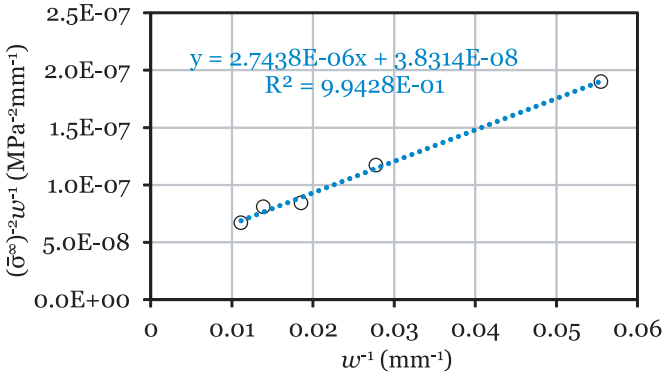

(a) *Dispersed* laminate: linear regression II.

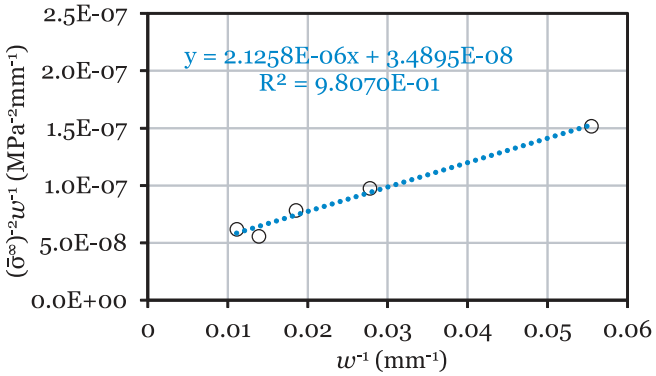

(b) *Blocked* laminate: linear regression II.

Fig. 5.123. Experimental results and best fitting for the size effect laws of the *dispersed* and *blocked* laminates calibrated from the CNT tests.

Table 5.19
Parameters of the $\mathcal{R}$-curves and fitting formulae of the *dispersed* and *blocked* laminates obtained from the CNT tests.

Laminate	l_{fpz} (mm)	$\mathcal{R}_{ss}$ (N/mm)	ζ (mm^{-1})	η (-)
Dispersed laminate	11.29	259	0.08727	1.768
Blocked laminate	9.60	284	0.1028	1.763

analytical envelopes. The parameters ζ and η that best fit the formula to the respective $\mathcal{R}$-curve, are given in table 5.19. These parameters were obtained using a nonlinear least squares method with a Trust-Region algorithm, available in the commercial software Matlab [278]. Figure 5.125 shows the $\mathcal{R}$-curves and the corresponding fitting curves for both laminates. As can be observed, the fitting formulae agree very well with the analytical envelopes. A comparison of the $\mathcal{R}$-curves of both laminates obtained from the CNT tests is given in figure 5.126.

Table 5.19 and figure 5.126 show that the $\mathcal{R}$-curves of the *dispersed* and *blocked* laminates determined from the size effect laws calibrated with the CNT tests are similar in shape and size. The length of the FPZ and the steady-state value of the fracture toughness of the *blocked* laminate are, respectively, 1.10 times smaller and 1.18 times higher than the *dispersed* laminate (table 5.19). This difference is related to the extent of subcritical damage mechanisms. Larger longitudinal split cracks and a more diffuse damage ahead of the notch tips of the *blocked* laminate delayed the onset of through-the-thickness intralaminar damage growth and postponed ultimate failure, resulting in a slightly higher fracture toughness at propagation.

Comparing with the $\mathcal{R}$-curves determined from the size effect laws calibrated with the DENT tests (figure 5.42), a length of the FPZ and a steady-state value of the fracture toughness almost twice as large was obtained. This difference is caused by the extent and stability of internal damage growth before ultimate failure.

Whereas the DENT test specimens are characterised by self-similar intralaminar damage propagation and unstable fracture across the notched plane, the CNT test specimens show a diffuse failure mode, with long split cracks and extensive internal damage growth ahead of the notch tips before ultimate failure. These damage mechanisms cause large changes in the stress field at the vicinity of the notch due to stress redistribution, blunting the stress concentration and virtually increasing the fracture toughness.

From the previous observations, and as stressed before, it becomes clear that the $\mathcal{R}$-curves determined from the size effect laws calibrated with the CNT tests do not characterise the mode I longitudinal tensile intralaminar fracture of the *dispersed* and *blocked* laminates, since no self-similar fracture propagation was obtained with these tests. This observation also justifies the use of the DENT tests by Catalanotti et al. [65] to determine the $\mathcal{R}$-curves of composite laminates due to the unstable character of fracture propagation in these specimens.

The present results also show that the $\mathcal{R}$-curves determined from the size effect laws calibrated with the DENT tests (figure 5.42) do not reflect the actual differences of the notched response of the *dispersed* and *blocked* laminates. A similar steady state fracture toughness, possibly slightly higher for the *blocked* laminate, would be expected given the trends observed in the scaled centre notched tension tests. As discussed in section 5.5.1, a larger DENT test specimen configuration would have to be tested to confirm the observed trends, and perhaps validate the assumption that, as the specimens become larger, the notched strengths of the *dispersed* and *blocked* laminates should tend to the same value.

Moreover, the results presented in table 5.19 and figure 5.126 can be helpful in understanding how the extent of internal damage growth in multidirectional laminates affects their notched response. They can also be used to understand how the notched response can be improved through appropriate laminate design.

For instance, laminate stacking sequences that promote fibre-matrix splitting in the 0° plies can be adopted to improve the notched response of composite laminates, as demonstrated in the present section. In fact, blocking the 0° plies effectively promoted longitudinal fibre-matrix splitting, which acts as an important notch blunting mechanism [121, 276], improving the notched response of the NCF thin-ply laminates studied in the present work.

It is also important to stress that undesirable damage mechanisms, such as delamination and transverse cracking,

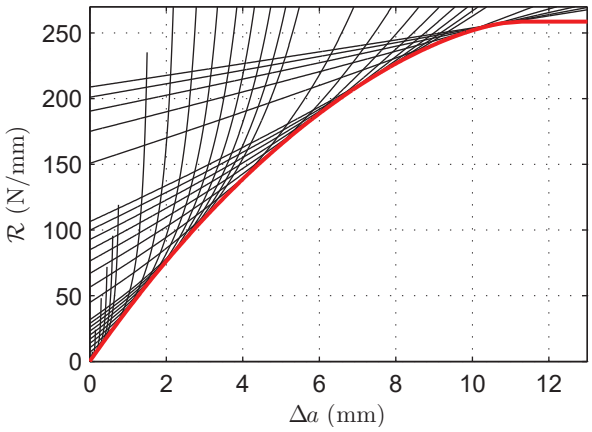

(a) *Dispersed* laminate.

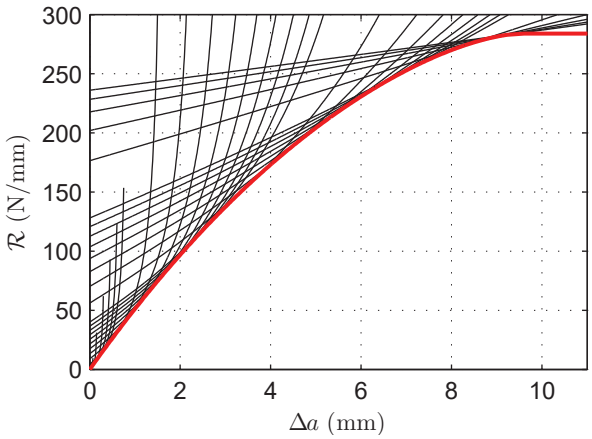

(b) *Blocked* laminate.

Fig. 5.124. Crack driving force curves and resulting $\mathcal{R}$-curves of the *dispersed* and *blocked* laminates obtained from the CNT tests.

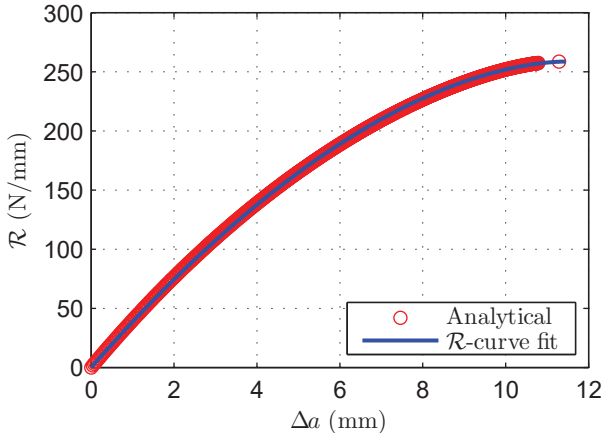

(a) *Dispersed* laminate.

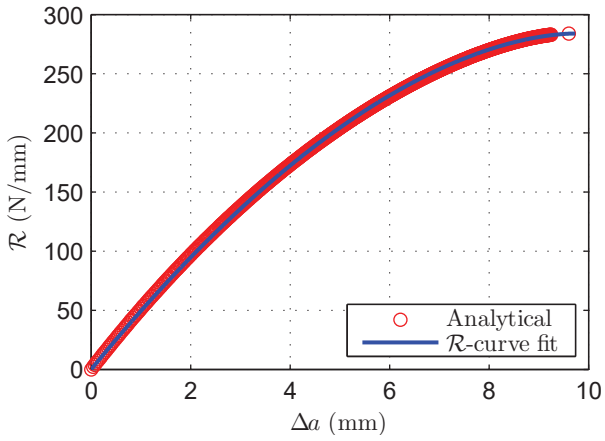

(b) *Blocked* laminate.

Fig. 5.125. Analytical and fitted $\mathcal{R}$-curves of the *dispersed* and *blocked* laminates obtained from the CNT tests.

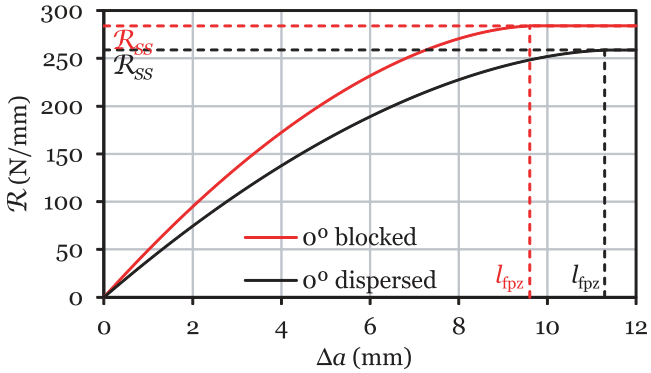

Fig. 5.126. Comparison of the $\mathcal{R}$-curves of the *dispersed* and *blocked* laminates obtained from the CNT tests.

must be delayed or even suppressed. These damage mechanisms are generally more detrimental to the laminate integrity, affecting considerably the unnotched strengths [58, 171], the compressive response [37, 58, 134, 169, 170] and the fatigue behaviour of laminates [53, 58, 173, 229, 230].

Therefore, combining thin transverse and off-axis plies with thicker 0° plies is seen as a promising solution to improve the notched response of laminates without compromising their unnotched behaviour (sections 5.5.3 and 5.5.4). A limited or even unnoticeable detrimental effect on the compressive notched response and fatigue behaviour is also expected.

5.5.6. Bolt-bearing test results

5.5.6.1. Bearing strengths

In this work, 3 bolt-bearing specimens of each laminate were tested to failure. All specimens exhibited a bearing failure mode, resulting from local compressive damage in the bearing hole region. Representative specimens after testing are shown in figure 5.127. Besides local compressive failure and crushing of the load-bearing surface, which is the typical failure mode observed in composite laminates subjected to bearing loads [122, 235], transverse and split cracking of the outer 90° ply has also occurred after permanent deformation of the hole. No relevant difference between the failure modes of the *dispersed* and *blocked* laminates is observed.

Figure 5.128 shows the bearing stress-bearing strain relations of both laminates. The bearing stress, σ^{br}, is determined using equation (4.22), and the bearing strain, ε^{br}, is determined from the total axial deformation of the specimen's gauge length, measured directly from the cross-head displacement of the testing machine, using equation (4.23), where Δ is the cross-head displacement and K is a parameter that depends on the bearing test configuration [237]. For double-shear tests $K = 1.0$ [237].

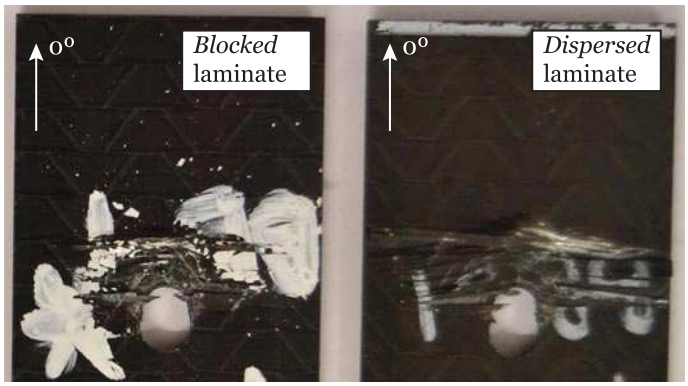

Fig. 5.127. Bearing hole region of representative bolt-bearing specimens after testing.

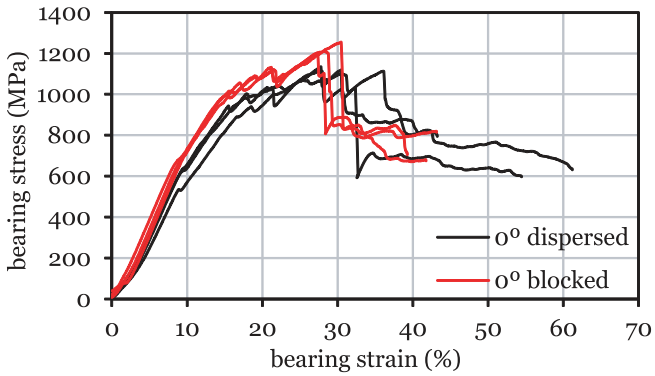

Fig. 5.128. Bearing stress-bearing strain relations for the bolt-bearing tests.

The bearing stress-bearing strain curves of both laminates are linear up to approximately 50% of the maximum bearing stress, exhibiting a small kink before the response becomes nonlinear. A similar response was already reported elsewhere [122]. This nonlinearity is attributed to the propagation of matrix cracks and to the initiation of fibre kink bands [122, 235]. For bearing stresses greater than the initial peak bearing stress, after the first load drop, extensive matrix cracking and fibre kinking are typically observed [235]. Subcritical damage mechanisms start to interact, resulting in permanent damage such as through-the-thickness shear cracks, whose propagation conducts to the sudden load drops shown in figure 5.128, as well as to permanent hole deformation.

The large load drop observed in both laminates at bearing strains around 30% were typically accompanied by a strong noise due to sudden damage propagation in the specimens' bearing region. After this large load drop, subsequent damage propagation takes place in a rather continuous way, with the bearing stress decreasing slowly, practically without load drops. At this point, extensive hole deformation occurs and continuous damage growth was audible until the test is finally stopped.

As explained in section 5.3.6, a clear interpretation of bearing strength does not exist, and different definitions can be used. Table 5.20 shows the average test results and respective coefficients of variation for the bearing strengths of the *dispersed* and *blocked* laminates adopting some of the most common definitions used in the literature, namely the average bearing stress at the onset of nonlinearity, the average bearing stress at the first load drop, the average bearing stress for an offset bearing strain of 2% and 6%, and the average maximum bearing stress. The offset bearing strains were determined following the ASTM D5961/D5961M – 13 test standard [237]. The offset is performed based on a bearing chord stiffness, E^{br}, determined from the bearing strain obtained from the total axial deformation of the specimen's gauge length, measured directly from the cross-head displacement, using equation (4.24), where $\Delta\sigma^{br}$ and $\Delta\varepsilon^{br}$ are the change in bearing stress and bearing strain over the chord stiffness range, respectively. Figure 5.129 shows two representative bearing stress-bearing strain curves indicating the bearing strength definitions adopted in table 5.20.

In a previous work [235], based on the experimental data obtained in both bolted and pinned joints, the first nonlinearity in the bearing stress-bearing strain relation was defined as the ultimate bearing strength. Using this definition, it is possible to increase the load before the load drops to lower values. Furthermore, there are no shear cracks in the material, and the resulting permanent hole deformation is small. However, the first nonlinearity in the bearing stress-bearing strain relation does not necessarily indicate that the actual load carrying capacity of a composite laminate subjected to bearing loads has been achieved, specially in bolted joints due to the lateral support provided in the bearing region. In fact, after the first nonlinearity, composite laminates exhibit an additional load-carrying capacity, which in some cases can duplicate the bearing stress before the load starts dropping (see, for instance, figure 5.129).

Hence, as an alternative, the bearing stress at the first load drop can be used as a reliable measure of the bolted joint bearing strength [122], in particular for the purpose of joint failure strength assessment and material/lay-up scrutiny. As noted in section 4.5.12, whereas the bearing stress at the onset of nonlinearity is related to the onset of damage [235] (i.e.

5.5. Experimental results and discussion

Table 5.20
Average test results for the bolt-bearing strengths and respective coefficients of variation (C.V.).

Results		*Dispersed* laminate	*Blocked* laminate
No. specimens		3	3
Average bearing stress at the onset of nonlinearity			
σ^{br}_{nonlin}	(MPa)	601	682
C.V.	(%)	7.8	2.5
Average bearing stress at the first load drop			
σ^{br}_{drop}	(MPa)	956	1024
C.V.	(%)	2.1	2.3
Average bearing stress for an offset bearing strain of 2%			
$\sigma^{br}_{2\%offset}$	(MPa)	812	938
C.V.	(%)	4.9	1.5
Average bearing stress for an offset bearing strain of 6%			
$\sigma^{br}_{6\%offset}$	(MPa)	992	1080
C.V.	(%)	3.0	0.3
Average maximum bearing stress			
σ^{br}_{max}	(MPa)	1121	1223
C.V.	(%)	0.9	1.9

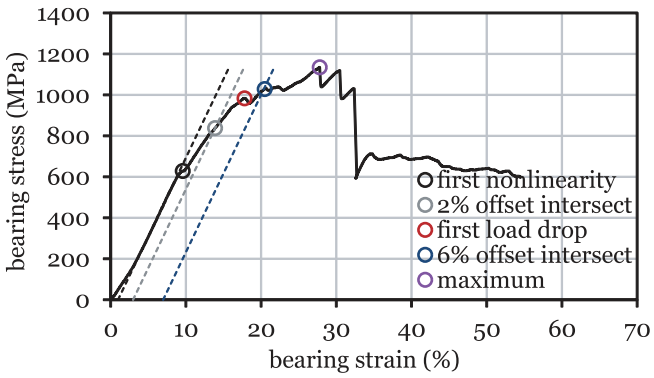

(a) *Dispersed* laminate.

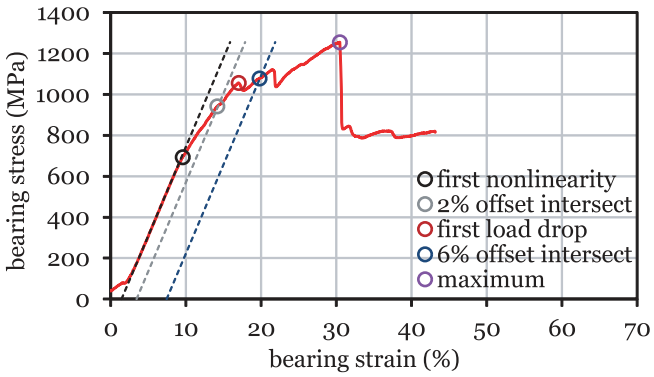

(b) *Blocked* laminate.

Fig. 5.129. Representative bearing stress-bearing strain curves and alternative definitions of bearing strength.

first-ply failure), the bearing stress at the first load drop is governed by the propagation of damage mechanisms such as matrix and shear cracking and fibre kinking (i.e. last-ply failure).

Composite joints loaded to high offset bearing strains or up to the maximum load sustained by the joint show already extensive damage, and present an excessively high permanent deformation of the hole. The maximum bearing stress is also associated with local catastrophic failure of the joint, and typically followed by large load drops (figures 5.128 and 5.129). Their use to characterise the bearing strength of a bolted joint is therefore undesirable. Nevertheless, the bearing strengths corresponding to these definitions were also included in table 5.20.

As can be observed in figure 5.128 and in table 5.20, the *blocked* laminate exhibit a higher bearing strength when compared with the *dispersed* laminate. Interestingly, the same trend is observed when comparing the bearing strengths of both laminates independently of the bearing strength definition used. The average bearing stress of the *blocked* laminate at the onset of nonlinearity and at the first load drop is respectively 13.5% and 7.1% higher than in the *dispersed* laminate.

Adopting a hard laminate configuration with blocked 0° plies resulted, therefore, in an improved bearing response with respect to both local first-ply and last-ply failure. A possible explanation for these results is the additional stability of the thicker 0° plies in the region confined by the lateral support provided by the bolt/washer assembly, increasing locally the laminate compressive strength. On the other hand, the brittler response of the thinner 0° plies of the *dispersed* laminate did not benefit equally from the additional support provided by the bolted joint. It is noted that, as reported in section 5.5.4, the ultimate unnotched strength of both laminates is virtually the same. Thus, it can be concluded that the lateral support provided by the bolt/washer assembly plays a key role in the improved bearing response of the *blocked* laminate.

5.5.6.2. Interrupted bolt-bearing test results

Seeking a more accurate identification of the difference of the bearing response of the *dispersed* and *blocked* laminates, interrupted bolt-bearing tests were performed in 3 specimens of each laminate, corresponding to three different loading levels: onset of nonlinearity, first load drop and offset bearing strain of 6%[1]. Each sample was subsequently analysed by optical microscopy. Micrographies on through-the-thickness sections of the bearing plane (figure 4.137) were obtained, providing a more precise picture of the failure process occurring on bearing tests, allowing the detailed identification of individual damage mechanisms [235, 238].

The same procedure explained in section 4.5.12.2 was used here in the preparation of the micrography samples. After loading each specimen, stopping the test and unloading from the desired load level, the surface to be analysed was marked, and the samples were obtained by cutting a section of each specimen using a diamond-coated disk (figure 4.137). To avoid inflicting additional damage on the bearing plane due to the cutting process, the sample was cut in a plane parallel to the surface to be analysed, at a distance of the bearing plane of approximately 1 mm. The sample was then embedded into an epoxy resin for handling. The surface of the resin parallel to the composite surface to be analysed was ground on a rotary grinder using watered silicon carbide grinding paper of 180, 320, 800, 2500 and 4000 grit. Final polishing was obtained using different cloths impregnated with 3 μm and 1 μm synthetic diamond particles.

Following section 4.5.12.2, the polished samples were examined at different magnification factors and the micrographies captured by a digital camera attached to the optical microscope. Starting from the through-the-thickness plane tangent to the hole (figure 4.137), micrographies were taken until no further damage was visible.

Figures 5.130 and 5.131 show, respectively, the through-the-thickness micrographies of the bearing planes of specimens of the *dispersed* and *blocked* laminates at the onset of nonlinearity. In the *dispersed* laminate (figure 5.130), the onset of matrix cracking can be observed at the loading surface. No fibre compressive failure can be identified. In the *blocked* laminate, though, wedge matrix cracking and fibre kinking can be observed (figure 5.131). As suggested in

[1] As in section 4.5.12.1, in the present study the bearing strain was determined from the total axial deformation of the specimen's gauge length, measured directly from the cross-head displacement of the testing machine (section 5.5.6.1), and not from the axial deformation of the region surrounding the hole, as specified in the ASTM D5961/D5961M – 13 test standard [237]. Consequently, an offset bearing strain of 2% does not yield permanent damage, occurring before the first load drop (figure 5.129). The bearing stress for an offset bearing strain of 6% has been used instead.

section 5.5.6.1, the onset of nonlinearity in the bearing stress-bearing strain relations (figures 5.128 and 5.129) is associated with the initiation of permanent damage mechanisms such as fibre kink bands and matrix shear cracks (see also Ref. [235]). However, the *dispersed* laminate has apparently the ability to delay the initiation of fibre kinking, as the first nonlinearity is mostly due to matrix cracking in the transverse and off-axis plies. It is also noted that the onset of nonlinearity occurs earlier in the *dispersed* laminate.

Whereas the thickness of the transverse and off-axis plies is exactly the same in both laminates, the thickness of the longitudinal plies, aligned with the loading direction, is doubled in the *blocked* laminate. On one hand, this indicates that thinner plies have the ability to delay the onset of compressive longitudinal fracture. On the other hand, in spite of having the same thickness, matrix cracking in the transverse and off-axis plies is apparently more detrimental in the case of the *dispersed* laminate. This can perhaps be attributed to a lower constraining effect imposed by the thinner 0° plies.

At the first load drop (figures 5.132 to 5.134), wedge matrix cracking and fibre kinking have already propagated considerably in both laminates. The interaction of these damage mechanisms leads to the formation of through-the-thickness shear cracks, conducting to the load drops observed in figures 5.128 and 5.129.

After the first load drop (figures 5.135 to 5.139), the first through-the-thickness shear cracks propagate across the laminate, and the continuously growing kink bands and wedge matrix cracks lead to the formation of new through-the-thickness shear cracks not only in the vicinity of the hole edge (figures 5.135 and 5.138), but also away from this region (figures 5.136, 5.137 and 5.139).

Comparing the damage morphology of the two laminates, a "brittler" through-the-thickness shear cracking failure mode can be observed in the *dispersed* laminate (figures 5.135 to 5.137), characterised by slenderer shear bands with signs of shear-driven fibre compressive failure (figures 5.135 and 5.136). In the *blocked* laminate (figures 5.135 and 5.136), on the other hand, a "softer" through-the-thickness shear cracking failure mode is identified, with enlarged shear bands characterised by a more gradual shear deformation of the off-axis plies and wider kink bands in the longitudinal plies (figure 5.138b). This "softer" damage morphology is apparently responsible for the improved bearing response of the *blocked* laminate, due to a more gradual damage process that allows the laminate the carry higher loads than the *dispersed* laminate, where damage propagation is more abrupt. As discussed in section 5.5.6.1, a possible explanation for these results is the additional stability of the thicker 0° plies of the *blocked* laminate in the region confined by the lateral support provided by the bolt/washer assembly, resulting in a more gradual damage process.

5.5.7. Pin-bearing test results

As described in section 5.3.7, pin-bearing tests were performed to understand the failure morphology of thin-ply laminates subjected to a local compressive effort, to assess the effect of the lateral support provided in the bearing region due to changes in the joint configuration, and assess the effect of lay-up and 0° ply thickness on the development of the damage mechanisms promoted by local compressive failure. With this purpose, 3 pin-bearing specimens of each laminate were tested to failure. Figure 5.140 shows representative specimens after testing. As expected, all specimens exhibited a bearing failure mode. Transverse and split cracking in the outer 90° ply can also be observed in figure 5.140, with no relevant difference between the failure modes of the *dispersed* and *blocked* laminates.

Figure 5.141 shows the bearing stress-bearing strain relations for the pin-bearing tests. The bearing stress, σ^{br}, and the bearing strain, ε^{br}, were determined using equations (4.22) and (4.23), respectively. As in section 5.5.6, the total axial deformation of the specimen's gauge length, measured directly from the cross-head displacement of the testing machine, was used to determine ε^{br}.

No relevant difference is observed between the bearing stress-bearing strain curves of the *dispersed* and *blocked* laminates. Linear bearing stress-bearing strain relations up to approximately 97% of the maximum bearing stress can be observed in figure 5.141. At failure, a large load drop occurs, reducing the applied bearing stress to approximately 50% of its maximum value. In pinned joints, as expected, once damage at the micro-level, such as matrix cracking and fibre kinking, starts to form, it quickly propagates into macro-cracks and crushing due to the lack of lateral support, reducing considerably the joints load-carrying capacity.

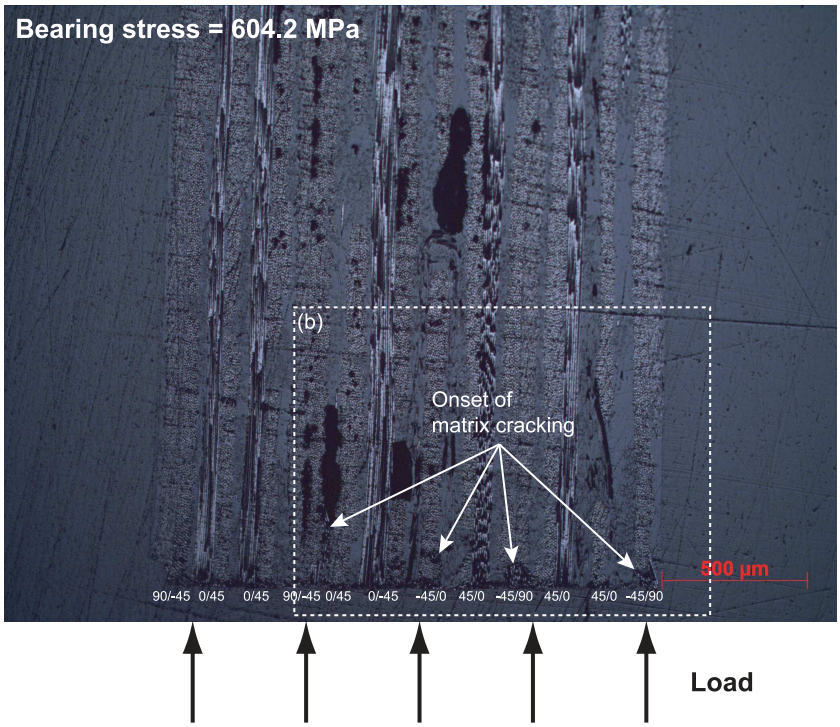

(a) Magnification factor of 5×.

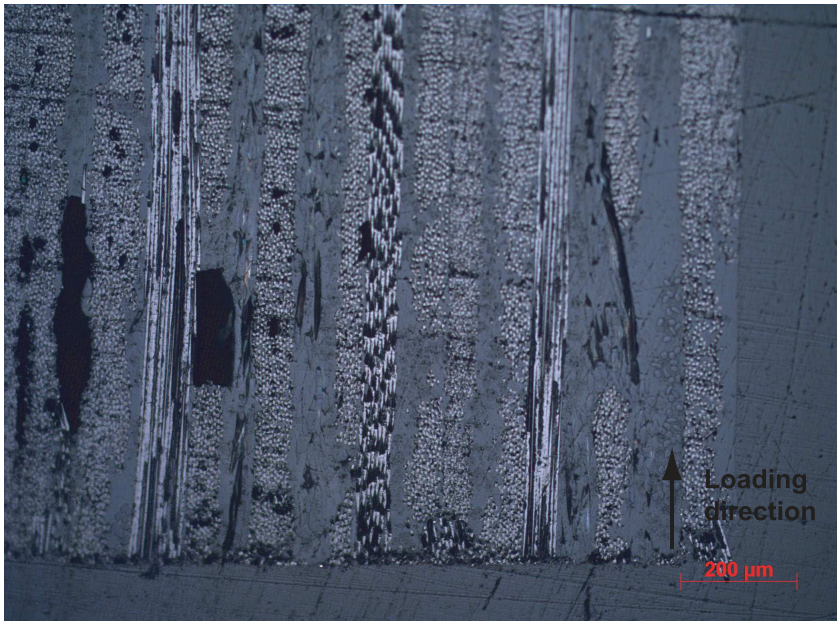

(b) Magnification factor of 10× (detail from (a)).

Fig. 5.130. Bearing plane of the *dispersed* laminate at the onset of nonlinearity.

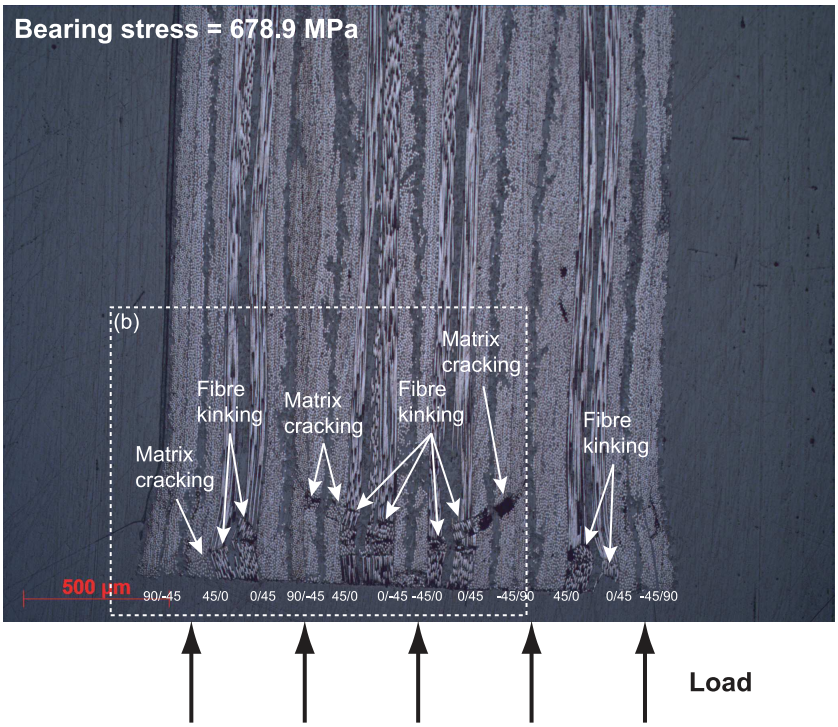

(a) Magnification factor of 5×.

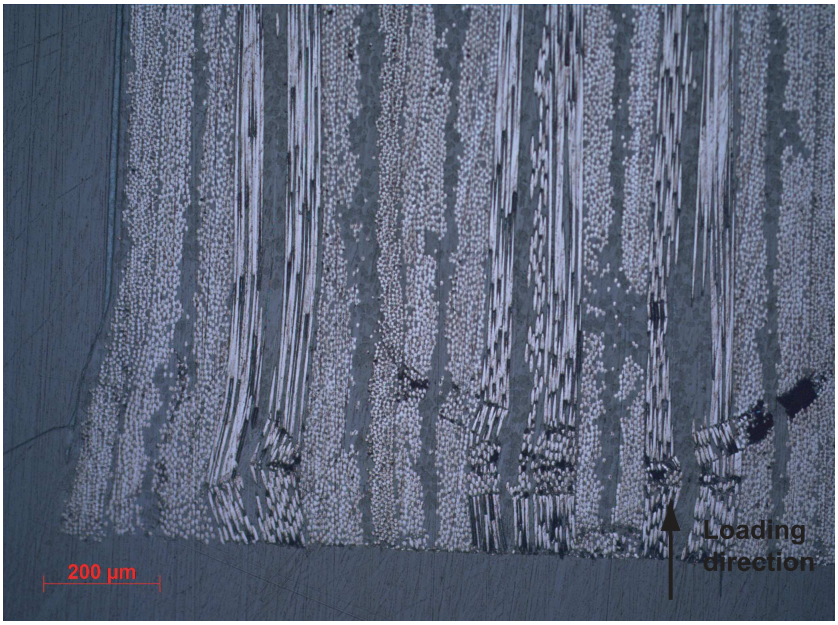

(b) Magnification factor of 10× (detail from (a)).

Fig. 5.131. Bearing plane of the *blocked* laminate at the onset of nonlinearity.

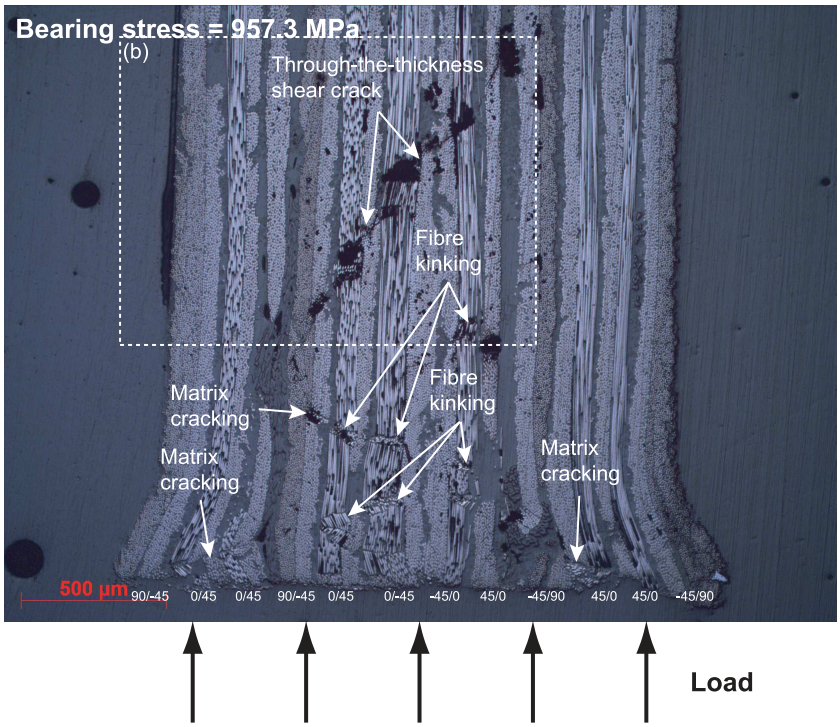

(a) Magnification factor of 5×.

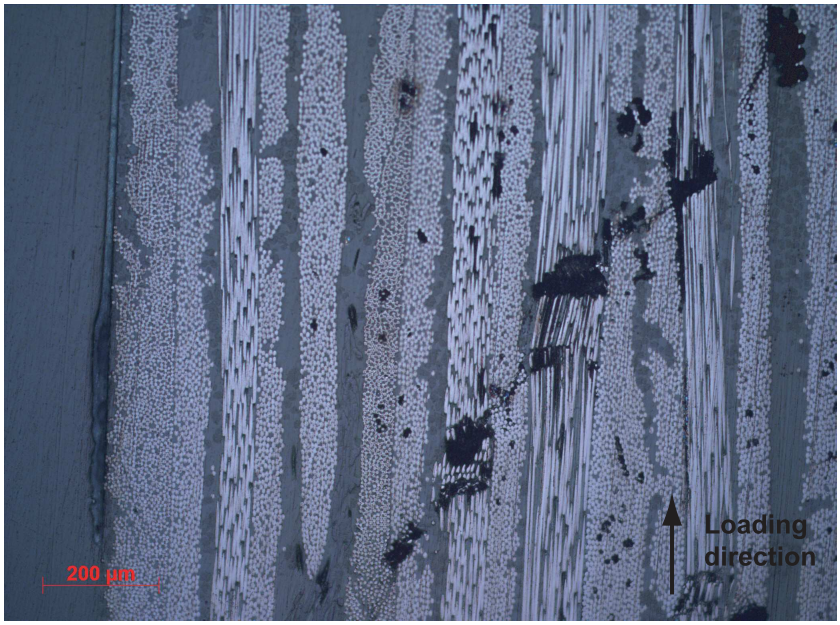

(b) Magnification factor of 10× (detail from (a)).

Fig. 5.132. Bearing plane of the *dispersed* laminate at the first load drop.

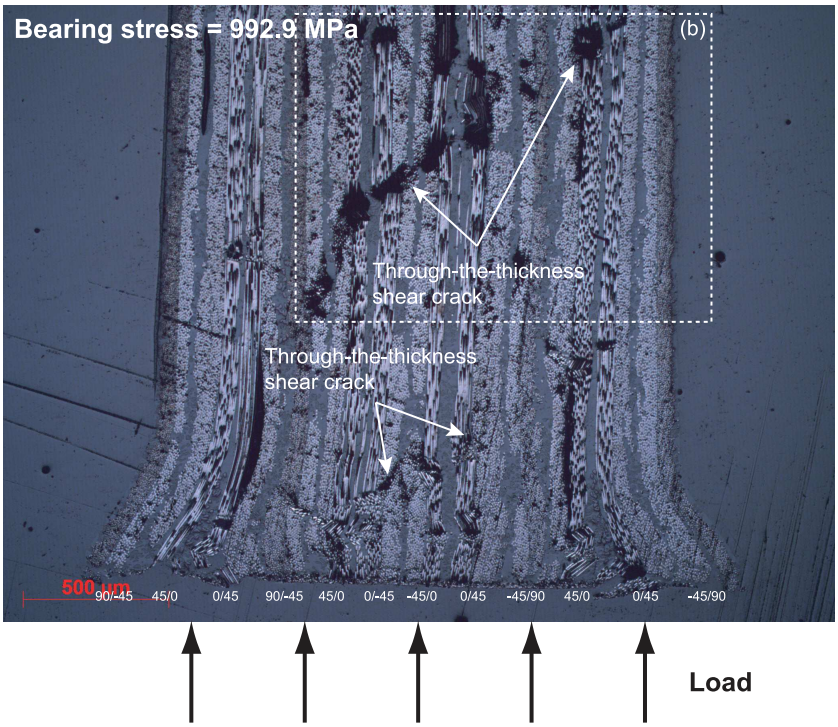

(a) Magnification factor of 5×.

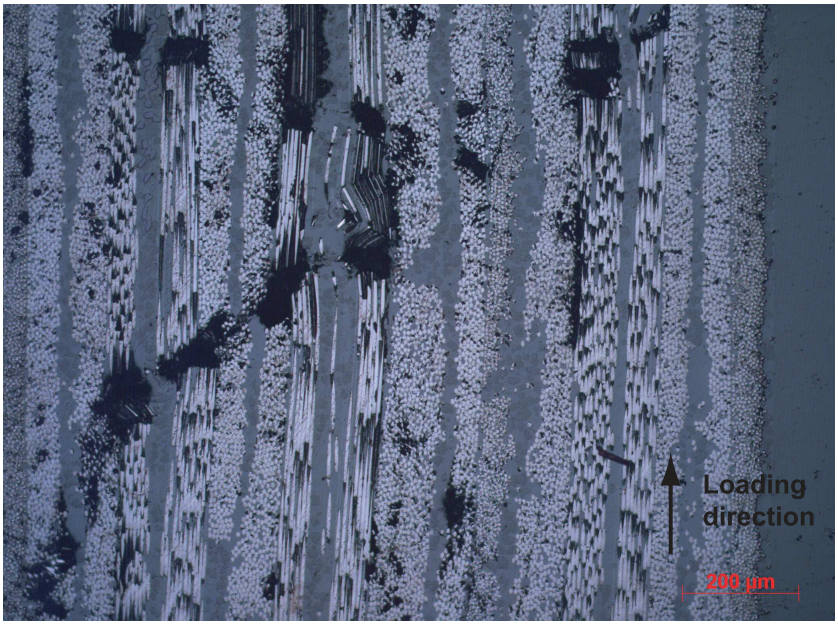

(b) Magnification factor of 10× (detail from (a)).

Fig. 5.133. Bearing plane of the *blocked* laminate at the first load drop.

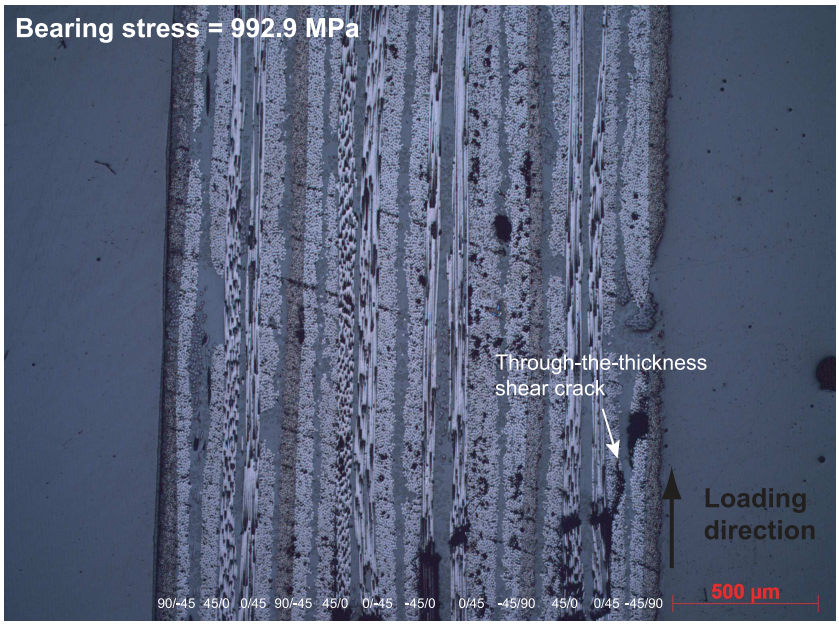

Fig. 5.134. Bearing plane of the *blocked* laminate at the first load drop at approximately 1.8 mm from the hole edge. Magnification factor of 5×.

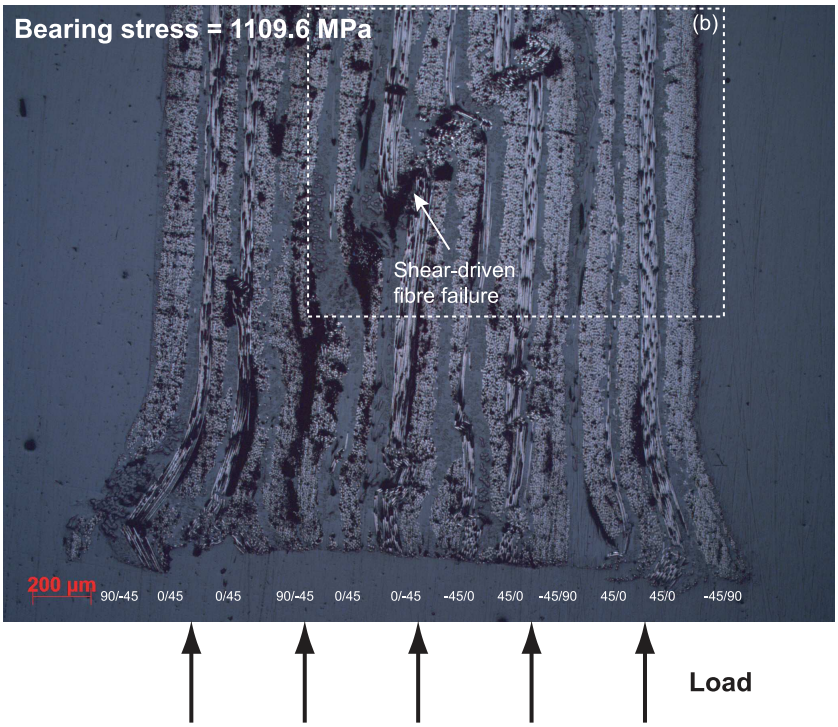

(a) Magnification factor of 5×.

(b) Magnification factor of 10× (detail from (a)).

Fig. 5.135. Bearing plane of the *dispersed* laminate at an offset bearing strain of 6%.

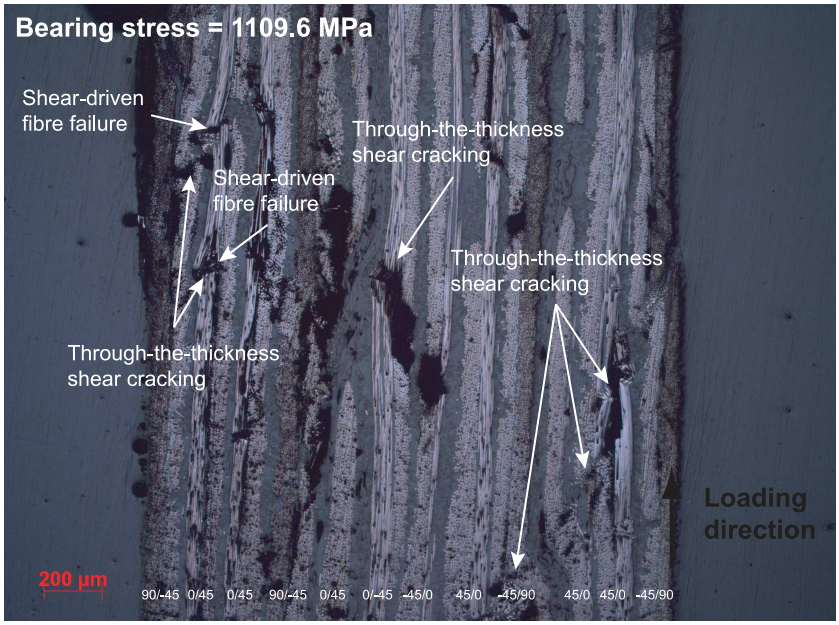

Fig. 5.136. Bearing plane of the *dispersed* laminate at an offset bearing strain of 6% at approximately 1.8 mm from the hole edge. Magnification factor of 5×.

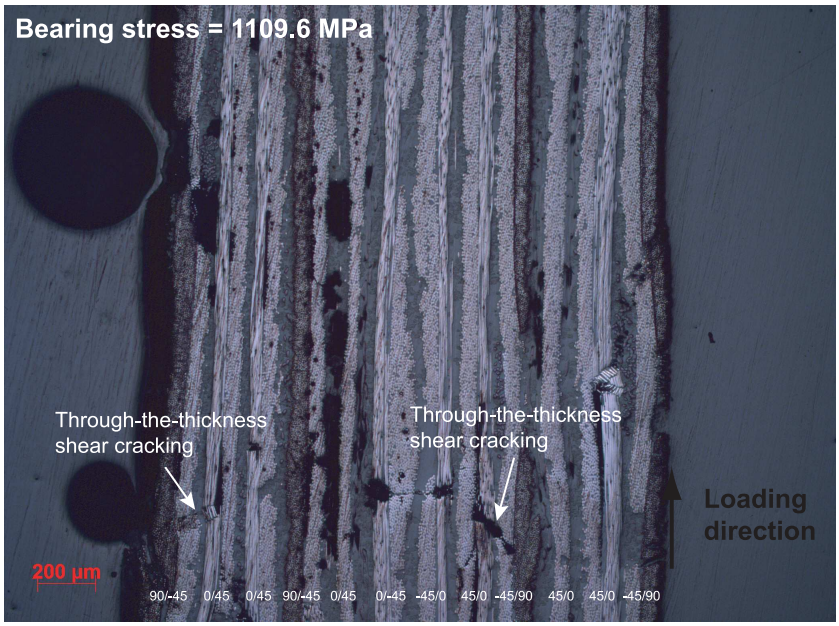

Fig. 5.137. Bearing plane of the *dispersed* laminate at an offset bearing strain of 6% at approximately 3.7 mm from the hole edge. Magnification factor of 5×.

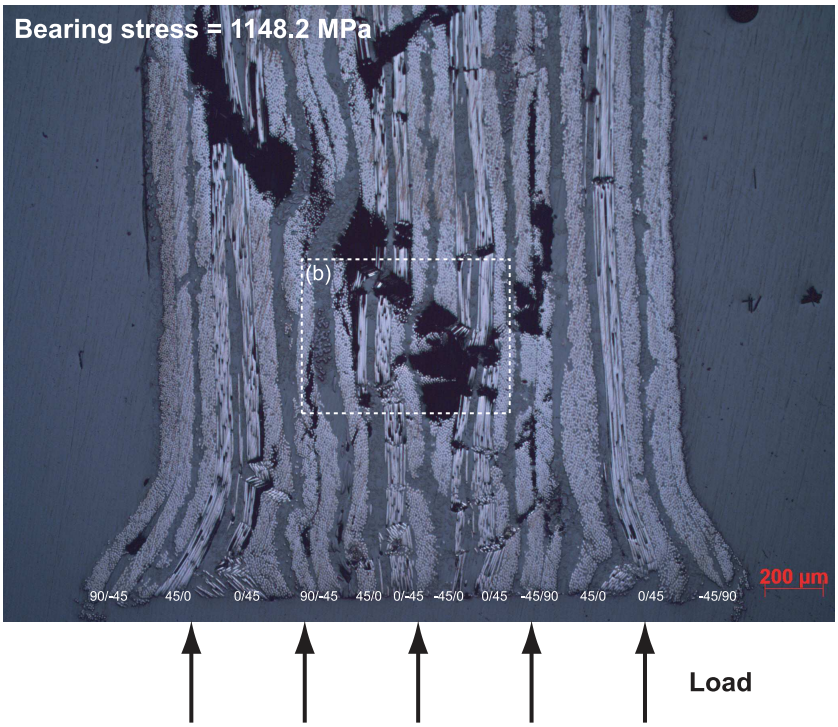

(a) Magnification factor of 5×.

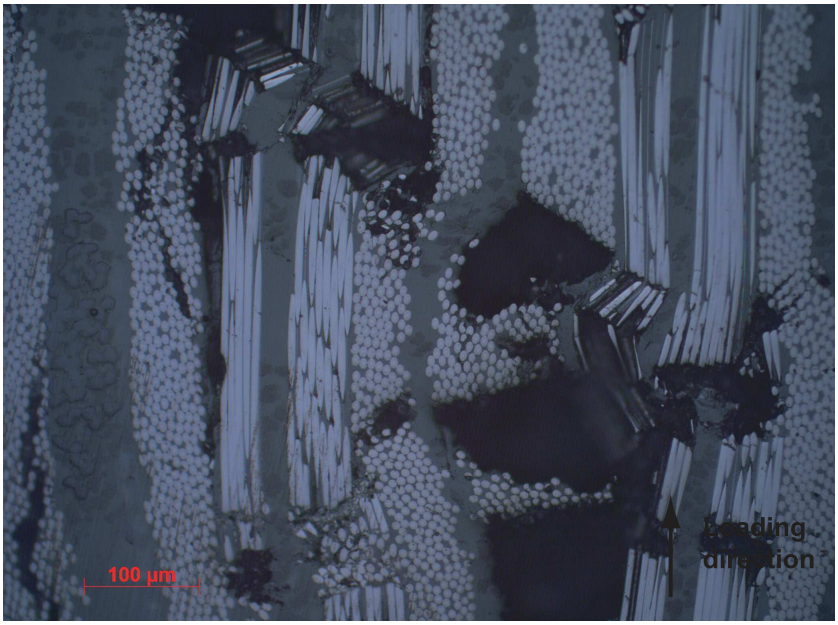

(b) Magnification factor of 20× (detail from (a)).

Fig. 5.138. Bearing plane of the *blocked* laminate at an offset bearing strain of 6%.

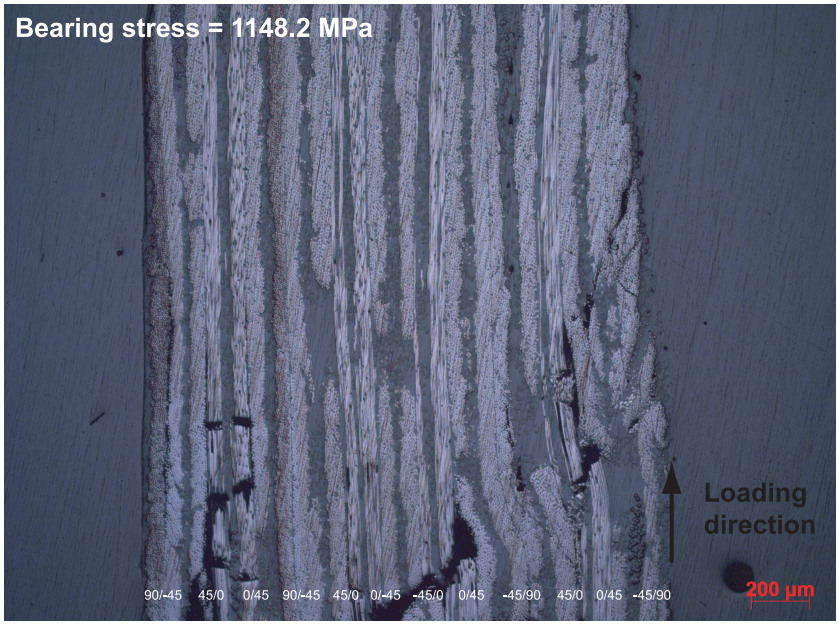

Fig. 5.139. Bearing plane of the *blocked* laminate at an offset bearing strain of 6% at approximately 1.8 mm from the hole edge. Magnification factor of 5×.

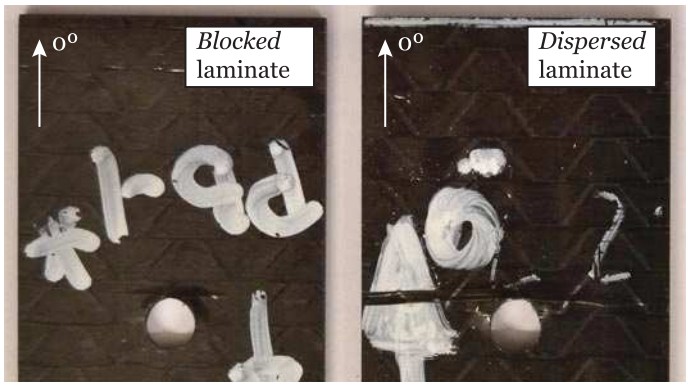

Fig. 5.140. Bearing hole region of representative pin-bearing specimens after testing.

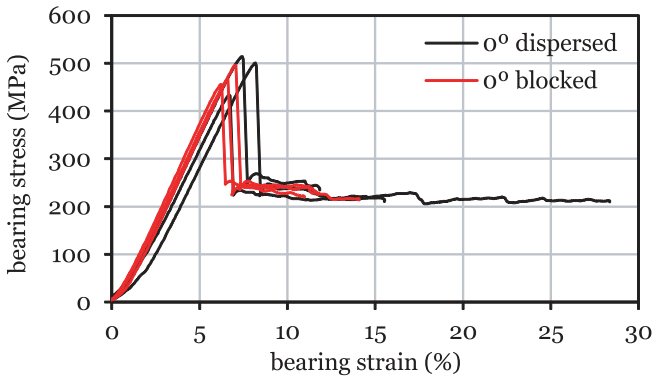

Fig. 5.141. Bearing stress-bearing strain relations for the pin-bearing tests.

Table 5.21 shows the average test results and respective coefficients of variation for the pin-bearing strengths of the *dispersed* and *blocked* laminates. Both average bearing stress at the onset of nonlinearity and the maximum bearing stress are reported.

Unlike the results for bolted joints, there is virtually no difference between the results of the *dispersed* and *blocked* laminates when subjected to pin-bearing loads (the mean values of the bearing stress at the onset of nonlinearity and maximum bearing stress obtained for the *blocked* laminate are less than 2% lower than the values obtained for the *dispersed* laminate, below the variation between experimental results). Figures 5.142 and 5.143 show a comparison between the pin-bearing and bolt-bearing responses of both laminates. As it can be observed, the lateral support provided by the bolt/washer assembly in the bolted joints effectively delays the onset of nonlinearity to values above the maximum bearing stress that occurs in the tests with pinned joints. In addition, comparing figures 5.142 and 5.143 and tables 5.20 and 5.21, it is clear that the delay in damage initiation is more effective in the *blocked* laminate. As suggested in section 5.5.6, the additional stability of the thicker 0° plies in the region confined by the lateral support provided by the bolt/washer assembly delays the onset and propagation of fibre kinking, increasing locally the laminate compressive strength. These results are therefore important in understanding not only how lateral support can help increasing the load carrying capacity of composite laminates with mechanical joints, but also how it affects local compressive damage growth in different laminates.

5.5.8. Net-tension test results

Net-tension tests were preformed in the present work to study the effect of 0° ply blocking on the net-tension failure mode of thin-ply laminates with bolted joints. With this purpose, 3 net-tension specimens of each laminate and geometry were tested to failure. Figure 5.144 shows representative specimens after testing. As expected, all specimens exhibited a fibre-dominated pull-out net-tension failure mode. Delaminations with a triangular shape can be observed, extending from the hole edge to the free edge and connected to matrix cracks in the 45° plies, starting where the fibre direction is tangent to the hole free edge. In the larger 12 mm wide specimens (figure 5.144b), some bearing damage has occurred at the hole boundary where load is applied. Nevertheless, no relevant difference between the failure modes of the *dispersed* and *blocked* laminates can be observed.

Figure 5.145 shows the bearing stress-bearing strain relations for the net-tension tests. The bearing stress, σ^{br}, and the bearing strain, ε^{br}, were determined using equations (4.22) and (4.23), respectively. As in section 5.5.6, the total axial deformation of the specimen's gauge length, measured directly from the cross-head displacement of the testing machine, was used to determine ε^{br}.

The 9 mm wide specimens of both laminates show a linear bearing stress-bearing strain relation up to the maximum bearing stress (figure 5.145a), followed by catastrophic net-tension failure. The 12 mm wide specimens, on the other hand, after a linear bearing stress-bearing strain relation, show a small nonlinear response close to the maximum bearing stress, in some cases accompanied by small load drops (figure 5.145b). This nonlinear response is apparently due to the onset of bearing damage in the hole boundary tangent to the bearing plane (figure 5.144b). Comparing figures 5.128 and 5.145b, it can be seen that the maximum bearing stress of the 12 mm wide specimens of both laminates is above the corresponding

Table 5.21
Average test results for the pin-bearing strengths and respective coefficients of variation (C.V.).

Results		*Dispersed* laminate	*Blocked* laminate
No. specimens		3	3
Average bearing stress at the onset of nonlinearity			
$\sigma^{br}_{\text{nonlin}}$	(MPa)	468	462
C.V.	(%)	7.0	3.8
Average maximum bearing stress			
σ^{br}_{max}	(MPa)	483	473
C.V.	(%)	7.3	3.6

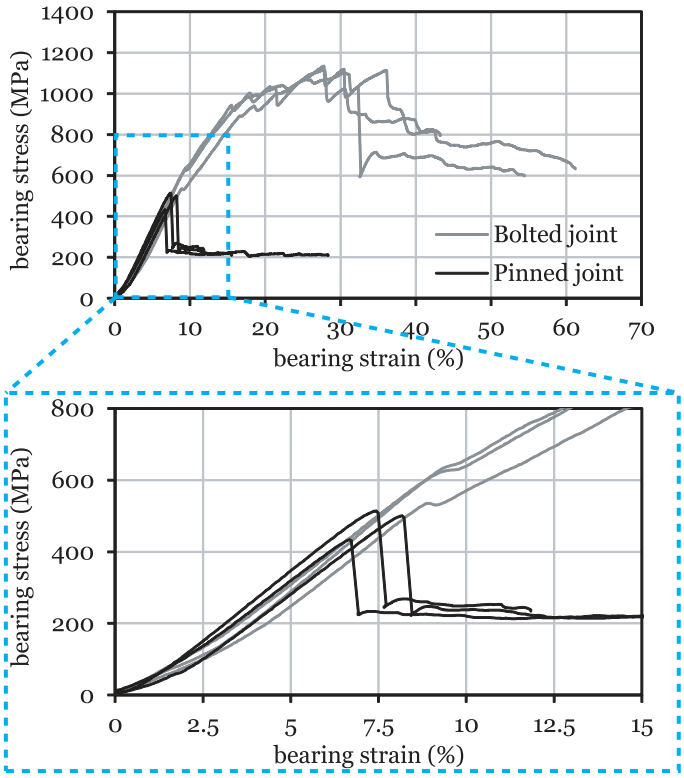

Fig. 5.142. Comparison between the bearing stress-bearing strain curves of the *dispersed* laminate for bolted and pinned joints.

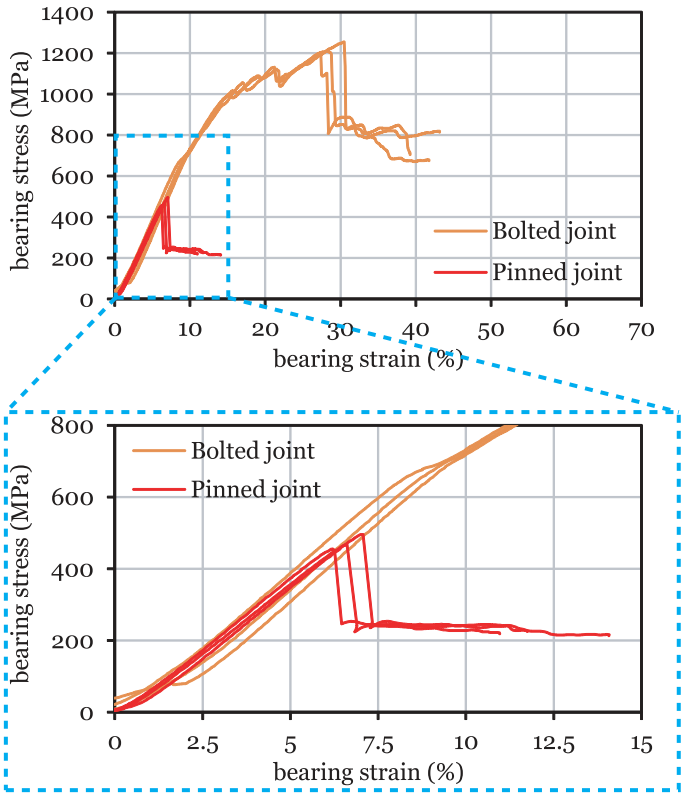

Fig. 5.143. Comparison between the bearing stress-bearing strain curves of the *blocked* laminate for bolted and pinned joints.

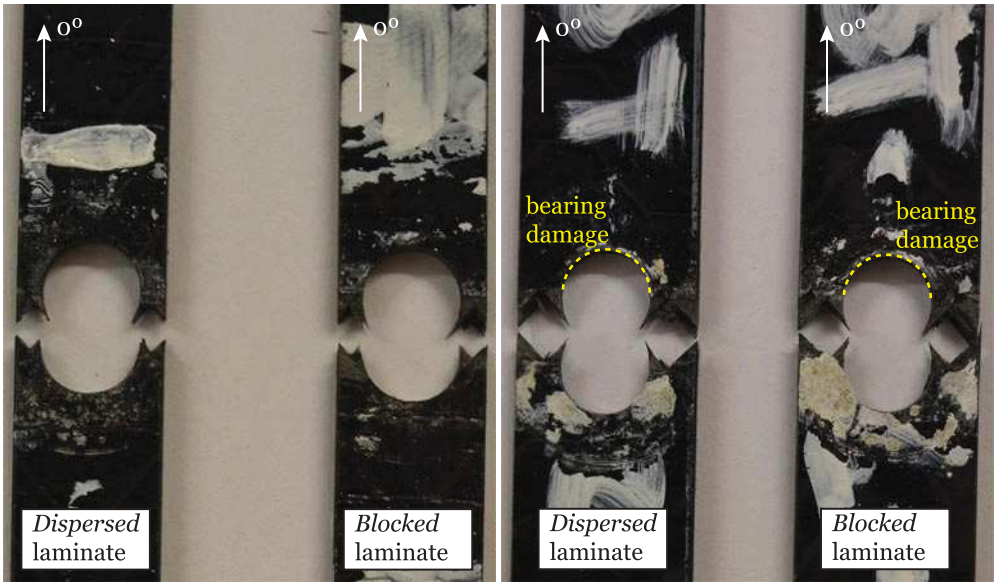

(a) Specimen width: 9 mm (small). (b) Specimen width: 12 mm (large).

Fig. 5.144. Bearing hole region of representative net-tension specimens after testing.

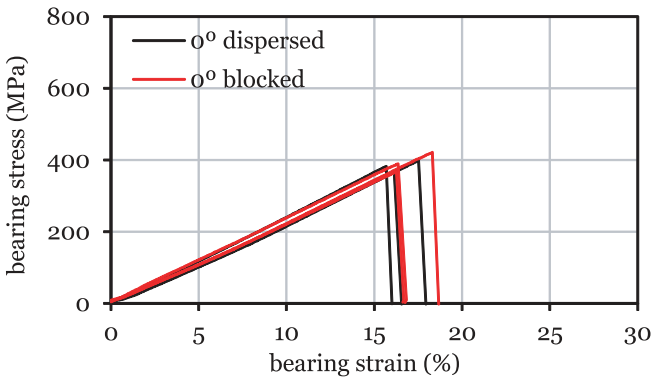

(a) Specimen width: 9 mm (small).

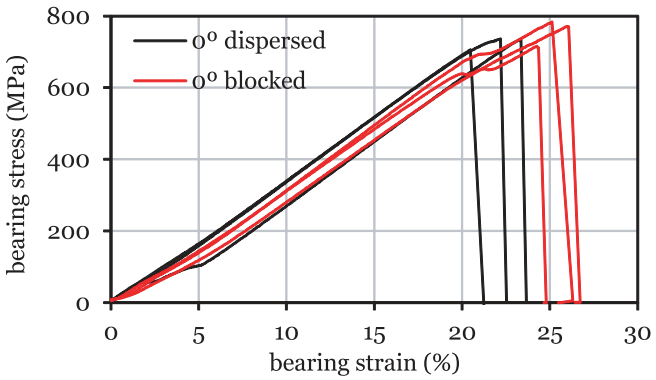

(b) Specimen width: 12 mm (large).

Fig. 5.145. Bearing stress-bearing strain relations for the net-tension tests.

Table 5.22
Mean ultimate bearing stresses ($\bar{\sigma}^{br}$) and coefficients of variation (C.V.) of the net-tension tests.

Results	Specimen width: 9 mm (small)		Specimen width: 12 mm (large)	
	Dispersed	*Blocked*	*Dispersed*	*Blocked*
No. specimens	3	3	3	3
$\bar{\sigma}^{br}$ (MPa)	382	392	726	757
C.V. (%)	3.5	5.7	2.0	3.9

bearing stress at the onset of nonlinearity observed in the bolt-bearing tests (section 5.5.6). This becomes more clear observing table 5.22, which shows the average test results and respective coefficients of variation for the net-tension tests.

Table 5.22 shows that the ultimate bearing stresses of the 9 mm wide *dispersed* and *blocked* laminates are virtually the same; the *blocked* laminate has an ultimate bearing stress only 2.7% higher than the *dispersed* laminate, which is below the variation of the tests. On the other hand, the ultimate bearing stress of the larger 12 mm wide *blocked* laminate is 4.3% higher than the ultimate bearing stress of the *dispersed* laminate. Due to the small ligament width of the 9 mm wide specimens, propagation of damage mechanisms such as matrix cracking in the off-axis plies and delamination along the short ligament section occurs rapidly in both laminates, making any differences in the blunting effects unnoticeable. A larger ligament width, as in the 12 mm wide specimens, results in a superior blunting effect in the *blocked* laminate due to the clustered 0° plies, which delays unstable net-section failure, resulting in a slightly higher net-tension strength.

Comparing the results in table 5.22 with the results from table 5.20, it is possible to confirm that the ultimate bearing stress of the 12 mm wide specimens is higher than the bearing stress at the onset of nonlinearity observed in the bolt-bearing tests. This observation explains the occurrence of bearing damage in these specimens (figure 5.144b). Nevertheless, it is believed that the occurrence of local compressive damage in the hole boundary did not affect the final net-tension strength of the tested specimens.

5.6. Concluding remarks

With the aim to improve the notched response of structural laminates, spread-tow thin plies were chosen to design a structural laminate based on a baseline of the aeronautical industry. With thin plies, detrimental subcritical damage mechanisms, such as transverse cracking and delamination, can be restrained or even suppressed. However, even though this damage suppression capability results in enhanced unnotched strengths [53, 58, 122, 134], improved compressive response [122, 134] and higher fatigue resistance [53, 58, 66, 134], it has a negative impact in notched structures loaded in tension [58], since it inhibits local stress redistribution at the vicinity of the notch. To improve local blunting near geometrical stress concentrations, such as holes or through-the-thickness cracks, a detailed study on the effect of 0° ply blocking on the structural behaviour of an aerospace-grade laminate was carried out, with particular emphasis on the blunting mechanisms (split cracking and local delamination) and notched response. Due to the intrinsic design advantages, thin-ply NCF layers were used.

To obtain the $\mathcal{R}$-curve associated, respectively, with the tensile and compressive mode I intralaminar fracture, tests on scaled DENT and DENC specimens were performed to calibrate the size effect law. Failure due to the development of a through-the-thickness intralaminar crack was observed in the DENT test specimens. Since strong strain relaxation due to the occurrence of subcritical damage mechanisms did not occur, the tests performed were deemed suitable for the determination of the $\mathcal{R}$-curve associated with tensile mode I intralaminar fracture.

For the smaller specimen configurations, the ultimate remote stresses of the *blocked* laminate were higher than in the *dispersed* laminate. However, as the size of the specimens increased, the notched strengths of both laminates tended to the same value, becoming slightly higher for the largest specimens of the *dispersed* laminate. This result showed that, as the size of the specimens increased, the effect of internal stress relaxation due to the blunting mechanisms promoted by the thicker blocks of 0° plies, namely internal split cracking, became less and less important. This is in accordance with the

general nonlinear fracture mechanics principles, which state that, for sufficiently large structures (or coupons), the size of the FPZ tends to a limit value that will become negligibly small compared to any characteristic dimension of the structure, and the fracture toughness reaches a constant (steady-state) value. Since the laminates under study have the same in-plane properties, and the change in the stacking sequence affects only internal subcritical damage mechanisms, which can be lumped into a damage process zone, it is expected that, as the specimens become sufficiently large, the difference in their notched response becomes negligible.

According to the DENT tests performed in this work, the *dispersed* laminate is characterised by a length of the FPZ 2.42 times larger and a steady-state value of the fracture toughness 1.33 times higher than the *blocked* laminate. However, from the observation of the damage mechanisms and failure modes of the tested specimens, in particular of the larger coupons, and taking into account that both laminates have the same material system, more similar $\mathcal{R}$-curves would be expected. This difference was attributed to a stronger strength reduction with size in the *blocked* laminate, despite its higher notched strength for the small coupons, resulting in a steeper size effect law. This is then translated into a brittler response and, consequently, in a shorter FPZ and lower steady-state value of the fracture toughness. Complementary tests on a larger specimen configuration are therefore suggested to understand if the notched strengths of both laminates tend, instead, to the same value (as suggested in the previous paragraph), and if a more reliable characterisation of the $\mathcal{R}$-curve of the *blocked* laminate can be obtained.

These results also highlight the importance of adequately selecting both specimen configurations and range of coupon dimensions in calibrating the size effect laws to accurately derive the $\mathcal{R}$-curves using this methodology. It is important to note that an $\mathcal{R}$-curve determined from the size effect law is defined such that the steady-state value of the fracture toughness is the energy required for crack growth in an infinitely large specimen, which is taken as size and geometry independent. However, because the size effect law is not exact, this should be regarded as an approximation. Yet, for structures until one order of magnitude larger than the larger specimen configuration used to calibrate the size effect law, the approximation should be regarded as acceptable [279, 280]. On the other hand, for some materials, the $\mathcal{R}$-curve may change slightly with specimen shape (e.g. Refs. [211, 277, 279, 280]). However, the differences in the $\mathcal{R}$-curve may result either from the statistical scatter of the experimental tests carried out to calibrate the size effect law (e.g. Ref. [211]), or due to the effect of the shape correction functions κ, which vary with the different specimen geometries [279, 280].

For the DENC tests, a very similar fracture response is observed in both *dispersed* and *blocked* laminates. Not only the ultimate remote stresses for each geometry are very close, but also the stresses at the onset of intralaminar damage growth. Moreover, a similar size effect is observed in both laminates. Hence, it can be concluded that the effect of grouping together the 0° plies in the compressive fracture response of hard laminates is negligible. Consequently, the compressive $\mathcal{R}$-curves of the *dispersed* and *blocked* laminates are very similar in shape and size, with approximately the same length of the FPZ and same steady-state value of the fracture toughness.

The unnotched response of the *dispersed* and *blocked* laminates was assessed testing smooth coupons in tension and compression. The unnotched tension tests revealed a highly catastrophic type of failure. A fibre-dominated pull-out failure mode, with the failure section perpendicular to the applied load, was observed in both laminates. However, the *blocked* laminate exhibited a higher susceptibility to grow subcritical damage mechanisms, as the extent of delamination and pulled-out fibre bundles in the failed regions was slightly higher. This was attributed to higher stress concentrations in the interfaces adjacent to the thicker 0° ply blocks, facilitating the occurrence of delamination and splitting, and to higher mismatch angles between some of the adjacent NCF bi-angle layers, which result in higher interlaminar stress concentrations between these plies, promoting delamination at these interfaces. It is interesting to note that transverse matrix cracking from the free edges of the smooth coupons loaded in tension was absent, showing the potential of thin transverse plies to suppress subcritical failure mechanisms. This transverse cracking suppression capability was attributed to the *in situ* effect [81].

Despite the small differences in the damage mechanisms that preceded failure of the smooth coupons, the tensile strengths of the tested laminates were virtually the same. As reported elsewhere [53, 58, 121, 122], blocking together the off-axis and transverse plies with the same orientation has a detrimental effect on the tensile unnotched strength of

multidirectional laminates. This is due to the higher interlaminar stresses and lower *in situ* strengths of laminates with thick plies, which cause early subcritical damage mechanisms adjacent to the load carrying 0° plies, acting as stress concentration points that promote early catastrophic longitudinal failure. However, restricting ply blocking to the 0° plies did not affect the final unnotched strength of the laminates, while potentiating the growth of damage mechanisms such as fibre-matrix splitting, which can be beneficial in improving the notched response of laminates.

The smooth coupons of both laminates tested in compression exhibited a net-section failure mode, characterised by a complex combination of failure mechanisms, including fibre kinking, brittle shear-driven fibre fracture, wedge transverse fracture, crushing and delamination, whose sequence is not easy to identify. In some specimens, multiple fracture planes, inclined with respect to the laminate midplane, were observed, revealing the catastrophic type of failure of this test configuration.

The *dispersed* laminate had apparently a brittler failure mode, as the occurrence of fibre kinking was more limited, and a high degree of abrasion of the inclined crack surfaces, typical of shear-driven brittle compressive failure [285], was observed. The *blocked* laminate exhibited more irregular failure surfaces, dominated by fibre kinking, suggesting that blocking the 0° plies results in a higher susceptibility to grow kink bands before compressive failure.

In fact, assuming that kink bands are triggered by localised matrix failure in the vicinity of misaligned fibres, an *in situ* effect associated with the onset of fibre kinking in constrained 0° plies is likely to exist. In other words, thicker 0° plies, which have lower *in situ* transverse strengths, will have lower resistance to localised matrix failure in the vicinity of misaligned fibres, thus lowering the resistance to the onset of fibre kinking.

Limiting the development of kink bands, as in the *dispersed* laminate, resulted in a more gradual failure mode. However, growth of severe damage apparently occurred earlier, initially as small events (first load drops), becoming more and more important as the specimen was loaded towards ultimate failure. In the *blocked* laminate, the development of kink bands had apparently the potential to delay the onset of discrete compressive damage growth, but conducted to sudden, unstable ultimate failure once fibre kinking initiated. It is interesting to note, though, that, despite the different failure behaviours of the *dispersed* and *blocked* laminates, the unnotched compressive strengths obtained were remarkably similar, suggesting that final longitudinal compressive failure was not governed by the mechanism leading to failure of the 0° plies, but by the fibre compressive strength itself. It is also interesting to note that, whereas blocking together the off-axis and transverse plies with the same orientation has a detrimental effect on the compressive unnotched strength of multidirectional laminates [121, 122], seemingly caused by higher interlaminar stresses and lower *in situ* strengths, restricting ply blocking to the 0° plies does not affect the final compressive unnotched strength of hard laminates, in spite of the changes in the damage mechanisms.

To study the notched response, the evolution of damage mechanisms and the effect of size on the notched strengths of the different thin-ply laminate configurations, CNT tests were performed in specimens with different sizes, scaled by a factor between 2 and 5. All CNT specimens of both laminates exhibited a fibre-dominated failure mode, caused by the catastrophic propagation of an intralaminar crack after extensive damage growth ahead of the notch tips. A highly diffuse damage process zone was observed, with stable damage propagation occurring predominantly along the off-axis ±45° directions, before unstable propagation across the width perpendicularly to the loading direction.

In the smaller specimens, regions of high strain concentration with a triangular shape in the vicinity of the notch tips were observed, attributed to the occurrence of localised transverse cracking and delamination in addition to intralaminar fracture and longitudinal splitting. As the size of the CNT specimens increased, longitudinal split cracks propagated quickly after slow damage growth from the notch tips along the off-axis ±45° directions. As expected, as the size of the specimens increased, the mean ultimate remote stress decreased.

In general, the ultimate remote stresses of the *blocked* laminate were higher than the ultimate remote stresses of the *dispersed* laminate. In the *blocked* laminate, the onset of intralaminar damage growth and ultimate failure were delayed due to higher stress relaxation in the vicinity of the notch tips caused by larger longitudinal split cracks in the 0° plies, blunting the notch and reducing the local stress concentration.

5.6. Concluding remarks

As the size of the specimens increased, stress relaxation caused by the superior blunting effect of split cracking and local delamination in the *blocked* laminate, potentiated by the thicker blocks of 0° plies, became less and less important. As discussed earlier, for sufficiently large structures the size of the FPZ tends to a limit value, and the fracture toughness reaches a steady-state value. Because the laminates under study have the same in-plane properties, and the change in the stacking sequence affects only internal subcritical damage mechanisms, it is expected that, as the specimens become sufficiently large, the difference in their notched response will become smaller.

Because the CNT tests were performed using geometrically similar specimens with positive geometry, these tests can be used to calibrate the size effect law and determine the laminate $\mathcal{R}$-curve associated with diffuse fracture of the *dispersed* and *blocked* laminates. In contrast with the results determined from the DENT tests, the $\mathcal{R}$-curves of the *dispersed* and *blocked* laminates determined from the size effect laws calibrated with the CNT tests were similar in shape and size. The length of the FPZ and the steady-state value of the fracture toughness of the *blocked* laminate are, respectively, 1.10 times smaller and 1.18 times higher than the *dispersed* laminate. This difference is related to the extent of subcritical damage mechanisms. Larger longitudinal split cracks and a more diffuse damage ahead of the notch tips of the *blocked* laminate delayed the onset of through-the-thickness intralaminar damage growth and postponed ultimate failure, resulting in a slightly higher fracture toughness at propagation.

Comparing with the $\mathcal{R}$-curves determined from the size effect laws calibrated with the DENT tests, a length of the FPZ and a steady-state value of the fracture toughness almost twice as large was obtained. This difference was attributed to the extent and stability of internal damage growth before ultimate failure. Whereas the DENT test specimens are characterised by self-similar intralaminar damage propagation and unstable fracture along the ligament section, the CNT test specimens show a diffuse failure mode, with long split cracks and internal damage growth before ultimate failure, causing large changes in the stress field at the vicinity of the notch due to stress redistribution.

Hence, the $\mathcal{R}$-curves determined from the size effect laws calibrated with the CNT tests do not characterise the mode I longitudinal tensile intralaminar fracture of the *dispersed* and *blocked* laminates, since no self-similar fracture propagation was obtained with these tests. This observation also justifies the use of the DENT tests by Catalanotti et al. [65] to determine the $\mathcal{R}$-curves of composite laminates, given the unstable character of fracture propagation observed in these specimens.

Nevertheless, the "virtual" $\mathcal{R}$-curves determined from the CNT tests are helpful in understanding how the extent of internal damage growth in multidirectional laminates affects their notched response, and how the latter can be improved through appropriate laminate design. For instance, by adopting a laminate stacking sequence that promotes fibre-matrix splitting in the 0° plies, which is an important notch blunting mechanism [20, 121, 276], while suppressing the more detrimental delamination and transverse cracking, a laminate with improved notched response can be obtained. In fact, the results of the present study show that combining thin transverse and off-axis plies and thicker 0° plies can be a promising solution to improve the notched response of thin-ply laminates without compromising their superior unnotched behaviour [53, 58, 122, 134], their improved compressive response [122, 134] and their enhanced fatigue resistance [53, 58, 66, 134].

To investigate the effect of 0° ply thickness on the structural performance of thin-ply laminates, bolt- and pin-bearing tests were performed. In the case of bolted joints, the *blocked* laminate exhibited a higher bearing strength when compared with the *dispersed* laminate. Not only the onset of local compressive damage, measured by the first nonlinearity in the bearing stress-bearing strain curve, was delayed, but also the growth of permanent damage, corresponding to the first load drop, occurred at a higher bearing stress. Interrupted testing at different load levels have shown that the *dispersed* laminate exhibits a "brittler" through-the-thickness shear cracking failure mode, characterised by slenderer shear bands with signs of shear-driven fibre compressive failure. In the *blocked* laminate a "softer" through-the-thickness shear cracking failure mode was identified, with enlarged shear bands characterised by a more gradual shear deformation of the off-axis plies and wider kink bands in the longitudinal plies. This "softer" damage morphology is apparently responsible for the improved bearing response of the *blocked* laminate, due to a more gradual damage process that allows the laminate to carry higher loads than the *dispersed* laminate, whose damage propagation is more abrupt.

In the the pin-bearing tests, no relevant difference was observed between the *dispersed* and *blocked* laminates. Once damage at the micro-level, such as matrix cracking and fibre kinking, started to form, it quickly propagated into macro-cracks and crushing due to lack of lateral support, reducing considerably its load-carrying capacity. In the bolted joints, the lateral support provided by the bolt/washer assembly effectively delayed the onset of nonlinearity to values above the maximum bearing stress observed in the pinned joints. These results are important in understanding not only how lateral support can help increasing the load carrying capacity of composite laminates with mechanical joints, but also how it affects local compressive damage growth in different laminates. In fact, it is noted that the lateral support provided by the bolt/washer assembly plays a key role in the improved bolt-bearing response of the *blocked* laminate.

Finally, in order to assess the effect of joint design in the structural response of the *dispersed* and *blocked* laminates, net-tension tests were also carried out. Both laminates exhibited a fibre-dominated pull-out net-tension failure mode. Delaminations with a triangular shape were observed, extending from the hole edge to the free edge and connected to matrix cracks in the 45° plies, starting where the fibre direction is tangent to the hole free edge. For the smallest, 9 mm wide specimens, the very small ligament width resulted in a fast propagation of matrix cracking in the off-axis plies and delamination along the short ligament section, making any differences in the blunting effects unnoticeable. A larger ligament width, as in the 12 mm wide specimens, resulted in a superior blunting effect in the *blocked* laminate due to the clustered 0° plies, which delayed unstable net-section failure, resulting in a slightly higher net-tension strength.

The present results show that, by changing the position of the 0° plies in a multidirectional laminate, a different structural response can be obtained. Moreover, it is clear from this experimental test campaign that a wise selection of the position of the 0° plies can result in improvements of the notched behaviour of structural laminates. For instance, by grouping together the 0° plies in thicker blocks, it is possible to promote fibre-matrix split cracking, which acts as an important notch blunting mechanism [20, 121, 276]. In addition, using spread-tow thin plies along the transverse and off-axis orientations, ensures that matrix cracking and delamination preceding ultimate failure can be effectively delayed or even suppressed, which is known to have a positive effect on the unnotched, compressive and fatigue behaviours [53, 58, 66, 122, 134], while potentiating increased residual strengths [20]. Following this approach, an improved structural response was obtained on scaled coupons with straight through-the-thickness notches and on mechanically fastened joints, without compromising the superior unnotched tensile and compressive strengths intrinsic to thin-ply laminates.

Part IV

Numerical and analytical modelling of ply damage mechanisms

Chapter 6

Micro-mechanical analysis of the *in situ* effect in polymer composite laminates

When embedded in a multidirectional laminate, the mechanical response of each ply can be significantly different from the behaviour of UD laminae, due to the constraining effect of the adjacent plies. In fact, it is recognised that the actual ply strengths are not only higher than those measured in UD coupons, but they reportedly increase with decreasing ply thickness. When dealing with the most recent spread-tow, ultra-thin grades, where dry ply thicknesses can be extremely low, the effect of ply thickness gains particular importance. However, fracture mechanics predictions of the *in situ* strengths yield asymptotic results when the ply thickness tends to zero. Therefore, an understanding of the *in situ* effect for such ply thinness is of crucial importance, namely for the development of physically meaningful analytical models applicable at this scale. A possible way through is the use of computational micro-mechanics. In the present chapter, a three-dimensional computational micro-mechanics framework is used to study the mechanical response of ultra-thin spread tows embedded in a multidirectional laminate. Varying the thickness of the 90° ply, it is possible to assess its effect on the mechanical response of laminated composites (i.e. the *in situ* effect). The results of the micro-mechanical model are then compared with the predictions from analytical models for the *in situ* effect, with the aim of validating both modelling strategies. In addition, a truthful insight into the mechanics of thin-ply laminates is sought using the proposed micro-mechanical model, including a better understanding of their damage mechanics and of the mechanisms that preclude both microcracking and delamination.

6.1. Introduction

The improved fibre dispersion resulting from tow spreading [32, 33] has motivated the study of the effect of ply thinness on the mechanical response of unidirectional (UD) laminae. Amacher et al. [58] performed an extensive experimental characterisation of the mechanical response of thin-ply laminates, including testing of UD carbon fibre-epoxy composites with ply areal weights ranging from ultra-thin to very high grades, all produced from the same batch of fibre and matrix. No significant influence of ply thinness on the elastic and strength properties of the UD composites was observed, except for longitudinal compression, where an enhancement of approximately 20% in average was observed, attributed to the more uniform microstructure of spread tow thin plies.

When embedded in a multidirectional laminate, the mechanical response of each ply can be significantly different from the behaviour of UD laminae, due to the constraining effect of the adjacent plies. For instance, plies whose fibre orientation is perpendicular to the loading direction develop a network of matrix cracks that do not occur on UD laminae subjected to transverse loads. These matrix cracks induce the deterioration of the mechanical performance of the laminate, promoting other damage modes (e.g. delamination), and creating pathways for substances contained in composite chemical tanks or pressure vessels [78].

6.1. Introduction

Transverse matrix cracking typically occurs at strains lower than the failure strain of the entire laminate [35, 38]. Consequently, the actual ply strengths are not only higher than those measured in UD laminae, but they reportedly increase with decreasing ply thickness [35, 81, 91–97, 287], due to the constraining effect imposed by the neighbouring plies, which delays damage propagation in the matrix [38, 58]. This is a deterministic size effect that occurs at the meso-scale, known as the *in situ* effect. The transverse tensile strength (Y_T) and the in-plane shear strength (S_L) are two examples of well known *in situ* strengths, which are function of ply thickness [35, 88, 89, 91–97, 120], fibre orientation (or stiffness) of the adjacent plies (e.g. figure 2.5) [94, 95], and ply's position in the laminate [81].

The *in situ* effect is typically taken into account by using fracture mechanics models that predict the relation between the ply thickness, its fracture toughness and the *in situ* strengths [81, 98], whose accurate determination is necessary for implementation of any physically based failure criteria for transverse fracture in multidirectional laminates [81, 99–108]. In fact, it has been shown that using as ply properties those measured directly from UD plies to predict the strength of multidirectional laminates results in very conservative predictions that could differ substantially from the experimental results [83, 95, 102, 109]. It is noted that, in the case of in-plane shear, Linear Elastic Fracture Mechanics (LEFM) alone is not able to accurately predict the *in situ* strength, and the nonlinear shear response typically observed in laminated composites must be included in the prediction models [81].

The delay of other ply matrix-dominated failure mechanisms in multidirectional laminates, such as wedge transverse compressive and shear fracture and fibre kinking, can also be attributed to the *in situ* effect. This has been addressed in the past through application of three-dimensional (3D) phenomenological failure criteria [128, 129]. According to these models, when embedded in a multidirectional laminate, not only the transverse tensile and in-plane shear strengths (calculated using e.g. the models proposed by Camanho et al. [81]), but also the transverse compressive and transverse shear strengths (Y_C and S_T, respectively) are *in situ* properties. In addition, assuming that kink bands are triggered by localised matrix failure in the vicinity of misaligned fibres [128, 129], the *in situ* effect has also a direct, positive influence on the resistance of embedded plies to fibre kinking.

The effect of ply thickness on the onset of ply damage (transverse cracking) finds particular significance when dealing with the most recent spread-tow, ultra-thin grades, where dry ply thicknesses can be extremely low. Fracture mechanics predictions of the *in situ* strengths yield asymptotic results when the ply thickness tends to zero. For example, the LEFM model for the *in situ* transverse tensile strength, Y_T^{is}, of a thick ply can be written as [81]:

$$\frac{Y_T^{is}}{Y_T} = 1.12\sqrt{2} \tag{6.1}$$

whereas for a thin embedded ply it can be written as [81]:

$$\frac{Y_T^{is}}{Y_T} = \lambda^{-1/2} \tag{6.2}$$

with:

$$\lambda = \frac{\pi\, b\, \Lambda_{22}^0}{8\, \mathcal{G}_{Ic}\, Y_T^2} \tag{6.3}$$

where b is the transverse ply thickness, Λ_{22}^0 is a parameter that depends on the material elastic properties [288]:

$$\Lambda_{22}^0 = 2\left(\frac{1}{E_{22}} - \frac{\nu_{12}^2}{E_{11}}\right) \tag{6.4}$$

and $\mathcal{G}_{Ic}$ is the fracture toughness associated with mode I intralaminar fracture parallel to the fibre direction. The distinction between thick- and thin-ply behaviour in equations (6.1) and (6.2), introduced by Dvorak and Laws [98] and Camanho

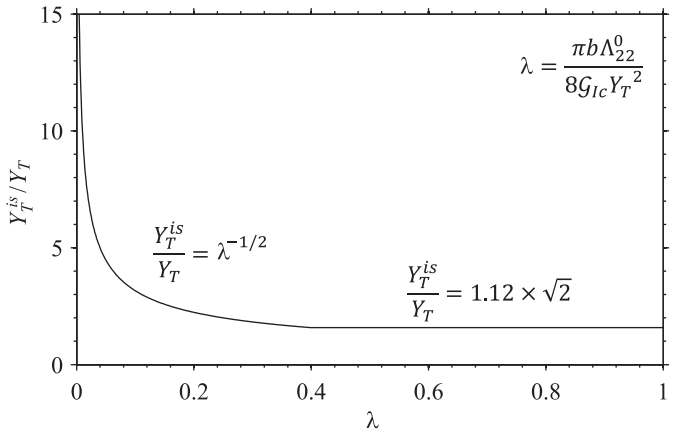

Fig. 6.1. Dimensionless representation of the *in situ* effect on the transverse tensile strength of an embedded ply.

et al. [81], was addressed in detail and confirmed numerically by van der Meer and Dávila [289]. In the thin-ply case, the *in situ* strength is related to stable crack propagation in the longitudinal direction after propagation through the ply thickness. On the other hand, in the thick-ply case, the *in situ* strength is related to the unstable through-the-thickness propagation of the transverse crack, as stable widthwise propagation occurs immediately after but at a lower applied stress. The theory shows that the transverse stress level at which unstable though-the-thickness crack propagation occurs is independent of the ply thickness, whereas stable widthwise propagation occurs at higher stress levels as the ply thickness decreases. For ply thicknesses in which the stress level needed for stable propagation in the longitudinal direction is higher than for unstable through-the-thickness propagation, increasing strength with decreasing ply thickness is observed.

Figure 6.1 shows a dimensionless representation of the *in situ* effect on the transverse tensile strength of an embedded ply. A similar representation would be obtained for the *in situ* in-plane shear strength, S_L^{is}.

As can be observed in figure 6.1, as the ply thickness decreases, the *in situ* strength asymptotically tends to infinity. Therefore, an understanding of the *in situ* effect for such ply thinness is of crucial importance, namely for the development of physically meaningful analytical models applicable at this scale. However, experimental analysis based on *in situ* observations of very thin plies are extremely difficult, not only because it is hard to identify any transverse damage at this scale, but also because the applied strains needed to develop such damage mechanisms are so high that conduct to failure (or severe damage) of the constraining material [87]. A possible way through for the understanding of the *in situ* effect is the use of computational micro-mechanics.

The ability of damage models to predict physical phenomena, such as the initiation and propagation of damage, strongly depends on the scale (or resolution) at which the damage mechanisms under consideration are modelled [138, 290] — see figure 6.2. In fact, the conceptual idealisation of the damage process, i.e., the identification, characterisation and formulation of the governing physical principles of damage evolution, may span from molecular dynamics scales to structural mechanics scales, including the intermediate micro- and meso-mechanics [290]. In the case of composite laminates, where the in-plane dimensions exceed the length-scale at which delamination, matrix cracking and fibre-matrix debonding take place by one to several orders of magnitude, the proper definition of the modelling scale has particular importance [138].

At lower structural scales, damage idealisations have higher resolution, higher kinematic freedom and are able to recreate all kinds of damage mechanisms, each of these captured with separate damage laws [260, 290, 292]. Micro-mechanical scale models, based on the constituent level, represent what is normally the smallest scale of composite damage idealisation [260, 290, 293]. Due to the sophistication of the modelling techniques and to the ever-increasing computational power, computational micro-mechanics has been emerging as an accurate and reliable tool to study the mechanical response of laminated composites.

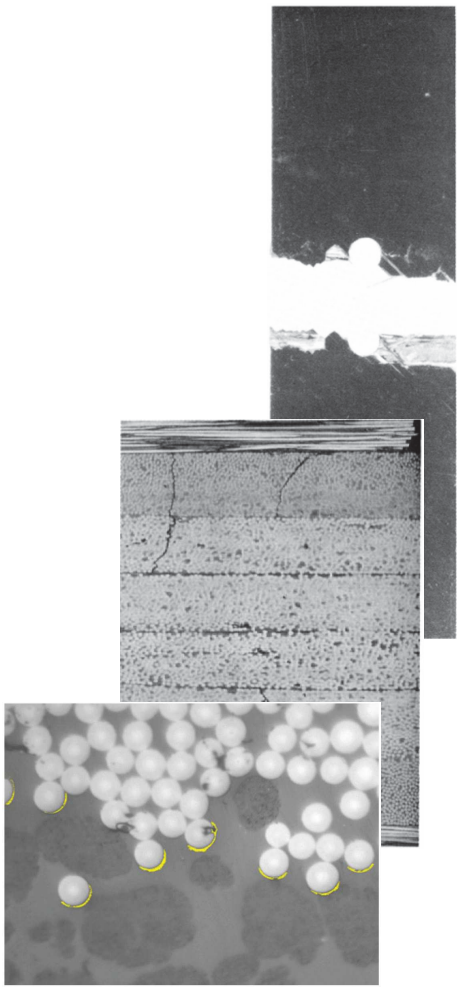

Fig. 6.2. View of the damage mechanisms on composite laminates at different scales [88, 291].

Within this framework, experimental data on the properties of the fibres and matrix materials, which are seen as individual homogeneous materials, and their interfaces are used to study the constitutive behaviour and to obtain the macroscopic properties of a composite lamina, not only the elastic constants, but also the strength properties under diverse loading conditions. Detailed matrix damage mechanisms, such as matrix plasticity and damage, and fibre-matrix interface cracking can be easily represented by means of the numerical simulation of the deformation and failure of a representative volume element (RVE) of the microstructure, where fibre, matrix and their interface are modelled with the appropriate constitutive equations. Therefore, the micro-scale is the ideal damage scale to analyse intralaminar fracture, in particular the ply thickness and constraining (*in situ*) effects on matrix damage initiation and propagation.

An RVE can be defined as the smallest volume fraction of the material whose properties are representative of the global mechanical performance of the material system [70, 71]. Therefore, an important issue when using computational micro-mechanics is the minimum size of the RVE.

RVEs cannot be too large, as it would endanger the possibility to numerically analyse them. In addition, RVEs cannot be too small, since they should contain all the necessary information about the statistical description of the microstructure, so that their average properties are independent of their size and position within the material [294, 295]. The critical size of an RVE depends on the phase and interface properties, as well as on the spatial distribution [294].

In addition to the size of the RVE, other important issues include fibre distribution, volume fraction and spatial arrangement of reinforcements in the matrix. This spatial arrangement is usually not periodic and it is highly dependent upon the

manufacturing process [295]. To accurately reproduce the onset and evolution of damage in the matrix, it is important to represent properly the transverse randomness of the fibre distribution (i.e. distance to first neighbours, occurrence of clusters of fibres, etc.) [295, 296].

However, in the computational analysis of composite materials, periodic RVE are often employed, assuming that the material has a deterministic and ordered distribution of fibres, mainly because this assumption leads to lower computational costs [296, 297]. To understand if this type of assumption conducts to worse results than when using RVEs with randomly distributed fibres, Trias et al. [297] compared the stress and strain distributions between a periodic and a random model for a carbon fibre reinforced polymer (CFRP), established in Ref. [296]. This comparison showed that periodic models can be used for the simulation of effective properties when the accuracy required is not so high (the difference in the Young's modulus was about 12% and in the Poisson's ratio about 6%); however, for any statistical analysis or for the simulation of local phenomena such as local damage or matrix cracking, random models must be considered. Clearly, this is an important feature to take into account in the micro-mechanical analysis of the *in situ* effect.

Recently, Saito et al. [35] experimentally evaluated transverse crack constraining on thin-ply carbon-epoxy cross-ply laminates. The thickness of the inner 90° layer varied between 0.040 mm (single ultra-thin ply) and 0.160 mm (block of four ultra-thin plies). In an interesting analysis approach, these authors reported a much lower crack-opening displacement (COD) for the thin 90° ply when compared to blocks of two and four plies. This was attributed to the constraining effect caused by the stiff 0° plies adjacent to the inner 90° ply.

Saito et al. [35] observed that, for the thickest transverse laminae, the matrix crack extension, which occurred suddenly through the thickness, led to stress relaxation, whereas, for the thinner transverse laminae, matrix cracking extended gradually, eventually without completely penetrating through the thickness, making stress relaxation much more difficult. The higher stress field maintained in the thinner transverse laminae caused, therefore, new matrix cracks to occur, increasing the crack density. A crack suppression effect was shown to exist, attributed to a decrease in the energy release rate (ERR) at the crack tip as the ply thickness decreased.

In a complementary study, Saito et al. [38] numerically investigated matrix cracking restriction in the inner transverse ply of a thin-ply laminate, and the effect of the stiffness of the adjacent plies, to clarify the mechanisms of transverse damage suppression in thin-ply laminates. A two-dimensional micro-mechanical model was used, including an RVE of an embedded ply subjected to transverse tensile loading, where fibres and matrix were discretely represented. A "weak interfacial strength" was assumed between matrix and fibres, modelled using cohesive elements at the interfaces. The fibres distribution in the RVE of the 90° ply was modelled mimicking the *in situ* observations on the actual specimens tested in Ref. [35]. The widths of the RVEs were defined using the experimentally observed crack density information, such that the area modelled along the length direction contained only one transverse crack. An initial thermal step was performed to account for the residual stresses of the curing process in the RVE. Standard boundary conditions were applied to the RVE. A bilinear elastic-plastic constitutive model was used to model the mechanical behaviour of the matrix. Failure was assumed to occur when the tensile or shear strains in the matrix reached their critical values, and the moduli of the failed matrix was reduced to 10% of the original values.

The numerical results presented by Saito et al. [38] were consistent with the experiments [35], with drastic penetration of the transverse cracks for the thicker 90° plies. With 45° plies adjacent to the inner 90° layer, matrix crack propagation was faster than when having 0° adjacent plies, confirming the effect of the stiffness of adjacent plies on the constraining imposed to the embedded 90° laminae [94].

To improve the analysis carried out in Ref. [38], a recent 3D computational micro-mechanics framework [298, 299] is used in the present work [84, 85]. This framework gives particular emphasis to the constitutive behaviour of the different constituents and to the characteristics of the RVEs under analysis, enabling an accurate representation of the micro-mechanical phenomena without relying on empirical observations.

In fact, a relevant aspect in the development of micro-mechanical models is the correct definition of the constitutive behaviour of the composite material's constituents, in particular of the matrix material. For example, epoxy resins,

which are typically used in advanced composite laminates, are known to be pressure dependent and extremely ductile under shear loading. Unlike the standard nonlinear models, such as the Mohr-Coulomb and the Drucker-Prager elastic-plastic models, or other alternative plastic models that do not consider hardening effects, Melro et al. [298, 299] proposed and implemented a new pressure dependent, elastic-plastic thermodynamically consistent damage model that is able to properly represent the most relevant characteristics of epoxy matrices, namely the pressure dependency on its yield and failure behaviour, and the shear nonlinear-almost perfectly plastic behaviour.

In this work, a micro-mechanical Finite Element (FE) model of a thin-ply carbon-epoxy sublaminate, consisting of an RVE of a 90° thin lamina in-between two homogenised $\pm\theta^\circ$ plies, is used to study the mechanical response of ultra-thin spread tows. This RVE is created using an adaptation of the algorithm proposed in Ref. [295], which is able to generate random fibre distributions (even for high values of the fibre volume fraction) that are materially and statistically equivalent to real distributions in the transverse cross-section of laminated composites.

A computational micro-mechanics framework proposed recently [298, 299], with a special focus on the matrix material behaviour and fibre-matrix interface, is used in this analysis. The matrix is modelled using a pressure dependent, elastic-plastic damage model, and cohesive elements are used to model the interface between matrix and fibres [298]. Cohesive elements are also used to simulate delamination between the 90° lamina and the adjacent homogenised $\pm\theta^\circ$ plies.

Varying the thickness of the 90° ply, it is possible to assess its effect on the mechanical response of laminated composites (i.e. the *in situ* effect). The results of the micro-mechanical model can then be compared with the predictions from the analytical models for the *in situ* effect based on LEFM [81] and phenomenological 3D failure criteria [128, 129], with the aim of validating both modelling strategies. In addition, a detailed insight into the mechanics of thin-ply laminates is sought using the proposed micro-mechanical model, including a better understanding of their damage mechanics and of the mechanisms that preclude both microcracking and delamination, as observed experimentally [23, 35, 53, 58, 66, 122, 123].

6.2. Constitutive modelling

The FE model of the thin-ply sublaminate consists of three main parts, a micro-mechanical RVE of a 90° thin lamina, two adjacent homogenised $\pm\theta^\circ$ plies, and the interfaces between the 90° lamina and the homogenised plies. The RVE of the 90° thin lamina is composed by a random distribution of carbon fibres, the epoxy matrix, and the interfaces between fibres and matrix.

The random distribution of fibres is generated using an adaptation of the algorithm proposed in Ref. [295], with imposed fibre continuity along the faces perpendicular to the y-direction for implementation of Periodic Boundary Conditions (PBCs) — figure 6.3. Here, the x-direction coincides with the longitudinal (fibre) direction of the discretised transverse ply (normal to the surface of the page), the y-direction coincides with the in-plane transverse direction of the discretised transverse ply (horizontal axis), and the z-direction coincides with the out-of-plane (through-the-thickness) transverse direction (vertical axis).

Unlike 3D random RVEs with PBCs for analysis of UD composites [295, 298], in the present study the entire thickness of the discretised transverse ply is explicitly represented, so its effect in the response of the sublaminate can be taken into account. The faces of the discretised transverse ply perpendicular to the z-direction (top and bottom faces) will be connected to the homogenised outer plies, and, therefore, in the generation of the RVE, fibres are not allowed to intersect these faces.

The homogenised $\pm\theta^\circ$ plies are intended to simulate the mesoscopic elastic behaviour of the surrounding laminae and its effect on the mechanical response and on the damage initiation and growth in the mid-90° ply. The interfaces between the 90° lamina and the homogenised plies, and the corresponding interlaminar damage onset and propagation, are simulated using cohesive elements. The constitutive models for each of these materials are briefly described in the following sections.

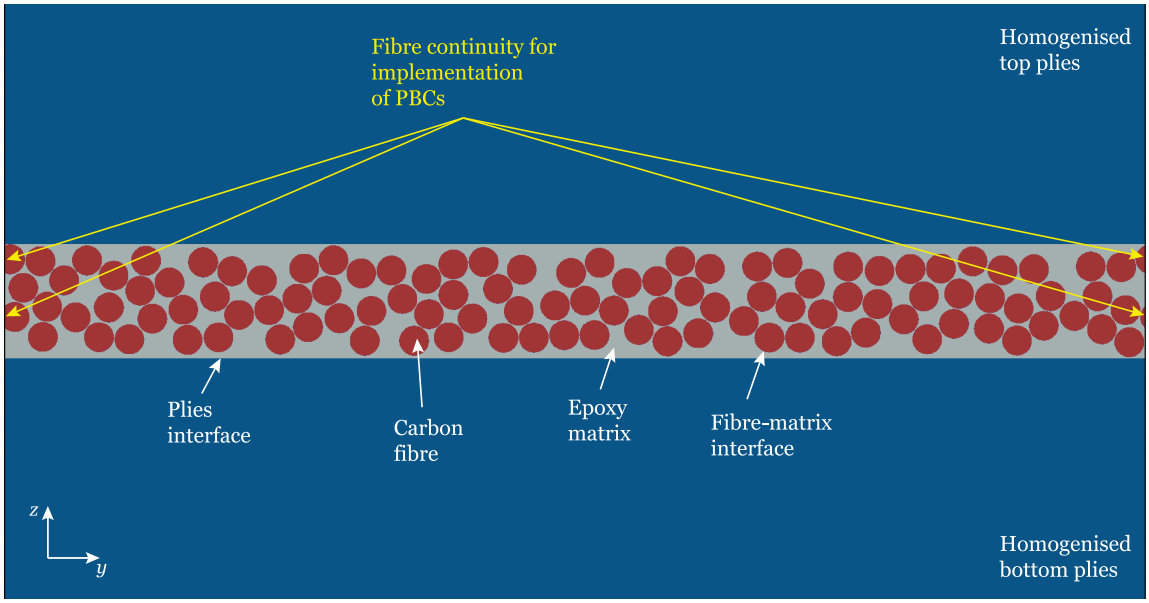

Fig. 6.3. RVE of a laminate with a discrete 0.020 mm thick 90° ply.

6.2.1. Reinforcing fibres

In this work, a simple transversely isotropic, linear-elastic constitutive model is used to simulate the individual reinforcing carbon fibres. The diameter of the individual fibres is considered constant in the entire RVE [299]. Table 6.1 shows the material properties of standard carbon fibres, used in the present micro-mechanical model.

6.2.2. Epoxy matrix

The epoxy matrix is modelled using the elastic-plastic constitutive model with damage proposed in Ref. [298], implemented as an UMAT user subroutine of the FE commercial software Abaqus [275]. The initial elastic behaviour is defined by a linear relation between the stress tensor and the elastic strain. A paraboloidal yield criterion, defined as a function of the stress tensor and of the compressive and tensile yield strengths, is used together with a non-associative flow rule, which allows for a correct definition of the volumetric deformation in plasticity. The tensile and compressive hardening functions are provided by two piecewise functions of the equivalent plastic strain. Since it is fully differentiable, the paraboloidal yield function is integrated by means of a general return mapping algorithm.

Damage in the epoxy matrix is modelled by a single damage variable that affects only the Young's modulus of the material once activated. This isotropic damage model is defined in a thermodynamically consistent way, ensuring irreversibility of the damage process.

Damage onset is defined by a damage activation function similar to the paraboloidal yield criterion, but using the final compressive and tensile strengths of the epoxy matrix, instead of yield strengths, and the concept of effective stress tensor, i.e., the stress tensor calculated using the undamaged stiffness tensor [298]. To avoid damage localisation (mesh size dependency), an approach based on the *crack band model* [300], which makes use of the characteristic length of the finite element and the fracture toughness of the epoxy matrix to regularise the computed dissipated energy, is implemented along with the definition of the damage evolution law [298]. The chosen damage evolution law forces damage localisation and strain softening in the material under tensile load, but under compressive load the influence of the hydrostatic pressure causes a different evolution of the damage variable. The progression of damage is softer than in the tensile case, which suggests a slower propagation of damage [298]. For more details, the reader is referred to Refs. [298, 299].

Fiedler et al. [301] characterised the stress-strain behaviour of a typical epoxy matrix material (Toho # 113) under tension, compression and shear. The relevant elastic and strength properties needed to model the material behaviour

Table 6.1
Properties of the carbon fibres.

Material property	Value
Fibre diameter	
$2R$ (mm)	0.0052
Fibre volume fraction	
V_f (%)	56.27
Young's moduli	
E_{11} (MPa)	276000
E_{22} (MPa)	15000
Poisson's ratio	
ν_{12}	0.2
Shear moduli	
G_{12} (MPa)	15000
G_{23} (MPa)	7000
Coefficients of thermal expansion	
α_{11} ($^\circ C^{-1}$)	-0.5×10^{-6}
α_{22} ($^\circ C^{-1}$)	15×10^{-6}
Critical energy release rate	
$\mathcal{G}_c$ (N/mm)	90
Tensile strength	
X_T (MPa)	5310
Compressive strength	
X_C (MPa)	3500
Density	
(kg/mm^3)	1.78×10^{-9}

of the epoxy matrix were extracted from these experimental results, as well as the hardening data for both tension and compression. The plastic Poisson's ratio has been determined by Guild et al. [302], which is considered a standard value for epoxy resins, and the fracture toughness (or critical energy release rate, $\mathcal{G}_c$) used in this work is a mean value of the values reported in the literature [299].

Table 6.2 shows the epoxy matrix material properties. The tensile and compressive hardening curves are shown in figure 6.4.

6.2.3. Fibre-matrix interface

The interface between fibre and matrix is modelled using the cohesive elements of the FE commercial software Abaqus [275]. The cohesive element behaviour is defined by a bilinear traction-separation damage law. The onset of cohesive damage is mode dependent, and is defined by the corresponding strengths in mode I (τ_3^0) and mode II ($\tau_1^0 = \tau_2^0$). The rate of damage progression is controlled by the fracture energy (or critical Energy Release Rate) of the cohesive elements under mode I, mode II, or mixed-mode, according to the Benzeggagh-Kenane (BK) law [303].

Table 6.3 shows the material properties of the fibre-matrix interface. The initial stiffness K is set to maintain continuity of the stress and strain fields between fibres and matrix. The values of the interface fracture energies $\mathcal{G}_{Ic}$ and $\mathcal{G}_{IIc}$, although somewhat low, are justified not only by experimental evidence (see, for instance, Varna et al. [304]), but also from previous micro-mechanical numerical analyses [299, 305], which have demonstrated that the brittle behaviour in transverse tension typical of composites is only captured for such low values of interfacial toughness [299].

6.2.4. Homogenised outer plies

The outer plies are modelled assuming a linear-elastic transversely isotropic material behaviour. Because the homogenised outer plies are introduced in the micro-mechanical model to assess the effect of the stiffness of the adjacent

Table 6.2
Properties of the epoxy matrix.

Material property	Value
Young's modulus	
E (MPa)	3760
Poisson's ratio	
ν	0.39
Coefficient of thermal expansion	
α ($^\circ C^{-1}$)	58×10^{-6}
Stress free temperature	
T_0 ($^\circ$C)	155
Plastic Poisson's ratio	
ν_p	0.3
Critical energy release rate	
$\mathcal{G}_c$ (N/mm)	0.277
Tensile strength	
X_T (MPa)	93
Compressive strength	
X_C (MPa)	350
Density	
(kg/mm^3)	1.3×10^{-9}

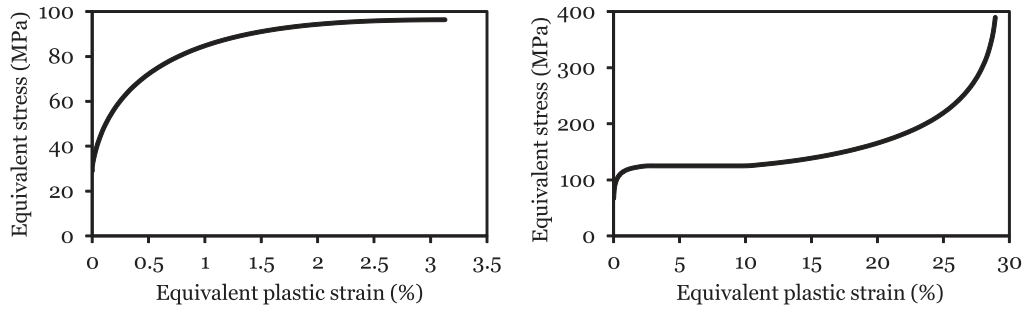

(a) Tensile hardening curve. (b) Compressive hardening curve.

Fig. 6.4. Yield curves given in equivalent stress vs. equivalent plastic strain.

plies in the mechanical response and damage evolution of the intermediate 90° lamina, no nonlinear or fracture behaviour are considered.

IM7/8552 carbon-epoxy is used to model the outer plies of the proposed RVE, as the corresponding material properties are available in several references (e.g. Refs. [171, 235, 265]). Table 6.4 shows the relevant material properties.

6.2.5. Plies interface

The interfaces between the intermediate 90° lamina and the adjacent homogenised $\pm\theta^\circ$ plies are modelled using the cohesive elements in Abaqus [275]. Similarly to the fibre-matrix interface, the cohesive element behaviour is defined by a mode dependent bilinear traction-separation damage law. Once again, the rate of damage progression is controlled by the fracture energy of the cohesive element under mode I, mode II, or mixed-mode, according to the BK law [303].

The interlaminar properties of the IM7/8552 carbon-epoxy composite laminate [235] are used to model the interfaces between the intermediate 90° lamina and the adjacent homogenised $\pm\theta^\circ$ plies. The main reason for this consideration is the use of the IM7/8552 elastic and physical properties to model the homogenised outer plies. Table 6.5 shows the corresponding material properties.

Table 6.3
Properties of the fibre-matrix interface.

Material property	Value
Interface stiffness	
K (N/mm^3)	10^8
Interface maximum strengths	
τ_1^0 (MPa)	75
τ_2^0 (MPa)	75
τ_3^0 (MPa)	50
Interface critical energy release rates	
$\mathcal{G}_{Ic}$ (N/mm)	0.002
$\mathcal{G}_{IIc}$ (N/mm)	0.006
$\mathcal{G}_{IIIc}$ (N/mm)	0.006
Mixed-mode interaction parameter (BK law [303])	
η	1.45

Table 6.4
Properties of the IM7/8552 homogenised outer plies.

Material property	Value
Young's moduli	
E_{11} (MPa)	171420
E_{22} (MPa)	9080
Poisson's ratio	
ν_{12}	0.32
Shear moduli	
G_{12} (MPa)	5290
G_{23} (MPa)	3920
Coefficients of thermal expansion	
α_{11} ($^\circ$C^{-1})	-5.5×10^{-6}
α_{22} ($^\circ$C^{-1})	25.8×10^{-6}
Density	
(kg/mm^3)	1.57×10^{-9}

6.3. Finite element modelling

6.3.1. Finite element discretisation

Figure 6.5 shows a schematic view of the thin-ply sublaminate RVE, where b is the thickness of the intermediate 90° lamina (z-direction), t is the thickness of each individual outer ply, constant and equal to 0.075 mm throughout the analysis, a is the RVE's width (y-direction), defined to ensure the representativeness of the different RVEs analysed in the present work (see table 6.6), c is the RVE's length (x-direction), and θ is the orientation of the outer plies. Different 3D RVEs of the thin-ply sublaminate, with varying transverse ply thickness (b) and, when necessary, varying RVE's width (a) were generated.

Several 90° ply thicknesses are studied, spanning from the ultra-thin 0.020 mm to the more conventional 0.140 mm. For some ply thicknesses, different random fibre distributions are analysed to assess the effect of microstructural randomness.

The width of the RVEs of the thin-ply sublaminates along the y-direction (figure 6.3) is 0.200 mm. This was defined to ensure the representativeness of the different RVEs analysed in the present work. In fact, it is important to note that the width of the RVEs should be defined in such a way that any diffuse damage, which might occur before a transverse crack has grown entirely through the thickness of the ply, can be captured [84, 85]. In a compromise between the computational

Table 6.5
Interlaminar properties of the IM7/8552 carbon-epoxy composite laminate.

Material property	Value
Interface stiffness	
K (N/mm^3)	10^8
Interface maximum strengths	
τ_1^0 (MPa)	93
τ_2^0 (MPa)	93
τ_3^0 (MPa)	71
Interface critical energy release rates	
$\mathcal{G}_{Ic}$ (N/mm)	0.277
$\mathcal{G}_{IIc}$ (N/mm)	0.788
$\mathcal{G}_{IIIc}$ (N/mm)	0.788
Mixed-mode interaction parameter (BK law [303])	
η	1.634

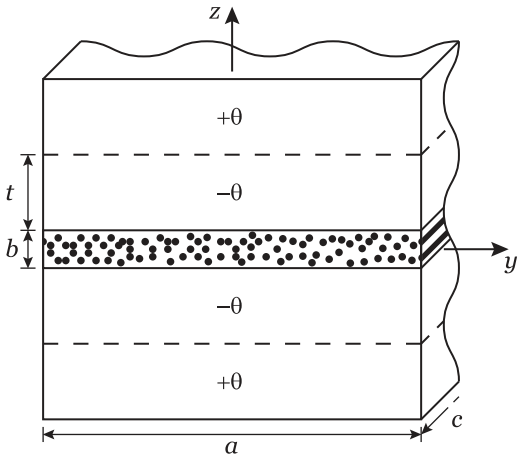

Fig. 6.5. Schematic of the RVE of a thin-ply sublaminate.

cost of the proposed models and the results obtained, it was observed that an RVE width of 0.200 mm was adequate to capture the diffuse damage occurring on the thinner transverse plies.

However, due to the enormous computational cost of these models, the RVEs of the sublaminates with transverse ply thicknesses above or equal to 0.100 mm were modelled to accommodate approximately a single transverse crack, reducing the total width of the RVEs to 0.120 mm. As the transverse ply gets thicker, the size of the models becomes so large that they cannot be handled.

Nevertheless, it was observed that, for such transverse ply thicknesses, the diffuse damage, before transverse cracking grew through the thickness, was very limited. Therefore, defining the width of the RVE such that a single transverse crack could be captured was sufficient to study the damage morphology and predict failure of the thicker transverse plies.

Reducing the RVE width from 0.200 mm to 0.120 mm for transverse ply thicknesses above 0.100 mm was enough to capture transverse cracking and keep the computational cost of the models in reasonable values. It is recognised that the size of the RVE may affect the predicted material response, particularly during softening [299]; however, the analysis of the RVEs with thicker transverse plies is still important to accurately address the causes of matrix transverse failure as the ply thickness increases.

The length of the micro-mechanical models (x-direction) is kept constant and approximately equal to two times the average element size of the mesh of the discretised transverse ply, or 0.2 times the fibre radius. A discretisation of two elements along the x-direction was used. The authors believe this is the most suitable choice for the compromise between

Table 6.6
Size of the sublaminate RVEs studied in the present work.

Ply thickness (b)	RVE's width, y-direction (a)
0.020 mm	0.200 mm
0.040 mm	0.200 mm
0.060 mm	0.200 mm
0.080 mm	0.200 mm
0.100 mm	0.120 mm
0.120 mm	0.120 mm
0.140 mm	0.120 mm

the computational cost of the present models and the quality of the results. Despite the increased computational cost of the 3D modelling approach, the flexibility of the present computational micro-mechanics framework to predict the mechanical response of UD composites and sublaminates subjected to general 3D loading conditions motivates its employment in the present study.

Following Melro et al. [299], linear hexahedral finite elements with reduced integration (Abaqus C3D8R) are used to generate the mesh of the 90° intermediate ply (both matrix and fibres). However, due to the randomness of the distribution of reinforcements and consequent difficulties to mesh this geometry, some linear wedge elements (Abaqus C3D6) are also included in the mesh. According to Melro et al. [299], the wedge elements have no influence in the meso-mechanical behaviour of the composite. Abaqus C3D8R elements are also used to generate the mesh of the homogenised outer plies. For the interface between fibres and matrix and for the interface between the mid-90° ply and the adjacent homogenised plies, 8-node cohesive elements (Abaqus COH3D8) are used. Figure 6.6 shows a representative FE discretisation of part of an RVE with a 0.040 mm thick 90° intermediate ply.

6.3.2. Loading and boundary conditions

PBCs are applied to the thin-ply sublaminate RVEs in the x- and y-directions. Although it is recognised that the use of this type of boundary conditions may affect the damage pattern results [299], and that additional studies have to be conducted to assess its impact, it is considered that the appropriate definition of boundary conditions in RVE-based modelling is outside the scope of the present work.

The imposition of PBCs in the Finite Element Analysis (FEA) follows Melro et al. [299]. Linear multi-point constraints are used, i.e., kinematic constraints imposed on the degrees of freedom of each pair of nodes belonging to opposite faces, edges or vertices of the RVE. These equations include the corresponding degrees of freedom, as well as the far-field applied strains. Depending on the nodes position — faces, edges or vertices — a different set of equations is applied to their degrees of freedom to solve compatibility issues between different kinematic constraints [299].

The effect of residual thermal stresses is not taken into account, since the focus of the present study is on the effect of ply thickness on the mechanical response of constrained transverse plies for validation of the theory and current analytical models for the *in situ* effect. The rationale followed here is consistent with the use of the *in situ* strengths in models of homogenised composite materials. In such models, the *in situ* strength is taken as a material and geometrical property and the different residual stresses resulting from different ply thickness are calculated from a stress analysis model. Therefore, including residual stresses in the micro-mechanical models could not allow a comparison between these models and the simple, closed-form solutions for the *in situ* effect.

6.4. Results

To validate the present framework, figure 6.7 shows the strain field along the transverse (y-) direction of an RVE with a 0.080 mm thick 90° ply subjected to transverse compression. It is noted that the present micro-mechanical simulations fully agree with the experimental observations carried out by Canal et al. [306], who have shown, by analysing the shape and intensity of the probability density functions for each constituent, that fibres are characterised by a very homogeneous

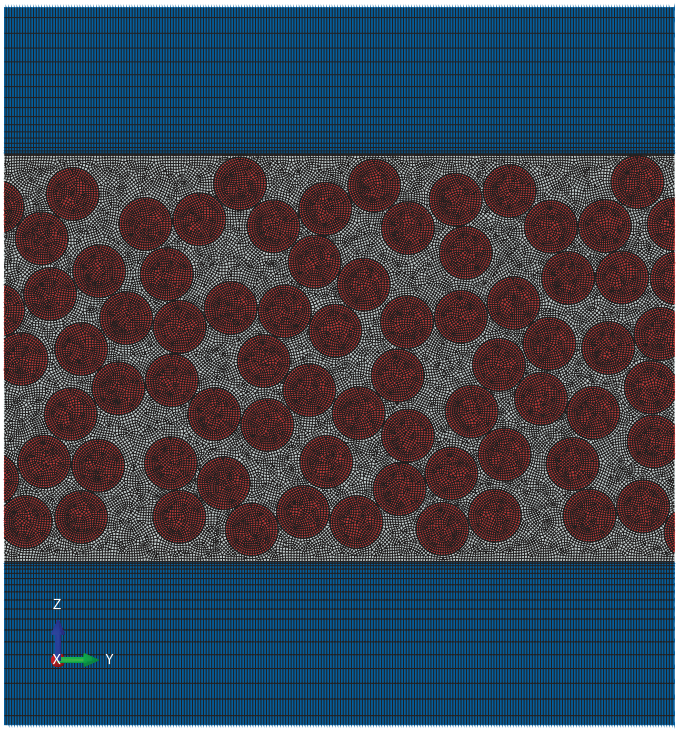

Fig. 6.6. Representative FE model of part of an RVE with a 0.040 mm thick transverse ply.

strain field, whereas the matrix shows a very inhomogeneous strain distribution. This preliminary result, together with the analysis carried out by Melro et al. [299], show the validity of the present framework in assessing the micro-mechanical response of polymer composite laminates.

6.4.1. Transverse tension

6.4.1.1. Transverse cracking

Figures 6.8 to 6.11 show the contour plots of the matrix damage variable on representative RVEs of 90° laminae with thicknesses between 0.020 mm and 0.080 mm at applied remote strains ranging from 0.6% to 2.0%. Only sublaminates with 0° outer plies are considered. Figure 6.12 shows the contour plots of the equivalent plastic strain in the matrix at an applied remote strain of 2.0%. Although only one random distribution of fibres is presented for each case, it is representative of other random distributions in terms of damage localisation.

As expected, a crack develops perpendicularly to the applied load (see figures 6.8 to 6.11). Similarly to what was observed experimentally from *in situ* observations [35] (and confirmed numerically in Ref. [38]), damage starts in the narrower portions of matrix between the closest adjacent fibres aligned with the loading direction at approximately the same applied remote strain (in the present case between 0.56% and 0.58%), first as fibre-matrix decohesions, then followed by matrix cracking. Even though not clear in figure 6.8a, due to the reduced COD, for an applied remote strain of 0.6%, fibre-matrix decohesion has also occurred in the thinner 0.020 mm thick transverse ply. This can be seen in more detail in figure 6.13, which shows the damage variable of the cohesive elements in the interface between fibre and matrix in a detail of the RVE with a 0.020 mm thick ply.

The *in situ* observations presented in Ref. [35] also showed that, for the thicker 90° plies, once a transverse crack is formed, it rapidly penetrates through the thickness. This was also observed in the present simulations, as shown in figures 6.14 to 6.16 for more conventional transverse ply thicknesses. As discussed in section 6.3.1, it is noted that, due to the enormous computational cost of these models, the sublaminate RVEs with transverse ply thicknesses above or equal to 0.100 mm were modelled to accommodate a single transverse crack (as in Ref. [38], for instance), with a reduction of

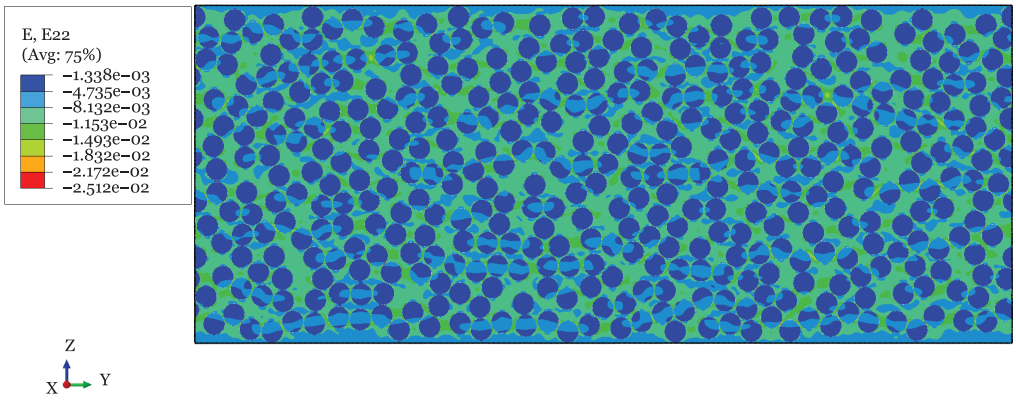

Fig. 6.7. Strain distribution along the transverse (y-) direction of an RVE with a 0.080 mm thick 90° ply subjected to transverse compression, at an applied remote strain of 0.66%.

the total width of the RVEs when compared to the thin-ply sublaminates. Nevertheless, even though the models for the thicker RVEs shown in figures 6.14 to 6.16 may not be completely representative in terms of damage progression after full extension of the first (single) transverse crack, they are useful in showing the differences in terms of damage evolution in a first stage of transverse crack propagation.

In the case of the thinner transverse plies, crack extension reportedly slows down with increasing applied remote strain [35]. In the numerical simulations presented in this work, the same trend is observed (compare, for example, figures 6.9 and 6.11 and the experimental observations reported in Ref. [35]). This becomes even more clear observing figure 6.17, showing the normalised crack length, obtained dividing the length of the transverse crack by the 90° ply thickness, as a function of the applied remote strain. The length of the transverse crack is given by the base distance between the nodes in the tips of the longer transverse crack in the RVE. The numerical results for a representative random distribution of sublaminate RVEs with 0.020 mm, 0.080 mm and 0.140 mm thick transverse plies are shown.

As reported by Saito et al. [35], for the thickest transverse laminae, the sudden matrix crack extension leads to stress relaxation, whereas thinner transverse laminae show a gradual extension of the transverse cracks, eventually without completely penetrating through the thickness (see figure 6.17 and section 6.4.1.2). Therefore, stress relaxation is much more difficult in the case of thinner transverse laminae.

Figures 6.18 and 6.19 show the transverse stress field (σ_{22}) in cracked 0.020 mm and 0.080 mm thick 90° plies, obtained from the proposed micro-mechanical models. As discussed in Ref. [35], a higher stress field in the thinner transverse laminae (figure 6.18) results in an increase of the crack density of the thinner plies, as can be observed in figures 6.8 to 6.11. It is noted that, as reported in the literature [87], the maximum crack density typically corresponds to a crack spacing of the order of the transverse ply thickness.

The ability of the proposed micro-mechanical models to predict the gradual, slow stress relaxation and progressive transverse cracking in thin and ultra-thin plies can also be observed analysing the homogenised stress-strain curves of the embedded 90° ply shown in figure 6.20 for the different sublaminate RVEs. The results for only one representative sublaminate RVE per 90° ply thickness were plotted, to facilitate the analysis. Volumetric homogenisation was performed to obtain the homogenised stress-strain curves [299]:

$$\sigma_{ij}^{0} = \frac{1}{V}\int_{V}\sigma_{ij}\mathrm{d}V = \frac{1}{V}\sum_{k=1}^{N_p}\sigma_{ij}^{k}V^{k} \tag{6.5}$$

where σ_{ij}^{0} is the homogenised stress component, σ_{ij}^{k} and V^{k} are, respectively, the stress component determined at integration point k and associated volume, and N_p is the total number of integration points in the RVE. It is noted that, after

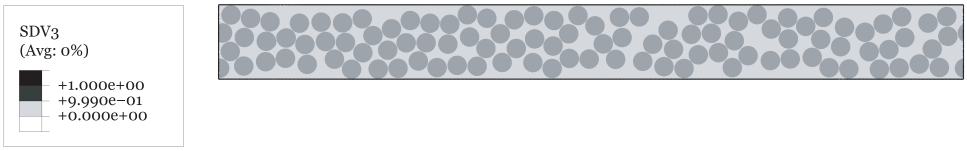

(a) Applied remote strain of 0.6%.

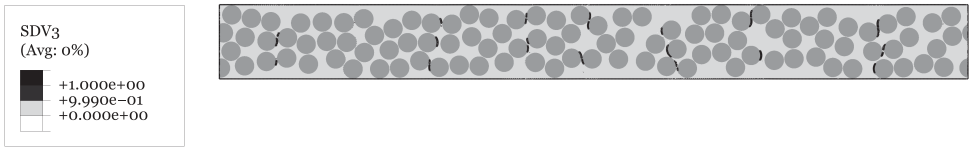

(b) Applied remote strain of 1.2%.

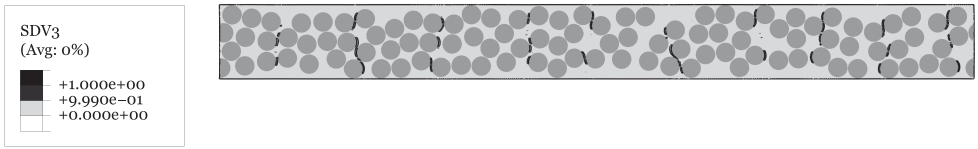

(c) Applied remote strain of 2.0%.

Fig. 6.8. Contour plots of the matrix damage variable on a representative RVE of a 0.020 mm thick 90° lamina of a sublaminate with 0° outer plies (only the 90° lamina is presented).

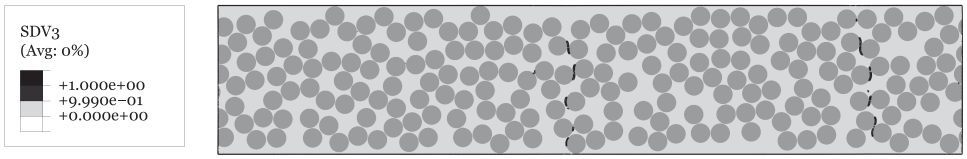

(a) Applied remote strain of 0.6%.

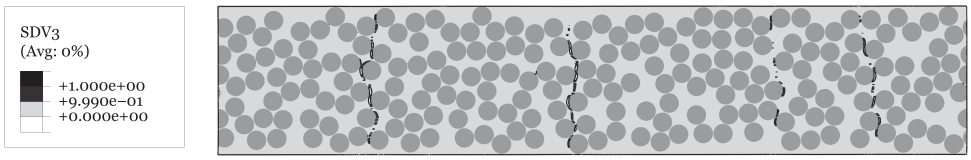

(b) Applied remote strain of 1.2%.

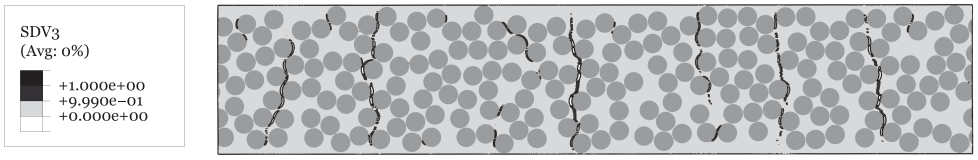

(c) Applied remote strain of 2.0%.

Fig. 6.9. Contour plots of the matrix damage variable on a representative RVE of a 0.040 mm thick 90° lamina of a sublaminate with 0° outer plies (only the 90° lamina is presented).

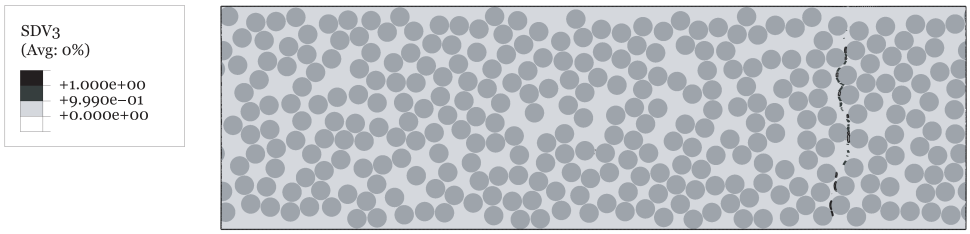

(a) Applied remote strain of 0.6%.

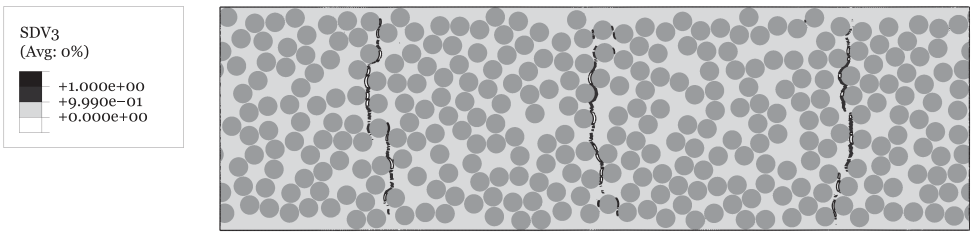

(b) Applied remote strain of 1.2%.

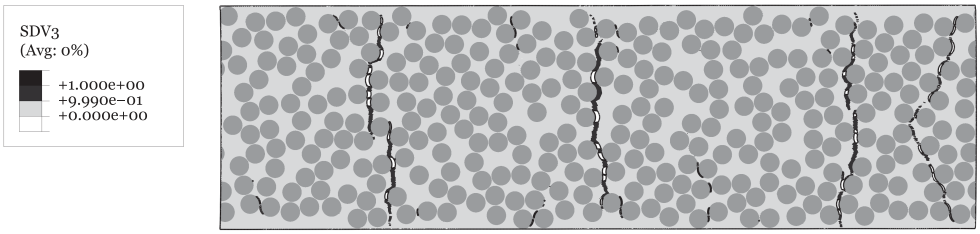

(c) Applied remote strain of 2.0%.

Fig. 6.10. Contour plots of the matrix damage variable on a representative RVE of a 0.060 mm thick 90° lamina of a sublaminate with 0° outer plies (only the 90° lamina is presented).

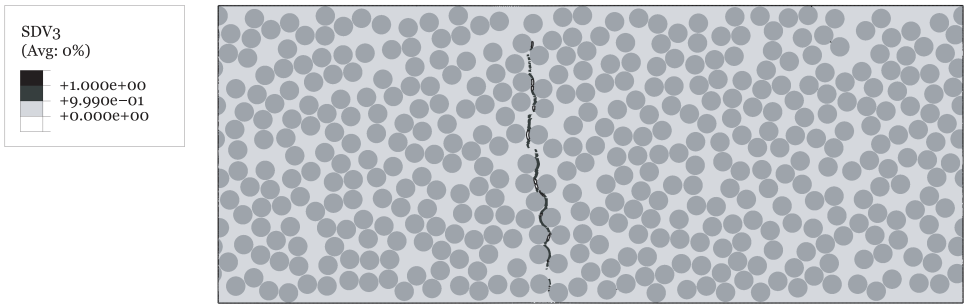

(a) Applied remote strain of 0.6%.

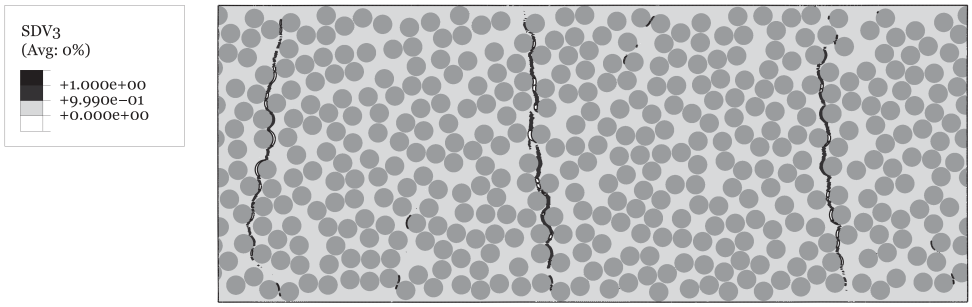

(b) Applied remote strain of 1.2%.

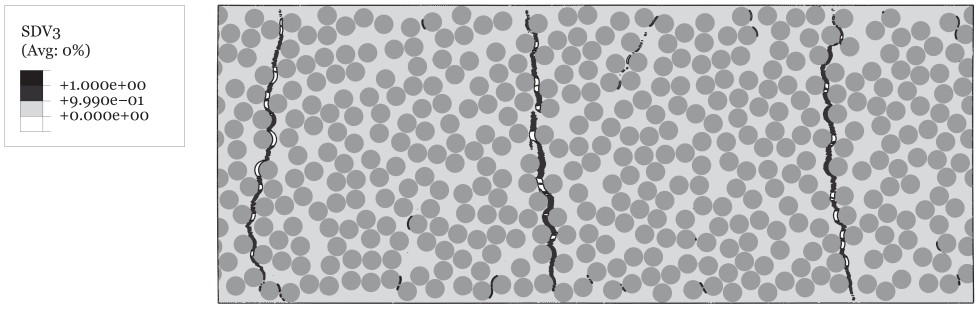

(c) Applied remote strain of 2.0%.

Fig. 6.11. Contour plots of the matrix damage variable on a representative RVE of a 0.080 mm thick 90° lamina of a sublaminate with 0° outer plies (only the 90° lamina is presented).

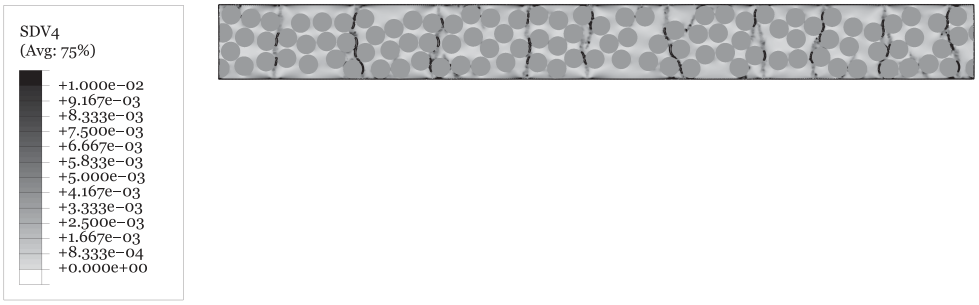

(a) 0.020 mm thick transverse ply.

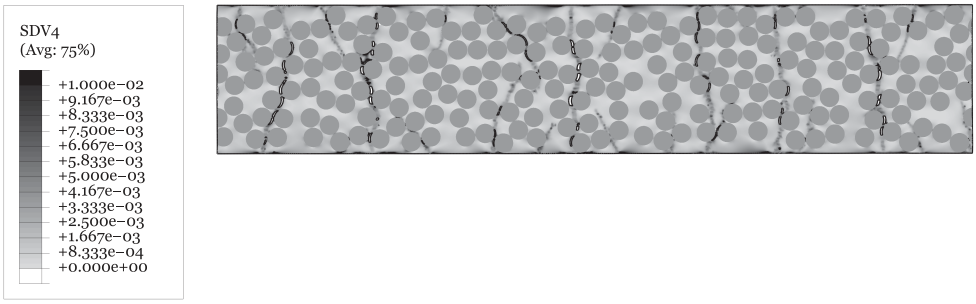

(b) 0.040 mm thick transverse ply.

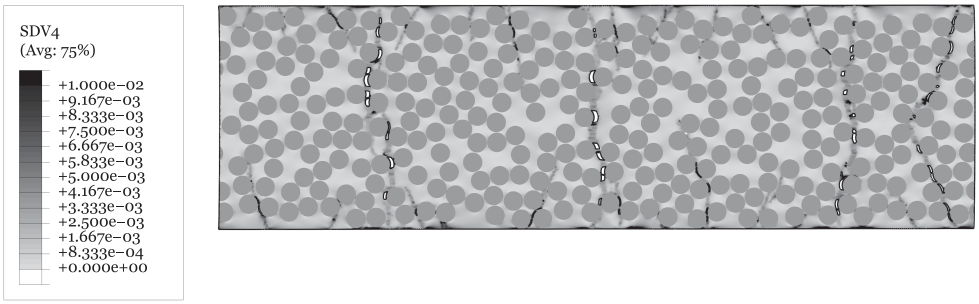

(c) 0.060 mm thick transverse ply.

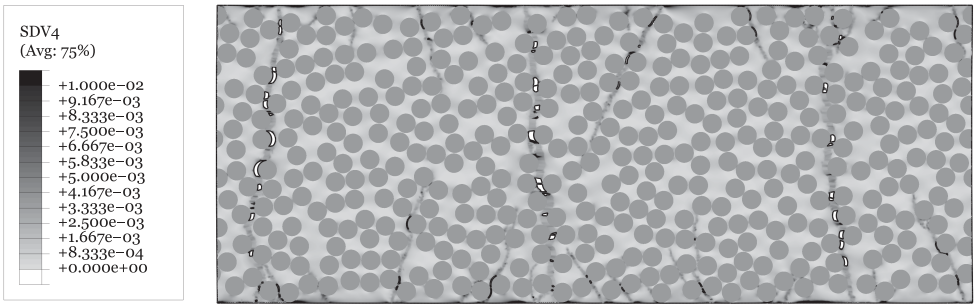

(d) 0.080 mm thick transverse ply.

Fig. 6.12. Contour plots of the equivalent plastic strain in the matrix of representative RVEs of 90° laminae on thin-ply sublaminates with 0° outer plies, at an applied remote strain of 2.0% (only the 90° laminae are presented).

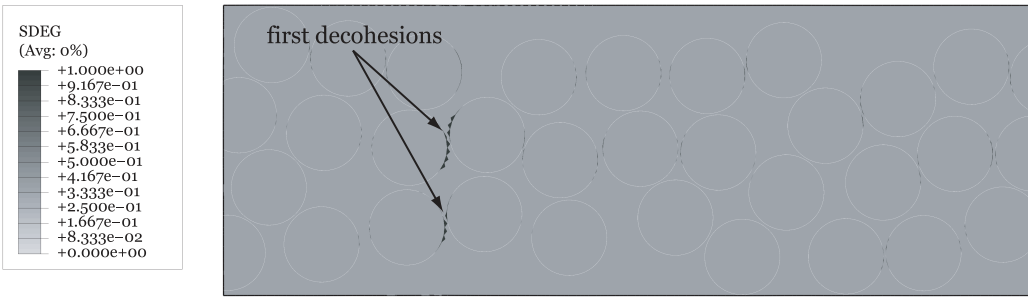

Fig. 6.13. Damage variable of the cohesive elements representing the interface between fibre and matrix in a detail of the 0.020 mm thick ply RVE at an applied remote strain of 0.6%.

the onset of damage, which occurs approximately at the same applied remote strain (as observed elsewhere [35, 38]), softening is more gradual for thinner transverse plies. In other words, as the 90° ply thickness increases, the discrete drops of the homogenised stress caused by discrete through-the-thickness transverse damage growth become larger and more spaced. These larger drops of the homogenised stress are associated with more unstable transverse damage growth through the thickness of the 90° ply, which occurs in larger discrete jumps (figures 6.8 to 6.11 and 6.17).

The discrete drops of the homogenised stress in the 90° ply (figure 6.20) are related to stress relaxation caused by transverse damage growth, with the extra load being transferred to the adjacent 0° plies. It is interesting to note that, as the applied remote strain increases, the homogenised stress level in thinner plies is consistently higher than in thicker plies, showing that lower stress relaxation occurs in the former, as observed in figures 6.18 and 6.19.

For more conventional ply thicknesses, above 0.100 mm, this progressive softening behaviour is not observed, and the appearance of the first crack generally corresponds to first-ply-failure (large drop of the homogenised stress in the 90° ply). However, as stressed earlier in this section, the sublaminate RVEs with the thickest transverse plies, due to the reduced size of the RVE justified by limitations in computational power, may not be completely representative in terms of damage progression after full extension of the first transverse crack, reason why the homogenised stress-strain curves are not shown in figure 6.20 for those cases. Nonetheless, the same trends can be expected.

These results (figure 6.18 to 6.20) are also useful in understanding how transverse cracking can be detrimental to the integrity of a laminate with thick transverse plies, and how thin plies can improve the performance of the load carrying plies aligned with the loading direction. In fact, once transverse damage initiates in a thick ply, it quickly penetrates through the thickness (e.g. figure 6.17), resulting in high local stress relaxation in the 90° ply, and consequently in a local stress concentration at the adjacent (load carrying) plies, promoting early failure of the latter. By reducing the 90° ply thickness, transverse damage growth is suppressed, resulting in low stress relaxation, and consequently in a lower stress concentration at the adjacent plies, pushing their longitudinal performance closer to that of the UD lamina.

Figures 6.9 to 6.12, specially the latter, also show that, for the particular material properties of the constituents employed in the present work, and except for the thinner 0.020 mm thick 90° ply, once through-the-thickness transverse cracking has saturated, damage localisation occurs close to the straight transverse cracks, starting near the interface between the mid-90° ply and the surrounding constraining plies. These oblique cracks, also observed experimentally for very thick transverse plies [125], are not perpendicular to the loading direction and propagate towards the straight transverse cracks, without joining them. This simulations have also shown that the oblique cracks typically do not penetrate through the ply thickness, except when joining with oblique cracks growing in the opposite direction in sufficiently thin plies, as can be observed in figure 6.21.

Another very interesting finding reported by Saito et al. [35] and also observed in the present simulations is related with the COD of the transverse cracks in 90° plies of different thicknesses. As observed experimentally [35], due to the constraining effect imposed by the adjacent 0° plies, the COD in thinner 90° plies (figures 6.8 to 6.11) is much smaller than observed in the thicker 90° plies (figures 6.14 to 6.16).

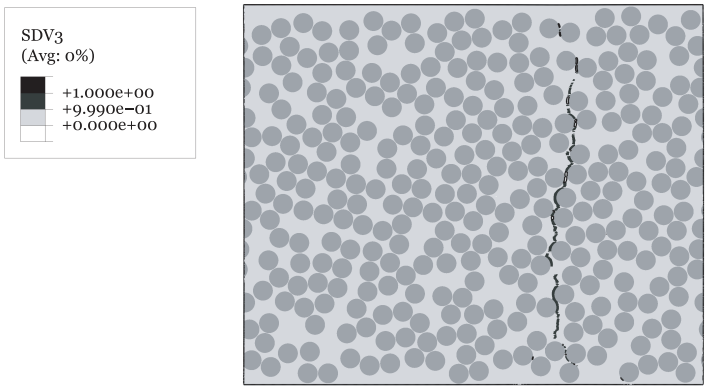

(a) Applied remote strain of 0.6%.

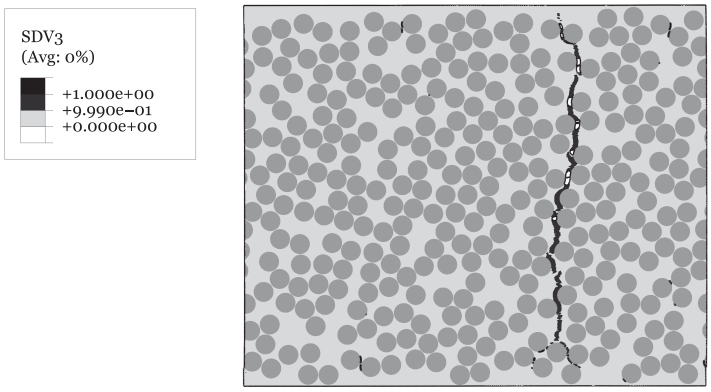

(b) Applied remote strain of 1.2%.

Fig. 6.14. Contour plots of the matrix damage variable on a representative RVE of a 0.100 mm thick 90° lamina of a sublaminate with 0° outer plies (only the 90° lamina is presented).

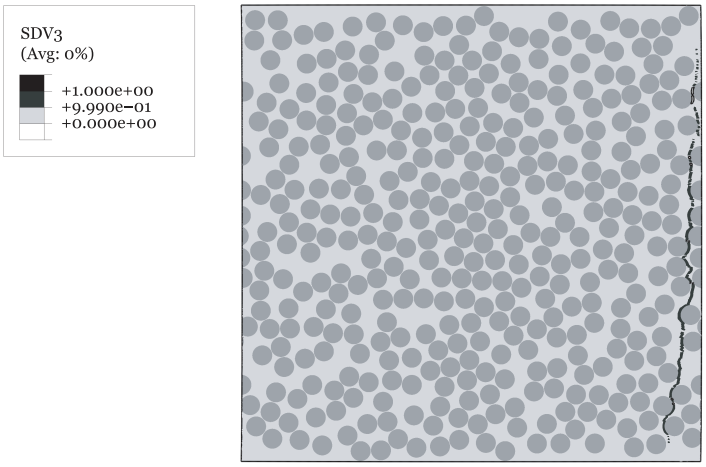

(a) Applied remote strain of 0.6%.

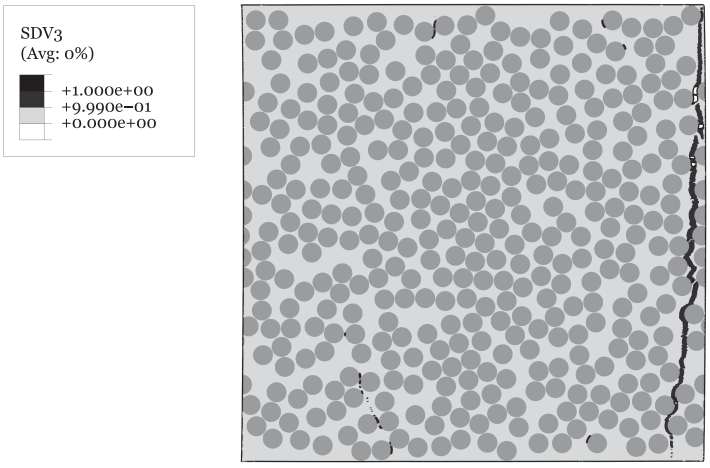

(b) Applied remote strain of 1.2%.

Fig. 6.15. Contour plots of the matrix damage variable on a representative RVE of a 0.120 mm thick 90° lamina of a sublaminate with 0° outer plies (only the 90° lamina is presented).

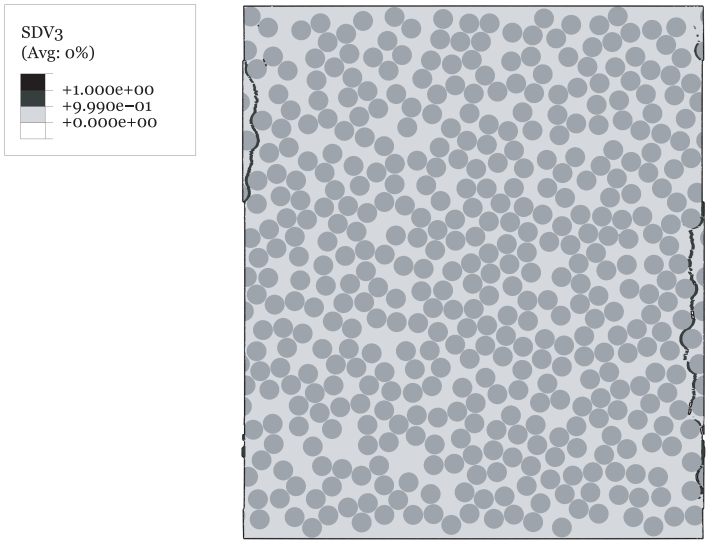

(a) Applied remote strain of 0.6%.

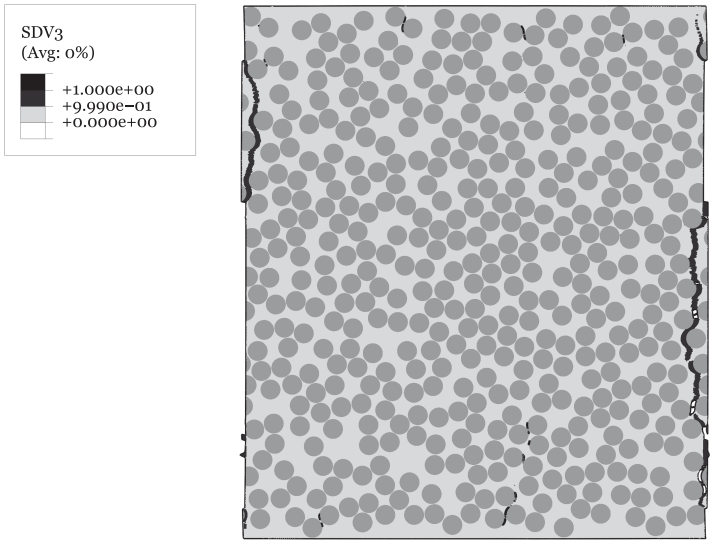

(b) Applied remote strain of 1.2%.

Fig. 6.16. Contour plots of the matrix damage variable on a representative RVE of a 0.140 mm thick 90° lamina of a sublaminate with 0° outer plies (only the 90° lamina is presented).

Figure 6.22 shows the COD as a function of the applied remote strain for sublaminate RVEs with 0.020 mm, 0.080 mm and 0.140 mm thick transverse plies. The COD is determined as the higher relative displacement between adjacent nodes in the surface of a transverse crack. Only one representative random distribution per sublaminate RVE is considered to facilitate the analysis. Similar trends to those reported in Ref. [35] can be observed.

Another interesting result of the numerical simulations, also confirmed by experimental evidence, is the formation of thin necks of matrix material around the regions where interfacial damage is more pronounced. This micro-scale damage mechanism was also reported in the numerical analyses presented by Melro et al. [299]. The *in situ* observations presented by Saito et al. [35] suggest that this phenomenon is potentiated by increasing ply thicknesses, since it could barely be seen in the thinnest 0.040 mm thick 90° plies, an effect also captured in the present simulations, as shown in figure 6.12. For a comparison with more conventional ply thicknesses, see also figure 6.23.

6.4.1.2. Mechanics of ultra-thin plies

Figures 6.24 and 6.25 show the contour plots of the matrix damage variable on representative RVEs with 0.020 mm and 0.040 mm thick 90° laminae at increasingly higher applied remote strains. As can be observed, for these ply thicknesses, transverse failure can be described as a distributed damage mechanism. In the case of 0.040 mm thick 90° plies, as shown in figure 6.25, transverse fracture is characterised by progressive fragmentation and multiple cracking, with reduced spacing between transverse cracks, followed by additional decohesions as onset sites for the development of oblique cracking close to the interface with the constraining plies. By reducing further the thickness of the 90° laminae, as can be observed in figure 6.24 for a 0.020 mm thick ply, damage is characterised by many decohesions occurring without extending completely through the ply thickness, similar to a continuous damage event, and leading to overall failure of the matrix material between the fibres before development of transverse cracking, as shown in figure 6.24c and d.

Even though it is recognised that this dispersed/non-localised matrix failure, observed on the thinnest, 0.020 mm thick 90° laminae, can be a purely numerical feature, as it may not be totally realistic, this result is important in showing that, at the mesoscopic scale, failure of these very thin plies can be accurately represented by conventional continuum damage mechanics frameworks, without the need to address discrete cracking as in smeared crack or discrete damage formulations. It is also important to note that the experimental observation of post-failure behaviour of embedded ultra-thin plies may not be possible, as the applied remote strains needed to cause these mechanisms (e.g. figure 6.24) may certainly exceed the failure strain of the adjacent material that imposes the constraining effect on these plies.

Moreover, it is interesting to note that this constraining effect also has its own importance on the failure and post-failure behaviour of embedded ultra-thin plies. Figures 6.26 and 6.27 show the contour plots of the matrix damage variable on RVEs with 0.020 mm thick 90° laminae with ±45° and 90° IM7/8552 outer plies, respectively. As can be observed in figures 6.24, 6.26 and 6.27, as the stiffness of the outer plies decreases, by this order, transverse crack growth through the

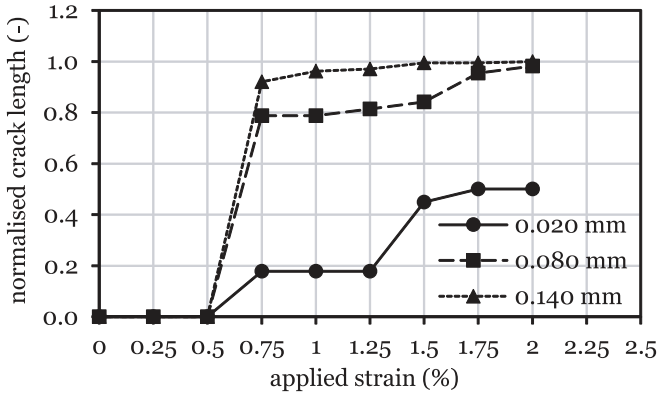

Fig. 6.17. Normalised crack length as a function of applied remote strain for sublaminate RVEs with 0.020 mm, 0.080 mm and 0.140 mm thick transverse plies.

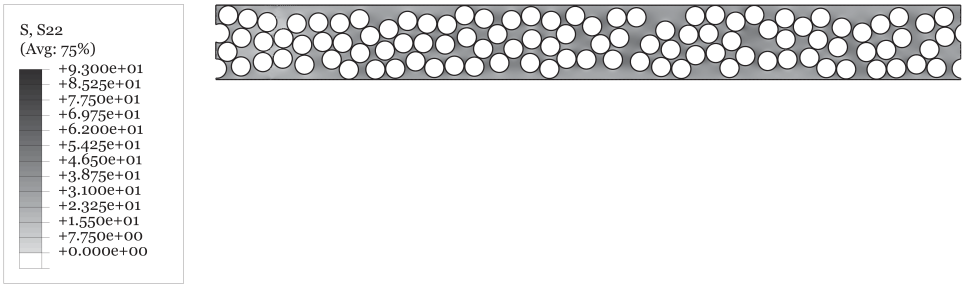

(a) Applied remote strain of 0.6%.

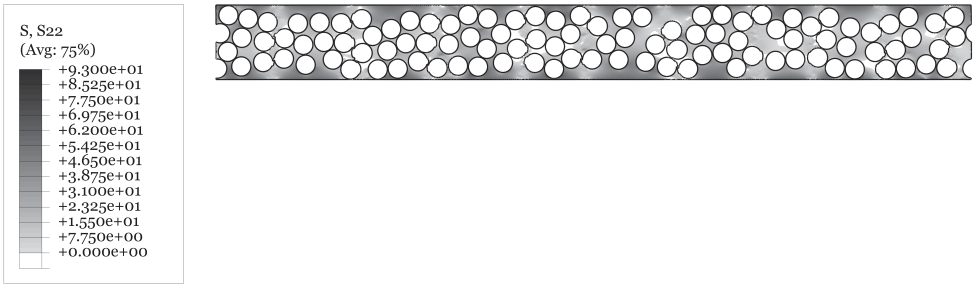

(b) Applied remote strain of 2.0%.

Fig. 6.18. Transverse stress field (σ_{22}) in a cracked 0.020 mm thick 90° ply of a sublaminate with 0° outer plies (only the matrix material of the 90° ply is presented).

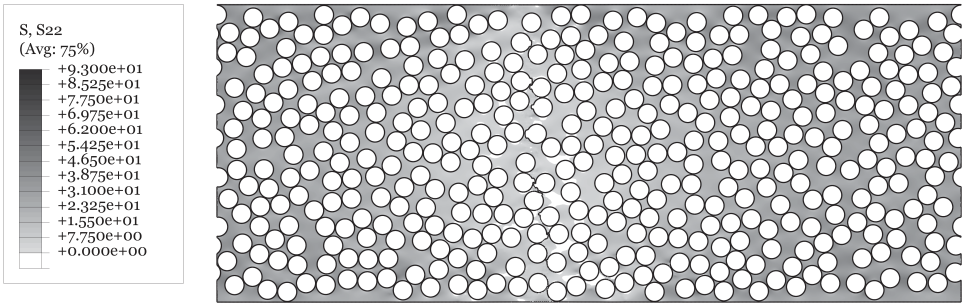

(a) Applied remote strain of 0.6%.

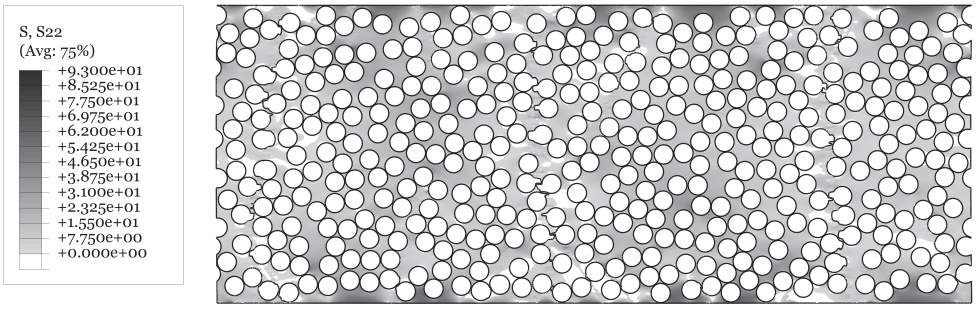

(b) Applied remote strain of 2.0%.

Fig. 6.19. Transverse stress field (σ_{22}) in a cracked 0.080 mm thick 90° ply of a sublaminate with 0° outer plies (only the matrix material of the 90° ply is presented).

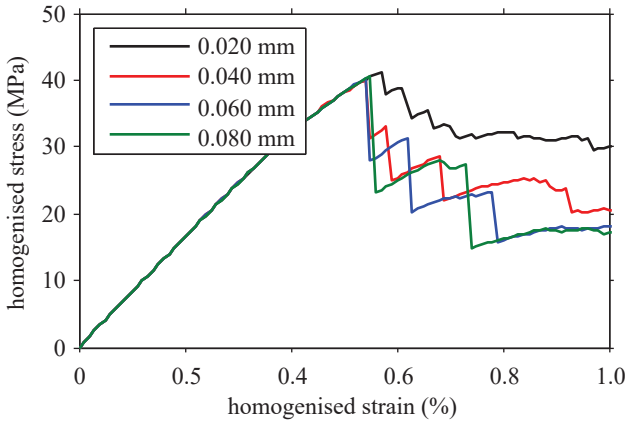

Fig. 6.20. Homogenised stress-strain curves of the embedded 90° ply for sublaminates with 0° outer plies.

ply thickness becomes easier (lower constraining effect), and damage tends to localise, as observed on RVEs with thicker transverse plies (e.g. figure 6.25).

The critical ply thickness below which damage localisation does not occur anymore, giving rise to a dispersed/non-localised matrix failure (figure 6.24d), apparently depends on the constraining imposed by the adjacent plies (i.e., on the stiffness of the adjacent material). In fact, the constraining effect imposed to an embedded ply depends on its thickness and on the stiffness of the adjacent material; the thinner the ply and the stiffer the adjacent material, the higher this constraining effect is (figure 2.5). Hence, as the stiffness of the adjacent material decreases, the critical ply thickness at which the post-failure behaviour changes also decreases.

6.4.1.3. *In situ* effect

Figure 6.28 shows the *in situ* transverse tensile strength as a function of the ply thickness determined from the micro-mechanical models presented in this work. These *in situ* strengths are calculated from the applied remote strain corresponding to the development of a damage localisation zone (for a value of the damage variable greater than 0.99) through the thickness of the 90° ply before the onset of secondary failure mechanisms (such as interlaminar damage localisation, oblique cracking or dispersed/non-localised matrix failure) and from the elastic properties determined from a linear-elastic analysis of the same RVE. Figure 6.28 also shows the predictions of the *in situ* transverse tensile strength calculated using the fracture mechanics model proposed by Camanho et al. [81]:

$$Y_T^{is} = 1.12\sqrt{2}Y_T \tag{6.6}$$

for a thick ply, or:

$$Y_T^{is} = \sqrt{\frac{8\mathcal{G}_{Ic}}{\pi b \Lambda_{22}^0}} \tag{6.7}$$

for a thin embedded ply [81]. The strength and elastic properties required by the analytical model were determined from a separate run of the micro-mechanical model using UD RVEs, as in Melro et al. [299] (table 6.7). As a first approximation, the fracture toughness associated with intralaminar fracture of the transverse ply (parallel to the fibre direction) was taken as 25% of the fracture toughness of the matrix. Although, at this stage, comparing the results from both models can only be seen as a qualitative analysis, the same trends have been obtained, emphasising the validity of the analytical and computational micro-mechanics representations.

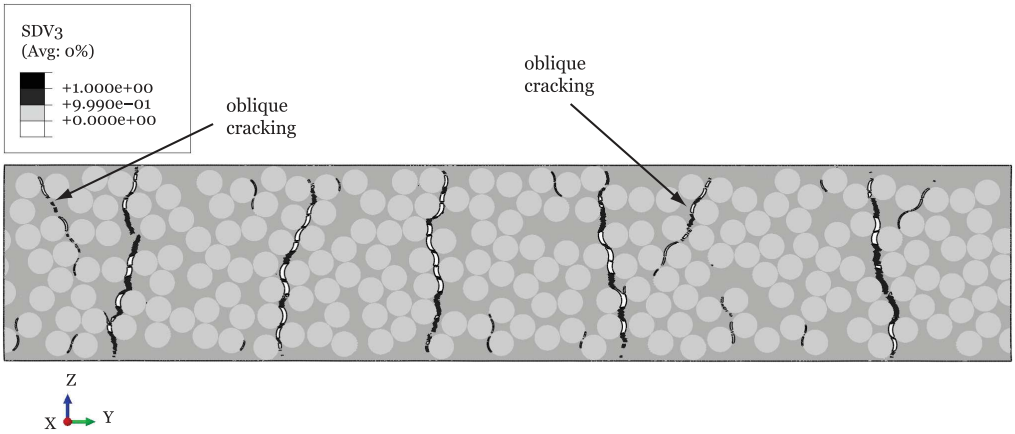

(a) Applied remote strain of 3.0%.

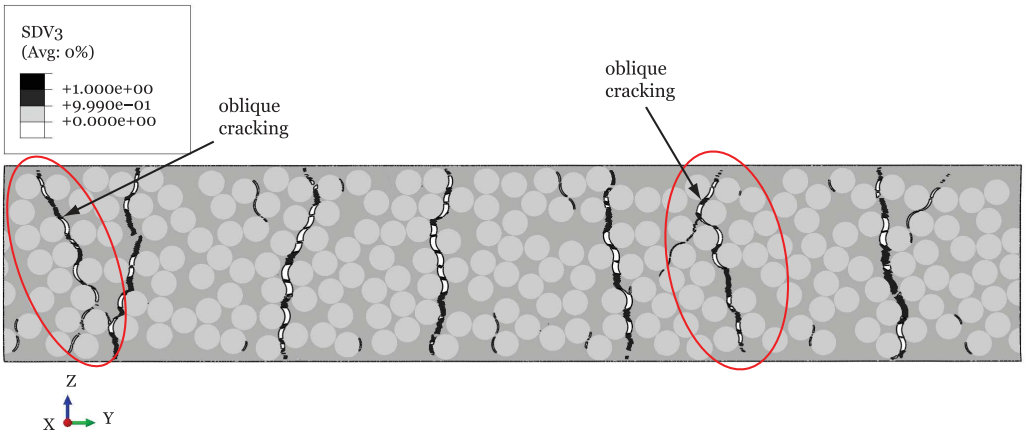

(b) Applied remote strain of 4.0%.

Fig. 6.21. Oblique cracking captured by the micro-mechanical analysis of a representative RVE of a 0.040 mm thick 90° lamina in a sublaminate with 0° outer plies (only the 90° lamina is presented).

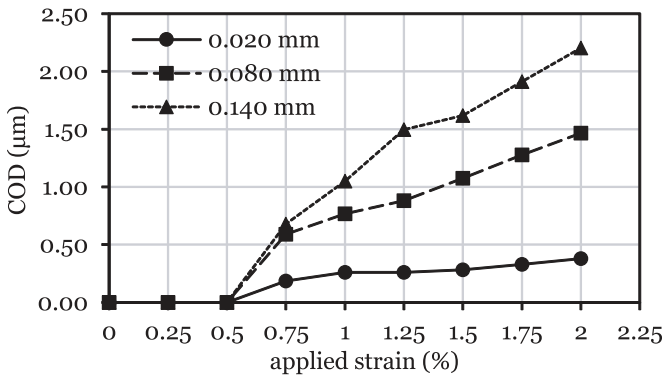

Fig. 6.22. COD as a function of applied remote strain for representative RVEs with 0.020 mm, 0.080 mm and 0.140 mm thick 90° laminae in a sublaminate with 0° outer plies.

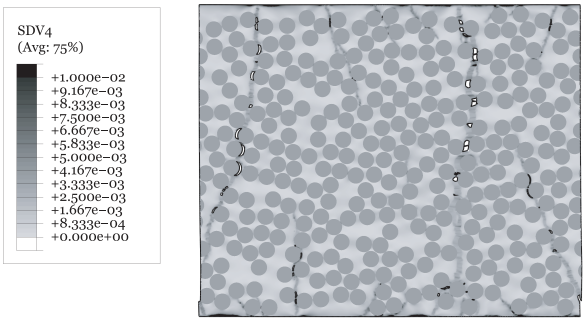

(a) 0.100 mm thick transverse ply.

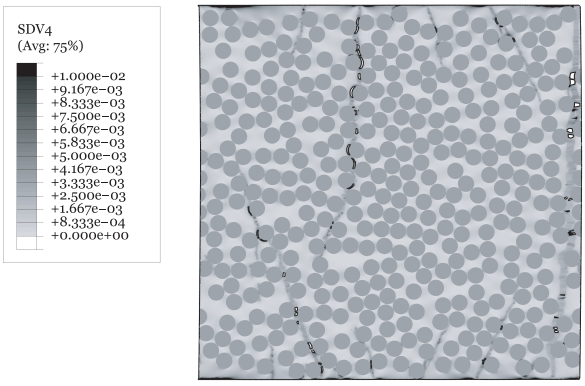

(b) 0.120 mm thick transverse ply.

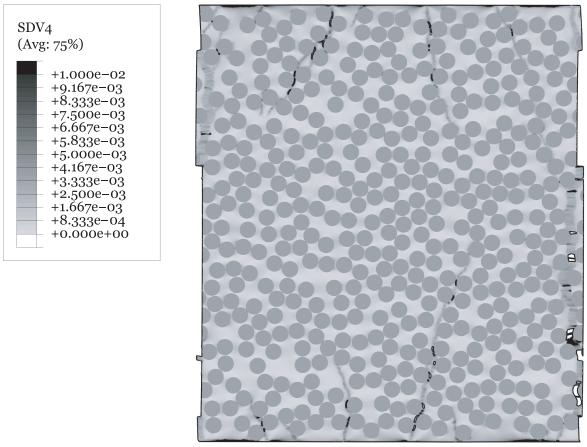

(c) 0.140 mm thick transverse ply.

Fig. 6.23. Contour plots of the equivalent plastic strain in the matrix of representative RVEs of 90° laminae in sublaminates with 0° outer plies, at an applied remote strain of 2.0% (only the 90° laminae are presented).

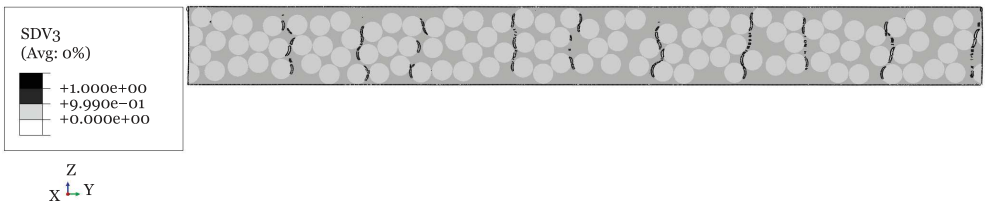

(a) Applied remote strain of 2.6%.

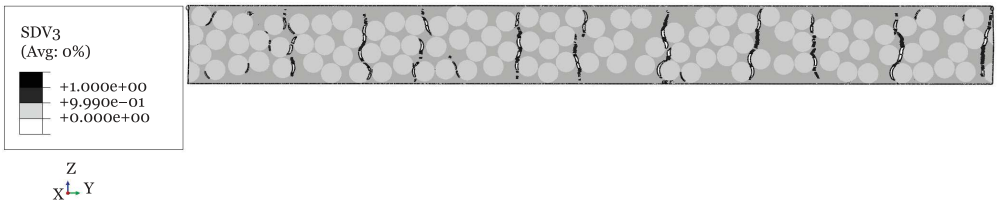

(b) Applied remote strain of 4.0%.

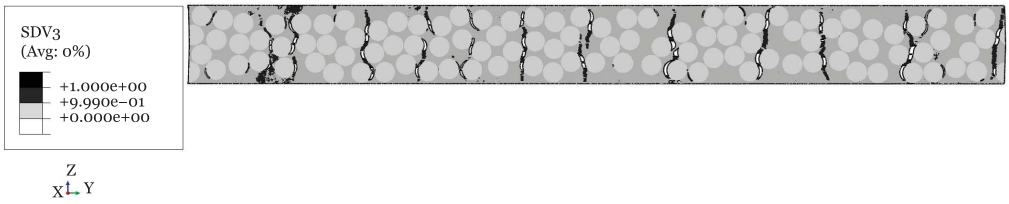

(c) Applied remote strain of 5.5%.

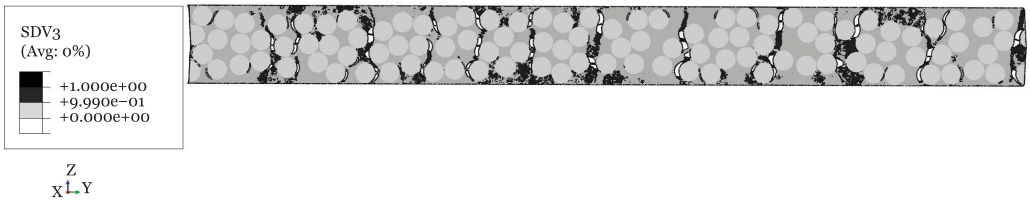

(d) Applied remote strain of 8.0%.

Fig. 6.24. Contour plots of the matrix damage variable on a representative RVE of a 0.020 mm thick 90° lamina of a sublaminate with 0° outer plies, and damage growth after matrix cracking (only the 90° lamina is presented).

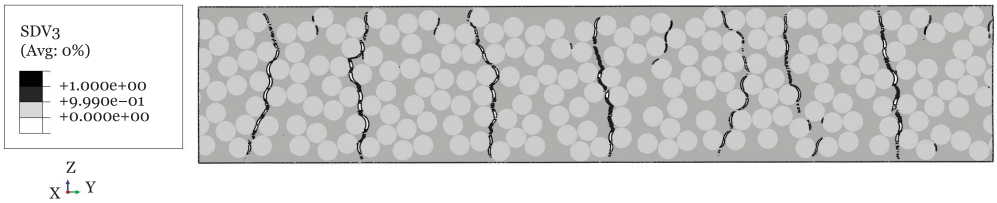

(a) Applied remote strain of 2.6%.

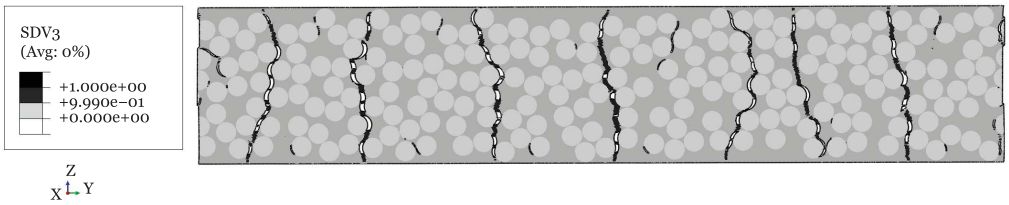

(b) Applied remote strain of 4.0%.

Fig. 6.25. Contour plots of the matrix damage variable on a representative RVE of a 0.040 mm thick 90° lamina of a sublaminate with 0° outer plies, and damage growth after matrix cracking (only the 90° lamina is presented).

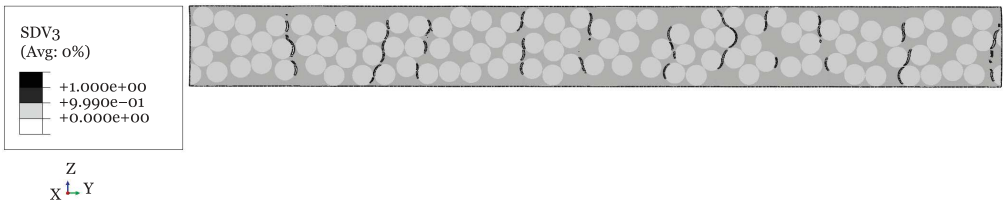

(a) Applied remote strain of 2.6%.

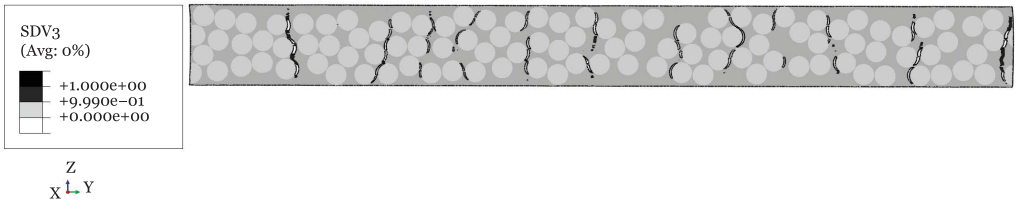

(b) Applied remote strain of 4.0%.

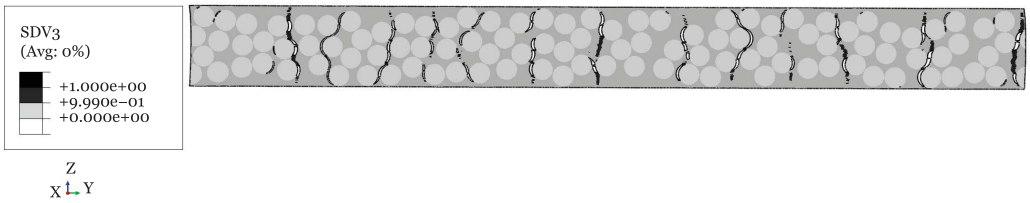

(c) Applied remote strain of 5.5%.

Fig. 6.26. Contour plots of the matrix damage variable on a representative RVE of a 0.020 mm thick 90° lamina of a sublaminate with ±45° IM7/8552 outer plies (only the embedded 90° lamina is presented).

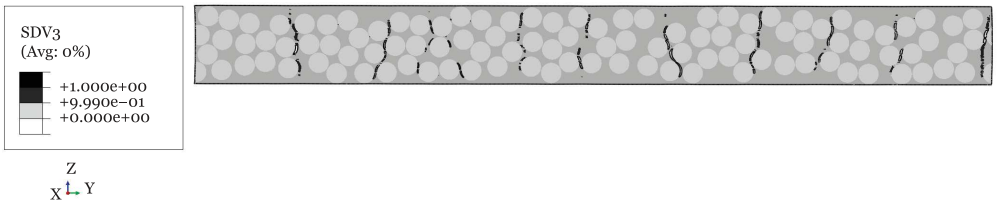

(a) Applied remote strain of 2.6%.

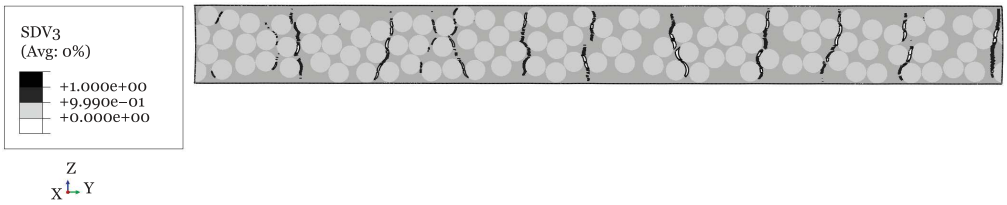

(b) Applied remote strain of 4.0%.

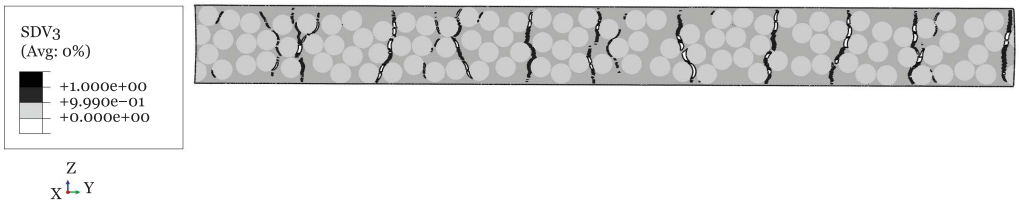

(c) Applied remote strain of 5.5%.

Fig. 6.27. Contour plots of the matrix damage variable on a representative RVE of a 0.020 mm thick 90° lamina of a sublaminate with 90° IM7/8552 outer plies (only the embedded 90° lamina is presented).

Table 6.7
UD properties determined from a separate run of the micro-mechanical model using UD RVEs (e.g. Ref. [299]).

Material property	Value
Elastic properties	
E_{11} (MPa)	152570
E_{22} (MPa)	8238
G_{12} (MPa)	4026
ν_{12} (-)	0.27
Strength properties	
Y_T (MPa)	37.3
Y_{BT} (MPa)	23.2
Y_C (MPa)	147.9
Y_{BC} (MPa)	349.9
S_T (MPa)	34.1
S_L (MPa)	61.7
Critical energy release rate	
$\mathcal{G}_{Ic}$ (N/mm)	0.069
$\mathcal{G}_{IIc}$ (N/mm)	0.139
Shear nonlinearity	
β (MPa^{-3})	3×10^{-8}
Fracture angle	
α_0 (°)	53
Friction coefficient	
η_L (-)	0.317

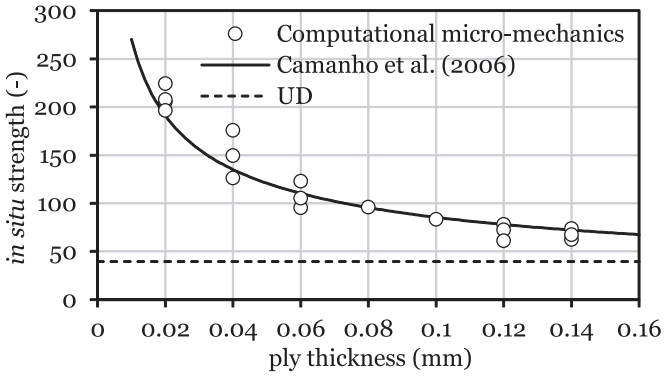

Fig. 6.28. *In situ* transverse tensile strength as a function of ply thickness.

The fact that the trends of the analytical and computational micro-mechanics models (figure 6.28) are in reasonable agreement not only for the thin-ply range (below 0.100 mm thick plies), but also for ply thicknesses above 0.100 mm, shows that the 0.120 mm wide RVEs, defined for the models with thicker plies to accommodate approximately a single transverse crack, were sufficiently accurate to capture the *in situ* effect and the underlying mechanisms for such ply thicknesses, validating the proposed approach. This observation also shows that these models may not benefit from a wider RVE, as suggested in section 6.3.1, due to the limited amount of diffuse damage before transverse crack growth through the thickness. The same conclusions will be obtained for the analysis of the *in situ* effect in transverse compression in section 6.4.2.

6.4.2. Transverse compression

Figures 6.29 to 6.33 show the contour plots of the equivalent plastic strain in the matrix of representative RVEs with ultra-thin and conventional 90° plies at applied remote strains of 2.0% and 2.5%. Only sublaminates with 0° outer plies have been considered.

As can be observed in figures 6.32 and 6.33 for cross-ply sublaminates with conventional 90° plies, failure caused by transverse compressive loading is dominated by fibre-matrix interface cracking and large localised plastic deformation of the matrix, forming a localised band of damage in a plane not aligned with the loading direction. This wedge shaped transverse fracture is in agreement with what has been described in the literature [102, 299] for the UD case. In the case of cross-ply sublaminates with ultra-thin plies, a similar damage pattern can be identified, but developing at higher applied remote strains, as shown in figures 6.29 to 6.31. In fact, looking at these figures, and comparing them with figures 6.32 and 6.33, a transverse crack suppression effect can be clearly identified. As the ply thickness decreases, damage progression becomes more and more gradual, and through-the-thickness transverse fracture is delayed. This fact indicates that there is an *in situ* effect in transverse compression; to the authors knowledge, it is the first time an *in situ* effect in transverse compression and its underlying mechanisms have been identified.

Figures 6.34 to 6.36 show the contour plots of the equivalent plastic strain in the matrix of representative RVEs with 0.020 mm, 0.040 mm and 0.060 mm thick 90° plies at applied remote strains ranging from 3.0% to 4.0%. Unlike conventional 90° plies subjected to transverse compressive loading (figures 6.32 and 6.33), whose fracture is characterised by a wedge shaped transverse crack, constrained ultra-thin plies show a dispersed damage mechanism, combining wedge cracking with ply fragmentation/separation, or just ply fragmentation/separation, as in the case of the thinnest plies (see figure 6.37). As for the tensile case (section 6.4.1.1), this dispersed type of damage observed on thin-ply sublaminates is the result of a less pronounced stress relaxation due to the constraining effect imposed by the surrounding plies, causing the development of progressive, overall ply damage instead of discrete transverse cracking.

This constraining effect, and how it affects stress relaxation in the transverse ply, is further highlighted observing figure 6.38, which show the stress distributions predicted for different ply thicknesses. This slower stress relaxation can also be identified observing the homogenised stress-strain curves of figure 6.39, where more gradual softening is observed

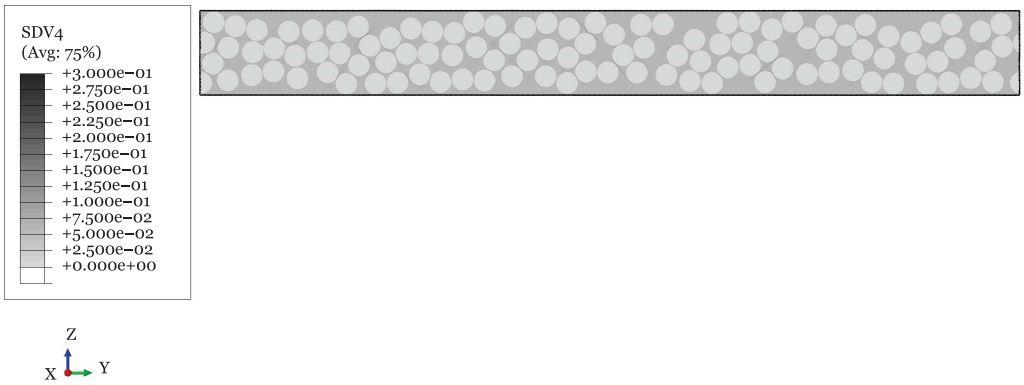

(a) Applied remote strain of 2.0%.

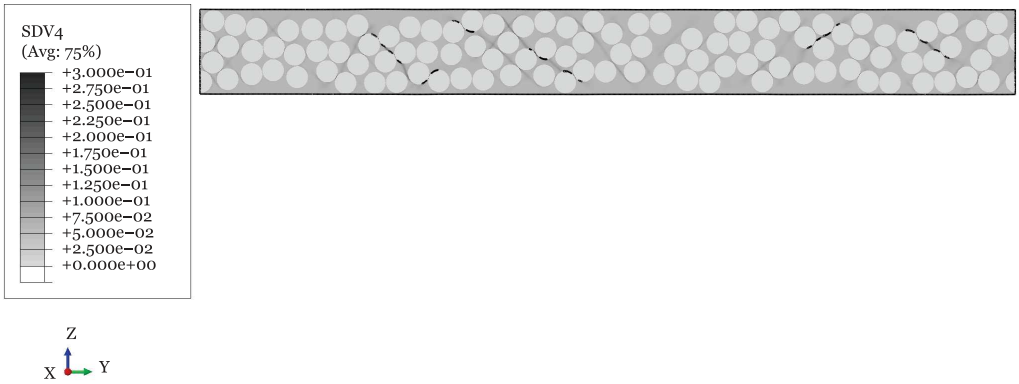

(b) Applied remote strain of 2.5%.

Fig. 6.29. Contour plots of the equivalent plastic strain in the matrix of a representative RVE with a 0.020 mm thick 90° ply, on a sublaminate with 0° outer plies (only the 90° ply is presented).

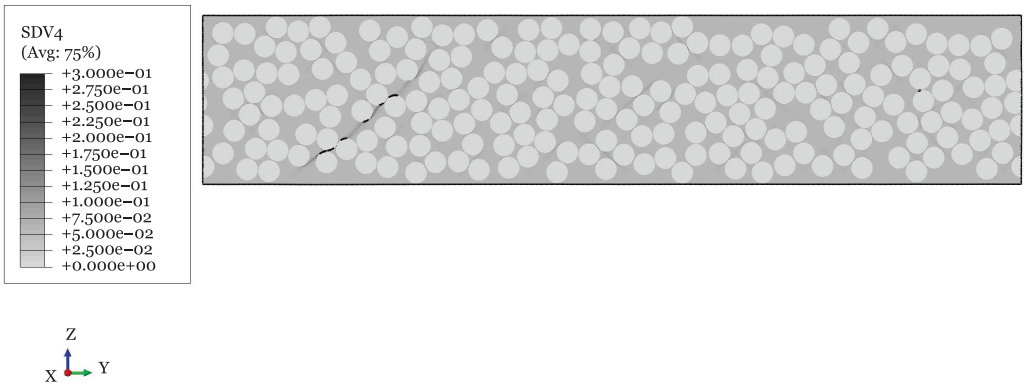

(a) Applied remote strain of 2.0%.

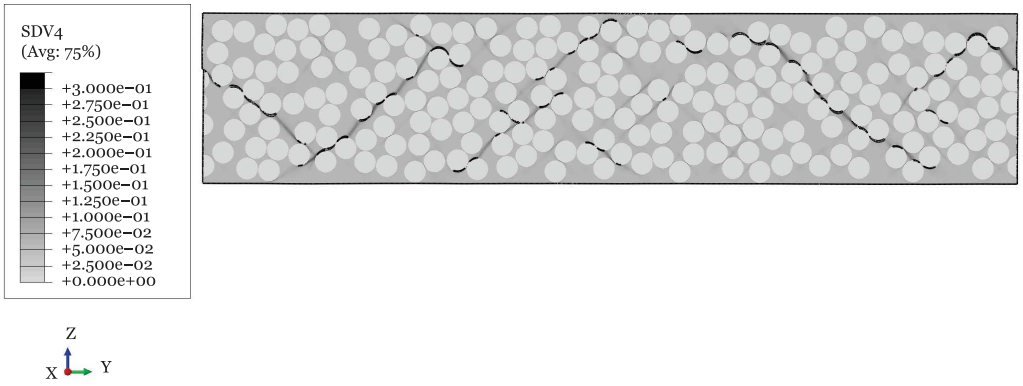

(b) Applied remote strain of 2.5%.

Fig. 6.30. Contour plots of the equivalent plastic strain in the matrix of a representative RVE with a 0.040 mm thick 90° ply, on a sublaminate with 0° outer plies (only the 90° ply is presented).

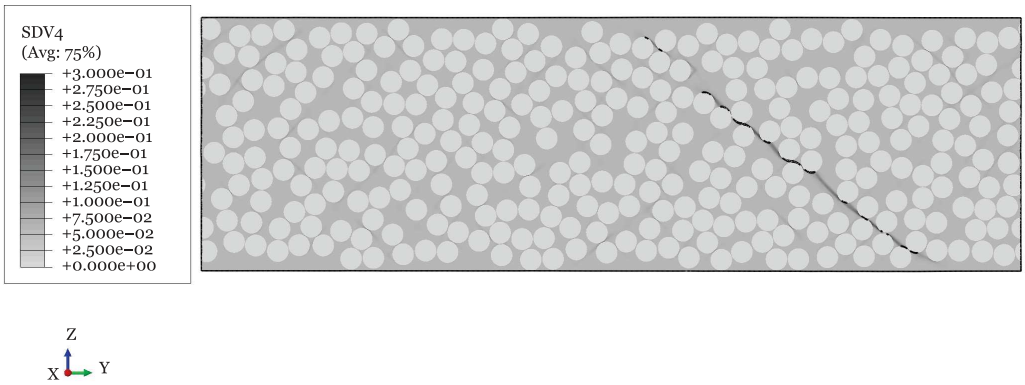

(a) Applied remote strain of 2.0%.

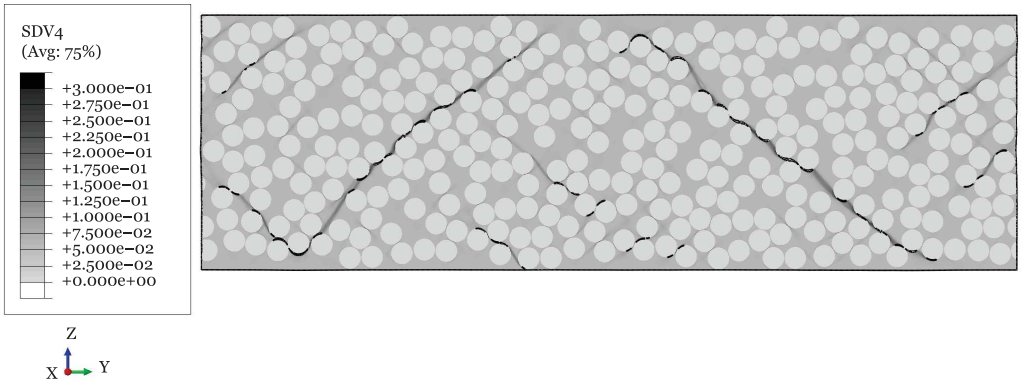

(b) Applied remote strain of 2.5%.

Fig. 6.31. Contour plots of the equivalent plastic strain in the matrix of a representative RVE with a 0.060 mm thick 90° ply, on a sublaminate with 0° outer plies (only the 90° ply is presented).

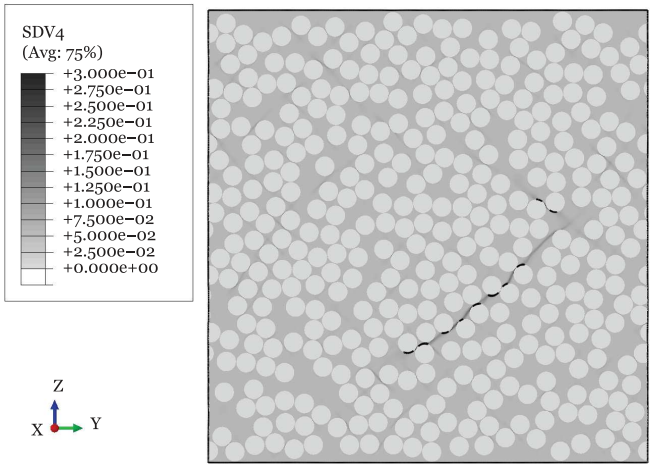

(a) Applied remote strain of 2.0%.

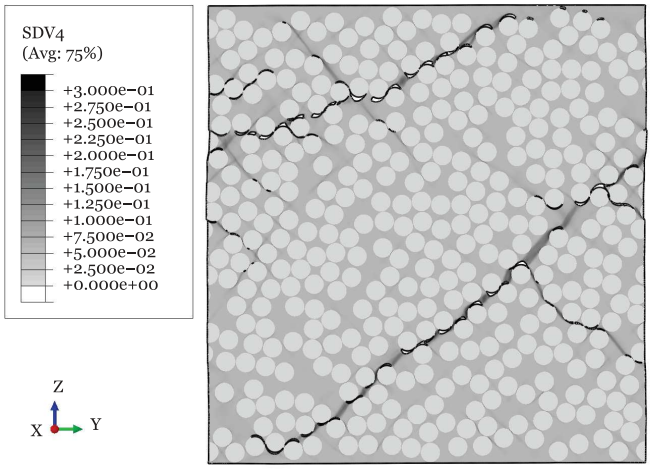

(b) Applied remote strain of 2.5%.

Fig. 6.32. Contour plots of the equivalent plastic strain in the matrix of a representative RVE with a 0.120 mm thick 90° ply, on a sublaminate with 0° outer plies (only the 90° ply is presented).

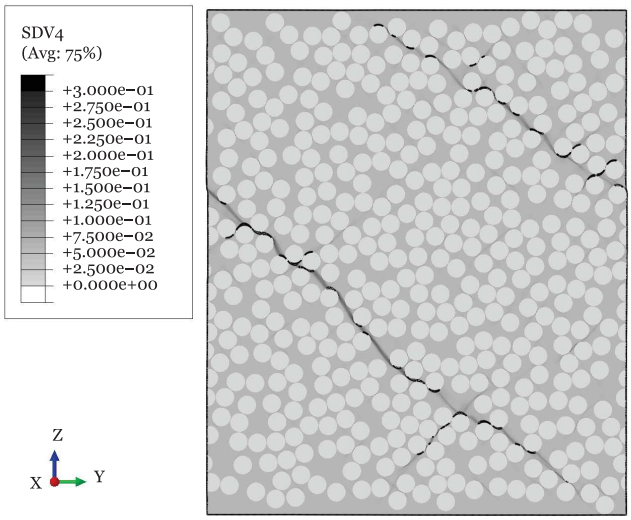

(a) Applied remote strain of 2.0%.

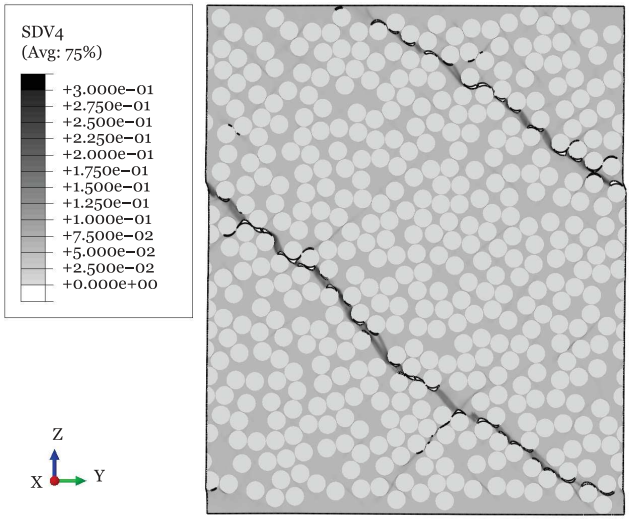

(b) Applied remote strain of 2.5%.

Fig. 6.33. Contour plots of the equivalent plastic strain in the matrix of a representative RVE with a 0.140 mm thick 90° ply, on a sublaminate with 0° outer plies (only the 90° ply is presented).

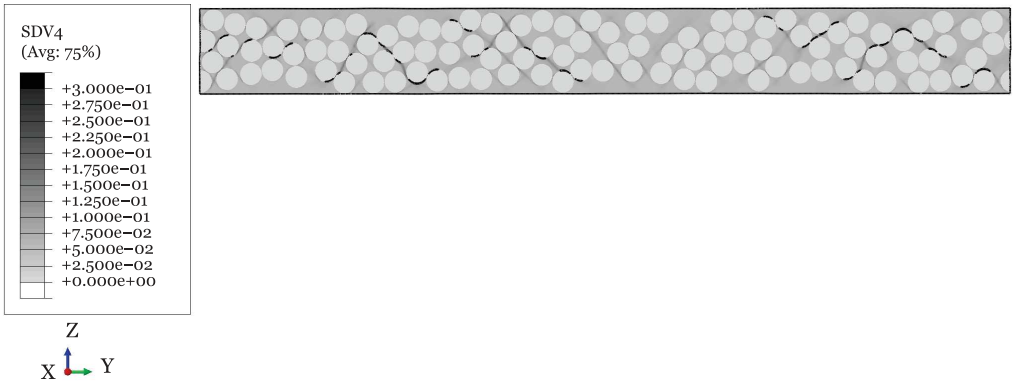

(a) Applied remote strain of 3.0%.

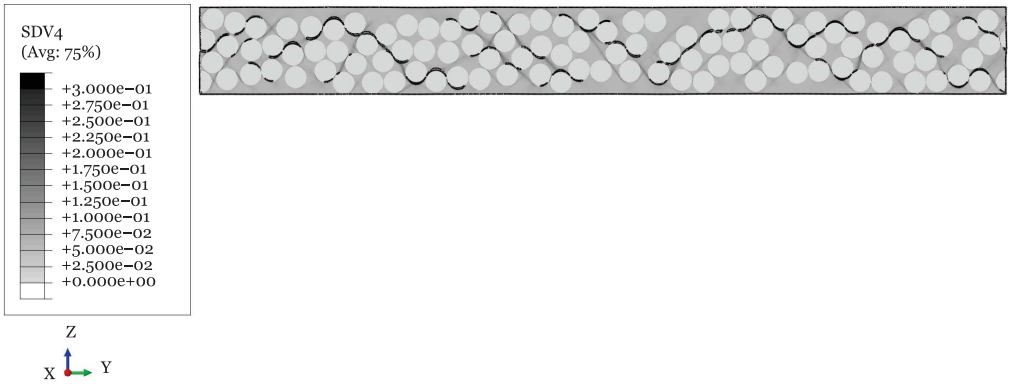

(b) Applied remote strain of 3.5%.

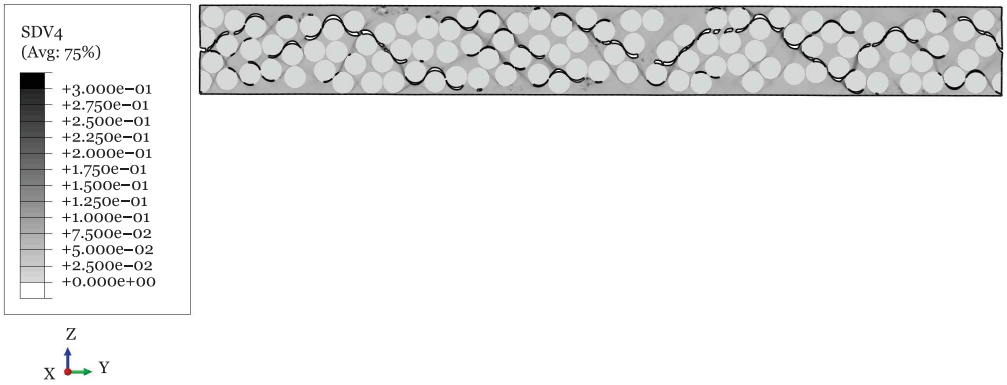

(c) Applied remote strain of 4.0%.

Fig. 6.34. Contour plots of the equivalent plastic strain in the matrix of a representative RVE with a 0.020 mm thick 90° ply, on a sublaminate with 0° outer plies (only the 90° ply is presented).

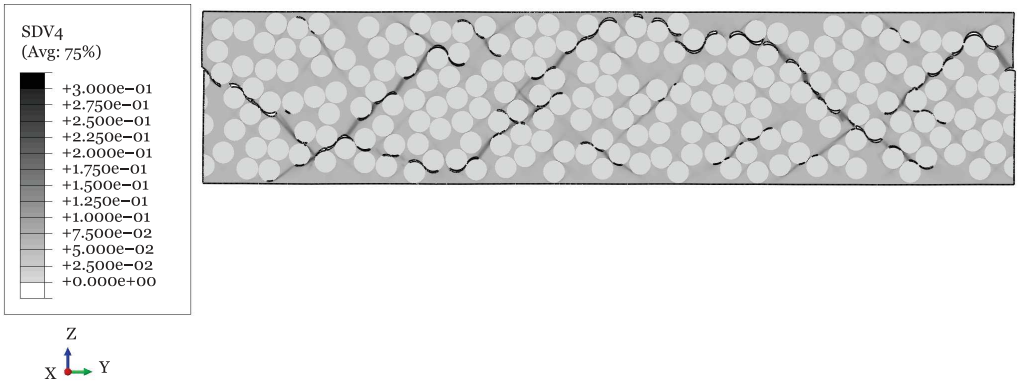

(a) Applied remote strain of 3.0%.

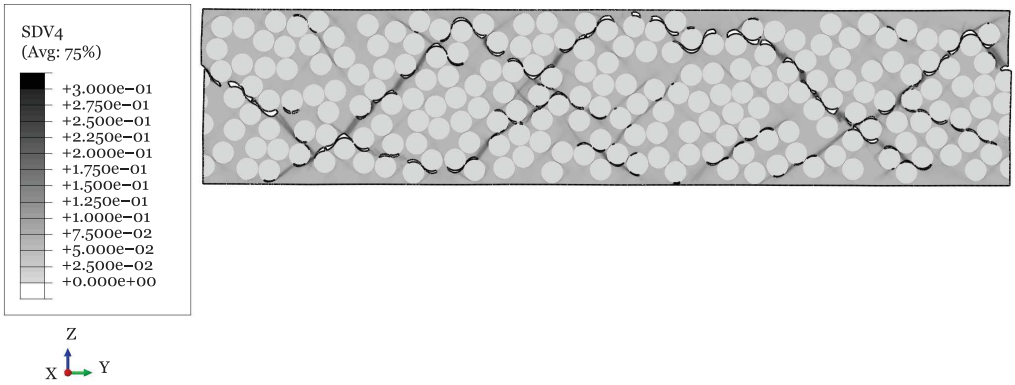

(b) Applied remote strain of 3.5%.

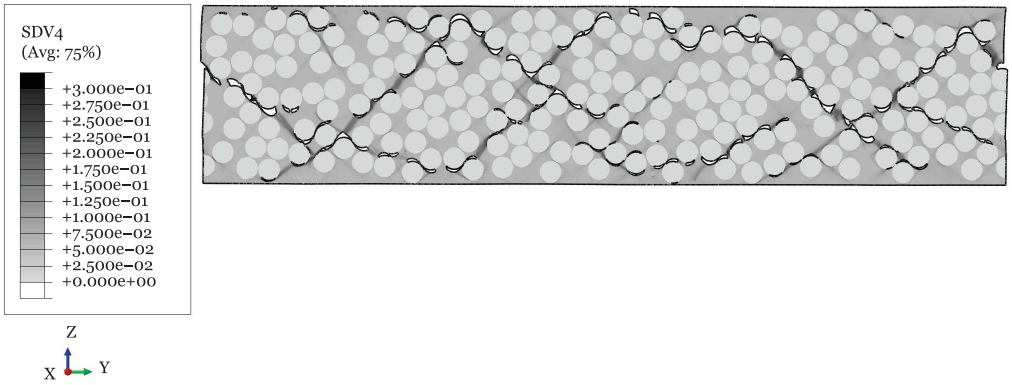

(c) Applied remote strain of 4.0%.

Fig. 6.35. Contour plots of the equivalent plastic strain in the matrix of a representative RVE with a 0.040 mm thick 90° ply, on a sublaminate with 0° outer plies (only the 90° ply is presented).

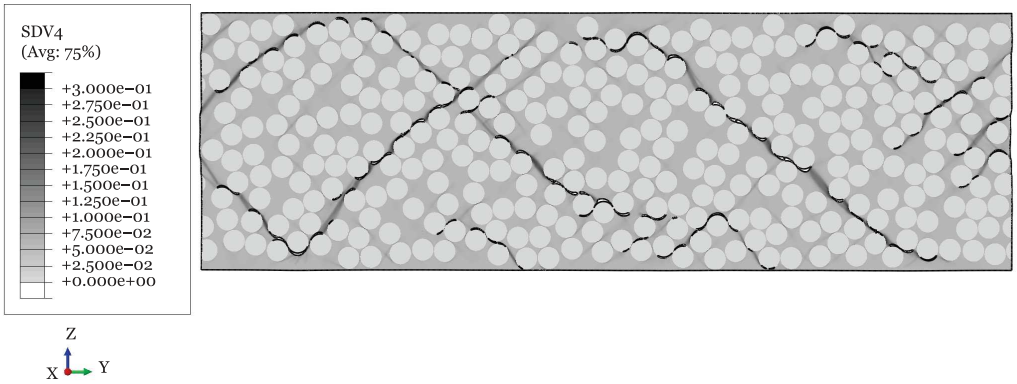

(a) Applied remote strain of 3.0%.

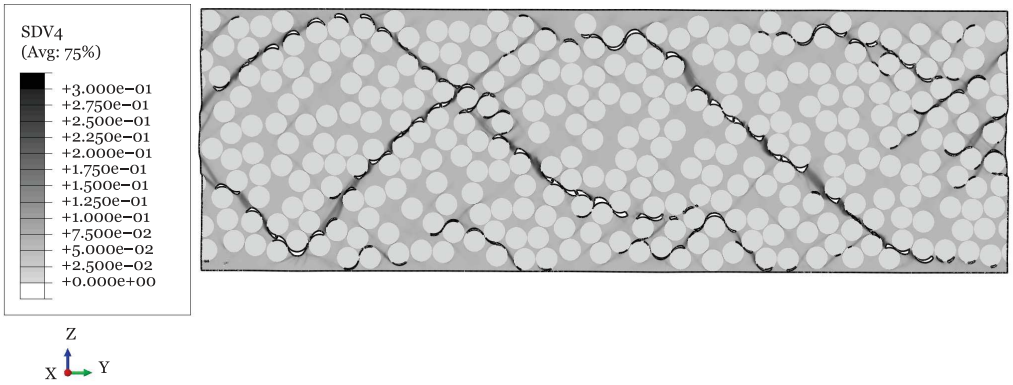

(b) Applied remote strain of 3.5%.

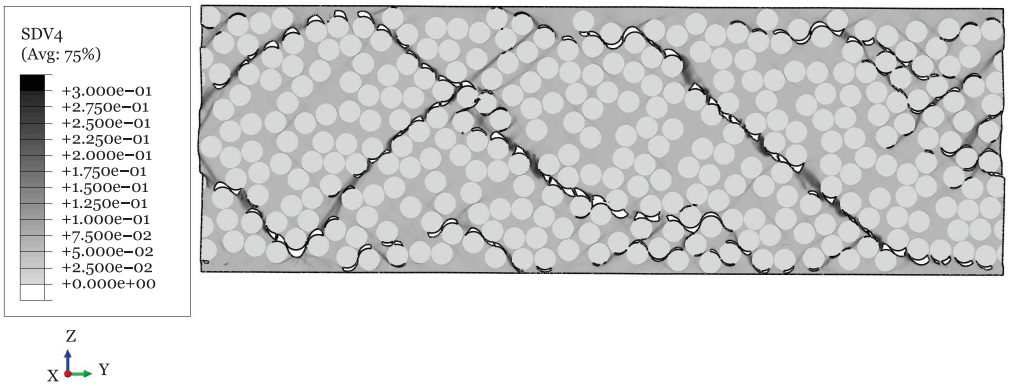

(c) Applied remote strain of 4.0%.

Fig. 6.36. Contour plots of the equivalent plastic strain in the matrix of a representative RVE with a 0.060 mm thick 90° ply, on a sublaminate with 0° outer plies (only the 90° ply is presented).

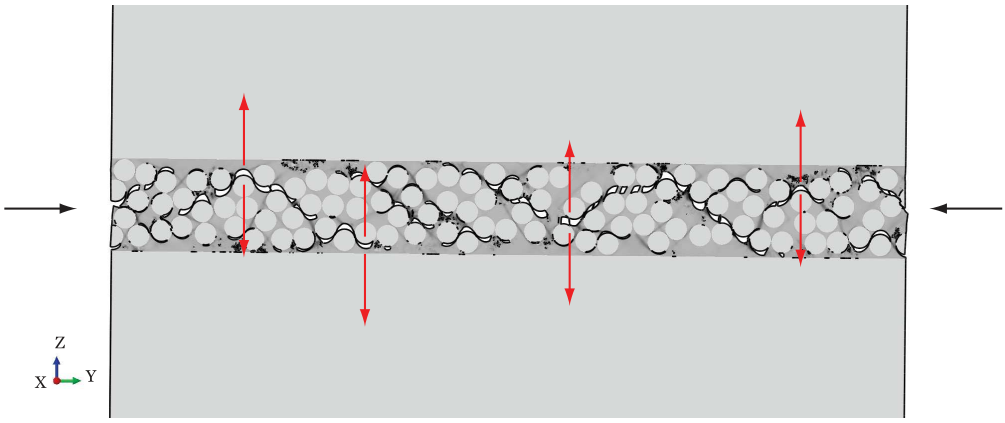

Fig. 6.37. Fragmentation/ply separation of a representative RVE with a 0.020 mm thick 90° lamina subjected to an applied transverse compressive strain of 4.9%, on a sublaminate with 0° outer plies.

on thinner transverse plies. As the ply thickness increases, larger and more spaced drops of the homogenised stress for increasing applied strains can be observed, resulting from more unstable discrete wedge fracture propagation.

Upon onset of transverse damage, the stress relaxation is much higher in the thicker transverse plies than in the thinner ones. This happens because the constraining effect imposed by the adjacent plies on the thicker transverse plies is not sufficient to delay transverse damage growth through the thickness. On the other hand, the higher stress levels maintained on the thinner transverse plies, which results from the higher constraining effect imposed by adjacent plies, conducts to diffuse transverse damage onset and growth before earlier damage has extended completely through the thickness.

Figure 6.40 shows the *in situ* transverse compressive strength, Y_C^{is}, as a function of the ply thickness determined from the micro-mechanical models presented in this work, and the predictions from the models for the *in situ* transverse compressive strength proposed by Catalanotti et al. [128] and, more recently, by Camanho et al. [129] (see also section 7.2.4). Several RVEs have been analysed, and the respective data has been plotted in figure 6.40.

The *in situ* strengths determined from the micro-mechanical models (figure 6.40) were calculated based on the applied remote strain corresponding to the development of through-the-thickness ply failure, characterised by a localised band of damage, as described before, and based on the elastic properties determined from a linear-elastic analysis of the same RVE. It is noted that, in the case of the thinner sublaminates, the development of the first through-the-thickness damage localisation band is delayed, and other regions of localised damage start propagating before failure of the thin transverse ply has occurred. Unless one of these damage bands penetrates completely through the ply thickness, the transverse ply is not considered to have failed. As the ply thickness decreases, the number of localised bands increases, but one eventually will be the first to penetrate through the thickness. That is the point that defines the strength of the thinner transverse plies. It is interesting to note that, once the first band penetrates through the thickness, the remaining will also penetrate progressively.

According to Catalanotti et al. [128], the *in situ* transverse compressive strength, Y_C^{is}, is explicitly given as:

$$Y_C^{is} = \frac{S_L^{is}(2\cos^2\alpha_0 - 1)}{\eta_L \cos^2\alpha_0} \tag{6.8}$$

where α_0 is the fracture angle and η_L is the friction coefficient [128]. The *in situ* in-plane shear strength, S_L^{is}, is calculated from the fracture mechanics model [81]:

$$S_L^{is} = \sqrt{\frac{(1+\beta\phi G_{12}^2)^{1/2} - 1}{3\beta G_{12}}} \tag{6.9}$$

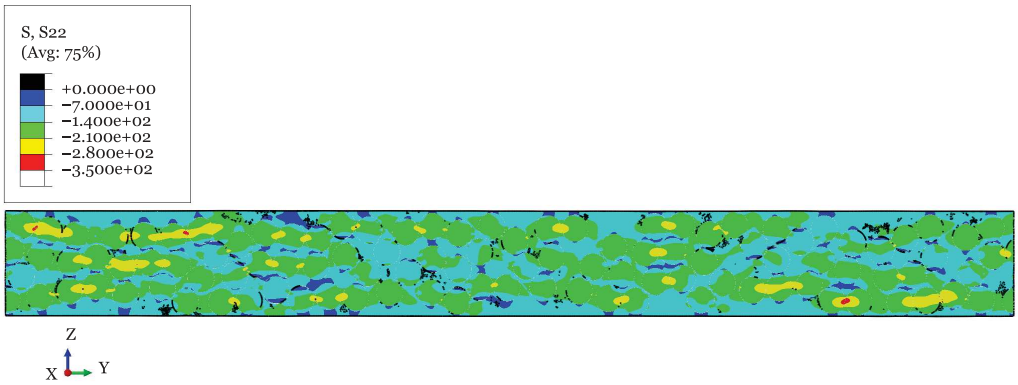

(a) 0.020 mm thick 90° ply.

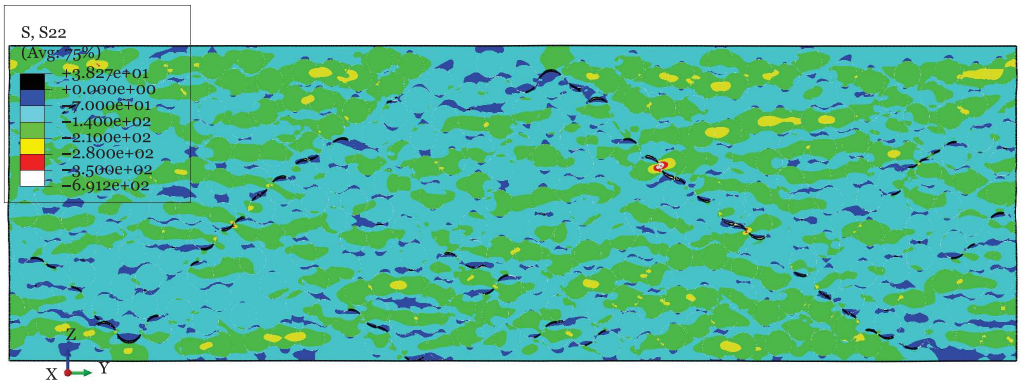

(b) 0.060 mm thick 90° ply.

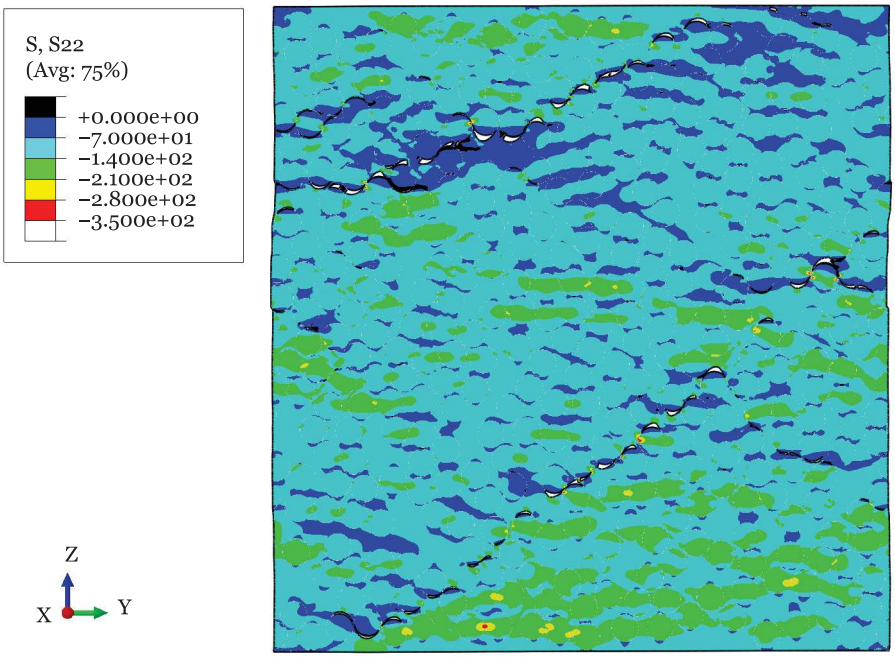

(c) 0.120 mm thick 90° ply.

Fig. 6.38. Stress field along the transverse (y-) direction of representative RVEs subjected to transverse compression, at an applied remote strain of 2.5% (only the 90° ply is presented).

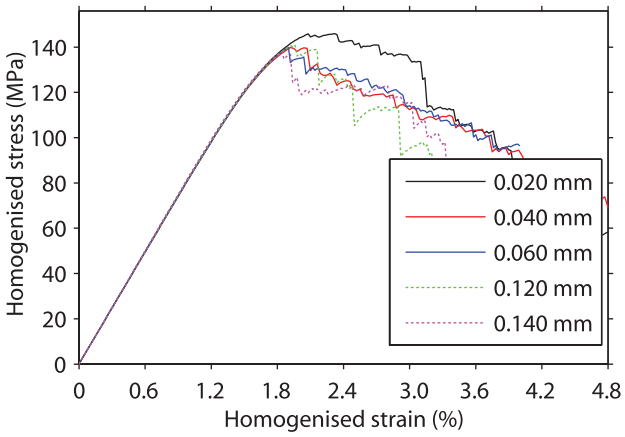

Fig. 6.39. Homogenised stress-strain curves of the embedded 90° ply for representative sublaminates with 0° outer plies subjected to transverse compression.

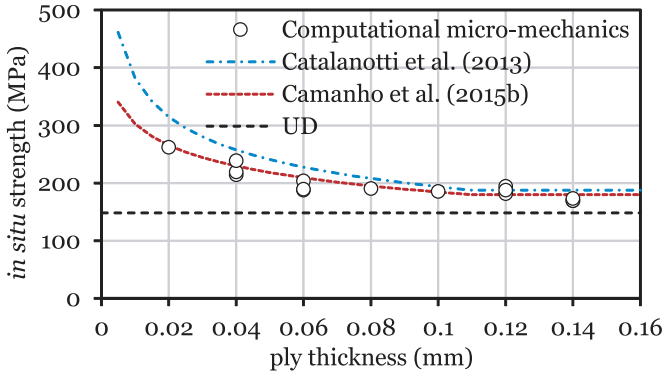

Fig. 6.40. *In situ* transverse compressive strength as a function of ply thickness.

where β is a parameter that defines the nonlinearity of the shear stress-shear strain relation [307], G_{12} is the shear modulus and the parameter ϕ is defined according to the configuration of a given ply. For a thick ply, ϕ is given as [81]:

$$\phi = \frac{12 S_L^2}{G_{12}} + 18 \beta S_L^4 \tag{6.10}$$

and, for a thin ply [81]:

$$\phi = \frac{48 \mathcal{G}_{IIc}}{\pi b} \tag{6.11}$$

where $\mathcal{G}_{IIc}$ is the fracture toughness associated with intralaminar fracture of the transverse ply (parallel to the fibre direction) in mode II. According to Camanho et al. [129], the *in situ* transverse compressive, transverse shear (S_T^{is}) and biaxial transverse tensile (Y_{BT}^{is}) strengths are calculated imposing:

$$\begin{cases} \eta_L^{(+)} = \eta_{L,is}^{(+)} \\ \eta_T^{(+)} = \eta_{T,is}^{(+)} \end{cases} \tag{6.12}$$

and, assuming that the biaxial transverse compressive strength is not an *in situ* property ($Y_{BC}^{is} = Y_{BC}^{ud}$), imposing one of the following relations:

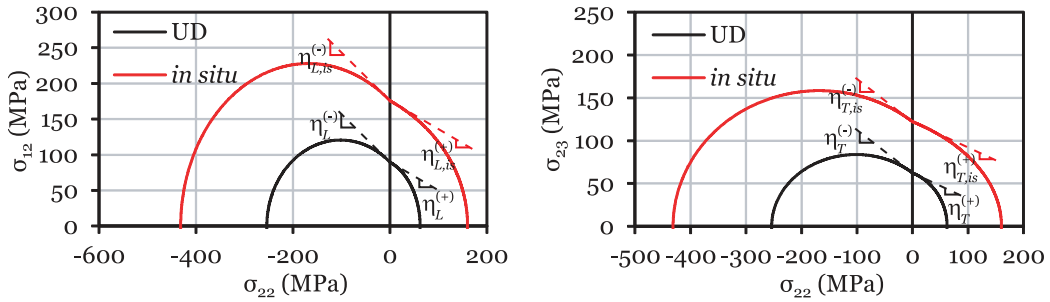

(a) $\sigma_{22} - \sigma_{12}$ failure envelope.

(b) $\sigma_{22} - \sigma_{23}$ failure envelope.

Fig. 6.41. Definitions of the parameters η_L and η_T (after Camanho et al. [129]).

$$\eta_L^{(-)} = \eta_{L,is}^{(-)} \tag{6.13}$$

$$\eta_T^{(-)} = \eta_{T,is}^{(-)} \tag{6.14}$$

where η_L and η_T are, respectively, the slopes in the σ_{22}–σ_{12} and σ_{22}–σ_{23} failure envelopes when $\sigma_{22} = 0$ [102], which depend on the sign of the stress component σ_{22} (figure 6.41). In other words, it is assumed that the slopes in the σ_{22}–σ_{12} and σ_{22}–σ_{23} failure envelopes when $\sigma_{22} = 0$ are not *in situ* properties [128, 129].

The strength and elastic properties required by the analytical models (table 6.7) were determined from a separate analysis of the micro-mechanical model using UD RVEs, following Melro et al. [299]. The micro-mechanical simulations included pure transverse tension and compression, transverse shear, in-plane longitudinal shear and biaxial transverse tension stress states. The biaxial transverse compressive strengths (Y_{BC}) was estimated based on the approach suggested by Vogler et al. [266]. As a first approximation, the fracture toughness associated with intralaminar fracture of the transverse ply (parallel to the fibre direction) in mode I was taken as 25% of the fracture toughness of the matrix, and in mode II as 50% of the fracture toughness of the matrix (or twice the fracture toughness of mode I). The parameter β was determined based on the results from the micro-mechanical computational model of UD RVEs subjected to pure longitudinal in-plane shear, fitting the polynomial approximation proposed by Hahn and Tsai [307]:

$$\gamma_{12} = \frac{1}{G_{12}}\sigma_{12} + \beta\sigma_{12}^3 \tag{6.15}$$

to the shear stress-shear strain curves obtained with three different RVEs (figure 6.42). For the model proposed by Catalanotti et al. [128], the fracture angle was assumed as $\alpha_0 = 53°$, and the friction coefficient $\eta_L = 0.317$ was determined by inverse identification from the UD transverse compressive strength, in-plane shear strength, and from the assumed fracture angle [128].

Comparing the predictions of the *in situ* effect for transverse compression with the results obtained using computational micro-mechanics in figure 6.40, similar trends are observed, showing that the analytical models are sufficiently accurate, and that there is an *in situ* effect in the transverse compressive failure of polymer composites. To the author's knowledge, this is the first time an *in situ* effect in transverse compression has been clearly identified, and the validity of the analytical models proposed in Refs. [128, 129] to predict this *in situ* effect demonstrated.

Figure 6.40 also shows that the predicted *in situ* transverse compressive strengths for ply thicknesses over 0.060 mm are very similar, in agreement with the available theoretical models for the *in situ* effect. This observation validates the results of the models with ply thicknesses above 0.100 mm, with 0.120 mm wide RVEs, defined to accommodate approximately a single transverse crack, and for which diffuse damage is very limited before transverse crack growth

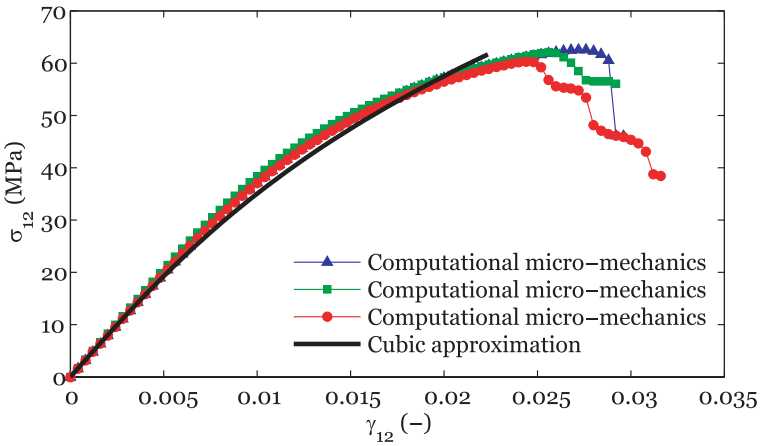

Fig. 6.42. Shear stress-shear strain curves from the micro-mechanical computational model for three different RVEs, and fitting curve using the cubic approximation proposed by Hahn and Tsai [307].

through the thickness. This observation also shows that these models may not benefit from a wider RVE, as suggested in section 6.3.1.

6.5. Concluding remarks

A 3D computational micro-mechanics framework [298, 299] was used in this chapter to study the micro-mechanics of the *in situ* effect in tow-spread, ultra-thin plies. In an analogy with a thorough experimental study on similar grades [35], it was observed that the proposed framework is able to accurately represent the micro-mechanical response of ultra-low grades, including:

(i) the mechanics of transverse cracking onset and propagation;

(ii) the constraining effect observed in the laminae embedded in multidirectional laminates;

(iii) the gradual, slow stress relaxation and progressive transverse cracking observed in very thin plies, and consequent increase of the crack density;

(iv) the reduction in COD of the transverse cracks with ply thinness, attributed to the constraining effect imposed by the adjacent stiffer laminae;

(v) the formation of thin necks of matrix material around the regions where interfacial damage is more pronounced, a phenomenon potentiated by increasing ply thicknesses;

(vi) the *in situ* effect, characterised by a reduction in the applied stress needed to extend a transverse crack through the thickness of the ply when the ply thickness increases.

As reported by Saito et al. [35], for the thickest transverse laminae, the sudden matrix crack extension leads to strong, local stress relaxation. In fact, once transverse damage initiates in a thick ply, it quickly penetrates through the thickness, resulting in a local stress concentration at the adjacent (load carrying) plies, promoting early failure of the latter. For thinner transverse laminae, though, a gradual extension of the transverse cracks, eventually without completely penetrating through the thickness, results in a substantially lower stress relaxation. Transverse damage growth is suppressed, resulting in lower stress concentration at the adjacent plies, pushing their longitudinal performance closer to that of the UD lamina.

The present work also showed that a change on the transverse fracture mechanisms due to in-plane tensile loading occurs for sufficiently thin plies. When embedded ultra-thin plies are subjected to transverse tensile loading, ply failure is characterised by progressive fragmentation and multiple cracking. For limit cases, damage is characterised by many

decohesions occurring without extending completely through the ply thickness, as a dispersed damage event, and leading to overall failure of the matrix material between the fibres before development of discrete transverse cracking.

The dispersed/non-localised matrix failure observed for very thin plies shows that, for this particular case, failure at the mesoscopic scale can be regarded by conventional continuous damage mechanics frameworks, without the need to address discrete cracking as in smeared crack or discrete damage formulations, potentially simplifying the analysis of thin-ply laminates. It is also important to note that this work must be seen as an improvement over initial models [38] with respect to the understanding and representation of the physics of matrix cracking suppression in very thin plies.

Regarding the response of constrained plies subjected to transverse compressive loading, the proposed computational micro-mechanics framework provided a detailed representation of the failure mechanisms involved. For cross-ply sublaminates with conventional, standard-thickness 90° plies, failure was dominated by fibre-matrix interface cracking and large localised plastic deformation of the matrix, forming a localised band of damage in a plane not aligned with the loading direction. The predicted wedge shaped transverse fracture is in agreement with what has been described in the literature [102, 299]. Unlike conventional 90° plies subjected to transverse compressive loading, constrained ultra-thin plies showed a dispersed damage mechanism, combining wedge cracking with ply fragmentation/separation, or just ply fragmentation/separation for the thinnest plies. As in the tensile case, this dispersed type of damage on thin-ply sublaminates is the result of a less pronounced stress relaxation due to the stronger constraining effect imposed by the surrounding plies. This results in the development of progressive ply damage instead of discrete transverse cracking. Therefore, a transverse crack suppression effect was observed.

It should be noted that, while there is no direct experimental evidence of the *in situ* effect for transverse compression, some recent test results obtained in structural details indicate that indeed the ply thickness affects the compressive strengths. For example, recent results show that the compressive unnotched strength [121, 122, 133, 134] and the bearing strength [58] increase with decreasing ply thickness. Superior unnotched compressive strengths were also obtained on the thinner spread-tow fabrics in chapter 4, attributed to an *in situ* effect and to the uniformity of the thinner tows. This well reported improved compressive behaviour of thin-ply laminates is justified by an increase of the transverse and longitudinal compressive strengths of thin plies.

When comparing the results of the computational micro-mechanics framework with the predictions from the analytical models available in the literature for the *in situ* effect [81, 128, 129], the same trends were obtained, emphasising the validity of both the computational micro-mechanics and analytical representations. The present results also show that, for realistic ply thicknesses, these analytical models can be considered fairly accurate and representative of the actual strengths characterising the response of transverse plies embedded in multidirectional laminates.

It should be noted that, generally, and in particular for thin transverse plies, matrix cracks first propagate through the thickness of the ply (namely at the free edges) and subsequently penetrate along the longitudinal direction as a steady state process [289]. However, the 3D computational micro-mechanics model has a limited dimension along this direction. Due to the imposition of PBCs, the onset and propagation of the transverse cracks are modelled as occurring instantaneously through the longitudinal direction. Nonetheless, given the advantages in terms of computational cost, which would increase severely if longer RVEs would have been employed, it is believed that the present approach provides sufficient insight into the micro-mechanical response of embedded transverse plies. In fact, having taken into account widthwise transverse crack propagation would most certainly provide the same results for the constraining effect imposed on through-the-thickness transverse crack propagation and consequent *in situ* effect, as transverse damage has to grow first through the thickness before penetrating longitudinally. Additionally, a consistent definition of the width of the RVEs is deemed considerably more important to accurately capture the stress relaxation caused by transverse damage growth, as discussed in section 6.4.

It should be also noted that Saito et al. [35] has shown that there is effectively a constraining effect imposed on the through-the-thickness propagation of transverse cracks, which was extremely well captured by the present simulations, and predicted analytically elsewhere [83]. In fact, looking at the detailed results from both numerical and experimental studies, it can be concluded that, whereas the transverse stress level for the onset of transverse cracking (first occurrence

of fibre-matrix decohesion) is independent of ply thickness, its through-the-thickness propagation is not, as higher stress levels are required to fully propagate a transverse crack through the thickness of thin plies.

Note also that the analytical solutions for the *in situ* effect [81, 98] are not intended to represent the intrinsic mechanisms of transverse crack initiation and propagation, but to represent the equilibrium point for final or steady state propagation of transverse cracking, whose mechanisms are phenomenologically different between thin and thick plies, as explained in great detail by van der Meer and Dávila [289]. These models capture the thick-ply solution by considering through-the-thickness transverse crack propagation and the thin-ply solution by considering through-the-width transverse crack propagation, since one of these two phenomena will become critical when the ply thickness changes. However, transverse crack propagation on each direction cannot be dissociated from each other. Based on the theoretical background presented in Refs. [81, 98, 289], and analysing the detailed simulations presented in this work [84], supported by experimental evidence [35], it can be concluded that:

- The *in situ* effect on thick transverse plies is characterised by unstable propagation of through-the-thickness transverse cracks [35, 84], which may expand quickly through the ply width [81, 98, 289], and an analytical solution formulated on the basis of a transverse slit crack propagating in the transverse direction of an embedded ply (thick-ply solution) [81] is able to represent the physical event associated with ply failure. Since this through-the-thickness propagation is unstable, the thick-ply solution for the *in situ* effect does not depend on the ply thickness.

- The *in situ* effect on thin transverse plies is characterised by slow propagation of through-the-thickness transverse cracks [35, 84], which, at the same time, may also grow slowly along the fibre direction [81, 98, 289]. Analytically, even though this stable through-the-thickness crack propagation cannot be represented, the *in situ* effect can be formulated on the basis of a constrained slit crack propagating in the longitudinal direction [81]. This is a steady-state phenomenon that can be associated with complete through-the-thickness ply failure, and, consequently, associated with the *in situ* strength for thin plies. Due to its nature, this stable mechanism naturally depends on the ply thickness. As it decreases, the effect on crack arrest caused by the constraining plies is stronger, delaying/slowing down through-the-thickness crack propagation and increasing the *in situ* strength.

It is important to note that any attempt to study the constraining effect on the widthwise propagation of transverse cracks using computational micro-mechanics would naturally require RVEs with a significant increase in their size along the longitudinal direction. Such huge micro-mechanical models have been recently used to study longitudinal failure mechanisms, namely kink band formation [308] and tensile fracture of intra-bundle hybrid composites [309].

Recently, Herráez et al. [124], based on an approach that resembles the work performed in this chapter (see also Refs. [84, 85, 310]), but employing a simpler constitutive, bi-dimensional model, argued that the transverse ply strength corresponding to the initiation and propagation of a transverse crack through the thickness was independent of the ply thickness. These authors also argued that this is in accordance with the thick-ply solution of the *in situ* effect theory [81, 98], since the model they employed could not capture widthwise propagation of the matrix cracks. However, this argument contradicts not only the numerical observations presented in this work (see also Refs. [84, 85]) and presented by Saito et al. [38], as it contradicts experimental evidence from Saito et al. [35]. Moreover, it is not clear whether taking the maximum homogenised stress in the transverse ply at the onset of damage growth, as Herráez et al. [124] did, is an appropriate measure of the actual strength of the embedded transverse ply. In fact, as discussed in section 6.4, the homogenised stress in a finite RVE of a transverse ply reflects the stress relaxation that occurs upon onset of transverse damage, with the extra load being transferred to the adjacent load carrying plies.

Another inconsistency of the results presented by Herráez et al. [124] is related with the growth of individual transverse cracks. These authors showed transverse cracks propagating from the interface between the inner and outer plies towards the centre of the ply. Even though this is a phenomenon typically seen on oblique cracking [125], which was captured by the present micro-mechanical model, transverse crack growth generally starts at the centre of the ply, where the constraining effect of the adjacent plies is minimum, and propagates towards the interfaces between plies, as predicted numerically [38, 84], analytically [83], and observed experimentally [35, 126].

6.5. Concluding remarks

Currently, the present methodology is also being applied to the cases of in-plane shear and transverse shear stress states. The cases of biaxial tensile and compressive loading, as well as longitudinal compression and kink band formation [308], can all be addressed in the future. In addition, emphasis will be given not only to the effect of the transverse ply thickness, but also to the effect of the stiffness of the adjacent plies and ply position in the laminate (for instance, placing the 90° ply RVE at the surface of the laminate). These analyses are intended to support the understanding of the micro-mechanical constitutive behaviour of ultra-thin plies and thin-ply laminates subjected to basic stress states, overcoming the complexities and limitations of experimental testing on these low grade materials. Moreover, the present framework can also be extremely helpful in understanding the behaviour of polymer composite laminates subjected to biaxial or multiaxial loading scenarios, for which there is still a fundamental lack of reliable experimental data [311]. It also has great potential for future material tailoring at the micro-scale, with important applications not only for the scientific community, but also for the composite materials industry: effects of fibre clustering (manufacturing process and realistic fibre distributions), effects of intra-bundle and intra-ply hybridisation (intermingled fibres of different grades or of different materials [309], or adjacent tows with different reinforcements), and effects of new matrix materials (e.g. enhanced resin formulations or thermoplastic matrices).

Chapter 7

Three-dimensional invariant-based failure criteria for fibre-reinforced polymer laminates

The development of accurate analytical and numerical tools that are able to predict the response of composites under general loading conditions and geometries is extremely important, whether the interest is to characterise the mechanical response of composite laminates or to assess the structural integrity of composite structures. In the absence of such tools, the design process will rely on costly matrices of mechanical tests based on a large number of test specimens and empirical knockdown factors. The effective use of polymer composite materials in load carrying structures depends, then, on the ability to obtain reliable predictions of the onset and propagation of the different failure mechanisms. Accordingly, the development of accurate, fully-benchmarked failure criteria that predict the onset of ply damage mechanisms in fibre-reinforced polymers is fundamental. In this chapter, new three-dimensional failure criteria for fibre-reinforced composite materials are presented, based on structural tensors that represent the material symmetries of the respective anisotropy class as an intrinsic material property, enabling an elegant coordinate system-free description of anisotropy using isotropic tensor functions. Then, a pragmatic approach is proposed to estimate the orientation of the fracture plane for composite laminates under transverse, matrix-dominated failure. To account for the effect of ply thickness when the laminae are embedded in a multidirectional laminate, proper definitions of the *in situ* properties are derived in the framework of the invariant-based failure criterion for transverse failure mechanisms. Finally, the proposed failure criteria are validated using several case studies available in the literature based on experimental testing and on a strategy employing computational micro-mechanics.

7.1. Introduction

When composites are used in structural parts, a design development programme is generally implemented during which the performance of the structure is assessed prior to use, in the case of aero-structures, relying on a "*building-block*" approach [25]. The process of substantiating the structural performance and durability of composite components generally consists of a complex combination of testing and analysis. While testing alone is prohibitively expensive and time consuming, analysis techniques alone are usually not sophisticated enough to adequately predict results under every set of conditions. Therefore, the development of accurate analytical and numerical tools that are able to predict the response of composites under general loading conditions and geometries is extremely important, whether the interest is to characterise the mechanical response of composite laminates or to assess the structural integrity of composite structures. In the absence of such tools, the design process will rely on costly matrices of mechanical tests based on a large number of test specimens and empirical knockdown factors.

7.1. Introduction

The effective use of polymer composite materials in load carrying structures depends, then, on the ability to obtain reliable predictions of the onset and propagation of the different failure mechanisms. Accordingly, the development of accurate, fully-benchmarked failure criteria that predict the onset of ply damage mechanisms in fibre-reinforced polymers (FRPs) is extremely important [312]. Indeed, this has been the subject of a great number of research studies in the literature for several years [103, 128, 313–319].

Failure criteria are especially useful in providing failure envelopes from relatively simple experimental data that can be used in the analysis, design and calculation of safety factors of composite structures subjected to complex loading and boundary conditions. Global stress- [320–325] and strain- [326] based criteria are generally "*purely empirical*" [321], and their replacement by phenomenological failure criteria, with a stronger physical basis, is more and more common [102, 103, 128, 282, 316, 318, 319, 327, 328]. Nevertheless, it should be noted that failure criteria must be simple enough for application in engineering problems while capturing the relevant physics of the problem [327].

To meet the most common design requirements, failure criteria must be applicable at the ply, laminate and structural level. Because failure at these levels is often the consequence of an accumulation of micro-level failure events, an understanding of the micro-mechanical damage mechanisms is crucial to develop accurate and physically-based failure theories [282]. Regarding the mathematical form of the failure criteria and the shape of the corresponding envelopes, there are some restrictions that must also be taken into account. For example, failure envelopes must be closed, in order to prevent infinite strength, and they must be convex, so that unloading from a stress state will not lead to additional failures [321].

Among the phenomenological failure criteria available in the literature, those proposed by Hashin [316] and by Puck and Schürmann [102, 327] for transverse failure are often used by the composites' research and design communities, with several other theories appearing as extensions to these criteria [103, 104, 128, 282, 328]. In particular, Puck's failure criterion for matrix transverse cracking [102, 327] is based on a modified Mohr/Coloumb theory for brittle transversely-isotropic materials. The tractions acting on the fracture plane, which needs to be determined, are used to assess failure under two fundamental regimes: transverse tension (positive normal stress) or transverse compression (negative normal stress). The orientation of the fracture plane is determined when the *plane of maximum stress effort* is found, i.e., the plane that maximises the failure index. This means that a maximisation problem needs to be solved, which is generally done by varying the orientation of the fracture plane, calculating the failure index for every angle, and recording the orientation giving the maximum value of the failure index.

In the design and analysis of thick composite laminates, general three-dimensional (3D) stress states should be accounted for, and reliable failure criteria must be formulated for these cases. Improved 3D failure criteria, based on the ideas presented by Puck and Schürmann [102, 327], were recently proposed by Catalanotti et al. [128] to address more general stress states in a consistent way, providing not only the predictions for the onset of ply damage, but also additional information regarding the type of failure and the orientation of the fracture plane.

In order to obtain a simpler, but elegant description of failure of laminated composites, Cuntze and Freund [318] presented a formulation of different failure criteria based on invariants for each individual failure mode observed in anisotropic, heterogeneous materials. This means that the formulations do not depend on coordinate-system transformations. Therefore, the search for the fracture plane is not necessary. Cuntze and Freund [318] suggest that the results of the invariant-based failure criteria can then be used for post-determination of the angle of the fracture plane; e.g., Cuntze and Freund [318] used Mohr/Coloumb theory, but considered only a state of plane stress, without including the shear stresses σ_{12} and σ_{13} (1 corresponds to the fibre direction, and 2–3 to the transverse directions). Cuntze and Freund [318] claim that, besides not predicting directly the orientation of the fracture plane, the invariant approach's simplicity can result in a certain loss of '*physical correctness*'.

In this chapter, new 3D failure criteria for fibre-reinforced composite materials based on the transversely isotropic yield function proposed by Vogler et al. [266, 329] are presented. The new 3D failure criteria have an invariant quadratic formulation based on structural tensors that accounts for the preferred directions of the anisotropic material [319]. With this formulation, anisotropy is derived using structural tensors and not symmetry conditions based on a refer-

ence coordinate system. The so-called structural tensors represent the material symmetries of the respective anisotropy class as an intrinsic material property, which enables an elegant *coordinate system-free* description of anisotropy using isotropic tensor functions. Moreover, finite fibre rotations can be regarded easily. It is noted that the 3D invariant-based failure criteria proposed in this work predicts failure in a single lamina, requiring the calculation of the strains and stresses of each ply of multidirectional laminates, which is a common procedure in the most recent failure criteria for FRPs [102, 103, 128, 282, 327].

For transverse failure mechanisms, a pragmatic approach is proposed to estimate the orientation of the fracture plane. Because in failure criteria based on the invariant theory a *coordinate system-free* description of failure is considered, there is no means of obtaining the local coordinate system associated with the *maximum effort* directly from the criteria, and the orientation of the fracture plane cannot be determined. With the proposed pragmatic approach, determining the orientation of the fracture plane of composite laminates under transverse, matrix-dominated failure is made possible, providing a useful evaluation tool, not only for comparison against other failure theories, but also in assessing failure mode types [330]. On the other hand, its knowledge is essential for the accurate representation of transverse cracking by means of smeared crack formulations, since the orientation of the transverse crack cannot be known in advance [108].

To account for the effect of ply thickness when the laminae are embedded in a multidirectional laminate, proper definitions of the *in situ* properties are derived in the framework of the invariant-based failure criterion for transverse failure mechanisms. This is important for application of the proposed criteria as damage initiation functions in advanced computational models that predict the inelastic and fracture behaviour of composites [106, 108, 183, 190].

Finally, the proposed 3D failure criteria are validated using several case studies available in the literature based on experimental testing. Moreover, a new validation strategy is explored based on computational micro-mechanics, showing the validity of both approaches for more complex stress states [319].

7.2. Invariant-based failure criterion for transverse failure

7.2.1. Failure criterion formulation

When formulating physically-based failure criteria for FRPs, it is essential to distinguish between transverse, matrix-dominated failure mechanisms, and longitudinal, fibre-dominated failure mechanisms [103, 128, 319, 327]. Regarding the transverse failure mechanisms, the proposed 3D invariant-based criterion [319] is formulated directly from the yield function presented by Vogler et al. [266, 329]. According to the invariant formulation of anisotropic constitutive equations [331], transversely isotropic materials can be characterised by a preferred direction $\mathbf{a}$. For unidirectional (UD) FRPs, this preferred direction $\mathbf{a}$ is the fibre direction [266, 332]. If it coincides with the x_1-direction, which is often the convention in UD fibre-reinforced laminates, it is given as:

$$\mathbf{a} = [1\ 0\ 0]^{\mathrm{T}} \tag{7.1}$$

The material response is invariant with respect to arbitrary rotations around the preferred direction $\mathbf{a}$, to reflections at planes parallel to the fibre direction, and with respect to the reflection at that plane, whose normal is the preferred direction $\mathbf{a}$ [266].

The structural tensor $\mathbf{A}$ of transverse isotropy, which represents the material's intrinsic characteristic direction, is an additional tensor argument to formulate the failure criterion as an isotropic tensor function. It is defined as the dyadic product of the preferred direction $\mathbf{a}$, i.e. [266, 332]:

$$\mathbf{A} = \mathrm{a} \otimes \mathrm{a} \tag{7.2}$$

According to the proposed invariant formulation, failure is a function, f_M, of the stress tensor $\boldsymbol{\sigma}$ and of the structural tensor $\mathbf{A}$, which are the argument tensors. The corresponding isotropic invariants form the functional basis for constructing

the function f_M as a scalar isotropic tensor function [266, 332].

This functional basis for transverse isotropy, formed by the argument tensors $\boldsymbol{\sigma}$ and $\mathbf{A}$, reads [266, 333]:

$$\operatorname{tr}\boldsymbol{\sigma}, \quad \operatorname{tr}\boldsymbol{\sigma}^2, \quad \operatorname{tr}\boldsymbol{\sigma}^3, \quad \operatorname{tr}(\mathbf{A}\boldsymbol{\sigma}) \quad \text{and} \quad \operatorname{tr}(\mathbf{A}\boldsymbol{\sigma}^2) \tag{7.3}$$

It should be noted that, according to the invariant theory, an arbitrary linear combination of the stress tensor $\boldsymbol{\sigma}$ can be used in equation (7.3). Furthermore, a linear combination of the basic invariants given in equation (7.3) can also be used, without loss of generality [266].

Vogler et al. [266] reformulated the quadratic ($\operatorname{tr}\boldsymbol{\sigma}^2$ and $\operatorname{tr}(\mathbf{A}\boldsymbol{\sigma}^2)$) and the linear ($\operatorname{tr}\boldsymbol{\sigma}$) invariants of the functional basis (7.3) in order to identify particular stress states with the corresponding invariants. The basic invariant $\operatorname{tr}\boldsymbol{\sigma}^3$ is neglected; the cubic invariant $\operatorname{tr}\boldsymbol{\sigma}^3$ is suitable for modelling metal plasticity, which is obviously not the case. The invariant $\operatorname{tr}(\mathbf{A}\boldsymbol{\sigma})$ can be used to regard yielding in the fibre direction, which is neglected when modelling (conventional) UD fibre-reinforced laminates.

Following Vogler et al. [266], the quadratic invariants $\operatorname{tr}\boldsymbol{\sigma}^2$ and $\operatorname{tr}(\mathbf{A}\boldsymbol{\sigma}^2)$ of the functional basis (7.3) are reformulated assuming a decomposition of the stress tensor $\boldsymbol{\sigma}$ in plasticity inducing stresses $\boldsymbol{\sigma}^p$ and reaction stresses $\boldsymbol{\sigma}^r$ [332]:

$$\boldsymbol{\sigma} = \boldsymbol{\sigma}^p + \boldsymbol{\sigma}^r \tag{7.4}$$

with:

$$\boldsymbol{\sigma}^r = \frac{1}{2}(\operatorname{tr}\boldsymbol{\sigma} - \mathbf{a}\boldsymbol{\sigma}\mathbf{a})\mathbf{1} - \frac{1}{2}(\operatorname{tr}\boldsymbol{\sigma} - 3\mathbf{a}\boldsymbol{\sigma}\mathbf{a})\mathbf{A} \tag{7.5a}$$

$$\boldsymbol{\sigma}^p = \boldsymbol{\sigma} - \boldsymbol{\sigma}^r \tag{7.5b}$$

The reaction stress tensor $\boldsymbol{\sigma}^r$ contains the hydrostatic pressure and the projection of the stress tensor onto the preferred direction $\mathbf{a}$. Since the fibre-dominated failure mechanisms are treated separately in the formulation of the failure criteria, the quadratic invariants of the functional basis are reformulated choosing the plasticity inducing stress tensor $\boldsymbol{\sigma}^p$. This procedure enables the identification of transverse shear loading and in-plane shear loading solely with invariants I_1 and I_2, respectively. The linear invariants $\operatorname{tr}\boldsymbol{\sigma}$ and $\operatorname{tr}(\mathbf{A}\boldsymbol{\sigma})$ of the functional basis (7.3) are used to define the third invariant I_3. With the invariant I_3, pressure dependent failure is regarded, which is experimentally observed in FRPs [334]. The set of transversely isotropic invariants used to formulate the failure surface reads [266]:

$$I_1 = \frac{1}{2}\operatorname{tr}(\boldsymbol{\sigma}^p)^2 - \mathbf{a}\,(\boldsymbol{\sigma}^p)^2\,\mathbf{a} \tag{7.6a}$$

$$I_2 = \mathbf{a}\,(\boldsymbol{\sigma}^p)^2\,\mathbf{a} \tag{7.6b}$$

$$I_3 = \operatorname{tr}\boldsymbol{\sigma} - \mathbf{a}\boldsymbol{\sigma}\mathbf{a} \tag{7.6c}$$

which, after substitution of equations (7.1), (7.2), (7.4) and (7.5), can be rewritten as:

$$I_1 = \frac{1}{4}\sigma_{22}^2 - \frac{1}{2}\sigma_{22}\sigma_{33} + \frac{1}{4}\sigma_{33}^2 + \sigma_{23}^2 \tag{7.7a}$$

$$I_2 = \sigma_{12}^2 + \sigma_{13}^2 \tag{7.7b}$$

$$I_3 = \sigma_{22} + \sigma_{33} \tag{7.7c}$$

Having defined the set of invariants (7.6) (or (7.7)), following Vogler et al. [266], the transversely isotropic failure criterion for transverse failure of UD fibre-reinforced laminates reads:

$$f_M = \alpha_1 I_1 + \alpha_2 I_2 + \alpha_3 I_3 + \alpha_{32} I_3^2 \leq 1 \tag{7.8}$$

with:

$$\begin{aligned} &\alpha_3 = \alpha_3^t, \alpha_{32} = \alpha_{32}^t \text{ if } I_3 > 0, \quad \text{and} \\ &\alpha_3 = \alpha_3^c, \alpha_{32} = \alpha_{32}^c \text{ if } I_3 \leq 0 \end{aligned} \tag{7.9}$$

The distinction concerning $I_3 > 0$ and $I_3 \leq 0$ allows the criterion to represent failure under biaxial stress states.

The failure criterion represented by equation (7.8) results in six failure parameters that, together with the respective invariants, are related to certain load states: transverse shear, in-plane shear, uniaxial tension/compression and biaxial tension/compression. These six failure parameters can be calculated imposing simple stress states and applying the failure criterion (for a detailed explanation, the reader is referred to Ref. [266]). Taking the x_1-direction as the fibre direction, the six failure parameters read [266]:

$$\alpha_1 = \frac{1}{S_T^2} \tag{7.10a}$$

$$\alpha_2 = \frac{1}{S_L^2} \tag{7.10b}$$

$$\alpha_{32}^t = \frac{1 - \dfrac{Y_T}{2Y_{BT}} - \alpha_1 \dfrac{Y_T^2}{4}}{Y_T^2 - 2Y_{BT}Y_T} \tag{7.10c}$$

$$\alpha_3^t = \frac{1}{2Y_{BT}} - 2\alpha_{32}^t Y_{BT} \tag{7.10d}$$

$$\alpha_{32}^c = \frac{1 - \dfrac{Y_C}{2Y_{BC}} - \alpha_1 \dfrac{Y_C^2}{4}}{Y_C^2 - 2Y_{BC}Y_C} \tag{7.10e}$$

$$\alpha_3^c = \frac{1}{2Y_{BC}} - 2\alpha_{32}^c Y_{BC} \tag{7.10f}$$

where S_T and S_L are respectively the transverse and in-plane shear strengths, Y_T and Y_C are respectively the transverse tensile and compressive strengths, and Y_{BT} and Y_{BC} are respectively the biaxial transverse tensile and compressive strengths.

A summary of the resulting failure conditions for matrix-dominated failure is shown in section 7.4.

7.2.2. Alternative model parameters identification

The transverse biaxial tensile and compressive strengths (Y_{BT} and Y_{BC}, respectively) of structural composites are seldom available. To overcome this drawback, an alternative model parameters identification procedure is proposed.

As described in section 7.2.1, the definition of the reaction stress tensor $\boldsymbol{\sigma}^r$ and the reformulation of the quadratic invariants of the functional basis using the plasticity inducing stress tensor $\boldsymbol{\sigma}^p$ instead of $\boldsymbol{\sigma}$, allows the identification of transverse shear loading and in-plane shear loading solely with invariants I_1 and I_2, respectively. Therefore, the parameters α_1 (equation (7.10a)) and α_2 (equation (7.10b)) do not impose any difficulty in their identification.

7.2. Invariant-based failure criterion for transverse failure

Following the same reasoning proposed by Vogler et al. [266], consider a transverse isotropic material subjected to a transverse uniaxial load. Applying the invariant-based failure criterion, at failure ($\sigma_{22} = Y_{T/C}$ and $\sigma_{ij} = 0$), the failure index f_M yields:

$$f_M = \alpha_1 \frac{Y_{T/C}^2}{4} + \alpha_3^{t/c}\, Y_{T/C} + \alpha_{32}^{t/c}\, Y_{T/C}^2 - 1 = 0 \tag{7.11}$$

To identify the parameters $\alpha_3^{t/c}$ and $\alpha_{32}^{t/c}$, a second stress state at failure must be known for the tensile and compressive cases. When biaxial data is not available, simple off-axis tests can be performed and the corresponding data used for parameter identification. Note that only off-axis tests exhibiting a transverse, matrix-dominated failure mode must be considered. For test procedures on off-axis compression the reader is referred, for example, to Ref. [265], and for test procedures on off-axis tension the reader is referred to Refs. [335, 336].

Consider a transversely isotropic material with its preferred direction at an angle ϕ (off-axis angle) with the loading direction[1]. Applying the invariant-based failure criterion, at failure ($\sigma = \sigma_u$), the failure criterion f_M yields:

$$\begin{aligned} f_M = \alpha_1 \left[\frac{1}{4} \left(\sigma_u^{t/c}\right)^2 \sin^2\phi_{t/c} \left(3\cos^2\phi_{t/c} + 1\right) - \left(\sigma_u^{t/c}\right)^2 \sin^2\phi_{t/c}\, \cos^2\phi_{t/c} \right] + \\ + \alpha_2 \left(\sigma_u^{t/c}\right)^2 \sin^2\phi_{t/c}\, \cos^2\phi_{t/c} + \alpha_3^{t/c}\, \sigma_u^{t/c} \sin^2\phi_{t/c} + \\ + \alpha_{32}^{t/c} \left(\sigma_u^{t/c}\right)^2 \sin^4\phi_{t/c} - 1 = 0 \end{aligned} \tag{7.12}$$

where $\sigma_u^{t/c}$ is the ultimate (tensile/compressive) stress applied to the off-axis specimen and $\phi_{t/c}$ is the corresponding off-axis angle. Equations (7.11) and (7.12) can now be solved for $\alpha_3^{t/c}$ and $\alpha_{32}^{t/c}$, yielding:

$$\alpha_3^{t/c} = \frac{1}{Y_{T/C}} - \frac{1}{4}\,\alpha_1\, Y_{T/C} - \alpha_{32}^{t/c}\, Y_{T/C} \tag{7.13a}$$

$$\begin{aligned} \alpha_{32}^{t/c} = & \frac{1 - \frac{1}{4}\,\alpha_1 \left(\sigma_u^{t/c}\right)^2 \sin^4\phi_{t/c} - \alpha_2 \left(\sigma_u^{t/c}\right)^2 \sin^2\phi_{t/c}\, \cos^2\phi_{t/c}}{\left(\sigma_u^{t/c}\right)^2 \sin^4\phi_{t/c} - Y_{T/C}\, \sigma_u^{t/c} \sin^2\phi_{t/c}} - \\ & - \frac{\frac{1}{Y_{T/C}} - \frac{1}{4}\,\alpha_1 Y_{T/C}}{\sigma_u^{t/c} \sin^2\phi_{t/c} - Y_{T/C}} \end{aligned} \tag{7.13b}$$

If the available experimental data is given, for example, as a $\sigma_{22} - \sigma_{12}$ relation (obtained, for instance, from a cylindrical specimen subjected to torsion and axial loading), a critical point, characterised by a maximum transverse (tensile/compressive) stress $\sigma_{22\,u}^{t/c}$ and the corresponding longitudinal shear stress $\sigma_{12\,u}^{t/c}$, can also be used for parameter identification. In this case, applying the invariant-based failure criterion, the failure index f_M yields:

$$f_M = \frac{1}{4}\,\alpha_1 \left(\sigma_{22\,u}^{t/c}\right)^2 + \alpha_2 \left(\sigma_{12\,u}^{t/c}\right)^2 + \alpha_3^{t/c}\, \sigma_{22\,u}^{t/c} + \alpha_{32}^{t/c} \left(\sigma_{22\,u}^{t/c}\right)^2 - 1 = 0 \tag{7.14}$$

Solving equations (7.11) and (7.14), the parameters $\alpha_3^{t/c}$ and $\alpha_{32}^{t/c}$ read:

[1] This is the case, for instance, of an UD laminate with an off-axis fibre orientation ϕ.

$$\alpha_3^{t/c} = \frac{1}{Y_{T/C}} - \frac{1}{4}\,\alpha_1\,Y_{T/C} - \alpha_{32}^{t/c}\,Y_{T/C} \tag{7.15a}$$

$$\alpha_{32}^{t/c} = \frac{1 - \left(\dfrac{1}{Y_{T/C}} - \dfrac{1}{4}\,\alpha_1\,Y_{T/C}\right)\sigma_{22\,u}^{t/c} - \dfrac{1}{4}\,\alpha_1\left(\sigma_{22\,u}^{t/c}\right)^2 - \alpha_2\left(\sigma_{12\,u}^{t/c}\right)^2}{\left(\sigma_{22\,u}^{t/c}\right)^2 - Y_{T/C}\,\sigma_{22\,u}^{t/c}} \tag{7.15b}$$

The set of equations (7.13) and (7.15) allow the identification of the parameters $\alpha_3^{t/c}$ and $\alpha_{32}^{t/c}$ without the need for complicated transverse biaxial tests. It is interesting to note the possibility of using simple off-axis tests for parameter identification. It should be stressed, however, that the failure predictions of the proposed failure criteria are more sensitive to the experimental data used for model parameters identification when the alternative procedure shown here is adopted (for example, in some cases, the $\sigma_{22} - \sigma_{33}$ failure locus may become open in the biaxial transverse compression range). Therefore, whenever biaxial data is available (in particular Y_{BC}), the model parameters identification procedure described by Vogler et al. [266] is recommended.

7.2.3. Orientation of the fracture plane: pragmatic approach

As discussed by Christensen and DeTeresa [330], determining the orientation of the fracture plane of composite laminates under transverse, matrix-dominated failure can be very interesting, since it provides a useful evaluation tool, not only in comparing the various failure theories, but also in assessing failure mode types. On the other hand, its knowledge is essential for the accurate representation of transverse cracking by means of smeared crack formulations, since the orientation of the transverse crack cannot be known in advance [108].

Phenomenological failure theories based on the approach proposed by Puck and Schürmann [102, 327] determine the orientation of the fracture plane through a maximisation problem, namely by searching for the *plane of maximum stress effort* (e.g. Refs. [103, 104, 128, 328, 337]). This is, therefore, a direct outcome of the failure criteria. However, for failure criteria based on the invariant theory, since a *coordinate system-free* description of failure is considered, there is no means of obtaining the local coordinate system associated with the *maximum effort* directly from the criteria, and the orientation of the fracture plane cannot be determined. Hence, a pragmatic approach has to be considered in order to obtain at least an estimate of the orientation of the fracture plane.

According to Thom [338], for a transverse compression-dominated failure mode, the stress normal to the fracture plane (t_n) remains constant and equal to the transverse shear strength (S_T). Thus, for $\sigma_{22} < 0$ (compression) and $|\sigma_{22}| \geq S_T$, the following relation can be assumed:

$$|t_n| = |\sigma_{22}|\cos^2\alpha = S_T \tag{7.16}$$

and the orientation of the fracture plane, α, can be estimated as:

$$\alpha = \arccos\sqrt{\frac{S_T}{|\sigma_{22}|}} \tag{7.17}$$

However, based on Puck's observations, Thom [338] suggested the use of a factor R_{23}, instead of the transverse shear strength S_T, derived from Mohr's circle based on transverse compression (see also Ref. [103]):

$$R_{23} = \frac{|Y_C|}{2}\cot\alpha_0 \tag{7.18}$$

where α_0 is the fracture angle for pure transverse compression. The orientation of the fracture angle, α, for a general transverse compression-dominated failure is then:

7.2. Invariant-based failure criterion for transverse failure

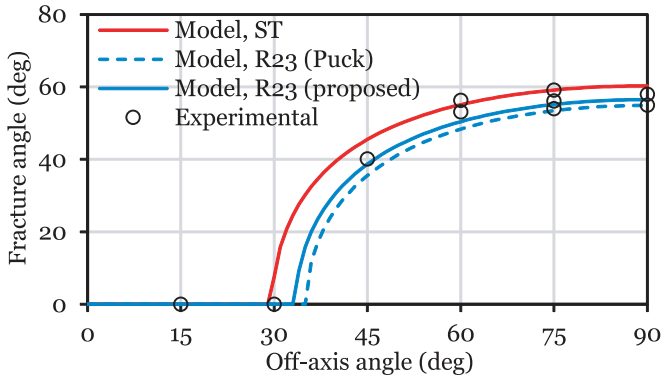

Fig. 7.1. Orientation of the fracture plane as a function of the off-axis angle of off-axis compression tests performed by Koerber et al. [265], and a comparison with the results from the proposed expressions used to estimate the fracture angle.

$$\alpha = \arccos \sqrt{\frac{R_{23}}{|\sigma_{22}|}} \tag{7.19}$$

If equations (7.18) and (7.19) are used to estimate the orientation of the fracture angle, it is observed, however, that, for pure transverse compression, the predicted fracture angle does not coincide with α_0, which is unreasonable. Therefore, instead of equation (7.18), the following expression should be used to calculate the factor R_{23}:

$$R_{23} = |Y_C| \cos^2 \alpha_0 \tag{7.20}$$

which can be obtained manipulating equation (7.17) and considering $\alpha = \alpha_0$ when $\sigma_{22} = Y_C$ (pure transverse compression).

Koerber et al. [265] performed off-axis compression tests on IM7/8552 carbon-epoxy and measured the orientation of the fracture plane. Figure 7.1 shows the orientation of the fracture plane as a function of the off-axis angle obtained by Koerber et al. [265], and a comparison with the results from the expressions presented before to estimate the orientation of the fracture angle. In figure 7.1, "*Model, ST*" refers to equation (7.17), whereas "*Model, R23 (Puck)*" and "*Model, R23 (proposed)*" refer to equations (7.18) and (7.19) and to equations (7.19) and (7.20), respectively.

Comparing the estimates shown in figure 7.1 with the experimental results, it is clear that equations (7.19) and (7.20) give the best predictions. When using equations (7.18) and (7.19), the predictions are also very good; however, as already mentioned, in spite of using the angle α_0 to calculate the factor R_{23}, the prediction of the orientation of the fracture plane for pure transverse compression does not coincide with α_0, which is, from a conceptual point of view, not reasonable. Therefore, if the fracture angle α_0 is known *a priori*, the author suggests the use of equations (7.19) and (7.20) to estimate the orientation of the fracture plane. Observing the predictions from equation (7.17), it can be seen that the estimates are reasonable, particularly when taking into account that the fracture angle α_0 is never used to obtain such estimates. Hence, it can be concluded that, in case α_0 is not known, equation (7.17) can be used to estimate the orientation of the fracture plane, without incurring on unrealistic predictions.

From figure 7.1, it is clear that, in the case of transverse compression-dominated failure for a state of plane stress, the proposed expressions give good predictions of the orientation of the fracture angle, without any kind of maximisation procedure or search for the *plane of maximum stress effort*. But for the general 3D case, other stress states and combinations of them should also be addressed. For example, when subjected to through-the-thickness transverse compression ($\sigma_{33} < 0$), a similar type of expressions to those presented for in-plane transverse compression ($\sigma_{22} < 0$) can be deduced. In this case, assuming a transverse compression-dominated failure mode ($\sigma_{33} < 0$ and $|\sigma_{33}| \geq R_{23}$), the orientation of the fracture plane can be estimated as:

$$\alpha = \arcsin \sqrt{\frac{R_{23}}{|\sigma_{33}|}} \tag{7.21}$$

where R_{23} is given by equation (7.20); if α_0 is not known *a priori*, $R_{23} = S_T$ can be adopted (as already shown for in-plane transverse compression). Notice that α_0 is the orientation of the fracture plane when pure in-plane transverse compression ($\sigma_{22} = Y_C$, $\sigma_{ij} = 0$) is applied. In the case of biaxial transverse compression, it is assumed that, when $|\sigma_{22}| > |Y_C|$ or $|\sigma_{33}| > |Y_C|$, the orientation of the fracture angle remains constant. Thus, equations (7.19) and (7.21) can be rewritten, respectively, as:

$$\alpha = \arccos \sqrt{\frac{R_{23}}{\min\{|\sigma_{22}|, |Y_C|\}}} \tag{7.22}$$

and

$$\alpha = \arcsin \sqrt{\frac{R_{23}}{\min\{|\sigma_{33}|, |Y_C|\}}} \tag{7.23}$$

For general transverse compressive failure ($I_3 < 0$), it is assumed that the highest transverse stress (in absolute value) will define the orientation of the fracture plane. In other words, when $I_3 < 0$, $|\sigma_{22}| > |\sigma_{33}|$ and $|\sigma_{22}| \geq S_T$, equation (7.22) holds; on the other hand, if $I_3 < 0$, $|\sigma_{33}| > |\sigma_{22}|$ and $|\sigma_{33}| \geq S_T$, equation (7.23) must be used.

When $I_3 < 0$ but $|\sigma_{22}| < S_T$ and $|\sigma_{33}| < S_T$, or when $I_3 > 0$, failure is either dominated by a transverse state of stress or by longitudinal shear. To assess which failure mode is dominating, the contribution of each type of stressing to the failure criterion can be used. Thus, if $\left|\alpha_1 I_1 + \alpha_3 I_3 + \alpha_{32} I_3^2\right| > |\alpha_2 I_2|$, the fracture angle can be estimated by the orientation of the plane of the secondary principal stresses:

$$\alpha = \frac{1}{2} \arctan\left(\frac{2\sigma_{23}}{\sigma_{22} - \sigma_{33}}\right) \tag{7.24}$$

otherwise, the orientation of the fracture angle can be estimated by the in-plane shear effort:

$$\alpha = \arctan\left(\frac{\sigma_{13}}{\sigma_{12}}\right) \tag{7.25}$$

Table 7.1 shows the experimental results for the orientation of the fracture plane under transverse tensile and compressive failure given by Christensen and DeTeresa [330], and a comparison with the predictions of the proposed pragmatic approach. For transverse compression, the relation $R_{23} = S_T$ was adopted. A very good correlation between experiments and predictions can be observed.

7.2.4. *In situ* properties

As discussed in chapter 6, when embedded in a multidirectional laminate, the actual strengths of the laminae whose fibre orientation is perpendicular to the loading direction are not only higher than those measured in UD coupons, as they reportedly increase with decreasing ply thickness [35, 81, 91–97, 287]. In fact, early research about the strength prediction of multidirectional laminates has shown that using as ply properties those measured directly from UD plies, regardless of ply orientation or laminate thickness, results in very conservative predictions that could differ substantially from the experimental results [83, 95, 102, 109].

This deterministic size effect, known as the *in situ* effect, is typically taken into account by using fracture mechanics models that predict the relation between the ply thickness, its fracture toughness and the *in situ* strengths [81, 98], whose accurate determination is necessary for implementation of any physically-based failure criteria for transverse fracture in

Table 7.1
Experimental results for the orientation of the fracture plane under transverse tensile and compressive failure [330], and a comparison with the predictions of the proposed pragmatic approach.

Material	Transverse strengths (MPa)	Orientation of the fracture plane (°)		
			Measured	Predicted
AS4/Ultem[a]	Tension	78.6	90	90
	Compression	191.0	38 (±1.2)[c]	39.9
AS4/3501-6[b]	Tension	64.8	90	90
	Compression	241.3	31 (±4.7)[c]	31.2

[a] AS4 carbon fibre-reinforced thermoplastic (Ultem polyetherimide)

[b] AS4 carbon fibre-reinforced 3501-6 untoughened epoxy

[c] Standard deviation

multidirectional laminates [81, 99–108]. In the case of in-plane shear, Linear Elastic Fracture Mechanics alone is not able to accurately predict the *in situ* strength, and the nonlinear shear response typically observed in laminated composites must be included in the prediction models [81].

To account for the effect of ply thickness when the laminae are embedded in a multidirectional laminate, proper definitions of the *in situ* properties must be accounted for in the criterion that predicts transverse fracture. The *in situ* transverse tensile and in-plane shear strengths, Y_T^{is} and S_L^{is} respectively, can be calculated using the analytical models proposed by Camanho et al. [81]. The remaining transverse strength properties, though, should be defined in the framework of the corresponding failure criterion [128, 129].

The *in situ* transverse shear strength, S_T^{is}, and the *in situ* biaxial transverse tensile strength, Y_{BT}^{is}, are calculated imposing [128]:

$$\begin{cases} \eta_L^{(+)} = \eta_{L,is}^{(+)} \\ \eta_T^{(+)} = \eta_{T,is}^{(+)} \end{cases} \tag{7.26}$$

where η_L and η_T are, respectively, the slopes in the σ_{22}–σ_{12} and σ_{22}–σ_{23} failure envelopes when $\sigma_{22} = 0$ [102] (figure 6.41). They depend on the sign of the stress component σ_{22} and, for the tensile case, can be defined as:

$$\eta_L^{(+)} = \left.\frac{\partial \sigma_{12}}{\partial \sigma_{22}^{(+)}}\right|_{\sigma_{22}=0^+} = -\frac{1}{2}\frac{\alpha_3^t}{\sqrt{\alpha_2}} \tag{7.27}$$

$$\eta_T^{(+)} = \left.\frac{\partial \sigma_{23}}{\partial \sigma_{22}^{(+)}}\right|_{\sigma_{22}=0^+} = -\frac{1}{2}\frac{\alpha_3^t}{\sqrt{\alpha_1}} \tag{7.28}$$

The system of equations (7.26) can be solved for S_T^{is} and Y_{BT}^{is} using, for example, a numerical procedure based on floating-point arithmetics.

In compression, it is assumed that the biaxial transverse compressive strength is not an *in situ* property, i.e. $Y_{BC}^{is} = Y_{BC}^{ud}$. This can be justified observing figure 7.2. Under transverse biaxial compression, the confinement is promoted by the surrounding pressure; therefore, it is assumed that the adjacent plies do not affect such constraining effect.

Assuming that $Y_{BC}^{is} = Y_{BC}^{ud}$, the *in situ* transverse compressive strength, Y_C^{is}, can be determined imposing one of the following relations (both giving the same result):

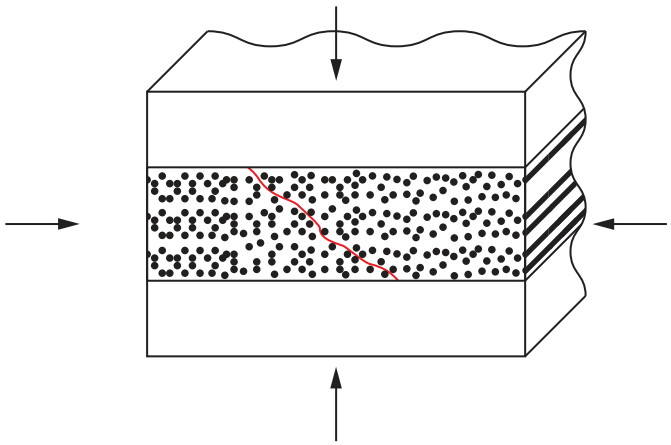

Fig. 7.2. Representative volume element of a multidirectional laminate subjected to biaxial transverse compression.

$$\eta_L^{(-)} = \eta_{L,is}^{(-)} \tag{7.29a}$$

$$\eta_T^{(-)} = \eta_{T,is}^{(-)} \tag{7.29b}$$

with:

$$\eta_L^{(-)} = \left.\frac{\partial \sigma_{12}}{\partial \sigma_{22}^{(-)}}\right|_{\sigma_{22}=0^-} = -\frac{1}{2}\frac{\alpha_3^c}{\sqrt{\alpha_2}} \tag{7.30}$$

$$\eta_T^{(-)} = \left.\frac{\partial \sigma_{23}}{\partial \sigma_{22}^{(-)}}\right|_{\sigma_{22}=0^-} = -\frac{1}{2}\frac{\alpha_3^c}{\sqrt{\alpha_1}} \tag{7.31}$$

Equation (7.29) can be solved for Y_C^{is} using a numerical procedure based on floating-point arithmetics.

As an example, table 7.2 shows the UD properties and the *in situ* properties for a 0.125 mm thick IM7/8552 carbon-epoxy inner ply, calculated using the procedure just described. E_{11} and E_{22} are respectively the longitudinal and transverse Young's moduli, G_{12} is the in-plane shear modulus, ν_{12} is the major in-plane Poisson's ratio, $\mathcal{G}_{Ic}$ and $\mathcal{G}_{IIc}$ are respectively the mode I and mode II transverse intralaminar fracture toughness, β is a parameter that defines the nonlinearity of the shear stress-shear strain relation [307] (equation (6.15)), and X_T and X_C are respectively the longitudinal tensile and compressive strengths. Figure 7.3 shows the relation between the ply thickness and the *in situ* strengths calculated using the same procedure. These values are not far from those obtained using alternative failure criteria [128].

7.2.5. Preliminary results

Following previous work [318, 338], it is assumed that the transverse shear strength, S_T, is equal to the transverse tensile strength, Y_T. This assumption is based on the observation that under pure transverse shear the fracture angle is roughly 45°. In this case, the first principal stress, σ_1, equals the shear transverse stress σ_{23} (figure 7.4). In other words, for pure transverse shear, σ_1 acts as in the case of transverse tension, but in a rotated frame. Therefore, at failure, the critical transverse shear stress, or transverse shear strength, S_T, equals the transverse tensile strength, Y_T.

Figure 7.5 shows the failure envelopes of IM7/8552 carbon-epoxy obtained with the invariant-based failure criterion for several stress states involving transverse failure mechanisms only. The material properties used to compute the failure envelopes are shown in table 7.2.

Table 7.2
IM7/8552 carbon-epoxy UD material properties and *in situ* transverse strengths for a 0.125 mm thick IM7/8552 inner ply embedded in a multidirectional laminate.

Properties		References
Elastic properties		
E_{11} (MPa)	171420	Camanho and Lambert [235]
E_{22} (MPa)	9080	Camanho and Lambert [235]
G_{12} (MPa)	5290	Camanho and Lambert [235]
ν_{12} (-)	0.32	Camanho and Lambert [235]
Fracture toughness		
$\mathcal{G}_{Ic}$ (N/mm)	0.277	Camanho and Lambert [235]
$\mathcal{G}_{IIc}$ (N/mm)	0.788	Camanho and Lambert [235]
Shear nonlinearity [307]		
β (MPa^{-3})	2.98×10^{-8}	Camanho and Lambert [235]
UD longitudinal strengths		
X_T (MPa)	2323.5	Catalanotti et al. [128]
X_C (MPa)	-1017.5	Catalanotti et al. [128]
UD transverse strengths		
Y_T (MPa)	62.3	Camanho and Lambert [235]
Y_{BT} (MPa)	38.7	Vogler et al. [266]
Y_C (MPa)	-253.7	Koerber et al. [265]
Y_{BC} (MPa)	-600.0	Vogler et al. [266]
S_L (MPa)	89.6	Catalanotti et al. [128]
S_T (MPa)	62.3	$S_T = Y_T$ (section 7.2.5)
***In situ* transverse strengths**		
Y_T^{is} (MPa)	160.5	Camanho et al. [81]
Y_{BT}^{is} (MPa)	102.1	Equation (7.26)
Y_C^{is} (MPa)	-344.1	Equation (7.29)
Y_{BC}^{is} (MPa)	-600.0	$Y_{BC}^{is} = Y_{BC}^{ud}$
S_L^{is} (MPa)	130.2	Camanho et al. [81]
S_T^{is} (MPa)	90.5	Equation (7.26)

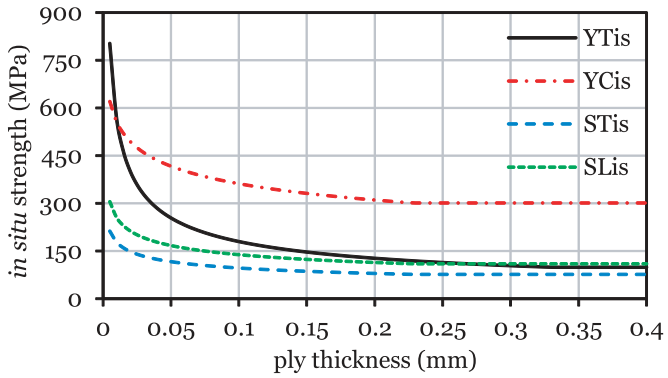

Fig. 7.3. Relation between ply thickness the *in situ* strengths for the IM7/8552 carbon-epoxy.

Observing the $\sigma_{22} - \sigma_{12}$ stress space (figure 7.5c), as expected, when the transverse stress σ_{22} becomes compressive, the apparent shear strength increases. It is noted, however, that, for transverse failure mechanisms, the transversely isotropic invariant-based failure criterion does not distinguish between the longitudinal shear stresses σ_{12} and σ_{13} (see equations (7.6b) and (7.7b)). Consequently, unlike what is observed in other phenomenological failure criteria [102, 103, 128, 282, 327, 328], the failure loci for the $\sigma_{22} - \sigma_{12}$ (figure 7.5c) and $\sigma_{22} - \sigma_{13}$ (figure 7.5d) stress spaces (or $\sigma_{33} - \sigma_{13}$ and $\sigma_{33} - \sigma_{12}$) are exactly the same. This does not respect the different interaction of the stress combinations $\sigma_{22} - \sigma_{12}$ and $\sigma_{22} - \sigma_{13}$ (or $\sigma_{33} - \sigma_{13}$ and $\sigma_{33} - \sigma_{12}$), which arises from a typical material asymmetry observed in laminated composites [318]. Because σ_{22} and σ_{13} (or σ_{33} and σ_{12}) act on different planes, no interaction between them should exist [128].

Cuntze and Freund [318], after *an intense trial and error search*, proposed an invariant term that respects such different interactions. Nevertheless, such term results in mathematical inconsistencies when applied to the proposed failure criterion for longitudinal compressive failure by fibre kinking (section 7.3.2). Because disrespecting the different interaction between the transverse stresses and longitudinal shear stresses acting on different planes is a side effect of the invariant theory, with negligible influence on the failure predictions for the typical load cases observed in composite structures, it is believed that the advantages of the proposed criteria, namely the elegant coordinate system-free description of failure and the ability to predict failure under high values of hydrostatic pressure (figure 7.6), overcome this limitation.

Figure 7.6 shows the $\sigma_{22} - \sigma_{33}$ failure envelopes when nonzero σ_{12} (figure 7.6a), σ_{13} (figure 7.6b), or σ_{23} (figure 7.6c) shear stresses are applied. Unlike other 3D failure criteria (e.g. Refs. [128, 328]), under biaxial transverse compression the failure envelopes are not open. Thus, the proposed failure criteria is able to predict material failure under high values of hydrostatic pressure, typically seen in the resins used in structural composites [334, 339]. Under hydrostatic tension, a gradual variation of the failure locus is observed, i.e. an interaction between $\sigma_{22} > 0$ and $\sigma_{33} > 0$ exists. Also, observing figure 7.6, it is shown that, for low values of negative transverse stresses ($\sigma_{22(33)} < 0$), the apparent transverse tensile strength ($\sigma_{33(22)} > 0$) increases slightly. Finally, figure 7.6 shows that, in relative terms, the effect of nonzero shear stresses (σ_{12}, σ_{13}, or σ_{23}) on the $\sigma_{22} - \sigma_{33}$ failure envelope is the same; increasing the shear stresses, the failure envelope is reduced.

Finally, figure 7.7 shows the $\sigma_{22} - \sigma_{12}$ failure envelopes when a nonzero transverse stress σ_{33} is applied. When $\sigma_{33} > 0$, the failure locus is reduced, either when the transverse stress σ_{22} is positive or negative. This result does not agree with the results obtained by Catalanotti et al. [128] when $\sigma_{33} > 0$ and $\sigma_{22} > 0$, who claim that, in this case, the failure envelope must remain constant. According to Catalanotti et al. [128], there is no interaction between σ_{22} and σ_{33} when they are both positive. However, the invariant-based failure criteria predicts such interaction, as observed in figure 7.6 (this has been validated using the results from a computational micro-mechanics framework — section 7.2.5).

It is also noted that, when $\sigma_{33} < 0$, the longitudinal shear stress σ_{12} increases slightly for low values of σ_{33} (figure 7.7), as a result of the interaction predicted by the invariant-based failure criteria for this stress-state, as discussed earlier. For

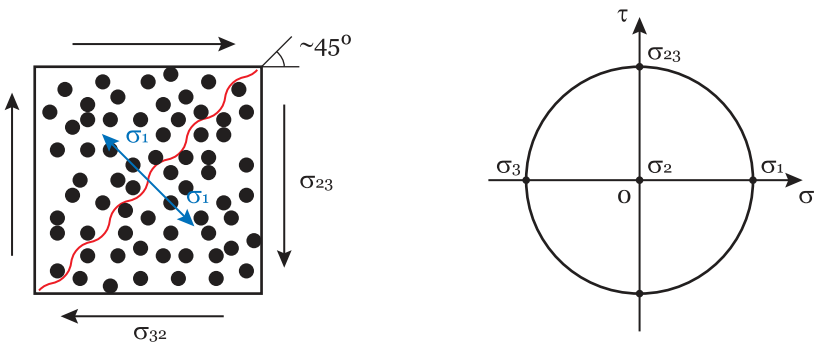

Fig. 7.4. Mohr's circle for pure transverse shear.

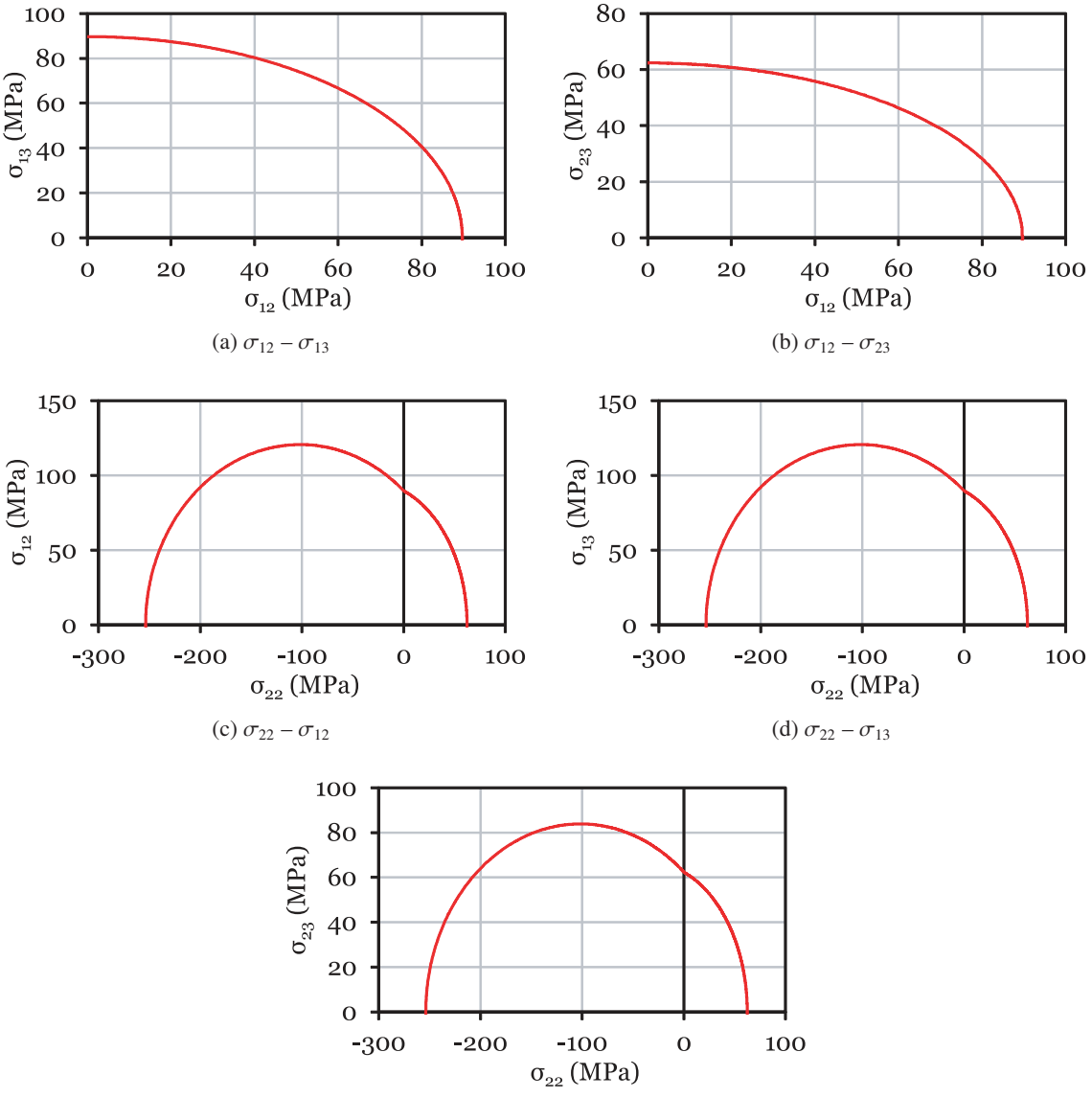

(a) $\sigma_{12} - \sigma_{13}$

(b) $\sigma_{12} - \sigma_{23}$

(c) $\sigma_{22} - \sigma_{12}$

(d) $\sigma_{22} - \sigma_{13}$

(e) $\sigma_{22} - \sigma_{23}$

Fig. 7.5. Failure envelopes of IM7/8552 carbon-epoxy for several stress states obtained with the invariant-based failure criterion for transverse failure mechanisms.

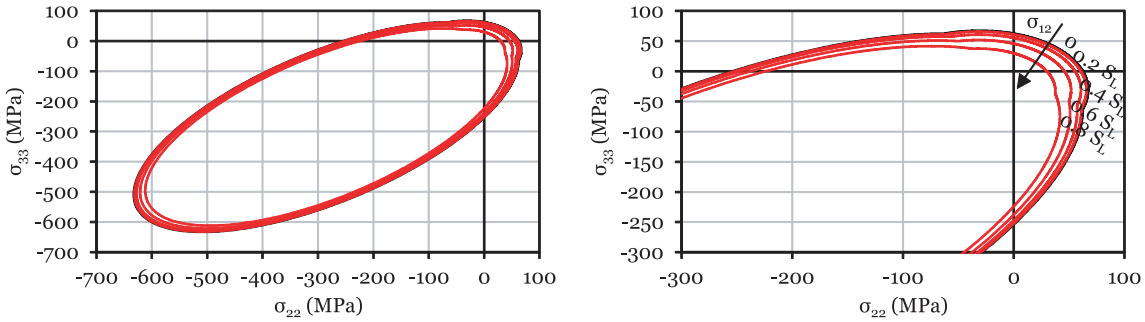

(a) Nonzero longitudinal in-plane shear stress σ_{12}.

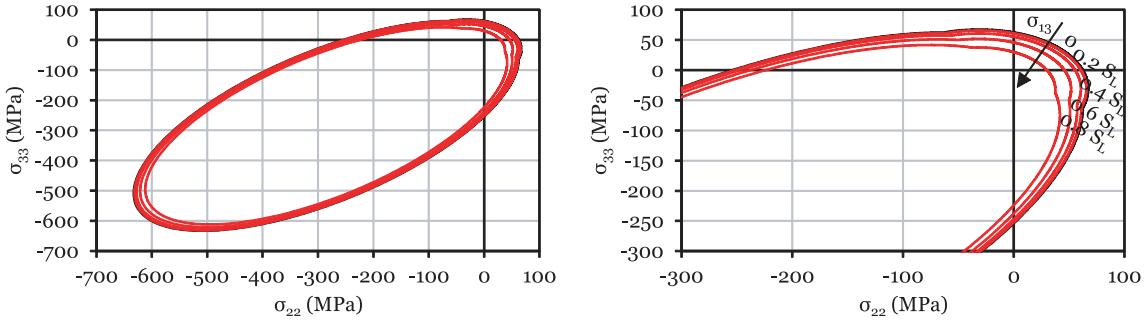

(b) Nonzero longitudinal out-of-plane shear stress σ_{13}.

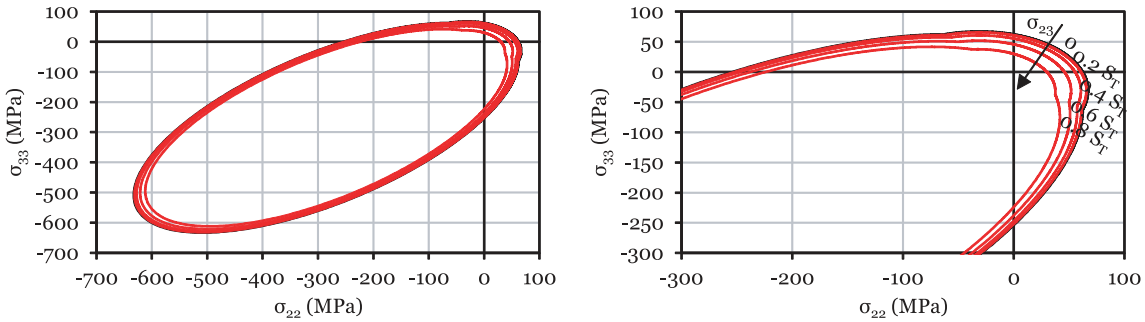

(c) Nonzero transverse shear stress σ_{23}.

Fig. 7.6. $\sigma_{22} - \sigma_{33}$ failure envelopes of IM7/8552 carbon-epoxy with nonzero σ_{12}, σ_{13} or σ_{23} shear stresses.

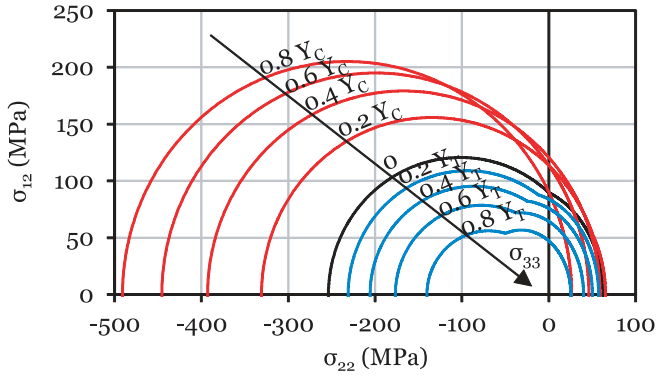

Fig. 7.7. $\sigma_{22} - \sigma_{12}$ failure envelopes of IM7/8552 carbon-epoxy when a nonzero transverse stress σ_{33} is applied.

higher values of σ_{33}, however, the longitudinal shear stress σ_{12} decreases considerably. On the other hand, negative values of σ_{33} have a substantial beneficial effect when $\sigma_{22} < 0$, in agreement with the results of Catalanotti et al. [128].

7.3. Criteria for longitudinal failure

7.3.1. Longitudinal fibre failure ($\sigma_{11} \geq 0$)

Based on experimental evidence, and similarly to other failure criteria [102, 103, 128, 282, 327], tensile fracture in the fibre direction ($\sigma_{11} \geq 0$) is predicted using a noninteracting maximum allowable strain criterion (see section 7.4):

$$f_F = \frac{\varepsilon_{11}}{\varepsilon_1^T} \leq 1 \tag{7.32}$$

where ε_{11} and ε_1^T are respectively the strain component and the tensile strain-to-failure in the fibre direction.

7.3.2. Invariant-based failure criterion for fibre kinking ($\sigma_{11} < 0$)

7.3.2.1. Failure criterion formulation and definition of the preferred direction $\mathbf{a}^{(R)}$ associated with the misaligned fibres in a kink band

The main hypothesis of the proposed model for fibre kinking is that longitudinal compressive failure of FRPs occurs from the collapse of the fibres as a result of damage of the supporting matrix [103, 282]. Because 3D stress states greatly affect the kinking failure mode [128, 328], a 3D kinking model relying on the invariant failure criterion previously formulated for transverse fracture is proposed.

The 3D kinking model assumes that fibre kinking is originated by local micro-structural defects that trigger a kink band when local matrix cracking occurs in the vicinity of the misaligned, micro-buckled fibres. These local micro-structural defects are represented in the model as a local initial fibre misalignment, which leads to shearing stresses between fibres that result in a micro-instability [103, 281, 282].

Figure 7.8 shows the kinking plane in the 3D kinking model. The coordinate system $1^0 2^0 3^0$ is aligned with the material axes of the composite, where 1^0 is the fibre direction and 2^0 and 3^0 are the transverse directions. The kinking plane is associated with the coordinate system $1^1 2^1 3^1$, obtained after rotating by an angle ψ (*angle of the kinking plane*) the $1^0 2^0 3^0$ frame around the 1^0 axis. The misaligned fibres are associated with the rotated $1^R 2^R 3^R$ coordinate system, originated from a rotation of the $1^1 2^1 3^1$ frame by an angle φ (*kinking-angle*) around the 3^1 axis.

Based on the previous assumptions, kinking failure is predicted using the invariant-based formulation for transverse failure in the misalignment frame. Here, the preferred direction, $\mathbf{a}^{(R)}$, is the direction of the misaligned fibres, which coincides with the 1^R-direction (see figure 7.8):

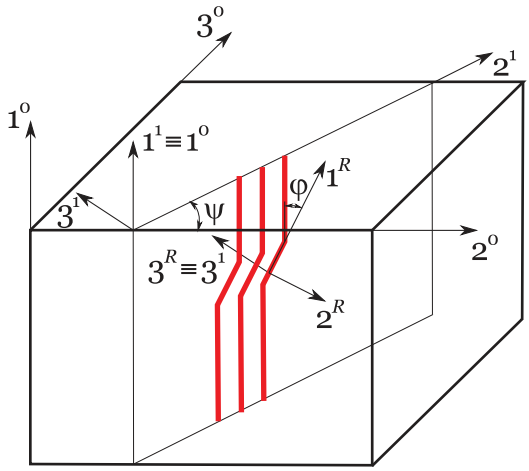

Fig. 7.8. 3D kinking model.

$$\mathbf{a}^{(R)} = [1\ 0\ 0]^{\mathrm{T}} \tag{7.33}$$

To express the preferred direction in the material coordinate system $1^0 2^0 3^0$, two successive transformations are necessary, i.e.:

$$\mathbf{a}^{(0)} = \mathbf{T}_{10} \cdot \mathbf{a}^{1} = \mathbf{T}_{10} \cdot \mathbf{T}_{R1} \cdot \mathbf{a}^{(R)} \tag{7.34}$$

where $\mathbf{T}_{10}$ and $\mathbf{T}_{R1}$ are, respectively, the $1^1 2^1 3^1$–$1^0 2^0 3^0$ and $1^R 2^R 3^R$–$1^1 2^1 3^1$ transformation matrices, defined as:

$$\mathbf{T}_{10} = \begin{bmatrix} 1 & 0 & 0 \\ 0 & \cos\psi & -\sin\psi \\ 0 & \sin\psi & \cos\psi \end{bmatrix} \tag{7.35}$$

and

$$\mathbf{T}_{R1} = \begin{bmatrix} \cos\varphi & -\sin\varphi & 0 \\ \sin\varphi & \cos\varphi & 0 \\ 0 & 0 & 1 \end{bmatrix} \tag{7.36}$$

Solving equation (7.34), the preferred direction in the material coordinate system yields:

$$\mathbf{a}^{(0)} = \begin{bmatrix} \cos\varphi \\ \cos\psi \sin\varphi \\ \sin\psi \sin\varphi \end{bmatrix} \tag{7.37}$$

7.3.2.2. Angle of the kinking plane (ψ)

The angle of the kinking plane, ψ, is the angle that maximises the fibre kinking failure index. It can be obtained applying the kinking failure criterion to a range of tentative angles ψ_i in the range $0 \leq \psi_i < \pi$ [328]. However, because this is a numerically expensive solution, an alternative (pragmatic) expression for ψ is considered, based on the works of Pinho et al. [328] and Catalanotti et al. [128]. Assuming that the angle of the kinking plane, ψ, is a function of the stress

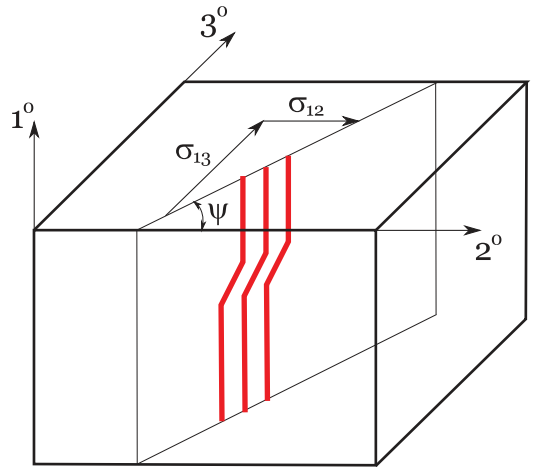

Fig. 7.9. Kinking plane and involved shear stresses (after Catalanotti et al. [128]).

state, in particular of the shear stresses that act on the 2-3 plane (see figure 7.9), the angle of the kinking plane can be calculated as [128]:

$$\psi = \arctan \frac{\sigma_{13}}{\sigma_{12}} \tag{7.38}$$

If both shear stress components σ_{12} and σ_{13} are equal to zero, the angle of the kinking plane can be calculated by the maximum principal stress that acts on the transversely isotropic plane [128]. Following the reasoning presented by Pinho et al. [328], if the shear stress $\sigma_{23}^{(1)}$ in the kinking plane is nonzero, an out-of-plane movement of the kinked fibres would occur, contradicting the evidence that fibres kink on this plane (see figures 7.8 and 7.9). Therefore, imposing $\sigma_{23}^{(1)} = 0$, and knowing that the stress tensor in the kinking plane, $\boldsymbol{\sigma}^{(1)}$, is given by the transformation $\boldsymbol{\sigma}^{(1)} = \mathbf{T}_{01} \cdot \boldsymbol{\sigma} \cdot \mathbf{T}_{01}^{\mathrm{T}} = \mathbf{T}_{10}^{\mathrm{T}} \cdot \boldsymbol{\sigma} \cdot \mathbf{T}_{10}$, the angle of the kinking plane is obtained as:

$$\psi = \frac{1}{2} \arctan\left(\frac{2\sigma_{23}}{\sigma_{22} - \sigma_{33}}\right) \tag{7.39}$$

7.3.2.3. Kinking-angle (φ)

7.3.2.3.1. Linear shear response Figure 7.10 shows the misalignment frame of an UD laminate volume element for generic loading conditions. The kinking-angle φ, or total misalignment, can be calculated as the sum of a constant initial misalignment angle φ_0 and, assuming the kinematics of deformation, an angle φ^R that is originated by the applied shear loading, and that depends on the constitutive law. The initial misalignment angle φ_0 can be taken as a representation of the local micro-structural defects from manufacture, or of the intrinsic fibre volume fraction oscillations in the material. For a material that exhibits linear shear response:

$$\varphi' = \varphi_0 + \varphi^R = \varphi_0 + \frac{\left|\sigma_{12}^{(R)}(\varphi_0, \psi)\right|}{G_{12}}, \text{ and } \varphi = \begin{cases} \varphi', \text{if } \sigma_{12}^{(R)}(\varphi_0, \psi) \geq 0 \\ -\varphi', \text{if } \sigma_{12}^{(R)}(\varphi_0, \psi) < 0 \end{cases} \tag{7.40a}$$

or

$$\varphi = \operatorname{sgn}\left\{\sigma_{12}^{(R)}(\varphi_0, \psi)\right\}\left(\varphi_0 + \frac{\left|\sigma_{12}^{(R)}(\varphi_0, \psi)\right|}{G_{12}}\right) \tag{7.40b}$$

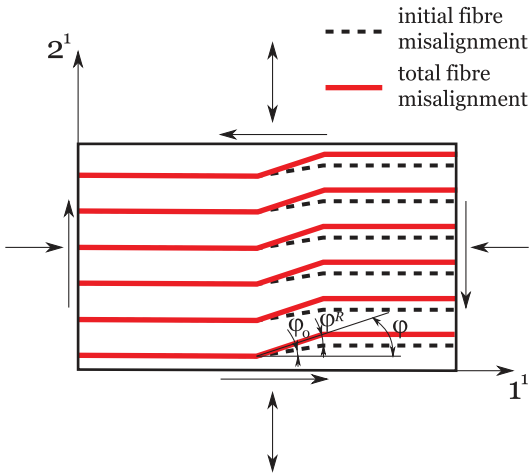

Fig. 7.10. Misalignment frame.

where $\sigma_{12}^{(R)}(\varphi_0, \psi)$ is the applied shear stress in the misalignment frame, which is a function of the initial misalignment angle φ_0 and of the angle of the kinking plane ψ; sgn$\{x\}$ represents the sign of x (i.e., sgn$\{x\} = 1$ if $x \geq 0$, and sgn$\{x\} = -1$ otherwise). In the misalignment frame, the stress state $\boldsymbol{\sigma}^{(R)}$ is given by the transformation of coordinate systems $\boldsymbol{\sigma}^{(R)} = \mathbf{T}_{1R} \cdot \boldsymbol{\sigma}^{(1)} \cdot \mathbf{T}_{1R}^{\mathrm{T}} = \mathbf{T}_{R1}^{\mathrm{T}} \cdot \boldsymbol{\sigma}^{(1)} \cdot \mathbf{T}_{R1}$, with $\boldsymbol{\sigma}^{(1)} = \mathbf{T}_{10}^{\mathrm{T}} \cdot \boldsymbol{\sigma} \cdot \mathbf{T}_{10}$, where the transformation matrices $\mathbf{T}_{10}$ and $\mathbf{T}_{R1}$ are given, respectively, by equations (7.35) and (7.36). Rewriting $\mathbf{T}_{R1}$ (equation (7.36)) with $\varphi = \varphi_0$, the applied shear stress in the misalignment frame, $\sigma_{12}^{(R)}(\varphi_0, \psi)$, yields:

$$\begin{aligned}\sigma_{12}^{(R)}(\varphi_0, \psi) = &\frac{1}{2}\left[-\sigma_{11} + \sigma_{22}\cos^2\psi + \sigma_{33}\sin^2\psi + \sigma_{23}\sin 2\psi\right]\sin 2\varphi_0 + \\ &+ (\sigma_{12}\cos\psi + \sigma_{13}\sin\psi)\cos 2\varphi_0\end{aligned} \tag{7.41}$$

The initial misalignment angle, φ_0, which is taken here as a material property, can be calculated taking the particular case when the material fails under pure longitudinal compression, i.e. when $\sigma_{11} = X_C$ and all the other components of the stress tensor are equal to zero. For this case, recalling equation (7.40b), the total misalignment angle, φ_C, reads:

$$\begin{aligned}\varphi_C &= \varphi_0 + \varphi_C^R \\ \therefore\ \varphi_0 &= \varphi_C - \varphi_C^R\end{aligned} \tag{7.42}$$

where φ_C^R is the angle φ^R when the material fails under pure longitudinal compression. Assuming linear shear behaviour, φ_C^R yields:

$$\varphi_C^R = \frac{|X_C \sin 2\varphi_0|}{2G_{12}} \tag{7.43}$$

Combining equations (7.42) and (7.43), the initial misalignment angle, φ_0, reads:

$$\varphi_0 = \varphi_C - \frac{|X_C \sin 2\varphi_0|}{2G_{12}} \tag{7.44}$$

which is a nonlinear equation in φ_0. Equation (7.44) can be solved numerically using, for instance, the Newton-Raphson method (as shown in section 7.4, assuming $\beta = 0$).

Alternatively, assuming small initial misalignment angles, equation (7.44) can be solved explicitly:

$$\varphi_0 = \varphi_C \left(1 + \frac{|X_C|}{G_{12}}\right)^{-1} \tag{7.45}$$

Finally, it is necessary to determine the misalignment angle at failure when a pure longitudinal compression is applied, φ_C. In this particular case, the stress tensor reads:

$$\boldsymbol{\sigma} = \begin{bmatrix} \sigma_{11} & 0 & 0 \\ 0 & 0 & 0 \\ 0 & 0 & 0 \end{bmatrix} \tag{7.46}$$

and the invariants (equation (7.6)), calculated in the misalignment frame (taking $\mathbf{a} = \mathbf{a}^{(0)}$ — equation (7.37)), yield:

$$I_1 = \frac{1}{4}\sigma_{11}^2 \sin^4\varphi \tag{7.47a}$$

$$I_2 = \sigma_{11}^2 \sin^2\varphi \cos^2\varphi \tag{7.47b}$$

$$I_3 = \sigma_{11} \sin^2\varphi \tag{7.47c}$$

For a pure longitudinal compressive stress state, $\sigma_{11} < 0$. Therefore, from equation (7.47c), $I_3 < 0$, and the failure criterion (equation (7.8)) reads:

$$f = \frac{1}{4}\alpha_1\sigma_{11}^2 \sin^4\varphi + \alpha_2\sigma_{11}^2 \sin^2\varphi\cos^2\varphi + \alpha_3^c\sigma_{11}\sin^2\varphi + \alpha_{32}^c\sigma_{11}^2\sin^4\varphi - 1 \tag{7.48}$$

Equation (7.48) can be rewritten as:

$$\begin{aligned} f = {} & \frac{1}{16}\alpha_1\,\sigma_{11}^2\left(1 - 2\cos 2\varphi + \cos^2 2\varphi\right) + \frac{1}{4}\alpha_2\,\sigma_{11}^2\left(1 - \cos^2 2\varphi\right) + \\ & + \frac{1}{2}\alpha_3^c\,\sigma_{11}(1 - \cos 2\varphi) + \frac{1}{4}\alpha_{32}^c\,\sigma_{11}^2\left(1 - 2\cos 2\varphi + \cos^2 2\varphi\right) - 1 \end{aligned} \tag{7.49}$$

which is a quadratic function of $\cos 2\varphi$. At failure, under pure longitudinal compression, $\sigma_{11} = X_C$ and $f = 0$, and equation (7.49) can be solved for $\varphi = \varphi_C$, yielding[2]:

$$\begin{aligned} \varphi_C = \frac{1}{2}\arccos\Big\{\Big[4\sqrt{\alpha_1 - 4\alpha_2 + \alpha_2^2 X_C^2 + \left(\alpha_3^c\right)^2 + 2\alpha_2\alpha_3^c X_C + 4\alpha_{32}^c} + \\ + \left(\alpha_1 + 4\alpha_{32}^c\right)X_C + 4\alpha_3^c\Big]\cdot\Big[\left(\alpha_1 - 4\alpha_2 + 4\alpha_{32}^c\right)X_C\Big]^{-1}\Big\} \end{aligned} \tag{7.50}$$

Having defined φ_0 and φ_C (equations (7.44) and (7.50), respectively), the kinking angle is calculated using equation (7.40).

7.3.2.3.2. Nonlinear shear response It is well known that UD composite materials show nonlinear response when subjected to in-plane shear stresses. This nonlinear response has two main effects [81]: (i) the shear modulus of the material is reduced in the loading-unloading cycles occurring after the onset of nonlinearity, as a result of the presence of microcracks in the matrix, and (ii) the presence of permanent shear deformations in the material, which result from the plastic or viscoplastic deformations of the matrix.

[2]Equation (7.49) has two solutions for φ, a real and an imaginary solution. Only the real one is considered.

According to Hahn and Tsai [307], the nonlinear shear response of a composite laminate can be approximated by the following polynomial:

$$\gamma_{12} = \frac{1}{G_{12}}\sigma_{12} + \beta\sigma_{12}^3 \tag{7.51}$$

where β defines the nonlinearity of the shear stress-shear strain relation. Taking into account the nonlinear shear behaviour, the kinking angle, φ, is given as:

$$\begin{aligned}\varphi &= \operatorname{sgn}\left\{\sigma_{12}^{(R)}(\varphi_0,\psi)\right\}\left(\varphi_0 + \varphi^R\right) \\ &= \operatorname{sgn}\left\{\sigma_{12}^{(R)}(\varphi_0,\psi)\right\}\left\{\varphi_0 + \left|\frac{\sigma_{12}^{(R)}(\varphi_0,\psi)}{G_{12}} + \beta\left[\sigma_{12}^{(R)}(\varphi_0,\psi)\right]^3\right|\right\}\end{aligned} \tag{7.52}$$

where $\sigma_{12}^{(R)}(\varphi_0,\psi)$ is given by equation (7.41). The initial misalignment angle, φ_0, is now written as:

$$\varphi_0 = \varphi_C - \varphi_C^R = \varphi_C - \left|\frac{X_C \sin 2\varphi_0}{2G_{12}} + \beta\frac{X_C^3 \sin^3 2\varphi_0}{8}\right| \tag{7.53}$$

where φ_C is given by equation (7.50). Because equation (7.53) is a nonlinear equation of φ_0, it has to be solved numerically using, for instance, the Newton-Raphson method (as shown in section 7.4).

Finally, it should be noted that taking $\beta = 0$ in equations (7.52) and (7.53) the solution for linear shear behaviour is recovered. Thus, the solution accounting for nonlinear shear behaviour presented before can be regarded as the general case; the degree of nonlinearity is controlled by the parameter β.

7.3.2.3.3. Alternative determination of φ According to Catalanotti et al. [128], physical incompatibilities may arise when a nonzero initial misalignment angle, φ_0, is assumed (e.g. Refs.[103, 319, 328] and sections 7.3.2.3.1 and 7.3.2.3.2). Therefore, in the present formulation, an alternative methodology proposed by Catalanotti et al. [128] is used to determine the kinking-angle φ. According to this methodology, the imperfections that trigger fibre kinking (local micro-structural defects from manufacture or the intrinsic fibre volume fraction oscillations in the material, for example) are taken into account by a micro-mechanical parameter (χ) associated with the creation of a kink-band:

$$\chi = -\frac{\sin(2\varphi_C)\, X_C}{2\varphi_C} \tag{7.54}$$

The kinking angle, φ, is then obtained imposing the stress equilibrium in a kink band and solving the corresponding nonlinear equation using, for instance, the Newton-Raphson method, as suggested by Catalanotti et al. [128].

A summary of the resulting failure conditions for the fibre-dominated failure modes is shown in section 7.4.

7.3.3. Preliminary results

For longitudinal kinking failure ($\sigma_{11} < 0$), two different approaches can be employed to determine the angle of the kinking plane (section 7.3.2.2): (i) maximising the kinking failure index, or (ii) assuming that the angle of the kinking plane is a function of the stress state, and calculating it using equations (7.38) or (7.39). The difference between these two approaches is negligible; therefore, the pragmatic approach based on equations (7.38) or (7.39), which reduces considerably the computational effort, is used.

Figure 7.11 shows the failure envelopes of IM7/8552 carbon-epoxy for stress states involving longitudinal failure mechanisms (nonzero σ_{11}). The invariant-based failure criterion for transverse failure mechanisms (section 7.2.1) was applied together with the failure criteria for fibre tensile failure (section 7.3.1) and for kinking failure (section 7.3.2). The

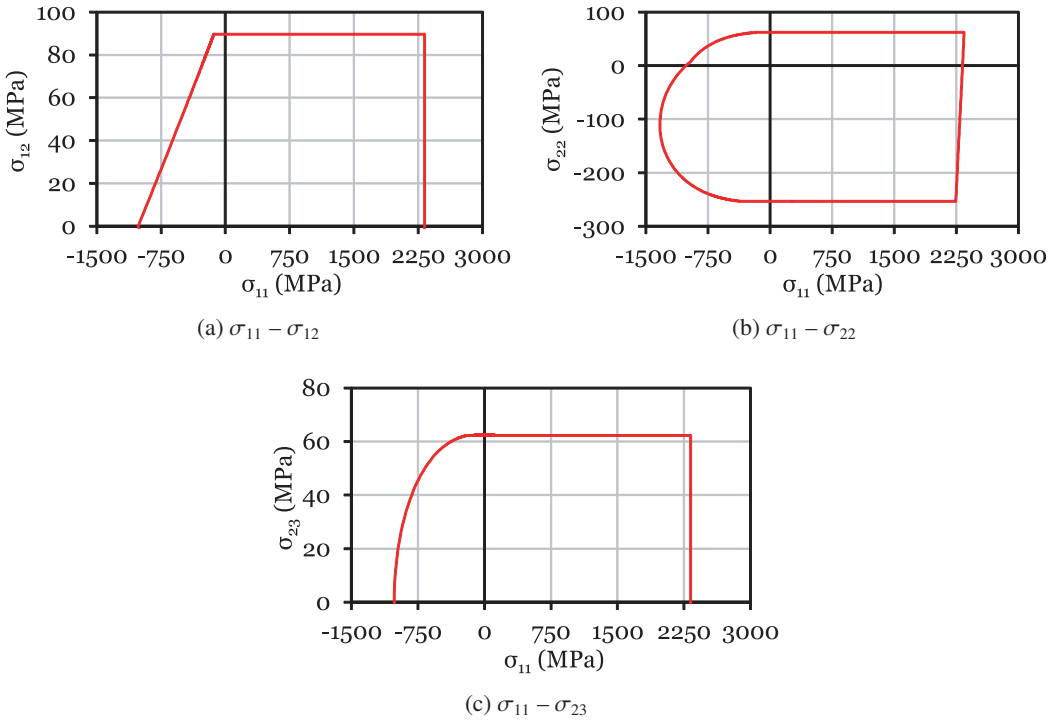

(a) $\sigma_{11} - \sigma_{12}$

(b) $\sigma_{11} - \sigma_{22}$

(c) $\sigma_{11} - \sigma_{23}$

Fig. 7.11. Failure envelopes of IM7/8552 carbon-epoxy for stress states involving longitudinal failure (nonzero σ_{11}).

material properties of IM7/8552 carbon-epoxy are reported in table 7.2. In figure 7.11, a linear shear response ($\beta = 0$) is assumed.

To assess the effect of the material's nonlinear shear response in the failure loci of IM7/8552 carbon-epoxy, the failure envelopes for both linear and nonlinear shear responses are presented in figure 7.12. In addition, figure 7.12 shows the effect of considering a small angles approximation for the determination of φ_0 (equation (7.45)); for this comparison, a linear shear response ($\beta = 0$) is assumed.

Figure 7.12 shows that, in the case of IM7/8552 carbon-epoxy, the effect of the nonlinear shear response in the failure loci including longitudinal compressive (or kinking) failure is marginal. However, for material systems comprising tougher resins or thermoplastic matrices, the material nonlinear shear behaviour may affect more remarkably the kinking failure response, and in such cases the use of a formulation accounting for the nonlinear shear response should be used. It is also noted that considering a small angles approximation for the determination of φ_0 (equation (7.45)) does not have any effect on the predicted failure envelopes, which means that, for this case, a nonlinear procedure to solve equation (7.44) does not need to be used, without loss of accuracy.

From figures 7.11b or 7.12b, which show the $\sigma_{11} - \sigma_{22}$ failure envelope, it is observed that, when $\sigma_{11} < 0$ and $\sigma_{22} < 0$, there is an increase of the apparent axial compressive strength. As explained by Catalanotti et al. [128], an increase of the apparent axial compressive strength when a biaxial compressive loading is applied is not physically reasonable. When $\sigma_{22} < 0$ (and $\sigma_{33} = 0$) the angle of the kinking plane (ψ) changes from 0° to 90° (equation (7.39)). If a transverse compressive loading in the 2-direction is applied, it will not have influence on fibre kinking because the fibres will kink in the perpendicular plane. From Ref. [128], it can be seen that this physical incompatibility can be solved adopting the alternative methodology to determine the kinking-angle φ described in section 7.3.2.3.3.

Figure 7.13 shows the $\sigma_{11} - \sigma_{22}$ failure envelope obtained with the invariant-based failure criteria using the alternative methodology proposed by Catalanotti et al. [128] to determine the kinking-angle φ (section 7.3.2.3.3). The effect of a negative transverse stress σ_{33} on the failure loci is also shown. Linear shear behaviour is assumed.

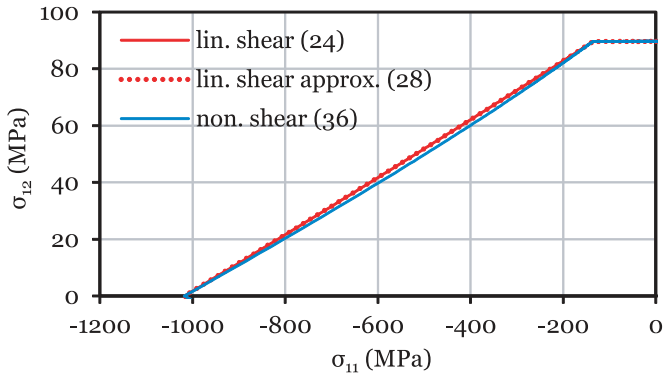

(a) $\sigma_{11} - \sigma_{12}$

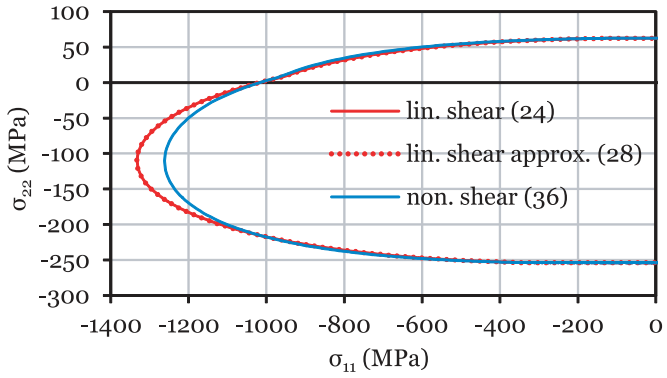

(b) $\sigma_{11} - \sigma_{22}$

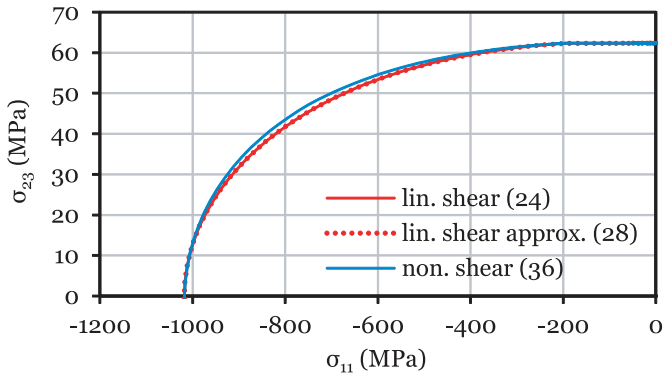

(c) $\sigma_{11} - \sigma_{23}$

Fig. 7.12. Kinking failure loci of IM7/8552 carbon-epoxy obtained with the invariant-based failure criteria. Effect of considering a small angles approximation for the determination of φ_0, and effect of the material nonlinear shear response.

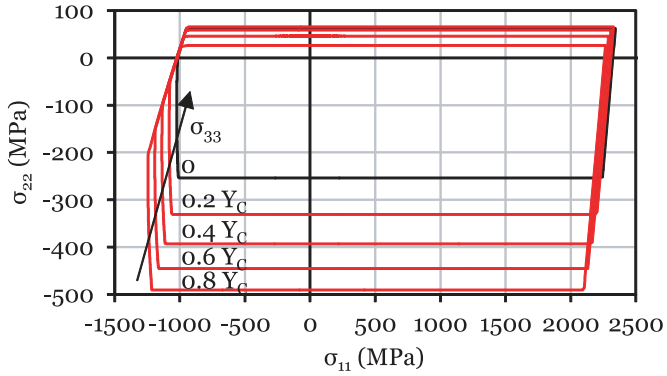

Fig. 7.13. $\sigma_{11} - \sigma_{22}$ failure loci of IM7/8552 carbon-epoxy obtained with the invariant-based failure criteria for different transverse compressive stresses σ_{33}. The alternative methodology proposed by Catalanotti et al. [128] to determine the kinking-angle φ is adopted (section 7.3.2.3.3). A linear shear response is assumed.

As proposed by Catalanotti et al. [128], when the transverse stress σ_{33} is zero, there is no increase of the apparent axial compressive strength. However, if both transverse stresses σ_{22} and σ_{33} are compressive, the creation of the kink-band that will conduct to longitudinal compressive failure is more difficult (the transverse stresses act together like a confining pressure), and an increase of the apparent axial compressive strength occurs, as shown in figure 7.13. Moreover, this increase of the apparent axial compressive strength agrees with experimental evidence [340].

7.4. Summary of the invariant-based failure criteria

Matrix failure

0. *Required UD properties*

Y_T, Y_{BT}, Y_C, Y_{BC}, S_L, S_T $(= Y_T)$

1. *Invariants*

$$I_1 = \frac{1}{4}\sigma_{22}^2 - \frac{1}{2}\sigma_{22}\sigma_{33} + \frac{1}{4}\sigma_{33}^2 + \sigma_{23}^2$$
$$I_2 = \sigma_{12}^2 + \sigma_{13}^2$$
$$I_3 = \sigma_{22} + \sigma_{33}$$

Matrix tension $(I_3 > 0)$	**Matrix compression** $(I_3 \leq 0)$

2. *Model parameters*

$\alpha_1 = \dfrac{1}{S_T^2}$	$\alpha_1 = \dfrac{1}{S_T^2}$
$\alpha_2 = \dfrac{1}{S_L^2}$	$\alpha_2 = \dfrac{1}{S_L^2}$
$\alpha_{32}^t = \dfrac{1 - \dfrac{Y_T}{2Y_{BT}} - \alpha_1 \dfrac{Y_T^2}{4}}{Y_T^2 - 2Y_{BT}Y_T}$	$\alpha_{32}^c = \dfrac{1 - \dfrac{Y_C}{2Y_{BC}} - \alpha_1 \dfrac{Y_C^2}{4}}{Y_C^2 - 2Y_{BC}Y_C}$
$\alpha_3^t = \dfrac{1}{2Y_{BT}} - 2\alpha_{32}^t Y_{BT}$	$\alpha_3^c = \dfrac{1}{2Y_{BC}} - 2\alpha_{32}^c Y_{BC}$

Matrix tension ($I_3 > 0$)	**Matrix compression** ($I_3 \leq 0$)

3. *Failure criteria*

$f_M = \alpha_1 I_1 + \alpha_2 I_2 + \alpha_3^t I_3 + \alpha_{32}^t I_3^2$	$f_M = \alpha_1 I_1 + \alpha_2 I_2 + \alpha_3^c I_3 + \alpha_{32}^c I_3^2$

Fibre failure

0. *Required UD properties*

ε_1^T (or X_T), X_C, Y_T, Y_{BT}, Y_C, Y_{BC}, S_L, S_T $(= Y_T)$, (G_{12}), (β)

• **Fibre tension** ($\sigma_{11} \geq 0$)

1. *Failure criteria*

$$f_F = \frac{\varepsilon_{11}}{\varepsilon_1^T}$$

• **Fibre compression** ($\sigma_{11} < 0$)

1. *Model parameters*

$$\alpha_1 = \frac{1}{S_T^2}$$
$$\alpha_2 = \frac{1}{S_L^2}$$
$$\alpha_{32}^t = \frac{1 - \dfrac{Y_T}{2Y_{BT}} - \alpha_1 \dfrac{Y_T^2}{4}}{Y_T^2 - 2Y_{BT}Y_T}$$
$$\alpha_{32}^c = \frac{1 - \dfrac{Y_C}{2Y_{BC}} - \alpha_1 \dfrac{Y_C^2}{4}}{Y_C^2 - 2Y_{BC}Y_C}$$
$$\alpha_3^t = \frac{1}{2Y_{BT}} - 2\alpha_{32}^t Y_{BT}$$
$$\alpha_3^c = \frac{1}{2Y_{BC}} - 2\alpha_{32}^c Y_{BC}$$

2. *Angle of the kinking plane* (ψ)

If $\sigma_{12} = 0$ and $\sigma_{13} = 0$	Otherwise
$\psi = \frac{1}{2}\arctan\left(\frac{2\sigma_{23}}{\sigma_{22} - \sigma_{33}}\right)$	$\psi = \arctan\frac{\sigma_{13}}{\sigma_{12}}$

3. *Misalignment angle at failure when a pure longitudinal compression is applied* (φ_C)

$$\varphi_C = \frac{1}{2}\arccos\left\{\left[4\sqrt{\alpha_1 - 4\alpha_2 + \alpha_2^2 X_C^2 + \left(\alpha_3^c\right)^2 + 2\alpha_2\alpha_3^c X_C + 4\alpha_{32}^c} + \right.\right.$$
$$\left.\left. + \left(\alpha_1 + 4\alpha_{32}^c\right) X_C + 4\alpha_3^c\right] \cdot \left[\left(\alpha_1 - 4\alpha_2 + 4\alpha_{32}^c\right) X_C\right]^{-1}\right\}$$

7.4. Summary of the invariant-based failure criteria

4. *Kinking-angle* (φ)

■ **First alternative** Initial nonzero misalignment angle ($\varphi_0 \neq 0$)

4.1. *Initial misalignment angle* (φ_0)

Linear shear and small angles	*Nonlinear shear*
$\varphi_0 = \varphi_C \left(1 + \dfrac{\lvert X_C \rvert}{G_{12}}\right)^{-1}$	Equation (7.53) is a nonlinear equation of φ_0, which can be solved numerically using, e.g., the Newton-Raphson method. Defining the function $F(\varphi_0)$ as: $F(\varphi_0) = \varphi_C - \varphi_0 - \left\lvert \dfrac{X_C \sin 2\varphi_0}{2G_{12}} + \beta \dfrac{X_C^3 \sin^3 2\varphi_0}{8} \right\rvert$ and calculating its derivative with respect to φ_0: $\dfrac{\mathrm{d}F}{\mathrm{d}\varphi_0} = -1 - \left\lvert \dfrac{X_C \cos 2\varphi_0}{G_{12}} + \beta \dfrac{3}{4} X_C^3 \sin^2 2\varphi_0 \cos 2\varphi_0 \right\rvert$ the initial misalignment angle, φ_0, can be computed using the following recursive formula: $\varphi_0^{i+1} = \varphi_0^i - \dfrac{F(\varphi_0^i)}{\left.\dfrac{\mathrm{d}F}{\mathrm{d}\varphi_0}\right\rvert_{\varphi_0 = \varphi_0^i}}$

4.2. *Shear stress in the misalignment frame* ($\sigma_{12}^{(R)}(\varphi_0, \psi)$)

$$\sigma_{12}^{(R)}(\varphi_0, \psi) = \frac{1}{2}\left[-\sigma_{11} + \sigma_{22}\cos^2\psi + \sigma_{33}\sin^2\psi + \sigma_{23}\sin 2\psi\right]\sin 2\varphi_0 + \\ + (\sigma_{12}\cos\psi + \sigma_{13}\sin\psi)\cos 2\varphi_0$$

4.3. *Kinking-angle* (φ)

$$\varphi = \operatorname{sgn}\left\{\sigma_{12}^{(R)}(\varphi_0, \psi)\right\}\left\{\varphi_0 + \left\lvert \frac{\sigma_{12}^{(R)}(\varphi_0, \psi)}{G_{12}} + \beta\left[\sigma_{12}^{(R)}(\varphi_0, \psi)\right]^3 \right\rvert\right\}$$

■ **Second alternative** Null initial misalignment angle ($\varphi_0 = 0$)

4.1. *Micro-mechanical parameter associated with the creation of a kink-band* (χ)

$$\chi = -\frac{\sin(2\varphi_C)\, X_C}{2\varphi_C}$$

4.2.*Kinking-angle* (φ)

Stresses in the frame of the kinking plane ($\boldsymbol{\sigma}^{(1)}$)

$$\sigma_{11}^{(1)} = \sigma_{11}$$
$$\sigma_{22}^{(1)} = \sigma_{22}\cos^2\psi + 2\sigma_{23}\cos\psi\sin\psi + \sigma_{33}\sin^2\psi$$
$$\sigma_{12}^{(1)} = \sigma_{12}\cos\psi + \sigma_{13}\sin\psi$$

Shear strain (γ_m)

For a material that exhibits a linear shear behaviour, it is assumed that:

$$\sigma_{12}^{(R)} = \chi\gamma_m$$

This is a nonlinear equation of γ_m that can be solved numerically using, e.g., the Newton-Raphson method.

Defining the function $F(\gamma_m)$ as:

$$F(\gamma_m) = \chi\gamma_m + \frac{1}{2}\left(\sigma_{11}^{(1)} - \sigma_{22}^{(1)}\right)\sin(2\gamma_m) - \left|\sigma_{12}^{(1)}\right|\cos(2\gamma_m)$$

and calculating its derivative with respect to γ_m:

$$\frac{\mathrm{d}F}{\mathrm{d}\gamma_m} = \chi + \left(\sigma_{11}^{(1)} - \sigma_{22}^{(1)}\right)\cos(2\gamma_m) + 2\left|\sigma_{12}^{(1)}\right|\sin(2\gamma_m)$$

the angle γ_m can be computed using the following recursive formula:

$$\gamma_m^{i+1} = \gamma_m^i - \frac{F(\gamma_m^i)}{\left.\dfrac{\mathrm{d}F}{\mathrm{d}\gamma_m}\right|_{\gamma_m=\gamma_m^i}}$$

Kinking-angle (φ)

$$\varphi = \mathrm{sgn}\{\sigma_{12}^{(1)}\}\,\gamma_m$$

5. *Preferred direction* (**a**)

$$\mathbf{a} = \begin{bmatrix} \cos\varphi \\ \cos\psi\sin\varphi \\ \sin\psi\sin\varphi \end{bmatrix}$$

6. *Structural tensor* (**A**)

$$\mathbf{A} = \mathbf{a}\otimes\mathbf{a}$$

7. *Reaction stress tensor* ($\boldsymbol{\sigma}^r$)

$$\boldsymbol{\sigma}^r = \frac{1}{2}(\mathrm{tr}\,\boldsymbol{\sigma} - \mathbf{a}\boldsymbol{\sigma}\mathbf{a})\mathbf{1} - \frac{1}{2}(\mathrm{tr}\,\boldsymbol{\sigma} - 3\mathbf{a}\boldsymbol{\sigma}\mathbf{a})\mathbf{A}$$

8. *Plasticity inducing stress tensor* ($\boldsymbol{\sigma}^p$)

$$\boldsymbol{\sigma}^p = \boldsymbol{\sigma} - \boldsymbol{\sigma}^r$$

9. *Invariants*

$$I_1 = \frac{1}{2}\mathrm{tr}\,(\boldsymbol{\sigma}^p)^2 - \mathbf{a}\,(\boldsymbol{\sigma}^p)^2\,\mathbf{a}$$
$$I_2 = \mathbf{a}\,(\boldsymbol{\sigma}^p)^2\,\mathbf{a}$$
$$I_3 = \mathrm{tr}\,\boldsymbol{\sigma} - \mathbf{a}\boldsymbol{\sigma}\mathbf{a}$$

Matrix tension ($I_3 > 0$)	**Matrix compression** ($I_3 \leq 0$)

10. *Failure criteria*

$f_K = \alpha_1 I_1 + \alpha_2 I_2 + \alpha_3^t I_3 + \alpha_{32}^t I_3^2$	$f_K = \alpha_1 I_1 + \alpha_2 I_2 + \alpha_3^c I_3 + \alpha_{32}^c I_3^2$

7.5. Validation studies

7.5.1. Off-axis failure of IM7/8552 carbon-epoxy

Koerber et al. [265] performed off-axis compression tests on IM7/8552 carbon-epoxy under quasi-static and dynamic loading. Figure 7.14 shows the predictions of the proposed failure criteria and a comparison with the experiments for quasi-static and dynamic loading. The material properties for quasi-static loading are shown in table 7.2, and for dynamic loading in table 7.3. Following section 7.2.5, it is assumed that the transverse shear strength, S_T, is equal to the transverse tensile strength, Y_T. This assumption is not only valid for IM7/8552 carbon-epoxy, but also for all validation studies presented in section 7.5. Since biaxial data is not available for IM7/8552 carbon-epoxy under dynamic loading, the alternative procedure for model parameters identification described in section 7.2.2 was adopted (equations (7.13)). In table 7.3, ϕ_t and ϕ_c and σ_u^t and σ_u^c are respectively the off-axis angles and the mean applied stresses at failure of the dynamic off-axis tension and compression tests used in the parameters identification.

Figure 7.15 shows the predicted relations between the off-axis angle and the failure stresses for IM7/8552 under quasi-static and dynamic loading. Linear shear response ($\beta = 0$) is assumed.

Table 7.3
IM7/8552 dynamic material properties.

Properties		References
G_{12} (MPa)	6612.5	Koerber et al. [265]
X_C (MPa)	-1428.0	Catalanotti et al. [128]
Y_T (MPa)	62.3	assumed value[a]
ϕ_t (°)	45.0	assumed value[b]
σ_u^t (MPa)	94.8	assumed value[b]
Y_C (MPa)	-368.9	Koerber et al. [265]
S_L (MPa)	122.3	Catalanotti et al. [128]
ϕ_c (°)	75.0	Koerber et al. [265]
σ_u^c (MPa)	-363.0	Koerber et al. [265]

[a] Same value as for quasi-static loading (table 7.2).

[b] Same value as for quasi-static loading [341].

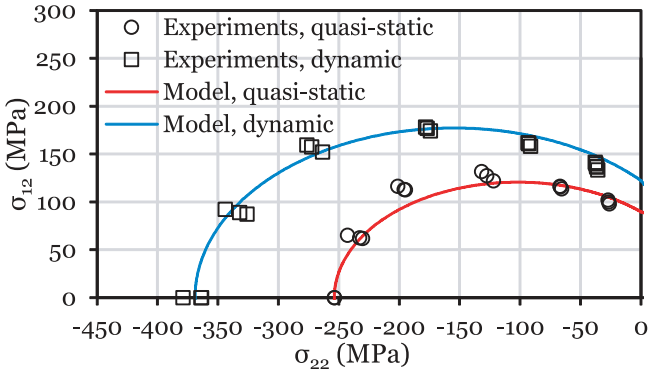

Fig. 7.14. Quasi-static and dynamic $\sigma_{22} - \sigma_{12}$ failure envelopes for IM7/8552 carbon-epoxy under transverse compression.

Table 7.4
AS4/55A material properties.

Properties		References
Y_T (MPa)	27.0	Swanson et al. [342]
$\sigma^t_{22\,u}$ (MPa)	12.0	Swanson et al. [342]
$\sigma^t_{12\,u}$ (MPa)	42.8	Swanson et al. [342]
Y_C (MPa)	-91.8	Swanson et al. [342]
$\sigma^c_{22\,u}$ (MPa)	-20.0	Swanson et al. [342]
$\sigma^c_{12\,u}$ (MPa)	63.3	Swanson et al. [342]
S_L (MPa)	51.3	Swanson et al. [342]

7.5.2. $\sigma_{22} - \sigma_{12}$ failure envelope for AS4/55A carbon-epoxy

Figure 7.16 shows the predicted $\sigma_{22} - \sigma_{12}$ failure envelope for AS4/55A carbon-epoxy, and a comparison with alternative 3D failure criteria [104, 128]. The experimental results obtained by Swanson et al. [342] are also shown. Table 7.4 shows the material properties used to identify the parameters of the invariant-based failure criteria.

Since biaxial data is not available for AS4/55A carbon-epoxy, the alternative procedure for model parameters identification described in section 7.2.2 was adopted (equations (7.15)). $\sigma^{t/c}_{22\,u}$ are the maximum transverse stress and $\sigma^{t/c}_{12\,u}$ the maximum longitudinal shear stress for a specimen subjected to combined transverse tensile (t)/compressive (c) and longitudinal shear loading.

7.5.3. Through-the-thickness off-axis failure of AS4/3501-6 carbon-epoxy

Daniel et al. [343] performed through-the-thickness off-axis tension and compression tests on AS4/3501-6 carbon-epoxy. Figure 7.17 shows the predicted relations between the off-axis angle and the ultimate stresses. The material properties are shown in table 7.5. Since biaxial data is not available, the alternative procedure for model parameters identification described in section 7.2.2 was adopted (equations (7.15)). Linear shear response is assumed.

7.5.4. $\sigma_{22} - \sigma_{12}$ failure envelope for AS4/3501-6 carbon-epoxy

Figure 7.18 shows the $\sigma_{22} - \sigma_{12}$ failure envelope for AS4/3501-6 carbon-epoxy obtained with the proposed failure criteria and a comparison with the experimental results presented by Daniel et al. [344]. The material properties are shown in table 7.5.

7.5.5. Off-axis compressive failure of AS4/3501-6 carbon-epoxy at intermediate and high strain rates

Daniel et al. [344] also performed dynamic off-axis compressive tests on AS4/3501-6 carbon-epoxy at intermediate (1 s^{-1}) and high (400 s^{-1}) strain rates. Figure 7.19 shows the predictions of the proposed criteria and a comparison with

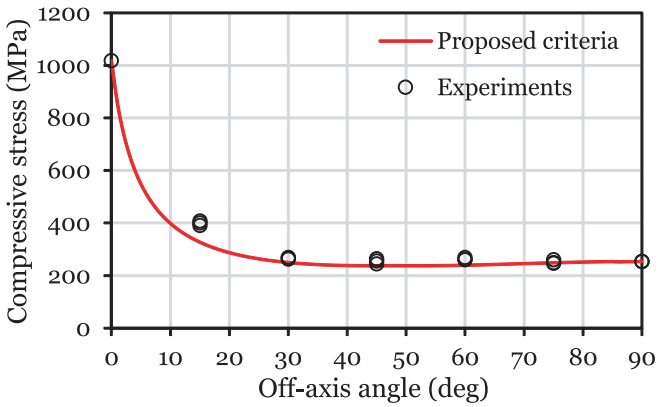

(a) Quasi-static loading.

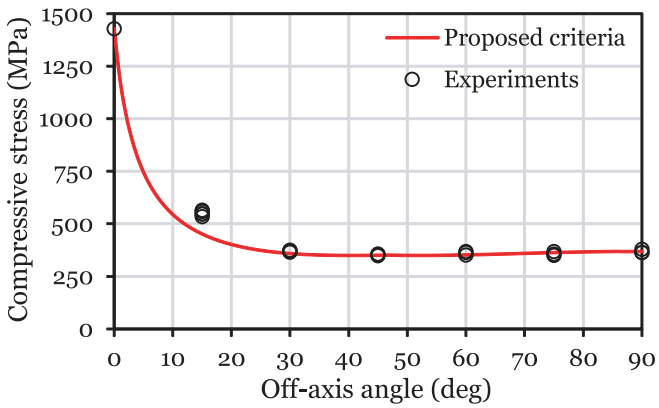

(b) Dynamic loading.

Fig. 7.15. Quasi-static and dynamic off-axis compression failure predictions for IM7/8552 carbon-epoxy.

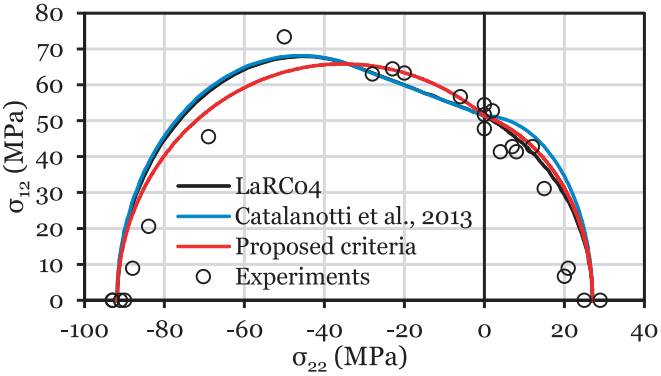

Fig. 7.16. $\sigma_{22} - \sigma_{12}$ failure envelopes for AS4/55A carbon-epoxy.

Table 7.5
AS4/3501-6 material properties.

Properties		References
G_{12} (MPa)	7000.0	Daniel et al. [344]
X_T (MPa)	2300.0	Daniel et al. [343]
X_C (MPa)	-1725.0	Daniel et al. [343]
Y_T (MPa)	65.0	Daniel et al. [344]
$\sigma^t_{22\,u}$ (MPa)	19.5	Daniel et al. [344]
$\sigma^t_{12\,u}$ (MPa)	72.4	Daniel et al. [344]
Y_C (MPa)	-285.0	Daniel et al. [344]
$\sigma^c_{22\,u}$ (MPa)	-117.0	Daniel et al. [344]
$\sigma^c_{12\,u}$ (MPa)	121.0	Daniel et al. [344]
S_L (MPa)	80.0	Daniel et al. [344]

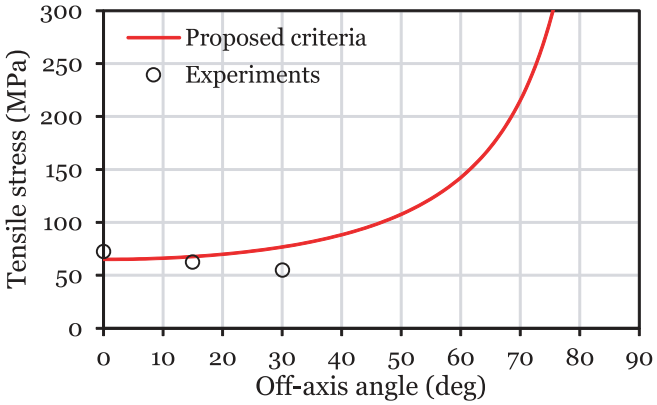

(a) Off-axis tension.

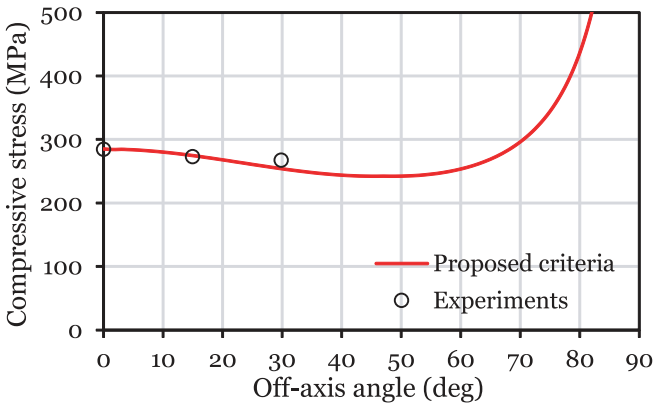

(b) Off-axis compression.

Fig. 7.17. Through-the-thickness off-axis failure predictions for AS4/3501-6 carbon-epoxy.

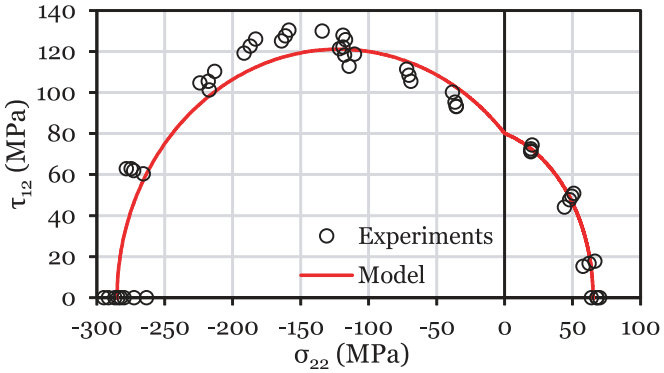

Fig. 7.18. $\sigma_{22} - \sigma_{12}$ failure envelope for AS4/3501-6 carbon-epoxy.

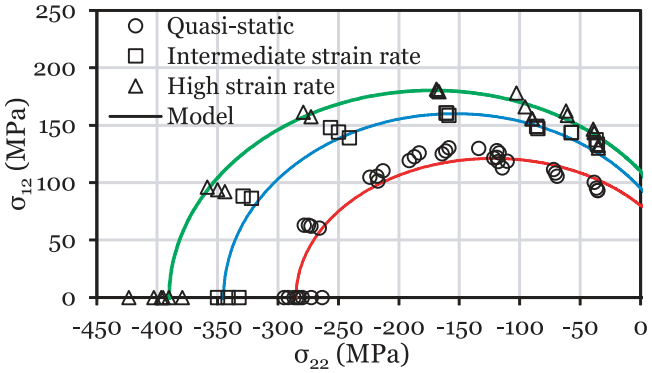

Fig. 7.19. $\sigma_{22} - \sigma_{12}$ failure envelopes for AS4/3501-6 carbon-epoxy under transverse compressive quasi-static and dynamic (intermediate and high strain rate) loading.

the experimental results presented by Daniel et al. [344]. The material properties for quasi-static loading are shown in table 7.5. Table 7.6 shows the compressive and shear matrix dominated material properties for the intermediate and high strain rates. Since biaxial data is not available, the alternative procedure for model parameters identification described in section 7.2.2 (equations (7.15)) was also adopted for dynamic loading.

7.5.6. $\sigma_{22} - \sigma_{12}$ failure envelope for E-Glass/LY556/HT907/DY063

Soden et al. [345] tested E-Glass/LY556/HT907/DY063 fibreglass-epoxy laminae under transverse and shear loading and obtained the $\sigma_{22} - \sigma_{12}$ failure envelope. Figure 7.20 shows the predicted $\sigma_{22} - \sigma_{12}$ failure envelope for this fibreglass-epoxy composite material obtained with the proposed criteria. The experimental results from Soden et al. [345] are also shown.

The material properties of E-Glass/LY556/HT907/DY063 fibreglass-epoxy used to identify the parameters of the invariant-based failure criteria are shown in table 7.7. It is noted that, since biaxial data is not available, the alternative procedure for model parameters identification described in section 7.2.2 was adopted (equations (7.15)).

7.5.7. Effect of hydrostatic pressure on E-Glass/MY750/HY917/DY063

Hine et al. [334] studied the effect of hydrostatic pressure on E-Glass/MY750/HY917/DY063 fibreglass-epoxy. Figure 7.21 shows the experimental results obtained by Hine et al. [334] for the effect of hydrostatic pressure on the in-plane shear response, and a comparison with the predictions of the proposed failure criteria.

Table 7.8 shows the material properties used to identify the parameters of the invariant-based criteria. Due to the lack of biaxial data, the transverse tensile and compressive biaxial strengths (Y_{BT} and Y_{BC}, respectively) were assumed.

Table 7.6
AS4/3501-6 dynamic material properties.

Properties	Average strain rate		References
	1 s^{-1}	400 s^{-1}	
Y_C (MPa)	-345.0	-390.0	Daniel et al. [344]
$\sigma^c_{22\,u}$ (MPa)	-160.0	-167.9	Daniel et al. [344]
$\sigma^c_{12\,u}$ (MPa)	159.9	180.2	Daniel et al. [344]
S_L (MPa)	95.0	110.0	Daniel et al. [344]

Table 7.7
E-Glass/LY556/HT907/DY063 material properties.

Properties		References
Y_T (MPa)	37.5	Soden et al. [345]
$\sigma^t_{22\,u}$ (MPa)	17.5	Soden et al. [345]
$\sigma^t_{12\,u}$ (MPa)	50.9	Soden et al. [345]
Y_C (MPa)	-130.3	Soden et al. [345]
$\sigma^c_{22\,u}$ (MPa)	-43.8	Soden et al. [345]
$\sigma^c_{12\,u}$ (MPa)	81.1	Soden et al. [345]
S_L (MPa)	66.5	Soden et al. [345]

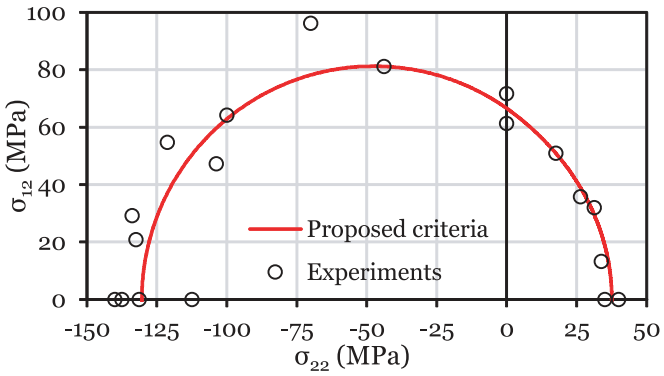

Fig. 7.20. $\sigma_{22} - \sigma_{12}$ failure envelope for E-Glass/LY556/HT907/DY063 fibreglass-epoxy.

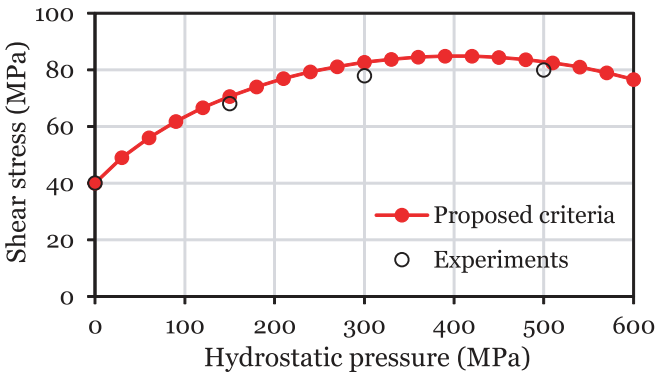

Fig. 7.21. Shear response of E-Glass/MY750/HY917/DY063 fibreglass-epoxy subjected to hydrostatic pressure.

Table 7.8
E-Glass/MY750/HY917/DY063 material properties.

Properties		References
G_{12} (MPa)	5830.0	Soden et al. [346]
X_T (MPa)	1266.7	Soden et al. [345]
X_C (MPa)	-783.3	Soden et al. [345]
Y_T (MPa)	40.0	Soden et al. [345]
Y_{BT} (MPa)	25.6	assumed value[a]
Y_C (MPa)	-110.0	Hine et al. [334]
Y_{BC} (MPa)	-860.0	assumed value
S_L (MPa)	40.0	Hine et al. [334]

[a] Assumed as equal to E-glass/LY556/HT907/DY063.

Table 7.9
Scotch-ply Type 1002 material properties.

Properties		References
Y_T (MPa)	19.61	Voloshin and Arcan [347]
$\sigma^t_{22\,u}$ (MPa)	9.72	Voloshin and Arcan [347]
$\sigma^t_{12\,u}$ (MPa)	26.71	Voloshin and Arcan [347]
Y_C (MPa)	-137.30	Voloshin and Arcan [347]
$\sigma^c_{22\,u}$ (MPa)	-26.73	Voloshin and Arcan [347]
$\sigma^c_{12\,u}$ (MPa)	57.33	Voloshin and Arcan [347]
S_L (MPa)	36.92	Voloshin and Arcan [347]

7.5.8. $\sigma_{22} - \sigma_{12}$ failure envelope for Scotch-ply Type 1002

Voloshin and Arcan [347] performed biaxial tests on Scotch-ply Type 1002 fibreglass-epoxy and obtained experimental data for the $\sigma_{22} - \sigma_{12}$ stress-space. Figure 7.22 shows the $\sigma_{22} - \sigma_{12}$ failure envelope predicted using the proposed criteria, and the experimental results from Voloshin and Arcan [347]. Table 7.9 shows the material properties. The alternative procedure for model parameters identification described in section 7.2.2 was adopted (equations (7.15)).

7.5.9. $\sigma_{11} - \sigma_{12}$ failure envelope for T300/914C carbon-epoxy

Figure 7.23 shows the predicted $\sigma_{11} - \sigma_{12}$ failure envelope for T300/914C carbon-epoxy obtained with the proposed criteria. The experimental results from Soden et al. [345] are also shown. Table 7.10 shows the material properties used to identify the parameters of the invariant-based criteria. Due to the lack of appropriate biaxial data for T300/914C carbon-epoxy, the transverse tensile and compressive biaxial strengths (Y_{BT} and Y_{BC}, respectively) were assumed.

7.5.10. $\sigma_{22} - \sigma_{12}$ failure envelope for T800/3900-2 carbon-epoxy

Figure 7.24 shows the predicted $\sigma_{22} - \sigma_{12}$ failure envelope for T800/3900-2 carbon-epoxy obtained with the proposed criteria. The experimental results from Swanson and Qian [348] are also shown. Table 7.11 shows the material properties used to identify the parameters of the invariant-based criteria. The alternative procedure for model parameters identification described in section 7.2.2 was adopted for the compressive case (equations (7.15)). For the tensile case, the identification of the model parameters was done assuming a value for the biaxial transverse tensile strength ($Y_{BT} = 30.3$ MPa).

All validation studies presented in section 7.5 indicate that the failure criteria proposed is able to predict first-ply failure with a satisfactory degree of accuracy.

7.6. Validation based on computational micro-mechanics

The examples in section 7.5 provide a preliminary validation of the proposed failure criteria. However, the range of stress states that can be imposed by means of experimental tests is limited by the complexity of the load introduction

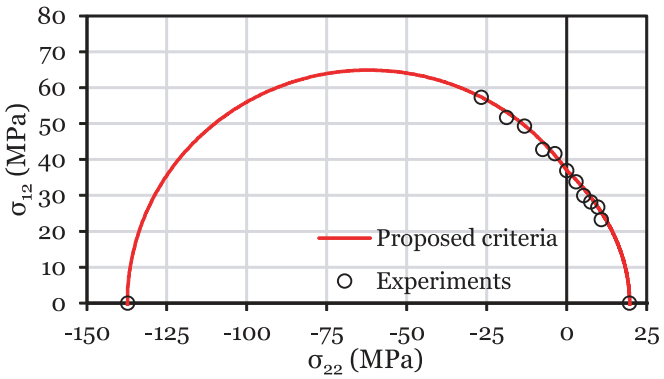

Fig. 7.22. $\sigma_{22} - \sigma_{12}$ failure envelope for Scotch-ply Type 1002 fibreglass-epoxy.

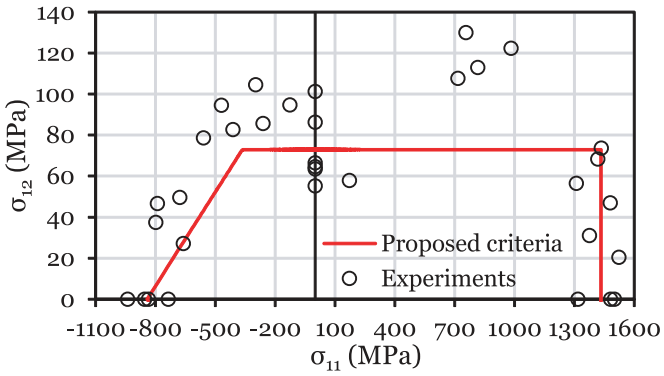

Fig. 7.23. $\sigma_{11} - \sigma_{12}$ failure envelope for T300/914C carbon-epoxy.

Table 7.10
T300/914C material properties.

Properties		References
G_{12} (MPa)	5500.0	Soden et al. [346]
X_T (MPa)	1433.6	Soden et al. [345]
X_C (MPa)	-841.4	Soden et al. [345]
Y_T (MPa)	27.0	Soden et al. [346]
Y_{BT} (MPa)	16.5	assumed value[a]
Y_C (MPa)	-200.0	Soden et al. [346]
Y_{BC} (MPa)	-769.8	assumed value[b]
S_L (MPa)	72.9	Soden et al. [345]

[a] Assumed as equal to AS4/55A.

[b] Assumed as equal to T800/3900-2.

Table 7.11
T800/3900-2 material properties.

Properties		References
Y_T (MPa)	48.8	Swanson and Qian [348]
Y_{BT} (MPa)	30.3	assumed value
Y_C (MPa)	-201.7	Swanson and Qian [348]
$\sigma^c_{22\,u}$ (MPa)	-140.0	Swanson and Qian [348]
$\sigma^c_{12\,u}$ (MPa)	119.1	Swanson and Qian [348]
S_L (MPa)	103.6	Swanson and Qian [348]

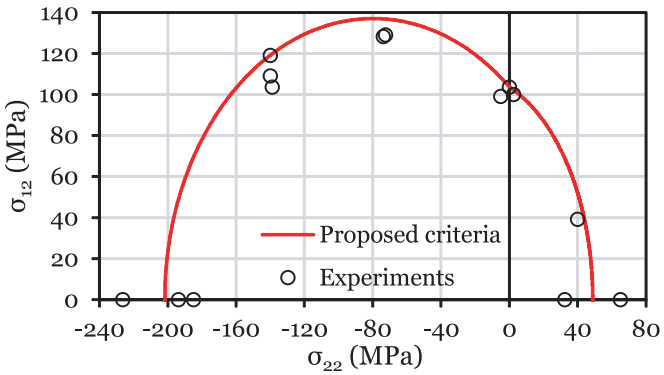

Fig. 7.24. $\sigma_{22} - \sigma_{12}$ failure envelope for T800/3900-2 carbon-epoxy.

systems. Therefore, a recently proposed approach based on computational micro-mechanics [299, 349, 350] is used here for generation of failure envelopes corresponding to stress states that cannot be experimentally imposed to the material or that would require very expensive test set-ups.

The approach requires the definition and implementation of thermodynamically consistent constitutive models for each of the constituents of a composite — fibre and matrix. The elastic and strength properties of the UD composite are predicted by the analysis of a Representative Volume Element (RVE) of a composite material under Periodic Boundary Conditions [351]. This RVE contains a random distribution of reinforcements generated by a specifically developed algorithm for the effect [295]. Each RVE has a transverse-side measure of 10 times the fibre radius and a thickness of 0.3 times the fibre radius in the longitudinal direction [299]. Melro et al. [299] addressed the effect of the choice of the boundary conditions and size of the RVEs, having assured the representativeness of the proposed computational micro-mechanics framework in the hardening stage for any stress state.

The material behaviour of the matrix is modelled using an elastic-plastic constitutive model with damage, recently proposed by Melro et al. [298] and used in chapter 6. This model is capable of accounting for the material nonlinear behaviour of the epoxy matrix under compression or pure shear, and considers the dependency of the material on hydrostatic pressure (section 6.2.2). The fibres are considered isotropic and linear elastic. Cohesive elements are used to model the interface between fibres and matrix [299].

The elastic and strength properties of the composite under uniaxial loading are estimated using computational micro-mechanics. The failure point is defined as the maximum homogenised stress in the RVE. Figure 7.25 shows representative homogenised stress-strain curves for some basic stress states analysed using the computational micro-mechanics framework [298, 299].

The values from the micro-mechanical analyses of the composite under pure uniaxial, pure biaxial and pure shear loading are used to feed the failure criteria presented in this work. Two failure envelopes are then generated from computational micro-mechanics, for several multiaxial stress combinations, and from the proposed failure criteria.

Tables 7.12 show the material properties used for this comparison. E_m is the Young's modulus, ν_m is the Poisson's ratio, ν_p is the plastic Poisson's ratio and $\mathcal{G}_c$ is the fracture toughness of the epoxy matrix. E_f and ν_f are respectively the Young's modulus and the Poisson's ratio of the glass fibres. X_T and X_C are respectively the tensile and compressive strengths of the constituents. Table 7.13 shows the material properties predicted by computational micro-mechanics for the UD composite, which were used to feed the failure criteria. Given the similarity of the values of the transverse shear strength, S_T, and transverse tensile strength, Y_T, of the UD composite (figures 7.25a and 7.25c), and following section 7.2.5, it is assumed that the these strength properties are equal.

Figures 7.26 to 7.32 show the comparison between the failure envelopes predicted by computational micro-mechanics and the failure criteria proposed in this work. In general, a good agreement between the two modelling strategies is observed.

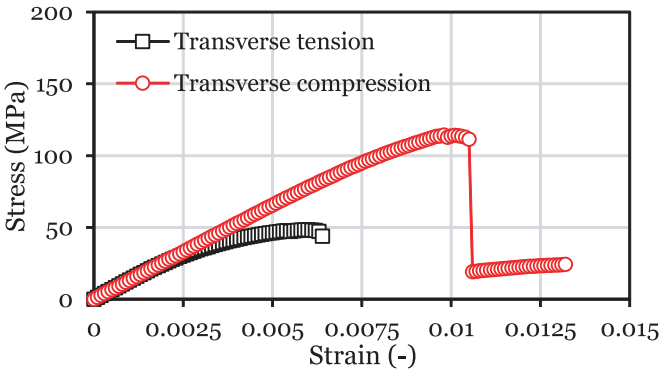

(a) Uniaxial transverse loading.

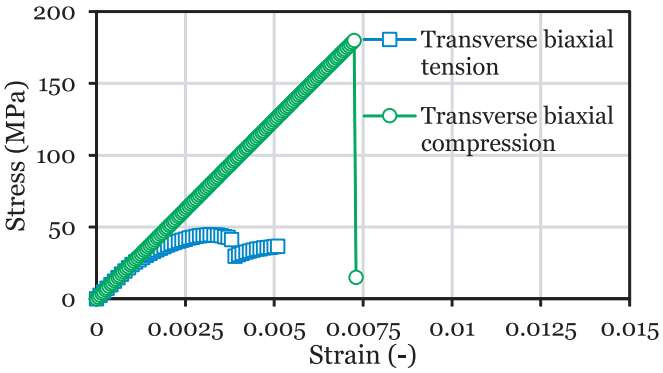

(b) Biaxial transverse loading.

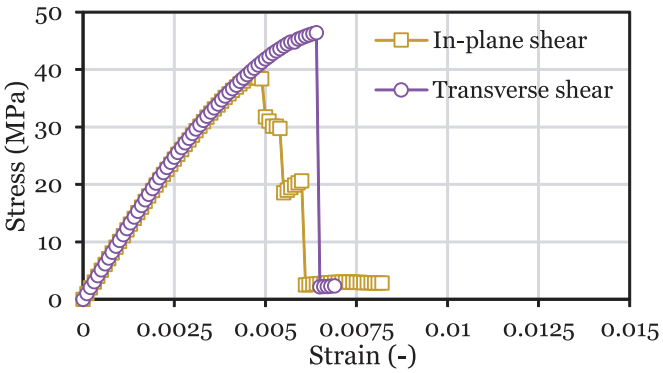

(c) Shear loading.

Fig. 7.25. Representative homogenised stress-strain curves for some basic stress states, obtained using a computational micro-mechanics framework [298, 299].

7.6. Validation based on computational micro-mechanics

Table 7.12
Material properties of the constituents used in the computational micro-mechanics predictions [298, 299].

Properties		Refs.
Material properties of the epoxy matrix		
E_m (MPa)	3760	Fiedler et al. [301]
ν_m (-)	0.39	Fiedler et al. [301]
ν_p (-)	0.30	Guild et al. [302]
$\mathcal{G}_c$ (N/mm)	0.09	assumed value
X_T (MPa)	93	Fiedler et al. [301]
X_C (MPa)	124	Fiedler et al. [301]
Material properties of the glass fibres		
Fibre diameter (μm)	5	Soden et al. [346]
Fibre volume (%)	60	Soden et al. [346]
E_f (GPa)	74	Soden et al. [346]
ν_f (-)	0.2	Soden et al. [346]
X_T (MPa)	2150	Soden et al. [346]
X_C (MPa)	1450	Soden et al. [346]

Table 7.13
Properties of the UD composite predicted by computational micro-mechanics [298, 299].

Properties	
Y_T (MPa)	48.32
Y_{BT} (MPa)	45.0
Y_C (MPa)	-114.4
Y_{BC} (MPa)	-180.0
S_L (MPa)	40.57

Figures 7.26 and 7.27 show a comparison between the predictions from computational micro-mechanics, from the proposed invariant-based failure criteria, and from Hashin's failure criteria [316]. The latter have been used intensively in the analysis of intralaminar failure of composite laminates under complex loading conditions characterised by triaxial stress states, such as damage occurrence at the free edge of blunt notches [352], bearing or pin loading in mechanically fastened joints [353–355], or low-velocity impact loading [356–361]. In addition, their two-dimensional version can be found in commercial finite element codes [275, 362]. However, as can be observed, Hashin's failure criteria are not able to predict the fracture of fibre-reinforced composites subjected to biaxial transverse loading. These failure criteria largely underpredict the biaxial tensile strength of laminated composites. Furthermore, they show an open failure envelope for the biaxial transverse compression quadrant, thus making such failure criteria unsuitable for representing the fracture of composites subjected to hydrostatic pressure. It is important to note that the accurate prediction of failure under these stress states is crucial to predict the mechanical response of very thick laminates (e.g. for applications in wind turbine blades and ship construction) or laminates subjected to complex triaxial stress states (e.g. indentation, low-velocity impact, crashworthiness, or bearing).

In figures 7.28 and 7.29, some deviations between the micro-mechanical predictions and the proposed model can be observed, respectively, for the $\sigma_{22} - \sigma_{12}$ and $\sigma_{22} - \sigma_{13}$ stress spaces. One possible reason is related with the random distribution of the reinforcing fibres in the numerical RVE, which results in some scatter of the numerical simulations. Still, the deviations are not large, in particular in figure 7.28, where the trend of the $\sigma_{22} - \sigma_{12}$ failure envelope is reasonably well predicted. Moreover, the observed deviations are in the range of the experimental scatter observed in section 7.5.

The deviations observed in figure 7.29 for the $\sigma_{22} - \sigma_{13}$ stress space are also due to the fact that the proposed failure criterion for transverse, matrix-dominated failure, formulated for a homogeneous transversely-isotropic material, does not distinguish between the in-plane (σ_{12}) and out-of-plane (σ_{13}) longitudinal shear stresses. Observing figures 7.28 and 7.29, it can be seen that the predictions of the proposed model for the stress combinations $\sigma_{22} - \sigma_{12}$ and $\sigma_{22} - \sigma_{13}$ are exactly the

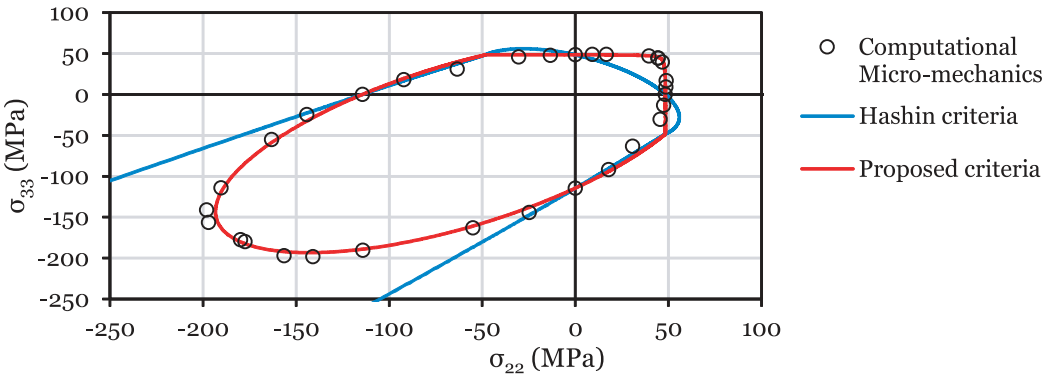

Fig. 7.26. $\sigma_{22} - \sigma_{33}$ failure envelope — micro-mechanics versus analytical failure criteria.

same. But, due to their morphology, long fibre-reinforced composites show different interaction of the stress combinations $\sigma_{22} - \sigma_{12}$ (or $\sigma_{33} - \sigma_{13}$) and $\sigma_{22} - \sigma_{13}$ (or $\sigma_{33} - \sigma_{12}$) [318], i.e. small compressive values of the normal transverse stress σ_{22} (or σ_{33}) results in an increase of the longitudinal shear strength acting on the same plane, σ_{12} (or σ_{13}), but does not affect the longitudinal shear strength acting on the perpendicular plane, σ_{13} (or σ_{12}), as discussed in section 7.2.5. This different interaction is captured by the micro-mechanical analysis, but it is not captured by the proposed model, conducting to the observed deviations. Nevertheless, it is believed that the advantages of the proposed criteria overcome this limitation (section 7.2.5). Moreover, the deviations for this particular stress state shall not affect the prediction capability of the proposed model for general stress states.

It is important to note that, even in those combinations of stress states where there are no experimental values available or the existing ones are scarce or unreliable (e.g., combination of σ_{13} and σ_{23}), computational micro-mechanics is capable of providing predictions. This capability evidences the potential of computational micro-mechanics to serve as a tool in the development and validation of accurate failure criteria.

7.7. Concluding remarks

New 3D invariant-based failure criteria for fibre-reinforced composite materials based on a transversely isotropic function were presented. The failure criteria include an invariant quadratic formulation based on structural tensors that accounts for the preferred directions of the transversely isotropic material. These new 3D failure criteria predict failure in a single UD ply, requiring the analysis of strains and stresses ply-by-ply when analysing multidirectional laminates.

Based on the failure envelopes for fibre kinking obtained for IM7/8552 carbon-epoxy, it was observed that accounting for the nonlinear shear behaviour in the failure criterion has a minor effect on the predicted failure load. In addition, it was observed that considering a small angles approximation for the determination of the initial misalignment angle associated with kink band formation does not affect the predicted failure envelopes, resulting in a simple implementation of the invariant-based failure criterion for fibre kinking. In general, the failure predictions were in agreement with previous 3D failure criteria (e.g. Ref. [128]).

Taking into account that the proposed failure criteria do not use geometrical information to predict failure (due to its invariant-based formulation), a pragmatic approach to estimate the orientation of the fracture plane was proposed. In spite of the simplicity of the approach, reliable estimates can be obtained for general 3D stress states. For instance, the ability to determine, in a simple way, the orientation of the fracture angle, can be very useful for future implementations of the invariant-based failure criteria in smeared crack models (e.g. Ref. [108]) to predict ply failure mechanisms in composite laminates (chapter 8).

To account for the effect of ply thickness when the laminae are embedded in a multidirectional laminate, the *in situ* properties were defined in the framework of the failure criterion for transverse damage mechanisms. It is important to note that an accurate determination of the *in situ* strengths is extremely important in implementing physically-based failure

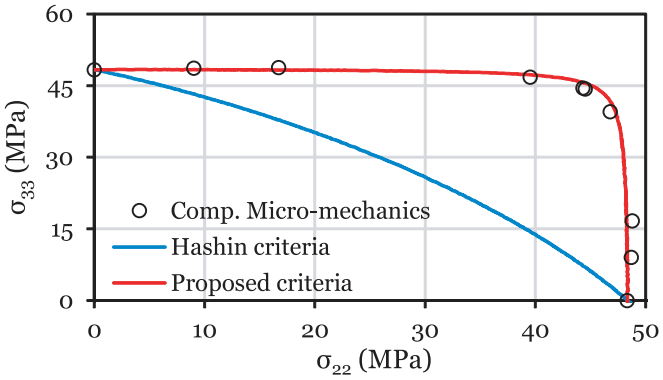

(a) First quadrant (biaxial transverse tension).

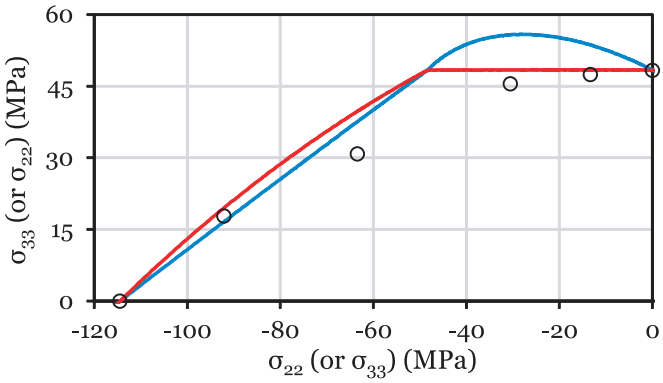

(b) Second (fourth) quadrant (transverse tension-transverse compression).

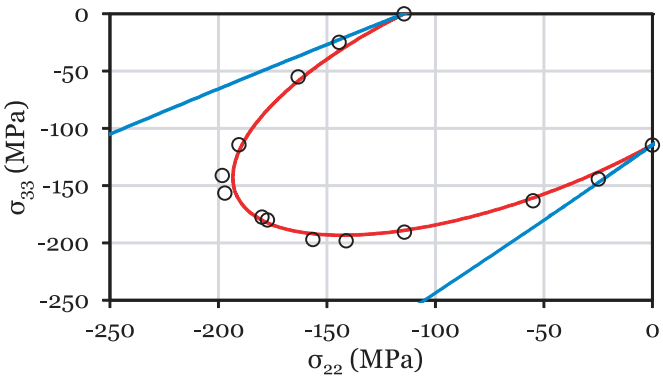

(c) Third quadrant (biaxial transverse compression).

Fig. 7.27. Detailed view of the $\sigma_{22} - \sigma_{33}$ failure envelope — micro-mechanics versus analytical failure criteria.

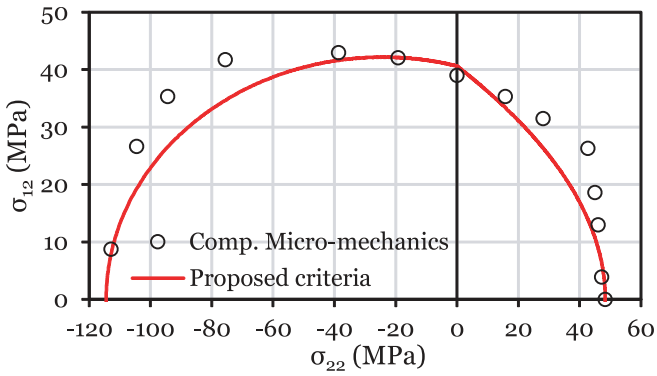

Fig. 7.28. $\sigma_{22} - \sigma_{12}$ failure envelope — micro-mechanics versus analytical failure criteria.

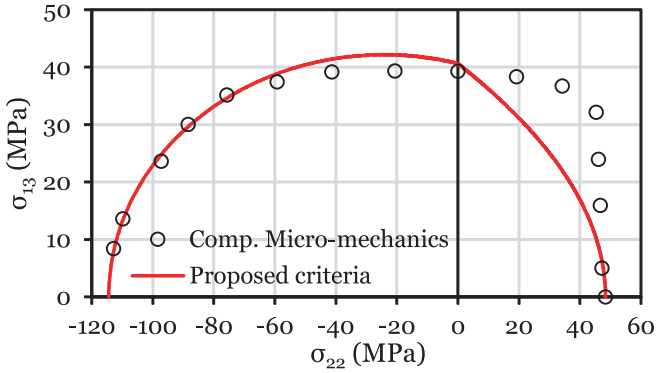

Fig. 7.29. $\sigma_{22} - \sigma_{13}$ failure envelope — micro-mechanics versus analytical failure criteria.

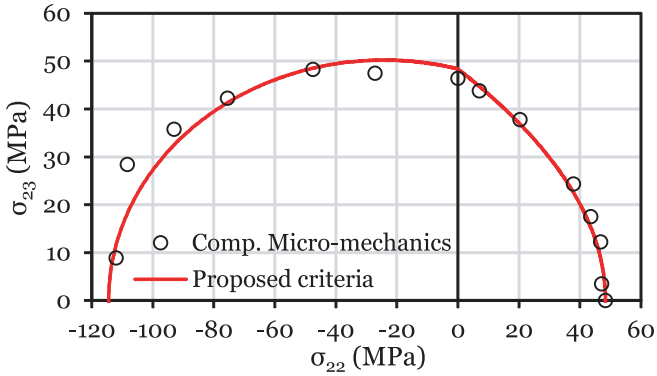

Fig. 7.30. $\sigma_{22} - \sigma_{23}$ failure envelope — micro-mechanics versus analytical failure criteria.

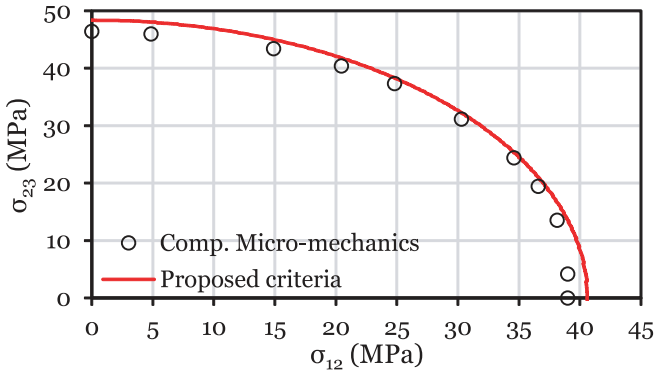

Fig. 7.31. $\sigma_{12} - \sigma_{23}$ failure envelope — micro-mechanics versus analytical failure criteria.

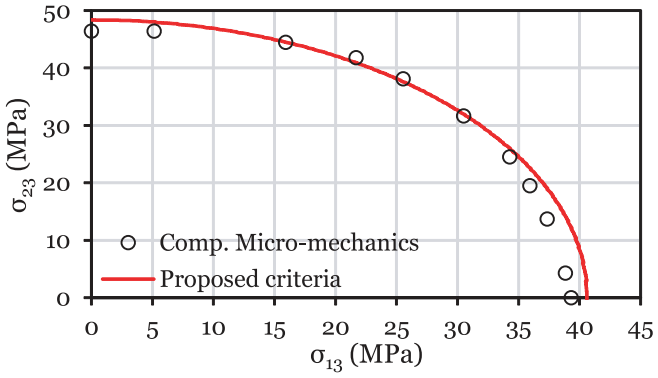

Fig. 7.32. $\sigma_{13} - \sigma_{23}$ failure envelope — micro-mechanics versus analytical failure criteria.

criteria and damage models for prediction of transverse damage mechanisms in multidirectional laminates [81, 99–108]. In fact, it has been shown that using as ply properties those measured directly from UD coupons to predict the strength of multidirectional laminates results in very conservative predictions that can differ substantially from the experimental results [83, 95, 102, 109].

When compared against experimental data available in the literature, good agreement for transverse failure modes, for failure under off-axis loading and for the effect of superposed hydrostatic pressure on failure of different FRPs was obtained. For more complex 3D stress states, where the test data available shows large scatter or is not available at all, a computational micro-mechanics framework was used to validate the failure criteria. A good correlation between the predictions of the two modelling strategies was obtained. Moreover, the computational micro-mechanics framework was shown to be a very useful tool to validate failure criteria under complex 3D stress states.

Chapter 8

Failure criteria implementation in a Smeared Crack Model

The onset and evolution of damage in composite materials is different and generally more complex than in metals, not only in the involved mechanisms but also in the effects on the mechanical properties. Due to the material heterogeneity and due to the anisotropy in both stiffness and strength properties, in composites the damage mechanisms develop at different levels, acting together under complex combinations. The models used to predict this complex damage behaviour typically take into account the progressive loss of stiffness and strength typical of these materials. In the present chapter, a Smeared Crack Model for transverse fracture of polymer composites is addressed. In particular, the new set of failure criteria described in chapter 7 is implemented in a smeared crack formulation, providing this numerical tool with a simpler model for damage onset prediction, and extending its ability to predict failure under high hydrostatic pressure.

8.1. Introduction

All materials exhibit irreversible nonlinearities, such as plasticity, damage, and fracture, resulting in either hardening or softening. The first is a macroscopic, distributed and irreversible material response that smears the stress concentrations and eliminates any stress singularities, while the latter corresponds to the development and coalescence of voids and microcracks, conducting, respectively, to damage localisation and elastic unloading along and adjacent to the fracture process zone [290].

The onset and evolution of damage in composite materials is different and generally more complex than in metals, not only in the involved mechanisms but also in the effects on the mechanical properties [159, 186]. Macroscopic fracture in composite materials is a result of the evolution of discrete damage events during the loading process, namely fibre/matrix debonding and subsequent pull-out, matrix cracking and yielding, delamination between plies, fibre breakage (longitudinal tension) or fibre kinking/microbuckling (longitudinal compression), and fibre-matrix split cracking.

Due to the material heterogeneity and due to the anisotropy in both stiffness and strength properties, in composites the damage mechanisms develop at different levels, acting together under complex combinations. Such combinations depend not only on the composite material (and its constituents), but also on the reinforcement configuration, stacking sequence and ply thickness, causing important stress redistributions in the damaged composite. While some combinations of damage may reduce local stress concentrations, others may conduct directly to structural collapse [290]. Therefore, a reliable methodology capable of predicting structural strength of composite materials must take into account both initiation and propagation of damage.

The models used to predict the complex damage behaviour of composite materials typically take into account the progressive loss of stiffness and strength typical of these materials, generally conducting either to too simplistic analytical so-

lutions or computationally demanding numerical models. However, the recent computational advances allowed numerous published demonstrations of successful representations of the initiation and propagation of damage in composite materials at different length scales, from detailed micro-mechanical approaches [67, 84, 85, 261, 294, 298, 299, 305, 308, 309, 349–351, 363–365], to models homogenised at the ply level (meso-scale) [106, 108, 183, 190, 287, 366–371] and at the laminate level (macro-scale) [7, 62, 372].

At the *micro-scale*, damage idealisations have higher resolution and higher kinematic freedom, allowing the prediction of the different damage mechanisms using separate damage laws applied at the constituent level (e.g. chapter 6). However, even though reliable estimations of the onset and propagation of damage can be obtained [294], the computational cost of micro-mechanical models makes them unsuitable for the prediction of damage localisation and ultimate failure in composite laminates with several laminae.

Alternatively, *meso-mechanical* models take the laminate layers or sublaminates as the basic homogeneous building blocks and use the orthotropic material properties related to the directions of the fibres to predict the behaviour of the whole laminate. The material properties can be determined from characterisation tests at the lamina level, or from micro-mechanical models. Models at the meso-scale are typically divided into *Continuum Damage Mechanics* (CDM) models and *Discrete Damage Mechanics* (DDM) models, depending on the approach used to model damage localisation.

In CDM models, damage propagation is modelled as a gradual, local loss of material integrity. CDM models assume that plies are composed of a homogeneous material, and the damage mechanisms are described explicitly, directly or indirectly representing the density and/or redistribution of the microscopic defects. Damage localisation is therefore represented as a "*soft discontinuity*" [290].

DDM models represent a new class of analysis methods in which the plies are represented at the meso-scale level as homogeneous materials, but the displacement discontinuities, such as cracks, are regarded as a zero- or finite-thickness cohesive process zone. Alternatively, embedded discontinuity models, such as the Extended Finite Element Method, are used to insert discrete damage in locations that are independent of the mesh orientation and without the need of re-meshing [373]. In DDM models, damage localisation is therefore represented as a "*hard discontinuities*" [290].

In structural-level (*macro-mechanical*) damage models, performing analyses is easier and the computational effort required is more reduced than in meso- and micro-mechanical models. The material is assumed homogeneous and the effects of the constituent materials and stacking sequence are represented by averaged apparent properties of the laminate. These models allow designers to study stress patterns and stress concentration regions in a component assuming the composite to be a homogeneous material. Damage can be represented either as hard discontinuities [372] or using a continuum damage approach [7, 62]. However, structural-level crack propagation criteria are strongly dependent on the material system and laminate configuration; therefore, a new set of material properties must be determined for each new material system and laminate stacking sequence, either through direct experimental testing or performing virtual testing using meso-mechanical models and experimental data at the ply level. For structural analyses, though, models at the macro-scale are often the most suitable analysis tools to predict the global mechanical response of composites parts and sub-components due to the relatively reduced computational cost of these models.

An alternative to performing different simulations at different length scales to obtain first the homogenised laminae or laminate properties and only then the structural response, is to link the different scale idealisations using "*multi-scale approaches*". These consider the various aspects of the entire structural problem at different levels of observation. The different levels at which analyses are carried out are connected either through *length scale transitions*, in which the structural behaviour at a given level is homogenised to arrive at mechanical properties at a next higher level (*hierarchical methods*), or through Finite Element Analysis (FEA) conducted at two different levels simultaneously (or concurrently), connected by matching the boundary conditions at both levels, usually invoking periodicity to reduce the amount of computations that need to be performed (*concurrent methods*) [374]. Hence, multi-scale analyses can be performed by using the best out of each level of analysis. For instance, in an information passing (or hierarchical) multi-scale approach, analyses on unit cells at the micro-scale can determine the stiffnesses and strengths of the unidirectional (UD) composite through homogenisation techniques, which are passed to a meso-mechanical model that accounts for the response of the

individual plies in a laminate and predicts its basic behaviour, providing stiffnesses and strengths for computations at the macro-scale [375].

From the previous discussion, it is clear that the development of reliable damage models at the different length scales is an important subject for the improved design development of composite structures. In the present chapter, a Smeared Crack Model (SCM) for transverse fracture of polymer composites [108] is addressed due to its ability to accurately represent the inelastic behaviour of composite laminates caused by matrix-dominated damage mechanisms.

Due to the CDM formulation, SCMs can be easily implemented in commercial Finite Element (FE) packages as a user-defined material. No intricate coding to take into account any additional degrees-of-freedom, special discretisation or re-meshing techniques is necessary.

However, CDM models typically suffer from lack of numerical objectivity, i.e., with successive mesh refinement, damage localises into a zone with a dimension that tends to zero. In the present model, this is obviated ensuring proper energy dissipation following the *crack band approach* [300].

The crack band model [300] uses the characteristic length of the finite element (which represents the crack band width) to regularise the computed dissipated energy due to the fracture process, independently of the numerical discretisation [376]. This avoids the need for *non-local techniques*, which, besides the complex implementation, require finer meshes and whose precise form of the averaging operator close to boundaries and material interfaces (important, for instance, when analysing multidirectional laminates) is still not clear [370, 376].

A computationally tractable approach to include the different damage modes in CDM models consists of using phenomenological failure criteria based on the homogenised stress (or strain) state at the ply level, which are able to predict the onset of the discrete failure mechanisms [290]. However, few criteria represent satisfactorily several relevant aspects of the failure process of laminated composites.

Important aspects of the failure process of laminated composites include the increase on apparent shear strength when applying moderate values of transverse compression, the effect of ply thickness (*in situ* effect), the detrimental effect of the in-plane shear stresses due to fibre misalignment under longitudinal compressive failure by fibre kinking, or the ability to predict failure under hydrostatic pressure [293, 312, 317, 377–381]. Many of the failure criteria that have been used in advanced damage models to predict the onset of matrix cracking and fibre fracture [102, 103, 128, 282, 315, 316, 327, 328] do not address all these limitations.

In chapter 7, new fully three-dimensional (3D) failure criteria for fibre-reinforced composite materials have been proposed, characterised by a simple, but elegant formulation, and based on a physical model for each failure mechanism [319]. These new 3D failure criteria have an invariant quadratic formulation based on structural tensors, which does not depend on coordinate-system transformations.

A thorough benchmarking of the failure criteria was presented in chapter 7, based on experimental results from the literature and based on a new strategy employing computational micro-mechanics [319]. A pragmatic approach was also proposed to estimate the orientation of the fracture plane, which is essential for the accurate representation of transverse cracking by means of a smeared crack formulation [129].

To account for the effect of ply thickness when the laminae are embedded in a multidirectional laminate, proper definitions of the *in situ* properties were also derived in the framework of the proposed invariant-based failure criterion for transverse failure mechanisms [129]. In addition, by including a linear invariant of the stress tensor $\boldsymbol{\sigma}$, the proposed criteria is able to account for pressure dependent fracture.

The objective of the present chapter is to implement a new set of failure criteria (chapter 7) in the SCM proposed by Camanho et al. [108]. This new implementation will provide the proposed SCM with a simpler formulation for damage onset prediction, avoiding the determination of the orientation of the fracture plane using a maximisation procedure (as originally proposed by Camanho et al. [108] based on Ref. [128]), and extend the ability of the SCM to predict fracture due to high hydrostatic pressure.

8.2. Failure models

8.2.1. Smeared Crack Model for transverse fracture

The mechanisms of transverse, matrix-dominated fracture include fibre-matrix decohesion and matrix cracking, which occur predominantly along a fracture plane whose orientation with respect to the mid-surface of a composite ply is not known in advance. The orientation of the fracture plane depends not only on the stress state, but also on the material properties. However, due to the morphology of fibre-reinforced polymers (FRPs), the fracture plane is always parallel to the fibre direction. The tractions acting on this fracture plane are assumed to govern the transverse fracture process, defining, together with the corresponding displacement jumps, the cohesive law that controls the propagation of transverse cracks on the UD ply.

The onset of transverse fracture and the orientation of the fracture plane, which are functions of the stress state $\boldsymbol{\sigma}$ and material properties, are predicted using the 3D invariant-based failure criterion for transverse damage mechanisms, following sections 7.2.1 and 7.2.3, respectively. Once the onset of transverse damage is predicted (equation (7.8)), i.e. when the condition $f_M(\boldsymbol{\sigma}) > 1$ is satisfied, where $f_M(\boldsymbol{\sigma})$ is the failure index for transverse damage mechanisms, the inelastic deformation associated with damage localisation must be determined.

First, the intersection with the failure surface is defined, to ensure that transverse cracking initiates when the condition $f_M(\boldsymbol{\sigma}) = 1$ holds. This is done employing an iterative scheme based on the Newton-Raphson method [382]. Having defined the conditions that trigger transverse failure mechanisms, a constitutive model that simulates the propagation of transverse matrix cracks under general loading conditions must be defined. Taking into account that, in such conditions, the orientation of the fracture plane is not known in advance, it is not possible to use cohesive zone models placed in predefined locations of the FE domain. Therefore, the use of a SCM, based on a '*fixed crack*' formulation [376], was proposed by Camanho et al. [108]. The SCM uses an additive decomposition of the strain tensor, which is divided into an elastic strain and a cracking strain, and it is based on a cohesive law that relates the tractions acting on the fracture plane with the corresponding displacement jumps across the crack faces. The following sections show the solution for the determination of the intersection with the failure surface, the definition of the traction tensor and a brief description of the SCM proposed by Camanho et al. [108]. The SCM was implemented in the FE package Abaqus/Explicit [275], which is an explicit dynamics analysis procedure based on the implementation of an explicit integration rule.

8.2.1.1. Intersection with the failure surface

When the onset of transverse damage is predicted, $f_M(\boldsymbol{\sigma}) > 1$, the stress state $\boldsymbol{\sigma}$ for such condition is unfeasible, because damage is assumed to initiate at the intersection with the failure surface, as shown in figure 8.1. For the sake of simplicity, a biaxial stress state composed of non-zero σ_{12} and σ_{22} stress components is considered. If, at a certain time increment, the stress state yields a point outside the failure surface, and if such stress state is taken as the condition for the onset of transverse failure mechanisms without returning to the original failure surface, the latter (solid line) is replaced by a new failure surface (dashed line) that overpredicts the onset of fracture. This may have a significant effect on the cohesive law governing the propagation of matrix cracks (figure 8.2). Because the condition that triggers the onset of transverse failure is overpredicted, and because the transverse fracture energy is constant (material property), the equivalent displacement jump at failure, and, consequently, the inelastic deformation at failure, are underpredicted. To represent accurately the conditions for the initiation of transverse cracks, it is therefore necessary to locate the intersection with the failure surface, i.e., the stress state at which $f_M = 1$.

For a given elastic stress increment $\boldsymbol{\Delta\sigma}_i$ at time increment i satisfying the failure criterion ($f_M > 1$), assuming that the intersection with the fracture surface can be given by a linear interpolation between the previous ($\boldsymbol{\sigma}_{i-1}$) and the new (purely elastic) stress state ($\boldsymbol{\sigma}_i = \boldsymbol{\sigma}_{i-1} + \boldsymbol{\Delta\sigma}_i$), valid for sufficiently small time (or stress) increments (typically the case in FEA with explicit integration rules), the location of the intersection of the elastic stress vector with the fracture surface can be determined imposing the following condition [382]:

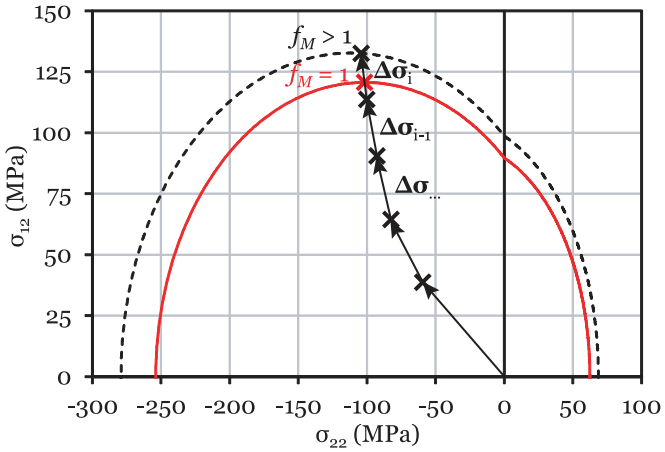

Fig. 8.1. Intersection with the fracture surface.

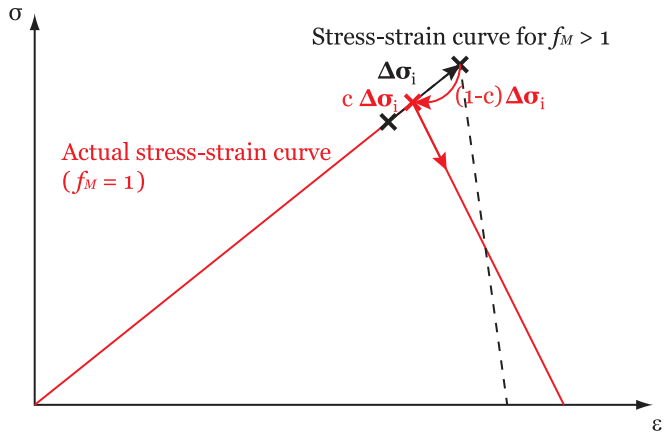

Fig. 8.2. Effect of determining the location of the intersection with the fracture surface on the inelastic response.

$$f_M\left(\boldsymbol{\sigma}_{i-1} + c\Delta\boldsymbol{\sigma}_i\right) = 1 \tag{8.1}$$

and solving it for c. In equation (8.1), the stress states $\boldsymbol{\sigma}_{i-1}$ and $\boldsymbol{\sigma}_{i-1} + \Delta\boldsymbol{\sigma}_i$ are such that the following two conditions must be satisfied:

$$f_M\left(\boldsymbol{\sigma}_{i-1}\right) < 1 \tag{8.2a}$$

$$f_M\left(\boldsymbol{\sigma}_{i-1} + \Delta\boldsymbol{\sigma}_i\right) > 1 \tag{8.2b}$$

Alternatively, defining an auxiliary function $F(\boldsymbol{\sigma}) = f_M(\boldsymbol{\sigma}) - 1$, equation (8.1) can be expressed as:

$$F\left(\boldsymbol{\sigma}_{i-1} + c\Delta\boldsymbol{\sigma}_i\right) = 0 \tag{8.3}$$

with:

$$F\left(\boldsymbol{\sigma}_{i-1}\right) < 0 \tag{8.4a}$$

$$F\left(\boldsymbol{\sigma}_{i-1} + \Delta\boldsymbol{\sigma}_i\right) > 0 \tag{8.4b}$$

It is noted that equation (8.3) can also be expressed in terms of strain increments (particularly useful in explicit FEA) as:

$$F\left[\mathbb{D}_e : (\boldsymbol{\varepsilon}_{i-1} + c\boldsymbol{\Delta\varepsilon}_i)\right] = 0 \tag{8.5}$$

where $\mathbb{D}_e$ is the elastic stiffness tensor [3].

To solve equation (8.3) (or equation (8.5)) for c, an iterative scheme can be set up using, for instance, a numerical procedure based on the Newton-Raphson method, with c as the only variable. Such iterative scheme might start with an initial estimate given as [382]:

$$c^{(0)} = -\frac{F|_{c=0}}{F|_{c=0} - F|_{c=1}} \tag{8.6}$$

where $F|_{c=0}$ and $F|_{c=1}$ are, respectively, $F(\boldsymbol{\sigma}_{i-1})$ and $F(\boldsymbol{\sigma}_{i-1} + \boldsymbol{\Delta\sigma}_i)$. The scalar c can be updated as:

$$c^{(k)} = c^{(k-1)} - \frac{F|_{c=c^{(k-1)}}}{\left.\dfrac{\mathrm{d}F}{\mathrm{d}c}\right|_{c=c^{(k-1)}}}, \quad k = 1, 2, \ldots \tag{8.7}$$

where k is the current iteration of the Newton-Raphson method. $F|_{c=c^{(k-1)}}$ is the function F evaluated taking $c = c^{(k-1)}$, which can be calculated from equations (7.6) (or (7.7)) and (7.8), knowing that $F = f_M - 1$ and making:

$$\boldsymbol{\sigma} = \boldsymbol{\sigma}_{i-1} + c^{(k-1)}\boldsymbol{\Delta\sigma}_i = \mathbb{D}_e : \left(\boldsymbol{\varepsilon}_{i-1} + c^{(k-1)}\boldsymbol{\Delta\varepsilon}_i\right) \tag{8.8}$$

$\left.\frac{\mathrm{d}F}{\mathrm{d}c}\right|_{c=c^{(k-1)}}$ is the derivative of F with respect to c for $c = c^{(k-1)}$. The derivative of F, $\frac{\mathrm{d}F}{\mathrm{d}c}$, is given as:

$$\frac{\mathrm{d}F}{\mathrm{d}c} = \alpha_1\frac{\mathrm{d}I_1}{\mathrm{d}c} + \alpha_2\frac{\mathrm{d}I_2}{\mathrm{d}c} + \alpha_3\frac{\mathrm{d}I_3}{\mathrm{d}c} + 2\alpha_{32}I_3\frac{\mathrm{d}I_3}{\mathrm{d}c} \tag{8.9}$$

with:

$$\begin{aligned}\frac{\mathrm{d}I_1}{\mathrm{d}c} &= \frac{1}{2}\left[\sigma_{22}(\Delta\sigma_{22} - \Delta\sigma_{33}) + \sigma_{33}(\Delta\sigma_{33} - \Delta\sigma_{22}) + c\left(\Delta\sigma_{22}^2 + \Delta\sigma_{33}^2\right)\right] + \\ &\quad + 2\Delta\sigma_{23}(\sigma_{23} + c\Delta\sigma_{23}) - c\Delta\sigma_{22}\Delta\sigma_{33} \qquad (8.10a)\\ \frac{\mathrm{d}I_2}{\mathrm{d}c} &= 2\left[\Delta\sigma_{12}(\sigma_{12} + c\Delta\sigma_{12}) + \Delta\sigma_{13}(\sigma_{13} + c\Delta\sigma_{13})\right] \qquad (8.10b)\\ \frac{\mathrm{d}I_3}{\mathrm{d}c} &= \Delta\sigma_{22} + \Delta\sigma_{33} \qquad (8.10c)\end{aligned}$$

I_1, I_2 and I_3 can be calculated from equation (7.6) (or (7.7)), making $\boldsymbol{\sigma} = \boldsymbol{\sigma}_{i-1} + c\boldsymbol{\Delta\sigma}_i = \mathbb{D}_e : (\boldsymbol{\varepsilon}_{i-1} + c\boldsymbol{\Delta\varepsilon}_i)$. The iterative procedure can be stopped either when the difference between two consecutive iterations is smaller than a predefined value (tolerance), or k is greater than the maximum number of iterations, which generally does not exceed 20.

Having determined c, the stress state $\boldsymbol{\sigma}_{i-1} + c\boldsymbol{\Delta\sigma}_i$ and the elastic strain $\boldsymbol{\varepsilon}_{i-1} + c\boldsymbol{\Delta\varepsilon}_i$ that define the intersection with the failure surface and, consequently, satisfy the condition $F = 0$ (or $f_M = 1$), are obtained. The stress state $\boldsymbol{\sigma}_{i-1} + c\boldsymbol{\Delta\sigma}_i$ establishes the conditions that trigger transverse failure mechanisms, defining the scalar components of the traction tensor on the fracture plane at the onset of transverse failure, $\bar{t}_i^{cr}$ [108]. The strain increment beyond the onset of transverse fracture, $(1 - c)\boldsymbol{\Delta\varepsilon}_i$ (figure 8.2), is responsible for the first cracking strain increment.

8.2.1.2. Traction tensor

Because in FRPs the fracture plane is always parallel to the fibre direction (figure 8.3), the unit vector normal to the fracture plane, $\mathbf{n}_2$, reads [128]:

$$\mathbf{n}_2 = \{0 \ \cos\alpha \ \sin\alpha\}^T \tag{8.11}$$

where α is the fracture angle estimated following the pragmatic approach described in section 7.2.3. The traction tensor acting on the fracture plane is then calculated using the stress tensor $\boldsymbol{\sigma}$ and the unit vector normal to the fracture plane $\mathbf{n}_2$ as [128]:

$$\boldsymbol{t} = \boldsymbol{\sigma} \cdot \mathbf{n}_2 \tag{8.12}$$

The normal, t_N, and shear components, t_L and t_T, of the traction tensor $\boldsymbol{t}$ are [128]:

$$t_N = \boldsymbol{t} \cdot \mathbf{n}_2 \ , \quad t_L = \boldsymbol{t} \cdot \mathbf{n}_1 \ , \quad t_T = \boldsymbol{t} \cdot (\mathbf{n}_1 \times \mathbf{n}_2) \tag{8.13}$$

with $\mathbf{n}_1 = \{1 \ 0 \ 0\}^T$. Alternatively, performing the necessary substitutions, the components of the traction tensor, equation (8.13), can be expressed as:

$$t_N = \frac{\sigma_{22} + \sigma_{33}}{2} + \frac{\sigma_{22} - \sigma_{33}}{2} \cos 2\alpha + \sigma_{23} \sin 2\alpha \tag{8.14}$$

$$t_L = \sigma_{12} \cos\alpha + \sigma_{13} \sin\alpha \tag{8.15}$$

$$t_T = (\sigma_{33} - \sigma_{22}) \sin\alpha \cos\alpha + \sigma_{23} \left(\cos^2\alpha - \sin^2\alpha\right) \tag{8.16}$$

The tractions are used in the SCM to define the cohesive law, established in terms of the displacement jumps across the crack faces ($\boldsymbol{\omega}^{cr}$) [108].

8.2.1.3. Smeared Crack Model

The SCM proposed by Camanho et al. [108] uses an additive decomposition of the strain tensor, where the total strain, $\boldsymbol{\varepsilon}$, is calculated as a function of the elastic strain, $\boldsymbol{\varepsilon}_e$, and of the cracking strain, $\boldsymbol{\varepsilon}_c$ as:

$$\boldsymbol{\varepsilon} = \boldsymbol{\varepsilon}_e + \boldsymbol{\varepsilon}_c = \boldsymbol{\varepsilon}_e + \mathbf{R} \cdot \boldsymbol{\varepsilon}_c^{cr} \cdot \mathbf{R}^T \tag{8.17}$$

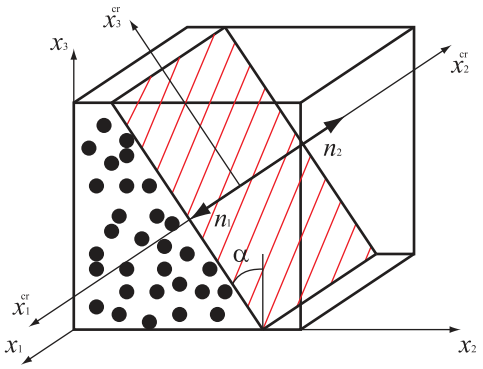

Fig. 8.3. Transverse fracture plane.

where $\boldsymbol{\varepsilon}_c^{cr}$ is the cracking strain projected in the crack coordinate system $x_1^{cr} x_2^{cr} x_3^{cr}$ (figure 8.3) and $\mathbf{R}$ is the rotation matrix that relates the global coordinate system to that associated to the fracture plane, whose components are functions of the fracture angle α.

The stress-strain relation reads [108]:

$$\boldsymbol{\sigma} = \mathbb{D}_e : (\boldsymbol{\varepsilon} - \boldsymbol{\varepsilon}_c) = \mathbb{D}_e : \boldsymbol{\varepsilon} - \mathbb{D}_e : \left(\mathbf{R} \cdot \boldsymbol{\varepsilon}_c^{cr} \cdot \mathbf{R}^T\right) \tag{8.18}$$

and the tractions acting on the fracture plane, projected onto the crack frame, can be expressed as [108]:

$$\boldsymbol{t}^{cr} = \mathbf{R}^T \cdot \boldsymbol{t} = \mathbf{R}^T \cdot (\boldsymbol{\sigma} \cdot \mathbf{n}_2) \tag{8.19}$$

The tractions $\boldsymbol{t}^{cr}$ can also be obtained by an appropriate cohesive law, which can be written as $\boldsymbol{t}^{cr} = g(\boldsymbol{\omega}^{cr})$, or, using equation (8.19) [108]:

$$\mathbf{R}^T \cdot (\boldsymbol{\sigma} \cdot \mathbf{n}_2) = \mathbf{g}\left(\boldsymbol{\omega}^{cr}\right) \tag{8.20}$$

resulting in a system of nonlinear equations [108].

Following Camanho et al. [108], the displacement jump $\boldsymbol{\omega}^{cr}$ is calculated using the relevant components of the cracking strain tensor, $\boldsymbol{\varepsilon}_c^{cr}$, and the characteristic length of the finite element, l^*:

$$\boldsymbol{\omega}^{cr} = \left[\left(2\boldsymbol{\varepsilon}_c^{cr} : \mathbf{n}_1^{cr} \otimes \mathbf{n}_2^{cr}\right)\mathbf{n}_1^{cr} + \left(\boldsymbol{\varepsilon}_c^{cr} : \mathbf{n}_2^{cr} \otimes \mathbf{n}_2^{cr}\right)\mathbf{n}_2^{cr} + \left(2\boldsymbol{\varepsilon}_c^{cr} : \mathbf{n}_2^{cr} \otimes \mathbf{n}_3^{cr}\right)\mathbf{n}_3^{cr}\right] l^* \tag{8.21}$$

where $\mathbf{n}_i^{cr}$ are the unit vectors acting on the fracture plane written in the crack coordinate system. In the present implementation, l^* is taken as the square root of the finite element's in-plane area.

To solve the system of nonlinear equations expressed by equation (8.20), Camanho et al. [108] defined a cohesive law in the context of the SCM using a modification of the constitutive model originally proposed by Turon et al. [137] to address delamination growth under general loading conditions. The proposed constitutive model imposes a linear softening cohesive law, defining the tractions $t_i^{cr}(d)$ acting on the fracture plane as [108]:

$$t_i^{cr}(d) = \left(\frac{1-d}{d}\right)\frac{\left|\omega_i^{cr}\right|}{\omega_f^m} \bar{t}_i^{cr} - \delta_{i2}\frac{\langle -\omega_2^{cr}\rangle}{\left|\omega_2^{cr}\right|}\left[\left(\frac{1-d}{d}\right)\frac{\left|\omega_i^{cr}\right|}{\omega_f^m}\bar{t}_i^{cr} - E_{22}\left(\varepsilon_{22}^{cr} - \varepsilon_{c_{22}}^{cr}\right)\right] \tag{8.22}$$

where d is a scalar damage variable, δ_{ij} is the Kroenecker delta, ω_f^m is the equivalent displacement jump at failure under mixed-mode loading conditions, ω_i^{cr} are the scalar components of the displacement jump vector $\boldsymbol{\omega}^{cr}$, E_{22} is the transverse Young's modulus, ε_{22}^{cr} and $\varepsilon_{c_{22}}^{cr}$ are respectively the scalar components of the total and cracking strain tensors $\boldsymbol{\varepsilon}^{cr}$ and $\boldsymbol{\varepsilon}_c^{cr}$ projected in the crack coordinate system, and $\langle \bullet \rangle$ are the Macaulay brackets.

Following Camanho et al. [108], the damage variable d is obtained from the loading function $\mathcal{L}(\boldsymbol{\omega}^{cr})$ proposed by Turon et al. [137] as:

$$d = \max\left\{0, \max\left[\mathcal{L}\left(\boldsymbol{\omega}^{cr}\right)\right]\right\} \tag{8.23}$$

with:

$$\mathcal{L}\left(\boldsymbol{\omega}^{cr}\right) = \min\left\{\frac{\lambda}{\omega_f^m}, 1\right\} \tag{8.24}$$

where λ is the equivalent displacement jump defined as [108]:

$$\lambda = \sqrt{(\omega_s^{cr})^2 + \langle\omega_2^{cr}\rangle^2} \tag{8.25}$$

with:

$$\omega_s^{cr} = \sqrt{\left(\omega_1^{cr}\right)^2 + \left(\omega_3^{cr}\right)^2} \tag{8.26}$$

The equivalent displacement jump at failure, ω_f^m, requires an appropriate criterion for crack propagation under mixed-mode loading conditions. Following Camanho et al. [108], the Benzeggagh-Kenane (BK) law [303] is adopted to predict the mixed-mode intralaminar fracture toughness associated with transverse failure mechanisms. The equivalent displacement jump at failure, ω_f^m, is then obtained as [108]:

$$\omega_f^m = \frac{2\left(\mathcal{G}_{Ic} + AB^{\eta}\right)}{\bar{t}^{cr}} \tag{8.27}$$

where $A = \mathcal{G}_{IIc} - \mathcal{G}_{Ic}$, B is the mode ratio and η is the mixed-mode interaction parameter used in the BK law, $\mathcal{G}_{Ic}$ and $\mathcal{G}_{IIc}$ are respectively the mode I and mode II intralaminar fracture toughness associated with transverse failure mechanisms, and $\bar{t}^{cr}$ is the norm of the traction tensor at the onset of transverse failure:

$$\bar{t}^{cr} = \sqrt{(\bar{t}_s^{cr})^2 + \langle\bar{t}_2^{cr}\rangle^2} \tag{8.28}$$

with:

$$\bar{t}_s^{cr} = \sqrt{\left(\bar{t}_1^{cr}\right)^2 + \left(\bar{t}_3^{cr}\right)^2} \tag{8.29}$$

The mode ratio B was derived by Camanho et al. [108], and it is given as:

$$B = \frac{\bar{t}_s^{cr}\beta}{\beta\left(\bar{t}_s^{cr} - \langle\bar{t}_2^{cr}\rangle\right) + \langle\bar{t}_2^{cr}\rangle} \tag{8.30}$$

with:

$$\beta = \frac{\omega_s^{cr}}{\omega_s^{cr} + \langle\omega_2^{cr}\rangle} \tag{8.31}$$

where ω_s^{cr} is given by equation (8.26).

Following Camanho et al. [108], equation (8.20) can be rewritten as:

$$\mathbf{r}\left(\boldsymbol{\varepsilon}_c^{cr}\right) = \mathbf{f}\left(\boldsymbol{\varepsilon}_c^{cr}\right) - \mathbf{g}\left(\boldsymbol{\varepsilon}_c^{cr}\right) \tag{8.32}$$

with:

$$\mathbf{f}\left(\boldsymbol{\varepsilon}_c^{cr}\right) = \mathbf{R}^T \cdot \left[\mathbb{D}_e : \boldsymbol{\varepsilon} - \mathbb{D}_e : \left(\mathbf{R} \cdot \boldsymbol{\varepsilon}_c^{cr} \cdot \mathbf{R}^T\right)\right] \cdot \mathbf{n}_2 \tag{8.33}$$

$\mathbf{r}\left(\boldsymbol{\varepsilon}_c^{cr}\right)$ is the residual for the system of nonlinear equations defined by equation (8.20), which can be solved for the cracking strain. The algorithm and the iterative procedure based on a multi-variable Newton-Raphson method used to numerically

solve this system of nonlinear equations were described by Camanho et al. [108]. Having determined the cracking strain, the stress tensor is easily obtained using equation (8.18).

8.2.2. Damage model for longitudinal fracture

The mechanisms of longitudinal failure include fracture of the fibres and matrix, as well as fibre-matrix pull-out in the tensile mode. Following Camanho et al. [108], the propagation of longitudinal failure mechanisms is addressed using the damage model proposed by Maimí et al. [106, 190]. However, in the present chapter, the onset of longitudinal fracture is predicted using the failure criteria proposed in section 7.3, based on a noninteracting maximum allowable strain criterion for longitudinal fibre failure ($\sigma_{11} \geq 0$), and based on a 3D invariant-based failure criterion for fibre kinking ($\sigma_{11} < 0$).

The choice for a noninteracting maximum allowable strain criterion for the prediction of the onset of tensile fracture in the fibre direction (section 7.3.1) is based on experimental evidence, and follows many other phenomenological failure criteria [102, 103, 128, 282, 327]. If the tensile strain-to-failure in the fibre direction, ε_1^T, is not known, assuming that the tensile behaviour of the composite in the fibre direction is linear-elastic until failure, equation (7.32) can also be written as:

$$f_F = \frac{\varepsilon_{11}}{\varepsilon_1^T} = \varepsilon_{11}\frac{E_{11}}{X_T} \leq 1, \quad \sigma_{11} \geq 0 \tag{8.34}$$

where ε_{11} and σ_{11} are respectively the strain and stress components in the fibre direction, E_{11} is the longitudinal Young's modulus, and X_T is the longitudinal tensile strength of the UD ply.

The proposed 3D kinking model (section 7.3.2) assumes that fibre kinking is originated by local micro-structural defects that trigger a kink band when local matrix cracking occurs in the vicinity of the misaligned, micro-buckled fibres. In the implementation used in the present damage model, these local micro-structural defects are represented by a micro-mechanical parameter (χ) associated with the creation of a kink-band (section 7.3.2.3.3) [128].

The damage evolution laws for fibre-dominated failure mechanisms must account for the different energy dissipating mechanisms associated with the propagation of a crack perpendicularly to the reinforcing fibres [108]. Following Camanho et al. [108], the bi-linear softening laws proposed by Maimí et al. [106, 190] are used. This bi-linear softening behaviour is defined by the maximum stress sustained by the material, by the stress corresponding to the modification of the softening slope (the so-called '*pull-out stress*'), and by the partition of the dissipated energy per unit volume associated with each softening regime. As suggested by Camanho et al. [108], the 'pull-out stress' and the partitions of the dissipated energy are identified using the procedure proposed by Dávila et al. [189] by means of the analysis of the crack resistance curve ($\mathcal{R}$-curve) obtained in the propagation of cracks or kink bands perpendicularly to the fibre direction [65, 187, 191]. The relevant quantities of the $\mathcal{R}$-curve are the lengths of the fracture process zones, l_{fpz}, and the steady state propagation values of the fracture toughness, $\mathcal{G}_{1+}^{ss}$ for tensile fracture propagation and $\mathcal{G}_{1-}^{ss}$ for kink band formation [108].

The details of the theoretical background and of the implementation of the damage model for longitudinal failure mechanisms are given in Refs. [106, 190]. It should be noted that, as suggested by Camanho et al. [108], the same characteristic length, l^*, is used for transverse and longitudinal failure mechanisms.

8.3. Preliminary verification and validation

Before presenting the validation results based on comparisons of the predictions of the proposed implementation of a new set of failure criteria in a SCM [108] with data from experimental tests, two preliminary verifications were performed to ensure that the results of the proposed model are numerically consistent. First, a verification based on single-element tests, subject to simple stress states, is performed. Secondly, following Camanho et al. [108], simple models of a single UD ply subject to uniaxial transverse tension are used to demonstrate that the predictions do not depend on the level of mesh refinement.

Table 8.1
Material properties of IM7/8552 carbon-epoxy UD tape.

Property			References
Elastic properties			
E_{11}	171.42	GPa	Camanho et al. [108]
E_{22}	9.80	GPa	Camanho et al. [108]
G_{12}	5.29	GPa	Camanho et al. [108]
ν_{12}	0.32	-	Camanho et al. [108]
ν_{23}	0.487	-	Camanho et al. [108]
Strength properties			
X_T	2806.0	MPa	Camanho et al. [108]
X_C	-1200.1	MPa	Camanho et al. [108]
Y_T	62.3	MPa	Camanho and Lambert [235]
Y_{BT}	38.7	MPa	Vogler et al. [266]
Y_C	-253.7	MPa	Koerber et al. [265]
Y_{BC}	-600.0	MPa	Vogler et al. [266]
S_L	89.6	MPa	Catalanotti et al. [128]
S_T	62.3	MPa	section 7.2.5
Fracture toughness			
$\mathcal{G}_{Ic}$	0.277	kJ/m^2	Camanho et al. [108]
$\mathcal{G}_{IIc}$	0.788	kJ/m^2	Camanho et al. [108]
η	1.634	-	Camanho et al. [108]
$\mathcal{G}^i_{1+}$	94.1	kJ/m^2	Camanho et al. [108]
$\mathcal{G}^{ss}_{1+}$	134.7	kJ/m^2	Camanho et al. [108]
l_{fpz}	3.4	mm	Camanho et al. [108]
$\mathcal{G}^i_{1-}$	47.5	kJ/m^2	Camanho et al. [108]
$\mathcal{G}^{ss}_{1-}$	150.0	kJ/m^2	assumed

The failure models presented in section 8.2 were implemented in Abaqus/Explicit [275] by means of a VUMAT user subroutine. The material selected, not only for the preliminary verification but also for the validation studies, is IM7/8552 carbon-epoxy UD tape, with a nominal ply thickness of 0.125 mm. The material properties are presented in table 8.1. G_{12} is the shear modulus, ν_{12} and ν_{23} are the Poisson's ratios, X_C is the longitudinal compressive strength, Y_T and Y_{BT} are respectively the uniaxial and biaxial transverse tensile strengths, Y_C and Y_{BC} are respectively the uniaxial and biaxial transverse compressive strengths, S_L and S_T are respectively the in-plane and transverse shear strengths, $\mathcal{G}^i_{1+}$ is the initiation value of the fracture toughness associated with crack propagation perpendicularly to the fibre direction, and $\mathcal{G}^i_{1-}$ is the initiation value of the fracture toughness associated with the propagation of a kink band.

To verify the correct implementation of the damage model in the VUMAT user subroutine, single-element tests were performed on cubic 8-node linear hexahedral finite elements with reduced integration (C3D8R) [275], with dimensions $0.1 \times 0.1 \times 0.1$ mm^3. Each element was subjected to a simple stress state, imposed by means of null-displacement and velocity boundary conditions applied to its surfaces. Figure 8.4 shows the corresponding traction-cracking strain relations for several pure uniaxial and pure shear stress states. The model was able to correctly predict the onset of transverse damage mechanisms, as well as the computed fracture energy, given, for instance, by the area below the traction-cracking strain relations.

To show that the predictions are independent of the finite element size, following Camanho et al. [108], simple models of an UD IM7/8552 carbon-epoxy [90] laminate, with a thickness of 0.125 mm, are used. A rectangular plate, 12 mm wide and 40 mm long, subjected to a remote tensile load is simulated. Three different levels of mesh refinement were generated. The nominal in-plane sizes of the finite elements are 0.3×0.3 mm^2, 0.5×0.5 mm^2 and 0.8×0.8 mm^2. One element along the thickness of the UD laminate is used. The SCM is applied to the elements placed on the fracture plane to simulate the onset and propagation of transverse cracking.

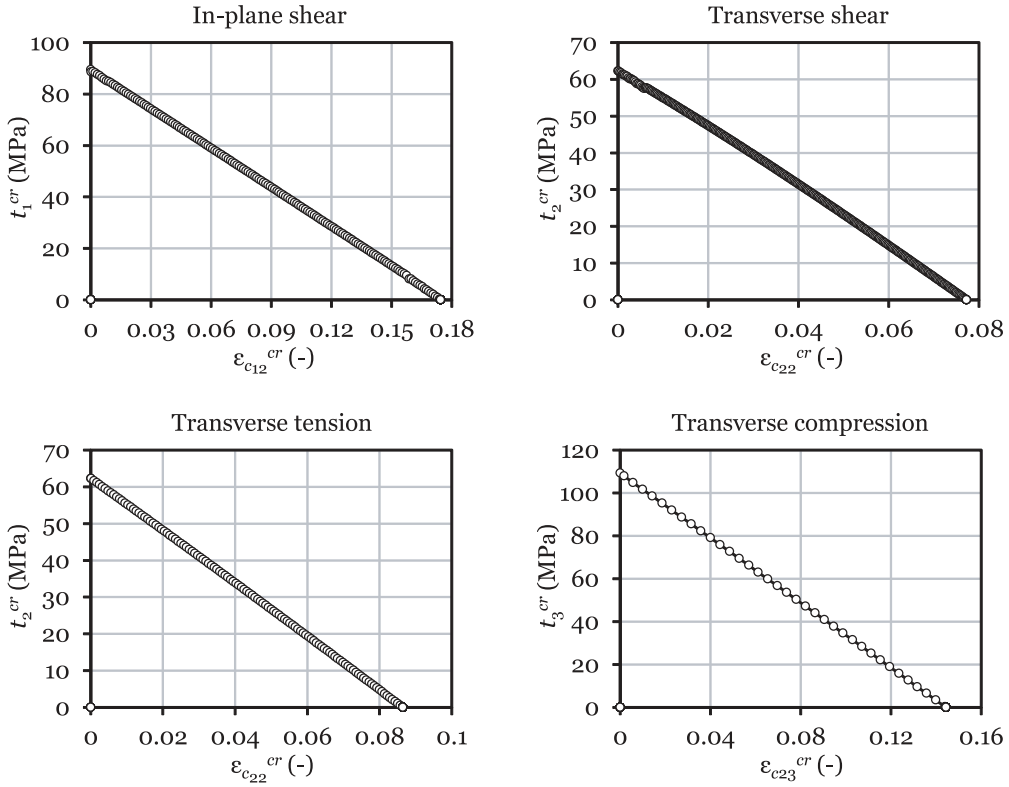

Fig. 8.4. Single-element test results.

Figures 8.5 and 8.6 show respectively the scalar damage variable that represents transverse matrix cracking at the peak loads and the relation between the remote stress and the applied displacement for each FE discretisation. As it can be observed, the predicted peak load is independent of the mesh refinement.

The previous preliminary verification show that the implementation of the SCM [108] is consistent with the proposed damage idealisation and that it does not suffer from lack of objectivity. However, it is now necessary to assess the accuracy of the proposed damage model, and understand how well it represents the inelastic response and failure behaviour of composite laminates and structural details subjected to different loading conditions. With this purpose, a comparison between the predictions of the proposed damage model and data obtained from experimental tests carried out on an IM7/8552 $[90/0/\pm 45]_{3S}$ laminate is presented. Test data includes results on unnotched and open-hole specimens loaded in tension and in compression.

The FE models were constructed using C3D8R finite elements [275]. Each ply of the IM7/8552 $[90/0/\pm 45]_{3S}$ laminate was modelled as a homogeneous material (table 8.1), with one element through the thickness. The constraining effect of the adjacent plies on the initiation of transverse damage growth in the embedded and outer plies was taken into account using as ply strengths the *in situ* strengths, calculated as described in section 7.2.4.

As discussed by Camanho et al. [108], ideally, the characteristic length l^* should be calculated as a function of the fracture angle and of the direction of crack propagation. However, in the present models, l^* is taken as the square root of the finite element's in-plane area (the element's thickness is constant and equal to the ply thickness). This means that the most accurate predictions are obtained with elements with in-plane aspect ratios close to one, with the element edges aligned with the crack propagation direction, and for cracks that are perpendicular to the symmetry plane of the laminate (e.g. uniaxial transverse tensile failure).

It is noted that the last condition is dependent on the stress state and on the material response (e.g. wedge fracture due to transverse compression), and therefore cannot be easily addressed when constructing the mesh for the FE models.

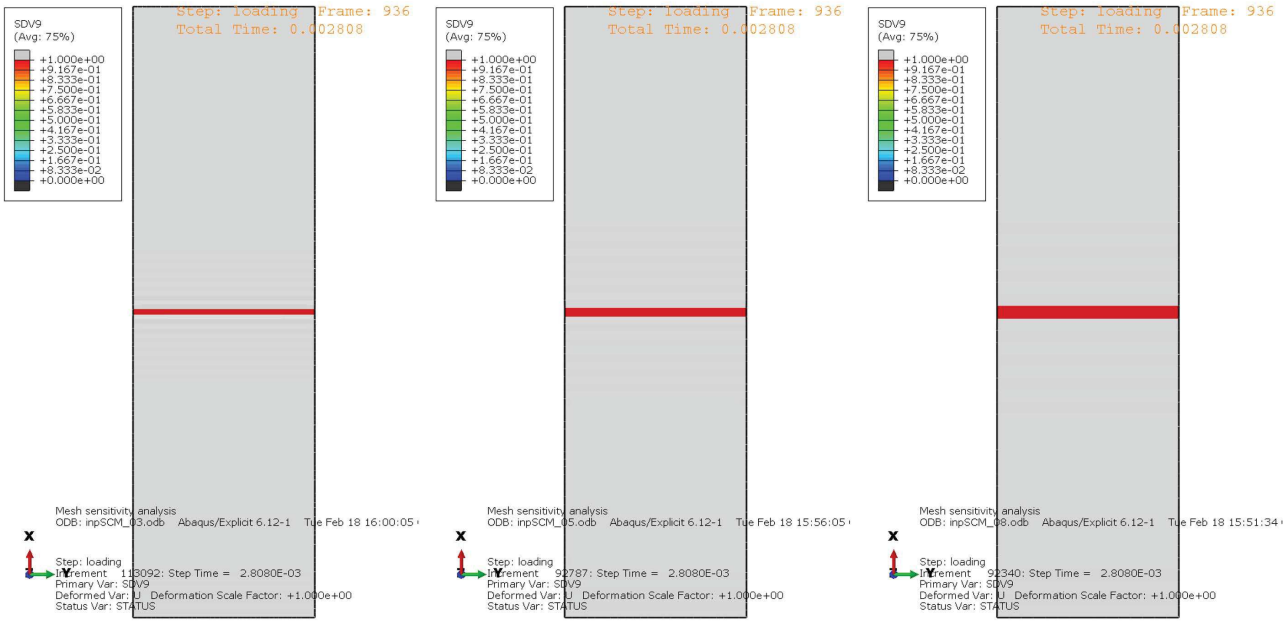

Fig. 8.5. Scalar damage variable that represents transverse matrix cracking at the peak load for different FE discretisations: (left) 0.3×0.3 mm^2, (centre) 0.5×0.5 mm^2 and (right) 0.8×0.8 mm^2.

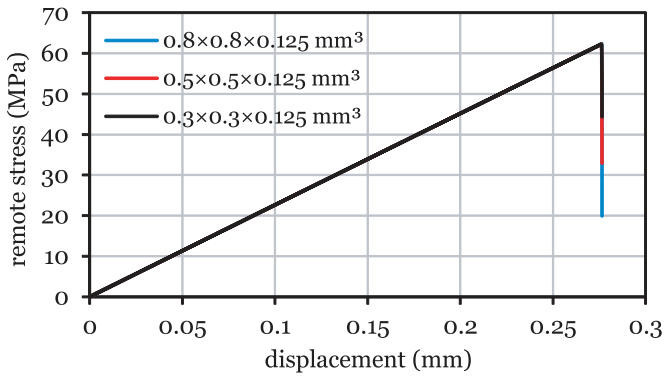

Fig. 8.6. Relation between the remote stress and the applied displacement for different FE discretisations.

On the other hand, due to the morphology of FRPs, the transverse crack propagation direction is always parallel to the fibres, whereas longitudinal failure typically occurs perpendicularly to the fibre direction. Hence, to ensure that the element edges are aligned with the crack propagation direction, a structured mesh aligned with the fibre direction was employed [206, 383]. Due to meshing difficulties in the off-axis ±45° plies of the open-hole specimens, 6-node linear wedge (C3D6) elements were included close to the edges of the open holes.

Cohesive surfaces, defined as surface interactions [275], were used to simulate delamination between plies. An uncoupled traction-separation behaviour, a maximum stress criterion for damage initiation, and an energy based damage evolution criterion were used [275]. The mixed-mode behaviour (based on the BK law [303]) was provided in tabular form [383]. Because delamination is a matrix-dominated failure mechanism, the transverse tensile and shear strengths, Y_T and S_L respectively, and the fracture toughness $\mathcal{G}_{Ic}$ and $\mathcal{G}_{IIc}$ (table 8.1) were used in the definition of the interlaminar properties used in the cohesive surfaces.

Abaqus/Explicit [275] was used to simulate the quasi-static behaviour of the IM7/8552 $[90/0/\pm 45]_{3S}$ laminate, while ensuring a low kinetic energy through out the simulations. Loading was applied my means of appropriate boundary conditions, imposing a velocity along the longitudinal direction of the specimens using a smooth step amplitude [383].

Table 8.2
Comparison between experiments [183, 206] and predictions [383] of the proposed implementation of the SCM [108]. Experimental results for unnotched and open-hole specimens of an IM7/8552 $[90/0/\pm 45]_{3S}$ laminate.

Specimen type	width (mm)	hole diameter (mm)	experiments (MPa)	predictions (MPa)	relative error
Unnotched specimens					
Tension	12	-	845.1	871.4	3.1%
Compression	12	-	532.6	540.5	1.5%
Open-hole specimens					
Tension	12	2	555.7	611.4	10.0%
Tension	24	4	480.6	529.6	10.2%
Tension	36	6	438.7	473.9	8.0%
Tension	48	8	375.7	438.9	16.8%
Tension	60	10	373.7	407.8	9.1%
Compression	12	2	383.1	414.5	8.2%
Compression	18	3	372.9	421.1	12.9%
Compression	24	4	365.2	387.8	6.2%
Compression	30	5	353.7	382.5	8.1%

In the FE models of the open-hole specimens, taking advantage of laminate symmetry, only one-half of the laminate was simulated to reduce computing time. In addition, the damage model was applied to the elements in the central region, where damage is expected to grow due to the presence of the geometric discontinuity. A linear-elastic material model, defined using only the elastic properties of IM7/8552 carbon-epoxy (table 8.1), was applied to the finite elements in the regions for from the centre.

Table 8.2 shows a comparison between the ultimate remote stresses obtained from experimental testing and from the predictions of the proposed damage model for both unnotched and open-hole specimens. The relative errors between experiments and predictions are also presented.

This preliminary validation study (table 8.2) shows that, in the case of the unnotched specimens, the predictions of the proposed implementation of the SCM [108] are only slightly above the experimental results in both loading scenarios, correlating very well with the corresponding ultimate remote stresses. However, in the case of the open-hole specimens, the numerical results overpredict the ultimate remote stresses obtained experimentally, with relative errors around 10%.

This larger overprediction can be attributed to the role of delamination in the failure behaviour of the notched specimens, since current implementations of cohesive surface interactions [275] are known to lack accuracy in the prediction of interlaminar damage growth [206]. Cohesive elements (e.g. Ref. [384]), on the other hand, are currently mature enough to accurately predict delamination in composite laminates. Unfortunately, the choice for an oriented, structured mesh, intended to improve the accuracy of the proposed damage model, does not allow the implementation of cohesive elements between the solid elements that represent each ply in the laminate. Nonetheless, the predictions of the unnotched specimens of the IM7/8552 $[90/0/\pm 45]_{3S}$ laminate, whose response is reasonably independent of delamination growth before ultimate failure, show that the proposed implementation of the SCM [108] can be seen as a valid tool to predict failure of multidirectional laminates using only properties determined from tests carried out at the lamina level (table 8.2).

8.4. Concluding remarks

In the present chapter, the SCM proposed by Camanho et al. [108] was extended by implementing the invariant-based failure criteria presented in chapter 7 as a new set of damage initiation functions. A preliminary verification, based on single-element tests and on simple models with different levels of refinement, and a preliminary validation study, where test results of unnotched and notched coupons of an IM7/8552 carbon-epoxy multidirectional laminate were compared with the predictions of the proposed damage model, show that the latter is not only consistent with respect to the proposed

damage idealisation and to mesh objectivity, but it can also be seen as a valid tool to predict failure of multidirectional laminates using only properties determined from tests carried out at the lamina level.

In the future, coupling with a reliable interlaminar damage model and further benchmarking based not only on simple coupons but also on more complex structural details should be performed to demonstrate the strengths of the proposed damage model. Case studies including laminates with thinner plies may also be desirable, given the ability of these laminates to suppress interlaminar damage growth before ultimate failure. This would certainly be the most desirable test cases to validate a numerical tool like the SCM, which is intended to simulate the inelastic and fracture response associated with intralaminar damage mechanisms.

It should be noted that, for very thin plies, the applicability of numerical tools formulated at the lamina level becomes questionable. In fact, compared to conventional ply grades, for the same laminate thickness, thin-ply laminates have to accommodate a much greater number of plies. If each of these plies need to be represented individually for application of a damage model at the ply level, the required discretisation and the size of the FE model will rapidly become impractical. On the other hand, the possibility to accommodate more plies means that the macro-mechanical response of thin-ply laminates is practically homogeneous. Moreover, thin-ply laminates develop much lower interlaminar stresses, resulting in a recognised delamination suppression capability, and they have considerably higher *in situ* strengths, precluding matrix cracking before ultimate laminate failure. Therefore, their mechanical and fracture response resemble that of a homogenised quasi-brittle material, making macro-mechanical models at the laminate level more suitable for their analysis. This is the subject of part V of this thesis.

Part V

Analysis models for laminate failure prediction

Chapter 9

Invariant-based approach to laminate design

Using thin plies, laminate homogenisation becomes simpler, even for very thin laminates. Consequently, suitable macro-mechanical tools become readily available, with accuracies hardly found when applied to conventional laminates. This chapter presents an overview of the recently proposed Trace theory and Master Ply concept, which employ an invariant-based approach to stiffness, with great potential to simplify design allowable generation. Then, an introduction to the concept of Omni Strain Failure Envelopes and to the Unit Circle failure criterion is presented. These concepts introduce a new invariant-based approach to strength that greatly simplifies the macro-mechanical failure analysis of homogenised laminates. Using the invariant-based approaches to stiffness and strength, a simple sizing method that is able to account for weight and lay-up time savings is described, making lay-up and material screening for a given application much easier.

9.1. Introduction

When a laminate is composed by a large number of repeated sublaminates, with dispersed plies, it becomes homogenised [3]. One consequence is that extension-bending coupling tends to zero and the flexural and in-plane stiffnesses converge to the same value [3]. Thus, the optimised laminate for in-plane loading is the same for flexural loading [55], and the design of homogenised composite laminates becomes similar to that of isotropic materials [385].

Heterogeneous laminates have a great number of possible stacking combinations, each originating a different macro-mechanical response. Optimal design is therefore an extremely difficult and time-consuming task. Optimisation of homogenised orthotropic laminates, though, is greatly simplified, because the macro-mechanical response is independent of the stacking sequence.

Other benefits of homogenisation includes null thermal warpage, making mid-plane symmetry irrelevant, increased toughness and strength, higher out-of-plane (delamination) strength, minimal residual stresses originated during the curing process, and simpler manufacturing [55].

Using thin plies, laminate homogenisation is possible even for very thin laminates, increasing the potential for cost and weight savings, while simplifying considerably laminate design and optimisation. Suitable macro-mechanical tools become readily available (e.g. [58, 135]), with accuracies hardly found when applied to conventional laminates.

In the following, an overview of the recently proposed Trace theory and Master Ply concept is presented, which employ an invariant-based approach to stiffness, with great potential to simplify design allowable generation. Then, the concept of Omni Strain Failure Envelopes and the Unit Circle failure criterion are briefly described. These concepts introduce a new invariant-based approach to strength that greatly simplifies the macro-mechanical failure analysis of homogenised

laminates. Using the invariant-based approaches to stiffness and strength, a simple sizing method that is able to account for weight and lay-up time savings is described, making lay-up and material screening for a given application much easier.

9.2. Trace theory and Master Ply concept

9.2.1. Overview

Tsai and Melo [55] recently proposed an invariant-based approach to describe the elastic properties of composite plies and laminates based on trace-normalised stiffness parameters. Following Tsai and Melo [55], the traces of the in-plane and flexural normalised stiffness matrices, tr$\mathbf{A}^*$ and tr$\mathbf{D}^*$, which are invariants with respect to coordinate transformations, have the same value:

$$\text{tr}\mathbf{Q} = \text{tr}\mathbf{A}^* = \text{tr}\mathbf{D}^* = Q_{11} + Q_{22} + 2Q_{66} \tag{9.1}$$

where $\mathbf{Q}$ is the plane stress stiffness matrix. Tsai and Melo [55] noted that, while the terms of $\mathbf{A}^*$ are independent of the stacking sequence, those of $\mathbf{D}^*$ are not. However, the trace of these matrices has the same value, and it is invariant with respect to the stacking sequence. In fact, for a given material, tr$\mathbf{A}^*$ and tr$\mathbf{D}^*$ are independent of the loading condition (in-plane or flexural), stacking sequence (symmetric or not), and material symmetry (isotropic, orthotropic or anisotropic). According to Tsai and Melo [55], *Trace* is, therefore, a material property.

Tsai and Melo [55] found that the stiffness of carbon-fibre reinforced polymers (CFRPs) normalised by their respective Trace are very close, especially the longitudinal stiffness, parallel to the fibre direction (with a coefficient of variation around 1.5% for 10 different material systems). In fact, it is noted that the transverse and shear properties of CFRPs are only a small fraction of their longitudinal properties[1], even if their variation is large (due to differences in the matrix formulations and curing processes) [55]. Based on these observations, Tsai and Melo [55] defined a *Master Ply* for CFRPs using the median values of the Trace-normalised stiffness properties (table 9.1).

Because the stiffness of CFRPs along the fibre direction is responsible for about 88% of the value of Trace (table 9.1), it is possible to determine the Trace of a given material using only the in-plane longitudinal stiffness component, E^0_{11}, without the need to measure the transverse and shear moduli. On the other hand, Classical Laminated Theory (CLT) can be used to generate Trace-normalised factors for the stiffness components of multidirectional laminates (figure 9.1). Trace can then be used to estimate the laminate in-plane elastic constants, E^0_x, E^0_y, G^0_{xy} and ν^0_{xy}, from one elastic lamina property (E^0_{11}) and from the Universal Laminate Factors. This is valid not only for unidirectional (UD) tapes, but also for woven fabrics [386].

Regarding the sensitivity of Trace and Trace-normalised properties to environmental conditions, Tsai and Melo [386] observed that, in the case of multidirectional laminates, even though the value of Trace for a given material varies with temperature, the Trace-normalised laminate factors remain unchanged. Hence, it is possible to determine the elastic properties of any laminate using the universal laminate factors in figure 9.1 (or using CLT and the Master Ply for other laminates) and the value of Trace obtained from the longitudinal stiffness of a coupon tested after exposure to the desired environmental conditions.

9.2.2. Analysis and predictions

To assess the accuracy of Trace theory, table 9.2 compares the predictions obtained with Trace and CLT for quasi-isotropic laminates of different carbon-epoxy systems (table 9.3). As can be observed, the correlation between the predictions of Trace and from CLT is remarkable. It is important to stress that whereas CLT requires the knowledge of four

[1] Tsai and Melo [55] noted that for glass-fibre reinforced polymers (GFRPs) the agreement between the Trace-normalised stiffness properties is not satisfactorily good, mostly because the transverse and shear properties correspond to larger fractions of the corresponding values of Trace when compared with CFRPs. This is attributed to the role played by the matrix and by the lower fibre volume fractions typical of GFRPs.

Table 9.1
Trace-normalised plane stress stiffness components of the carbon Master Ply.

Q^*_{11}	Q^*_{22}	Q^*_{12}	Q^*_{66}
0.8815	0.0499	0.0164	0.0342

Universal laminate factors

	$E_x{}^0/Tr$	$E_y{}^0/Tr$	$G_{xy}{}^0/Tr$	$\nu_{xy}{}^0$
Master Ply	0.880	0.052	0.031	0.320
[0/90]	0.468	0.468	0.031	0.036
[π/4]	0.336	0.336	0.129	0.308
[0_7/±45/90]	0.662	0.175	0.070	0.310
[0_5/±45_2/90]	0.518	0.208	0.109	0.423
[0_2/±45/90]	0.445	0.289	0.109	0.308
[0/±45_4/90]	0.217	0.217	0.187	0.552
[0/±45]	0.370	0.155	0.161	0.734
[0/±45/0]	0.499	0.141	0.129	0.701
[0/±30]	0.510	0.074	0.129	1.220
[0/±30/0]	0.611	0.072	0.104	1.079
[±12.5]	0.764	0.053	0.066	0.913

Fig. 9.1. Universal laminate factors obtained from the Master Ply using CLT (after Tsai and Melo [386]).

ply elastic properties (E_{11}, E_{22}, G_{12} and ν_{12}), which need to be measured from different coupons (including the complex, highly nonlinear in-plane shear test), the elastic properties of multidirectional laminates predicted using Trace were obtained from the universal laminate factors for the [π/4] laminate (figure 9.1) and from the value of Trace (table 9.3), calculated from the longitudinal stiffness of the UD lamina (E_{11}) using the Master Ply concept. Characterisation of the elastic properties of composite laminates using Trace requires just one test on a 0° coupon, simplifying considerably the number and complexity of the tests needed to be performed, for instance, in material scrutiny programmes.

Figures 9.2 and 9.3 show a comparison between the experimental data obtained from the unnotched tension tests in chapters 4 and 5, respectively, and the predictions of Trace theory. Table 9.4 shows the ply properties of T700GC/M21 carbon/epoxy and the corresponding value of Trace. These properties were determined from in-plane tensile tests on 0° laminae of a *prepreg* with an areal weight of 268 g/m^2 (cured ply thickness of 0.262 mm) [88]. Nevertheless, as stressed in chapter 4, the effect of ply areal weight on the basic UD properties of composite materials is negligible (except on the longitudinal compressive strength, attributed to the more uniform microstructure of spread tows) [58].

The correlation between the elastic responses obtained experimentally and predicted using Trace theory are, once again, remarkable. It is noted, though, that the multidirectional laminate built with 240 g/m^2 spread-tow fabrics (STFs) exhibits a nonlinear behaviour (figure 9.2b), which naturally cannot be captured by Trace, which is an elastic property. It is also noted that whereas the STFs tested in chapter 4 were made of T700SC fibres, the elastic properties in table 9.4 were obtained from *prepregs* with T700GC fibres, which use a different sizing. Nevertheless, the effect of fibre sizing on the elastic properties should be negligible.

9.3. Omni Strain Failure Envelope and Unit Circle

9.3.1. Overview

Tsai and Melo [55] also proposed an invariant-based approach to failure, with the aim to define a strength property independent of laminate lay-up composition. Using a failure criterion based on a tensor polynomial in strain space, Tsai and Melo [55] defined an *Omni Strain Failure Envelope* for a laminate with many ply orientations by selecting the controlling ply in each orientation of the strain space.

It is noted that, in the case of composite materials, the use of strain space for the representation of failure envelopes is preferred over stress space because in strain space failure envelopes are invariant [55], i.e. their shapes are independent

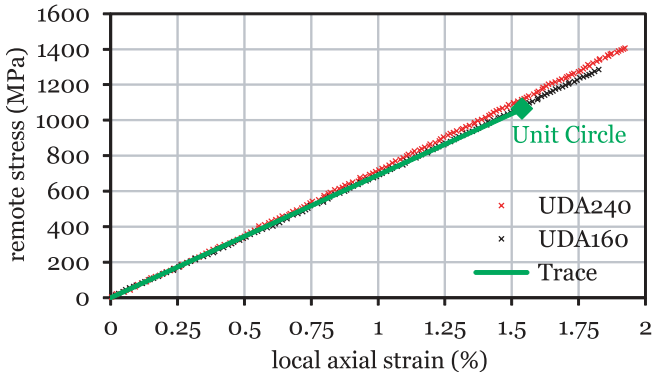

(a) Cross-ply laminate.

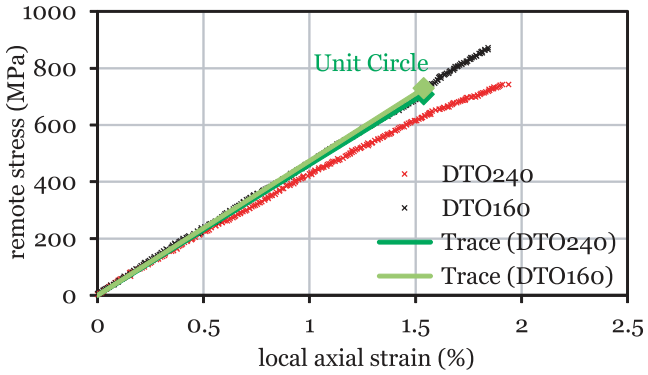

(b) Multidirectional laminate.

Fig. 9.2. Comparison between the experimental data obtained from unnotched tensile testing on spread-tow fabric T700SC/M21 carbon/epoxy laminates (chapter 4) and the elastic response and strength predictions of Trace theory and Unit Circle failure criterion.

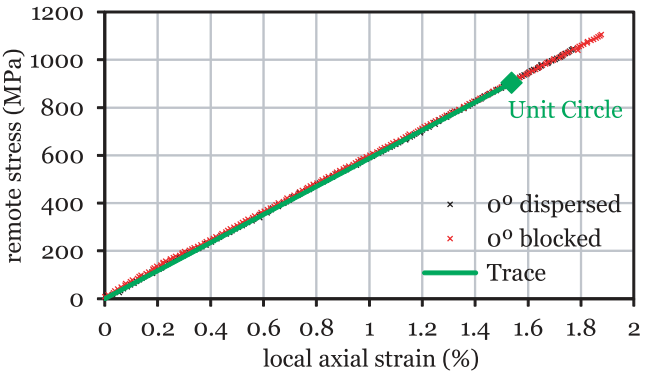

Fig. 9.3. Comparison between the experimental data obtained from unnotched tensile testing on multidirectional non-crimp fabric thin-ply T700GC/M21 carbon/epoxy laminates (chapter 5) and the elastic response and strength predictions of Trace theory and Unit Circle failure criterion.

Table 9.2
Predictions of the elastic properties of quasi-isotropic laminates of different carbon-epoxy systems using CLT and Trace, and relative errors (ϵ_r).

Elastic properties		IM7/8552			T800/M21		
		CLT	Trace	ϵ_r (%)	CLT	Trace	ϵ_r (%)
E_x	(MPa)	64513	65451	1.5	64401	65673	2.0
E_y	(MPa)	64513	65451	1.5	64401	65673	2.0
G_{xy}	(MPa)	24600	25129	2.1	24517	25214	2.8
ν_{xy}	(-)	0.311	0.308	−1.0	0.313	0.308	−1.7
		T700/AR2527			M40JB/ThinPreg 80EP/CF		
		CLT	Trace	ϵ_r (%)	CLT	Trace	ϵ_r (%)
E_x	(MPa)	42572	42000	−1.3	80197	84764	5.7
E_y	(MPa)	42572	42000	−1.3	80197	84764	5.7
G_{xy}	(MPa)	16306	16125	−1.1	30494	32543	6.7
ν_{xy}	(-)	0.305	0.308	0.8	0.315	0.308	−2.2

Table 9.3
Ply properties and value of Trace for different carbon-epoxy systems.

Material system	E_{11} (MPa)	E_{22} (MPa)	G_{12} (MPa)	ν_{12} (-)	X_T (MPa)	X_C (MPa)	Trace (MPa)
IM7/8552 [169, 171, 183]	171420	9080	5290	0.320	2410	1690	194795
T800/M21 [206]	172000	8900	5000	0.320	3039	1669	195455
T700/AR2527 [122]	110000	7400	4200	0.300	2300	1500	125000
M40JB/ThinPreg 80EP/CF [58]	222000	7010	4661	0.314	2250	1052	252273

of the presence of other plies. Superimposing the envelopes of the constituent plies forms the failure envelope for a given laminate. Hence, an inner envelope that covers all controlling plies, or Omni Strain Failure Envelope, essentially defines a material property that is independent of laminate lay-up configuration, representing any laminate constructed from a given material [55]. Even though this is a conservative approach, it greatly simplifies laminate failure prediction by avoiding ply-by-ply failure analysis.

The Omni Strain Failure Envelope for a given composite material is determined from the ply elastic (E_x, E_y, G_{xy} and ν_{xy}) and strength properties (X_T, X_C, Y_T, Y_C and S_L) [55]. Moreover, Omni Strain Failure Envelopes (figure 9.4) can be generated either from first-ply failure (FPF) analysis [55], using intact ply properties, or from last-ply failure (LPF) analysis [386, 387], using degraded ply properties.

Tsai and Melo [387] found that the LPF Omni Strain Failure Envelopes of CFRPs are invariably controlled by the 0° and 90° plies (figure 9.4). Hence, the longitudinal tensile and compressive strains-to-failure (ε_{1T} and ε_{1C} respectively) define the tensile and compressive anchor points in the axes of the principal strain space (figure 9.5).

To make laminate failure analysis simpler, the LPF Omni Strain Failure Envelope can be approximated by a *Unit Circle* in the *normalised principal strain space* using the uniaxial tensile and compressive failure strains as normalising factors (figure 9.5) [387]. The Unit Circle failure envelope is inscribed in the LPF Omni Strain Failure Envelope [387], resulting in a more conservative approach. However, whereas Omni Strain Failure Envelopes require complete ply characterisation, based on the Unit Circle, a laminate failure envelope can be generated from the longitudinal tensile and compressive strains-to-failure of an UD ply. Hence, ply characterisation can be reduced from several tests on different lamina configurations to just two tests of a 0° coupon: longitudinal tension and longitudinal compression. The potential gains in terms of test complexity, time and cost reductions are outstanding.

Tsai and Melo [387] also showed that the Unit Circle failure criterion is applicable to cold-dry and hot-wet environmental conditions. In this case, the 0° coupon must be tested after exposure to the corresponding conditions, and the resulting anchor points used to define the cold-dry/hot-wet Unit Circle failure envelope.

Table 9.4
0° ply properties of T700GC/M21 carbon-epoxy and respective values of Trace [88].

E_{11} (MPa)	X_T (MPa)	Trace (MPa)
130000	2000	147727

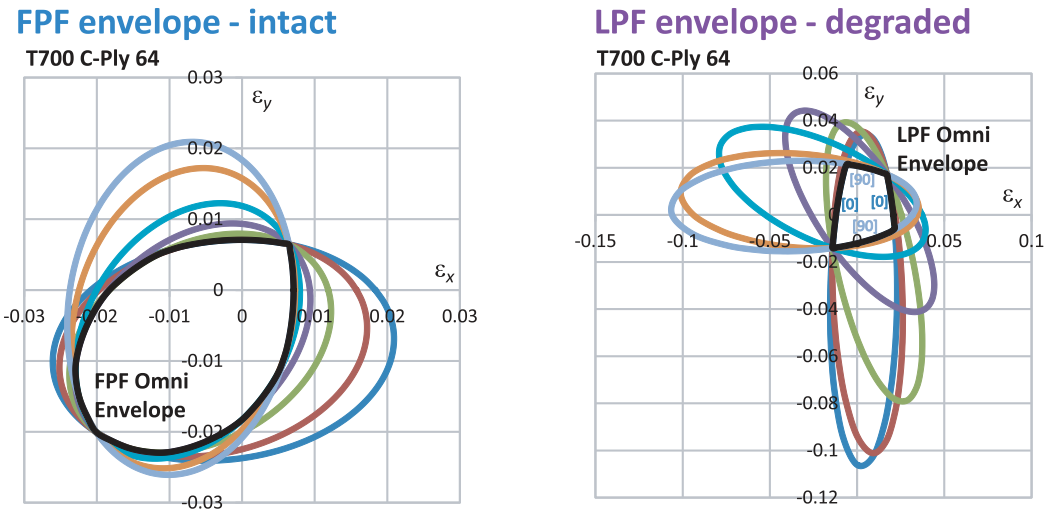

Fig. 9.4. FPF (intact) and LPF (degraded) Omni Strain Failure Envelopes for T700 C-Ply 64 CFRP, obtained using the Tsai-Wu failure criterion (interaction term $F^*_{xy} = -1/2$) in strain space (after Tsai and Melo [386, 387]). In the LPF analysis, property degradation was only applied to the matrix-dominated elastic properties (E_y, G_{xy} and ν_{xy}), to the longitudinal compressive strength (X_C) due to loss of shear modulus, and to the interaction term (F^*_{xy}), using a matrix degradation factor of 0.15.

9.3.2. Analysis and predictions

Table 9.5 shows a comparison between the failure predictions (X^L_T and X^L_C) obtained with the Unit Circle failure criterion and the experimental results reported in the literature for quasi-isotropic laminates of different carbon-epoxy systems. To generate these predictions, only the stiffness (E_{11}) and the tensile and compressive strengths (X_T and X_C respectively) of the 0° lamina were used (table 9.3).

In general, the failure predictions are reasonably accurate (only the T800/M21 laminate compressive strength was largely over-predicted compared with the experiments [121]). In fact, it is interesting to note that the laminates exhibiting the higher level of homogeneity, i.e. the laminates with a larger number of sublaminate repetitions, IM7/8552 (8 and 16 sublaminate repetitions for tension and compression, respectively) [169, 171] and M40JB/ThinPreg 80EP/CF (20 sublaminate repetitions) [58], provided the results closest to the Unit Circle failure criterion, with relative errors below 2%.

Figures 9.2 and 9.3 also show a comparison between the experimental data obtained from the unnotched tension tests in chapters 4 and 5, respectively, and the failure predictions of the Unit Circle failure criterion. These predictions were obtained from the 0° ply properties of an UD T700GC/M21 carbon-epoxy *prepreg* of a different grade and, in some cases, with a different fibre sizing, tested elsewhere [88] (table 9.4). As can be observed, the Unit Circle failure criterion systematically underpredicted the failure stress of the unnotched cross-ply and multidirectional laminates. However, fibre sizing, ply thickness and reinforcement structure are all known to affect the strengths of laminates; therefore, these results may be interpreted as a preliminary assessment, and no definite conclusions can be drawn at this stage.

9.4. Sizing of homogenised laminates based on Trace

Tsai et al. [385] used a Trace-based scaling approach to study the optimal design of beams made of homogenised composite laminates, and compare directly the optimal solutions between isotropic materials and composite laminates

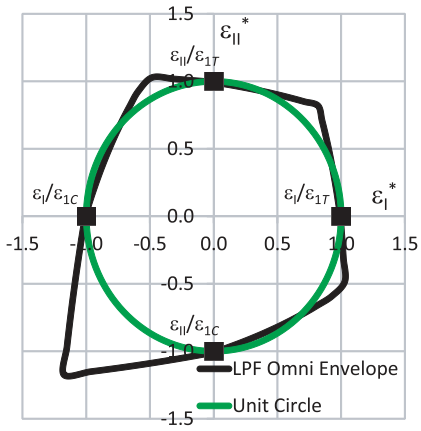

Fig. 9.5. LPF Omni Strain Failure Envelope for T700 C-Ply 64 CFRP and Unit Circle failure criterion in normalised principal strain space (after Tsai and Melo [387]).

Table 9.5
Failure predictions of quasi-isotropic laminates of different carbon-epoxy systems using the Unit Circle failure criterion, and comparison with experimental results from the literature. The relative errors (ϵ_r) between predictions and experiments are also shown.

Laminate strengths		IM7/8552 [169, 171]			T800/M21 [121]		
		Experiments	Unit Circle	ϵ_r (%)	Experiments	Unit Circle	ϵ_r (%)
X_T^L	(MPa)	929	920	−0.9	1054	1160	10.1
X_C^L	(MPa)	644	645	0.2	539	637	18.3
		T700/AR2527 [122]			M40JB/ThinPreg 80EP/CF [58]		
		Experiments	Unit Circle	ϵ_r (%)	Experiments	Unit Circle	ϵ_r (%)
X_T^L	(MPa)	800	878	9.7	847	859	1.4
X_C^L	(MPa)	540	573	6.0	-	402	-

in terms of weight savings. Using the proposed Trace-based scaling approach, Tsai et al. [385] performed thickness optimisation of tapered beams for minimum weight. After finding the optimal profile, which can be determined from any homogeneous material, whether it is isotropic or orthotropic, Trace-based scaling was applied to other material and laminate combinations without the need for recalculation. Tsai et al. [385] noted that this straightforward, yet highly accurate, process is only possible for the homogenised laminates, and could not be applicable if the composite laminates were heterogeneous. Tsai et al. [385] also noted that, whereas material scaling based on Trace is always possible, laminate scaling for the same material is only applicable in cases where there is one determinant loading axis, such as in slender beams, and scaling based on the laminate factor $E_x^* = E_x/Tr$ (figure 9.1) can be performed; in the case of biaxial loading, the full stiffness matrix is required, making scaling not trivial.

However, the Trace-based scaling approach proposed in Ref. [385] was limited to stiffness-driven design requirements, which were analysed using Trace theory. Moreover, the only focus was on weight optimisation, with no references to manufacturing. Hence, more recently, Tsai et al. [388] proposed a direct sizing method based on Trace of the plane stress stiffness matrix and based on the Unit Circle failure criterion for weight and lay-up speed optimisation. According to the proposed method, the tapering profile of a homogenised composite panel subjected to in-plane loading is first determined for a baseline material from the strength-driven criterion based on the upper-bound value of the failure index. Due to its simplicity, and because it is scalable, the Unit Circle failure criterion was used. Multiple load cases can be dealt with. The structural component can then be scaled linearly to meet the stiffness requirements that include deformation, deflection, natural frequency or buckling. If the boundary-value problem is statically determinate, direct strength- and stiffness-scaling provide an optimum profile that meets both strength- and stiffness-driven design requirements without the need for an iterative procedure. Lay-up optimisation is, therefore, very simple and very fast. Material selection by Trace-based scaling is the last step in the sizing method, as in Ref. [385].

Tsai et al. [388], for higher efficiency in laminate design, suggested the use of bi-angle and tri-angle tapes as repeated sub-laminates to reach homogeneity. In addition to the manufacturing advantages, due to faster lay-up along only the 0° and 90° axes, tapering also becomes greatly simplified. To decide for the optimum design, both weight reductions over an aluminium design and lay-up speed improvements over the traditional 4-axis lay-up were considered. Even though intrinsically conservative, due to the use of the Unit Circle failure criterion (section 9.3.1), the approach proposed by Tsai et al. [388] is conceptually simple, easy to implement and not material specific.

9.5. Concluding remarks

The invariant-based approaches to stiffness and strength have demonstrated their value as simplifying methodologies to laminate design. Using Trace theory and the Master Ply concept to determine the elastic properties of multidirectional laminates from the longitudinal ply stiffness component, and using the Omni Strain Failure Envelope or, more specifically, the Unit Circle failure criterion to predict LPF of multidirectional laminates from the strengths of the 0° ply only makes material screening similar to that of metals, since only 0° coupons need to be tested in tension and compression. Moreover, laminate design becomes substantially simpler, as the invariant-based approaches to stiffness and strength provide more efficient and straightforward computations of the mechanical and failure response of composite laminates.

However, full applicability of these concepts is only guaranteed to applications on homogenised laminates. As stressed by Tsai et al. [388], the virtues of laminate homogenisation for simpler and faster design procedures, in particular through the use of thin plies, which make laminate homogenisation possible even for the thin laminates currently used in the airframe construction, must be embraced by designers so all benefits from the superior specific properties of advanced composites can keep improving the performance of high-end applications.

Chapter 10

Failure prediction of notched laminates

The residual strength of composite laminates with large through-the-thickness cracks is a topic of great interest in the aeronautical field, namely because tests on large panels with discrete sources of damage are generally used not only for design, but also for certification purposes. Experiments show that composite laminates exhibit high resistance to propagation of large cracks and a remarked crack-bridging effect. In this chapter, analysis methods based on simple solutions formulated at the homogenised laminate level are used to predict the notched response of composite laminates. Even though existing models predict with reasonable accuracy the notched response of small coupons, they are not able to capture the bridging processes that occur in the presence of large through-the-thickness cracks. Consequently, Large Damage Capability is systematically underestimated by traditional analysis methods. By taking into account the crack resistance curve of the material in a recently proposed Finite Fracture Mechanics model, it is expected that good predictions of the notched response of laminated plates with large through-penetration damage can be obtained using only independently measured material properties and without requiring fitting parameters or complex Finite Element Analyses.

10.1. Introduction

In spite of today's large scale application of composite materials, the understanding about the mechanical response of composite laminates subjected to large through-penetration damage is still limited, despite previous efforts in identifying the critical material and laminate variables and in evaluating failure criteria [20, 25]. In fact, due to the interest of the aeronautical industry, several analytical models have been developed to analyse large through-penetration damage of composites under tensile loading, a structural characteristic usually designated as *Large Damage Capability* (LDC) or *Large-Notch Capability* [25]. However, it is well known that the tensile residual strength of composite laminates in the presence of through-the-thickness notches is significantly affected by size [25]. Nonetheless, most studies in the literature addressing the notched response of composite laminates (e.g. Refs. [121, 122, 144, 163, 169, 170, 172–174, 184]) are restricted to the notched response of small scale samples, with only a few studies addressing LDC [20, 166, 182, 195].

In general, it is possible to distinguish between *small-notch* and *large-notch* strengths. The analysis methods should be able to capture and predict these distinct material behaviours, providing failure predictions beyond the notch sizes and structural geometries tested during material screening, which are typically based on small scale coupons [20].

To ensure this extrapolation capability, suitable models must be based on the actual physics of the problem [20]. Additionally, it is desirable to minimise the number of material properties required for the analysis models to reduce the material testing requirements [20, 25].

However, existing analytical models, such as the Inherent Flaw Model (IFM) [175] and the Point-Stress (PS) and Average-Stress (AS) models [176], use empirical "*characteristic distances*" that, in practice, are determined from notched strength data. They are often thought as correction factors that account for apparent changes in the stress distribution or

in the fracture toughness with increasing crack size, with limited physical meaning [20]. Although analysis models that include characteristic distances are better at predicting small crack experimental trends than classical Linear Elastic Fracture Mechanics (LEFM) models, they all fail to describe the notch response of composite laminates with large through-penetration damage [20], typically yielding conservative estimates [25].

An alternative approach is the Mar-Lin model [389], which is based on the assumption that the stress distribution at the crack tip of inhomogeneous materials, such as laminated composites, may not be limited to the square-root singularity. This model captures the reduced sensitivity of composite materials to large changes in notch size by allowing the singularity, n, to be other than the square-root (as in LEFM). This model was successfully used to predict LDC from smaller notch data, avoiding excessive conservatism. However, the exponent n is an additional empirical parameter that also needs to be experimentally determined (typically by curve-fitting). In addition, a precise, verified method for determining the appropriate singularity value in the absence of large notch data has not been developed. In fact, caution should be exercised in selecting exponents for extrapolation, since it is possible to select values that over-predict LDC (unconservative results). In general, verification tests should be conducted with sufficiently large notch lengths, or, in the absence of LDC data, a conservative selection of the exponent must be adopted to avoid potential design problems [25].

The objective of this chapter is to assess the validity of traditional analysis methods in predicting the notched response of carbon fibre-reinforced polymer (CFRP) laminates, including coupons with large through-the-thickness cracks. The Finite Fracture Mechanics (FFMs) model, recently proposed to predict the notched response of laminates with open-holes [179], is extended to address the notched response of centre-notched plates in tension, and it is used, together with the classical LEFM model, the IFM [175] and the PS and AS models [176], in the analysis of hole size effects and LDC of composite laminates. The Mar-Lin model [389] is not addressed in this work because it requires extensive experimental testing in centre-cracked plates to obtain all necessary parameters. The LDC analysis results are compared against experimental data obtained from comprehensive test campaigns.

10.2. Review of analysis methods

10.2.1. Classical Linear Elastic Fracture Mechanics (LEFM) model

The LEFM model is the classical method of predicting the residual strength of homogeneous materials, and therefore it can be applied to the analysis of LDC. Assuming that a through-the-thickness crack of length $2a$ exists, for classical continuum theories, the stress distribution at the crack tip is singular. In LEFM, a square-root singularity is assumed, and the residual strength $\bar{\sigma}^{\infty}$ is predicted as:

$$\bar{\sigma}^{\infty} = \frac{\mathcal{K}_{Ic}}{\sqrt{\pi a}} \tag{10.1}$$

where $\mathcal{K}_{Ic}$ is the critical Stress Intensity Factor (SIF), or fracture toughness, calculated from a specimen with a central crack. However, this approach suffers from the physically unacceptable situation of infinite stresses at the crack tip, and the residual strength increases rapidly with decreasing a. At the limit, as $a \to 0$, $\bar{\sigma}^{\infty} \to \infty$.

In order to account for finite-width and material orthotropy effects, correction factors have to be included in equation (10.1). According to the orthotropy rescaling technique [269, 270], the SIF $\mathcal{K}_I(a)$ for a centre-cracked plate can be written as:

$$\mathcal{K}_I(a) = \chi(\rho)\, Y(2a/W)\, \sigma^{\infty} \sqrt{\pi a} \tag{10.2}$$

where $\chi(\rho)$ is the correction factor for the orthotropy of the material and $Y(2a/W)$ is the finite-width correction (FWC) factor. Following the orthotropy rescaling technique [269, 270], the geometry dependence, $Y(2a/W)$, is the same of that of an isotropic material. The simple FWC factor proposed by Chen et al. [286] is used in this work. This FWC factor

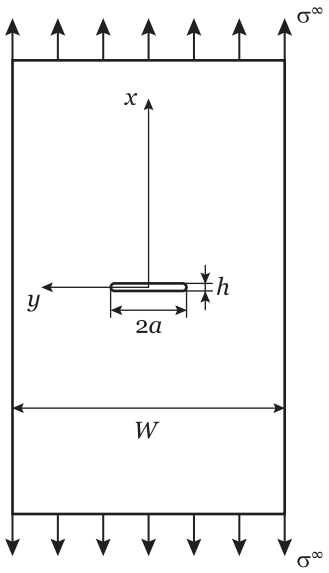

Fig. 10.1. Centre-notched plate.

was derived imposing equilibrium between the remotely applied stress and the stress in the elastic material, and it is given as [286]:

$$Y(2a/W) = \frac{1}{\sqrt{1 - \left(\frac{2a}{W}\right)^2}} \tag{10.3}$$

where W is the plate width. The orthotropy dependence $\chi(\rho)$ (equation (5.3)) is expressed as a single function of a dimensionless elastic parameter ρ (equation (4.7)), in which E_x and E_y are the Young's moduli, G_{xy} the shear modulus, and ν_{xy} and ν_{yx} the Poisson's ratios in the respective preferred axes, as shown in figure 10.1.

As reported in Ref. [270], equations (10.2) and (5.3) are only valid for materials with $0 \leq \rho \leq 4$. As discussed in Ref. [65], for highly orthotropic materials, with $\rho > 4$ (which is typically the case of cross-ply laminates, for example), a new correction factor for equation (10.2), κ, which takes into account both geometry and orthotropy dependence, should be determined. Nevertheless, it is noted that, in general, multidirectional laminates typically used in airframe construction fall in the range $0 \leq \rho \leq 4$.

For the general case, taking both geometry (Y) and orthotropy (χ) correction factors, $\bar{\sigma}^{\infty}$ is now predicted by the LEFM model as:

$$\bar{\sigma}^{\infty} = \frac{\mathcal{K}_{Ic}}{\chi Y \sqrt{\pi a}} \tag{10.4}$$

10.2.2. Inherent Flaw Model (IFM)

In order to address the physically unacceptable situation of infinite stresses at the crack tip predicted by LEFM models, several theories, which generally rely on a characteristic distance, were proposed. One of these theories is the IFM. It was originally developed by Waddoups et al. [175] to predict the residual strength of notched or centre-cracked laminates with infinite widths under tensile loads, and extended to finite widths by introducing a finite-width correction factor [390]. The IFM is based on LEFM; it assumes that a composite laminate containing a notch is analogous to a crack in an isotropic material. According to this model, the noncritical damage mechanisms can be lumped into a constant "*intense energy*

region", or "*inherent flaw*", of length a_0 [175]. Approximating the central notch of length $2a$ by a through-the-thickness crack, the SIF is given by equation (10.2). For a quasi-isotropic laminate ($\rho = 1.0$ and $\chi = 1.0$), assuming that an inherent flaw exists at each notch tip, at failure, the fracture toughness is given as:

$$\mathcal{K}_{Ic} = \frac{\bar{\sigma}^{\infty}\sqrt{\pi(a+a_0)}}{\sqrt{1-\left[\frac{2(a+a_0)}{W}\right]^2}} \tag{10.5}$$

Assuming that the fracture toughness of an unnotched specimen can be predicted by letting the notch length tend to zero, i.e.:

$$\mathcal{K}_{Ic} = \frac{X_T^L\sqrt{\pi a_0}}{\sqrt{1-\left(\frac{2a_0}{W}\right)^2}} \tag{10.6}$$

where X_T^L is the laminate tensile unnotched strength, combining equations (10.5) and (10.6) results in:

$$\bar{\sigma}^{\infty} = X_T^L\sqrt{\frac{a_0}{a+a_0}}\sqrt{\frac{1-\left[\frac{2(a+a_0)}{W}\right]^2}{1-\left(\frac{2a_0}{W}\right)^2}} \tag{10.7}$$

Accordingly, the strength of a notched laminate is predicted using two parameters, the length of the inherent flaw, a_0, that needs to be calculated from a baseline specimen, and the unnotched tensile strength of the laminate, X_T^L. It is noted that, unlike Aronsson and Bäcklund [390], a FWC factor is used in equation (10.6) to calculate the critical SIF when the notch length tends to zero.

Although this is a simple approach, since it does not require complex Finite Element (FE) implementations, the IFM only provides reasonable predictions for specimens with geometries close to that used to calibrate the model [183]. Moreover, the IFM is only applicable to quasi-isotropic laminates, since it is formulated assuming that a composite laminate containing a notch is analogous to a crack in an isotropic material.

10.2.3. Point-Stress (PS) and Average-Stress (AS) models

The residual strength of homogeneous materials can also be determined using stress-based criteria, such as the PS and AS models proposed by Whitney and Nuismer [176]. These models predict failure when the stress at a given distance (PS model) or the stress averaged over a characteristic distance (AS model) reach the unnotched strength of the laminate. Considering the coordinate axes shown in figure 10.1, the PS and AS models can be written respectively as:

$$\sigma_{xx}(0,y)|_{y=a+r_{ot}} = X_T^L \tag{10.8}$$

$$\frac{1}{r_{ot}}\int_a^{a+r_{ot}}\sigma_{xx}(0,y)\,\mathrm{d}y = X_T^L \tag{10.9}$$

Hence, each model requires that the unnotched laminate strength X_T^L and a characteristic distance r_{ot} (without any physical relation between them) must be determined from an unnotched and from a notched specimen, respectively. The characteristic distances r_{ot} are not material properties, and need to be identified every time the material/lay-up or the geometry are modified. Therefore, a large amount of empirical data from expensive experimental programmes to account for the different geometries and lay-ups that are typically used in the aerospace and aeronautical industries is required.

Approximating the centre notch by an elliptical opening of major axes ($2a$) equal to the notch length, and minor axes ($2b$) such that the ellipse's curvature in the major axis is equal to the notch tip radius, as proposed in Ref. [135], and assuming that the normal stress profile of a finite plate, $\sigma_{xx}(0,y)$, is identical to that of an infinite plate, $\sigma_{xx}^{\infty}(0,y)$, except for an FWC factor, the longitudinal stress distribution along the y-axis is given as [258]:

$$\sigma_{xx}(0,y) = \frac{K_T}{K_T^{\infty}}\sigma_{xx}^{\infty}(0,y) \tag{10.10}$$

with:

$$\begin{aligned}\frac{\sigma_{xx}^{\infty}(0,y)}{\sigma^{\infty}} = &\frac{\lambda^2}{(1-\lambda)^2} + \frac{(1-2\lambda)\gamma}{(1-\lambda)^2\sqrt{\gamma^2-1+\lambda^2}} + \frac{\lambda^2\gamma}{(1-\lambda)\left(\gamma^2-1+\lambda^2\right)^{\frac{3}{2}}} - \\ &-\frac{\lambda^7}{2}\left(K_T^{\infty}-1-\frac{2}{\lambda}\right)\left[\frac{5\gamma}{\left(\gamma^2-1+\lambda^2\right)^{\frac{7}{2}}}\frac{7\lambda^2\gamma}{\left(\gamma^2-1+\lambda^2\right)^{\frac{9}{2}}}\right]\end{aligned} \tag{10.11}$$

where σ^{∞} is the applied remote stress, K_T^{∞} and K_T are, respectively, the stress concentration factors at the edge on the axis normal to the applied load of the centre elliptical notch of an infinite orthotropic plate and a finite orthotropic plate, given as [258]:

$$K_T^{\infty} = 1 + \frac{1}{\lambda}\sqrt{2\left(\sqrt{\frac{E_x}{E_y}} - \nu_{xy}\right) + \frac{E_x}{G_{xy}}} \tag{10.12}$$

$$\begin{aligned}\frac{K_T^{\infty}}{K_T} = &\frac{\lambda^2}{(1-\lambda)^2} + \frac{1-2\lambda}{(1-\lambda)^2}\sqrt{1+\left(\lambda^2-1\right)(2a/W)^2} - \\ &-\frac{\lambda^2}{(1-\lambda)^2}\frac{(2a/W)^2}{\sqrt{1+\left(\lambda^2-1\right)(2a/W)^2}} + \\ &+\frac{\lambda^7}{2}\left(\frac{2a}{W}\right)^6\left(K_T^{\infty}-1-\frac{2}{\lambda}\right)\left\{\left[1+\left(\lambda^2-1\right)\left(\frac{2a}{W}\right)^2\right]^{-\frac{5}{2}} - \right. \\ &\left.-\left(\frac{2a}{W}\right)^2\left[1+\left(\lambda^2-1\right)\left(\frac{2a}{W}\right)^2\right]^{-\frac{7}{2}}\right\}\end{aligned} \tag{10.13}$$

and:

$$\lambda = \frac{b}{a} \tag{10.14}$$

$$\gamma = \frac{y}{a} \tag{10.15}$$

For quasi-isotropic laminates, $K_T^{\infty} = 1 + 2/\lambda$, and equations (10.13) and (10.11) are considerably simplified. Using equations (10.10) to (10.13) in equations (10.8) and (10.9), the PS and AS failure models for a centre-notched laminate read, respectively [258]:

$$\frac{\bar{\sigma}^{\infty}}{X_T^L} = \frac{K_T^{\infty}}{K_T}\left\{\frac{\lambda^2}{(1-\lambda^2)} + \frac{(1-2\lambda)\xi_1^{-1}}{(1-\lambda)^2\sqrt{\xi_1^{-2}-1+\lambda^2}} + \frac{\lambda^2\xi_1^{-1}}{(1-\lambda)\left(\xi_1^{-2}-1+\lambda^2\right)^{3/2}} - \right.$$
$$\left. -\frac{\lambda^7}{2}\left(K_T^{\infty}-1-\frac{2}{\lambda}\right)\left[\frac{5\xi_1^{-1}}{\left(\xi_1^{-2}-1+\lambda^2\right)^{7/2}} - \frac{7\lambda^2\xi_1^{-1}}{\left(\xi_1^{-2}-1+\lambda^2\right)^{9/2}}\right]\right\}^{-1} \tag{10.16}$$

$$\frac{\bar{\sigma}^{\infty}}{X_T^L} = \frac{K_T^{\infty}}{K_T}\left(\xi_2^{-1}-1\right)\left\{\frac{\lambda^2}{(1-\lambda^2)}\xi_2^{-1} + \frac{1-2\lambda}{(1-\lambda)^2}\sqrt{\xi_2^{-2}-1+\lambda^2} - \frac{\lambda^2}{(1-\lambda)\sqrt{\xi_2^{-2}-1+\lambda^2}} + \right.$$
$$\left. +\frac{\lambda^7}{2}\left(K_T^{\infty}-1-\frac{2}{\lambda}\right)\left[\left(\xi_2^{-2}-1+\lambda^2\right)^{-5/2} - \lambda^2\left(\xi_2^{-2}-1+\lambda^2\right)^{-7/2}\right]\right\}^{-1} \tag{10.17}$$

where ξ_1 and ξ_2 are given as [258]:

$$\xi_1 = \xi_2 = \frac{a}{a+r_{ot}} \tag{10.18}$$

10.3. Finite Fracture Mechanics model

10.3.1. Model overview and predictions

A new model based on FFMs was proposed by Camanho et al. [179] to predict the open-hole tensile strength of composite laminates. Failure is predicted when both stress-based and energy-based criteria are satisfied. This model is based on an analytical solution, and no empirical adjusting parameters are required, but only the ply elastic properties, the laminate unnotched strength (X_T^L) and the laminate fracture toughness ($\mathcal{K}_{Ic}$). Camanho et al. [179] and Arteiro et al. [135] showed that the model predictions are very accurate, resulting in improvements over the traditional strength prediction methods. The FFMs model was also used to assess the notch sensitivity and brittleness of composite laminates by means of versatile design charts and by the identification of a dimensionless parameter designated *notch sensitivity factor* [135, 179].

According to the coupled FFMs model [179], failure in an open-hole specimen occurs when the following system os equations is satisfied:

$$\begin{cases} \frac{1}{l}\int_R^{R+l}\sigma_{xx}(0,y)\mathrm{d}y = X_T^L \\ \frac{1}{l}\int_R^{R+l}\mathcal{K}_I^2(a)\mathrm{d}a = \mathcal{K}_{Ic}^2 \end{cases} \tag{10.19}$$

where R is the hole radius, $\sigma_{xx}(y,0)$ is the stress distribution along the y-axis, perpendicular to the loading direction, $\mathcal{K}_I(a)$ is the mode I SIF, and l is the crack extension at failure.

To verify the accuracy of the FFMs model to predict the notched response of thin-ply laminates, the experimental data obtained in chapter 3 for the hole size effect of quasi-isotropic laminates built of 0.03 mm thick and 0.10 mm thick plies (*THIN* and *INTERMEDIATE* laminates, respectively), which exhibited fibre-dominated failure modes, is compared with the results of the analytical model. It is noted that, for the laminates with thicker plies (*THICK* and *THICK - PLY LEVEL* laminates), which exhibited a matrix-dominated failure mode, an inverse hole size effect was observed, rendering the FFMs model unapplicable. In fact, the analysis of laminates exhibiting predominantly matrix-dominated failure requires complex nonlinear FEA tools to accurately predict their notched response.

As stressed before, the FFMs model only needs two independently measured material properties, the laminate tensile unnotched strength and the mode I laminate fracture toughness. The former is obtained from an unnotched specimen (table 3.4), and the latter can be calculated from the centre-notched specimen tested in the experimental programme described in chapter 3 following the FFMs analysis proposed by Arteiro et al. [135]. Figure 10.2 shows the predictions of the FFMs model for the normalised notched strength, $\bar{\sigma}_N$, of the *THIN* and *INTERMEDIATE* laminates, for a hole diameter range between 1 mm and 30 mm (the width-to-hole diameter ratio is constant and equal to 6). The values of the laminate fracture toughness, $\mathcal{K}_{Ic}$, are also shown in figure 10.2.

For reference, the experimental results and respective relative errors are also shown in figure 10.2, as well as the predictions for a notch-sensitive material, whose normalised strength is a function of the stress concentration factor K_t ($\bar{\sigma}_N = 1/K_t$), and the predictions for a notch-insensitive material, whose normalised strength is a function of the geometry ($\bar{\sigma}_N = 1 - d/W$). For a quasi-isotropic laminate with a centrally located circular hole, the stress concentration factor K_t is calculated using equation (3.2).

Observing the results in figure 10.2, and comparing the FFMs predictions with the experimental results, it can be seen that, for these geometries, the FFMs model captures very well the experimentally observed size effect. For the *THIN* laminate, errors below 4% were obtained for the tested geometries (figure 10.2a), an accuracy comparable to that obtained with advanced nonlinear numerical models (e.g. Ref. [183]). The explanation for these good predictions lies in the intrinsic behaviour of this laminate. Because subcritical damage mechanisms such as matrix cracking and delamination are almost absent, unstable fracture propagates soon after an intralaminar fracture process zone (FPZ) has formed in the vicinity of the notch tip. Therefore, the simplifying assumptions of the analytical FFMs model are all met, resulting in a very accurate representation of the physical phenomenon.

In the case of the *INTERMEDIATE* laminate, because subcritical damage mechanisms have developed prior to ultimate failure, resulting in a pull-out failure mode, the accuracy of the predictions (figure 10.2b) is not as good as for the *THIN* laminate. Nevertheless, the size effect trend is well represented, with errors below 9% for the tested geometries. This accuracy is within the range acceptable for fast analysis tools [121, 135, 179, 391], useful for preliminary design and optimisation.

It is important to stress that, unlike alternative strength prediction models, only two parameters obtained from two independent tests were used to obtain the predictions shown in figure 10.2. No calibration from a baseline specimen with an open hole was performed.

It is also important to note that, as already discussed elsewhere [58, 135], the mechanical response of thin-ply laminates can be predicted with great accuracy using simple, analytical models. This is a clear advantage of this type of advanced composites, because preliminary design and optimisation of composite structures become more reliable and less time consuming than it is nowadays. In addition, employing physically-based tools such as the FFMs model reduces the number of tests required in the early stages of design and optimisation, resulting in lower costs associated with preliminary material and lay-up characterisation.

10.3.2. Analysis of centre-notched plates

10.3.2.1. Model description

In the present section, the coupled FFMs model proposed by Camanho et al. [179] for the prediction of the notched response of laminated composites with open-holes (equation 10.19), is extended to address the notched response of laminates with centre notches (figure 10.1). In this case, failure is predicted when the following system of equations is satisfied:

$$\begin{cases} \dfrac{1}{l}\displaystyle\int_a^{a+l} \sigma_{xx}(0,y)\,\mathrm{d}y = X_T^L \\ \dfrac{1}{l}\displaystyle\int_a^{a+l} \mathcal{K}_I^2(a)\,\mathrm{d}a = \mathcal{K}_{Ic}^2 \end{cases} \tag{10.20}$$

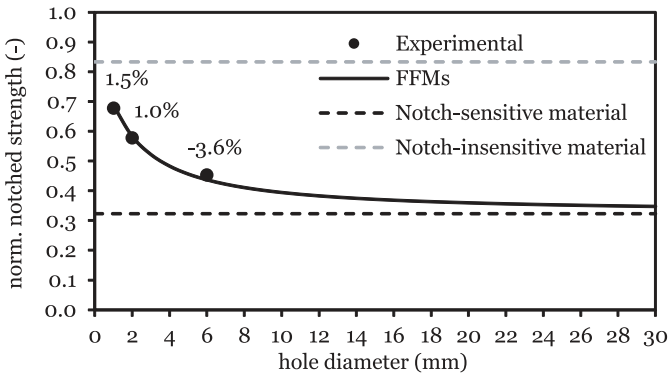

(a) *THIN* laminate ($\mathcal{K}_{Ic}$ = 35.7 MPa $\sqrt{\text{m}}$).

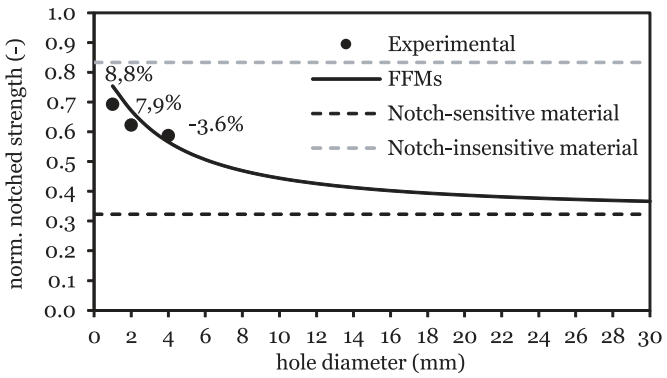

(b) *INTERMEDIATE* laminate ($\mathcal{K}_{Ic}$ = 49.4 MPa $\sqrt{\text{m}}$).

Fig. 10.2. FFMs predictions for the notched response of laminates exhibiting fibre-dominated failure modes.

where l is the crack extension at failure, $\sigma_{xx}(0, y)$ is the longitudinal stress distribution along the y-axis, X_T^L is the laminate tensile unnotched strength, $\mathcal{K}_I(a)$ is the mode I SIF, and $\mathcal{K}_{Ic}$ is the mode I laminate fracture toughness.

Approximating the central notch by an elliptical opening of major axes ($2a$) equal to the notch length, and minor axes ($2b$) such that the ellipse's curvature in the major axis is equal to the notch tip radius [135], the longitudinal stress distribution along the y-axis, $\sigma_{xx}(0, y)$, is given by equation (10.10). Integrating equation (10.10) and using it in the system of equations (10.20), the first member of the first equation reads [258]:

$$\frac{1}{l}\int_a^{a+l} \sigma_{xx}(0, y)\,\mathrm{d}y = \frac{K_T}{K_T^\infty}\sigma^\infty f_\sigma \tag{10.21}$$

with:

$$f_\sigma = \frac{1}{\xi^{-1}-1}\left\{\frac{\lambda^2}{(1-\lambda^2)}\xi^{-1} + \frac{1-2\lambda}{(1-\lambda)^2}\sqrt{\xi^{-2}-1+\lambda^2} - \frac{\lambda^2}{(1-\lambda)\sqrt{\xi^{-2}-1+\lambda^2}} + \right.$$
$$\left. + \frac{\lambda^7}{2}\left(K_T^\infty - 1 - \frac{2}{\lambda}\right)\left[\left(\xi^{-2}-1+\lambda^2\right)^{-5/2} - \lambda^2\left(\xi^{-2}-1+\lambda^2\right)^{-7/2}\right]\right\} \tag{10.22}$$

where σ^∞ is the applied remote stress, λ is the aspect ratio, given by equation (10.14), K_T^∞ is the stress concentration factor at the edge of the elliptical opening of an infinite plate, given by equation (10.12), K_T is the stress concentration factor at the edge of the elliptical opening of a plate of finite width, given by equation (10.13), and ξ is given as:

$$\xi = \frac{a}{a+l} \tag{10.23}$$

The SIF solution $\mathcal{K}_I(a)$ required to solve the energy-based criterion corresponds to a central notch that is extended by two cracks of finite dimension, which can be reasonably approximated by a plate with a centre crack. For an orthotropic plate, $\mathcal{K}_I(a)$ is given by equation (10.2). Replacing the SIF solution $\mathcal{K}_I(a)$ in the system of equations (10.20), the first member of the second equation reads:

$$\frac{1}{l}\int_a^{a+l} \mathcal{K}_I^2(a)\,\mathrm{d}a = (\sigma^\infty)^2\,\frac{\pi}{8}\chi^2\frac{W^2}{l}f_K \tag{10.24}$$

with:

$$f_K = \ln(W+2a) + \ln(W-2a) - \ln(W+2a+2l) - \ln(W-2a-2l) \tag{10.25}$$

Using equations (10.21) and (10.24) in (10.20), and dividing the second equation in (10.20) by the square of the first one yields:

$$\frac{\pi\chi^2 W^2 f_K}{8l\left(\dfrac{K_T}{K_T^\infty}\right)^2 f_\sigma^2} = \left(\frac{\mathcal{K}_{Ic}}{X_T^L}\right)^2 \tag{10.26}$$

which is a nonlinear equation with only one unknown, the crack extension at failure l. After solving equation (10.26) for l, the notched strength $\bar{\sigma}^\infty$ of a centre-notched laminate can be calculated using, for example, the first equation in (10.20), i.e.:

$$\bar{\sigma}^{\infty} = \frac{K_T^{\infty}}{K_T} f_{\sigma}^{-1} X_T^L \tag{10.27}$$

Equations (10.26) and (10.27) can be used to calculate the residual strength of centre-notched laminates with a variety of geometries using only two material properties: the unnotched strength X_L^T and the fracture toughness $\mathcal{K}_{Ic}$. The latter can be calculated by means of a FFMs analysis of a specimen with a centre notch using the same set of equations, as described in Ref. [135], or from a specimen with a different geometry. No characteristic distance calculated from a baseline specimen is necessary.

10.3.2.2. Large damage capability and crack resistance curve

Experimental characterisation of several composite materials and different lay-ups has shown that composite laminates exhibit a fracture resistance behaviour resembling a crack resistance curve ($\mathcal{R}$-curve) type of response, characterised by an increasing critical Energy Release Rate (ERR) with crack growth. This damage growth resistance has been attributed to (i) load redistribution resulting from microcracking, splitting and/or delamination, which relieve the stress concentration and delays fracture to higher applied loads [20, 182, 194–196], and (ii) bridging by the intact fibres of the plies that are adjacent to the principal load-carrying plies with broken fibres [194, 195].

Laminates characterised by a remarked $\mathcal{R}$-curve effect show a large, stable FPZ developing before final fracture. However, the analysis methods described in sections 10.2 and 10.3.2 assume that fracture occurs unstably, as a singular event, regardless of the crack length. For small cracks, this assumption is valid, because the FPZ develops just before final fracture (e.g. Ref. [122]), and the predictions typically yield good results. However, for large crack lengths, this assumption is no longer valid, and, from a macro-mechanical point of view, the bridging mechanisms that cause the development of a stable FPZ must be lumped into the crack tip in a physically admissible way, to take them into account in the macro-mechanical model. One possibility is to take into account the effect of the $\mathcal{R}$-curve in the analysis method. This was already done to predict net-tension failure of mechanically fastened joints in composite laminates using the FFMs model [181], and no other analysis method seems to be able to account for this effect.

The effect of the $\mathcal{R}$-curve in determining the crack length corresponding to unstable fracture of a centre-notched laminate can be taken into account using the FFMs model by rewriting the system of equations (10.20) as:

$$\begin{cases} \dfrac{1}{l}\displaystyle\int_a^{a+l} \sigma_{xx}(0,y)\,\mathrm{d}y = X_T^L \\ \displaystyle\int_a^{a+l} \mathcal{G}_I(a)\,\mathrm{d}a = \int_0^l \mathcal{R}(\Delta a)\,\mathrm{d}\Delta a \end{cases} \tag{10.28}$$

where $\mathcal{G}_I(a)$ is the mode I ERR and $\mathcal{R}(\Delta a)$ is the $\mathcal{R}$-curve, expressed in terms of a critical ERR, of the laminate. To simplify the implementation of the $\mathcal{R}$-curve in numerical or analytical models, Catalanotti et al. [65] used equation (4.21) to fit the $\mathcal{R}$-curve, where l_{fpz} is the length of the FPZ, $\mathcal{R}_{ss}$ is the steady-state value of the fracture toughness and ζ and η are two parameters obtained fitting the formula to the $\mathcal{R}$-curve.

Equation (4.21) can be used in the system of equations (10.28) to take into account the $\mathcal{R}$-curve of the laminate in the FFMs predictions. The first equation in (10.28) (stress equilibrium) is equal to the first equation of the system of equations (10.20), and no modifications are necessary. However, the second equation in (10.28) (energy equilibrium) is now written in terms of the ERR $\mathcal{G}_I(a)$. Using equation (4.5) in the system of equations (10.28), and using equation (10.2) to compute the SIF, the first member of the second equation of (10.28) reads, after integration:

$$\int_a^{a+l} \mathcal{G}_I(a)\,\mathrm{d}a = (\sigma^{\infty})^2 \frac{\pi}{8} \frac{1}{\acute{E}} \chi^2 W^2 f_K \tag{10.29}$$

where $\acute{E}$ is the equivalent modulus (equation (4.6)) and f_K is given by equation (10.25).

The second member of the second equation in (10.28) can be obtained using the formula in equation (4.21), yielding, after integration:

$$\int_0^l \mathcal{R}(\Delta a)\,\mathrm{d}\Delta a = \mathcal{R}_{0-l} = \\ = \begin{cases} \mathcal{R}_{ss}\,\dfrac{\zeta l + \eta\zeta l + (1-\zeta l)^{\eta} - (1-\zeta l)^{\eta}\zeta l - 1}{\zeta(\eta+1)} & , \; l \le l_{fpz} \\ \mathcal{R}_{ss}\left[\dfrac{\zeta l_{fpz} + \eta\zeta l_{fpz} + (1-\zeta l_{fpz})^{\eta} - (1-\zeta l_{fpz})^{\eta}\zeta l_{fpz} - 1}{\zeta(\eta+1)} + l - l_{fpz}\right], & l > l_{fpz} \end{cases} \tag{10.30}$$

Using equations (10.21), (10.29) and (10.30) in (10.28), dividing the second equation in (10.28) by the square of the first one yields:

$$\frac{\pi}{8}\left(\frac{K_T^{\infty}}{K_T}\right)^2 \frac{1}{\acute{E}}\chi^2 W^2 \frac{f_K}{f_{\sigma}^2} = \frac{\mathcal{R}_{0-l}}{\left(X_T^L\right)^2} \tag{10.31}$$

which is a nonlinear equation with only one unknown, the crack extension at failure l. After solving equation (10.31) for l, the residual strength $\bar{\sigma}^{\infty}$ of a centre-notched laminate can be calculated using, for instance, equation (10.27).

10.3.2.3. Experimental validation

Recently, an extensive experimental test programme [122] and a study of the applicability of traditional analysis methods to predict the open-hole tensile and compressive response of CFRP laminates [135] were conducted to assess the notched response, size effects and brittleness of non-crimp fabric (NCF) carbon/epoxy C-Ply™ T700/AR-2527 thin-ply laminates. A size effect on the strength was observed for both the open-hole tension and compression tests, and the associated notch sensitivity of thin-ply NCFs were similar to those observed in typical aerospace-grade unidirectional (UD) pre-impregnated CFRPs. It was also shown that simple analysis models, namely the PS and AS models [176] and the FFMs model [179], are able to predict with reasonable accuracy the observed size effects in both tension and compression. However, all tests were limited to small-scale coupons.

In order to assess the LDC of thin-ply NCFs, a $[(0/-45)/(45/0)/(90/45)/(-45/90)]_S$ 16-ply thick panel with a centre notch was tested. This laminate, manufactured at VX Aerospace (Leesburg, Virginia USA) using vacuum bagging, was built from a carbon NCF C-Ply™ T700/AR-2527 epoxy *prepreg* system from Aldila (Poway, CA USA), which includes the spread-tow C-Ply™ T700 $(0/-45)$ NCF from Chomarat (Le Cheylard, France), with an areal weight of 150 g/m^2 per bi-angle layer (or 75 g/m^2 per ply). It has a fibre volume fraction around 50% and a nominal ply thickness of 0.08 mm. The 0° fibre orientation is coincident with the loading direction and the ply properties were reported in Ref. [122].

A centre-notched plate, 270 mm wide (W) and 400 mm long (L), was tested in tension. The nominal length of the notch ($2a$) was 36 mm. The central notch was obtained using a milling machine, ensuring a distance of 1 mm between the notch faces. The notch tip was not sharpened, since, based on the previous work [212], no relevant difference between the fracture toughness of specimens with and without sharpened notch tips is expected.

The plate was instrumented with seven strain gauges, installed on the −45° surface-ply along the longitudinal (x) direction, as shown in figure 10.3. In addition, the digital image correlation (DIC) technique was used to evaluate the displacement and strain fields of the 0° surface-ply, by means of a single-camera, and assess damage formation and development near the notch tips. The ARAMIS DIC-2D v6.0.2 system developed by GOM [257] was used, equipped with an 8-bit Baumer 138 Optronic FWX20 camera (resolution of 1624×1236 pixels^2 and sensor format of 1/1.8”). The digital camera was coupled with a Nikon AF Micro-Nikkor 200 mm f/4D IF-ED lens for image grabbing. The working distance (defined between the plate’s surface and the support of the camera) was set to 2730 mm. The lens aperture was set to f/11 to improve the depth of field, and the shutter time was set to 25 ms to maximise the grey levels distribution over the 8-bit dynamic range of the camera while avoiding saturation of the image [253]. The captured region was

Table 10.1
Configuration of the DIC system.

Camera-lens optical system	
CCD camera	Baumer 138 Optronic FWX20 camera
	8-bit
	Resolution: 1624×1236 pixels^2
	Sensor format of 1/1.8”
Lens	Nikon AF Micro-Nikkor 200 mm f/4D IF-ED
	Lens aperture: f/11
Shutter time	25 ms
Working distance	2730 mm
Captured region	100×76 mm^2
Conversion factor	0.0636 mm/pixel
Acquisition frequency	1 Hz
DIC measuring parameters	
Subset size	15×15 pixels^2
Subset step	13×13 pixels^2
Strain base length	5 subsets
Strain validity code	55.0%
Strain computation method	Total
DIC resolution	
Spatial resolution	2×10^{-2} pixels [187]
Strain resolution	0.01-0.04% [187]

of approximately 100×76 mm^2 (conversion factor of 0.0636 mm/pixel), and the acquisition frequency was 1 Hz. The measuring parameters used in the DIC analyses were a subset size of 15×15 pixels^2, a subset step of 13×13 pixels^2, and a strain base length of 5 subsets. The adopted configuration, which leads to an expected spatial resolution in the order of 2×10^{-2} pixels and a strain resolution in the range 0.01-0.04% [187], is summarised in table 10.1. In order to ensure the perpendicularity between the image grabbing setup and the sample’s surface, a laser pointer fixed to the camera support and a mirror placed on the sample’s surface and parallel to it were used to achieve a correct alignment.

The LDC test was performed under displacement control, at a controlled speed of 1.0 mm/min, in a servo-hydraulic MTS 810 testing machine with a load capacity of 250 kN, equipped with a 250 kN load cell. The acquisition frequency was set to 5 Hz.

The load introduction device is made of an upper and a bottom tool, each of which has two rows of holes used to fasten M5 bolts through the CFRP plate, applying pressure in a region corresponding to the gripping area (figure 10.4). The resulting grip-to-grip length is of approximately 250 mm, and the width-to-gauge length ratio is 1.1. It is noted that, according to a numerical study conducted by Catalanotti et al. [65] addressing the effect of finite gauge length on the finite width and orthotropy correction factors obtained from the orthotropy rescaling technique [269, 270], neglecting the effect of finite gauge length for a width-to-gauge length ratio of 1.1 incurs an error of approximately 5%. Nevertheless, taking into account that the analysis becomes much simpler, the authors believe this is an acceptable error for the objectives of the present paper. It is also important to note that no bearing damage was observed in the holes of the CFRP plate after testing.

Figure 10.5 shows the longitudinal displacement (u_x)-remote longitudinal stress (σ_x^∞) and the far-field (*SG0*) longitudinal strain (ε_x)-remote longitudinal stress (σ_x^∞) relations for the tested centre-notched plate (figure 10.3). Observing figure 10.5a, it can be seen that the longitudinal displacement-remote longitudinal stress relation is linear up to approximately 75% of the peak load. On the other hand, observing figure 10.5b, it can be seen that the onset of nonlinear behaviour in figure 10.5a coincides with the onset of unstable behaviour of the far-field longitudinal strain-remote longitudinal stress relation.

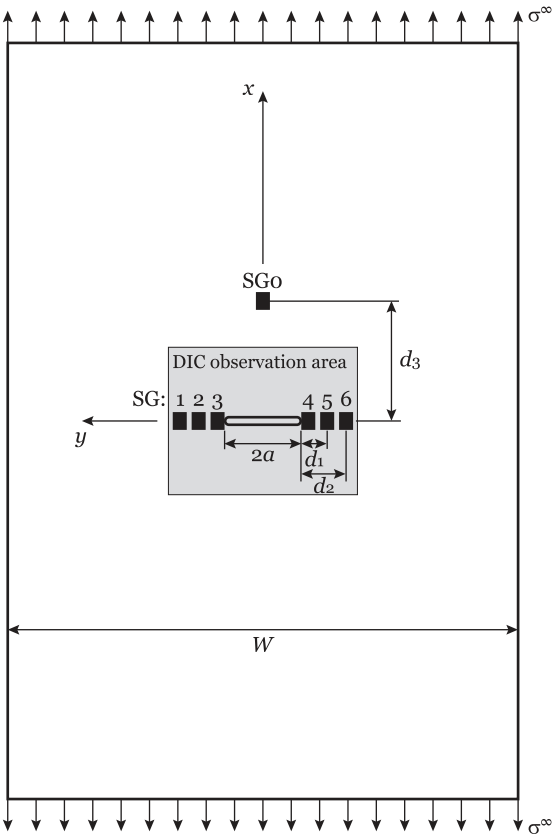

Fig. 10.3. Centre-notched plate. Position of the strain gauges (d_1 = 11.5 mm, d_2 = 21.5 mm, and d_3 = 63.5 mm) and DIC observation area.

This behaviour is related with the onset of a FPZ ahead of the notch tips, whose propagation can be analysed observing figure 10.6. Here, the surface longitudinal strain (ε_x) fields measured using the DIC technique for four different stages of the development of the FPZ are shown, together with the time-stress curve showing the points corresponding to these stages. The surface longitudinal strain (ε_x) measured along a cutting line centered along the notch (red line in the charts on the left-hand side) are shown in the plots on the right-hand side.

At the onset of the fracture process (figure 10.6 (b)), corresponding to the first load drop, the strain concentration moves from the notch tip, perpendicularly to the loading direction. A visible, finite region of high strained material ahead of the notch tip can be observed. In the subsequent stages, the location of the strain concentration can be used to identify the tip of the FPZ. Observing figure 10.6 (a), it can be seen that the point in the time-stress relation for the onset of the fracture process (point (b)) coincides with the onset of nonlinear behaviour (compare with figure 10.5). Thereafter, the strain concentration does not increase further, and, as shown in figure 10.6, the front of the FPZ propagates perpendicularly to the loading direction (i.e., in the x-direction).

Figure 10.7 shows the longitudinal strain (ε_x)-remote longitudinal stress (σ_x^∞) relations ahead of the notch tips, obtained using *physical* (figure 10.7a and b) and *virtual* (figure 10.7c and d) strain gauges. The far-field longitudinal strain is also shown. The measurements for the virtual strain gauges were obtained using the DIC technique, averaging the strain values in the area equivalent to the gauge area of the physical strain gauges. It should be noted that, in the unloading regime, the longitudinal strain (ε_x) in the notch plane cannot be obtained because, after unstable fracture of the plate, the signal from both physical and virtual strain gauges is lost due to the presence of a transverse intralaminar crack in that plane.

As observed in previous works [121, 187], and in spite of having been obtained in plies with different orientations, no substantial difference can be found in figure 10.7 between the results of the physical or virtual strain gauges (from

(a) Upper tool of the load introduction device.

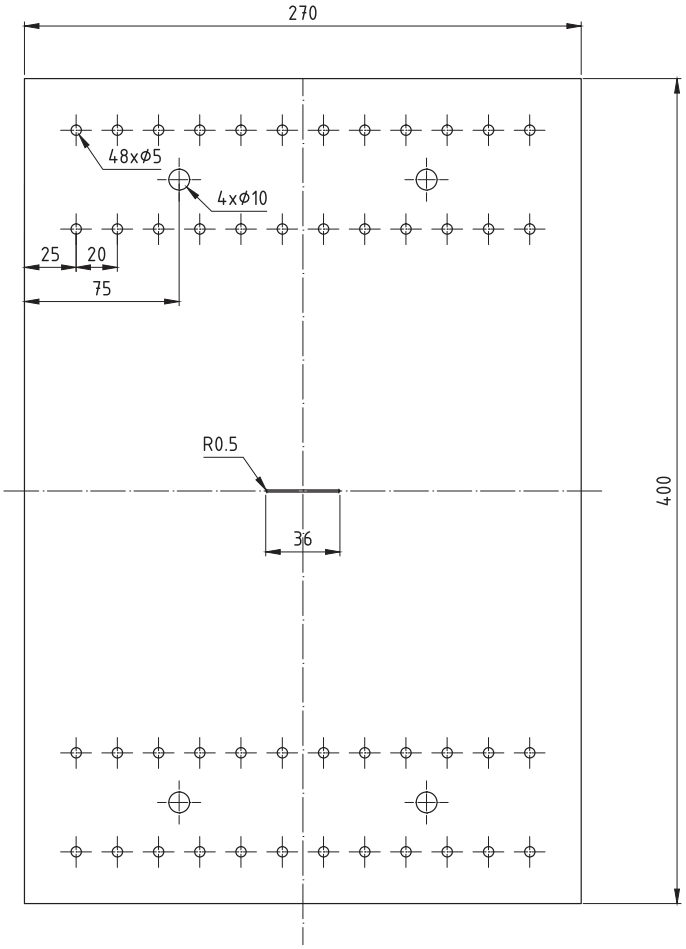

(b) Specimen drawing.

Fig. 10.4. Load introduction mechanism and specimen drawing.

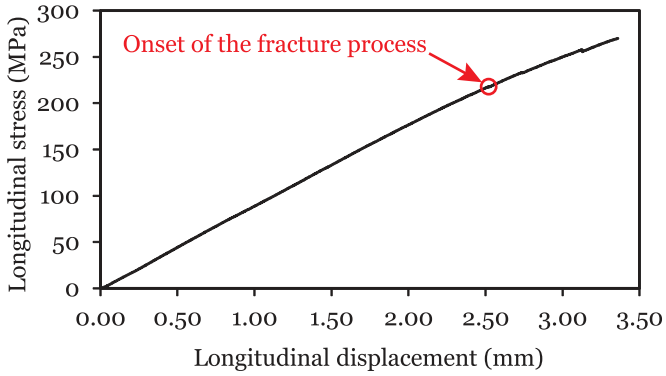

(a) Longitudinal displacement (u_x)-remote longitudinal stress (σ_x^∞) relation.

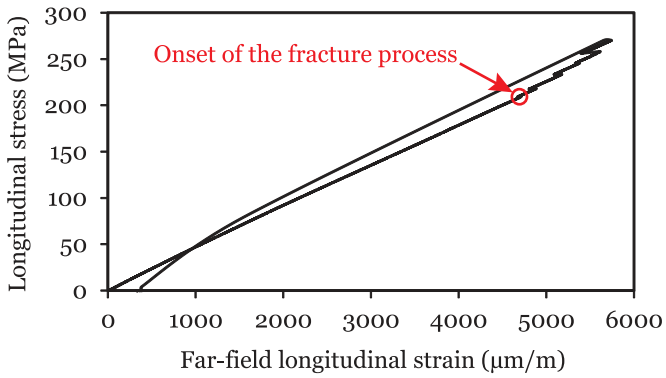

(b) Far-field (*SG0*) longitudinal strain (ε_x)-remote longitudinal stress (σ_x^∞) relation.

Fig. 10.5. Centre-notched plate test results.

DIC), except for the notch tips; however, it should be noted that, as the distance to the notch tips decreases, the strain gradient considerably increases, and a small difference between the positions of the physical strain gauge and the averaged region used in the DIC technique may led to large differences in the strain measurements. Still, the correlation between the measured strains at the notch tips is satisfactory. Both techniques show that the local longitudinal strains (ε_x) considerably increase with its proximity to the notch tips. In addition, observing the notch tip longitudinal strains captured by the virtual strain gauges (which do not suffer from premature failure), it can be seen that the remote stress at the onset of the fracture process (corresponding to a sudden increase in strain) relates very well with the onset of nonlinear behaviour observed in figures 10.5 and 10.6.

Before final fracture, and contrary to what was observed for small notch coupons [122], the crack that propagates from the notch tips extends significantly along the notch plane, although not very regularly, as shown in figures 10.6 and 10.8. From a macro-mechanical point of view, the development of the FPZ occurs in discrete, finite steps, which result from a bridging process at the crack tip. This bridging process prevents unstable fracture along the ligament width, increasing the fracture toughness of the laminate as the crack length increases, until a maximum is reached, after which final fracture occurs.

This notched response clearly shows that the tested laminate is characterised by an $\mathcal{R}$-curve. Accordingly, some small load drops can be observed (figure 10.5a), resulting from the development of the FPZ, which have some effect on the stiffness of the centre-notched plate, causing the nonlinear behaviour mentioned before. This bridging process and the $\mathcal{R}$-curve effect are fundamental in the analysis of LDC, as perviously discussed.

Figure 10.9 shows the centre-notched plate after testing. In the vicinity of the notch tips, some fibre splitting can

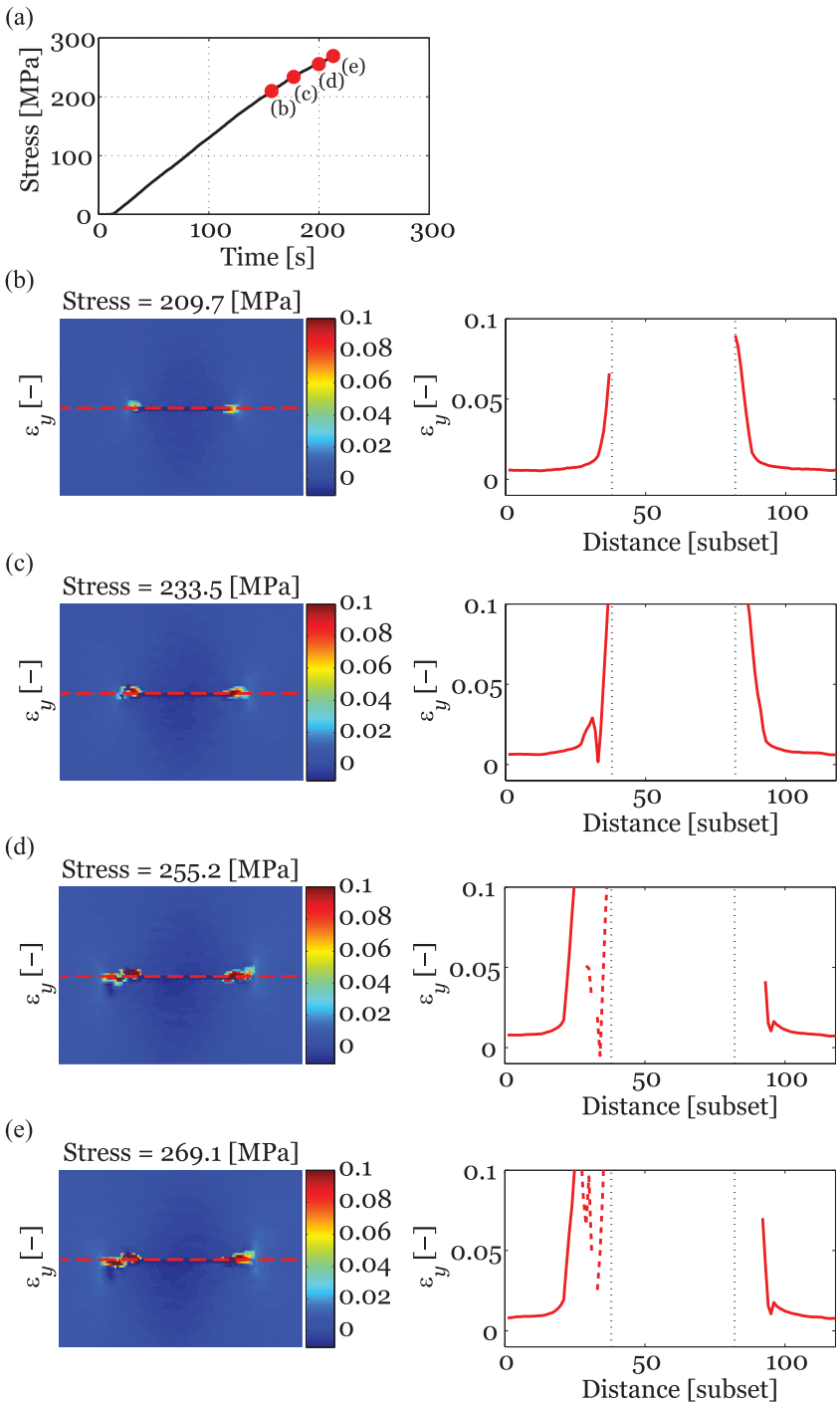

Fig. 10.6. Post-processing of the DIC measurements: (a) time-stress relation showing some points corresponding to the development of the FPZ; surface longitudinal strain (ε_x) fields, and surface longitudinal strain (ε_x) measured along a cutting line centered along the notch, for the stages corresponding to (b) the onset of the fracture process, (c) and (d) its development, and (e) just before ultimate failure.

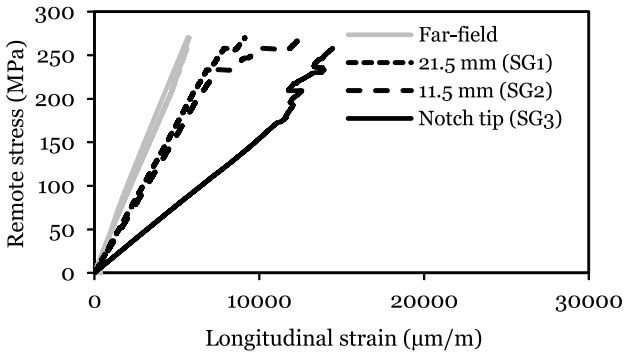

(a) Physical strain gauges, notch left-hand side.

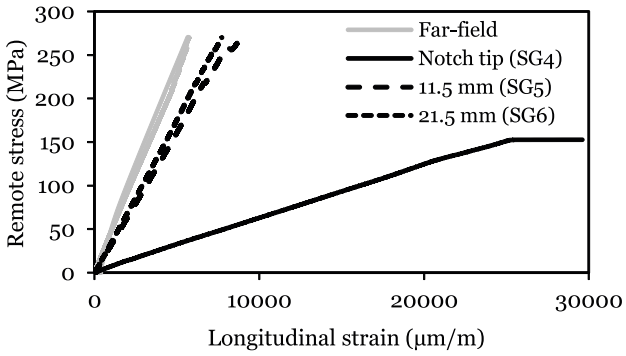

(b) Physical strain gauges, notch right-hand side.

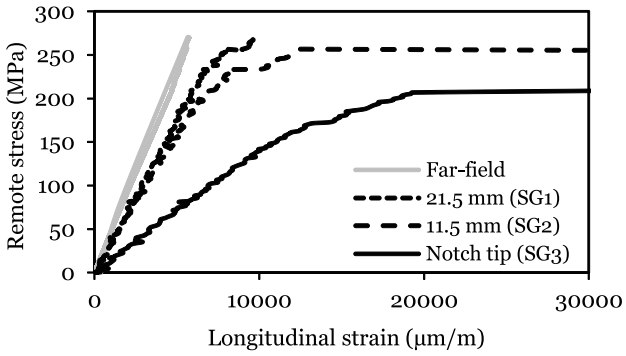

(c) Virtual strain gauges, notch left-hand side.

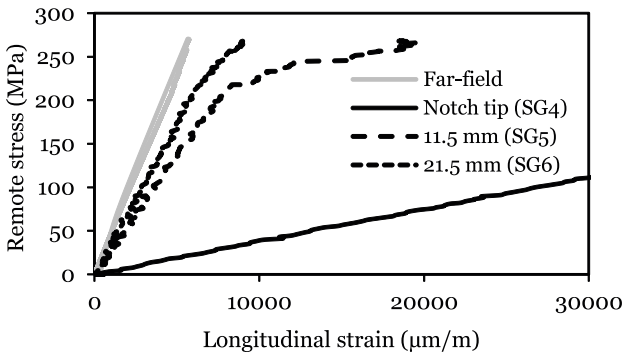

(d) Virtual strain gauges, notch right-hand side.

Fig. 10.7. Longitudinal strain (ε_x)-remote longitudinal stress (σ_x^{∞}) relations ahead of the notch tips.

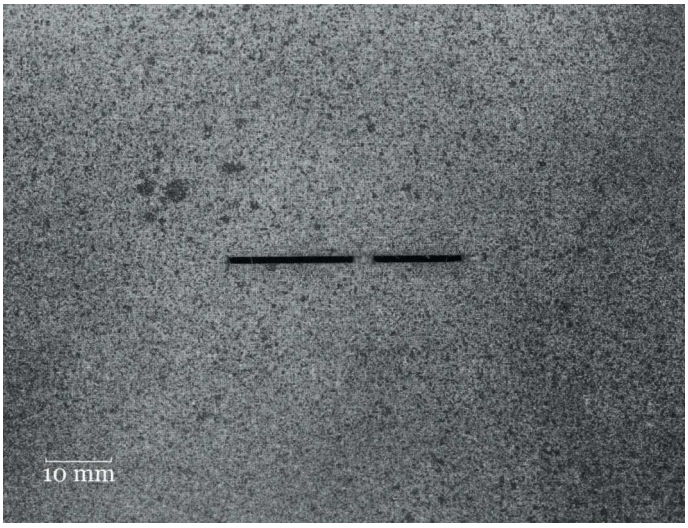

(a) Before testing.

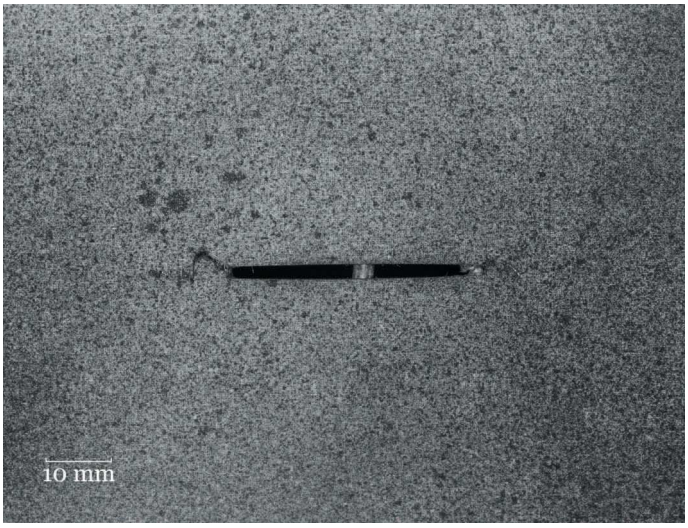

(b) Just before final fracture.

Fig. 10.8. Centre notch region of the tested centre-notched plate.

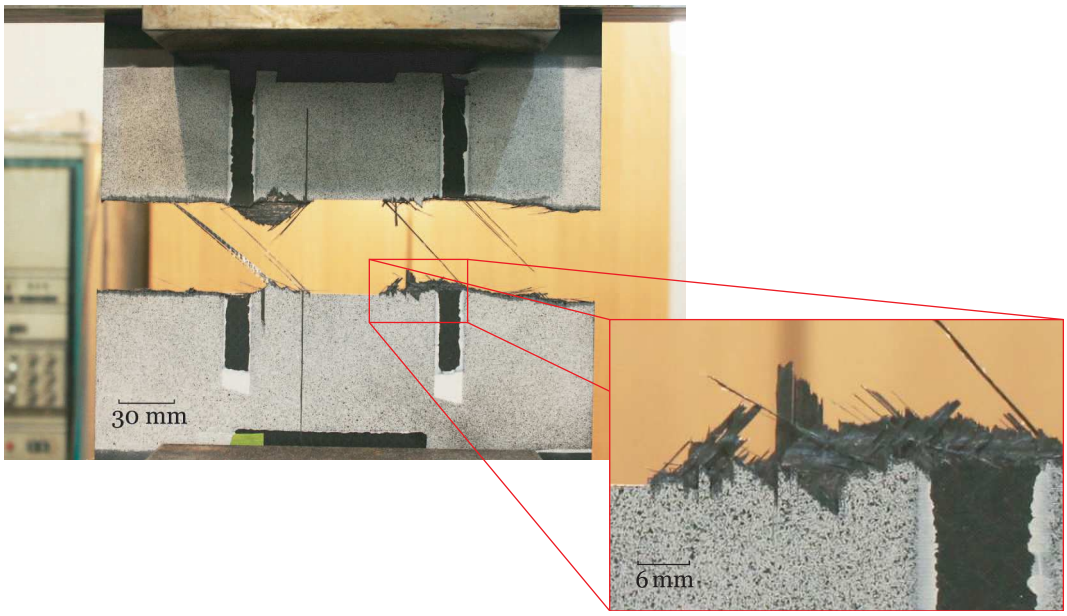

Fig. 10.9. Centre-notched plate after testing. (The two black vertical stripes in the plate's surface are just two unpainted regions used to help delimitating the DIC observation area).

Table 10.2
Material properties and empirical factors for the macro-mechanical models.

Model	a_0 (mm)	r_{ot} (mm)	$\mathcal{K}_{Ic}$ (MPa $\sqrt{\text{m}}$)	X_L^T (MPa)
LEFM	-	-	38.1	-
IFM	1.79	-	-	710.3
PS	-	0.76	-	710.3
AS	-	3.36	-	710.3
FFMs	-	-	53.1	710.3

be observed in both 0° and −45° surface-plies, as well as some separated plies due to delamination. However, these damage mechanisms, whose extent was reduced, only occurred after unstable fracture along the ligament width, since they were not observed in figures 10.6 and 10.8. In addition, similarly to what was observed in the small notch coupons after testing [122], a brittle type of net-section failure mode can be identified. Therefore, it is possible to conclude that the development of the FPZ observed in figures 10.6 and 10.8 resulted from stable (although not regular) intralaminar damage growth, and that subcritical damage mechanisms such as delamination, transverse cracking or fibre splitting did not play an important role in the LDC of the tested thin-ply laminate, even if a stacking sequence more susceptible to subcritical damage growth was used [122]. Nevertheless, it is recognised that related studies in the future should include non-destructive inspection data of the coupons during testing [166] to verify the previous conclusions.

The test results obtained in Ref. [122] for the $[(0/-45)/(45/0)/(90/45)/(-45/90)]_S$ NCF thin-ply tensile specimens with a 4 mm long centre notch are used to calculate the fracture toughness $\mathcal{K}_{Ic}$, and calibrate the IFM and the PS and AS models by calculating the length of the inherent flaw a_0 and the characteristic distances r_{ot}, respectively. The laminate tensile unnotched strength X_L^T is also obtained from Ref. [122]. The values of the properties required by each macro-mechanical model are summarised in table 10.2.

Figure 10.10 shows the predictions of the tensile residual strength of a $[(0/-45)/(45/0)/(90/45)/(-45/90)]_S$ NCF thin-ply centre-notched plate obtained using the macro-mechanical models described in sections 10.2 and 10.3.2. The height of the centre notch (h) and the $W/(2a)$ ratio are kept constant and equal to 1 mm and 7.5, respectively. Figure 10.10 also shows the experimental results for the centre-notched specimen ($2a = 4$ mm) [122], and for the centre-notched plate ($2a = 36$ mm). For the latter, both stresses at the initiation of the fracture process and at the final fracture are shown.

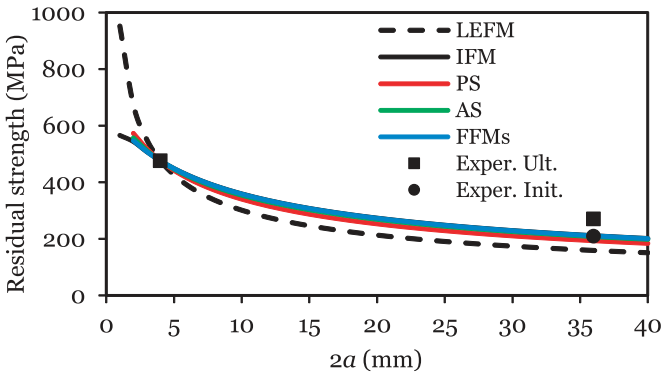

Fig. 10.10. Predictions and experimental results for the tensile residual strength of the NCF thin-ply laminate.

Table 10.3
LDC predictions and relative errors.

Model	$\bar{\sigma}^{\infty}$ (MPa)	Relative error (ϵ_r) (%)	
		init. fract.	ult. stress
LEFM	159	−24.3	−41.2
IFM	211	0.9	−21.6
PS	193	−7.8	−28.4
AS	208	−0.8	−22.9
FFMs	211	0.6	−21.8

It is noted that subcritical damage mechanisms such as delamination and splitting are neglected when using the models presented in sections 10.2 and 10.3.2, an assumption acceptable for laminates whose failure in dominated by through-the-thickness intralaminar damage.

From figure 10.10, it becomes clear that the LEFM model is not able to capture the right trend of the residual strength with changing notch length. Regarding the remaining analysis models, they all show similar trends, with slightly different predictions of LDC (table 10.3).

All models fail to predict the residual strength of the laminated plate with a large through-the-thickness notch. However, interestingly, the predictions of these models (with the exception of the LEFM model) match with reasonable accuracy the stress at the initiation of the fracture process, with errors below 1% for the IFM, AS model and FFMs model. Therefore, it seems that these models are able to capture the onset of the fracture process, which, for small crack lengths, is close to final fracture [122], yielding, in this case, good predictions. For large crack lengths, though, the onset of the fracture process occurs considerably before final fracture, consequently yielding conservative estimates.

As discussed in section 10.3.2.2, for large crack lengths, the bridging mechanisms that cause the development of a stable FPZ must be taken into account in the macro-mechanical models to accurately predict LDC. One possibility is to take into account the effect of the $\mathcal{R}$-curve in the analysis method.

To solve the system of equations (10.28), the $\mathcal{R}$-curve of the material must be first determined. However, no standard test method exists to characterise the $\mathcal{R}$-curve associated with intralaminar fracture of composite laminates.

Compact Tension (CT) test specimens are normally used to measure this property in composite laminates [191, 197, 198, 200]. Over-height Compact Tension (OCT) specimens [197], complemented with an anti-buckling support, as proposed by Li et al. [198], were used to measure the $\mathcal{R}$-curve of the $[(0/-45)/(45/0)/(90/45)/(-45/90)]_S$ NCF thin-ply laminate. Unfortunately, buckling of the unnotched end was observed (figure 10.11), despite the use of the anti-buckling support, and no crack propagation occurred. This buckling phenomenon resulted from the low thickness of this laminate (about 1.3 mm), which easily promotes such instabilities, but also from the reasonably high resistance of this material to unstable fracture, despite the brittle type of net-section failure mode exhibited in previous experiments [122].

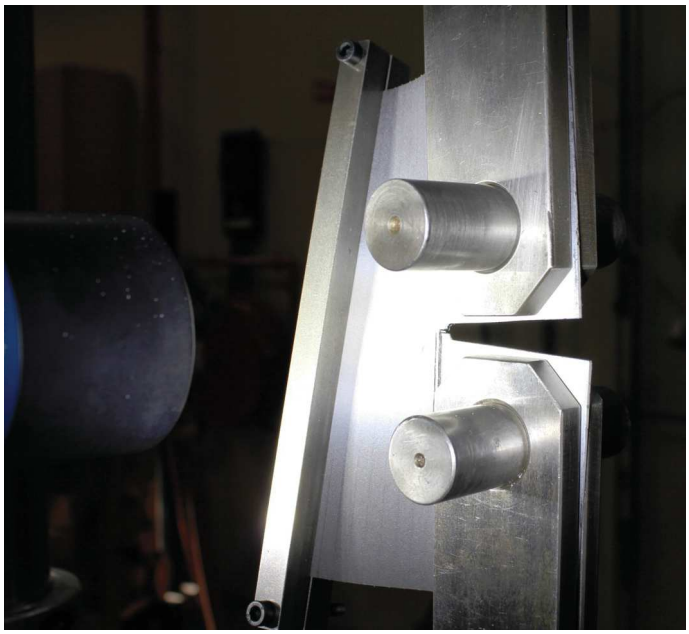

Fig. 10.11. OCT specimen during testing, showing overall buckling of the unnotched end.

In order to circumvent the previous difficulties found in the characterisation of the $\mathcal{R}$-curve of the tested laminate using the OCT test, a recent methodology based on the size effect law [209] to measure the fracture toughness and the $\mathcal{R}$-curve of composite laminates was adopted [65]. According to this methodology, the $\mathcal{R}$-curve of a composite laminate can be measured taking into account that, for different characteristic sizes w_n, assuming that the size effect law, $\bar{\sigma}^{\infty} = \bar{\sigma}^{\infty}(w)$, is known, the driving force curves $\mathcal{G}_I$ at the ultimate remote stresses $\bar{\sigma}^{\infty}(w_n)$ are tangent to the $\mathcal{R}$-curve. In other words, the $\mathcal{R}$-curve can be determined as the envelope of the driving force curves at the ultimate remote stresses (e.g. Ref. [211]).

Catalanotti et al. [65] measured the $\mathcal{R}$-curve of the $[(0/-45)/(45/0)/(90/45)/(-45/90)]_S$ NCF thin-ply laminate, investigated in the present work, using scaled Double Edge-Notched Tension specimens. Specimens of width $2w$ in the range of 10 mm to 35 mm and an edge notch length-to-width ratio $a/w = 0.6$ were tested. The length of the FPZ and the fracture toughness at propagation reported by Catalanotti et al. [65] for this laminate were respectively $l_{fpz} = 1.92$ mm and $\mathcal{R}_{ss} = 101.5$ kJ/m^2.

Figure 10.12 shows the $\mathcal{R}$-curve of the $[(0/-45)/(45/0)/(90/45)/(-45/90)]_S$ NCF thin-ply laminate, obtained as the envelope of the crack driving force curves [65]. To simplify the implementation of the $\mathcal{R}$-curve in numerical or analytical models, Catalanotti et al. [65] used equation (4.21) to fit the $\mathcal{R}$-curve. For the $[(0/-45)/(45/0)/(90/45)/(-45/90)]_S$ NCF thin-ply laminate, the best fit is obtained with $\zeta = 0.4226$ mm^{-1} and $\eta = 4.004$.

It is noted that, unlike most experimental results available in the literature, which consider the $\mathcal{R}$-curve to start from some initial nonzero value of $\mathcal{R}$, the $\mathcal{R}$-curve presented in figure 10.12 starts from zero. However, as stressed, for instance, in Ref. [277], an $\mathcal{R}$-curve that starts from some initial nonzero value implies that the crack tip can sustain a singular stress field without showing any damage, which is unreasonable.

The fact that the $\mathcal{R}$-curve starts from zero means that the process zone forms right at the beginning of loading and that there is never any singularity at the crack tip, which is more physically reasonable. For CFRPs exhibiting a relatively large bridging zone, however, it is observed that the initial rising part of the $\mathcal{R}$-curve is considerably steep, which is the reason why, in practice, a nonzero initial value of $\mathcal{R}$ is used. According to Bažant and Kazemi [277], this relatively large initial slope can be explained by assuming that the matrix itself will, on a smaller scale, exhibit a microscopic, relatively fast-rising $\mathcal{R}$-curve.

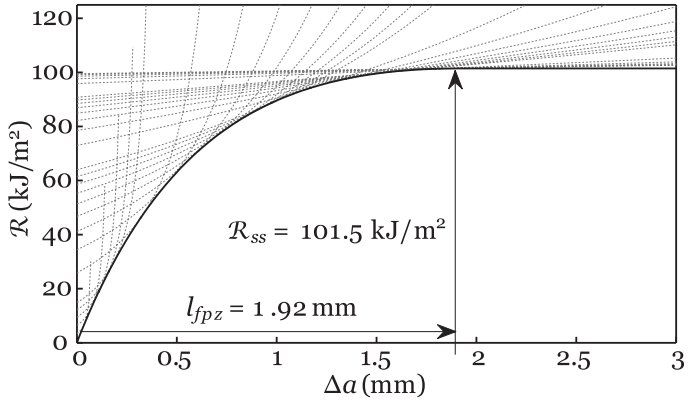

Fig. 10.12. $\mathcal{R}$-curve of the tested NCF thin-ply laminate (after Catalanotti et al. [65]).

It is also worth noting that the $\mathcal{R}$-curve determined using the size effect law is defined such that the fracture energy at propagation, $\mathcal{R}_{ss}$, corresponds to the energy required propagate a crack in an infinitely large specimen, which is taken as size and geometry independent. However, because the size effect law is not exact, this should be regarded as an approximation. Nonetheless, for structures until one order of magnitude larger than the end of the size range for which the size effect law has been calibrated, which is the case here, the approximation is acceptable (e.g. Refs. [279, 280]). On the other hand, for some materials, the $\mathcal{R}$-curve may change slightly with specimen shape (e.g. Refs. [211, 277, 279, 280]). However, the differences in the $\mathcal{R}$-curve may result either from the statistical scatter of the experimental tests carried out to calibrate the size effect law (e.g. Ref. [211]), or due to the effect of the shape correction functions, which vary with the different specimen shapes. In fact, it is noted that the length of the FPZ is dependent not only on the shape correction functions, but also on their derivatives, making l_{fpz} more sensitive to experimental or numerical error than $\mathcal{R}_{ss}$ [279, 280]. Although the authors did not assess the effect of coupon shape on the determination of the $\mathcal{R}$-curve of CFRPs using the size effect law, based on the previous discussion, the hypothesis of a unique $\mathcal{R}$-curve is considered acceptable.

Figure 10.13 shows the predictions of the tensile residual strength of a $[(0/-45)/(45/0)/(90/45)/(-45/90)]_S$ NCF thin-ply centre-notched plate for a wide range of crack lengths ($2a$), obtained using the FFMs model taking into account the $\mathcal{R}$-curve of the laminate. Figure 10.13 also shows a comparison with the experimental results for the centre-notched specimen ($2a$ = 4 mm) [122] and for the centre-notched plate ($2a$ = 36 mm), and corresponding relative errors.

Observing table 10.3, and comparing with the results from figure 10.13, it is clear that accounting for the $\mathcal{R}$-curve in the FFMs formulation results in a significant improvement of the predictions of LDC. Using the traditional analysis methods, the relative errors of the predictions ranged from −41.2% to −21.6% for a centre-notched plate with a crack length $2a$ = 36 mm, whereas the FFMs prediction that takes into account the $\mathcal{R}$-curve of the laminate has a relative error

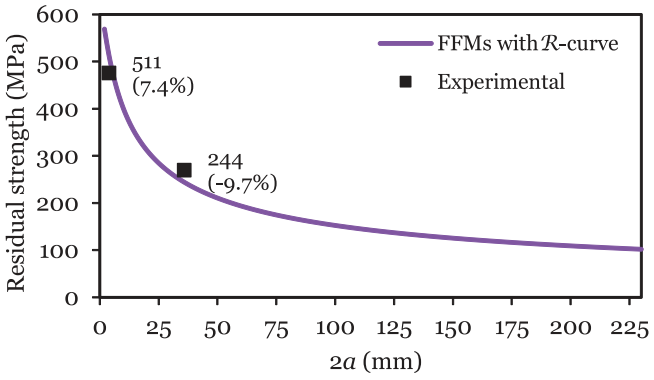

Fig. 10.13. FFMs predictions and corresponding relative errors, taking into account the $\mathcal{R}$-curve of the laminate.

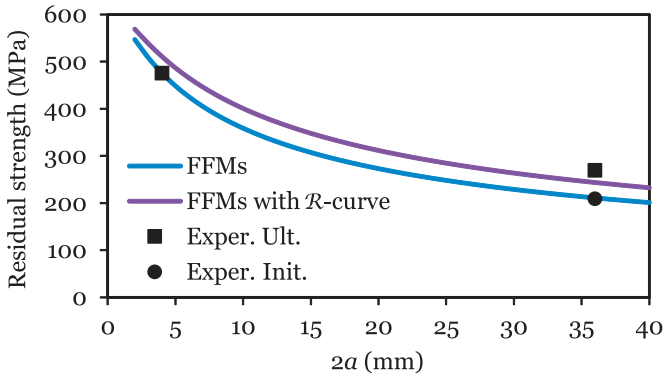

Fig. 10.14. FFMs predictions, not taking and taking into account the $\mathcal{R}$-curve of the laminate.

of −9.7%, which is within the range typically obtained by the traditional analysis methods for small damage coupons (e.g. Refs. [121, 135, 179]).

For the small notch coupons, the FFMs analysis that takes into account the $\mathcal{R}$-curve of the laminate seems to overpredict the residual strength, with a relative error of 7.4% for the centre-notched specimen with a crack length $2a = 4$ mm. However, such error is again within the range typically obtained by the traditional analysis methods for specimens with small notches that are not used for calibration. It should be noted that the centre-notched specimens with this geometry were used to calibrate the IFM and the PS and AS models, and calculate the fracture toughness required by the LEFM and FFMs models, whereas an independent test was used to determine the $\mathcal{R}$-curve.

Finally, figure 10.14 shows a comparison between the FFMs predictions that do not take and that take into account the $\mathcal{R}$-curve of the laminate. It is clear from this figure that, by including the $\mathcal{R}$-curve in the formulation of the FFMs model, and consequently taking into account the bridging process that delays unstable fracture and increases the fracture toughness as the FPZ advances, more reliable analyses of large through-penetration damage of composites are obtained without requiring fitting parameters or complex Finite Element Analyses (FEA). Taking into account that the FFMs model relies on a closed-form, macro-mechanical solution, it can be used in preliminary design and implemented in optimisation codes, without the need of verification tests or fine tuning parameters that account for scale modifications. Furthermore, because it is physically-based, only independently measured material properties are necessary (the laminate strength and the $\mathcal{R}$-curve), which can be easily included in material screening programmes that are often carried out in the composites industry.

10.4. Concluding remarks

Several analysis methods were presented and applied to estimate the residual strength and LDC of NCF thin-ply laminates, namely the LEFM model, the IFM [175], the PS and AS models [176], and the FFMs model [179]. It was observed that the classical LEFM model is not able to capture the right trend of the residual strength with changing notch length. Regarding the remaining analysis models, they all showed similar trends, with slightly different predictions for the smaller and larger notch lengths. However, all models failed to predict the residual strength of laminated plates with large through-the-thickness cracks.

Interestingly, the predictions matched with reasonable accuracy the stress at the initiation of the fracture process (except the LEFM model), with errors below 1% for the IFM, AS model and FFMs model. Hence, these models were able to capture the onset of the fracture process, which, for small crack lengths, is close to final fracture [122], yielding good predictions. Nevertheless, for large crack lengths, the onset of the fracture process occurs considerably before final fracture, consequently yielding conservative estimates.

The previously developed analysis methods assume that fracture occurs unstably, as a singular event, regardless of the crack length. However, the composite laminates generally exhibit a remarked $\mathcal{R}$-curve effect, developing an extensive,

stable FPZ before ultimate failure. Therefore, to predict LDC of laminated composites with a non-negligible FPZ, the bridging mechanisms associated with the fracture process must be lumped into the crack tip in a physically admissible way, in order to be able to take them into account in the macro-mechanical model. One possibility is to take properly into account the effect of the $\mathcal{R}$-curve in the analysis method.

Reformulating the FFMs model to take into account the $\mathcal{R}$-curve of the material resulted in a significant improvement of the predictions of LDC. In fact, more reliable analyses of large through-penetration damage of composites can be obtained without fitting parameters or complex FEA. The analytical FFMs model can be used in preliminary design and implemented in optimisation codes. Furthermore, only independently measured material properties are necessary (the laminate strength and the $\mathcal{R}$-curve), which can be easily included in the experimental characterisation programmes that are often carried out in the composites industry. In fact, the number of tests required in the early stages of design and optimisation can be reduced, and more reliable experimental programmes can be established, resulting in lower costs associated with preliminary material and lay-up characterisation.

Regarding the LDC of thin-ply laminates, it was observed that extensive, stable FPZ develop before final fracture. It is interesting to note that, from a macro-mechanical point of view, the development of the FPZ took place in discrete, finite steps, which resulted from a bridging process at the crack tip. This bridging process delayed unstable fracture along the ligament width, increasing the fracture toughness of the laminate as the crack length increased, until a maximum was reached, after which final fracture occurred. This is rthe typical $\mathcal{R}$-curve effect.

In the vicinity of the notch tips, a reduced extent of fibre splitting was observed in both 0° and -45° surface plies, as well as some separated plies due to delamination. However, this subcritical damage mechanisms occurred after unstable fracture of the panel, which exhibited a brittle type of net-section failure mode. In spite of this brittle type of failure, the tested thin-ply laminate exhibited stable (although not regular) intralaminar damage, typical of tougher materials, where subcritical damage mechanisms such as delamination, transverse cracking or fibre splitting typically do not play an important role.

As already discussed elsewhere [58, 135], the characteristic failure behaviour of thin-ply laminates makes them particularly suitable for analysis that employ simple analytical tools. The mechanical response of thin-ply laminates can be predicted with great accuracy using simple models, making preliminary design and optimisation more reliable and less time consuming. In fact, it is important to stress that, in the case of laminates exhibiting matrix-dominated failure modes, governed by the propagation of large delaminations, complex nonlinear FEA tools are required to predict their notched strength.

Part VI

Conclusions and future work

Chapter 11

Conclusions and future work

The work presented in this thesis aimed at improving the understanding of the structural mechanics of thin-ply laminates. Previous preliminary experimental data and theoretical and numerical analyses on the notched response of thin-ply laminates has been complemented by means of extensive experimental testing and by new analysis performed at different length-scales. This chapter presents the main conclusions of the work carried out in this thesis, and enumerates the topics that should be subject of future analysis and further development.

11.1. Conclusions

Even though high-end composites technology has evolved in the aerospace industry only in the last thirty years, it rapidly expanded in the recent past. In fact, nowadays nearly all aeroplanes use composites extensively [3], including in primary structural components. And there is still great potential for further application.

In spite of the improved specific properties of composite laminates and despite new technological developments, the heterogeneity of these materials at the meso-scale still poses some limitations regarding their mechanical performance. In this thesis, the thin-ply technology was proposed to reduce, or even suppress these limitations.

Studies assessing the mechanics of thin-ply laminates only appeared in recent years, and most of them were preliminary. Furthermore, the effect of ply thinness and the use of thin plies in different reinforcement configurations, such as woven or non-crimp fabrics, as well as the comprehensive assessment of the damage mechanisms involved in the failure of thin-ply laminates and the applicable analysis tools, were not studied in detail in an industrial context.

11.1.1. Current state-of-the-art and lessons (to be) learned

The state-of-the-art of the spread-tow thin-ply technology was presented, with special remarks on manufacturing and design with thin-ply laminates and a description of some of the commercially available spread-tow reinforcements. It is recognised that ultra-thin plies produced using this technology exhibit a series of advantages, including (i) potential to use heavy tow yarns to cost-effectively obtain low-grade and thin-ply tows, (ii) improved surface appearance, fibre orientation and distribution, and better dispersion and uniformity of plies, (iii) smoother ply drops, (iv) reduced crimp angle and tow flexure when used in woven fabrics, (v) laminate homogenisation, (vi) possibility of using smaller relative fibre orientations between adjacent plies, and (vii) faster and simpler design due to the absence of subcritical damage mechanisms such as matrix cracking and delamination, showing potential for better optimised laminates and higher consistency in defining safety factors. The spread-tow thin-ply technology is therefore highly attractive, having gained a featured place in the advanced composites market in the form of different configurations, including ultra-thin unidirectional (UD) tapes, spread-tow fabrics (STFs) and thin-ply non-crimp fabrics (NCFs).

A comprehensive literature review was also presented in this thesis. The microstructural effect of ply thinness, the effect of ply thickness scaling, and current applications of thin plies were described and discussed.

In terms of structural performance, the literature shows that some advantages are intrinsic to the ply thinness obtained with the spread-tow thin-ply technology. Either as a result of the particular microstructural uniformity or as a result of subcritical damage suppression, thin plies provide (i) higher UD longitudinal compressive strength, (ii) higher *in situ* strengths, (iii) higher resistance to delamination due to lower interlaminar energy release rates, (iv) higher laminate tensile and compressive strengths, (v) higher low-velocity impact resistance, (vi) improved fatigue response, and (vii) higher bearing strengths.

However, the damage suppression capability of thin-ply laminates has also a potential negative effect on the mechanical response of coupons or structures containing notches. In this case, damage suppression reduces the blunting effect that provides conventional notched composites with a more gradual failure behaviour. Consequently, notched coupons or structures made of thin plies are prone to early unstable failure across the ligament sections, resulting in lower notched strengths.

Other aspects of the structural performance of spread-tow thin-ply laminates are not so clear. For instance, it is not clear what is the effect of ply thinness on the intralaminar fracture toughness associated with tensile and compressive longitudinal fracture perpendicular to the fibre direction. It is recognised that ply thickness affects the sequence and type of damage occurring prior to ultimate failure, and that modifications of the mechanisms leading to final rupture may induce substantially different notched responses, virtually changing the fracture toughness of laminates of the same material system but with plies of different thickness. The experimental campaign conducted in the present work systematically addressed this issue, even though definite conclusions could not be obtained due to constraints related to specimens' size and availability (section 11.1.2).

In addition, contradicting results about the effect of ply thickness scaling on the compressive notched strength and damage tolerance of advanced composite laminates were found in the literature. Nevertheless, it is becoming clear that, in compression, the ability of thin-ply laminates to delay or suppress the occurrence of subcritical damage mechanisms before ultimate failure prevents early unstable fracture of the longitudinal plies or yarns, resulting in improved notched strengths (e.g. section 11.1.2).

The understanding of the effect of ply thickness on the damage tolerance of multidirectional laminates is more challenging. In fact, due to a reduction of the laminate bending stiffness, the residual compressive strength of laminated composites decreases if the size of the delaminations created by impact is large, which is expected to occur in thick-ply laminates. On the other hand, if the number of delamination planes increases, as in the case of thin-ply laminates, the plate bending stiffness decreases too, reducing the residual compressive strength (or damage tolerance). Hence, a thorough understanding of the effect of ply thickness on damage tolerance requires reliable experimental testing and analytical [220] and numerical [228] modelling, which was out of the scope of the present research.

11.1.2. Effect of ply thinness on the integrity of structural laminates

An extensive experimental test campaign on different reinforcement configurations with different areal weights was performed aiming at assessing in greater detail the effect of ply thickness on the structural mechanics of advanced composites and at understanding the advantages and potential weaknesses of thin-ply laminates.

In a first assessment, the hole size effect on laminated composites incorporating spread-tow UD tapes was studied. Open-hole and centre-notched tension tests were performed on laminates with the same nominal thickness produced from *prepregs* of the same material system but with different ply thicknesses.

In accordance with the results available in the literature (e.g. Refs. [144, 163]), thick-ply laminates exhibited an inverse size effect, attributed to a characteristic matrix-dominated failure mode comprising extensive delamination and transverse cracking of the ±45° and 90° plies. Even though thick-ply laminates do not fail catastrophically, they lose their structural integrity due to complete gauge section delamination. An interesting conclusion was that no significant difference was found on the notched response of thick-ply laminates manufactured with high grade thick plies or by blocking together several thin plies with the same fibre orientation.

For ply thicknesses in the range of the low-grade systems, a fibre-dominated pull-out failure mode was observed, with extensive subcritical damage including split cracks in the 45° outer plies. Thin-ply laminates, on the other hand, in general exhibited a brittle type of net-section failure mode, where subcritical damage such as transverse cracking or delamination were absent.

For small open holes, when normalised for the same fibre volume fraction, the notched strength tends to increase with decreasing ply thickness. For the thin-ply and low-grade laminates the notched strengths are approximately the same, but for the high-grade laminates it can be considerably lower. Hence, in this case (small hole diameters), all laminates are characterised by a constant normalised notched strength, with respect to the corresponding tensile unnotched strengths. However, increasing the specimens' size, a decrease of the notched strengths of the laminates with thin and low-grade plies is observed, which tend to a notch-sensitive material response, whose mechanical behaviour depends strongly on the stress concentration factor at the hole boundary. On the other hand, the tensile notched strengths of the high-grade laminates tend to their unnotched strengths. Delamination propagation across the ligament width causes strong stress relaxation at the hole edge, and the 0° plies remain intact. Delamination takes place along the unnotched gauge section and failure eventually occurs due to complete gauge section delamination as in the unnotched specimens [58], resulting in tensile notched strengths approximately equal to the tensile unnotched strengths. It is important to stress, though, that the development of large-scale subcritical damage, in particular delamination, which may propagate unstably in finite, abrupt steps, is typically highly undesirable due to the early loss of structural integrity and due to the severe reduction of the laminates' residual compressive and shear strengths.

Given the promising role of structural textile composites on advanced applications, namely in the aeronautical industry, an experimental test campaign was carried out to study the structural response of aerospace-grade plain weave spread-tow fabrics of different grades, including a detailed assessment of the structural response of laminates based on a baseline of the aeronautical industry. Special focus was given to the study of the effect of tow thickness on the structural response of these textile composites.

In general, the effect of using thin plies observed in laminates produced from UD tapes [53, 58, 122] was also present in the spread-tow textile composites. In spite of an unexpectedly low tensile longitudinal strength of the thinner STF, its ability to delay or suppress subcritical damage growth resulted in an improved tensile unnotched strength when incorporated in a structural multidirectional laminate. However, suppressing the subcritical damage mechanisms reduced the blunting effect in the presence of stress concentrations, resulting in premature failure of the notched configurations loaded in tension. This was particularly evident in the case of the UD STF laminates used for characterisation of the mode I tensile $\mathcal{R}$-curves of the STFs. In structural multidirectional laminates, though, the typical notched strength reduction due to subcritical damage suppression was not so evident, on one hand due to excessive subcritical damage growth in the low-grade STF laminate, and, on the other hand, due to an effective blunting effect in the thin-ply STF laminate promoted by the selected lay-up.

The damage suppression capability of the thin-ply STFs resulted in superior longitudinal compressive and (estimated) in-plane shear strengths, and superior laminate unnotched and notched compressive strengths. Due to the positive effect of the uniformity of the crimp configuration and homogeneity of the individual yarns, which benefit from a thinner configuration, a substantial improvement of the compressive response of the thin-ply configuration over a low-grade configuration was observed, demonstrating the merit of ultra-thin reinforcements in improving the compressive response of composite laminates. Subcritical damage growth tended to promote early unstable fracture of the spread-tow yarns aligned with the loading direction due to an early loss of the lateral support provided to the highly compressed fibres, conducting to premature compressive failure of the thicker configurations.

In the case of mechanically fastened joints, the effect of using thin plies observed elsewhere [58, 122] was not observed in the STF configurations, despite the improved compressive response of the thinner STF and corresponding multidirectional laminate. If at the coupon level the uniformity of the thinner STFs played an important role in delaying the micro-instabilities that conducted to compressive failure, at the local level of bearing damage the same role was expectably smaller, even though a compressive damage constraining effect, promoted by the yarns thinness, was observed.

Finally, as the detrimental effect of thick transverse and off-axis plies becomes clear due to lower *in situ* strengths and higher interlaminar stresses, which promote transverse cracking, off-axis splitting, delamination and complex interactions thereof, the effect of 0° ply blocking on the blunting mechanisms and notched response of a structural laminate based on a baseline of the aeronautical industry was investigated. In addition, recognising that longitudinal fibre-matrix splitting can act as an important blunting mechanism [20, 121, 276], the present study also aimed at improving the notched response of structural thin-ply laminates.

Due to the intrinsic design advantages, thin-ply NCF laminates were produced. As expected, by changing the position of the 0° plies, a different structural response could be obtained. Improvements of the notched behaviour of structural laminates were observed when adopting a laminate configuration with blocked 0° plies and spread-tow thin plies along the transverse and off-axis orientations. Whereas the former promoted longitudinal split cracking from the notch tips, blunting the stress concentration, the latter ensured that matrix cracking and delamination preceding ultimate failure could be effectively delayed or even suppressed, leaving the laminate practically intact far from the notched region. A superior structural response was obtained on scaled coupons with straight through-the-thickness notches and on fastened joints. More importantly, this was achieved without compromising the unnotched tensile and compressive strengths of thin-ply laminates. These observations follow the recent results of Furtado et al. [248] obtained on quasi-isotropic (QI) laminates of the same NCF material system designed with a similar understanding of the effect of 0° ply blocking on the notched response of thin-ply laminates. It is also shown that the benefits of selective ply-level hybridisation is not restricted to QI laminates [248], and that this concept can be wisely used in the design of better laminates.

11.1.3. Modelling of ply thinness effects

In this thesis, different numerical and analytical modelling strategies of the ply damage mechanisms at different scales were presented. Analyses were performed at the micro- and meso-scales, depending on the detail of the damage mechanisms that were considered.

Computational micro-mechanical analyses were carried out to study the mechanical response of ultra-thin spread tows embedded in a multidirectional laminate and to understand the effect of ply thickness on the meso-mechanical behaviour of composite laminae. Given the importance of accurately taking into account the microstructure in the onset and growth of transverse damage, in particular in the case of very thin plies, modelling of damage evolution at the constituent level was key in understanding the constraining, or *in situ*, effect observed on thin plies embedded in multidirectional laminates.

The proposed three-dimensional (3D) computational micro-mechanics framework was able to accurately represent the micro-mechanical response of ultra-low grades, including (i) the mechanics of transverse cracking onset and propagation, (ii) the constraining effect observed in the laminae embedded in multidirectional laminates, (iii) the gradual, slow stress relaxation and progressive transverse cracking observed in very thin plies and consequent increase of the crack density, (iv) the reduction in crack opening displacement of the transverse cracks with ply thinness, attributed to the constraining effect imposed by the adjacent stiffer laminae, (v) the formation of thin necks of matrix material around the regions where interfacial damage is more pronounced, a phenomenon potentiated by increasing ply thicknesses, and (vi) the *in situ* effect, characterised by a reduction in the applied stress needed to extend a transverse crack through the thickness of the ply when the ply thickness increases. For sufficiently thin plies, a change on the transverse fracture mechanisms was observed. When embedded ultra-thin plies are subjected to transverse tensile loading, ply failure is characterised by progressive fragmentation and multiple cracking. For limit cases, damage is characterised by many decohesions occurring without extending completely through the ply thickness, as a dispersed damage event, and leading to overall failure of the matrix material between the fibres before development of discrete transverse cracking. The dispersed/non-localised matrix failure observed for very thin plies shows that, for this particular case, failure at the mesoscopic scale can be regarded by conventional continuous damage mechanics frameworks, without the need to address discrete cracking as in smeared crack or discrete damage formulations, potentially simplifying the analysis of thin-ply laminates.

Regarding the response of constrained plies subjected to transverse compressive loading, the proposed computational micro-mechanics framework was able to provide a detailed representation of the failure mechanisms involved. For cross-

ply sublaminates with conventional, standard-thickness 90° plies, failure was dominated by fibre-matrix interface cracking and large localised plastic deformation of the matrix, forming a localised band of damage in a plane not aligned with the loading direction, in agreement with what has been described in the literature [102, 299].

Unlike conventional 90° plies subjected to transverse compressive loading, constrained ultra-thin plies showed a dispersed damage mechanism, combining wedge cracking with ply fragmentation/separation, or just ply fragmentation/separation for the thinnest plies. As in the tensile case, this dispersed type of damage on thin-ply sublaminates is the result of a less pronounced stress relaxation due to the stronger constraining effect imposed by the surrounding plies. This results in the development of progressive ply damage instead of discrete transverse cracking. It should be noted that, while there is no direct experimental evidence of the *in situ* effect for transverse compression, some recent test results obtained in structural details indicate that indeed the ply thickness affects the compressive strengths [58, 121, 122, 133, 134].

When comparing the results of the computational micro-mechanics framework with the predictions from the analytical models available in the literature for the *in situ* effect [81, 128, 129], the same trends were obtained, emphasising the validity of the computational micro-mechanics and analytical representations. The present results also show that, for realistic ply thicknesses, these analytical models can be considered fairly accurate and representative of the actual strengths characterising the response of transverse plies embedded in multidirectional laminates.

Even though models at the micro-scale can provide reliable estimates of the onset and propagation of damage, the computational cost of micro-mechanical models makes them unsuitable for the prediction of damage localisation and ultimate failure in composite laminates with several laminae. Hence, models at the meso-scale, which consider a ply as a homogeneous material, need to be introduced. These models need to be formulated in order to take into account the effects observed at the micro-scale, so damage accumulation at the constituent level can be lumped into a crack or damage process zone representative of the actual lamina failure response.

With this objective, new 3D failure criteria were presented. These failure criteria are based on structural tensors, enabling an elegant coordinate system-free description of anisotropy using isotropic tensor functions. They predict failure in a single UD ply, requiring the analysis of strains and stresses ply-by-ply when analysing multidirectional laminates. In addition, a pragmatic approach to estimate the orientation of the fracture plane for composite laminates under transverse, matrix-dominated failure was proposed. To account for the effect of ply thickness when the laminae are embedded in a multidirectional laminate, appropriate definitions of the *in situ* properties were derived in the framework of the invariant-based failure criterion for transverse failure mechanisms.

In general, the failure predictions were in agreement with previous 3D failure criteria (e.g. Ref. [128]). When compared against experimental data available in the literature, good agreement for transverse failure modes, for failure under off-axis loading and for the effect of superposed hydrostatic pressure on failure of different fibre-reinforced polymers was obtained. For more complex 3D stress states, where the test data available shows large scatter or is not available at all, a computational micro-mechanics framework was used to validate the failure criteria. A good correlation between the predictions of the failure criteria and the predictions of computational micro-mechanics was obtained. Finally, in spite of the simplicity of the pragmatic approach proposed to estimate the orientation of the fracture plane, reliable estimates were obtained for general 3D stress states.

The ability to determine, in a simple way, the orientation of the fracture angle, and the possibility to account for the *in situ* effect in the framework of the proposed failure criterion for transverse damage mechanisms, enabled the implementation of the invariant-based failure criteria in a Smeared Crack Model [108] to predict ply failure mechanisms in composite laminates. A preliminary verification, based on single-element tests and on simple models with different levels of refinement was performed. Also, a preliminary validation study, where test results of unnotched and notched coupons of an IM7/8552 carbon-epoxy multidirectional laminate were compared with the predictions of the proposed damage model, was presented. Both showed that the proposed implementation was not only consistent with respect to the proposed damage idealisation and to mesh objectivity, but it can also be seen as a valid tool to predict failure of multidirectional laminates using only properties determined from tests carried out at the lamina level.

11.1.4. Failure prediction of thin-ply laminates

For very thin plies, the applicability of numerical tools formulated at the lamina level becomes questionable. In fact, compared to conventional ply grades, for the same laminate thickness, thin-ply laminates have to accommodate a much greater number of plies. If each of these plies need to be represented individually for application of a damage model at the ply level, the required discretisation and the size of the finite element model will rapidly become impractical.

The possibility to accommodate more plies also means that the macro-mechanical response of thin-ply laminates in practically homogeneous. Moreover, thin-ply laminates develop much lower interlaminar stresses, resulting in a recognised delamination suppression capability, and they have considerably higher *in situ* strengths, precluding matrix cracking before ultimate laminate failure. Therefore, their mechanical and fracture responses resemble those of a homogenised quasi-brittle material, making macro-mechanical models at the laminate level more suitable for their analysis.

Hence, macro-mechanical analysis methods based on analytical tools formulated at the homogenised laminate level were proposed to enhance the predictive capability of the strength and failure of composite structures, and for more reliable and easier design methodologies. First, an overview of the recently proposed Trace theory and Master Ply concept, which employ an invariant-based approach to stiffness, was introduced. In addition, the concept of Omni Strain Failure Envelopes and the Unit Circle failure criterion were described, which introduce a new invariant-based approach to strength that greatly simplifies the macro-mechanical failure analysis of homogenised laminates.

The combination of the invariant-based approaches to stiffness and strength, valid for homogenised laminates, shows great potential to simplify design allowable generation. In fact, using Trace theory and the Master Ply concept to determine the elastic properties of multidirectional laminates from the longitudinal ply stiffness component, and using the Omni Strain Failure Envelope or, more specifically, the Unit Circle failure criterion to predict last-ply failure of multidirectional laminates from the strengths of the 0° ply only, makes material screening similar to that of metals, since only 0° coupons need to be tested in tension and compression. Moreover, laminate design becomes substantially simpler, as the invariant-based approaches to stiffness and strength provide more efficient and straightforward computations of the mechanical and failure response of composite laminates.

To predict the notched response of composite laminates, and since traditional analysis methods are not able to capture the bridging processes that occur in the presence of large through-the-thickness cracks, a recently proposed Finite Fracture Mechanics model was reformulated to take into account the crack resistance curve of the material. With the proposed model, more reliable analyses of the notched response of laminated plates with large through-penetration damage were obtained without requiring fitting parameters or complex Finite Element Analyses (FEA). Furthermore, only independently measured material properties are necessary (the laminate strength and the crack resistance curve), which can be easily included in the experimental characterisation programmes that are often carried out in the composites industry. In fact, the number of tests required in the early stages of design and optimisation can be reduced, and more reliable experimental programmes can be established, resulting in lower costs associated with preliminary material and lay-up characterisation.

As discussed elsewhere [58, 135], the characteristic failure behaviour of thin-ply laminates makes them particularly suitable for analysis that employ simple analytical tools. The mechanical response of thin-ply laminates can be predicted with great accuracy using simple models, making preliminary design and optimisation more reliable and less time consuming.

It is important to stress that, in the case of laminates exhibiting matrix-dominated failure modes, governed by the propagation of large delaminations, complex nonlinear FEA tools are required to predict their notched strength. Moreover, as stressed by Tsai et al. [388], the virtues of laminate homogenisation for simpler and faster design procedures, in particular through the use of thin plies, which make laminate homogenisation possible even for the thin laminates currently used in the airframe construction, must be embraced by designers so all benefits from the superior specific properties of advanced composites can keep improving the performance of high-end applications.

11.2. Future work

In spite of the increasing number of publications that address the effect of ply thickness scaling on the mechanical and structural response of advanced composite laminates, a thorough study addressing laminates made of different spread-tow reinforcement configurations with different areal weights ("apples-to-apples" comparison) is still missing. In particular, a detailed case study of a structural component designed to take advantage of thin plies versus current composite technologies was not performed yet.

After a first assessment of the hole size effect on laminated composites incorporating spread-tow unidirectional (UD) tapes and on the structural mechanics of aerospace-grade spread-tow fabrics and non-crimp fabrics, in the future, complementary tests on larger specimens and different notch geometries could provide interesting additional information on the effect of ply thinness on the intralaminar fracture toughness and crack resistance curve, Large Damage Capability, and open-hole, filled-hole and unnotched size effects, namely in compression. Impact resistance, damage tolerance and buckling/crippling analyses are also still missing. These would certainly boost the understanding of the structural behaviour of spread-tow composite laminates. The introduction of enhanced resin formulations or nano-reinforcements and the study of the effect of lay-up and the effect of inter- and intra-ply hybridisation on the structural response of laminates with conventional and spread-tow reinforcements would be of great value as well.

A further understanding of the effect of ply thinness on the mechanical response and on the structural performance of composite structures must also be sought not only by means of the available computational and design tools, but most importantly by means of new modelling strategies that can more effectively address the material behaviour of thin plies. Currently, the computational micro-mechanics framework proposed in chapter 6 is being applied to the cases of in-plane shear and transverse shear stress states. The cases of biaxial tensile and compressive loading, as well as longitudinal compression and kink band formation [308], can all be addressed in the future. In addition, emphasis will be given not only to the effect of the transverse ply thickness, but also to the effect of the stiffness of the adjacent plies and ply position in the laminate. These analyses are intended to support the understanding of the micro-mechanical constitutive behaviour of ultra-thin plies and thin-ply laminates subjected to basic stress states, overcoming the complexities and limitations of experimental testing on these low grade materials.

This computational micro-mechanics framework can also be extremely helpful in understanding the behaviour of polymer composite laminates subjected to biaxial or multiaxial loading scenarios, for which there is still a fundamental lack of reliable experimental data [311]. It also has great potential for future material tailoring at the micro-scale, with important applications not only for the scientific community, but also for the composite materials industry, including effects of fibre clustering, effects of intra-bundle and intra-ply hybridisation, and effects of new matrix materials.

For more reliable detailed modelling of the composite laminate behaviour, coupling of the proposed implementation of the Smeared Crack Model with a reliable interlaminar damage model and further benchmarking based not only on simple coupons but also on more complex structural details should be performed. Case studies including laminates with thinner plies may also be addressed.

For laminate failure prediction, embracing simpler analysis models and the virtues of laminate homogenisation for simpler and faster design procedures is seen as an essential step towards more competitive composite structures. And thin-ply laminates are essential for the feasibility and reliability of these concepts, in particular for the most advanced applications, where laminates must be kept thin enough for improved efficiency.

For instance, the development of integrated tools applicable at the homogenised laminate level combining analysis models for the prediction of the elastic and strength properties of laminates with and without discrete sources of damage or geometrical discontinuities would provide a great enhancement to the predictive and design capability of composite structures. Such integrated tools would preferably be conceived requiring a minimum of input material properties, obtained exclusively at the UD lamina level. An example of an integrated tool would combine the invariant-based approaches to stiffness [55] and strength [55, 387] for prediction of the elastic and strength properties of smooth laminates with the Finite Fracture Mechanics model to predict the notched strength [179, 182]. Integrating also the analytical model

to predict the fracture toughness of the laminate from the fracture toughness of the 0° ply [212] would provide a predictive tool with the ability to estimate the structural response of any homogenised laminate just from tests on 0° and/or cross-ply coupons with smooth and notched configurations.

Finally, it is recognised that the apparent brittle failure behaviour of thin-ply laminates may be unsuitable for applications with unpredictable loading conditions, where high safety factors may have to be used to ensure the risk of catastrophic failure is acceptably low [26]. In this case, laminate design concepts based on combinations of thin-thick plies [222, 248], pseudo-ductile lay-ups [243] or hybrid configurations [23, 161], which exhibit higher structural "*forgiveness*", can help widening the range of applications of composite structures.

References

[1] Daniel IM, Ishai O. Engineering Mechanics of Composite Materials. Oxford: Oxford University Press; 2008.

[2] Gay D, Hoa SV. Composite Materials: Design and Applications. 2nd ed.; Boca Raton: CRC Press, Taylor and Francis Group; 2007.

[3] Tsai SW. Strength and Life of Composites. Composites Design Group, Department of Aeronautics and Astronautics, Stanford University; 2008.

[4] Linde P. Overview of test prediction and damage simulation of composite aircraft structures. In: Proceedings of the 2nd International Conference on Buckling and Postbuckling Behaviour of Composite Laminated Shell Structures. Braunschweig: DLR, Institute of Composite Structures and Adaptive Systems; 2008, p. 1.

[5] Laurin F, Charrier JS, Lévêque D, Maire JF, Mavel A, nez PN. Determination of the properties of composite materials thanks to digital image correlation measurements. Procedia IUTAM 2012;4:106–15.

[6] Davies G. Future trends in automotive body materials. In: Materials for Automobile Bodies; chap. 9; second ed. Oxford: Butterworth-Heinemann; 2012, p. 357–96.

[7] Cousigné O, Moncayo D, Coutellier D, Camanho P, Naceur H. Numerical modeling of nonlinearity, plasticity and damage in CFRP-woven composites for crash simulations. Compos Struct 2014;115:75–88.

[8] Behrens BA, Rolfes R, Vucetic M, Reinoso J, Vogler M, Grbic N. Material modelling of short fiber reinforced thermoplastic for the FEA of a clinching test. Procedia CIRP 2014;18:250–5.

[9] Linde P, Heltsch N, Kruse T, Das S, Vernier C. Second generation composites. In: 19. Nationales Symposium — SAMPE Deutschland E. V. Hamburg; 2013, p. 1–2. In German.

[10] Ogihara S, Takeda N, Kobayashi A. Experimental characterization of microscopic failure process under quasi-static tension in interleaved and toughness-improved CFRP cross-ply laminates. Compos Sci Technol 1997;57:267–75.

[11] Nash NH, Young TM, McGrail PT, Stanley WF. Inclusion of a thermoplastic phase to improve impact and post-impact performances of carbon fibre reinforced thermosetting composites — A review. Mater Design 2015;85:582–97.

[12] Aymerich F, Pani C, Priolo P. Damage response of stitched cross-ply laminates under impact loadings. Engng Fract Mech 2007;74:500–14.

[13] Aymerich F, Priolo P. Characterization of fracture modes in stitched and unstitched cross-ply laminates subjected to low-velocity impact and compression after impact loading. Int J Impact Eng 2008;35:591–608.

[14] Cox BN, Flanagan G. Handbook of Analytical Methods for Textile Composites. NASA Contractor Report 4750; Langley Research Center; Hampton, Virginia; 1997.

[15] Abdalla MM, Setoodeh S, Gürdal Z. Design of variable stiffness composite panels for maximum fundamental frequency using lamination parameters. Compos Struct 2007;81:283–91.

References

[16] Blom AW, Abdalla MM, Gürdal Z. Optimization of tow-placed, tailored composite laminates. In: Proceedings of ICCM-16. Kyoto; 2007, p. 1–8.

[17] Blom AW, Lopes CS, Kromwijk PJ, Gürdal Z, Camanho PP. A theoretical model to study the influence of tow-drop areas on the stiffness and strength of variable-stiffness laminates. J Compos Mater 2009;43(5):403–25.

[18] Blom AW, Setoodeh S, Hol JMAM, Gürdal Z. Design of variable stiffness conical shells for maximum fundamental eigenfrequency. Comput Struct 2008;86:870–8.

[19] Blom AW, Tatting BF, Hol JMAM, Gürdal Z. Fiber path definitions for elastically tailored conical shells. Compos Part B-Eng 2009;40:77–84.

[20] Walker TH, Avery WB, Ilcewicz LB, Poe, Jr. CC, Harris CE. Tension fracture of laminates for transport fuselage. Part I: material screening. In: Soderquist JR, Neri LM, Bohon HL, editors. Proceedings of the 9th DoD/NASA/FAA conference on fibrous composites in structural design; vol. II. Lake Tahoe, Nevada; 1991, p. 747–87.

[21] Lopes CS, Camanho PP, Gürdal Z, Tatting BF. Progressive failure analysis of tow-placed, variable-stiffness composite panels. Int J Solids Struct 2007;44:8493–516.

[22] Lopes CS, Gürdal Z, Camanho PP. Variable-stiffness composite panels: Buckling and first-ply failure improvements over straight-fibre laminates. Comput Struct 2008;86:897–907.

[23] Czél G, Wisnom MR. Demonstration of pseudo-ductility in high performance glass/epoxy composites by hybridisation with thin-ply carbon prepreg. Compos Part A-Appl S 2013;52:23–30.

[24] González EV, Maimí P, Sainz de Aja JR, Cruz P, Camanho PP. Effects of interply hybridization on the damage resistance and tolerance of composite lmainates. Compos Struct 2014;108:319–31.

[25] MIL-HDBK-17-3F. Composite Materials Handbook, volume 3. Polymer Matrix Composites Materials Usage, Design and Analysis. Department of Defense Handbook; 2002.

[26] Diao H, Bismarck A, Robinson P, Wisnom MR. Production of continuous intermingled CF/GF hybrid composite via fibre tow spreading technology. In: Proceedings of ECCM16. Seville; 2014, p. 1–8.

[27] Pimenta S, Robinson P. Modelling the tensile response of unidirectional hybrid composites. In: Proceedings of ECCM16. Seville; 2014, p. 1–8.

[28] Yu H, Potter KD, Wisnom MR. A novel manufacturing method for aligned discontinuous fibre composites (High Performance-Discontinuous Fibre method). Compos Part A-Appl S 2014;65:175–85.

[29] Czél G, Pimenta S, Wisnom MR, Robinson P. Demonstration of pseudo-ductility in unidirectional discontinuous carbon fibre/epoxy prepreg composites. Compos Sci Technol 2015;106:110–9.

[30] Yu H, Jalalvand M, Wisnom MR, Potter KD. Hybrid composites with aligned discontinuous fibres. In: Proceedings of ECCM16. Seville; 2014, p. 1–8.

[31] Chen XL, Liew KM. Buckling of rectangular functionally graded material plates subjected to nonlinearly distributed in-plane edge loads. Smart Mater Struct 2004;13:1430–7.

[32] Kawabe K, Matsuo T, Maekawa Z. New technology for opening various reinforcing fiber tows. J Soc Mat Sci Jpn 1998;47(7):727–34. In Japanese.

[33] Kawabe K. New spreading technology for carbon fiber tow and its application to composite materials. Sen-i Gakkaishi 2008;64(8):262–7. In Japanese.

[34] Tao J, Sun CT. Influence of ply orientation on delamination in composite laminates. J Compos Mater 1998;32(21):1933–47.

[35] Saito H, Takeuchi H, Kimpara I. Experimental evaluation of the damage growth restraining in 90° layer of thin-ply CFRP cross-ply laminates. Adv Compos Mater 2012;21:57–66.

[36] Amacher R, Cugnoni J, Botsis J. Experimental characterization and modeling of thin ply-size effect. In: Proceedings of CompTest-2013. Aalborg; 2013, p. 33–4.

[37] Amacher R, Cugnoni J, Botsis J. Thin ply composites: experimental characterization and modeling. In: Proceedings of ICCM-19. Montréal; 2013, p. 1–13.

[38] Saito H, Takeuchi H, Kimpara I. A study of crack suppression mechanism of thin-ply carbon-fiber-reinforced polymer laminate with mesoscopic numerical simulation. J Compos Mater 2014;48(17):2085–96.

[39] Guillamet G, Turon A, Costa J, Renart J. Damage evolution in thin and thick-ply regions of NCF thin-ply laminates under off-axis uniaxial loading. In: Proceedings of ECCM16. Seville; 2014, p. 1–5.

[40] Athreya SR, Ma L, Barpanda D, Jacob G, Verghese N. Estimation of in-plane elastic properties of stitch-bonded, non-crimp fabric composites for engineering applications. J Compos Mater 2014;48(2):143–54.

[41] Kawabe K, Tomoda S. Multi-filament split-yarn sheet and method and device for the manufacture thereof. United States Patent Number: 6032342; 2000.

[42] Kawabe K, Tomoda S. Method of producing a spread multi-filament bundle and an apparatus used in the same. United States Patent Number: 7571524 B2; 2009.

[43] Kawabe K, Tomoda S. Method of producing a spread multi-filament bundle and an apparatus used in the same. United States Patent Number: 7832068 B2; 2010.

[44] Daniels CG. Pneumatic spreading of filaments. United States Patent Number: 3795944; 1974.

[45] Daniels CG. Pneumatic spreading of filaments. United States Patent Number: 3873389; 1975.

[46] Baucom RM, Marchello JM. LaRC dry powder towpreg system. Tech. Rep. 102648; NASA Langley Research Center; Hampton, Virginia; 1990.

[47] Baucom RM, Marchello JM. Powder towpreg process development. Tech. Rep. N93-30844; NASA Langley Research Center; Hampton, Virginia; 1991.

[48] Baucom RM, Snoha JJ, Marchello JM. Process for application of powder particles to filamentary materials. United States Patent Number: 5057338; 1991.

[49] Bayha TD, Osborne PP, Thrasher TP, Hartness JT, Johnston NJ, Marchello JM, et al. Processing, properties and applications of composites using powder-coated epoxy towpreg technology. Tech. Rep. N93-30844; NASA Langley Research Center; Hampton, Virginia; 1991.

[50] Kim C, Gray Jr. RA. Pneumatic induction fiber spreader with lateral venturi restrictors. United States Patent Number: 5446952; 1995.

[51] Everett RK, Hernshaw WF. Carbon fiber reinforced metal matrix composites. United States Patent Number: 4853294; 1989.

[52] Shinkado H. Fiber opening apparatus for mass fibers. United States Patent Number: 7596834 B2; 2009.

[53] Sihn S, Kim RY, Kawabe K, Tsai SW. Experimental studies of thin-ply laminated composites. Compos Sci Technol 2007;67:996–1008.

[54] El-Dessouky HM, Lawrence CA, McGrail T, Broughton WR. Ultra-lightweight carbon fibre/thermoplastic composite material using spread tow technology. Compos Part B-Eng 2013;50:91–7.

[55] Tsai SW, Melo JDD. An invariant-based theory of composites. Compos Sci Technol 2014;100:237–243.

References

[56] Baker N, Butler R, York CB. Damage tolerance of fully orthotropic laminates in compression. Compos Sci Technol 2012;72:1083–9.

[57] Cadena DSA. Improvement in damage tolerance and buckling behaviour of a composite fuselage panel using thin plies. Master's thesis; Politecnico de Milano, Facoltà di Ingegneria Industriale; Milan; 2014.

[58] Amacher R, Cugnoni J, Botsis J, Sorensen L, Smith W, Dransfeld C. Thin ply composites: Experimental characterization and modeling of size-effects. Compos Sci Technol 2014;101:121–32.

[59] Tsai SW, Papila M. Thin-ply NCF: design for deformation through anisotropy. JEC Compos Mag 2011;68:66–7.

[60] Tsai SW. Weight and cost reduction by using unbalanced and unsymmetric laminates. In: Proceedings of ICCM-18. Jeju Island; 2011, p. 1–2.

[61] Wysocki M, Szpieg M, Hellström P, Ohlsson F. The out-of-plane behaviour of spread-tow fabrics. In: Proceedings of ECCM16. Seville; 2014, p. 1–6.

[62] Cousigné O, Moncayo D, Coutellier D, Camanho P, Naceur H, Hampel S. Development of a new nonlinear numerical material model for woven composite materials accounting for permanent deformation and damage. Compos Struct 2013;106:601–14.

[63] Alif N, Carlsson LA, Boogh L. The effect of weave pattern and crack propagation direction on mode I delamination resistance of woven glass and carbon composites. Compos Part B-Eng 1998;29B:603–11.

[64] Shamsudin MH, York CB. Mechanically coupled laminates with balanced plain weave. Compos Struct 2014;107:416–28.

[65] Catalanotti G, Arteiro A, Hayati M, Camanho PP. Determination of the mode I crack resistance curve of polymer composites using the size-effect law. Engng Fract Mech 2014;118:49–65.

[66] Nishikawa Y, Okubo K, Fujii T, Kawabe K. Fatigue crack constraint in plain-woven CFRP using newly-developed spread tows. Int J Fatigue 2006;28:1248–53.

[67] Jacques S, De Baere I, Van Paepegem W. Application of periodic boundary conditions on multiple part finite element meshes for the meso-scale homogenization of textile fabric composites. Compos Sci Technol 2014;92:41–54.

[68] Asp LE, Varna J, Marklund E, Olsson R. Multiscale modelling of non-crimp fabric composites. In: Proceedings of the ASME IMECE2012. Houston, Texas; 2012, p. 1–10.

[69] Kuraishi A, Itoh T, Kimoto J, Ochi S, Hirano N. Applicability of C-ply Bi-angle™ NCF to aircraft parts. In: Proceedings of ICCM-19. Montréal; 2013, p. 1–11.

[70] Tessitore N, Riccio A. A novel FEM model for biaxial non-crimp fabric composite materials under tension. Comput Struct 2006;84:1200–7.

[71] Petriccione A, Annicchiarico D, Antonucci V, Giordano M, Riccio A, Scaramuzzino F. A stiffness volume averaging based approach to model non-crimp fabric reinforced composites. Compos Sci Technol 2012;72:360–9.

[72] Massard T, Harry R, Sanial P, Lorriot T. Characterization of the equivalent unidirectional thin ply from NCF. JEC Compos Mag 2011;68:55–6.

[73] Tsai SW, Nettles AT. Representative test data on bi-angle thin-ply NCF. JEC Compos Mag 2011;68:62–3.

[74] Suo Z, Bao G, Fan B. Delamination *R*-curve phenomena due to damage. J Mech Phys Solids 1992;40(1):1–16.

[75] Albertsen H, Ivens J, Peters P, Wevers M, Verpoest I. Interlaminar fracture toughness of CFRP influenced by fibre surface treatment: Part 1. Experimental results. Compos Sci Technol 1995;54:133–45.

[76] Sørensen BF, Jacobsen TK. Large-scale bridging in composites: R-curves and bridging laws. Compos Part A-Appl S 1998;29A:1443–51.

[77] Airoldi A, Dávila CG. Identification of material parameters for modelling delamination in the presence of fibre bridging. Compos Struct 2012;94:3240–9.

[78] Yokozeki T, Aoki T, Ogasawara T, Ishikawa T. Effects of layup angle and ply thickness on matrix crack interaction in contiguous plies of composite laminates. Compos Part A-Appl S 2005;36:1229–35.

[79] Quaresimin M, Carraro PA. On the investigation of the biaxial fatigue behaviour of unidirectional composites. Compos Part B-Eng 2013;54:200–8.

[80] Nairn JA. Matrix microcracking in composites. In: Zweben C, Kelly A, editors. Comprehensive Composite Materials; vol. 2; chap. 12. Oxford: Pergamon; 2000, p. 403–32.

[81] Camanho PP, Dávila CG, Pinho ST, Iannucci L, Robinson P. Prediction of in situ strengths and matrix cracking in composites under transverse tension and in-plane shear. Compos Part A-Appl S 2006;37:165–76.

[82] Andersons J, Joffe R, Spārniņš E, Rubenis O. Progressive cracking mastercurves of the transverse ply in a laminate. Polym Composite 2009;30(8):1175–82.

[83] García IG, Mantič V, Blázquez A, París F. Transverse crack onset and growth in cross-ply $[0/90]_s$ laminates under tension. Application of a coupled stress and energy criterion. Int J Solids Struct 2014;51:3844–56.

[84] Arteiro A, Catalanotti G, Melro AR, Linde P, Camanho PP. Micro-mechanical analysis of the *in situ* effect in polymer composite laminates. Compos Struct 2014;116:827–40.

[85] Arteiro A, Catalanotti G, Melro AR, Linde P, Camanho PP. Micro-mechanical analysis of the effect of ply thickness on the transverse compressive strength of polymer composites. Compos Part A-Appl S 2015;79:127–37.

[86] Tan SC, Nuismer RJ. A theory for progressive matrix cracking in composite laminates. J Compos Mater 1989;23:1029–47.

[87] Berthelot JM. Transverse cracking and delamination in cross-ply glass-fiber and carbon-fiber reinforced plastic laminates: Static and fatigue loading. Appl Mech Rev 2003;56(1):111–47.

[88] Huchette C. Sur la complémentarité des approches expérimentales et numériques pour la modélisation des mécanismes d'endommagement des composites stratifiés. Ph.D. thesis; Université Paris 6; Paris; 2005. In French.

[89] Laurin F, Carrere N, Huchette C, Maire JF. A multiscale hybrid approach for damage and final failure predictions of composite structures. J Compos Mater 2013;47(20–21):2713–47.

[90] Adolfsson E, Gudmundson P. Matrix crack initiation and progression in composite laminates subjected to bending and extension. Int J Solids Struct 1999;36:3131–69.

[91] Garrett KW, Bailey JE. Multiple transverse fracture in 90° cross-ply laminates of a glass fibre-reinforced polyester. J Mater Sci 1977;12:157–68.

[92] Parvizi A, Garrett KW, Bailey JE. Constrained cracking in glass fibre-reinforced epoxy cross-ply laminates. J Mater Sci 1978;13:195–201.

[93] Parvizi A, Bailey JE. On multiple transverse cracking in glass fibre epoxy cross-ply laminates. J Mater Sci 1978;13:2131–6.

[94] Flaggs DL, Kural MH. Experimental determination of the in situ transverse lamina strength in graphite/epoxy laminates. J Compos Mater 1982;16:103–16.

[95] Chang FK, Chen MH. The in situ ply shear strength distribution in graphite/epoxy laminated composites. J Compos Mater 1987;21:708–33.

[96] Boniface L, Smith PA, Bader MG. Transverse ply cracking in cross-ply CFRP laminates — Initiation or propagation controlled? J Compos Mater 1997;31(11):1080–112.

[97] Sebaey TA, Costa J, Maimí P, Batista Y, Blanco N, Mayugo JA. Measurement of the *in situ* transverse tensile strength of composite plies by means of the real time monitoring of microcracking. Compos Part B-Eng 2014;65:40–6.

[98] Dvorak GJ, Laws N. Analysis of progressive matrix cracking in composite laminates II. First ply failure. J Compos Mater 1987;21:309–29.

[99] Flaggs DL. Prediction of tensile matrix failure in composite laminates. J Compos Mater 1985;19:29–50.

[100] Chang FK, Chang KY. Post-failure analysis of bolted composite joints in tension or shear-out mode failure. J Compos Mater 1987;21:809–33.

[101] Chang KY, Liu S, Chang FK. Damage tolerance of laminated composites containing an open hole subjected to tensile loadings. J Compos Mater 1991;25:274–301.

[102] Puck A, Schürmann H. Failure analysis of FRP laminates by means of physically based phenomenological models. Compos Sci Technol 2002;62:1633–62.

[103] Dávila CG, Camanho PP, Rose CA. Failure criteria for FRP laminates. J Compos Mater 2005;39(4):323–45.

[104] Pinho ST, Dávila CG, Camanho PP, Iannucci L, Robinson P. Failure models and criteria for FRP under in-plane or three-dimensional stress states including shear non-linearity. Tech. Rep. NASA/TM-2005-213530; NASA Langley Research Center; Hampton, Virginia; 2005.

[105] Maimí P, Camanho PP, Mayugo JA, Dávila CG. A thermodynamically consistent damage model for advanced composites. Tech. Rep. NASA/TM-2006-214282; NASA Langley Research Center; Hampton, Virginia; 2006.

[106] Maimí P, Camanho PP, Mayugo JA, Dávila CG. A continuum damage model for composite laminates: Part I — Constitutive model. Mech Mater 2007;39:897–908.

[107] Mayugo JA, Camanho PP, Maimí P, Dávila CG. Analytical modelling of transverse matrix cracking of $\{\pm\theta/90^n\}^s$ composite laminates under multiaxial loading. Mech Adv Mater Struc 2010;17:237–45.

[108] Camanho PP, Bessa MA, Catalanotti G, Vogler M, Rolfes R. Modeling the inelastic deformation and fracture of polymer composites — Part II: Smeared crack model. Mech Mater 2013;59:36–49.

[109] Cuntze RG. Efficient 3D and 2D failure conditions for UD laminae and their application within the verification of the laminate design. Compos Sci Technol 2006;66:1081–96.

[110] Herakovich CT. Influence of layer thickness on the strength of angle-ply laminates. J Compos Mater 1982;16:216–27.

[111] Lavoie JA, Soutis C, Morton J. Apparent strength scaling in continuous ber composite laminates. Compos Sci Technol 2000;60:283–99.

[112] Lavoie JA, Adolfsson E. Stitch cracks in constraint plies adjacent to a cracked ply. J Compos Mater 2001;35(23):2077–97.

[113] Yokozeki T, Aoki T, Ishikawa T. Transverse crack propagation in the specimen width direction of CFRP laminates under static tensile loadings. J Compos Mater 2002;36(17):2085–99.

[114] Sasayama H, Kawabe K, Tomoda S, Ohsawa I, Kageyama K, Ogata N. Effect of lamina thickness on first ply failure in multidirectionally laminated composites. J Jpn Soc Compos Mater 2004;30(4):142–8. In Japanese.

[115] Pierron F, Green B, Wisnom MR. Full-field assessment of the damage process of laminated composite open-hole tensile specimens. Part I: Methodology. Compos Part A-Appl S 2007;38:2307–20.

[116] Pierron F, Green B, Wisnom MR, Hallett SR. Full-field assessment of the damage process of laminated composite open-hole tensile specimens. Part II: Experimental results. Compos Part A-Appl S 2007;38:2321–32.

[117] O'Higgins RM, McCarthy MA, McCarthy CT. Comparison of open hole tension characteristics of high strength glass and carbon fibre-reinforced composite materials. Compos Sci Technol 2008;68:2770–8.

[118] Takagi K, Nakatani H, Suga K, Koike A, Ogihara S. Effect of ply thickness on mechanical property of CFRP symmetric angle-ply laminates. In: Proceedings of ICCM-18. Jeju Island; 2011, p. 1–4.

[119] Ogihara S, Nakatani H. Effect of ply thickness on mechanical properties in CFRP angle-ply laminates. In: Proceedings of ECCM15. Venice; 2012, p. 1–6.

[120] Takeuchi H, Saito H, Kimpara I. Restraining effects of transverse cracking in 90° layer of thin-ply CFRP cross-ply laminates. In: Proceedings of ACCM-7. Taipei; 2010, p. 1–4.

[121] Erçin GH, Camanho PP, Xavier J, Catalanotti G, Mahdi S, Linde P. Size effects on the tensile and compressive failure of notched composite laminates. Compos Struct 2013;96:736–44.

[122] Arteiro A, Catalanotti G, Xavier J, Camanho PP. Notched response of non-crimp fabric thin-ply laminates. Compos Sci Technol 2013;79:97–114.

[123] Guillamet G, Turon A, Costa J, Renart J, Linde P, Mayugo JA. Damage occurrence at edges of non-crimp-fabric thin-ply laminates under off-axis uniaxial loading. Compos Sci Technol 2014;98:44–50.

[124] Herráez M, Mora D, Naya F, Lopes CS, González C, Llorca J. Transverse cracking of cross-ply laminates: A computational micromechanics perspective. Compos Sci Technol 2015;110:196–204.

[125] Jalalvand M, Wisnom MR, Hosseini-Toudeshky H, Mohammadi B. Experimental and numerical study of oblique transverse cracking in cross-ply laminates under tension. Compos Part A-Appl S 2014;67:140–8.

[126] París F, Blázquez A, McCartney LN, Barroso A. Characterization and evolution of matrix and interface related damage in $[0/90]_S$ laminates under tension. Part II: Experimental evidence. Compos Sci Technol 2010;70:1176–83.

[127] Chang FK, Scott RA, Springer GS. The effect of laminate configuration on characteristic lengths and rail shear strength. J Compos Mater 1984;18:290–6.

[128] Catalanotti G, Camanho PP, Marques AT. Three-dimensional failure criteria for fiber-reinforced laminates. Compos Struct 2013;95:63–79.

[129] Camanho PP, Arteiro A, Catalanotti G, Melro AR, Vogler M. Three-dimensional invariant-based failure criteria for transversely isotropic fibre-reinforced composites. In: Camanho PP, Hallett SR, editors. Numerical Modelling of Failure in Advanced Composite Materials; chap. 5. Cambridge: Woodhead Publishing; 2015, p. 111–50.

[130] Budiansky B, Fleck NA, Amazigo JC. On kink-band propagation in fiber composites. J Mech Phys Solids 1998;46(9):1637–53.

[131] Bažant ZP. Size effect. Int J Solids Struct 2000;37:69–80.

[132] Christensen RM. Compressive failure of composites using a matrix-controlled failure criterion with the kink band mechanism. Mech Mater 2000;32:505–9.

[133] Kawabe K, Sasayama H, Kageyama K, Ogata N. Effect of ply thickness on compressive properties in multidirectionally laminated composites. J Jpn Soc Compos Mater 2008;34:173–81. In Japanese.

[134] Yokozeki T, Aoki Y, Ogasawara T. Experimental characterization of strength and damage resistance properties of thin-ply carbon fiber/toughened epoxy laminates. Compos Struct 2008;82:382–9.

[135] Arteiro A, Catalanotti G, Xavier J, Camanho PP. Notched response of non-crimp fabric thin-ply laminates: Analysis methods. Compos Sci Technol 2013;88:165–71.

[136] Ogihara S, Takeda N. Interaction between transverse cracks and delamination during damage progress in CFRP cross-ply laminates. Compos Sci Technol 1995;54:395–404.

[137] Turon A, Camanho PP, Costa J, Dávila CG. A damage model for the simulation of delamination in advanced composites under variable-mode loading. Mech Mater 2006;38:1072–89.

[138] de Borst R, Remmers JJC. Computational Methods for Debonding in Composites. In: Camanho PP, Dávila CG, Pinho ST, Remmers JJC, editors. Mechanical Response of Composites; vol. 10 of *Computational Methods in Applied Sciences*; chap. 1. Dordrecht: Springer; 2008, p. 1–25.

[139] Herakovich CT. Mechanics of composites: A historical review. Mech Res Commum 2012;41:1–20.

[140] O'Brien TK. Characterization of delamination onset and growth in a composite laminate. NASA Technical Memorandum, NASA-TM-81940; NASA Langley Research Center; Hampton, Virginia; 1981.

[141] de Moura MFSF, Gonçalves JPM, Marques AT, de Castro PMST. Prediction of compressive strength of carbon-epoxy laminates containing delamination by using a mixed-mode damage model. Compos Struct 2000;50:151–7.

[142] Camanho PP, Dávila CG, de Moura MF. Numerical simulation of mixed-mode progressive delamination in composite materials. J Compos Mater 2003;37(16):1415–38.

[143] Turon A, Dávila CG, Camanho PP, Costa J. An engineering solution for mesh size effects in the simulation of delamination using cohesive zone models. Engng Fract Mech 2007;74:1665–82.

[144] Wisnom MR, Hallett SR. The role of delamination in strength, failure mechanisms and hole size effect in open hole tensile tests on quasi-isotropic laminates. Compos Part A-Appl S 2009;40:335–42.

[145] Ashari SE, Mohammadi S. Delamination analysis of composites by new orthotropic bimaterial extended finite element method. Int J Numer Meth Engng 2011;86:1507–43.

[146] Camanho PP, Arteiro A, Turon A, Costa J, Guillamet G. Structural integrity of thin-ply laminates. JEC Compos Mag 2012;71:49–50.

[147] Canturri C, Greenhalgh ES, Pinho ST, Ankersen J. Delamination growth directionality and the subsequent migration processes — The key to damage tolerant design. Compos Part A-Appl S 2013;54:79–87.

[148] Zubillaga L, Turon A, Maimí P, Costa J, Mahdi S, Linde P. An energy based failure criterion for matrix crack induced delamination in laminated composite structures. Compos Struct 2014;112:339–44.

[149] O'Brien TK. Analysis of local delaminations and their influence on composite laminate behavior. NASA Technical Memorandum 85728/USAAVSCOM Technical Report 83-B-6, NASA-TM-85728; NASA Langley Research Center/U.S. Army AVSCOM; Hampton, Virginia; 1984.

[150] Dávila CG, Camanho PP. Analysis of the effects of residual strains and defects on skin/stiffner debonding using decohesion elements. Tech. Rep. AIAA Paper 2003-1465; NASA Langley Research Center; Hampton, Virginia; 2003.

[151] Andersons J, König A. Dependence of fracture toughness of composite laminates on interface ply orientations and delamination growth direction. Compos Sci Technol 2004;64:2139–52.

[152] de Moura MFSF, Gonçalves JPM, Marques AT, de Castro PMST. Modelling compression failure after low velocity impact on laminated composites using interface elements. J Compos Mater 1997;31(15):1462–79.

[153] O'Brien TK. Interlaminar fracture toughness: the long and winding road to standardization. Compos Part B-Eng 1998;29B:57–62.

[154] Standard test method for mode I interlaminar fracture toughness of unidirectional fiber-reinforced polymer matrix composites, ASTM D5528 – 13. ASTM International; West Conshohocken, PA, USA; 2013.

[155] Wisnom MR. Size effects in the testing of fibre-composite materials. Compos Sci Technol 1999;59:1937–57.

[156] Camanho PP, Turon A, Costa J, Dávila CG. Simulation of delamination under high cycle fatigue in composite materials using cohesive models. Tech. Rep.; NASA Langley Research Center; Hampton, Virginia; 2006.

[157] Turon A, Costa J, Camanho PP, Dávila CG. Simulation of delamination propagation in composites under high-cycle fatigue by means of cohesive-zone models. Tech. Rep. NASA/TM-2006-214532; NASA Langley Research Center; Hampton, Virginia; 2006.

[158] Turon A, Costa J, Camanho PP, Dávila CG. Simulation of delamination in composites under high-cycle fatigue. Compos Part A-Appl S 2007;38:2270–82.

[159] Farahmand B. Fracture Mechanics of Metals, Composites, Welds, and Bolted Joints: Application of LEFM, EPFM, and FMDM theory. Boston / Dordrecht / London: Kluwer Academic Publishers; 2001.

[160] Chen BY, Tay TE, Baiz PM, Pinho ST. Numerical analysis of size effects on open-hole tensile composite laminates. Compos Part A-Appl S 2013;47:52–62.

[161] Czél G, Wisnom MR. Study of non-linear tensile behaviour of discontinuous carbon-epoxy prepreg composites. In: Proceedings of ICCM-19. Montréal; 2013, p. 1–9.

[162] Arca MA. Strengtheninh of L-shaped composite laminates using carbon nanotube reinforcement and thin ply non-crimp fabrics. Master's thesis; Graduate School of Natural and Applied Sciences, Middle East Techincal University; Ankara; 2014.

[163] Green BG, Wisnom MR, Hallett SR. An experimental investigation into the tensile strength scaling of notched composites. Compos Part A-Appl S 2007;38:867–78.

[164] Bažant ZP. Size effect on structural strength: a review. Arch Appl Mech 1999;69:703–25.

[165] Bažant ZP, Yavari A. Is the cause of size effect on structural strength fractal or energetic-statistical? Engng Fract Mech 2005;72:1–31.

[166] Xu X, Wisnom MR, Mahadik Y, Hallett SR. An experimental investigation into size effects in quasi-isotropic carbon/epoxy laminates with sharp and blunt notches. Compos Sci Technol 2014;100:220–7.

[167] Bažant ZP. Scaling laws in mechanics of failure. J Eng Mech-ASCE 1993;119(9):1828–44.

[168] Bažant ZP, Hubler MH, Salviato M, Kirane K, Le JL. Fracture scaling and safety of quasibrittle structures: atomistic basis, computational challenges and new advances. In: Proceedings of CFRAC 2013. Prague; 2013, p. 1–6.

[169] Lee J, Soutis C. Measuring the notched compressive strength of composite laminates: Specimen size effects. Compos Sci Technol 2008;68:2359–66.

[170] Soutis C, Lee J. Scaling effects in notched carbon fibre/epoxy composites loaded in compression. J Mater Sci 2008;43:6593–8.

[171] Wisnom MR, Khan B, Hallett SR. Size effects in unnotched tensile strength of unidirectional and quasi-isotropic carbon/epoxy composites. Compos Struct 2008;84:21–8.

[172] Wisnom MR, Hallett SR, Soutis C. Scaling effects in notched composites. J Compos Mater 2010;44(10):195–210.

[173] Nixon-Pearson OJ, Hallett SR, Withers PJ, Rouse J. Damage development in open-hole composite specimens in fatigue. Part 1: Experimental investigation. Compos Struct 2013;106:882–9.

[174] Hallett SR, Green BG, Jiang WG, Wisnom MR. An experimental and numerical investigation into the damage mechanisms in notched composites. Compos Part A-Appl S 2009;40:613–24.

[175] Waddoups ME, Eisenmann JR, Kaminski BE. Macroscopic fracture mechanics of advanced composite materials. J Compos Mater 1971;5:446–54.

[176] Whitney JM, Nuismer RJ. Stress fracture criteria for laminated composites containing stress concentrations. J Compos Mater 1974;8:253–65.

[177] Eriksson I, Aronsson CG. Strength of tensile loaded graphite epoxy laminates containing cracks, open and filled holes. J Compos Mater 1990;24:456–82.

[178] Bao G, Suo Z. Remarks on crack-bridging concepts. Appl Mech Rev 1992;45(8):355–66.

[179] Camanho PP, Erçin GH, Catalanotti G, Mahdi S, Linde P. A finite fracture mechanics model for the prediction of the open-hole strength of composite laminates. Compos Part A-Appl S 2012;43:1219–25.

[180] Martin E, Leguillon D, Carrère N. A coupled strength and toughness criterion for the prediction of the open hole tensile strength of a composite plate. Int J Solids Struct 2012;49:3915–22.

[181] Catalanotti G, Camanho PP. A semi-analytical method to predict net-tension failure of mechanically fastened joints in composite laminates. Compos Sci Technol 2013;76:69–76.

[182] Arteiro A, Catalanotti G, Xavier J, Camanho PP. Large damage capability of non-crimp fabric thin-ply laminates. Compos Part A-Appl S 2014;63:110–22.

[183] Camanho PP, Maimí P, Dávila CG. Prediction of size effects in notched laminates using continuum damage mechanics. Compos Sci Technol 2007;67:2715–27.

[184] Lee J, Soutis C. Thickness effect on the compressive strength of T800/924C carbon fibre-epoxy laminates. Compos Part A-Appl S 2005;36:213–27.

[185] Laffan MJ, Pinho ST, Robinson P, Iannucci L. Measurement of the in situ ply fracture toughness associated with mode I fibre tensile failure in FRP. Part I: Data reduction. Compos Sci Technol 2010;70:606–13.

[186] Chang JB, Goyal VK, Klug JC, Rome JI. Composite structures damage tolerance analysis methodologies. Tech. Rep. NASA/CR-2012-217347; NASA Langley Research Center; Hampton, Virginia; 2012.

[187] Catalanotti G, Xavier J, Camanho PP. Measurement of the compressive crack resistance curve of composites using the size effect law. Compos Part A-Appl S 2014;56:300–7.

[188] Catalanotti G, Xavier J. Measurement of the mode II intralaminar fracture toughness and R-curve of polymer composites using a modified Iosipescu specimen and the size effect law. Engng Fract Mech 2015;138:202–14.

[189] Dávila CG, Rose CA, Camanho PP. A procedure for superposing linear cohesive laws to represent multiple damage mechanisms in the fracture of composites. Int J Fract 2009;158:211–23.

[190] Maimí P, Camanho PP, Mayugo JA, Dávila CG. A continuum damage model for composite laminates: Part II — Computational implementation and validation. Mech Mater 2007;39:909–19.

[191] Pinho ST, Robinson P, Iannucci L. Fracture toughness of the tensile and compressive fiber failure modes in laminated composites. Compos Sci Technol 2006;66:2069–79.

[192] Laffan MJ, Pinho ST, Robinson P, McMillan AJ. Translaminar fracture toughness testing of composites: A review. Polym Test 2012;31:481–9.

[193] Standard test method for translaminar fracture toughness of laminated polymer matrix composite materials, ASTM E 1922 – 97. ASTM International; West Conshohocken, PA, USA; 1997.

[194] Coats TW, Harris CE. A progressive damage methodology for residual strength predictions of notched composite panels. Tech. Rep. NASA/TM-1998-207646; NASA Langley Research Center; Hampton, Virginia; 1998.

[195] Coats TW, Harris CE. A progressive damage methodology for residual strength predictions of notched composite panels. J Compos Mater 1999;33(23):2193–224.

[196] Caminero MA, Lopez-Pedrosa M, Pinna C, Soutis C. Damage monitoring and analysis of composite laminates with an open hole and adhesively bonded repairs using digital image correlation. Compos Part B-Eng 2013;53:76–91.

[197] Kongshavn I, Poursartip A. Experimental investigation of a strain-softening approach to predicting failure in notched fibre-reinforced composite laminates. Compos Sci Technol 1999;59:29–40.

[198] Li X, Hallett SR, Wisnom MR, Zobeiry N, Vaziri R, Poursartip A. Experimental study of damage propagation in Over-height Compact Tension tests. Compos Part A-Appl S 2009;40:1891–9.

[199] Standard test method for plane-strain fracture toughness of metallic materials, ASTM E 399 – 90 (Reapproved 1997). ASTM International; West Conshohocken, PA, USA; 1990.

[200] Catalanotti G, Camanho PP, Xavier J, Dávila CG, Marques AT. Measurement of resistance curves in the longitudinal failure of composites using digital image correlation. Compos Sci Technol 2010;70:1986–93.

[201] Laffan MJ, Pinho ST, Robinson P, Iannucci L. Measurement of the in situ ply fracture toughness associated with mode I fibre tensile failure in FRP. Part II: Size and lay-up effects. Compos Sci Technol 2010;70:614–21.

[202] Teixeira RF, Pinho ST, Robinson P. Translaminar fracture toughness of CFRP: from the toughness of individual plies to the toughness of the laminates. In: Proceedings of ECCM15. Venice; 2012, p. 1–8.

[203] Fernandes MFC. Translaminar fracture of thin-ply composite laminates. Master's thesis; Faculdade de Engenharia, Universidade do Porto; Porto; 2014.

[204] Bergan AC, Dávila CG, Leone FA, Awerbuch J, Tan TM. Mode I cohesive law characterization of through-crack propagation in a multidirectional laminate. Tech. Rep. NF1676L-18222; NASA Langley Research Center; Hampton, Virginia; 2014.

[205] Xu X, Wisnom MR, Mahadik Y, Hallett SR. Scaling of fracture response in Over-height Compact Tension tests. Compos Part A-Appl S 2015;69:40–8.

[206] Erçin GH. Stress gradient effects in laminated composites. Ph.D. thesis; Faculdade de Engenharia, Universidade do Porto; Porto; 2013.

[207] Catalanotti G, Camanho PP. Measurement of the intralaminar fracture toughness and R-curve of polymer composites laminates using the size effect law. In: Proceedings of ECCM16. Seville; 2014, p. 1–8.

[208] Blanco N, Trias D, Pinho ST, Robinson P. Intralaminar fracture toughness characterisation of woven composite laminates. Part II: Experimental characterisation. Engng Fract Mech 2014;131:361–70.

[209] Bažant ZP, Planas J. Fracture and Size Effect in Concrete and Other Quasibrittle Materials. CRC Press LLC; 1997.

[210] Bažant ZP, Daniel IM, Z ZL. Size effect and fracture characteristics of composite laminates. Mater Struct 1996;118:317–24.

[211] Bažant ZP, Kim JK, Pfeiffer PA. Nonlinear fracture properties from size effect tests. J Struct Eng-ASCE 1986;112:289–307.

[212] Camanho PP, Catalanotti G. On the relation between the mode I fracture toughness of a composite laminate and that of a 0° ply: Analytical model and experimental validation. Engng Fract Mech 2011;78:2535–46.

[213] Aoki Y, Suemasu H, Ishikawa T. Damage propagation in CFRP laminates subjected to low velocity impact and static indentation. Adv Compos Mater 2007;16:45–61.

[214] Sutherland LS, Soares CG. The use of quasi-static testing to obtain the low-velocity impact damage resistance of marine GRP laminates. Compos Part B-Eng 2012;43:1459–67.

[215] Guillamet G, Liv Y, Turon A, Marín L, González EV, Mayugo JA, et al. Design of non-conventional CFRP laminates for improved damage resistance and damage tolerance. In: Proceedings of ECCM16. Seville; 2014, p. 1–7.

[216] Hitchen SA, Kemp RMJ. The effect of stacking sequence on impact damage in a carbon fibre/epoxy composite. Composites 1995;26:207–14.

[217] Richardson MOW, Wisheart MJ. Review of low-velocity impact properties of composite materials. Compos Part A-Appl S 1996;27A:1123–31.

[218] Reis L, de Freitas M. Damage growth analysis of low velocity impacted composite panels. Compos Struct 1997;38(1–4):509–15.

[219] de Freitas M, Reis L. Failure mechanisms on composite specimens subjected to compression after impact. Compos Struct 1998;42:365–73.

[220] González EV, Maimí P, Camanho PP, Lopes CS, Blanco N. Effects of ply clustering in laminated composite plates under low-velocity impact loading. Compos Sci Technol 2011;71:805–17.

[221] Yokozeki T, Kuroda A, Yoshimura A, Ogasawara T, Aoki T. Damage characterization in thin-ply composite laminates under out-of-plane transverse loading. Compos Struct 2010;93:49–57.

[222] Sebaey TA, González EV, Lopes CS, Blanco N, Costa J. Damage resistance and damage tolerance of dispersed CFRP laminates: Effect of ply clustering. Compos Struct 2013;106:96–103.

[223] Fuoss E, Straznicky PV, Poon C. Effects of stacking sequence on the impact resistance in composite laminates — Part 1: parametric study. Compos Struct 1998;41:67–77.

[224] Saito H, Morita M, Kawabe K, Kanesaki M, Takeuchi H, Tanaka M, et al. Effect of ply-thickness on impact damage morphology in CFRP laminates. J Reinf Plast Comp 2011;30:1097–106.

[225] Olsson R. Analytical prediction of damage due to large mass impact on thin ply composites. Compos Part A-Appl S 2015;72:184–91.

[226] González EV, Guillamet G, Costa J, Cugnoni J, Turon A, Maimí P, et al. Drop-weight impact tests and compression after impact tests on ultra-thin ply based laminates. Journal not defined; 2014. In preparation.

[227] Lopes CS, Seresta O, Coquet Y, Gürdal Z, Camanho PP, Thuis B. Low-velocity impact damage on dispersed stacking sequence laminates. Part I: Experiments. Compos Sci Technol 2009;69:926–36.

[228] Lopes CS, Camanho PP, Gürdal Z, Maimí P, González EV. Low-velocity impact damage on dispersed stacking sequence laminates. Part II: Numerical simulations. Compos Sci Technol 2009;69:937–47.

[229] Naghipour P, Bartsch M, Voggenreiter H. Simulation and experimental validation of mixed mode delamination in multidirectional CF/PEEK laminates under fatigue loading. Int J Solids Struct 2011;48:1070–81.

[230] Allegri G, Wisnom MR. A non-linear damage evolution model for mode II fatigue delamination onset and growth. Int J Fatigue 2012;43:226–34.

[231] Nishikawa Y, Miki T, Okubo K, Fujii T, Kawabe K. Fatigue behaviour of plain-woven CF/epoxy composites using spread tows (effect of tow thickness on crack formation). Trans Jpn Soc Mech Eng A 2005;71(710):1356–61. In Japanese.

[232] Lee WHCSS, Yeh JT. Three-dimensional contact stress analysis of a composite laminate with bolted joint. Compos Struct 1995;30:287–97.

[233] Camanho PP, Matthews FL. Stress analysis and strength prediction of mechanically fastened joints in FRP: a review. Compos Part A-Appl S 1997;28A:529–47.

[234] Camanho PP, Tavares CML, de Oliveira R, Marques AT, Ferreira AJM. Increasing the efficiency of composite single-shear lap joints using bonded inserts. Compos Part B-Eng 2005;36:372–83.

[235] Camanho PP, Lambert M. A design methodology for mechanically fastened joints in laminated composite materials. Compos Sci Technol 2006;66:3004–20.

[236] Cooper C, Turvey GJ. Effects of joint geometry and bolt torque on the structural performance of single bolt tension joints in pultruded GRP sheet material. Compos Struct 1995;32:217–26.

[237] Standard test method for bearing response of polymer matrix composite laminates, ASTM D5961/D5961M – 13. ASTM International; West Conshohocken, PA, USA; 2013.

[238] Camanho PP. Application of numerical methods to the strength prediction of mechanically fastened joints in composite laminates. Ph.D. thesis; Centre for Composite Materials, Imperial College of Science, Technology and Medicine; London; 1999.

[239] Camanho PP, Matthews FL. Delamination onset prediction in mechanically fastened joints in composite laminates. J Compos Mater 1999;33(10):906–27.

[240] Garbo SP, Ogonowski JM. Effect of variances and manufacturing tolerances on the design strength and life of mechanically fastened composite joints. Volume 1 - Methodology development and data evaluation. Final report AFWAL-TR-81-3041; Flight Dynamics Laboratory, Air Force Wright Aeronautical Laboratories; Air Force Systems Command, Wright-Patterson Air Force Base, Ohio; 1981.

[241] Moon JB, Kim MG, Kim CG, Bhowmik S. Improvement of tensile properties of CFRP composites under LEO space environment by applying MWNTs and thin-ply. Compos Part A-Appl S 2011;42:694–701.

[242] Czél G, Jalalvand M, Wisnom MR. Development of pseudo-ductile hybrid composites with discontinuous carbon- and continuous glass prepregs. In: Proceedings of ECCM16. Seville; 2014, p. 1–8.

[243] Fuller J, Wisnom MR. Damage suppression in thin-ply angle-ply carbon/epoxy laminates. In: Proceedings of ICCM-19. Montréal; 2013, p. 1–9.

[244] Fuller J, Wisnom MR. Pseudo-ductility and damage suppression in thin ply CFRP angle-ply laminates. Compos Part A-Appl S 2015;69:64–71.

[245] Fuller J, Wisnom MR. Exploration of the potential for pseudo-ductility in thin ply CFRP angle-ply laminates via an analytical method. Compos Sci Technol 2015;112:8–15.

[246] Fuller J, Jalalvand M, Wisnom MR. Pseudo-ductility by fragmentation of central unidirectional plies in thin CFRP angle-ply laminates. In: Proceedings of ECCM16. Seville; 2014, p. 1–9.

[247] Baley C, Lan M, Davies P, Cartié D. Porosity in ocean racing yacht composites: a review. Appl Compos Mater 2015;22:13–28.

[248] Furtado C, Arteiro A, Catalanotti G, Xavier J, Camanho PP. Selective ply-level hybridisation for improved notched response of composite laminates. Compos Struct 2016;145:1–14.

[249] Bäcklund J, Aronsson CG. Tensile fracture of laminates with holes. J Compos Mater 1986;20:259–86.

[250] Geers MGD. Experimental Analysis and Computational Modelling of Damage Fracture. Ph.D. thesis; Technische Universiteit Eindhoven; Eindhoven; 1997.

[251] Lecompte D, Smits A, Bossuyt S, Sol H, Vantomme J, Van Hemelrijck D, et al. Quality assessment of speckle patterns for digital image correlation. Opt Laser Eng 2006;44:1132–45.

[252] Grégoire D. Initiation, propagation, arrêt et redémarrage de fissures sous impact. Ph.D. thesis; L'Institut National des Sciences Appliquées de Lyon; 2008.

[253] Crammond G, Boyd SW, Dulieu-Barton JM. Speckle pattern quality assessment for digital image correlation. Opt Laser Eng 2013;51:1368–78.

[254] Yaofeng S, Pang JHL. Study of optimal subset size in digital image correlation of speckle pattern images. Opt Laser Eng 2007;45:967–74.

[255] Haddadi H, Belhabib S. Use of rigid-body motion for the investigation and estimation of the measurement errors related to digital image correlation technique. Opt Laser Eng 2008;46:185–96.

[256] Xavier J, de Jesus AMP, Morais JJL, Pinto JMT. Stereovision measurements on evaluating the modulus of elasticity of wood by compression tests parallel to the grain. Constr Build Mater 2012;26(1):207–15.

[257] GOM International AG. Bremgarterstrasse 89B, CH-8967 Widen, Switzerland; 2000.

[258] Tan SC. Stress Concentrations in Laminated Composites. Lancaster: Technomic; 1994.

[259] Charrier JS. Développement de méthodologies dédiées à l'analyse robuste de la tenue de structures composites sous chargements complexes tridimensionnels. Ph.D. thesis; École Nationale Supérieure d'Arts et Métiers; Paris; 2013. In French.

[260] Melro AR. Analytical and numerical modelling of damage and fracture of advanced composites. Ph.D. thesis; Faculdade de Engenharia, Universidade do Porto; Porto; 2011.

[261] Melro AR, Camanho PP, Pires FMA, Pinho ST. Numerical simulation of the non-linear deformation of 5-harness satin weaves. Comp Mater Sci 2012;61:116–26.

[262] Standard test method for tensile properties of polymer matrix composite materials, ASTM D3039/D3039M – 14. ASTM International; West Conshohocken, PA, USA; 2014.

[263] Koerber H, Xavier J, Camanho PP, Essa YE, Martín de la Escalera F. High strain rate behaviour of 5-harness-satin weave fabric carbonepoxy composite under compression and combined compressionshear loading. Int J Solids Struct 2015;54:172–82.

[264] Bing Q, Sun CT. Specimen size effect in off-axis compression tests of fiber composites. Compos Part B-Eng 2008;39:20–6.

[265] Koerber H, Xavier J, Camanho PP. High strain rate characterisation of unidirectional carbon-epoxy IM7-8552 in transverse compression and in-plane shear using digital image correlation. Mech Mater 2010;42:1004–19.

[266] Vogler M, Rolfes R, Camanho PP. Modeling the inelastic deformation and fracture of polymer composites — Part I: Plasticity model. Mech Mater 2013;59:50–64.

[267] Koerber H, Vogler M, Kuhn P, Camanho PP. Experimental characterisation and modelling of nonlinear stress-strain behaviour and strain rate effects for unidirectional carbon-epoxy. In: Proceedings of ECCM16. Seville; 2014, p. 1–8.

[268] Mandel U, Taubert R, Hinterhölzl R. Mechanism based nonlinear constitutive model for composite laminates subjected to large deformations. Compos Struct 2015;132:98–108.

[269] Suo Z, Bao G, Fan B, Wang TC. Orthotropy rescaling and implications for fracture in composites. Int J Solids Struct 1991;28(2):235–48.

[270] Bao G, Ho S, Suo Z, Fan B. The role of material orthotropy in fracture specimens for composites. Int J Solids Struct 1992;29(9):1105–16.

[271] Bažant ZP, Kim JJH, Daniel IM, Becq-Giraudon E, Zi G. Size effect in compression strength of fiber composites failing by kink band propagation. Int J Fracture 1999;95:103–41.

[272] Standard test method for open-hole compressive strength of polymer matrix composite laminates, ASTM D6484/D6484M – 14. ASTM International; West Conshohocken, PA, USA; 2014.

[273] Standard test method for open-hole tensile strength of polymer matrix composite laminates, ASTM D5766/D5766M – 11. ASTM International; West Conshohocken, PA, USA; 2011.

[274] Camanho PP, Fink A, Obst A, Pimenta S. Hybrid tytanium-CFRP laminates for high-performance bolted joints. Compos Part A-Appl S 2009;40:1826–37.

[275] ABAQUS 6.12 Documentation. Dassault Systèmes Simulia Corp.; Providence, RI, USA; 2012.

[276] Iarve EV, Mollenhauer D, Kim R. Theoretical and experimental investigation of stress redistribution in open hole composite laminates due to damage accumulation. Compos Part A-Appl S 2005;36:163–71.

[277] Bažant ZP, Kazemi MT. Size effect in fracture of ceramics and its use to determine fracture energy and effective process zone length. J Am Ceram Soc 1990;73(7):1841–53.

[278] Matlab R2014a Documentation. MathWorks; Natick, MA, USA; 2014.

[279] Bažant ZP, Kazemi MT. Determination of fracture energy, process zone length and brittleness number from size effect, with application to rock and concrete. Int J Fract 1990;44:111–31.

[280] Bažant ZP, Gettu R, Kazemi MT. Identification of nonlinear fracture properties from size effect tests and structural analysis based on geometry-dependent *R*-curves. Int J Rock Mech Min 1991;28(1):43–51.

[281] Vogler TJ, Kyriakides S. On the initiation and growth of kink bands in fiber composites: Part I. experiments. Int J Solids Struct 2001;38:2639–51.

[282] Dávila CG, Camanho PP. Failure criteria for FRP laminates in plane stress. Tech. Rep. NASA/TM-2003-212663; NASA Langley Research Center; Hampton, Virginia; 2003.

[283] Tada H, Paris PC, Irwin GR. The stress analysis of cracks handbook. Hellertown, Pennsylvania: Del Research Corporation; 1973.

[284] Camanho PP, Tavares CML, Almeida JB, Bandeira PM, Portela PM, Guedes RM. Test plan and test procedures. Technical note ICFRP_INEGI_TN_002; INEGI, CEFAD — Structural Integrity Division; 2003.

[285] Gutkin R, Pinho ST, Robinson P, Curtis PT. On the transition from shear-driven fibre compressive failure to fibre kinking in notched CFRP laminates under longitudinal compression. Compos Sci Technol 2010;70:1223–31.

[286] Chen DL, Weiss B, Stickler R. A new geometric factor formula for a center cracked plate tensile specimen of finite width. Int J Fracture 1992;55:R3–8.

[287] Abisset E, Daghia F, Ladevèze P. On the validation of a damage mesomodel for laminated composites by means of open-hole tensile tests on quasi-isotropic laminates. Compos Part A-Appl S 2011;42:1515–24.

[288] Maimí P, González EV, Camanho PP. Comment to the paper 'Analysis of progressive matrix cracking in composite laminates II. First ply failure'. J Compos Mater 2014;48(9):1139–41.

[289] van der Meer FP, Dávila CG. Cohesive modeling of transverse cracking in laminates under in-plane loading with a single layer of elements per ply. Int J Solids Struct 2013;50:3308–18.

[290] Dávila CG, Rose CA, Iarve EV. Modeling fracture and complex crack networks in laminated composites. In: Mantič V , editor. Mathematical Methods and Models in Composites; vol. 5 of *Computational and Experimental Methods in Structures, Aliabadi FMH, Series editor*; chap. 8. London: Imperial College Press; 2014, p. 297–347.

[291] Prombut P. Caracterisation de la propagation de delaminage des stratifies composites multidirectionnels. Ph.D. thesis; Université Toulouse III Paul Sabatier; Toulouse; 2007. In French.

[292] Ladevèze P, Lubineau G, Violeau D, Marsal D. A computational damage micromodel for laminate composites. In: Sadowski T, editor. IUTAM Symposium on Multiscale Modelling of Damage and Fracture Processes in Composite Materials. Springer; 2006, p. 1–12.

[293] Soden PD, Kaddour AS, Hinton MJ. Recommendations for designers and researchers resulting from the world-wide failure exercise. Compos Sci Technol 2004;64:589–604.

[294] González C, Llorca J. Mechanical behavior of unidirectional fiber-reinforced polymers under transverse compression: Microscopic mechanisms and modeling. Compos Sci Technol 2007;67:2795–806.

[295] Melro AR, Camanho PP, Pinho ST. Generation of random distribution of fibres in long-fibre reinforced composites. Compos Sci Technol 2008;68:2092–102.

[296] Trias D, Costa J, Turon A, Hurtado JE. Determination of the critical size of a statistical representative volume element (SRVE) for carbon reinforced polymers. Acta Mater 2006;54:3471–84.

[297] Trias D, Costa J, Mayugo JA, Hurtado JE. Random models versus periodic models for fiber reinforced composites. Comp Mater Sci 2006;38:316–24.

[298] Melro AR, Camanho PP, Pires FMA, Pinho ST. Micromechanical analysis of polymer composites reinforced by unidirectional fibres: Part I - Constitutive modelling. Int J Solids Struct 2013;50:1897–905.

[299] Melro AR, Camanho PP, Pires FMA, Pinho ST. Micromechanical analysis of polymer composites reinforced by unidirectional fibres: Part II - Micromechanical analyses. Int J Solids Struct 2013;50:1906–15.

[300] Bažant ZP, Oh BH. Crack band theory for fracture of concrete. Mater Struct 1983;16(93):155–77.

[301] Fiedler B, Hojo M, Ochiai S, Schulte K, Ando M. Failure behavior of an epoxy matrix under different kinds of static loading. Compos Sci Technol 2001;61:1615–24.

[302] Guild FJ, Potter KD, Heinrich J, Adams RD, Wisnom MR. Understanding and control of adhesive crack propagation in bonded joints between carbon fibre composite adherents II. Finite element analysis. Int J Adhes Adhes 2001;21:445–53.

[303] Benzeggagh M, Kenane M. Measurement of mixed-mode delamination fracture toughness of unidirectional glass/epoxy composites with mixed-mode bending apparatus. Compos Sci Technol 1996;56:439–49.

[304] Varna J, Berglund LA, Ericson ML. Transverse single-fibre test for interfacial debonding in composites: 2. Modelling. Compos Part A-Appl S 1997;28A:317–26.

[305] Vaughan TJ, McCarthy CT. Micromechanical modelling of the transverse damage behaviour in fibre reinforced composites. Compos Sci Technol 2011;71:388–96.

[306] Canal LP, González C, Molina-Aldareguía JM, Segurado J, Llorca J. Application of digital image correlation at the microscale in fiber-reinforced composites. Compos Part A-Appl S 2012;43:1630–8.

[307] Hahn HT, Tsai SW. Nonlinear elastic shear behavior of unidirectional composite laminae. J Compos Mater 1973;7(1):102–18.

[308] Bai X, Bessa MA, Melro AR, Camanho PP, Guo L, Liu WK. High-fidelity micro-scale modeling of the thermo-visco-plastic behavior of carbon fiber polymer matrix composites. Compos Struct 2015;134:132–41.

[309] Tavares RP, Melro AR, Bessa MA, Turon A, Liu WK, Camanho PP. Mechanics of hybrid polymer composites: analytical and computational study. Comput Mech 2016;57:405–21.

[310] Arteiro A, Melro AR, Camanho PP. Mechanics of thin-ply laminates. In: Suleman A, Camanho PP, editors. Proceedings of the IV ECCOMAS Thematic Conference on the Mechanical Response of Composites. Ponta Delgada, S. Miguel — Azores; 2013, p. 1–2.

[311] Gan KW, Wisnom MR, Hallett SR. Effect of high through-thickness compressive stress on fibre direction tensile strength of carbon/epoxy composite laminates. Compos Sci Technol 2014;90:1–8.

[312] Hinton MJ, Kaddour AS, Soden PD. Evaluation of failure prediction in composite laminates: background to 'part C' of the exercise. Compos Sci Technol 2004;64:321–7.

[313] Puck A. Calculating the strength of glass fibre/plastic laminates under combined load. Kunstst German Plast 1969;55:18–19. Original in German.

[314] Puck A, Schneider W. On failure mechanism and failure criteria of filamentwound glass-fibre/resin composites. Plast Polym 1969;37:33–44.

[315] Tsai SW, Wu EM. A general theory of strength for anisotropic materials. J Compos Mater 1971;5(1):58–80.

[316] Hashin Z. Failure criteria for unidirectional fibre composites. J Appl Mech 1980;47:329–34.

[317] Hinton MJ, Soden PD. Predicting failure in composite laminates: the background to the exercise. Compos Sci Technol 1998;58:1001–10.

[318] Cuntze RG, Freund A. The predictive capability of failure mode concept-based strength criteria for multidirectional laminates. Compos Sci Technol 2004;64:343–77.

[319] Camanho PP, Arteiro A, Melro AR, Catalanotti G, Vogler M. Three-dimensional invariant-based failure criteria for fibre-reinforced composites. Int J Solids Struct 2015;55:92–107.

[320] Christensen RM. Stress based yield/failure criteria for fiber composites. Int J Solids Struct 1997;34(5):529–43.

[321] Liu KL, Tsai SW. A progressive quadratic failure criterion for a laminate. Compos Sci Technol 1998;58:1023–32.

[322] Sun CT, Tao J. Prediction of failure envelopes and stress/strain behaviour of composite laminates. Compos Sci Technol 1998;58:1125–36.

[323] Hart-Smith LJ. Predictions of a generalized maximum-shear-stress failure criterion for certain fibrous composite laminates. Compos Sci Technol 1998;58:1179–208.

[324] Sun CT, Tao J, Kaddour AS. The prediction of failure envelopes and stress/strain behavior of composite laminates: comparison with experimental results. Compos Sci Technol 2002;62:1673–82.

[325] Kuraishi A, Tsai SW, Liu KKS. A progressive quadratic failure criterion, part B. Compos Sci Technol 2002;62:1683–95.

[326] Hart-Smith LJ. Predictions of the original and truncated maximum-strain failure models for certain fibrous composite laminates. Compos Sci Technol 1998;58:1151–78.

[327] Puck A, Schürmann H. Failure analysis of FRP laminates by means of physically based phenomenological models. Compos Sci Technol 1998;58:1045–67.

[328] Pinho ST, Iannucci L, Robinson P. Physically-based failure models and criteria for laminated fibre-reinforced composites with emphasis on fibre kinking: Part I: Development. Compos Part A-Appl S 2006;37:63–73.

[329] Vogler M, Ernst G, Rolfes R. Invariant based transversely-isotropic material and failure model for fiber-reinforced polymers. CMC-Comput Mater Con 2010;16(1):25–49.

[330] Christensen RM, DeTeresa SJ. Failure plane orientations for transverse loading of a unidirectional fiber composite. Int J Solids Struct 2003;40:7055–62.

[331] Boehler JP, editor. Applications of Tensor Functions in Solid Mechanics. CISM Courses and Lectures — No. 292; Wien: Springer - Verlag; 1987.

[332] Spencer AJM. Kinematic constraints, constitutive equations and failure rules for anisotropic materials. In: Boehler JP, editor. Applications of Tensor Functions in Solid Mechanics; chap. 10. CISM Courses and Lectures — No. 292; Wien: Springer - Verlag; 1987, p. 187–201.

[333] Boehler JP. Yielding and failure of transversely isotropic solids. In: Boehler JP, editor. Applications of Tensor Functions in Solid Mechanics; chap. 5. CISM Courses and Lectures — No. 292; Wien: Springer - Verlag; 1987, p. 66–97.

[334] Hine PJ, Duckett RA, Kaddour AS, Hinton MJ, Wells GM. The effect of hydrostatic pressure on the mechanical properties of glass fibre/epoxy unidirectional composites. Compos Part A-Appl S 2005;36:279–289.

[335] Sun CT, Berreth SP. A new end tab design for off-axis tension test of composite materials. J Compos Mater 1988;22:766–79.

[336] Sun CT, Chung I. An oblique end-tab design for testing off-axis composite specimens. Composites 1993;24(8):619–23.

[337] Wiegand J, Petrinic N, Elliott B. An algorithm for determination of the fracture angle for the three-dimensional Puck matrix failure criterion for UD composites. Compos Sci Technol 2008;68:2511–7.

[338] Thom H. A review of the biaxial strength of fibre-reinforced plastics. Compos Part A-Appl S 1998;29A:869–86.

[339] Hoppel CPR, Bogetti TA, Gillespie, Jr. JW. Literature review — Effects of hydrostatic pressure on the mechanical behavior of composite materials. J Thermoplast Compos 1995;8:375–409.

[340] Pae KD. Influence of hydrostatic pressure on the mechanical behavior and properties of unidirectional, laminated, graphite-fiber/epoxy-matrix thick composites. Compos Part B-Eng 1996;27B:599–611.

[341] Bessa M. Meso-mechanical model of the structural integrity of advanced composite laminates. Master's thesis; Faculdade de Engenharia, Universidade do Porto; Porto; 2010.

[342] Swanson SR, Messick MJ, Tian Z. Failure of carbon/epoxy lamina under combined stress. J Compos Mater 1987;21:619–630.

[343] Daniel IM, Luo JJ, Schubel PM, Werner BT. Interfiber / interlaminar failure of composites under multi-axial states of stress. Compos Sci Technol 2009;69:764–771.

[344] Daniel IM, Werner BT, Fenner JS. Strain-rate-dependent failure criteria for composites. Compos Sci Technol 2011;71:357–364.

[345] Soden PD, Hinton MJ, Kaddour AS. Biaxial test results for strength and deformation of a range of E-glass and carbon fibre reinforced composite laminates: failure exercise benchmark data. Compos Sci Technol 2002;62:1489–514.

[346] Soden PD, Hinton MJ, Kaddour AS. Lamina properties, lay-up configurations and loading conditions for a range of fibre-reinforced composites laminates. Compos Sci Technol 1998;58:1011–22.

[347] Voloshin A, Arcan M. Failure of unidirectional fiber-reinforced materials - New methodology and results. Exp Mech 1980;20:280–4.

[348] Swanson SR, Qian Y. Multiaxial characterization of T800/3900-2 carbon/epoxy composites. Compos Sci Technol 1992;43:197–203.

[349] Totry E, González C, Llorca J. Failure locus of fiber-reinforced composites under transverse compression and out-of-plane shear. Compos Sci Technol 2008;68:829–39.

[350] Totry E, González C, Llorca J. Prediction of the failure locus of C/PEEK composites under transverse compression and longitudinal shear through computational mechanics. Compos Sci Technol 2008;68:3128–36.

[351] Melro AR, Camanho PP, Pinho ST. Influence of geometrical parameters on the elastic response of unidirectional composite materials. Compos Struct 2012;94:3223–31.

[352] McCarthy CT, O'Higgins RM, Frizzell RM. A cubic spline implementation of non-linear shear behaviour in three-dimensional progressive damage models for composite laminates. Compos Struct 2010;92:173–81.

[353] Camanho PP, Matthews FL. A progressive damage model for mechanically fastened joints in composite laminates. J Compos Mater 1999;33(24):2248–80.

[354] McCarthy CT, McCarthy MA. Three-dimensional finite element analysis of single-bolt, single-lap composite bolted joints: Part II - effects of bolt-hole clearance. Compos Struct 2005;71:159–75.

[355] Zhou Y, Yazdani-Nezhad H, McCarthy MA, Wan X, McCarthy C. A study of intra-laminar damage in double-lap, multi-bolt, composite joints with variable clearance using continuum damage mechanics. Compos Struct 2014;116:441–52.

[356] Palazotto AN, Herup EJ, Gummadi LNB. Finite element analysis of low-velocity impact on composite sandwich. Compos Struct 2000;49:209–27.

[357] Foo CC, Chai GB, Seah LK. A model to predict low-velocity impact response and damage in sandwich composites. Compos Sci Technol 2008;68:1348–56.

[358] Wang SX, Wu LZ, Ma L. Low-velocity impact and residual tensile strength analysis to carbon fiber composite laminates. Mater Design 2010;31:118–25.

[359] Batra R, Gopinath G, Zheng JQ. Damage and failure in low energy impact of fiber-reinforced polymeric composite laminates. Compos Struct 2012;94:540–7.

[360] Maio L, Monaco E, Ricci F, Lecce L. Simulation of low velocity impact on composite laminates with progressive failure analysis. Compos Struct 2013;103:75–85.

[361] Farooq U, Myler P. Ply level failure prediction of carbon fibre reinforced laminated composite panels subjected to low velocity drop-weight impact using adaptive meshing techniques. Acta Astronaut 2014;102:169–177.

[362] ANSYS Release 15.0 Documentation. ANSYS, Inc.; Canonsburg, PA, USA; 2013.

[363] Totry E, Molina-Aldareguía JM, González C, Llorca J. Effect of fiber, matrix and interface properties on the in-plane shear deformation of carbon-fiber reinforced composites. Compos Sci Technol 2010;70:970–80.

[364] Vaughan TJ, McCarthy CT. A micromechanical study on the effect of intra-ply properties on transverse shear fracture in fibre reinforced composites. Compos Part A-Appl S 2011;42:1217–28.

[365] Canal LP, González C, Segurado J, Llorca J. Intraply fracture of fiber reinforced composites: Microscopic mechanisms and modeling. Compos Sci Technol 2012;72:1223–32.

[366] Pinho ST, Iannucci L, Robinson P. Physically-based failure models and criteria for laminated fibre-reinforced composites with emphasis on fibre kinking. Part II: FE implementation. Compos Part A-Appl S 2006;37:766–77.

[367] Zobeiry N, Forghani A, McGregor C, Vaziri R, Poursartip A. Progressive damage modeling of composite materials under both tensile and compressive loading regimes. In: Camanho PP, Dávila CG, Pinho ST, Remmers JJC, editors. Mechanical Response of Composites; vol. 10 of *Computational Methods in Applied Sciences*; chap. 9. Dordrecht: Springer; 2008, p. 179–95.

[368] Van der Meer FP, Sluys LJ. A phantom node formulation with mixed mode cohesive law for splitting in laminates. Int J Fract 2009;158:107–24.

[369] Van der Meer FP, Sluys LJ. Mesh-independent modeling of both distributed and discrete matrix cracking in interaction with delamination in composites. Engng Fract Mech 2010;77:719–35.

[370] Iarve EV, Gurvich MR, Mollenhauer DH, Rose CA, Dávila CG. Mesh-independent matrix cracking and delamination modeling in laminated composites. Int J Numer Meth Engng 2011;88:749–73.

[371] Song K, Li Y, Rose CA. Continuum damage mechanics models for the analysis of progressive failure in open-hole tension laminates. Tech. Rep. NF1676L-12382; NASA Langley Research Center; Hampton, Virginia; 2011.

[372] Areias P, Rabczuk T, Camanho PP. Initially rigid cohesive laws and fracture based on edge rotations. Comput Mech 2013;52:931–47.

[373] Benvenuti E. A regularized XFEM framework for embedded cohesive interfaces. Comput Methods Appl Mech Engrg 2008;197:4367–78.

[374] Belytschko T, Song JH. Coarse-graining of multiscale crack propagation. Int J Numer Meth Engng 2010;81:537–63.

[375] Rolfes R, Ernst G, Vogler M, Hühne C. Material and failure models for textile composites. In: Camanho PP, Dávila CG, Pinho ST, Remmers JJC, editors. Mechanical Response of Composites; vol. 10 of *Computational Methods in Applied Sciences*; chap. 2. Dordrecht: Springer; 2008, p. 27–56.

[376] Jirásek M, Grassl P. Evaluation of directional mesh bias in concrete fracture simulations using continuum damage models. Engng Fract Mech 2008;75:1921–43.

[377] Soden PD, Hinton MJ, Kaddour AS. A comparison of the predictive capabilities of current failure theories for composite laminates. Compos Sci Technol 1998;58:1225–54.

[378] Hinton MJ, Kaddour AS, Soden PD. Evaluation of failure prediction in composite laminates: background to 'part B' of the exercise. Compos Sci Technol 2002;62:1481–8.

[379] Hinton MJ, Kaddour AS, Soden PD. A comparison of the predictive capabilities of current failure theories for composite laminates, judged against experimental evidence. Compos Sci Technol 2002;62:1725–97.

[380] Kaddour AS, Hinton MJ, Soden PD. A comparison of the predictive capabilities of current failure theories for composite laminates: additional contributions. Compos Sci Technol 2004;64:449–76.

[381] Hinton MJ, Kaddour AS, Soden PD. A further assessment of the predictive capabilities of current failure theories for composite laminates: comparison with experimental evidence. Compos Sci Technol 2004;64:549–58.

[382] Crisfield MA. Non-linear Finite Element Analysis of Solids and Structures; vol. 1. Chichester: John Wiley & Sons; 1991.

[383] Branco AAPD. Virtual testing of advanced polymer composite materials. Master's thesis; Faculdade de Engenharia, Universidade do Porto; Porto; 2015.

[384] González EV, Maimí P, Turon A, Camanho PP, Costa J. Simulation of delamination by means of cohesive elements using an explicit finite element code. CMC-Comput Mater Con 2009;9(1):51–92.

[385] Tsai SW, Sihn S, Melo JDD. Trace-based stiffness for a universal design of carbon-fiber reinforced composite structures. Compos Sci Technol 2015;118:23–30.

[386] Tsai SW, Melo JDD. Composite Materials Design and Testing — Unlocking mystery with invariants. Stanford: Composites Design Group, Department of Aeronautics and Astronautics, Stanford University; 2015.

[387] Tsai SW, Melo JDD. A unit circle failure criterion for carbon fiber reinforced polymer composites. Compos Sci Technol 2016;123:71–78.

[388] Tsai SW, Arteiro A, Melo JDD. A trace-based approach to design for manufacturing of composite laminates. J Reinf Plast Comp; 2015. DOI 10.1177/0731684415624770.

[389] Mar JW, Lin KY. Fracture mechanics correlation for tensile failure of filamentary composites with holes. J Aircraft 1977;14:703–4.

[390] Aronsson CG, Bäcklund J. Tensile fracture of laminates with cracks. J Compos Mater 1986;20:287–307.

[391] Maimí P, González EV, Gascons N, Ripoll L. Size effect law and critical distance theories to predict the nominal strength of quasibrittle structures. Appl Mech Rev 2013;65(2):020802–1.